LIF measurement of laser plasma plume produced by KrF excimer laser ablation of graphite target

S. Aoqui[1], T. Ikegami[2] and K. Ebihara[3]

[1] *Department of Electrical System & Computer Engineering , SOJO University, Japan*
[2] *Graduate School of Science and Technology, Kumamoto University, Japan*
[3] *Department of Electrical and Computer Engineering, Kumamoto University, Japan*

Pulsed laser ablation (PLA) technique has been used to produce thin films of a variety of light element materials such as diamondlike carbon (DLC), carbon Nanotubes, carbon nitride (CNx), boron carbide (B_4C) and boron nitride (BN). Metastable amorphous films have been studied intensively, both theoretically and experimentally, due to the unique combination of functional properties such as ultra hardness, highly optical transparency, chemical inertness and high resistively. Owing to their excellent performance, vast opportunities for electronic applications have been expected. However when it comes to a theoretical explanation of this phenomenon of PLA, no complete solution has yet been given. So we carried out the investigation of ablation of phenomenon of graphite target by using laser induced fluorescence (LIF) method. A carbon plasma plume was produced in a vacuum by ablating a graphite target using KrF excimer laser, Nd:YAG laser second harmonic and fundamental light. Emission spectroscopy, two-dimensional LIF (2D-LIF), spectral absorption and ion probe diagnostics measurements were used to measure C atoms, C^+ ions, C_2 and C_3 molecules in the carbon plasma plume versus laser wavelength and laser fluence. Fig. 1 shows an observation direction of 2D-LIF and the PLA system. The 2D-LIF images examined the temporal and spatial profiles of C_2 and C_3 near the target surface. Fig. 2 shows comparison of experimental and computed rotational-vibrational spectra of C_2. It was found that the KrF laser of 248 nm ablated species of carbon atoms and ions with highly excited electronic states from the target, and C_2 and C_3 were also found near the target. Nd:YAG laser light of 532 nm more effectively produced C, C^+ than the fundamental Nd:YAG laser light of 1064 nm. The carbon species produced by the Nd:YAG laser of 1064 nm were thought to result from the thermal evaporation of the target by laser heating.

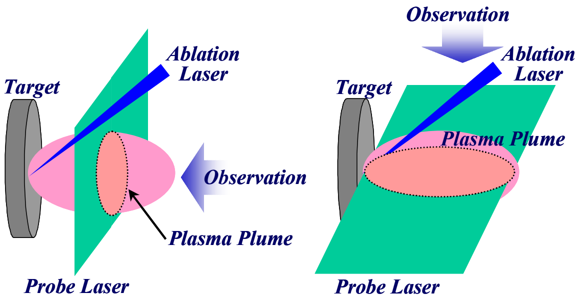

Fig.1 Observation direction of 2D-LIF images

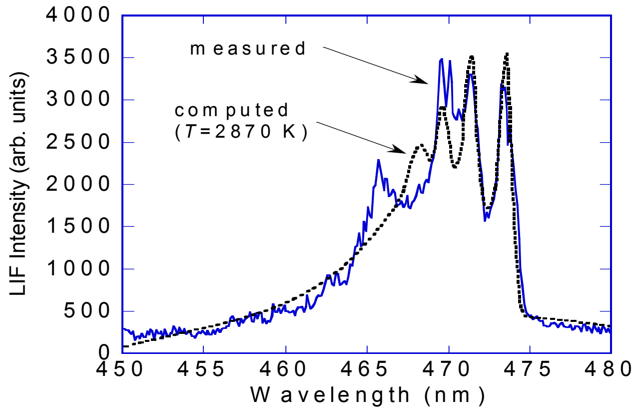

Fig. 2 Comparison of experimental and computed rotational-vibrational spectra of C_2 （$d^3\Pi_g(v'=1)$-$a^3\Pi_u(v''=0)$, $\Delta v=1$）.

Fabrication of carbon films via UHF micrometer-scale plasma CVD

Yoshiki Shimizu[1], Takeshi Sasaki[1], Tsuyohito Ito[2], Kazuo Terashima[2], and Naoto Koshizaki[1]

[1.] Nanoarchitectonics Research Center, National Institute of Advanced Industrial Science and Technology,
Central 5, 1-1-1 Higashi, Tsukuba, Ibaraki 305-8565, Japan
[2.] Department of Advanced Materials and Science, Graduate School of Frontier Science, The University of Tokyo,
5-1-5 Kashiwanoha, Kashiwa, Chiba 227-8562, Japan

Abstract

We developed an inductively coupled UHF micrometer-scale plasma (microplasma) CVD apparatus, which can be operated easily in air at atmospheric pressure with a few tens of watts of UHF power and enables us to deposit material on any kind of substrates. In the CVD processing of carbon using CH_4/Ar at atmospheric pressure in ambient air, spherical products of carbon, composed of concentric graphitic shells, were deposited on the substrate without additional heating at a growth rate of about 2 μm/min, which is much higher than by conventional plasma CVD.

1. Introduction

Micrometer-scale plasma, i.e., microplasma, has been intensively studied, and utilized for industrial applications such as light sources and analytical instruments. Recently, applications of microplasma to material processing were reported by a few groups [1,2]. In these studies, direct current discharges between coplanar film electrodes, or between a stainless steel capillary tube and a metal plate electrode, have been employed to generate a microplasma. The products by these techniques, however, were deposited only on the electrodes surface. To improve this point, we developed the CVD system, which employed inductively coupled UHF (450 MHz) microplasma generated in the glass capillary. In this system, the substrate for deposition is independent of the plasma generator, and thus we can deposit the materials on any kinds of substrates such as glass, resin, and so on. In this paper, we will present a new apparatus for inductively coupled UHF microplasma CVD we are developing and some experimental results on the characterization of carbon deposits on the substrates without additional heating.

2. Inductively coupled UHF microplasma CVD apparatus

Fig. 1 is a schematic illustration of the UHF microplasma CVD system. This microplasma generator consists of a quartz capillary (100 to 500 μm inner diameter) joined to a metal tube, a five-turn copper coil, and tungsten wire (50 μm in diameter) inserted into the capillary. One end of the coil is connected to a 450-MHz UHF generator (5 to 30 W) via a matching circuit, while the other end is grounded. When UHF power is supplied to the coil, the tungsten wire is inductively heated and emits thermoelectrons to sustain stable microplasma generation. A dc power supply (15 kV) connected to the metal tube is employed to ignite the microplasma easily. Plasma gas (Ar) and carbon source gas (CH_4) are introduced into the capillary via the metal tube, and the flow rates can be controlled by mass flow controllers. The substrate folder is movable in the X, Y and Z directions (as indicated in Fig. 1) with a micrometer. We can thus vary the site for deposition on the substrate and the gap distance between the tip of capillary and the substrate. A microscope equipped with a CCD system is employed to precisely measure the gap distance and observe the CVD processing.

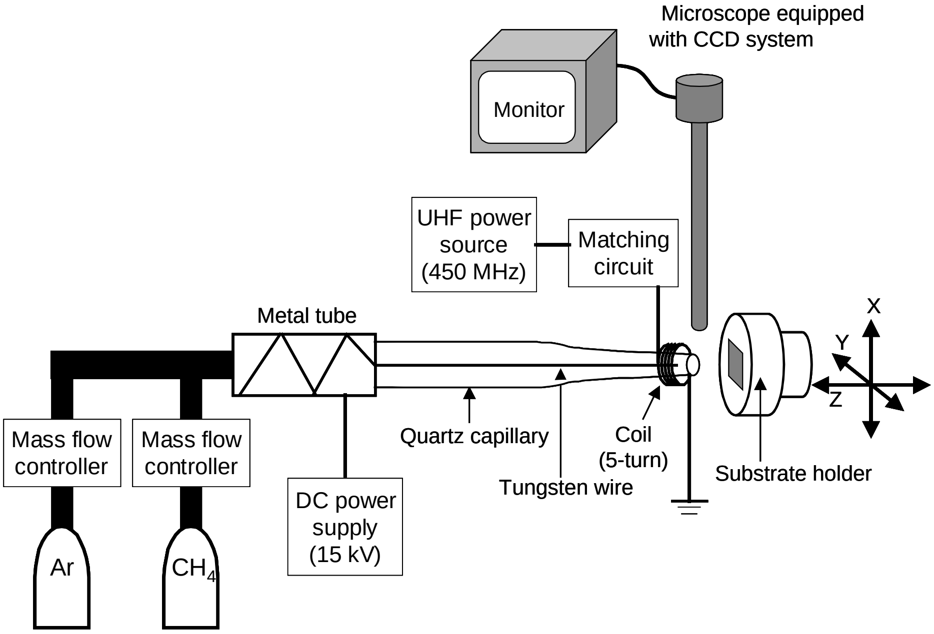

Fig. 1 Schematic illustration of an inductively coupled UHF microplasma CVD system.

3. Experimental

In this study, carbon was deposited in air at atmospheric pressure. A mixed gas of CH_4 (0.5%) / Ar was introduced into the capillary at a flow rate of 100 ccm. The capillary had an inner diameter of 100 μm, and a tungsten wire (50 μmϕ) was inserted into it. Hastelloy (C-276), employed as the substrate for deposition, was set at a gap distance of 250 μm. Under these conditions, the microplasma was generated at UHF powers of 10, 20, and 30 W to investigate the effect of the UHF power on this CVD process. The time for deposition was varied between 30 and 120 seconds to clarify the carbon formation process. The deposits were observed with a scanning electron microscope (Hitachi S-800), and a transmission electron microscope (JEOL JEM-2000FX, JEM-2010, 200 kV).

4. Results and discussions

Fig. 2 shows a whole SEM image of products for 120 seconds at the UHF power of 10 W. The products were deposited in a circular region about 200 μm in diameter, approximately twice that of the inner diameter of capillary. Similar results were observed for the products prepared at the UHF power of 20 and 30 W.

Fig. 3 shows magnified SEM images of the deposits for 120 seconds for various UHF powers. The morphologies of the deposits at 10 and 20 W were spherical with a rugged surface (Fig. 3 (b), (c)), but that of the deposit at 30 W was a spherical with a smooth surface (Fig. 3 (a)).

The thickness of the deposits was estimated by the observations of the peeled edge. The observations indicated that the deposits were about 4 µm thick near the center of the deposit, and gradually became thinner with distance from the center. This growth rate of about 2 µm/min is much higher than that of conventional plasma CVD. Such a high growth rate might be due to the high-rate feeding of the chemical species caused by the high speed of the microplasma jet, which can be estimated to be about 300 m/s.

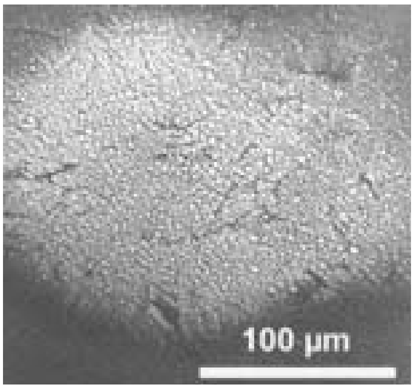

Fig. 2 Whole SEM image of the products via the UHF microplasma CVD system, deposited in a circular region of about 200 µm (UHF power 10 W; deposition time 120 seconds).

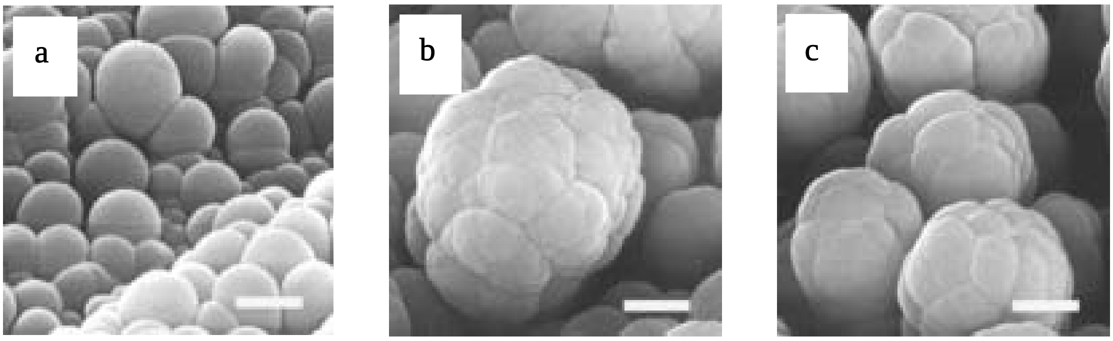

Fig. 3 SEM images of the deposits for 2 min at UHF powers of (a) 30 W, (b) 20 W, and (c) 10 W, indicating the morphological changes with UHF power (bar = 1 µm).

Fig. 4 shows a high resolution TEM image of a part of the spherical product prepared at 30 W, indicating that the spherical product is crystalline and consisted of concentric graphitic shells (spherical graphite). Spherical graphite similar to that seen in Fig. 4 was also observed in the deposits at lower UHF power.

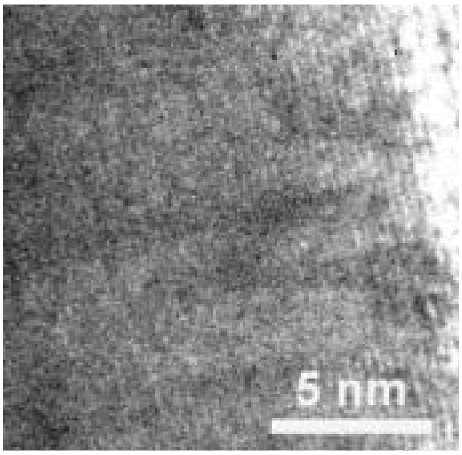

Fig. 4 A typical high resolution TEM image of a part of a spherical product (UHF power 30 W)

The SEM observations of these spherical graphites prepared for 30 to 120 seconds revealed that the increase of the size with deposition time, suggesting that the growth of the spherical products proceeded not in vapor phase but on the substrate in this process.

The crystal growth on the substrate without additional substrate heating should be discussed based on the heat conduction from the microplasma jet. A few hundred micrometer region on the substrate, 250 μm away from the tip, is thought to be heated by conduction through the microplasma jet, and the temperature could be enough to promote the crystal growth.

Morphological changes with UHF power as seen in Fig. 3 can also be related to the temperature of the microplasma jet. Reducing the UHF power reduces the plasma jet temperature and the temperature of the deposition area, which should be a critical parameter affecting morphology. However, we have not yet clarified the specific relationship between the morphology and temperature.

These results indicate that CVD processing with inductively coupled UHF microplasma enables us to deposit crystalline films at a high rate in a micrometer-scale region of the substrate without additional heating in air and at atmospheric pressure. This can be considered to be a new CVD process with a very simple operation compared to the conventional CVD method, and may be utilized in the near future for repairing micro-cracks of materials, maskless patterning, and so on.

5. Summary

We developed an inductively coupled UHF micrometer-scale plasma (microplasma) CVD apparatus, which can be operated easily in air at atmospheric pressure with a few tens of watts of UHF power and enables us to deposit material on any kind of substrate. In the CVD processing of carbon using CH_4/Ar at atmospheric pressure in ambient air, spherical graphites were deposited on the substrate without additional heating at a growth rate of about 2 μm/min, which is much higher than by conventional plasma CVD.

Acknowledgement

This work was financially supported by a Grant-in-Aid for Scientific Research (B) (Grant No. 14350362), from The Ministry of Education, Culture, Sports, Science and Technology.

References

[1] T. Ito, T. Izaki, and K. Terashima, Thin. Solid. Films. **386**, 300-304 (2001)
[2] R. M. Sankaran, and K. P. Giapis, J. Appl. Phys. **92**, 2406 (2002)

Adsorbability Improvement of Activated Carbon by DBD Plasma Treatment in Atmospheric Pressure

Dongsoo Lee[1], Yoon-Ho Choi[1], Kwang-Hyun Paek[2], Won-Tae Ju[2] and Sang Hee Hong[1]

[1] *Department of Nuclear Engineering, Seoul National University, Seoul, 151-742, Korea*
[2] *PLASNIX CO. Ltd., Seoul, 151-742, Korea*

Abstract

Granular activated carbon has been treated by dielectric barrier discharge (DBD) plasma for the purpose of enhancing its adsorbability of metal cations. A mixture gas of helium and oxygen is used as a feeding gas to create oxygen radicals in the plasma for oxidizing the surface of activated carbon by adjusting the oxygen flow rate. The present experimental results show that the activated carbon treated by the helium-oxygen DBD plasma improves its adsorbability in low pH solutions.

1. Introduction

Activated carbons have been widely used as adsorbents for many industrial applications, such as purification of water in sewage facilities and filtration of air in toxicity-treating factories. So there have been considerable attempts to change their chemical and physical properties for getting better adsorbability. Among various methods for improving their adsorption capability, a plasma treatment can be a promising candidate for producing plenty of chemically active species in a clean and dry atmospheric environment. And there have been several treatment experiments of activated carbon with oxygen plasma [1, 2].

In this experimental study, activated carbon is treated with a helium-oxygen plasma generated in a DBD reactor of planar type because the helium DBD reactor with small amount of oxygen can easily produce homogeneous plasma including active species such as ions, radicals and high energy electrons. This homogeneous plasma can treat activated carbon more uniformly than a pure oxygen plasma which usually has many streamers in the discharge region, thus in this respect the helium-based DBD plasma has great advantages for the activated carbon treatment. Especially, the oxygen content in the mixture gas enables the discharge to create oxygen radicals that react on the surface of activated carbon, resulting in the introduction of weakly acidic functional groups which play an important role in adsorbing metal cations [3]. Therefore it is of great importance to know the effect of oxygen in the helium DBD plasma in order to examine the adsorbability of activated carbon.

OES (Optical Emission Spectroscopy) is used to identify the species in the DBD plasma. The electric power delivered into the DBD reactor is measured by drawing Lissajous diagrams. The adsorption experiments are conducted with cobalt metal cations (Co^{2+}) in aqueous solutions, and the amount of adsorption is measured by ICP-AES (Inductively Coupled Plasma – Atomic Emission Spectroscopy). FT-IR (Fourier Transform - Infrared spectroscopy) is employed to investigate the surface properties of the activated carbon treated by the DBD plasma.

2. Experimental Setup and Diagnosis

2.1 DBD plasma reactor and diagnostic equipment

Figure 1 depicts a schematic of the experimental setup and diagnostic equipment used in this experiment on the DBD plasma treatment of activated carbon. A DBD plasma reactor of parallel-plate type has a plate electrode size of 217×200 mm, a barrier thickness of 3.0 mm, and a barrier-to-barrier gap of 3.0 mm. Glass is used for the barrier materials and stainless steel for the electrodes. A commercial product of granular activated carbon (Kwang-Woon C&S, made of coconut char) is used as a specimen for the adsorption experiment, and the fine carbon grains weighing 1.0 g are evenly spread over the lower barrier surface in the reactor. The feeding gas consists of helium mixed with oxygen in atmospheric pressure (1 atm), and the two mixture gases are independently controlled with the respective mass flow controllers

(MFC). The flow rate of helium is fixed at 5 slm and the oxygen flow rate is varied from 0 to 200 sccm. The DBD plasma is generated by applying a power supply with an audio-frequency of 10 kHz and a peak voltage of 5 kV. All the activated carbon samples are treated for 5 minutes in the DBD reactor. The input electric powers delivered to the reactor at various oxygen flow rates are measured by taking advantage of Lissajous diagrams, which are obtainable from the voltage signals recorded in a digital oscilloscope (LeCroy 9310A DUAL 400 MHz) with the help of two high voltage probes (Tektronix P6015A, 1000X) and a capacitor (1500 pF) inserted in series into the discharge circuit. And the OES diagnosis is carried out to find out a dominant species produced in the DBD plasma.

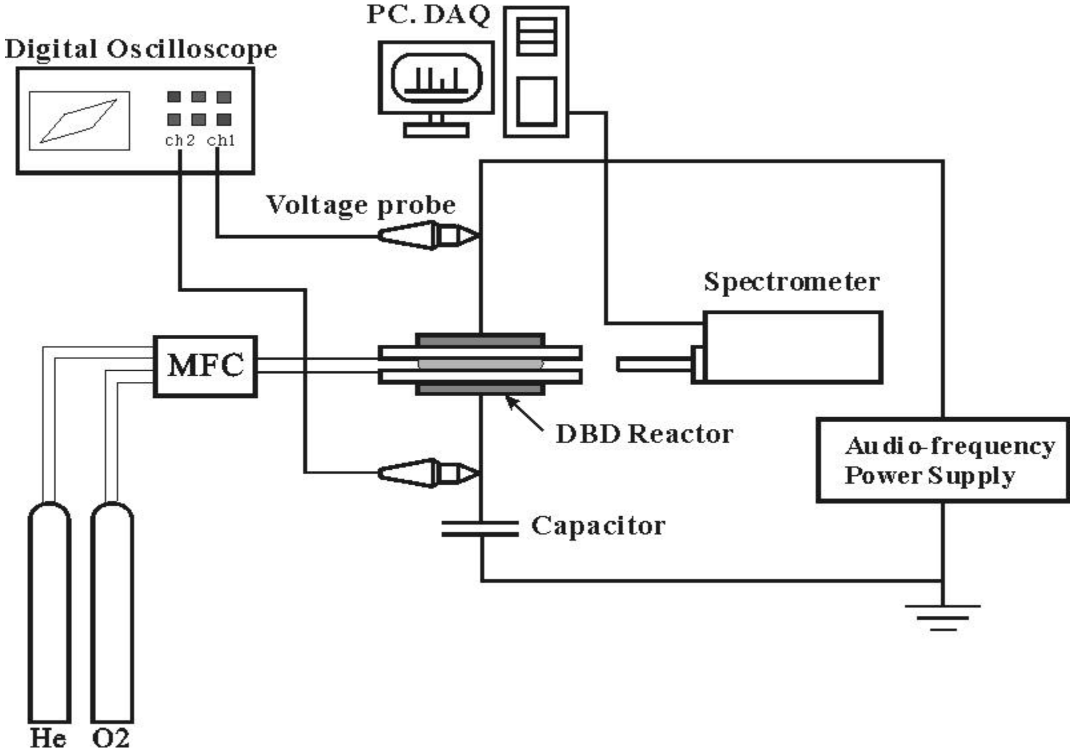

Fig. 1. Schematic diagram of an experimental setup and diagnostic equipment for the DBD plasma treatment

2.2 Characterization of activated carbon

The transmission IR spectra of the carbon samples are obtained by using the KBr technique and Jasco Model FT-IR 200 spectrometer to analyze surface functional groups on the activated carbon treated by the plasma.

2.3 Cobalt adsorption experiments

The mixtures of activated carbon and cobalt ion solutions are prepared for the adsorption experiments. Cobalt (Co) is chosen for this experiment because its ion is a typical metal cation found in wastes from nuclear power plants. Since the adsorption of metal cations is greatly dependent on pH of the aqueous solution [4, 5], two solutions of different concentrations, 20 and 100 ppm, are made by diluting a Co standard solution (1000 ppm of Co in 1 wt.% HNO_3, Aldrich) with distilled water. Titrations are carried out to adjust the initial pHs of the Co solutions to 2.57 and 6.88 by the addition of 1.0 N sodium hydroxide solution. After the DBD plasma treatment, the activated carbon of 0.3 g is put into a flask containing 20 ml of Co solution, and this mixture solution is kept in the room temperature for 48 hours without being shaken. The untreated activated carbon is also experimented with the Co solutions in the same way. Then the final concentrations of Co in the solutions are measured by the ICP-AES (Shimadzu ICPQ 1000).

3. Results and Discussion

3.1 Characteristics of DBD plasma

The emission spectra from the DBD plasma measured by OES are shown in Fig. 2. The atomic oxygen lines of 777 and 845 nm distinctly appear in the spectra because the presence of helium in the discharge helps to produce atomic oxygen radicals efficiently via the Penning reaction with less demanding reaction energy [6]. It is expected that the atomic oxygen produced in the DBD plasma reactor might influence the oxidization of the activated carbon.

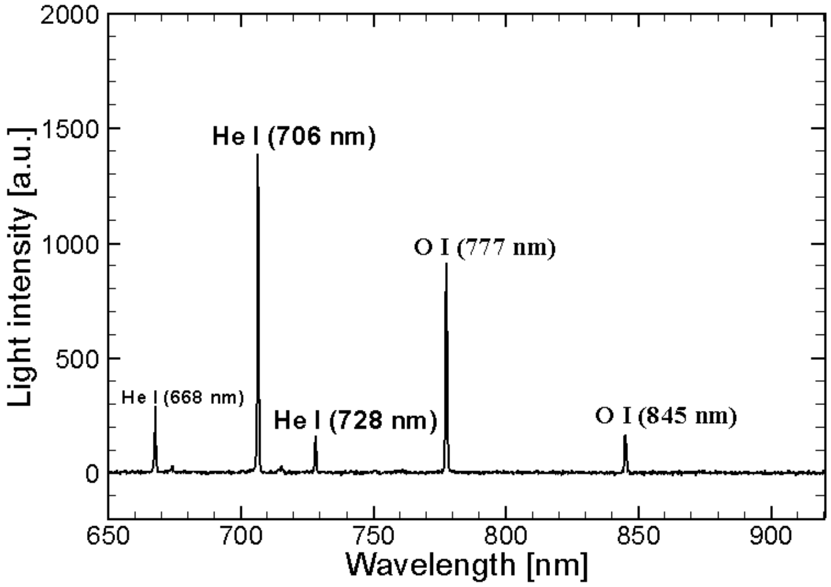

Fig. 2. OES spectra measured from the helium-oxygen DBD plasma

Figure 3 shows one of the Lissajous diagrams to be used for calculations of the electric powers delivered to the DBD reactor for a case of 5 kV applied peak voltage and 3 % O_2/He fraction. The averaged power turns out to be 27.7 W, which corresponds to a power density of 212.7 mW/cm^3. As seen in Fig. 4., the input power slowly increases with the increment of O_2/He fraction at each applied peak voltage because of variance of the plasma load with oxygen flow rate.

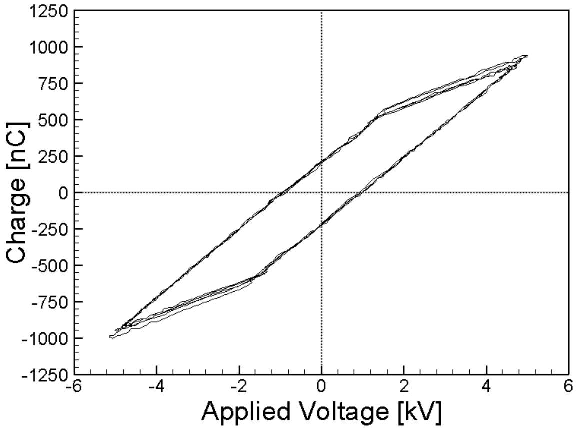

Fig. 3. Lissajous diagram obtained during the DBD operation for 5 kV applied peak voltage and 3 % O_2/He fraction

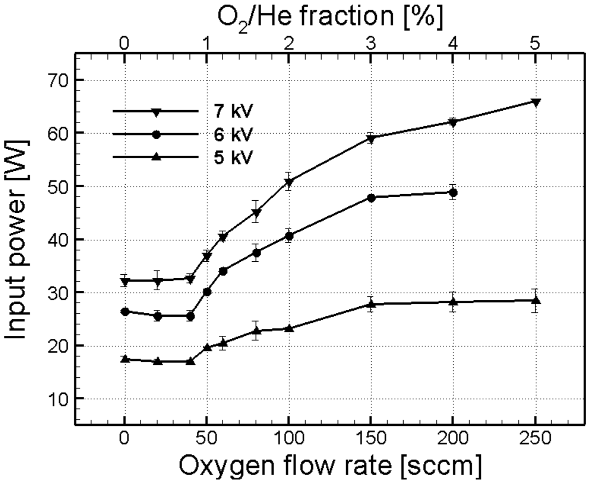

Fig. 4. Dependence of input power on oxygen flow rate (or O_2/He fraction) at different applied peak voltages

3.2 Adsorbability enhancement by the plasma treatment

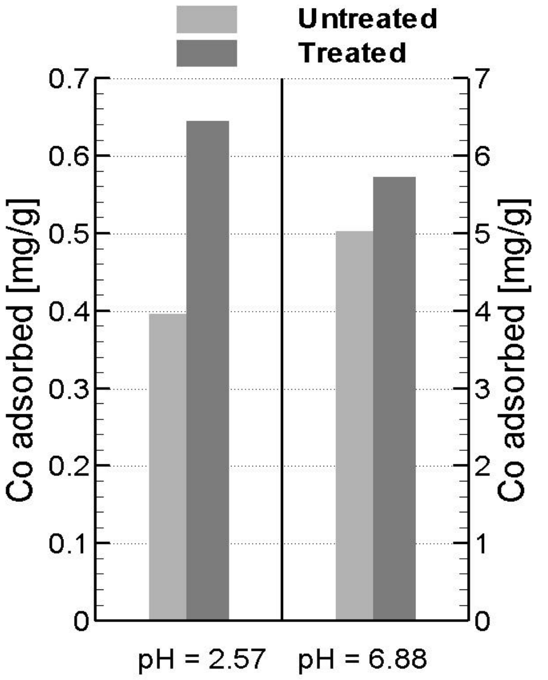

Fig. 5. Comparison of Co quantities adsorbed onto the activated carbons untreated and treated by the DBD plasma at two pH conditions with different O_2/He fractions of 2 % and 0.8 %, respectively.

Figure 5 presents the measured results of Co adsorption by the activated carbons untreated and treated by the DBD plasma, respectively. In this figure, the two different pH conditions are introduced because the quantity of Co adsorption has been normally observed to increase greatly in the higher pH of the initial mixture solution. This increase of adsorption with pH can be explained from the fact that as pH of the solution increases, the exchange of metal cations and hydrogen ions on the surface of activated carbon also enhances and more increased metal adsorption accordingly follows [4].

In the low pH solution, the absolute amount of Co adsorption per activated carbon is lower than that in the high pH solution by more than ten times (0.39 vs. 5.0 mg/g) in the untreated case. On the contrary, a considerable adsorbability enhancement is achievable in the low pH with the plasma-treated activated carbon by about 1.6 times compared with the untreated one at 2 % of O_2/He fraction. On the other hand, even though the high pH solution yields much larger quantity of adsorption than the low one, the plasma treatment of activated carbon with the high pH solution is not practically effective for improving the adsorbability as illustrated in Fig. 5 for pH = 6.88, where only about 15 % increase of Co adsorption is achieved.

Figure 6 shows the dependence of Co adsorption by activated carbons on the oxygen flow rate (or oxygen fraction). Fig. 6 (a) indicates in the low pH solution that high adsorbability enhancement is obtainable by the plasma treatment at oxygen flow rates of 100 ~ 150 sccm. But, such a high improvement of adsorbability is not appeared in Fig. 6 (b) for the high pH solution.

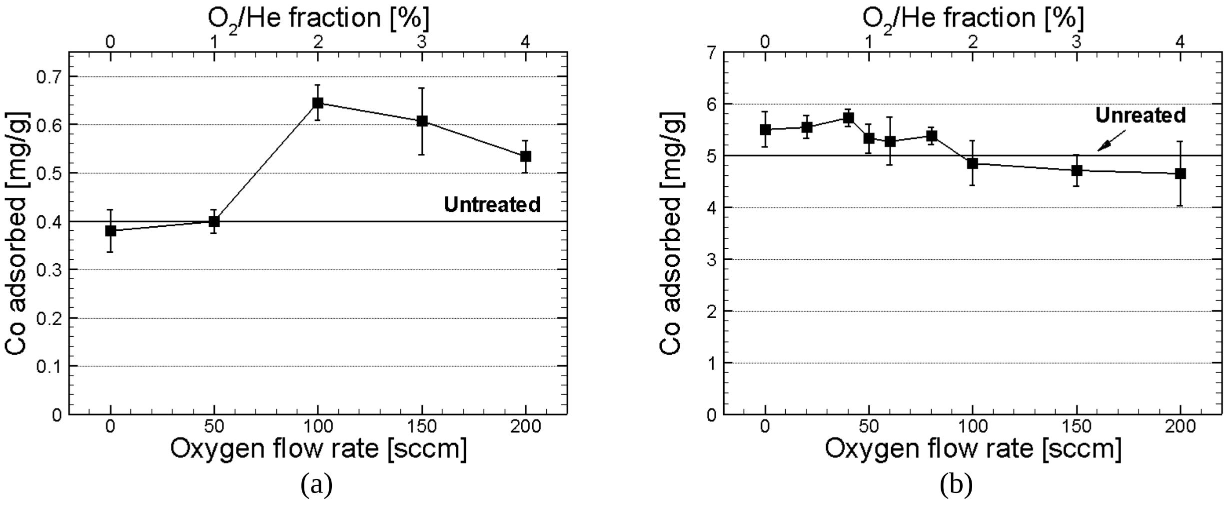

(a) (b)

Fig. 6. Dependence of adsorbability on oxygen flow rate (or O_2/He fraction) at different pH conditions: (a) pH = 2.57 (initially acidic solution) and (b) pH = 6.88 (initially neutral solution)

The FT-IR spectra of the untreated and treated activated carbons are plotted in Fig. 7. The best adsorption improvement was observed in the low pH adsorption experiment when the oxygen flow rate was 100 sccm. It was, therefore, expected that there would be a decrease in the transmittance at about 1717 cm^{-1} in the spectral lines of the plasma-treated carbon showing the feature of stretching vibrations of C=O carbonyl bond in carboxylic acid groups [3]. But, a noticeable transmittance decrease is not seen at this spectral line in Fig. 7. With regard to this measured result, it is considered that there are not detectably enough acidic properties on the surface of the plasma-treated activated carbon though an enhanced adsorbability appeared.

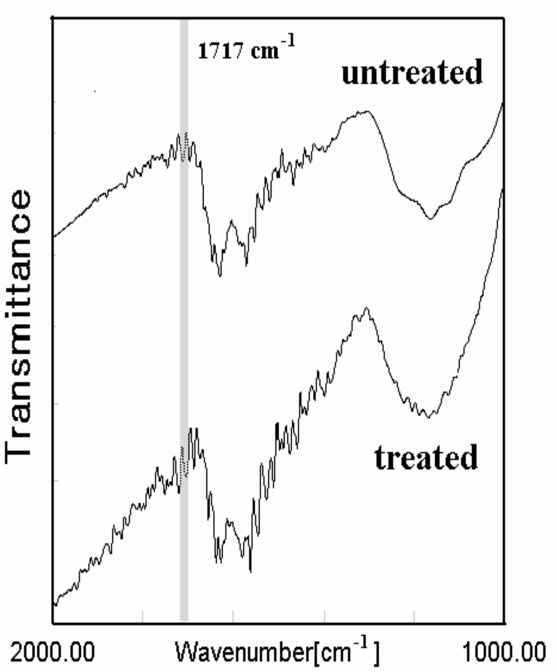

Fig. 7. FT-IR spectra of the activated carbons untreated and treated by DBD plasma.

4. Conclusion

In order to improve the adsorbability of activated carbon in cobalt cation solutions, the DBD treatments are conducted by using the helium plasma mixed with oxygen. The measured results show that the adsorbability of plasma-treated activated carbon can be improved about 1.6 times higher than that of untreated one at 2 % content of oxygen in helium when the pH of the initial cobalt solution is sufficiently low. But the DBD plasma treatment of activated carbon in a high pH solution does not seem to improve the adsorbability effectively.

Acknowledgement

This work has been supported by Ministry of Science & Technology in the Republic of Korea.

References

[1] Ana B. García et. al., Fuel **77**, 6 (1998).
[2] Satoshi Kodama et. al., Thin Solid Films **407** (2002).
[3] Y. F. Jia, K. M. Thomas, Langmuir **16** (2000).
[4] J. Paul Chen, M. Lin, Carbon **39** (2001).
[5] M. Sánchez-Polo, J. Rivera-Utrilla, Eviron. Sci. Technol. **36** (2002).
[6] G. Placinta et. al., J. Appl. Polym. Sci. **66** (1997).

Aerosol Particles Generated in a Plasma Process and Penetrations through an Airfilter

A. Yamamoto[1], K. Matsubayashi and M.Suzuki[1]

[1] *Department of Chemical Engineering, Tokyo Institute of Technology, Tokyo, Japan*

Abstract

The processes of metal particle generations in a plasma process could be studied, synthetically. We simulated evaporation phenomena with the lattice Boltzmann method and obtained evaporation rate of metal surrounded by inert gas. Simulations for particle growth by taking the consideration of the experimental results into account were carried out. Particle amounts penetrating through an airfilter were calculated by using simulated particle data and reported filtration efficiency of an airfilter.

1. Introduction

When a thermal plasma is used in a nuclear energy industrial process, the generation of fine particles is a problem from the viewpoint of safety. Plasma has high temperature and high enthalpy and is suitable for treatments of metal having high melting point. However, fine metal particles generate through evaporation. Those fine particles are not desirable, because they are harmful in itself and it is more if they have radioactivity, so that we have studied their characteristics. In considering safety, important data are amounts and size distribution of generated particles in a process, and also those of particles passing a filter when they are collected by using it. It is an objective in this study to estimate an amount of metal aerosol particles generated in a plasma process and their particle size distribution, and to make the characteristics of those particles that penetrate through an airfilter clear. We simulated evaporation phenomena to estimate the generated particle amount, and preparatory experiments and simulations for particle growth were carried out to obtain size distribution of generated particles. Those obtained information about generated particles in a plasma process and the filtration efficiency of a typical airfilter were used to study the characteristics of particle filtration.

The first step of particle generation is evaporation of metals. Evaporation phenomena have been studied in losses of light bulb filaments by many researchers. Effects of surrounding gas pressure on the evaporation rate of filament metal are reported [1]. Experimental results that are reported have wide range and theoretical work is scarce except Langmuir's ideal evaporation rate. In the present study, the evaporation phenomenon was simulated with the lattice Boltzmann method. The lattice Boltzmann method (LBM) is based on microscopic models and mesoscopic kinetic equations. The LBM uses description for the evaluation of the velocity distribution function of a fluid [2]. Applying multi-speed to discrete velocity model to represent the velocity distribution function makes it possible to use energy equations, and therefore to simulate thermohydrodynamics [3]. Two-component and three-speed LBM was used in the present study to simulate the evaporation phenomena. The evaporation rates of metals surrounded by inert gases were obtained from the simulated results. And we also discussed the effects of energy of evaporating metal gas on the evaporation rate.

Evaporated gas of a metal grows up to be particles through collisions and subsequent coalescences. Particle growth has been studied very well. Numerical simulation of the particle growth is governed by the general dynamic equations (GDE). When particle size distribution is not assumed, the discrete-sectional model is popular in modeling of particle size [4]. Agglomerate consisting of spherical primary particles that are easy to recognize is represented by using a fractal dimension [5]. Particle growth was studied by using preparatory experiments with DC-arc plasma and simulations in the present study. We made the rigorous model of particle growth where the experimental results were taken into account. The GDEs about zeroth and first moment with the discrete-sectional model were used. An additional quantity, the number density of primary particles, makes it possible to treat agglomerates consisting of primary particles with size distribution. Particle size and particle size distribution were obtained and the effects of size distribution of primary particles on particle growth as agglomerates were studied.

Generated metal particles have to be collected in a practical industrial process. Aerosol particles are generally collected by using airfilters, which originated in the nuclear industry and have been highly developed in the semiconductor industry. The collection efficiency of an airfilter, such as a high efficiency particulate air (HEPA) filter and an ultra low penetration air (ULPA) filter, which are typical ones, is very high and exceeds 99%. In the present study, it is presumed that particles were collected with an airfilter. We used reported data on an airfilter, the collection efficiency as a function of particle size, and simulated data on particles, size and size distribution. Particle amounts penetrating through an airfilter were calculated and the characteristics of them were discussed.

2. Evaporation

Masstransfer for evaporation of metals surrounded by an inert gas at high temperature was simulated by using the lattice Boltzmann method, and the evaporation rate defined as the net flux at an evaporation surface was obtained. Ideal evaporation rate in a vacuum is theoretically derived by Langmuir and is the following form [6],

$$J = P_{\mathrm{s}}\sqrt{\frac{1}{2\pi MRT}}, \quad (1)$$

where P_{s} is the vapor pressure, M the molecular weight, T the temperature, and it is assumed that evaporating vapor is saturated at a surface of evaporation. Evaporation rates obtained in this study were normalized with ideal evaporation rate. The governing equations of the lattice Boltzmann method is the Boltzmann equation with BGK type single relaxation model in the collision term [7],

$$\frac{\partial f}{\partial t} + \mathbf{c}\cdot\frac{\partial f}{\partial \mathbf{x}} = -\frac{f - f^{\mathrm{eq}}}{\tau}, \quad (2)$$

where f is the distribution function, f^{eq} is the equilibrium distribution function and τ is the relaxation time. Simulations for evaporation phenomena need two-component system, evaporating gas and surrounding gas, and each component has own governing equation such as eq. (2). The distribution function is represented with discrete velocities. We applied the three-speed model, the one-dimension and seven-velocity model (1D7V model) that includes stationary particles to make simulations stable. The Maxwell-Boltzmann distribution of the equilibrium distribution function is expanded though the Taylor expansion and the unknown coefficients appeared in the expansion are obtained by using the definitions of macroscopic fluid variables, mass, momentum, energy and pressure, and comparing to the coefficient of the Navier-Stokes equation. The relaxation time τ is generally obtained by connecting the Boltzmann equation with the N-S equation. In the present study the relaxation time is, however, derived microscopically [8]. Relaxation is originated by collisions with like particles and unlike particles. Momentum is also considered because of two components having different masses. The relaxation time of the first component is the following form,

$$\tau_1 = \frac{n_1}{N_{11}\dfrac{m_1}{m_1 + m_1} + N_{12}\dfrac{m_2}{m_1 + m_2}}, \quad (3)$$

where m_i is the molecular mass of component i and the number of collisions between component i and j, N_{ij} is,

$$N_{ij} = \frac{1}{2} n_i n_j \left(d_i + d_j\right)^2 \sqrt{2\pi k_{\mathrm{B}} T\left(\frac{1}{m_i} + \frac{1}{m_j}\right)}, \quad (4)$$

where d_i is the molecular diameter of component i and it is assumed that colliding particles are rigid sphere. The relaxation time of the second component is derived, similarly. Diameter of an evaporating molecule is given by [9],

$$d = 1.221V^{1/3}, \quad (5)$$

where V is the molecular volume of solid metal at its melting temperature. Two operators of eq. (2), translation term and relaxation term, are split, then one time step have two steps. Evolution of the local distribution function, $f(\mathbf{x},t)$, is analyzed. The translation term is discretized with up-wind scheme and the term of time evolution is treated explicitly.

Fundamental simulated results are reported in ref. [10], where it is assumed that molecules of an evaporating gas have energy predicted as equilibrium condition. However, evaporating molecules can have higher energy than predicted as equilibrium condition at an evaporation surface. In the present study, we discussed the effect of energy of an evaporating gas on the evaporation rate in detail. Simulations for evaporating particles whose energy were determined with the 500[K] higher temperature and whose saturated amounts were determined with the original temperature, were carried out. Obtained evaporation rates in the simulations are shown in Figs. 1 and 2, where an evaporating metal is iron and a surrounded gas is argon, and original temperatures are 1810[K] of the melting point and 3020[K] of the boiling point, respectively. Reduced pressure was defined as the ratio of the metal saturated vapor pressure to the total pressure. Knudsen number denoted by Kn is the ratio of the mean free path to the simulation zone size. When reduced pressure is large, which means near the boiling point, metal molecules are dominant species and, therefore, there is no decrease of the evaporation rate. On the other hand, it is shown that decrease of the evaporation rate is remarkable and the phenomenon is diffusion, when reduced pressure is not large. Though the evaporation rates of higher energy gas are higher, the differences are hardly observed in low reduced pressure, where diffusion is dominant because evaporated metal gas can be relaxed, sufficiently. Remarkable effects of high energy are appeared where reduced pressure is moderate, such as 0.5. The tendencies of the effect of higher energy in Figs. 1 and 2 are similar.

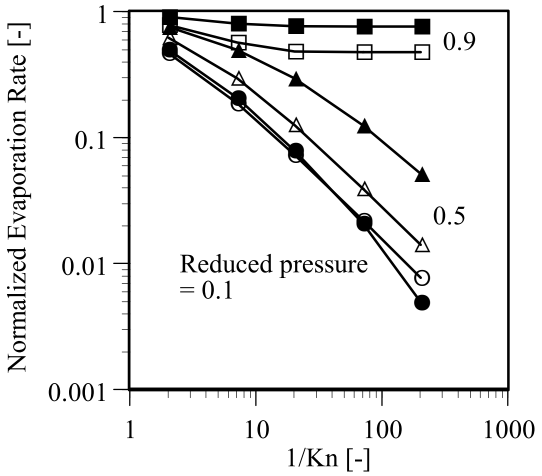

Fig. 1 Evaporation Rate, Comparison of energies of evaporating atoms. The temperature of evaporating atoms to determine their energies is 1810 K for open symbols or 2310 K for closed symbols.

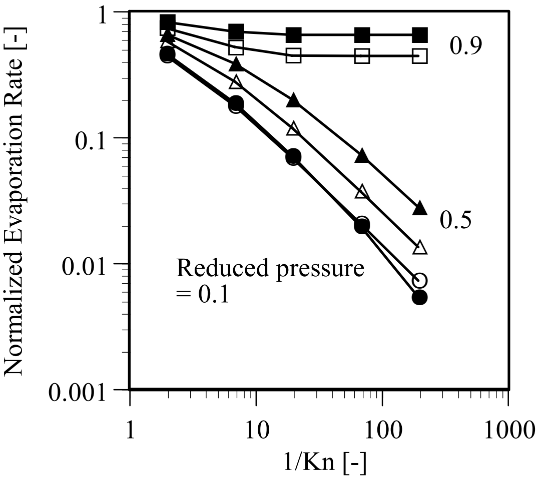

Fig. 2 Evaporation Rate, Comparison of energies of evaporating atoms. The temperature of evaporating atoms to determine their energies is 3020 K for open symbols or 3520 K for closed symbols.

3. Particle Growth

First, we observed practical particles generated in a plasma process. In the experiments with DC-arc argon plasma, generated particles of iron were collected with a membrane filter. Spherical primary particles, which were easy to recognize and to measure size, were observed by using scanning electron microscope. The primary particles were about 20[nm] in diameter and their size distributions were lognormal. Mean diameter hardly changed at various conditions. We used the relation of the collection efficiency, collection mechanism and particle size of the membrane filter that we had used in the experiments, and, therefore, confirmed that particles were agglomerates in a gas phase, which consist of spherical primary particles.

We carried out computations of particle growth by taking the consideration of the experimental results, mentioned above, into account. Since detailed information is, however, required in application to safety assessment in the nuclear field, we pay attention to size distribution of particles with the discrete-sectional model. Particles grow through collisions and subsequent coalescences. Our numerical simulation for particle growth is governed by GDEs, rate equation of losses and products of particles at each size. The GDEs about zeroth and first moment, number density and mass density, respectively, were used to simulate. In the free-molecule regime, the collision rate between v and $\tilde{v}$ in volume is,

$$\beta(v,\tilde{v})=\frac{1}{2}\left(d+\tilde{d}\right)^2\sqrt{2\pi k_B T\left(\frac{1}{m}+\frac{1}{\tilde{m}}\right)}, \quad (6)$$

which is derived from the kinetic theory of gases [8]. And number density of primary particles is an additional conserved quantity and is used to consider size distribution of primary particles. The additional number density makes it possible to simulate particle growth of agglomerates consisting of primary particles with any kind of size distributions. The fractal dimension *Df* is useful to represent agglomerate consisting of spherical primary particles. The fractal dimension linked to agglomerate consisting of primary particles with size distribution is defined by the following equation,

$$v=\xi^{3/Df} i v_{\mathrm{m}}, \quad (7)$$

where ξ is the number of primary particles of an agglomerate, i the number of molecules of a primary particle and v_{m} the volume of a molecule. Particle growth divided into two parts, condensation and coagulation. In condensation part, particles collide and coalesce, then spherical particles generate ($Df=3.0$). In coagulation part, particles collide and stick together, then agglomerates generate ($Df\neq3.0$).

The merit of the simulation model that we have improved is to treat particle growth of agglomerates consisting of primary particles with various size distribution, polydisperse sized primary particles. As mentioned above, primary particles have size distribution and are not monodisperse size. Therefore, the effects of size distribution of primary particles on particle growth as agglomerate were studied. Figure 3 shows time evolution of the geometric mean diameter of particles, particle growth, at two states of agglomerate (Df=2.0 and 2.5) and is comparison between results of monodisperse sized primary particles and those of polydisperse sized primary particles, whose distribution was simulated, rigorously. Particle growth rate is overestimated if it is assumed that primary particles are same size, monodisperse. The overestimation is caused by the difference of the initial conditions where the total masses of particles of two simulations are equal. Size distributions of agglomerates when mean size of agglomerates consisting of polydisperse sized primary particles are d_g=100[nm] are compared in Fig. 4. It is hard to recognize the slight difference of size distributions seen in Fig. 4, in the experimental results.

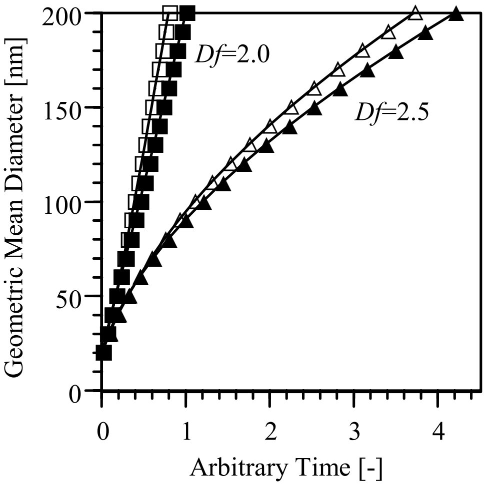

Fig. 3 Particle growth, two kinds of size distribution of primary particles as initial conditions. Agglomerates consist of monodisperse sized primary particles (open symbol) and polydisperse sized primary particles (closed symbol).

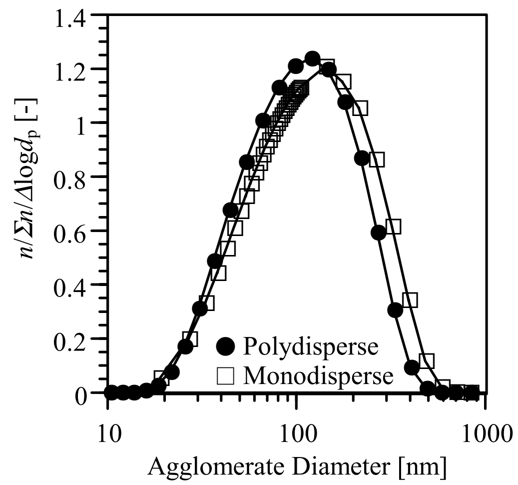

Fig. 4 Particle size distribution of agglomerates, two kinds of size distribution of primary particles as initial conditions. (Df=2.0)

4. Filtration

It is required that generated particles are collected appropriately, in order to keep safety against particles. We presumed that generated metal particles were collected with an airfilter, and studied characteristics of particles penetrating through an airfilter. The penetrating particles were estimated by using simulated data of particles mentioned above and reported data of an airfilter. The collection efficiency of a typical HEPA filter reported by Yamada *et al.* [11] was used. The collection efficiency of an airfilter heavily depends on particle size and has a minimum at about 100 [nm] in diameter. At the minimum, so-called the most penetrating particle size (MPPS), mechanism of collection of an airfilter changes from diffusion to inertial impaction or interception. The MPPS of the airfilter reported in ref. [11] is 108 [nm], where face velocity is 5.3 [m/s]. Figure 5 shows particle size distributions of initial particles, before filtration, and particles penetrating through an airfilter, after filtration, where the geometric mean diameter of initial particles is d_g=100 [nm]. It is assumed that the geometric mean diameter of primary particles is 19 [nm] and particles are of iron. After filtration, the geometric mean diameter of particles penetrating through the filter is d_g=107.4 [nm], and the distribution shifts toward 108 [nm] that is a minimum of the filter. The width of the distribution gets narrow and the geometric standard deviation changes from σ_g =1.608 to 1.370. On the other hand, the distribution of collected particles is the same as initial one because almost all particles are collected, over 99%. The total fractional penetration is calculated by,

$$PN_{\mathrm{T}} = \frac{\int_{d_{\mathrm{p}}} PN(d_{\mathrm{p}}) \times Q(d_{\mathrm{p}}) dd_{\mathrm{p}}}{\int_{d_{\mathrm{p}}} Q(d_{\mathrm{p}}) dd_{\mathrm{p}}}, \quad (8)$$

where $PN(d_p)$ is the fractional penetration of particles with diameter d_p and Q is the mass density of particles before penetration. The total fractional penetrations at various fractal dimension denoted by *Df*, states of agglomerates, are compared in Fig. 6. Penetration of particles with the rigorously simulated distribution and a lognormal distribution where the geometric mean diameter and the geometric standard deviation are of simulated data, are compared in Fig. 7. In the practical particle size range, penetration is underestimated if the assumption of a lognormal distribution is applied. However, the difference between those two distributions is a little. Although simulations where geometric mean diameter of primary particles is 20 [nm], are also carried out, results correspond to the simulations for 19 [nm].

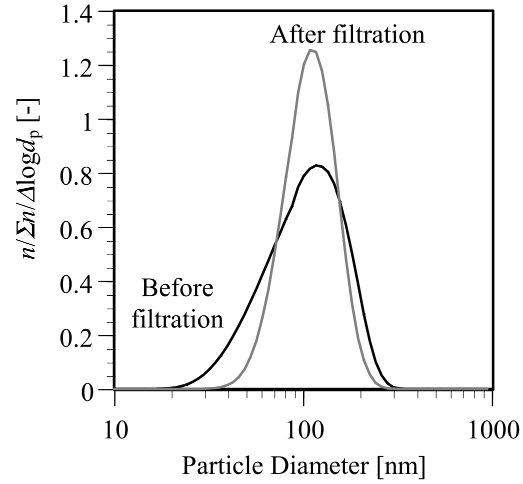

Fig. 5 Particle size distributions of before and after filtration (Primary particle size d_g=19 [nm], iron particles).

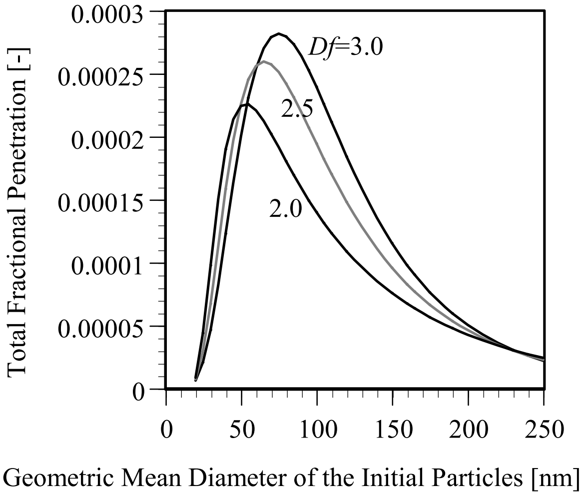

Fig. 6 Total fractional penetrations of particles through an airfilter at various states of agglomerates (*Df*).

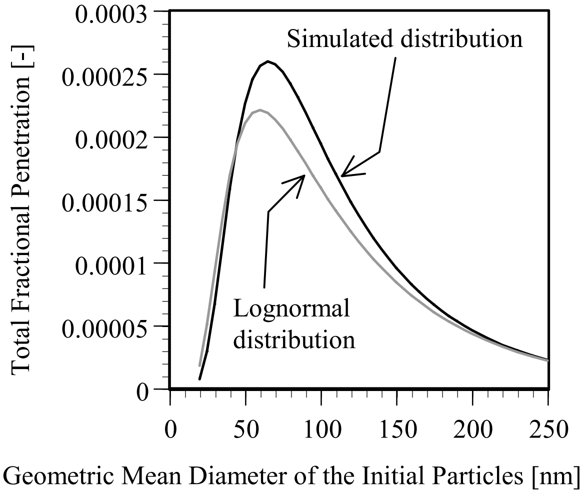

Fig. 7 Total fractional penetrations of particles through an airfilter at various particle size distributions.

5. Conclusion

The processes of undesirable metal particle generations in a plasma process could be studied, synthetically. Since it is hard to obtain detailed particle information in an experiment, the simulation models are useful tools to understand particle generations. The beginning of metal particle generation is evaporation of melting metals. We simulated evaporation phenomena with the lattice Boltzmann method and obtained evaporation rate of metal surrounded by inert gas, defined as a net flux of an evaporation surface. The effect of energy of evaporating metal molecules was discussed. Observations of practical metal particles generated in the experiments in which DC arc plasma was used to generate iron particles, particles were collected with a membrane filter, and they were observed in pictures of SEM, showed that spherical particles existed and their size distributions were lognormal. We used the relation of the collection efficiency of the membrane filter and particle size, and, therefore, confirmed that particles were agglomerates in a gas phase, which consist of spherical primary particles. A model to simulate particle growth in detail was made by taking the consideration of the experimental results into account. Typical simulation model that was based on collision rate of particles was improved to treat agglomerates that consist of spherical primary particles with a size distribution. Simulations for particle growth of the agglomerates consisting of primary particles with size distribution were carried out and results were compared to simulations for that of the agglomerates consisting of primary particles with uniform size. We presumed that generated particles are collected with an airfilter and particle amounts penetrating through an airfilter were calculated by using simulated particle data and reported filtration efficiency of a typical airfilter. The effects of agglomerate state and size distribution were discussed and the characteristics of the filtration of particles clear.

References

[1] E. Fromm, Metallurg. Trans. A **9A**, 1835 (1978).
[2] S. Chen and G. D. Doolen, Ann. Rev. Fluid Mech. **30**, 329 (1998).
[3] F. J. Alexander, S Chen and J. D. Sterling, Phys. Rev. E **47**, R2249 (1993).
[4] Y. Xioing and S. E. Pratsinis, J. Aerosol Sci. **22**, 637 (1991).
[5] T. Matsoukas and S. K. Friedlander, J. Colloid Inter. Sci. **146**, 495 (1991).
[6] I. Langmuir, Phys. Rev. **2**, 329 (1913).
[7] P. L.Bhatnager, E. P. Gross and M. Krook, Phys. Rev. **94**, 511 (1954).
[8] S. Chapman and T. G. Cowling, The Mathematical Theory of Non-uniform Gases (third edition, 1970).
[9] P. Grieveson and E. T. Turkdogan, J. Phys. Chem. **68**, 1547 (1964).
[10] A. Yamamoto and M. Suzuki, J. Chem. Eng. Japan **35**, 944 (2002).
[11] Y. Yamada *et al.*, Japanese J. Health Phys. **29**, 283 (1994), in Japanese.

Nano-insulating Bench with using Plasma Processes

Mikinori Suzuki, Md. Abul Kashem and Shinzo Morita

Department of Electronics, Graduate School of Engineering, Nagoya University,
Furo-cho, Chikusa-ku, Nagoya 464-8603, Japan

Abstract

Nano-lithography for single electron transistor (SET) working at a room temperature is the most interesting target for the lithography works after Likharev [1] and others. There are however many problems to realize the technology. According to our preliminary calculation, single electron transistor (SET) is formed by a conducting dot array at about 10 nmϕ with about 1 nm space. Whereas the device should be fabricated at a thickness and/or a step small than a few nm. Nano-insulating bench technology was proposed to fulfill the above demands for the SET device process, which include insulating layer and conducting circuit on Si wafer in a barrier free condition. To realize nano-insulating bench technology, a fine lithography process is necessary. Monolayer resist process was proposed for the lithography according to ESCA analization of resist and Si wafer interface. As a parallel work, a quantum dots nature of C-Au-S is under evaluation.

1. Introduction

Nano-lithography for single electron transistor (SET) working at a room temperature is the most interesting target for the lithography works after Likharev and others. There are many problems to realize the technology. In order to realize SET working at a room temperature, quantum dot diameter of conducting material must be about 10 nmϕ and the dots must be arranged with about 1 nm space. Whereas the device should be fabricated at a thickness and/or a step small than 10 nm.
Nano-insulating bench technology was proposed to fulfill the above demands for the SET device process, which forms insulating layer, and conducting part on Si wafer in a barrier free condition. The bench will be formed as following; nanometer size polls or walls are formed on Si wafer by a lithography, the polls and walls on Si wafer are oxidized, then the polls and walls are etched off to flat arise then the Si wafer surface is composed with an insulating and conducting area. Because the positions of polls and walls are not oxidized.

For quantum dots, C-Au-S film at about 1nm will be deposited on the bench. The quantum dot nature of C-Au-S film was discussed in other paper, which will be appeared else wais. Whereas the quantum dot structure will be discussed in this work.

For the nano-insulating bench fabrication, a key process is fabrication of polls and walls at nanometer size. For example, Y. Ochiai, et al. realized about 10 nm dot polystyrene (Molecular weight: 800) resist patterns on Si wafer with using an electron-beam patterning at 37.5 fC/dot and development by isopropyl-alcohol for 30 s. The dose rate is about 200 mC/cm^2 for the resist at a thickness of 20-40 nm.

In the previous paper [3], chemical bonds between the resist molecule and Si wafer are affecting on the plasma etching process. Whereas, the interface properties was focused to analyze in order to realized a nano-meter lithography with a resist, and a new etching technologies [4][5].

In this paper, the estimated mechanism of resist is aimed to be clarified by analyzing the surface bond structure between the resist and the substrate surface using ESCA measurements.

2. Experiment

Plasma graft polymerized styrene was formed by a plug flow reactor with a parallel plate electrode and a pulsed 13.56 MHz power source modulated as ON:OFF of 0.1:0.9 sec [5]. The substrate was Si wafer that was treated in HF to eliminate the oxide. Plasma graft polymerized styrene film was formed at a gas pressure of 0.6 Torr and a discharge power of 10 W. The resist thickness on Si wafer was varied by changing the number of pulse.

Conventional polystyrene was also used for the comparison.

The ESCA measurement was performed using ESCALAB210(V.G.SCIENTIFIC LIMITED).

3. Experiment Results and Discussion

For the ESCA measurement, two kinds of polystyrene were formed at a thickness of 40 nm and 1 nm.

For the plasma graft polymerized styrene, the film thickness of 40 nm and 1 nm were obtained by 500 and 2 pulses, respectively. As shown in Fig. 1, the ESCA spectrum of 40 nm film showed two peaks at 286 eV and 534 eV, which are referred to carbon and oxygen, respectively. The oxygen was expected to be introduced in the film by oxidization of carbon radicals in the air [6]. The carbon peak has a large simple peak.

As shown in Fig. 2, the film of 1 nm thickness showed two peaks at 286 eV and 100 eV, which are referred to carbon and silicon, respectively. Both peaks of carbon and silicon showed multiple peaks. Detected silicon peak will be referred to the silicon wafer because the thickness is too thin. The multiple peaks of carbon and silicon means existence of chemical bond between the carbon and silicon.

For conventional polystyrene of molecular weight of 2000, two kinds of thickness were formed by using different dilution rates. The film of 40 nm thickness was formed using 1 mol% of polystyrene in benzene at a spinning rate of 5000 rpm and dried at 120 ℃ for 30 min. The film of 1 nm thickness was formed using 0.1 mol% of polystyrene in benzene at a spinning rate of 5000 rpm and dried at 120 ℃ for 30 min.

For ESCA spectrum of 40 nm film, only one peak at 286 eV was observed. For the film of 1 nm thickness, two peaks of carbon and silicon at 286 eV and 100 eV were measured as shown in Fig. 3. They are simple large peaks. These facts mean they are no chemical bonds between the polystyrene and Si wafer. The polystyrene is supposed to be adsorbed physically. After Ar plasma treatment of the spin coated polystyrene film, the peak shape was changed. The carbon and silicon peaks became multiplied peaks as shown in Fig. 4. This means that a new chemical bond was formed between the carbon and silicon substrate by the treatment. Similar change was observed when the spin coated resist at 1nm was irradiated by the electron beam.

From the ESCA measurements on two kinds of polystyrene at thickness of 40 and 1nm, the plasma graft polymerized styrene is formed with chemical bonds on Si wafer from the beginning. However, the conventional polystyrene film is only physical adsorbed onto the substrate. The physically adsorbed polystyrene was however chemically bonded by Ar ion or the electron beam delineation.

For the negative resist, physically adsorbed molecule formation is supposed to be important to realize fine pattern. We still interested in plasma polymerized resist for the fine lithography, therefore a new plasma polymerization method must be developed.

For the conventional polystyrene resist, 2000 of molecular weight was used in this work, but the clear nanometer patterns have not been realized compared to the polystyrene of 800 molecular weight. Why are there so large difference between the molecular weight of 2000 and 800. Presently, we have no clear answer, but our possible explanation will be referred to the molecular chain activity. The differences will affect on the resist pattern resolution.

4. Nano-insulation bench

The nano-insulation bench is fabricated as a processes shown in Fig.5. Initially, nanometer size dots and wall are fabricated on Si wafer by using nanometer lithography. Secondly, the dots and walls structure are oxidized by a wet oxidation process. At next process, the oxidized dots and walls are etched off and the surface of Si wafer will be flattered. Whereas the Si wafer surface has an insulated and conducting part.

5. C-Au-S quantum dots

C-Au-S film with about 10 atoms% of gold(Au) atom will have quantum dot of C-Au-S molecular group, which has a few nanometer size. To form quantum dots on nano-insulating bench. C-Au-S film with about 1 nm thickness must be deposited by co-operation process of plasma CVD and supporting [8] . The quantum dot nature will be evaluated by a scanning probe microscope technology with STM (scanning tunneling microscope) and AFM (atomic force microscope) in a vacuum.

4. Conclusion

Two kinds of polystyrene with the two kinds of thickness were prepared for ESCA measurements. Two thick films showed only one carbon simple peak. Some times small oxygen peak was observed, which was referred to the oxidized carbon after the film formation in the air. For thin film at about 1nm, two peaks of carbon and silicon were observed. For the plasma graft polymerized styrene, multiple peaks for each atom were referred to chemical bond. For the conventional polystyrene, two peaks of carbon and silicon were simple single peak for both atoms, which means the film was adsorbed physically on Si wafer. However the simple peak was changed to multiple peaks after Ar ion bombardment or the electron beam irradiation, which means chemical bond was induced between the film and Si wafer.

Whereas the chemical bond formation by the electron beam irradiation is essential for the negative pattern on resist which is physically adsorbed on the substrate. The nanometer resist pattern is expectant to be form by using monolayer resist electron beam lithography.

References

[1] Single Electronics. K. K. Likharev in Granular Nanoelectronics; NATO ASI Series B, Physics Vol. 251. Edited by David K. Ferry et al. Plenum Press, 1991.
[2] Y.Ochiai, S.Manako, J.Fujita, and E.Nomura; J.Potopolym. Sci. and Tech., **10**(4)(1997), 641-646
[3] M.Suzuki, S.Ogawa, G.J.Phatak, and S.Morita; J.Photopolym. Sci. and Tech., **12**(4)(1999), 583-584
[4] Ryoichi Inanami, Toshihito Uchida and Shinzo Morita; J. Electrochem. Soc., **143**(11)(1996)3754-3756.
[5] Tomoya Yamada, Ryoichi Inanami and Shinzo Morita; Thin Solid Films, **316**(1998)13-17.
[6] G.K. Vinogradov, G. Yusa, T. Uchida and S. Morita; J. Photopolym. Sci. Tech., **10**(1997), 151-158.
[7]Mitchel Shen and Alexis T.Bell; Plasma Polymerization; American Chem. Sci.(1978)
[8]Md. Abul Kashem, Matushita, and Shinzo Morita; ; J.Potopolym. Sci. and Tech., **15**(2)(2002), 317-322

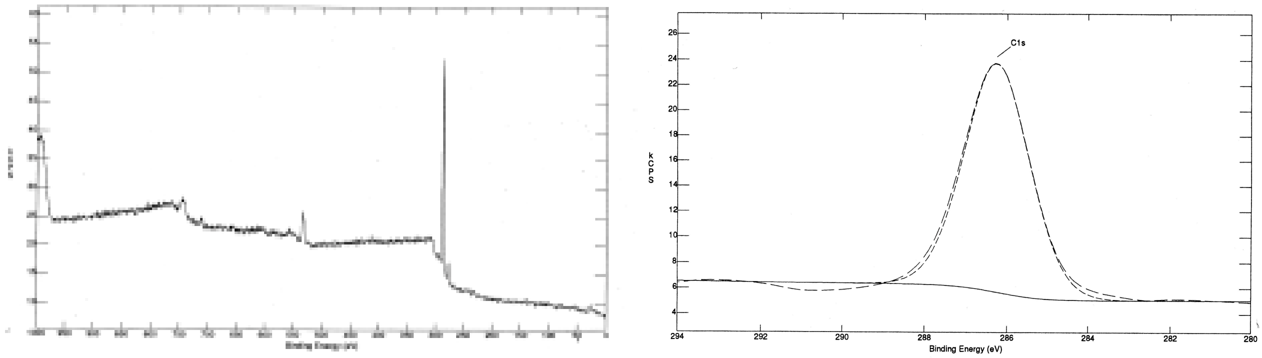

Fig. 1: ESCA spectrum of plasma graft polymerized styrene (thickness; about 40 nm)

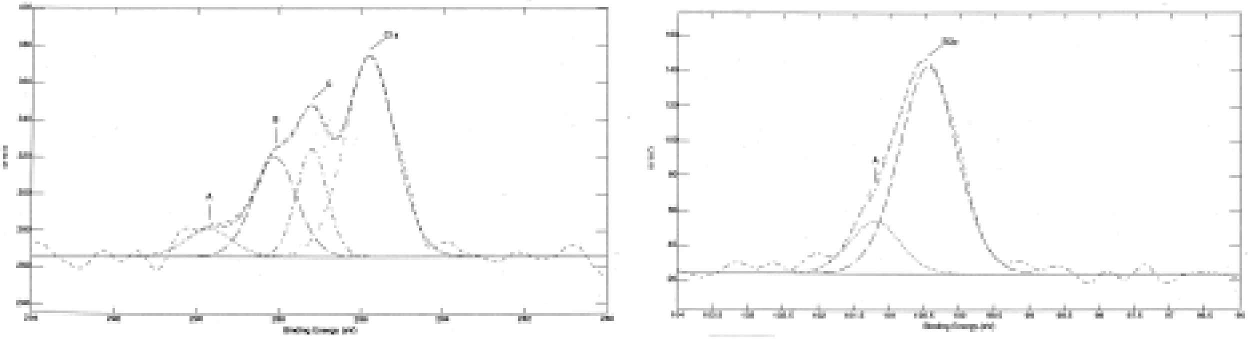

Fig. 2: ESCA spectrum of plasma graft polymerized styrene (thickness; about 1 nm)

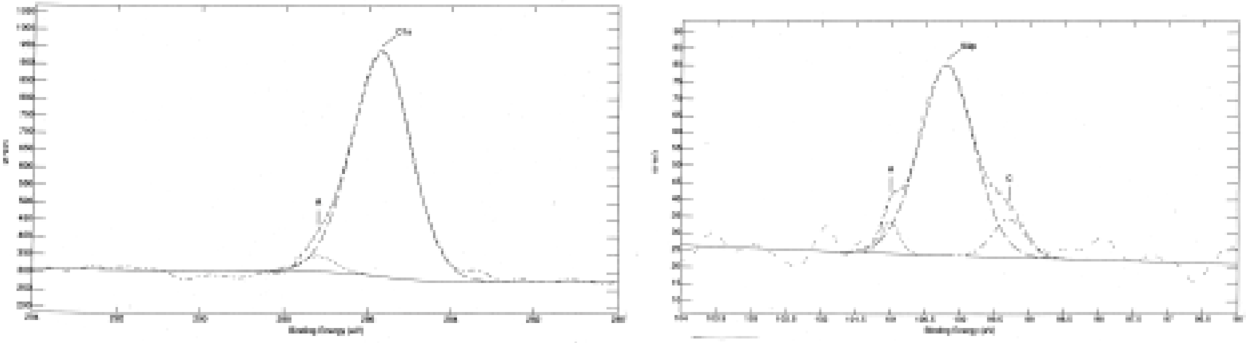

Fig. 3: ESCA spectrum of spin coated polystyrene (thickness; about 1 nm)

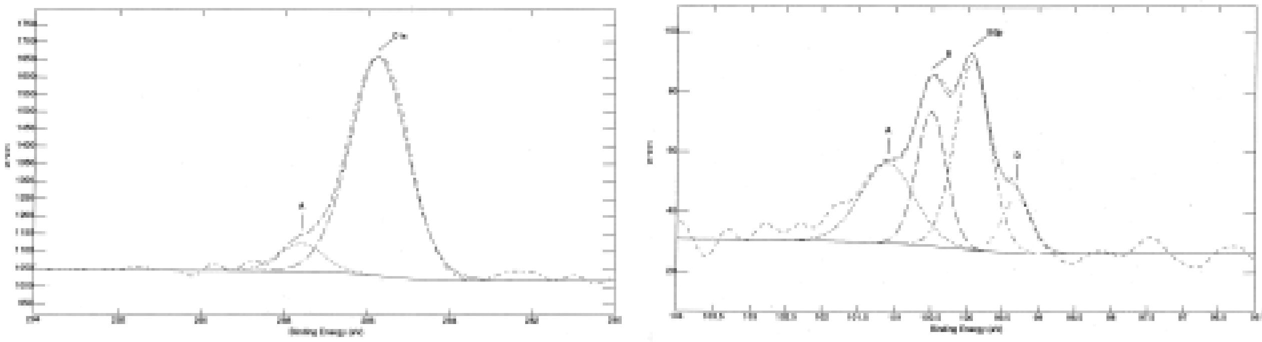

Fig. 4: ESCA spectrum of spin coated polystyrene after Ar ion treatment (thickness; about 1 nm)

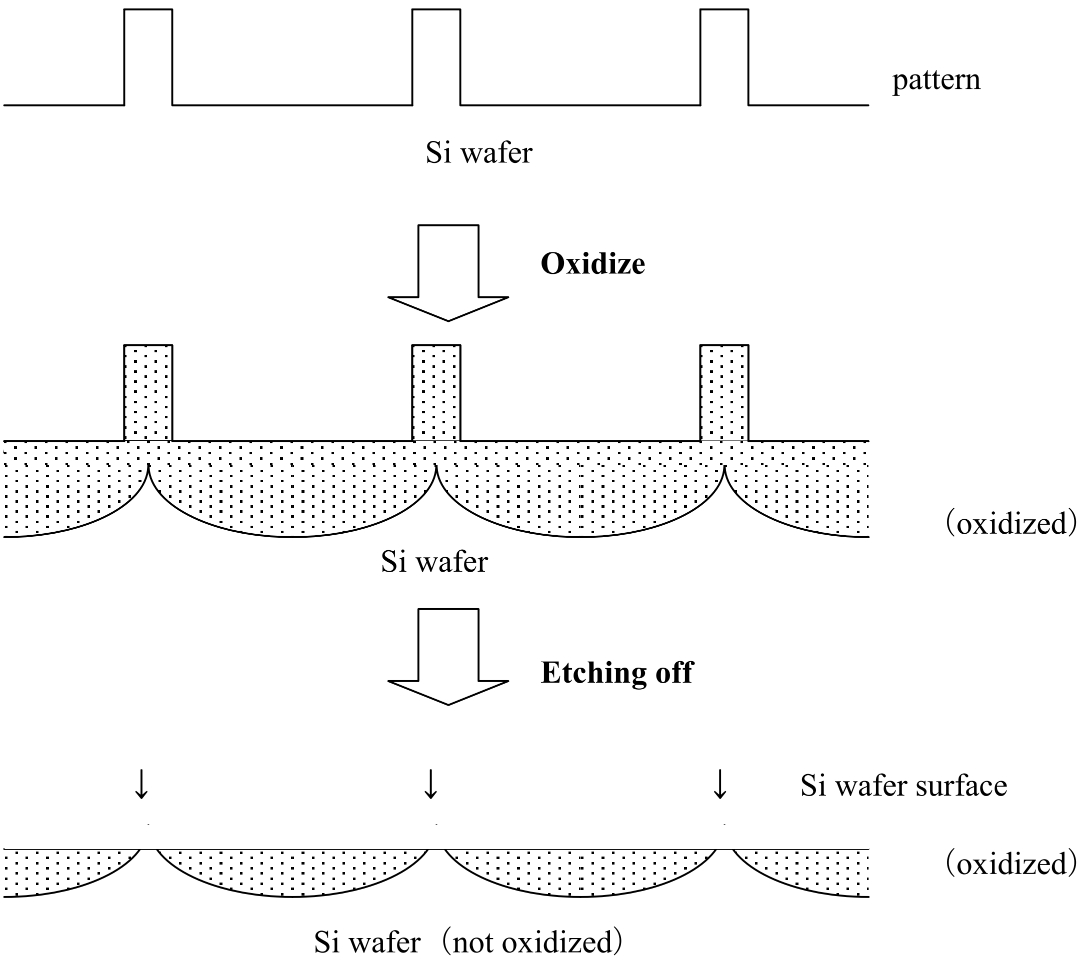

Fig.5: Nano-insulating bench fabrication process

APPLICATION OF NON-THERMAL PLASMAS TO NATURAL GAS UTILIZATION

S. Kado[1], Y. Sekine[2], N.Muto[1], T. Nozaki[1] and K. Okazaki[1]

[1] *Department of Mechanical and Control Engineering, Tokyo Institute of Technology, Tokyo, Japan*
[2] *Department of Applied Chemistry, Waseda University, Tokyo, Japan*

Abstract

Direct dehydrogenation of methane was examined using low temperature plasmas such as DBD, corona and spark discharge at room temperature and atmospheric pressure. In spark discharge, acetylene was produced with high selectivity and higher energy efficiency than that in DBD and corona discharge. By the emission spectroscopy, it was found that gas temperature in spark discharge channel remained as low as 420-460 K. The specific energy requirement for acetylene was 12.1 kWh/kg-C_2H_2 as same as Huels process.

1. Introduction

From a point of view of chemical utilization of natural gas, methane conversion into valuable products such as hydrogen, synthesis gas, C_2 and higher hydrocarbons has been examined under various conditions. The activation of methane requires a high reaction temperature due to its thermal stability. Even in the industrial process to produce hydrogen by steam reforming, the operating temperature is higher than 1073 K in the presence of catalysts. The higher temperature is favorable for promoting the reaction, but is not suitable for the selective formation of ethane/ethylene and oxygen-containing liquid compounds by oxidative coupling and partial oxidation. That is one of the reasons why the high yield of these products, sufficient for the commercialization, has not been obtained.

To resolve these problems, we have paid attention to the low temperature plasma having a property of high electron temperature and low gas phase temperature, and succeeded in the formation of acetylene with high yield at ambient temperature in gas phase homogeneous reaction using the spark discharge [1]. The formation of synthesis gas by carbon dioxide or steam reforming and partial oxidation was also examined with and without catalyst [2-4]. In this work, the reactivity and the energy efficiency of the spark discharge were compared with those of other cold plasmas such as dielectric barrier discharge (DBD) and corona discharge. In addition, the emission spectroscopic diagnostics of the spark discharge was done to know the gas phase temperature in the discharge channel and the reaction mechanism.

2. Experimental

Reaction Apparatus. The differences of the reactivity including the conversion, products selectivity and energy efficiency among DBD, corona and spark discharge were examined with the reactors as shown in Fig. 1. A flow type reactor composed of a quartz tube with 16.5 mm i.d. and 19.5 mm o.d. (1.5 mm thickness) was used through all experiments under the conditions of room temperature and atmospheric pressure without any catalysts. The reactant was a 99.9999% purity of methane. In this study, the effect of the residence time was investigated by varying the flow rate under the same discharge conditions.

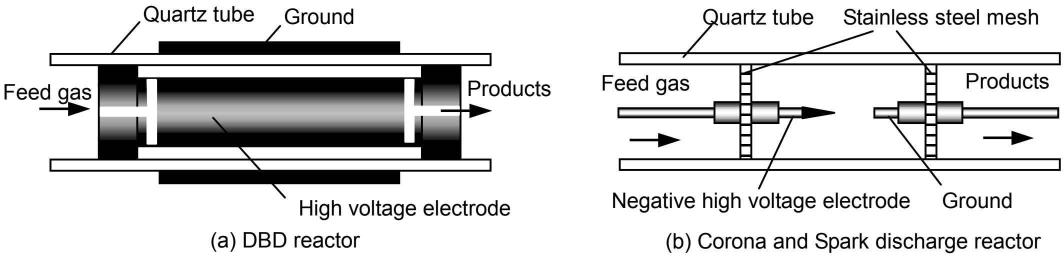

(a) DBD reactor (b) Corona and Spark discharge reactor

Fig. 1. Schematic diagram of reactors.

In DBD, the electrodes configuration was the coaxial type as shown in Fig. 1-(a). Inside of the reactor, the high voltage electrode of copper with 14.5 mm o.d. was inserted and fixed at the center. The outside of the reactor was covered with aluminum tape and grounded. The quartz glass of the reactor played a role of the dielectric material. The gap distance and the length of the discharge region were 1.0 mm and 40 mm, which corresponded to 2.0 cm^3 volume of the discharge region. AC high voltage with 75 kHz frequency was applied between the electrodes, and the supplied discharge power was fixed at 17 W.

In corona and spark discharge, the same reactor was used as shown in Fig. 1-(b). The electrodes configuration was needle to needle type. The stainless steel rods with 1mmϕ were used as the electrodes. The electrodes were centered and supported with the stainless steel mesh with 5.0 mm gap distance. DC negative high voltage was applied between the electrodes. In corona discharge, 1 MΩ high voltage resistor was inserted between the power supply and the electrode. The corona current was estimated from the decrease in the voltage at the resistor, and the discharge power was fixed at 4.6 W.

The intermittent spark discharge occurred periodically with 50 Hz pulse frequency (20 ms pulse period) and *ca.* –5 kV inception voltage. From the detail measurement of voltage of one pulse, it was clear that there were a dozen of spikes at one pulse. The number of spikes at a pulse was uncertain and distributed from 5 to 19 spikes. The average number of spikes was decided to be 12.6 spikes per pulse. The voltage recovered to 0 V in a few hundreds of nanoseconds, and the pulsed current occurred. The pulsed current reached 20-30 A with a width of 300-500 ns. This short width of current contributed to non-equilibrium plasma having characteristics of extremely high electron temperature and low gas phase temperature.

The discharge energy at a spike (P_S) was defined as follows.

$$P_S = \sum_i (|V_i \times I_i| + |V_{i+1} \times I_{i+1}|) \times (t_{i+1} - t_i) / 2$$

Total energy injection rate of spark discharge (P) in watts was defined as follows from P_S, average number of spikes (N_S) and pulse frequency (F), and fixed at 1.4 W.

$$P = P_S \times N_S \times F$$

Analysis. The waveforms of applied voltage and current were measured with the digital oscilloscope (Tektronix TDS644A, 500 MHz band width, 2 Gsamples/s maximum sampling rate) using voltage probe (Tektronix P6015A, 75 MHz band width, 1000:1) and current probe (Tektronix P6021, 60 MHz band width, 10:1). The gaseous products were analyzed by gas chromatography equipped with FID (G-950 column and Porapk N column) and TCD (SHIN-carbon column). The amount of deposited carbon was estimated from the total amount of CO and CO_2 in the combustion of deposited materials in the air at 923 K. The conversion of methane was defined as follows.

Conversion (%) = (moles of methane consumed) / (moles of methane introduced)×100.

The selectivities of products were defined as follows.

Product selectivity (%) = (carbon based moles of product) / (moles of methane consumed)×100.

The deposited materials were also characterized by Raman spectroscopy (Green laser 532 nm). The emission from the discharge region was continuously recorded by an ICCD camera with 50 ms exposure, and a 500 mm spectrometer with 1200 grating was used.

3. Results and Discussion

Reactivity of Low Temperature Plasmas. Figure 2 shows the products selectivity and methane conversion when pure methane was fed. In DBD, the oligomerization to hydrocarbons higher than C_3 was the main reaction (others in Fig. 2 were considered to be the liquid hydrocarbons). The main component in C_2 hydrocarbons was ethane formed by the coupling of CH_3 radicals. In corona discharge, although the formation of C_2 hydrocarbons was dominant, the consecutive dehydrogenation of ethane to ethylene and acetylene was observed. In addition, a large amount of carbon was deposited on the electrodes with the increase in the conversion. On the other hand, in spark discharge, acetylene was produced with the selectivity of 85% with small amount of carbon deposition.

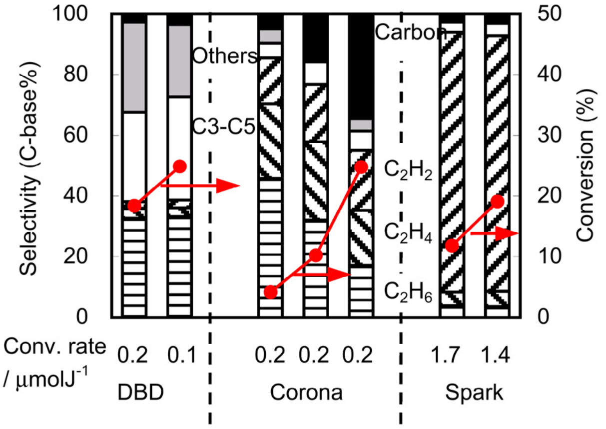

Fig. 2. Comparison of selectivity and conversion among DBD, corona and spark discharge in pure methane flow.

From a point of view of the energy efficiency, methane conversion rate (μmol/J) was estimated. Methane conversion rates of DBD and corona discharge were almost the same at 0.2 μmol/J, while the spark discharge reaction showed the high efficiency of 1.7 μmol/J. When the spark discharge was considered for acetylene synthesis method, the power required to produce 1 kg acetylene was 14.6 kWh/kg-C_2H_2. The spark discharge has a possibility to become more efficient process than Huels process (12.1 kWh/kg-C_2H_2) by the optimization of the reaction and discharge conditions.

Emission Spectroscopy. Figure 3 shows the emission spectra obtained in DBD, corona and spark discharge in methane flow. The spectrum obtained in spark discharge in hydrogen flow is also shown in Fig. 3. They were quite different among these three types of low temperature plasmas. The rotational band of 431.5 nm due to an $A^2\Delta$ - $X^2\Pi$ (0,0) transition had the highest intensity in DBD. The low intensity of emission derived from C_2 swan band system (517 nm, $A^3\Pi_g - X^3\Pi_u$ (0,0)) was observed. In corona discharge, the emission intensity of CH rotational band was almost the same as that of C_2 swan band system. The continuous radiation was observed in corona discharge, which was cause by carbon deposition in discharge channel.

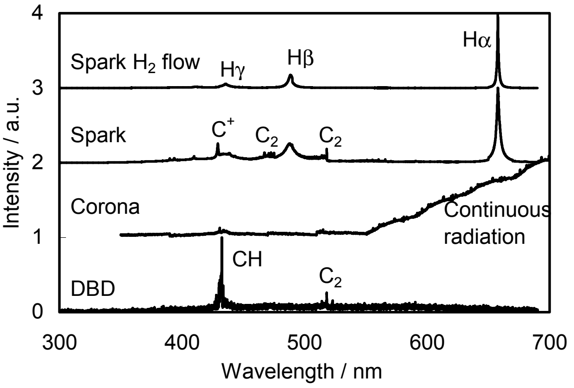

Fig. 3. Emission spectra of DBD, corona and spark discharge in pure methane flow and that of spark discharge in pure hydrogen flow.

In spark discharge, the emission intensity of CH rotational band was relatively low, while the strong emission of C_2 swan band system and atomic carbon (C^+, 427 nm) was observed. In addition, when the spectra in methane flow are compared with those obtained in hydrogen flow, it is clear that almost the same spectra of H Balmer series were observed. These facts of the strong intensity of atomic spectra of carbon and H Balmer series in methane flow indicate that methane was highly dissociated into C and H by the electron impact. These results are consistent with the previous work investigating the reaction mechanism using isotopes [5].

Gas Temperature Estimation in Discharge Channel. T. Nozaki et al. have developed a diagnostic method based on the emission spectroscopy of a rotational band of CH (431.5 nm) to determine the gas temperature [6]. As shown in Fig. 4, the results of DBD and corona discharge show a straight line in the Boltzmann plot. From the given slope, the rotational temperature was calculated to be 533 K and 959 K in DBD and corona discharge. In the spark discharge, the estimated gas temperature was as low as 418 K although the Boltzmann plot did not agree with the approximate line.

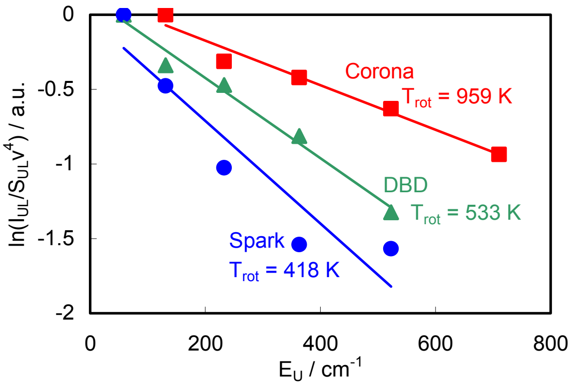

Fig. 4. Boltzmann plot obtained from measured spectra in DBD, corona and spark discharge.

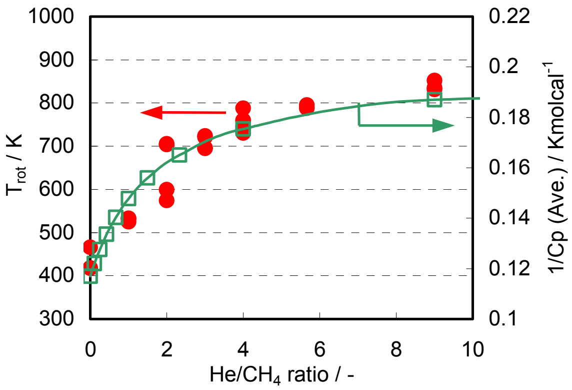

Fig. 5. Behavior of rotational temperature in spark discharge toward He/CH_4 ratio and its relationship with average heat capacity.

In the spark discharge, the dilution of methane with helium gave the strong intensity of CH emission enough to calculate the reliable rotational temperature. Figure 5 shows the effect of He/CH_4 ratio on the temperature and the average heat capacity. The behavior of the temperature showed the good agreement with the behavior of the average heat capacity. From this, the rotational temperature of 418 K in the spark discharge was reasonable.

Improvement of Energy Efficiency. To improve the energy efficiency for the production of acetylene and hydrogen with spark discharge, the optimization of reaction conditions were examined besides the discharge conditions. The maximum diameter of the discharge channel was estimated to be *ca.* 0.9-1.3 mm from the image of spark discharge taken with an ultra high-speed digital imaging system [7]. This indicated that most of methane might pass through the discharge region without contacting with the discharge channel.

Figure 6 shows the effect of internal diameter of the reactor on the selectivity and conversion under the condition of the same residence time of 0.6 s. The residence time was determined from the reactor volume between the electrodes defined as a reaction volume. With the decrease in the internal diameter, methane conversion increased while the main product remained acetylene although the selectivity to carbon slightly increased. Figure 7 shows methane conversion rate and specific energy requirement for C_2H_2. Methane conversion rate increased from 1.7 μmol/J (16.5 mmϕ) to 2.1 μmol/J (10.4 mmϕ), but decreased gradually with further decrease in the internal diameter of the reactor. The lowest specific energy requirement for C_2H_2 was 12.1 kWh/kg-C_2H_2 obtained with 10.4 mm i.d. reactor. The decrease in the energy efficiency with thin reactor tube was considered caused by high methane conversion, which led to low methane concentration and energy loss in the products decomposition.

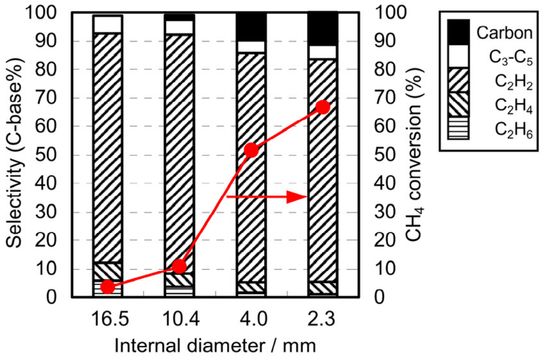

Fig. 6. Effect of internal diameter of reactor on reactivity of spark discharge in pure methane flow.

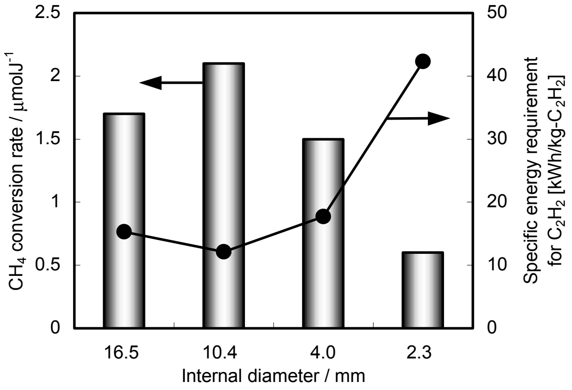

Fig. 7. Effect of internal diameter of reactor on energy efficiency.

Using 2.3 mmϕ i.d. reactor, the effect of residence time was examined under the conditions of 1.4 W and 4.0 W energy injection rate. It was natural that longer residence time gave higher methane conversion at the same energy injection rate, and higher energy injection rate gave higher methane conversion at the same residence time without affecting the selectivity so much. From Fig. 8, too short and too long residence time was not favorable to efficient production of acetylene and hydrogen. There was an optimum condition in residence time, and in this case, it was 20 ms, which corresponded to pulse period. Under this condition, the reactant gas was replaced per pulse. The efficient feed of reactant and removal of products are necessary. And the necessity of the optimization of energy injection rate was indicated from the fact that higher energy injection rate increased the specific energy requirement for C_2H_2.

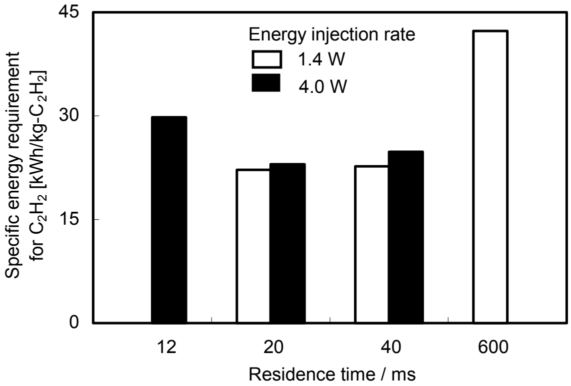

Fig. 8. Effect of residence time and energy injection rate on specific energy requirement for C_2H_2 (2.3 mmϕ i.d. reactor).

In addition, the specific energy requirement for C_2H_2 obtained with 2.3 mmϕ i.d. reactor was higher than that obtained with 10.4 mmϕ i.d. shown in Fig. 7. This indicates that the diffusion in the direction perpendicular to the discharge channel is also important. Figure 9 shows the effect of residence time on specific energy requirement for C_2H_2 when 10.4 mmϕ i.d. reactor was used. The lowest specific energy requirement for C_2H_2 of 12.1 kWh/kg-C_2H_2 was obtained at 0.6 s residence time, which was much longer than pulse period. These experiments were conducted in pure methane flow with relatively large amount of deposited carbon, so it is possible that this energy cost will be improved by mixing moderate concentration of oxygen to prevent carbon deposition and enhance methane conversion [4].

The obtained energy cost of 12.1 kWh/kg-C_2H_2 is as same as that of Huels process, which was industrialized as acetylene plant using thermal plasma of DC arc discharge [8]. At this optimized condition, methane conversion rate and energy efficient were 2.1 µmol/J and 32.3 %. Yao et al. used the similar reactor and achieved 2.73 µmol/J with high frequency pulsed discharge (9.92 kHz) [9]. They have reported that methane conversion rate increased with the increase in the pulse frequency, and our system showed much higher methane conversion rate as compared with their system at the same frequency as low as 50 Hz. It is also necessary to optimize the pulse frequency in our system.

Figure 10 summarizes methane conversion of all experiments conducted in this study as a function of specific input energy (eV/molecule). The results of DBD and corona discharge were dotted on the same curve. On the other hand, methane conversions obtained in spark discharge were much higher than those of DBD and corona discharge at the same specific input energy. Even in spark discharge, the energy efficiency decreased drastically in the range of methane conversion higher than *ca.* 60%. In the pulsed microwave plasma, this problem was overcome and linear increase in methane conversion was observed up to 80% [10]. At this stage, our pulsed spark discharge has an advantage in relatively low energy injection rate.

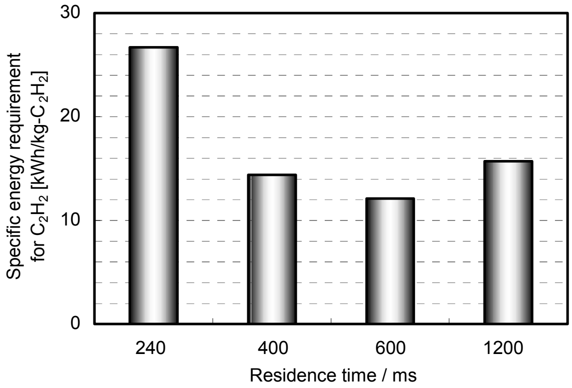

Fig. 9. Effect of residence time on specific energy requirement for C_2H_2 (10.4 mmϕ i.d. reactor).

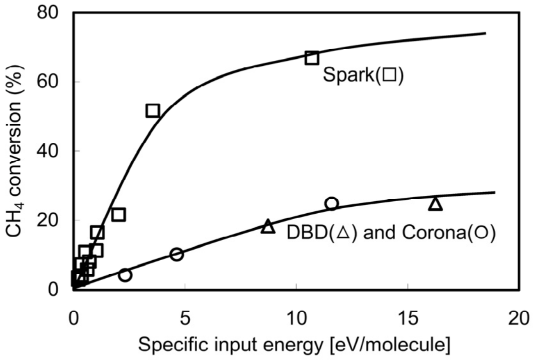

Fig. 10. Comparison of methane conversion among DBD, corona and spark discharge as a function of specific input energy.

4. Conclusion

Comparison of the properties among DBD, corona and spark discharge was made under the conditions of room temperature, atmospheric pressure and pure methane flow. The spark discharge showed much higher reactivity and selectivity to acetylene than those of DBD and corona discharge. From emission spectroscopic study, it was found that methane was highly dissociated to atomic carbon and hydrogen by the collision of electrons, and that the gas temperature in spark discharge channel was as low as 420-460 K, which indicated that the high selectivity to acetylene was not caused by thermal reaction. The highest energy efficiency of 32.3 % for the production of acetylene was obtained by the optimization of reactor size and residence time. Under this condition, the specific energy requirement for acetylene was 12.1 kWh/kg-C_2H_2, which was as same as that in Huels process using DC arc plasma.

Acknowledgment. S. Kado is grateful for his Research Fellowship from the Japan Society for the Promotion of Science (JSPS) for Young Scientists.

References

[1] S. Kado, Y. Sekine, K. Fujimoto, Chem. Commun., **24**, 2485 (1999).
[2] S. Kado, K. Urasaki, Y. Sekine, K. Fujimoto, Chem. Commun., **5**, 415 (2001).
[3] S. Kado, K. Urasaki, H. Nakagawa, K. Miura, Y. Sekine, Am. Chem. Soc., Div. Fuel Chem., in print.
[4] S. Kado, K. Urasaki, Y. Sekine, K. Fujimoto, Fuel, in print.
[5] S. Kado, K. Urasaki, Y. Sekine, K. Fujimoto, Therm. Sci. Eng., **11** (2003) in print.
[6] T. Nozaki, Y. Unno, Y. Miyazaki, K. Okazaki, J. Phys. D: Appl. Phys., **34**, 2504 (2001).
[7] S.L. Yao, E. Suzuki, A. Nakayama, Plasma Chem. Plasma Process., **21**, 651 (2001).
[8] H. Gladisch, Hydrocarbon Process. Petrol. Refiner, **41**, 159 (1962).
[9] S.L. Yao, E. Suzuki, N. Meng, A. Nakayama, Plasma Chem. Plasma Process., **22**, 225 (2002).
[10] M. Heintze, M. Magureau, M. Kettlitz, J. Appl. Phys., **92**, 7022 (2002).

PE-CVD of Ultra Low-*k* Thin Films and Its Gas Phase Diagnostics Using IR Spectroscopy

Tatsuru Shirafuji[2], Akio Tsuchino[1], Toshihiro Nakamura[1] and Kunihide Tachibana[1]

[1]*Department of Electronic Science and Engineering, and* [2]*International Innovation Center,*
Kyoto University, Yoshida Honmachi, Sakyo-Ku, Kyoto 606-8501, Japan

Abstract

Low-*k* a-C:F films have been prepared from C_6F_6/C_5F_8 using a PE-CVD method. The films prepared from 75% C_6F_6 show *k*=1.6 after thermal treatment at 400°C, which is explained by void formation due to desorption of some tissues in the films. Thickness reduction of 80% has been observed for the first 5 min treatment. However, no further reduction has been observed after that, which has relationships to inclusion and cross-linking of the aromatic carbon rings supplied from C_6F_6.

1. Introduction

In future ultra large scale integrated circuits (ULSIs), quite low dielectric constant *k* of inter-metal dielectric (IMD) films are required for decreasing resistance-capacitance time delay. For the next-generation ULSIs using 50 nm rule, IMD films of *k*<1.5 are required. This is achieved only by using porous materials[1,2]. Porous silica films have already proposed by other researchers[3,4]. In this paper, we report on a possibility of preparing low-*k* porous *carbon* films using a PE-CVD method.

2. Experimental

Films were deposited on Si substrates using an inductively coupled RF (13.56 MHz) PE-CVD reactor[5]. The diameter of the dielectric window and the distance between the window and grounded substrate holder were 20 and 150 mm, respectively. Typical deposition condition is summarized in **Table I**. Structure, refractive index and dielectric constant of the deposited films were characterized using FT-IR, XPS, spectroscopic ellipsometry and capacitance measurements before and after the thermal treatment at 400°C for 30 min in N_2 ambient. Void concentration in the films has been calculated using Bruggeman's effective medium approximation[6]. Gas phase diagnostics were performed using *in situ* Fourier transform infrared spectroscopy (FT-IR), optical emission spectroscopy (OES) and infrared laser absorption spectroscopy (IR-LAS)[5] for detecting gas phase stable species and radicals for the purposeof discussion on deposition mechanisms.

Table I. Typical deposition condition

RF power	150 W
Total flow rate	7.5 sccm
Total pressure	52 mTorr
Substrate temperature	Room temperature
RF power	150 W

3. Results and discussion

3.1 Deposition rate

Figure1 shows deposition rate as a function of C_6F_6 mixing ratio. By changing the mixing ratio from C_5F_8 to C_6F_6, deposition rate increases from 10 to 80 nm/min, which means C_6F_6 is much more polymerizable than C_5F_8. In addition, mixing ratio dependence of the deposition rate is linear, which can be explained by assuming that deposition precursors generated from C_6F_6 and C_5F_8 deposit independently of each other.

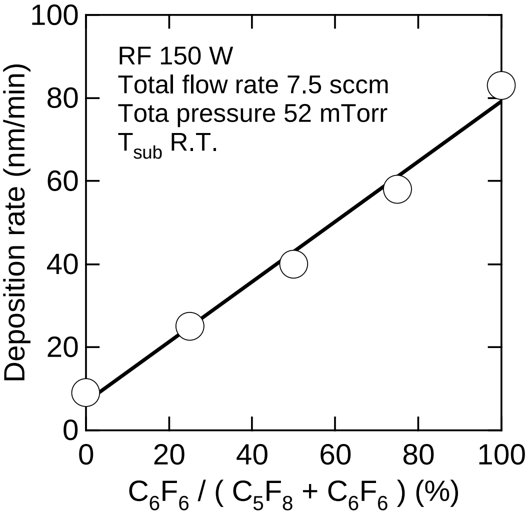

Fig.1 Deposition rate as a function of C_6F_6 mixing ratio.

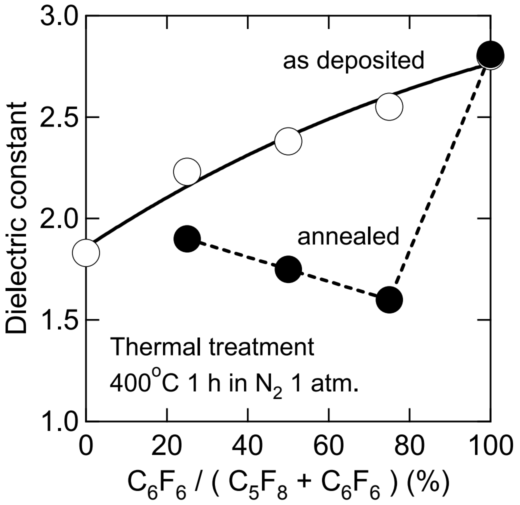

Fig.2 Volumetric fraction of voids in the films after thermal treatment.

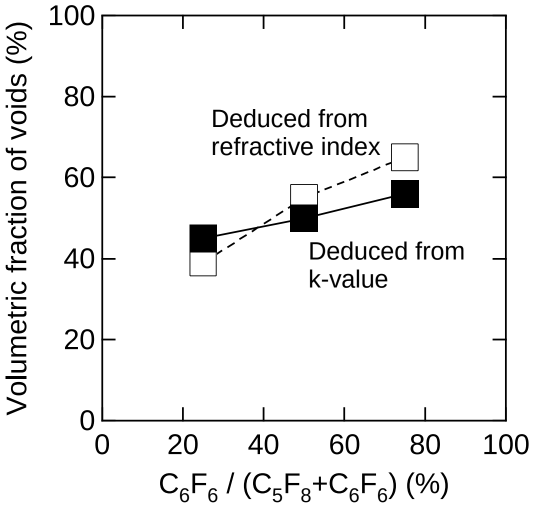

Fig.3 Volumetric fraction of voids in the films after thermal treatment.

3.2 Dielectric constant

Figure2 shows dielectric constant (*k*-value) of the films. Dielectric constant for as-deposited films varies from 1.8 to 2.7 with increasing C_6F_6 mixing ratio, which means that the precursors from C_5F_8 tends to create lower-*k* film structure while those from C_6F_6 brings about *k*-value higher than 2.0. This difference is due to difference in fluorine/carbon concentration ratio in the films as described in the section for XPS characterization of the films. Linear characteristics of *k*-value shown in **Fig.2** is corresponding to those for the deposition rate described above, where the deposition precursors from each monomer contribute to film composition independently of each other.

Concerning the films after thermal treatment, the films for 50 and 75% C_6F_6 show reduction of *k*-value after the thermal treatment. Final *k*-value is 1.6. This suggests that the voids might be formed in the films due to desorption of the tissues from C_5F_8 as we have expected. On the other hand, the film from 100% C_6F_6 does not show reduction in *k*-value although this film also shows thickness reduction of 80% after the thermal treatment. Therefore, the frame structure being left in the films for 50 and 75% C_6F_6 after the thermal treatment might have structures similar to those for 100% C_6F_6.

Figure 3 shows void concentration in the films as a function of C_6F_6 mixing ratio, in which one of the data have been derived from fitting of spectroscopic ellipsometry data, and another ones have been derived from dielectric constant. In this analysis, the films have been assumed to be composed of voids and the dense parts having *k*-value for 100% C_6F_6, because C_6F_6 film has not shown variation in *k*-value due to the thermal treatment. As can be seen in the figure, the void concentration increases from 40-45 to 60-65% with increasing C_6F_6 mixing ratio. The amount of 60% is quite high value, and which might bring about surface roughness. However, as long as characterize the surface with DekTak-3surface profiler, there was no macroscopic roughness, and interference color was also observed for the films. This might be due to overestimation of *k*-value (=2.8) for the dense part (frame structure) in the films after the thermal treatment.

3.3 Residual thickness

Figure 4 shows residual thickness after thermal treatmentat at 400°C for 30 min in N_2 ambient. The film prepared from 100% C_5F_8 has been removed almost completely. On the other hand, the film pre-

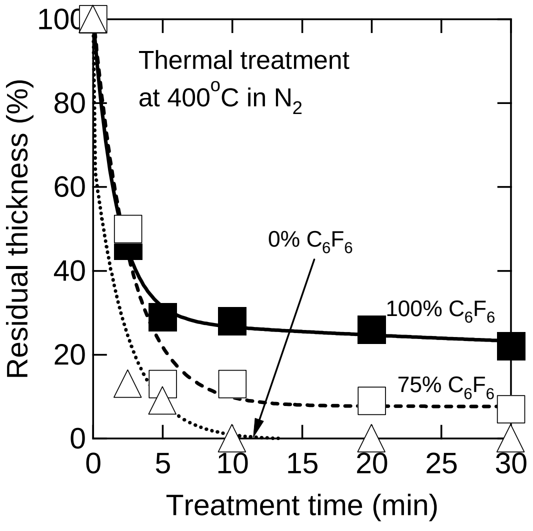

Fig.4 Volumetric fraction of voids in the films

pared from 100% C_6F_6 shows higher residual thickness of 20% although it is not enough for practical application at this moment. As seen in the figure, thickness reduction occurs during the first 5 min. After that, no marked thickness reduction is observed. This result means that the films have two components even for the film prepared from only C_6F_6. One is easily decomposed and/or vaporized by thermal treatment. Another is thermally stable up to 400°C and can be the frame structure after void formation. As seen in the characteristics for the film from 75% C_6F_6, the latter component must be incorporated because this film shows *k*-value of 1.6 which cannot be obtained without void formation, and thermally stable at 400°C. In order to clarify which structure is thermally stable, film structure has been characterized by FT-IR and XPS.

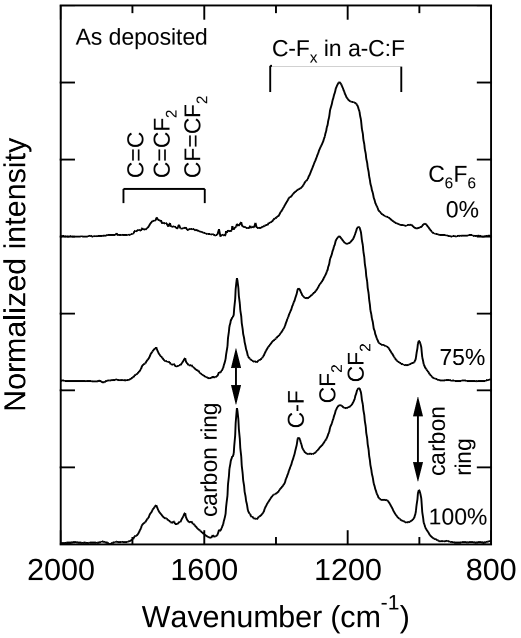

Fig.5 Normalized FT-IR spectra of the films prepared using 0, 75 and 100% C_6F_6 plasma.

3.4 Film structure

Figure 5 shows FT-IR spectra of as-deposited films. The spectrum for 100% C_5F_8 contains a broad C-F_x peaks at 1200 cm^{-1} and C=C related peaks at 1600-1800 cm^{-1}[7,8]. On the other hand, the spectrum for 75 and 100% C_6F_6 shows quite different spectral profile in which there exist several sharp peaks. This means that the films prepared with C_6F_6 do not have simple amorphous structure. Han *et al* have reported similar FT-IR spectra for the films deposited using pentafluorostyrene and perfluoroallylbenzene with pulsed plasma, in which the sharp peaks at 1500 and 1000 cm^{-1} are assigned to fluoroaromatic carbon ring vibrations[9]. The fact that the ring structure in the monomer has been included in the films means that the deposition precursors keep the ring structure even after electron impact dissociation of the monomer, and incorporated in the films. The cause of higher thermal stability of the films prepared from C_6F_6 can be attributed to inclusion of the ring structure as Han *et al* suggested[9].

Figure 6 shows XPS spectra of as-deposited films. As seen in the figure, the film from C_6F_6 has higher amount of C-CF and CF bonds relative to CF_2 and CF_3. Incorporation of carbon ring structure in the films observed in the FT-IR spectra can explain this density ratio, because aromatic rings are composed of C-C and CF bonds. On the other hand, the film from C_5F_8 has higher amount of CF_x bonds relative to C-CF bonds, which means that the film is composed of many domains surrounded by CF_x.

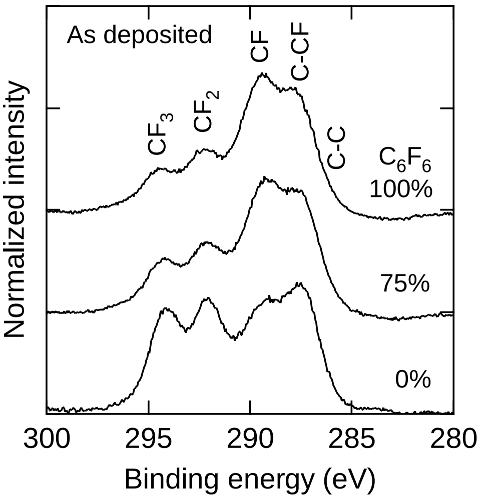

Fig.6 Normalized XPS spectra of the films prepared using 0, 75 and 100% C_6F_6 plasma.

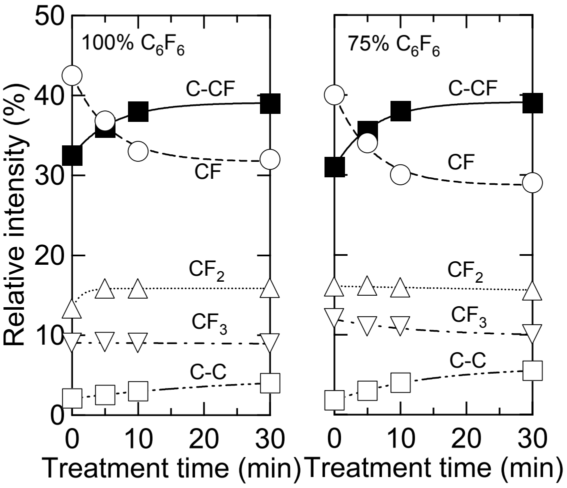

Fig.7 Thermal-treatment-time dependence of relative integrated intensity for the peaks observed in XPS spectra of the films deposited using 100 and 75% C_6F_6.

This might be a cause of the fact that the films from C_5F_8 can be vaporized at high temperature.

In order to study temperature dependence of the film structure, thermal-treatment time dependence of the XPS spectra has been investigated. **Figure 7** shows relative integrated intensity for the detectedchemical bonds as a function of the treatment time.The integrated intensity for each chemical bonds has been calculated through the deconvolution procedure of the spectra. The spectra after the thermal treatment has common feature that C-CF peak intensity increases and becomes highest. This variation occurs during the first 10 min, which is the similar time constant for the variation in FT-IR spectra ofthe films during the thermal treatment, and supports the previous discussion that reconstruction of the film structure needs more time in comparison to desorption of the thermally instable portion in the films.

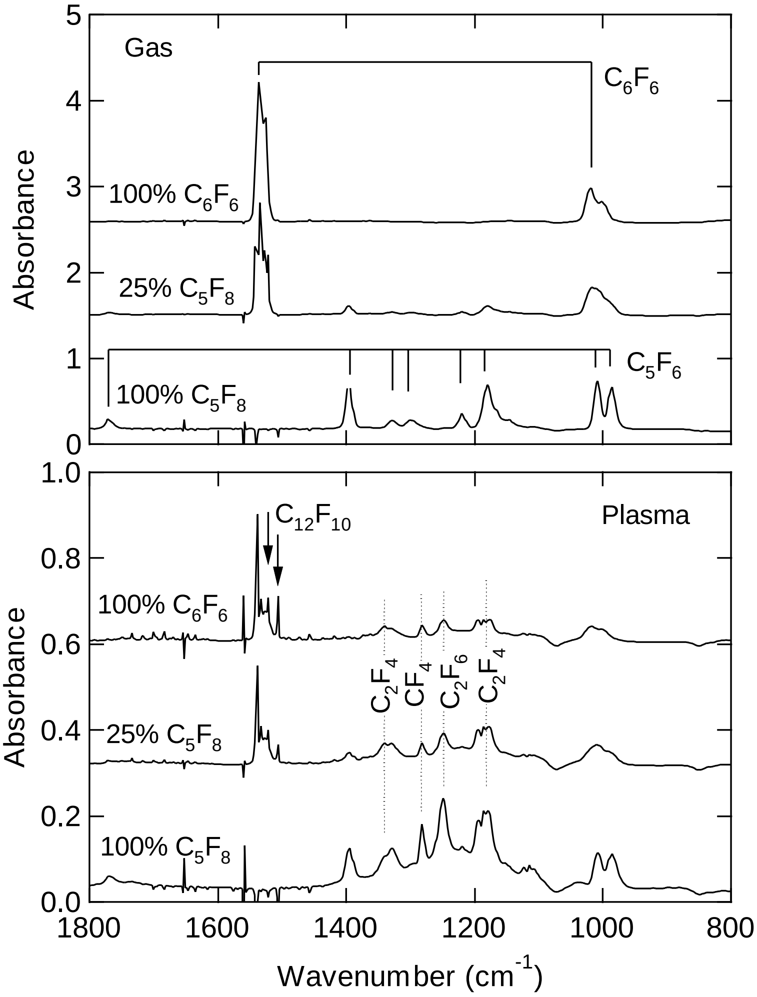

Fig.8 Gas phase FT-IR spectra for C_6F_6/C_5F_8 gases and plasmas. The spectra for the plasma have been measured during discharge.

As seen in the figure, the chemical bond which shows the opposite variationto C-CF is CF bonds. As the most of CF bonds are attributed to those accompanied with aromatic ring structure, this variation by the thermal treatment can be explained by the scheme that some of the CF bonds in the aromatic ring structure have been used for cross-linking to the other aromatic rings. The film after 10 min thermal treatment shows no structural variation even after further treatment. Therefore, the structure of cross-linked aromatic rings might be a cause of higher thermal stability. If all the carbons in the aromatic rings have been cross-linked, there are no space for incorporating voids in the films. In order to explain incorporation of 40-60% of voids in the films, these aromatic rings are considered to be partially cross-linked.

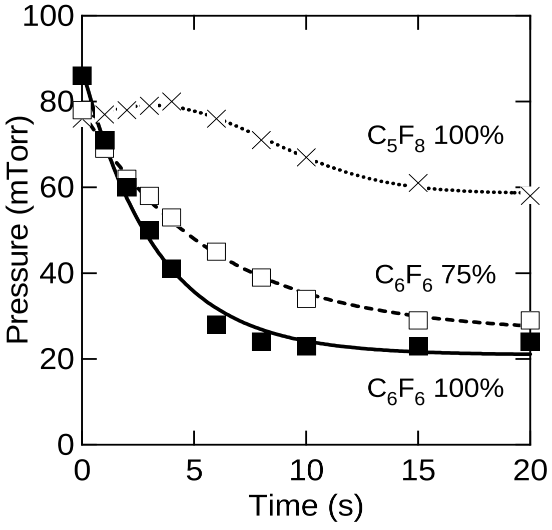

Fig.9 Pressure reduction observed for C_6F_6/C_5F_8 plasmas after turning discharge on.

3.5 Gas-phase diagnostics

Figure 8 shows FT-IR spectra of the gas-phaseof C_5F_8 and C_6F_6 gas and plasma. Concerning the FT-IR spectra for C_5F_8, many peaks appear when the peaks for parent monomer disappear by igniting plasma. The products observed in the plasma are CF_4, C_2F_4 and C_2F_6. As these species have lower molecular weight in comparison to the parent monomer, the parent monomer is considered to be highly fragmented by electron impact dissociation. This is the common feature that is known also for C_2F_4 and C_4F_8[5]. Concerning the deposition precursors for C_5F_8 plasma, Takahashi *et al* have already clarified that variation of CF_x radicals has no direct correlation with the deposition tendency, and that the presence of high-mass and less-stable species in the gas phase in the C_5F_8 plasma was suggested to be responsible for the deposition of polymers with a higher rate and larger fluorine content[6].

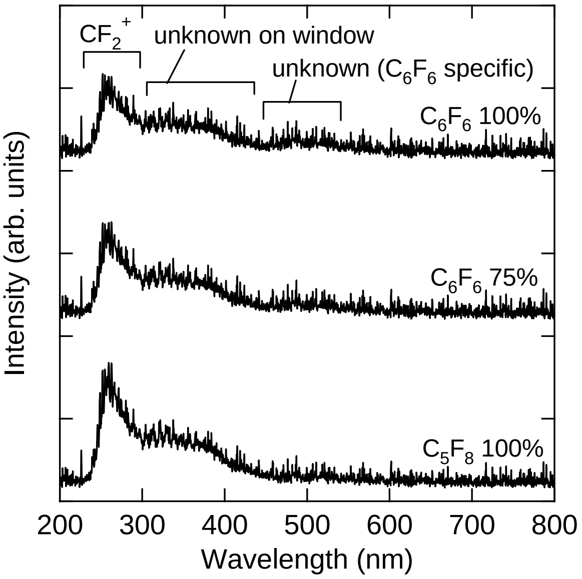

Fig.10 OES spectra for 0, 75 and 100% C_6F_6/C_5F_8 plasmas.

Concerning the gas phase of C_6F_6, two peaks for the parent monomer are observed at around 1500 and 1000 cm^{-1} in the spectrum without plasma. These are both aromatic carbon rings, which appear also in the FT-IR spectra of the films as mentioned above. The spectrum for C_6F_6 plasma is quite different from the result for C_5F_8, where intensity of products is quite smaller than that for C_5F_8 plasma even though dissociation degree of C_6F_6 is close to 100%. Possible explanation for this phenomenon is that the monomer has highly polymerizable nature, which is supported by higher deposition rateof the films. **Figure 9** shows total pressure before and after plasma ignition. As can be seen in the figure, marked reduction in total pressure is observed for C_6F_6, which also indicates that the product from C_6F_6 can be easily polymerized and deposited. As the aromatic ring structure has been incorporated in the deposited films, it is expected that the ring structure of C_6F_6 is not fully decomposed by electron impact.

An additional peak has been observed at around 1500 cm^{-1}. This peak position is almost the same to that for parent monomer C_6F_6. However, its shape is quite different from that for the parent monomer. The sharp peaks around1500-1700 might be attributed to H_2O existing inthe optical path, but its intensity is much smaller than the peak at around 1500 cm^{-1}.

According to the report by H. Bai and B. S. Ault, IR absorption peak for $C_{12}F_{10}$ is observed at 1502 and 1521 cm^{-1}[10]. These are corresponding to the sharp peaks observed at the same position. As the parent monomeris expected to be fragmented partially as mentioned above, following reactions can be proposed for explaining polymerization in C_6F_6 plasma,

$$C_6F_6 + e \rightarrow C_6F_5 + F + e,$$
$$C_6F_5 + C_6F_5 \rightarrow C_{12}F_{10}.$$

As the emission of fluorine was not observed in the OES spectra as shown in **Fig.10**, F radicals must be consumed through the following reaction,

$$C_6F_6 + F \rightarrow C_6F_5 + F_2.$$

These polymerization can occur both in the gas phase andon the surface. Quite high deposition rate of C_6F_6 plasma suggests that similar reaction schemes occur on the surface for film deposition.

In the previous discussion, small radicals such as CF_x is not considered in the film deposition scheme. Concerning the C_5F_8 plasma, Takahashi *et al* have already clarified that CF_x radicals cannot be the pre-

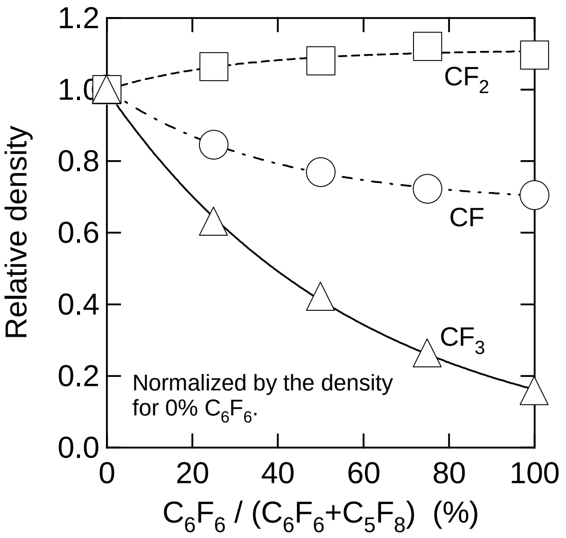

Fig.11 Relative density of CF_x radicals as a function of C_6F_6 mixing ratio.

cursors for film deposition[6]. In this work, similar experiments using IR-LAS have been performed. **Figure11** shows relative density of CF_x radicals in the C_6F_6/C_5F_8 plasma. As can be seen in the figure, all the density variations do not have direct correlation with the deposition rateshown in **Fig.1**. This means that CF_x radicals cannot be responsible for film deposition in both of C_5F_8 and C_6F_6 plasmas. Although marked variationis seen in the density of CF_3 while the other species do not show large variation as a function of gas mixing ratio, its cause is not clarified yet at present.

4. Conclusions

Low *k* a-C:F films have been prepared from C_6F_6 and C_5F_8 gas mixture by a PE-CVD method. The films from 100% C_5F_8 have volatile nature, and they are vaporized by heating up to 400^{o}C. On the other hand, the films prepared with 100% C_6F_6 have higher thermal stability. After thermal treatment of the composite films, the dielectric constant of the films has been reduced to 1.6, although residual thickness of the films are only 20%. This result suggests that the tissue from C_5F_8 are vaporized by the thermal treatment and voids are formed in the films. Void concentration in the films estimated to be 40-60%. These structural variation stops after 5-10 min thermal treatment, and no marked structural changes have been observed for further thermal treatment. This means that a-C:F films with *k*-value of 1.6 can be prepared with high thermal stability by annealing procedure although the thickness reduction is quite large. Cause of higher thermal stability of the films prepared with C_6F_6 has been attributed to the fact that cross-linked aromatic ring structure has been incorporated in the films. Gas-phase diagnostics of the deposition processes revealed that C_6F_6 is highly polymerizable. Together with the fact that the aromatic ring structures have been incorporated in the films, these results suggest that C_6F_6 is partially fragmented and its original ring structure has been incorporated in the films, which has brought about higher thermal stability.

Acknowledgement

The authors gratefully acknowledge Zeon Corporation for their cooperation in providing the C_5F_8. The authors express their deep gratitude to Mr. Keiichi Asamura for the numerous experimental help. This research was partially supported NEDO/MIRAI Project, and by the Grant-in-Aid of the Ministry of Education, Science, Sports and Culture.

Referemces

[1] M. Sekine: Appl. Surf. Sci. **192,** 270 (2002).
[2] R. D. Miller, R. Beyers, K. R. Carter, R. F. Cook, M. Harbison, C. J. Hawker, J. L. Hedrick, V. Lee, E. Liniger, C. Nguyen, J. Remenar, M. Sherwood, M. Trollsas, W. Volksen and D. Y. Yoon: Mater. Res. Soc. Symp. Proc. **565,** 3 (1999).
[3] Y. Uchida, T. Katoh, S. Sugahara, M. Matsumura: Jpn. J. Appl. Phys. 2, Lett. **39,** L1155 (2000).
[4] P. T. Liu, T. C. Chang, K. C. Hsu, T. Y. Tseng, L. M. Chen, C. J. Wang, S. M. Sze: Thin Solid Films **414** 1 (2002).
[5] K. Takahashi, A. Itoh, T. Nakamura and K. Tachibana: Thin Solid Films **374**, 303 (2000).
[6] D. E. Aspnes: Thin Solid Films **89**, 249 (1982).
[7] R. d'Agostino, F. Cramarossa, F. Fracassi and F. Illuzzi: *Plasma Deposition, Treatment, and Etching of Polymers*, Ed. R. d'Agostino, Academic Press, New York, 1990, Chapter 2.
[8] A. Milella: *Plasma Deposition and Treatments of Polymers: Modulated vs. Continuous Deposition of Fluorocarbon Films and Processes for the Reduction of Hydrophobic Recovery*, Ph. D. thesis, Universitá degli studi di Bari, Italia, 2002.
[9] L. M. Han, R. B. Timmons and W. W. Lee: Mater. Res. Soc. Symp. Proc. **511,** 93 (1998).
[10] T. Shirafuji, Y. Miyazaki, Y. Nakagami, Y. Hayashi and S. Nishino: Jpn. J. Appl. Phys. **38,** 4520 (1999).
[11] H. Bai and B. S. Ault: Chem. Phys. **169**, 317 (1993).

Measurement of atomic oxygen density in processing plasmas by vacuum ultraviolet laser absorption spectroscopy

Takashi Yokomizo and Kunihide Tachibana

Department of Electric Science and Engineering, Kyoto University,
Yoshida-Honmachi, Sakyo-ku, Kyoto 606-8501, Japan

Abstract

The absolute oxygen (O) atom density in an inductively coupled plasma (ICP) source was measured by using vacuum ultraviolet (VUV) laser absorption spectroscopy (LAS) with the resonance lines of oxygen atoms at 130 nm. The tunable VUV laser was generated by two-photon resonance four-wave difference-frequency mixing technique in Kr gas. The obtained values varied from 2×10^{12} to 1×10^{13} cm^{-3}, depending on the source gas and operating conditions of plasma source.

1.Introduction

It has been known that light element atoms such as H, C, N, O and F contribute to a variety of plasma material processing technologies. Therefore, quantitative *in situ* diagnostics of such radical densities as well as plasma parameters are strongly required to clarify the kinetics of plasmas including these species in the gas phase and on the surface in order to control plasma processes more precisely. Especially, Oxygen atoms have very important roles in the resist ashing process for the fabrication of ultra-large scale integrated circuits (ULSIs). Oxygen atoms with high reactivity are also used in the oxidation processes of Si to produce gate insulators for ULSIs and thin film transistors (TFTs).

Although many studies have been made on the quantitative measurements of molecular radicals, there have been few quantitative and reliable measurements of atomic radicals. Some methods have been developed for the measurement of the absolute density of these atomic species, such as two-photon absorption laser-induced fluorescence (TALIF) [1], vacuum ultraviolet absorption spectroscopy (VUV-AS) with incoherent light source [2] and so on. However, TALIF needs a laser source with a sufficient power level, and absolute density calibration is not an easy task. In the case of VUV-AS, other errors in the derivation of absolute density may have been caused by the influence of background absorption by source gas molecules and species produced in plasmas as well as by imprecise estimation of the line shape of the light source. Therefore, we have been developing an alternative measurement system for these species by using vacuum ultraviolet laser absorption spectroscopy (VUV-LAS) [3]. In this method, the VUV laser is generated by a two-photon resonance four-wave mixing technique, and its tunability permits accurate determination of absolute atomic density from the integrated absorption line shapes.

In this study, we report on the measurement of the absolute O atom density with the tunable VUV laser around 130 nm in order to understand the chemistry during processing using oxygen atoms.

2.Experimental Procedure

Figure 1 shows a schematic diagram of the experimental setup for the measurement of O atom density using VUV-LAS. In order to generate a tunable VUV laser of wavelength around 130 nm, we used a two-photon resonance four-wave difference-frequency mixing technique in Kr gas as the nonlinear medium ($\nu_{VUV} = 2\nu_1 - \nu_2$). Two dye lasers pumped simultaneously by a Xe-Cl excimer laser or a Nd:YAG laser provided the frequencies (wavelengths) of $\nu_1(= c/\lambda_1)$ and $\nu_2(= c/\lambda_2)$, where c is the light velocity. The energy of two photons $2h\nu_1$, where h is the Planck constant, was tuned to be resonance with the excitation energy level of Kr ($4p^5 5p[1/2,0]$) from the ground state at $\lambda_1 = 212.55$ nm, while λ_2 was varied between 570 and 578 nm to obtain a tunable VUV laser in the range from 130.2 to 130.6 nm (Fig. 2). Two dye laser beams were aligned collinearly and focused by a lens of $f = 20$ cm into the VUV generation chamber where these frequencies were mixed. Kr gas was filled in the chamber at 30 Torr with an MgF_2 sealing window at the exit side. The generated VUV laser was reflected by the surface of an uncoated concave quartz plate of 1 m curvature, which was placed in another small chamber at an incident angle of 65°. The quartz plate acts

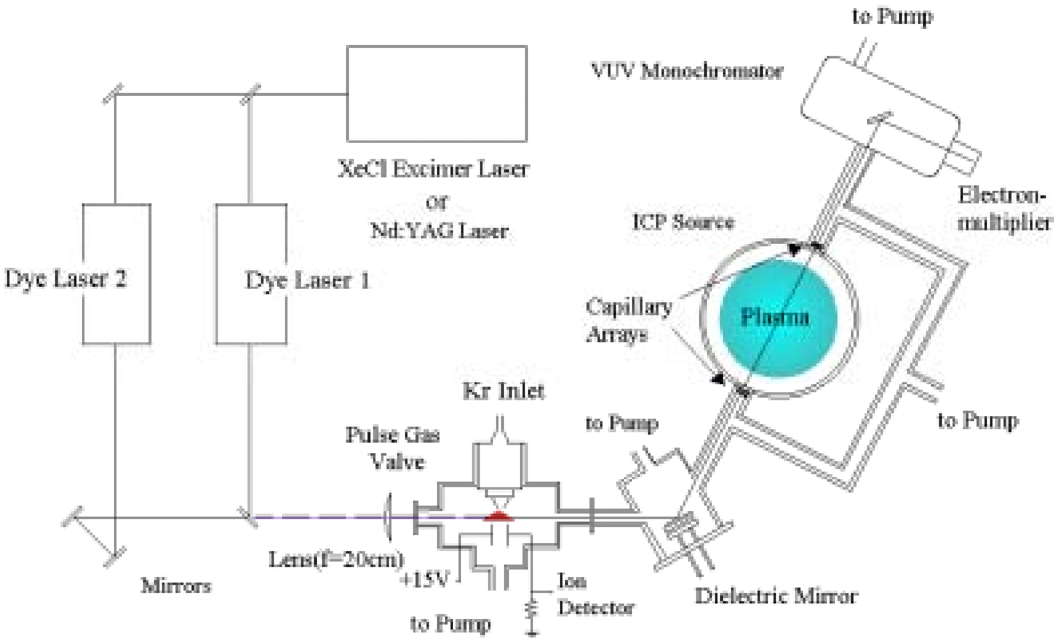

Fig. 1. Experimental setup for VUV-LAS measurement combined with an ICP plasma reactor.

partially in collimating the VUV beam and also in separating it from the fundamental wavelengths.

The ICP chamber was 32 cm in inner diameter and 15 cm in height. A substrate holder of 22 cm in diameter was located at 8.5 cm below the quartz plate. The rf (13.56 MHz) power up to 600 W was supplied by a flat spiral four-turn antenna coil into the plasma reactor through a quartz plate of 19 cm in diameter and 1.5 cm in thickness. Source gases (O_2, CO and CH_4) were introduced into the chamber from a side port

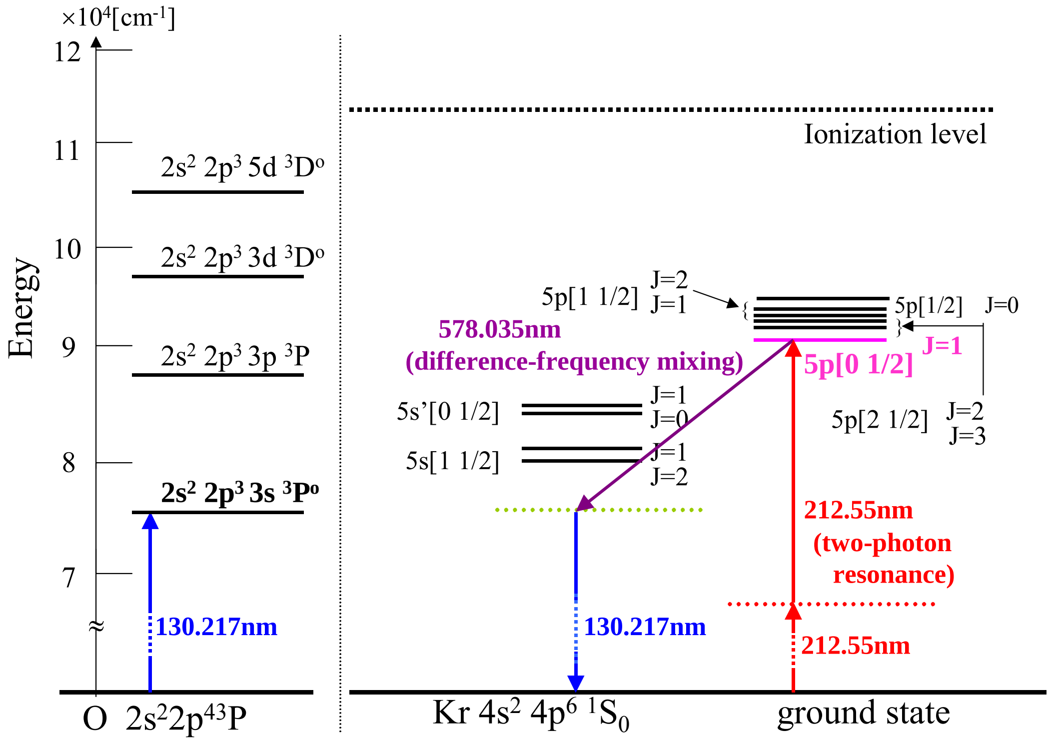

Fig. 2. Partial energy level diagrams of Kr and O atoms as explanations of VUV generation and VUV-LAS measurement.

of the chamber at a pressure range from 30 to 75 mTorr. The laser beam was fed into the chamber through the capillary array windows mounted on the both sides at 2 cm above the substrate holder. The VUV laser path was differentially pumped, so that the windows also functioned for sustaining the pressure difference. In the configuration, the absorption length through the plasma was 32 cm. The VUV probe beam coming out of the chamber was further filtered by a VUV monochromator of f = 20 cm and detected by a solar blind photo-multiplier.

The energy level diagram of O atom is shown in Fig. 3. The absorption measurement was performed on the $2s^22p^{4}{}^3P_J$ (J = 0, 1, 2) – $2s^22p^33s^3S_1$ transition at 130 nm. Provided the corresponding transition probability A is known, the absolute density populated on each lower level N can be derived from the integrated area of the profile of absorption coefficient per unit length $k(\nu)$ as follows,

$$N = \frac{8\pi g_1}{\lambda^2 g_2 A}\int k(\nu)d\nu \qquad (1)$$

where λ is the wavelength and g_1 and g_2 are the statistical weights of the lower and upper levels of the transition.

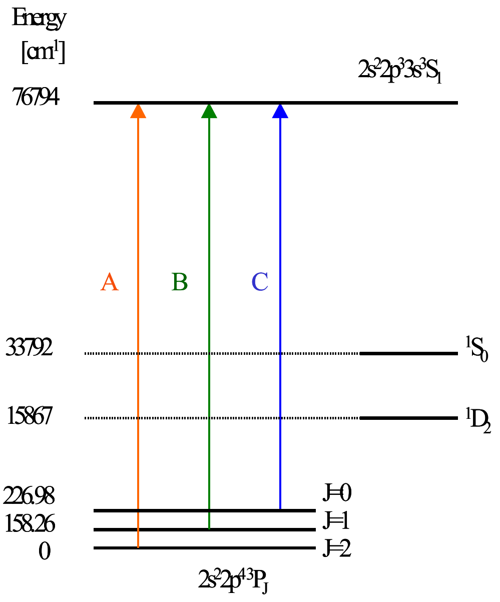

Fig. 3. Partial energy level diagram of O atom and corresponding resonance lines.

3.Results and Discussion

The signals observed in the spectral range between 130.217 and 130.603 nm in a pure O_2 plasma are shown in Fig. 4. The flow rate of O_2 gas was 10 sccm, the pressure was 30 mTorr, and the supplied rf power was 300 W. The absorption feature composed of the three isolated lines in Fig. 3 is clearly seen in the figure according to a fairly high resolution of our VUV-LAS technique. Each population densities on the $^3P_0$, $^3P_1$ and $^3P_2$ levels were derived by using Eq. (1), and the total density of O atoms in the ground state was obtained from the sum of them.

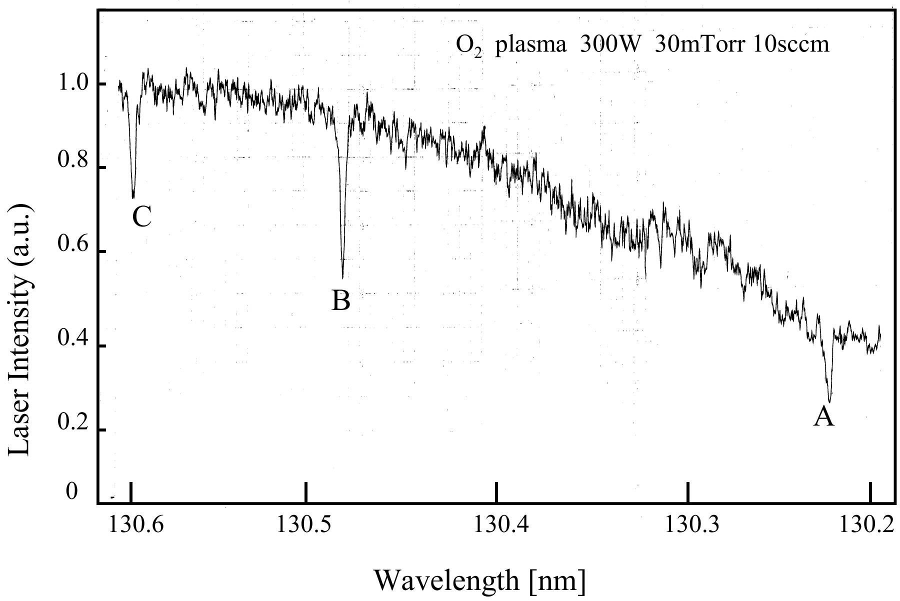

Fig. 4. Measured absorption spectra of the $2s^22p^43P_J$ (J = 0, 1, 2) – $2s^22p^33s^3S_1$ transition group.

Figure 5 shows an example of the observed absorption spectrum as a function of frequency ν for the 130.217 nm ($2s^22p^{43}P_2 - 2s^22p^33s^3S_1$) line. Its full width at half maximum (FWHM) was estimated to be 2.26 × 10^{-3} nm, which was much larger than that of the Doppler profile at 300 K, i.e., 0.40 × 10^{-3} nm. The difference may be attributed mostly to the finite spectral width of our VUV laser, but there may be a contribution from the non-thermalized velocity distribution of O atoms produced by electron collisional dissociation. Nevertheless, the absolute density can be derived accurately from the integrated area over the absorption coefficient profile given in Eq. (1) without any influence of the instrumental width.

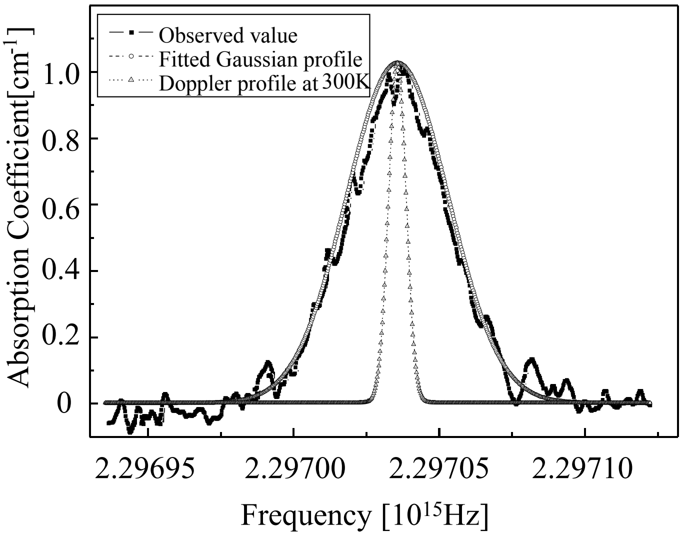

Fig. 5. Typical absorption line profile of 130.217 nm ($2s^22p^43P_2 - 2s^22p^33s^3S_1$) line.

Figure 6 shows the O atom density measured in O_2 and CO plasma as a function of the rf power, respectively. The pressure was kept at 30 mTorr, and the flow rates of source gas were 10 sccm. Obtained values were about 1×10^{13} cm^{-3} in O_2 plasma and 2×10^{12} cm^{-3} in CO plasma at 400 W, and in both charts the density increased almost linearly with the rf power. Assuming the Boltzmann distribution within the ground state levels at a temperature of 400 K, the ratio of O atom densities on the $^3P_0$, $^3P_1$ and $^3P_2$ levels deduced from the respective statistical weights should be 1:3.5:11.3. However, the ratio of O atom obtained from measured values was 1:1.2:1.3 in O_2 plasma and 1:2.0:3.8 in CO plasma. Therefore, the population within the ground state levels of O atom could not be explained by the Boltzmann distribution. The cause of this disagreement may be attributed to the fact that the measurements have been performed in active plasma region, which is closely located at 6 cm from the antenna coil. Therefore, it may be considered that O atoms do not come into thermal equilibrium and remain in the state just after the production of O atoms.

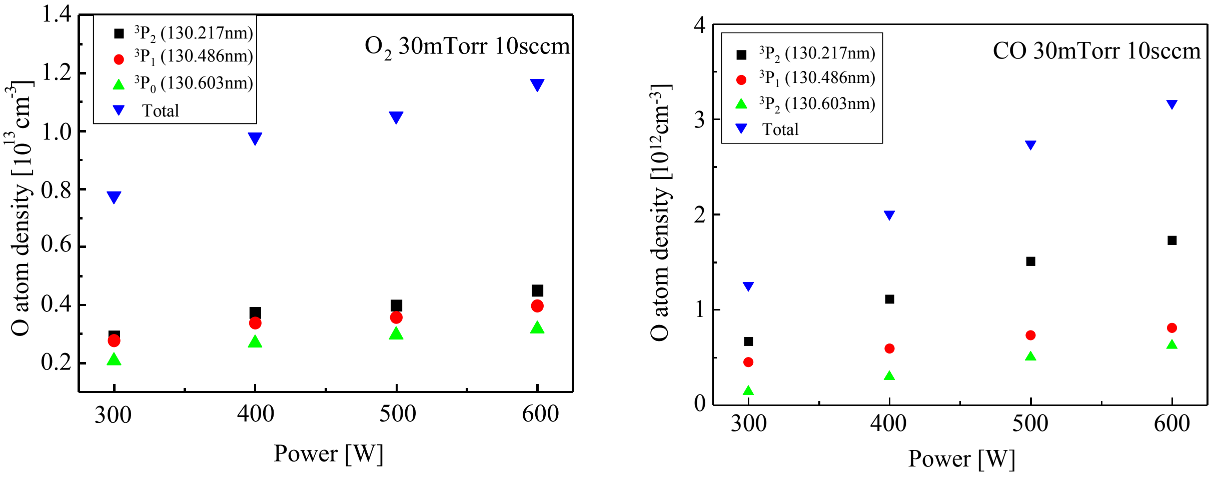

(a) (b)

Fig. 6. rf power dependence of O atom densities measured in (a) O_2 plasma and (b) CO plasma.

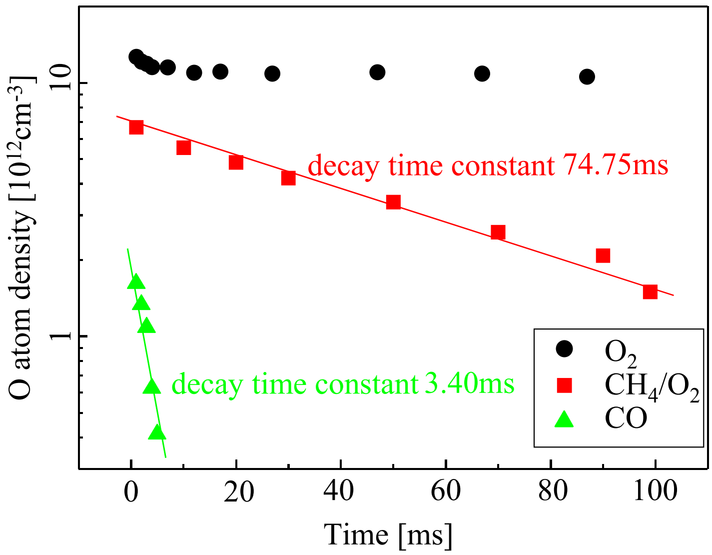

Fig. 7. Time decay dependence of O atom densities measured in O_2, CO and O_2/CH_4 by pulsing the discharge.

The decay of total O atom density in the ground state was measured in O_2, CO and O_2/CH_4 by pulsing the discharge. The results are shown in Fig. 7. In each source gas, the supplied rf power was kept at 300 W and the total pressure was 50 mTorr, and the flow rates of source gas and CH_4 were 10 sccm. The decay of O atom was hardly seen in O_2 plasma, while the exponential decay of O atoms was observed in CO and O_2/CH_4 plasma, and the decay time constants were 3.40 and 74.75 ms, respectively. We tried to measure the temporal variation of the O atom densities over further longer time range concerning the O_2 plasma in which the decay was scarcely seen in the observed time range. Therefore, we fixed the VUV laser at 130.217 nm where the absorption was maximum, and then turned off the discharge. The temporal variation of transmitted laser intensity is shown in Fig. 8(a), from which the O atom density is estimated by taking account of the broadening of measured absorption spectrum as shown in Fig. 8(b). The O atom density starts to decrease after about 1 s after the discharge is turned off, and almost disappears after 5 s. Since the mean residence time of gas particles in the chamber is about 4.5 s for our experimental condition, it may be considered that O atoms are exhausted mostly by pumping.

On the other hand, the O atom density in CO plasma decreased fairly rapidly. This rapid reduction of oxygen density may be caused by the reaction with other species in gas phase and the diffusion toward the chamber wall. However, the former is not likely in consideration of extremely small reaction rates given as follows [4];

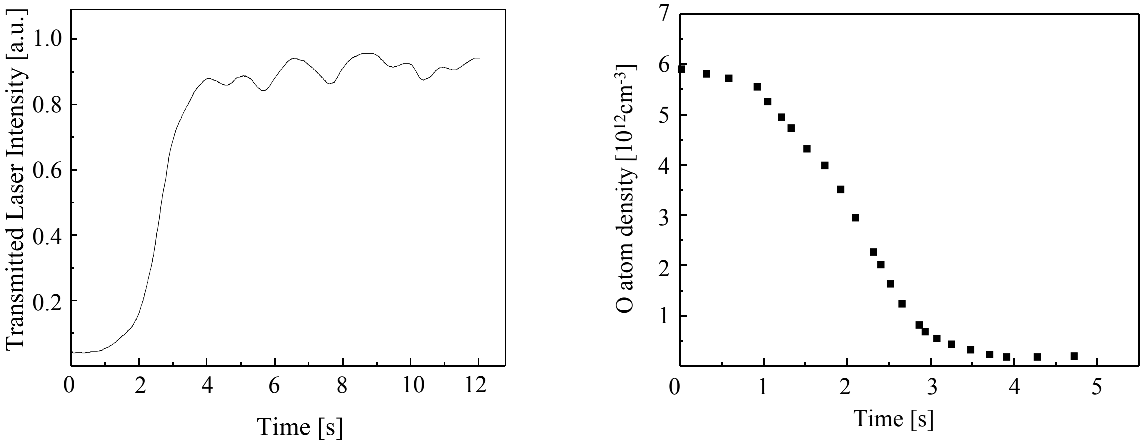

(a) (b)

Fig. 8. (a) The temporal variation of transmitted laser intensity at 130.217 nm where the absorption was maximum after O_2 plasma was turned off, and (b) the O atom density estimated from this transmission efficiency by taking account of the broadening of measured absorption spectrum.

$$\mathrm{C + O + M \rightarrow CO + M} \qquad k = 1.2 \times 10^{-32}\ \mathrm{cm^6 molecule^{-2} s^{-1}} \qquad (2)$$
$$\mathrm{CO + O + M \rightarrow CO_2 + M} \qquad k = 1.7 \times 10^{-31}\ \mathrm{cm^6 molecule^{-2} s^{-1}} \qquad (3)$$
$$\mathrm{CO_2 + O \rightarrow CO + O_2} \qquad k = 4.0 \times 10^{-26}\ \mathrm{cm^3 molecule^{-1} s^{-1}} \qquad (4)$$

For example, in the second reaction (Eq. (3)), even if we take the densities of CO and the third body M as the feeding gas density corresponding to the pressure of 50 mTorr, the estimated rate only becomes 0.4 s^{-1}. The third one (Eq. (4)) is a two-body reaction, but the rate constant is too small. Thus, the surface reaction of O atoms transported to the wall by diffusion can only be a cause of their fast decay. Actually, a deposit like soot was observed on the wall after the operation with CO gas.

In O_2/CH_4 plasma, a slower decay of O atom than that in CO plasma was observed. It is considered that O atoms react with CH_X radicals in gas phase as follows [5];

$$\mathrm{CH_3 + O \rightarrow CH_2O + H} \qquad k = 9.4 \times 10^{-11}\ \mathrm{cm^3 molecule^{-1} s^{-1}} \qquad (5)$$

In order to be consistent with the decay time constant of 75 ms, the estimated density of CH_3 should be about 1.4×10^{11} cm^{-3}. This is a reasonable value in a typical plasma with CH_4 gas [6].

4.Conclusions

A tunable VUV laser around 130 nm range was generated by the two-photon resonance four-wave difference-frequency mixing technique in Kr gas, and the absolute atomic oxygen density in an ICP source was successfully measured by using absorption spectroscopy. The absolute values of O atom density were about 1×10^{13} cm^{-3} in O_2 plasma and 2×10^{12} cm^{-3} in CO plasma at the rf power of 400 W and the pressure of 30 mTorr, and increased linearly with the increase of the rf power. However, the ground state levels of O atom could not be explained by the Boltzmann distribution, and O atoms did not come into thermal equilibrium state. In the case of time decay dependence of O atom densities, the decay of O atom was scarcely seen in O_2 pulsed plasma, while the decay of O atom was exponentially observed in CO and O_2/CH_4 pulsed plasma, and the decay time constants were 3.40 and 74.75 ms, respectively. This reduction of oxygen density may be caused by the diffusion toward the chamber wall in CO plasma and the reaction with CH_x radicals in gas phase in O_2/CH_4 plasma.

References

[1] G. C. Herring, M. J. Dyer, L. E. Jusinsky and W. K. Bischel, Opt. Lett. **13**, 360 (1988).
[2] D. Husain and L. J. Kirsch, Trans. Faraday Soc. **67**, 2025 (1971).
[3] K. Tachibana and H. Kamisugi, Appl. Phys. Lett. **74**, 2390 (1999).
[4] H. Ito, K. Teii, H. Funakoshi, M. Ito and T. Goto, J. Appl. Phys. **88**, 4537 (2000).
[5] P.W. Seakins and S. R. Leone, J. Phys. Chem., **96**, 4478 (1992).
[6] S. Naito, M. Ikeda, N. Ito, T. Hattori and T. Goto, Japn. J. Appl. Phys. **32**, 5721 (1993).

Control of glow/streamer transition in pulse-driven dielectric barrier discharge

T.Somekawa[1], Y.Kishimoto[1], M.Kubo[1], T.Shirafuji[2], K.Tachibana[1]

[1]Department of Electronic Science and Engineering, and [2]International Innovation Center,
Kyoto University, Yoshida Honmachi, Sakyo-Ku, Kyoto 606-8501, Japan

Abstract

Current-voltage characteristics and optical images have been investigated for an atmospheric pressure dielectric barrier discharge driven by asymmetric pulse voltage supply. We have controlled transitions between glow sustained discharge and streamer sustained discharge by means of changing voltage and frequency.

1. Introduction

Today, plasma process is essential to make micro-electronic devices such as semiconductor, opto-electronic and photo-voltaic devices. The “glow discharge” type of plasma is used for these processing. Glow discharge is uniform discharge. Therefore, it enables uniform treatment of surfaces. As the pressure range of glow discharge is usually 0.01~10 Torr, many plasma processing were done in a vacuum. However, considerable space and time are required, which is disadvantage from economical view points. The processing in atmospheric pressure could be a candidate for overcome this issue.

Dielectric-barrier-discharges (DBDs) are used in atmospheric pressure, and are self-sustained non-equilibrium electrical gas discharges. These are characterized by insulating layers on one or both electrodes or on dielectric structures inside the discharge gap. Due to this structure, continuos current flow and transition to arc discharge are inhibited, which enables operation up to high power levels in

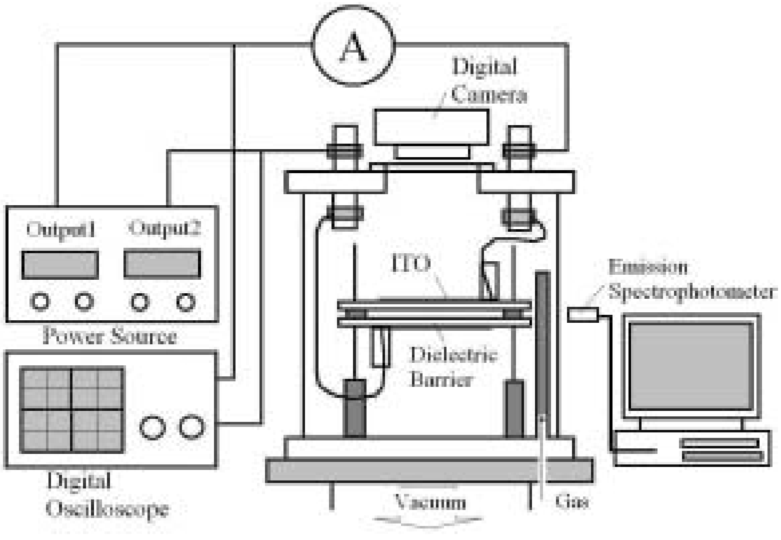

Fig.1 Schematic diagram of experimental equipment.

megawatt range. DBDs are used in many applications such as ozone generation [1], high-power CO_2 lasers [2], excimer lamps [3, 4], plasma display panels and so on. However discharges in these applications are inhomogeneous and have many filamentary discharges [5], which are called “streamers”, which makes it difficult to apply DBDs for uniform surface treatments. Therefore, atmospheric pressure dielectric barrier glow (APDBG) discharges are required. Although APDBG discharges have already been realized[6, 7], higher density plasma is required for faster processing. For achieving high density plasma without transition to filamentary discharges, we are trying to control the transition from glow-sustained and streamer-sustained discharges. In this work, we report on several parameters whichi enable us to control the transition between these two discharge schemes.

2. Experimental equipments

A schematic diagram of experimental equipment is shown in **Fig.1**. We used dielectric plates made of quartz and evaporated Indium-Tin-Oxide (ITO) electrodes on them. The thickness of this plates and ITO electrodes was 1.2 mm and 150 nm, respectively. The diameter of the plates and the electrodes was 100.0 mm and 60.0 mm, respectively. The width of spacers between two electrodes, which were made of Al_2O_3, was 5.0 mm. Power source was connected by copper wire to the electrodes. After pumping of the chamber, discharge gas was introduced into the chamber up to atmospheric pressure through plastic tube. Concerning the pulse-driven power source, duty ratio was fixed at 20%. Frequency was changed from 1 kHz to 14 kHz. Raising time was 10 V/ns. Here, voltage between the electrodes means the value of output1-output2. **Fig.2** shows the shape of output waveform supplied from power

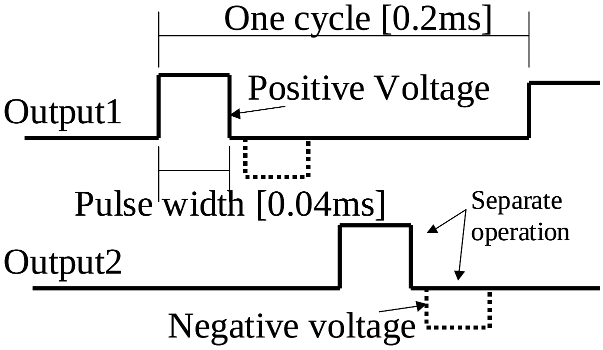

Fig.2 The shape of power source output waveform.

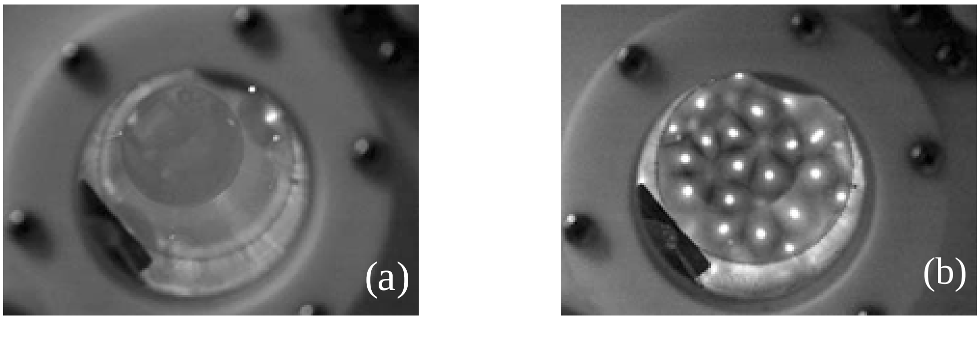

Fig.3 Two types of DBD of Ar opreted pulse voltage source. Top view through dielectric plates. (a) Glow sustained discharge for 3.00kV supply (b) Streamer sustained discharge for 4.00kV supply.

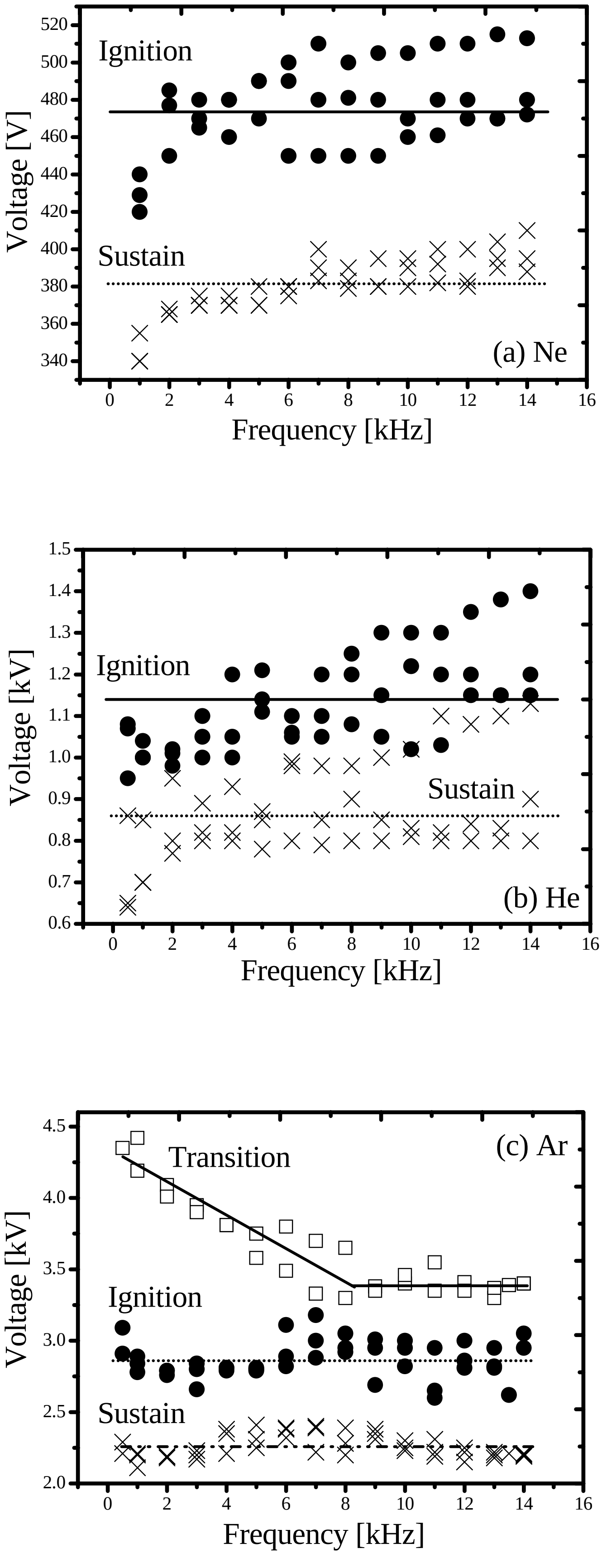

Fig.4 Ignition,Sustain and transiton voltage of atmospheric pressure (a) Ne, (b) He and (c) Ar.

source. Current-voltage (I-V) characteristics were measured by current probe (HP6021). Optical images were taken by a digital camera through the quartz window which was mounted on the top of the chamber. Optical emission was measured by a spectrophotometer and a photomultiplier also from the side of chamber.

3. Results and discussion

3.1. Discharge characteristics

In helium and neon gases, the type of discharge was always glow sustained discharge even when higher voltage was applied. In argon gas, it was also glow sustained discharge when discharge was ignited. However transition from glow- to streamer- sustained discharge happened when higher voltage was applied. When discharge was disappearing, streamer sustained discharges sometimes appeared. **Fig.3** shows optical images of (a) glow- and (b) streamer- sustained discharge. Streamers were filamentary and brighter than glow sustained discharges, and spread over the dielectric surfaces.

3.2. Ignition/Sustain/Transition voltage

Fig.4 show frequency dependence of the ignition, sustain and transition voltages for discharge of neon, helium and argon gases. In all gases, ignition and sustain voltage were almost constant. They did

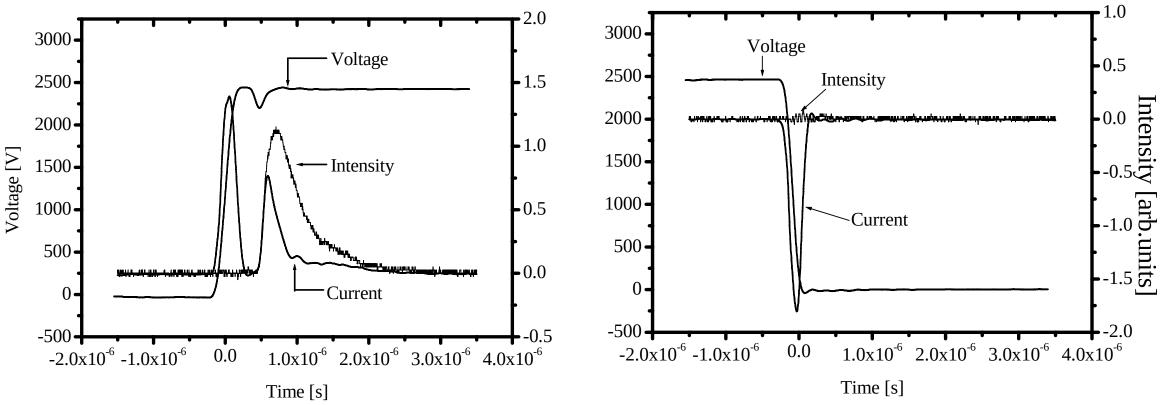

(a) Output1 rising edge.

(b) Output1 falling edge.

Fig.5 Current-voltage characteristics and light emitting for glow-sustained discharge.

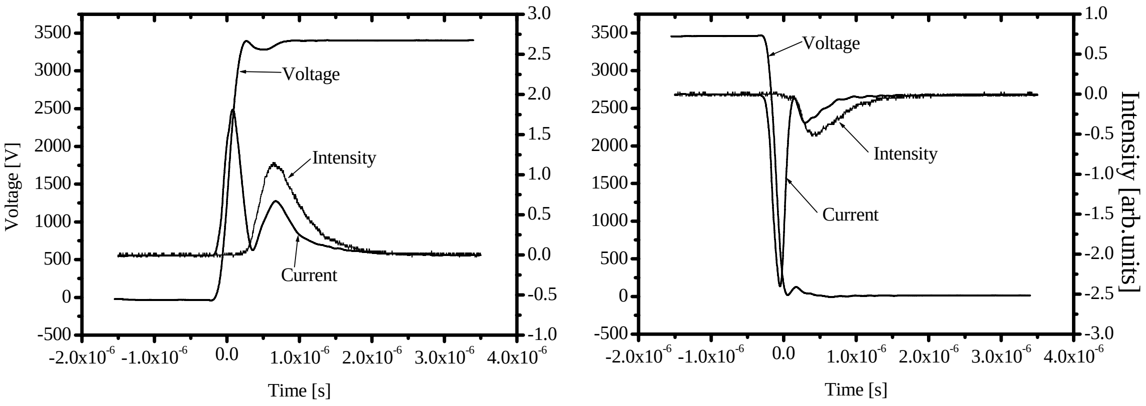

(a) Output1 rising edge.

(b) Output1 falling edge.

Fig.6 Current-voltage characteristics and light emitting for streamer-sustained discharge.

not depend on frequency. In the case of argon gas, transition voltage decreased with increasing frequency and it became almost constant for the frequency higher than 8 kHz.

When sinusoidal voltage was applied, ignition voltage rose at lower frequency [8]. On the contrary, however, it did not occur when pulse voltage was applied. This is due to the fact that rising time of pulse voltage did not depend on frequency. Moreover, when sinusoidal voltage was applied, the transition voltage decreased with increasing frequency [8]. However, as mentioned before, it became almost constant by using pulse-driven power source. This means that uniform and high-speed plasma processing can be realized at high frequency, because increase of frequency means that higher averaged power deposition rate.

3.3. Current-Voltage Characteristics

I-V characteristics and timing of light emission for these two discharge schemes are shown in **Fig.5** and **Fig.6**. In this I-V characteristics, we can see two components, one is for charging into dielectrics and another is discharge current after that. The transition from glow- to streamer- sustained discharge was observed when the time-delay between charging and discharge current became less than 0.5 ms. Simultaneously, peak value of the discharge current decreased and self-erasing discharge occured at failing edges of voltage.

In order to realize uniform glow sustained discharge, we need sufficient supply of charge on dielectric surfaces. As mentioned before, we can see streamer sustained discharge when discharge is disappearing. This is due to the fact that sufficient voltage is not supplied, and distribution of charge on surfaces slants and discharge happened locally. On the other hand, we can see streamer sustained discharge when too high voltage is applied. This is due to the fact that self-erasing discharge occurs, and charges on surfaces locally disappear, and distribution of charges slants.

3.4. Optical emission spectroscopy

Optical emission spectroscopy was performed for these two kinds of discharges. At this moment,

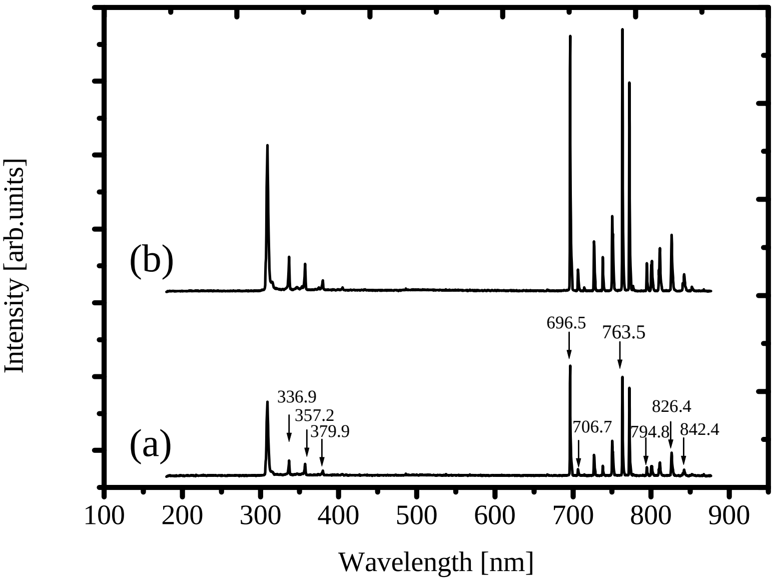

Ar I	[nm]
357.2	
696.5	
706.7	
763.5	
794.8	
826.4	
842.4	
Ar II	[nm]
379.9	
Ar III	[nm]
336.9	

Fig.7 Optical emission spectra of (a) glow- and (b) streamer- sustained discharge of Ar.

only space/time-averaged data was available, which means that the spectrum contains the mixed information from the regions of streamers and glow. Results are shown in **Fig.7**. Although we have expected different spectral profile due to difference in electron temperature in streamer and glow regions, there are no marked differences in the spectral profile except for the total intensity.

4. Conclusion

In this paper, we have presented basic results obtained by asymmetric pulse voltage suppllу for atmospheric-pressure dielectric barrier discharge. However, in order to clarify mechanisms of glow sustained discharge and streamer sustained discharge in detail, we need to measure the distribution of charge on dielectric surfaces.

In addition, refering to this atmospheric-pressure discharge, we are trying to realize micro-scale plasma which can be used for MEMS (Micro Electro Mechanical System), micro TAS (Total Analysis Systems).

Acknowledgement

The authors thank Dr. Y. Sawada and Mr. N. Taguchi for fruitfull discussion on the DBDs and experimental supports. The authors also thank Mr. K. Matsunaga and Haiden Research Laboratory for offering of the unique power source. This work was partly supported by Kyoto Nanotechnology Cluster.

References

[1] R.Hippler, S.Pfau, M.Schmidt and K.H.Schoenbach – Low Temperature Plasma Physics (WILLEY-VCH, Berlin, 2001) Chap.13, p.331

[2] S.Yagi, and N.Tabata, Proc. IEEE/OSA Conf. on Lasers and Opto-Electronics, Washington DC, 22 (1981).

[3] Y.Tanaka, J. Opt. Soc. Am. **45**, 710 (1995).

[4] G.A.Volkova, N.N.Kirillova, E.N.Pavlovskaya, and A.V. Yakovleva, J. Apply. Spectronic. **41**, 1994 (1984).

[5] W.Seimens, Poggendorffs Ann. Phys. Chem. **102**, 66(1857)

[6] S.Kanazawa, M.Kogoma, T.Moriwaki, and S.Okazaki , J. Phys. D **21**, 838 (1988).

[7] M.Kogoma, and S.Okazaki, J. Phys. D **27**, 1985 (1994)

[8] N.Gherardi, and F.Massines, IEEE Trans. Plasma Sci. **29**(2001)

The optimization of discharge conditions for the downstream ashing process with jet-type plasma reactor at atmospheric pressure

K. Tanaka[1], T. Kamada[1] and M. Kogoma[1]

[1] *Department of Chemistry, Faculty of Science and Technology, Sophia University*

Abstract

We tried to use N_2O as an oxygen source for the ashing treatment with a jet-type APG plasma reactor with a wide slit nozzle. The ashing rates of the N_2O plasma were much slower than that of the O_2 plasma. According to the simulation calculation of the oxygen concentration in the plasma gas blew out from the slit, the slow ashing rate was assumed that the oxygen atoms in the plasma gas were quenched by NO generated from the dissociation of N_2O. The fast ashing rate was obtained at the discharge power 600 W, the total gas flow rate 13 $\mathrm{Lmin^{-1}}$ with O_2/Ar gas.

1. Introduction

In the printed wiring board (PWB) industry, cleaning of the land surface on the PWB is an indispensable process for reducing the number of soldering failures [1, 2]. This process has usually been carried out by wet methods. However, the development of a practical dry treatment method is strongly desired to avoid pollution from the chemical baths. In our previous studies, we found that O_2/He or O_2/Ar plasma treatments could ash an organic compound (a photoresist, OFPR-800) in a jet-type reactor at atmospheric pressure; the ashing rate was as rapid as that of some low-pressure plasma treatments [3-5].

The relationships between the plasma parameters and the ashing rate indicated that the ashing rate became faster if one increased the discharge power and the total volume flow rate of gas. However, excessive discharge power generated a discharge between the reactor and the sample; this phenomenon would break the electric devices on the PWD. The other hand, the higher gas flow rate, in turn, increased the gas velocity emerging from the nozzle, thereby reducing the transit time of the gas from the nozzle to the sample surface. Although the shorter transit time made the ashing faster, the much gas flow would increase the treatment cost.

In the present research, to make the ashing rate much faster without increasing the cost, we tried to use N_2O (dinitrogen monooxide) instead of O_2 as an oxygen atom source since we could expect that N_2O plasma would generate more oxygen atoms than O_2 plasma because of the weak N_2-O bond energy. Moreover, we tried to optimize the plasma parameters to obtain the fastest ashing rate.

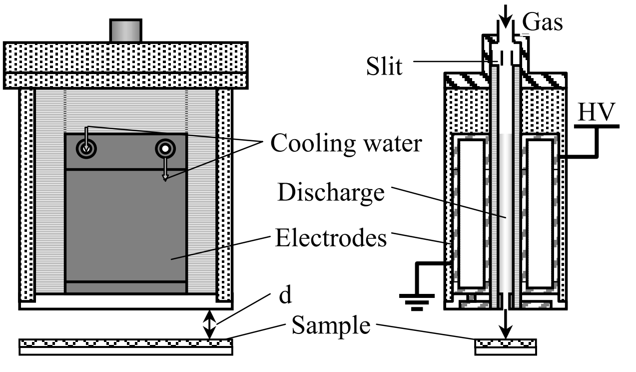

Fig. 1 Schematic diagram of the reactor.

Table 1 Discharge Conditions

Discharge Frequency / MHz	13.56
Discharge Power / W	200 – 800
He or Ar Flow Rate / $\mathrm{L\cdot min^{-1}}$	5 – 9
O_2 or N_2O Flow Rate / $\mathrm{cm^3 min^{-1}}$	25 – 180
Distance, d / mm *1	3.0 - 8.0

*1 The distance from slit to sample surface, as shown with a two-headed arrow in Fig. 1.

2. Experimental

The jet-type reactor used in this study, shown in Fig. 1, was a capacitively coupled reactor, comprising two quartz glass plates between the electrodes. The discharge volume was 5.25 $\mathrm{cm^3}$ (the electrode height was 70 mm). The electrode width was 50 mm and the distance between the quartz glass plates was 1.5 mm. A rectangular slit, of dimensions 0.5 mm × 50 mm, was located at the bottom of the reactor. The ashing treatments were carried out as follows: O_2 or N_2O diluted with He or Ar was introduced from the top of the reactor and made to pass through the discharge zone, following which it blew over the sample, all at atmospheric pressure. Table 1 shows details of the discharge conditions. We used a photoresist, OFPR-800 (Novolak Resin, Tokyo Ohka Kogyo), to simulate an organic impurity in this study [3-5]. The thickness of sample films were about 1.2 μm after being spin-coated on a silicon wafer; each film was pre-baked

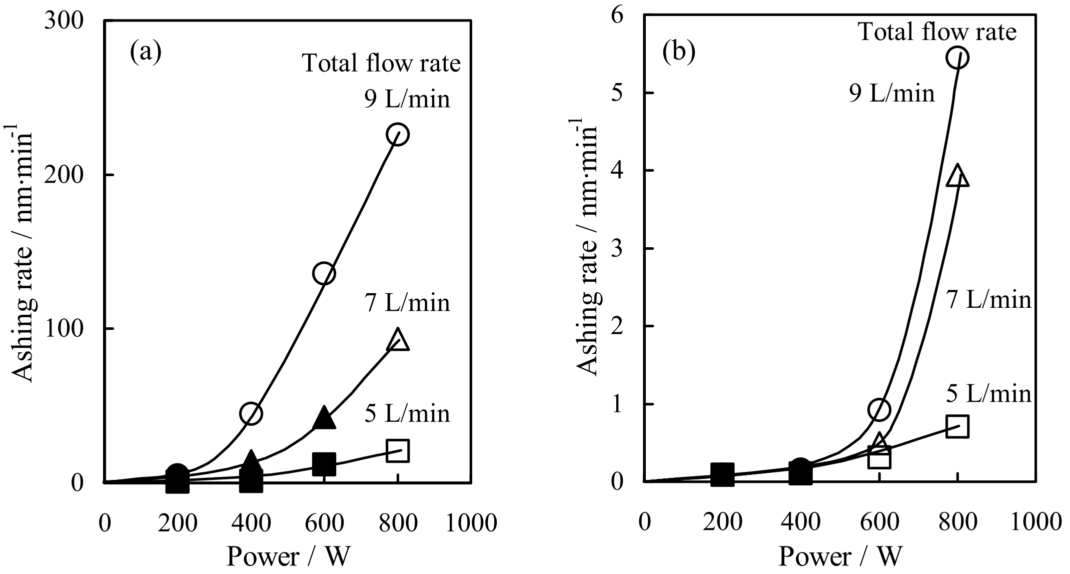

Fig. 2 The variations of the ashing rate as a function of the discharge power on the (a) O_2/He and (b) N_2O/He system. The O_2 content was 1.0 %. The marks show different total flow rates. The open symbols indicate that the plasma blew out from the slit.

at 90 °C for 30 min. The ashing rate was calculated from the resist thicknesses before and after ashing, which were measured with a surface profile measuring system (DEKTAK IIA, Sloan). The details of the thickness measurement were described in Ref. 3.

3. Results and discussion

Figures 2 and 3 show the variation of the ashing rate as a function of the discharge power on the He and Ar systems, respectively. The ashing rates of N_2O plasmas were increased with increasing the discharge power and the total flow rate as same as that of O_2 plasmas. And both results indicated that the ashing rates using N_2O gas were much slower that that of O_2 gas systems. The ashing rate of the open symbols became faster extremely than those of the solid symbols since the plasma blew out from the slit under these conditions. However, those conditions were not suitable for treatment of printed wiring boards where

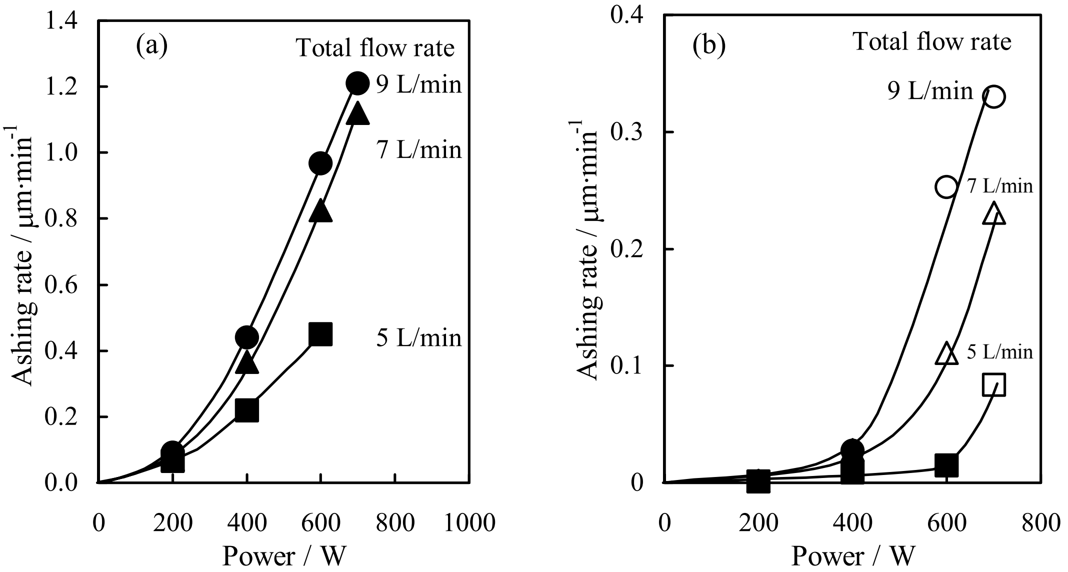

Fig. 3 The variations of the ashing rate as a function of the discharge power on the (a) O_2/Ar and (b) N_2O/Ar system. The O_2 content was 1.0 %. The marks show different total flow rates. The open symbols indicate that the plasma blew out from the slit.

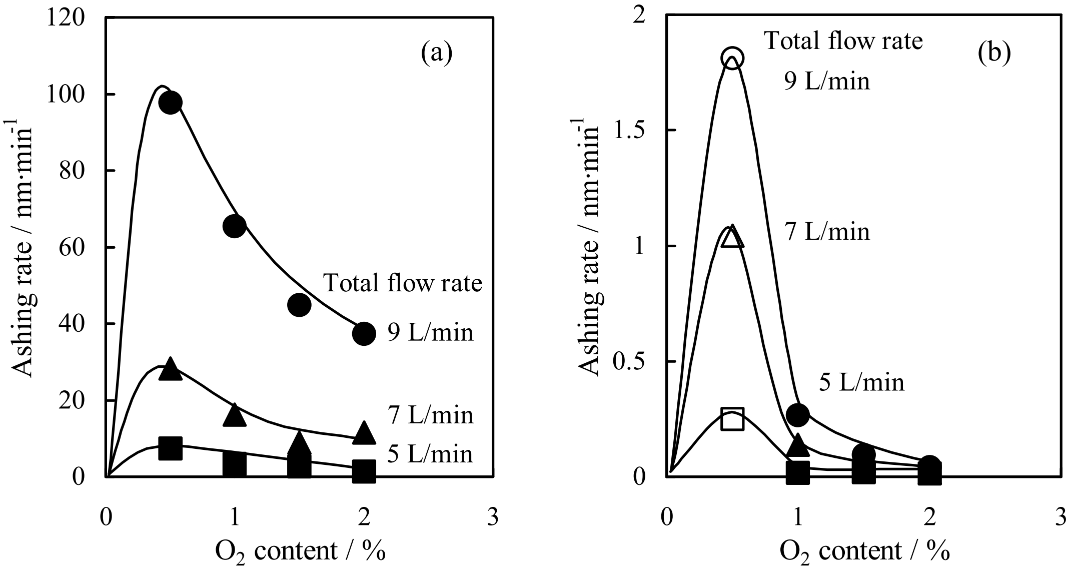

Fig. 4 The variations of the ashing rate as a function of the O_2 content at 400 W on the (a) O_2/He and (b) N_2O/He system. The marks show different total flow rates. The open symbols indicate that the plasma blew out from the slit.

electronic parts were already mounted because the electrons and ions in the plasma might break them.

Figures 4 and 5 show the variations of the ashing rate as a function of the O_2 content at 400 W on the He and Ar system, respectively. The variations of the ashing rate of O_2 plasmas have maximum points. Since the discharge energy per one O_2 was decreased by increasing the O_2 content, we considered that the dissociation reaction of O_2 was reduced. The other hand, although it seems that the variations of the ashing rate of N_2O plasmas have maximum points, we could not obtain more details because the discharge area extended to the sample surface.

Figure 6 shows the dependence of ashing rate on residence time for He and Ar systems. We assumed that the ozone formation (O + O_2) was one of the reasons of the decay of the ashing rate. If that was right, we expected that the decay rate would be decreased if only we used N_2O gas. However, O_2 and N_2O plasmas shown almost the same decay rates. Then, we did a simulate calculation of the time variation of the gas species concentrations, such as oxygen atoms, in the plasma gas blew out from the slit. We used the elementary reactions shown in table 2 for the simulate calculation and carried out the calculation on the

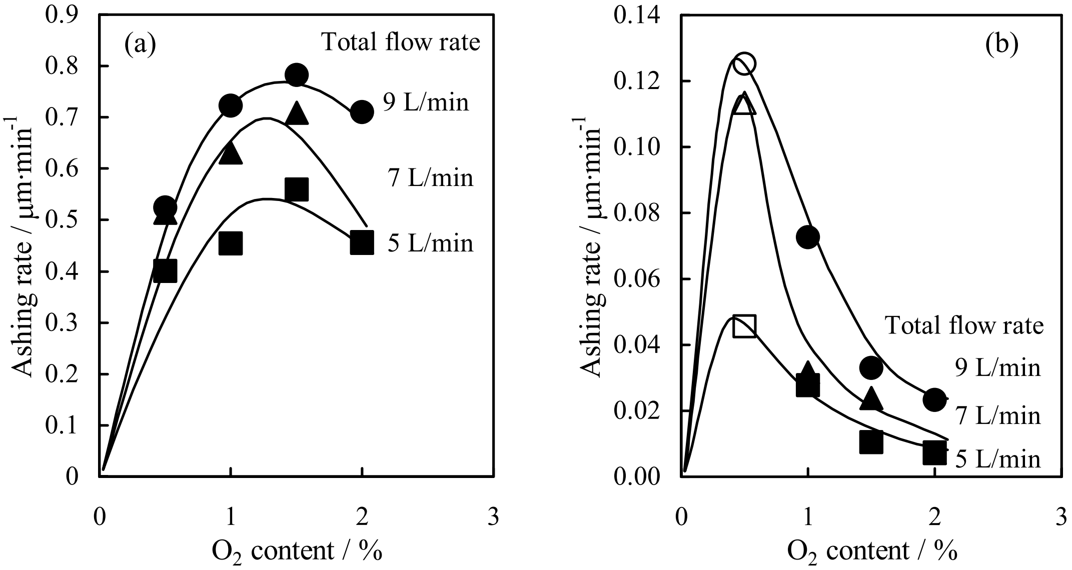

Fig. 5 The variations of the ashing rate as a function of the O_2 content at 400 W on the (a) O_2/Ar and (b) N_2O/Ar system. The marks show different total flow rates. The open symbols indicate that the plasma blew out from the slit.

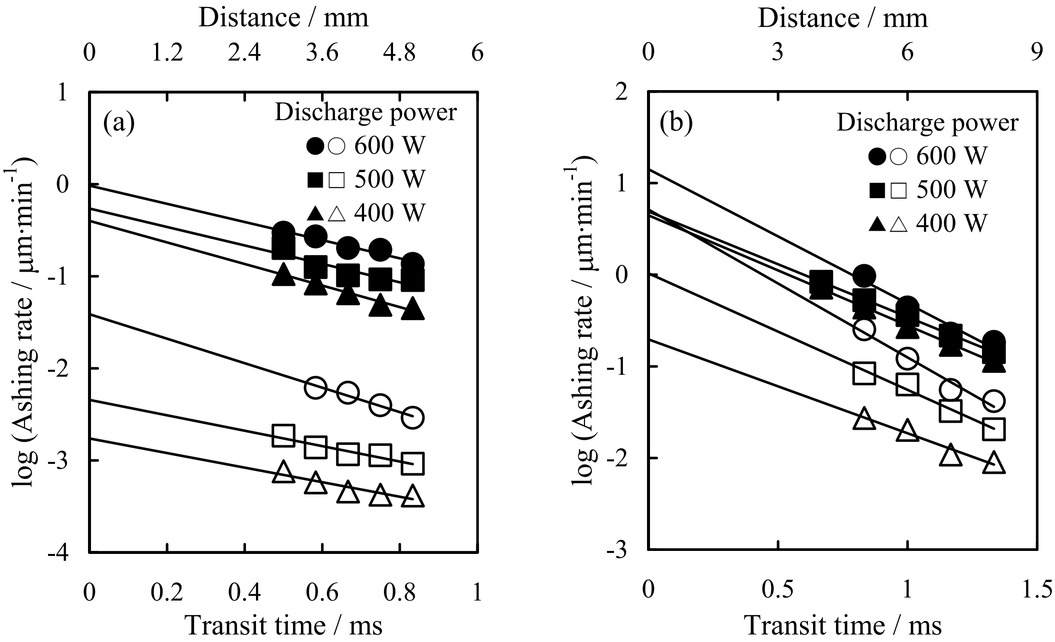

Fig. 6 The dependence of ashing rate on residence time for (a) He and (b) Ar systems. The marks show different discharge powers. The full and open symbols show results of the O_2 and N_2O plasmas, respectively. The plasma conditions were as follows: the gas velocity was 6.0 m·s^{-1}, and the O_2 and N_2O concentrations was 1 %.

different initial concentrations, which were the values at the slit (time = 0). Figure 7 shows the result of the simulation calculation. The round solid symbol shows the result of the O_2 plasma and the others show N_2O plasma. The decay of the N_2O plasma without NO was slower than that of the O_2 plasma as we expected. However, if only there was quite few NO in the plasma gas, the oxygen atoms were quenched via the chain reaction (Reaction No. 8 and 9). In fact, we detected several ppm NO in the N_2O plasma at the slit by means of an NO detector tube. Thus, we considered that the ashing rates of the N_2O plasma were so slow.

According to these results, we concluded that the oxygen gas was the most suitable oxygen atom source; of course, there are the other gas molecules such as SO_2, CO and CO_2. They are, however, toxic or consume the oxygen by itself.

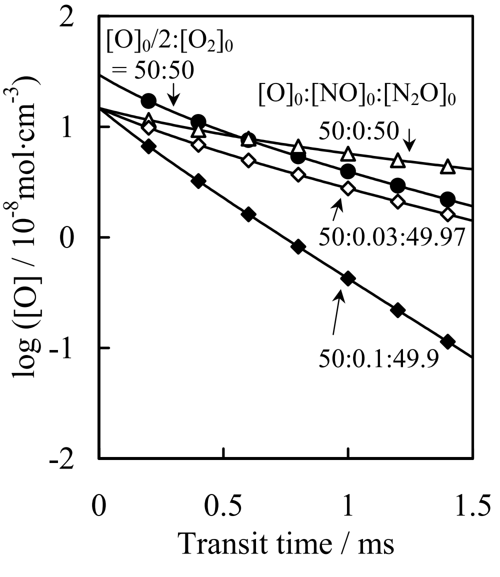

Fig. 7 The time variations of the oxygen atom concentration obtained from the simulate calculation. The marks show different initial concentration ratios.

Table 2 The elementary reactions used for the simulate calculation

No	Reactions		Rate constant / cm^{3}mol^{-1}s^{-1}	Ref.
1	$O + O_2 + M$	$\rightarrow O_3 + M$	$k_1^{2nd} = 2.39\times10^9$	6
2	$O + O + M$	$\rightarrow O_2 + M$	$k_2^{2nd} = 4.67\times10^9$	7
3	$O + O_3$	$\rightarrow 2O_2$	$k_3 = 3.72\times10^{10}$	8
4	$O + N + M$	$\rightarrow NO + M$	$k_4^{2nd} = 8.43\times10^{10}$	9
5	$N + N + M$	$\rightarrow N_2 + M$	$k_5^{2nd} = 1.34\times10^{11}$	10
6	$O + N_2O$	$\rightarrow NO + NO$	$k_6 = 1.20$	11
7	$O + N_2O$	$\rightarrow N_2 + O_2$	$k_7 = 0.355$	11
8	$O + NO$	$\rightarrow NO_2$	$k_8 = 2.01\times10^{13}$	8
9	$O + NO_2$	$\rightarrow O_2 + NO$	$k_9 = 5.21\times10^{12}$	11

T=423.5 K, P=1 atm, [M](≈[He],[Ar])≈2.95×10^{-5} mol cm^{-3}

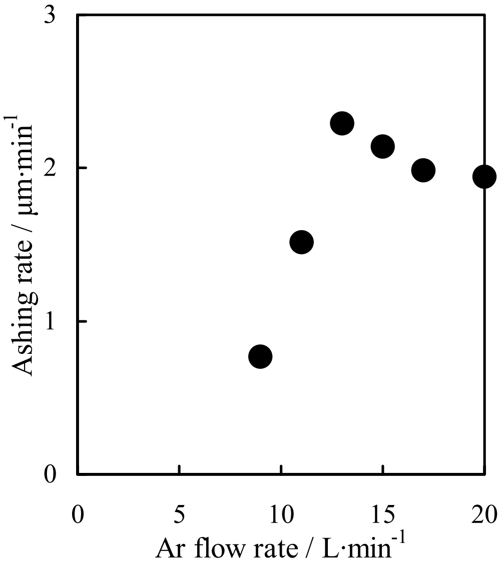

Fig. 8 The variations of the ashing rate as a function of the Ar flow rate. The discharge power was 600 W. The O_2 content was 1.5 %. The distance d was 10 mm.

Finally, to obtain the maximum ashing rate on the reactor used in this study, the discharge parameters were optimized. The O_2/Ar mixture gas was preferred to the O_2/He mixture gas. The discharge power, the oxygen content and the d5stance d were restricted to less than 600 W, more than 1 % and more than 10 mm, respectively, to prevent the occurring the discharge between the slit and the sample. Thus, only the gas flow rate could be changed. Figure 8 shows the variations of the ashing rate as a function of the Ar flow rate. The maximum ashing rate was 2.3 μm·min^{-1}. The reason of the decrease of the ashing rate above 13 L·min^{-1} was only a shortage of the residence time of the gas in the plasma region [4]. Thus, although this maximum value was enough to use this system to the practical use, increasing the discharge volume and the gas flow rate would increase the ashing rate.

References

[1] J. Jellison, IEEE Trans. Parts, Hybrids and Pack., **11**, 3, 206 (1975).
[2] R. D. Rust, D. A. Doane, IEEE Trans. Components Hybrids and Manufacturing Technol., **14**, 573 (1991).
[3] K. Tanaka, T. Inomata and M. Kogoma, Plasmas and Polymers, **4**, 4, 269 (1999).
[4] K, Tanaka and M. Kogoma, Plasmas and Polymers, **6**, 1/2, 27 (2001).
[5] K. Taniguchi, K. Tanaka, T. Inomata and M. Kogoma, J. Photopolymer Sci. Tech., **10**, 1, 113 (1997).
[6] H. Hippler, et al., J. Chem. Phys., **93**, 6560 (1990).
[7] W. Tsang, et al., J. Phys. Chem. Ref. Data, **15**, 1087 (1986).
[8] R. Atkinson, et al., J. Phys. Chem. Ref. Data, **26**, 1329 (1997).
[9] I. M. Campbell, et al., Chem. Phys. Lett. **18**, 607 (1973).
[10] O. M. Knipovich, et al., Russ. J. Phys. Chem., **62**, 867 (1988).
[11] W. Tsang, et al., J. Phys. Chem. Ref. Data, **20**, 609 (1991).

Discharge under a high-pressure carbon dioxide environment up to a supercritical condition

Tsuyohito Ito, Hideyuki Fujiwara, Takaaki Tomai, and Kazuo Terashima

Department of Advanced Materials Science, Graduate School of Frontier Sciences, The University of Tokyo,
5-1-5 Kashiwanoha, Kashiwa-shi, Chiba 277-8561, Japan

Abstract

Dc discharges with 1-μm-gap and 30-μm-gap electrodes and dielectric barrier discharges (gap distance: 30-50 μm) are performed under a high-pressure carbon dioxide environment up to a supercritical condition (T_c: 7.38 MPa, P_c: 304.2 K). Peculiar *Pd* curves in breakdown voltages, which consist of an inflection around 3 MPa and a trough near the critical point, are only observed with a 1-μm gap in this study. Moreover, applying dielectric barrier discharges allows us to generate much more stable discharges under a supercritical carbon dioxide environment than that of a micrometer-scale dc discharge.

1. Introduction

Micrometer-scale discharges have been attracted much interest and studied energetically [1-9]. Micrometer-scale discharges are used in many cases as a method of generating discharge without extremely high temperature under a high-pressure environment, such as an atmospheric-pressure environment. Moreover, micrometer-scale discharge allows easy generation not only under a high-pressure gaseous environment but also under a supercritical fluid (SCF) environment, which is the intermediate state of matter between gaseous and liquid states. The use of SCF offers several advantages for processing [11], particularly in the transport phenomena. During the past decade, these advantages have been successfully applied in materials processing [12, 13, 14], such as very-high-rate ruthenium-catalyzed hydrogenation of carbon dioxide to formic acid [13, 14]. Therefore, discharge in a SCF environment might be promising in processing, due to a combination of merits such as highly activated state of discharge and highly effective transport phenomena of SCF. Also, the discharge might be an unique state and described as being in a complex plasma state, which consists of various species, such as atoms, molecules, clusters, radicals, electrons and ions exhibiting the phenomena of clustering and ionization. Recently, our first trial of discharge generation in a supercritical carbon dioxide (sc CO_2, T_c: 7.38 MPa, P_c: 304.2 K) environment with micrometer-scale-gap platinum coplanar film electrodes (CFE [4, 6]) was performed [8]. Peculiar *Pd* (pressure x distance) curves have been observed, in which there exist a trough in breakdown voltages near the critical point, and an inflection around 2.5 MPa. But the duration time was not long, a few seconds, due to a damage of electrodes.

Here, as a basic study of discharges under a high-pressure gaseous environment up to a supercritical condition of carbon dioxide, which is one of the most promising media in SCFs due to its mild critical point condition and chemical characteristics [11], we report breakdown voltages of dc discharges for 1-μm-gap electrodes and 30-μm-gap electrodes and breakdown voltages of 50-μm-gap dielectric barrier discharges (DBD). Generation of DBD is performed with a motivation to realize a more stable discharge under sc CO_2 environment without extremely high temperature.

2. Experimental

Figure 1 shows a schematic diagram of the apparatus. The apparatus for discharges is almost the same as the previous report [8], except that the internal volume of the cell is approximately 100 cm^3 and a stirrer exists for keeping temperature more uniform. For 1-μm-gap dc discharges, we have employed 1-μm-gap tungsten CFE (as shown as d in fig.1) with 0.5 μm thickness and 50 μm width (*w*), which were produced on the sapphire substrate by a lithography technique. For 30-μm-gap dc discharges, nickel electrodes, made with 250-μm-diameter wire have been employed. Figure 2 shows a schematic diagram of the electrodes used for dielectric barrier discharges. This consists of partially thin quartz tube (thickness: 20 μm) fabricated using micropipette puller (Sutter Instrument Co. P-2000), conductive paste, and tungsten tip, which is fabricated by electrochemically etching for realizing a strong electric field and whose top curvature is about 100 nm, inserted into the tube. The gap distance between the top of the tip and the quartz is about 50 μm. Applied power for DBD is rf-7 kHz, 0-10 kVp-p (offset: 0 V).

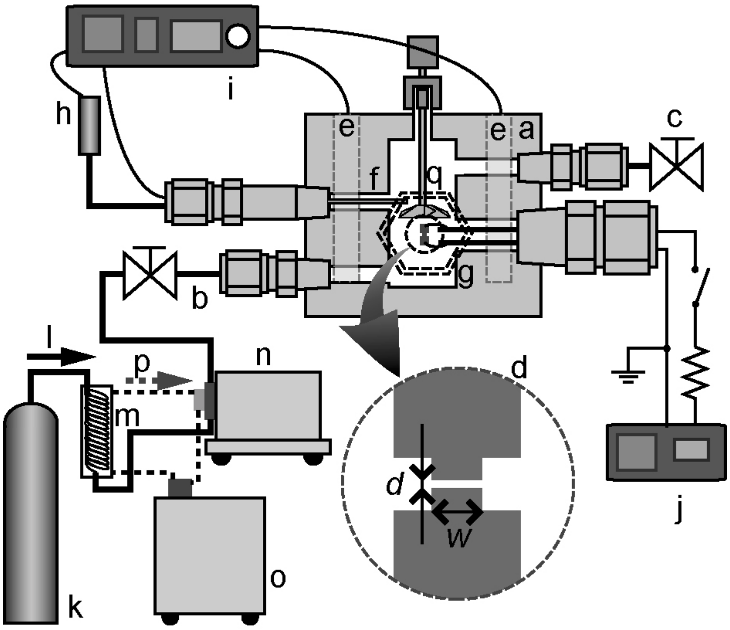

Fig.1 A schematic diagram of the apparatus for the discharge in very high-pressure CO_2, a: SCF cell, b: CO_2 inlet, c: CO_2 outlet, d: electrodes, e: heaters, f: thermocouple, g: window, h: pressure sensor, i: controller, j: DC power source, k: CO_2 cylinder, l: CO_2 flow, m: condenser, n: pump, o: cooling system, p: cooling water flow, q: stirrer.

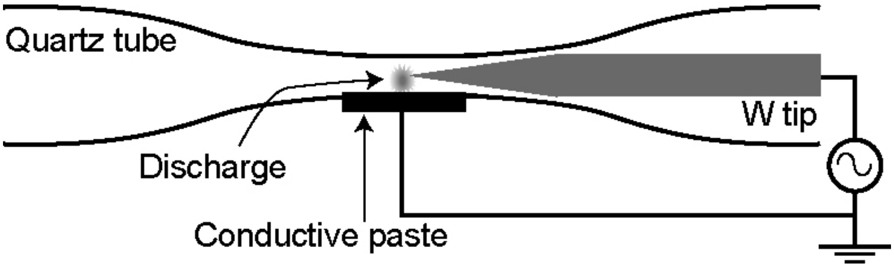

Fig.2 A schematic diagram of the electrodes for dielectric barrier discharges.

3. Results and Discussion

3.1 Breakdown voltages for 1-μm-gap dc discharge

Figure 3 shows breakdown voltages for high-pressure CO_2 as a function of an environmental pressure for 1-μm-gap tungsten CFE at 305.65 K. Compared with a normal Paschen's curve, there exist two peculiar characteristics: inflections at around 3 MPa and troughs near the critical point. The measurements were also performed at 308.15 K and 313.15 K, respectively [10]. From these results, it was confirmed that with the rise in temperature, the location of the trough shifts to the high-pressure range, and the sharpness and the depth decrease. This tendency is similar to the density fluctuations shown in Fig. 4, which typically indicate clustering. The density fluctuation F_D is obtained from the equation [15]

$$F_D = \left\langle (\Delta N)^2 \right\rangle / N = (N/V)\kappa_T k_B T = \kappa_T / \kappa_T^0 , \tag{1}$$

and the isothermal compressibility κ_T is obtained from the reported equation of state [16] using the relation

$$\kappa_T = (-1/V)(\partial V/\partial P)_T , \tag{2}$$

where V is the volume, T is the temperature, N is the number of molecules, k_B is Boltzmann's constant, κ_T^0 is compressibility of a perfect gas, and P is the pressure.

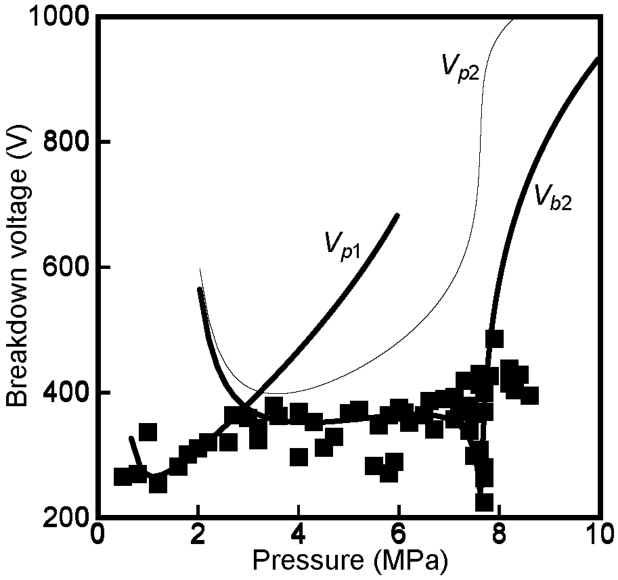

Fig.3 Breakdown voltages for high-pressure CO_2 at 305.65 K as a function of pressure (P) for 1-µm-gap tungsten coplanar film electrodes (CFE), with theoretical curves V_p and V_b.

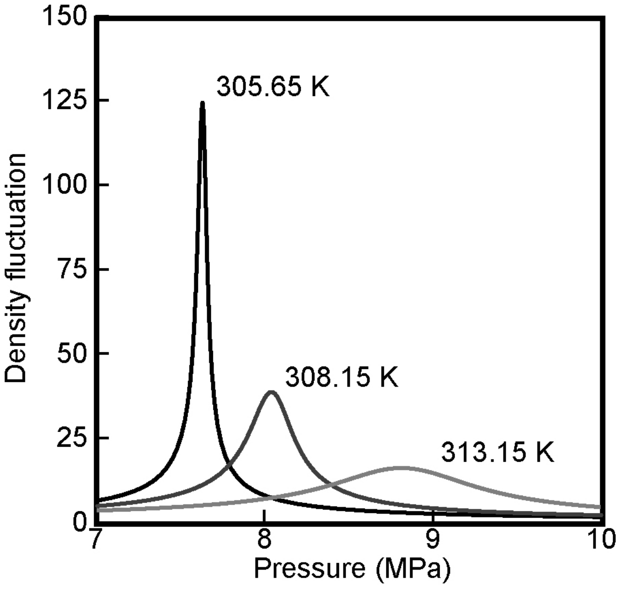

Fig.4 Density fluctuation estimated for temperatures of 305.65 K, 308.15 K, and 313.15 K.

To explain the decrease in pressure environments higher than 3 MPa, we have proposed the correlation between the breakdown voltage V_b and density fluctuation, based on the gaseous breakdown theory [10], to be

$$V_b = \alpha V_p {F_D}^{\beta}, \tag{3}$$

where α and β are individual coefficients. V_p is the breakdown voltage based on the Townsend theory [17] as

$$V_p = \frac{dn\sigma\varphi_i}{AB}\left\{\frac{1}{\ln(dn\sigma)-\ln(\ln(1/\gamma'+1))}\right\} \tag{4}$$

and B is a coefficient associated with Lorentz's internal field [18] and is described as

$$B = \frac{1}{3}(\varepsilon + 2), \tag{5}$$

where d is the interelectrode distance, σ is the electron-to-particle cross section, φ_i is the ionization potential, A is the effective coefficient related to the electrode sharpness, γ' is the second Townsend coefficient, and ε

is the dielectric constant. Third approximation for the density determined from the Clauius-Mossotti function reported by Obriot *et al* [19] was employed for estimation of ε.

$$n = N_A\left[\frac{1}{A_\varepsilon}\left(\frac{\varepsilon-1}{\varepsilon+2}\right)-\frac{B_\varepsilon}{A_\varepsilon}\left\{\frac{1}{A_\varepsilon}\left(\frac{\varepsilon-1}{\varepsilon+2}\right)\right\}^2+\frac{2B_\varepsilon^2-A_\varepsilon C_\varepsilon}{A_\varepsilon^2}\left\{\frac{1}{A_\varepsilon}\left(\frac{\varepsilon-1}{\varepsilon+2}\right)\right\}^3-\cdots\right] \tag{6}$$

where N_A is Avogadro's constant, A_ε, B_ε, C_ε are respectively the first, second, third dielectric virial coefficient. (A_ε, B_ε, C_ε) for 305.65 K, 308.15 K, and 313.15 K are, respectively, (7.363 cm^3mol^{-1}, 56.6 cm^6mol^{-2}, -2725 cm^9mol^{-3}), (7.356 cm^3mol^{-1}, 55.7 cm^6mol^{-2}, -2694 cm^9mol^{-3}), and (7.355 cm^3mol^{-1}, 53.9 cm^6mol^{-2}, -2631 cm^9mol^{-3}). We extrapolated the values of the coefficients for 305.65 K from the values reported by Obriot *et al* [19].

While in the region lower than about 3 MPa (V_{p1} shown in Fig. 3), σ of 8.5 x 10^{-16} cm^{-2} and γ' of 2.0 x 10^{-4} are employed for agreement with the experimental results, in the region higher than about 3 MPa (V_{p2} and V_{b2} shown in Fig. 3), σ of 3.4 x 10^{-16} cm^{-2} and γ' of 2.5 x 10^{-6} are employed. For all estimations, φ_i of 13.77 eV, A of 1.2, α of 1 and β of -0.25 are employed. However, in the high-pressure region above the location of existing troughs, in which the state is believed to be more similar to the liquid state than the gaseous one, these estimations based on the breakdown in the gaseous state probably cannot be employed. This agreement might mean that the decrease of the breakdown voltages can be explained by the clustering near the critical point. The differences of σ and γ', between lower and higher regions than about 3 MPa, probably indicates the possibility of any changes of the environment. Further details about these micrometer-scale discharges are presented elsewhere [10].

3.2 Breakdown voltages for 30-μm-gap dc discharges

Figure 5 shows breakdown voltages for a high-pressure CO_2 at 305.65 K as a function of density for 30-μm-gap nickel electrodes. This indicates $dV/dn > 0$ ($dV/dP > 0$) and $d^2V/dn^2 < 0$. There don't exist any inflections and troughs. From comparison with the results of 1-μm-gap one, the peculiar breakdown voltage curve is probably not only due to the clustering but also due to its scale of plasma. We think that one of the factors occurring this specific phenomena and resulting from its scale (high (electrode area)/(plasma volume) ratio) is an electron attachment by emitted from the cathode to a cluster existing in a dense carbon dioxide, because the density-normalized mobility of negative charge rapidly decreases around 3MPa at 305.65 K [20] and this is believed to indicate that electron attachment to clusters existing in dense carbon dioxide begins at around this point.

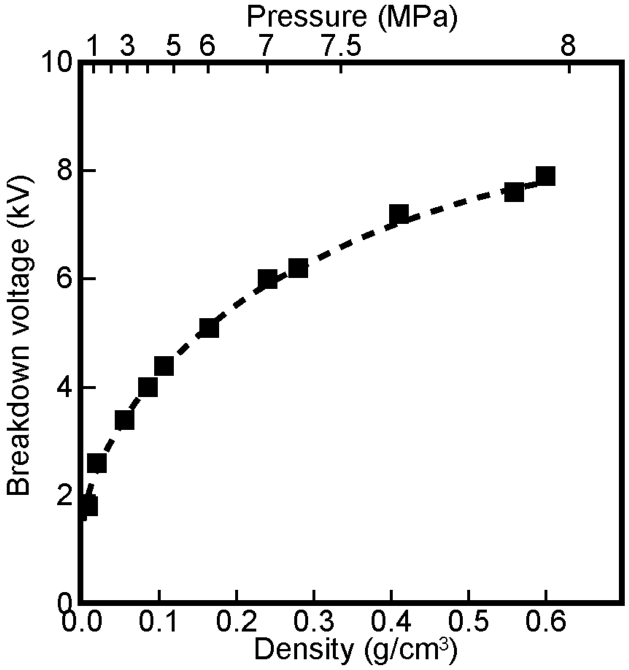

Fig.5 Breakdown voltages for high-pressure CO_2 at 305.65 K as a function of density for 30-μm-gap nickel electrodes.

3.3 Dielectric barrier discharges

The breakdown voltages of dielectric barrier discharges for high-pressure CO_2 at 305.65 K as a function of pressure (*P*) for 50-μm-gap (tip-quartz distance) electrodes were shown in fig.6. There don't exist any troughs and inflections. This might be also due to its scale. However, DBD was successfully generated under a high-pressure CO_2 environment up to a supercritical condition. For the example, figure 7 shows the photograph of DBD under a sc CO_2 environment. Moreover, from the optical emission spectra, which have CO^+ peak near 470 nm and 510 nm, we have also confirmed the generation of CO_2-DBD.

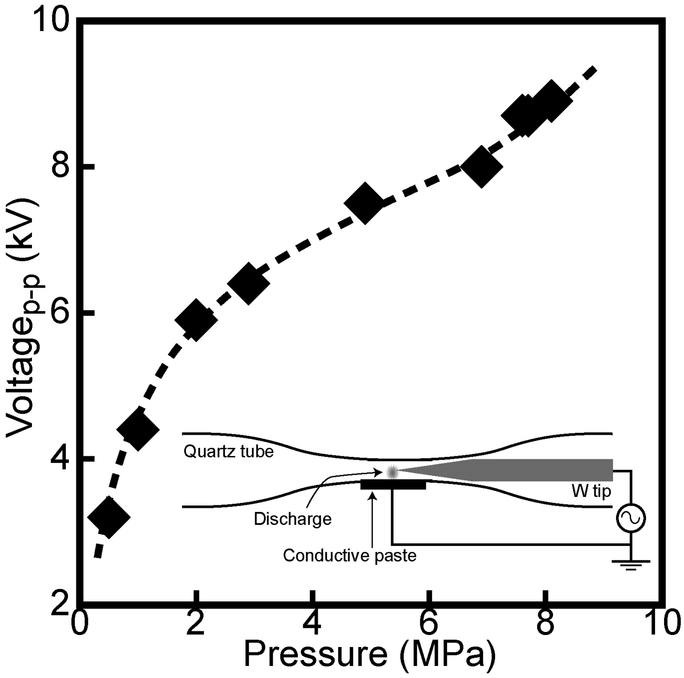

Fig.6 Breakdown voltages (frequency: 7 kHz, offset: 0 V) of dielectric barrier discharges for high-pressure CO_2 at 305.65 K as a function of pressure (*P*) for 50-μm-gap (tip-quartz distance) electrodes.

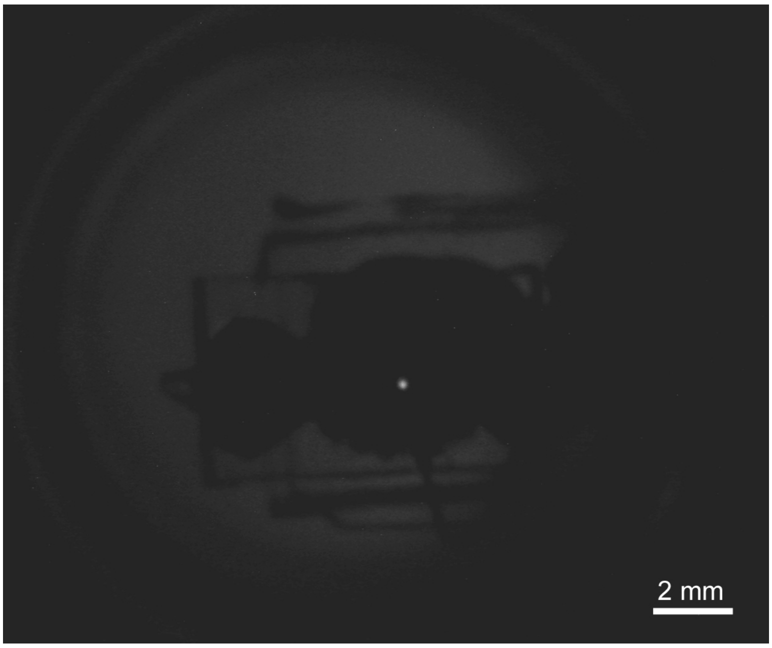

Fig.7 Dielectric barrier discharge under 7.6MPa and 305.65 K with rf power of 7 kHz-8.0kVp-p (offset: 0 V) generated with 30-μm-gap (tip-quartz distance) electrodes.

The duration time was from 2 minutes to 30 minutes: it strongly depends on the condition of electrodes. Although we have not yet confirmed the real factors of the difference of duration time, the increase of top curvature of the tungsten tip after the generation was observed by scanning electron microscope (SEM) measurements and this might be a reason of the disappearance of the discharge resulting from a weaker electric field.

4. Conclusion

We have performed dc discharges with 1-μm-gap and 30-μm-gap electrodes and DBD (50-μm-gap or 30-μm-gap) and measured breakdown voltages under a high-pressure carbon dioxide environment up to a supercritical condition. The peculiar *Pd* curves revealed with 1-μm gap might be not special for dc discharges, but for its smaller scale, which yields higher surface/volume ratio (higher efficiency of the electrodes). Moreover, applying DBD allowed us to generate more stable discharges under a sc CO_2 environment. The duration time of 2-30 minutes is not enough for industrial demands, however, we hope that it will yield new processing with a discharge under a sc CO_2 environments, which have a combination of merits such as highly activated state of discharge and highly effective transport phenomena of SCF, in the near future.

Acknowledgement

The authors are grateful to Professor Yoshida for his discussion and encouragement. This work was supported in part by Grants-in-Aid for the Research Fellowship for Young Scientists to T.I. from the Japan Society for the Promotion of Science.

References

[1] K. Terashima, L. Howald, H. Haefke, H. Guntherodt - Thin Solid Films **282**, 634 (1996).
[2] K.H. Schoenbach, R. Verhappen, T. Tessnow, W.W. Byszewski - Appl. Phys. Lett. **68,** 13 (1996).
[3] J. Hopwood, O. Minayeva, Y. Yin - J. Vac. Sci. & Technol. A **15**, 1220 (1997).
[4] T. Ito, T. Izaki, K. Terashima - Proc. 14th Int. Symp. Plasma Chem. (ISPC-14), ed. M. Hrabovsky, Prague **2**, 967 (1999).
[5] T. Ito, T. Izaki, K. Terashima – Surf. Coat. Technol. **133**, 497 (2000).
[6] T. Ito, T. Izaki, K. Terashima - Thin Solid Films **386**, 300 (2001).
[7] T. Ito, K. Terashima - Thin Solid Films **390**, 234 (2001).
[8] T. Ito, K. Terashima - Appl. Phys. Lett. **80**, 2854 (2002).
[9] T. Ito, K. Terashima - Appl. Phys. Lett. **80**, 2648 (2002).
[10] T. Ito, H. Fujiwara, K. Terashima - submitted.
[11] C. A. Eckert, B. L. Knutson, P. G. Debenedetti - Nature **383**, 313 (1996).
[12] J. M. Blackburn, D. P. Long, A. Cabanas, J. J. Watkins - Science **294**, 141 (2001).
[13] P. G. Jessop, T. Ikariya, R. Noyori - Nature **368**, 231 (1994).
[14] P. G. Jessop, T. Ikariya, R. Noyori - Science **269**, 1065 (1995).
[15] H. E. Stanley - *Introduction to Phase Transitions and Critical Phenomena.* Oxford University Press, Oxford, 1971.
[16] F. Huang, M. Li, L. L. Lee, K. E. Starling, F. T. H. Chung - J. Chem. Eng. Jpn. **18**, 490 (1985).
[17] Y. P. Raizer - *Gas Discharge Physics.* Springer-Verlag, Berlin, 1991.
[18] B. K. P. Scaife - *Principles of Dielectrics.* Clarendon Press, Oxford, 1989.
[19] J. Obriot, J. Ge, T. K. Bose, J. –M. St-Arnaud - Fluid Phase Equilibria **86**, 315 (1993).
[20] F. M. Jacobsen, G. R. Freeman - J. Chem. Phys. **84**, 3396 (1986).

Experimental investigation of characteristics of the glow discharge in air

S.V. Avtaeva, D.K. Otorbaev and A.V. Skornyakov

Kyrgyz-Russian Slavic University, Bishkek, Kyrgyzstan

Abstract

The determination of characteristics of the glow discharge in air using double Langmuir probes, an emission spectroscopy and thermocouple method is reported. The electric field, gas temperature, vibrational temperature of N_2 molecules, electron temperature, and positive ion density as functions of discharge current are determined. The discharge current was adjusted in the range of 5÷25 mA, steady voltage was adjusted in the range of 1000÷2600 V, and air pressure of 10 Pa was maintained.

1. Introduction

In recent years interest to investigations of gas discharges in air or air-like mixtures has increased [1-3]. This connects with using air discharges in different novel technologies such as waste utilization and other. However, glow discharges in air remains not enough studied that caused to complexity of physical-chemical processes as well to only a few applications. In this work characteristics of the glow discharge in air was investigated.

2. Experimental details

Two nickelized copper electrodes with diameter 30 mm and interelectrode distance 60 mm was disposed in the cylindrical glass-steal chamber (diameter – 25cm, height - 23 cm), which was evacuated by a rotor pump to pressure 10 Pa. The thermocouple sensor was used to air pressure control. A steady voltage 1000÷2600 V was applied to electrode, dc current of the glow discharge was varied in the range of 5÷25 mA. The glow discharge characteristics were studied experimentally. Electrotechnical method was employed for observing the current-voltage characteristic. Axial and radial distributions of electric field, plasma density and average electron energy in the glow discharge were determined with probe methods. Radial distributions of gas temperature were determined with thermocouple. Spectral methods were used to observation of emission specter of the glow discharge in air and distributions of nitrogen molecules in the ground electronic state on vibrational energy levels.

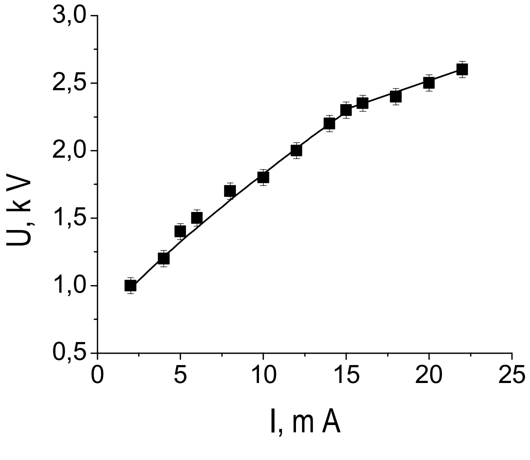

Figure 1. Current –voltage characteristic of the glow discharge in air.

3. Current-voltage characteristic and electric field distribution in the glow discharge

Current-voltage characteristic of the glow discharge in air is shown in figure 1. In particular experimental conditions discharge glowing was abnormal, the steady voltage increases with increasing discharge current. It was observed that discharge resistance at current about 15 mA changes sharply.

Axial and radial distributions of the electric field are shown in figures 2(a) and 2(b). The axial distance was counted off from the cathode and the radial distance was counted off from the discharge axis. As it can be seen in picture 2(a), spaces of the cathode sheath, the dark cathode space, the negative glow, the Faraday’s dark space and the positive column are clearly distinguished in the air glow discharge. The radial distributions of electric field are typical for the positive column of glow discharges. The radial electric field become zero in the axis and increases with a radius, the electric field penetrates far outside the boundaries of a cylinder with electrodes in bases and increases up to the chamber walls.

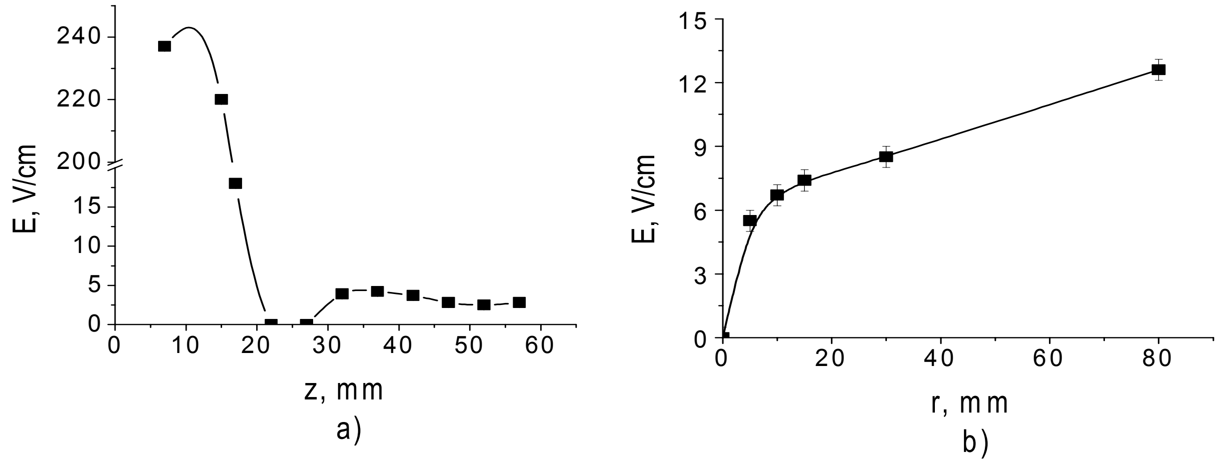

Figure 2. Axial (a) and radial (b) electric field distributions of the glow discharge in air.

Electron temperature and positive ion density

The electron temperature and the positive ion density were measured with the double probe. The double probe has always-negative potential relative to plasma that minimizes the influence of negative ions on probe current. As evaluations showed the negative ions density in the air glow discharge can reach approximately 10÷20% of the electron density. The probe was made from molybdenum wire of diameter 0.14 mm with a free tip length of 4 mm. The probe can be immersed in any position inside the chamber. Calculations of the electron temperature and the positive ion density were made in accordance with a method described earlier [4].

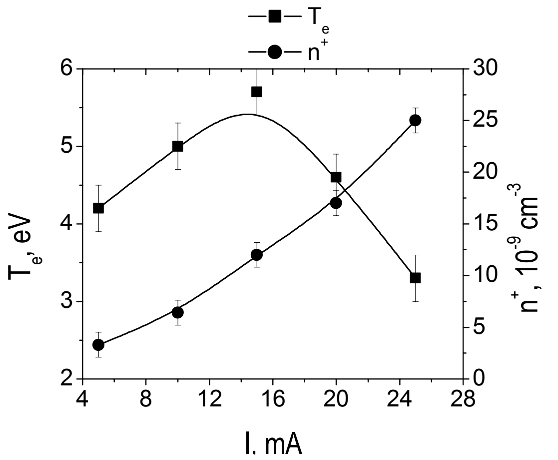

Figure 3. The electron temperature and the positive ion density as a function of a discharge current.

The electron temperature and the positive ion density as functions of a discharge current are shown in figure 3. The electron temperature has maximum at the discharge current 15 mA. The positive ion density increases with increasing discharge current. The dependence of the positive ion density on discharge current changes its behavior at the discharge current 15 mA, the density begins to increase with current rapidly.

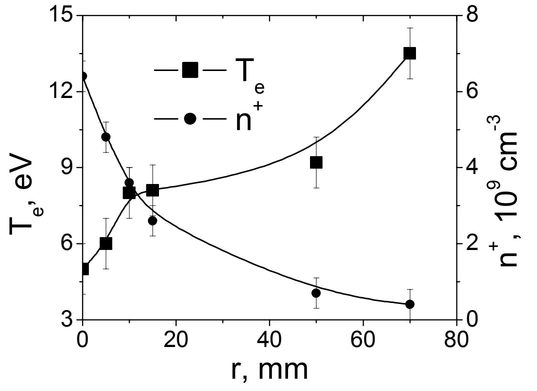

Figure 4. Radial distributions of the electron temperature and the positive ion density.

The positive ion density decreases with radial distance (figure 4), the radial distribution of the positive ion density agrees with the classic theory of the positive column (the diffusion regime) [5] only qualitatively. This is, possibly, because of the glow discharge is not limited by pipe walls. Non-limited discharge volume causes also to the positive ion density not vanish at the radial distance, being approximately equal to the electrode radius (R_e=15 mm). The space of week discharge glow is observed up to the radial distance of 50 mm at discharge current 10 mA.

The electron temperature increases with a radial distance. Apparently, this caused to increase of the

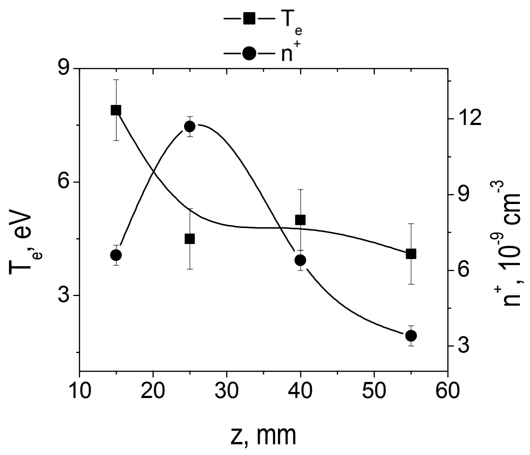

Figure. 5. Axial distributions of the electron temperature and the positive ion density.

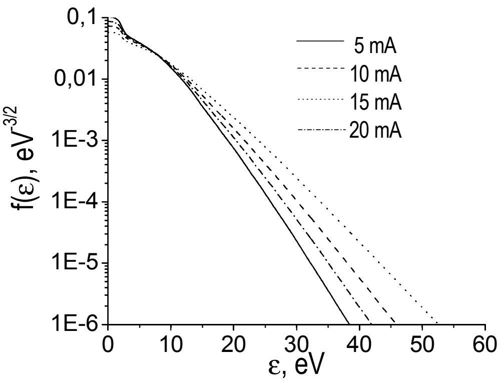

Figure 6. EEDF in the glow discharge in 78%N_2:21%O_2:1%Ar mixture, E/n=240 Td; 1-culculated with BOLZIG; 2-Maxwellian for <ε>=4эВ.

radial electric field and to exit of fast electrons beyond the glow discharge spaces because of absence of wall limited the discharge.

Axial distributions of the electron temperature and the positive ion density are shown in figure 5. Maximum in the positive ion density is observed in the negative glow space. In the dark cathode space the positive ion density is significantly lower. The positive ion density decreases monotonic with the distance from cathode in the positive column. The electron temperature (average electron energy) has maximum in the cathode sheath, where the large electric field exists. In this space of the discharge the electron temperature decreases following decrease in electric field.

In spaces of the Faraday's dark space and the positive column the electron temperature is practically constant in so far as electric field is low and changes slowly.

5. Electron energy distribution function

The electron energy distribution function (EEDF) in the positive column of the glow discharge was calculated for experimental values of the parameter E/n, with E denoting the electric field and n denoting the gas density. The program "BOLZIG" of Kinema software & CPAT [6] was used for calculation of EEDF. The program allows to calculate EEDF in two-terms approximation for local values of the parameter E/n. Air composition was assumed as mixture of 78% N_2-21%O_2-1%Ar. Typical shapes of the calculated EEDF is shown in figure 6. As it can be seen in figure 6, the EEDF in the glow discharge in air is not Maxwellian-like, the EEDF is depleted by fast electrons.

6. Gas temperature

Measurements of the gas temperature were carried out by thermocouple. The gas temperature in the positive column at the glow discharge axis varies in the range of 320÷420 K, when discharge current increase from 5 mA to 25 mA. The gas temperature decreases in radial direction, near chamber wall the gas temperate approaches to the room temperature.

7. Glow discharge spectrum

Emission spectrum of the glow discharge in air was observed in the wavelength range between 350 and 800 nm. A high-resolution spectrograph DFS-8-3 and photomultiplier were used for recording the spectrum intensity. Molecular bands of the first and second positive systems of nitrogen, the first positive system of nitrogen ions, the atmospheric system of oxygen, the first negative system of oxygen ions, the red system of cyan and atomic lines of the Balmer series of hydrogen were observed in the spectrum of the glow discharge.

8. Vibrational excitation of nitrogen molecules

Distributions of nitrogen molecules on vibrational levels of the excited $N_2(C^3\Pi_u)$ and ground $N_2(X^1\Sigma^+_g)$ states in the air glow discharge were experimentally investigated. The intensities of vibrational bands of the second positive system (2 PS) of nitrogen ($C^3\Pi_u$-$B^3\Pi_g$ –transition, Δv=-2) were used to studying the excited state $N_2(C^3\Pi_u)$ vibrational distribution function. The (0-2), (1-3), (2-4) and (3-5) vibrational bands of the 2 PS with wavelengths of 380.4 nm, 375.5 nm, 371.0 nm and 367.1 nm, respectively, were observed. The

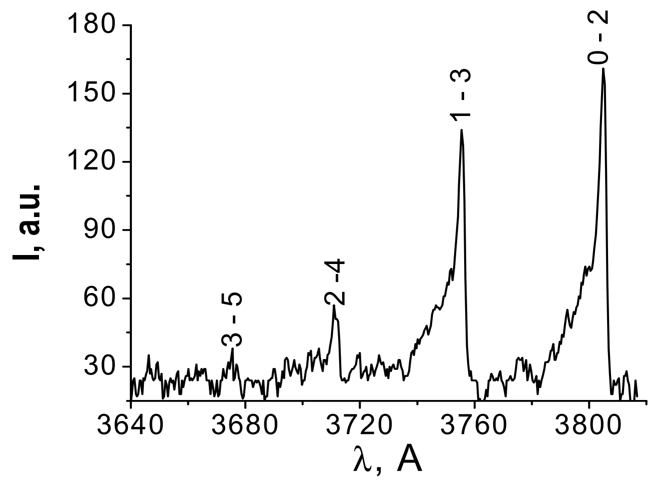

Figure 7. Molecular bands of second positive nitrogen system (Δv = -2) emitted by the glow discharge in air. P=10 Pa, I= 10 mA.

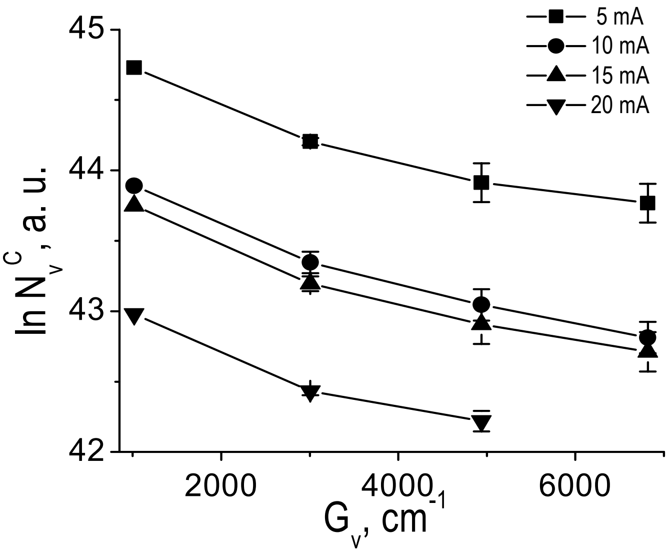

Figure 8. Distribution of nitrogen molecules on vibrational levels of the exited electronic state $C^3\Pi_u$ in the air glow discharge.

typical view of molecular bands of second positive nitrogen system (Δv = -2) emitted by the glow discharge in air is shown in figure 7. The total emitted intensity of the vibrational band is determined as

$$I_{v'v''}=C'S_e\nu_{v'v''}{}^4\cdot N_{v'}q_{v'v''}\ , \qquad (1)$$

where S_e is the electronic transition strength, $\nu_{v'v''}$-is the transition frequency, $q_{v'v''}$ is Franck-Condon factor, $N_{v'}$ is the population of the v'-vibrational level of the $N_2(C^3\Pi_u)$ state and C' is a constant. Typical distributions of nitrogen molecules on vibrational levels of the exited electronic state $C^3\Pi_u$ in the air glow discharge are shown in figure 8 . As it can be seen, distributions of nitrogen molecules on vibrational energy levels of the excited $N_2(C^3\Pi_u)$ state are non-Maxwellian. Detailed analysis showed that this distributions are close to Treanor distribution [7]:

$$f_T(v)=\text{const}\cdot\exp(-\frac{\hbar\omega v}{T_v}+x_e\frac{\hbar\omega v^2}{T_g})\ ,(2)$$

where ħω is quantum of the vibrational energy, x_e is correction for non-harmonic vibration, T_g is gas temperature, T_v is vibrational temperature of the first level, determined as

$$T_v=-(E_2-E_1)/(\ln N_2-\ln N_1).$$

Hier E_1, E_2 denote energies of first and second vibrational levels, N_1, N_2 denote populations of the levels and v denotes vibrational quantum number.

Populations of vibrational levels of the excited state $N_2(C^3\Pi_u)$ are related to vibrational distribution of nitrogen molecules in ground state $N_2(X^1\Sigma^+_g)$ as [8]

$$N_{v'_c}=c\cdot\frac{\sum_{v''_x} q_{v''_x v'_c}\cdot\sqrt{\varepsilon^*_{v''_x v'_c}}\cdot f(\varepsilon^*_{v''_x v'_c})\cdot\varphi(v''_x)}{\sum_{v''_b}\left|R_e(r_{v'_c v''_b})\right|^2\cdot q_{v'_c v''_b}}$$

(3). Hear $N_{v'_c}$ is population of v′-vibrationallevel of $N_2(C^3\Pi_u)$ state, $q_{v''_x v'_c}$, $q_{v'_c v''_B}$ is Franck-Condon factors for transitions $X^1\Sigma^+_g \leftarrow C^3\Pi_u$ [9] and $C^3\Pi_u \rightarrow B^3\Pi_g$ [10], respectively, $\varepsilon^*_{v''_x v'_c}$ is threshold value of excitation energy, f(ε) is EEDF, φ(v″$_x$) is the ground state vibrational distribution function of molecules, $R_e(r_{v'_c v''_B})$ is the momentum of electronic transition [11], assuming constant $R_e(r_{v'_c v''_B})$ =12. Threshold values of $X^1\Sigma^+_g$, v''→ $C^3\Pi_u$, v' transition energy were calculated with using molecular constants from work [12].

The expression (3) was used to derivation of the ground state vibrational distribution function of nitrogen molecules from determined molecule vibrational distribution in the excited state $N_2(C^3\Pi_u)$. Ground state

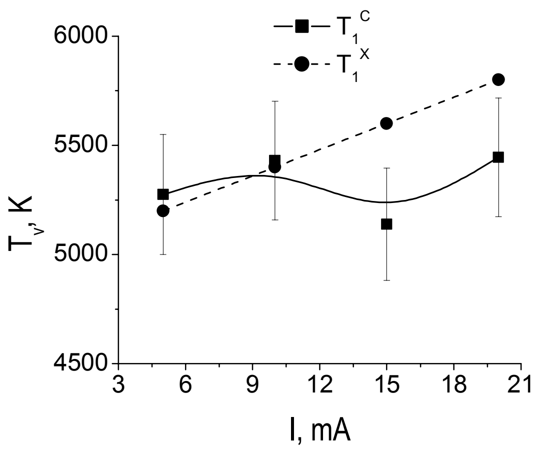

Figure 9. Vibrational temperatures of first vibrational level of N2 ($C^3\Pi_u$) and N_2 ($X^1\Sigma_g^+$) states as a function of the discharge current.

vibrational distribution functions were selected when experimental and calculated N_2 molecule vibrational distributions in the excited state $N_2(C^3\Pi_u)$ coincided well. Maximal agreement between experimental and calculated N_2 molecule vibrational distributions in the excited state $N_2(C^3\Pi_u)$ was reached for the Treanor-like ground state vibrational distribution function. So ground state vibrational distribution functions are close to the Treanor distribution function. Vibrational temperatures of the first vibrational level of the exited ($C^3\Pi_u$) and the ground ($X^1\Sigma_g^+$) states of nitrogen as a function of the discharge current are shown in figure 9.

The evaluated values of different excitation and de-excitation flows for the first vibrational level of the ground state $N_2(X^1\Sigma_g^+)$ are presented in table 1. The two-level scheme, consisted from zero and first vibrational levels, is used for evaluations of the flows. The values k_{eV}=2,5·10^{-9} см^3/с, k_{VT}^{N2} =10^{-18} см^3/с, k_{VV}^{N2}=5·10^{-14}см^3/с were used for rate coefficients of vibrational excitation by electron impact, VT-relaxation and VV-relaxation [7, 13]. The rate coefficient of de-excitation by electronic impact was calculated with principle of the detail equilibrium. For rate coefficients of the non-resonant V-V' exchange on oxygen molecules $k_{VV'}^{O2}$, the V-T relaxation on oxygen molecules k_{VT}^{O2} and argon atoms k_{VT}^{Ar} were used values $k_{VV'}^{O2}$ =5·10^{-15} см^3/с, k_{VT}^{O2}=10^{-17} см^3/с and k_{VT}^{Ar}=10^{-19} см^3/с, which satisfy to conditions $k_{VV}^{N2} > k_{VV'}^{O2}$, $k_{VT}^{O2} > k_{VT}^{N2}$ and $k_{VT}^{Ar} < k_{VT}^{N2}$.

Table 1. The excitation and de-excitation flows for the first vibrational level of the ground state $N_2(X^1\Sigma_g^+)$ evaluated for the air glow discharge at current 10 A.

Reaction	eV - excitation	eV' - de-excitation	VT – relaxation on N_2	VT – relaxation on O_2	VT – relaxation on Ar	Resonant VV – exchange	Non-resonant VV' – exchange
Flow, см$^{-3}$с$^{-1}$	1,7 ·10^{16}	8,6 ·10^{15}	6,0 ·10^{11}	2,5 ·10^{13}	1,2 ·10^{9}	1,5 ·10^{16}	6,2 ·10^{14}

Evaluations showed that the strong vibrational-vibrational exchange between nitrogen molecules in zero and first vibrational levels of the ground state has a decisive effect on population of the first vibrational level. As it was be shown in the original work [7], the vibrational-vibrational exchange results in formation of the Treanor-like molecule distribution on vibrational energy levels.

9. Conclusions

As one would expect, thermal equilibrium in the air glow discharge not exists ($T_e >> T_v >> T_g$), EEDFs are non- Maxwellian and molecule distributions on vibrational energy levels are different from the Boltzmann distribution. Experimental investigations of nitrogen molecule distribution on vibration energy levels were sown that Treanor-like vibrational distribution of nitrogen molecules in the excited ($C^3\Pi_u$) and ground ($X^1\Sigma^+_g$) states are released in the air glow discharge.

Radial distributions of the electron temperature and the positive ion density in the positive column of the discharge not correspond to classic theories of the positive column in diffusion regime. The glow discharge is strong non-uniform in radial direction. Interest induces a rise in intensity of radial electric field and the electron temperature outside the electrode boundaries up to chamber walls. On periphery of the discharge electron temperature increases with approaching to chamber wall where it reaches the value of 10-15 eV. Charged particles and electric field embrace a space, exceeding size of the cylinder with electrodes in bases. Axial distribution of electric field in the discharge is typical for glow discharges. Axial distributions of the positive ion density and the electron temperature are close to typical distributions of the parameters in glow discharges in pipes.

Referenses

[1] I.A.Kossyi, A.Yu Kostinsky, A.A. Matveyev and V.P. Silakov – Plasma Sourses Sci. Technol. **1**, 207 (1992).

[2] St. Kröpke and A.Holländer- ISPC-15. Orlean. France. **4**, 1503 (2001).

[3] V.Guerra and J. Loureiro - Plasma Sourses Sci. Technol. **8**, 110 (1999).

[4] O.V. Kozlov - Electric probe in plasma. Moscow. Atomizdat (1969).

[5] V.L. Granovsky - Electric current in gas. Established current. Moscow. Nauka (1971).

[6] W.L. Morgan, J.-P. Boeuf and L.C. Pitchford - KINEMA SOFTWARE & CPAT. http://www.kinema.com

[7] V.D.Rusanov, A.A.Fridman - Physics of chemical active plasma. Moscow. Nauka (1984).

[8] V.N. Ochkin, S.Yu. Savinov, N.N.Sobolev - Works of PI AS. Moscow. Nauka. **157**, 62 (1985).

[9] R.N. Zare, E.O. Larson and R.A. Berg - J. Molec. Spectr. **15**, No.1 (1965).

[10] W. Benesch, J.T. Vanderslice, S.G. Tilford. et al. - Astrophys. J. **144**, 408 (1966).

[11] A.A. Kon'kov, V.Ya. Neiland, V.M. Nikolaev et.al. – High Temperature. **7**, 140 (1969).

[12] K.P. Huber and G. Herzberg - Constants of diatomic molecules. Moscow. Mir. V. **2** (1984).

[13] K.A. Vereshyagin, V.V. Smirnov and V.A. Shakhatov.-JTP. **67**, 34 (1997).

Steam reforming of hydrocarbons and alcohols using non-equilibrium pulsed discharge

Y. Sekine[1], K. Urasaki[1], S. Kado[2], S. Asai[1], M. Matsukata[1] And E. Kikuchi[1]

[1] *Department of Applied Chemistry, Waseda University, Tokyo, Japan*
[2] *Department of Mechanical Engineering and Science, Tokyo Institute of Technology, Tokyo, Japan*

Abstract

For the purpose of hydrogen production and supply for PEMFC, steam reforming of various hydrocarbons and alcohols using non-equilibrium pulsed discharge was investigated under the conditions of low temperature (393 K) and atmospheric pressure without a catalyst. In each case, steam reforming proceeded without coking and hydrogen was produced as a main product. Moreover steam reforming using non-equilibrium pulsed discharge has a lot of advantages such as fast start-up, quick response and simple and small system, which catalytic steam reforming does not have.

1. Introduction

In recent years, fuel cells have attracted a lot of attentions because fuel cells have high energy efficiency and clean exhaust gases. Above all, proton exchange membrane fuel cell (PEMFC) is expected to be applied for transportation applications and small-scale power generation due to its small size, light weight, and low operating temperature (~ 363 K). One of the problems of commercializing PEMFC is the difficulty regarding hydrogen supply. Because hydrogen is gaseous fuel, transportation and storage are very difficult and energy per weight is low. Therefore, hydrogen production by steam reforming of natural gas, LPG, gasoline, methanol and ethanol is very attractive technology of supplying hydrogen for PEMFC. Table 1 shows the steam reforming reactions of various hydrocarbons and alcohols.

Unfortunately, catalytic steam reforming has some difficulties. In case of steam reforming of natural gas, LPG and gasoline, which can be using the existing infrastructure, steam reforming reaction of hydrocarbon is strongly endothermic as shown in table 1 and high reaction temperature is required. The high reaction temperature restricts the selection of materials for reactor, causes very slow start-up and enlarges and complicates the PEMFC systems. Above all, the drawback of slow start-up is fatal in case of transportation applications. Moreover, coking(1), (2) and deactivation of a catalyst decrease the operating time of PEMFC systems and make it difficult to quickly adjust the amount of hydrogen produced. Every steam reforming catalyst has these difficult problems. On the other hand, ethanol is very attractive fuel because it can be produced from various renewable sources. However steam reforming of ethanol has the same problems as steam reforming of hydrocarbons has, due to its high reaction temperature or deactivation of a catalyst. In case of steam reforming of methanol, the high reaction temperature is not required. However the obstacles of slow start-up and responsiveness and deactivation and coking of a catalyst remain.

Table 1 Steam reforming reactions

Reaction	ΔH° / kJ*mol^{-1}	Reaction temperature
$CH_4 + H_2O \rightarrow CO + 3H_2$	206	700 ~ 1000 K
$C_3H_8 + 3H_2O \rightarrow 3CO + 7H_2$	498	700 ~ 1000 K
$C_6H_{14} + 6H_2O \rightarrow 6CO + 13H_2$	955	700 ~ 1000 K
$CH_3OH \rightarrow CO + 2H_2$	91	~ 500 K
$CH_3OH + H_2O \rightarrow CO_2 + 3H_2$	50	~ 500 K
$C_2H_5OH + H_2O \rightarrow 2CO + 4H_2$	256	~ 800 K

In this study we investigated how non-equilibrium pulsed discharge can be used in the steam reforming of hydrocarbons and alcohols under conditions of atmospheric pressure and low temperature (393 K) without a catalyst. As its name suggests, this discharge is one of the non-equilibrium plasmas(3), (4), (5), (6). When exposed to a pulsed discharge, a large amount of electrons can be irradiated (30 - 40 A) in very short time (less than 1 μs) at constant intervals (in the order of milliseconds). Molecules decomposed by electron impact even if they were very stable molecules like methane. Because of the very short irradiation time, discharge can be kept stable under atmospheric pressure and the supplied energy can be held down. Moreover, the temperature of gas phase do not increase despite very high electron temperature; thus, useless side-reactions can be suppressed. So far, this method can be utilized effectively for acetylene synthesis, dry reforming and other applications(7), (8).

2. Experimental

In all experiments a quartz tube of 4.0 mm inner diameter was used as a flow type reactor as shown in Fig. 1. Two stainless steel rods of 2.0 mm diameter inserted from each end of the quartz tube were used as electrodes. A power supply (Matsusada precision inc. HARb-40R30) was used to produce non-equilibrium pulsed discharge and discharge occurred between the gap of the rods. Reaction temperature was set at 393 K for the sole purpose of preventing condensation of reactant gases such as steam, higher hydrocarbons and alcohols. No catalyst was used. All products were analyzed using gas chromatography equipped FID and TCD (Shimadzu GC14-B) and GC-MS (Shimadzu QP1100EX). The waveforms of current and voltage were observed by means of a digital signal oscilloscope (Lecroy 9314C).

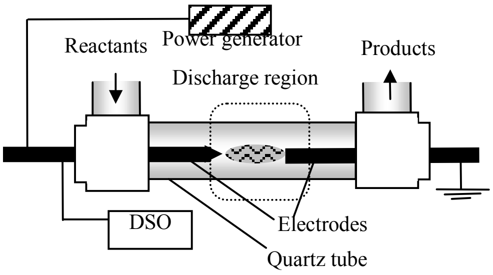

Fig. 1 experimental setup and configuration

3. Results and discussion

3.1 Steam reforming of methane using non-equilibrium pulsed discharge

Fig. 2 shows the current and voltage waveforms of non-equilibrium pulsed discharge and energy injection on various pulse frequencies. The energy injection was calculated according to following equation [1] using current and voltage waveforms.

$$\text{Energy injection} = F * \sum\{(V_{i+1} + V_i)/2\}\{(I_{i+1} + I_i)/2\}(t_{i+1} - t_i) \quad [1]$$

F, V_i, I_i, and t_i are respectively, pulse frequency in hertz, voltage in volts, current in amperes and time in seconds.

As shown in Fig. 2(A), the irradiation time was very short less than 1 μs and the current and voltage waveforms were not influenced by pulse frequency, dramatically. Therefore, the energy injection increased in proportion to pulse frequency. By changing the pulse frequency, we controlled the energy injection.

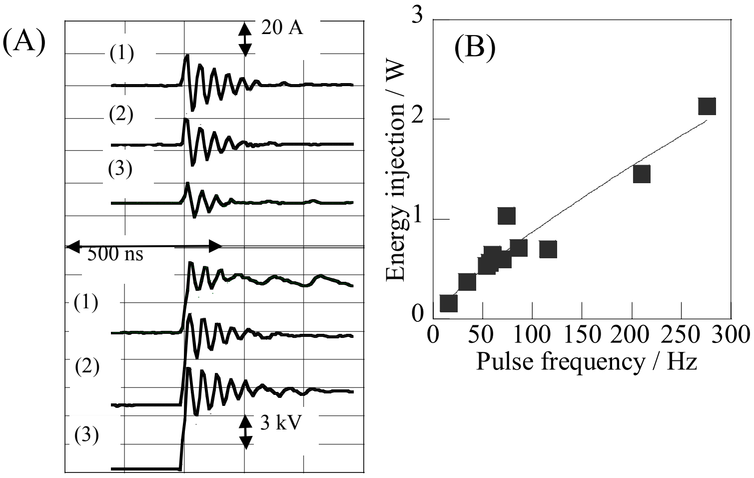

Fig. 2 (A)Current and voltage waveforms on various pulse frequencies. (1)35 Hz, (2)86 Hz, (3)210 Hz. (B)Energy injection on various pulse frequencies. Conditions; methane flow rate; 10 cm^3*min^{-1}, $H_2O/CH_4 = 1/1$, distance between electrodes; 2.1 mm, temperature; 393 K, atmospheric pressure.

Steam reforming of methane by means of non-equilibrium pulsed discharge was performed under the various frequencies. Methane is a model of natural gas. Fig. 3 shows the result. In each frequency, steam reforming of methane proceeded effectively and hydrogen was produced as a main product. With an increase in frequency, methane conversion rate and formation rate of hydrogen increased. In this experiment, the formation rate of hydrogen and methane conversion rate reached about 400 $\mu mol*min^{-1}$ and 55 %, respectively when the pulse frequency was 210 Hz and the injection energy was 2.1 W. In addition to hydrogen, carbon monoxide, C2 compounds and a small amount of carbon dioxide were produced. The selectivity to these products was not influenced by the frequency. Other products such as higher hydrocarbons or oxygenated compounds were not detected. Formation of C2 compounds lowers the amount of hydrogen obtained. However, the influence of C2 compounds formation is relatively small in case of steam reforming of methane using non-equilibrium pulsed discharge method because the main component of C2 compounds was acetylene, and the selectivity to hydrogen was very high more than 90 %. Moreover, the selectivity to C2 compounds can be controlled by changing the mixing ratio of methane and steam. (See below further details)

Carbon deposition and wax formation are very serious problems in steam reforming of methane because these cause a blockage in the reactor or deactivation of a steam reforming catalyst. In order to prevent these problems, the catalytic steam reforming process requires a surplus of steam, thereby lowering the net energy efficiency of the PEMFC system. In case of non-equilibrium pulsed discharge, even a small amount of carbon deposition or wax formation causes stop or instabilization of discharge. However, there was a trace amount of carbon deposition and wax formation under the condition of molar H_2O/CH_4 = 1 in each frequency and discharge could be kept stable for a long period of time.

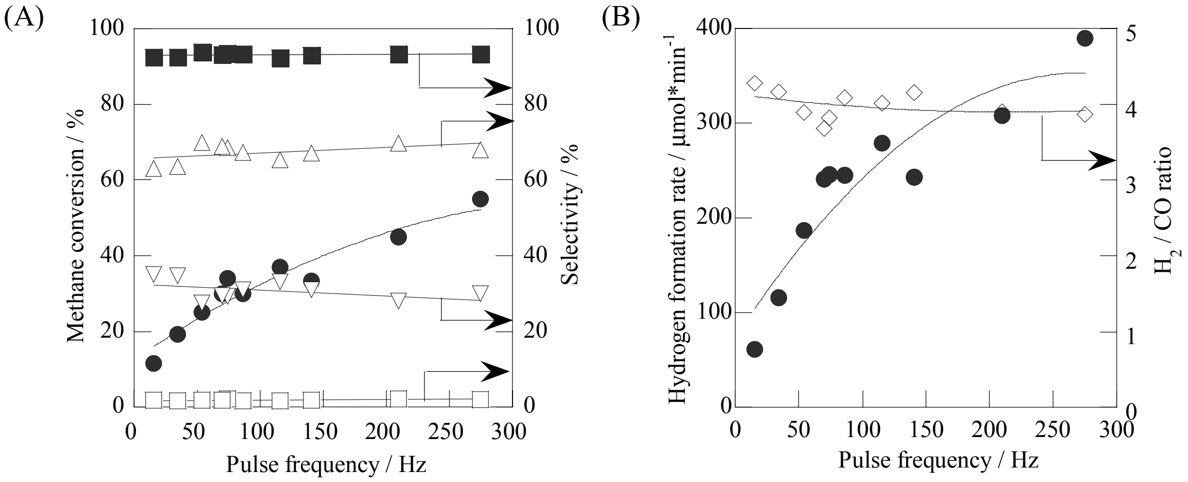

Fig. 3 Effect of pulse frequency on steam reforming of methane: ((A) (●)methane conversion rate, (▲)selectivity to CO, (▼)selectivity to C2, (■)selectivity to CO_2, (□)selectivity to H_2, (B) (●)hydrogen formation rate, (◊)H_2/CO molar ratio). Conditions; methane flow rate; 10 cm^3*min^{-1}, H_2O/CH_4 = 1/1, distance between electrodes; 2.1 mm, temperature; 393 K, atmospheric pressure.

We investigated influence of some parameters (distance between electrodes, partial pressure of steam, flow rate of reactant gas and so on) on the results of steam reforming of methane using non-equilibrium pulsed discharge. In case of changing the parameters of distance between electrodes and flow rate of reactant gas, the methane conversion rate increased with an increase in distance between electrodes and decreased in flow rate of reactant gas. The result of changing distance between electrodes is shown in table 1. On the other hand, the selectivity to products except hydrogen was hardly influenced by these parameters.

Table 2 Effect of distance between electrodes on steam reforming of methane.

Distance between electrodes / mm	Conversion / %	Selectivity / %			
		CO	C2	CO_2	H_2/CO ratio
0.7	21.4	62.6	35.6	1.8	4.08
2.1	29.2	66.4	31.8	1.8	3.83

Conditions; pulse frequency; 100 Hz, $H_2O/CH_4/Ar$ = 1/1/1.5, Total flow rate; 35 cm^3*min^{-1}, temperature; 393 K, atmospheric pressure.

In contrast to the experiments of changing pulse frequency, distance between electrodes and flow rate of reactant gas, the selectivity to products other than hydrogen was strongly influenced by partial pressure of steam. The result is shown in Fig. 4. The higher the partial pressure of steam, the larger the selectivity to carbon monoxide and the smaller the selectivity to C2 compounds.

In our recent investigation of acetylene synthesis from methane using non-equilibrium pulsed discharge, we consider that a reaction scheme in which methane is not dissociated hydrogen by hydrogen (i.e., $CH_4 \rightarrow CH_3$

→ CH_2 → CH) but is directly dissociated into a CH_x fragment due to electron impact and CH_x fragment reacting with steam produced carbon monoxide, while CH_x fragment reacting with each other produced acetylene. Therefore, the number of CH_x fragment increased, as did their reactions with steam when partial pressure of steam was high.

The selectivity to carbon dioxide increased slightly. This is because the water gas shift reaction (shown in equation [2]) proceeded.

$$CO + H_2O \rightarrow CO_2 + H_2,\ \Delta H^\circ = -41\ kJ*mol^{-1} \qquad [2]$$

We calculated the energy efficiency according to the following equation [3].

$$\text{Energy efficiency} = \{(\sum \Delta H^\circ * FR)/P\}*100 \qquad [3]$$

FR and P are respectively, formation rate of products in mole per minutes and injection energy in watts. The result is shown in Fig. 5. The energy efficiency was 30 ~ 60 %. We consider that this result was no way inferior to the energy efficiency of catalytic steam reforming and the energy efficiency can be improved by developing a new power supply, in order to optimize the current and voltage waveforms suitable for steam reforming. With an increase in frequency, the energy efficiency decreased slightly. When the frequency and injection energy increase and the concentration of product molecules such as hydrogen, carbon monoxide, carbon dioxide and C2 compounds, the number of electrons which interact with not methane and steam which are reactant molecules, but the product molecules increase. Therefore, the energy loss increase with an increase in frequency and the energy efficiency decrease.

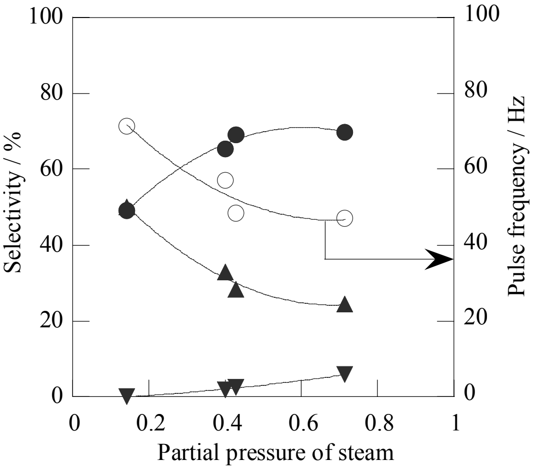

Fig. 4 Effect of partial pressure of steam on steam reforming of methane: ((○)pulse frequency, (●)selectivity to CO, (▲)selectivity to C2 compounds, (▼)selectivity to CO_2). Conditions; methane flow rate; 10 cm^3*min^{-1}, total flow rate; 35 cm^3*min^{-1}, distance between electrodes; 2.1 mm, temperature; 393 K, atmospheric pressure.

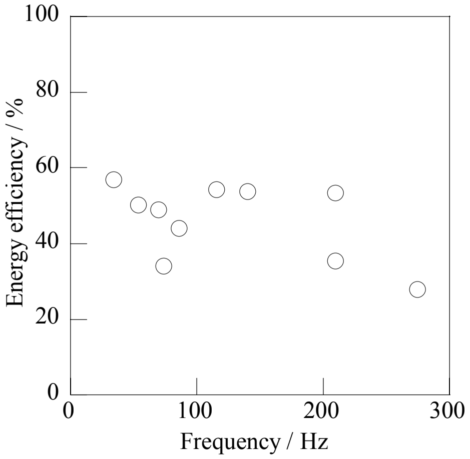

Fig. 5 Energy efficiency on steam reforming of methane. Conditions; methane flow rate; 10 cm^3*min^{-1}, total flow rate; 20 cm^3*min^{-1}, distance between electrodes; 2.1 mm, temperature; 393 K, atmospheric pressure.

3.2 Steam reforming of various hydrocarbons and alcohols using non-equilibrium pulsed discharge

In addition to steam reforming of methane, we investigated about steam reforming of other hydrocarbons and alcohols using non-equilibrium pulsed discharge. Propane served as a model for LPG and n-hexane and cyclohexane served as a model for gasoline. The results are shown in Fig. 6. Argon was added as carrier gas in case of steam reforming of n-hexane, cyclohexane, methanol and ethanol. In each case, steam reforming reactions proceeded efficiently and selectively, and hydrogen was obtained as a main product. The product yield of hydrogen was more than 50 % in each case. There was a trace amount of carbon deposition and wax formation.

In addition to hydrogen, carbon monoxide C2 compounds (mainly acetylene except for steam reforming of methanol) carbon dioxide and methane (except for steam reforming of methane) were produced. In case of steam reforming of n-hexane and cyclohexane, small amount of C3 and C4 compounds were produced. Other products such as higher hydrocarbons and oxygenated compounds were not observed. The formation of methane, C2 compounds, and C3, C4 compounds lowers the amount of hydrogen obtained. As mentioned above, we consider that the influence of C2 compounds formation on the selectivity to hydrogen is small, because the main product of C2 compounds was acetylene. Moreover, the C2 compounds could be controlled by changing the S/C ratio in each case. On the other hand, the formation of methane, C3, C4 compounds is not a serious problem because the amount of methane and C3, C4 compounds is very small, about 10 % and less than 1 %, respectively.

The selectivity to methane was hardly influenced by changing S/C ratio in contrast to the influence of S/C ratio on the selectivity to carbon monoxide or C2 compounds. Fig. 7 shows the influence of various parameters on selectivity to methane on steam reforming of propane. We consider that the reaction scheme of methane formation differs from that of carbon monoxide or acetylene formation.

The amount of carbon monoxide was very high in case of steam reforming of methanol and the amount of C2 compounds was extremely small. The main component of C2 compounds was ethylene. We suppose that the role of steam is very small on hydrogen formation from methanol and carbon monoxide and hydrogen were produced by decomposition of methanol in case of steam reforming of methanol.

The results of our experiments of steam reforming of various hydrocarbons and alcohols demonstrated the subtle advantages the non-equilibrium pulsed discharge method. Operating temperature has a great significance. Compared to the demand of catalytic steam reforming, non-equilibrium pulsed discharge operated at a very reasonable temperature (393 K), resulting in shortened start-up time. Moreover, the operating temperature simplifies the overall PEMFC systems, related its size by eliminating the need for a large heat exchanger and heated, and holds down the cost of reactor material.

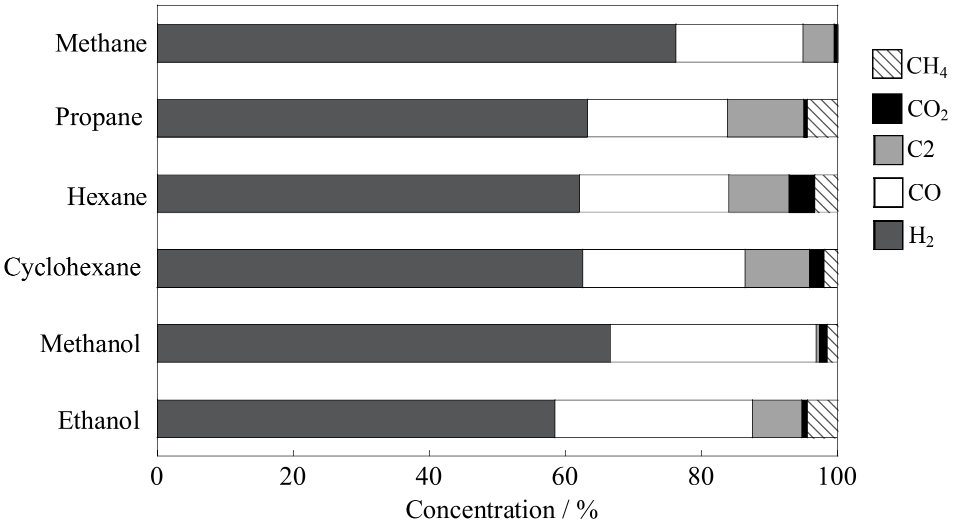

Fig. 6 Steam reforming of various fuels using non-equilibrium pulsed discharge.
Conditions; conversion; 30 %, distance between electrodes; flow rate; 20 ~ 35 cm^3*min^{-1}, 2.1 mm, S/C = 1, temperature; 393 K, atmospheric pressure.

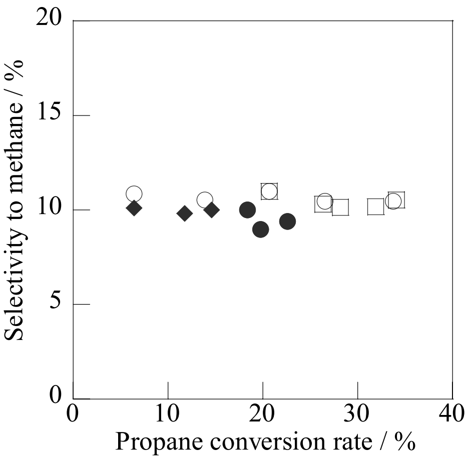

Fig. 7 Selectivity to methane on steam reforming of propane: ((●)pulse frequency, (○) distance between electrodes, (♦) partial pressure of steam, (□) flow rate).

4. Conclusions

We found that the steam reforming of hydrocarbons and alcohols by means of non-equilibrium pulsed discharge proceeded efficiently and selectively, demonstrating many advantages not shared by catalytic steam reforming. The advantages include;

Steam reforming reactions proceed under the atmospheric pressure and low temperature (393 K).

Start-up and stop-off are very quick (less than 1.0 second).

There are trace amount of carbon deposition or wax formation though the S/C ratio of reactant gas was 1 (stoichiometric ratio) and hydrogen can be supplied stably for long time

The amount of methane formation is very small and the selectivity was less than 10 %.

The hydrogen production system using non-equilibrium pulsed discharge does not have the faults of the catalyst system. Thus, the use of carbon monoxide removal technology in combination with the catalytic water gas shift reaction and combustion or the use of a membrane for hydrogen separation, we consider that a hydrogen production system employing non-equilibrium pulsed discharge can be applied to practical use.

References

[1] D. L. Trimm - Catal. Today **37**, 233 (1997)
[2] J. R. Rostrup-Nielsen - Catal. Today. **37**, 225 (1997).
[3] B. Eliasson, U. Kogelschatz - IEEE T. Plasma Sci. **19**, 1063 (1991).
[4] Y. Li, G. H. Xu, C. J. Liu, B. Eliasson, B. Z. Xue - Energy & Fuels **15**, 299 (2001).
[5] S. L. Yao, M. Okumoto, A. Nakayama, E. Suzuki - Energy & Fuels **15**, 1295 (2001).
[6] K. Okazaki, T. Kishida, K. Ogawa, T. Nozaki - Energy Convers. Manage. **43**, 9 (2002).
[7] S. Kado, Y. Sekine and K. Fujimoto - Chem. Commun. 2485 (1999).
[8] S. Kado, K. Urasaki, Y. Sekine, K. Fujimoto - Chem. Commun. 415 (2001).

Influence of Pulse-Modulation of High-Power ICP on Hydrogen Doping to Improve UV Emission of ZnO

T. Ishigaki, N. Ohashi, H. Taguchi, and H. Haneda

National Institute for Materials Science, Advanced Materials Laboratory,
1-1 Namiki, Tsukuba-shi, Ibaraki 305-0044, Japan
E-mail: ISHIGAKI.Takamasa@nims.go.jp

Abstract

Pulse-modulated (PM) operation of ICP was adopted for intensive doping with hydrogen. High flux of chemically active hydrogen radicals and controlling of sample temperature can be simultaneously achieved by using the PM-ICP method. Powder compacts, sintered bodies and single crystals of ZnO were irradiated by PM-ICP with variable plasma parameters, and show the effects of hydrogen doping on luminescence properties of ZnO.

1. Introduction

Newly developed pulse-modulated high-power inductively coupled plasma (ICP) is expected to offer the unique physico-chemical condition for materials processing, because of the increased concentration of chemically reactive species, as well as the appropriate heat flux[1-4]. Total energy of plasma can be decreased, while the maximum temperature remained unchanged, that is, the plasma temperature, 12,000K, in the pulse-on time was almost the same as that of continuous generation. Also, it is suggested by optical emission spectroscopy that the pulse-modulated RF plasma could produce intentionally a non equilibrium state of particle temperatures and the high flux density of radical species.

Zinc oxide (ZnO) is a candidate material for both visible (VIS) and ultraviolet (UV) applications, such as phosphor for field emission displays and UV light emitting diodes. Recent investigations on ZnO have resulted in many remarkable achievements, e.g., quantum effect in super lattices, laser emission, and a hetero junction LED. It was suggested that hydrogen plasma irradiation was appropriate for passivation of radiative recombination centers giving VIS emission[5]. The green emission centered at 2.3 eV was suppressed and UV emission efficiency was improved by exposing ZnO to the micro-wave hydrogen plasma.

Pulse modulated (PM) operation of ICP was adopted in the present study for intensive doping with hydrogen. In the previous case of micro-wave plasma irradiation, heating ZnO in hydrogen (reductive) atmosphere sometimes caused formation of defects, e.g., oxygen vacancies, or evaporation of ZnO. Thus, non-thermal way of hydrogen doping is required. High flux of chemically active hydrogen radicals and controlling of sample temperature can be simultaneously achieved by using the PM-ICP method[6,7]. In this work, we irradiate powder compacts, sintered bodies and single crystals of ZnO with variable plasma parameters, and show the effects of hydrogen doping on luminescence properties of ZnO.

2. Experiments

Schematic of PM plasma generation system has been shown elsewhere[1]. The inverter-type solid state power source supplies the electric power of 22 kW continuously with nominal frequency of 1 MHz. The RF power was modulated by imposing the external pulse signal from a pulse generator to switch a static induction transistor(SIT). As shown in Fig. 1, the mixture of Ar and H_2 was injected with swirl at the flow rate of 98 and 6 l/min, respectively. The torch design is the same as that used in our previous study for continuous steady operation[8]. Operation conditions are as follows. The plasma was firstly generated at the continuous power level of 13 kW and the reactor pressure was controlled at 26.6 kPa. Then, the external pulsing signal was imposed to switch to the pulse-modulated mode with pulse-on and -off times of 10 and 5 ms, respectively. The shimmer current level, which is the current ratio of the lower level of pulse-off time to the higher one of pulse-on time, is 0.53. There kinds of specimen were used for the plasma treatment. Powder compact bodies were formed from ZnO powders by isostatical pressing. The compacts were fired at 1050°C in air to get sintered bodies, whose sintered density was over 90%. Single crystal specimens grown by a hydrothermal method was also irradiated in plasmas. Specimens were put on the water-cooled molybdenum holder and irradiated for 5 minutes in Ar-H_2 plasma of CN and PM generation modes.

Luminescence properties of the samples were characterized by cathodoluminescence (CL) and photoluminescence (PL). The PL spectra excited by an He-Cd laser (325 nm, 10 mW) were recorded with an RPM-2000 (Accent Optical Technologies, OR, USA). The CL spectra were obtained with a secondary electron microscope equipped with an optical spectrometer. The CL equipment has been described elsewhere.[1] The CL spectra were measured at 20-300 K, and the current of the 5 keV electron beam was about 1 nA. The hydrogen concentrations in the samples were qualitatively analyzed by depth profiling with SIMS. Most of the analyses were carried out for ^{2}D plasma irradiated samples. The instrument was imf-4 (CAMECA, France), and a Cs-ion incident ion beam was selected. For the qualitative analyses, the sensitivity of the SIMS equipment was calibrated with a standard sample prepared with an ion implantation method.[2]

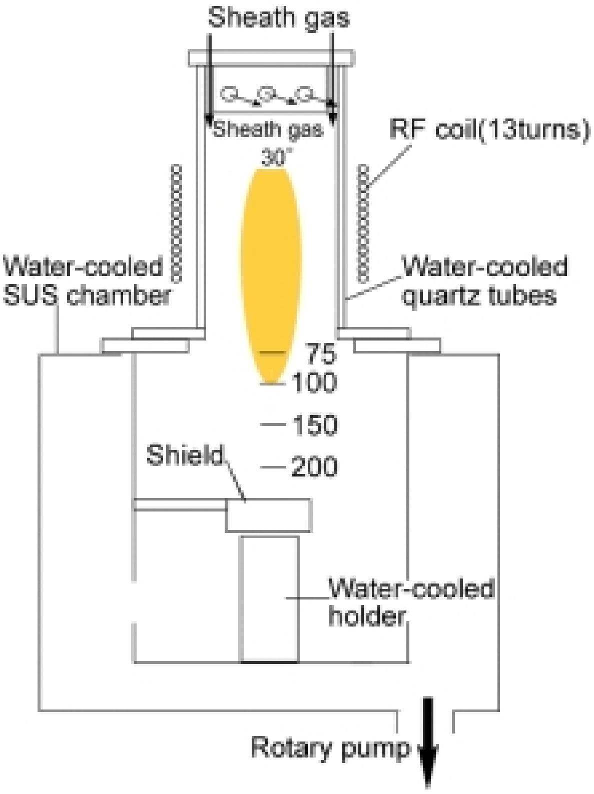

Fig. 1 Schematic of plasma torch and reactor.

3. Results and Discussion

Specimens treated in the CN plasma were damaged by plasma irradiation. The specimens put the position of 100 and 150 mm below the bottom of RF coil in Fig. 1 suffered some evaporation and showed the weight loss of 21.2 and 1.7%, respectively. On the other hand, Specimens treated in PM plasma had no weight loss even at 100 mm, where the plasma tail reaches the specimen. The influence of PM plasma irradiation was compared with the CN plasma irradiation on the cathodoluminescence. The effects of CN and PM plasma irradiation were considerably different on the emission spectra. As is clearly seen in Fig. 2, the

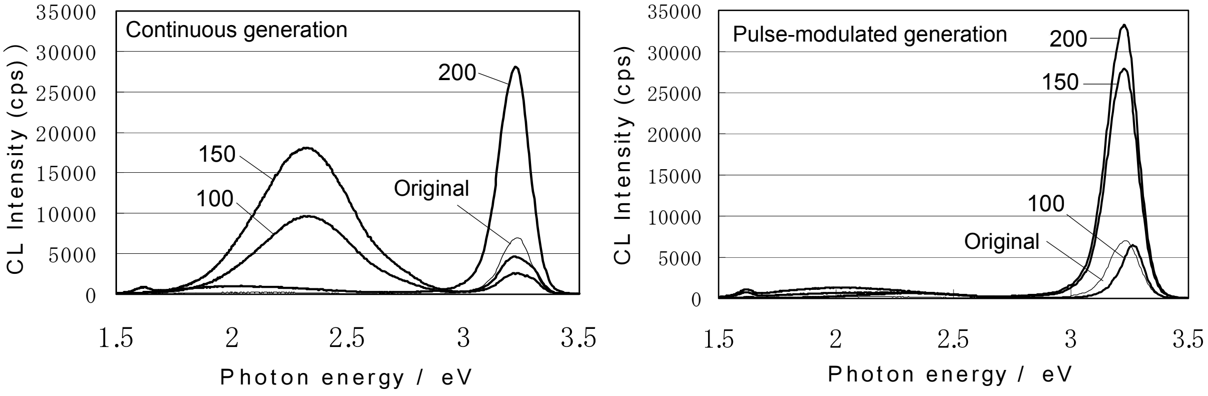

Fig. 2 Cathodoluminescence spectra of original and plasma-treated ZnO compacts.

CN irradiation at the positions of 100 and 150 mm gave the broad emission spectra in visible light region, while the UV emission at 3.3 eV decreaswed. To the contrary, the PM irradiation did not give rise to the visible light emission, but the efficiency of UV luminescence was significantly improved. The broad luminescence in the visible light region is believed to attribute to the thermally stabilized lattice defect in ZnO.

In order to suppress the increase of sample temperature during the plasma irradiation and show the influence of hydrogen radical irradiation, sintered bodies were treated in the argon-hydrogen plasma. As the sintered bodies have higher density, that is, higher thermal conductivity, than powder compacts, samples of sintered bodies can be cooled more efficiently by water-cooled sample holder.

The plasma irradiation on sintered bodies showed distinct difference in luminescence spectra shown in Fig. 3. The original sintered body has the broad emission from 450 to 800 nm in the visible light region as well as the UV emission at 375 nm. By the hydrogen-containing plasma irradiation, the luminescence in the visible light region disappeared and the UV luminescence intensity increased significantly. Comparing the samples treaded in CN and PM plasma at the same position, the PM irradiared samples showed the higher PL intensity than the CN irradiated samples at each positions. It is noteworthy that the sample irradiated in the PM irradiation at the position of 75 mm, where is in the plasma tail and high concentration of hydrogen radials is expected to irradiate the ZnO sample, the highest UV emission intensity was obtained. The UV intensity at 75 mm was over 15 times higher than that of the original sintered body sample.

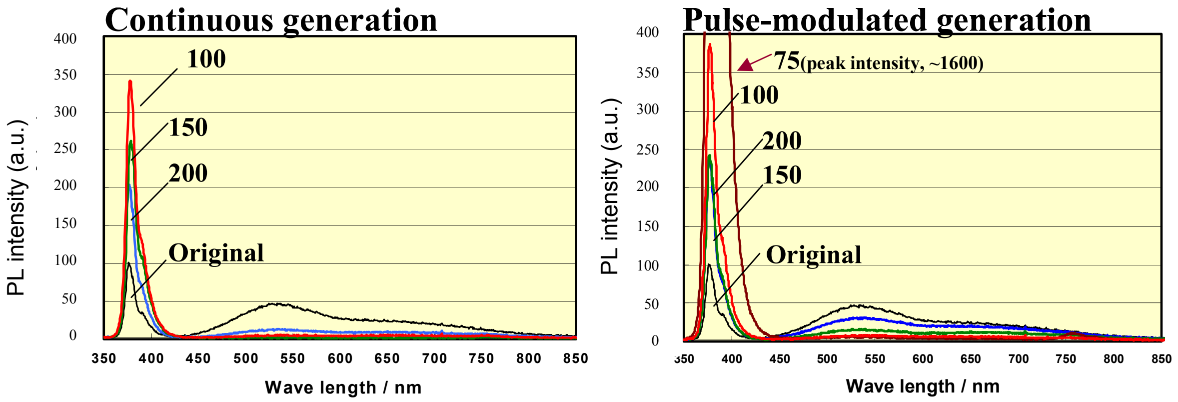

Fig. 3 Photoluminescence of plasma-irradiated and original ZnO sintered bodies.

The hydrogen irradiation in ZnO was measured by a secondary ion mass spectroscope[SIMS]. As the detection of low concentration of hydrogen in oxide materials is difficult due to the interference of residual gas in vacuum chamber, the single crystal of zinc oxide was irradiated in argon-duterium plasma of the same condition as the argon-hydrogen plasma irradiation of pulse-modulated mode at 100 mm. In Fig. 4, the PL spectra form the single crystal are shown before and after the plasma irradiation. The plasma irradiation doubled the UV emission at 380 nm. In Fig. 5, the diffusion profile of deuterium in the single crystal ZnO is shown. It is recognized that deuterium diffused into the specimen, up to 0.1 micro meters in depth. Comparing with a standard specimen detection, the surface concentration of deuterum is estimated to be some tens of ppm.

For these samples, the most likely reason for this improvement is passivation of non-radiative recombination centers. As proposed by Van de Walle[9], it is likely that hydrogen in ZnO is of the proton state, by injecting an electron. This means that doping of hydrogen results in charge compensation for acceptors and ionized donors. Namely, it is expected that the shift of the Fermi level by doping with hydrogen causes a change in the ionic charge state of both the impurities and the native defects. Two possible charge transfers from hydrogen are given in Eqs. 1,

$$V_O^{\bullet} + \frac{1}{2}H_2 \rightarrow V_O^{x} + H_i^{\bullet}, \qquad \text{1a}$$

$$V_{Zn}^{x} + H_2 \rightarrow V_{Zn}^{''} + 2H_i^{\bullet}. \qquad \text{1b}$$

Here, neutralization of oxygen vacancy (Eq. 1a) and ionization of zinc vacancy (Eq. 1b) are assumed.

Experimental and theoretical studies have recently indicated that a proton dimer can occupy the zinc vacancy site in ZnO. This means that Eq. 1.b can be modified into Eq. 2,

$$V_{Zn}^{x} + H_2 \rightarrow [2H^{\bullet}]_{Zn}^{x} . \qquad 2$$

It is quite reasonable that a proton occupies the cation site in ZnO. Assuming that the zinc vacancy is a non-radiative recombination center to reduce the total emission efficiency of ZnO, Eq. 1a is a likely mechanism for improving the total emission efficiency of ZnO by reducing the probability of non-radiative recombination. There is no evidence against Eq. 1a as the mechanism for the emission efficiency improvement. However, from the viewpoint of Madelung potential, it is not expected that a proton occupie the oxygen vacancy site, which is coordinated by positive Zn ions.

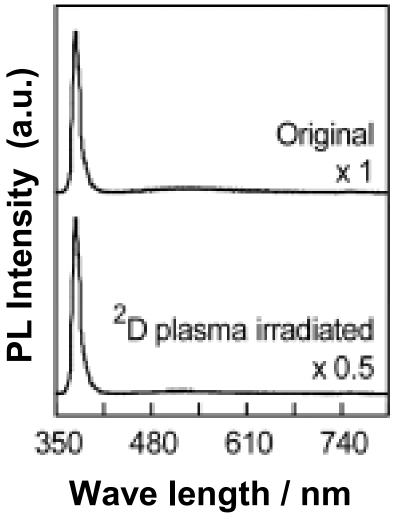

Fig. 4 Photoluminescence spectra, before and after hydrogen plasma irradiation, of ZnO single crystal grown by the hydrothermal method.

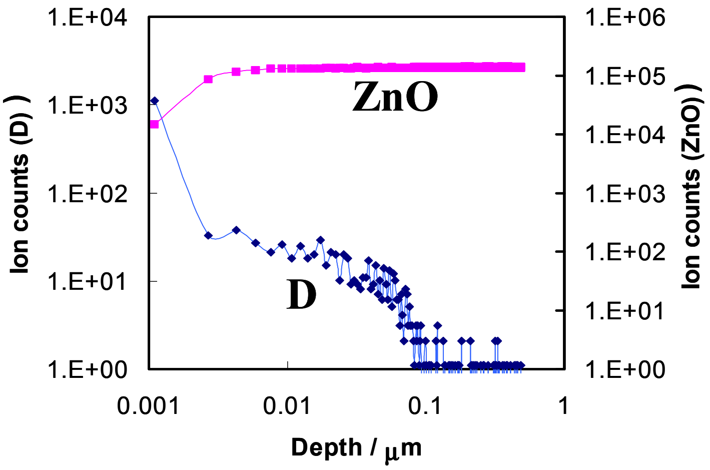

Fig. 5 Diffusion profile of deuterium obtained by secondary ion mass spectroscopy [SIMS].

Reference

[1] T. Ishigaki, X. Fan, T. Sakuta, T. Banjo and Y. Shibuya, *Appl. Phys. Lett.*, **71**, 3787 (1997) .
[2] T. Sakuta and T. Ishigaki, *Pure Appl. Chem.*, **71**, 1845(1999).
[3] T. Ishigaki, N. Okada, N. Ohashi, H. Haneda and T. Sakuta, *Pure Appl. Chem.*, **74**, 435(2002).
[4] T. Ishigaki, H. Haneda, N. Okada and S. Ito, *Thin Solid Films*, **390**, 20(2001).
[5] T Sekiguchi, N. Ohashi, and Y. Terada, *Jpn. J. Appl. Phys. Part 2*, **36**, L289 (1997).
[6] N. Ohashi, T. Ishigaki, N. Okada, I. Sakaguchi, T. Sekiguchi and H. Haneda, *Appl. Phys. Lett.*, **80**, 2869(2002).
[7] N. Ohashi, T. Ishigaki, N. Okada, H. Taguchi, I. Sakaguchi, S. Hishita, T. Sekiguchi and H. Haneda, J. *Appl. Phys.*, in press.
[8] T. Ishigaki, Y. Moriyoshi, T. Watanabe, and A. Kanzawa, *J. Mater. Res.*, **11** (1996) 2811.
[9] C. G. Van de Walle, *Phys. Rev. Lett.*, **85**, 1012 (2000).

Spectroscopic Measurements of Electric Fields in a Hollow Cathode Discharge and a Beam-Plasma Discharge

E.K. Cherkasova[1], V.P. Gavrilenko[2,3], A.I. Zhuzhunashvili[4]

[1]Moscow Institute of Physics and Technology, Dolgoprudnyi 141700, Russia
[2]General Physics Institute, Russian Academy of Sciences, Department of Plasma Physics, Vavilov Street 38, 119991, GSP-1, Moscow, Russia
[3]Center for Surface and Vacuum Research, Russian State Committee for Standards, Vavilov Street 38, 117334 Moscow, Russia
[4]Russian Research Center "Kurchatov Institute", Kurchatov square, 123182 Moscow, Russia

Abstract

Three spectroscopic methods for the measurements of electric fields in a plasma were experimentally realized. The first method was based on the emission spectroscopy of helium atoms, whereas the second and third methods were based on the fluorescent spectroscopy of atomic hydrogen and BH molecules, respectively. These diagnostic methods were applied to measure the electric fields of plasma turbulence in a beam-plasma discharge as well as the electric fields in a hollow cathode discharge.

1. Introduction

Electric field is one of the main parameters in physics of discharges. Electric field in a discharge determines the charged particles energy distribution functions and the charged particle fluxes. Knowledge of these characteristics is of great importance for improving modeling and control of plasma discharges. At present, for the diagnostics of electric fields in plasma, spectroscopic methods based on the Stark effect of atoms and molecules are widely used (see, e.g., the review article [1]). The main objective of the present paper is the development of the new methods of electric fields in a discharge plasma. This paper presents the results of the spectroscopic measurements of electric fields in two kinds of discharges: (a) a beam-plasma discharge, and (b) a hollow cathode discharge.

2. Spectroscopic measurements of turbulent electric fields in a beam-plasma discharge

Experimental set-up of a beam-plasma discharge is shown in Fig. 1. Electron beam of the density of $N_b = 10^8 - 10^9$ cm^{-3} is injected through the differential vacuum resistance into the vacuum chamber filled with a gas. The typical energy of electrons in a beam is $\varepsilon = 1 - 10\,\text{keV}$. Due to the interaction of the beam electrons with the gas, a non-equilibrium plasma is produced. Under the action of the electron beam, non-equilibrium Langmuir oscillations occur in a plasma. The electron beam can transfer a substantial portion of its energy (up to 70 %) to plasma oscillations. In turn, the plasma electrons can be heated as a result of their interaction with plasma oscillations. Finally, the kinetic energy of the plasma electrons can be transferred to the working gas that passes through the discharge region. This energy is used for the excitation of the internal degrees of freedom of the working gas, which leads to its selective dissociation and ionization. The particles that appear in a beam-plasma discharge due to the dissociation and ionization, can be used for the plasma processing.

In our work, we performed spectroscopic measurements of electric fields of Langmuir turbulence in a plasma of a beam-plasma discharge. In our experiments, the discharge was produced in helium. We recorded emission spectrum of helium in the vicinity of the spectral line corresponding to the 2^1P-4^1D transition ($\lambda \approx 492.2$ nm). This spectrum was recorded along the *y*-axis that was directed along the radius of the cylindrical vacuum chamber (see Fig. 1). The *z*-axis coincided with the direction of the electron beam. Two polarizations (***x***- and *z*-polarizations) of the radiation from helium were observed. It turned out that the emission spectrum of helium contained not only the dipole-allowed spectral line at $\lambda \approx 492.2$ nm (the 2^1P-4^1D transition), but also a spectral line at $\lambda \approx 491.1$ nm. The latter line corresponded to the dipole-forbidden 2^1P-4^1P transition in helium. The appearance of the dipole forbidden line at $\lambda \approx 491.1$ nm was due to the Stark mixing of the wave functions of the two upper levels, 4^1P and 4^1D, under the turbulent electric field. We obtained that the intensities of the allowed line (at $\lambda \approx 492.2$ nm) were approximately equal for both ***x***- and *z*-polarizations. At the same time the intensity of the forbidden line (at $\lambda \approx 491.1$ nm) for *z*-polarization was greater than that for *x*-polarization approximately by the factor 2.65. This indicated that the turbulent electric fields were predominantly directed along the *z*-axis. In Table 1 are given the experimental data for the ratio of intensities I_F / I_A of forbidden (491.1 nm) and allowed (492.2 nm) spectral lines of helium (see the seventh column of Table 1).

Table 1.

I (A)	U (kV)	W (kW)	P (Pa)	T$_e$ (eV)	N$_e$ (cm^{-3})	I_F / I_A	polarization	F (V/cm)
1.4	2.2	3.0	6.6×10^{-2}	4.0	8.0×10^{11}	2.0×10^{-5}	z	500
						7.96×10^{-5}	x	525
1.8	2.8	5.0	2.2×10^{-1}	5.2	2.0×10^{12}	5.0×10^{-5}	z	775
						2.0×10^{-5}	x	790

In Table 1, the first column presents the current that flowed through the discharge. The second column gives the voltage that was applied to accelerate the beam electrons. The third column presents the power W that is the product of the current I and voltage U. The forth column shows the pressure of helium in a discharge. The values of T$_e$ and N$_e$ presented in Table 1 are the plasma electron temperature and density, respectively.

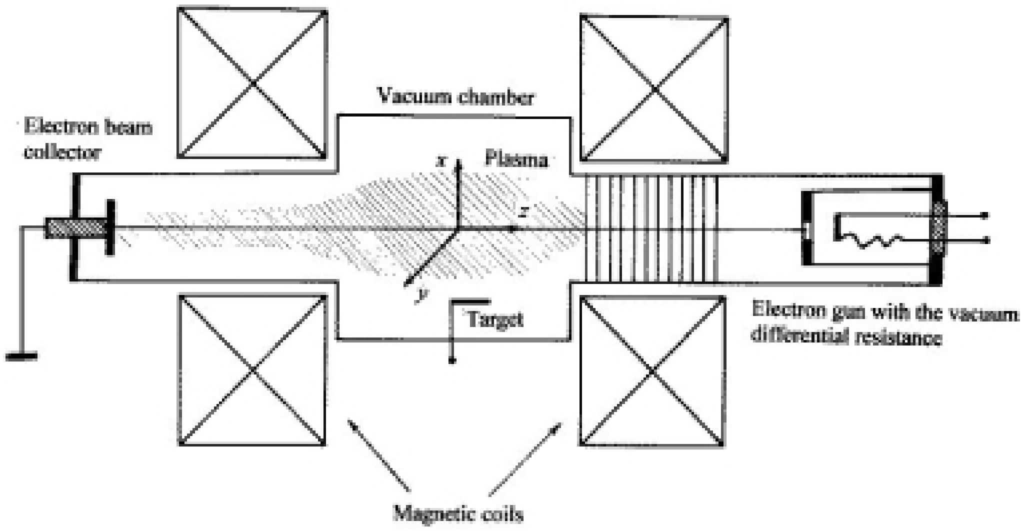

Fig. 1. Experimental apparatus for the beam-plasma discharge.

Performing the quantum mechanical calculations, we obtained the following formulas for the ratio of intensities of allowed line (at $\lambda \approx 492.2$ nm) and forbidden line (at $\lambda \approx 491.1$ nm) versus the electric field strength F

$$\left(\frac{I_F}{I_A}\right)^{(x)} \approx 3.189\times10^{-11} F^2 , \qquad \left(\frac{I_F}{I_A}\right)^{(z)} \approx 8.343\times10^{-11} F^2 . \qquad (1)$$

While obtaining the formulas (1), it was assumed that the electric field $\vec{F}$ is directed parallel to the z-axis. Using the experimental ratios of intensities I_F / I_A presented in Table 1, we obtained with the help of formulas (1) the strength of the turbulent electric field in a beam-plasma discharge. The corresponding values of the field strength are given in the ninth column of Table 1. We note that in both cases (for $W = 3.0$ kW and $W = 5.0$ kW) the strength of the turbulent field F obtained from the ratio $(I_F / I_A)^{(x)}$ is close to that obtained from the ratio $(I_F / I_A)^{(z)}$. This fact supports our conclusion that the turbulent electric fields were predominantly directed along the z-axis. This means that the amplitude-angular distribution of the turbulent electric fields looks like a “sausage” with the main axis aligned parallel to the z-axis.

3. Spectroscopic measurements of electric fields in a hollow cathode discharge

The measurements of the electric fields in a hollow cathode discharge were performed with the help of two different spectroscopic techniques. The first technique was based on the effect of Stark splitting of highly lying energy levels of hydrogen. In this technique a double resonance in hydrogen atoms interacting with two laser beams was realized. The first laser was in the resonance with the $n=2 \to n=3$ transition in a hydrogen atom (the H_α transition), whereas the second laser was tuned to the Stark components of the $n=3 \to n=8$ transition (the P_ε transition), and a signal of fluorescence at the $n=8 \to n=3$ transition was detected. Here n is the principal quantum number. We would like to note that for hydrogen our excitation scheme shares some common features with the schemes used in Refs. [2,3]. The second technique employed the laser-induced excitation of the transitions in polar diatomic molecules BH. This technique was based on the effect of appearance of dipole-forbidden lines in the fluorescent spectrum of the BH molecules. The same hollow cathode discharge was used as a plasma source for both techniques. The cylindrical hollow cathode was of the inner diameter of 8 mm and of the length of 40 mm. The BH molecules and the hydrogen atoms were produced in the discharge due to the decomposition of pentaborane, B_5H_9. The gas pressure in a hollow cathode discharge was 13.3 Pa.

3.1. Stark spectroscopy of atomic hydrogen

The experimental set-up is shown in Figure 2. In our work, a tunable dye laser ($\lambda \approx 656$ nm) pumped by a copper vapor laser was used for the excitation of the transition $n=2 \to n=3$ in hydrogen. As a tunable IR laser at the P_ε transition ($\lambda \approx 955$ nm), a ruby laser pumped color center laser was used. The beams of the dye laser and the color center laser were nearly counter-propagating: the angle between the wave vectors of the beams was 165 degrees. The laser beam at 656 nm was directed parallel to the axis of the cylindrical cathode (the *z*-axis).

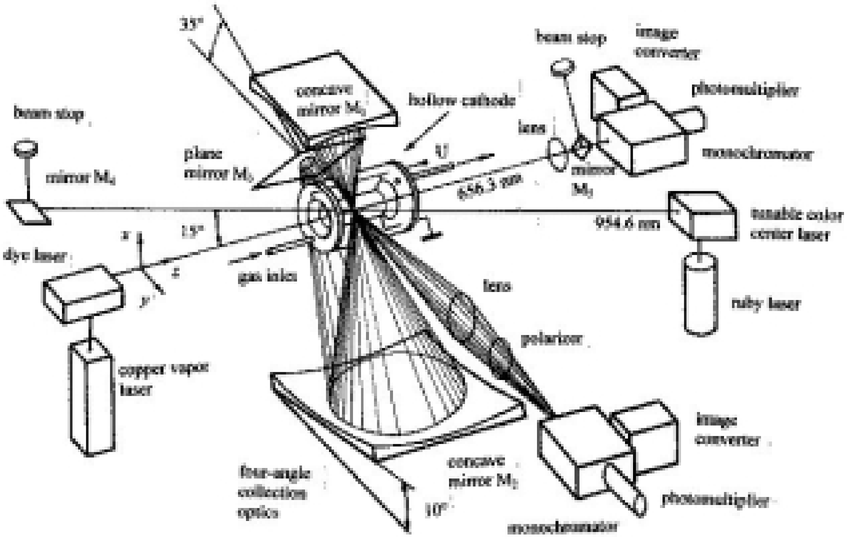

Fig. 2. Experimental setup for the measurements of electric fields in a hollow cathode discharge with the use of laser and Stark spectroscopy of hydrogen.

In our work the fluorescent measurements at the P_ε transition were performed in two regions. The first one was the cathode dark space region for which the measurements were performed at the radial distance $r=3$ mm from the cylindrical cathode axis. The second one was the negative glow region when the beam of the dye laser was directed along the cathode axis (this corresponds to $r=0$ mm). The LIF spectra were recorded orthogonal to the axis of the cylindrical cathode (along the *y*-axis). Figure 3 demonstrates the typical experimental LIF spectra in hydrogen recorded in the dark space region. The voltage between the cathode and the anode was 500 V, and the discharge current was 0.2 A. The experimental points are shown by squares. These experimental points are connected by polygonal line. Figure 3(a) shows the P_ε fluorescent spectrum of *x*-polarization, whereas Figure 3(b) shows the P_ε fluorescent spectrum of *z*-polarization. In Fig. 3, the vertical lines show the Stark components for P_ε spectrum calculated with the assumption that the electric field vector is parallel to the *z*-axis, and the field strength is equal to 2530 V/cm. We can see that the theoretical spectra calculated for *x*- and *z*-polarizations are in accordance with the experimental fluorescent spectra. In particular, this means that the direction of the electric field was close to the axis of the cylindrical cathode. Stark spectra similar to those shown in Fig. 3 were also recorded from the negative glow region. We found out that the typical field strengths in the dark space region and in the negative glow region were 1-3 kV/cm and 0.2-0.3 kV/cm, respectively, depending on the voltage *U* that was applied between the cathode and the anode (*U*=250-500 V).

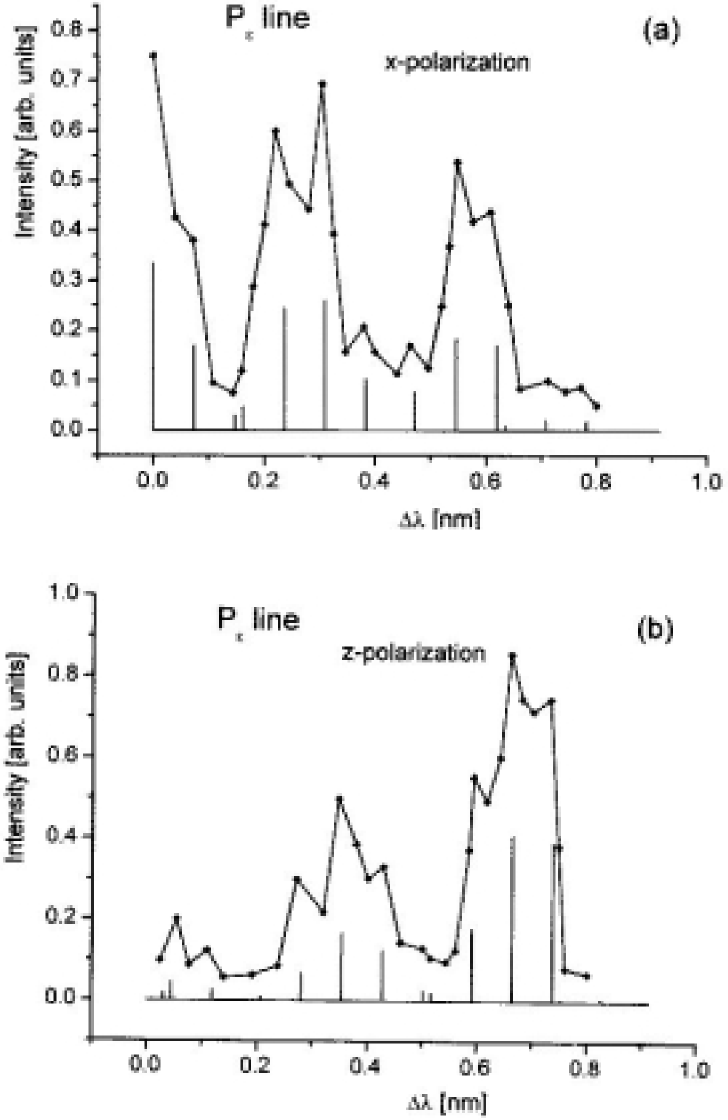

Fig. 3. Stark spectra (the “red” halves) of the P_ε spectral line ($\lambda \approx 955$ nm) of hydrogen. A polygonal line shows spectra of the P_ε line recorded from a hollow cathode discharge. (a) *x*-polarization of the radiation at the P_ε spectral line; (b) *z*-polarization of the radiation at the P_ε spectral line. Vertical lines show theoretical Stark spectra of the P_ε line of hydrogen. Theoretical Stark spectra of the P_ε line were calculated for the case when the electric field strength was equal to 2530 kV/cm, and the electric field vector was directed along the *z*-axis.

3.2. Stark spectroscopy of BH molecules

A method for laser-induced fluorescence (LIF) measurements of electric fields in plasmas and gases based on Stark effect of polar diatomic molecules was suggested and tested in Ref. [4]. Since then it was implemented in a number of experiments [5-9]. The primary characteristic feature of the method is its high sensitivity with respect to electric fields that can be explained in the following way. The laser is tuned to an allowed $X^1\Sigma{-}^1\Pi$ transition in a polar diatomic molecule (see Fig. 4). Each rotational level of the molecule in the $^1\Pi$ state is split into two closely spaced sublevels (Λ- doublet splitting). Therefore, even moderate electric field can significantly intermix the wave functions of the Λ- doublet sublevels, and hence, even moderate electric field can produce considerable modification of the LIF spectrum of such molecule. Although there exists a large number of polar diatomic molecules and radicals [10], until recently only three molecules, BCl, NaK, and CS, were used for LIF measurements of electric fields. However, it is desirable to have a larger choice of molecules that can be used for LIF measurements of electric fields. This is due to the fact that for a specific discharge it is better to utilize for diagnostics the molecules that are either present in the discharge, or could be added to the discharge without changing significantly its properties. From this point of view, the boron monohydride (BH) molecule is of considerable interest. First, its ground electronic state is $X\,^1\Sigma^+$, and as the upper electronic state the $A\,^1\Pi$ state can be chosen. Second, there are the reference data on the dipole moment d_Π and the Λ-doublet splitting $\Delta\nu_{ef}$ for the $A\,^1\Pi$ state of the BH molecule (see [10]). Third, the BH molecules may be present in many discharges in hydrogen that are used for the boron nitride deposition. The scheme of the experimental apparatus is similar to that shown in Fig. 2. The main difference between two schemes is that for the measurements of electric fields with the use of LIF in BH only one tunable laser was used. This was the dye laser pumped by a nitrogen laser. The dye laser operated at $\lambda \approx 395-430$ nm. The output of the dye laser had pulse duration of 20 ns, a spectral width of 0.01 nm, and an output energy of about 1.5 mJ. The laser beam was directed to the hollow cathode plasma parallel to the axis of the cylindrical cathode. The LIF spectra were recorded orthogonal to the direction of the laser beam.

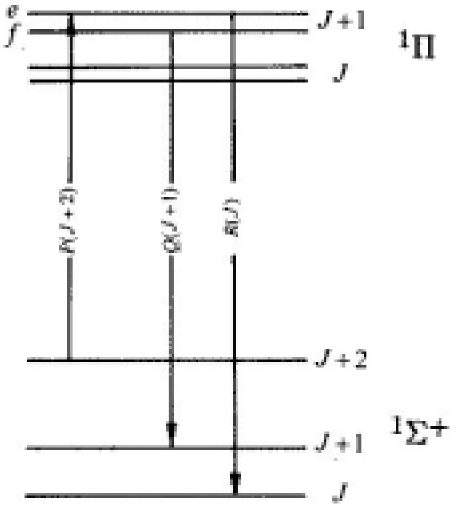

Fig. 4. Energy levels of a polar diatomic molecule. Laser radiation excites the transition belonging to the P-branch. Fluorescent radiation is recorded at the transitions belonging to the Q- and R-branches.

In our work, we employed the laser excitation of the transition belonging to the P-branch, and we used the ratio of intensities of the LIF signal spectral lines belonging to the Q- and R-branches for the electric field measurements. For weak electric fields this ratio is a quadratic function of F. Figure 5 shows, as an example, the experimental fluorescence spectrum of BH with the Q- and R-lines recorded from the dark space region in the case when the beam of the dye laser was directed at the radial distance of $r = 3$ mm from the cathode axis, and the voltage applied between the cathode and the anode was U=350 V. This spectrum was recorded when the dye laser was tuned to the P(7) transition. From the ratio of intensities of Q- and R-lines presented in Fig. 5, we deduced the following strength of the electric field $F \approx 1.7$ kV/cm. We note that the results of the measurements of electric fields in a hollow cathode discharge obtained with the use of LIF in BH molecules were in a good agreement with the corresponding results obtained with the use of Stark spectroscopy of hydrogen.

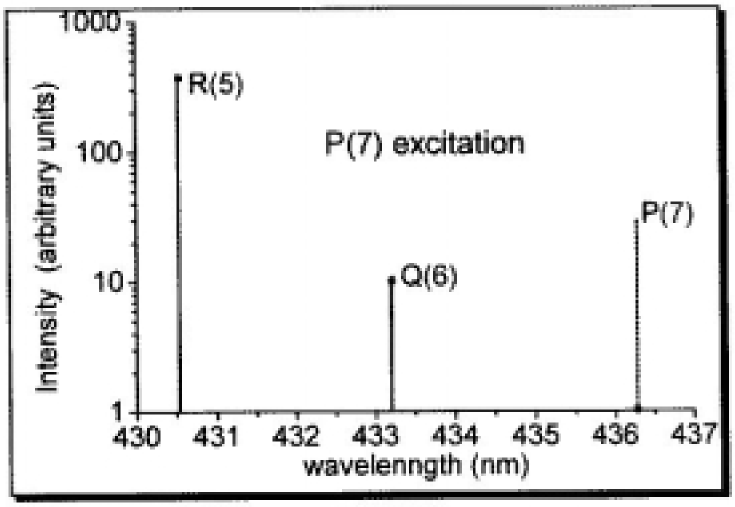

Fig. 5. Spectrally resolved laser-induced fluorescence from excitation of the P(7) transition in the (0,0) band of the BH $A^1\Pi - X\ ^1\Sigma^+$ system. The voltage applied between the cathode and anode of a hollow cathode discharge is 350 V.

4. Conclusions

Thus, in the present work three different spectroscopic techniques for the measurements of electric fields in a discharge plasma were experimentally realized. The first technique was based on the emission spectroscopy of helium. In the second and third techniques, the laser-induced fluorescence in atomic hydrogen and BH molecules was used. With the use of these spectroscopic techniques, the electric fields in a beam-plasma discharge and a hollow cathode discharge were measured. We note that the minimum electric fields that were measured in a hollow cathode discharge were of the order of 200 V/cm.

Acknowledgements

This work was supported in part by the Russian Foundation for Basic Research (project no. 01-02-17810) and the International Science & Technology Center (project no. 2098). For V.P.G., this work was also supported by the Alexander von Humboldt Foundation.

References

[1] V.P. Gavrilenko, V.N. Ochkin, S.N. Tskhai, “Progress in plasma spectroscopic diagnostics based on Stark effect of atoms and molecules”. *In: Proceedings of the International Society for Optical Engineering (SPIE)*, **4460**, pp.207-229 (2002).
[2] J.P. Booth, M. Fadlallah, J. Derouard, N. Sadeghi - *Appl. Phys. Lett.* **65**, 819 (1994).
[3] U. Czarnetzki, D. Luggenhölsher, H.F. Döbele - *Phys. Rev. Lett.* **81**, 4592 (1998).
[4] C.A. Moore, G.P. Davis, R.A. Gottscho - *Phys. Rev. Lett.* **52**, 538 (1984).
[5] R.A. Gottscho, M.L. Mandich - *J. Vac. Sci. Technol. A* **3**, 617 (1985).
[6] J. Derouard, N. Sadeghi - *Optics Commun.* **57**, 239 (1986).
[7] M.D. Bowden, T. Nakamura, K. Muraoka, Y. Yamagata, B.W. James, M. Maeda - *J. Appl. Phys.* **73**, 3664 (1993).
[8] S. Maurmann, H.-J. Kunze, V.P. Gavrilenko, E. Oks - *J. Phys. B: At. Mol. Opt. Phys.* **29**, 25 (1996).
[9] S. Maurmann, V.P. Gavrilenko, H.-J. Kunze, E. Oks - *J. Phys. D: Appl. Phys.* **29**, 1525 (1996).
[10] K.P. Huber, G. Herzberg - *Molecular Spectra and Molecular Structure. IV. Constants of Diatomic Molecules*, Van Nostrand, New York, 1979.

On the Possibility of Diagnosing the Time-Dependent Weak Electric Fields in Low-Density Plasmas with the Use of Laser-Induced Fluorescence of Polar Diatomic Molecules

V.P. Gavrilenko[1,2,3]

[1] *Institut für Experimentalphysik V, Ruhr-Universität Bochum, D-44780 Bochum, Germany*
[2] *General Physics Institute, Russian Academy of Sciences, Department of Plasma Physics, Vavilov Street 38, 119991, GSP-1, Moscow, Russia*
[3] *Center for Surface and Vacuum Research, Russian State Committee for Standards, Vavilov Street 38, 117334 Moscow, Russia*

Abstract

Laser-induced fluorescence of polar diatomic molecules interacting with time-dependent plasma electric fields is studied theoretically. The obtained results enable performing sensitive measurements of plasma density and plasma electric fields in low temperature plasmas.

1. Introduction

One of the most sensitive methods for the diagnostics of static (time-independent) electric fields (EFs) in discharge plasmas is a spectroscopic method based on the laser-induced fluorescence (LIF) of polar diatomic molecules. This method was proposed in [1] and has been used since in many experimental investigations (see, e.g., [2-9]). The high sensitivity of the LIF method to the EF is due to the fact that molecules that have a state $^1\Pi$ as the upper electronic state are utilized. Each rotational level of these states is split into two nearby Λ doublet sublevels that can be coupled by the EF. Therefore, even rather weak EFs can produce considerable modifications of the LIF spectrum of these molecules. At present, four molecules (BCl, NaK, CS, and BH) are employed [1-9] to measure static EFs in discharge plasma.

In many practical situations the EFs in a plasma are time-dependent rather than static fields. First, the EF in plasma can be the oscillating field of the following form $\vec{E}(t) = \vec{E}_0 \cos \omega t$. The presence of the oscillating EF $\vec{E}(t)$ in plasma is typical, e.g., for microwave discharges. Second, these fields can be the plasma ion microfields (PIMs). The typical PIM frequency can be estimated as $\Omega \approx vN^{1/3}$ where v is the typical ion velocity ($v \approx \sqrt{2kT_i / M_i}$), and N is the plasma density. Assume that the ion temperature T_i exceeds 0.5 eV, and that the plasma density N is higher than 10^{10} cm^{-3}. Then the frequency Ω can be of the order or higher than 2.0×10^{-9} s^{-1}. The latter value of Ω can be of the order or higher than the typical separation between the Λ doublet sublevels of a polar diatomic molecule. In this case a static electric field approximation for the molecule is not valid. In the present paper, we consider theoretically the modification of the LIF spectrum of a polar diatomic molecule interacting with time-dependent electric fields in a plasma.

2. Modification of the fluorescent spectra of polar diatomic molecules interacting with time-dependent electric fields

We assume that the ground electronic state of a polar diatomic molecule is the $^1\Sigma$ state, and the upper electronic state of the molecule is the $^1\Pi$ state. Each rotation level of the $^1\Pi$ state is split into two closely spaced sublevels (Λ-doublet sublevels). The structure of energy levels for such a molecule is shown in Fig. 1. Let us consider the case when the time-dependent electric field $\vec{E}(t)$ acts on the polar diatomic molecule in a plasma. We assume that the typical frequencies $\tilde{\omega}$ of the electric field $\vec{E}(t)$ are much smaller than the splitting ε_{21} of the Λ - doublet sublevels of the upper rotational level J_τ.

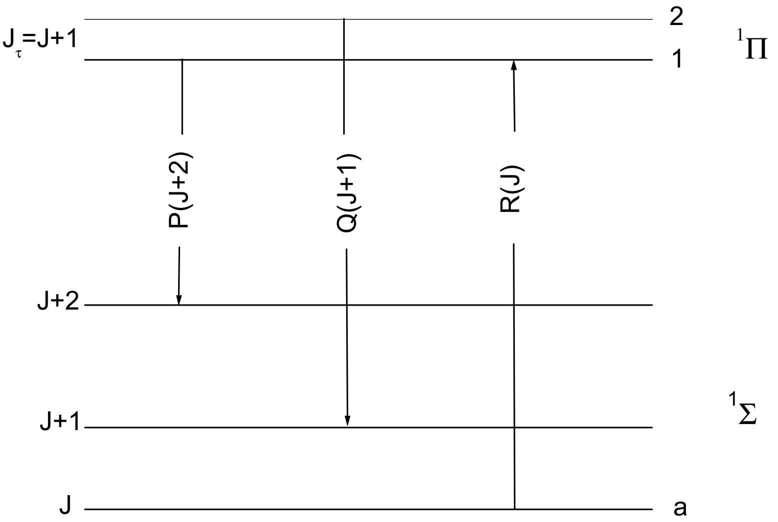

Figure 1. Scheme of energy levels of a polar diatomic molecule. The laser radiation populates the $\Lambda-$doublet sublevels 1 and 2 by excitation of the R branch transition. The Q and P branch transitions are observed in the fluorescence spectrum.

Then the wave functions of this $\Lambda-$doublet sublevels (sublevels 1 and 2) can be represented as

$$\begin{aligned}\Phi_{1m}(t) &= \{\chi_{1m}\cos(b_m(t)/2)-\chi_{2m}\sin(b_m(t)/2)\}\exp(-i\int_0^t \omega_{1m}(t')dt'),\\ \Phi_{2m}(t) &= \{\chi_{1m}\sin(b_m(t)/2)+\chi_{2m}\cos(b_m(t)/2)\}\exp(-i\int_0^t \omega_{2m}(t')dt').\end{aligned} \tag{1}$$

Here we assume that the quantization axis z is chosen along the direction of the electric field $\vec{E}(t)$. In Eqs. (1), m is the quantum number of the projection of the total angular momentum of the molecule on the z axis, χ_{1M} and χ_{2M} are the unperturbed wave functions of the sublevels 1 and 2, and $\omega_{qm}(t)$ (q=1,2) are the "instantaneous" energies of the sublevels. In Eqs. (1) and further we use the atomic units: $\hbar = m_e = e = 1$. The values $\omega_{qm}(t)$ and $b_m(t)$ can be expressed as follows

$$\begin{aligned}&\omega_{qm}(t) = [\varepsilon_1^{(0)}+\varepsilon_2^{(0)}+(-1)^k\varepsilon_{21,m}(t)]/2, \qquad q=1,2,\\ &\varepsilon_{21,m}(t) = \varepsilon_{21}[1+\sigma_m^2E^2(t)]^{1/2}, \qquad \varepsilon_{21}=\varepsilon_2^{(0)}-\varepsilon_1^{(0)},\\ &\sigma_m = 2\mu m/[J_\tau(J_\tau+1)\varepsilon_{21}],\\ &b_m(t) = \arctan[\sigma_m E(t)].\end{aligned} \tag{2}$$

In Eq. (2), μ is the dipole moment of the polar molecule in the upper electronic state $^1\Pi$.

Designating the lower level for the $R(J)$ transition by "a", we assume that the transition $a \rightarrow 1$ is optically allowed, whereas the transition $a \rightarrow 2$ is optically forbidden in the absence of the electric field.

For determining the evolution of the molecules under superposition of the laser field $\vec{E}_L(t)$ and the plasma field $\vec{E}(t)$ we solved the equation for the density matrix in the interaction representation

$$
\begin{aligned}
&i\partial\rho/\partial t = [V_1 + V_2, \rho] + i\gamma\rho, \\
&V_1 = -\vec{d}\vec{E}_L(t), \qquad V_2 = -d_z E(t).
\end{aligned}
\tag{3}
$$

In Eq. (3), γ is the relaxation operator allowing for spontaneous radiative transfer from the $\Lambda-$doublet sublevels 1,2, d_z is the $z-$component of the operator of the dipole moment $\vec{d}$ of the molecule. The laser bandwidth was assumed to be larger than the frequency separation ε_{21} and the natural width Γ of the sublevels 1 and 2. For solving Eq. (3) in the case when the electric field $\vec{E}(t)$ is the oscillating field ($\vec{E}(t) = \vec{E}_0 \cos\omega t$), we used the Fourier series expansion of the functions $\omega_{qm}(t), \varepsilon_{21,m}(t), b_m(t)$ presented in Eqs. (2). In the case when the electric field $\vec{E}(t)$ is the plasma ion microfield, we used the Model Microfield Method proposed in [10]. The intensity of the fluorescent radiation for the transition from the $\Lambda-$doublet sublevels 1 and 2 to some lower level q of the $^1\Sigma$ state can be represented in the form

$$
I = \sum_{k,k',m,m'} \rho_{km,k'm} \left\langle \Phi_{k'm}(t) \middle| \vec{d} \middle| \varphi_{qm'} \right\rangle \left\langle \varphi_{qm'} \middle| \vec{d} \middle| \Phi_{km}(t) \right\rangle,
$$

where $\varphi_{qm'}$ is the wave function of the m' state of the level q. Figure 2 presents as an example the results of the calculations of the ratio of time average intensities of the Q and P lines in the fluorescence spectrum of a polar diatomic molecule interacting with the oscillating electric field $\vec{E}(t) = \vec{E}_0 \cos\omega t$ versus the reduced amplitude of the oscillating field $\xi = \mu E_0 /(3\hbar\varepsilon_{21})$. It is assumed that laser radiation excites the transition R(1) in the polar diatomic molecule (see Fig. 1).

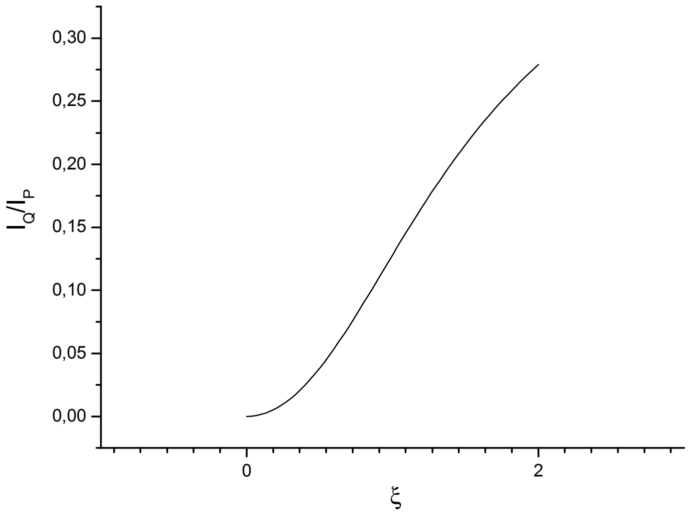

Figure 2. The ratio of time average intensities of Q and P lines in the fluorescence spectrum of a polar diatomic molecule as a function of the reduced amplitude of the regular oscillating electric field $\xi = \mu E_0 /(3\hbar\varepsilon_{21})$. The ration Γ/ω was assumed to be equal to 1.0.

In Fig. 3 is given the ratio of intensities of the Q and P lines in the fluorescence spectrum of a polar diatomic molecule as a function of plasma density N_e. In our calculations, we assumed that the polar diatomic molecule has the following parameters: $\mu = 1.0$ Debye, $\varepsilon_{21} = 5\times10^{-5}$ cm^{-1}. Similar to Fig. 2, it is assumed that the laser radiation excites the transition R(1) in the polar diatomic molecule. For the curve 1 the ion motion effects in a plasma were taken onto account. The curve 2 corresponds to the case when the ion motion is neglected. It can be seen that the ion motion effects can be important for the formation of the fluorescence spectrum of a polar diatomic molecule.

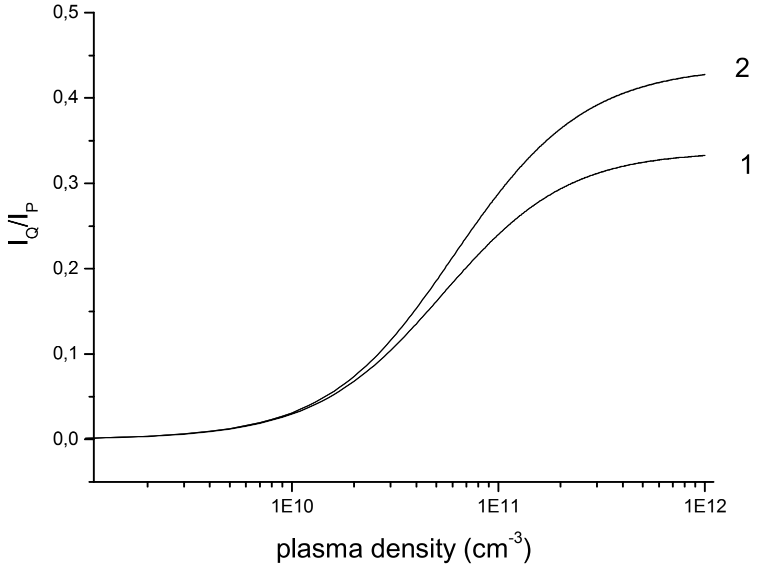

Figure 3. The ratio of intensities of the Q and P lines in the fluorescence spectrum of a polar diatomic molecule versus the plasma density N_e. Curve 1: ion motion effects are taken into account. Curve2: ion motion effects are not taken into account.

3. Conclusions

In the present work we calculated the intensities in the fluorescence spectrum of a polar diatomic molecule interacting with time-dependent plasma electric fields. Two types of electric fields were considered: (1) the regular oscillating electric field $\vec{E}(t) = \vec{E}_0 \cos\omega t$, and (2) the electric field produced by chaotically moving ions in a plasma. We obtained that taking into account the time dependence of the electric field can be important for correct describing the intensities of spectral lines in the fluorescence spectrum of a polar molecule. The results presented in our work can be used for spectroscopic measurements of electric fields and plasma density in a low temperature plasma.

Acknowledgements

This work was supported in part by the Alexander von Humboldt Foundation, the Royal Society (the Royal Society Grant gt/fSU/JP), the Russian Foundation for Basic Research (project no. 01-02-17810), and the International Science & Technology Center (project no. 2098). The author thanks Prof. V.N. Kolokoltsov (Nottingham Trent University, Nottingham, UK) for fruitful discussions.

References

[1] C.A. Moore, G.P. Davis, R.A. Gottscho - *Phys. Rev. Lett.* **52**, 538 (1984).
[2] R.A. Gottscho, M.L. Mandish – *J. Vac. Sci. Technol.* **A3**, 617 (1985).
[3] J. Derouard, N. Sadeghi - *Optics Commun.* **57**, 239 (1986).
[4] C.E. Gaebe, T.R. Hayes, R.A. Gottscho – *Phys. Rev. A* **35**, 2993 (1987).

[5] H. Debontride, J. Derouard, P. Edel, R. Romestain, N. Sadeghi, J.P. Boeuf – *Phys. Rev. A* **40**, 5208 (1989).
[6] M.D. Bowden, T. Nakamura, K. Muraoka, Y. Yamagata, B.W. James, M. Maeda - *J. Appl. Phys*. **73**, 3664 (1993).
[7] S. Maurmann, H.-J. Kunze, V.P. Gavrilenko, E. Oks - *J. Phys. B: At. Mol. Opt. Phys.* **29**, 25 (1996).
[8] S. Maurmann, V.P. Gavrilenko, H.-J. Kunze, E. Oks - *J. Phys. D: Appl. Phys.* **29**, 1525 (1996).
[9] E. K. Cherkasova, V.P. Gavrilenko, A.I. Zhuzhunashvili, *These proceedings.*
[10] A. Brissaud, U. Frisch – *J. Quant. Spectrosc. Radiat. Transfer* **11**, 1767 (1971).

Functionalisation of cotton fabrics with (meth)acrylate monomers by glow discharge plasma

L. Corsi[1], S. Nesti[1], E. Fatarella[2], V. Castelvetro[2], G. Ciardelli[1,3] and F. Zulli[4]

[1]*Tecnotessile, National Society of Technological Research r.l. Prato*
[2]*Department of Chemistry and Industrial Chemistry, University of Pisa, Italy*
[3]*current address: Dep. of Chemical Engineering, Industrial Chemistry and Material Science, University of Pisa, Italy*
[4]*Dep. of Department of Physics, University of Pisa, Italy*

Abstract

Preliminary attempts to modify the surface of cotton fabrics by means of low temperature plasma treatment with glycidilmethacrylate [GMA] (epoxide group can react with a wide variety of different functional groups) is presented.

Introduction

Over the past three decades research on low temperature plasma technology was also focused on fimproving the surface properties of polymeric materials without changing the bulk properties[1-5]. Research was also oriented to improve wettability, water repellency, soiling, soil release, printing, dyeing and other finishing processes of textile fibres and fabrics by using plasma technology [6-10].

Plasma treatments for the surface modification of textiles are usually performed by applying two main procedures, i.e. deposition or non-deposition plasmas. In the case of deposition plasmas, the plasma is usually applied by using saturated and unsaturated gases such as fluoro- and hydro-carbons or vapours or monomers such as acetone, methanol, allylamine and acrylic acid. Several reactive etching (Ar, He, O_2, N_2, F_2) or non-polymerisable gases (H_2O, NH_3) are used in the non-deposition plasmas.

Plasma processing is a clean, simple and multifunctional process that meets today's strict economic and ecological demands. As noted in many previous studies, the main advantages of plasma treatments are shorter processing times and the absence of water [11-13].

In this present study, the low-temperature plasma methods were used to modify the cotton fibres prior to graft a methacrylate monomer. Two methods were employed: either the direct application of the monomer in the reaction chamber after plasma activation of cotton fabric; or a two-stage application involving exposure to gas plasma followed by immersion in a monomer solution.

Experimental

Materials

Methanol and Acetone were reagent grade.

Glycidyl methacrylate (GMA, 97%, b.p. 189 °C), 3,3,4,4,5,5,6,6,7,7,8,8,9,9,10,10,10-Heptadecafluorodecyl methacrylate was supplied by Aldrich and was used as such.

Mercerised cotton was supplied by Tecnotessile.

Equipments

Plasma treatments have been realised by a Plasma system including an RF generator (0-600 W; 13.56 MHz in a continuous wave or pulse mode); an RF impedance matching network; a vacuum pump with a capacity of 18 m^3/h; two planar electrodes shielded against RF radiation and appropriate meters and gauges for measuring power output and pressures. Inside dimensions of the cylindrically-shaped steel reactor are 50 cm in diameter and 50 cm in length for a total volume of 7850 cm^3. Four inlets into the reactor are present: the first one for the introduction of the gaseous monomer, downstream from the electrodes; the other three ones for process gases (Argon, Oxygen, Nitrogen or a mixture of them). The square sample older is formed from steel net-support, optimised to suspend the sample with minimum contact.

Impregnation of fabrics with monomers has been realised by a FL 500/V Foulard machine (Gavazzi S.r.l.).

Plasma treatment

Unless otherwise indicated, a target square fabric specimen (20 x 20 cm) was centrally located in the reactor between electrodes. The vacuum pump was started: when a pressure of 0.04 mbar was attained, processing gas was introduced into the system. After the pressure returned to 0.2 mbar, the RF generator was turned on and the RF power adjusted to the processing power value ranging from 150-550 W. Samples were subjected to the gas plasma for various time ranging from 0-300 sec, after which RF power was turned off and the system was allowed to return to atmospheric pressure. Fabric specimens were removed, conditioned at 105 °C for 4 hours, cooled over silica-gel in a desiccator and weighed.

Grafting Procedure by Discontinuous Plasma (DP) Process

The plasma-treated cotton sample was placed into a reaction flask containing a 500 ml of a 20% (v/v) GMA solution in methanol/water (1:1). The flask contents were kept in a thermostatic oil bath at the temperature of 85 °C under methanol reflux for 4 hours. After the reaction time was over, the sample was removed and consecutively washed with: a hot solution (T=85 °C) of methanol/water (1:1) for 1 h; a solution of methanol/water (1:1) at ambient temperature for 1 h; and with acetone at ambient temperature for 1 h twice. The sample was then squeezed and dried in an oven at 105°C for a period of 4 h, cooled over silica-gel in a desiccator and weighed.

Grafting Procedure by Continuous Plasma (CP) Process

After the plasma treatment of the cotton sample, the valve of gas inlet was turned off, while the vacuum pump valve was still opened: when a pressure of 0.04 mbar was attained, the monomer (GMA) in vapour phase was introduced into the system. The monomer was previously degassed with Argon for 2 hours. The time of treatment was in the range from 60-300 min. After the reaction time, the sample was removed and washed as described in previously paragraph.

Qualitative Estimation of Cotton Macroradical

Electron Spin Resonance (ESR) Confirmation

The cotton macroradical generation was confirmed by ESR analysis. The ESR spectra were recorded using a continuous wave ER 200 D-SRC spectrometer in collaboration with Prof. Giordano of the Department of Physics at the University of Pisa.

Estimation of Percentage of Graft Add-on

Gravimetric Method

The percentage of graft add-on was calculated on a dry-weight basis. This was determined by storing the heated material at 105°C for a period of 4 h over silica-gel at room temperature in a vacuum dessicator until a constant weight was obtained:

$$\text{Percent graft add-on} = \frac{(W_2 - W_1)}{W_1} \times 100$$

where W_2 is the dry weight of the grafted sample and W_1 is the dry weight of cotton fabric after the plasma treatment.

Attenuated total reflectance Infrared analysis (ATR-IR)

The grafting was confirmed by IR analysis. The ATR-IR spectra were recorded using a Perkin-Elmer Spectrum GX spectrometer, at room temperature.

Results and Discussion

Effect of the kind of Gas on the Amount of Cotton Macroradical Generated by Plasma Process

Mercerised cotton samples were treated by different gas plasmas at constant RF power and treatment time (250 W; 180 sec); after treatment, samples was placed into a reaction flask containing GMA and treated as described. Table I shows the relation between the amount of GMA grafted onto the cotton sample (related to the amount of free radicals generated onto the cotton surface) as a function of the kind of gas used in the plasma process.

Table I - Functionalisation of cotton with GMA by different gas plasmas

Sample	*Power*	*Time*	*Gas*	*GMA add-on*[a]	*GMA add-on*
	(W)	*(sec)*		*(g)*	*(%)*
Cot1-1	250	180	Ar	0,1829	5,30
Cot1-2	250	180	air	0,0487	1,43
Cot1-3	250	180	O_2/Ar (1:1)	0	0
Cot1-4	250	180	O_2	0	0
Cot1-5	250	180	N_2	0,0613	1,83

[a] material grafted onto cotton surface $(W_2\text{-}W_1)$

IR spectra of treated materials after washing resulted quite complex. However, the band at 1730 cm^{-1} (stretching of C=O) can be considered diagnostic for the presence of grafted poly-GMA (Figure 1).

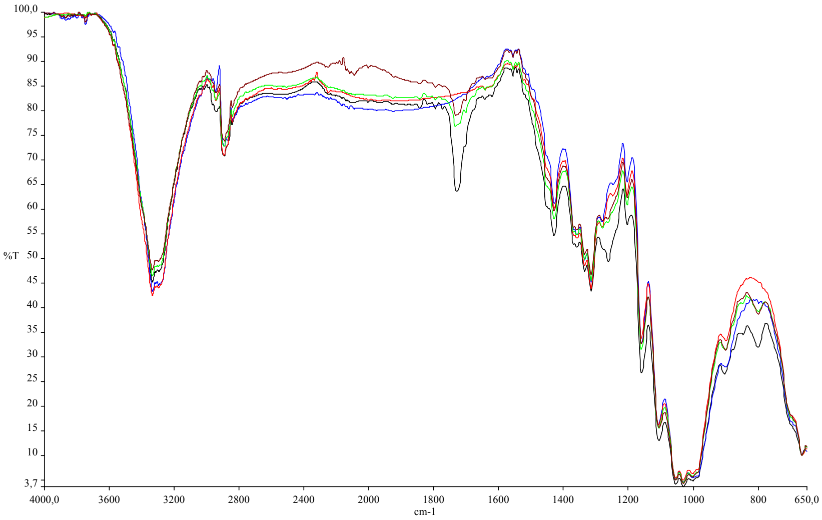

Figure 1- ATR spectra of plasma treated cotton samples using different gases, after functionalisation with GMA (black Cot-1; bordeau Cot1-2; blue Cot1-3; red Cot1-4; green Cot1-5)

Results obtained indicate that the best percent of graft add-on value was obtained using Argon as processing gas probably because Argon generates the larger number of free radicals on the surface of the fabric. Argon does not generate secondary reactions leading to the physical ablation of material from the fabric surface.. In the case of Argon/Oxygen mixture the generation of active species on the fabric surface due to Argon, competes with the substitution of functional groups on the material surface by -OH, -C=O and –COOH groups, due to the presence of oxygen.

In order to verify the nature of the radical species onto the cotton surface an ESR study on some samples of cotton treated by argon-plasma for 180 seconds, at varying RF powers and contact time with air (simulating the conditions for continous plasma treatment) was carried out. Results are shown in Table II and Figure 2.

Table II – Argon-plasma treatment of cotton fabrics

Sample	RF power (W)	Air exposition
1	150	YES
2	250	YES
3	350	YES
4	450	YES
5	550	YES
6	100	NO
7	200	NO
8	300	NO

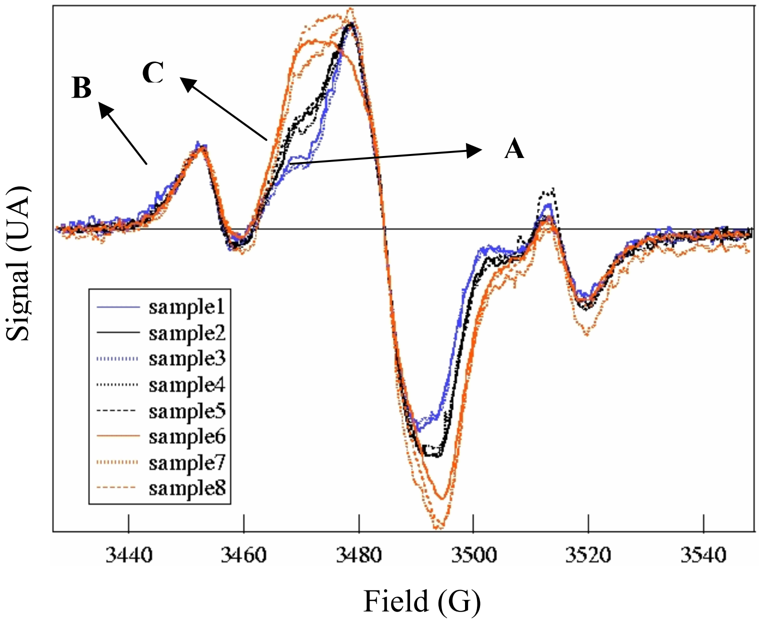

Figure 2 – ESR spectra of cotton samples treated by argon-plasma and typical bands of radical species A, B and C.

Radical species held for responsible for spectra reported in Figure 2are sketched in Scheme I.

Scheme I– Possible radical species generated by argon plasma on cotton fibres.

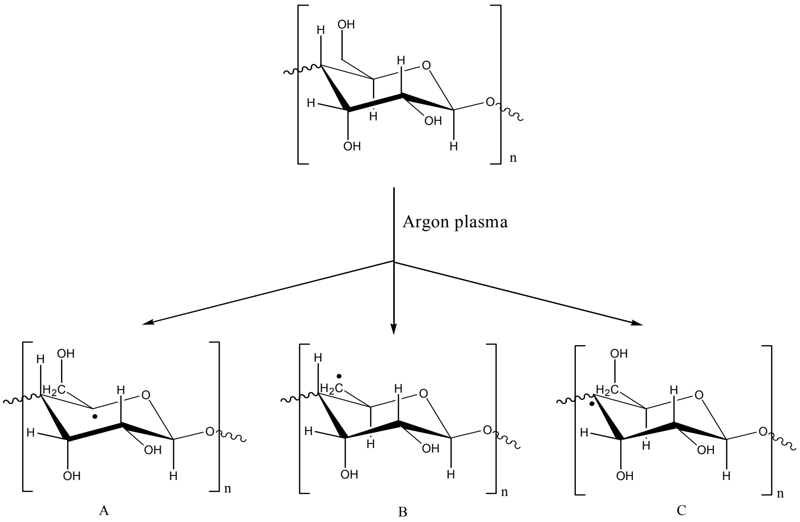

Effect of Plasma Power and Time of Treatment on Percent Graft Add-on in the DP Process

Figure 3 shows the effect of RF power on the graft add-on. The percent of graft add-on decreases by increasing the power, probably because at higher power a higher instantaneous concentration of radicals is generated, promoting coupling reaction that lead to the inactivation of active sites.
Moreover, at higher RF power, the energy value required to generate radicals is reached more quickly giving more time to etching reaction to become competitive.

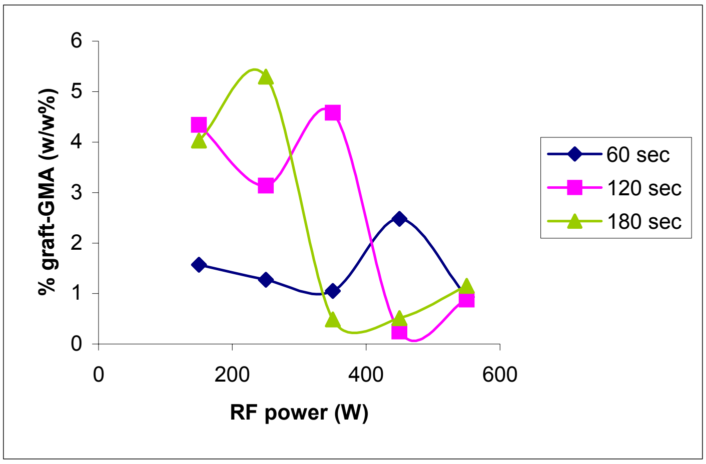

Figure 3 – Percent graft add-on of GMA as function of RF power.

Figure 4 shows the effect of time on the graft add-on. At long treatment time and lower RF power higher % of graft add-on is observed. In these conditions the generation of radicals is continuous and therefore radical coupling reactions are less likely to occur and the formation of stable active sites is favoured.

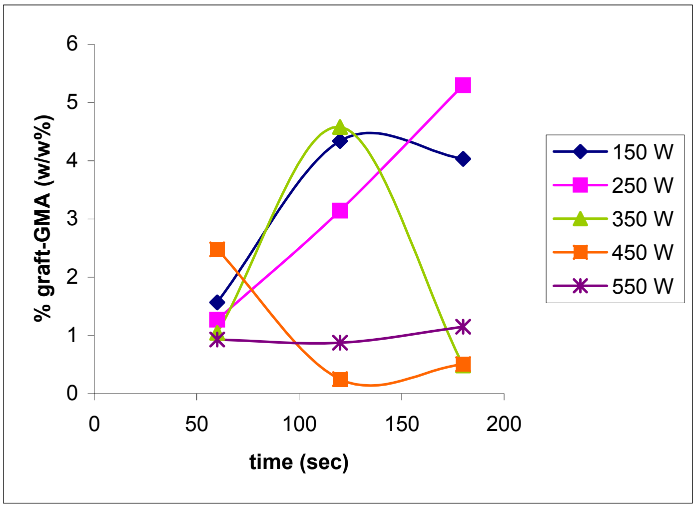

Figure 4 – Percent graft add-on of GMA as function of plasma treatment times

Effect of Plasma Power and Time of Treatment on Percent Graft Add-on in the CP Process

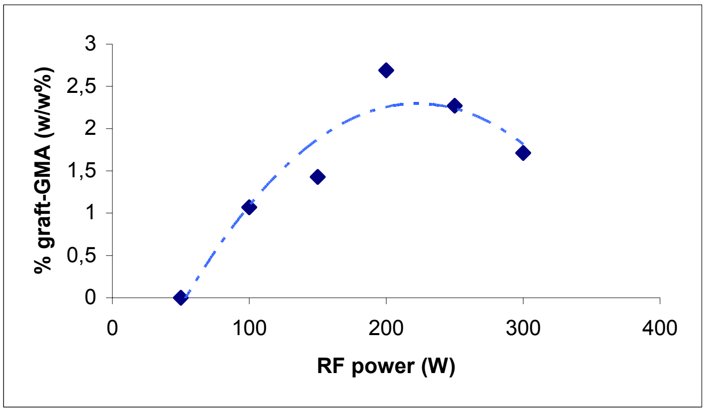

Figure 5 - Percent graft add-on of GMA as function of RF power at constant treatment time (180 sec.).

The graft add-on (Figure 5) shows a similar trend to that observed in the discontinuous process, as the maximum yield is recorded at RF powers between 200 and 250 W.

Conclusions

Plasma treatment is a promising technique for the modification of fabric surfaces for commercial purposes in tha apparel sector. The present work confirmed the possibility to graft an acrylic monomer on natural fibers by either continous or discontinous treatment through plasma surface activation. Future work is in progress to extend the precisely established operating conditions for GMA to a wider palette of acrylic monomers carrying functionalities which will be able to improve different characteristics of fabrics according to the more stringent requirements of the market.

References

[1] J.K. Hollahan, A.T. Bell – Techniques and Applications of Plasma Chemistry (New York: John Wiley and Sons, 1974).
[2] D.T. Clark, W.J. Feast – Application of Plasmas to the Synthesis and Surface Modifications of Polymers (New York: John Wiley and Sons, 1978).
[3] H. Yasuda – J. Polym. Sci.: Macromol. Rev. **16**, 199 (1981).
[4] H. Yasuda – Plasma Polymerisation (Orlando: Academic Press Inc., 1985).
[5] R. D’Agostino – Plasma Depositation, Treatment and Etching of Polymers (New York: Academic Press Inc., 1991).
[6] G.A. Byrne, K.C. Brown – J.S.D.C. **86**, 113 (1974).
[7] A.M. Wrobel, M. Kryszewski, M. Gazicki – Polymer **17**, 673 (1978).
[8] C.J. Jahagirdar, S. Venkatarkrishnan – J. Appl. Polym. Sci. **41**, 117 (1990).
[9] T. Okuno, T. Yasuda, H. Yasuda – Text. Res. J. **62**, 474 (1992).
[10] A.M. Sarmadi, Y.A. Kwon – Text. Chem. Colorist **25**, 33 (1993).
[11] M. Radetic, D. Jocic, P. Jovancic, R. Trajkovic, Z.L. Petrovic – Text. Chem. Colorist Amer. Dyestuff Rep. **32**, 55 (2000).
[12] H. Grzegorz, W. Urbanczyk, B.L. Symonowicz, S.T. Kowalska – Melliand Textilber. **64**, 838 (1983).
[13] T. Oktem, H. Ayhan, N. Seventekin, E. Piskin – J.S.D.C. **115**, 274 (1999).

Plasma assisted polymer coatings on ceramic nano particles

Zhigang Guo[1], Luting Yan[2], Wei He[1], Yikang Pu[1] and Wenjie Si[2]

[1] *Department of Engineering Physics, Tsinghua University, Beijing, 100084, China*
[2] *Department of Materials, Tsinghua University, Beijing, 100084, China*

Agglomeration occurs usually among ceramic nanoparticles because of their high surface energy. Polymer coatings on the surface of nanoparticles have the effect of oxidation reduction and decrease of surface energy. Furthermore, polymer coated ceramic powders are easily dispersed in plastic and this leads to an improvement of the formability of the ceramic powder by injection molding.

In this work, polymers are coated on the ZrO_2 and SiC nano powder by an inductively coupled plasma in a quartz tube. Either ethane or styrene and their mixture with nitrogen serve as the feed gases. The total pressure ranges from 30 Pa to 100 Pa and the RF power is between 20 W and 100 W. The active radicals produced by electron impact processes are monitored by optical emission spectroscopy. Thermogravimatric analysis of the treated samples indicates that 3% weight is added on the sample by the plasma process. Transmission Electron Microscopy (TEM) graph shows that 3-8 nm thick polymers is deposited on the surface of the nanoparticles. The diffuse reflection FT-IR spectroscopy is employed to determine the component of the polymer. Experimental results under different plasma conditions are compared and analyzed.

[1] Donglu Shi, S. X.. Wang, Wim J. van Ooij, L. M. Wang, Jiangang Zhao, Zhou Yu. Uniform deposition of ultrathin polymer films on the surface of Al_2O_3 nanoparticles by a plasma treatment. *Applied Physics Letters*, **78**(9), 2001, pp.1243-1245.

Surface Wave Oxygen Plasma Production with High Permittivity Microwave-Window

K. Fujiwara[1], K. Matsuo[1], K. Kawamura[2] and H. Shindo[1]

[1]*Department of Electronics, Tokai University, 1117 Kitakaname, Hiratsuka 259-1292, Japan*
[2]*Process Equipment Division, Canon Sales Corporation, 2-13-29 Kounan, Minato-ku, Tokyo 108-0075, Japan*

Abstract

As a novel method of large-diameter plasma production for ultra large-scale integrated (ULSI) circuit processes, microwave plasma production employing a high-permittivity material window is proposed. A systematic plasma density enhancement is found to occur in conjunction with increase in the permittivity value of the dielectric window material. The results are shown to be due to the surface wave, and the microwave power consumption mainly occurs near the window in the high permittivity. This plasma production can provide a good downstream plasma with a large diameter for ULSI processes.

1. Introduction

Plasma processes such as etching, deposition and resist ashing are one of the key technologies for large-scale integrated (LSI) circuit fabrication. In these processes, a large-diameter plasma source is required to meet the forthcoming demand of 300 mm diameter wafer fabrication. Microwave plasma is a potential candidate as a large-diameter plasma source. One issue in large-diameter microwave plasma sources is the dielectric window material required for the introduction of microwaves. As the plasma diameter is increased, the mechanical stress on the window material is significantly enhanced. Therefore, the thickness of the window material increases, making plasma production ineffective. To avoid this problem, the introduction of microwaves by slot antenna has already been proposed [1]. This device enables suppression of the window area, but the plasma uniformity remains questionable. In this method, microwaves were introduced as a surface wave [1-3]. In order to attain good plasma uniformity, the microwaves should be introduced through a large-area window, and the window material should be as thin as possible.

We have previously reported that plasma production employing an alumina window resulted in a density enhancement; this was found by comparison with quartz window material [4].

The objective of this work is to perform a systematic investigation into the effect of the permittivity of the window material on plasma production. In particular, the permittivity dependence of the electron density as well as its axial variations is examined for a wide range of permittivities of windows. The electron energy distribution function and its axial variation are also examined to find the total effect of the permittivity on plasma properties, thus providing an aspect of microwave power consumption. It is extremely important to clarify the total effect of the permittivity for future development of large-diameter microwave plasma sources. It would be particularly beneficial to carry out experiments with a practical process gas of oxygen for applications. The oxygen plasmas are important media for oxidation and resist ashing in silicon processes.

2. Experimental

The plasma was produced in an aluminum chamber of 360 mm in diameter as shown in Fig. 1. At the one end of the chamber, a microwave of frequency 2.45 GHz was introduced through a dielectric window of disc plates of 240 and 360 mm in diameter. Before introducing the microwaves into the dielectric window, the microwave mode was converted from TE_{10} at the rectangular wave guide to TM_{01} at the circular one.

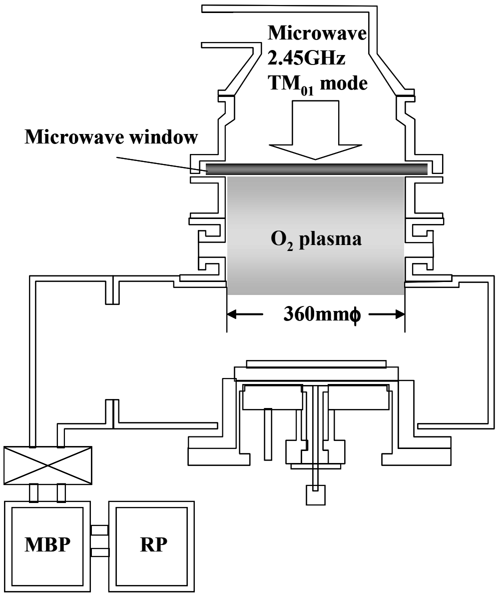

Fig. 1. Schematic illustration of the experimental apparatus.

Four kinds of dielectric windows, quartz, alumina and two commercially available aluminum nitrides, with different permittivities were employed in this experiment; their permittivities were, respectively, 3.86 (14.9 GHz), 9.7 (10 GHz), 8.5 (14.9 GHz) and 10.9 (14.9 GHz), where the frequencies used for the permittivity measurements are given in parentheses. The microwave frequency for plasma production is different from those used for the permittivity measurements, but their values at 2.45 GHz do not differ significantly from their measured values [5]. The permittivity for one of the aluminum nitrides is as high as 10.9, more than double that for quartz, 3.86. The plasma parameters were measured using a Pt plane probe of diameter 1 mm in diameter with the aid of a PMS-8051 probing system (Nihon Kousyuha). The microwave magnetic field was also measured by a small pick-up coil [4], to show how the microwave travels into the plasma volume at different conditions. Hereafter, the experimental data of the oxygen plasma will be shown as a function of the radial distance R from the chamber axis and the axial distance Z from the inner surface of the microwave window. In this experiment, all the measurements were carried out under the conditions of a microwave power of 1 kW with zero reflected power and an O_2 gas pressure of 1-3 Torr.

3. Results and Discussions

In Fig. 2, the permittivity dependence of the measured electron density is shown for 3 Torr O_2 gas pressure. One notes, however, that the electron density values plotted in Fig.2 are all averaged values for each radial plane with the constant Z. This is carried out because the measured local values of electron density are greatly affected by the microwave mode, making the data plots complicated. In Fig. 2, a marked dependence on the permittivity of the window material can be clearly observed for all axial distances of Z, particularly at low Z of the upstream. At Z=1 cm, the permittivity dependence is quite prominent in spite of the averaged values of the electron density, suggesting that the plasma production mechanism involves a significant effect of the permittivity of the window. In the figure, the cutoff density for the 2.45 GHz microwave is indicated by a broken line, and one data point for the lowest permittivity of quartz is just below this value even in the case of Z=1 cm upstream. Thus the electron density under this condition is just below the cutoff density in the entire volume of plasma. This suggests that the microwave does not become the surface wave mode in the case of the quartz. This property can also be confirmed by the following data.

Figure 3 shows the plots of the measured microwave magnetic flux density as a function of the axial distance Z, where the radial component Br is compared for the four windows. The behaviors of the microwave magnetic field are highly consistent with those of the electron density as shown above. In the case of the quartz, the microwave magnetic field does not decay as much in the plasma volume and maintains still high values, indicating that the microwave travels into the plasma volume. In the cases of higher permittivity such as for the alumina and aluminum nitrides, on the other hand, the field decays rapidly

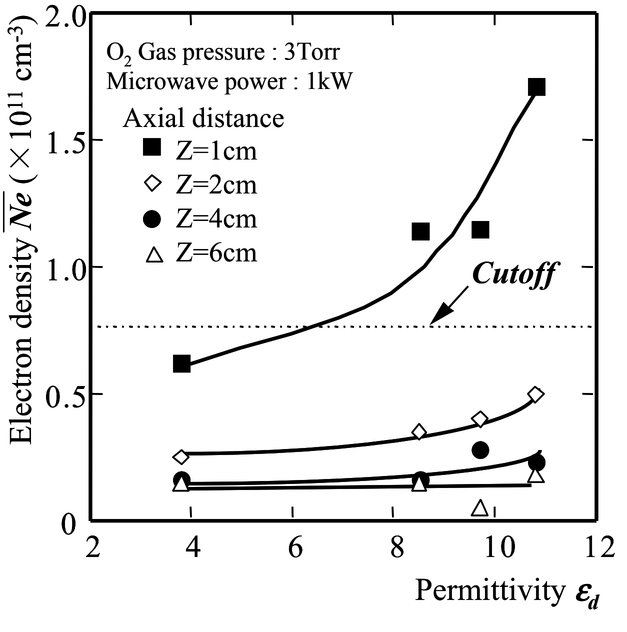

Fig. 2. Electron density as a function of the permittivity of the microwave window materials.

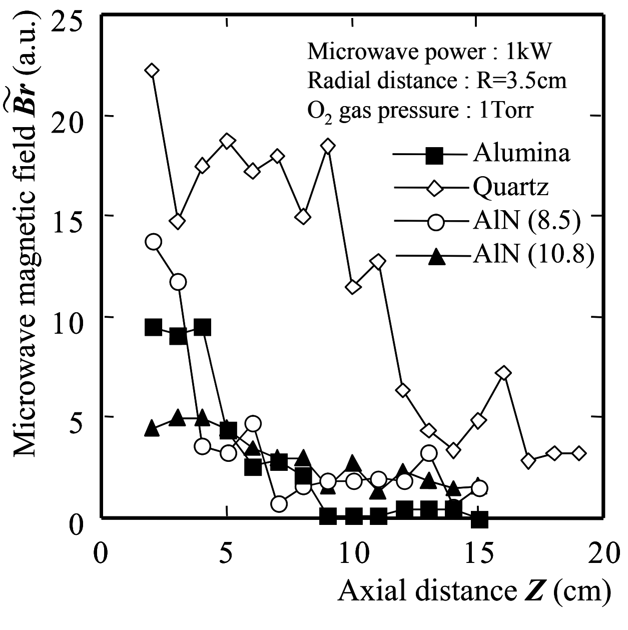

Fig. 3. Axial variations of the microwave magnetic field.

with the axial distance and reaches a quite low level even at Z=10 cm, indicating that the microwave is in the surface wave mode. It should be noted, furthermore, that the decay is closely related to the value of permittivity, as higher permittivity increases the rate of decay. This feature is consistent with the data shown in Fig. 2.

As demonstrated above, for the lowest permittivity of the quartz the microwave is not in the surface wave mode and travels into the volume of the plasma. This microwave behavior has another effect on plasma parameters. The electron energy distribution functions (EEDF) were measured by a Langmuir probe for two typical cases of the alumina and quartz, and the axial variation of the electron energy distribution functions was analyzed. These axial variations of the electron energy distribution function were quite reasonable. In the alumina with the higher permittivity, the electron energy decreases drastically below Z=10 cm, in accordance with the microwave field shown in Fig. 3. To be specific, since the microwave is in the surface wave mode in the alumina and the electron acceleration field decays rapidly in the downstream, the electron gains less energy there. For the quartz, on the other hand, the axial decay of the electron energy is not as evident, and only the density decay is relatively visible, which is also consistent with the microwave field shown in Fig. 3. Since the microwave field does not decay as much under this condition, the electron energy maintains a high level even in the downstream.

In Fig. 4, the energy in which the distribution function shown has a peak is plotted and compared for the two cases. It is clearly demonstrated in Fig. 4 that the axial variations of the electron energy are essentially different between the two window materials. In the alumina window with the higher permittivity, the electron energy decays rapidly with axial distance, while the energy in the quartz shows almost no decay.

As described thus far, the plasma produced by employing a higher permittivity window readily reaches high density, and the microwave power is supplied by the surface wave in this case. In other words, the microwave power is consumed in the immediate vicinity of the window, providing a powerful means to produce a good downstream plasma, where chemically reactive species are rich and less energetic charged-particles are presented.

One possible explanation for the mechanism of the density enhancement is as follows. The microwave passing through the interface between the dielectric and the plasma is governed by the boundary conditions for the field, and one of these conditions is the continuity of the normal component of the dielectric flux density. The normal component of the dielectric flux density is required to be the same at both media, and one way to meet this requirement is to have the same permittivity for the plasma as that of the window material. For the higher window permittivity, therefore, the electron density becomes higher to elevate its own permittivity. In this requirement, however, the evanescent wave, hence the surface wave is only allowable for the microwave in the transverse magnetic wave (TM) mode [6].

When the microwave is not in the surface wave but the volume mode, a different dependence on the permittivity appears and the plasma behaves differently. Under these plasma conditions, the electron density is relatively low and its permittivity ε_p is just below unity as $\varepsilon_p=1-(\omega_p/\omega)^2$, where ω_p and ω are the frequencies of the plasma oscillation and the microwave respectively. Since ε_p is fairly low compared with that of the window, its effect on the electron density is small. If the microwave power is fairly high and the electron density is increased, the plasma permittivity ε_p becomes negative, and this further requires another condition that the microwave must be evanescent for the TM mode. In this regime, the electron density depends markedly on the permittivity ε_d of the window and is enhanced, so as to fulfill the relation $\varepsilon_p+\varepsilon_d=0$. This is precisely the condition we found experimentally as shown in Fig. 2. The skin depth δ for the microwave in plasma is also affected by the permittivity ε_d, because the tangential wave number is the same for both media, and δ becomes smaller with the higher ε_d. In other words, the microwave power is consumed only in the vicinity of the window.

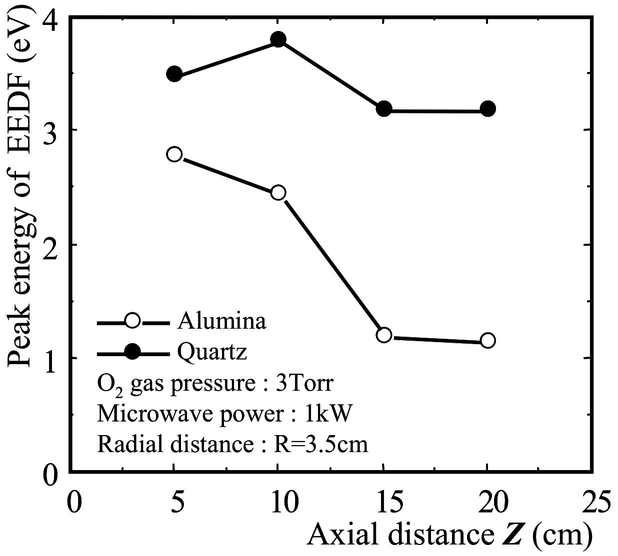

Fig. 4. Axial variation of the peak energy in the electron energy distribution function.

The microwave electric field in plasma also depends on the permittivity ε_d and in the case of the volume wave mode, the field strength increases as the permittivity is increased, providing that the electron density is constant. The higher electric field may be a driving force in causing the microwave to become a surface wave. In other words, it is easier for the microwave to be evanescent with higher permittivity ε_d of the microwave window. A more exact description of this mechanism, however, requires a further investigation involving the simulation of the plasma production mechanism; this is a subject for future study.

As described above, the introduction of microwave power using a high-permittivity window material provides a higher electron density if the microwave is in the surface-wave mode. The choice of a high-permittivity window material provides one method of realizing a large-diameter microwave plasma source for the forthcoming large-diameter wafer processes.

References

[1] M. Nagatsu, G. Xu, M. Yamage, M. Kanoh and H. Sugai: Jpn. J. Appl. Phys. **35**(1996)L341.

[2] I. Ghanashev, M. Nagatsu and H. Sugai: Jpn. J. Appl. Phys. **36**(1997)337.

[3] Z. Zakrezewski and M. Moisan: Microwave Discharges, eds. C. M. Ferreira and M. Moisan (Plenum Press, New York, 1993) p. 117.

[4] M. Furukawa, N .Saito, K. Kawamura and H. Shindo: Jpn. J. Appl. Phys. **37**(1998)L1005.

[5] A. R. Von Hippel: Handbook of Materials and Processes for Electronics, (McGraw Hill, New York, 1970) p. 110.

[6] H. Sugai, I. Ganashev and M. Nagatsu: Plasma Sources Sci. Technol. **7**(1998)192.

Negative-Ion Silicon Trench Oxidation in Surface-Wave Oxygen Plasma

H. Shindo, M. Takahashi, Y. Sugiura and K. Fujiwara

Department of Electronics, Tokai University, 1117 Kitakaname, Hiratsuka 259-1292, Japan

Abstract

For one application of negative ions in plasma, silicon trench oxidation at low temperature was studied by employing negative oxygen ions in surface-wave plasma. The oxidation depth showed a strong dependence on RF bias frequency, and thus it was concluded that the trench oxidation was due to the negative ions. The experimental result reveals that the bias has an optimum frequency at which maximum oxidation depth is realized.

1. Introduction

A low temperature and low damage silicon oxidation technique [1] is highly required in various ULSI processes. In particular for trench isolation of a memory cell to realize further integrations, the oxidation should be ion-assisted for directionality but with low damage. For this purpose, a new method of negative ion assisted silicon oxidation has been proposed employing a microwave O_2 plasma, and the high rate and low temperature silicon oxidation has been demonstrated [2].

The objective of this work is to study silicon oxidation characteristic in a silicon trench by negative ions under the RF bias. For a practical application of this method, the oxidation should be preceded under the RF bias, because the DC bias becomes ineffective as the oxide film is grown. In this work, the oxidation characteristics were intensively studied in silicon trench to form a shallow trench insulation layer for cell isolation of MOS transistor. In particular, the bias frequency was concerned to show an optimum condition of the oxidation at the trench bottom.

2. Experimental

The plasma was produced in a 6 inch stainless-steel chamber as shown in Fig. 1 and the downstream plasma was mainly considered due to the reason that this region was highly populated with negative ions. The plasma parameters were measured using a Pt Langmuir probe, especially for the saturation currents I^+ at the positive and I^- at the negative probe bias. Silicon oxidation was made on a stage 10 to 25 cm downstream from the microwave window, and the stage was biased by the DC voltage as well as the RF bias to irradiate both negative and positive ions. The RF bias voltage was applied to the stage with a transformer, and the secondary of the transformer was biased by DC voltage at the same time. Thus the substrate voltage was varied artificially from the negative to the positive during the cycle. During the oxidation a slight temperature rise in the substrate was observed if it is not heated. Hence, the oxidation experiment was also performed at the substrate temperature of 300 ^{o}C, and no temperature change was observed in this condition. The substrate temperature was monitored at the back of Si wafer using a thermocouple.

The oxide film quality thus produced was analyzed by X ray photoelectron spectroscopy (XPS). The oxide film thickness was measured by the XPS and ellipsometry methods. The sample used for oxidation was a P type crystal Si (100) and its surface was treated by 5% B-HF before oxidation. The oxygen plasma was generated for oxidation was at microwave power of 500 W and at pressure of 50 mTorr, unless stated otherwise. Hereafter the experimental data are

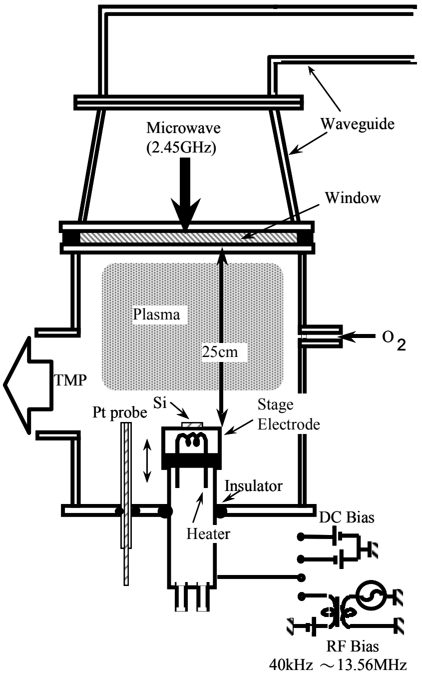

shown as a function of distance Z from the microwave entrance window. The oxidation characteristics was also examined in a silicon trench of 0.15 μm width and 0.2 μm depth.

3. Results and Discussion

For a detailed study of the negative ion behavior, silicon oxidation under the RF bias was examined, and a typical result is shown in Fig. 2, where the oxidation depth obtained with a flat silicon substrate at Z=18.5 cm is plotted against the frequency. The frequency of the bias was varied with keeping the RF voltage of 30 V peak-to-peak and DC voltage of +20 V. This value of +20 V is just the plasma potential observed [2] at the distance Z=18.5 cm. The oxidation depth in this case was determined from the step observed on the sample surface etched by B-HF. It is clearly demonstrated, in Fig. 2, that the oxidation strongly depends on the frequency and there is an optimum frequency. We have already reported that there is a limitation of oxidation at both sides of frequency [3, 4]. In particular, a high frequency limitation of oxidation has been concerned therein, and since the limitation began at about 1 MHz which was close to the negative ion plasma frequency, it was confirmed that the oxidation was negative ion-assisted. The frequency dependence of the oxidation depth shown in Fig. 2 is more detailed one, showing that the oxidation is maximum at the frequency of 1100 kHz. This value of the frequency is very close to the one found in our previous report [4]. In this condition, the oxidation depth becomes as high as 1600 Å, giving the rate of oxidation of 53 Å/min in the rate. At the axial distance Z=18.5 cm, the ratio of the positive bias probe saturation current I^+ to the negative one I^- was found about 5, indicating that the electron density in this condition is several order less than the negative ion density. Since the positive ion density can be estimated as 5×10^{10} cm^{-3} as the molecular oxygen ion O_2^+, almost the same amount of the negative ion O^- contributes to the high speed silicon oxidation as shown in Fig. 2.

For the frequency dependence shown in Fig. 2, more detailed explanations can be made as below. The condition in which the oxidation depth has a maximum value corresponds to a maximum ion flux onto the silicon surface. The maximum ion flux is attained in the condition where the ion traveling time from plasma to the substrate is just the same as the period of the RF bias. This is exactly the definition of the ion plasma frequency. Below this frequency, the ion energy cannot become large because the substrate voltage is increased relatively slow. At higher frequency, on the other hand, the ion is experienced deceleration as well as acceleration. Thus the ion flux becomes a maximum around the ion plasma frequency, and this is the reason why the oxidation depth has a maximum as shown in Fig. 2 [3].

In Fig. 3, the substrate bias current observed at various axial distances is demonstrated against the frequency for the same plasma condition as in Fig. 2. The substrate bias current in peak-to-peak volt. shows a strong frequency dependence at every distance Z. The gradual increase in the substrate current may be due to the displacement current, because it is proportional to the frequency. At the same time, a very localized peak is apparently seen for each curve, and it appears around the frequency of 1100 kHz. This localized peak may be due to the negative oxygen ion, because the frequency of the peak is close to the negative ion plasma frequency. The same explanation for the mechanism is possible as in the above mentioned about the oxidation depth shown in Fig. 2. Thus, it is clearly demonstrated that the frequency at

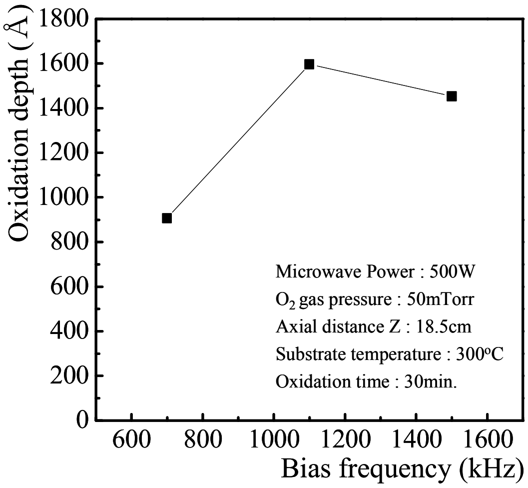

Fig. 2. Oxidation depth obtained with flat silicon as a function of bias frequency.

which the oxidation rate shows a maximum value corresponds to the one of localized substrate current peak due to the negative ion.

The condition which was found in the flat silicon oxidation above was applied to the trench oxidation. In Fig. 4, a typical example of the silicon trench oxidation is demonstrated, where the oxidation depth at various portion of the trench is plotted as a function of the bias frequency. The oxidation depth also shows strong frequency dependence, and most of the curve has a maximum at the same frequency as in Fig. 2. The oxidation at the top of the trench can be explained by the same mechanism as in the flat silicon. However, the oxidation at the trench bottom may be considered by a more detailed mechanism. For the trench bottom oxidation, the frequency of 1100 kHz also gives a maximum. However the ratio of the oxidation of the bottom to the top of trench is further enhanced at this frequency. To be specific, the ratio at the frequency 1100 kHz becomes as high as 0.65, while at 1500 kHz the ratio is limited to only 0.25. This enhancement in the oxidation at the bottom may be due to ion motion with more directed nature to the trench bottom at this frequency. For more detailed discussions on the mechanism, further study will be needed about the ion motions, and this is a next step of this work.

In the figure, the oxidation depth on the side wall is also shown, as one of important trench oxidation parameters. In actual formation of oxidation layer, the side wall oxidation is more important, and it should be as small as possible. In Fig. 4, however, the side wall oxidation at 1100 kHz is fairly high compared with the bottom. This is due to the nature of the silicon trench which was prepared this time. The silicon trench side wall showed a fairly strong taper as will be seen in Fig. 5. Thus the fairly high oxidation depth on the side wall in Fig. 4 is mainly due to the tapered nature of the side wall, and its actual oxidation can be expected smaller than as shown in Fig. 4. In Fig. 5, one example of SEM photographs in the oxidized trench is shown, where the oxidation was made in the condition of 1100 kHz. In

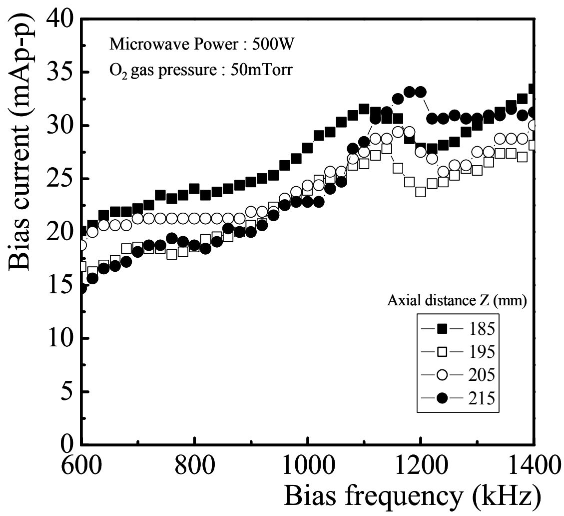

Fig. 3. Substrate bias current as a function of the frequency with the parameter of the distance Z.

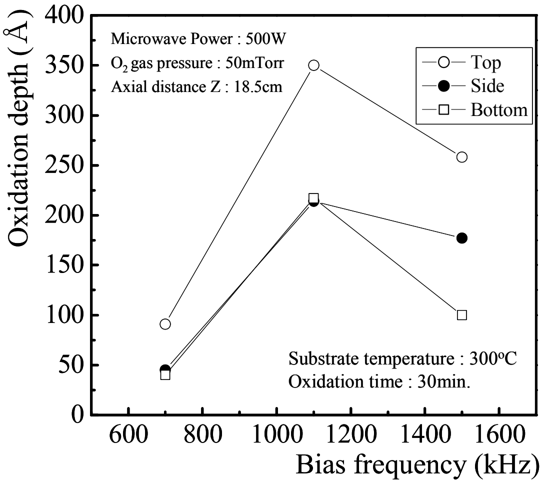

Fig. 4. Silicon trench oxidation characteristics as a function of the bias frequency.

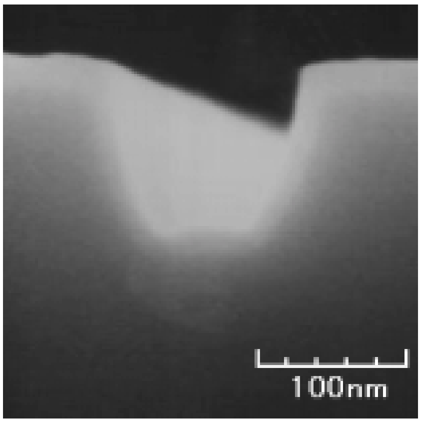

Fig. 5. SEM photograph of trench cross section oxidized at 1100 kHz.

this condition, the layer boundary between the silicon and silicon dioxide can be clearly seen, indicating that the good quality silicon dioxide film is formed.

By means of the substrate bias, the negative ion is attracted into the bottom of the trench, and the oxidation rate is drastically enhanced. This behavior is obviously originated from an ion dominated silicon oxidation reaction, and it is quite advantageous in the formation of a shallow trench isolation layer. Thus the negative ion silicon oxidation has a potential of an innovative technique.

References

[1] S. Taylor, J. F. Zhang and W. Eccleston: Semicond. Sci. Technol. **8**(1993)1426.
[2] T. Koromogawa, T. Fujii, Y. Horiike and H. Shindo: Jpn. J. Appl. Phys. **37**(1998)5028.
[3] T. Koromogawa, A. Yamashita, T. Urayama, Y. Horiike and H. Shindo: Proc. 15th Symp. Reactive Plasma, Hamamatsu, Japan, 1998, p.17.
[4] T. Fujii, H. Aoyagi, K. Kusaba, Y. Horiike and H. Shindo, Jpn. J. Appl. Phys., **38**(1999)L1466.

Surface treatment of a polymer bottle by plasma-based ion implantation

N. Sakudo[1], Y. Ohmura[1], R. Yoneda[1], H. Endo[1], N. Ikenaga[2], D. Mizutani[1], H. Takikawa[3]

[1] *Kanazawa Institute of Technology, Advanced Materials Science R & D Center, 3-1 Yatsukaho, Matto Ishikawa 924-0838, Japan*
[2] *Shibuya Kogyo Co. Ltd., 2-232, Wakamiya, Kanazawa, Ishikawa 920-0054 Japan*
[3] *Toyohashi University of Technology, Dept. of Electrical & Electronic Eng., Toyohashi, Aichi 441-8580 Japan*

Abstract

In order to enhance the gas barrier characteristics of PET (polyethylene terephthalate) the film surface of the material is changed to DLC (diamond like carbon) by PBII (plasma-based ion implantation). The change is confirmed by FT-IR and Laser Raman spectroscopy. Then, a new technique to implant ions into the inner surface of a PET bottle is proposed. The principle is simply described and new experimental equipment for treating a real bottle is constructed.

1. Introduction

PET is widely used as beverage containers and food or medicine packages due to the easy handling as well as the low cost. It is also suitable for recycling. However, the barrier characteristics against a certain kind of gases such as CO_2 and O_2 are not so good that the long-period maintenance of quality is hard for some beverages, beers, wines and medicines. The use of other polymer, PEN (Poly ethylene naphthalate) is effective to some extent for resolving the gas barrier problem [1]. But, the cost is higher and the material is not suitable for recycling. Recently, a European company developed a new technique that deposits thin DLC on the inner surface of a PET bottle in order to enhance the gas barrier characteristics [2]. It has shown that thin-DLC deposit of 0.02 to 0.04 micron enhances the barrier characteristics more than ten times as large as the uncoated PET. However, as far as they use coating technique, there remains a peeling problem of the deposit [3].

Then, we have proposed to use surface modification by ion implantation in order to simultaneously resolve the both problems, the low gas barrier and the DLC-deposit peeling. We have previously reported the experimental results of modifying PET film surface by PBII (plasma based ion implantation) [4]. In the experiment the PET film was put in plasma on a metallic holder that was supplied with negative high voltage pulses. Ion implanted PET film was investigated by both ATR (Attenuated Total Reflection) FT-IR and Laser Raman spectroscopy. It has been shown that most PET molecules in the near surface volume are destroyed and amorphized by 10 keV N_2^+ ion implantation with dose of 10^{16} cm^{-2}.

In this paper we develop a new PBII technique to implant ions into the inner surface of a PET bottle instead of PET-film surface while plasma is generated inside the bottle.

2. Preliminary experiment for modifying PET film surface into DLC

2.1 Experimental setup

Ion implantation into PET film is carried out with the experimental equipment as shown in Fig.1. Nitrogen plasma is generated at a pressure of around 10^{-2} Pa by off-resonant microwave discharge in magnetic field [5]. Plasma density of 10^{10} to10^{11} cm^{-3} is obtained with microwave power of 50 to 200 W. Usually, microwave nitrogen plasma generated at this condition consists of roughly equal amounts of N^+ and N_2^+ ions [6]. The ratio of atomic ion N^+ increases with higher microwave power and/or at lower pressure.

Sometimes, ion implantation into insulator has a problem due to ion-charge accumulation on the surface. This often causes big troubles in the ion implantation processes of mass-production factories for semiconductor devices [7, 8]. However, plasma-based ion implantation that performs the implantation in pulses as shown in Fig.2 resolves this problem. Ion charges accumulate on the sample surface during the on time of the high voltage pulse, resulting in the linear increase of the surface voltage of insulator. Then, during the off time the charges are quickly neutralized by the electrons from plasma as shown in Fig.3. A piece of PET film, 10 mm square in area and 0.1 mm in thickness, is placed on the sample holder in the plasma. The sample holder, which is made of copper, is supplied with negative high-voltage pulses of 10 kV in height and 5 microseconds in width. Since the pulse repetition is 1000 Hz, the duty of the high voltage is 0.5 percent. Just at the instant when the high voltage is supplied to the sample holder, the PET surface facing the plasma is elevated to the same potential as the sample holder, since the capacitance

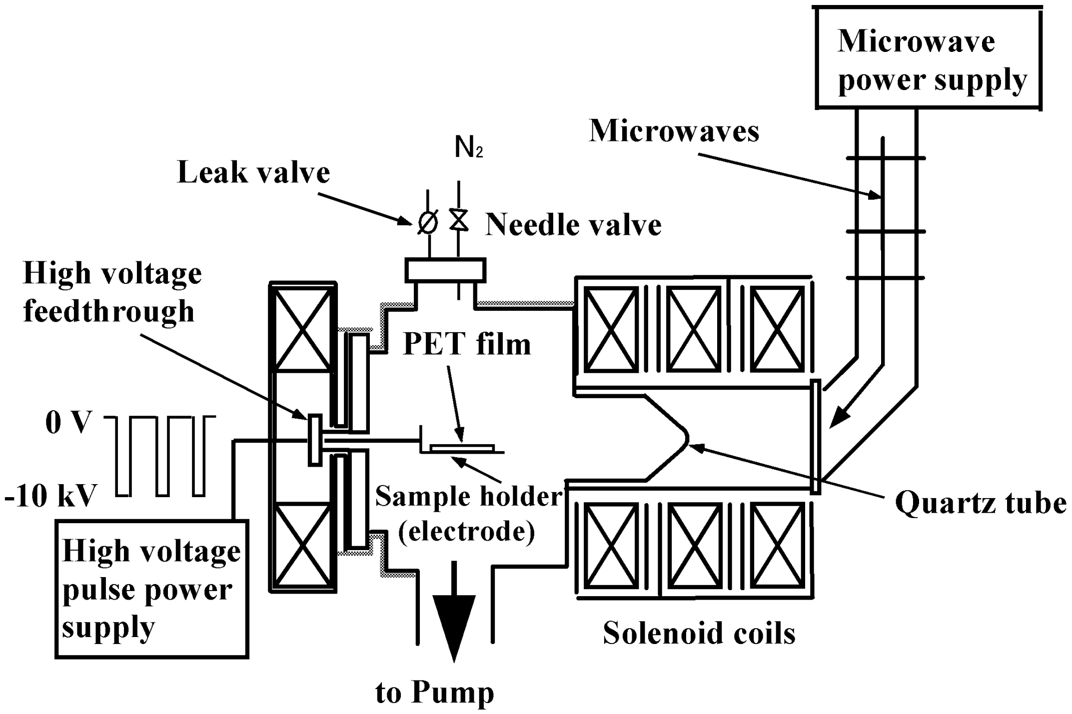

Fig.1 Experimental equipment for plasma-based ion implantation. Plasma is generated by microwave discharge in magnetic field.

between the back and the front of PET film is much larger than that between the PET front surface and the vacuum-chamber inner surface (earthed). But then, the front-surface potential against the sample holder, V_c, which is determined with the surface charge and the PET film capacitance, increases as positive ions are implanted into PET. The potential-increase rate is proportional to the plasma density. From a simple calculation, it is easily found that in case of the plasma of 10^{11} cm^{-3} in density and 10 eV in electron temperature, the PET surface potential against the holder becomes about 600 V at the end of high voltage pulse. Accordingly, the implant energy varies from 10 keV to 9.4 keV during 5 microseconds of the pulse duration. This value of energy variation does not cause any significant problem to the surface modification of PET as far as concerned with our purpose described above.

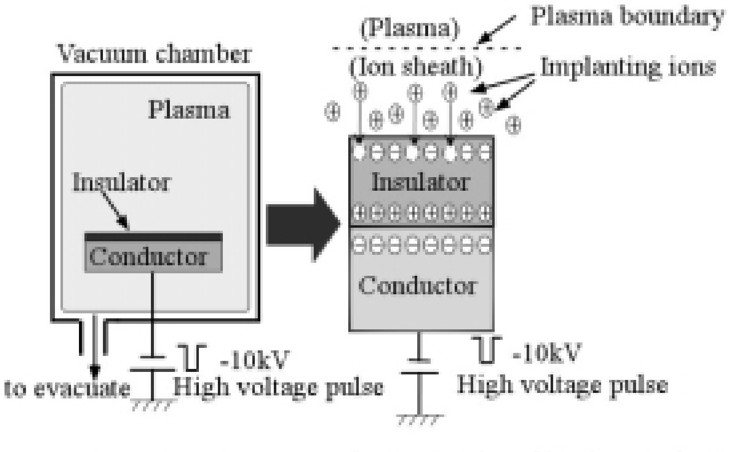

(a) PBII of insulator (b) Ion charging of insulator surface

Fig.2 Principle of ion implantation into insulator

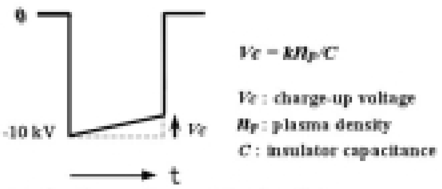

(b) Surface voltage of the insulator

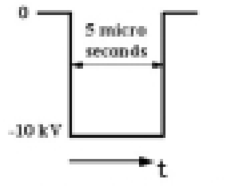

(a) Supplied voltage

Fig.3 Voltage variation on the insulator surface

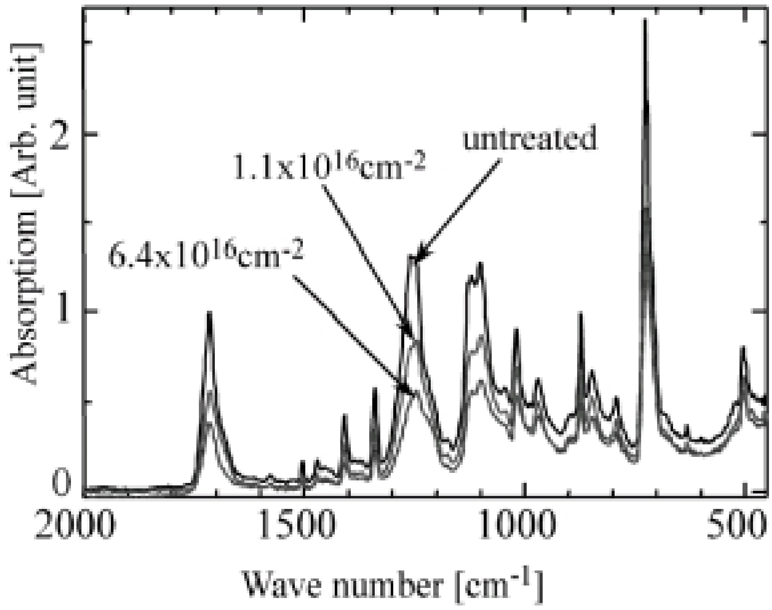

Fig. 4 ATR-FTIR spectra of surface-modified PET films.

2.2 Characterization of ion-implanted PET films

Ion implanted PET films are measured by FT-IR spectrometer in order to see how the organic structure of PET is destroyed by ion irradiation. Since the modified layer is very thin, we use ATR (attenuated total-reflection type) FT-IR spectrometer (Perkin Elmer, 1650PC-DC). The prism (or internal reflection element) material is KRS-5. Infrared absorption spectra of surface-modified PET films are shown in Fig.4. In this figure, the peaks at the wave numbers, 1714, 1250, 1120, 1046 and 726 cm^{-1} are specific for PET. The absorption spectrum obtained by ATR method is generally considered lacking quantitativity, since the signals are very changeable depending on the contact conditions between the prism and the sample surface. Thus, in order to get a relative comparison of the absorption spectra we have to mount each sample on the instrument under the same contact conditions as possible. From Fig.4 we can see the tendency that the specific absorption peaks decrease with dose.

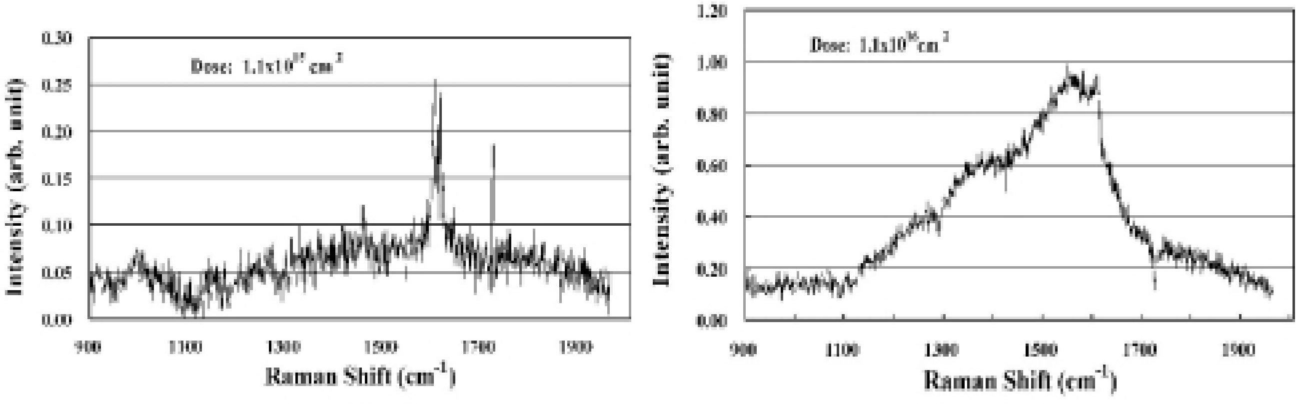

(a) 1.1x10^{15} cm^2

(b) 1.1x10^{16} cm^2

Fig.5 Laser Raman spectra of surface- modified PET films. DLC is formed over the dose of 10^{16} cm^2.

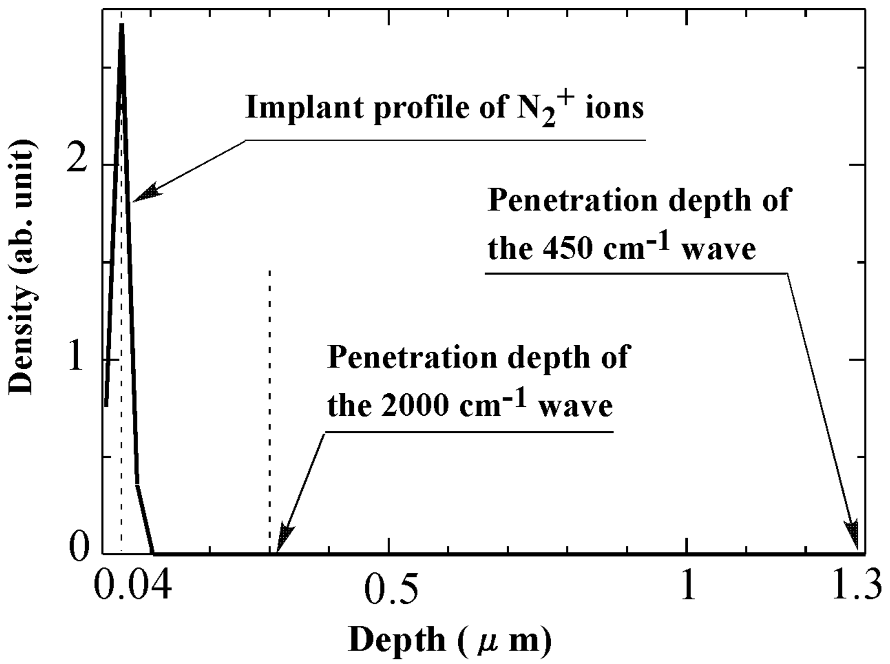

Fig.6 Implanted-ion profile calculated with the simulation software TRIM-98.

Then, the same samples are measured by a laser Raman spectrometer (Jusco, NRS-1000). The wave length is 532 nm. Figure 5 shows the Raman spectra of the ion implanted PET films with different doses of (a) 1.1 x 10^{15}, and (b) 1.1 x 10^{16}. It shows that the Raman spectrum changes over the dose of 10^{16} cm^{-2}. The spectrum of (b) has an asymmetric broad peak around 1550 cm^{-1}. Those with asymmetric broad distributions are often seen on the ion plated carbon deposit that is called amorphous carbon or DLC [9]. From the spectra we can see that PET molecules in the modified layer are completely changed into DLC, if we take the above-mentioned results from ATR FT-IR spectrometry into account.

Regarding the measurement by ATR FT-IR spectroscopy as shown in Fig.4, the specific peaks for PET decrease with dose. Up to the dose of 6.4x10^{16} cm^{-2}, there is no indication that the specific peaks would become zero with further higher doses. However, this does not mean that a lot of complete organic structures remain in the ion-implanted layer. Because the modified layer thickness is much thinner than the penetration depth of the evanescent wave used for the measurement. The mean projected range of 10 keV N_2^+ ions that are implanted into PET is calculated with the simulation software TRIM-98 to be about 0.04 micron, assuming the PET density of 1.33g/cm^3 as shown in Fig.6. As mentioned above, implanted ions contain a lot of N^+ ions with same energy. Therefore, the modified-layer thickness will be about 0.1 micron, if we take the mean projected range of N^+ ions and their standard deviation into account. On the other hand, the penetration depths of the evanescent waves differ with their wave numbers, that is, the depth is inversely proportional to the wave number. Typically, the penetration depth for the wave number of 1000 cm^{-1} is 0.6 micron, which is about 6 times as large as the ion-implanted layer thickness. Thus, the absorption spectra in Fig.4 are considered to be the summation of those from the ion implanted layer and from the un-implanted part beneath the implanted layer. The power density P of the evanescent wave inside PET is expressed as a function of the depth z as follows;

$$P = P_0 \cdot \exp(-z/d_p), \qquad (1)$$

where P_0 is the wave power density on the PET surface, and d_p, the penetration depth of the wave power. Since the wave power density is concentrated near the surface area, the ratio of spectrum signals from the two parts is determined not by the depths ratio but by the ratio of the depth integrations of equation (1). Therefore, as far as we observe only the ion-implanted layer, a considerable proportion of PET molecules is destroyed.

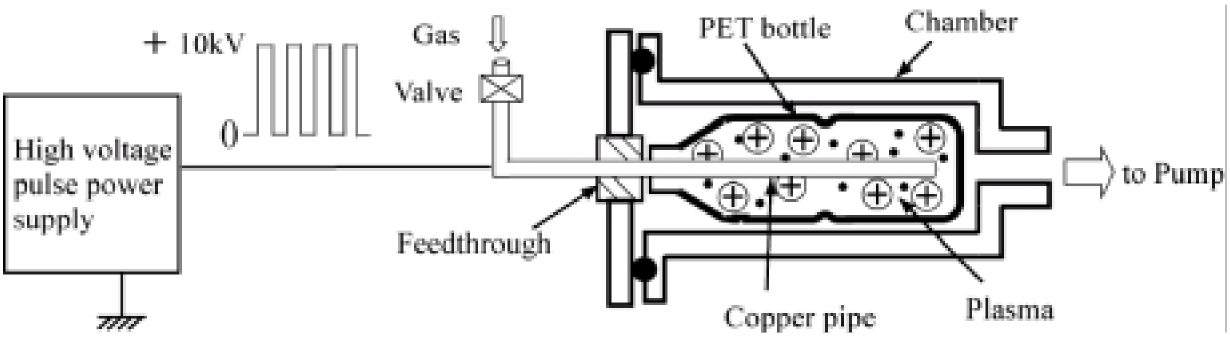

Fig. 7 A new equipment for modifying the inner surface of PET bottle to DLC.

The result by a laser Raman spectroscopy as shown in Fig.5 confirms this speculation. The Raman spectrum is very similar to those of typical DLC's, which are made by plasma PVD or ion plating using hydrocarbon gases such as methane, ethane or ethylene. Since the wave length in the laser Raman spectrometer (532 nm) is roughly one order shorter than that in the FT-IR, the penetration depth is considered sufficiently smaller than the thickness of ion implanted layer.

3. Ion implantation into an inner surface of a PET bottle

In the above-mentioned preliminary experiment a sample of PET film was placed in a microwave plasma. However, during the experiment we found that plasma of considerable density was easily generated only by the high voltage pulses at a pressure of around 1 Pa, where PBII was carried out. Therfore, we constructed a new equipment for modifying the inner surface of PET bottle without using any microwave power suply. Figure 7 shows the schematic drawing of the equipment as well as the new method to implant ions into the inner surface of bottle[10]. An electrode that is supplied with positive high-voltage pulses differently from negative ones as in the previous experiment is inserted into the bottle. Since the plasma potential is kept close to that of the electrode, positive ions are accelerated to bombard the inner surface with the kinetic energy corresponding to the pulse voltage. The surface charging by ions is neutralized by electrons from plasma during the pulse off time. The inner surface of the PET bottle is investigated by both ATR FT-IR and Laser Raman spectroscopy, too. The result shows that the new method can also perform surface modification of the PET-bottle inner surface similarly to the previous experiment for PET film. The details will be reported elsewhere.

4. Discussions and conclusion

In order to enhance the barrier characteristics of PET film against CO_2 and O_2 gases, a new technique for surface modification was investigated. PBII of nitrogen plasma was proved to be able to change PET-film surface into DLC that is similar to those made by plasma PVD or ion plating. Since the technique is basically the materials modification by ion implantation differently from coating, there will be no peeling problems. Regarding the gas barrier characteristics, we consider that they will be at least comparable to those tested with plasma-coating technique by a European company [1], because the thickness of the ion-implanted PET layer by the new technique is almost same or slightly larger and the Raman structure is very close to those of the typical DLC's.

For PET bottle modification a new method to apply positive high-voltage pulses to the electrode inserted into the bottle is proved to be effective. Since the pressure at which the modification is carried out is one to several Pa, the evacuation time from atmospheric pressure will be shorter than 1 minute when a high-speed dry pump is used.

References

[1] H. Forcinio, "Food manufacturing & packaging", Prepared Foods, March (1997) 75-78

[2] J. Briem, "Die Bombe ist geplatzt", Verpackungs-Rundschau, No.6 (1999) 42-43

[3] B. Olliver, S. J. Dowey, S. J. Young and A. Matthews, J. Adhesion Sci. Technol., **9**, No.6 (1995) 769

[4] N. Sakudo, D. Mizutani, Y Ohmura, E. Endo R. Yoneda N. Ikenaga and H. Takikawa, “Surface modification of PET film by plasma-based ion implantation”, 13th International Conference on Ion Beam Modification of Materials, Kobe, Japan Sept.1-6 (2002), to be published in Nucl. Instrum. and Methods.
[5] N. Sakudo, Rev. Sci. Instrum. **71** (2000) 1016
[6] N. Sakudo, K. Tokiguchi, T. Seki, Materials Science and Engineering, **A116** (1989) 221
[7] C. M. McKenna, Radiat. Eff. **44** (1979) 93
[8] G. Ryding and M. Farley, Nucl. Instrum.and Meth. **189** (1981) 295
[9] M. Iwaki, M. Matsunaga, K. Terashima, H. Watanabe, Ion Implantation Technology-98 (1999) 1026
[10] N. Sakudo and N. Ikenaga, Kanazawa Inst. of Technol., Japanese Patent Application No. 2000-156572.

C_2 and CH diagnostics in methane / helium and methane / argon plasmas

S. Meir[1,2], U. Fantz[1]
[1] *Lehrstuhl für Experimentelle Plasmaphysik, Universität Augsburg, D-86136 Augsburg, Germany*
[2] *Max-Planck-Institut für Plasmaphysik, EURATOM Association, Boltzmannstr. 2, D-85748 Garching, Germany*

Abstract

Methane plasmas are investigated in an ECR discharge and particle densities are obtained by using emission spectroscopy and a residual gas analyzer. The radiation of the C_2 molecule (Swan system) and the CH molecule (A – X system) and their correlation with CH_4, CH, C_2H_2 and C_2 densities have been studied. The dominant dissociation chain of hydrocarbons for C_2 formation was identified by a simple particle balance. The influence of argon on the formation process of C_2 is shown.

1. Introduction

Methane plasmas are commonly used for technical applications, i.e. diamond-like coatings. For an optimization of plasma processes the knowledge of the radical densities, i.e. the dissociation products, is essential. For the determination of radical densities different diagnostic techniques can be applied. Optical emission spectroscopy has the advantage of minor experimental equipment and easy handling. In the visible range the radiation of the CH radical, the C_2 molecule, the Balmer lines and carbon lines is detectable and can be used to determine the radical densities of CH, C_2, H and C, respectively. The densities of molecular hydrogen, methane and other hydrocarbons (C_2H_y) are measured by a residual gas analyzer.

Methane / helium and methane / argon plasmas at two different mixtures (5%CH_4 / background gas, 95%CH_4 / background gas) in the range from 4 – 18 Pa have been investigated in an ECR microwave discharge. The radiation is recorded with a 1 m spectrometer and ICCD camera in the visible range and a 1 m VUV spectrometer equipped with a photomultiplier. Both spectroscopic systems are absolutely calibrated and detect the same plasma volume. The electron density of 10^{17} m^{-3} has been determined by microwave interferometry. Langmuir probe measurements indicate a Maxwellian electron energy distribution function. The electron temperature, derived from the radiation of a helium line, varies with pressure and gas mixture between 1.5 and 3 eV. The gas temperature is 450 K, the degree of ionization is typically 10^{-4}.

Detailed investigations are carried out to correlate the radiation of the C_2 molecule with the density of the C_2H_y group and the radiation of the CH radical with the methane density in the plasma. Suitable emission bands are presented and total densities are shown. To understand the formation mechanisms of C_2 molecules simulations are applied. It will be discussed if the intensity ratio can be used as a monitoring tool for the density ratio of C_2H_y to CH_4.

2. Radiation of molecular carbon and CH radical

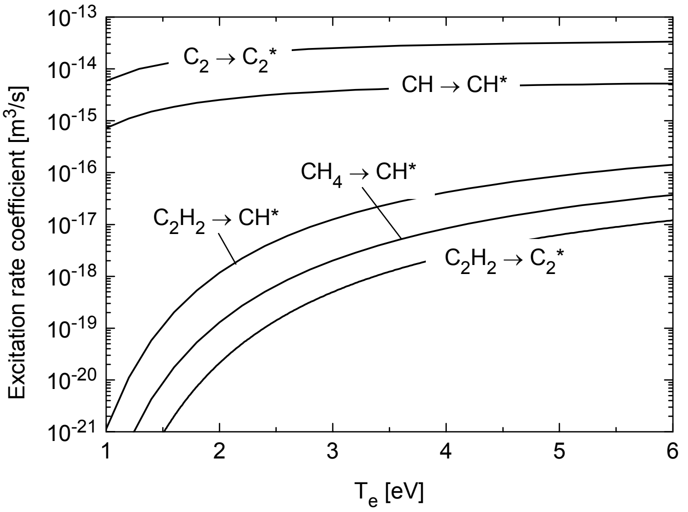

Fig.1: Emission rate coefficients for direct and dissociative excitation of the C_2 Swan and the CH A-X band.

In case of the C_2 molecule the Swan band system (d $^3\Pi_g$ – a $^3\Pi_u$) has several intense vibrational bands in the visible spectral range. The most prominent vibrational transition is the v'=0 – v''=0 transition with a band head at 516.52 nm, degrading to the blue. In the UV range, the Mulliken system (D $^1\Sigma_u^+$ – X $^1\Sigma_g^+$) emits the diagonal vibrational transitions v'=v''=0,...,3 around 231.3 nm.

The upper states of both emission bands can be populated by either, direct excitation from ground state and metastable state of the C_2 molecule, or dissociative excitation of higher hydrocarbons. Since cross sections of electron impact excitation are considerable higher for optically allowed transitions than for forbidden transitions, it is sufficient to take into account the direct excitation from the lower state of the corresponding transition. These rate coefficients are calculated by using the Impact Parameter Method for atoms (IPProg, [1]) applied to molecules using the corresponding oscillator strengths (Swan: f = 0.024, Mulliken: f = 0.055).

Cross sections for dissociative excitation from the C_2H_2 molecule are available [2]. The rate coefficient for the dissociative excitation of C_2 from C_2H_2 is four to seven orders of magnitude smaller than the rate coefficient for direct excitation; for both, Swan and Mulliken. However, the rate coefficients for dissociative excitation have to be weighted with the density of C_2H_2.

As measured by the residual gas analyzer C_2H_2 is the dominant higher hydrocarbon species of the C_2H_y group which is a factor of 10 – 100 below the methane density (depending on pressure and mixture, see section 3). Therefore, the above mentioned dissociative excitation mechanism stands for the higher hydrocarbons.

For the analysis an extended corona model was applied:

$$\varepsilon_{ph} = n_{C_2} n_e X^{direct}_{C_2 \to C_2^*}(T_e) + n_{C_2H_2} n_e X^{dissociative}_{C_2H_2 \to C_2^*}(T_e) \qquad (1)$$

Since the plasma parameters are well known the C_2 density is the remaining parameter. The two parts which contribute to the measured radiation ε_{ph} can be calculated and are presented together with T_e in Fig. 2 for the Swan band. The situation is very similar for the Mulliken emission. It is obvious that the direct excitation channel is dominant. Thus, the measured radiation refers to excitation out of C_2. This means, that the analysis of the Swan band yields the density of the metastable state and the Mulliken band refers to the density of the ground state.

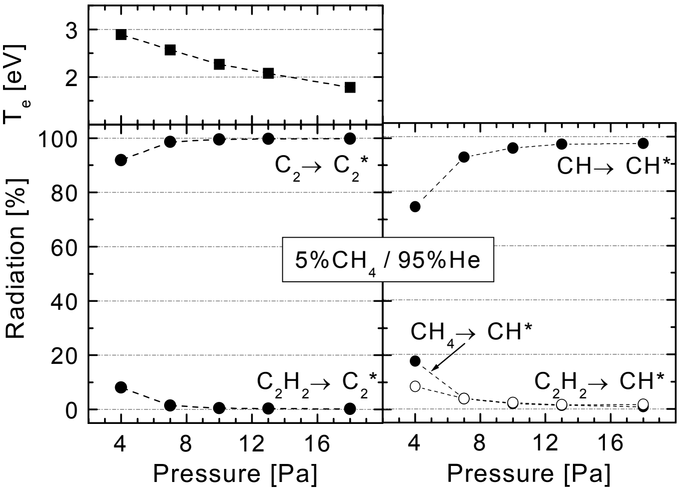

Fig.2: Percentage of the radiation originating from direct and dissociative excitation for C_2^* and CH^*.

In case of CH radiation the most prominent band is the $A^2\Delta - X^2\Pi$ transition with the v'=0 – v''=0 bandhead at 431.42 nm. Furthermore, the $B^2\Sigma - X^2\Pi$ transition around 390 nm (v'=0 – v''=0) is observed. Like in the case of C_2, the upper states can be populated either by direct excitation from the ground state of CH or by dissociative excitation of methane and also higher hydrocarbons. Rate coefficients for the dissociative excitation from CH_4 and C_2H_2 are determined from the corresponding cross sections [3,4]. The rate coefficient for direct excitation is calculated by using the Impact Parameter Method for atoms [1]. These rate coefficients are also shown in Fig. 1 for the $A^2\Delta - X^2\Pi$ transition. Investigations on the radiation of the A – X transition show that in plasmas with 95%CH_4/He the dissociative excitation of CH_4 becomes important, while in plasmas with 5%CH_4/He excitation from the ground state of CH is the dominant excitation channel, as shown in Fig. 2. As a consequence the radiation of CH is correlated with the CH density for mixtures with 5% methane. In case of methane dominated plasmas the radiation of the CH molecule refers to the CH_4 density.

3. Methane plasmas

Besides CH and C_2 densities, carbon and atomic hydrogen densities, are determined by spectroscopy as well. For carbon, the resonance line at 165.7 nm was evaluated taking into account direct and dissociative excitation channels. The radiation of the Balmer line H_γ can originate directly from the ground state of atomic hydrogen and from dissociation of H_2, CH_4, and C_2H_y. Using a residual gas analyzer the densities of CH_4, hydrocarbons of the C_2H_y group and H_2 are measured. As shown in section 2 this is needed to consider dissociative excitations channels. Fig. 3 shows the results for 5% methane in helium plasmas. As can be seen, the methane density is considerably reduced (up to a order of magnitude) in the plasma and convoluted mostly into molecular hydrogen. The sum of the densities of the hydrocarbons of the C_2H_y group is a factor five below this density. Here, the dominating hydrocarbon species is C_2H_2. The density of atomic hydrogen is at the same order of magnitude. This means the degree of dissociation for H_2 is around a few percent. The densities of atomic carbon and the CH radical are both around a factor 10^{-3} below the methane density in the plasma. The C_2 density, which is the lowest, is given by the sum of the metastable state a $^3\Pi_u$ and the ground state X $^1\Sigma_g^+$ determined from the radiation of the Swan and Mulliken band, respectively. Due to the low energy gap of 0.0887 eV between these two states, the metastable state remarkable populated.

In the mixture with 95%CH_4 in helium the dissociation of methane is much less. The densities of C_2H_y are about one percent of the density of methane. Again, C_2H_2 is the dominant molecule of the C_2H_y group. Unfortunately, the intensity of the Mulliken band was below the sensitivity of the spectroscopic system and the population ratio of a $^3\Pi_u$ / X $^1\Sigma_g^+$ is taken from the 5%CH_4 / 95%He mixture in order to determine the total C_2 density. The C_2 density decreases to 10^{-5} below the C_2H_2 density.

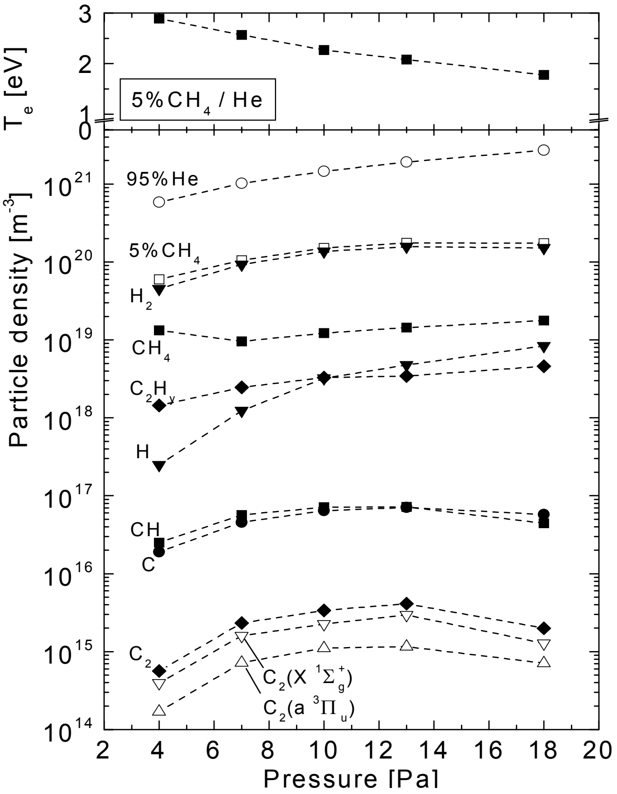

Fig.3: Particle densities and T_e in 5% methane in helium plasmas. Open symbols of CH_4 and He show the densities filled in.

4. Influence of background gas

To investigate the influence of a background gas, helium was replaced by argon. CH_4/Ar plasmas show an enhancement of C_2 radiation while the radiation of the CH bands does not change. However, the electron temperature decreases from helium dominated plasmas to argon dominated plasmas (ΔT_e=0.6 eV). This indicates higher densities of both radicals in the argon plasma. Since the energy of the metastable argon atoms is around 11.5 eV, the dissociation of methane which needs around 10 eV can be easily enhanced by energy transfer. Metastable argon atoms also offer additional reaction channels for the formation of C_2 out of C_2H_2 which will be discussed in detail in section 5. Therefore, an enhancement of the C_2 density is expected. As suggested before, the line ratio of the Swan band system of C_2 and the A – X transition of CH is applied to diagnose the C_2 / CH density. In Fig 4. intensity ratios of C_2 to CH are presented. For the measurements in methane plasmas the ratio is a factor of two higher for argon dominated plasmas than for helium dominated plasmas. The measurements show clearly that the formation of C_2 is increased. The intensity ratios are also measured for C_2H_y (y=2, 4, 6) in helium and argon gas mixtures. As expected, the intensity ratio increase drastically in any case (one order of magnitude). Again, argon dominated plasmas yield a higher ratio than helium dominated plasmas (factor of two).

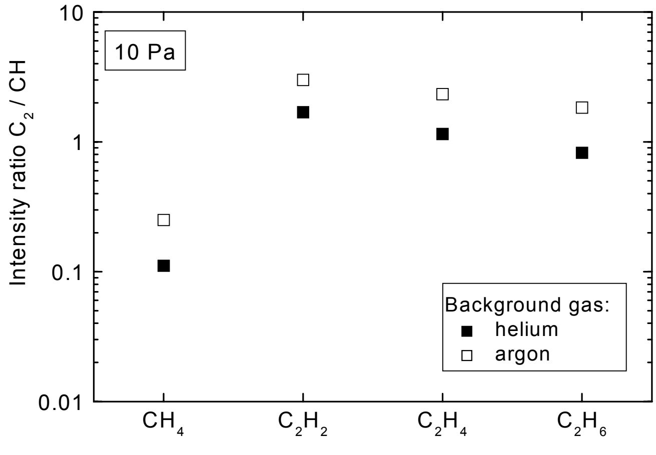

Fig.4: Intensity ratio of the radiation of the C_2 Swan band and the A $^2\Delta$-X $^2\Pi$ transition of the CH radical in different mixtures (typically 5% hydrocarbons).

5. Modeling the formation of C_2

The formation of C_2 in the plasma has been studied with a 0-dim. particle balance (MEDICUS code [5]) using the measured plasma parameter n_e, T_e, T_{gas} as input data. Rate coefficients for electron impact dissociation were taken from [6], those for heavy particle collisions from [7,8]. In a first step, dissociation only from C_2H_2 was taken into account, which is formed by electron impact dissociation of methane and heavy particle collisions of methane radicals. Since an direct formation chain from methane to C_2 is only possible via volume recombination of C with a low rate coefficient, the contribution of the methane channel is negligible.

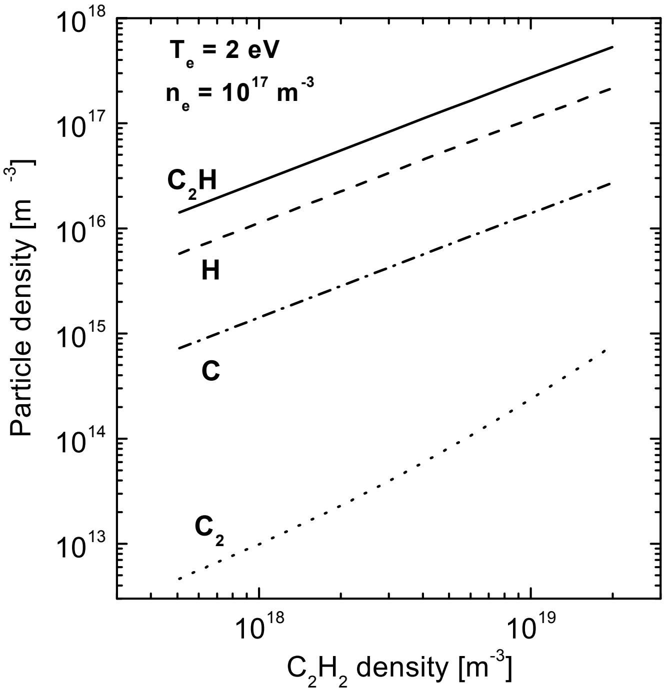

Fig.5: Calculation of radical densities formed by C_2H_2 dissociation as a function of the C_2H_2 density.

To study dominant formation mechanism the following reactions are implemented:

(1) $C_2H_2 + e \rightarrow C_2H + H + e$,
(2) $C_2H + C_2H \rightarrow C_2 + C_2H_2$
(3) $C_2H + e \rightarrow C + C + H + e$
(4) $C + C \rightarrow C_2$
(5) $C_2H_2 + M \rightarrow C_2 + H_2 + M$
(6) $C_2H + H \rightarrow C_2H_2$
(7) $C_2 + H_2 \rightarrow C_2H + H_2$
(8) $C_2 + e \rightarrow C + C + e$
(9) $CH + CH \rightarrow C_2 + H_2$
(10) $CH + CH \rightarrow C_2H + H$
(11) $C + CH \rightarrow C_2 + H$
(12) $CH_4 + C_2 \rightarrow CH_3 + C_2H$
(13) $CH_4 + C_2H \rightarrow CH_3 + C_2H_2$.

Fig 5. shows calculated particle densities for several species (C_2H, H, C and C_2) as a function of C_2H_2 density. Electron temperature and electron density be 2 eV and 10^{17} m^{-3}, respectively. The most dominant radical in this reaction chain is C_2H, which plays an important role in the formation of C_2 (reaction *(1)* and *(2)*). The density of C_2H is about a factor of 50 below the density of C_2H_2. To check the influence of C_2H on the formation of C_2 the calculation was repeated with an additional inlet of C_2H. The increase of C_2H by a factor of ten yields a factor of ten more C_2 density. Since the density of C also raises by factor of 10 the densities were re-calculated this time with additional inlet of C. Here, only a small increase in the C_2 density took place. This proves, that the whole reaction chain is dominated by the C_2H density.

In Fig 6. calculated densities are compared with results from measurements in the 5%CH_4 / He mixture. Measured electron temperatures and C_2H_2 densities are used as input parameters. Since also reactions with not specified heavy particles (M), i.e. reaction *(5)*, and molecular hydrogen take place, these densities were re-adjusted to the value measured in the experiments.

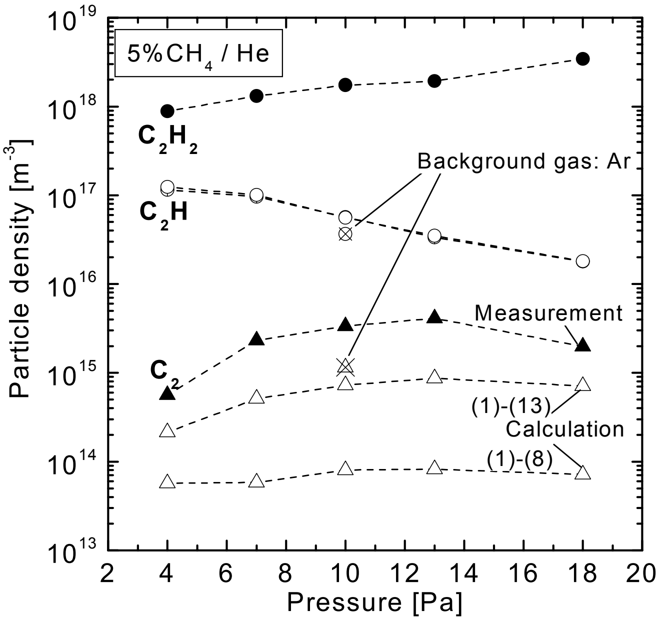

Fig.6: Comparison of simulation and measurement of the C_2 density. Additional simulation at 10 Pa for argon as background gas.

In a first step, the reactions *(1)-(8)* are used, since no significant influence of CH_x molecules on the formation of C_2 is expected. As shown in Fig 6. the calculations underestimate the density of C_2 more than one order of magnitude. Including reactions *(9)-(13)* a better agreement with measurements is observed. This demonstrates the importance of heavy particle collisions with CH_y radicals, in particular reactions *(9)-(11)*.

In order to study the influence of metastable argon (Ar^*) further reactions

(14) $C_2H_2 + Ar^* \rightarrow C_2H + H + Ar$
(15) $C_2H + Ar^* \rightarrow C_2 + H + Ar$

were added, the rate coefficients are taken from [8]. For a pressure of 10 Pa, the results are shown in Fig 6. It was taken into account that the electron temperature in argon is 0.6 eV lower than in plasmas with helium. Typical relative densities of metastable argon are about 10^{-4}, therefore, this value is used in the calculation. The simulation shows a decrease in the C_2H density of a factor of 1.5, in comparison to helium mixtures. The C_2 density increases by a factor of 2 and demonstrates therefore the influence of metastable argon.

6. Conclusions

Measured densities for two different methane / helium mixtures in an ECR discharge were presented. The particle densities of C_2 and CH are determined by optical emission spectroscopy based an extended corona model whereas CH_4, and H_2 are measured with a residual gas analyzer. It was shown that the radiation of CH (A - X transition) correlates with the CH density or with the CH_4 density, depending on the gas mixture. Since CH is related with the electron impact dissociation of CH_4, the radiation of CH delivers an indicator for the CH_4 density in the plasma. Detailed analysis of the radiation of C_2 (Swan transition) yields a correlation with the C_2 density in the discharge. To investigate the formation processes of C_2 the dissociation channels of C_2H_2 are modeled. A clear correlation with the C_2 density is observed. Systematic variations in input densities demonstrate the dominant role of the C_2H density. The deduced correlation of C_2 radiation with C_2H_2 density offers a possibility to determine the C_2H_2 density in the plasma by optical emission spectroscopy. In particular, the intensity ratio of C_2 to the CH band provides a simple, fast tool for monitoring the ratio of the C_2H_y to the CH_4 density by emission spectroscopy.

Applying this method, the influence of argon on the dissociation chain was demonstrated. As proved by calculations, the metastable argon atoms enhance the dissociation of hydrocarbons, e.g. C_2H_y and therefore the formation of C_2. Furthermore, methane in helium plasma was replaced by C_2H_2, C_2H_4 and C_2H_6. These mixtures show an increase in the intensity ratio of C_2 / CH which represents an increase of the C_2 density in comparison to methane plasmas. Again, a further enhancement was observed in case of argon.

References

[1] A. Burgess, H.P. Summers - Mon. Not. R. Astr. Soc. **174**, 345 (1976)
[2] H. Tawara, *et al.* - NIFS-DATA-6, (1990)
[3] J.F.M. Aarts, *et al.* - Physica **53,** 32 (1971)
[4] C.I.M. Beenaker, F.J. de Heer - Chem. Phys. **6**, 291 (1974)
[5] U. Fantz, M Berger - MEDICUS code
[6] J.N. Brooks, *et al.* - ANF/FPP/TM-**297** (1999)
[7] H. Tahara, *et al.* - Jpn. J. Appl. Phys. **34**, 1 (1995)
[8] C. Riccard, *et al.* - Czech. J. Phys. **50 S3**, 389 (2000)

Effects of surface modification on electrochemical properties of MCMB powder treated in reactive ICP

H. Tanaka[1], T. Osawa[1], Y. Moriyoshi[1], M. Kurihara[2], S. Maruyama[2], T. Ishigaki[3]

[1] Hosei University, Department of Materials Science, 3-7-2 Kajino-cho, Koganei-shi, Tokyo 184-0002, Japan
[2] TDK Corp,. R&D Center, 2-15-7 Higashi-Owada, Ichikawa-shi, Chiba 272-8558,
[3] National Institute for Materials Science, Advanced Materials Laboratory,
1-1 Namiki, Tsukuba-shi, Ibaraki 305-0044, Japan

Abstract

We investigated the effect of surface modification on electrochemical properties of mesocarbon microbeads (MCMB) powders treated in RF inductively coupled plasmas (RF-ICP). Through the plasma treatment, the surface morphology, structure, and chemical composition of the powders were modified. Plasma modification made MCMB particles surface disordered, and gave rise to an improvement of the electrochemical properties, and made it suitable for use as the anode of lithium-ion rechargeable battery.

1. Introduction

The carbonaceous materials come into being a variety of forms, such as fibers, balls, flakes and sheets, and each of them has its own unique characteristics. Many types of carbonaceous materials have been investigated extensively as anodes of lithium-ion rechargeable batteries. Li-ion rechargeable batteries are now widely used in consumer electronic devices, such as cellular telephones, camcorders and portable computers because they have excellent performances in terms of high voltage, high specific energy and long cycle life. Recently, there is a strong interest in utilizing Li-ion rechargeable battery for transportation application. Among carbonaceous materials, graphitic or graphitized carbon, were mainly used as an anode material. Graphite materials show better electrode performance than other compounds such as transition metal oxide, lithium alloy, or lithium metal because they can store various kinds of species between the crystalline sheets to form graphite intercalation compounds (GICs), which have high discharge capacity, low electrode potential, high charge/discharge efficiency, long cycle life and high level of safety. The discharge capacity and initial charge/discharge efficiency are most important electrode characteristics which determine the nominal capacity of batteries. The capacity of graphite electrode is limited to the theoretical value of 372mA/g, which corresponds to a stoichiometry of LiC_6. The initial charge/discharge efficiency is defined in terms of the ratio of discharge capacity to charge capacity during the first charge-discharge cycle, and it decrease with increasing extent of irreversible reaction. Carbon electrode always suffers complex irreversible reactions when it is electrochemically firstly intercalated by lithium. These irreversible reactions, involving the electrolyte, solvent, and the carbon electrode, cease when electric insulating solid electrolyte interface (SEI) forms between the carbon electrode and the liquid solvent. The nature of SEI film plays a significant role in the electrochemical performance of the graphite anode. The SEI composition and properties depend strongly on the electrolyte and surface characteristics of carbon electrode, and the SEI causes the decreasing of initial charge/discharge efficiency, so, surface properties as well as bulk one should be key factors for electrochemical properties. Recently, there has been a lot of research on SEI of graphite powders possess various bulk and surface properties.

The thermal plasma has great advantages in material modification and some chemical reactions, because it has very high temperature and can easily produce active species. The peak temperature in an atmospheric-pressure thermal plasma, whether generated by direct current (DC) or by RF induction, is ～10,000K or more, and reactants injected into such a plasma are exposed to temperatures of at least 4,000~5,000K. RF inductively coupled thermal plasma (ICP) generation is one method used to generate a thermal-plasma, and it has the following features: (1) The volume of the relatively high-temperature region is large (30～40mm in diameter); (2) The plasma flow velocity is low (20~50 m/s); (3) Plasma having various atmospheres, such as oxidative, reductive and reactive, can be generated by this method. It has been reported that many kinds of unique materials have been prepared by RF thermal plasma processes [1-17]. Powders injected into thermal plasma are subjected to modifications of their shape, surface morphology, chemical composition, and crystal structure in a moment. It is expected that the plasma-treated carbon powders could have characteristics different from those of the conventionally heat-treated powders. The present authors have reported the thermal plasma treatment of glassy carbon and spherical phenolic resin powders, and their improved electrochemical properties [18-19]. The plasma-treated carbon powders subjected to modifications in chemical composition, surface morphology and graphitization in the bulk. The modifications led to a higher capacity than that of the untreated powders when used as the anode of lithium-ion rechargeable battery.

In this study, we tried to create the functional surface of mesocarbon microbeads (MCMB) powder, which is known as spherical artificial graphite, through the in-flight interaction between thermal plasma and particles, and to improve electrochemical properties of MCMB powder. The electrochemical properties of plasma-treated powder and the influence of water-vapor adsorption on the surface for electrochemical properties were investigated as anode of lithium-ion rechargeable battery.

2. Experiments

The ICP torch and reactor chamber used in the present work have been reported elsewhere [1]. MCMB powder (Osaka Gas Co., 10 μm average particle size) was used as the original carbon powder. MCMB powder was prepared by heating at ～2800°C to carbonize and graphitize the mesophase, which was obtained by heating pitches at around 400°C in an inert atmosphere. The MCMB powder granules, a sort of artificial graphite that is highly graphitized and composed of lamella graphite grains, are spherical and the powder has a 99.9% or more carbon content. MCMB powder can be fed easily and a uniform plasma reaction can be expected. The powder was treated in Ar-H_2, Ar-N_2, Ar-H_2-CO_2, and Ar-N_2-CO_2 induction thermal plasmas generated at the power level of 40 kW and the pressure of 53 kPa. The powder-feed rate was adjusted to be 4 g/min, a rate at which the optimal condition for heating the powders was attained. To control the adsorbed amount of water-vapor during the collection procedure, the plasma-treated powders without air exposure were collected in argon atmosphere, while the powders were normally collected in the air. The plasma generating and powder feeding conditions are summarized in Table 1. The powders were observed by scanning electron microscopy (SEM, JEOL, JSM-5410) to characterize their surface morphologies, and by X-ray diffractometry (XRD) to identify the bulk structure formed through the induction thermal-plasma treatment. Crystallinity in the surface of several nanometers depth was observed by Raman scattering spectroscopy (JASCO, NR-1800). The Brunauer-Emmett-Teller (BET) surface area was also measured (BEL JAPAN, BELSORP18). The content of oxygen, nitrogen, and hydrogen in the bulk were measured by means of an oxygen/nitrogen analyzer (Horiba, EMGA-650) and a hydrogen analyzer (Horiba, EMGA-621), respectively. The adsorption species on the surface of powder were analyzed using thermal desorption spectroscopy (ESCO EMD-WA1000).

Table 1 Plasma generating and powder feeding conditions

Sample	a	b	c	d
Plasma gas	Ar	Ar	Ar	Ar
Sheath gas(1)	Ar	Ar	Ar	Ar
Sheath gas(2)	H_2	H_2	N_2	N_2
Powder carrier gas(1)	Ar	Ar	Ar	Ar
Powder carrier gas(2)		CO_2		CO_2
R.F. Frequency / MHz	2			
Plate power / kW	40			
Reactor pressure / kPa	27			
Powder feed rate / g/min	4			

Electrochemical measurements as an anode for lithium-ion rechargeable battery were performed in non-aqueous solvents containing 1M $LiCLO_4$. Sample electrodes were prepared to examine the anode properties of lithium-ion rechargeable batteries as follows: Poly vinylidene fluoride as the binder and a slurry were spread on copper foil and dried at 150℃ under vacuum for one hour; A 1mol/cm^3 solution of $LiClO_4$ in a 50:50 mixture of ethylene carbonate (EC) and diethyl carbonate (DEC) was used as the electrolyte; A counter lithium electrode and a reference lithium electrode were used; The electrochemical cell set up in a dry box under argon atmosphere and the charge/discharge behavior of the cell was measured galvanostatically at the current density of 0.25 mA/cm^2 between 0 to 3 V vs. Li/Li^+ at 25℃.

3. Results and Discussion

The lattice parameter of plasma-treated and original MCMB powders were determined to be d_{002}=0.337(nm). The lattice parameter and half-width of the plasma-treated MCMB powders were almost the same as those of the original MCMB powder. The crystalline sizes in c-direction (Lc) and a-direction (La) of the plasma-treated MCMB powder determined by XRD were Lc = 37 nm and La= 68nm, which are equal to the value of original. The plasma-treated MCMB powders did not show any further graphitization in bulk.

Figure 1 shows the typical morphology obtained from the original and plasma-treated MCMB powders. As is seen in Fig. 1(b), the Ar-N_2 plasma-treated powder had a surface morphology that was covered with fine particles of several tens of nanometers in size. The MCMB powders were heated and partially evaporated followed by the formation of a condensate through the coagulation from a vapor phase, and covered the surface of the particles. The Ar-N_2-CO_2 plasma-treated powder in Fig. 1(c) showed a rough surface. In the Ar-N_2-CO_2 plasma treatment, the evaporated species were almost burned off by oxygen atoms, which were formed by the decomposition of CO_2, then, the surface was chemically etched and lamellar structure peculiar to the MCMB was disclosed on the surface.

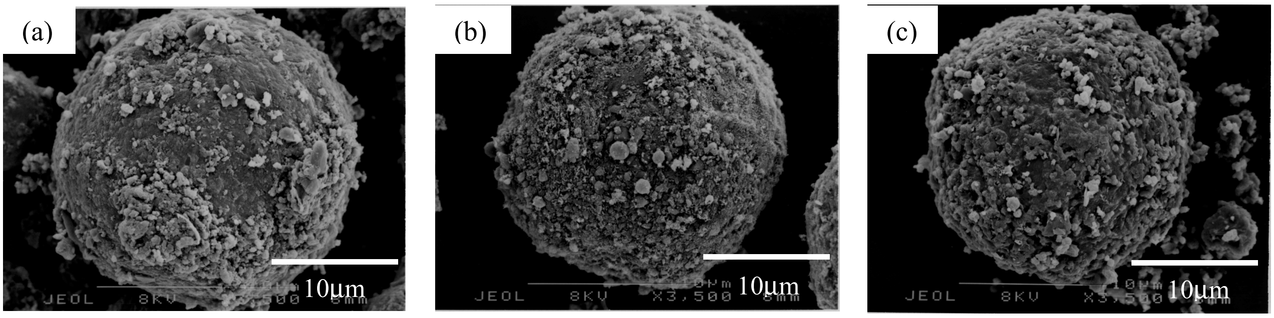

Fig.1 Surface morphology of the (a) original and plasma-treated powders. (b):Ar-N_2, (c):Ar-N_2-CO_2 bar:10μm

The BET surface area of the original, and Ar-H_2, Ar-N_2, Ar-H_2-CO_2 and Ar-N_2-CO_2 plasma-treated MCMB powders were 1.83, 2.22, 4.68, 1.94 and 1.59, respectively. The BET surface area changed corresponding to the variation with the surface morphology, and changed with plasma atmospheres. The Ar-N_2-CO_2 plasma-treated powder had a BET surface area smaller than that of the original, while the BET surface area of the Ar-N_2 plasma-treated powder was over two times larger than that of the original. In the powders treated in the reactive atmospheres containing CO_2, the increase of the surface area was quite small. The hydrogen, oxygen, and nitrogen contents in the samples were shown in Fig. 2. The plasma-treated powders showed a unique variation in their chemical composition. The change of hydrogen, oxygen, and nitrogen contents induced by plasma treatment was dependent on the composition of the plasma. In all plasma treatments, both the hydrogen and oxygen contents increased. In particular, the content of nitrogen in the Ar-N_2 plasma-treated powder was three times larger than that of the original one. All the changes in chemical composition predominantly took place in the surface region.

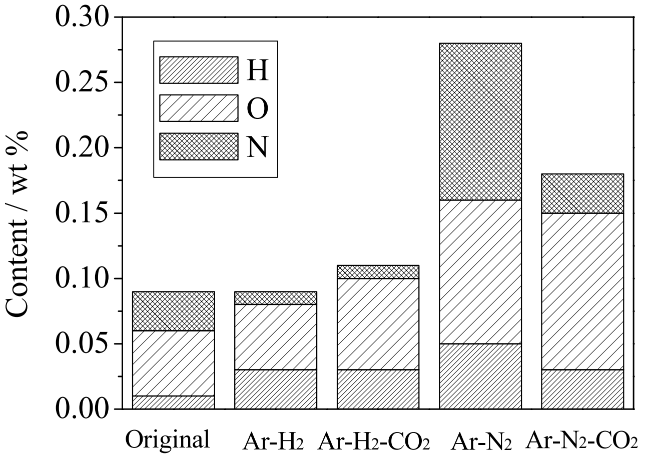

Fig.2 The hydrogen, oxygen and nitrogen contents of the original and plasma-treated powders

Raman spectroscopy is a useful tool for evaluating a carbon surface. Since carbon materials are black, scattered light can be absorbed. The escape depth of Raman scattered light is limited to several nanometers. In the Raman spectroscopy, two peaks appeared at about 1580 cm^{-1} and at about 1350 cm^{-1}. The band at 1580 cm^{-1} is assigned to the Raman active E_{2g2} mode of graphite-lattice vibration. The band at 1350 cm^{-1} originates from the disordered structure of carbon. Thus, the ratio of intensity of the band at 1580 cm^{-1} (I_{1580}) and that at 1350 cm^{-1} (I_{1350}), (I_{1350}/I_{1580} (=R)), can be an indicator of the graphitization. The halfvalue width of the band at 1580 cm^{-1} is also used as the degree of crystallinity. Figure 3 shows the Raman spectra of the original and plasma-treated MCMB powders. The surface on the plasma-treated MCMB particles can be recognized to have a disordered carbon structure. In the Raman spectra of the Ar-N_2-CO_2 plasma-treated powder, the Raman band at 1580 cm^{-1}, which is attributed to the graphite structure, was sharp. The R-values of the original, Ar-N_2-CO_2 and Ar-N_2 plasma-treated powder, were 0.108, 0.178 and 0.301, respectively. The R-values of all plasma-treated powders became larger than that of the original. The values of the Ar-N_2 plasma-treated MCMB powder in particular became much larger. The halfvalue width of the band at 1580 cm^{-1} for the original, Ar-N_2-CO_2 and Ar-N_2 plasma-treated powders, were 24cm^{-1}, 23.7cm^{-1} and 24.5cm^{-1}, respectively. The halfvalue width of the bands at 1580 cm^{-1} also showed a tendency similar to that of the R-value. In Ar-N_2 plasma treatment, the fine surface powder showed low crystallinity, while in the Ar-N_2-CO_2 plasma treatment, the disclosed surface heated and roughened by the plasmas had relatively high crystallinity.

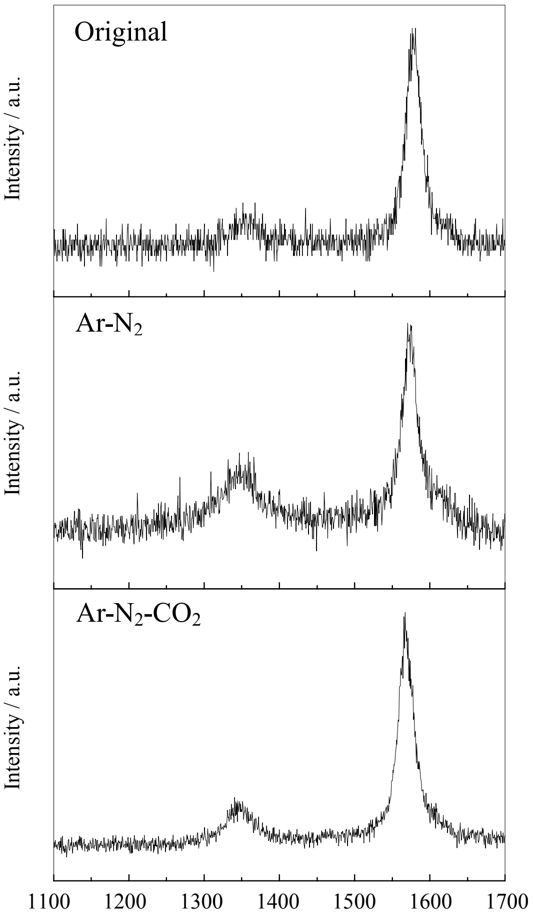

Fig.3 Raman spectra of the original and plasma-treated MCMB powders.

The first charge/discharge efficiency of the original, and Ar-H_2, Ar-N_2, Ar-H_2-CO_2 and Ar-N_2-CO_2 plasma-treated MCMB powders were 90.3, 90.1, 88.7, 91.6 and 91.0, respectively. The difference in surface structure influenced the initial charge/discharge efficiency. It is noteworthy that plasma treatment is able to improve the initial charge/discharge efficiency. In the powder treated in the CO_2 containing atmosphere, first charge/discharge efficiency was improved appreciably. On the other hand, the first charge/discharge efficiency of the Ar-N_2 plasma-treated powder showed a slight decrease. The initial charge/discharge efficiency has a tendency to decrease with increase of the surface area because of the capacity loss by the side reactions, which are believed to form a SEI on the surface of graphite [20]. Thus, the initial charge/discharge efficiency of the Ar-N_2 plasma-treated powder decreased.

The relative discharge capacity of the Ar-H_2, Ar-N_2, Ar-H_2-CO_2 and Ar-N_2-CO_2 plasma-treated powders (the discharge capacity of the original was set to be 100) were 107, 106, 108 and 108, respectively. As a result, the plasma treatment gave rise to a 6% - 8% increase in the discharge capacity. It was reported by Mabuchi et al. that in heat-treatment processes at 2000°C or higher, the discharge capacity of MCMB shows a tendency with increases of the heat-treatment temperature [21]. It is believed that in this treatment temperature range, the interlayer spacing d(002), which is the space between graphite layers, approaches a fixed value, 3.354Å, and crystal growth accumulates on a graphite layer in the direction of the C axis and spreads in the direction of the A axis. Therefore, any increase in charge/discharge capacity is dependent on the stack and spread of the graphite layer. Since no appreciable difference in the peaks obtained before and after plasma treatment was found in the XRD, it was thought that the growth of graphite crystallite had not been advanced. Since the surface characteristics of the plasma-treated powders were different, the mechanisms are still unclear now. Further investigation is required to properly clarify the mechanism.

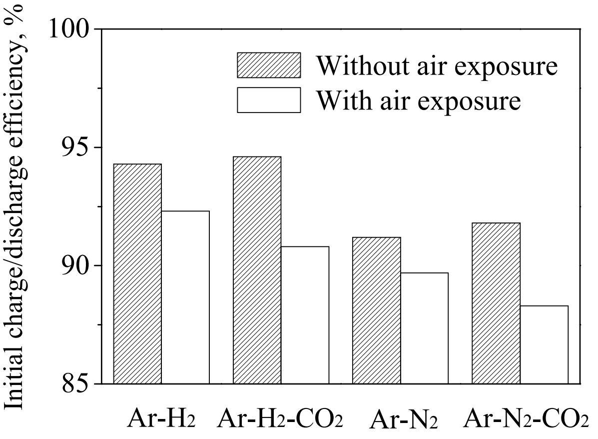

Fig.4 Influence of air exposure on initial charge/discharge efficiency

In order to clarify the influence of adsorbed species on the surface of MCMB powders, especially water-vapor, we prepared the plasma-treated MCMB powders without air exposure. The samples were collected in argon atmosphere in order to protect adsorptions from air. The initial charge/discharge efficiency was measured for the plasma-treated MCMB powders without air exposure. Figure 4 shows the initial charge/discharge efficiency of the comparison of MCMB powder without air exposure and MCMB powder exposed to the air. All the powders without air exposure showed higher initial charge/discharge efficiency than that of the exposed powders. The increase in initial charge/discharge efficiency of the MCMB powder without air exposure was 1.5 - 3.8%. Especially, the powder treatment containing CO_2 atmosphere, the initial charge/discharge efficiency was improved to as high as 95%. Initial charge/discharge efficiency of the Ar-N_2 plasma-treated powder without air exposure showed more than 90%. The protection from surface adsorption of spices gave rise to an improvement in electrochemical properties. The improvement of initial charge/discharge efficiency means, in other words, the decrease of irreversible capacity. A general understanding is that irreversible capacity of lithium ion intercalation into the graphite electrode during the first few cycle is associated with the formation of SEI film, from this result, it was found that surface properties greatly influence the irreversible capacity. To characterize the surface properties of the plasma-treated powders, the H_2O and CO_2 adsorption was measured by thermal desorption spectroscopy (TDS). Thermal desorption spectroscopy is used to determined the desorption properties of materials. In TDS, the temperature of a material is elevated at a controlled step rate, and the molecules desorbed at each temperature are analyzed using a mass spectrometer. The quantity and type of molecules desorbed from the sample with increasing of temperature provide invaluable information about the properties of material at high temperature. The TDS spectra at low temperature and high temperature show the properties of the surface and the underneath of surface, respectively. The sample was placed on the black quartz boat in the chamber and heated from 60°C to 1000°C in vacuum with a heating rate of 30°C/min. During this heating process, the out-gassed species and amounts were measured by quadrupole mass spectrometer (QMS). The evolved gases were mainly H_2, CH_4, H_2O, CO and CO_2 in all plasma-treated powders, and NH_3 were detected in the atmospheres containing N_2. The major out-gassed species were physically adsorbed H_2O and chemical reaction product CO_2. Figure 5 shows the TDS spectra of original and plasma-treated

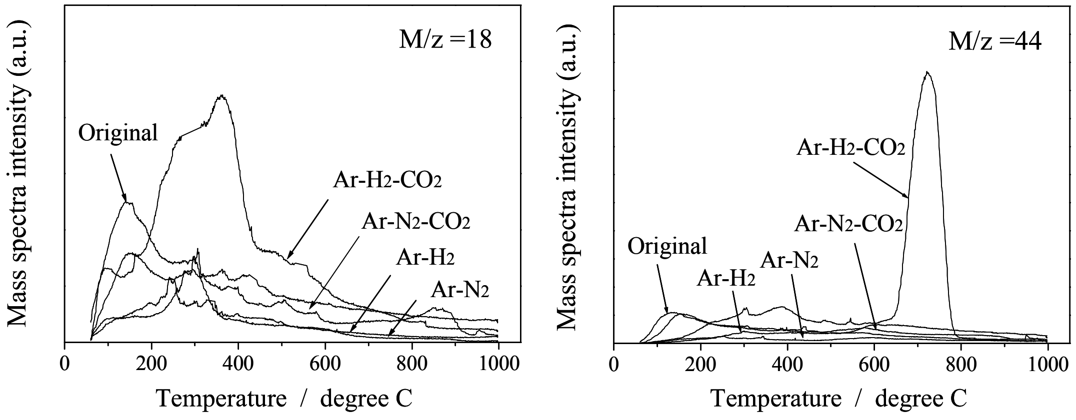

Fig.5 TDS spectra from original and plasma-treated powder without air exposure of H_20 (mass 18) and CO_2 (mass 44).

powders without air exposure for adsorbed H_2O (mass 18) and CO_2 (mass 44) on the plasma-treated powder surface. Especially, there are much desorption amount in the Ar-H_2-CO_2 plasma-treated powder. The peak at around 130°C in the original powder, which would be attributed to water adsorption on the surface, became smaller. The decreasing of the peak at around 130°C was due to water evaporatation by plasma heating. The peak shift to around 300°C was caused by plasma treatment. Remarkable peak of CO_2 at relatively higher temperature (more than 600°C) occurred only for the plasma treatment in the Ar-H_2-CO_2. The out-gassed CO_2 should be due to the decomposition of the sample, not the physical absorption. This result indicated that the surface layer or the underneath of the surface was modified by reactive plasmas including CO_2. It also suggested that new surface on the MCMB particles have some functional groups including of oxygen atom by the plasma treatment. The electrochemical properties, such as discharge capacity and initial charge/discharge efficiency, may be related to the adsorbed species on the surface. These results showed that the modification of surface morphology and chemical composition by plasma treatment increase the discharge capacity, and the protection of adsorbing spices on the surface lead to the improvement of the initial charge/discharge efficiency.

Reference

[1] T. Ishigaki, Y. Moriyoshi, T. Watanabe, and A. Kanzawa., *J. Mater. Res.*, **11** (1996) 2811.
[2] X. Fan, T. Ishigaki, Y. Suetsugu, J. Tanaka, and Y. Sato., *J. Am. Ceram. Soc.*, **81** (1998) 2517.
[3] Y.L. Li, T. Ishigaki., *Chem. Phys. Lett.*, **367** (2003)561.
[4] T. Ishigaki, Y. Bando, Y. Moriyoshi, and M.I. Boulos., *J. Mater. Sci.*, **28** (1993) 4223.
[5] T. Ishigaki, J. Jurewicz, J. Tanaka, Y. Moriyoshi, and M. I.Boulos., *J. Mater. Sci.*, **30** (1995) 883.
[6] X. Fan, T. Ishigaki, and Y. Sato, *J. Mater. Res.*, **12** (1997) 1315.
[7] X. Fan and T. Ishigaki., *Plasma Chem. Plasma Process.*, **18** (1998) 487.
[8] X. Fan, T. Ishigaki, and Y. Sato., *J. Am. Ceram. Soc*, **82** (1999) 281.
[9] X .Fan, and T. Ishigaki., *J. Am. Ceram. Soc.*, **82** (1999) 1965.
[10] T. Ishigaki., *J. Sur. Fin. Soc. Jpn*, **51** (2000) 161.
[11] T. Ishigaki., *Bull. Cer. Soc. Jpn*, **35** (2000) 525.
[12] T. Ishigaki., *J. Vac. Soc. Jpn*, **43** (2000) 863.
[13] T. Ishigaki., *J. Plasma and Fusion. Res.*, **77** (2001) 1088.
[14] Y.L. Li, T. Ishigaki., *J. Am. Ceram. Soc.*, **84** (2001)1929.
[15] T. Ishigaki., *J. High. Temp. Soc.*, **28** (2002) 98.
[16] Y.L. Li, T. Ishigaki, M. Uchida and Y.Matsui., *J. Ceram. Soc. Jan*, **110** (2002)830.
[17] Y.L. Li, T.Ishigaki., *Mater. Sci. and Eng A.*, **345** (2003)301.
[18] M. Kurihara, S. Maruyama, K. Ohe, T. Ishigaki., *Chem. Lett.*, (**1998**) 715.
[19] S. Maruyama, M. Kurihara, T. Ishigaki, K. Watanabe, T. Takizawa, and Y. Moriyoshi., *NIPPON KAGAKU KAISHI*, (**2002**) 27.
[20] K. Zahib, K. Tatsumi, H. Abe, T. Ohsaki, Y. Sawada, and S. Higuchi., *J. Electrochem. Soc.*, **145** (1998) 210.
[21] A. Mabuchi, H. Fujimoto, K. Tokumitu, and T. Kasuh., *J. Electrochem. Soc.*, **142** (1995) 3049.

Development of Liquid Fuel Reformer Using Low Energy Pulse Discharge at Room Temperature

Y. Sekine[1], S. Asai[1], K. Urasaki[1], S. Kado[2], E. Kikuchi[1], M. Matsukata[1],.

[1] *Department of Applied Chemistry, School of Engineering and Science, Waseda University, Tokyo, Japan*
[2] *Department of Mechanical Engineering and science, Tokyo Institute of Technology, Tokyo, Japan*

Abstract

Using low energy pulsed discharge and carbon fiber, it could be possible to make a compact and more efficient device for hydrogen production by hydrocarbon reforming. This process does not require such equipments as heater and evaporator for liquid fuel. So if the improvement of controlling Voltage and Current system progresses, it will be suitable to load this reformer into a fuel cell vehicle in the future.

1. Introduction

Recent years, fuel cell system attracts considerable attentions as an efficient and clean energy supply / use technology. PEMFC (Polymer Electrolyte Membrane Fuel Cell) which is the representation rank of various fuel cells is expected to serves as a fuel cell vehicle (FCV) or a home cogeneration system. But, there are various problems with the present technology, (for example, the transportation and storage of Hydrogen) so it is need to research innovative technological know-how's. Then, we examined to apply low energy pulse (LEP) discharge to this system. This new technique has brilliant feature. Using this, reforming reaction proceeded at ambient temperature and under atmospheric pressure. So we aim at unifying supply and storage system with using liquid fuel and LEP discharge in a small space, and improving energy efficiency. Specifically, mixed solution of C_2H_5OH and H_2O is sucked up by carbon fiber, and LEP discharge under ambient temperature and atmospheric pressure was performed and examined.

2. Experimental methods

Previous and present fuel delivery systems were shown in Fig. 2-1. When reforming was carried out using pulse discharge and previous reformer, water and alcohol like methanol or ethanol must be evaporated, so the process needed something like pre-heater. Then, even if the efficiency of the reaction itself was good, the efficiency in the whole process was unfortunately not good. Then the method as shown in the following Fig. 2-1 was able to be considered. Here, C_2H_5OH and H_2O were used as mixed solution. In this present method, C_2H_5OH and H_2O are sucked up to discharge space by capillary tube phenomenon of carbon fiber. And, Joule heat which was generated from internal resistance was utilized effectively for evaporating liquid. The liquid fuel is evaporated, and discharged. At last, produced gas was collected to a gas bag equipped in upper part of the device. And produced gas is analyzed by gas-chromatography.

In this study, both reactors as shown in Fig. 2-1 were used under atmospheric pressure condition and under room temperature. No catalyst was used, and argon was used as carrier gas. Distance between electrodes was fixed at 3.0 mm. All products were analyzed using a gas chromatography equipped with FID and TCD (ShimadzuGC14-B). the waveforms of current and voltage were observed by a digital signal oscilloscope (DSO) (Lecroy 9314C). And the diameter of carbon fiber is 8.0μ, the length is 7 cm, 14 cm both, and we used 84 thousand fiber bound up.

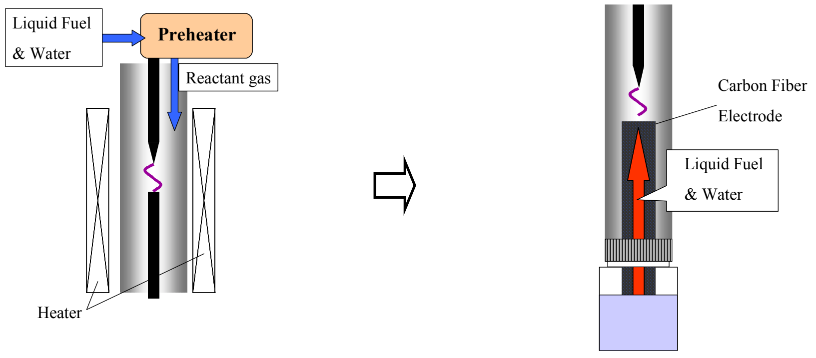

Previous method for fuel supply present method for fuel supply

Fig. 2-1 Fuel supply system.

3. Experimental results

3-1 Capacity of Fiber Carbon for Fuel Supply

At first, the amount of liquid sucked up per time was investigated when number of fibers and fiber length were changed. It turns out that the amount of liquid sucked up become large in proportion to a fiber number and fiber length, and it sucked up 30 cc/min with a 8.4×10^5 number of fiber, if the liquid converted as gas.

Influence on sucking up rate which the concentration of mixed solution gave was small. So in the following experiments, the mixture ratio of ethanol and water was equivalent as far as there were no directions.

3-2 Comparison of Previous System and Present System

Here, the comparison between the previous system and the present system was carried out. In both cases, The results is shown in Fig. 3-1. H_2 and the lower hydrocarbon compounds: CO, CH_4, CO_2, C_2H_4, and C_2H_6 were produced, and amount of produced gas increased in proportion to the increase of the distance between electrodes. But there is no influence of the distance between electrodes on carbon selectivity. Since it cannot be said that experiment conditions were completely the same, it was difficult to compare both. But in what performed reforming using carbon fiber, the result is almost equivalent to that of reforming in gas phase.

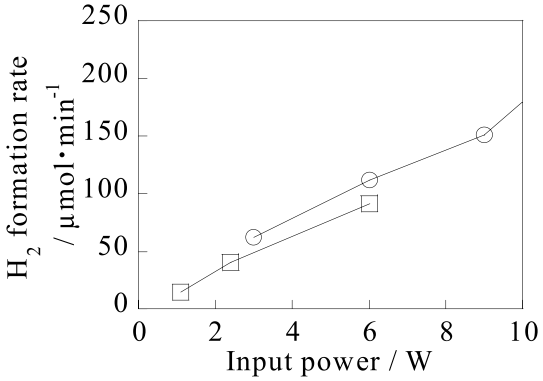

Fig. 3-1 comparison of previous and present reaction system
(○) Reforming in gas phase; mixture ratio, $C_2H_5OH / H_2O = 1 / 1$;
distance between electrodes, 2.1 mm; temperature, 393 K; atmospheric pressure.
(□) Reforming using carbon fiber; mixture ratio, $C_2H_5OH / H_2O = 1 / 1$;
distance between electrodes, 3.0 mm; room temperature; atmospheric pressure.

For this reason, it is possible to make the size of device compact, and to make this process more efficient, because of the needless to install such equipments as heater and to evaporate liquid fuel.

3-3 Effect of Discharge Stabilizer

It turned out that H_2 formation rate was equivalent to a former gaseous phase reaction from the experiment 3.2., this fiber engaged in the reaction in the case where carbon fiber is used as electrodes as it was. So it was con However, the orange color of plasma's flame was observed, and the color originates carbon (fiber) reacting. For this reason possibility to burn or deteriorate the fiber were considered, and it was not desirable. So we put SUS electrode into the middle of the fiber to prevent it from reacting. And we tried to send the solution evaporated into discharging area using the joule heat generated in internal resistance.

The result is shown in Fig. 3-2. H_2 formation rate of the case of putting SUS electrode was a few bigger than that of the case of not putting it. It could be seemed to understand that the stability of discharge is improving by leaps and bounds judging from flame color of discharge space. In former experiment, the flame color was orange, which was derived from carbon reacting. But in this way, the flame color was blue or purple, which meant that liquid fuel was steadily provided in the discharging space.

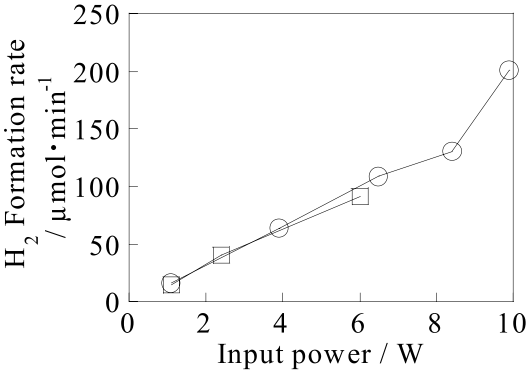

Fig. 3-2 Comparison of the case of putting SUS electrode and of not putting
(○) putting SUS electrode, (□) not putting SUS electrode
Conditions; mixture ratio, C_2H_5OH / H_2O = 1 / 1;
distance between electrodes, 3.0 mm; room temperature; atmospheric pressure.

3-4 Effect of Input Power

In this section, we investigated effect of input power on ethanol consumption rate and carbon selectivity. The results of C_2H_5OH consumption rate and carbon selectivity are plotted against the input power in Fig. 3-3. Carbon selectivity was almost fixed as an indication of Fig. 3-3. It's characteristic feature of this system that CO Sel. (about 80 %) was very high.

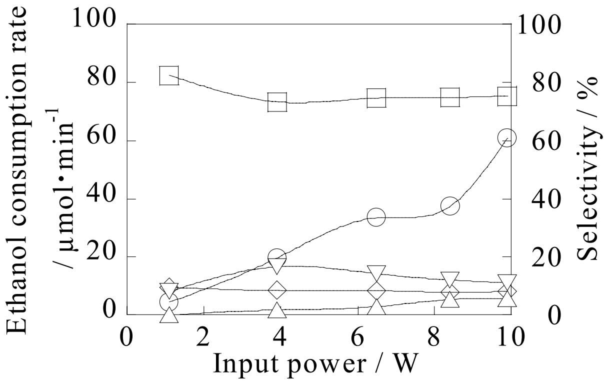

Fig. 3-3 Effect of input power on ethanol consumption rate and on Carbon selectivity.
(○) ethanol consumption rate, (□) CO Sel., (◇) CH_4 Sel., (△) CO_2 Sel., (▽) C2 Sel.
Conditions; mixture ratio, C_2H_5OH / H_2O = 1 / 1;
distance between electrodes, 3.0 mm; room temperature; atmospheric pressure.

3-5 Effect of Concentration of C_2H_5OH and H_2O

In this section, we investigated effect of concentration of C_2H_5OH and H_2O to search the effective concentration. It means high H_2 formation rate in addition to low C2 formation rate. At first, H_2 and O_2 were not generated when H_2O concentration was 100 %. So the electrolysis reaction of water did not advance. Next, at the decomposition reaction of C_2H_5OH 100 %, carbon deposited was gradually observed and finally the reaction stopped with time progress. But the discharge could be stabilized for a long time and could be continued in steam reforming without stopping the reaction.

The results were shown in Fig. 3-4. The larger C_2H_5OH concentration is, the more produced H_2. And in the area of high ethanol concentration, C2 selectivity was high, (it was about 30 %) compared to that in the area of low ethanol concentration. So it seems to say that the reaction of which C_2H_5OH concentraton is from 20 to 50 percent is the highest efficiency at a present stage. Because C2 selectivity was not high, and carbon deposited was not observed. So the reaction was continued with the grate ease.

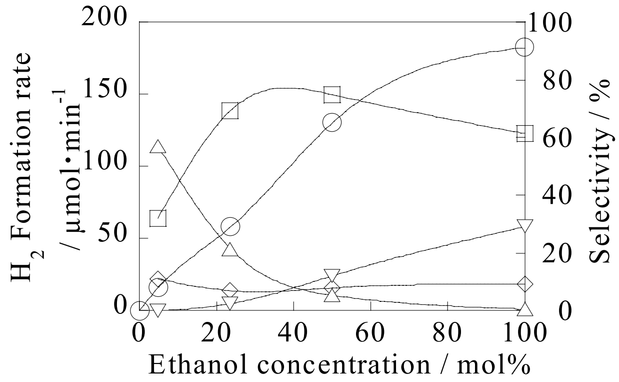

Fig. 3-4 Effect of ethanol concentration on H_2 formation rate and on Carbon selectivity.
(○) H_2 Formation rate, (□) CO Sel., (◇) CH_4 Sel., (△) CO_2 Sel., (▽) C2 Sel.
Conditions; input current 7.0 mA, distance between electrodes,
3.0 mm; room temperature; atmospheric pressure.

3-6 Energy Efficiency

Input power was regarded as the power consumption in the discharging space. And it was calculated from integration value which is current multiply by voltage, picked up from the waveforms of the oscilloscope. Here, input power was computed based on the following approximation formula. In this formula, Input power was computed by having multiplied power consumption per one discharge and pulse frequency.

$$\Sigma \{(v_i+v_{i+1})/2\} \cdot \{(c_i+c_{i+1})\} \cdot (t_{i+1}-t_i) \times f \quad [1]$$

On the other hand, output power was regarded as addition of A and B as follows. A was the difference of the standard enthalpy of formation between the amount of liquid fuel converted and the amount of produced compounds. And B was energy which required for the mixed solution to evaporate. Finally energy efficiency was calculated by making output power into the numerator and by making input power into the denominator.

And, if it's supposed that input and output power were calculated such a way, energy efficiency was 50–60 %. The efficiency in this experiment was exceeding that of the former way. Furthermore, it is possible to improve the result by controlling Voltage and Current system. For example, using AC power system in which it is easy to short half-band width technically.

4. Conclusions

Using carbon fiber, it could be possible to make the size of device compact, and to make this process more efficient, because of the needless to install such equipments as heater and to evaporate liquid fuel without spoiling its functions. So if the improvement of controlling Voltage and Current system progresses, it will be suitablew to load this reformer into a fuel cell vehicle in the future.

5. References

[1] S.L. Yao, M. Okumoto, A.Nakayakma and E. Suzuki, Energy Fuel., 2001,15,1295.
[2] S. Kado, Y. Sekine, and K, Fujimoto, Chem Commun., 1999,2485.
[3] S. Kado, K. Urasaki, Y. Sekine and K. Fujimoto, Chem. Commun., 2001,415.

Novel Abatement of PFCs Using Microwave Excited Non-Equilibrium Atmospheric Pressure Plasma

M. Nagai [1], K. Yamakawa [1], M. Ito[2], M. Hori [1], and T. Goto[1]

[1] Department of Quantum Engineering, Graduate School of Engineering, Nagoya University, Japan
[2] Department of Opto-Mechatronics, Faculty of Systems Engineering, Wakayama University, Japan

The atmospheric non-equilibrium plasma was applied to the novel abatement of PFCs where the PFCs were converted to the solid particles for the first time. As a result, the spherical-shaped particles were successfully fabricated using the CF_4/He and C_4F_8/He atmospheric plasma. Furthermore, the effect of H_2 addition on the CF_4/He plasma was investigated, and CF_4 was decomposed successfully over 80%. This process will be useful for the abatement of PFCs.

1. Introduction

Perfluorinated compounds (PFCs) are widely used in the dielectric film etching and chemical vapor deposition chamber cleaning process. It is well known that PFCs cause a serious environmental problem due to the high global warming potentials (GWP) and long atmospheric lifetimes. In particular, CF_4 is generated as a byproduct after the CVD processing using PFCs, of which lifetimes exceed 50000 years. Therefore, it is an important issue in the worldwide semiconductor industry to reduce the emission of PFCs into the atmosphere and to abate PFCs.

Non-equilibrium plasmas sustained at the atmospheric pressure have been widely studied because the material processing using arc plasma is limited due to the high gas temperature. To produce non-equilibrium plasmas, several attempts have been proposed, such as corona discharges [1] and dielectric barrier discharges [2]. However, the default of these sources is that plasmas do not uniformly extend throughout the electrode. Kono et al. reported the generation of high-density non-equilibrium plasma at the atmospheric pressure using microwave-excited discharge [3]. In the report, a high-density (n_e= ~10^{15} cm^{-3}) non-equilibrium plasma was produced continuously by using micro-gap electrodes. The micro-gap plasma with the microwave excitation enables us to etch, deposit and synthesize materials at low temperatures, and may be suitable for a wide range of applications.

Recently, we have developed a environmentally benign etching process using a solid material (PTFE) evaporation technique instead of PFCs [4]. A solid-state recovery process, where the exaust PFCs after the etching process are polymerized by atmospheric plasma and hereby particles are formed, enables us to develop the zero-emission recycle etching process without the use and emission of PFCs. Therefore, we have developed a novel abatement of PFCs employing the atmospheric micro-gap discharge with the microwave excitation to convert PFCs to solid particles. To our knowledge, syntheses of fluorocarbon particles from PFCs in non-equilibrium atmospheric plasma have been never reported. The method of conversion of PFCs to solid particles will attract much attention as a novel abatement.

In this study, we have demonstrated the abatement of PFCs and the synthesis of solid particles employing the atmospheric micro-gap plasma with the microwave excitation. The high decomposition efficiency of CF_4 gas was obtained by mixing H_2 gas to the CF_4/He atmospheric plasma.

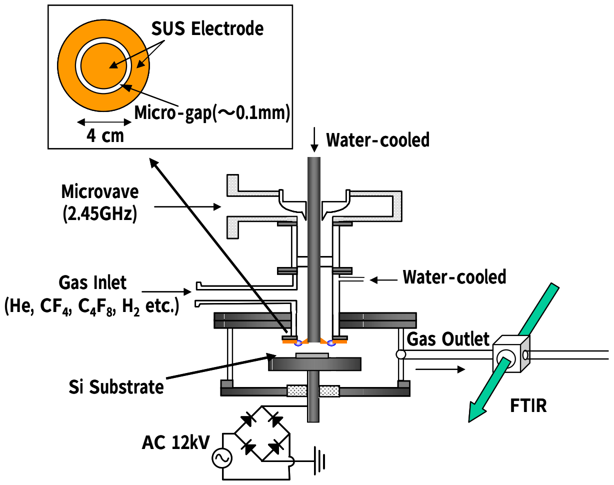

Fig. 1. The atmospheric micro-gap plasma using microwave excititation for the abatement of PFCs.

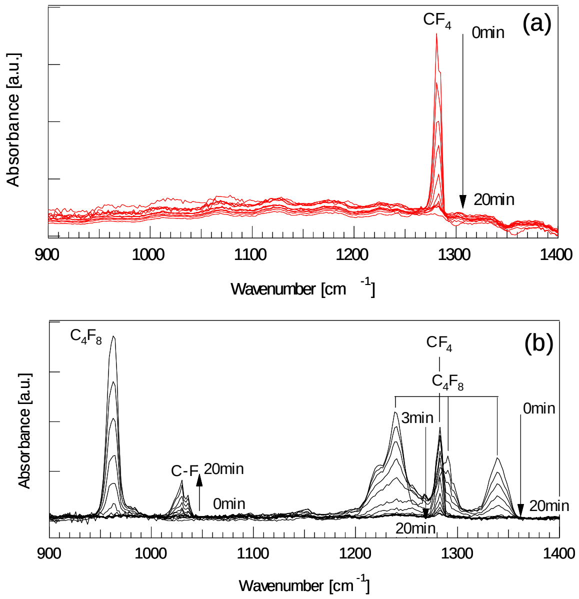

Fig. 2. Time evolution of FT-IR spectrum of (a) CF_4/He and (b) C_4F_8/He atmospheric plasma at a microwave power of 400 W, a total pressure of 1 atom, and a PFC concentration of 0.5 %.

2. Experimental

Figure 1 shows a schematic diagram of the atmospheric micro-gap discharge system using the microwave excitation for the abatement of PFCs. The Microwave (2.45 GHz) was converted to a coaxial mode through the rectangular-coaxial transducer and propagated along a water-cooled coaxial line to a ring micro-gap electrode with the gap distance of 0.1 mm. The ring plasma (40 mm in diameter) was generated between the micro-gap electrodes. The PFCs mixtures were introduced through the upper part of micro-gap. In this system, it was found that the arrangement of the gap distance was a key point to produce the stable plasma. In gap distances more than 0.1 mm, the plasma was not formed uniformity at good between electrodes.

Fourier transform infrared absorption spectroscopy (FT-IR) was performed for the analysis of exhaust gases from the reactor. The decomposition efficiency of CF_4 in the atmospheric plasma was calibrated from the IR speak ratio of CF_4 (1283cm^{-1}) before and after discharge. The morphology and chemical structure of synthesized fluorocarbon particles were evaluated using scanning electron microscopy (SEM) and energy dispersive x-ray spectroscopy (EDS), respectively.

3. Results and Discussions

A. Abatements of PFCs Using the Atmospheric Micro-gap Plasma

The atmospheric micro-gap plasma with the microwave excitation was applied to the abatement of PFCs and syntheses of solid paricles were demonstrated. We have investigated whether PFCs were decomposed or not using atmospheric CF_4/He and C_4F_8/He plasma on the condition of a microwave power of 400 W, a total pressure of 1 atom, and a PFCs concentration of 0.5 %.

Figure 2 shows the time evolution of FT-IR spectrum of (a) CF_4/He and (b) C_4F_8/He atmospheric plasma. In the case of CF_4/He atmospheric plasma, the absorption intensity at ν_3 CF_4 (1283 cm^{-1}) [5-7] was decreased monotonously with increasing discharge time. In the case of the C_4F_8/He atmospheric plasma, the absorption peak at ν_s ring in C_4F_8 (963 cm^{-1}) [8], C-F (1136 cm^{-1}) [9], ν_a C-F_2 (1152 cm^{-1}) [9, 10], ν_s C-F_2 in C_4F_8 (1239 cm^{-1}), and ν_a C-F_2 in C_4F_8 (1290 and 1340 cm^{-1}) [8] were observed. The absorption intensity of C_4F_8 was decreased with the discharge time, while the absorption intensity of C-F was increased. CF_4 molecule was generated as C_4F_8 molecule was decomposed. CF_4 molecular began to decompose after 3 min. It was considered that PFCs were conversed to other species by the atmospheric plasma, resulting in the formation of particles with C-F bonds.

Figure 3 shows the SEM images of particles fabricated for 2 min employing the atmospheric CF_4/He and C_4F_8/He plasma. Particles fabricated by the abatement of PFCs were collected on the Si substrate, which was

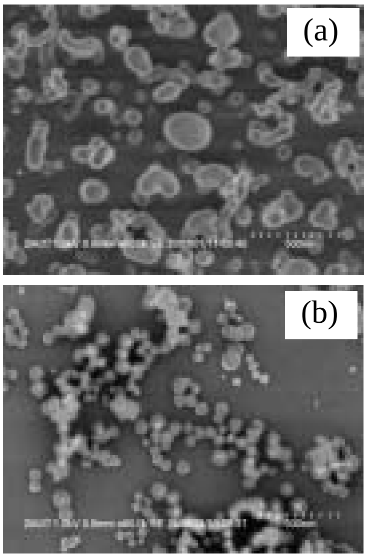

Fig. 3. SEM image of particles fabricated employing (a)CF_4/He and (b)C_4F_8/He atmospheric plasma at a microwave power of 400 W, a total pressure of 1 atom, a PFC concentration of 0.5 %, and discharge time of 2 min.

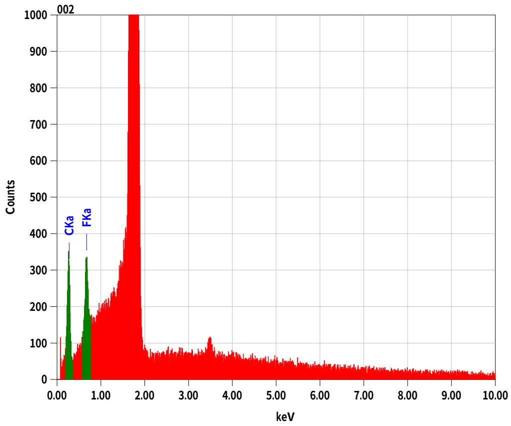

Fig. 4. EDS spectrum of SEM image of particles in Fig. 3(b).

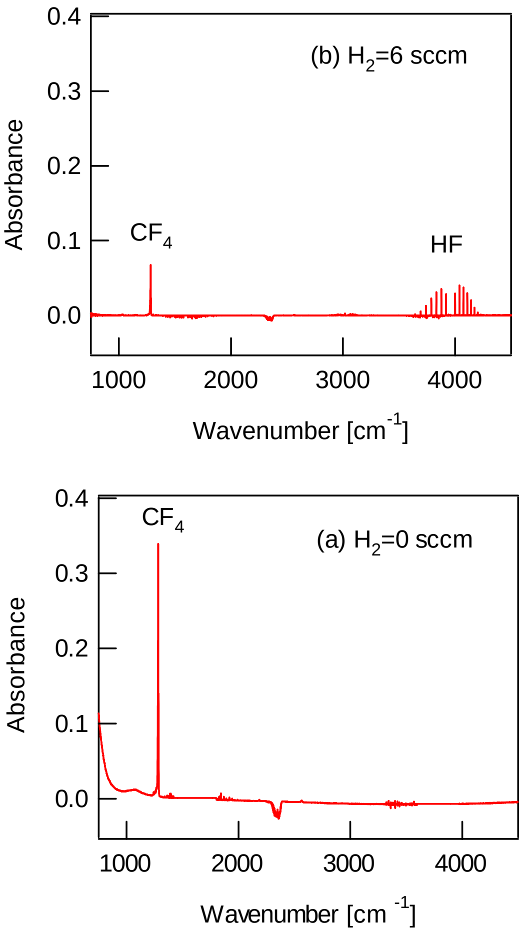

Fig. 5. FT-IR spectra of the exhaust gas from the atmospheric micro-gap plasma with/without H_2 addition at a microwave power of 400 W, a total pressure of 1 atom, a gas flow rate of He/CF_4/H_2=2000/1/x(x=0 and 6) sccm.

cooled by water and supplied with AC 12 kV (60 Hz) as the substrate bias. As shown in Fig. 3, the spherical-shaped particles of approximately 50-120 nm in diameter were fabricated at the short discharge time. The surface of the particles seems smooth. The particles consisted of carbon and fluorine composition from EDS analysis in Fig. 3(b). These results indicated that the cw non-equilibrium microwave-excited atmospheric discharge employing PFCs mixture worked effectively as the abatement and zero-emission recycling system to convert PFCs to solid particles. Furthermore, the spherical-shaped particles fabricated using this technique would be useful in the industrial application.

B. Effect of H_2 Addition on the Abatement of CF_4

The decomposition of CF_4 was performed in the gas flowing with atmosphere. The effect of a H_2 addition on the abatement of CF_4 at the condition of a microwave power of 0 - 1000 W, a total pressure of 1 atom, and a gas flow rate of CF_4/He/H_2 =1/2000/x (x=0-6) sccm. Figure 5 shows FT-IR spectra of the exhaust gas from the atmospheric micro-gap plasma with/without H_2 addition. When H_2 was added to CF_4/He atmospheric micro-gap plasma, the absorption intensity of CF_4 was dominantly decreased and the absorption peak of HF appeared. The generation of HF can be explained by reactions of H atoms with CF_x (x=1-3) radicals and F atom, for example,

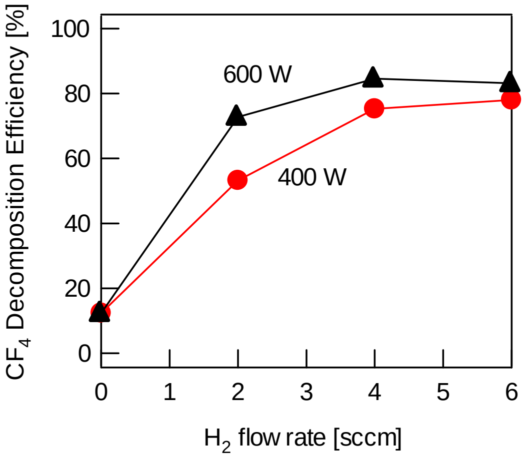

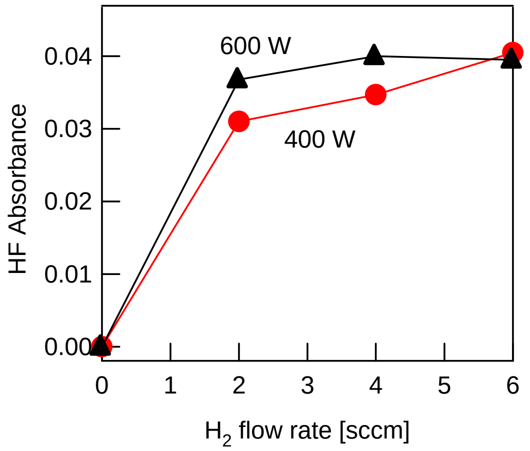

Fig. 6. Dependencies of (a) the decomposition efficiency of CF_4 and (b) the absorption intensity of HF on the H_2 flow rate at a microwave power of 400 or 600 W, a total pressure of 1 atom, a gas flow rate of $He/CF_4/H_2$=2000/1/x(x=0-6) sccm.

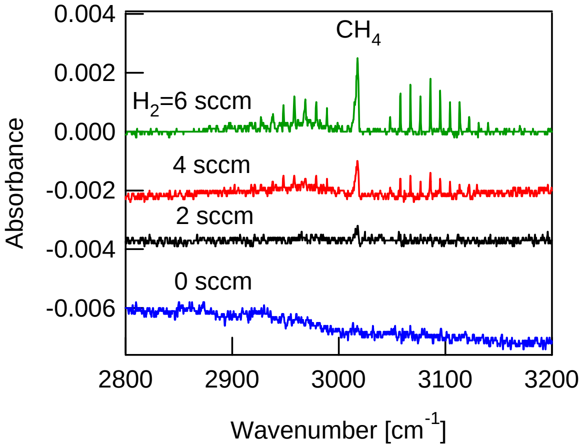

Fig. 7. The detailed FT-IR spectra around 2800–3200 cm^{-1} at a microwave power of 400, a total pressure of 1 atom, a gas flow rate of $He/CF_4/H_2$=2000/1/x(x=0-6) sccm.

$$CF_3 + H \Rightarrow CF_2 + HF \qquad (1.1)$$

$$CF_2 + H \Rightarrow CF + HF \qquad (1.2)$$

$$CF + H \Rightarrow C + HF \qquad (1.3)$$

$$F + H \Rightarrow HF \qquad (1.4)$$

$$F + H_2 \Rightarrow HF + H \qquad (1.5)$$

The rate constants for reactions (1.1)-(1.3) are of the order of 10^{-11} cm^3/s, which are considerably large [11]. The reaction in (1.4) is the third-body association, and HF is generated easily in the gas phase as compared with low pressure condition. H atom was generated not only by electron dissociation, but also by H abstraction reaction with F atoms and H_2 molecule as shown in the equation (1.5), where the rate constant is 8.27 x 10^{-12} cm^3/s [12].

On the other hand, H atoms are less likely to react with feed molecular.

$$CF_4 + H \Rightarrow products \qquad (1.6)$$

The rate constant is ~10^{-36} cm^3/s, which is much smaller than those for reactions (1.1)-(1.3), (1.5). The abstraction reaction with CF_x (x=1-3) radicals and the reduction of F atoms suppressed the recombination of CF_x (x=1-3) radicals with F atoms. Furthermore, it was reported that in the addition of H_2 to the fluorocarbon gas, the generation of fluorocarbon radicals is mainly dominated not by electron impact dissociation but by F abstraction with increasing the gas pressure [13]. It was thought that the high fluorocarbon radical density due to a high-density (n_e= ~10^{15} cm^{-3}) plasma [3] and the reduction of F atoms caused the high decomposition efficiency. Furthermore, it was considered that fluorocarbon radicals were lost in gas phase by the recombination as following, for example,

$$\begin{aligned} CF_2 + CF_2 &\Rightarrow C_2F_4 \\ &\Rightarrow C_xF_y \end{aligned} \qquad (1.7)$$

Figure 6 shows the dependence of decomposition efficiency of CF_4 and the absorption intensity of HF on the H_2 flow rate at a microwave power of 400 and 600 W. The decomposition efficiency of CF_4 in the atmospheric micro-gap plasma was calibrated from the IR speak ratio of CF_4 before and after discharge. As the H_2 flow rate was increased, the decompositon

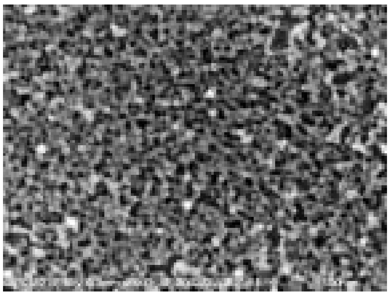

(a) H_2=0sccm

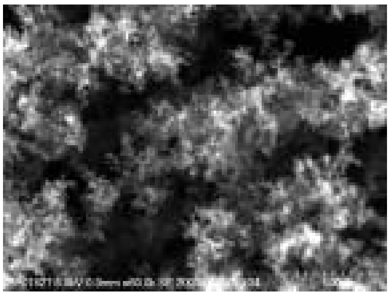

(b) H_2=2sccm

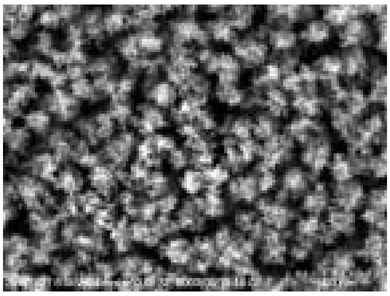

(c) H_2=4sccm

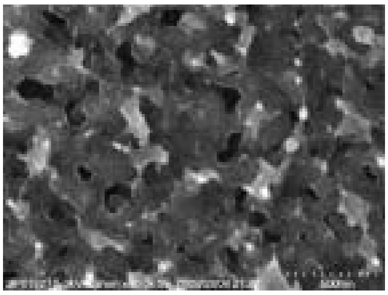

(d) H_2=6sccm

Fig. 8. SEM images of particles collected on the Si substrate at a microwave power of 600 W, a total pressure of 1 atom, a gas flow rate of $He/CF_4/H_2$=2000/1/0-6 sccm.

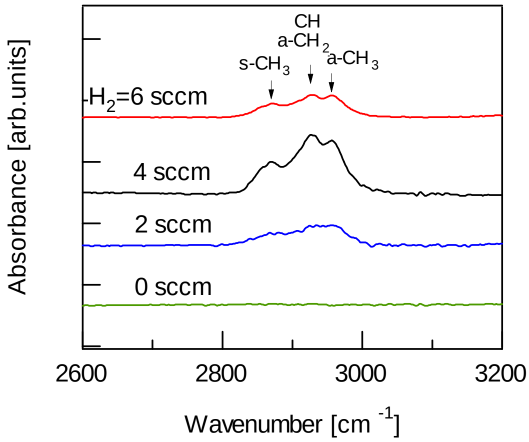

Fig. 9. FT-IR spectra obtained from four different samples, which were corresponded to the samples identified with Fig. 9(a), (b), (c) and (d), respectively.

efficiency of CF_4 was increased from 12 to 85 %, and saturated at the H_2 flow rate of 4 sccm. The behavior of decomposition efficiency was similar to that of the generation of HF. These results indicated that the F abstraction reaction in equations (1.1)-(1.5) contributed greatly to the decomposition.

Figure 7 shows the detailed FT-IR spectra around 2800–3200 cm^{-1}. The absorption peak of CH_4 around 3018.4 cm^{-1} was observed. The absorption peak of CH_4 was increased monotonously with increasing the H_2 flow rate in contrast with the decompositon efficiency of CF_4 as shown in Fig. 6. CH_4 was konwn to the greenhouse gas as well as PFCs. Therefore, the large amount of the H_2 addition should be avoided.

Figure 8 shows the SEM images of particles collected on the Si substrate. As shown in Fig. 4(a) (H_2=0 sccm), the spherical-shaped particles of 50 nm in diameter were selectively fabricated in the CF_4/He atmospheric micro-gap plasma. The particles seemed monodispersed as compared with the results of Fig. 3. In the atmospheric micro-gap plasma, the particles are produced possibly by the reaction in the gas phase because of the abundant three body reaction due to high pressure and high radical density. Therefore, the monodispersed particles may be formed by introducing gas flow and controlling the residence time through the plasma. In particular, the residence time can be easily controlled because of the small plasma volume, where the atmospheric plasma is generated between the micro-gap of $100\mu m$ width as shown in Fig. 1.

As H_2 was added to CF_4/He atmospheric micro plasma, the structures of particles were varied as shown in Figs. 8(b)-(d). In the case of H_2=2 and 4 sccm, the particles seemed to be the agglomerate of the polymerized tube-like fragment and in H_2=6 sccm, the particles formed a film. The difference of the surface structure may influence the formation of the particles in the atmospheric plasma. In order to investigate the chemical bond of the particles, FT-IR technique was performed as follows.

Figure 9 shows FT-IR spectra obtained from four different samples, which were corresponded to the samples identified with Figs. 8(a), (b), (c) and (d), respectively. Under the H_2 flow rate conditions of 2-6 sccm, three obvious absorption peaks at 2870, 2930, and 2960 cm^{-1} are due to the hydrogen in CH_3 (asymmetric), both CH_2 and (asymmetric) and CH, and CH_3 (asymmetric), respectively [14]. In our previous study, it was reported that the H_2 dilution in atmospheric $CH_4/H_2/He$ discharge suppressed the polymerized reaction in gas phase from the observation of Mie scattering [15]. The generation of CH_2 and CH_3 bonding in the fluorocarbon polymer may suppress the polymerized reaction due to the surface structures without a bridged bond. Therefore, it was thought that the structures of particles were varied from polymerized particles to film with increasing H_2 flow rate. CH_4 molecule was increased monotonously in contrast with the decomposition efficiency of CF_4. This fact indicated that the high H_2 dilution ratio supppressed the polymerized reaction in the gas phase due to the association reaction of C and H atom.

4. Conclusions

The atmospheric micro-gap discharge system with the microwave excitation was applied to the abatement of PFCs. CF_4 and C_4F_8 were successfully decomposed and the syntheses of the solid particles were performed. H atom caused the abstraction reaction with CF_x (x=1-3) radicals and F atom generated by the electron dissociation, and suppressed the recombination of CF_x (x=1-3) radicals with F atom. As a result, the CF_4 decomposition efficiency over 80% was achieved. These results indicated that the atmospheric micro-gap plasma with the microwave excitation employing PFCs would work to convert PFCs to solid particles effectively as the abatement and zero-emission recycling system. Furthermore, the polymerized particles fabricated using this technique will be useful in the industrial application.

Acknowledgements

The authors would like to Prof. Akihiro Kono of Nagoya University and Dr. Shoji Den of KATAGIRI ENGINEERING CO., LTD. for helpful advice and discussions in developing the atmospheric micro-gap plasma using the microwave excitation for the PFC abatement system.

References

[1] M. Goldman and R. S. Sigmond, ‘‘Corona and insulation,’’ IEEE Trans. Elect. Insulation, vol. EI-17, no. 2, pp. 90-105, 1982.
[2] B. Eliasson and U. Kogelschatz, ‘‘Nonequilibrium volume plasma chemical processing,’’ IEEE Trans. Plasma Sci., vol. 19, pp. 1063-1077, Dec. 1991.
[3] A. Kono, T. Sugiyama, T. Goto, H. Furuhashi, and Y. Uchida, Jpn. J. Appl. Phys. 40, L238 (2001).
[4] K. Fujita, M. Ito, M. Hori, and T. Goto, J. Vac. Sci. Technol. A 17, 3260 (1999).
[5] M. Haverlag, E. Stoffels, W.W. Stoffels, G.M.W. Kroesen, and F.J. de Hoog, J. Vac.Sci. Technol. A 12, 3102 (1994).
[6] F.W. Breitbarth, D. Berg, K. Dumke, and H.-J. Tiller, Plasma Chem. Plasma Process. 17, 39 (1997).
[7] I.M. Mills, W.B. Person, J.R. Scherer, and B. Crawford, Jr., J. Chem. Phys. 28, 851 (1958).
[8] F.A. Miller and R.J. Capwell, Spectrochim. Actra, Part A 27, 1113 (1971).
[9] R. d’Agostino, F. Cramarossa, F. Fracassi, and F. Illuzzi, Plasma Deposition Treatment and Etching of Polymers, edited by R. d’Agostino (Acadmic, New York,1990), pp. 95-162.
[10] S.J. Limb, K.K. Gleason, D.J. Edell, and E.F. Gleason, J. Vac. Sci. Technol. A 15, 1814 (1997).
[11] C. Tsai and D.L. McFadden, J. Phys. Chem. 93, 2471 (1989).
[12] M.A. Ioffe, Yu.M. Gershenzen, V.B. Rozenshtein and S.Ya. Umanskii, Chem. Phys. Lett. 154, 131 (1989).
[13] H. Doh, J. Kim, S. Lee, and K. Whang, J. Vac. Sci. Technol. A 14(5), 2827 (1996).
[14] B. Dischler, A. Bubenzer, and P. Koidl, Solid State Commun. 48, 105 (1983).
[15] M. Nagai, A. Matsushita, K. Yamakawa, M. Hiramatsu, M. Hori, and T. Goto, Proc. Symp. Dry rocess, (Tokyo, 2002), p. 233.

Quantum Chemical Study on Organic Low Dielectric Constant Film Etching

Toshihiro Nakamura[1], Hideki Motomura[2], Tatsuru Shirafuji[3], and Kunihide Tachibana[1]

[1] *Department of Electronic Science and Engineering, Kyoto University, Kyoto, Japan*
[2] *Department of Electrical and Electronic Engineering, Ehime University, Matsuyama, Japan*
[3] *International Innovation Center, Kyoto University, Kyoto, Japan*

Abstract

The reaction schemes in organic low dielectric constant (low-*k*) film etching were investigated using an *ab initio* molecular orbital and density functional theory calculations. We calculated the charge distributions of the possible gas-phase species in H_2/N_2 and NH_3 plasmas. The local surface structures of organic low-*k* polymer films were modelled using various simple molecules. The interaction between the gas-phase species and local surface models of organic low-*k* dielectric materials was discussed.

1. Introduction

The resistance-capacitance time delay must be reduced by using new materials to achieve high performance ultralarge-scale integrated circuits without compromising the requirements of driving speed, crosstalk tolerance, and dynamic power dissipation imposed by the small feature sizes [1]. Recently, various low dielectric constant (low-*k*) materials for interlayer dielectrics have been developed. One of the most promising approaches to the decrease of the dielectric constant is to use organic polymer materials such as FLARE^{TM} (Honeywell) and SiLK^{TM} (Dow Chemical).

Etching of the organic low-*k* dielectric is an important step in fabricating a damascene structure. In order to make multilevel interconnects with a damascene-structure, it is indispensable for developing an etching technology that suppress the reactive ion etching (RIE) lag, bowing profile tendency, microtrenching, and hard-mask shrinkage. Several experimental studies have been performed to investigate the etching mechanism in H_2/N_2 and NH_3 plasmas [2-5]. The ratio of H and N radical densities was reported to be important for the etching of organic low-*k* film employing N–H plasmas [2]. That is, H radicals were found to be important species for organic low-*k* film etching, while N radicals were found to be effective for the formation of protection layer on the sidewall against the etching by the H radicals. Etching of organic low-*k* dielectric using H_2/N_2 and NH_3 plasmas involves several charged species as well as neutral ones. N_2^+ and N_2H^+ charged species are considered to be dominant under the experimental conditions that give a low microloading profile. In particular, the N_2^+ ion was reported to play a role in the formation of sidewall protection C-N sp^3 film [3]. However, the role of the individual N_xH_y and $N_xH_y^+$ species is still not well understood.

An approach from the theoretical point of view is expected to yield some solutions for this problem [6,7]. In the present work, we investigated the reaction mechanisms in organic low-*k* dielectric etching using an *ab initio* molecular orbital (MO) and density functional theory (DFT) calculations. The scope of this work is to study the trends in reactivity of the possible gas-phase species such as N_xH_y and $N_xH_y^+$ with organic low-*k* dielectric materials.

2. Computational Methods

All the *ab initio* MO and DFT calculations have been carried out using the GAUSSIAN 98 program [8]. The Hartree-Fock (HF) calculations with the 6-31G* basis set were performed as preliminary quantum chemical calculations. In the DFT calculations, Becke's three-parameter exchange functional with the Lee-Yang-Parr correlational functional (B3LYP) was employed. The equilibrium geometry was optimized by B3LYP calculations with the 6-311G** basis set. The stability of the optimized geometries was verified by the calculation of the Hessian, showing that all vibration frequencies are real.

3. Results and Discussion

3.1. Analysis of the possible gas-phase species

In this work, NH, NH_2, NH_3, and N_2H are investigated as the possible gas-phase species in H_2/N_2 and NH_3 plasmas. Calculations for the lowest spin multiplicities of these neutral species show that the singlet and doublet states have the lowest energy. The only exception is NH, whose lowest electronic state is triplet. The net atomic charges calculated by Mulliken population analysis are presented for these neutral species in Fig. 1. The charges of the H atoms are nearly equal for all the ions (+0.2e). The negative charge is localized at the N atoms. Therefore, the attack of the N atoms to the positively charged sites on the surface of organic low-*k* films is preferentially expected.

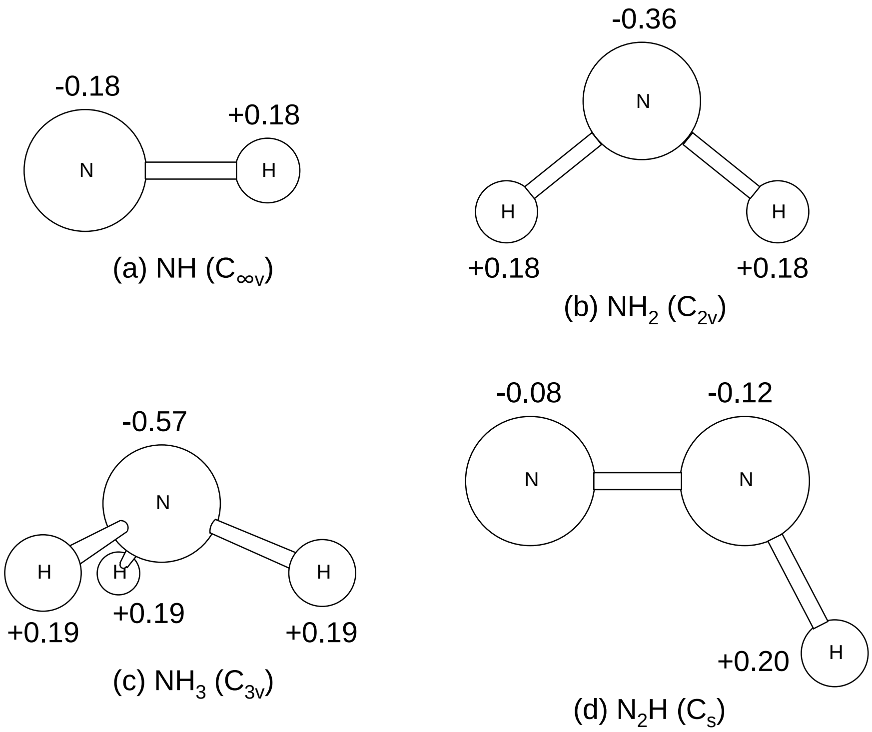

(a) NH ($C_{\infty v}$)

(b) NH_2 (C_{2v})

(c) NH_3 (C_{3v})

(d) N_2H (C_s)

Figure 1. Atomic charges of neutral species N_xH_y. The geometries were optimized by B3LYP/6-311G** calculation. These values were calculated by Mulliken population analysis.

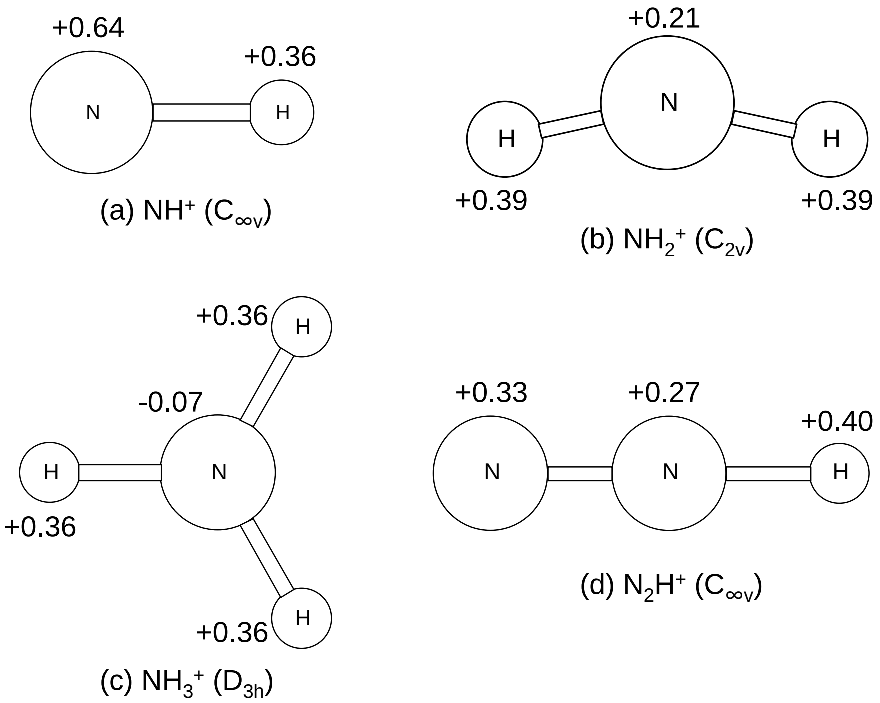

(a) NH^+ ($C_{\infty v}$)

(b) NH_2^+ (C_{2v})

(c) NH_3^+ (D_{3h})

(d) N_2H^+ ($C_{\infty v}$)

Figure 2. Atomic charges of cation species $N_xH_y^+$. The geometries were optimized by B3LYP/6-311G** calculation. These values were calculated by Mulliken population analysis.

Figure 2 shows the charge distribution (Mulliken population) of the corresponding positive ions at the optimized geometries of the cations. Calculations for the lowest spin multiplicities of these ions show that the singlet and doublet states have the lowest energy. The only exception is NH_2^+. For this ion, a triplet state is more stable. The N atoms as well as the H atoms have positive charges with the exception that the N atom of NH_3 has a small negative charge. The attack of the N atoms of these cations to the negatively charged sites on the surface of organic low-*k* films is expected to be possible.

3.2. Modelling of the local surface structures of the organic low dielectric constant films

In this work, we focus our attention on two species of low-*k* dielectric organic aromatic polymers: They are FLARE^{TM} and SiLK^{TM}. FLARE^{TM}, organic spin-on polymer from the Honeywell Electronic Materials Company, is a bridged poly-arylene ether with a dielectric constant of 2.8, and SiLK^{TM}, organic dielectric resin from the Dow Chemical Company, is an aromatic hydrocarbon polymer with a dielectric constant of 2.65 [9]. The chemical structure of FLARE^{TM} is shown in Fig. 3 [2].

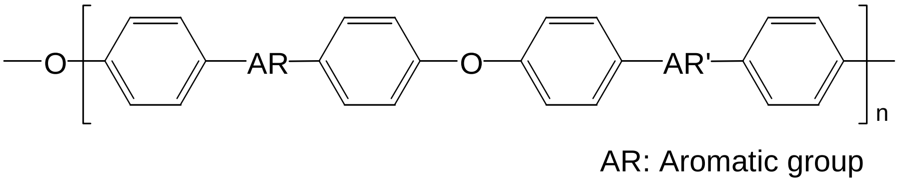

Figure 3. Chemical structure of FLARE^{TM} [2].

In order to model the chemical reactions that take place on a film surface, we approximated chemical structures of the organic low dielectric constant films using simple configurations. Figure 4 shows the structural models for the film surface. We modelled the aromatic group using benzene or biphenyl and the O-containing moiety using methyl alcohol, phenol, or diphenylether. In particular, a diphenylether molecule can be regarded as a typical monomer unit for organic polymers like poly-arylene ether such as FLARE^{TM}. The net atomic charges calculated by Mulliken population analysis are presented for these surface models in Fig. 5. The C and H atoms of benzene and biphenyl have small negative and positive charge, respectively. In the model molecules containing an oxygen atom, the relatively large negative charge is localized at the O atom.

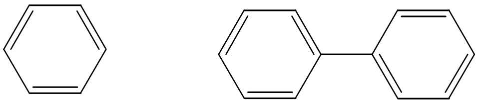

(a) benzene (b) biphenyl

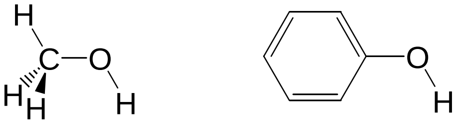

(c) methyl alcohol (d) phenol

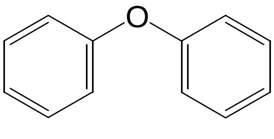

(e) diphenylether

Figure 4. Model molecules for surface structures of organic low dielectric constant films.

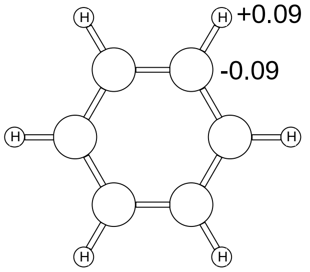

(a) benzene (D_{6h})

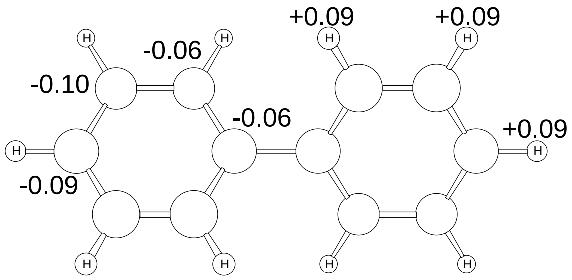

(b) biphenyl (D_2)

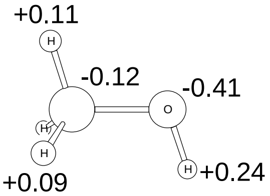

(c) methyl alcohol (C_s)

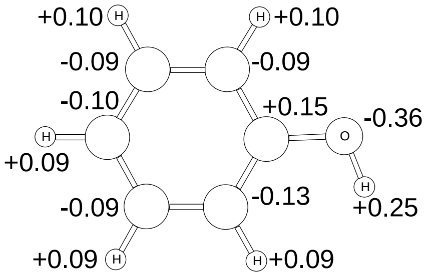

(d) phenol (C_s)

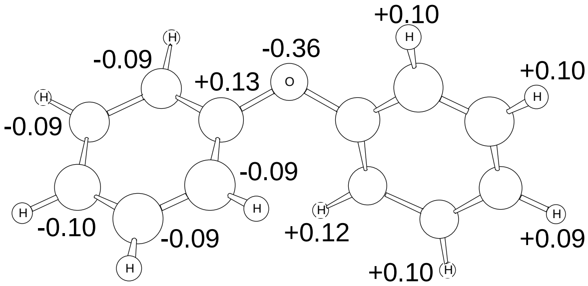

(e) diphenylether (C_2)

Figure 5. Atomic charges of the model molecules for surface structures of organic low dielectric constant films. The geometries were optimized by B3LYP/6-311G** calculation. These values were calculated by Mulliken population analysis.

The detail in the chemical structure of SiLK^{TM} is also unpublished. Infrared absorption spectroscopic measurements can provide some information on the chemical structure of the material. Figure 6 shows the typical infrared absorption spectrum of SiLK^{TM}/Si. This observed spectrum was found to resemble closely an infrared absorption spectrum of a diphenylether molecule. We carried out the vibrational mode analysis of a diphenylether molecule by HF/6-31G* calculation. The results for four relatively intense peaks are shown in Fig. 7. The calculated wavenumbers show good agreement with the corresponding ones of the observed spectrum of SiLK^{TM}/Si. This finding suggests that SiLK^{TM} can be approximated using a chemical structure similar to FLARE^{TM}.

3.3. Interaction between the gas-phase species and the local surface structures

We optimized the atomic configurations when N_xH_y or $N_xH_y^+$ species attack the sites on the surface. The computational surface models employed in this work are shown in Fig. 5. Figure 8 shows the approximate bonding geometry for the interaction between NH and benzene. This is considered as one of the first step of the etching reaction of an organic low-*k* dielectric material. The change of atomic configurations indicates that the attack of N_xH_y or $N_xH_y^+$ species initiates a switching process involving the formation of the C-N bond. The lowest potential energy path of the N_xH_y or $N_xH_y^+$ attack reaction gives the most probable route for organic low-*k* dielectric etching.

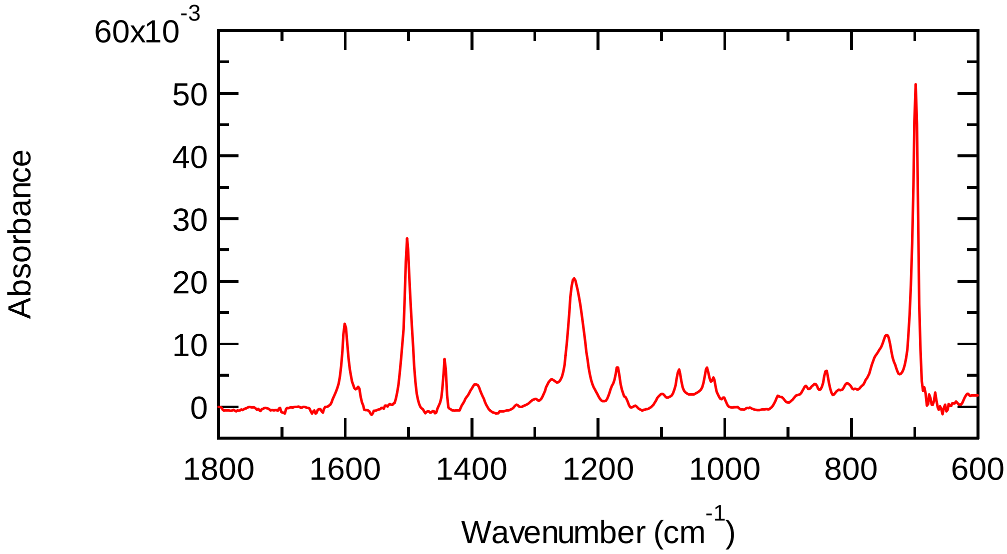

Figure 6. Typical infrared absorption spectrum of SiLK^{TM}/Si.

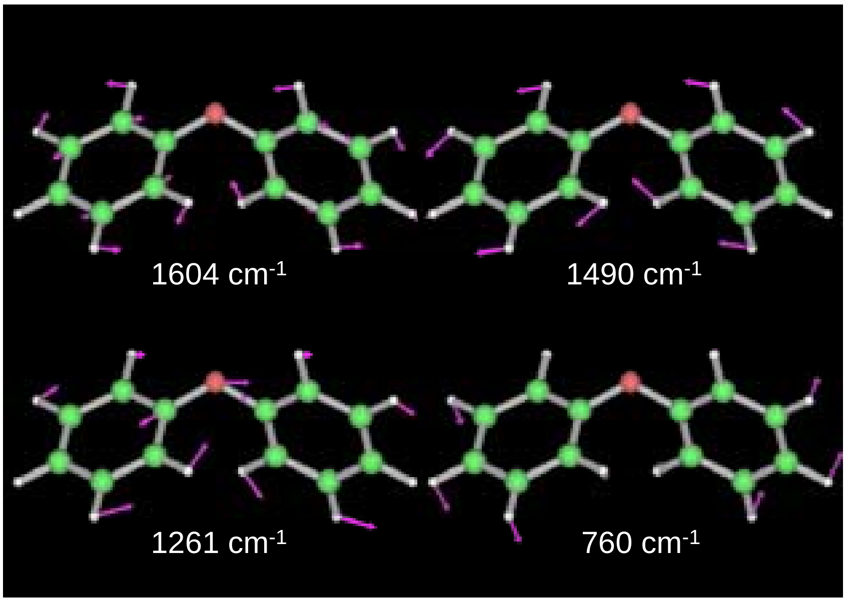

Figure 7. Vibrational mode analysis of a diphenylether molecule by HF/6-31G* calculation.

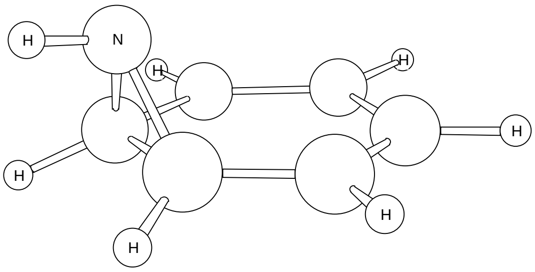

Figure 8. Bonding geometry for the interaction between NH and benzene. This structure is a global minimum.

Acknowledgement

This work has been supported partially by NEDO (New Energy and Industry Developments Organization) through ASET (Association of Super-advanced Electronics Technologies).

References

[1] Z. -C. Wu, Z. -W. Shiung, R. -G. Wu, Y. -L. Liu, W. -H. Wu, B. -Y. Tsui, M. -C. Chen, W. Chang, P. -F. Chou, S. -M. Jang, C. -H. Yu, M. -S. Liang - J. Electrochem. Soc. **148**, F109 (2001).
[2] H. Nagai, S. Takashima, M. Hiramatsu, M. Hori, T. Goto - J. Appl. Phys. **91**, 2615 (2002).
[3] Y. Morikawa, S. Yasunami, W. Chen, T. Hayashi, T. Uchida - J. Vac. Sci. Technol. A **19**, 1747 (2001).
[4] M. Mizumura, R. Fukuyama, Y. Oomoto - Jpn. J. Appl. Phys. **41**, L425 (2002).
[5] H. Nagai, M. Hiramatsu, M. Hori, T. Goto - Jpn. J. Appl. Phys. **42**, L212 (2003).
[6] T. Nakmaura, H. Motomura, K. Tachibana - Jpn. J. Appl. Phys. **40**, 847 (2001).
[7] T. Nakmaura, K. Tachibana - Appl. Phys. Lett. **80**, 3904 (2002).
[8] M. J. Frisch, G. W. Trucks, H. B. Schlegel, G. E. Scuseria, M. A. Robb, J. R. Cheeseman, V. G. Zakrzewski, J. A. Montgomery, Jr., R. E. Stratmann, J. C. Burant, S. Dapprich, J. M. Millam, A. D. Daniels, K. N. Kudin, M. C. Strain, O. Farkas, J. Tomasi, V. Barone, M. Cossi, R. Cammi, B. Mennucci, C. Pomelli, C. Adamo, S. Clifford, J. Ochterski, G. A. Petersson, P. Y. Ayala, Q. Cui, K. Morokuma, D. K. Malick, A. D. Rabuck, K. Raghavachari, J. B. Foresman, J. Cioslowski, J. V. Ortiz, A. G. Baboul, B. B. Stefanov, G. Liu, A. Liashenko, P. Piskorz, I. Komaromi, R. Gomperts, R. L. Martin, D. J. Fox, T. Keith, M. A. Al-Laham, C. Y. Peng, A. Nanayakkara, C. Gonzalez, M. Challacombe, P. M. W. Gill, B. Johnson, W. Chen, M. W. Wong, J. L. Andres, C. Gonzalez, M. Head-Gordon, E. S. Replogle, and J. A. Pople, *Gaussian 98 (Revision A.7),* (Gaussian, Inc. Pittsburgh, PA, 1998).
[9] K. Postava, T. Yamaguchi, M. Horie - Appl. Phys. Lett. **79**, 2231 (2001).

The removal characteristics of oxide layer on carbon steel by cathode spots in low vacuum

Y. Kubo[1], T. Iwao[2], K.Takeda[3], T.Inaba[1]

[1] *Department of Electrical, Electronic, and Communication Engineering, Chuo University, Tokyo, Japan*
[2]*JSPD Research Fellow, Institute of Science and Engineering, Chuo University*
[3]*Department of Machine Intelligence and Systems Engineering, Akita Prefectural University, Akita, Japan*

Abstract

The cathode spots of low vacuum arc can remove and evaporate the oxide layer on the metallic surface. The influence of arc current and thickness of oxide layer on removal rate on the surface of carbon steel is investigated. The results are compared with measured characteristics and theoretical analysis of the oxide on stainless steel. As the result, the removal characteristics are similar to stainless steel, and iron oxides of multi-layer formed on carbon steel influence on the removal rate.

1. Introduction

Oxide layers stably grow up on the surface of steel materials during a manufacturing process. The cathode spots of low vacuum arc can evaporate and remove the oxide layer on the metallic surface[1,2]. Decontamination of the oxide including radioactive substance is expected. Furthermore, the surface after removal of the oxide layer is also formed to be rough. Therefore, application for pre-treatment at thermal spray coating has been examined[3-5]. Grid blasting and chemical decontamination are widely used for the current treatment, but these are unfriendly for environment to scatter sludge, noise and to generate liquid waste. It is carefree for noise and sludge to apply low vacuum arc, because the treatment is carried out in an enclosed space.

The cathode spots are characterized[1,6] by (1) a multitude of arc spots on the cathode, (2) vapor emission of a cathode material due to the extremely intense power density at the cathode spot, (3) rapid movement of the spots on the cathode surface in a random manner[1], and (4) preferential formation on the oxides[1]. Therefore, the oxides under the cathode spots are vaporized and removed instantaneously.

Only a few reports deal with the cleaning action of the cathode spots in the process of Low Pressure Plasma Spray(LPPS)[3-5]. Recently, removal characteristics of the oxide layer on stainless steel were reported[1,7]. In this paper, the authors investigated the removal characteristics of the cathode spots in the removal of oxide on the carbon steel SS400. The experimental results are compared with those of the oxide on stainless steel by using theoretical analysis[7]. Finally, the influence of arc current and iron oxide thickness of multi-layer formed on carbon steel on the removal rate is investigated.

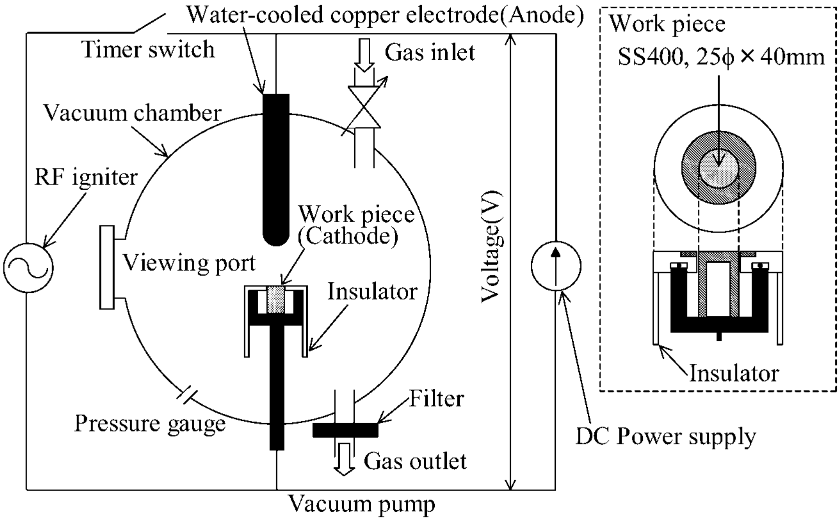

Fig.1. Schematic illustration of experimental set-up

2. Experimental

2.1 Experimental set-up for removal of oxide layer by cathode spots

As shown in Fig.1, an experimental set-up is composed of a vacuum chamber with electrodes inside, a water cooled copper electrode as an anode, a DC power supply (the open circuit voltage is 200V) for the arc, an evacuation system with a rotary pump. A work piece is made of SS400 carbon steel, the surface of which is oxidized. It is connected with a negative polarity of the power supply and serves as a cathode. The distance between the surfaces of the anode and the cathode (work piece) is kept to be 20mm.

The experimental procedure was as follows: Once inside of the chamber was evacuated down to 30Pa. Argon gas was introduced into the chamber up to 0.1MPa, again it was evacuated down to 30Pa. This operation was carried out twice. Finally, pressure inside the chamber was controlled by adjusting the needle valve of the gas inlet. In this time, the pressure was adjusted at 100Pa. A transferred-arc is ignited by an RF igniter, and then the magnitude of an arc current is adjusted at 10-120A in the constant current mode. Arc time can be controlled by a timer by 0.1s. For the measurement of instantaneous removal rate, a work piece is taken out from and back to inside the chamber after every short arc duration time. The area of removal oxides can be clearly recognized by silver-metallic luster, because the color of carbon steel oxide is black. Therefore, the removal area was measured by a digital image scanner before, in and after the removal.

2.2 Work pieces covered with oxide layer

Table 1 shows chemical components of SS400 carbon steels as work pieces. Its dimension is 25ϕ in diameter and 40mm in height. Table 2 shows oxide thickness D_0 with heating temperature T_h and component ratio of oxide layer on SS400 carbon steel as test pieces. First, the upper surface is polished by a buff wheel, and then an ultrasonic cleaning with acetone is carried out for some minutes. Finally, they are heated in an electrical furnace with the heating temperature T_h at 773, 873 and 973K for an hour. The thickness of oxides is analyzed by GDS(Glow Discharge Spectroscopy), and adopted its half value of the oxygen peak. The surface of test pieces was observed to be uniformly covered with a black oxide. The thickness of oxides exponentially increases with T_h, and the component ratio in each condition is different. The main component is Fe_3O_4 or FeO in each heating temperature.

Fig.2 shows distribution of Fe and O elements to depth direction and comparison of a work piece with real mill scale. On SS400 carbon steel, the oxide layer forms iron oxides of multi-layer, and it changes in order of Fe_2O_3, Fe_3O_4, FeO from the surface. In Fig.2, one of the real mill scale on SS400 manufactured by hot rolling is also represented, and both the components of multi-layer are resemble.

Table 1 Chemical components of SS400 carbon steel

(%wt)

Components	P	S	C	Si	Mn	O
SS400	0.01	0.03	0.17	0.04	0.35	0.05

Table 2 Oxide thickness D_0 and component ratio of oxide layer on SS400 carbon steel

Heating temperature T_h (K)	Initial thickness of oxide layer D_0 (m)	Component ratio(%wt)		
		Fe_2O_3	Fe_3O_4	FeO
773	2.3×10^{-6}	16	84	0
873	6.7×10^{-6}	9	91	0
973	25.2×10^{-6}	3	22	75
Real mill scale	20.2×10^{-6}	4	22	74

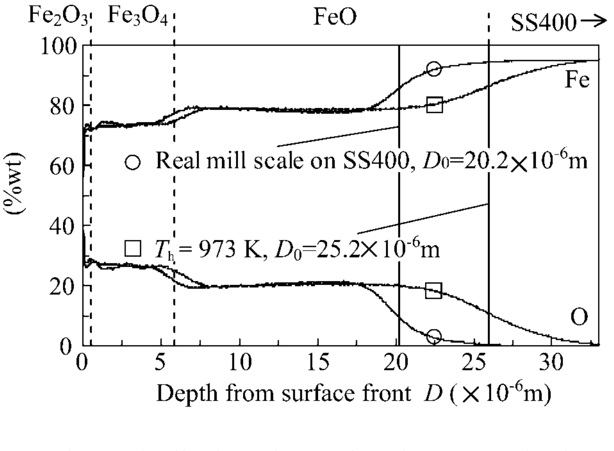

Fig.2. Distribution of Fe and O elements to depth direction and comparison of a work piece with real mill scale

3. Result

3.1 Number of cathode spots

The change of the arc current results in the change of the spot number as shown in Fig.3. Therefore, the cathode spot on the oxide of SS400 is also classified to Multi Cathode Spot (MCS)[6]. Roughly saying, the number of spots N proportionally increases with arc current I as follow:

$$N=I/i \tag{1}$$

Where, i is the current of one cathode spot. It is evaluated to be 10.5A on the average in the present SS400. This value is only 60% of that of SUS430.

3.2 Removal of oxide layer by cathode spots

The removal characteristics, mainly removal rate of oxide, are investigated by changing arc current and initial thickness of oxide layer defined as D_0 in Fig.2 on average with each heating temperature. Experimental result on the rate change of the oxide removal is shown with thickness of oxide layer D_0 and arc current in Fig.4. The rate decreases inversely with the increase of the thickness. On the other hand the proportional increase of removal rate is observed with the increase of arc current. These characteristics close to the behavior of cathode spots on SUS430 stainless steel[1].

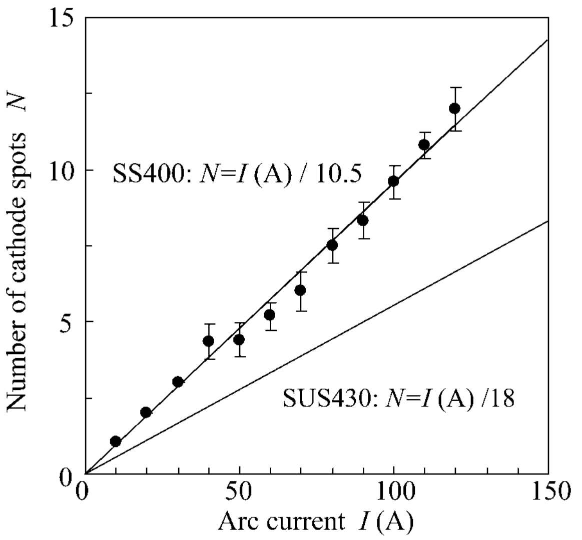

Fig.3. Change in the number of cathode spots with arc current for the present SS400 and SUS430[1] covered with oxide layer.

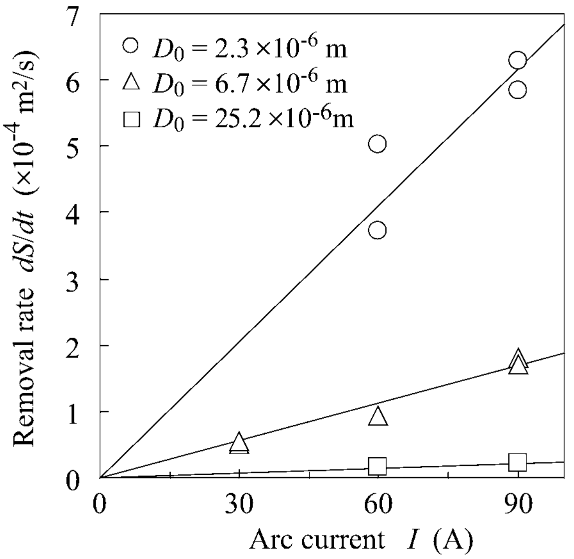

Fig.4. Change of the removal rate with arc current at different oxide thickness

4. Discussion

4.1 The modeling of removal action

In this section, the removal characteristics by cathode spots are considered between stainless steel and carbon steel by using existing model based on the energy balance at a cathode spot on SUS430 substrate covered with Cr_2O_3[1,7].

The energy balance is indicated as follows:

$$Q_{\mathrm{cathode}} = Q_{\mathrm{vapor}} + Q_{\mathrm{substrate}} + Q_{\mathrm{radiation}} + Q_{\mathrm{electron}} \tag{2}$$

The heat flux from the arc to the cathode, Q_{cathode} is written as

$$Q_{\mathrm{cathode}} = \eta \cdot iV, \tag{3}$$

where the η denotes the ratio of cathode input to the total energy supplied into the arc and V is arc voltage. The heat flux conveyed away by the vapor of the oxide, Q_{vapor} is represented by

$$Q_{\mathrm{vaper}} = -s(dD/dt)\,H_v \tag{4}$$

where H_v and D symbolize the amount of the heat necessary for the evaporation of the unit volume oxide, and the thickness of an oxide at an arbitrary time t, respectively. s is minimum unit of removal area of a cathode spot which was determined by the cathodic creator size, when it was eroded by short pulse. Here, H_v as oxides components of multi-layer assumes following decomposition reactions:

$$\begin{array}{cccc} \mathrm{FeO\ (s)} & \rightarrow & \mathrm{Fe\ (g)} + & \mathrm{O\ (g)} \\ \mathrm{Fe_2O_3\ (s)} & \rightarrow & \mathrm{2Fe\ (g)} + & \mathrm{3O\ (g)} \\ \mathrm{Fe_3O_4\ (s)} & \rightarrow & \mathrm{3Fe\ (g)} + & \mathrm{4O\ (g)} \end{array} \tag{5}$$

Here (s) and (g) mean solid and gas states, respectively. And vaporized gases are heated up to 3,000K. The heat flux due to the radiation, $Q_{\mathrm{radiation}}$ is neglected due to too small amount compared to others or so[1], and the emission of electrons from the cathode surface, Q_{electron} is approximated as:

$$Q_{\mathrm{electron}} = i\phi \tag{6}$$

ϕ denotes the work function of the oxide. The heat flow into the cathode by heat conduction, $Q_{\mathrm{substrate}}$ is expressed in the following form:

$$Q_{\mathrm{substrate}} = -s\kappa\nabla T \tag{7}$$

where κ and T represent thermal conductivity and temperature. On this model heat conduction is applied to a nonstationary state of one dimension perpendicular to a semi-infinite solid surface.

Here, two characteristic times are defined as τ_1 and τ_2. τ_1 is the time necessary to heat up the surface temperature to a boiling point, and the following equation from Eq.(2) is considered:

$$(i/s)(\eta V-\phi) = -\kappa(\partial^2T/\partial x^2)_{x=0} \qquad \text{for } 0 < t < \tau_1 \tag{8}$$

The origin ($x = 0$) of the coordinate x is fixed at the surface of the oxide. Furthermore, τ_2 is the time necessary to remove the oxide by evaporation, so the equation of the next time step is also written as follows:

$$(i/s)(\eta V-\phi) = -(dD/dt)H_v - \kappa(\partial^2T/\partial x^2)_{x=0} \qquad \text{for } \tau_1 < t < \tau_1+\tau_2 \tag{9}$$

and the boundary condition for Eq.(8) is $T(t,0) = T_v$, where T_v is the boiling point of each in component in a pressure at 10^2Pa. τ_1 is obtainable to solve Eq.(8) with the heat conduction equation by using above boundary condition and an initial condition of

$$\tau_1 = \frac{\pi}{\alpha}\left(\frac{\kappa T_v}{2E}\right) \tag{10}$$

where α is thermal diffusivity, and E is the power density at the cathode as:

$$E = (i/s)(\eta V-\phi) \tag{11}$$

and then the temperature distribution is written as following equation:

$$T = T_v\,\mathrm{erfc}(x/\sqrt{4\alpha(t-\tau_1)}\ ) \tag{12}$$

and erfc(y) denotes the complementary error function. Furthermore τ_2 can be obtainable to solve the function $D(t)$ from Eq.(9) which decreases with the time, then by $D(\tau_1+\tau_2) = 0$;

$$\tau_2 = \frac{1}{E^2}\left(2\kappa^2 T_{\mathrm{v}}^{\ 2} + D_0 E H_{\mathrm{v}} + \frac{2\kappa T_{\mathrm{v}}}{\pi\alpha}\sqrt{\kappa^2 T_{\mathrm{v}}^{\ 2} + D_0 E H_{\mathrm{v}}\,\pi\alpha} \right) \tag{13}$$

The time $t = \tau_1 + \tau_2$ denotes that a cathode spot removes the oxide in the area of S. Therefore, the removal rate dS/dt of a cathode spot is finally expressed as,

$$dS/dt = s/(\tau_1+\tau_2) = i(\eta V-\phi)/[(\tau_1+\tau_2)E] \tag{14}$$

Table 3 Physical properties of oxides on steel materials for the calculations

Material	Physical properties of oxides on steel materials								
	α (m^2/s)	κ (W/mK)	Tv (K)	i (A)	Hv (J/m^3)	r (m)	V (V)	η	ϕ (V)
Cr_2O_3[1,7]	3.5×10^{-6}	14	2400	18	1.00×10^{-11}	5×10^{-6}	20	1/3[1]	4.5
FeO	5.7×10^{-6}[8]	3.2[8]	2200	10.5	1.13×10^{-11}	5×10^{-6}	18		3.8[1]
Fe_2O_3	2.5×10^{-6}[8]	1.2[8]	2160		8.93×10^{-11}				
Fe_3O_4	3.5×10^{-6}[8]	1.5[8]	2160		8.49×10^{-11}				

4.2 Comparison with removal rates of the oxide layer on SUS430 stainless steel and SS400 carbon steel

Table 3 shows physical properties of oxides on steel materials for the calculation. In case of oxide layer on SUS430, chromium oxide is assumed[1,7]. Thermodynamic calculation software FactSage(GTT Technology, Germany) was used for calculation of H_{v} and T_{v}. The multi-layer composed of Fe_2O_3, Fe_3O_4, FeO dealt with individual layer. Radius of cathode spot r, η and V were obtained by former experiment.

Moreover, the values of removal rates in Fig.5 can denote a removal rate per a cathode spot to divide the removal rate dS/dt by number of cathode spots N from Eq.(1) because both the N and removal rate are in proportion to arc current, which is called a unit removal rate.

Fig.5 shows comparison of the unit removal rates predicted from the modeling with experimental values in each arc current. As the result, the difference of removal rate in arc current in Fig.4 can be roughly condensed to an ability of removal by a cathode spots. The experimental unit removal rates for SS400 and SUS430[1,7] roughly vary in inverse proportion to the initial thickness of oxide, and the result of this experiment gives good agreement with the theoretical characteristics obtained by the plots of Eq.(14). Here the the theoretical curve of Fe_2O_3 is almost same to that of Fe_3O_4. However all of theoretical data indicates a little bit higher removal rate than experimental data. The slopes of unit removal rate of iron oxides in the experiment are a little different from theoretical slopes of them. The reason can be explained by difference of component ratios in surface oxides in Table 2 *i.e.* the main component of SS400 is Fe_3O_4 or FeO in each heating temperature.

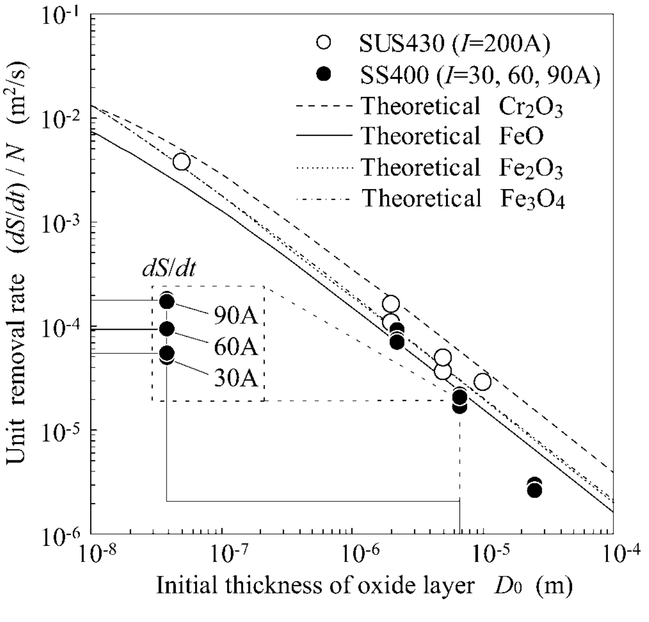

Fig.5. Change of the removal rate with arc current at different oxide thickness & its normalization using unit removal rate. dS/dt is indecated in the box of broken line ⬚ in arc current at 30, 60, 90A and the oxide thickness at 6.7×10^{-6}m.

Conclusions

In removal action of cathode spots at low vacuum of 100Pa, the influence of arc current and thickness of oxide layer on removal rates on the surface of SS400 carbon steel was investigated and compared with that of stainless steel.

As the result, the removal characteristics of carbon steel are similar to stainless steel, and iron oxides of multi-layer formed on carbon steel influence on its removal rate as follows:

(1) The behavior of cathode spots on oxide layer on the surface of SS400 carbon steel is nearly resembled to it on SUS430 stainless steel.

(2) The number of cathode spots is nearly in proportion to the arc current. The average of current/spot is 10.5A at the oxide layer on SS400.

(3) Removal rate changes in proportion to the arc current and in inverse proportion to the initial thickness of oxide layer.

(4) The removal rate can be expressed as a unit removal rate denoted as the removal rate/spot number. It can be compared with removal rates of different surface materials. It is also inverse proportional to the initial thickness of the oxide.

(5) The unit removal rate of oxide on carbon steel is 1.5-2 times as low as that on stainless steel.

(6) Oxide layer on a carbon steel is formed in multi-layer which is composed of Fe_2O_3, Fe_3O_4, and FeO. It significantly influenced on the removal rate.

Acknowledgements

The authors would like to gratefully acknowledge the enthusiastic supervision of Dr. T.Ootsuka during this work, and also thank Mr.Maezono, Mr. Umemoto, Mr.Kimitsuka and Mr.Nemoto for the help on the experiment and the digital image analysis. Attendance to this conference is to be supported by "IEEJ(Institute of Electrical Engineers of Japan) Sakurai Fund".

References

[1] K.Takeda, S.Takeuchi, Materials transactions, JIM, Vol.38(1997), 636-642
[2] A.E.Guile, B.Juttner, IEEE Trans. on Plasma Sci., Vol.PS-8(1991), 259-268
[3] R.Henne, M.V. Bradke, W.Schnurnberger and W.Weber, Proc. of 12th Int. Thermo. Spraying Conf., 112(1991), 245-186
[4] K.Takeda, M.Ito and S.Takeuch, Pure and Appl. Chem., **62**(1990), pp.1773-1782
[5] K.Honda, I.Chida, T.Fuse, T.Murakami, K.Kobayashi, Quarterly Journal of JWS, **3**(1996), pp.510-??.
[6] R.L.Boxman, D.M.Sanders and P.J.Martin, Handbook of Vacuum Arc Science and Technology, Fundamentals and Applications, Noyes Publ, Park Ridge, New Jersey, (1995)
[7] K.Takeda, S.Takeuch, Thin solid films **407**(2002), 163-168
[8] M.Trres, R.Colas, J. Mater. Proc. Technol. **105**(2000), 258-263

VUV-LIF measurements of ro-vibrationally excited hydrogen molecules

P. Vankan, S.B.S. Heil, D.C. Schram and R. Engeln

Centre for Plasma Physics and Radiation Technology(CPS),Department of Applied Physics,
Eindhoven University of Technology, P.O. Box 513, 5600 MB Eindhoven, The Netherlands

Abstract

For the spatially resolved detection of rotationally and vibrationally excited hydrogen molecules a Vacuum Ultra-Violet Laser Induced Fluorescence (VUV-LIF) setup has been built. Coherent anti-Stokes Raman scattering measurements are used to absolutely calibrate the VUV-LIF measurements. State-selective measurements in the shock structure of a hydrogen plasma expansion show that the rotational and vibrational density distributions cannot be described with one temperature.

Introduction

Ro-vibrationally excited hydrogen molecules ($H_2^{r,v}$) can influence the hydrogen kinetics in plasmas to a large extent. Molecular reactions with ro-vibrationally excited molecules can be much more efficient compared to reactions with ground state molecules. This increased reactivity is caused by the extra energy stored in rotation and vibration. The production of the hydrogen negative ion (H^-) via dissociative attachment, for example, becomes 5 orders of magnitude more efficient when the vibration of the hydrogen molecule is increased from v=0 to v=5 [1].
Another example of the increased reactivity of ro-vibrationally excited molecules is the charge exchange of H^+ with H_2. This process becomes resonant for v=4, which increases the cross section several orders.

To understand the influence of $H_2^{r,v}$ in plasmas it is vital to have information on the density distribution over the different levels. In low temperature plasmas, molecular hydrogen levels having high rotational excitation (J>5) are generally found to be overpopulated compared to a Boltzmann (i.e a thermal) distribution. High vibrational levels have also been found to be overpopulated [2]. These rotational and vibrational overpopulations are related to the creation of the $H_2^{r,v}$. The main creation processes for $H_2^{r,v}$ are the direct and indirect electron excitation processes (e-V and E-V) [3,4]. The non-thermal distributions are now believed to be caused by the high energy tail of the electron energy distribution function in combination with a less effective excitation exchange of the higher levels. The creation processes depend critically on the electron density and on the electron energy distribution function. However, in environments, where the electron density and electron energy tail are low, the electron excitation processes are very inefficient. In such environments surfaces may influence the vibrational and rotational excitation to a large extent.
On a surface, molecular hydrogen ions [5] as well as atomic hydrogen radicals [6,7] can recombine forming ro-vibrationally excited H_2. Eenshuistra *et al.* [6] and Hall *et al.*[7], for example, measured vibrational overpopulations produced in hot-filament reactors, where the electron density is very low. They explained the overpopulated density distribution by surface recombination of hydrogen atoms into high vibrationally excited hydrogen molecules.

Measuring the population distribution over the rotational and vibrational levels necessitates state selective and often spatially resolved measurements. Such measurements are commonly performed using laser spectroscopy. In the case of H_2 however, laser spectroscopy is not straightforward since pure ro-vibrational transitions are not allowed and the energy gap to the first electronically excited state ($B^1\Sigma_u^+$) is large (about 11 eV). A technique, which is successfully used to measure the density of the lower vibrational levels, is Coherent anti-Stokes Raman Scattering (CARS) [8]. However, for higher vibrational levels ($v \geq 2$) the CARS technique has serious limitations. In order to probe the higher vibrational levels, Laser Induced Fluorescence (LIF) with excitation to the $B^1\Sigma_u^+$ state can be used. To excite to this state, radiation is needed with a wavelength below 165 nm, the vacuum UV region(VUV). This VUV radiation can be produced using the Stimulated Anti-Stokes Raman Scattering (SARS) process [9].

In this contribution we present an experimental setup which can measure $H_2^{r,v}$ from v=2 to v=13, i.e. with wavelengths between 120 and 165 nm. The setup will be described in detail. Some spectra and a ro-vibrational distribution will be presented. CARS measurements are used to calibrate the VUV-LIF measurements.

Experimental set up

As a hydrogen source a cascaded thermal arc is used. The cascaded arc produces a sub-atmospheric and partially ionized and partially dissociated hydrogen plasma. The power input is typically 2 to 10 kW. The plasma supersonically expands into a vacuum chamber, at typical pressures of 10 to 200 Pa . The expanding plasma jet collides with the background gas in the vacuum chamber forming a shock structure. After the shock the plasma jet is subsonic [10,11].
The plasma source can be moved parallel to the expansion axis as well as perpendicular to the expansion axis. This enables spatially resolved measurements throughout the complete expansion structure. In order to perform measurements near a surface, a temperature controlled substrate can be used. The substrate material can be changed. Furthermore the substrate can also move perpendicular and parallel to the expansion axis, enabling spatially resolved measurements in front of the surface.

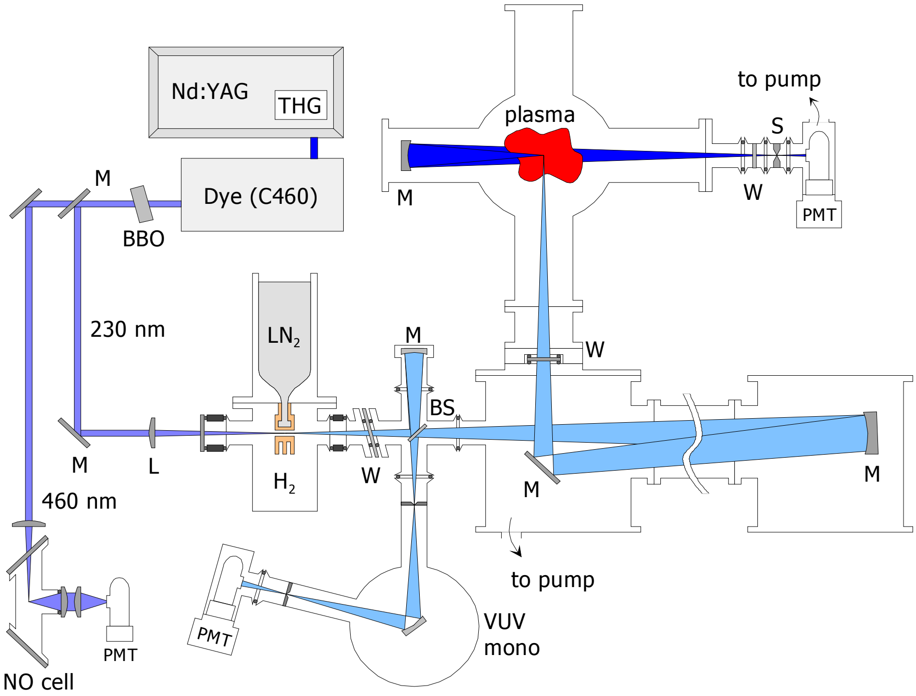

Figure 1: Schematic view of the VUV LIF setup

A scheme of the experimental arrangement is shown in Figure 1. A frequency doubled Nd:YAG laser (Spectra Physics GCR230) operated at 20 Hz is used to pump a tunable dye laser (Sirah Precisionscan) producing light between 430 and 470 nm. This light is frequency doubled in a BBO crystal resulting in 5 ns pulses of 5 to 10 mJ, with a bandwidth of 0.15 cm^{-1}. After separation of the dye laser fundamental beam using 3 dielectric mirrors, the light is focussed into a Raman cell using a 19 cm focal distance quartz lens. The details of the Raman cell and the principles of anti-Stokes generation are described elsewhere [9,12]. In short, the Raman cell contains hydrogen at a pressure of about 2 bars and a cold copper finger in the centre of the cell. This copper finger is cooled with liquid nitrogen. The laser is focussed into a cylindrical hole in the cold finger. In the laser focus, the high power density produces a set of laser beams, the so called Stokes (S) and Anti-Stokes (AS) laser beams, via the SARS process. Every anti-Stokes order is shifted up in

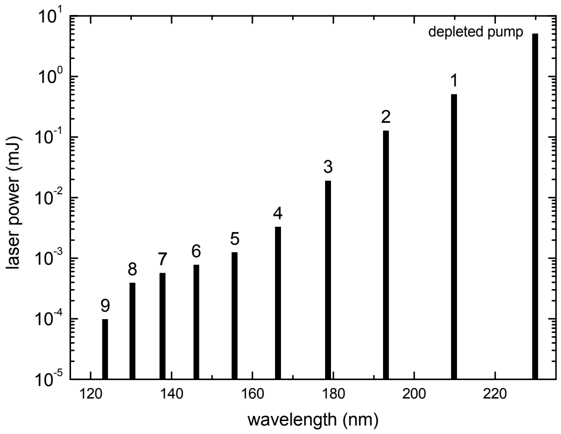

Figure 2: Pulse energy of the AS laser beams. The fundamental pump beam had an energy of 8 mJ.

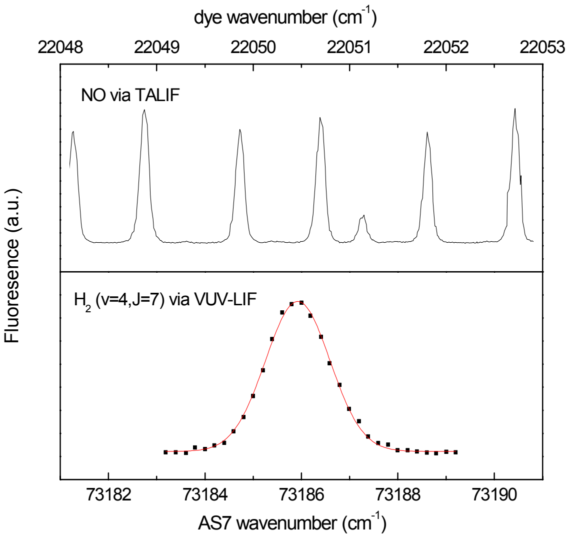

Figure 3: Simultaneous measurement of part of the NO spectrum and a H_2 transition

frequency by the vibrational Raman shift of H_2, i.e. 4155.23 cm^{-1}. This can also be seen in Figure 2, where the AS pulse energy is plotted as function of wavelength that in this way tunable, narrow band laser light can be produced covering the complete Vacuum UV (VUV) region from 200 nm down to 120 nm. This (V)UV laser light is used to excited hydrogen molecules from a ro-vibrational state in the electronic ground state to the first electronically excited state, i.e. one of the Lyman transitions in the $X^1\Sigma_g^+ \rightarrow B^1\Sigma_u^+$ -band [13]. The density in the $B^1\Sigma_u^+$ state radiatively decays to the ground state. The fluorescence, generated in this LIF process, is detected and gives information on the density and temperature of the initial state in the electronic ground state.

In order to accurately determine the wavelength of the dye laser, the light of the dye laser fundamental beam that is not used in the doubling process has been used to excite nitric monoxide (NO) in a reference cell via a two-photon transition of the γ-band. The fluorescence to the NO ground state has been imaged onto a PMT (Hamamatsu R7154). The resulting spectrum is well known from literature and can thus be used to calibrate the wavelength axis. In a typical measurement the fluorescence of the hydrogen and the NO spectrum can be recorded simultaneously as shown in Figure 3, where the H_2 line ($X(v=4,J=7) \rightarrow B(v=0,J=6)$) is scanned.

All the Raman orders, Stokes and anti-Stokes, together with the depleted pump radiation leave the Raman cell simultaneously. The laser beams are focused using a concave VUV mirror and redirected into the vacuum chamber using a flat VUV mirror. In order to reduce the stray light, which is mainly caused by the depleted pump beam, a metal disc can be placed at the centre of the concave VUV mirror. Since the spatial beam profiles of the Stokes and depleted pump beams are close to Gaussian whereas the profiles of the AS beams are concentrical rings the disc can block the relatively high power pump beam and Stokes beams reducing the stray light. A thin MgF_2 plate just after the Raman cell reflects a small part of the laser light onto a concave mirror, which focuses the light onto the entrance slit of a 50 cm VUV monochromator (McPherson). A solar blind PMT (Hamamatsu R7639) detects the AS used for the excitation for reference. In Figure 2 the relative AS intensities are plotted as function of the wavelength. This measurement was performed at a H_2 pressure in the Raman cell of 1.5 bar and a laser energy of around 8 mJ per shot. The measured intensities have been corrected for the quantum efficiency of the photomultiplier tube.

The laser induced fluorescence is detected perpendicular to the laser beam. A concave VUV mirror focuses the fluorescence onto a slit mask. The detection volume is defined by the waist of the focus (≈ 200 μm) and by the slit mask (1x0.5 mm^2). The fluorescence is detected by a solar blind PMT (Hamamatsu R1259). The PMT can be gated to protect it from the plasma radiation. Both the reference and the fluorescence signal are recorded shot-to-shot by a 2 GSample/s oscilloscope (LeCroy LT372). Since the VUV radiation is efficiently absorbed by oxygen the complete optical system after the Raman cell (reference branch, AS focussing and detection branch) is operated under vacuum at a pressure of around 10^{-5} mbar.

The fluorescence is recorded as function of the excitation wavelength in typically 50 steps. At every wavelength typically 100 shots are recorded. Since the number of fluorescence photons can be relatively small (in the order of 100 photons) the fluorescence is averaged prior to the correction for laser intensity, calculated from the average reference signal. From the area under the fluorescence peaks the density can be calculated. From the width of the Doppler broadened peaks the temperature is determined.

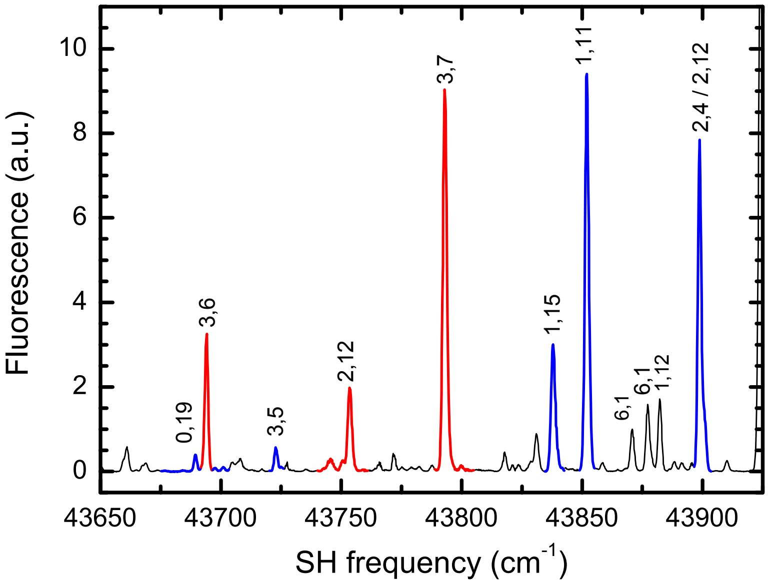

Figure 4: Part of the VUV-LIF Lyman spectrum measured with the setup shown in Figure 1. The numbers depict the v,J values of the levels in the ground state.

Results

To demonstrate the working of the setup, part of the Lyman band spectrum has been recorded, as can be seen in Figure 4. In this Figure the fluorescence is plotted as function of the pump beam wavelength, i.e. the Second Harmonic (SH) of the dye laser. When the dye laser, and thus the second harmonic, is scanned, all the anti-Stokes beams are scanned as well. The fluorescence from the different peaks in the spectrum can be induced by different AS orders, belonging to different wavelengths. The wavelength or energy scale of the spectrum is therefore the addition of all the energy scales of all the AS beams used for the excitation. This is the so-called multiplexing of the AS orders. The wavelength calibration was necessary in order to identify the peaks in the spectrum and their corresponding excitation AS beam.

When recording transitions from different lower levels one can measure the population distribution. Such a population distribution has been plotted in Figure 5. The density divided by the degeneracy ((2*J*+1)(2*N*+1), with *J* the angular momentum quantum number and *N* the nuclear spin quantum number) is plotted as function of the energy of the corresponding state. To deduce these relative densities, the measurements have been corrected for the excitation efficiency (Einstein coefficient, laser energy, and transmission through the optics in the excitation branch) and for the wavelength dependent detection efficiency (window transmission, mirror reflectivity and quantum efficiency of the PMT).
The relative LIF densities have been calibrated using previous Coherent anti-Stokes Raman Scattering (CARS) measurements [8]. These CARS measurements show overlap with the VUV-LIF measurements. Both techniques have been applied to the $H_2(X)$ (v=2,J=3) state. Using the VUV-LIF technique densities down to 10^{15} m^{-3} can be detected. The expected lower densities at higher vibrational levels can be measured comparably easy since the expected density drop is compensated by the higher laser energy at lower order anti-Stokes.

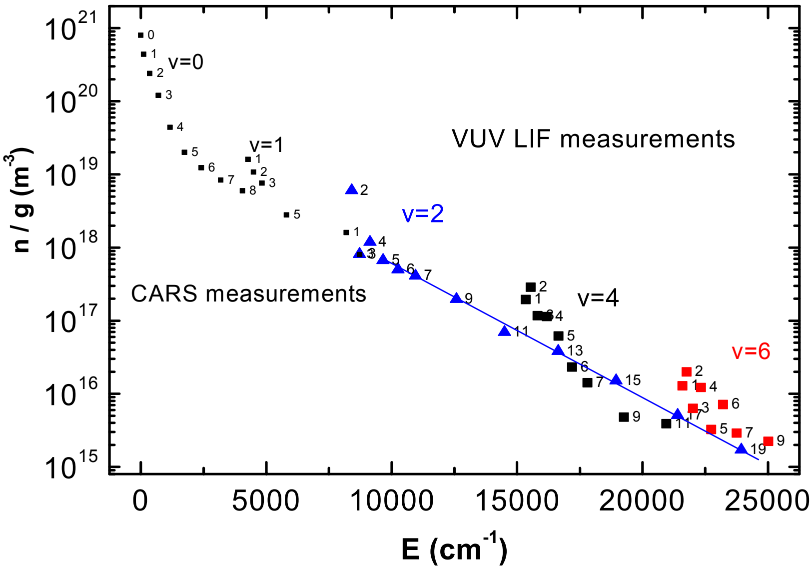

Figure 5: The density per statistical weight as function of the energy of the ro-vibrational state in the electronic ground state. The VUV-LIF measurements are calibrated using CARS measurements [8]. The solid line is drawn assuming a Boltzmann distribution with a temperature of 3600 K.

From the lower rotational levels a rotational temperature can be determined, assuming a Boltzmann distribution. This temperature is in the order of 400 K and is approximately equal to the temperature determined from the width of the fluorescence lines. This indicates that the lower rotational levels are in thermal equilibrium. However both the CARS and the VUV-LIF measurements show overpopulation of the higher rotational levels (J>5) compared to the Boltzmann distribution determined from the lower levels. For example in the v=6 state the population in the rotational levels J=7 and J=9 is clearly higher than a Boltzmann distribution determined from J=1 to J=5. In the state v=2 rotational levels have even been observed up to J=19. The temperature that is determined from these higher levels is approximately 3600 K. This is in the order of the vibrational temperature rather then the translational temperature, determined from the line widths. It can therefore be concluded that the higher rotational levels are not in equilibrium. Probably this is due to the large energy gap between the high rotational levels making collisional relaxation very inefficient.

The cumulative density of the levels v=1 and higher is in the order of a few percent of the total density. The density of the hydrogen atoms, believed to be the main reactive species, is around 10 %. The influence of hydrogen molecules with ro-vibrational excitation on the hydrogen kinetics can therefore not be neglected.

This work is part of the research program of the “Stichting voor Fundamenteel Onderzoek der Materie (FOM)”, which is financially supported by the “Nederlandse Organisatie voor Wetenschappelijk Onderzoek”. We acknowledge Prof. H.F. Döbele for his help during designing and building the VUV-LIF setup and Ries van de Sande, Jo Jansen, Herman de Jong and Bertus Hüsken for their technical assistance..

References

[1] A. Peet Hickman, Phys. Rev. A, **43**, 3495 (1991)

[2] T. Mosbach and H.-M. Katsch, and H. F. Döbele, Phys. Rev. Lett., **85**, 3420 (2000)

[3] R. Celiberto, R. K. Janev, A. Laricchiuta, M. Capitelli, J. M. Wadehra and D. E. Atems, Atomic Data and Nuclear Data Tables, **77**, 161 (2001)

[4] J. R. Hiskes, J. Appl. Phys., **70**, 3409 (1991)

[5] J. R. Hiskes and A. M. Karo, J. Appl. Phys., **67**, 6621 (1990)

[6] P.J. Eenshuistra, J.H.M. Bonnie, J. Los, and H.J. Hopman, Phys. Rev. Lett. **60**, 341 (1988)

[7] R.I. Hall, I. Cadez, M. Landau, F. Pichou and C. Shermann, Phys. Rev. Lett. **60**, 337 (1988).
[8] R.F.G. Meulenbroeks, R. A. H. Engeln, J.A.M. van der Mullen, and D. C. Schram, Phys. Rev. E, **53**, 5207 (1996)
[9] H. F. Döbele, Plasma Sources Sci. Technol., **4**, 224 (1995)
[10] R. Engeln, S. Mazouffre, P. Vankan, D.C. Schram, and N. Sadeghi, Plasma Sources Sci. Technol. **10**, 595 (2001)
[11] S. Mazouffre, M.G.H. Boogaarts, . J.A.M. van der Mullen, and D. C. Schram, Phys. Rev. Lett. **84**, 2622 (2000)
[12] M. Spaan, A. Goehlich, Schulz-von der Gathen, V. and H. F. Döbele, Appl. Opt., **33**, 3865 (1994)
[13] H. Abgrall, E. Roueff, F. Launay, J.-Y. Roncin and J.-L Subtil, Astron. Astrophys. Suppl. Ser., **101**, 273 (1993)

Ultrahigh Rate Etching of SiO_2 Film Employing Microwave Excited Non-equilibrium Atmospheric Pressure Plasma

K. Yamakawa[1], S. Den [2], T. Katagiri[2], M. Hori[1] and T. Goto[1]

[1] *Department of Quantum Engineering, Nagoya University, Nagoya, Japan*
[2] *Department of Engineering, Katagiri Engineering Co., LTD, Kawasaki, Japan*

Abstract

We have developed the non-equilibum microwave excited atmospheric pressure plasma source for the SiO_2 (BPSG) etching process. NF_3 and He mixture gases with bubbling H_2O were used as process gases. The etching rate of SiO_2 film was 14 μm/min while the etching rate of Si was a negligible small, that is the etching selectivity was estimated to be 200. The ultrahigh etch rate of SiO_2 and high selectivity (SiO_2 / Si) was firstly realized by using the non-equilibum microwave excited atmospheric plasma.

1. Introduction

Recently, the application of non-equilibrium discharge plasma operating at the atmospheric pressure has been studied in various fields, such as the treatment of exhaust gases (the removal of NO_X and SO_X)[1-3], the surface treatment (hydrophilicity or hydrophobic surface)[4,5], the thin film modification and so on. Moreover, in fields of microelectromechanical systems (MEMS) and bio-nanotechnology, the deep etching over 10 μm of SiO_2 is required and so the high-speed etching of SiO_2 is strongly demanded to minimize the process time.

The atmospheric pressure plasma produces considerably the high-density active species such as radicals and ions. Therefore, the atmospheric pressure plasma will be one of the most promising candidates for obtain the material process at the high speed. A number of methods for producing stable non-equilibrium plasma at the atmospheric pressure have been proposed [6,7]. Particularly, at the atmospheric pressure using microwave excited discharge, the generation of non-equilibrium plasma of high electron densities above 10^{15} cm^{-3} has been reported [8].

In this study, we have developed the microwave excited non-equilibrium atmospheric pressure plasma source employing the He and NF_3 mixture gases for the material process, and applied it to the high speed etching of SiO_2 film (BPSG).

The etch rate of SiO_2 (BPSG) has been investigated by changing the ratio of NF_3 and He flow rate, the distance between the electrode and the substrate, and the substrate temperature. The SiO_2/Si selectivity was investigated. The plasma diagnostics has been performed by optical emission spectroscopy (OES) and Fourier transform infrared spectroscopy (FT-IR).

2. Experimental

Figure 1 shows the etching equipment employing the microwave excited non-equilibum atmospheric pressure plasma. The 2.45 GHz cw microwave was introduced into the knife-edge of electrodes through the quartz window. A stable glow discharge was sustained between two knife-edge electrodes facing each other across a 200 μm micro-gap in the atmospheric pressure because the electric field was concentrated on the tip of two knife-edges. The width of electrodes was 60 mm. The discharge width was about 30 to 50mm under the present conditions. At the high pressure and high electron densities, the plasmas tend to be in the thermal equilibrium because of frequent collisions between electrons and gas molecules. However, if the size of the plasma is sufficiently small, the rate of heat flow from gas molecules to the wall should be fast enough to keep the gas temperature low. Since the discharge region was 200 μm in this study, the gas temperature was much smaller than the electron temperature even at the atmospheric pressure, and so the non-equilibum plasma was realized.

The mixture gases of NF_3, He and H_2O were used. The H_2O was mixed in the He carrier gas. These gas mixtures were introduced into the chamber from the upper part of micro-gap, the active species such as radicals and ions produced by plasma were exposed to the substrate through the micro gap. The substrate was set from 3mm to 40mm at the downstream region from electrodes. The substrate temperature was controlled from –15 ºC to 20 ºC by the coolant water. The total pressure in the chamber was 760 Torr. The microwave power was 500 W.

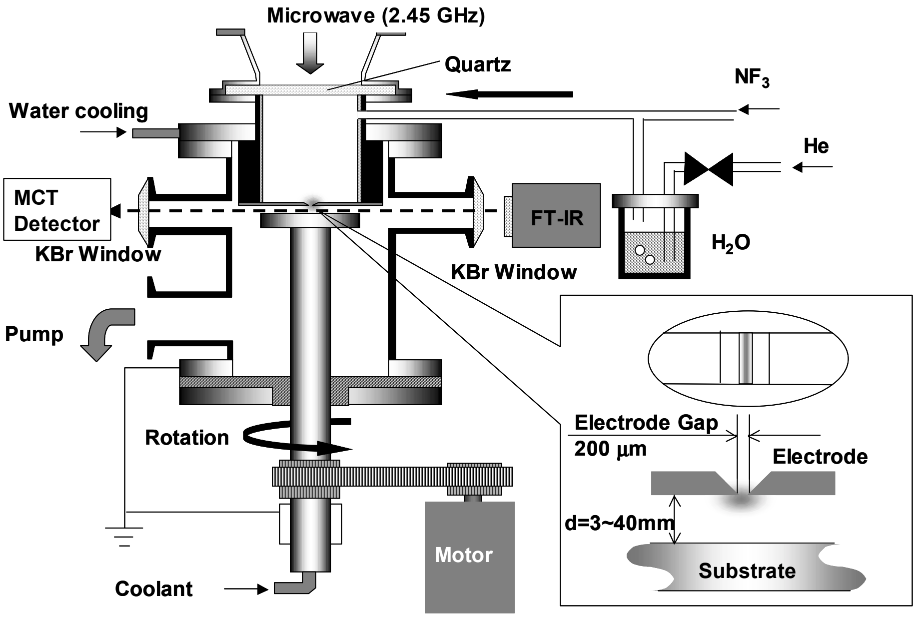

Fig. 1. Etching equipment using cw non-equilibrium microwave excited atmospheric plasma.

3. Results and Discussion

Figure 2(a) shows the photographs of He plasma region observed from the horizontal window at He flow rates of 8 L/min to 53 L/min. L is the length of plasma injected from electrodes. Figure 2(b) shows the length (L) of plasma as a function of He flow rate. L increased from 0.7 mm to 1.1 mm with increasing He injection flow rate since the charged species produced in the plasma diffused by the gas flow.

Figure 3 shows the etch rate of SiO_2 (BPSG) as a function of NF_3 flow rate. The H_2O was introduced into the chamber by the carrier gas of He (8 L/min, 16 L/min). The SiO_2 etch rate in a He flow rate of 16 L/min increased with increasing the NF_3 flow rate. Ultrahigh etch rate of about 14 μm/min was achieved at a NF_3

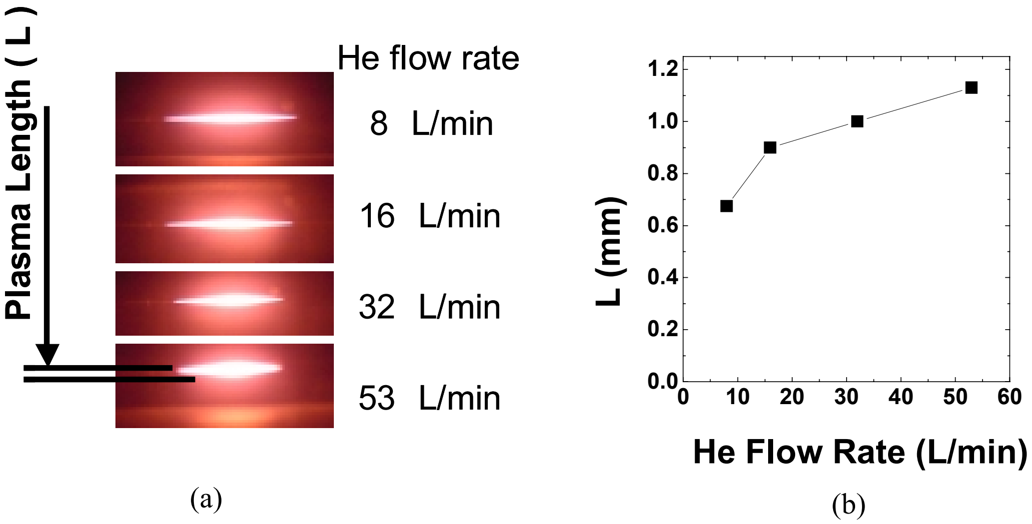

(a) (b)

Fig. 2. (a) The photographs of He plasma region seen from the horizontal window.
(b) The length (L) of injection plasma as a function of the He flow rate.

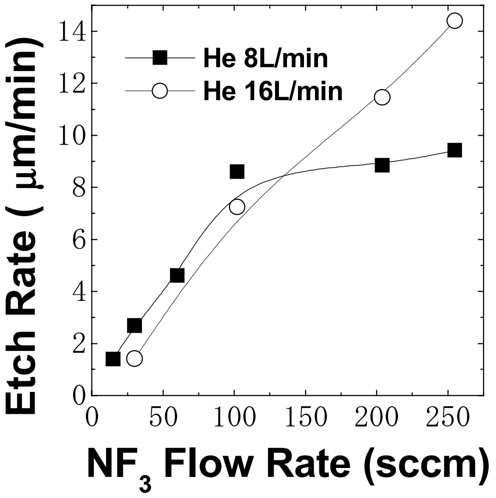

Fig. 3. Etch Rate of SiO_2 (BPSG) in He flow rate (8 L/min, 16 L/min) as a function of NF_3 flow rate. The microwave power was 500 W. The total pressure was 760 Torr. The distance between the electrode and the substrate was 5 mm.

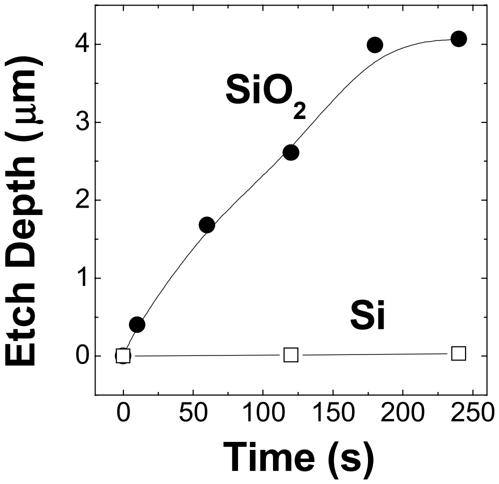

Fig. 4. The etch depth of SiO_2 (BPSG) and Si as a function of etch time. The NF_3 flow rate was 30 sccm. He flow rate with H_2O was 8 L/min. The microwave power was 500 W. The total pressure was 760 Torr. The distance between the electrode and the substrate was 5 mm.

flow rate 250 sccm. In general, the SiO_2 etch rate using the conventional low-pressure high-density plasma was about 1 µm/min. Therefore, the ultrahigh etch rate of SiO_2 was firstly realized by using the non-equilibum microwave excited atmospheric pressure plasma. On the other hand, in the He flow rate of 8 L/min, the SiO_2 etch rate was saturated at a NF_3 flow rate of 100 sccm. The amount of H_2O introduced into the reactor is dependent of the flow rate of He carrier gas. The amount of H_2O addition in the He flow rate of 8 L/min was smaller than that of 16 L/min. It was found that the amount of NF_3 and H_2O contributed to the SiO_2 etching.

Figure 4 shows the etch depth of SiO_2 and Si as a function of etch time. The SiO_2 etch rate was about 1.7 µm/min. On the other hand, the etch depth of Si was negligibly small on the same conditions. The Si etch rate was estimated about 0.008 µm/min. It was found that the SiO_2/Si selectivity was more than 200.

Figure 5 shows the etch rate of SiO_2 (BPSG) as a function of distance between the electrode and the substrate. The etch rate of SiO_2 increased drastically with decreasing the distance.

The plasma diagnostics have been performed by optical emission spectroscopy (OES) and Fourier transform infrared spectroscopy (FT-IR).

Figure 6 shows the intensity of optical emission for NF_3, He and H_2O mixture gas plasma. The measured wavelength was 300nm to 800nm. The NF_3 gas was dissociated into N and F, and the N_2 molecule will be produced by the recombination of N atoms. The H_2O was dissociated into H and OH, and furthermore, the OH was dissociated into H and O.

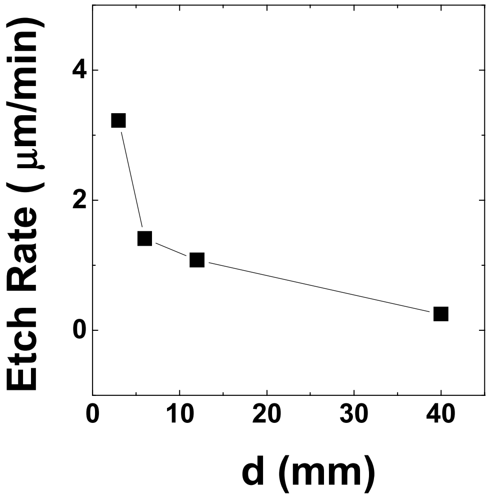

Fig. 5. Etch Rate of SiO_2 (BPSG) as a function of distance (d) between electrode and sample. The NF_3 flow rate was 30 sccm. He flow rate with H_2O was 16 L/min. The microwave power was 500 W. The total pressure was 760 Torr.

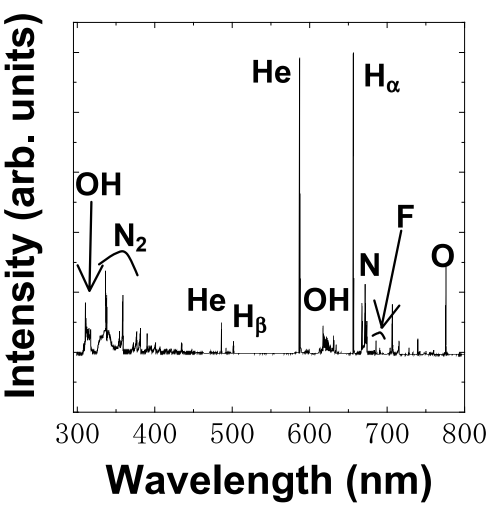

Fig. 6. Optical emission spectrum for NF_3, He and H_2O plasma. The He flow rate with H_2O was 8L/min. The NF_3 flow rate was 60 sccm. The microwave power was 500 W.

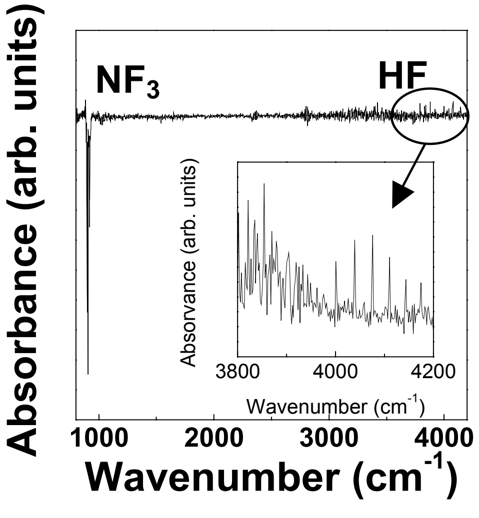

Fig. 7. FT-IR spectra of process gases (NF_3, He, H_2O) in the plasma discharge at the atmospheric pressure.

The emission intensity of OH and H increased with increasing the He flow rate. This result indicated that the amount of additional H_2O was controlled by He flow rate.

Figure 7 shows FT-IR spectra of NF_3 and He with H_2O plasma discharge. This absorption spectrum was obtained by subtracting the background spectrum without discharge from the spectrum with discharge. The downward peak at the asymmetric stretching vibration of NF_3 (~907cm^{-1}) [9] indicated that NF_3 molecules were decreased by the plasma discharge. The degree of NF_3 gas dissociation was estimated about 20 %. The upward peaks H-F bonds were distributed in the range from 3800 to 4200 cm^{-1} [10], indicating the formation of HF by the plasma discharge of NF_3, He and H_2O gases. The HF molecules were produced by a chemical reaction of NF_3 and H_2O from OES and FT-IR measurements.

The peak intensity of HF absorption was investigated as a function of NF_3 flow rate. The peak intensity of HF absorption increased with increasing NF_3 flow rate. This behavior was almost the same as the SiO_2 etch rate as a function of NF_3 flow rate as shown in Fig.3. It was found that the amount of HF molecules generated by plasma have played an important role for etching of SiO_2.

Figure 8 shows the etch rate of SiO_2 (BPSG) as a function of substrate temperature. The SiO_2 etch rate increased generally with increasing substrate temperature. It is considered that the HF_2^- will be enhanced by increasing the temperature of the substrate.

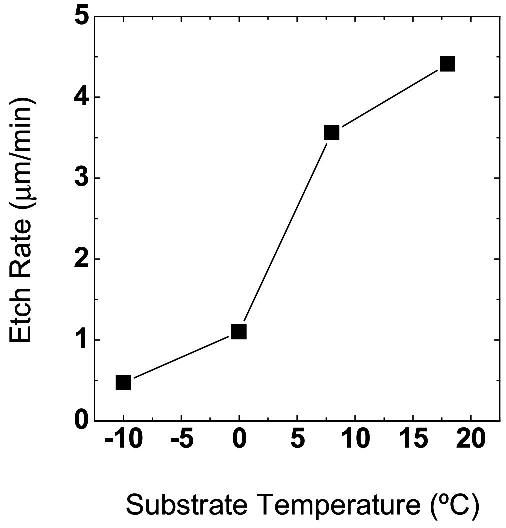

Fig. 8. The etch rate of SiO_2 (BPSG) as a function of substrate temperature. The NF_3 flow rate was 60sccm. The He flow rate was 8 L/min with H_2O. The microwave power was 500 W. The total pressure was 760 Torr. The distance between the electrode and the substrate was 5 mm.

4. Summary

We have developed the non-equilibum microwave excited atmospheric pressure plasma source for the material process, and performed ultrahigh-speed (14 μm/min) etching of SiO_2 (BPSG) by addition of H_2O. Moreover, it was found that the Si etch rate was negligibly small, and the SiO_2/Si selectivity was more than 200.

The HF molecules were found to be produced by a chemical reaction of NF_3 and H_2O from OES and FT-IR measurements. Moreover, it was found that the HF molecules produced by plasma played an important role for etching of SiO_2.

The non-equilibum microwave excited atmospheric plasma enables the ultrahigh speed etching of materials.

Reference

[1] B. M. Penetrant, J. N. Bardslry and M.C. Hsiao: Jpn. J. Appl. Phys. **36** (1997) 5007.
[2] J. S Chang: Oyo Butsuri 69 (2000) **268** [in Japanese].
[3] M.Higashi, S. Uchida, N. Suzuki and K. Fujii: IEEE Trans. Plasma Sci. **20** (1992) 1.
[4] A. Iwata and S. Moriyama: Japan Patent 2935772 (1999).
[5] N. Takashita and T. Hara: Japan Patent 2935774 (1999).
[6] S.Okazaki, M. Kogoma, M. Uehara and Y. Kimura: J. Phys. D **26** (1993) 889.
[7] K. H. Schoenbach, A. El-Habachi, W. Shi and M. Ciocca: Plasma Sources Sci. Technol. 6 (1997) 1156.
[8] A. Kono, T. Sugiyama, T. Goto, H. Furuhashi and Y. Uchida: Jpn. J. Appl. Phys. **40,** (2001) 238.
[9] H. Ogawa, T. Arai, M. Yanagisawa, T. Ichiki and Y. Horiike: Jpn. J. Appl. Phys. **41** (2002) 5349.
[10] M. Saito, Y. Kataoka, T. Homma and T. Nagatomo: J Electrochem. Soc. **147** (2000) 46

Particle-in-Cell Simulation of Ion Thruster with Multiple Plasma Channels Extracted from High-Density Helicon Plasma Source

H. Yamamoto, Y. Setsuhara, K. Takahashi, K. Ono

Department of Aeronautics and Astronautics, Graduate School of Engineering, Kyoto University,
Yoshida-Honmachi, Sakyo-ku, Kyoto 606-8501, Japan

Abstract

An ion thruster with multiple plasma channels, through which ions are extracted from high-density helicon plasma source, was modeled using two-dimensional particle-in-cell simulation. In this simulation, a single plasma channel was treated in the axial symmetry and the plasmas were assumed to be collisionless. Both electrons and ions were dealt with as macro particles. The potential distribution and ion trajectories in the channel are presented. The present model exhibits that the thrust density as high as 6 N/m^2 can be achieved.

1. Introduction

Development of high-performance and high specific-impulse ion thrusters has been desired as a propulsion system for future deep space exploration and/or efficient orbital adjustments of artificial satellites, in which exhaust capability with high ion current is required. As a candidate of such an ion thruster, there have been a number of experimental and numerical studies on the development of a cross-field stationary plasma thruster (SPT), also known as Hall thruster [1-5]. SPT have a coaxial acceleration plasma channel configuration in which radial magnetic fields and axial electric fields are applied and 1-2 kW-class SPT can obtain the thrust of 50-100 mN and the thrust efficiency of 40-50 % at the specific-impulse of 1000-2000 sec.

However, the exhaust ion current in SPT is uncontrollable independently from the ion acceleration voltage, since the plasma production is characterized by E x B configuration driven by anode voltage, which roughly determines the ion acceleration voltage. In the typical situation, the acceleration voltage is in the order of 200-300 V, and the radial magnetic field reaches a peak of 200 G at the exhaust, which decreases toward the anode.

In this paper we propose a novel high-performance ion thruster regime using helicon wave-excited high-density plasma source, in which the plasma channel in a SPT is replaced by the multiple plasma channels filled with high-density plasma flow extracted from the positively biased helicon source. Helicon wave-excited plasmas are characterized as a source for obtaining extremely high-density plasmas (10^{12}-10^{13} cm^{-3}) and high ionization ratio ($\lesssim$ 10 %), which are suitable for development of high ion current and efficient propulsion system.

2. Thruster design

In our design of the ion thruster, the ions are generated in the high-density helicon wave-excited plasma source. The helicon wave-excited plasmas are produced using a helical antenna (3-turn) with an azimuthal mode number of m=0. The helical antenna is coupled to an RF power generator at 13.56 MHz via a matching box. The discharge chamber is surrounded with magnetic coils to apply the static magnetic field (~ 1000 G) for excitation of helicon wave. Typical plasma densities of the helicon wave-excited plasmas are plotted in Fig. 1, which shows that high-density plasmas of 10^{12}-10^{13} cm^{-3} are produced at RF powers as low as 200 W at the pressure of several mTorrs. The schematic diagram of our thruster is presented in Fig. 2.

From the helicon plasma source, ions are extracted through the multiple plasma channels, which are formed by a dielectric disk with multiple holes, by an acceleration electric field established between the positively biased helicon source (plasma anode) and the ground. The dielectric disk is located at the axial boundary of the helicon plasma source and the plasma

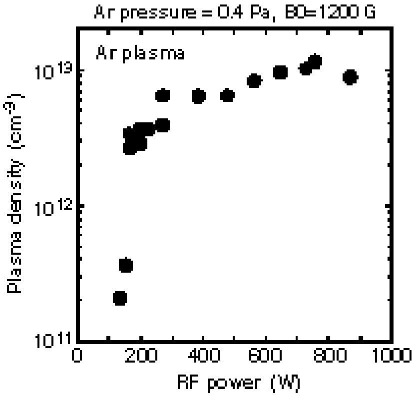

Fig. 1. Variation of argon plasma density as a function of input RF power

channels are formed by the high-density plasma flow through the multiple holes drilled in the disk. An electron source is also installed as in the SPT configuration and electrons are released there as needs arise. It plays a role as a neutralizer in order to prevent a spacecraft from being negatively charged. Our thruster is the simple design compared with conventional ion thrusters with multiple grids.

3. Simulation

3.1. Overview

In this paper, the ion trajectories and potential distribution are calculated in the plasma channel using the electrostatic axis-symmetric collisionless particle-in-cell (PIC) simulation. In the simulation a single plasma channel is considered in order to save calculation time. The parameters of the helicon source were taken from the experimental results, which gives the boundary condition of the plasma channel facing to the source. In the PIC simulation, a group of particles is represented by a single macro particle [6]. Both ions and electrons are dealt with as macro particles. The particle motions are assumed to be two-dimensional for space and three-dimensional for velocity. Influence of neutrals and multiply charged ions is not taken into account in this model. The calculated conditions of the thruster are summarized in Table 1.

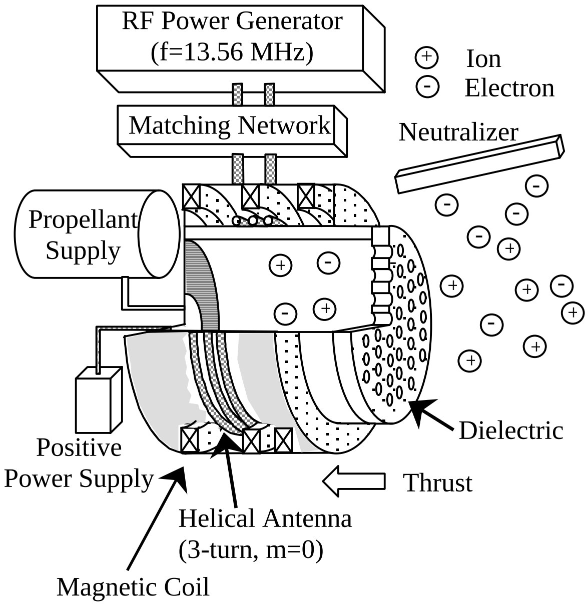

Fig. 2. Schematic diagram of the proposed ion thruster.

Table 1. Calculated conditions of the thruster.

Species	Argon
Plasma density (cm^{-3})	1×10^{13}
Electron temperature (eV)	3
Acceleration voltage (V)	2000
Plasma channel length (mm)	2
Plasma channel radius (mm)	1

3.2. Time step

For the stability of the PIC simulation, a time step is required to be adjusted on the order of the reciprocal of a plasma frequency. In this case, approximately 10^{-9} sec for ions and 10^{-11} sec for electrons are required. In addition, the charged particles influenced by fields are not allowed to move beyond a cell within a time step. In the simulation, a time step is set at 10^{-11} sec for ions and 10^{-12} sec for the electrons in order to describe particle motions with accuracy.

3.3. Grid

In this code the R-Z coordinates with non-equidistant grids are used to obtain the information with respect to local ion, electron and charge densities, electric potential and field. The volumes of cells near the central axis are increased in order to mitigate the instability around the symmetry axis which results from the shortage of the particles in the cells. In the area farther than plasma channel radius, the equidistant radial grid spacing is applied. On the other hand, in the axial direction, equidistant grid spacing is employed throughout the simulation space for simplicity.

3.4. Grid weighting

Both ions and electrons are mapped to the grid points with shape factors at every time step to conserve the charge density [7]. In the axial direction, linear PIC shape factors are used for particle-to-grid weighting of these macro particles. In the radial direction, the cell boundaries are adjusted so that the correct densities are obtained for the given shape factors. Particle-to-grid weighting is accomplished by area-weighting in the PIC scheme with the shape factors as

$$S_n(r) = \begin{cases} \dfrac{r^2 - r_{n-1}^2}{r_n^2 - r_{n-1}^2}, & r_{n-1} \le r \le r_n, \\ \dfrac{r_{n+1}^2 - r^2}{r_{n+1}^2 - r_n^2}, & r_n \le r \le r_{n+1}, \\ 0, & \text{otherwise,} \end{cases} \tag{1}$$

where S_n is the shape factor at the n-th radial grid point r_n and r is the radial position. These shape factors are also used in order to weight the electric fields to the charged particles.

3.5. Governing equations

In the simulation space, an electrostatic potential is governed by the Poisson's equation:

$$\nabla^2 V = -\frac{\rho}{\varepsilon}, \tag{2}$$

where V is an electrostatic potential, ε is the permittivity and ρ is the charge density derived from the ion density n_i and the electron density n_e. An electric field is derived from the electric potential with

$$\mathbf{E} = -\nabla V, \tag{3}$$

where $\mathbf{E}$ is a local electric field.

The behaviors of ions and electrons influenced by an electric field are governed by

$$\frac{d\mathbf{v}}{dt} = \frac{q}{m}\mathbf{E}, \tag{4}$$

$$\frac{d\mathbf{x}}{dt} = \mathbf{v}, \tag{5}$$

where $\mathbf{v}$ is the particle velocity, q is the particle charge, m is the particle mass, and $\mathbf{x}$ is the particle position. The equations of motions for particles are solved in combination with the Poisson's equation in order to trace the particle trajectory and to obtain the potential distribution in the plasma channel.

3.6. Boundary conditions

The ions are injected from the source plasma with a half Maxwellian velocity distribution characterized by a temperature of 0.1 eV. The electrons are injected from the source plasma and the neutralizer with a half Maxwellian velocity distribution based on a temperature of 3 eV. Number of ions and electrons injected from source plasma is determined by the experimental measurements of plasma densities. The electrons provided by a electron source are assumed to be enough to neutralize the space charge. Ions and electrons are deleted when reaching the axial boundaries of the plasma channel facing both to source plasma and neutralizer. Charged particles are also deleted when arriving at the surface of the dielectric disk although their charge is left on the insulating surface, which give the boundary conditions when solving the Poisson's equation. Any particles coming at the radial boundary except the dielectric disk are reflected and placed backed into the simulation space. This gives the periodic boundary condition, where similar plasma channels exist around the considered channel and calculation results include their influence. At the axial boundary facing to the source plasma, the electric potential is set at 2000 V and the axial electric field is zero at the boundary facing to the neutralizer.

3.7. Calculation procedures

The basic calculation procedures are presented in Fig. 3. First, the particles are laid out in the simulation space. The appropriate arrangement of the particles at the initial conditions is useful to decrease the calculation time to obtain steady state quantities. Second, ion and electron density calculations are conducted at each grid point. The densities are estimated on the basis of particle positions with the shape factors mentioned above. Third, the electrostatic potentials are calculated at each grid point for solving an R-Z coordinate Poisson's equation with the above boundary conditions and the evaluated charge densities at the last step. The electric fields at each grid point are obtained from equation (3) using a finite difference method. Forth, equations (4) and (5) are used to determine particle positions and velocities influenced by the obtained electric field. The electric field at each particle position is interpolated from fields at the nearest four grid points using the shape factors again. The difference equations of equations (4) and (5) are formed with a

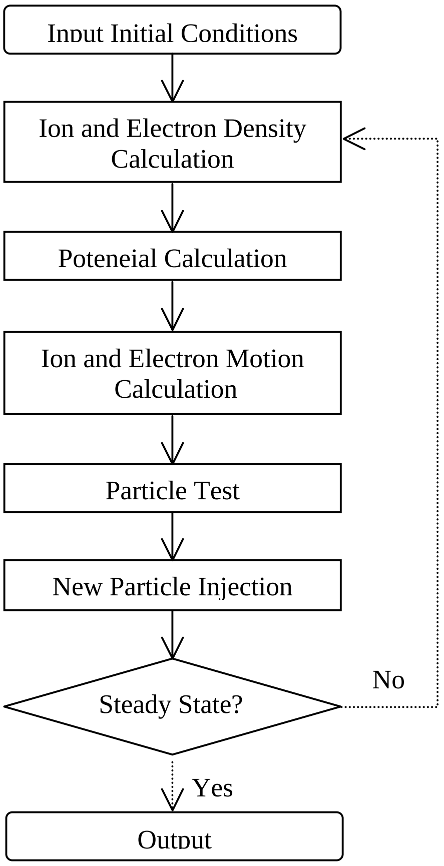

Fig. 3. Flow chart of the calculation procedures.

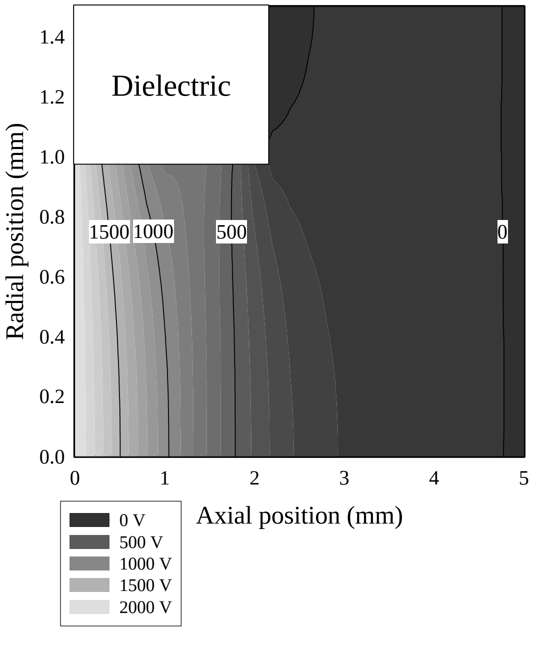

Fig. 4. Potential distribution in the plasma channel.

time-centered leapfrog finite difference method. Fifth, the particles are tested about whether they are inside or outside of the simulation space. The particles that get out of the simulation space are handled according to the boundary condition and are deleted or reflected on the boundary. Sixth, new particles required by the boundary conditions are injected from the source plasma and neutralizer. A source plasma density is assumed to be constant in this code. Then, we go back to the second step and the calculation is repeated until the steady state is reached. Particle number in the simulation space is about 500000 on a typical condition. This means 30 particles per cell on the average.

4. Results and discussion

The potential distribution in the plasma channel is presented in Fig. 4. The electric potential decreases in the axial direction. The potential map is determined by the boundary condition, namely the surface charge on the dielectric disk in this case. The potential in the plasma channel is compelled to drop by the negative charge on the insulating surface. The distribution of ion densities in the plasma channel is presented in Fig. 5. The density decreases rapidly near the source plasma along with the electric potential reduction. This is caused by the rapid potential drop as seen in Fig. 4. The distribution of electron densities is presented in Fig. 6. The electron density increases in the vicinity of the symmetry axis. The electrons are collected near the central axis by means of the relatively weak radial electric field.

Ion trajectories are shown in Fig. 7. Ions are injected from the plasma source and are accelerated in the axial direction. Some of ions are impinged on the dielectric disk in the plasma channel and does not contribute to the thrust. The ion impingement is critical to the lifetime of the propulsion system. Electron trajectories are shown in Fig. 8. Electrons are injected from the neutralizer and end up in the plasma source. Some electrons are repelled at the negatively charged dielectric disk in the downstream region, which greatly alters the trajectory.

In the simulation the potential distribution is affected by the excessive charge accumulation on the dielectric disk. It is unnatural that the electric potential goes down significantly in the vicinity of the dielectric surface. The typical sheath potential drop between a plasma and a dielectric wall is of the order of an electron temperature. Since the sheath potential is negligible compared to the acceleration voltage, we modify the model on the assumption that the electric field normal to the boundary is zero on the dielectric surface. The particles touching the dielectric disk are deleted and the charge is neutralized. The potential distribution in this situation is shown in Fig. 9, in which the acceleration voltage is set at 1000 V. The electric potential is comparably flat in the plasma channel and drops in the downstream region,

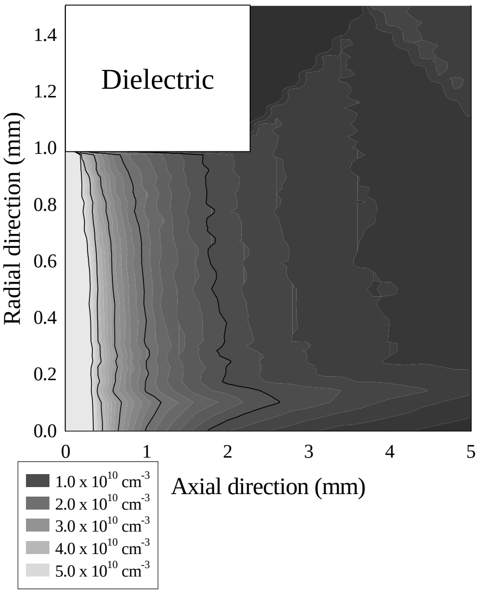

Fig. 5. Spatial distribution of the ion density in the plasma channel.

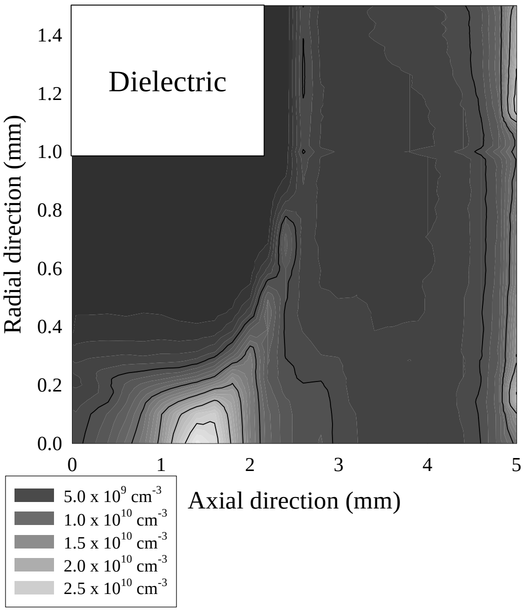

Fig. 6. Spatial distribution of the electron density in the plasma channel.

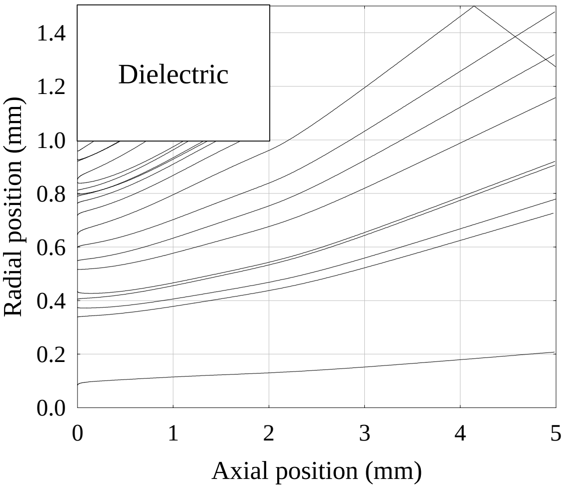

Fig. 7. Ion trajectories from source plasmas.

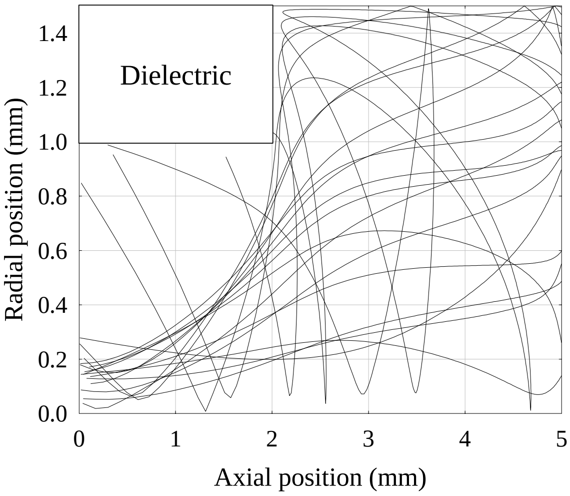

Fig. 8. Electron trajectories from neutralizer.

which is caused by the electron released from the neutralizer. The electrons from neutralizer reduce the electric potential roughly at the ground potential due to the negative charge although the potential is somewhat unstable at the exhaust. The ion exhaust current is limited both by source plasma densities and the space charge limited current. Electrons from neutralizer increase the electron densities at the exhaust, which cancels the ion space charge. In this configuration the high ion current is extracted compared to the space charge limited current.

The thrust density reaches 6 N/m^2 at the acceleration voltage of 2000 V. The corresponding ion current density is 140 A/m^2. The average ion velocity at the exhaust is approximately 10^5 m/s. Specific impulse is also derived from

$$I_{sp} = \frac{U_s}{g}, \tag{6}$$

where I_{sp} is the specific-impulse, U_s is the exhaust velocity and g is the gravitational constant. In this simulation, the specific impulse is approximately 10000 sec.

5. Summary

We proposed a novel ion thruster regime with multiple plasma channels using helicon wave-excited plasma source. A two-dimensional PIC simulation of the designed ion thruster based on the axis-symmetric collisionless model has been developed. The results of the simulation showed the capability of providing the high ion current in the downstream region. Ion impingement on the dielectric disk is still observed in this simulation, which is crucial to the engine lifetime. On the condition that reasonable amount of electrons is provided by the electron source at the exhaust, the space charge is cancelled successfully and the high ion current is extracted. The boundary conditions greatly influence the potential distribution and ion trajectories in the plasma channel and in the downstream region.

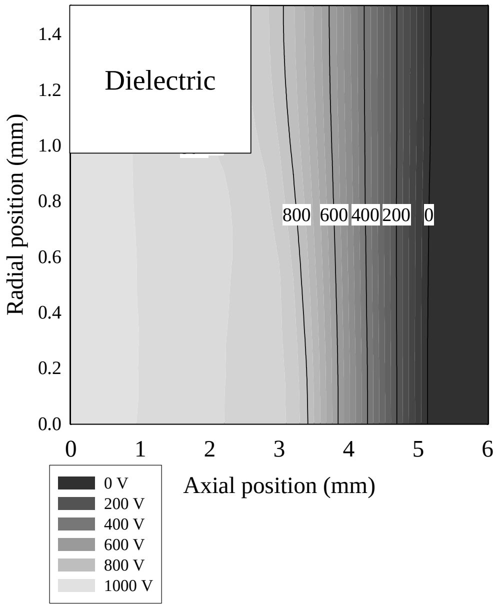

Fig. 9. Potential distribution in the plasma channel on the assumption that the electric field normal to the boundary is zero on the dielectric surface.

References

[1] K. Komurasaki, Y. Arakawa - Acta Astronautica, **38**, 185 (1996)

[2] J. P. Boeuf, L. Garrigues - J. Appl. Phys, **84**, 3541 (1998)

[3] V. Kim,G. Popov, V. Tikhonov, V. Garkusha, V, Murashko - *26th Int. Electric Propulsion Conf.* IEPC-99-004 (1999)

[4] D. Goto, H. Tahara - *26th Int. Electric Propulsion Conf.* IEPC-99-121 (1999)

[5] M. Keider, I. D. Boyd, I. I. Beilis - Phys. Plasmas, **8**, 5315 (2001)

[6] C. K. Birdsall, A. B. Langton - *Plasma Physics via Computer Simulation* (Adam Hilger, Bristol, 1991)

[7] W. M. Ruyten - J. Comput. Phys, **105**, 224 (1993)

Synthesis of Carbon Nanostructure Using Microwave Excited Non-Equilibrium Atmospheric Pressure Plasma Enhanced Chemical Vapor Deposition

A. Matsushita[1], K. Yamakawa[1], M. Hiramatsu[2], M. Hori[1] and T. Goto[1]

[1]*Department of Quantum Engineering, Nagoya University, Chikusa-ku, Nagoya, Japan*
[2]*Nano Factory, Graduate School of Science and Technology, Meijo University, Tenpaku-ku Nagoya, Japan*

Abstract

The microwave excited non-equilibrium atmospheric pressure plasma was applied to chemical vapor deposition and multi-walled carbon nanotubes were synthesized by the atmospheric pressure CVD for the first time employing mixture gases of $He/H_2/CH_4$. This system enabled to synthesize nanotubes at a very short period of 1 min. It was found that the high H_2 dilution ratio to CH_4 gas facilitated the synthesis of CNTs through surface reaction. The field emission properties for the CNTs films were observed. This CVD system has a great potential for the mass fabrication of nanotubes.

1. Introduction

Carbon nanostructures, such as fullerene, nanocrystalline diamond, carbon nanofiber, carbon nanohorns and carbon nanotubes (CNTs) have attracted great attention for several applications, e.g. nanoscale electronic devices (field effect transistor, memory and so on), storage materials for hydrogen gas, scanning probe microscopy, and so on, since they have the outstanding physical, chemical and mechanical properties. Especially, the excellent field emission property of CNTs [2] is focused on the electron emitter for a field emission display (FED)[3].

Since the first report of CNTs by Iijima in 1991[1], CNTs have been synthesized in many methods, such as arc discharge, laser ablation, pyrolysis and several kinds of chemical vapor deposition (CVD) [4]-[6]. Among a variety of synthesizing methods for CNTs, the plasma enhanced CVD [7] is becoming one of the most important methods, because this method has the potentiality of synthesis of CNTs at the low temperature and the large amounts compared with other methods. Therefore, PECVD is one of the promising synthetic techniques in a view of the industrial applications.

In this study, the atmospheric pressure plasma was developed as a plasma source for PECVD system. Recently, atmospheric pressure plasmas have been used in several processes. However, most of them are arc discharge or plasma jet, and their application to material processing with controlling gas chemistry is limited strongly due to the high gas temperature in these plasmas. On the other hands, the high-density non-equilibrium plasma at the atmospheric pressure using continuous-wave (cw) microwave-excited discharge was developed [8]. In this plasma, the electron density is considerably high, that is, on the order of 10^{15}cm^{-3} and the electron temperature is low (about 1 eV). Using this source, a number of radicals and ions can be produced, which enable us to synthesize new materials at a low temperature with a high speed. Accordingly, this type of atmospheric pressure plasma may be applied in a wide range of fields.

In this paper, the cw non-equilibrium microwave-excited atmospheric pressure plasma source was developed for the synthesis of CNTs for the first time. CNTs were synthesized with a high speed at a low temperature. The structures of grown CNTs were investigated in detail. Furthermore, the gas phase reaction during CNTs grown was investigated using laser light scattering methods.

2. Experiment

Figure 1 shows the schematic diagram of non-equilibrium microwave excited atmospheric pressure plasma CVD system used in this study. Prior to growth run, a deposition chamber made of stainless steel was evacuated to 10^{-6} Torr using a turbomolecular pump and a rotary pump. The cw microwave (2.45 GHz) was introduced from the top of deposition camber to the micro-gap electrode. The slit separation of the micro-gap electrode was 0.2 mm. The gas mixtures (He/H_2/CH_4) were introduced from the upper part of microwave cavity and pumped out from the lower part of chamber, so that the inside of the chamber was maintained at atmospheric pressure. Using this system, a stable slit plasma was successfully generated at the atmospheric pressure.

CNTs were synthesized at a microwave power of 300 W, a total pressure of 1 atm, a substrate temperature of 600 ˚C, and gas flow rates of He/H_2/CH_4 = 5000/x/50-x (x=0-48) sccm. Growth experiments were conducted for 1-10 min.

Prior to growth, the patterned Ni catalyst layer of 10 nm in thickness were formed on the SiO_2 substrate using an electron-beam evaporation through the mesh (200 mesh) as mask.

Synthesized CNTs were evaluated using scanning transmission electron microscopy (STEM), transmission electron microscopy (TEM), scanning electron microscopy (SEM), and Raman spectroscopy. The sample of TEM observation was made using microgrid mesh. A microgrid mesh was used for the TEM observation. Synthesized CNTs were scraped from the substrate and ultrasonicated in methanol, and this solution was dropped on the microgrid mesh and dried for 24 hours. Laser light scattering (LLS) method was used in order to observe the formation of various particles in the gas phase. The field emission properties of CNTs were measured using the spherical stainless steel anode of 3 mm diameter in a vacuum. The anode (spherical)-cathode (CNTs substrate) distance was kept at 80 μm.

3. Results and discussion

CNTs were successfully synthesized using this system at a very short period of 1 min. The deposition period required for CNT growth was much shorter than that using conventional CVD methods. Averaged length of grown CNTs increased with the increase of growth period in the range investigated.

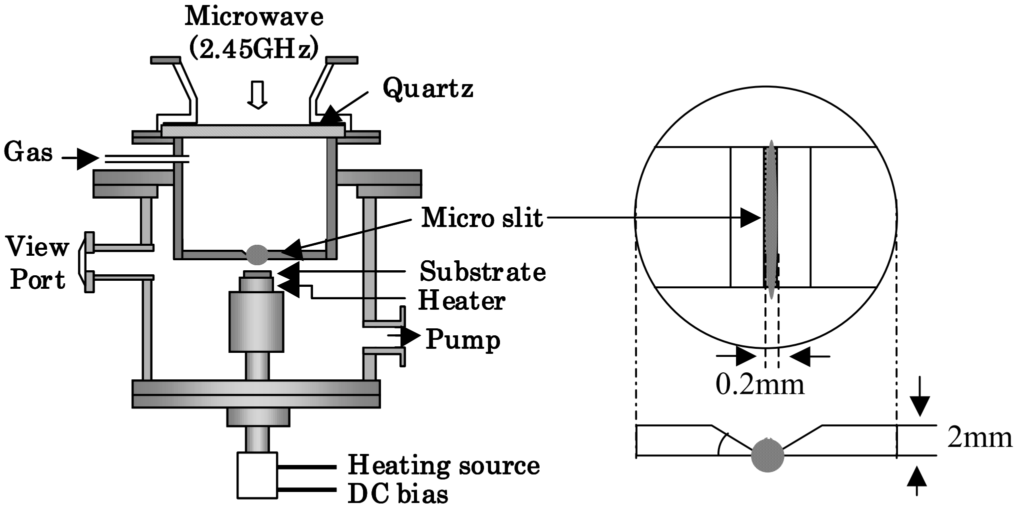

Fig. 1. Schematic of atmospheric pressure plasma CVD system.

Figure 2 shows typical STEM and TEM images of CNTs grown at He/H_2/CH_4=5000/45/5 [sccm] for 5 min. The diameters of the grown CNTs were approximately 30 nm. As shown in Fig. 2, TEM images reveal the multiwall nature of the CNTs Here, we observe an about 10nm inner diameter, a clear inner channel [Fig. 2(a)], and approximately 30 concentric walls [Fig. 2(b)].

Figures 3(a)-3(c) shows SEM images of carbon nanostructures grown at He/H_2/CH_4=5000/45/5, 5000/25/25 and 5000/0/50 [sccm], respectively, for 2 min. The surface morphologies of the carbon nanostructure were drastically changed with the hydrogen flow rate. At the typical growth condition for CNTs using the present system, as shown in Fig. 3(a), a large amount of CNTs with average diameters of about 20 nm, which had the spaghetti-like structure, were synthesized on the Ni surface (not on the synthesized SiO_2 surface). As shown in Fig. 3(b), on the other hand, CNTs were not formed in the case of low flow rate of hydrogen. Without hydrogen, polymer-like particles were formed as showed in Fig. 3(c). These particles piled upon the whole substrate regardless of Ni and SiO_2.

Figure 4 shows the Raman spectra obtained from three samples corresponded to Figs. 3(a), (b), and (c). The spectrum (a) clearly shows a strong peak at 1596 cm^{-1} (G band), indicating the formation of graphitized structure, and the G peak is stronger than the D peak (1334 cm^{-1}, caused by amorphous carbon or the lattice defect of graphite), which is similar to the typical Raman spectrum of CNTs [9]. On the other hand, for the Raman spectra (b) and (c), the G peak is nearly equal to the D peak, indicating the deposits of Figs. 3(b) and (c) were not graphitized, but almost amorphous or DLC.

. In order to investigate the formation mechanism of CNTs, the laser light scattering (λ=633 nm) was performed during deposition of CNTs. Figure 5 shows the scattered intensity as a function of $H_2/(H_2+CH_4)$ flow rate ratio. Scattering intensity was strong in the low H_2 flow rate ratio, and decreased rapidly with increase of H_2 flow rate ratio and became constant at the H_2 flow rate ratios more than 20 %. The results indicate that the low H_2 flow rate result in the polymerization reaction in the gas phase. Therefore, the

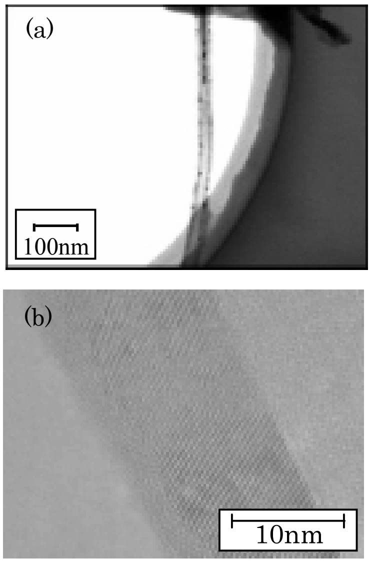

Fig. 2. (a) STEM images of CNTs fabricated by atmospheric plasma. (b)TEM image, magnified figure of side-wall

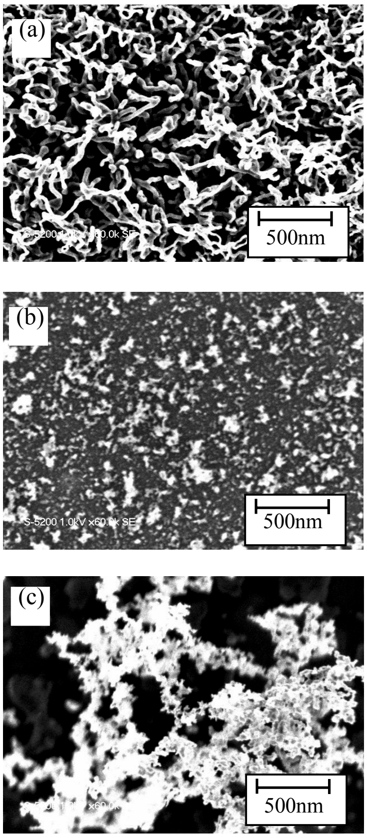

Fig. 3. SEM images of CNTs fabricated by atmospheric plasma on the condition of He/ H_2/CH_4 = (a) 5000/45/5, (b) 5000/25/25 and (c) 5000/0/50 [sccm].

deposits in Fig. 3(c) were not grown on the substrate surface but produced in the gas phase. It is suggested that H radicals play an important role in the reduction of polymerization in gas phase.

The field emission property of CNTs was investigated. Figure 6 shows the characteristic curve of the electron emission current density as a function of the field strength for the CNTs films shown in Fig. 3(a). The threshold electric field was 14 V/μm. Here, the field strength for the sample is calculated by using the applied voltage divided by the cathode (sample) to anode spacing. Corresponding Fowler-Nordheim plot (i.e. J/E^2 vs. E^{-1}) was shown in the inset of Fig. 8. This plot is well fitted by the straight line, indicating that the field emission property can be explained by a tunneling mechanism. The threshold field of 14V/μm was not good, but it will be possible to obtain a lower threshold electric field by controlling the size of Ni catalytic islands prior to the growth and aligned growth of CNTs.

4.Conculsions

Non-equilibrium atmospheric pressure $He/H_2/CH_4$ plasma was applied for the first time to the synthesis of CNTs. This system enabled us to grow CNTs at the short period of 1 min. Furthermore, it was found that the H_2/CH_4 flow rate ratio had a great influence on the growth of CNTs on the catalytic surface and reduction of polymerization reaction in the gas phase. From the laser light scattering measurement, it was indicated thet the high H_2 dilution was effective for the suppression of polymerization of carbon in gas phase, resulted in the contribution of CNT growth on the catalyst surface. The synthesized CNTs showed the field emission properties. This result indicates that the atmospheric pressure CVD system will be a promising tool to synthesize CNTs.

References

[1] S. Iijima, Nature (London) **354**, 56 (1991).

[2] Y. Chen, S. Patel, Y. Ye, D.T. Shaw, and L. Guo, Appl. Phys. Lett. **73**, 2119 (1998).

[3] W.B. Choi, D.S. Chung, J.H. Kang, H.Y.Kim, Y.W. Jin, I.T. Han, Y.H. Lee, J.E. Jung, N.S. Lee,G.S. Park, and J.M. Kim, Appl. Phys. Lett. **75**, 3129 (1999).

[4] S. Iijima and Ichihashi, Nature (London) **363**, 603 (1993).

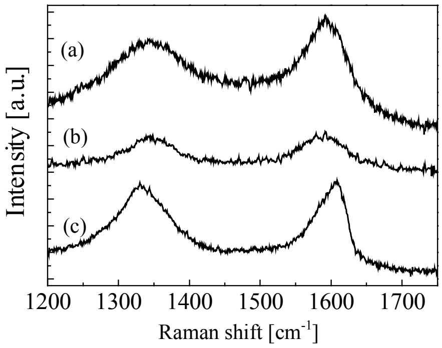

Fig. 4. Raman spectra obtained from three different H_2/CH_4 flow rate (a) 45/5 (b) 25/25 (c) 0/50 [sccm].

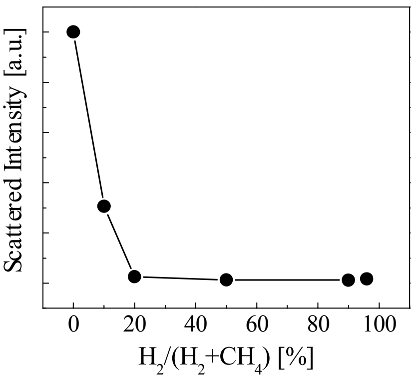

Fig. 5. Scattered intensity as a function of $H_2/(H_2+CH_4)$ flow ratio.

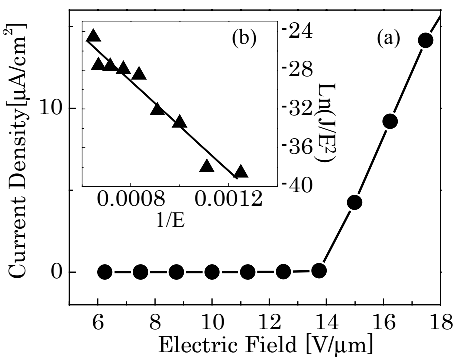

Fig. 6. (a) Field emission results from the synthesized CNT. (b) Fowler-Nordheim plot.

[5] T. Guo, P. Nikolaev, A. Thess, D.T. Colbert, R.E. Smalley , Chem. Phys. Lett. **243**, 49 (1995).
[6] H. Dai, A.G. Rinzler, P. Nikolaev, A. Thess, D.T. Colbert, R.E. Smalley , Chem. Phys. Lett. **260**, 471 (1996).
[7] Z.F.Ren, Z.P. Huang, J.W. Xu, J.H. Wang, P. Bush, M.P. Siegal and P.N. Provencio, Science **282** 1105 (1998)
[8] A.Kono, T. Sugiyama, T. Goto, H. Furuhashi, and Y. Uchida, Jpn. J. Appl. Phys. **40**, L238 (2001).
[9] F. Rohmund, R.-E. Morjan, G. Ledoux, F. Huisken, and R. Alexandrescu. J. Vac. Sci. Technol. B **20**, 802 (2002)

Synthesis of Fine Ag Particles Using Transferred-Arc Plasma

A.C. Doring[1], H. Toku[1], O.W. Bender[1], P.K. Kiyohara[2] , A.L. Silva[3], and A.C. da Cruz[1]

[1]*Institute for Technological Research – IPT - São Paulo, SP, Brazil*
[2]*Physics Institute of the University of São Paulo, SP, Brazil*
[3]*Independent Consultant for the research*

Abstract

Production of Ag fine powders was investigated using transferred-arc plasma. The experimental setup included evaporation and cooling chambers and a bag filter. Production rates of 500 g/h were attained with a rated power of 15 kW. The behavior of the fine Ag powder in the production of finely microstructured Ag/C compacts was studied. Results were compared with available commercial product that is used as electrical contacts.

1. Introduction

Commercially available silver (Ag) powder is classified as microcrystalline, spheroidal, or lamellar, according to its particle shape[1]. All three types, which differ in method of manufacture, have specific areas of use. The most important method of production of microcrystalline Ag powder is precipitation by reducing agents. These powders were used almost entirely in sintering technology for a long time. Today, they are also used in stoving preparations (e.g., metallization of ceramics) and in pastes used in the manufacture of heated rear windows of motor vehicles. Spheroidal Ag powder is produced by atomization of molten silver by compressed air, inert gas, a water jet, or a rapidly rotating knife. These powders are mainly used in sintering technology. Lamellar particles are obtained by ball milling microcrystalline silver powder. Flakes and bronzes are incorporated into paints and adhesives, where they impart electrical conductivity to the polymer matrix due to the good particle-to-particle electrical contact.

The present study has for main objective to produce Ag powder finer than the powders commercially available, intended for sintering of electrical contacts. Particularly, we look after the production of sintering compacts with a refined microstructure which is not possible to be achieved with the commercially available powder.

Based on the DC transferred-arc process previously presented, Ag fine powders were produced based on an evaporation/condensation process and further characterized. To evaluate the potentiality of these powders with respect to the production of sintered bodies for the above specified application, samples were prepared from a mixture of Ag/C.

2. Experimental

A schematic diagram of the experimental apparatus is shown in Fig. 1. The reactor mainly comprised an evaporation and a cooling chamber, according to the transferred-arc concept previously introduced[2]. Inside the first chamber (500 mm dia. x 400 mm high) Ag was evaporated from a molten bath (3 ~ 5 kg) contained in a graphite crucible that worked as the anode of a DC transferred-arc. Argon gas was used as plasma an Ag vapor carrier gas, and also as the cooling gas which was fed in the cooling chamber against the hot stream that issued from the evaporation chamber. Metal particles which formed in the cooling chamber were collected in a bag filter installed after a heat exchanger. The exhaustion line included also a vacuum pump used to keep constant pressure (close to 100 kPa) inside the evaporation chamber in spite of the head loss observed through the bag filter. The external walls of reactor were water cooled to guarantee dimensional stability.

Typical operating conditions are presented in Table I. Ar was fed in the arc chamber through the cathode assembly at 100 lpm flow rate, and as the cooling gas at 80 lpm at the exit of same chamber. In all experiments, steady state condition at a plasma chamber off gas temperature of 1500 K was achieved after 1 hr operation, approximately, with the DC transferred-arc plasma rated at 15 kW (60 V x 250 A). Using an optical pyrometer, bath temperatures of the order of 2400 K were measured right after shutting down the arc. At the given conditions, Ag powder was produced at a 500 g/h rate. Evaluation of quenching conditions in terms of the average after quenching temperature for each of the experiments considered are shown in Tab. II.

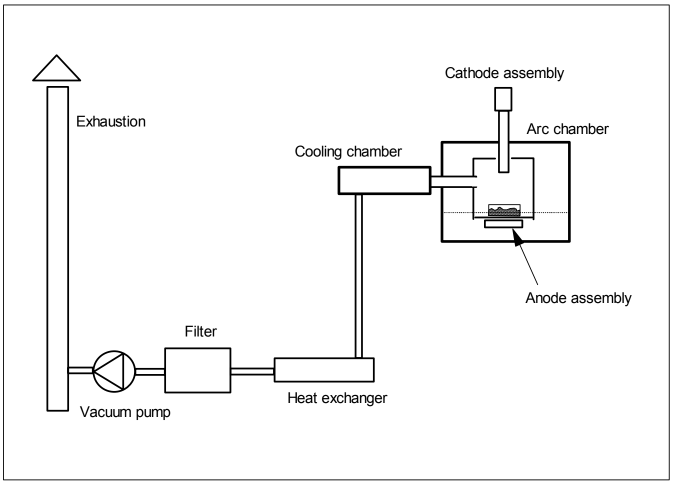

Fig. 1 – Schematic diagram of the plasma reactor for the vapor phase synthesis of Ag fine powder.

The Ag powders produced were characterized for particle size distribution using laser scattering analysis and particle size and morphology using scanning electron microscopy (SEM).

In order to evaluate the degree of homogeneity of the microstructure resulting from the preparation of sintered compacts having electrical-contact characteristics, 1 kg of powder was produced from which mixtures with both graphite powder (Fisher mean diameter of 0.001 mm) and carbon black (Degussa Printex G) in a 95%Ag / 5%C mass ratio were prepared. Typically, such compacts are prepared from the dry mixture of commercial Ag powder with graphite powder. Because this practice did not provide good results for the fine Ag powder we produced, its mixture with C was carried out using a suspension of the constituent powders in isopropyl alcohol. Compacts (15 mm dia. x 5 mm height) were prepared and sintered at 800 ^{o}C in H2/N2 atmosphere. Their microstructure was analyzed from simple polished (non chemically attacked) metallographic preparations observed in an optical microscope. For the sake of comparison, the same analysis was carried out with a commercial insert used as electrical contact.

Tab. I – Operating conditions applied in the plasma experiments for the preparation of fine Ag powders.

Starting material	Ag - 99,9% mín.
Ar flow rate (cathode assembly)	120 lpm[1]
Amount of Ag in the crucible	3,5 ~ 5,0 kg
Arc voltage	60 V
Arc current	250 A
Arc power	15 kW
Gas temperature at evaporation chamber outlet	1500 K
Cooling gas flow rate, exp. # 1 and #3 (Ar)	80 - 140 lpm
Cooling gas flow rate, exp. # 5 (N_2)	160 lpm

[1] Gas flow rates (lpm) referred to 298 K and 100 kPa.

Results and discussion

Fig. 2 shows the particle size distribution (PSD) of powders produced in different synthesis experiments. The transition which is observed between PSDs with many peaks (exps. #1 and #3) and the practically log-normal PSD of the powder produced in experiment #5 results from different cooling conditions applied to the plasma chamber off gas stream. These different experiments were conducted with a same carrier gas flow rate of 120 lpm (Ar), but with different cooling gas flow rates and gas composition: 80 lpm Ar in case of exp. #1; 140 lpm Ar in case of exp. #3; and 160 lpm N_2 in case of exp. #5. SEM micrographs of typical agglomerates occurrences in exp. #3 and exp. #5 are shown in Fig. 3. A more detailed SEM analysis on the sizes of primary particles indicates that they are about the same (100 ~ 200 nm). Possibly, for the geometry of the plasma chamber and the operating conditions which were common to all experiments, the gas-to-condensed phase transition giving rise to the formation of primary particles started in the duct that connects the evaporation and cooling chamber, before the hot gas stream was quenched by the cold gas jets. Therefore, definition of primary particle size, which in principle can be controlled by quenching intensity, remained little affected by the amount and composition of the cold gas injected at the entrance of the cooling section. Nevertheless, the cooling variables do affected primary particles agglomeration, as can be observed from the micrographs shown in Fig. 3: a stronger quenching (average temperatures after quenching are shown in Tab. II) seems to prevent a more intense agglomeration which otherwise might result from primary particles collision at higher temperatures. A modeling study was carried out which confirms these conclusions and whose results are presented in another paper in this symposium[3].

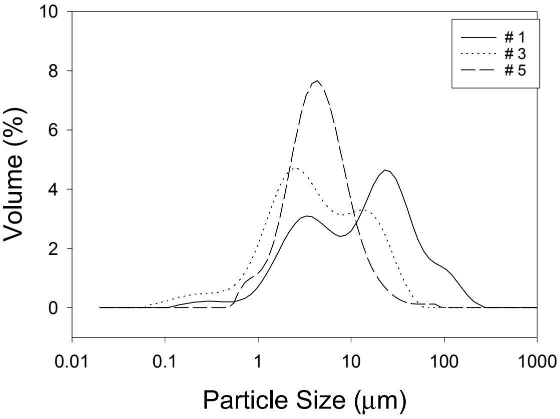

Fig. 2 – Particle size distribution (plasma) of powders produced in different plasma synthesis experiments.

Because of its well defined PSD and absence of large agglomerates, the powder from exp. #5 was chosen to carry Ag/C mixture sintering experiments. For the sake of comparison, the PSDs of this powder and of a commercially available Ag powder are shown in Fig. 4. The morphology of particle agglomerates of both commercial and plasma synthesized powders are shown in the SEM micrographs of Fig. 5(a) and Fig. 5(b), respectively. Commercial powder was produced by chemical precipitation A size difference of about one order of magnitude is observed, which applies to both primary particles and agglomerates.

Tab. II – Evaluation of quenching conditions for each of the experiments considered.

	Exp. #1	**Exp. #3**	**Exp. #5**
Carrier gas	Ar (1500 K) 120 lpm	Ar (1500 K) 120 lpm	Ar (1500 K) 120 lpm
Quenching gas	Ar (298 K) 80 lpm	Ar (298 K) 140 lpm	N2 (298 K) 160 lpm
After quenching average temperature	1011 K	846 K	706 K

Silver melting point: 1234 K; boiling point: 2483 K.

A comparison between graphite and carbon black powder which were used in the sintering preparation is shown in Fig. 6. Particle morphology of these powders are shown in the SEM micrographs of Fig. 7. The graphite particles have a flack like morphology, while the carbon black although agglomerated have a granular primary particle structure.

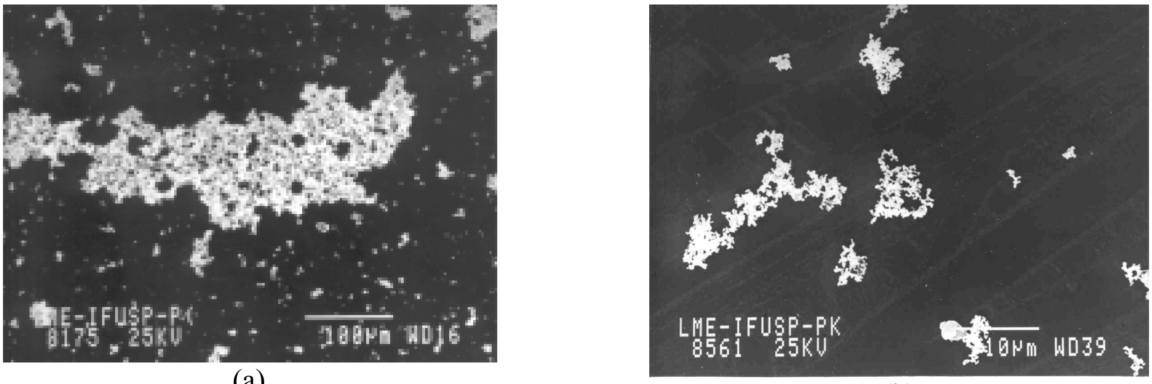

(a)

(b)

Fig. 3 – Particle agglomerates observed in different plasma synthesis experiments: a) exp. #3); and b) exp. #5.

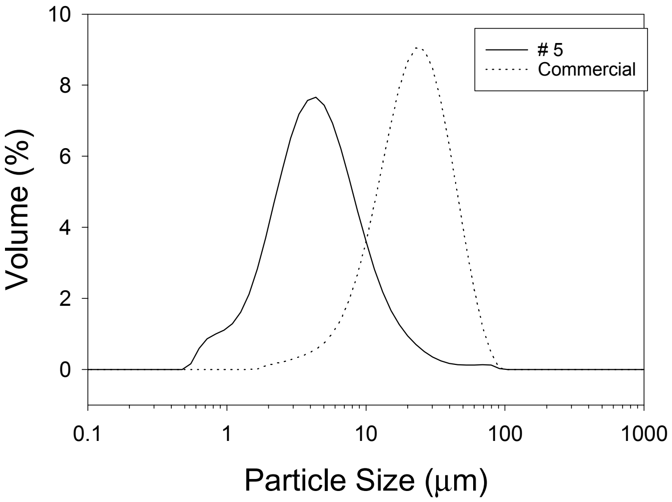

Fig. 4 – Comparison of PSD of plasma synthesized and commercial Ag powders.

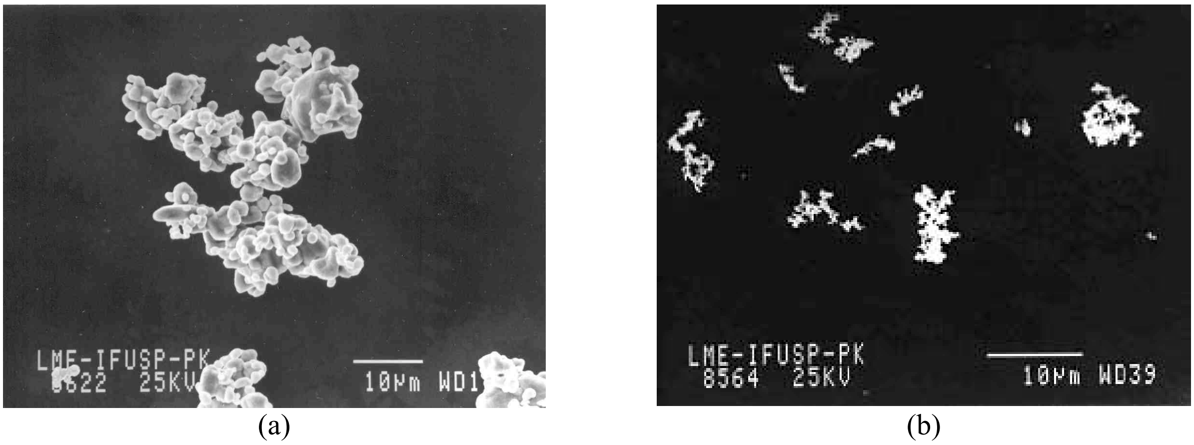

(a)

(b)

Fig. 5 – Agglomerates morphology of commercial (a) and plasma synthesized [exp. #5, (b)] Ag powders.

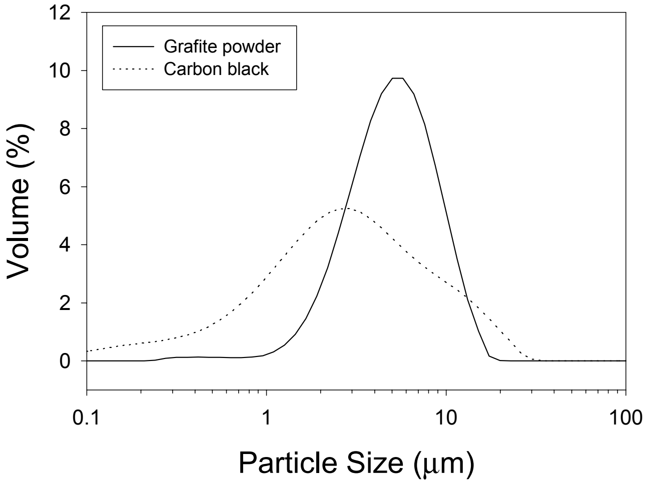

Fig. 6- PSDs of graphite (Fisher size 0.001 mm) and carbon black (Degussa Printex G) powders used in the sintering experiments.

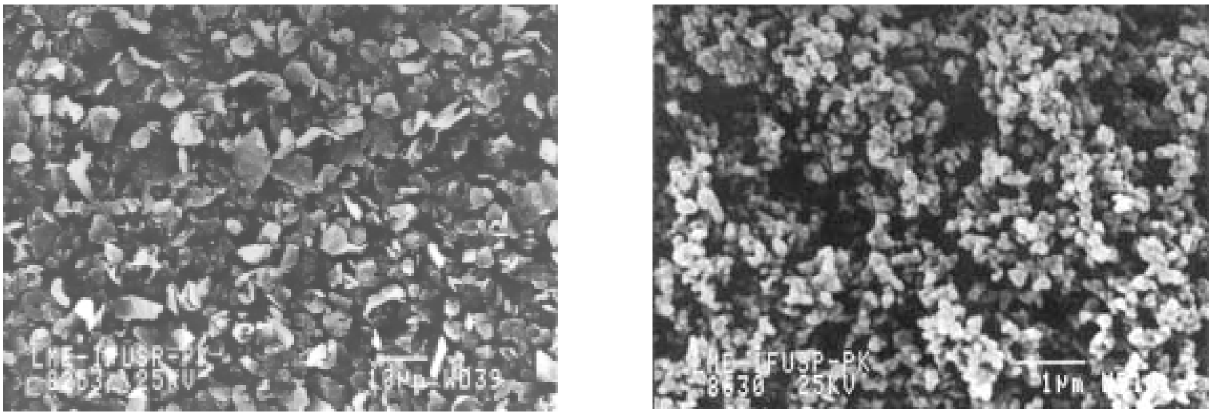

(a) (b)

Fig. 7 – Graphite and Carbon Black powders used in the Ag/C sintering experiments, respectively: (a) Fisher 0.001 mm; and (b) Degussa Printex G.

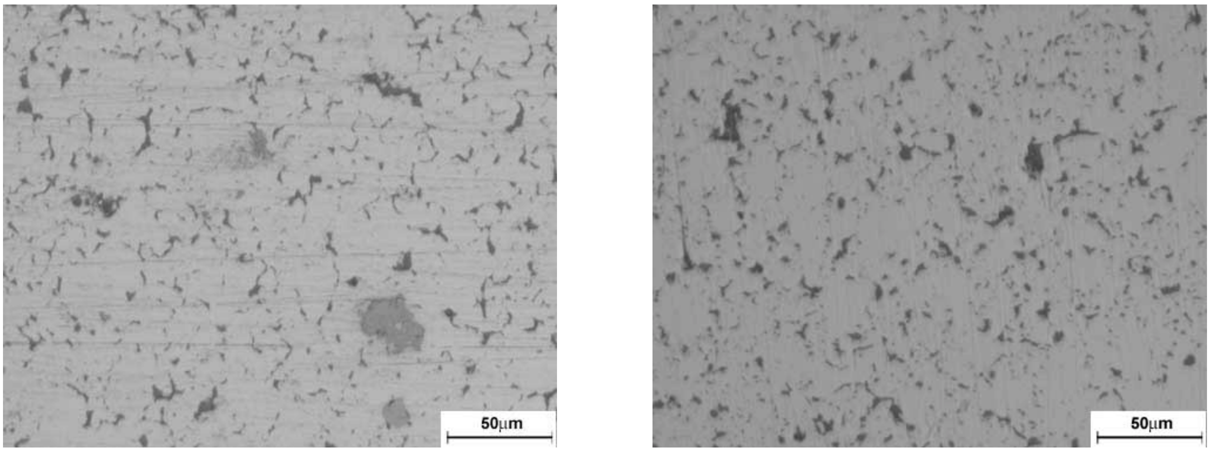

(a) (b)

Fig. 8 – Metallographic preparation of Ag/5%C sintered compacts using graphite powder and: (a) commercial Ag powder; (b) plasma synthesized powder (exp. #5).

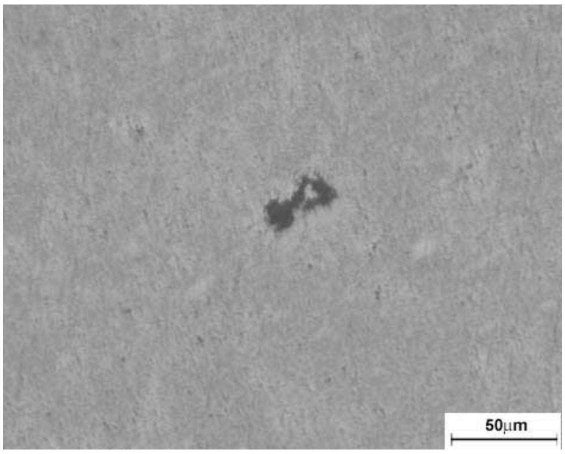

Fig. 9 – Metallographic preparation of Ag/5%C sintered compacts using plasma synthesized powder (exp. #5) and carbon black.

Fig. 8 shows micrographies of non-attacked metallographic preparations of an Ag/5C commercial electrical contact insert and a sintered compact produced with the plasma synthesized Ag powder. In both cases the graphite powder shown in Fig. 7(a) was used as the C bearing material. No relevant difference between commercial and experimental preparation can be noticed. On the other hand, a considerable homogeneity improvement has been achieved with the preparation obtained with the powder of exp. #5 mixed with the carbon black powder (Fig. 8).

Conclusion

Fine Ag powders were produced at a 500 kg/h rate using a transferred-arc synthesis reactor basically formed by evaporation and condensation separate chambers. It is observed that the powders produced are formed by agglomerates which may vary in size depending upon cooling conditions, but are basically constituted of primary particles in the same range (100 – 200 nm). The expected influence of cooling conditions on primary particle size was not observed. Analysis of this result suggests that gas-to-condensed phase transition occurs possibly inside the evaporation chamber and along the transition duct that exists between the two chambers. The particle size of the plasma synthesized powders are considerably smaller than the one observed in the commercially available powders. Sintered compacts of 95%Ag / 5%C mixture ratio where produced using one of the plasma Ag powders using both graphite and carbon black powders. The microstructure of the sintered compacts produced using the plasma Ag and graphite powders is about the same the one observed in commercial electrical contact insert of same composition. A considerably finer microstructure was observed for the plasma Ag powder mixed with carbon black, observing same composition.

Acknowledgment

The authors thankfully acknowledge the financial support given by Fundação de Amparo à Pesquisa do Estado de São Paulo – FAPESP, Brazil (Process No. 98/14864-5).

References

[1] Ullmann´s Encyclopedia of Industrial Chemistry, 6th Edition, 1998, Electronic Release.
[2] R.J. Munz, T. Addona, A.C. da Cruz, Application of transferred arcs to the production of nanoparticles, Pure Appl. Chem. **71,** 10, pp. 1889-1897 (1999).
[3]H. Toku and A.C. da Cruz, Modelling of Ag fine particles production using a transferred-arc plasma, ISPC 16 (2003).

Modelling of Ag Fine Particles Production Using a Transferred-Arc Plasma

H. Toku and A.C. da Cruz

Institute for Technological Research – IPT - São Paulo, SP, Brazil

Abstract

A modelling study was carried out intended to provide theoretical support to experimental investigation on the synthesis of Ag fine powder using transferred-arc plasma. A bi-dimensional numerical simulates de phase transition process, based on the method of moments of PSD. Results indicate that particle nucleation occurs before the quenching region and, therefore, primary particles size can not be controlled by cooling variables in the present operating conditions.

1. Introduction

The present modelling work was carried out with the objective to provide theoretical support to the experimental investigation of the vapour phase synthesis of silver (Ag) powders using a transferred-arc plasma evaporator. The experimental work, which is reported in another paper presented in this same symposium[1], involved a plasma evaporator coupled to a tubular section in which the plasma chamber hot gases were cooled. The model is adapted from the previous work involving both AlN and pure Al synthesis presented elsewere[2]. A bi-dimensional numerical model was applied to determine the fields of temperature, velocities, species concentrations, and to simulate de phase transition process inside the cooling chamber, based on the method of moments of particle size distribution.

2. Numerical model

The geometry and dimensions for the quenching section are shown in Fig.1. Ag vapor is produced by the transferred-arc and is carried out the plasma chamber by a hot argon (Ar) stream (Q1) through a connection duct into a quenching section where it is mixed with radial jets of room temperature Ar (Q2).

Hot gas containing Ag vapour coming from an evaporation chamber enters a circular port of diameter 40 mm. Room temperature Ar gas is fed through a circumferential gap 0.1 mm thick at 175 mm far from the entrance port. The total length of the quenching section is taken as 435 mm.

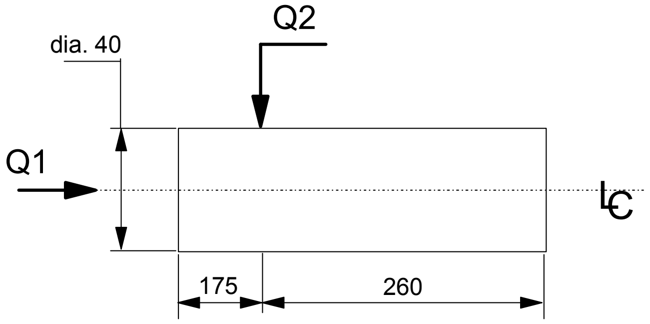

Fig. 1 – Schematic representation of the modeled region, dimensions in mm.

The many conservation equations describing both fluid flow conditions and phase transition phenomena are solved in two steps: (i) first, the fields for velocity, temperature, and chemical species concentration are calculated; (ii) following, the particle nucleation and growth process arising from the mixing of a hot gas flux carrying Ag(v) and a radial jet of a cold Ar gas mixture is determined. The following conservation equations are solved in the first step, assuming laminar axi-symmetric flow:

Continuity: $$\vec{\nabla} \cdot (\rho\vec{u}) = 0 \tag{1}$$

Moment conservation: $$\vec{\nabla} \cdot (\rho\vec{u}\vec{u}) = \vec{\nabla} \cdot (\mu\vec{\nabla}\rho\vec{u}) - \vec{\nabla}p \tag{2}$$

Chemical species conservation: $$\vec{\nabla} \cdot (\rho\vec{u}w_i) = \vec{\nabla} \cdot (\rho D_{i,Ar}\vec{\nabla}w_i) + S_i \tag{3}$$

Energy conservation: $$\vec{\nabla}\cdot(\rho\vec{u}h)=\vec{\nabla}\cdot\left(\frac{k}{C_p}\vec{\nabla}h\right)+\vec{\nabla}\cdot\left[\sum_i h_i\left(\frac{k_i}{C_{p_i}}-\frac{k}{C_p}\right)\vec{\nabla}w_i\right]+S_h \tag{4}$$

The particle nucleation and growth problem is solved using the method of moments of the particle size distribution. It is assumed that particles are spherical and transported by convection, Brownian diffusion, and thermophoresis. It is also assumed that particles can grow by condensation and heterogeneous reaction and coagulation. The kth-moment conservation is written as:

$$\frac{\partial M_k}{\partial t}+\vec{\nabla}\cdot(\vec{u}+\vec{u}_{th})M_k=\vec{\nabla}\cdot(D_p\vec{\nabla}M_k)+v_{cr}{}^{k}J-\int_0^\infty v^k\frac{\partial}{\partial v}(Gn)dv+(B-D)_k \tag{5}$$

A nucleation equation that considers the effect of heterogeneous reaction in the AlN system[3] is included in the birth and death term:

$$J=\frac{n(v_1)\beta s_1}{3S_{Ag}}\sqrt{\frac{\theta}{\pi}}\exp\left[-\frac{4}{27}\frac{\theta^3}{\ln S_{Ag}}\right] \tag{6}$$

These two sets of conservation equations were written in the form of algebraic equations and solved using the SIMPLER computational method as developed by Patankar[4].

3. Simulation results

Considering a plasma gas flow rate of 20 lpm at 2000 K at the entrance of the quenching section, a comparison is carried out between the nucleation and growth of Al (which was studied before[5]) and Ag with radial quenching by 7 lpm of Ar at room temperature and pressure (298 K, 100 kPa). The corresponding temperature field is shown in Fig. 2.

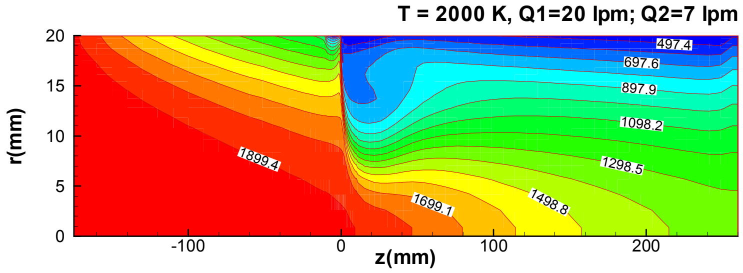

Fig. 2 – Distribution of temperature inside the quenching section.

Assuming a metal vapor concentration of 0.002 in both cases, the nucleation rate fields obtained for Al and Ag are presented in Fig. 3. It is observed that for these conditions the Al nucleation occurs near the wall, before the region of stronger cooling and along the jets. The Ag nucleation on the other hand occurs only in the cooling region and in a broader volume. The vapor pressure and surface free energy of Al and AlN as a function of temperature are graphically shown in Figs. 5 and 6, respectively. Considering the changes of these properties, for a same cooling condition and initial vapor concentration, it is observed that the absolute value of the Gibbs free energy change associated with the gas-to-condensed phase transition of Ag is smaller than in the case of Al. The Gibbs free energy change in this case being given by:

$$\frac{\Delta G}{k_B T}=-(i-1)\ln S+i^{2/3}\theta \tag{7}$$

This fact explains the result shown in Fig. 3 according to which Ag vapor takes longer than Al to nucleate.

NUCLEATION RATE

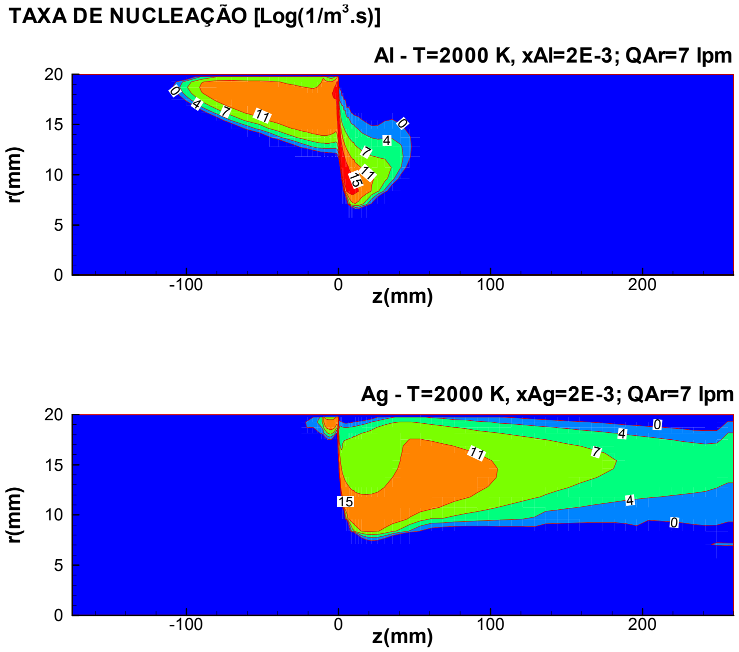

Fig. 3 – Distribution of the nucleation rates simulated for Al and Ag fine particle synthesis.

Vapor pressure

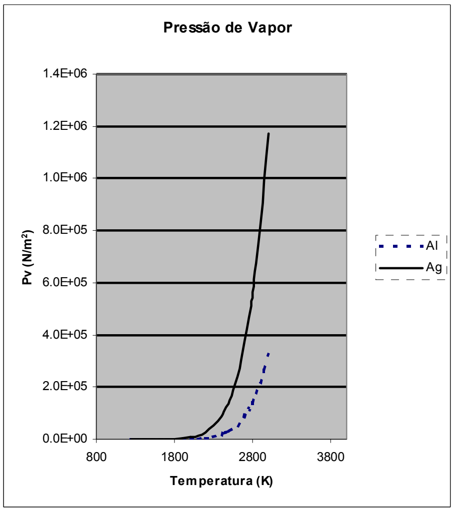

Fig. 5 – Change of the vapor pressure as a function of temperature for Al e Ag.

Dimensionless Surface Energy

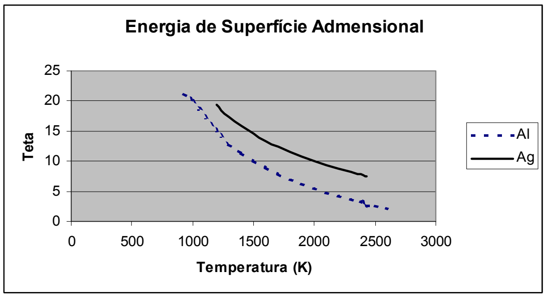

Fig. 6 – Change of the dimensionless surface energy as a function of temperature for Al e Ag.

Considering same operating conditions, the higher volatility of Ag with respect to Al contributes to its easier evaporation. Experimental[1,5] data point out to Ag vapor mole fractions which are about one order of magnitude higher than could be obtained for Al evaporation experiments carried out at a higher temperature level[6] (1500 K in case of Ag vs. 2000 K in case of Al). Based on this observation a new simulation was carried out whose results are presented next.

The temperature distribution obtained for the simulation of 40 lpm of Ar (Q1) at 1500 K entering the quenching section, 10 lpm of room temperature Ar (Q2) in the radial jets is shown in Fig. 8. Two different Ag vapor concentrations (mole fraction) are considered: 0.002 and 0.02 (Fig. 9). For the lower concentration situation the nucleation occurs near the wall before the radial jets and also along the jets. The simulation of a concentration one order of magnitude higher on the other hand points out to the nucleation predominantly at the very entrance of the quenching section. This situation is in agreement with the experimental results[1] according to which the primary particle size did not depend on the cooling conditions imposed in the quenching section.

Fig. 10 shows the fields for the average particle size diameter, based on the specific surface area (d_{BET}), determined for the two Ag vapor concentrations considered. It is observed that the higher concentration results in larger particle diameter.

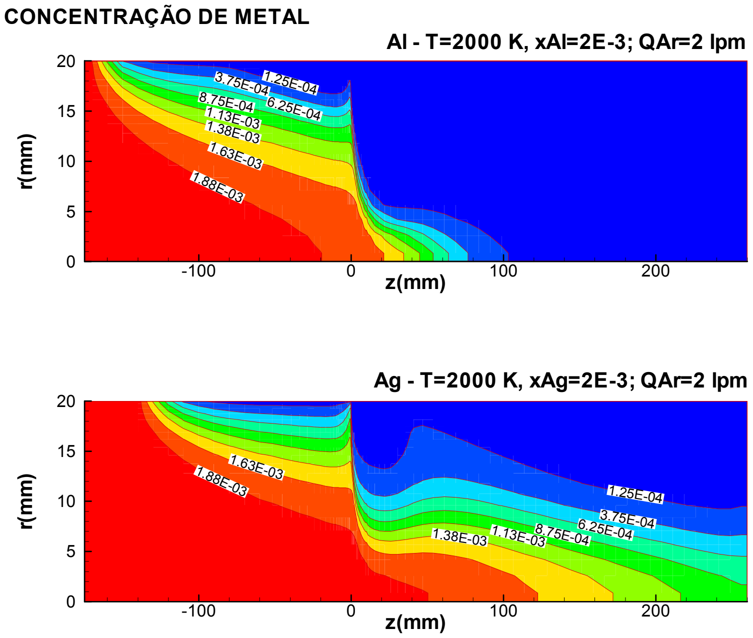

Fig. 7 – Distribuição das concentrações de vapor metálico, simuladas para o alumínio e para a prata.

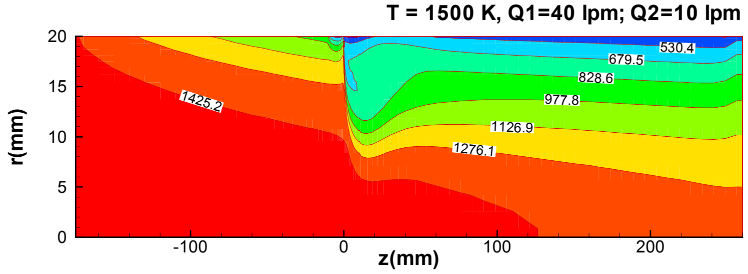

Fig. 8 – Distribuição de temperatura.

Conclusion

A model for the nucleation and growth of particles from the vapor phase was applied to the study of the synthesis of Ag fine powder. A comparison between Ag and Al was carried out which indicates a more intense nucleation in case of Al, for the same simulation conditions. The simulation of the synthesis of Ag particles based on experimental data indicates that the nucleation predominantly occurs at the entrance of quenching section. This simulation result fully agrees with the experimental observation that, for the adopted reactor geometry and operating conditions, the size of primary Ag particles is practically independent on the cooling intensity that is imposed in the chamber next to the evaporation section.

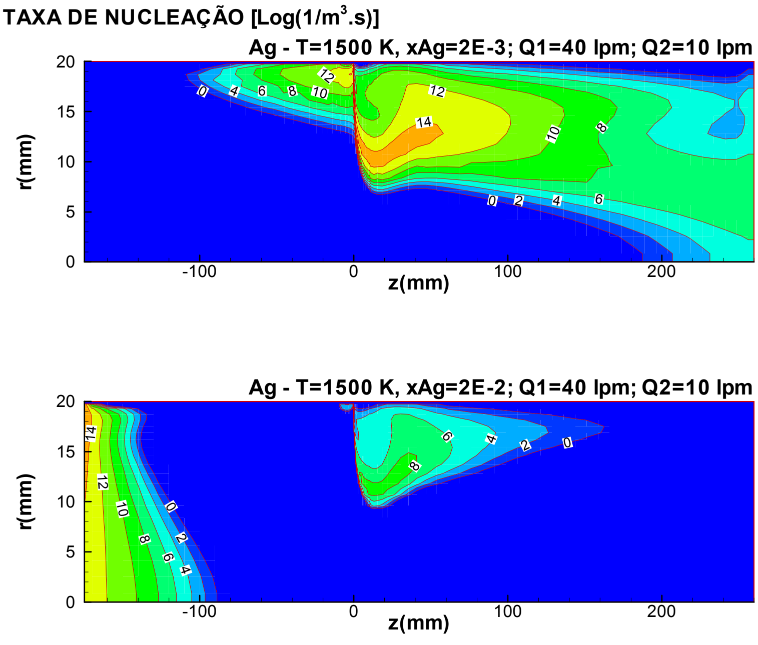

Fig. 9 – Distribution of the nucleation rate for different vapor concentrations at the entrance of the quenching section.

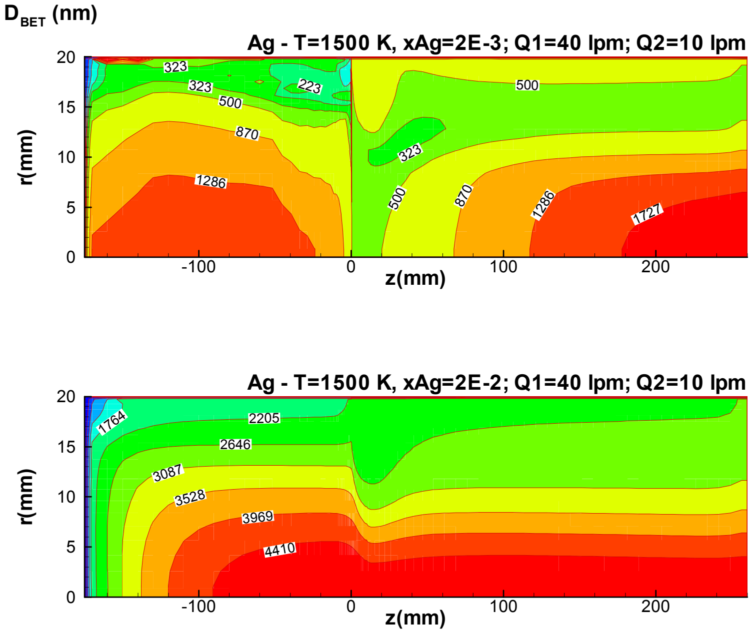

Fig. 10 – Particle size distribution fields based on the specific surface area determined for two metal vapor concentrations.

Acknowledgment

The authors thankfully acknowledge the financial support of Fundação de Amparo à Pesquisa do Estado de São Paulo – FAPESP, Brazil (Process No. 98/14864-5).

Nomenclature

B = birth term in the moment conservation equation
C_p = specific heat (J/kg.K)
D = mass diffusivity (m^2/s); death term in the moment conservation equation
Dp = particle diffusivity (m^2/s)
G = surface growth rate (m^3/s); Gibbs free energy
h = enthalpy (J/kg)
i = chemical species index (Ar, or Ag)
J = nucleation rate ($1/m^3.s$)
k = thermal conductivity (W/m.K)
M_k = k^{th}-moment of particle size distribution (k = 0, 1 ou 2)
n = particle number density ($1/m^3$)
p = pressure (N/m^2)
t = time (s)
T = temperature (K)
r = radius (m)
S_h = energy conservation equation source term
S_{Ag} = Ag supersaturation ratio
S_i = chemical species conservation equation source term
SSA = specific surface area (g/m^2)
u = velocity (m/s)
u_{th} = thermoforese velocity de termoforese (m/s)
w = mass fraction
z = longitudinal distance (m)
v = particle volume (m^3)
v_{cr} = critical particle volume (m^3)
v_g = geometric average particle volume (m^3)

Greek letters

β = impingement (or condensation) rate ($1/m^2/s$)
③ = viscosity (kg/m.s)
⑧ = gas density (kg/m^3)
⑨$_g$ = geometric standard deviation

ReferEnces

[1] A.C. Doring, H. Toku, O.W. Bender, P.K. Kiyohara , A.L. Silva, and A.C. da Cruz,_Synthesis of fine Ag particles using transferred-arc plasma, ISPC 16 (2003).
[2] A.C. da Cruz, O.W. Bender and H.N. Yoshimura, Modelling Study of the production of AlN nanoparticles in a new version of a Plasma Synthesis reactor, ISPC 15 (2001).
[3] A.C. da Cruz and R.J. Munz, Aerosol Science and Technology, 34, 1-13 (2001).
[4] S.V. Patankar, Numerical Heat Transfer and Fluid Flow. McGraw Hill (1980).
[5] Da Cruz, A.C., Bender, O.W., Doring, A.C., Thomas, O., Coelho, K.C., Kiyohara, P.K., (in Portuguese) Produção de pó de alumínio ultrafino em nova versão de reator a plasma, 14$^{o.}$ CEBCIMAT, São Pedro, SP (2000).
[6] A.C. da Cruz, Experimental and modelling study of the plasma vapour-synthesis of AlN powders, PhD thesis, McGill University, Canada (1997).

Application of Pulse Modulated RF Discharge Plasma to CVD of Carbon Materials from C_2H_2-H_2 Mixture

Kazuhiro ISHIMARU

Department of Mechanical Engineering, Gifu National College of Technology, Gifu, Japan

Abstract

RF discharge plasma is often used for various processes in material developments, and this plasma can form highly nonequilibrium condition. In addition, RF discharge with pulse modulated mode can realize process characteristics which is not realized in a steady state. In this study, nonequilibrium plasma chemical reactions by this discharge were applied to CVD of carbon materials from acetylene and hydrogen mixture. This discharge characteristics were investigated, and its mechanism was estimated.

1. Introduction

Recently various carbon materials, such as diamond, amorphous carbon and fullerene are studied and are developed. These properties are greatly different by a molecular structure. Since its first observation in 1991, carbon nanotubes [1] have been one of the most actively studied carbon materials due to their chemical stability, and unique structural, electrical, and mechanical properties [2]. Utilization of these properties with individual or ensembles of carbon nanotubes have led to advanced scanning probes [3], gas and electrochemical energy storage [4], molecular-filtration membranes [5], nanoelectronic devices [6], and the electron field emission source [7]. CVD (Chemical Vapor Deposition) is suitable for synthesizing great quantities of these materials. However, these qualities are not sufficient for applications to industrial products.

In the case of CVD processes of various materials, a plasma-enhancement method is often used, and especially, the excitation by RF (Radio Frequency) discharge plasma is used for various CVD processes, such as semiconductor manufacturing processes. This plasma forms highly nonequilibrium condition that electrons only have high energy, and it can realize chemical reactions which are generally difficult to produce. Because the motion of ions of which the mass is large can not follow for very quick change of the electric field. In addition, RF discharge plasma with pulse modulation along time constants of generation and disappearance of the particles and chemical reactions can realize process characteristics which is not realized in a steady state by using the transient phenomena [8,9]. In this case, the relaxation time of energy of electrons and the time of incomplete discharge plasma structure are effectively used.

In this study, nonequilibrium plasma chemical reactions using CCP (Capacitively Coupled Plasma) by pulse modulated RF discharge were applied to CVD of carbon materials from acetylene (C_2H_2) and hydrogen (H_2) mixture, and characteristics of this method were examined. As a result, it has been clarified that the pulse modulated RF discharge can control the generation process of active chemical species in this reaction system and is suitable for CVD of new carbon materials.

2. Experimental apparatus and procedure

Figure 1 shows the experimental apparatus. This consists of a CVD chamber ,RF (13.56MHz) power supply, supply system of reaction gases and measurement system of discharge characteristics. Plasma reactor, CVD chamber, is made of cylindrical quartz glass of 50mm diameter and 100mm length, so that the discharge phenomena and the plasma structure could be easily observed from the outside. Two parallel, flat-plate, coppered circular electrodes are set inside the reactor. Each electrode is 20mm in diameter and the distance between the electrodes is 5mm, and the RF electrode is upper side and the grounded electrode is lower side. Although this distance is variable, it was fixed in this study. Therefore this discharge system becomes a type which CCP is formed by applying RF power to these two electrodes through an impedance matching box. Although the plasma density of this type is not comparatively high, it is an effective method in CVD for a large area. And it is possible that the substrate is set on either electrode. An Asymmetric discharge which the grounded electrode is larger than the RF electrode is substantially formed because the reactor main body is grounded, and self-bias voltage (negative DC voltage) is generated. RF power supply is equipped with pulse generator system (pulse board and pulse controller), and pulse modulated RF voltage can be output. It is possible that the pulse frequency (from

200Hz to 100kHz) and the pulse duty ratio (from 20% to 80%) optionally change.

The mixed gas added hydrogen (H_2) for the synthesis of carbon nanotubes [10] to acetylene(C_2H_2) for the syntheses of carbon fibers and carbon micro coils [11,12] was used as raw materials. The flow rates of each gas were controlled by flow controllers, and then, these gases were supplied into the reactor. The reactor was decompressed by a rotary pump, and its internal pressure was measured by an absolute pressure gage. As standard condition in this study, the flow rates of acetylene and hydrogen were 30ml/min and 120ml/min respectively. This flow rate ratio has result of the synthesis of carbon nanotubes [10]. The residence time of the mixed gas in the discharge reaction part is about 0.6 second. Because its time is sufficiently longer than the characteristic time of the discharge, the discharge characteristics are hardly affected in the flow rate of the gas.

In the measurement of RF discharge characteristics, applied voltage and current were measured by the high speed digital oscilloscope with high voltage probe from the output terminal of impedance matching box and current probe respectively. These values were evaluated by maximum height of waveform.

The electric power was measured by using a forward wattmeter and a reflect wattmeter of RF power supply attachment, and then, it was evaluated by the difference in each measured electric power. In the case of pulse modulated RF discharge, this electric power was evaluated by peak value.

3. Results and discussion

3.1 Discharge condition

The waveform of pulse modulated RF voltage is shown in Fig. 2. Figure 2 (a) shows the appearance of the applied voltage waveform, and Figure 2 (b) shows the rising part of pulse modulated voltage in detail. A short period is required for rising of the voltage.

Figure 3 shows photograph of pulse modulated RF discharge. (Electric power: 30W, Pulse frequency : 1kHz, Pulse duty ratio : 50%) Strong light emission parts are observed on two electrodes respectively, and a kind of ion sheath can be confirmed.

3.2 Fundamental characteristics of continuous RF discharge

As a first step, fundamental characteristics of RF discharge were examined by using continuous mode. Figure 4 and 5 show P (electric power) -V (applied voltage) and I (current) - V characteristics at each pressure respectively, where the flow rates of acetylene and hydrogen were 30ml/min and 120ml/min respectively. In P-V characteristics, the electric power increases with raising the applied voltage, and this gradient increases as the pressure rises. This result means that although the discharge is difficult to be generated at high pressure because reduced electric field (electric field / pressure) is low, the discharge rapidly develops with raising the applied voltage after the discharge is generated. In I-V characteristics, these characteristic curves have the minimum

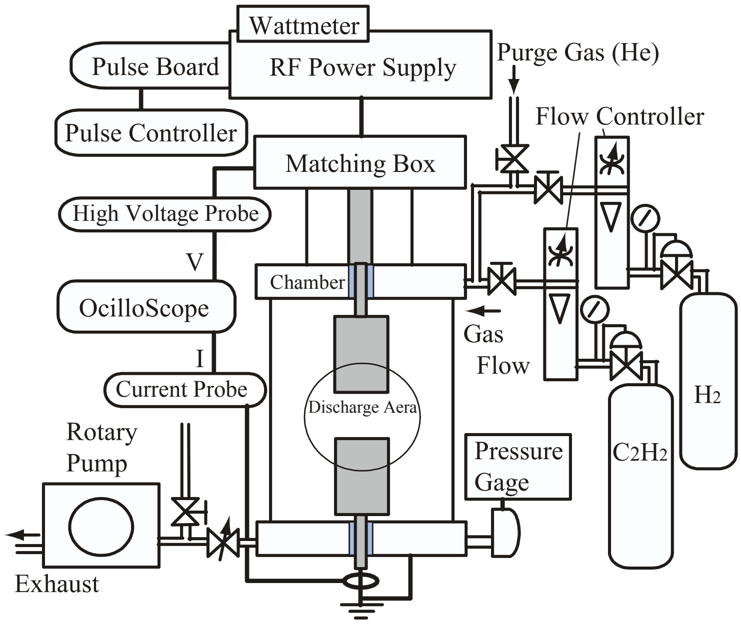

Fig. 1 Experimental apparatus

values. However, it is predicted that most of these measured currents are components of displacement current because the plasma density is not comparatively high and the frequency of applied voltage is very high. Therefore the change of the static capacitance of space, namely the change of the plasma structure may be generated at the points of the minimum value.

Figure 6 shows P-V characteristics at each acetylene-hydrogen mixture ratio, where the pressure was 10 Torr. The electric power increases with raising applied voltage, and this gradient increases as the mixture ratio (C_2H_2/H_2) increases. This result means that although the discharge is difficult to be generated at high mixture ratio because the breakdown voltage of acetylene is high, the discharge rapidly develops with raising applied voltage after the discharge is generated.

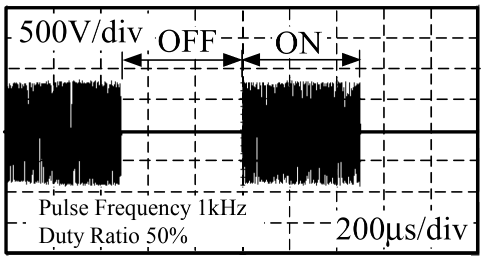

(a) Appearance of applied voltage waveform

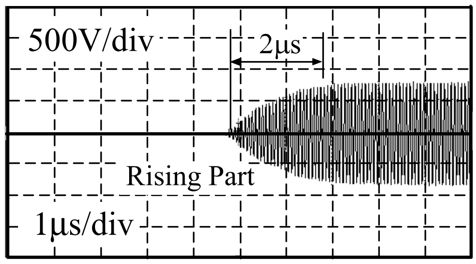

(b) Rising part of pulse modulated RF voltage

Fig. 2 Wave form of pulse modulated RF voltage

Fig. 3 Photograph of pulse modulated RF discharge

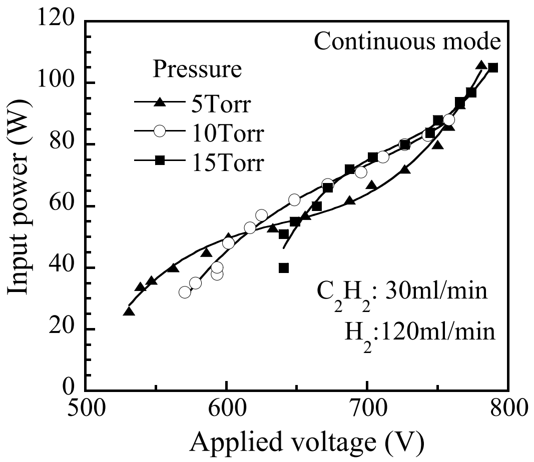

Fig.4 P-V characteristics (Effect of pressure)

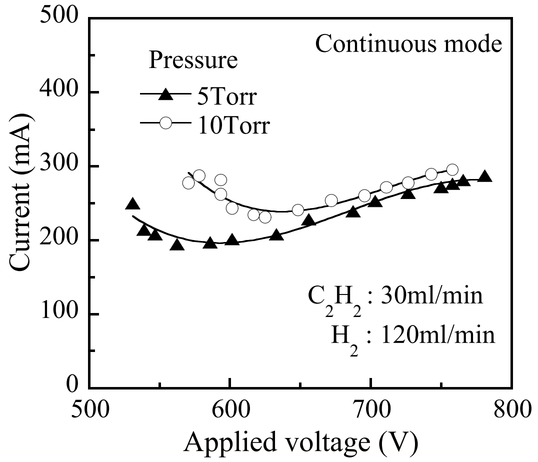

Fig. 5 I-Vcharacteristics (Effect of pressure)

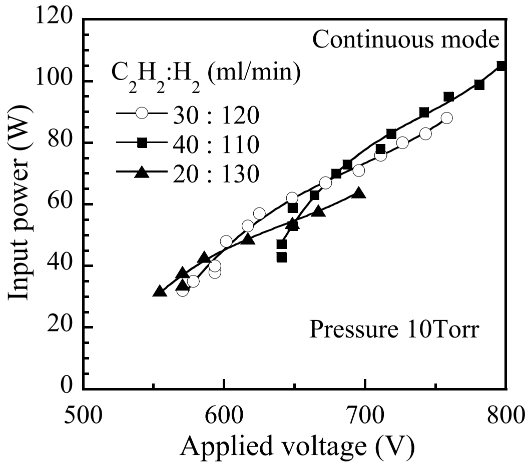

Fig.6 P-V characteristics (Effect of mixture ratio)

3.3 Characteristics of pulse modulated RF discharge

3.3.1 Effects of pulse frequency and pulse duty ratio

Figure 7 shows the effect of the pulse frequency on the minimum maintenance voltage of discharge, where the minimum maintenance voltage is minimum voltage which can maintain the discharge after the discharge is generated. The minimum maintenance voltage increases with raising pulse frequency. Charged particles are not sufficiently generated by shortening the discharge period. Therefore it is considered that most of these disappear even in the short non-discharge period and the discharge of next period is difficult to be generated.

Figure 8 shows the effect of the pulse duty ratio on the minimum maintenance voltage of discharge. The minimum maintenance voltage decreases with increasing the pulse duty ratio. When the non-discharge period is short for the discharge period which charged particles are generated, the remaining quantity of charged particles in the non-discharge period increases. Therefore it is considered that the discharge of next period is generated easily.

Furthermore, figure 9 shows the effect of the pressure on the minimum maintenance voltage of discharge. The pulse duty ratio was fixed to be 50%. The discharge is difficult to be generated at high pressure because reduced electric field is low. Therefore this voltage increases with raising the pressure.

It is considered that these results was determined by time constants of generation and disappearance of charged particles. In these results, charged particles were controlled by the pulse frequency and the pulse duty ratio. Therefore the relation between the discharge period and the non-discharge period has not been clarified. In next section, this relation is examined by the concrete time. And the pressure was fixed to be 10 Torr. This is higher pressure (gas density) which stabilized discharge is obtained.

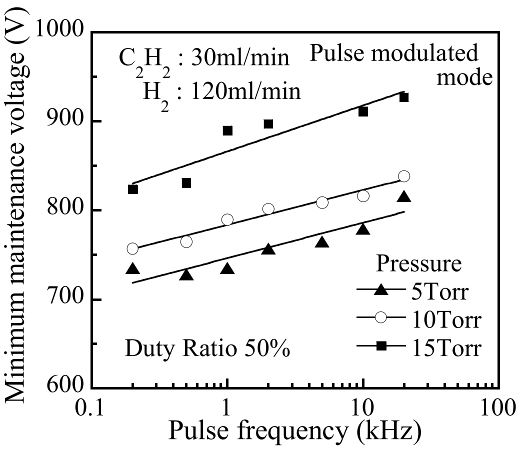

Fig.7 Effect of pulse frequency on minimum maintenance voltage

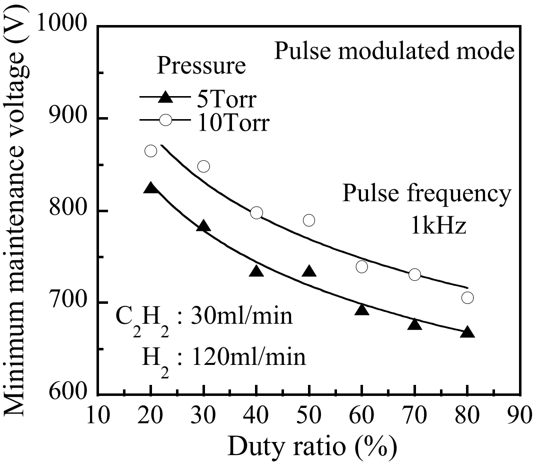

Fig.8 Effect of pulse duty ratio on minimum maintenance voltage

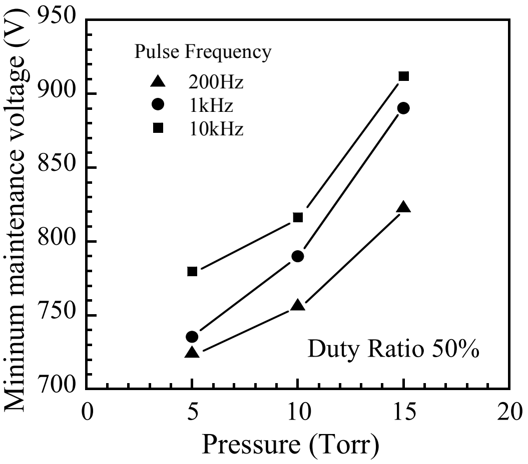

Fig.9 Effect of pressure on minimum maintenance voltage

3.3.2 Effects of discharge period and non-discharge period

Figure 10 shows the effect of the non-discharge period on the minimum maintenance voltage of discharge. The minimum electric power measured with this voltage is also shown in this figure. The discharge period was fixed in the period. The minimum maintenance voltage increases with lengthening the non-discharge period. Charged particles generated in the discharge period are gradually decreased in the non-discharge period. Therefore it is considered that the discharge of next period is difficult to be generated. However, the length of non-discharge period hardly affects the minimum maintenance voltage when charged particles are sufficiently generated by lengthening the discharge period. Furthermore, it is also considered that charged particles with long life are generated.

Figure 11 shows the effect of the discharge period on the minimum maintenance voltage of discharge. The minimum electric power measured with this voltage is also shown in this figure. The non-discharge period was fixed in the period. The minimum maintenance voltage decreases with lengthening the discharge period. Many charged particles are generated by lengthening discharge period. Therefore it is considered that many charged particles remain in the non-discharge period and the discharge of next period is generated easily.

These characteristics may be affected by high breakdown voltage of acetylene. (Breakdown voltage of acetylene is about 4.9 times of its voltage of hydrogen) Although the minimum electric power approximately shows the tendency which is equivalent to the minimum maintenance voltage, the gradient of the minimum electric power is slightly small. Therefore it is predicted that the discharge current decreases with raising the minimum maintenance voltage.

These results indicated that quantity and type of important charged particles and active chemical species in the process can be controlled if appropriate pulse modulation is conducted to RF discharge.

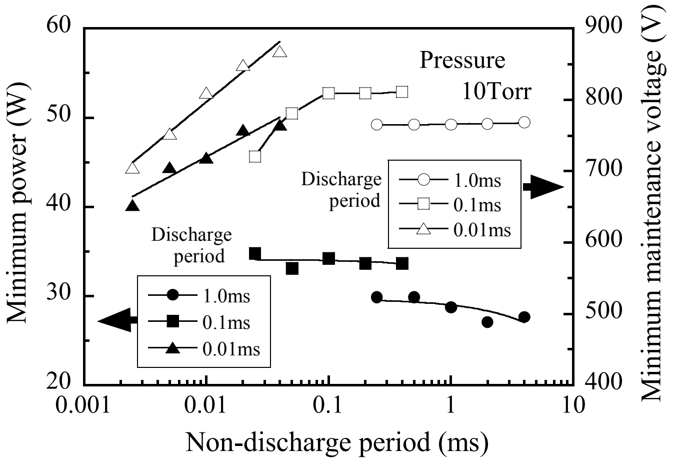

Fig.10 Effect of non-discharge period on minimum maintenance voltage and minimum power

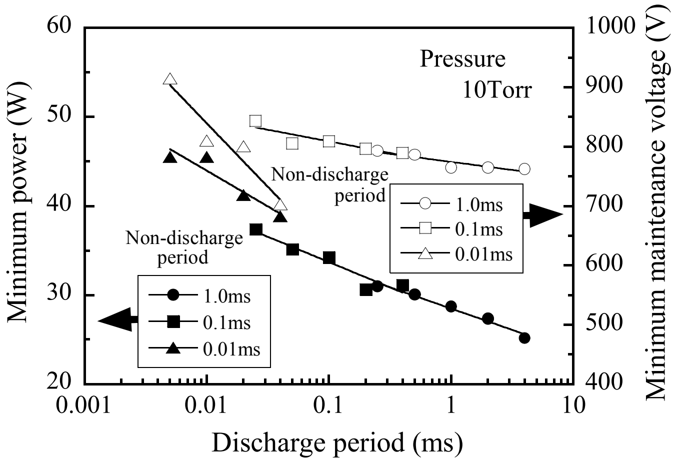

Fig. 11 Effect of discharge period on minimum maintenance voltage and minimum power

3.4 Application of pulse modulated RF discharge to CVD process

In the reaction process by RF discharge plasma using continuous mode or pulse modulated mode, the synthesis of carbon materials was confirmed on the both electrodes, and large quantities of these carbon materials are observed on the grounded electrode. Although the both electrodes is heated by the discharge, positive heating by a heater is not carried out. Generally, the acceleration of ions by the sheath is generated when the self-bias voltage is generated. Therefore, a substrate is set on the RF electrode in the process of desiring ion collisions, and on grounded electrode in the process of not desiring ion collisions. In this study, it is considered that the carbon materials with separate structure and form are synthesized on each electrode.

From this result and characteristics of pulse modulated RF discharge, it is predicted that the pulse modulated RF discharge is effective method for the control of CVD process of carbon materials

4. Conclusion

In this study, it has been shown that pulse modulated RF discharge can control the generation process of charged particles and active chemical species in the reaction system by acetylene and hydrogen mixture and this discharge is suitable for the CVD of new carbon materials. This process is concretely controlled by the pulse frequency and the pulse duty ratio of the pulse modulated voltage. As a result, the guideline for the CVD of carbon materials has been obtained .

It is predicted that substrate heating and addition of appropriate catalysts are required in concrete CVD of new carbon materials.

Reference

[1] S.Iijima, Nature, 354, (1991).

[2] T.W.Ebbesen, Phys. Today, 49, (1996).

[3] H.J.Dai, J.H.Hafner, A.G.Rinzler, D.T.Colbert and R.E.Smalley, Nature, 384, (1996).

[4] G.E.Gadd, M.Blakford, S.Moricca, N.Webb, P.J.Evans, A.M.Smith, G.Jacobsen, S.Leung, A.Day and Q.Hua, Science, 278, (1997).

[5] K.B.Jirge, J.C.Hulteen and C.R.Martin, Science, 278, (1997).

[6] S.Tans, A.Verschueren and C.Dekker, Nature, 393, (1998).

[7] W.A.de Heer, A.Chatelain and D.Ugarte, Science, 270, (1995).

[8] S. Samukawa and S. Furuoya, Appl. Phys. Lett., 63, 15(1993).

[9] Y.Watanabe and M.Shiratani, Plasma Sources Sci. Technol., 3, 3(1994).

[10] Y.H.Wang, J.Lin, C.H.A.Huan and G.S.Chen, Appl.Phys.Lett, 79, 5(2001).

[11] N.M.Rodriguez, J.Mater.Res., 8, 12(1993).

[12] S.Motojima and X.Chen, J.Appl.Phys, 85, 7(1999).

Arc plasma deposition of TiN/ZrN and TiN/(Ti,Zr)N superlattice hard coatings

M. Balaceanu[1], V. Braic[1], M. Braic[1], A. Manea[2], I. Tudor[3], A. Popescu[3], G. Pavelescu[1]

[1]Tehnoprof Center, National Institute for Optoelectronics, Magurele-Bucharest, Romania
[2]National Institute for Material Physics, Bucharest, Romania
[3] Petroleum-Gas University of Ploiesti, Ploiesti, Romania

The properties of TiN/ZrN and TiN/(Ti,Zr)N nano-structured hard films ("superlattice" – type [1], [2]) and their dependence on the deposition parameters were investigated. The coatings were deposited on Si, plain carbon steel and high-speed steel substrates in a cathodic arc deposition unit equipped with Ti and Zr cathodes [3]. Very thin alternating ZrN (or (Ti,Zr)N) and TiN films, with a "stacking period" of 4 ÷ 30 nm, were obtained by using rotating shutters. The main deposition parameters were varied in the ranges: N_2 pressure = 10^{-2} ÷ 1 Pa, arc current = 90 ÷ 120 A, substrate bias voltage = 50 ÷ 225 V, deposition temperature = 180 ÷ 340^0C, deposition time = 30 ÷ 90 min. The films were analyzed in terms of some of their microchemical (chemical composition, phase composition), microstructural (texture, morphology, surface topography), mechanical (microhardness, thickness, adhesion) and tribological (wear resistance, friction coefficient) properties. A comparison with TiN, ZrN and (Ti,Zr)N single-layer film properties was made.

Optical and scanning electron microscopy were used to determine the film thickness, the compositional modulation period Λ and the surface topography. Almost all multilayer coatings, with thicknesses in the range 1 ÷ 5 μm and Λ = 4 ÷ 30 nm, exhibited a compact microstructure and a smooth surface topography. Chemical composition investigations, using energy dispersive X-ray (EDX) spectroscopy, showed that N/Ti or N/Ti+Zr ratio was close to 1 over a wide range of the deposition parameters, whereas Ti/Zr ratio was dependent on the arc current and Λ values. X-ray diffraction patterns exhibited mainly TiN and ZrN peaks with a (111) preferred orientation. Vickers microhardness measurements revealed that the film microhardness depended primarily on the N_2 pressure, Ti/Zr ratio and Λ. Under the best deposition conditions, microhardness exceeding 33 GPa was obtained. The experiments also showed that the deposition rates both for the TiN and ZrN single layers increased almost linearly with the arc current and depended slightly on the gas pressure and on the substrate bias. For the nanostructured coatings deposited on high-speed steel substrates, scratch tests under standard conditions indicated an excellent adhesion, with critical load values higher than 65 N. Tribological performance of the coatings was evaluated by using a testing apparatus consisting mainly of a rotating roller pressed on a coated flat specimen. As compared with the single-layer coatings, the superlattice films exhibited a better wear resistance. In general, the film characteristics were found to mainly depend on N_2 pressure, Ti/Zr ratio and Λ values, whereas the substrate bias – in the range 50 ÷ 225 V – has only a slight influence of the investigated properties.

[1] S. Veprek, J. Vac. Sci. Technol. **A 17(5)**, 2401 (1999)
[2] P.C. Yashar, W.D. Sproul, Vacuum **55**, 179 (1999)
[3] M. Balaceanu, V. Braic, D. Macovei, M. Genet, A. Manea, D. Pantelica, M. Braic, F. Negoita, J. Optoel. Adv. Mat., **4(1)**, 107 (2002)

Wear-corrosion behavior of biocompatible hard coatings deposited by cathodic arc techniques

M.Balaceanu[1], V.Braic[1], S.Zamfir[2], I.Tudor[3], A.Popescu[3], A.Vladescu[1], M.Braic[1]

[1]National Institute for Optoelectronics, Magurele-Bucharest, Romania
[2]"POLYTEHNICA" University of Bucharest, Romania
[3]Petroleum-Gas University of Ploiesti, Romania

Abstract

Corrosion and wear resistance in artificial physiological solution of some transition metal nitrides coatings (TiN, ZrN, (Ti,Zr)N) were investigated. The coatings were deposited on austenitic stainless steel samples by the cathodic arc method. Corrosion behavior was studied by means of an electrochemical experiment, whereas for the wear resistance evaluation a testing apparatus consisting of a coated rotating roller pressed on a flat specimen was used. An analysis of the main film characteristics using EDX and XRD techniques, microhardness measurements and adhesion tests was also performed.

1. Introduction

Considerable attention has been given recently to the development of biocompatible materials to be inserted in biological internal environment. Beside metals and alloys such as titanium and cobalt-chrome alloys, austenitic stainless steels have proved in general to fulfill the requirements imposed by a successful biomaterial. An increase of the life expectancy of surgical implants made of stainless steel could be obtained by coating these parts with materials having high corrosion and wear resistance. Many transition metal nitrides, especially TiN and TiAlN, have been used to protect medical implants or prothesis against corrosion and wear [1]-[3]. Nevertheless, there are few data so far leading to decisive conclusions for an adequate choose of a material to be used as an efficient coating in surface biomedical.

The objective of the current work was to compare the corrosion and wear behavior in artificial physiological solution of TiN, ZrN and (Ti,Zr)N hard coatings. The films were prepared on 316L stainless steel specimens by the cathodic arc method [4]. For the corrosion resistance analysis, an electrochemical experiment was performed. A wear-corrosion test was carried out in order to determine the wear resistance of mobile coated samples immersed in artificial physiological solution. Additional information on the film characteristics was obtained by energy-dispersive X-ray (EDX) and X-ray diffraction (XRD) analyses, microhardness measurements and adhesion tests.

2. Experimental procedures

The experimental set-up has been described elsewhere [5]. The deposition chamber was equipped with Ti and Zr cathodes and the base pressure was of about 10^{-3}Pa. Specimens to be coated were ultrasonically cleaned with trichloroethylene and mounted on a rotating holder. Prior to deposition, the samples were sputtered by Ti ion bombardment (1000V; 5 min).

EDX technique was used to determine the elemental composition of the films by means of a XL-30-ESEM TMP scanning electron microscope. Phase composition and texture were obtained by XRD analysis using an X-ray DRON diffractometer with Cu K_a radiation. Microhardness (Vickers) measurements were performed with a microhardness tester at 30 g load. Scratch tests under standard conditions were undertaken to determine the coating adhesion. The critical load (L_c) values were determined by optical microscopy (L_c is defined as the load where film flaking starts).

A PHOM 4 pH/mV-meter was used to investigate the corrosion resistance of the coatings. The samples for the corrosion test consisted of square plates (23x23x4 mm) made of 316L stainless steel and carefully polished. The electrolyte was artificial physiological solution (composition: NaCl – 8.44 g/l, Na HCO_3 – 0.35 g/l, NaH_2PO_4 – 0.06 g/l, Na $H_2PO_4\cdot H_2O$ – 0.06 g/l) at the room temperature and the test duration was 180 min. Corrosion behavior was appreciated by measuring time dependent variation of the free corrosion potential V_{corr}.

The wear behavior of different coatings in artificial physiological solution was determined with a testing apparatus consisting of a rotating coated roller pressed on a flat sample (sliding shoe). Both the roller and the shoe were immersed in solution. The roller, 40 mm in diameter and 8 mm in width, and the shoe were made of 316L stainless steel with a hardness of 250 $HV_{0.1}$. The testing parameters were: sliding speed - 0.3 m/s, load – 10 N, temperature of the solution – 24 ^{0}C. The wear behavior was investigated by measuring the removed volume from the roller. The volume loss V was evaluated by an indentation test on the coated sample, using a Vickers diamond tip at 30 kg load. The diagonal of the indent was measured with an optical microscope before and after the wear testing. Geometrical considerations lead to the following expression for the volume loss V:

$$V = \pi u B(D - u)$$

where u = 0.143(D_0 – D_1), D is the roller diameter, B – roller width, D_0 – diagonal of the indent before wear, D_1 – diagonal of the indent after wear.

3. Results and discussion

Deposition parameters are listed in Table 1, where P_{N2} – nitrogen pressure, I_{aTi} and $I_{a\,Zr}$ – arc current at the titanium and zirconium cathodes, respectively, V_s – substrate bias voltage, T – deposition temperature, t- deposition duration, D_R – deposition rate. The parameters were selected on the base of the results of TiN deposition experiments (presented in a previous paper [5]), to obtain coatings with adequate microstructural and microchemical properties. The deposition duration was chosen to prepare coatings with almost the same thickness: 2.8-3.1 µm.

Table 1 Deposition parameters

Sample No	Coating	P_{N2} (Pa)	$I_{a\,Ti}$ (A)	$I_{a\,Zr}$ (A)	V_S (U)	T (^{0}C)	t (min)	D_R (µm/min)
1	TiN	1×10^{-1}	90	-	220	310	70	0.04
2	ZrN	1×10^{-1}	-	110	220	320	50	0.05
3	(Ti,Zr)N	1×10^{-1}	90	110	220	325	45	0.06

3.1 Microchemical and mechanical characteristics of the coatings

The chemical composition of the coatings, obtained by EDX analysis, is given in Table 2. It can be seen that the TiN films were slightly overstoichiometric, while the ZrN coating was substoichiometric. For the (Ti,Zr)N film, Zr content is significantly higher that Ti content (Ti/Zr= 0.45). The presence of a small amount of oxygen (2.7 – 3.6 %) is due both to residual gas incorporated in the chamber walls and to the film contamination during the time elapsed between the film preparation and the composition analysis.

Table 2 Elemental composition of the coatings

Sample No	Coating	Elemental concentration (at. %)				N / M*	Ti/Zr
		Ti	Zr	N	O		
1	TiN	45.6	-	50.6	3.8	1.11	-
2	ZrN	-	53.1	44.0	2.9	0.83	-
3	(Ti,Zr)N	15.3	33.9	49.7	2.7	0.99	0.45

M* - metal in the compound

X-ray diffraction patterns for TiN, ZrN and (Ti,Zr)N coatings are shown in Fig.1. All layers exhibit a strong (111) preferred orientation, as already reported (e.g. [4], [6]). For the (Ti,Zr)N coating, the diffraction lines were located nearby the positions of the lines found for the ZrN film, but with a slight shift (0.5-0.7 ^{0}) towards higher Bragg angles. This shows, as it was evidenced by the analysis of the elemental composition, that the Zr concentration in the film is substantially higher than that of Ti. One may conclude that the investigated layer crystallized in a face centered cubic ZrN lattice with reduced lattice parameters.

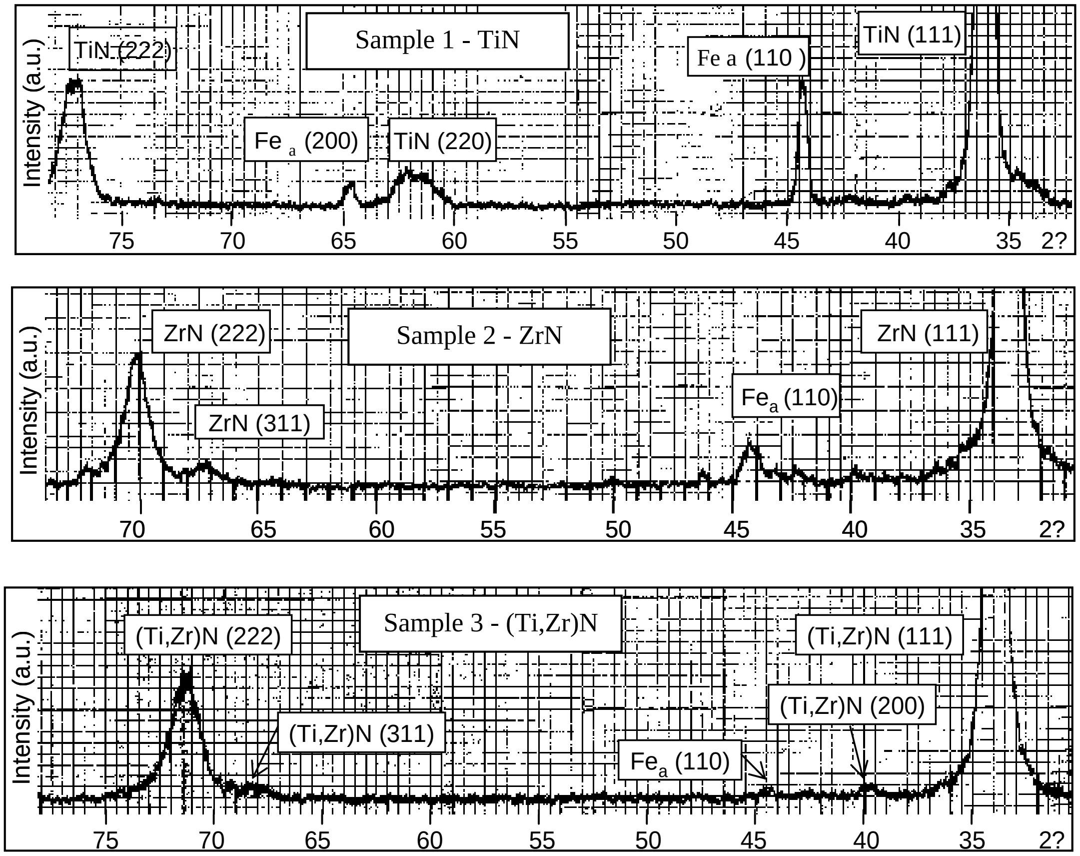

Fig.1 X-ray diffraction patterns of the coatings

Vickers microhardness $HV_{0.03}$ and critical loads L_c are presented in Table 3. It would be noticed that highest microhardness values were found for (Ti,Zr)N coating. It can also be seen that in general all films exhibited a good adhesion (L_c = 38N).

Table 3 Microhardness and adhesion of the coatings

Sample No	Coating	$HV_{0.03}$	L_c (N)
1	TiN	2280	46
2	ZrN	1920	38
3	(Ti,Zr)N	2720	40

3.2 Corrosion resistance

Time evolution of the free corrosion potential V_{corr} of the coated 316L stainless steel samples is shown in Fig.2. For comparison, the corrosion behavior of an uncoated sample is also illustrated. As compared with the uncoated sample, the TiN and ZrN coatings exhibited good corrosion behavior: the free corrosion potential is stabilized at relatively high positive values very soon after the beginning of the experiment. For the ternary compound (Ti,Zr)N the corrosion resistance was not better than that of the steel substrate. Moreover, fluctuations of the potential were observed, indicating the presence of a pitting corrosion process.

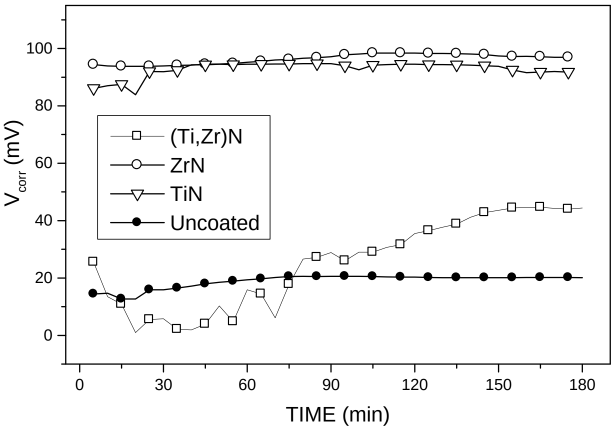

Fig. 2 Corrosion resistance of the coatings

3.3 Wear resistance

The wear resistance of the coatings in artificial physiological solution is illustrated in figures 3 – 4.

The maximum sliding distance L_{max} (the distance at which the damage of the coating occurs, commonly associated with a marked increase of the friction coefficient) was different for various coatings (Fig. 3). It can be seen that all coatings exhibited almost the same L_{max} values (2200-2500 m). It is interesting to note that though the (Ti,Zr)N had the highest microhardness (~2700 $HV_{0.03}$), this did not result in the highest wear life.

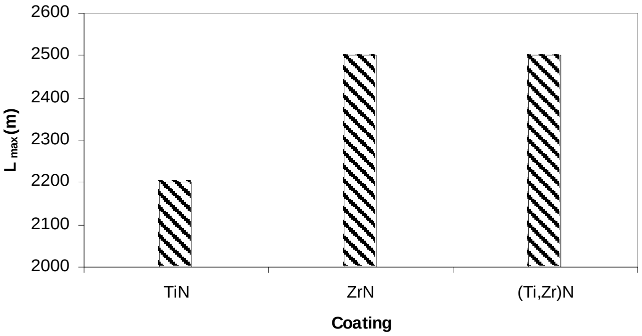

Fig.3 The maximum sliding distance L_{max} of the coatings

The wear behavior of the coatings can also be examined in Fig.4, where the volume loss from the roller as a function of the sliding distance is shown.

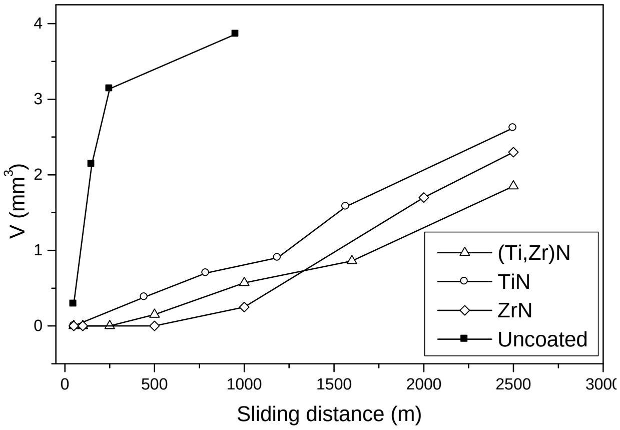

Fig.4 Wear resistance of the coatings as a function the sliding distance

The most important result is that all coated rollers exhibited a better wear resistance in comparison with that of the uncoated roller. Only slight differences in the wear behavior of various coatings were found. However, for a sliding distance up to 2500 m, at which the single layer coatings began to flake, the best wear resistance was found for (Ti,Zr)N , followed by ZrN and TiN.

If we take into account the results from both corrosion and wear experiments we can say that the ZrN coating revealed the best behavior

4. Summary and conclusions

Coatings of transition metal nitrides (TiN, ZrN, (Ti,Zr)N) were deposited on 316L substrates in order to enhance the corrosion and wear resistance in artificial physiological solution of austenitic stainless steels. Corrosive behavior was appreciated by means of an electrochemical test, while for the wear resistance experiments a testing apparatus consisting mainly of a rotating coated roller pressed on a flat specimen was used. The coatings were also characterized with respect to elemental composition, phase composition, texture, microhardness and adhesion.

Chemical composition analysis showed that nitrogen /metal ratio values were in the range 0.83 – 1.14. For the (Ti,Zr)N film, Zr content was much higher than that of Ti (Ti/Zr = 0.45). All films exhibited a strong (111) preferred orientation ((111), (200), (220), (311) and (222) diffraction lines were detected). Vickers microhardness $HV_{0.03}$ values were in the range 1920 (for ZrN) – 2720 (for (Ti,Zr)N). A good adhesion of the films was found (critical loads of 38 – 46 N were measured).

As compared with the uncoated sample, the binary compounds TiN and ZrN exhibited a superior corrosion and wear resistance. The (Ti,Zr)N coating showed to be the most wear resistant coating, but had not a corrosion behavior better than that of the stainless steel substrate.

REFERENCES

[1] S. Black, “Biological performance of materials: fundamental of biocompatibility”, 3rd edition, Ed. Dekker, New York (1999)
[2] J.Helsen, H.Breme, Metals as Biomaterials, Ed.Wiley, New York (1998)
[3] D.Hill, Design Engineering of Biomaterials for Medical Devices, Ed.Wiley, New York (1998)
[4] Handbook of Vacuum Arc Science and Technology, Ed.R.L.Boxman, D.M.Sanders, P.J.Martin, Noyes Publications, Park Ridge, N.J.U.S.A. (1995)
[5] M. Balaceanu, M. Braic, D.Macovei, M.J.Genet,A.Manea, D.Pantelica, V. Braic,F.Negoita, J.Optoel.Adv.Mat., **4/1** (2002) 107
[6] N.M.Mustapha, R.P.Howson, Vacuum, **60** (2001) 361

Micro Plasma Thruster Using Azimuthally Symmetric Surface Wave Discharges Excited by Microwaves: A Numerical and Experimental Study

Y. Takao, K. Ono, K. Takahashi and Y. Setsuhara

Department of Aeronautics and Astronautics, Graduate School of Engineering, Kyoto University, Kyoto, Japan

Abstract

This paper presents numerical and experimental investigations of the microplasma excited by azimuthally symmetric surface waves and its application to ultra small thrusters on next-generation small spacecrafts. The numerical results showed that the power efficiency to establish microplasma depends on applied microwave frequency and on relative permittivity of the dielectric chamber walls. The Ar plasma discharges excited by 2.45-GHz microwaves in a quartz tube 4 mm in inner diameter were observed in the experiment.

1. Introduction

In recent years, there has been a growing interest in developing microplasma sources [1, 2]. Miniaturized sources of gaseous plasma have applications in microsystems including mass spectrometers, thrusters, plasma displays, and so forth. Such microplasma sources are now obtained by dc plasma, capacitively coupled plasma (CCP), inductively coupled plasma (ICP), and microwave-excited plasma discharges. For space systems, the ongoing trend has been focused on decreasing the mass, dimension, and overall complexity to reduce the mission cost [3, 4]. The microspacecraft concept has supported a new approach to develop accurate, reliable, and low-cost micropropulsion systems. Small satellites less than 100 kg have already been launched, and some research is on going for several kg, and even less than 1 kg satellites. Such very small crafts require micropropulsion systems particularly for high-accuracy station-keeping and attitude control.

This paper presents a numerical and experimental study of a microplasma thruster. We have employed azimuthally symmetric surface wave discharges excited by microwaves because of their simple structure as a plasma source. The plasma source has no electrodes to generate plasma, which makes us expect long lifetime; in practice, for example, dc arc jet thrusters have a serious lifetime problem caused by the erosion of electrodes. The low power to sustain plasmas is also one of the advantages of a microwave plasma source. The microplasma thruster presented here consists of a plasma source and a micro nozzle. The plasma source serves as a high enthalpy reservoir with atmospheric pressures, and the micro nozzle changes a subsonic flow into a supersonic flow. The plasma source is composed of a cylindrical dielectric tube made of quartz glass (its relative permittivity ε_d = 3.7) or ceramics (ε_d = 10), whose outside is covered with a metal grounded, as shown in Fig. 1. The diameter and length of the tube are a few millimeters and a centimeter, respectively. The nozzle has a converging and diverging section, whose shape leads to a supersonic flow at the exit of the nozzle, and we use argon for a working medium. The numerical model consists of two modules; (i) an electromagnetic model and (ii) a fluid model. The former gives the combination of a volume-averaged global model [5] and a two-dimensional cylindrical (*r*-*z*) analysis based on the finite-difference time-domain (FDTD) approximation to Maxwell's equations and nonmagnetized plasma-electron equations [6], to predict the characteristic of plasmas in the reservoir; on the other hand, the latter gives a two-dimensional fluid analysis based on the compressible two-temperature Navier-Stokes equations, to analyze the plasma flow inside the nozzle [7, 8]. A preliminary experiment was also conducted to confirm the plasma discharges

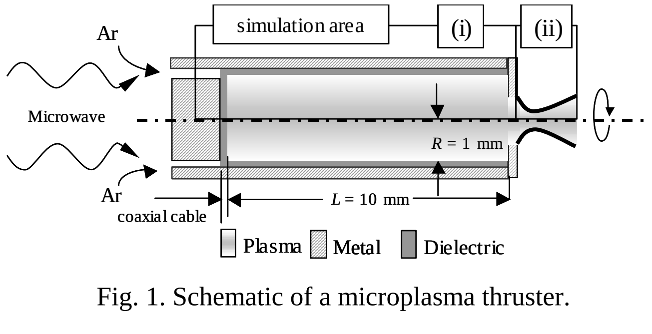

Fig. 1. Schematic of a microplasma thruster.

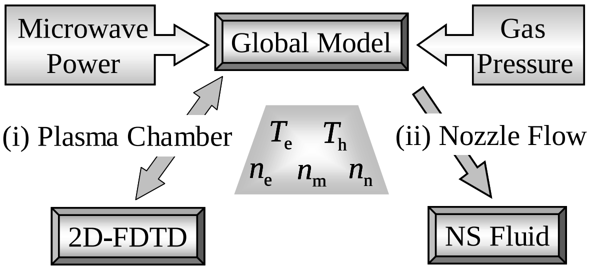

Fig. 2. Numerical flowchart.

excited by microwaves inside a small quartz tube.

2. Numerical Model

The numerical flowchart of the present simulation is depicted in Fig. 2. Given the plasma absorbing power and pressure in the plasma chamber, we employ the global model to obtain plasma parameters, such as electron density, temperature, and metastable density. We also employ the FDTD analysis of electromagnetic waves in the chamber with the parameters obtained. Then, we calculate plasma flow characteristics in the micro nozzle by solving the two-temperature Navier-Stokes equations, where the plasma parameters in the chamber are used for the inlet boundary condition of the micro nozzle flow.

2.1. Micro plasma chamber

The plasma chamber concerned is 1 mm in radius and 10 mm in length. The global model is employed not only to obtain the relationship between the plasma absorbing power and electron density, but also to take account of the effect of particle diffusion to the tube walls, because the effect cannot be neglected owing to the high ratio of the surface area to volume of the chamber. Moreover, the volume recombination is also taken into account using the principle of detailed balancing and Saha's equilibrium equations since the plasma is generated at atmospheric pressures,. The dependence of plasma density and other parameters on absorbing power is determined by solving the energy and particle balance equations. At atmospheric pressures of interest, the continuous wave heated plasmas tend to be in thermal equilibrium because of frequent collisions between electrons and gas molecules [9], and so we assume that the electron temperature is equal to the heavy particle temperature. The reactions taken into account in the present simulation are:

$$\mathrm{Ar} + \mathrm{e}^- \leftrightarrow \mathrm{Ar}^+ + 2\mathrm{e}^-, \tag{1}$$

$$\mathrm{Ar} + \mathrm{e}^- \leftrightarrow \mathrm{Ar}^* + \mathrm{e}^-, \tag{2}$$

$$\mathrm{Ar}^* + \mathrm{e}^- \leftrightarrow \mathrm{Ar}^+ + 2\mathrm{e}^-, \tag{3}$$

In the FDTD analysis, we solve the following set of equations consisting of Maxwell's equations and plasma-electron equations with a given uniform density,

$$\nabla \times \mathbf{B} = \mu_0 \mathbf{j} + \varepsilon_0 \mu_0 \frac{\partial \mathbf{E}}{\partial t}, \tag{4}$$

$$\nabla \times \mathbf{E} = -\frac{\partial \mathbf{B}}{\partial t}, \tag{5}$$

$$m_\mathrm{e} \frac{\partial \mathbf{u}_\mathrm{e}}{\partial t} = q_\mathrm{e} \mathbf{E} - m_\mathrm{e} \nu_\mathrm{eff} \mathbf{u}_\mathrm{e}, \tag{6}$$

$$\mathbf{j} = q_\mathrm{e} n_\mathrm{e} \mathbf{u}_\mathrm{e}, \tag{7}$$

where **E** and **B** are the electric and magnetic fields, respectively, **j** is the plasma current density, ε_0 is the electric permittivity of vacuum, μ_0 is the magnetic permeability of vacuum, q_e is the electron charge, m_e is the electron mass, ν_eff is the effective electron collision frequency, and $\mathbf{u}_\mathrm{e}$ is the electron velocity. The central differencing based on Yee's method [10] is applied to Eqs. (4) - (7). Under the assumption of $\partial/\partial\theta = 0$ or the azimuthal symmetry of the configuration, only the transverse magnetic (TM) waves occur with $\mathbf{E} = (E_r, 0, E_z)$ and $\mathbf{B} = (0, B_\theta, 0)$. The simulation area for FDTD consists of the plasma chamber and a coaxial cable as shown in Fig. 1, being 1.5 mm in radius by 15.5 mm in length. We solve these equations with $\mathbf{j} = \mathbf{0}$ except the plasma region, and ε_0 is multiplied by the relative permittivity ε_d in the dielectric region.

2.2. Micro nozzle

We make a two-dimensional, cylindrical, compressible flow analysis, where the plasma is treated as a two-phase, two-temperature medium that consists of heavy particles (neutral atoms, ions, and metastables) and light particles (electrons). The mass of electrons are so small that their momentum can be neglected in comparison with the heavy particles' momentum, and both phases are assumed to have the same convective velocity field. In these descriptions on the model, the following assumptions are made: (a) the flow is laminar and axisymmetric; (b) the plasma is quasi-neutral; (c) the radiative energy transfer is negligible;

(d) heavy particles have the same temperature; (e) the sheath structure is negligible. Thus, the plasma flow of interest is macroscopically described by the following set of equations:

$$\frac{\partial}{\partial t}\rho + \nabla\cdot(\rho\mathbf{u}) = 0, \tag{8}$$

$$\frac{\partial}{\partial t}(\rho\mathbf{u}) + \nabla\cdot(\rho\mathbf{u}\mathbf{u}) = -\nabla p + \nabla\boldsymbol{\tau}, \tag{9}$$

$$\frac{\partial}{\partial t}n_{\mathrm{e}} + \nabla\cdot(n_{\mathrm{e}}\,\mathbf{u}) = \nabla\cdot(D_{\mathrm{a}}\nabla n_{\mathrm{e}}) + J_{\mathrm{Ge}} - J_{\mathrm{Le}}, \tag{10}$$

$$\frac{\partial}{\partial t}n_{\mathrm{m}} + \nabla\cdot(n_{\mathrm{m}}\,\mathbf{u}) = \nabla\cdot(D_{\mathrm{m}}\nabla n_{\mathrm{m}}) + J_{\mathrm{Gm}} - J_{\mathrm{Lm}}, \tag{11}$$

$$\frac{\partial}{\partial t}\left(\frac{3}{2}n_{\mathrm{h}}k_{\mathrm{B}}T_{\mathrm{h}}\right) + \nabla\cdot\left(\frac{3}{2}n_{\mathrm{h}}k_{\mathrm{B}}T_{\mathrm{h}}\,\mathbf{u}\right) = -p_{\mathrm{h}}(\nabla\cdot\mathbf{u}) + \boldsymbol{\tau}:\nabla\mathbf{u} + \nabla\cdot\mathbf{q}_{\mathrm{h}} + Q_{\mathrm{elas}}, \tag{12}$$

$$\frac{\partial}{\partial t}\left(\frac{3}{2}n_{\mathrm{e}}k_{\mathrm{B}}T_{\mathrm{e}}\right) + \nabla\cdot\left(\frac{3}{2}n_{\mathrm{e}}k_{\mathrm{B}}T_{\mathrm{e}}\,\mathbf{u}\right) = -p_{\mathrm{e}}(\nabla\cdot\mathbf{u}) + \nabla\cdot\mathbf{q}_{\mathrm{e}} - Q_{\mathrm{elas}} - Q_{\mathrm{ion}} - Q_{\mathrm{ex}}, \tag{13}$$

$$p = n_{\mathrm{e}}k_{\mathrm{B}}T_{\mathrm{e}} + (n_{\mathrm{i}} + n_{\mathrm{m}} + n_{\mathrm{n}})k_{\mathrm{B}}T_{\mathrm{h}} = n_{\mathrm{e}}k_{\mathrm{B}}T_{\mathrm{e}} + n_{\mathrm{h}}k_{\mathrm{B}}T_{\mathrm{h}}, \tag{14}$$

where ρ, p, T, n, k_{B}, $\mathbf{u}$, τ, and $\mathbf{q}$ are the density, pressure, temperature, number density, Boltzmann constant, convective velocity vector, stress tensor, and heat flux vector, respectively. J_{G} is the particle source term and J_{L} is the particle loss term. The subscripts, e, i, n, m, and h stand for electrons, ions, neutral atoms, metastables, and heavy particles, respectively. Moreover, D_{a} is the ambipolar diffusion constant for ions and electrons, D_{m} is the diffusion constant for metastables, Q_{elas} is the net volumetric energy exchange between electrons and heavy particles through elastic collisions, Q_{ion} is the energy sink for ionization of neutral atoms or the source for ion-electron recombination, and Q_{ex} is the energy loss or gain through inelastic excitation of heavy particles. The viscous dissipation term is neglected in comparison with p_{e} in Eq. (13).

In these calculations, the plasma parameters at the nozzle inlet are taken from the results of the global model. The inlet radial velocity is assumed to be zero, while the inlet axial velocity is obtained by extrapolation from the interior. In practice, all valuables are calculated based on an extrapolation from the interior points at the exit, even though some portion of the exit flow near the nozzle walls is subsonic. The wall is assumed to be adiabatic, where the no-slip condition is used despite a relatively Knudsen number near the exit. Here, the Knudsen number is defined as the ratio of the mean free path to the characteristic length of the flow field.

3. Preliminary Experiments

A schematic of the experimental apparatus is shown in Figs. 3 and 4. The micro plasma source, made of a quartz tube 4 mm in inner diameter, is installed inside a stainless-steal chamber. The quartz tube is connected to a stainless-steal pipe through which argon gas is introduced. The 2.45-GHz transverse electromagnetic (TEM) waves are injected into the quartz tube through a semi-rigid type coaxial cable, and deposit the power into the plasma. A set of mechanical booster and rotary pumps are used in operation.

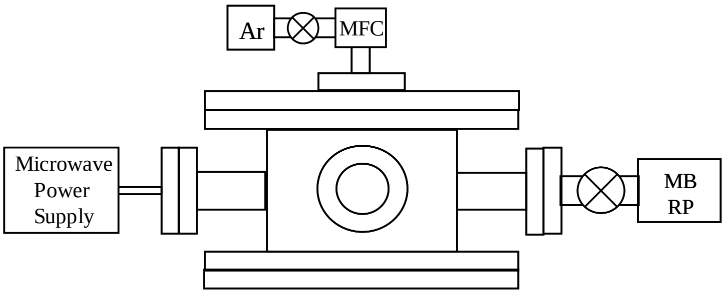

Fig. 3. Schematic of the experimental apparatus.

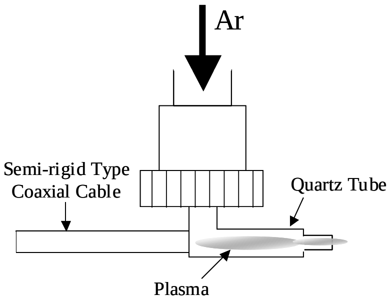

Fig. 4. Schematic of the setup inside of the chamber.

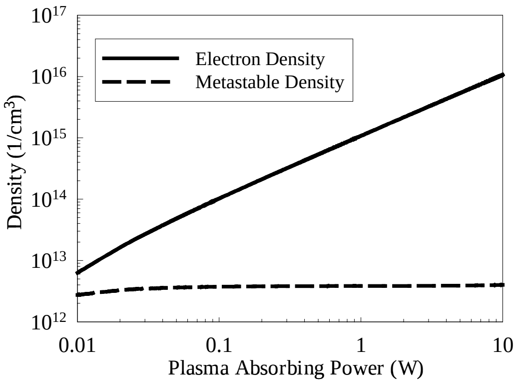

Fig. 5. Relationship between the plasma absorbing power and the particle densities.

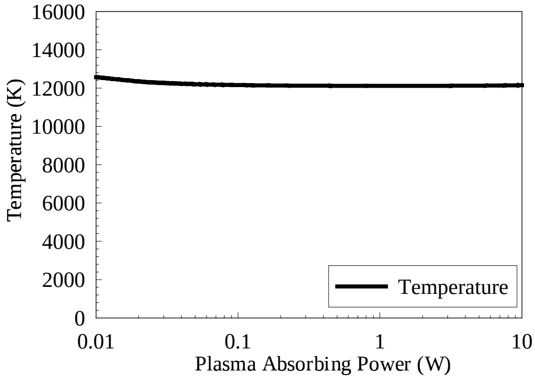

Fig. 6. Relationship between the plasma absorbing power and the temperature

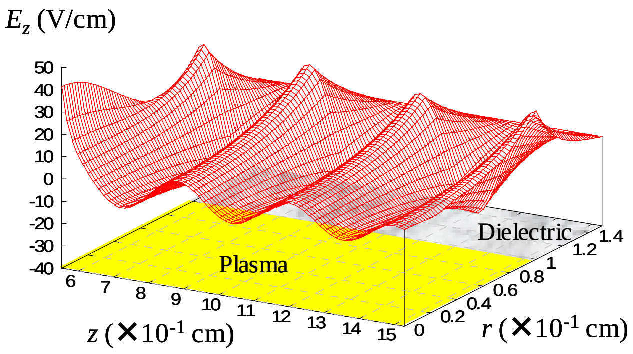

Fig. 7. Snapshot of the two-dimensional distribution of the axial component E_z of electromagnetic waves.

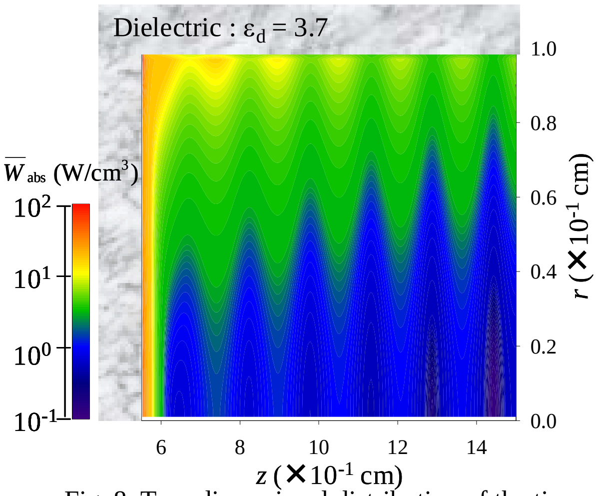

Fig. 8. Two-dimensional distribution of the time averaged power deposition per unit volume.

4. Results and Discussion

4.1. Plasma simulation in the micro plasma chamber

The global model and FDTD analyses were performed at the chamber pressure $p = 1.0 \times 10^5$ Pa for different plasma absorbing powers $P_{\rm abs}$ of f = 24.5-GHz microwaves, where the relative permittivity of the dielectric chamber walls is $\varepsilon_{\rm d}$ = 3.7. Figures 5 and 6 show the relationship between the plasma absorbing power and the electron density, temperature, and metastable density achieved, indicating that the electron density increases linearly with increasing power, whereas the temperature and metastable density remain almost unchanged.

Figure 7 shows a snapshot of the two-dimensional distribution of the axial component E_z of electromagnetic waves for $P_{\rm abs}$ = 0.1 W, where the electron density, the neutral density, and the electron and heavy particle temperature were $n_e = 1.0 \times 10^{14}$ cm $^{-3}$, $n_n = 6.2 \times 10^{17}$ cm $^{-3}$, and $T_e = T_h = 1.2 \times 10^4$ K, respectively; moreover, the ratio of the effective electron collision frequency to the microwave angular frequency was $\nu_{\rm eff} / \omega = 0.08$. Figure 8 shows the corresponding two-dimensional distribution of the time averaged power deposition per unit volume $\overline{W}_{\rm abs}$, where the cut-off density for surface waves is $n_{\rm cr} = 3.5 \times 10^{13}$ cm $^{-3}$. We can see that the axial electric field E_z decays exponentially in the radial direction from the plasma-dielectric boundaries (R = 1.0 mm) to the plasma, indicating that the plasma is excited by surface waves discharges. The distribution of the averaged power deposition exhibits that the plasma almost absorbs the microwave power in the vicinity of the plasma-dielectric boundaries.

The simulations was also performed for different microwave frequencies and relative permittivities: f = 2.45, 5.0, 10.0, and 24.5 GHz and $\varepsilon_{\rm d}$ = 3.7, 10.0, and 50.0. Table 1 and Fig. 9 show the dependence of power

Table 1. Microwave input power to achieved the electron density as high as $n_e = 5.4\times10^{14}$ cm^{-3}, where P_{abs} = 0.5 W, $T_e = T_h = 1.2\times10^4$ K, $p = 1.0\times10^5$ Pa, and $n_n = 6.2\times10^{17}$ cm^{-3}.

	ε_d = 3.7	ε_d = 10	ε_d = 50
2.45GHz	107 W	12 W	2.3 W
5GHz	16 W	5.0 W	2.0 W
10GHz	5.3 W	2.5 W	1.7 W
24.5GHz	2.2W	1.4 W	1.1 W

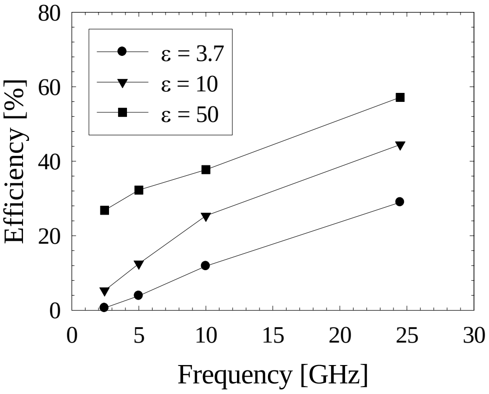

Fig. 9. Dependence of the power efficiency on microwave frequency and relative permittivity.

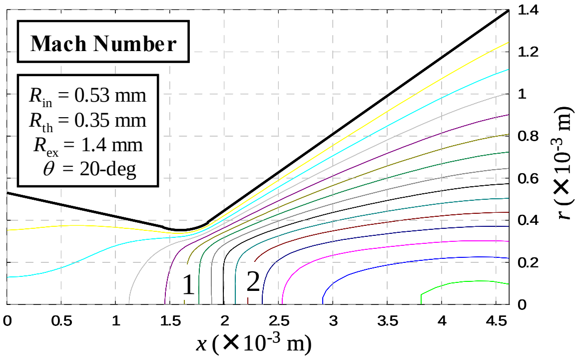

Fig. 10. Mach number contours for a 20-deg half-angle conical nozzle.

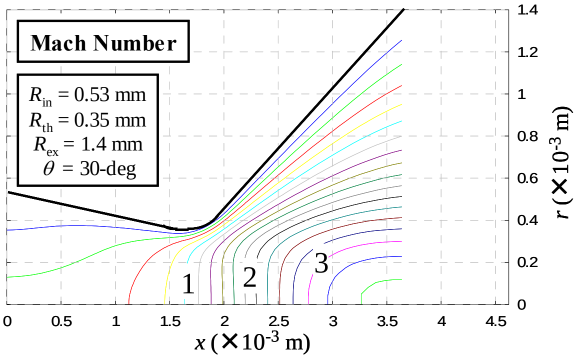

Fig. 11. Mach number contours for a 30-deg half-angle conical nozzle.

efficiency on microwave frequency and relative permittivity, where the power efficiency is defined as the ratio of the plasma absorbing power to microwaves input power. The table and figure demonstrate that higher microwave frequencies and higher relative permittivities of the dielectric tube lead to higher power efficiencies for the plasma source concerned.

4.2. Fluid simulation in the micro nozzle

Calculations were made for a chamber pressure of 0.1 MPa and a temperature of 12000 K, which were given by the global model. To check of the validity of the numerical solution, an integration scheme was used to confirm the conservation of mass. In practice, the rate of mass inflow across the entrance to the computational domain was compared to that of mass outflow across the exit plane; the deviation between mass flow rates at the entrance and the exit was less than 0.2 percent. We investigated the inside flow of two types of nozzles: one is a 20-deg. half-angle conical nozzle and the other is a 30-deg. half-angle conical nozzle, where both nozzles have the same area ratio of the inlet to the throat and of the exit to the throat; the inlet, throat, and exit radii are R_{in} = 0.53, R_{th} = 0.35, and R_{ex} = 1.4 mm, respectively.

Figures 10 and 11 show the Mach number contours for the two-type nozzles presently investigated, indicating that the subsonic inflow rapidly accelerates to supersonic through the converging-diverging nozzle and that the viscous layers along the nozzle walls are very thick. High gas temperatures lead to the high dynamic viscosity, and so the small scale of the nozzles gives a very small Reynolds number. Thus, although a quasi one-dimensional model based on the inviscid Euler equations gives an exit Mach number of 6, the present calculations show a considerably less Mach number, especially for the 20-deg. half-angle conical nozzle. The thrust and specific impulse are 44.4 mN and 330 sec, respectively, for the 20-deg. half-angle conical nozzle, while they are 44.1 mN and 328 sec, respectively, for the 30-deg. half-angle conical nozzle. Theses values are almost the same, because the viscous loss of the 20-deg. half-angle conical nozzle is larger than that of the 30-deg. one, while the divergence loss of the 20-deg. half-angle conical nozzle is smaller than that of the 30-deg. one. The thrust and specific impulse presently obtained are enough for very

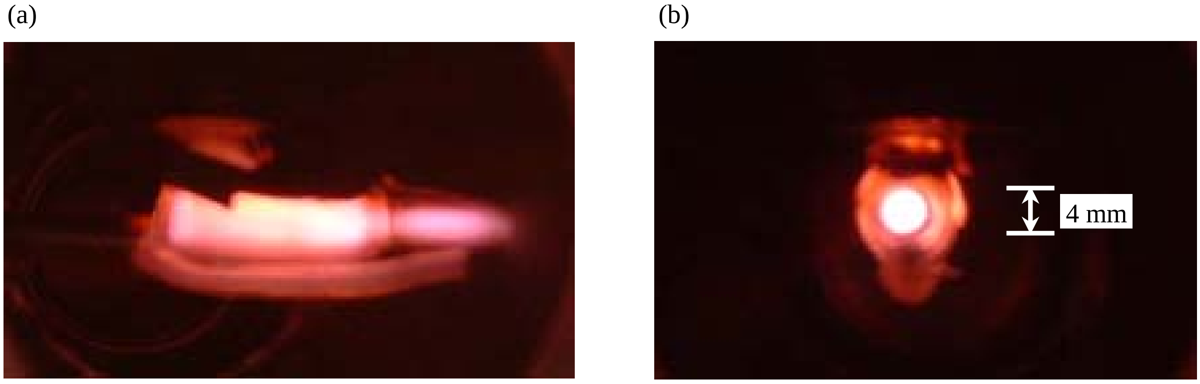

Fig. 12. Typical (a) side and (b) end views of Ar plasma discharges inside the quartz tube 4 mm in inner diameter.

small spacecrafts less than 1 kg; however, a more efficient shape of nozzles has to be investigated, and the chamber gas temperature should be lowered to reduce the viscosity near the walls, implying that we may require non-equilibrium high-pressure plasmas.

4.3. Experimental results

Figure 12 shows typical side view and end views of the discharge inside the quartz tube. The input power of 2.45-GHz microwaves was less than 10 W and the Ar gas flow rates was 5 sccm, where the back pressure inside the chamber was 45 mTorr. The plasma discharges ware established in the range up to 50 sccm (the maximum flow rate in the present apparatus) at the same microwave power. Further experiments are now underway.

5. Conclusions

Numerical investigations have been conducted to clarify the characteristic of micro plasma sources and that of micro nozzle flows. The volume-averaged global model and FDTD analyses were combined to simulate the micro plasma excited by azimuthally symmetric surface waves, and the two-temperature Navier-Stokes equations were solved for the flow in micro nozzles. The plasma simulation showed that the power efficiency to establish microplasmas depends on applied microwave frequency and dielectric relative permittivity. Higher microwave frequencies and higher relative permittivities of the dielectric tube lead to higher power efficiencies for the plasma source in the present configuration. The fluid simulation showed that the micro nozzle has a very thick viscous layer and that its thrust and specific impulse are typically 40 mN and 300 sec, respectively, which are enough for a very small spacecrafts (< 1 kg). We also made a preliminary experiment of the plasma discharges inside a micro quartz tube, and confirmed the plasma ignited and sustained inside the tube. Further experiments are now ongoing.

References

[1] J. Hopwood, O. Minayeva and Y. Yin - J. Vac. Sci. Technol. B **18**, 2446 (2000).
[2] A. M. Bilgic, U. Engel, E. Voges, M. Kückelheim and J. A. C. Broekaert - Plasma Sources Sci. Technol. **9**, 1 (2000).
[3] C. Rossi, M. D. Rouhani and D. Esteve - Sensors and Actuators A **87**, 96 (2000).
[4] D. H. Lewis Jr., S. W. Janson, R. B. Cohen and E. K. Antonsson - Sensors and Actuators A **80**, 143 (2000).
[5] M. A. Lieberman and A. J. Lichtenberg - *Princeples of Plasma Discharges and Materials Processing*, (Wiley, New York, 1994).
[6] H. Kousaka and K. Ono - Jpn. J. Appl. Phys. **41**, 2199 (2002); - Plasma Sources Sci. Technol. (2003), in press.
[7] S. C. Kim - Journal of Spacecraft and Rockets **31**, 259 (1994).
[8] J. J. Beulens, D. Milojevic, D. C. Schram and P. M. Vallinga - Phys. Fluids B **3**, 2548 (1991).
[9] A. Kono, T. Sugiyama, T. Goto, H. Furuhashi and Y. Uchida - Jpn. J. Appl. Phys. **40**, L238 (2001).
[10] K. S. Yee - IEEE Trans. Antennas Propagat. **14**, 302 (1966).

Preliminary study on plasma auxiliary coal gasification[*]

Mingdong Li, Weiwei Deng, Xiaolei Liu, Yonsan Fan

Department of Engineering Mechanics, Tsinghua University, Beijing, 100084, P. R. China

Gasification is an important means of clean and effective coal utilization. Gasification temperature is a principal factor that affects the gasification rate and thus the output per unit volume (OPUV) of gasification furnaces. In the conventional coal gasification methods where the system temperature is kept by the heat energy of coal combustion, the gasification temperature is usually not higher than 2000°C, so the OPUV is limited. Therefore, gasification furnaces employing conventional gasification methods for large-scale industrial equipments are usually bulky, which means high equipment investments and running costs and makes their manufacture and transportation very inconvenient. If an oxygen plasma torch that is rich of active particles is introduced into the conventional coal gasification methods as an auxiliary high-grade heat source, the gasification temperature can be raised to 3000K or higher, the concentration of active particles in the system can be largely enhanced, and the specific surface area of gasification can be increased because of explosion and fragmentation of coal particles caused by thermal stress and expansion pressure of volatile matter during rapid pyrogenation in the plasma torch. As a result of the above factors, an accelerated gasification rate and a higher OPUV can be obtained [1-4], which makes it possible to greatly reduce the equipment investments and running costs of large-scale gasification equipments.

C-H-O-N-S thermodynamic equilibrium systems on coal gasification are computed in this paper according to Zhao et al's means [5]. Calculation results show that: (I) in the equilibrium system in the temperature range from 1600K to 2500K, CO and H_2 are the principle components with the maximal total concentration above 98%, and the concentration of H_2 increases with the increase of the mole ratio H_2O/O_2; (II) at the temperature above 1600k, H_2S and N_2 are the main impurities with very low concentration not higher than 10^{-3}. Accordingly, it is appropriate to take the exit gas temperature of gasification furnaces as 1600K to obtain high-concentration CO and H_2, and the concentration of H_2 in the product gas may be higher at a bigger mole rate H_2O/O_2. Based on these results, a new scheme for plasma auxiliary coal gasification is addressed, where coal is supplied at twice into a two-stage gasification furnace with the exit gas temperature designed as 1600K. In the first-stage reactor, an oxygen plasma torch is introduced, and a portion of pulverized coal and corresponding oxygen are injected into the jet, which builds an active center with the average temperature between 3000K and 3300K permitted by refractory materials. In order to make full use of the heat energy above 1600K of the first stage's high-temperature gas, another portion of pulverized coal and corresponding water vapors are supplied near the entry of the second-stage reactor, because the water gas reaction is endothermic, which can adjust the exit gas temperature to 1600K and enhance the concentration of H_2 in the product gas as well.

Theoretical energy balance of this scheme is estimated, which shows that the plasma torch is only auxiliary with the electrical energy consumption of about 4% of the total coal heat value. Preparatory experiments are performed, which proves the feasibility of the new scheme.

[1] A. Cuesta, A. Martínez-Alonso, J.M.D. Tascón – Carbon, **39**, 1135-1146(2001)
[2] A.F. D'yakov, E.I. Karpenko - Thermal Engineering, **45**, 467-472(1998).
[3] D. Sasongko, J.F. Stubington - Chemical Engineering Science, **51**, 3909-3918(1996).
[4] R.A. Halinenko, A.P. Kuznekor, A. Levitsky et al - Plasma chem. and Plasma Proc., **13**, 141-167(1993).
[5] M.Y. Zhao, B.K. Xu - Calculation of complex chemical equilibrium (In Chinese), Jilin Univ. press, (1990).

---

[*] Grateful acknowledgements are made to the National Natural Science Foundation of China (No.19935010) and the Special Funds for Major State Basic Research Projects (G1999022106)

Study on quenching rate in process of coal pyrolysis in hydrogen plasma to produce acetylene[*]

Mingdong Li, Bo Dai, Weiwei Deng, Xiaolei Liu, Yonsan Fan

Department of Engineering Mechanics, Tsinghua University, Beijing, 100084, P. R. China

According to computation results of C-H thermodynamic equilibrium systems as shown in Fig.1, acetylene is the most principal hydrocarbon in C-H equilibrium system in the temperature range from 2800K to 3800K, but its concentration is much lower when the temperature is less than 2000K [1]. If pulverized coal is injected into a hydrogen plasma jet that is rich of active hydrogen atoms, acetylene will be directly produced through fast heterogeneous reactions [2], which may realize the efficient conversion from coal to chemical products because acetylene is an important basic material of organic chemical industry. However, the concentration of acetylene will drop down largely if the pyrolyzed products of coal is cooled slowly following the equilibrium path. In order to prevent the acetylene produced at high temperature from decomposing, the pyrolyzed products must be quenched in time to the temperature at which acetylene is steady [1, 3]. Maximal yield of acetylene may be acquired by selecting adequate quenching rate, which is estimated in this paper by employing a chemical dynamic method.

Acetylene's thermal decomposition reaction appears to be second order at the point of view of chemical kinetics [4], so the decomposition reaction rate can be written in the Arrhenius form as folllows:

$$-\frac{d[C_2H_2]}{dt} = k[C_2H_2][C_2H_2] \qquad (1)$$

where $[C_2H_2]$ represents acetylene's concentration in the reaction system, t represents time, and k is the reaction rate constant.

Quenching processes applied in plasma processes generally have the similar quasi-exponent time-temperature history [5], so the decrease of temperature in the quenching process could be assumed to follow an exponent form, i.e.

$$T = (T_0 - T_w) \times \exp(-t/\tau_q) + T_w \qquad (2)$$

where T_0 and T_w represent the beginning temperature and the ending temperature of quenching process respectively (T_w is taken as 300K in this paper), and τ_q is defined as quenching time constant. According to equation (2), the quenching rate in this paper is defined as the variation rate of temperature at the beginning of the quenching process, i.e.

$$Q=(T_0-T_w)/\ \tau_q \qquad (3)$$

By assuming that the system has already reached thermodynamic equilibrium condition before the beginning of quenching process, the effects of quenching processes with different quenching rates on preventing acetylene from decomposing are calculated according to the above model. It is shown that fixing ratio of acetylene (defined as the ratio of the final acetylene's concentration to the initial one at the beginning of quenching process) increases with the lowering of the beginning temperature of quenching process and the increasing of quenching rate. In order to obtain high yield of acetylene in the product gas, the optimal quenching process should begin at the temperature between 3000K and 3500K with an initial quenching rate of $(0.77\sim5.8)\times10^8$K/s, which can retain above 90% of the acetylene in the high-temperature equilibrium system.

Keywords：Acetylene, Coal, Hydrogen plasma, Quenching rate, Chemical dynamics

[1] B. Dai, Y.S. Fan, J.Y. Yang et al - Chem. Eng. Sci. **54**, 957-959(1999).
[2] D. Bittner, W. Wanzi - Fuel Processing Technology. **24**, 311-316(1990).
[3] M.D. Li, Y.S. Fan, B. Dai et al - Thin Solid Films. **390**, 170-174(2001).
[4] J.H. Kiefer, W.A. Von Drasek - International Journal of Chemical Kinetics. **22**, 747-786(1990).
[5] W.J. Pitz, C.K. Westbrook - Combustion & Flame. **63**, 113(1986).

---

[*] Grateful acknowledgements are made to the National Natural Science Foundation of China (No.19935010) and the Special Funds for Major State Basic Research Projects (G1999022106)

Properties of silicon based deposit realized by Glow Dielectric Barrier Discharge

Steve Martin, Serge Carré, Christel Jimenez, Nicolas Gherardi and Françoise Massines

Laboratoire de Génie Electrique, Université Paul Sabatier, Toulouse, France

Abstract

The aim of this work is to determine the properties and to understand the growth mechanisms of silicon-based coatings realised with an atmospheric pressure glow dielectric barrier discharge. Mixtures of SiH_4 and N_2O, diluted in N_2 to reach the atmospheric pressure, are used to obtain silicon oxide thin films. The deposits are characterized through thickness measurements, SEM observations, ellipsometry and infrared spectroscopy.

1. Introduction

Rather than plasmas at low pressures, the discharges operating at atmospheric pressure allow the exposure of substrate material to the plasma without the requirement of expensive vacuum devices. The main advantages are that materials can be treated on-line in a continuous manner at ambient temperature. Dielectric barrier discharge (DBD), operating at atmospheric pressure, can be used to produce thin film coatings [1-5]. Among the different DBD, the glow one leads to homogeneous and well-controlled surface treatment. The optimisation of this new surface process requires a large understanding of the discharge physics which has been largely initiated previously [6-7]. This discharge is obtained in rare gases and in nitrogen. To realise surface treatments, a small amount of reactive gas is added to the vector gas. The criterion is that the reactive gas percentage does not significantly change the discharge physics i.e. the glow regime is kept, and neither streamers nor discharge localisation occurs. As this physics depends a lot on the density of the main gas metastables, the maximum proportion of reactive gas is dependent on its ability to quench the metastables. As for example, the O_2 concentration in N_2 is limited to 500ppm [8] while several thousands ppm of N_2O can be added.

The GDBD behaviour is intermediate between that of low-pressure glow discharge and that of low temperature plasma at atmospheric pressure. The electron density is lower than $10^{11}/cm^3$ but the mean free paths are in the range of micrometers. The first step is to determine the specificities of thin films realised with GDBD. For that first step we choose to work with silane and nitrous oxide diluted in nitrogen. The objective is to elaborate SiO_2-like deposit. This material is suitable for many applications as microelectronic, optics, foods packaging, … Our approach consists in studying the coating properties as a function of the reactive gas decomposition and transformation level. The other parameters of this study are the silane and nitrous oxide rates and the plasma power. After the description of the experimental set-up, results concerning the structure and the chemistry of the coating are presented and discussed.

2. Experimental set-up

The dielectric barrier discharge used to elaborate the deposits is a low-frequency discharge obtained between two parallel electrodes, both covered by a dielectric layer (figure 1). The substrate (2 inches intrinsic silicon wafer) is placed on the lower electrode which is maintained to a potential near to the walls one, avoiding the formation of an electric arc outside of the discharge.

After a primary vacuum of 10^{-1} Pa, the vessel is filled up to atmospheric pressure (10^5 Pa) with nitrogen. Total gas flow (a N_2-SiH_4-N_2O mixture) of 5l/min is then added and the atmospheric pressure is kept by a slight pumping. A longitudinal gas injection is chosen in order to study both the silane and nitrous oxide molecular decomposition and the consumption from the gas inlet side to the outlet (figure 1). For this purpose, the different layer characterizations have been performed as a function of the distance from the discharge edge at the side of the gas inlet.

The coating thickness is measured with a Tencor profiler after a step has been made by etching the deposit with a HF solution. The thickness measurement resolution is lower than 1nm. Refractive index is determined ex-situ with a Jobin Yvon UVISEL ellipsometer. Results have been analysed assuming a multi-layer structure with a Bruggman approximation. Each layer is a mixture of air and SiO_2. Results validity is checked by comparing the sum of the thickness of layers with the one measured with the profiler. The chemical composition is determined by FTIR and XPS. FTIR spectra are obtained with a Perkin Elmer 1760-

x, providing a resolution of 4 cm^{-1}. The spot size (Ø=2mm) allows a space resolution. Surface has also been analysed with a XPS Scienta 200 using the monochromatized AlKα line. The analysed area is 0.2 x 4 mm^2.

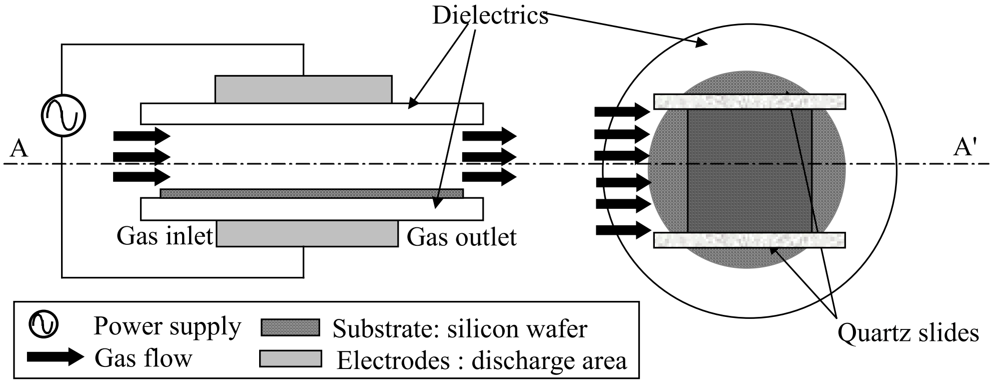

Figure 1: schematic diagram of the reactor

Most of the results shown in this paper have been obtained with a power, W, dissipated in the gas gap equal to 3.4 W/cm^3 which corresponds to a power per surface unit (Ws) equal to 0.34W/cm^2. Silane and nitrous oxide are diluted in N_2 with a rate of respectively 5 and 400 ppm. It is interesting to note that the partial pressure of reactive gases (0.5 Pa for SiH_4 and 40 Pa for N_2O) is about the same as that used in RF-low-pressure plasmas. The N_2 flow rate is 5l/min. The gas velocity, calculated assuming that the flow is laminar, is 2.6m/s. Then, for a molecule located at 10 mm from the gas inlet, the residence time in the discharge is about 3.9 ms, and the associated energy (t x W) is 13mJ/cm^3 or 1.3 mJ/cm^2. When not indicated, the deposit duration is 20 min.

3. Results

Figure 2 shows the thickness profile as a function of the position. The thickness is not constant, as usual for a longitudinal injection because the reactive gases are progressively consumed. However, the occurrence of two maxima lets think that there are two different growth mechanisms which have different kinetics. The first maximum is very close to the gas entrance in the discharge (1-2 mm) while the second is 10 times further.

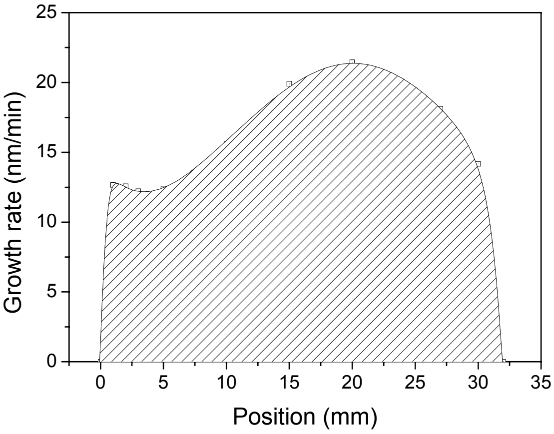

Figure 2: Growth rate profile with the distance from the gas inlet (W=3,4W/cm^3, SiH_4=5ppm, N_2O=400ppm)

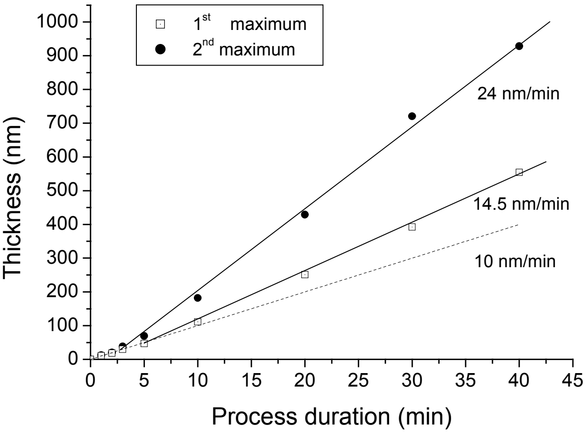

Figure 3: Thickness variation with the deposit duration at the first and the second profile maxima

The kinetic difference between the two maxima is confirmed by the figure 3 which shows the thickness variation of these two maxima as a function of the deposit duration. During the first minutes, the growth rate is 10 nm/min. Then, the slope of the thickness as a function of time increases to 14 nm/min for the first maximum and to 24 nm/min for the second one. Scanning electronic microscope pictures of the coating section at the two maxima (Figure 4a, 4c) for 20 min. deposit confirms the difference between the coating properties. For residence times shorter than 1.2ms (3mm), a columnar coating is observed in agreement with an island nucleation followed by a growth due to neutral or ionised light-siliconed radicals. For residence time longer than 6 ms (15mm) the layer appears like small particles (ø=20nm) heap. In between, the roughness is higher and large aggregates of 230 nm are observed at the surface (figure 4b). The basis element of these aggregate has about the same diameter has the particles which make the second maximum.

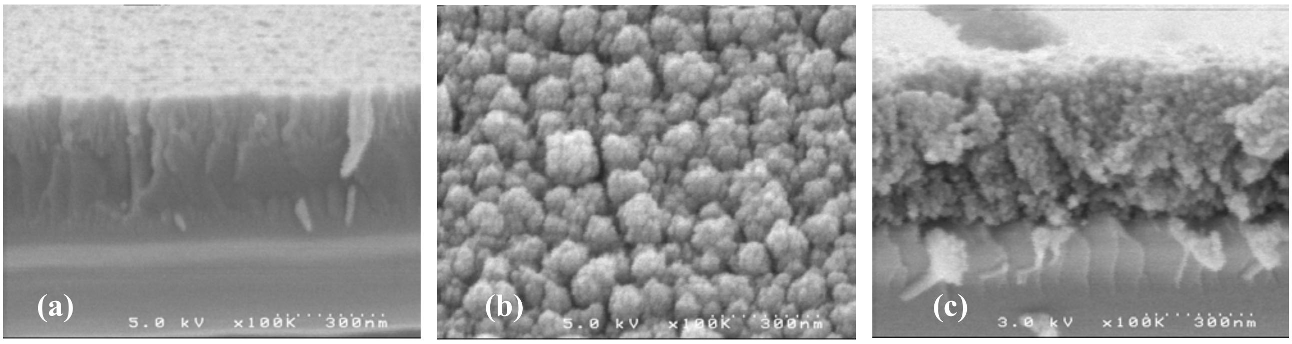

Figure 4: SEM pictures of (a) the coating section at the first maximum (b) the coating surface in between the two maxima (c) the coating section at the second maximum

To try to understand that behaviour, the chemical composition has been studied through XPS and IRTF measurements. XPS analysis shows that whatever the position on the sample, no N is introduced in the coating, and O/Si ratio is about 2.4. The decomposition of the O and Si peaks shows that they are constituted of only one component respectively centred at 533.2 eV and 103.8 eV which corresponds to SiO_2 environment. IRTF spectra confirm that the coating chemical composition does not significantly change with the position on the sample. Spectra are that of silica. The Si-O-Si rocking, bending and stretching vibrations are observed. Si-H and Si-N are never observed, whatever the position. H_2O and Si-OH are detected in the range of 950 cm-1 and 3000-3800cm-1. Water and Si-OH concentration are respectively 2 and 3 times higher at the second maximum. But the largest difference concerns the shift position and the Si-O-Si stretching peak width which indicates [9] that the Si-O-Si bound stress and the layer disorder significantly vary [10]. This is in agreement with the SEM pictures.

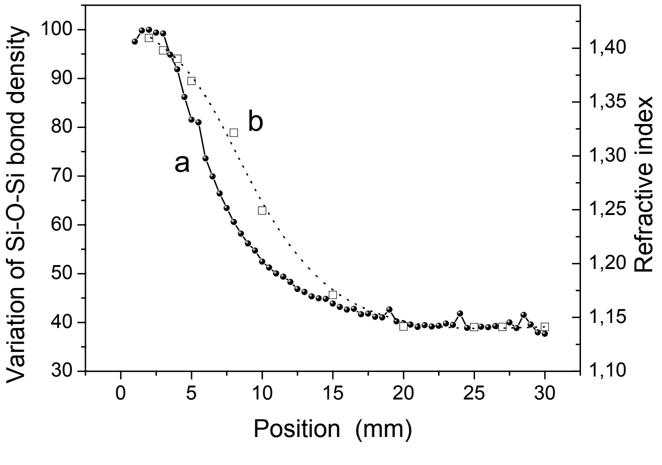

Figure 5: (a) Density of Si-O-Si bonds determined from the ratio of the Si-O-Si stretching FTIR peak area / thickness and (b) refractive index versus the distance from the gas inlet

To try to quantify the coating density variation, the density of Si-O-Si bonds has been determined by dividing the area of Si-O-Si stretching peak by the coating thickness. The Si-O-Si concentration (Figure 5a) decreases by more than a factor 2 from the entrance to the outlet. Ellipsometry results (Figure 5b) confirm that conclusion. The refractive index, drastically decreases with the gas residence time and the sample porosity varies from 0,1% at the first maxima to 65% at the second one.

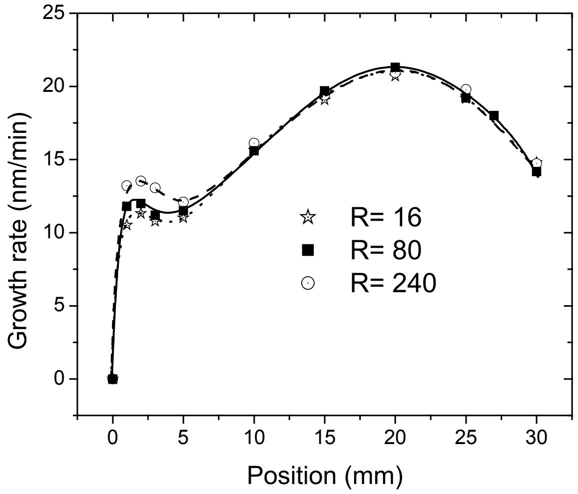

Figure 6: Growth rate profiles with the distance from the gas inlet for different N_2O/SiH_4 ratios R

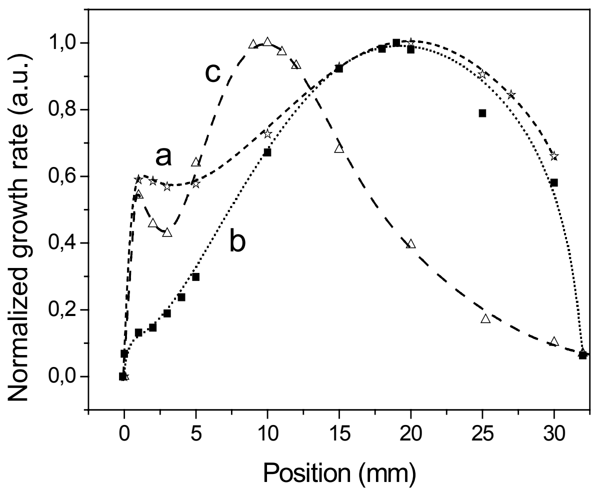

Figure 7: Thickness profile normalized on their maximum as a function of the distance from the gas inlet for (a) W=3.4 W/cm^3, SiH_4=5ppm, (b) SiH_4= 40 ppm, W=3,4W/cm^3, (c) W= 14,5 W/cm^3, SiH_4= 5ppm

The N_2O/SiH_4 ratio has been varied from 4 to 240. As it can be seen on figure 6, it does not influence the maxima position or the second maximum growth rate. However, it slightly changes the growth rate of the first maximum. Keeping the N_2O rate equal to 400 ppm, the SiH_4 rate has been increased up to 40ppm. As shown in figure 7, the maxima position does not change even if the growth kinetic significantly increases, from 15 to 35 nm/min for the first maximum and from 26 to 800nm/min for the second one. The power has also been varied by a factor close to ten: from 0.166 W/cm^2 to 1.45 W/cm^2. When it increases, the second maximum tends to be closer to the gas entrance and the growth rate increases too.

4. Discussion

It clearly appears that the gas residence time in the GDBD has no significant effect on the chemical composition of the coating but it drastically changes the layer porosity and structure. An increase of the gas residence time induces a decrease of the layer density and the Si-O-Si bond angle. These observations have to be related to the GDBD optical emission spectroscopy [5]. The gas analysis shows that emission related to SiH_4 radicals are observed even for very short gas residence time. Then, the GDBD is able to very quickly dissociate the SiH_4. When a silane radical is created, it can (i) reach the surface and stick on it (ii) make a collision with an other radical and begin to nucleate a particle (iii) stick on a particle. The probability of each of these mechanisms depends on particles density and on the distance between the surface and the radical. As the radical mean free path is in the range of micrometer, only those created very close to the surface will reach it, the others being at the origin of particles nucleation or growth. After a while, all these radicals are consumed at the surface. The flow being laminar and the diffusion coefficient rather low, no more radicals are able to reach the surface. During that time, particles grow in the gas bulk and participate more and more to the coating. Then, a possible explanation of our results is that the first maximum is due to radicals created in a kind of boundary layer close to the surface while the radicals created in the gas bulk leads to the formation of particles. In the boundary layer, close to the gas entrance, the gas is continuously renewed, and then radicals significantly contribute to the growth leading to a dense layer (figure 4a). Then, the roughness area occurs (figure 4b). In that area, both radicals and particles reach the surface inducing the formation of large aggregates because the particles are linked by the radicals. At the end, no more radicals reach the surface. Only particles contribute to the deposit (figure 4c) leading to the second maximum structure made of particles heap. Then, we can considered that two mechanisms contribute to the GDBD coating growth: the first one is based on radicals, the second one on small size (20nm in diameter) particles. Particles growth being homogeneous, it is more rapid than the surface growth which explained the difference between the growth rate at the first and the second maxima (Figure 3).

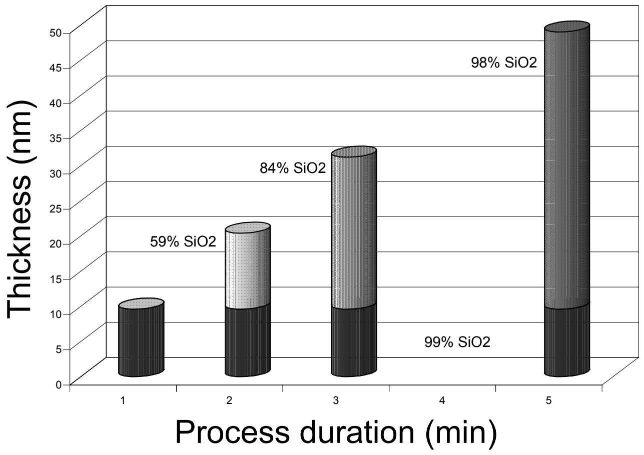

Figure 8: Thickness and density of the 2 layers model used to analyse the ellipsometry measurements made at the first maximum for 4 different deposit durations

Another special feature of figure 3 is the growth rate variation between 3 and 5 minutes of deposit. Ellipsometry measurements realised at the first maximum for different process duration allows to understand it. Figure 8 represented the thickness and density of the 2 layers deduced from the ellipsometry analysis at the first maximum position. It shows that during the first minute a dense layer (99% of SiO_2) of 10 nm thick is formed. For longer deposit duration, this layer is covered by a coating of variable density: SiO_2 percentage increases from 60% to 98% at 5 minutes while the thickness of that part of the coating increase from ten to 40 nm. According to the literature [11], such a variation of the growth rate can be attributed to an island growth: at first the deposit is constituted of small islands. These islands size increases due to a 3D growth which induces a density increase. Then they coalesce leading to a more or less flat surface on which the growth rate is higher because there is no more hole to fill. The growth becomes a 2D one. This behaviour is not observed at the second maximum: first there is a 10nm dense layer then the coating thickness increases and becomes less and less dense. Then, a possible explanation of the growth rate variation at the second maxima is a variation of particles sticking coefficient on the surface.

The residence time associated to each of these mechanisms depends on the power but neither on the SiH4 concentration nor the N_2O/SiH4 ratio. Concerning the N_2O/SiH_4 ratio, it is interesting to note that in the range considered here (from 4 to 240), it does not influence at all what happened at the second maximum. On the other hand, by plotting the growth rate at the first maximum versus the N_2O/SiH_4 ratio (figure 9), it clearly appears that this growth rate is limited by the amount of N_2O for values of N_2O/SiH_4 lower than 16. This shows that for low N_2O/SiH_4 ratios, the SiH_4 decomposition is limited by the amount of oxidizing species created in the discharge.

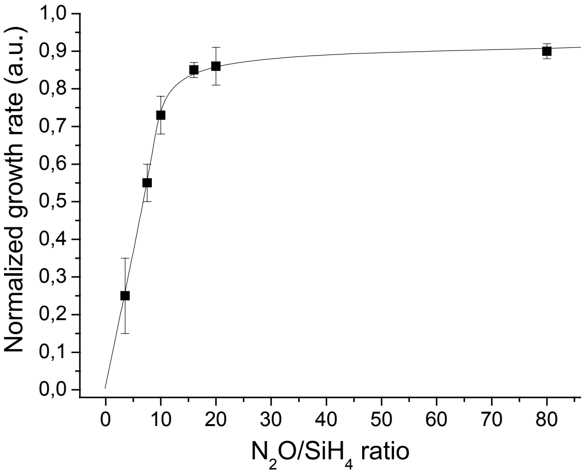

Figure 9: Relative growth rate variations at the first maximum as a function of the N_2O/SiH_4 ratio

According to the thickness profile (Figure 7a, 7b), when the silane rate increases, the particle kinetic is not affected but their density drastically increases: the contribution of the second mechanism is proportional to the square of the SiH_4 concentration.

When the power increases, the particle kinetic is more rapid as shown by the position of the second maximum (figure 7b, 7c). This can be attributed to a larger dissociation of SiH_4 molecules. In the same time, the growth rates at both maxima increase. However, the growth rate at the first maximum saturates for high power values (figure 10a) while the growth rate at the second maximum increases linearly (figure 10b). This can be explained taking into account the fact that precursors leading to the first maximum are coming from the boundary layer close to the surface. Then the results observed on figure 10 suggest that the SiH_4 present in this layer is entirely decomposed when the power is increased.

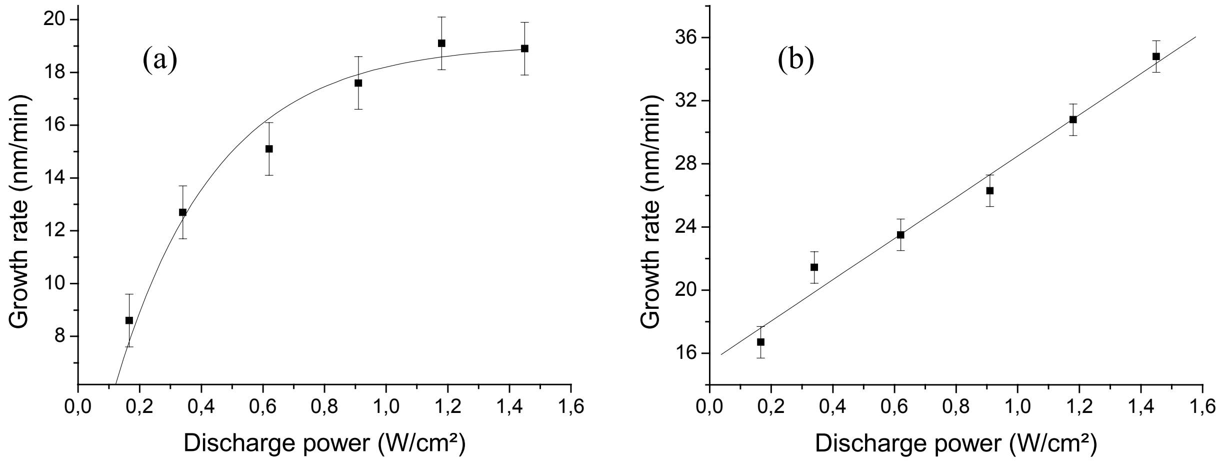

Figure 10: Growth rate as a function of the discharge power (a) at the first maximum (b) at the second maximum

5. Conclusion

In conclusion, the first important point is that a dense layer controlled by a radicalar growth is obtained with a glow dielectric barrier discharge. The second one is that particles of nanometric sizes can be introduced in the coating. However, the chemical composition of the coating due to radicals and that due to particles is the same. The experimental conditions in which these results have been obtained are compatible with a roll-to-roll system in controlled atmosphere.

References

[1] R. Foest, F. Adler, F. Sigeneger and M. Schmidt, *Surf. Coat. Tech.* **163-164** 323 (2003)
[2] Y. Sada, S. Ogawa and M. Kogoma, *J. Phys.D: Appl. Phys* **28** 1661 (1995)
[3] Thyen R., Weber A. and Klages C.P., *Surf. Coat. Techno.* **97** 426 (1997)
[4] A. Sonnenfeld, T. M. Tun, L. Zajickova, K. V. Kozlov, H. E. Wagner, J. F. Behnke and R. Hippler, *Plasmas-and-Polymers* **6(4)** 237 (2001)
[5] S. Martin, N. Gherardi, C. Jimenez et F. Massines, *Proc. 15th Int. Symp. Plasma Chemistry, ISPC 15,* Orléans (2001) p. 127
[6] N. Gherardi et F. Massines, *IEEE Transaction on Plasma Science* **29(3)** 536 (2000)
[7] F. Massines, P . Ségur, N. Gherardi, C. Khamphan, A. Ricard, *Surf. Coat. Technol.,* in press
[8] S.F. Miralaï, E. Monette, R. Bartnikas, G. Czeremuszkin, M. Latreche and M. R. Wertheimer, *Plasmas and Polymers* **5(2)** (2000).
[9] P.N. Sen and M.F. Thorpe, *Phys. Rev. B* **15** 4030 (1977)
[10] C.T. Kirk, *Phys. Rev. B* **38** 1255 (1988)
[11] K. Tsukamoto, D. Cheng, H. Komiyama, Y. Nishimoto, *Jpn. J. Appl. Phys.* **38** 68 (1999)

Scalable Multi-magnetron CVD Reactor

V.V. Dvorkin[1], N.N. Dzbanovsky[1], A.F. Pal[2], N.V. Suetin[1]

[1] Nuclear Physics Institute, Moscow State University, Leninskie Gory, Moscow, 119992, Russia
[2] Troitsk Institute for Innovation and Fusion Research, 142190, Troitsk, Moscow Reg., Russia

Abstract

A new approach is proposed solving the problem of the growth of large (more than 15 cm. in diameter) thin films. New method for creating of the scalable MW plasma reactor for thin films CVD is developed. Discharge is excited with system of magnetrons started one after another. Increasing amount of magnetrons it's possible to obtain plasma layer having desired square. On the built plant we got plasma layer of about 25 cm in diameter at pressures up to 10 Torr.

1. Introduction

Microwave plasma assisted chemical vapour deposition (MWCVD) the thin films is successfully used for a long time for creating of the different materials, particularly carbon films while other discharge types don't always comply with the requirements of microelectronics, technically complex or economically inefficient.

Uniform films production technologies used now don't let to grow thin films on squares more than some centimetres in diameter. Generation frequency of most widely used magnetrons is 2.45 GHz, which results in limitation of plasma ball size in 5-12 cm range. Attempts to increase of deposition area in the MWCVD system with the resonator type reactor by applying the larger wavelength led to sharp grow of the device price and operation cost. It should be noted that films of about 20 cm in diameter can be obtained in such devices [1]. Using of slot antenna structures [2, 3, 4] has the same problems.

One of possible ways of a microwave input in a reactor is usage of slow-wave circuits: comb-type profiles, concentric ribs and so on. For a long time it was offered to use such constructions in a microwave ovens. Applying of this principle to microwave CVD reactors allowed achieving of 20 cm in diameter plasma layer. Unfortunately, shortcoming of such systems is high cost and hard difficulties on a way of further extending of plasma layer and creation of non-planar discharge configurations.

The goal of our work was the development of a method of creation of a scalable plasma reactor for large size thin films MWPACVD having discharge excited by a system of synchronized magnetrons working in a pulse-mode regime. Such approach is attractive by cheapness of engineering implementation and flexibility of design solutions permitting to construct plasma reactors of the different configurations in compliance with the additional technological requirements.

In this work the possibility of enough homogeneous plasma creation on the space of 250 mm in diameter with aid of a system of "dotty" microwave emitters arranged near to a working surface of a reactor (outside of evacuated volume) was demonstrated. Plasma composition and uniformity was characterized with optical emission spectroscopy (OES), in a wide pressure range and in number of gas mixtures usually used during carbon thin films deposition.

2. Description of the experimental system

The flowchart of the system is presented on Fig. 1. Main parts of the device are: (1) reactor, (2) power supply units, (3) magnetrons unit, (4) flue gas path, (5) power absorber and (6) substrate holder.

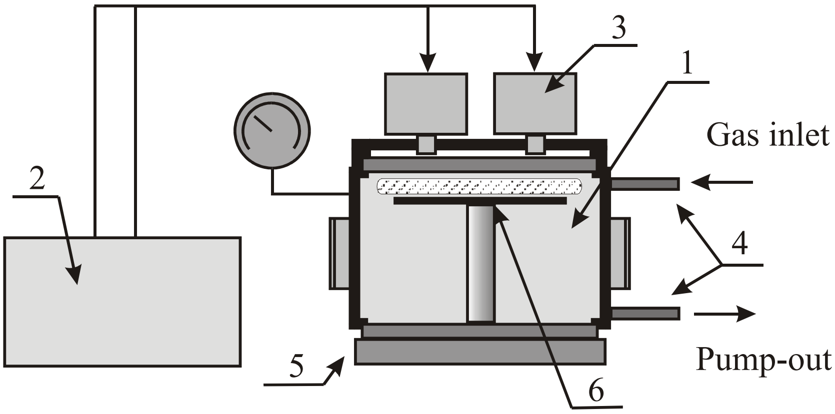

Fig. 1. System flowchart.

The reactor is a hollow cylinder of stainless steel with an inside diameter of 360 mm. It is cooled by running water. In a wall of the reactor there are inspection windows and a load port. From both butt ends the reactor is enclosed by quartz glass windows (QGW). Outside of the reactor from one butt end the power absorber is placed, and from another the magnetrons unit is arranged.

The power supply unit serves for high voltage (3-4 kV) producing, its fine control and distribution of power to all (from one up to four) magnetrons. It is possible to achieve a smooth variation of mean microwave power emitted by a separate magnetron from 100 up to 600 W. For exception of interference of magnetrons against each other the principle of time separation of magnetrons was realized. It enables to utilize advantages of the plasma excitation in pulse mode. In a time gap between pulses there is a recombination of ions and radicals. The difference between different plasma components' recombination velocities allows shifting the deposition process to formation of one or another material with aid of variation of pulses' parameters. Besides in a pulse mode it's possible to put in unit of plasma volume essentially larger power, than in a CW regime.

Thus, when using a pulse mode during films growth, a modulation frequency and on-off time ratio are additional macroparameters, defining channel of growth [5]. Applying to diamond films deposition the problem was studied in detail in [6]. The ability of a power supply unit allows achievement of a pulse mode of each magnetron with modulation frequency from 100 Hz up to 3 kHz having 2.5 kW pulse power.

The magnetrons unit consists of four magnetrons fixed in such a way the emitters are laid out on the duralumin disk at apexes of the square having 100 mm side, with centre situated on a reactor symmetry axis. The disc is fixed outside to one of butt ends of the reactor. As there is practically no reflecting surfaces on the way of the radiated wave, each magnetron works in conditions, when the load (plasma and the power absorber), nearly completely absorbs electromagnetic energy. It releases the system from necessity for decoupler. In the device the standard cheap magnetrons, used in home microwave ovens, insensitive to reflected power is utilized. For the increase of a generation mean power the magnetrons are furnished with water cooling, that allows to double the emitting power.

The power absorber is indispensable for removal, whenever possible, reflex of microwaves emitted by magnetrons that promotes more uniform plasma combustion and moderates likelihood of malfunctions in generation. The power absorber is microwave transparent vessel full of running water. The substrate holder was either 100 mm stainless steel disk or 180 mm in diameter ceramic heater, put 3-5 cm from QGW surface on quartz glass tube.

In our experiments we used H_2, H_2:CH_4 (usually utilized in carbon films growth processes) and H_2:CH_4:Ar gas mixtures under pressure ranging from 1 up to 10 Torr. Magnetrons modulation frequency was varied between 500 Hz and 3 kHz; on-off ratio was equal to 4. Average microwave power does not exceed 400 W per magnetron.

To characterize the discharge we used optical emission spectroscopy with aid of developed home made spectroscopy system which can control the wavelength range from 350 nm to 800 nm. System resolution was 0.05 nm that was achieved with B&M Spektronik BM-100 monochromator having 100 cm focal length and 0.83 nm/mm dispersion. The light-sensitive element was a Toshiba TCD1201 CCD linear sensor. Spectroscopy system was connected to the inspection port by way of quartz optical fibre equipped with the system of focusing lens. Spectra were collected and processed by the computer having spectral data analyzer program. To control the plasma uniformity with OES we used digital camera having objective closed with interference filter. In our experiments we had 658 nm, 515 nm and 431 nm Andover Corporation interference filters (bandwidth 10 nm) to view the spectral ranges in which H_α (n=3→n=2, 656.3 nm), C_2 ($d^3\Pi_g \rightarrow a^3\Pi_u$, 516.5 nm) and CH ($A^2\Delta \rightarrow X^2\Pi_r$, 431.4 nm) lines are arranged. Observation of the intensity emitted in every range by plasma can give the notion about film growth rate. At the same time picture obtained by division of pixels having coordinates (x, y) from photo made in one spectral range by (x, y) pixel from photo made in other spectral range can give the information about resulting film phase uniformity. Relative intensities of $[H_\alpha]$, $[C_2]$ and [CH] can be indicators of the relative concentrations of corresponding plasma specimen and, thus, serve for appraisal of different phase growth rates.

3. Results and Discussion

In our reactor and energy emitters configuration the plasma arises just under a magnetron under a quartz glass window, at a distance from side walls of the reactor and from a microwave emitter as well, near the maxima of an electrical field. Such field pattern could be explained with interference of a spatial electromagnetic wave and surface waves originating on a gas-quartz interface. To prevent arising of an undesirable plasma areas on the reactor edges, having small radius of curvature, we have installed a special ring-type electrode changing the configuration of an electromagnetic field in such a manner that plasma in peripheral area does not arise.

In 1 kHz one magnetron regime, at hydrogen pressure of 1 Torr, at smooth power increase up to 400 W the following evolution of plasma allocation near a quartz glass surface were watched: at 100 W the discharge ignited under the magnetron energy emitter. With the power increase the plasma was on all internal perimeter of the ring and forms a layer practically under all QGW surface. At the same time the intensity of glow under QGW surface at highest possible output of the magnetron rather essentially varied. With activation of remaining magnetrons at 200 W per magnetron the picture was a superposition of operation of separate magnetrons. As result, the rather uniform distribution of plasma on all QGW surface was derived. One can expect that with increase of an overall mean power up to 1.5 kW the plasma uniformity will improve well. Also we observed more plasma uniformity at lower pressures.

In order to ensure that no considerable distortion will be brought in plasma distribution under the QGW and, therefore, upon the substrate surface, we placed substrate holders of different diameters, from 100 mm up to 180 mm in working volume, in a region at the bottom of plasma layer. No obvious distortion (see Fig. 2 and Fig. 3) could be observed that gives us a reason to make a further OES experiments to characterize plasma uniformity without substrate.

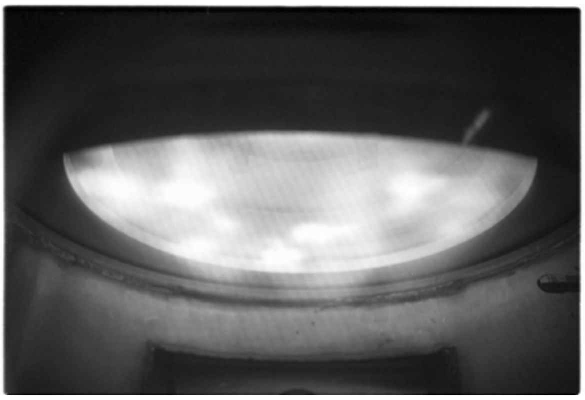

Fig. 2. Hydrogen plasma at 1 Torr without substrate holder

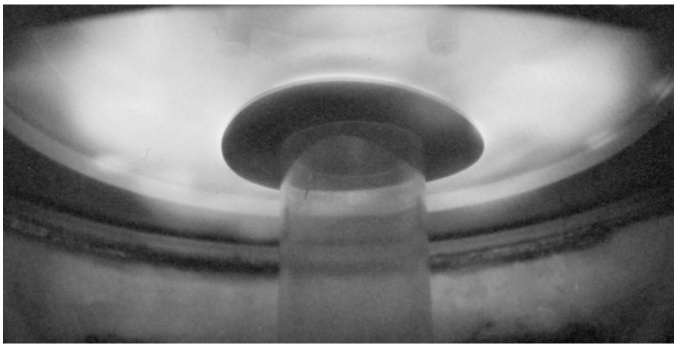

Fig. 3. Hydrogen plasma at 1 Torr with 100 mm substrate holder

With addition of the methane up to 16% the picture changes slightly (Fig. 4). Plasma luminescence uniformity for this case is shown on Fig. 5.

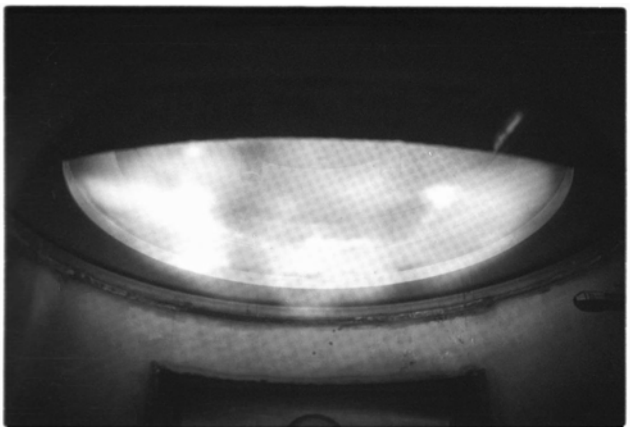

Fig. 4. The photo of the discharge (1 kHz, four magnetrons at 800 W, 1 Torr of H_2:CH_4)

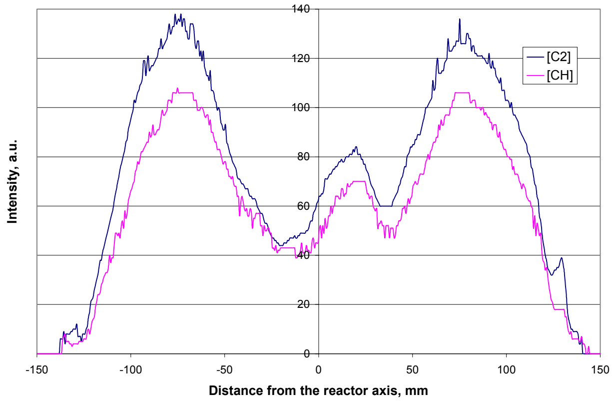

Fig. 5. [C_2] and [CH] intensities along QGW diameter at conditions given for Fig. 2

To make clear the uniform thin films growth possibility we have token some plasma pictures using interference filters and then we divided [C_2] photo by [CH] photo (as it was described in previous section). Experiments were carried out on modulation frequencies ranged from 800 Hz to 2 kHz. Resulting picture at 2 kHz is presented on Fig. 6. On Fig. 7 the cross section of Fig. 4 at QGW diameter is shown. A well uniform relative intensity distribution with variation no more than 10% was derived on diameter no less than 200 mm. This result makes us believe that grown film phase structure will have a good uniformity on square at least 200 mm in diameter.

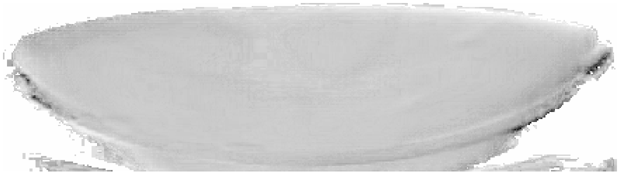

Fig. 6. [C_2]/[CH] picture of the discharge at 2 kHz

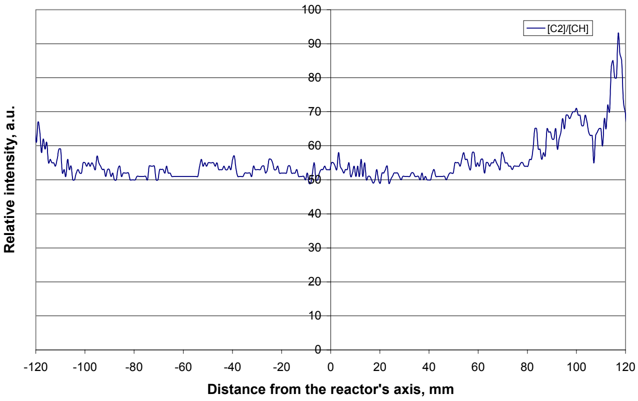

Fig. 7. [C_2]/[CH] graph along QC diameter at 2 kHz

In some papers devoted to thin films growth [7, 8] the positive role of an argon addition to hydrogen-containing microwave plasma was demonstrated. It's shown that the dilution of the feeding gas with an argon helps to increase the growth rates of films. At the same time its known, that addition of argon even in small (some percents) concentrations carry on to originating the plasma instabilities which influences negatively in uniformity and quality of a film.

We carried out a series of experiments in H_2:CH_4:Ar mixture at pressure of 10 Torr, both in continuous and pulse modes on a series of frequencies. The concentration of argon in our experiments was driven up to 75 %. In a continuous mode of plasma excitation we observed the great instability of a discharge that shows in form of arising of plasma filaments. In a pulse mode when the modulation frequency approaches to 1 kHz the discharge was completely steadied and plasma is shone under control in all range of concentration of argon. The carried out experiments have shown an advantage of the pulse way of plasma excitation at discharge stabilizing in our experimental conditions.

4. Conclusions

In our work we have designed and built the four-magnetron device, in working volume of the reactor it was obtained a flat layer of microwave plasma at the diameter of 250 mm. It was established, that with increase of microwave power the discharge becomes more homogeneous. Also, the stabilizing role of the pulse plasma mode is shown, by the example of H_2:CH_4:Ar plasma. Preliminary experiments have demonstrated ability to grow of homogeneous films on square of about 200 mm in diameter on the developed device. The ability to increase of the discharge square and square of grown films by means of installation of an additional magnetrons, working in time-sharing mode, is demonstrated.

With help of OES we have demonstrated that visible plasma heterogeneity on moderate power level will not result in film phase composition modification along film surface but can affect film growth rate. However, experiments that we carried out during the study show that effect of growth rate inequality could be extinguished with further power increase.

Acknowledgements

The work was supported in part by NATO SfP-974354 project and ISTC project No. 2484.

References

[1]. ASTeX, Technology overview. Published by Applied Science and Technology, Inc., Woburn, 1993.
[2]. M. Nagatsu et al., J. Phys. D: Appl. Phys. 33 (2000) 1143-1149.
[3]. M. Nagatsu et al., Jpn. J. Appl. Phys. 39 (2000) L929-L932.
[4]. Y. Yasaka et al., Plasma Sources Sci. Technol. 8 (1999) 530-533.
[5]. J. Khachan et al., Appl. Phys. Lett. Vol. 77 No. 19 (2000) 2973-2975.
[6]. L. de Poucques et al., J. Phys. D: Appl. Phys. 34 (2001) 896-904.
[7]. D. Zhou et al., J. Appl. Phys. 83 (1) 1998 540-543.
[8]. D. Zhou et al., J. Appl. Phys. 84 (4) 1998 1981-1989.

Hydrophobic/Hydrophilic Characterization of Plasma Polymerized Diglyme Thin Films

C. C. P. Rita, M. A. Algatti*, R. P. Mota, R. Y. Honda,
M. E. Kayama, E. C. Rangel and N. C. Cruz

Universidade Estadual Paulista "Júlio de Mesquita Filho", Faculdade de Engenharia, Departamento de Física e Química, Av. Ariberto Pereira da Cunha 333, Pedregulho, 12516-410, Guaratinguetá, SP, Brazil
*Corresponding author: (e-mail: algatti@feg.unesp.br, phone:(+55 12)31232841

Abstract

Polymeric Films were deposited from RF excited low-pressure $CH_3O(CH_2CH_2O)_2CH_3$ diethylene glycol dimethyl ether (diglyme) plasmas on polymethylmethacrylate, PMMA, substrates for RF power and pressure of 5 W and 12.6 Pa respectively. The results showed that the contact angle changed from 75 degrees to 45 degrees after diglyme deposition. These results suggest that the experimental conditions were profitable for producing hydrophilic biocompatible polymeric surfaces.

Keywords: Plasma polymers, hydrophilic coatings, diglyme plasmas

1. Introduction

Materials processing using low-pressure RF excited plasmas are of great importance in many current scientific and technological issues encompassing microelectronics, optical and biomaterials industries [1-10]. The main reason is that within such kind of plasmas electrons may attain an energy excess of some eV in comparison with the heavy particles present in the discharge. This unusual thermal non-equilibrium situation is very profitable in molecular fragmentation through electronic impact. This feature of such plasmas gives rise to a very reactive chemistry in a relative cold environment [4-8] whose kinetics is not easily controlled. Therefore is of paramount importance to set many plasma diagnostics in order to probe the trends of chemical species as well as the electrons behavior for different plasma parameters such RF power coupled to the plasma chamber, gas pressure, gas flux and so on [11-14].

In the field of biomaterials science and technology, plasma polymerized polyethylene glycol di-methyl ether is a material that has been keeping the attention of the scientific community due to its non-fouling properties [15-19]. If the appropriate plasma parameters are set these films may be synthesized keeping a molecular structure quite similar to the polyethylene oxide-like (PEO-like) with the advantage that these films are not soluble in water. The aqueous solubility of PEO makes it less appropriate in many biomaterials applications. In order to retain the monomer structure within the plasma deposited films and consequently its functionality, many different issues have been addressed in recent literature as for instance the film deposition under low mean RF power level by controlling the power supply on/off ratio [11,20], the decreasing of monomer residence time and consequently the reduction of its interaction with the plasma environment [20], the cooling of substratum with liquid nitrogen [13], the energy reduction of the ions reaching the substratum [14], and so on.

In order to set the appropriate experimental parameters that would result customized hydrophilic film structures in plasma polymerization of PEO-like coatings this paper deals with plasma polymerization of diglyme at relatively low RF power levels using PMMA plates as substrates. The trends of different chemical species were monitored through mass spectrometry [21]. The hydrophilic character of diglyme films was investigated using the contact angle measurements [22].

2. Experimental Setup and Plasma Diagnostics

The glow discharges were generated by a RF power supply operating in the range from 5 to 45 W in $CH_3O(CH_2CH_2O)_2CH_3$ (diglyme) atmospheres ranging from 16 Pa (120 mTorr) to 40 Pa (300 mTorr) within a stainless steel cylindrical, 210 mm of internal diameter and 225 mm long, parallel plate electrodes plasma reactor. This reactor is provided with eight lateral entrances, positioned at the mid plane between the electrodes, that may be used for setting optical, electrical and mass diagnostics and the low (mechanical pump) and high (turbo-molecular pump) vacuum systems. The vacuum inside the plasma chamber is monitored by pirani^{TM} (thermocouple) and penning^{TM} (inverse magnetrom) gauges. The turbo-molecular pump is coupled to the chamber through a gate valve and is used for cleanness purposes. The pressure is pumped down to 1.33 x 10^{-4} Pa (10^{-6} Torr), being the chamber purged with argon several times before each running of the experiment. The inner side of the plasma chamber was polished up to the optical quality (roughness of 0.5 microns or less) in order to minimize the retention of impurities and facilitate the cleaning process. The plasma chamber walls were heated with a temperature- controlled belt in order to minimize the monomer's condensation as well as the humidity. Diglyme was placed inside a stainless steel bottle and was fed into the plasma chamber through a needle valve. The plasmas were excited by a RF power supply operating in 13.56 MHz whose output intensity could be varied from 0 to 300 W (Tokyo HY-Power model RF-300^{TM}). The RF power was coupled to the plasma reactor through an appropriate matching network (Tokyo HY-Power model MB-300^{TM}) that allows one to minimize the reflected RF power. The mass spectrometry was realized using a mass spectrometer and energy analyzer (Hiden Analytical model EQP-300^{TM}), operating in the mass and energy range from 1 to 300 amu and from 0 to 100 eV respectively. The background mass spectra with the plasma turned off were carried out at the same pressure conditions of each diglyme plasma polymerization processes. These spectra allowed one to control the number of chemical species resulting from the fragmentation within the mass spectrometer as well as to control the presence of contaminants resulting from the plasma chamber cleaning process[21]. The block diagram of the experimental setup is presented in figure 1.

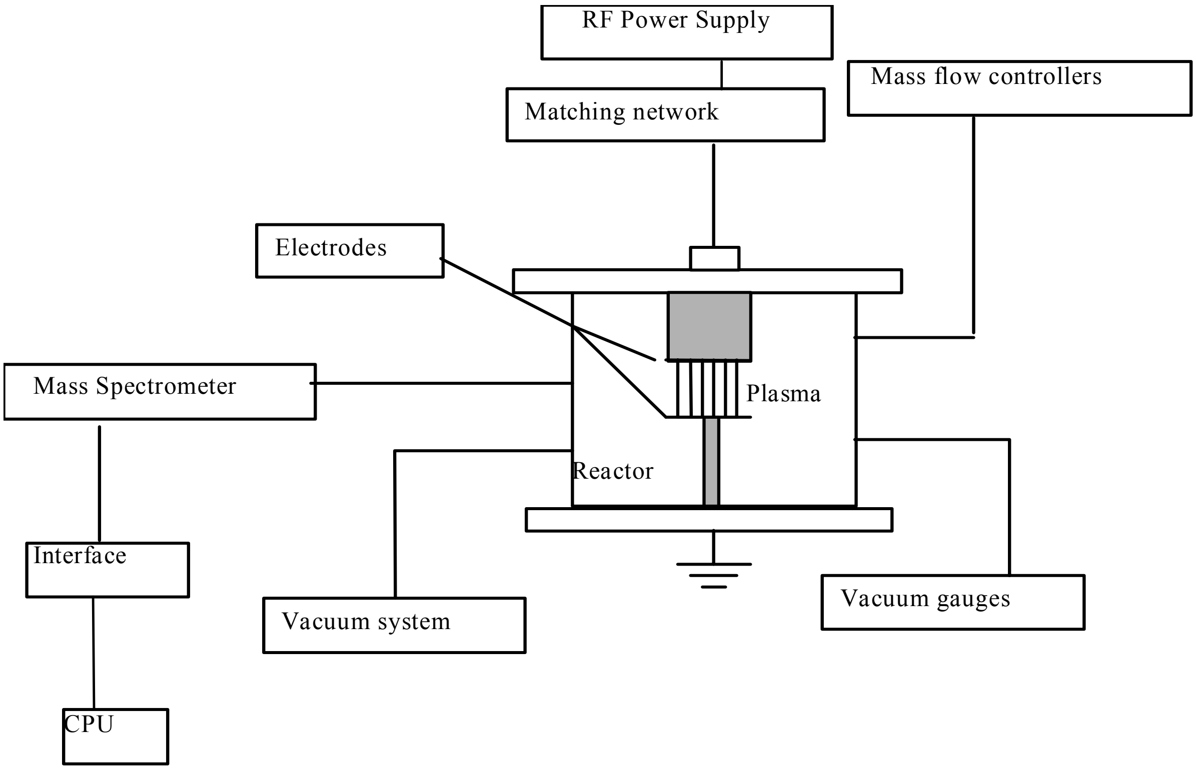

Figure 1. Block diagram of the experimental setup used in plasma polymerization of diglyme for different values of pressure and RF power coupled to the reactor.

The photograph of the stainless steel plasma chamber with the mass spectrometer coupled to it is shown in figure 2.

The hydrophobic/hydrophilic characteristics of plasma-polymerized diglyme were investigated through contact-angle measurements using water as a liquid probe. The contact angle measurements were carried out using an automated goniometer (Ramé-Hart 100-00). The apparatus, whose photograph is shown in figure 3, is composed by a CCD camera that allows one to record the image of a liquid drop (typically 0.2 µl in volume) put on the sample's surface by a syringe provided with an embolus that can be moved by a micrometer screw. An image-processing software (RHI 2001) was used for determining the liquid drop-surface contact angle.

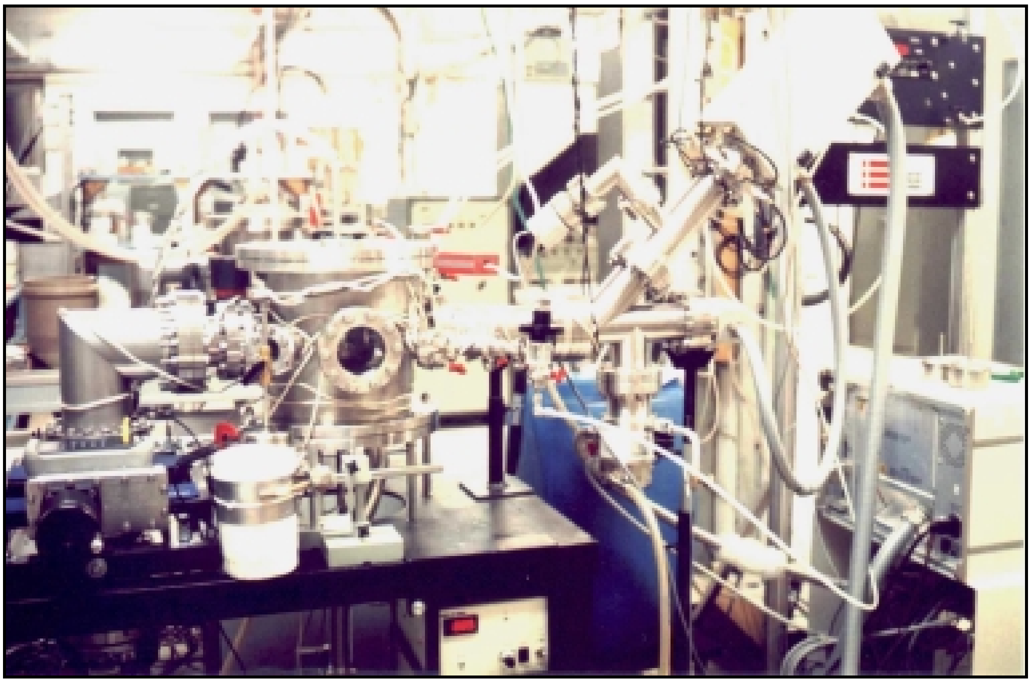

Figure 2. Photograph of the experimental setup used in plasma polymerization of diglyme for different values of pressure and RF power coupled to the reactor.

A picture of the liquid drop's image and the geometry used by the software for contact-angle determination is shown in figure 4. The contact-angle is defined by the straight line tangent to the semi-circle representing the liquid drop and the line parallel to the substrate-liquid drop interface as can be seen in figure 4 (right).

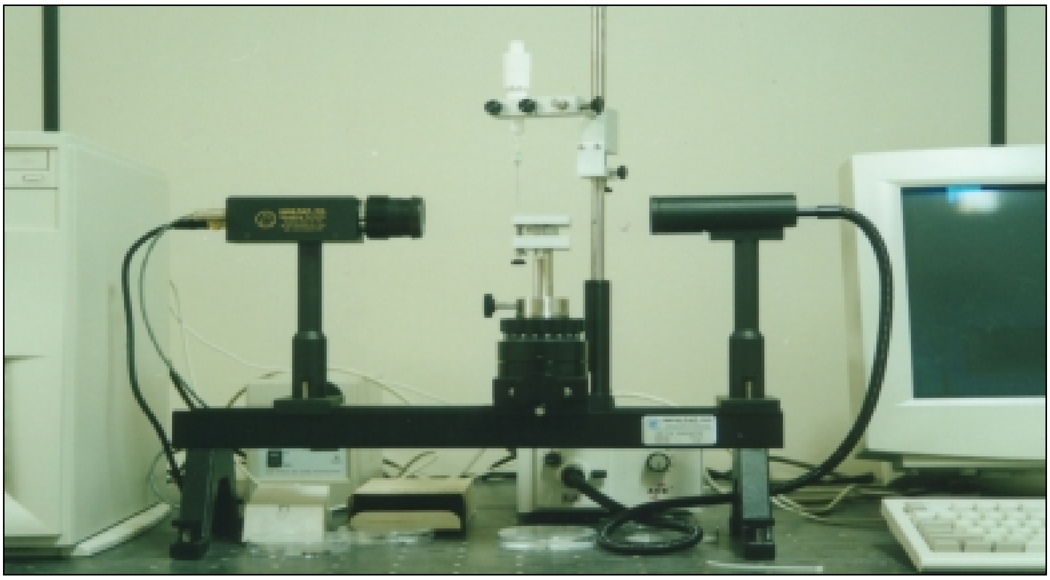

Figure 3. Photograph of the experimental setup used for water contact-angle measurements of plasma-polymerized hydrophilic coatings.

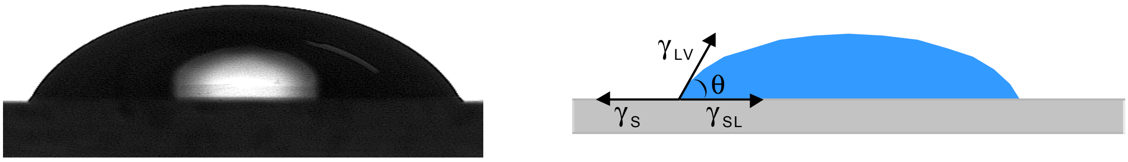

Figure 4. Photograph of the shadow of the water drop over plasma polymerized diglyme films deposited over PMMA substratum (left) and the geometry used for contact-angle measurements (right).

3. Results and Discussions

Figure 5 shows the contact angle (left) and surface energy (right) as a function of the days elapsed after the deposition of plasma-polymerized diglyme films over PMMA substrates. It may be appreciated that the initial contact angle of PMMA of 64^0 dropped to 55^0 after the deposition of plasma polymerized diglyme films. The hydrophilic characteristic of the films degraded as the post deposition period increased. The degradation of the hydrophilic characteristic occurs mainly due the rotation of polymeric chains at and nearby the polymeric film's surface. The recombination and neutralization of unbalanced chemical bonds of free radicals presented at polymeric film structure with oxygen contributes significantly for the decreasing of the surface energy of the film as can be appreciated in figure 5 (left). This behavior of the plasma polymerized diglyme films was observed for all samples. This suggests one that a post-treatment like PIII (plasma immersion ion implantation), for instance, is essential for polymeric chains stabilization at the surface as already was pointed out in recent literature [22].

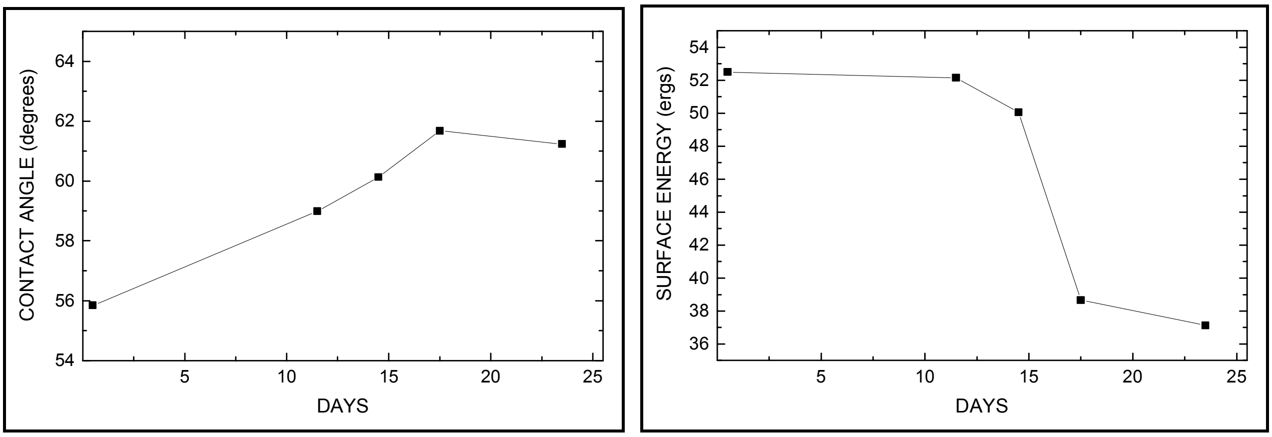

Figure 5. Time dependence of water contact-angle (left) and surface energy (right) for PMMA recovered with plasma-polymerized diglyme films.

4. Conclusions

One can conclude from the presented results that the operation of the plasma reactor at low RF power levels is appropriate if one wants to preserve the monomer functionality since it enhances the predominance of heavier chemical species within the discharge [21]. This is reinforced by the hydrophilic characteristic of diglyme films obtained for all samples soon after the deposition processes. The measurements of contact angle revealed that all samples aged recovering the initial contact angle value, i.e.; approximately the same value of the PMMA contact angle. As was already pointed out a post treatment of polymeric films surface must be carried out in order to stabilize the polymeric chains. The alternate use of plasma enhanced CVD and PIII techniques would provide a polymeric structure much more cross-linked that would keep the polar groups at the polymeric film's surface. The presence of such radicals would increase the coupling of PMMA surface with a polar liquid, like water for instance, that results in a small value of surface-liquid drop contact angle. Such kind of PMMA surfaces, in principle, would provide hard contact lenses as comfortable as a soft one. The hydrophilic diglyme polymeric films in principle would provide non-fouling polymeric surface that would make difficult the appearance of bacterial colonies [23,24].

Acknowledgments

The authors would like to thank FAPESP, (Fundação de Amparo à Pesquisa do Estado de São Paulo) for financial support and José Benedito Galhardo for technical assistance during the plasma chamber construction.

References

[1]– A. Bogaerts, E. Neyts, R. Gijbels and J. van der Mullen, Spectrochimica Acta **B57**, 609-658, (2002).

[2] R. J. Shul and S. J. Pearton (eds.) Handbook of Advanced Plasma Processing Techniques, Springer Verlag, Berlin, Germany, (2000).

[3] P. K. Chu, J. Y. Chen, L. P. Wang and N. Huang, Mat. Science and Engineering Reports **36**, 143-206, (2002).

[4]– R. d'Agostino, P. Favia and F. Fracassi (eds.) Plasma Processing of Polymers, NATO ASI series E: Applied Sciences vol. 346, Kluwer Academic Publishers, Dordrecht, The Netherlands, (1997).

[5]- N. Inagaki, Plasma Surface Modification and Plasma Polymerization, Technomic Publishing Company, Inc., Lancaster, USA, (1996).

[6]– H. Biederman and Y. Osada, Plasma Polymerization, Plasma Technology, vol. 3, Elsevier, Amsterdam, (1992).

[7]- R. d'Agostino (ed.) Plasma Deposition, Treatment and Etching of Polymers, Academic Press, Inc, San Diego, USA, (1990).

[8]- H. Yasuda, Plasma Polymerization, Academic Press, Inc., New York, USA, (1985).

[9]- B. D. Ratner and D. G. Castner (eds.) Surface Modification of Biomaterials, Plenum Press, New York, USA, (1997).

[10]– B. D. Ratner, A. S. Hoffman, F. J. Shoen and J. E. Lemons (eds.) Biomaterials Science: An Introduction to Materials in Medicine, Academic Press, San Diego, USA, (1996).

[11]– G. Cicala, M. Creatore, P. Favia, R. Lamendola and R. d'Agostino, App. Phys. Lett. **75**, 37-39, (1999).

[12]– P. Favia and R. d'Agostino, Surf. Coat. Technol. **98**, 1102-1106, (1998).

[13]– H. Biederman and D. Slavínská, Surf. Coat. Technol. **125**, 371-376, (2000).

[14]– R. Itatani, Plasm. and Ions, **1**, 37-44, (1998).

[15]– S. K. Hendricks, K. Kwok, M. Shen, T. A. Horbett, B. D. Ratner and J. D. Bryers, J. Biomed. Mater. Res. **50**, 160-170, (2000).

[16]– M. N. Mar, B. D. Ratner and S. S. Yee, Sensors and Actuators B **54**, 125-131, (1999).

[17]– C. S. Kwok, T. A. Horbett and B. D. Ratner, J. Control. Release **62**, 301-311, (1999).

[18]– G. P. Lopez, B. D. Ratner, C. D. Tidwell, C. L. Haycox, R. J. Rapoza and T. A. Horbett, J. Biomed. Mater. Res. **26**, 415-439, (1992).

[19]– N. A. Alcantar, E. S. Aydil and J. N. Israelachvili, J. Biomed. Mater. Res. **51**, 343-351, (2000).

[20]- C. Oehr, M. Müller, B. Elkin, D. Hegemann and U. Vohrer, Surf. Coat. Technol. **116-119**, 25-35, (1999).

[21]– C. C. P. Rita, M. A. Algatti, R. P. Mota, R. Y. Honda, M. E. Kayama, E. C. Rangel and N. C. Cruz, Paper presented in this Symposium, paper 358.

[22]– G. Gadioli, E. C. Rangel, R. P. Mota, R. Y. Honda, M. A. Algatti and N. C. Cruz, Anais do 6^0 Congresso Brasileiro de Polímeros/ XI International Macromolecular Colloquium, CD-rom, Gramado, Brazil, pp. 1609-1611, (2001).

[23]– M. K. Kim, I. S. Park, H. D. Park, W. R. Wee, J. H. Lee, K. D. Park, S. H. Kim and Y. H. Kim, J. Cataract. Refract. Surg., **27**, 766-774, (2001).

[24]– G. M. Bruisma, H. C. van der Mei and H. J. Busscher, Biomaterials, **22**, 3217-3224, (2001).

Spectral diagnostics for a DBD plasma in air and He/N_2 gas mixture

Alina Chiper, V. Anița, C. Agheorhiesei, V. Pohoața, Maria Anița and G. Popa

Plasma Physics Department, "Al.I.Cuza" University, Iasi – 6600, ROMANIA

Abstract

Experimental results obtained by emission spectroscopy on dielectric barrier discharges in helium and air or nitrogen gas mixtures are presented. Transition between glow mode and filamentary mode of the dielectric barrier discharge was pointed out and electrical power transferred to the discharge was calculated. Dependence of the rotational temperature versus nitrogen gas flow rate was investigated.

Introduction

In the last period a large interest can be observed for Dielectric Barrier Discharges (DBD) due to their large area of applications: ozone generation, surface treatment, pollution control, excimer UV lamps, CO_2 lasers and plasma display panels. The DBD contains non-equilibrium highly collisional plasma produced at rather high gas pressure by high voltage pulse applied to special system of electrodes [1,2]. Moreover, the DBD is produced in most cases in rare and/or reactive gas mixtures. Consequently, plasma diagnostic in such a system is rather difficult. The electrical probes are not suitable but optical and spectral methods may provide good information about atomic and molecular species, their excited and ionization state and some other plasma parameters.

Experimental set-up

The experimental set-up (fig.1) consists of two copper plane-parallel electrodes of 10.5cm^2 surface area each. Two glass plates of 1.2 mm thickness and 30cm^2 area were used as dielectric barrier. The glass plates were placed on both high voltage and ground electrodes, respectively. The distance between the two glass plates was 2.5 mm. The high voltage power supply (1 to 20 kV) generates mono or bipolar pulses width of 10 to 45 μs and frequency in the range of 10 Hz to 10 kHz. The gas flow rate of each component as helium (He), nitrogen (N_2) and air was kept constant using flow meter controllers (SCHAEFER). Total pressure of the gas mixture was about 1.05bar.

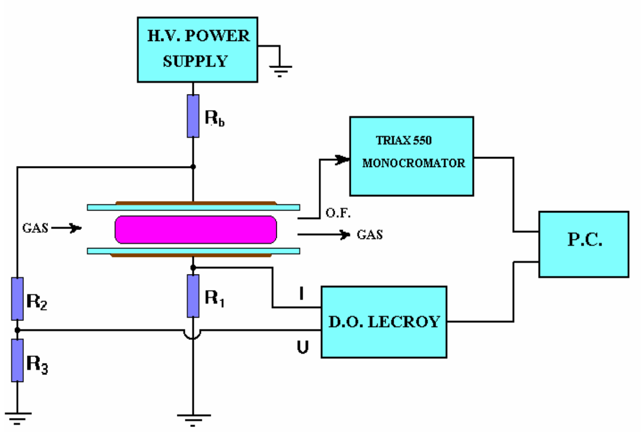

Fig.1 Experimental set-up
R_b=7,5kΩ, R_1=120Ω, R_2/R_3=1000

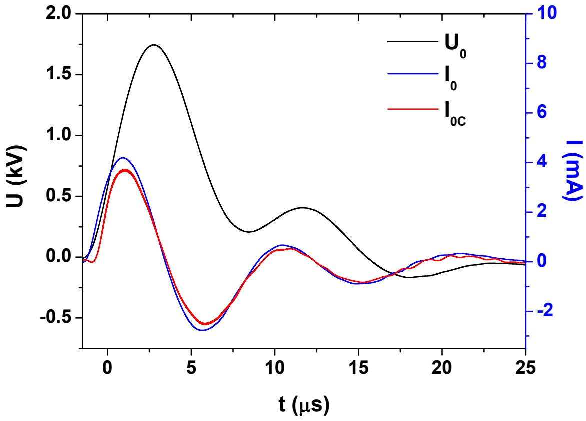

Fig.2 Oscillogram of the voltage (U_0) and of the current intensity measured (I_0) and calculated (I_{0C}) without discharge

Potential (U) applied on the electrodes and current intensity (I) through the system have been measured using a digital oscilloscope (LeCroy 9304CM). The current intensity was measured via voltage drop across the resistance R_1=120Ω connected series to the ground as in Fig.1. The voltage across the copper electrodes was also measured using the resistance system R_2, R_3.

In Fig. 2 the oscillograms of the both voltage (U_0) and current intensity (I_0) are presented for the case when discharge plasma is not present between the plates. In this case the equivalent electric circuit of the system is that presented in Fig.3a where the C_d and C_g are the equivalent capacity of dielectric (glass with relative dielectric permittivity ε_d=6) region and gas (relative dielectric permittivity ε_g =1) region, respectively. Using geometrical size of the electrodes presented above capacitive reactance of the system can be calculated as $X_C \cong 10^5$ Ω. Because the $X_C >> R_1$ impedance of the electrical circuit is almost pure capacitive and $I_{0C} \approx C(dU_0/dt)$, where $C=C_d\, C_g/(C_d + C_g)$. The I_{0C} is also presented in Fig.2 and it fits very well with the current intensity I_0 experimentally measured.

a) b)

Fig.3. Equivalent electric circuit a) without discharge plasma and b) with discharge plasma between the plates.

Spectra of the discharge light emission were acquired with a TRIAX 550 monocromator in UV-VIS (200 – 750 nm) with resolution of 0.01nm

Results and Discussions

One of the main feature of the DBD is the fact that it may present two regimes of working, so-called glow discharge mode (GD) and filamentary discharge mode (FD), respectively [3,4]. The former mode corresponds to a rather uniform discharge within the whole space between the electrodes and discharge current intensity (I) has a single peak (Fig.4). The latter mode corresponds to a rather non-uniform plasma region consisting of multifilamentary micro-discharges, which appear as spiky discharge current intensity (Fig5). The micro-discharges may produce a series of very short peak current intensity. Moreover, micro-discharges are produced randomly in space and time during potential pulse applied to the system..

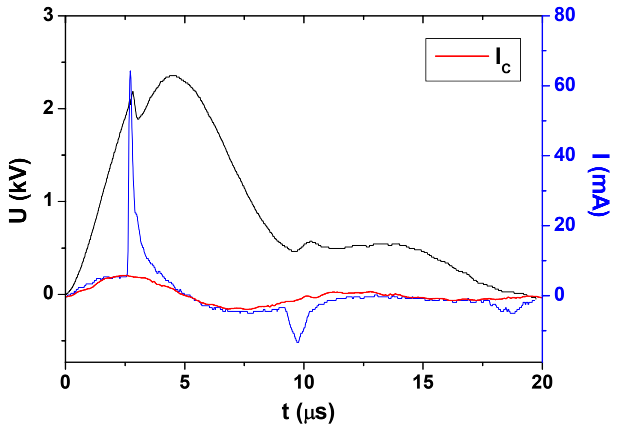

a)

Fig.4 Time evolution of the discharge voltage (U) and discharge (I) and capacitive (I_0) current intensity for GD mode. (Q_{He}=90cm^3/min Q_{N2}=20cm^3/min), p=1.05 bar

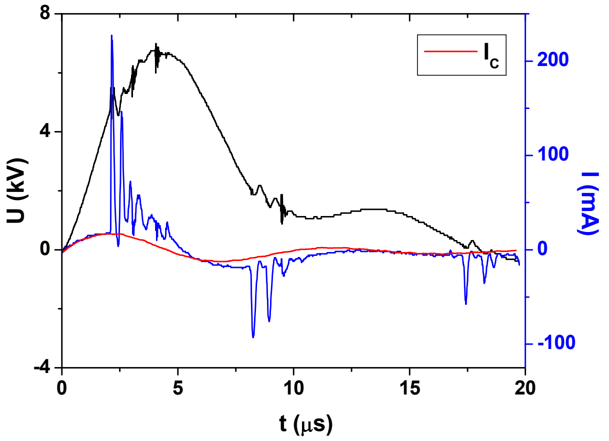

b)

Fig.5 Time evolution of the discharge voltage (U) and discharge (I) and capacitive (I_0) current intensity for FD mode. (Q_{He}=15 cm^3/min, Q_{N2}=5 cm^3/min), p=1.05 bar

For both GD and FD modes the discharge current intensity (I) can be much larger comparing with capacitive current (I_0) which can be also measured during the potential pulse (U) applied on the electrode system. For better presentation the calculated form of I_0 is also depicted in both cases GD mode (Fig 4) and FD mode

(Fig 5), respectively. In general, the FM is obtained for higher amplitude of the potential and at higher percentage of N_2 in the gas mixture.

Typical shape of the discharge current for GD mode presented in Fig.4 shows a time constant around 200 ns while typical shape of the discharge current for FD mode presented in Fig.5 shows that duration of a micro-discharge is around 100 ns. The discharge current intensity of GD mode decreases almost exponentially in time while, the amplitude of the discharge currents within one group of FD mode decreases faster. This characteristic may have important consequences on the mechanisms of production and destruction of different species of plasma particles. In both cases the plasma particles and their excited states are produced mainly during discharge current and they may disappear both by volume and surface processes during and after the pulse of the discharge current. In the GD mode plasma is almost uniform in any direction parallel to the electrodes. Consequently, relaxation processes are mainly controlled by diffusion towards the electrodes and by surface process on these electrodes.

In the FM mode, plasma is produced as filaments randomly distributed in space and time during the potential applied on the electrodes. In that case plasma is strongly non-homogenous in any direction also parallel to the electrodes. Moreover, relaxation processes are strongly influenced by the larger gradients around filaments and plasma parameters may behave differently between the two modes. These large un-homogeneities of the FD mode plasma may explain shorter duration of the filaments and consequently, shorter duration of the peak current intensity.

In the following we have paid more attention to the glow discharge mode. Thus, in Fig. 6 the evolution of the power dissipated on the discharge during the current peak is presented for different mass flow rate of the nitrogen in the N_2/He mixture and constant pressure.

The power was calculated as standard technique in such configuration [5]. It appears that with increasing of the N_2 flux in the system the power dissipated on the discharge decreases almost monotonically. This can be explained by the fact that more nitrogen molecules in the system correspond to more energy accumulated within internal degree of freedom. As a result the electrons may rapidly be cooled down and higher electrical field is needed to maintain the constant discharge current intensity. But experiments were made at constant amplitude of the potential applied of the electrodes so that the discharge current intensity has to decrease.

Moreover, at a given threshold of the N_2/He ratio the GD mode turns into FD mode. This transition is shown by additional peaks, which appear after the main discharge during the evolution of the potential applied to the electrodes.

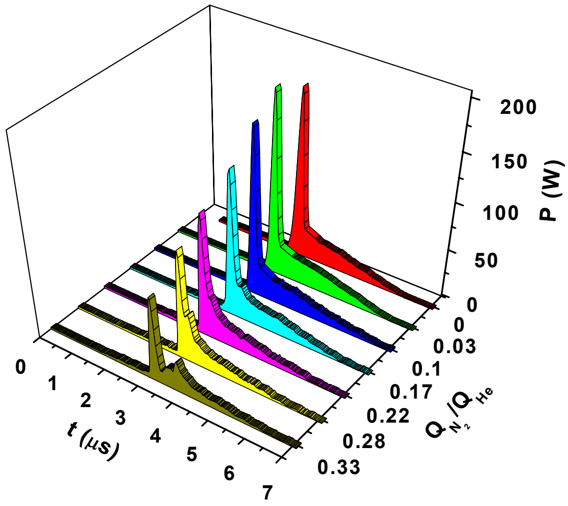

Fig.6 Time evolution of the electric power in GD mode for different ration of Q_{N2}/Q_{He} , p=1.05 bar

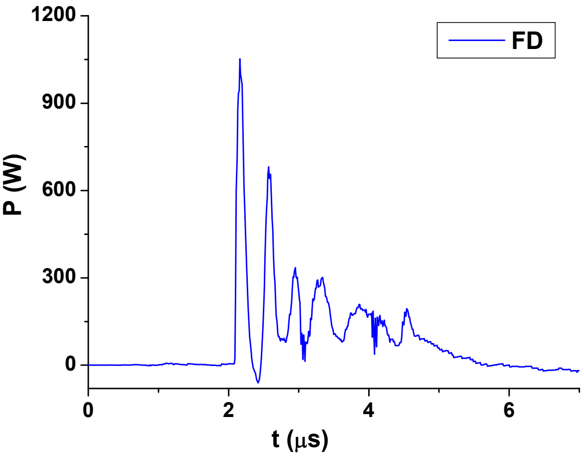

Fig.7 Time evolution of the electric power in FD mode for Q_{N2}/Q_{He}=0.333, p=1.05 bar

Time evolution of the power transferred to the discharge for the FM mode of operation is shown in Fig.7. It preserves mainly the structure of the current discharge intensity. The fact that the power transferred to the plasma also decreases almost exponentially within the high potential pulse it shows that the final stage of the series of micro-discharges is similar to that of the GD mode. The series of micro-discharges ends by polarization of the dielectric plates, which limits the gas gap and a new breakdown of the discharge is not possible before a depolarization process.

The energy transferred to the plasma may also serve to produce excited state of different species of plasma particles. Some of these particles can be observed by emission spectra. Emission spectra of both GD and FD mode, respectively, in the range 200 nm to 750 nm for helium and air gas mixture are presented in Fig 8. The peak power of 270W and $5*10^{-5}$ J/pulse were used for GD mode while for FD mode both the peak power of 2.1KW and total energy of $2,3*10^{-4}$J/pulse were larger. In spite of that the line intensity and number of excited species are larger for the GD mode then those of the FD mode. These features might suggest that the GD mode is more efficient in producing the active and excited particles in the energetic range investigated. A detail of emission spectra is presented in Fig.9 as the first negative system of the ion molecular transition $B(^2\Sigma_u^+, v_B=0) \rightarrow X(^2\Sigma_g^+, v_X=0)$ of nitrogen obtained in GD mode in helium/air mixture.

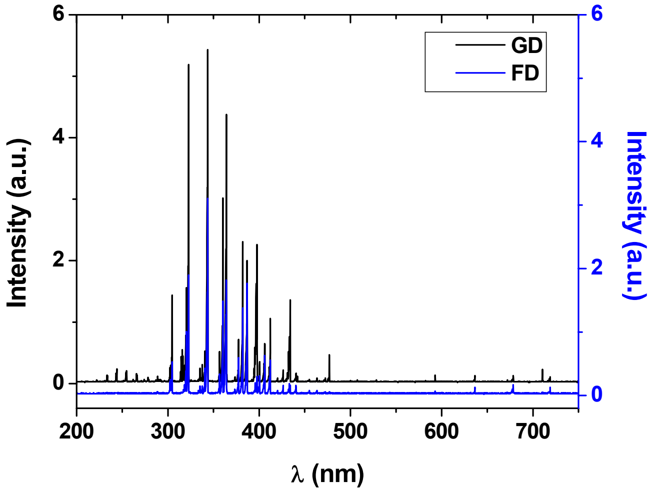

Fig 8 Emission spectra for glow DBD mode (Q_{He}=45 cm^3/min, Q_{aer}=6 cm^3/min) and filamentary DBD (Q_{He}=10 cm^3/min, Q_{air}=6 cm^3/min) mode, respectively, in He/air mixture

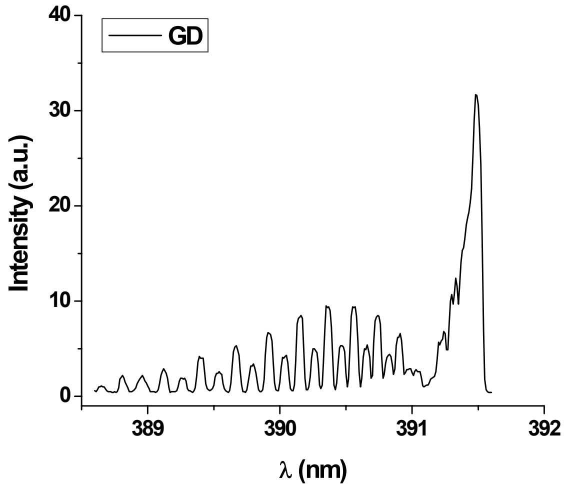

Fig 9 Emission spectra of the N_2^+ ($B_0 \rightarrow X_0$) in a He/air mixture for glow DBD (Q_{He}=90cm^3/min, Q_{N2}=6cm^3/min)

Moreover, representative for particular behavior of the GD mode is characteristic spectra of the radical OH. In the GD mode plasma the emission spectra of the molecular transition $A(^2\Sigma^+, v_A=0) \rightarrow X(^2\Pi, v_X=0)$ (Fig.10a) is very intensive while the same transition practically disappeared in the FD mode (Fig.10b) even if the energy transferred from the power supply to plasma is almost double in the FD mode with respect to GD mode.

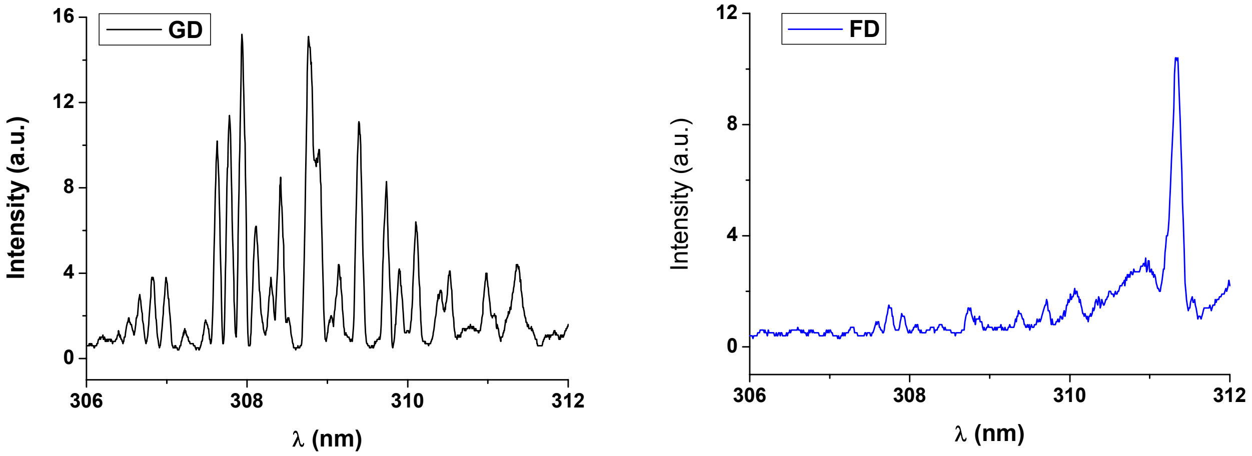

a)

b)

Fig 10 Emission spectra of the OH ($A_0 \rightarrow X_0$) in a He/air mixture for:
a) glow DBD (Q_{He}=90cm^3/min, Q_{air}=6cm^3/min) and b) filamentary DBD (Q_{He}=10cm^3/min, Q_{air}=6cm^3/min).

Taking into account these properties of the system we have restricted our self to investigation in more details the glow discharge mode produced in helium/nitrogen mixture or helium/air mixture. It is rather well known that in such experiments the spectral transition $B_0 \rightarrow X_0$ of the molecular ion of nitrogen may be used for measurement of the gas temperature [3,6].

Rotational temperature was measured by standard method using eq. (1). The slope of semi-logarithmic plot (fig.11) of the intensities of rotational lines versus a quantity corresponding to the energy of the rotational levels allows to determine the T_r. [6,7].

$$\ln\left(I_{j+1,j}\right) = \ln(F\nu_{j+1,j}^{4}) - \frac{Bhc(j+1)(j+2)}{kT_r} \tag{1}$$

where: j – the rotational quantum number, $\nu_{j+1,j}$ - the frequency of the radiation, F - coefficient which depend Hönl-London factor and degeneration of the rotational level, B - the molecular rotational constant, - Plank's constant, c – the speed of light, k – Boltzmann's constant.

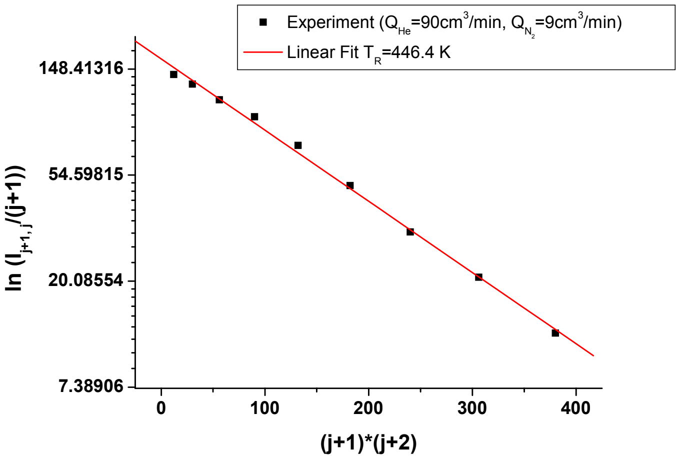

Fig. 11 Semilogaritmic plot of the intensities of rotational lines versus (j+1)*(j+2)

Dependence of the gas temperature measured by this method on ratio of mass flow rates of nitrogen (Q_{N2}) and helium (Q_{He}) was found. The result is presented in Fig 12. It shows that gas temperature increases about 10 % with increasing of Q_{N2}/Q_{He} ratio up to about 0.1 and then saturates and start to decrease when the GD mode pass into FD mode of operation..

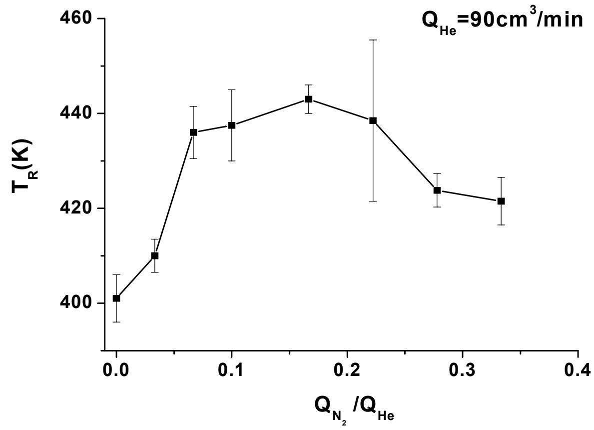

Fig.12 Rotational temperature in GD versus mass flow ratio Q_{N2}/Q_{He}

Increasing of the gas temperature presented in Fig 12 might be even larger if we take into account that measurements were performed at constant discharge voltage and according to results presented in Fig. 6 the energy transferred to plasma decreases with increasing of Q_{N2}/Q_{He} ratio. This result shows that relaxation mechanism of excited states of molecular nitrogen may have a rather complicated dependence on the ratio of the mass flow rates of nitrogen and helium.

Conclusions

Two modes of operation of the DBD as glow discharge (GD) mode and filamentary discharge (FD) were investigated versus amplitude of the potential applied on the electrodes and versus ratio between the mass flow rates of molecular nitrogen and helium. The GD mode can be obtained in pure helium and at rather low nitrogen concentration in N_2/He mixture and low discharge potential. The FD mode is obtained at high discharge voltage and high concentration of nitrogen in N_2/He or air/He mixture. The GD mode is more efficient in producing of the molecular and atomic exited state than FD mode. Rotational temperature of the nitrogen ion molecule increases with increasing of the nitrogen mass flow rate within the Q_{N2}/Q_{He} ratio

References

[1] U. Kogelschatz, B. Eliasson, W. Egli - Pure Appl. Chem., **71**, 10 (1999)
[2] U. Kogelschatz, B. Eliasson and W. Egli – ICPIG XXIII, July 17-22, Toulouse, France (1997)
Company-Amsterdam
[3]F. Massines and G. Gouda - J. Phys. D: Appl. Phys. **31** (1998)
[4] N.K. Bibinov, A.A. Fateev, K. Wiesemann – J. Phys. D: Appl. Phys. **34** (2001)
[5] S. Liu and M. Neiger – J. Phys. D: Appl. Phys. **34** (2001)
[6] N.K. Bibinov, A.A. Fateev, K. Wiesemann – Plasma Sources Sci. Technol. **10** (2001)
[7] "Plasma Diagnostics" edited by W. Lochte – Holtgreeven Kiel University, North – Holland Publishing

TiN coated debris shields and mirrors for EUV radiation

Mariana Braic[1], Peter Choi[2], Viorel Braic[1], Serguei Zakharov[2],
Carmen Dumitrescu[2], Mihai Balaceanu[1]

[1]*Tehnoprof Center, National Institute for Optoelectronics, Magurele-Bucharest, Romania*

[2] *EPPRA sas, 16 Ave du Québec, 706 SILIC, Courtaboeuf 91961, France*

The road map of the world semiconductor industry demands the availability of a next generation lithography system by 2005 for commercial production of microelectronics with feature size below 70 nm. Currently EUVL is one of the most favoured options, being considered as one of the keys for the 50 nm technology node. The paper presents an investigation, regarding the use of the 15 nm radiation of Xe X band instead of the 13.5 nm radiation of the Xe XI lines obtained from a Xe dense plasma radiation source. The advantage is a higher EUV energy output of the source, in a broader wavelength span for the emitted radiation centered around 15 nm, over a broader range of plasma temperature. This will decrease the pressure imposed on the EUV source power output. Calculation of the overall relative gain in the emitted EUV radiation intensity of the 15 nm centered region compared with 13.5 nm region have been made, using spectral emission data obtained from detailed 2D radiation MHD simulation with code Z*. The repetitive EUV source was operated in the range of frequencies 60 to 2000 Hz [1]. Simulations for multi-layered Mo/Si mirror with maximum reflectivity in the 12 - 15 nm region are presented, considering integrated emission output, showing that the radiation intensity in EUVL can be increased by matching of the EUV source emission and collection optics, modifying different parameters of the multi-layers and/or the incidence radiation angle.

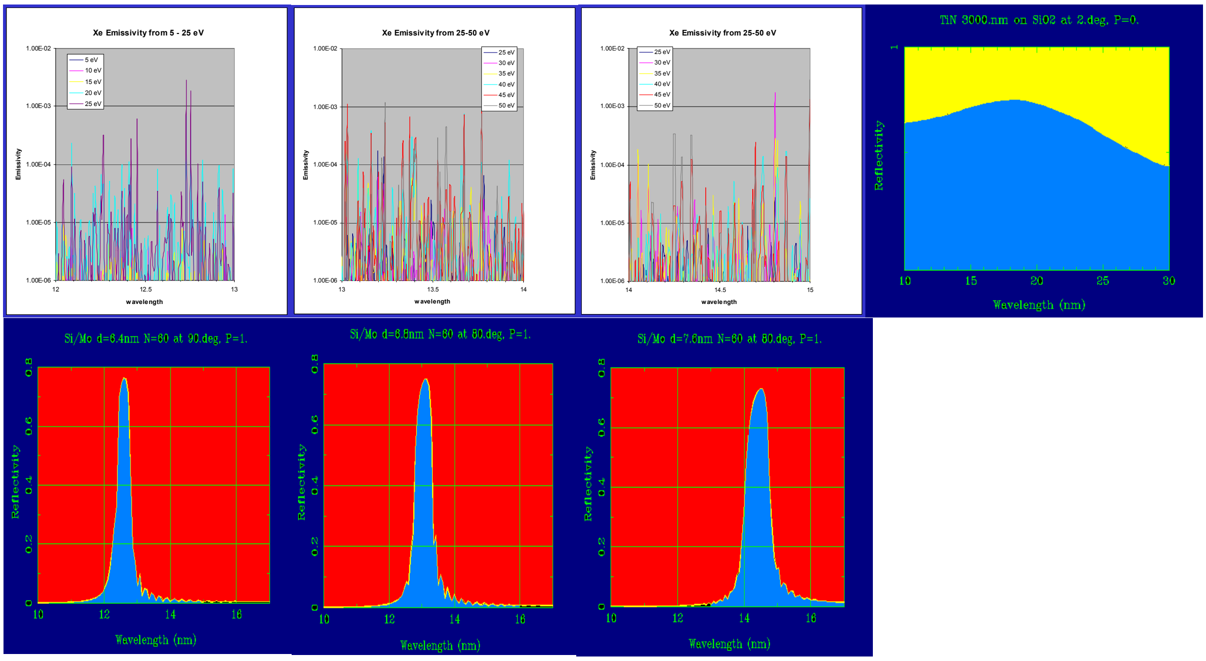

Fig. 1 Predicted reflectivity of multi-layers of Mo/Si (red-blue) and of 3µm TiN (yellow-blue) surface at different incidence angles - in connection with the source predicted emission within three bands in the region 12 - 15 nm.

A grazing off-axis ellipsoid covered with resistant, anti-abrasive coatings of TiN, with a superior heat conductivity in order to dissipate the heat load resulting from the EUV emitting source is proposed to be used as a collector and as well as a debris shield. The TiN coatings deposited on Si and glass by cathodic arc deposition and magnetron sputtering were characterized as debris shields for fast particles emerging from the EUV source.

[1] A high repetition rate discharge EUV Source, P. Choi , A. Conti, C.Dumitrescu, M.Favre, E.Wyndham, A. Yuan, S. Zakharov , 1st Intl. EUVL Symp. SEMATECH, Texas, USA, Oct. 2002

Control growth of carbon nanotube using glow barrier discharge

Tomohiro NOZAKI, Yoshihito KIMURA, Shigeru KADO, Ken OKAZAKI

Department of Mechanical and Control Engineering, Tokyo Institute of Technology
2-12-1 O-okayama, Meguro, Tokyo, JAPAN 152-8551.
tnozaki@mech.titech.ac.jp

Keywords: Multi-wall carbon nanotube, Glow barrier discharge, Catalytic CVD, Negative glow, Nano particle.

1. Introduction

The authors first achieved multi-walled carbon nanotube (CNT) deposition using glow barrier discharge, and discussed minimum requirements for CNT growth in terms of gas composition and growth temperature [1-2]. Several important aspects are as follows: (1) H_2/CH_4 ratio was at least higher than 5. (2) Substrate temperature must be above 600°C. (3) Streamer-like barrier discharge cannot achieve CNT synthesis. (4) Intense negative glow must be formed near substrate [3]. (4) Aggregation of catalyst nanoparticles likely leads to imperfect graphite structure of CNT. In addition, nanotube diameter tended to be thicker owing to particle aggregation. Based on these facts, this study discusses the improvement of the processes of catalytic CVD as well as nanotube quality.

2. Experimental

Barrier discharge reactor and fundamental growth parameters are shown in Fig.1 and Table 1. The reactor was placed in a vacuum chamber. The chamber was evacuated below 10^{-3} Torr with rotary pump, and then $CH_4/H_2/He$ mixture was introduced at constant flow rate. CH_4/H_2 mixture was diluted with helium by 90%. Detailed conditions and procedure was detailed elsewhere [2]. This study especially focused on Ni catalyst and combination with catalyst support. Deposited materials were characterized by Raman spectroscopy, HRTEM, and FE-SEM.

3. Creation of glow barrier discharge

Generally, operating frequency, gap distance, and gas additives are recognized as dominate parameters to determine whether He-based barrier discharge is uniform or filamentary. However, these parameters mutually influence each other and situation is more complicated than expected. The relationship among these parameters could be explained by Eq. 1 that accounts for ion trapping mechanism between gas gap. Ion trapping frequency at given conditions is called critical frequency, and derived from momentum transfer equation of ion. Critical frequency gives quantitative information about how remaining ion affects plasma history, which is important guideline to achieve glow condition.

Critical frequency was calculated for various positive ions presented in helium, and plotted against

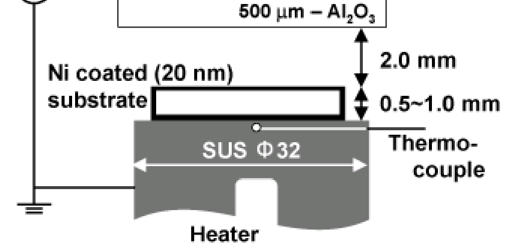

Fig. 1 Reactor configuration

Table 1 Experimental conditions

Growth temp.	400-750°C
Growth time	5-30 min
Pressure	760 Torr
Power	~4 W /cm^2
He dilution	90%
H_2/CH_4 ratio	0-10

Catalyst	Ni
Support	Quartz, Si.
Substrate	Heating rate (1-30°C/sec), Final temp. (~800°C)
Pretreatment	Hydrogen atmosphere without plasma

reduced field strength as shown in Fig. 2. In addition, reduced field strength derived from Lissajous figure was plotted with respect to operating frequency (Fig. 3). The gap distance was 1 mm in each case.

$$\nu_0 = \frac{eE_{eff}}{\pi m \nu_c}, \qquad \nu_c = \mu E N_0 < \sigma_m > \ [s^{-1}] \qquad \text{Eq 1}$$

ν_0	Critical frequency [s^{-1}]
e	Elementary charge [C]
m	Ion mass [kg]
ν_c	Collision frequency between ion and molecule [s^{-1}]
E_{eff}	Field strength [V/cm]
μ	Positive ion mobility [4]
$<\sigma_m>$	Momentum transfer cross section [cm^2] [4]
N_0	Molecule density [cm^{-3}]

In ideally pure helium, He_2^+ ion is the dominant ion at atmospheric pressure since three body collision leads to a creation of large number of excited dimers. Critical frequency for He_2^+ (and also He^+) ions exhibits highest value at given conditions, and tends to decrease with increasing molecular weight. If a small amount of impurity was injected, Penning ionization become remarkable for secondary electron production, and thus positive ions resulted from impurity would become major ion. At the same time, Penning ionization also decreases reduced field strength as shown in Fig. 3. The existence of impurity in helium simultaneously

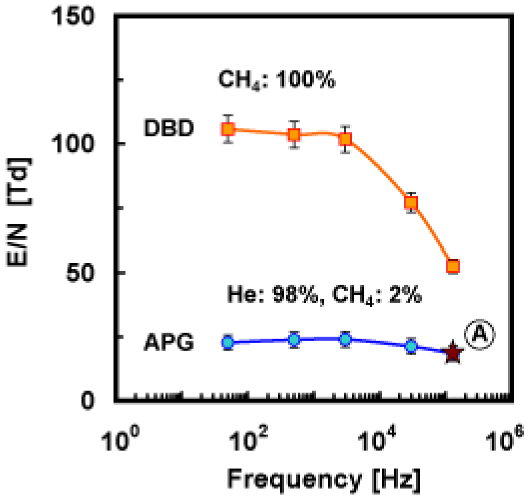

Fig. 3 Reduced field strength derived from Lissajous figure vs Operating frequency.

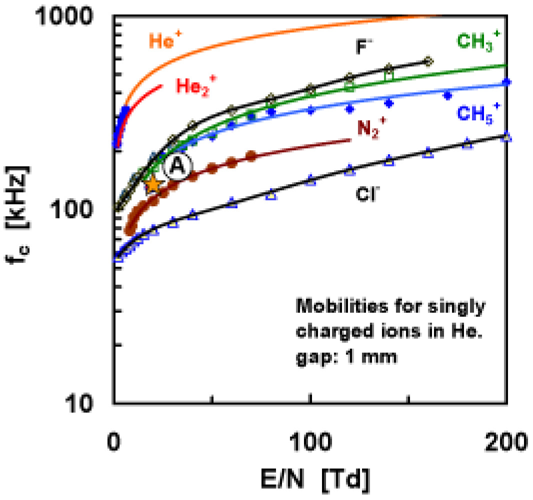

Fig. 2 Critical frequency for singly charged ions in He. Eq. 1 with 1 mm gap.

decreases critical frequency and reduced filed strength. In our experiment, reduced field strength and operating frequency was accordingly chosen as indicated by "★" in Fig. 3 and Fig. 4.

4. Results and discussion

4.1 Ni/Quartz suport

Most experiments were carried out using Ni coated quartz substrate since Ni catalyst coated on quartz (SiO_2) substrate provide most effective catalyst and support combination for nanotube growth [5]. Fig. 4 shows SEM micrograph of multi-wall carbon nanotube deposited by glow barrier discharge. Results were more successfull than other conditions, but Ni nanoparticle teneded to aggregate in this case. In addition, diameter of nanotube become thick and widely distributed. TEM pictures clealy show number of Ni grain aggregate each other.

4.2 Ni/Si suport

Figure 6 shows the SEM micrograph of CNT deposited on Si substrate. The growth rate was about 0.2 μm/min. We could not confirm specific improvement of wall structure from Raman spectra, but diameter of CNT became much thinner when deposited on Ni-coated Si wafer. However, Si seems to form Si-Ni chemical compounds at elevated temperature, so nanotube was sometimes missing. Si-SiO_2-Ni double layer coating probably works much better than those two types of substrate.

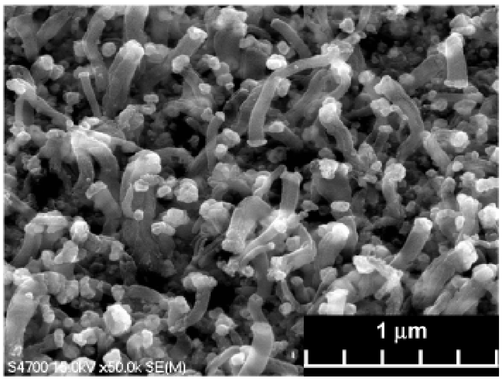

Fig. 4 SEM: Ni coated (20 nm) quartz substrate (650°C, H_2/CH_4 = 5).

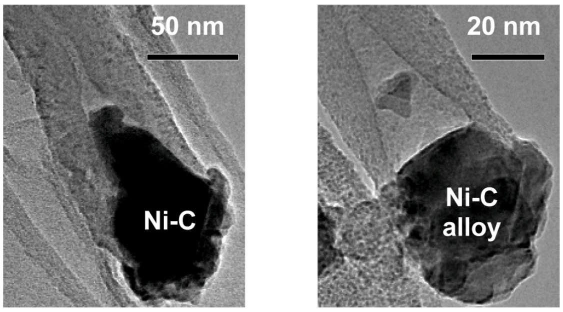

Fig. 5 TEM: Corresponding to Fig. 4.

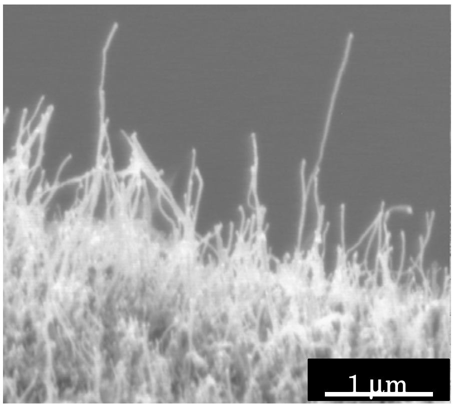

Fig. 6 SEM: Ni coated (20 nm) Si substrate (700°C, H_2/CH_4 = 5).

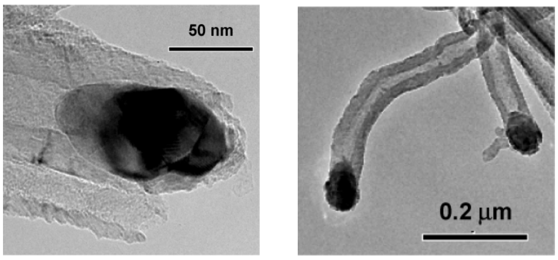

Fig. 7 TEM corresponding to Fig. 6

4. Conclusions

1. Nanotube was successfully deposited on both Ni-Si and Ni-quartz substrate.
2. Nanotube was easily deposited on Ni-quartz substrate, but Ni grain tended to aggregate each other, thus nanotube diameter was widely distributed.
3. Narrow and well-aligned nanotube was obtained with Ni-Si substrate.

References

1. T Nozaki, Y Kimura and K Okazaki, 16th ESCAMPIG and 5th ICRP Joint Conference, Grenoble France, July 14-18, Vol.1, (2002) 37-38.
2. T Nozaki, Y Kimura, K Okazaki, Journal of Physics D; Applied Physics, **35** (2002) 2279-2784.
3. T Nozaki, Y Unno, K Okazaki, Plasma Sources Science and Technology, **11** (2002) 431-438.
4. H. W. Ellis, Transport properties of Gaseous Ions over A Wide Energy Range. Part Ⅲ, At. Dat. and Nucl. Dat. Tables, vol.31, no.1, pp.113-151, 1984.
5. K Otsuka, S Kobayashi, and S Takenaka, Applied Catalysis A: General, 201 (2001) 371-379.

Acknowledgements

This work was partly granted by Venture Business Laboratory (VBL) of Tokyo Institute of Technology. Authors also would like to thank Prof Joachim Heberlein and Prof Uwe Kortshagen on University of Minnesota, High Temperature & Plasma Lab. for intensive discussion.

Micro-plasma reactor for direct liquefaction of natural gas

Tomohiro NOZAKI, Akinori HATTORI, Shigeru KADO, Ken OKAZAKI

Department of Mechanical and Control Engineering, Tokyo Institute of Technology
2-12-1 O-okayama, Meguro, Tokyo, JAPAN 152-8551.
tnozaki@mech.titech.ac.jp

Abstract

This paper describes fundamental electrical and optical characteristics of micro-plasma reactor used for partial oxidation of natural gas. The micro-scale non-thermal plasma reactor can process combustible gas mixture at atmospheric pressure and near room temperature without explosion, realizing energy efficient one-stage partial oxidation of natural gas to provide syngas and liquid fuels. Reactor configuration was quite similar to that of conventional barrier discharge reactor, but wall effect became remarkable in the micro scale plasma reactor. It favorably minimized excess temperature increase in the reactor. At the same time, the averaged electron density was decreased by the factor of 10^2.

Keywords: Micro-plasma, Barrier discharges, Methane, Syngas,Methanol, GTL,
Quenching length, Partial oxidation.

1. Introduction

The non-thermal, micro-scale plasma reactor was developed for direct conversion of natural gas into liquid fuels at 760 Torr and room temperature. Wide range of CH_4/O_2 mixtures was directly processed without explosion in the temperature range between 20°C and 100°C. Highly reactive non-thermal plasma stimulates chemical conversion processes even at room temperature, whereas perfect oxidation of methane that leads to CO_2 and H_2O could be minimized due to low temperature synthesis. One-stage partial oxidation of methane to produce liquid fuels proceeds almost independently of chemical and thermal equilibrium. In addition, low temperature synthesis enhances non-equilibrium nature of the reaction system: Liquid fuels including water vapor condenses inside the reactor, and thus re-decomposition of those products by electron impact can be effectively avoided.

2. Experimental

Figure 1 shows micro-scale plasma reactor used in the experiment [1]. Reactor consists of thin glass tube (600~1500 μm) and twisted stainless steel wire (200 μm) as a high voltage electrode. According to Pschen's law, possible minimum inner diameter of the tube would be 10 μm in order to ignite discharges at 760 Torr molecular gas, whereas maximum size is limited by 2000 μm considering quenching diameter of CH_4/O_2 flame: Quenching diameter is the minimum distance that a flame can propagate through a combustible mixture. The quenching property can be

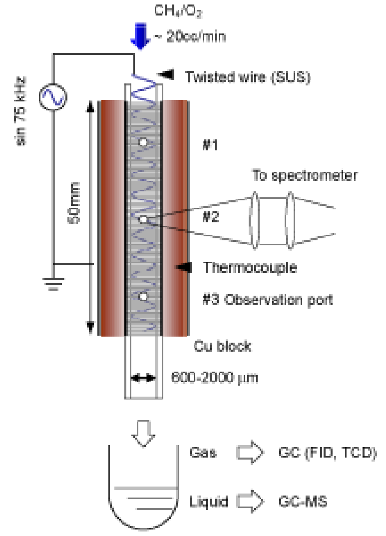

Fig. 1 Micro-plasma fuel converter

determined by the heat loss through reactor wall. The external tubular electrode had three observation ports. Emission from CH ($A^2\Delta \rightarrow X^2\Pi$: 431.5nm) was measured through each port, and analyzed for rotational temperature.

3. Result and discussion

3-1. Electric properties

Steady state discharge model provides time- and space-averaged electric properties of barrier discharges and commonly used for macroscopic characterization purposes. This model is expressed by the following relation.

$$\overline{N_e} = \frac{\kappa}{eN\overline{V_e}} \frac{\overline{W}}{\overline{(E/N)}Sd} \qquad \text{Eq 1}$$

κ	Part of energy carried by electrons. Generally assumed to be 0.5 [-]
W	Discharge power [W]
S	Electrode area [cm^2]
d	Gap [cm]
e	Elementary charge [°C]
E/N	Reduced field strength [Td (=10^{-17} Vcm^2)]
V_e	Drift velocity of electron [cm/s]
N	Molecular density [cm^{-3}]

Average electron number density was plotted against reduced field strength as shown in Fig. 2. The electric property for micro-plasma reactor was compared to co-axial barrier discharge reactor having 0.5, 1.0 mm gap separation that pretends typical barrier discharge reactors [2-3]. Three dotted lines show constant power line. Generally, high frequency operation significantly increases electron number density, whereas reduced field strength gradually approaches breakdown field of methane (83 Td) (curve A). In addition, there is no significant difference between 0.5mm and 1.0mm gap barrier discharge reactors. On the other hand, in micro-plasma reactor, field strength was weakened below breakdown field due to strong effect of charge accumulation on chamber wall. Electron number density was also decreased two orders of magnitude at the same time.

3-2. Syngas manufacturing

Three different CH_4/O_2 mixtures were processed at the constant flow rate (30 cc/min). The results are summarized in Table 1. When CH_4/O_2 ratio was 2.0, 70% of reacted methane was converted into liquid fuels such as methanol and formic acid, and 10% was wasted as CO_2 and C_2 hydrocarbons. Higher O_2 content (CH_4/O_2 = 1.0) can be processed without explosion, but selectivity for liquid fuels was decreased by 50%. Various kinds of liquid fuels were produce with reducing O_2 content. CO was also one of the major product throughout experiment. Micro plasma reactor extends the capability of manufacturing CO directly from methane. However, H_2 was likely to become H_2O even at low temperature processing.

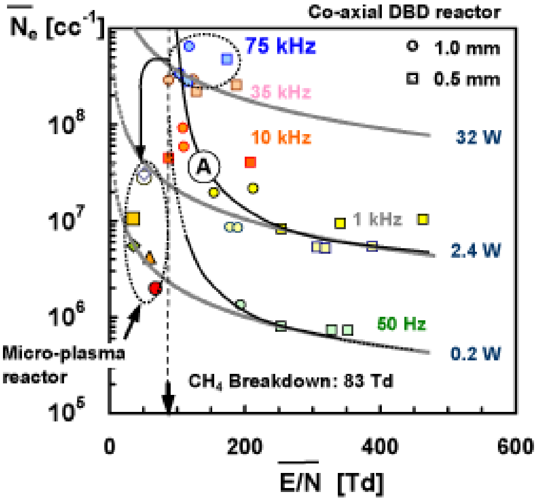

Fig. 2 E/N vs Ne: This figure compares electric properties between conventional co-axial DBD reactors and micro-plasma reactor.

Table 1 Operating condition and representative results

(Total flow rate: 30 cc/min, Discharge power: 3~4 W)

CH_4/O_2	T_{wall}	Conv.	Selectivity (relative value)						
		CH_4	CO	CO_2	C_2	Methanol	Formic Acid	Acetic Acid	Form aldehyde
1.0	80°C	23	38	12	3	(9)	(38)	(-)	(-)
2.0		27	19	7	3.5	(14)	(49.5)	(7)	(-)
5.0		14	21	8	8.5	(12.5)	(46)	(10)	(3)

3-3. Spectroscopic characterization

We analyzed emission spectrum of CH for rotational temperature. Rotational temperature sufficiently reflects gas temperature where chemical and electric processes take place. Not only wall temperature, but also plasma gas temperature was simultaneously analyzed. Fig 3 (A) shows numerically reproduced $CH(A^2\Delta)$ band spectrum that consists of three different vibrational components. Rotational and vibrational temperature was assumed to be 423K and 10000K, respectively. Relative emission intensity for v(0,0) vibration spectrum is similar to that for v(1,1) and closely overlapped each other. Emission intensity for v(2,2) vibration band is negligible weak, still we can identify unique band head near 432.5 nm. Another vibration mode such was v(3,3) is virtually negligible. Fig. 3 (B) shows emission spectrum due to $A^2\Delta \rightarrow X^2\Pi$ (431.5 nm) transition of CH observed at 80°C of wall temperature. Rotational temperature can be determined from relative intensity ratio of individual R line of CH spectrum. Background spectrum must be substituted before measuring relative intensity of R branches. When I_{UL} is emission intensity of a single R branch of wave number ν, then

$$I_{UL} \propto S_{UL}\nu_{UL}{}^4 \exp\left(-\frac{E_U hc}{kT_{rot}}\right) \tag{Eq 2}$$

S	Line strength
E	Rotational term
k	Boltzmann constant
h	Planck's constant
c	The velocity of light
T_{rot}	Rotational temperature

Subscripts $_U$ and $_L$ denote upper and lower electronic states

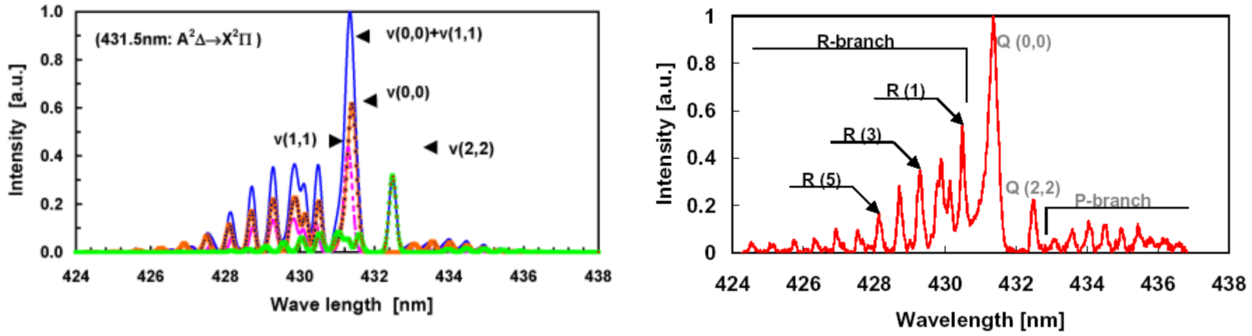

(A) Numerical

(B) Experimental

Fig. 3 Emission spectrum of CH band

The logarithmic plot of ln(I_{UL}) - ln($S_{UL}\nu_{UL}^4$) against ($E_U$hc/k) is called Boltzmann plot and will provide a straight line when rotational state of excited CH($A^2\Delta$) established equilibrium with respect to translational gas temperature: gas temperature can be derived from given slope of Boltzmann plot. Detailed numerical procedure to derive rotational temperature from measured data and reliability of measurement has been extensively discussed by Nozaki et al [4-6].

Although reactor temperature was maintained at room temperature, rotational temperature (i.e. gas temperature in the plasma) reached 200°C. Local gas heating due to streamer formation leads to remakable temperature increase although streamer duration was several nano-seconds. It increased by 300°C with increasing wall temperature. Rtational temperature was almost independent of CH_4/O_2 ratios. Heat produced by streamers as well as exothermic reaction was effectivelly removed through reactor wall.

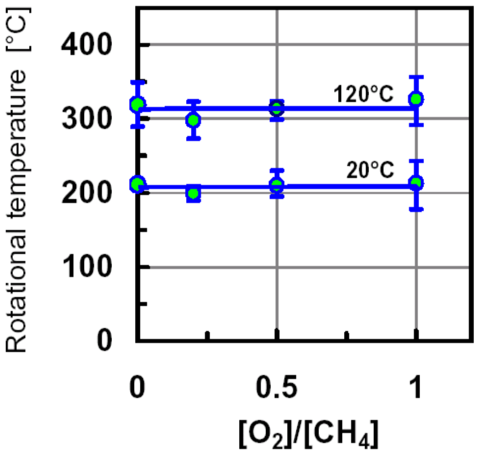

Fig. Rotaitonal temperature

4. Conclusions

Although rotational temperature reached 200°C higher than wall temperature, it was almost independent of O_2/CH_4 ratio in micro scale plasma reactor. Moderate methane oxidation was successfully achieved. Main products were CO and liquid hydrocarbons such as methanol and formic acid. Small amount of hydrogen was detected. Yield of oxygenates was decreased with increasing oxygen content.

References

1. T Nozaki, A Hattori, S Kado, and K Okazaki, Characterization of micro-plasma reactor and application to methane liquefaction, The 3rd International Workshop on Basic Aspects of Non-equilibrium Plasmas Interacting with Surfaces, Vol.1, p28, 2003.
2. D W Larkin, et al, Oxygen Pathways and Carbon Dioxide Utilization in Methane Partial Oxidation in Ambient Temperature Electric Discharges, Energy & Fuels, 1998.
3. S Tanabe, et al, Partial Oxidation on Methane with Nitrous Oxide in a dielectric-Barrier discharge System, Chemistry Letters, 1999.
4. T Nozaki, Y Unno, K Okazaki, Thermal Structure of Atmospheric Pressure Non-equilibrium Plasmas, Plasma Sources Science and Technology, Vol.11, pp431-438, 2002.
5. T Nozaki, Y Unno, Y Miyazaki, K Okazaki, Optical diagnostics for determining gas temperature in microdischarges generated in methane-fed DBD, Journal of Physics D; Applied Physics, Vol.34, No.16, pp2504-2511, 2001.
6. T Nozaki, Y Miyazaki, Y Unno, K Okazaki, Energy Distribution and Heat Transfer Mechanisms in Atmospheric Pressure Non-equilibrium Plasmas, Journal of Physics D; Applied Physics, Vol.34, No.23, pp3383-3390, 2001.

Acknowledgements

This work was supported in part by The Murata Science Foundation.

Effects of Current Limitation Through the Dielectric in Atmospheric Pressure Glows in Helium

L. Mangolini, C. Anderson, K. Sittig, P. Zhang, M. Hur, J. Heberlein and U. Kortshagen

Department of Mechanical Engineering, University of Minnesota, Minneapolis, Minnesota, USA

Abstract

In the current paper, we investigate the current limiting effects of varying the dielectric thickness and material in an atmospheric pressure glow (APG) discharge in high purity Helium. As the impedance of the dielectric barriers is increased, we observe a shift in the discharge regime from a glow-like to a Townsend-like discharge structure. Electrical and optical measurements are presented along with comparisons to results of a one-dimensional model.

1. Introduction

Uniform atmospheric pressure glow (APG) discharges have been demonstrated in the literature in different atmospheres and different discharge regimes. Initial studies focused on helium, in which the APG was first found with a distinct discharge structure that resembled that of a DC glow discharge [1]: A cathode layer, a Faraday dark space and a positive column were observed. The authors of this study proposed that the positive column is essential for the uniform, non-filamentary character of the discharge in that it traps electrons. Those electrons would later provide a sufficient level of pre-ionization before the next discharge pulse so that a Townsend breakdown rather than a streamer breakdown would occur. However, just recently in the experiments in ref. [2] a Townsend-like discharge in helium without positive column was demonstrated. The transition between both discharge regimes and the multiple current peak structure observed in [2] were recently studied in a theoretical investigation in ref. [3]. Townsend-like discharges were also observed in nitrogen [4,5], in which so far no glow-like mode could be established.

Experimental studies of glow- and Townsend-like APGs in helium have so far not been systematic. While thin alumina dielectrics were used in ref. [1], thick glass dielectrics were used in ref. [2]. As pointed out in ref. [3], the current limitation by the dielectric is crucial in establishing one or the other discharge regime. In this paper we demonstrate that the operating point of the APG in helium can continuously be adjusted between the glow-like and Townsend-like discharge through an appropriate choice of the dielectric barrier. We also compare our measurements with results of a one-dimensional, time-dependent model for the APG. Close agreement between experiments and model results are found.

2. Experimental Set-up

The discharge chamber is constructed of stainless steel, with an internal volume of 40 liters. It is designed to support the electrode assembly in its center, reducing the risk of arcing between these electrodes and the chamber walls. The electrodes are 4 cm–diameter Aluminum discs with rounded edges to reduce edge enhancements of the electric field. A TREK 20/20B amplifier and a Tektronix AFG320 function generator supply the high voltage for the system. The applied voltage signal from the discharge is taken using a 1:1000 high voltage probe to monitor, while other voltage signals are fed directly into the Tektronix 460A oscilloscope. An intensified CCD camera is used to study the light emission from the discharge. The camera is capable of exposure times down to 2 nanoseconds, and is synchronized with the applied signal from the function generator. The gating ability of the camera is used to produce time-sequenced images of the discharge evolution. These measurements are all compiled onto a PC for analysis.

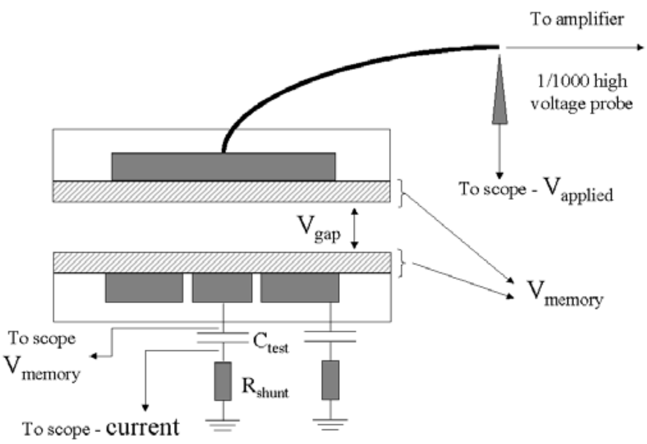

Figure 1: Schematic of electrical system. Arrows denote oscilloscope measurement points.

Figure 1 shows a schematic of the electrical system. The lower electrode is segmented consisting of two insulated sections. The center section has an area of 1 cm^2, which allows the direct measurement of the discharge current density at the center of the electrode where the effects of field distortion through edge effects are small. This is important in the comparison to the one-dimensional model, which assumes that there is no electric field in the radial direction. Both electrode sections are connected to ground through two separate R-C circuits. The capacitance and resistance values are chosen to minimize the difference in the voltage drops of the two electrode sections. A shunt resistor ($R = 500\ \Omega$) and a test capacitor ($C = 1$ nF) are used to measure, respectively, the discharge current through the Helium gap and the "memory voltage" drop across the dielectric plates (V_{memory}). The memory voltage is proportional to the voltage drop across the test capacitor (V_{test}) by a factor of $C_{test}/C_{dielectrics}$. Hence, the voltage across the discharge gap can be found as follows:

$$V_{gap} = V_{applied} - V_{memory} - (V_{shunt} + V_{test}) = V_{applied} - V_{test}\,(1 + C_{test}/C_{dielectics}) - V_{shunt} \qquad (1)$$

The discharge is produced between the two dielectric plates, separated by a fixed gap distance of 5 mm. Multiple materials were used for this investigation, including 5 mm thick glass plates ($\varepsilon_r = 4.6$), and multiple alumina plates (96% Al_2O_3, $\varepsilon_r = 9$) with .635 mm, 1 mm, 1.5 mm, 2.5 mm, and 4 mm thickness. A small amount of silicon vacuum grease is used between the electrodes and the dielectrics to ensure uniform surface contact.

Prior to operation, the chamber is evacuated using a rotary pump reaching a pressure on the order of 10^{-2} Torr. After some time, it is refilled with ultra-high purity Helium, and maintained at a pressure of 760 Torr. A flow rate of around 4 slm of Helium is used during operation of the experiment. Once the discharge is initiated, it is allowed to run for a few minutes in order to reach steady-state operation, effectively cleaning the dielectric surfaces of any contaminants in the process.

3. Modeling

In order to better understand the discharge mechanism, a one-dimensional fluid model has been developed. The simulation includes the presence of electrons, both atomic and molecular Helium ions (He^+, He_2^+), Helium metastables ($He[2^3S]$), and Nitrogen ions (N_2^+). We experienced the same problem as other researchers [1,3] in that no stable solution could be achieved in pure helium. Hence we assumed a slight impurity of nitrogen as also chosen in ref. [3]. This choice is supported by the fact that indeed we observe nitrogen molecular lines in the optical emission of our discharge.

The code solves simultaneously the continuity equations for all considered species, the momentum equations for all positive ions, and Poisson's equation. The boundary conditions for Poisson's equation are given in terms of the electric field at the interface of the Helium gap and dielectric plate [3]:

$$\varepsilon_r \cdot \varepsilon_0 \cdot E_{dielec} + \sigma_0 = \varepsilon_0 \cdot E_{plasma} \qquad (2)$$

Here σ_0 is the charge density at the dielectric surface, ε_0 is the vacuum permeability, and ε_r is the dielectric constant. The continuity equations are solved using a finite volume method, with an exponential scheme used for the charge carrier flux calculations [6]. Secondary electron emission from the dielectric surface is included.

The numerical code makes use of a non-uniform grid, with smaller cell sizes at the interface with the dielectrics, where the field is expected to be higher. An adaptive time step is used, which is a multiple of the Courant time step, generally by a factor of 10. The values for transport properties and reaction rates are taken from the literature [7-11]. The excitation rates for Helium from ground state atoms to the metastable states were computed using a Boltzmann solver. Cross section data from [12,13] were used and rate coefficients were calculated as a function of the applied reduced electric field strength. The treatment of Nitrogen ions assumes that N_2^+ ions are converted to N_4^+ ions immediately after their creation. This process can take place with Helium or Nitrogen as the third body. Since the background density of Helium is large, we can assume that this conversion rate is high, and that N_4^+ is the most important Nitrogen ion to consider. Based on the base pressure of the evacuated chamber achieved in our experiments, the level of Nitrogen impurities in the simulation was assumed to be equal to 100 ppm.

4. Results

Figure 2 shows the glow-like and Townsend-like regimes realized in an APG through the choice of the dielectric. The gap is 5 mm, with an applied signal frequency of 15 kHz. The applied voltage is varied in such a way as to maintain a constant amplitude of the gap voltage in the absence of breakdown. The left figure shows the light emission during the positive discharge pulse using the 5 mm glass dielectrics. A cathode layer is seen to develop. However, no positive column appears under these conditions, indicating that the discharge operation is close to that of a Townsend discharge. The maximum current density for this case is 0.4 mA/cm^2. The right figure shows the light emission for similar conditions but using 0.635 mm alumina dielectrics. In this case, the discharge exhibits a glow-like structure with pronounced cathode layer, Faraday dark space and positive column. The current density is much greater at 3.5 mA/cm^2. It should be noted that the exposure times and number of accumulations with the CCD camera were significantly different in both cases. Areas of similar brightness are actually significantly brighter in the glow than in the Townsend-like case due to the much shorter exposure time and the smaller number of accumulations in the glow case.

While the different discharge regimes observed in Fig. 2 are likely related to the current limitation through the dielectric, this conclusion is not unambiguous due to the different barrier materials used. For instance, different secondary electron emission coefficients of glass and alumina are expected to influence the discharge behavior as well. Hence we performed a set of measurements with alumina dielectric plates of different thicknesses. For this case, the Helium gap is again fixed at 5 mm, while the applied sinusoidal waveform frequency is set to 10 kHz.

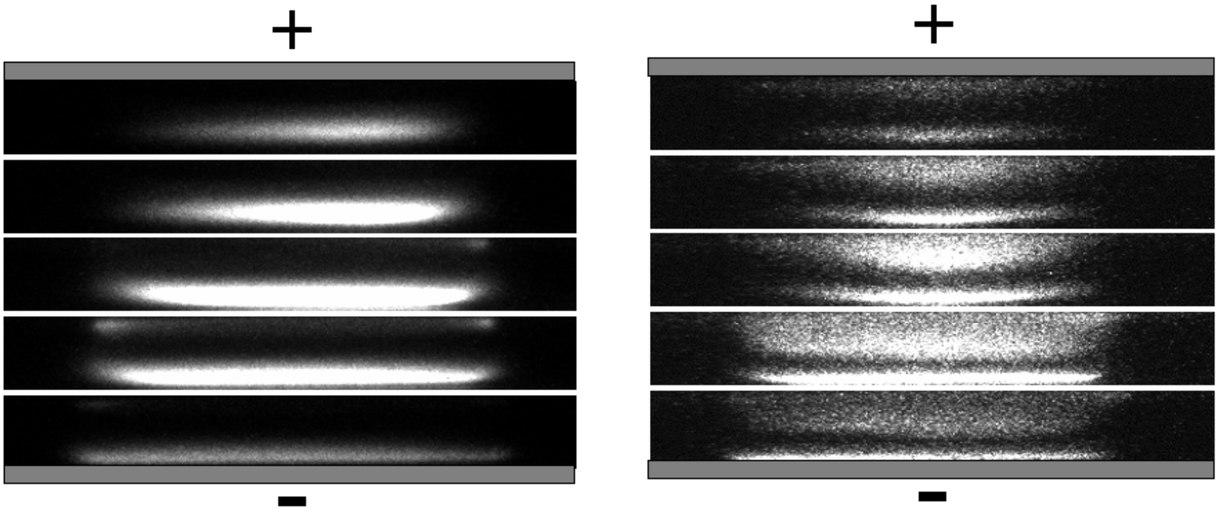

Figure 2: Light emission during positive current pulse. Left: Dielectric barriers are 5 mm thick glass plates. Exposure time is 300 nsec. with 800 accumulation on the CCD chip. Right: Dielectric barriers are 0.635 mm thick alumina plates. Exposure time is 13 nsec. with 100 accumulation on the CCD chip.

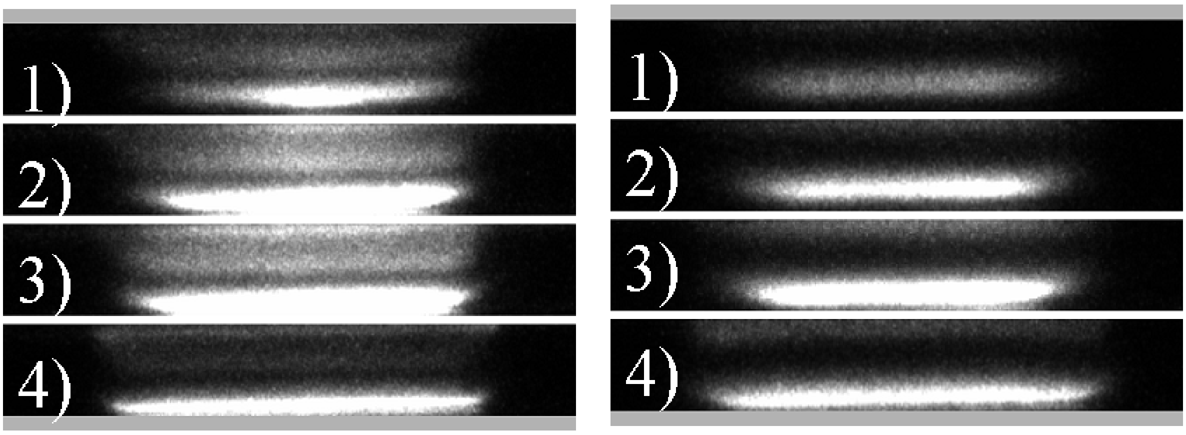

Figure 3: Light emission in the Helium gap over one positive current pulse for 1 mm alumina (left) and 4 mm alumina (right). The momentary cathode is on bottom. Frame number 2) corresponds to current maximum.

Figure 3 shows the light emission in the gap during the positive current pulse for the 1 mm and 4 mm alumina dielectrics. A glow-like discharge with a positive column is clearly observed for the 1 mm dielectric. The positive column disappears for the 4 mm dielectric and the discharge is Townsend-like. In fact, measurements with several intermediate dielectric thicknesses were performed and the disappearance of the positive column is observed to be a gradual process. The results in Fig. 3 indicate that the current limitation through the dielectric is responsible for the shift in discharge regime.

The one-dimensional model discussed above was used to simulate the experiments in Fig. 3. The code was run for several cycles until a periodic solution was found. The waveforms of the applied voltage, gap voltage, and current density are compared with results of measurements in Fig. 4.

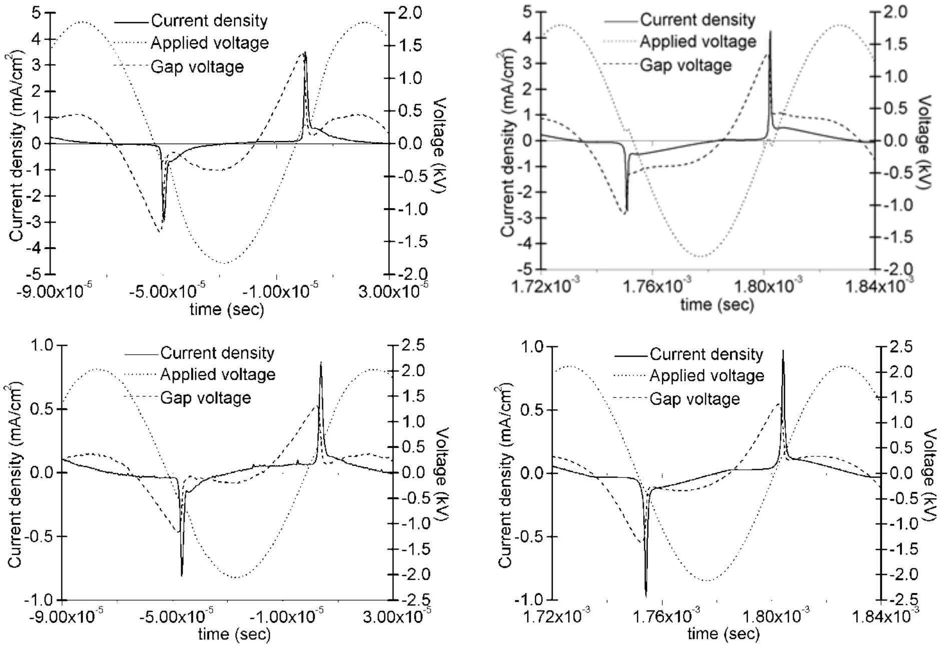

Figure 4: Measured electrical characteristics (left) and numerical simulation (right) for 1 mm alumina (top) and 4 mm alumina (bottom).

Obviously, excellent agreement between the model and measurements is obtained. For the case of the 4 mm dielectrics, the measured current density is by about 20% smaller than the measured peak current density. However, in this case the distance between the electrodes is 13 mm (5 mm gap plus two 4 mm dielectrics) while the electrode radius is 20 mm. The measured current density at the center may be affected by edge effects that are not accounted for in the one-dimensional model.

The calculated electric field distributions and the excitation rate of metastable atoms for the moment of maximum discharge current are shown in Figure 5. Since at present we have not performed detailed measurements of the spectral emission of the discharge, we consider the profile of the metastable atom excitation rate as indicative for the profiles of optical emission. For the 1 mm case, we observe a narrow maximum in the region of large electric field close to the cathode, which represents the emission by the cathode layer. The electric field drops to almost zero at about 0.6 mm. The metastable excitation rate around this position is also almost zero and indicates the Faraday dark space. Towards the anode, the electric field increases again and the rise of the metastable excitation rate signals the presence of the positive column. The electric field has a peak value of 18,000 V/cm at the momentary cathode dropping quickly to nearly 0 V/cm in the region of the Faraday dark space. The 4-mm-dielectric case shows less intense electric field strength at the cathode with about 10000 V/cm. After a more gradual decrease, it essentially levels off, without reaching a clear minimum value between the cathode fall and the anode. Correspondingly a broader profile of the metastable excitation rate in the region of the cathode layer is observed. Due to the lower electric field in the vicinity of the anode, the positive column is absent, indicating the same Townsend-like discharge regime as observed in the experiments. The overall qualitative agreement between the computed metastable excitation rate and the integral optical emission profiles is very good.

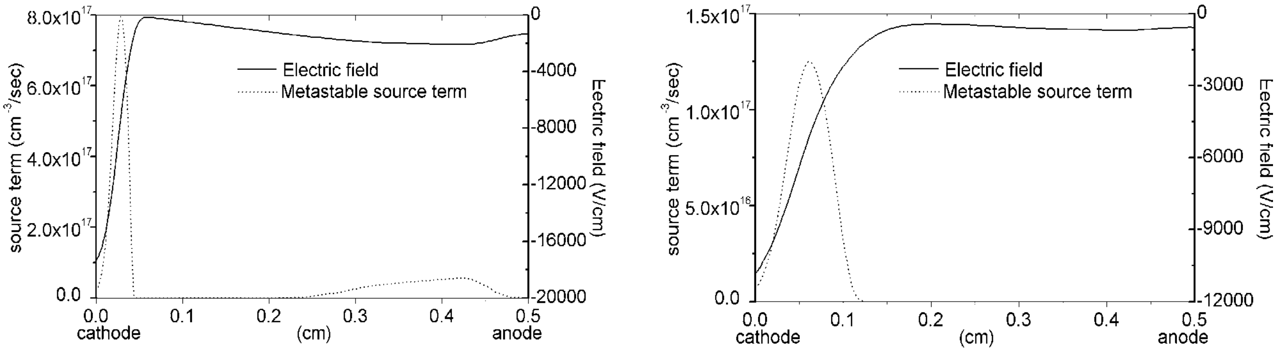

Figure 5: Electric field distribution and metastable source term for 1 mm alumina (left) and 4 mm alumina (right). Both distributions evaluated at discharge current maximum.

5. Conclusions

We have studied the characteristics of an APG discharge in Helium using both experimental and numerical techniques. It was demonstrated that the current limiting effect of the dielectric barriers can be used to adjust the discharge operating point between a glow-like and Townsend-like regime. A larger impedance of the dielectric either through thicker dielectrics or smaller dielectric constant of the barriers shifts the discharge regime towards a Townsend-like discharge. The experimental observations were supported by the results of our one-dimensional model. Good agreements with experiments in terms of the electrical characteristics (applied voltage, gap voltage, and current density) were found. The metastable excitation rate showed close similarity to the optical emission confirming the transition from the glow to the Townsend-like regime observed in the experiments.

Acknowledgments

This work is supported by the Department of Energy under grant DE-FG02-00ER54583 and by the University of Minnesota Supercomputing Institute.

References

1. Massines, F., A. Rabehi, P. Decomps, R.B. Gadri, P. Ségur, and C. Mayoux, *Experimental and theoretical study of a glow discharge at atmospheric pressure controlled by dielectric barrier.* J. Appl. Phys., 1998. **83**: p. 2950.
2. Mangolini, L., K. Orlov, U. Kortshagen, J. Heberlein, and U. Kogelschatz, *Radial structure of a low-frequency atmospheric-pressure glow discharge in helium.* Appl. Phys. Lett., 2002. **80**: p. 1722-1724.
3. Golubovskii, Y.B., V.A. Maiorov, J. Behnke, and J.F. Behnke, *Modelling of the homogeneous barrier discharge in helium at atmospheric pressure.* 2003.
4. Gherardi, N., G. Gouda, E. Gat, A. Ricard, and F. Massines, *Transition from glow silent discharge to micro-discharges in nitrogen gas.* Plasma Sources Sci. Technol., 2000. **9**: p. 340.
5. Gherardi, N. and F. Massines, *Mechanisms controlling the transition from glow silent discharge to streamer discharge in nitrogen.* IEEE Transactions on Plasma Science, 2001. **29**(3): p. 536-544.
6. Patankar, S.V., *Numerical Heat Transfer and Fluid Flow*. 1980, New York: McGraw-Hill Book Company.
7. Raizer, Y.P., *Gas Discharge Physics*. 1991, Berlin: Springer.
8. Mitcher, M. and C. Kruger, *Partially Ionized Gases*. 1973, New York: Wiley&Sons.
9. Kossyi, I.A., A.Y. Kostinsky, A.A. Matveyev, and V.P. Silakov, *Kinetic scheme of the non-equilibrium discharge in nitrogen-oxygen mixtures.* Plasma Sources Sci. Technol., 1992. **1**(3): p. 207-220.
10. Ueno, T. and Y. Hatano, *Measurement of the rate constant of the penning ionization of nitrogen by helium metastable states as studied by pulse radiolysis.* Chem. Phys. Letters, 1976. **40**(2): p. 283-286.
11. Gherardi, N., E. Gat, F. Massines, S. Lemoing, and P. Segur. *Light emission spatial and temporal evolutions in a glow dielectric barrier discharge in nitrogen: experiments and modelling*. in *15th International Symposium on Plasma Chemistry*. 2001. Orleans, France: GREMI, CNRS/University of Orleans.
12. Kato, T. and R. Janev, *Atomic and plasma-material interaction data for fusion.* Supplement Journal Nucl. Fusion, 1992. **3**(33-39).
13. Brunger, M.J., S.J. Buckman, L.J. Allen, I.E. McCarthy, and K. Ratnavelu, *Elastic electron scattering from helium: absolute experimental cross sections, theory and derived interaction potentials.* J. Phys. B: At. Mol. Phys., 1992. **25**(8): p. 1823-1838.

Deposition of Ammonia-free Silicon Nitride
Using Inductively Coupled Plasma at Low Temperatures

H. Zhou[1], C. Sim[1], C. Hodson[2], R. Kinsey[2], C. D. W. Wilkinson[1]

[1] *Nanoelectronics Research Centre, Department of Electrical and Electrical Engineering,*
Glasgow University, Glasgow G12 8QQ, United Kingdom
[2] *Oxford Instruments Plasma Technology, North End, Yatton, Bristol, United Kingdom*

Abstract

Room temperature ammonia-free silicon nitride films have been deposited by inductively coupled plasma enhanced chemical vapor deposition technique. The effects of a wide range of deposition parameters, such as RF power, deposition pressure, substrate temperature, and the gases flux ratio SiH_4/N_2, on the deposition rate and refractive index of the silicon nitride films using SiH_4-N_2 plasma are investigated. The properties of the films, such as stress, composition, and dielectric strength are briefly discussed.

References

[1] S. V. Nguyen, J. Vac. Sci. Technol. **B4**, 1159 (1986).
[2] M. Maeda and Y. Arita, J. Appl. Phys. **53**, 6852 (1982).
[3] S. Matsuo and M. Kiuchi, Jpn. J. Appl. Phys. **22**, 210 (1983).
[4] T. Hamasaki, M. Ueda, A. Chayahara, M. Hirose, and Y. Osakkka, Appl. Phys. Lett. **44**, 1049 (1984).
[5] F. S. Pool, J. Appl. Phys. **81**, 2839 (1997).
[6] S. Y. Shapoval, V. T. Petrashov, O. A. Popov, M. D. Yoder, P. D. Maciel, and C. K. C. Lok, J. Vac. Sci. Technol. **A9**, 3071 (1991).
[7] D. V. Tsu and G. Lucovsky, J. Vac. Sci. Technol. **A4**, 480 (1986).
[8] H. Mito and A Sekiguchi, J. Vac. Sci. Technol. **A4**, 475 (1986).
[9].J. R. Flemish and R. L. Pfeffer, J. Appl. Phys. **74**, 3277 (1993).
[10] C. Juang, J. H. Chang, and R. Y. Hwang, J. Vac. Sci. Technol. **B10**, 1221 (1992).
[11] R. S. Rosler, W. C. Benzing, and James Baldo, Solid State Technol. **XX**, 45 (1976)
[12] S. Lee and A. Gopinath, J. Vac. Sci. Technol. **B8**, 402 (1990).
[13] H. Mito aand A. Sekiguchi, J. Vac. Sci. Technol. **A4**, 475 (1986).
[14] C. Blaauw, J. Appl. Phys. **54**, 5064 (1983).
[15] S. Hasegawa, Y. Amano, T. Inokuma, and Y. Kurata, J. Appl. Phys. **75**, 1493 (1994).

1. Introduction

There have been extensive studies of the properties of silicon nitride (SiN) films due to its extensive applications in silicon and III-V electronic and optoelectronic device technologies. Main properties that make SiN an important dielectric in very large-scale integrated circuit (VLSI) technology are low current leakage, high breakdown voltage, and low interface-state density. These characteristics are dependent on the Si/N ratio and hydrogen content in deposited films [1, 2]. Conventional SiN deposition techniques include low-pressure chemical vapor deposition (LPCVD) and plasma-enhanced CVD (PECVD). The disadvantage of LPCVD is that it is a high temperature technique (>600^{o}C), which is not compatible with all device structures on a wafer or compatible with compound semiconductors. The PECVD technique is able to reduce the deposition temperature (~300^{o}C). But unlike LPCVD silicon nitride (Si_3N_4), the PECVD silicon nitride (SiN) is not confined to the stoichiometric Si_3N_4 composition, as it contains amounts of bonded hydrogen [1]. PECVD SiN films can possess markedly different characteristics, which depend greatly on the deposition conditions.

There is considerable interest of dielectric films that can be deposited at temperatures lower than 300^{o}C. Recently, the electron cyclotron resonance microwave (ECR CVD) technique has been developed [3, 4] and has deposited SiN films with very good qualities [5, 6]. The inductively coupled plasma CVD (ICP CVD) technique has also been developed [7, 8]. In the early stage, although high-density plasma was obtained, the deposition pressures were several hundred mTorr and the plasma was not expanded over a wide area. In the recent years, ICP sources have been able to produce high-density and large-diameter plasmas in low-pressure range. The main advantages of ECR CVD and ICP CVD systems over conventional PECVD system are the high-density plasma, low deposition pressures and temperatures. These advantages will result in minimizing film contamination, promoting film stoichiometry, reducing radiation damage caused by direct ion-surface interaction, and eliminating device degradation at high temperatures. ICP CVD system also has other advantages, such as no magnetic field on the wafer processing position; easy production of large-diameter uniform plasmas, a compact and simple source.

Room temperature ammonia-free silicon nitride films have been deposited by inductively coupled plasma enhanced chemical vapor deposition technique. Properties of the silicon nitride films using SiH_4-N_2 plasma are investigated versus various deposition parameters such as RF power, deposition pressure, substrate temperature, and flow rate ratio of SiH_4 to N_2. The effects of deposition conditions on refractive index, deposition rate, uniformity, stress, composition, and dielectric strength are discussed.

In this paper, we present the work on the deposition of high quality SiN films using SiH_4-N_2 plasma by the ICP CVD technique at the substrate temperature as low as 20°C on Si substrates. The effects of a wide range of deposition parameters, such as RF power, deposition pressure, substrate temperature, and the gases flux ratio SiH_4/N_2, on the deposition rate and refractive index of SiN films are investigated. The film properties, such as stress, composition, and dielectric strength are briefly discussed.

2. Experimental systems

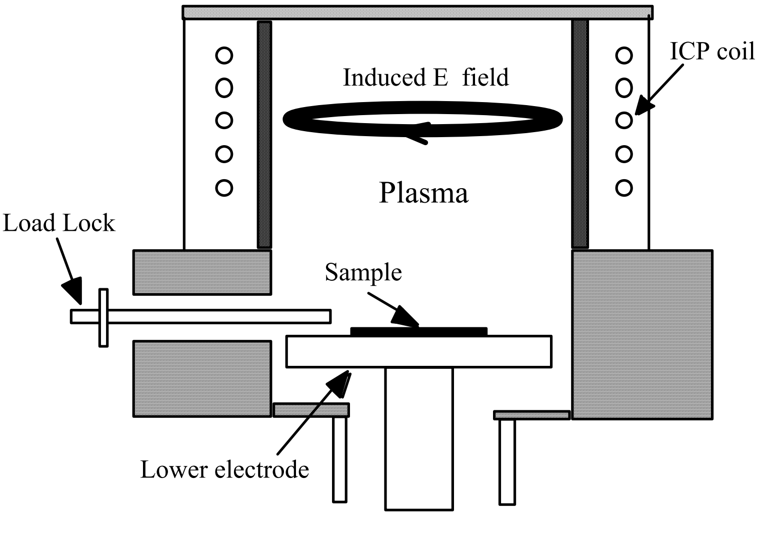

Fig. 1. Schematic diagram of the ICP CVD system.

The system used for deposition SiN films was a Plasmalab System 100 ICP180 from Oxford Instruments Plasma Technology. Schematic diagram of the ICP CVD system is shown in Fig. 1. The inductively coupled coil is connected to a 13.56 MHz, 2.5kW RF generator via a matching unit. The RF current through the coil generates the RF magnetic flux along the axis of the cylinder. At the same time, this RF magnetic flux induces a RF electric field inside the cylinder. This induced E field accelerates electrons. Finally these accelerated electrons produce high-density plasma in the ICP system. The ICP coil power controls the dissociation of the plasma and the density of the incident ions in the chamber. The lower electrode is separately powered by another 13.56 MHz 300W generator, which allows independent control of the bias voltage, i.e. the energy of the ions stricken on the sample. In order to reduce the plasma-induced damage during deposition processes and the stress level in deposited films, the ICP CVD system has been operated in a purely "ICP" mode by applying RF power (100 to 700W) to only the ICP coil, but no RF power on the lower electrode.

Samples were loaded automatically from an evacuated load lock into the main chamber to maintain good stability of chamber vacuum and hence excellent repeatability of deposition results. The 4inch silicon wafers were mechanically clamped to a temperature-controlled electrode. Helium pressure was applied to the back of the wafers to provide good thermal contact between chuck and wafer. The system has precise control of substrate temperature from -150°C to +200°C by using electrical heater and liquid nitrogen. This wide temperature range is important for the advanced plasma deposition processes of different substrate materials.

Since the total hydrogen content in a SiN film and the type of hydrogen bonds has a strong effect on the film properties. To reduce the hydrogen content in a PECVD SiN film, ammonia (NH_3) is generally replaced by N_2. High purity N_2 was introduced into the ICP source chamber at flow rates of 5-20sccm, while pure silane (100% SiH_4) was introduced into the deposition chamber through a gas distribution ring at rates of 3-20sccm. The gas flow rates were controlled by mass flow controllers (MFC) accurate to ~ 5% of the setting flow rate. Automatic pressure controller (APC) controlled the pressure (2 to 20mTorr).

3. Results and discussion

To study the effects of the deposition parameters at low temperature using SiH_4-N_2 plasma, Figs. 2,3,4, and 5 show deposition rate and refractive index as a function of chamber pressure, RF power, substrate temperature, and silane flow ratio, respectively. Refractive index and thickness of SiN films deposited on Si substrates were measured by a Gaerrner ellipsometer with manual polariser and analyzer. From the values of P1, A1 and P2, A2, refractive index and thickness were calculated. Film thickness was from 70 to 110nm. Dektak Stylus Profiler was also used to directly confirm the thickness measurements.

The deposition rate and refractive index as a function of chamber pressure are shown in Fig. 2. It is very interesting to note that at pressures lower than 10mTorr the deposition rate is constant, almost independent on the pressure. However, as increasing pressure just above 10mTorr, the deposition rate sharply increases to three times higher than that at 10mTorr. After pressure above 15mTorr, the deposition rate increases slowly again. The refractive index has the maximum 2.15 at the lowest pressure 4mTorr. At pressures lower than 10mTorr, the refractive index decreases slightly, and then almost constant. However, as the pressure increases just above 10mTorr, the refractive index sharply decreases to less than 1.5. After pressure above 15mTorr, the refractive index is almost independent on the pressure and then increases slowly again. The SiN films deposited at pressures higher than 15mTorr show poor qualities. The increased deposition rate at higher pressures may be a manifestation of lower film density and greater hydrogen incorporation. We should point that this pressure dependence of deposition rate and refractive index of SiN films deposited by ICP CVD is quite similar to that obtained by ECR CVD method [9].

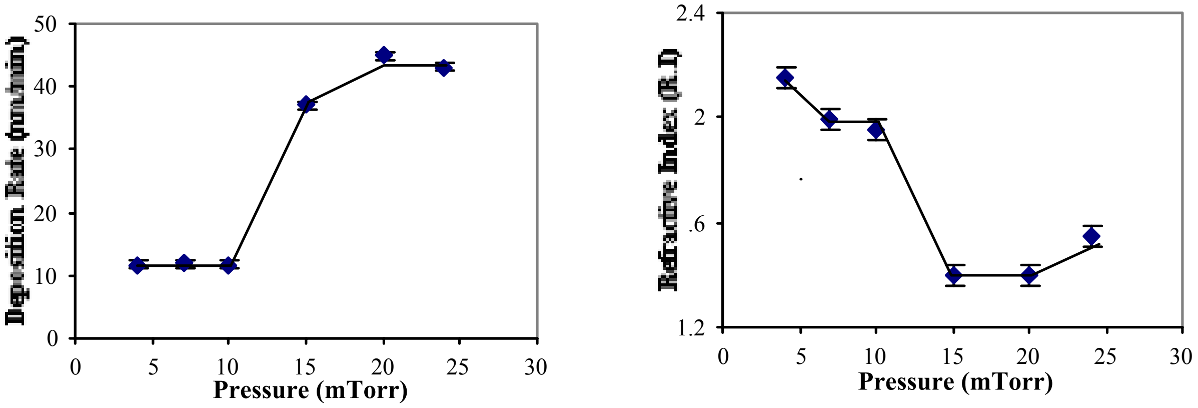

(a) (b)

Fig. 2. Pressure dependence of the deposition rate (a) and refractive index (b) of SiN films.
(SiH_4/N_2 = 6:6sccm, T = 20°C, RF power = 100W).

As shown in Fig. 3, the deposition rate and refractive index strongly depend on the RF power in the range of 100-500W. It is understandable that RF power provides energy to induce chemical reactions. This energy is important to the reactions especially when the substrate temperature is low. The increasing of RF power speeds up the reactions (deposition rate). This suggests a reaction-controlled rather than a transfer-controlled type of mechanism at low temperature [10]. We can see that the deposition rate first linearly increases with the power till ~ 300W, due to the enhanced dissociation of SiH_4/N_2 gases by the increased power. However in the range of 300-500W, the deposition rate has a slow increase and tends to saturate. At the same time, we see a symmetric effect on the refractive index, which first decreases with power till ~ 300W, and then is almost constant in the range of 300-500W. This may be explained by the fact that the N_2 has higher dissociation energy than the SiH_4, so that the fraction of the N_2 dissociated compared to the SiH_4 dissociation increases with increasing the power [11]. Therefore the SiN films changes from Si rich to N rich, which results in the decrease of the refractive index with power. This RF power dependence of deposition rate and refractive index of SiN deposited by ICP CVD is similar to that obtained by ECR CVD [12].

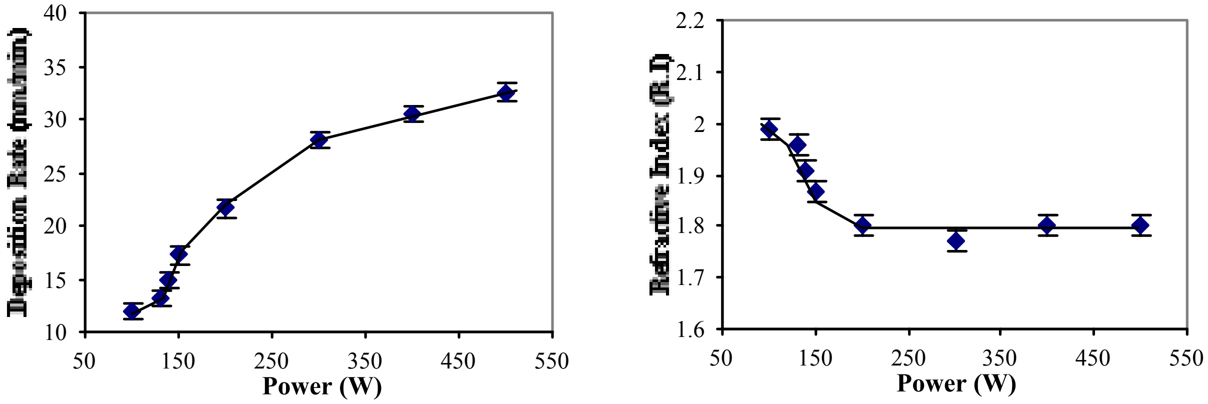

(a) (b)

Fig. 3. RF power dependence of the deposition rate (a) and refractive index (b) of SiN films. (SiH_4/N_2 = 6:6sccm, T = 20°C, pressure = 7mTorr).

In Fig. 4, we can see that in the range of 20-200^{0}C, the substrate temperature can significantly change the deposition rate. This is expected because increasing temperature will reduce hydrogen content and increase the film density [12]. Higher density is a consequence of both lower hydrogen content and a lower deposition rate. However, the substrate temperature has small influence on the refractive index, which only increases slightly in the range 20-100^{0}C, and then decreases with very small slope.

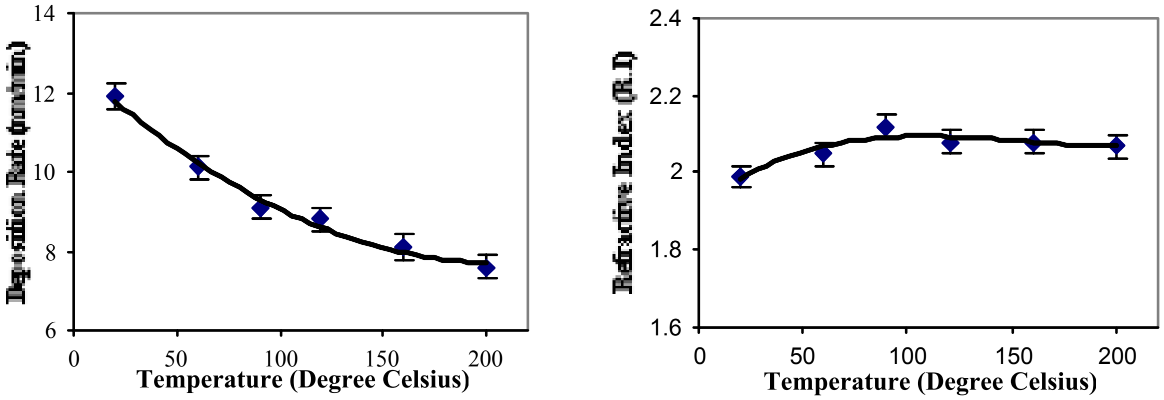

(a) (b)

Fig. 4. Temperature dependence of the deposition rate (a) and refractive index (b) of SiN films. (SiH_4/N_2 = 6:6sccm, pressure = 7mTorr, RF power = 100W).

It is interesting to note that in Fig. 5, the deposition rate only has small variations when the SiH_4/N_2 flow rate ratio has changed from 0.5 to 1.33. It is thought that this situation in deposition rate is caused by the limited feed rate of N radicals [13]. However, at the same time, a small amount change of SiH_4 flow rate can increase the refractive index rapidly. This is quite reasonable because increasing SiH_4/N_2 ratio corresponds to increasing Si/N ratio, which results in a significant increase in refractive index [12]. This also indicates that more Si atoms are incorporated in SiN films with increasing SiH_4 flow rate.

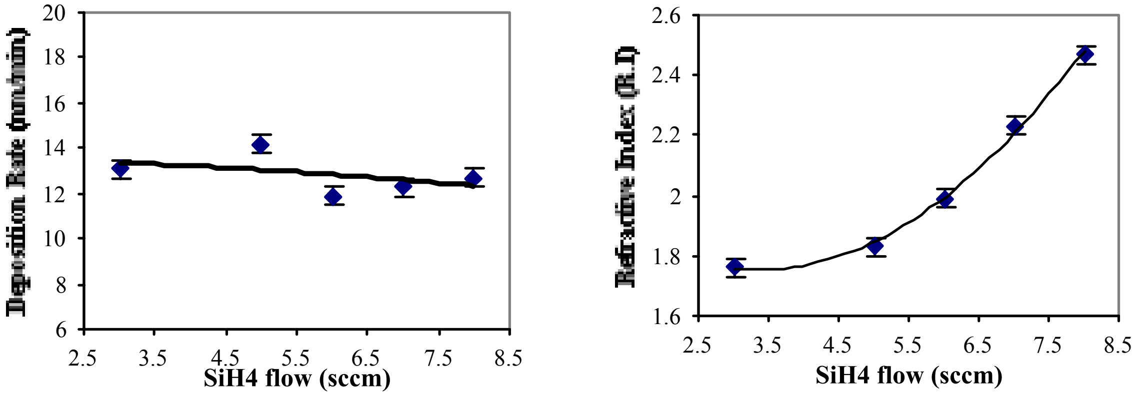

(a) (b)

Fig. 5. SiH_4 flow rate dependence of the deposition rate (a) and refractive index (b) of SiN films.

(N_2 = 6sccm, T = 20°C, pressure = 7mTorr, RF power = 100W).

Film stress was measured using Dektak Stylus Profiler and calculated by Stress Measurement Software from Veeco Metrology Group. The stress calculation was based on the formula below:

$$\sigma = (E_S t_S^2) / 6 (1 - \nu_S) t_f R$$

where σ is the stress in the film, t_S and t_f are the thickness of substrate and film, respectively, E_S is Young's modulus of the substrate, ν_S, is Poisson's ratio of the substrate, and R is its radius of curvature [14]. Using above formula to calculate film stress, the key parameter is the radius of curvature of the substrate, before and after film deposition. The radius of curvature is calculated from scan height data. The film stress has been investigated as a function of deposition pressure, RF power and substrate temperature, respectively. We observed that film stress is strongly dependent on the RF power and deposition pressure. Detailed results will be presented in another paper. For SiN films with 500nm thickness deposited by ICP CVD, both the lowest tensile stress 2.7×10^8dyne/cm^2 and compressive stress 2.5×10^8dyne/cm^2 have been obtained at room temperature deposition.

The electronic properties of the SiN films have been investigated as a function of deposition pressure, RF power and substrate temperature, respectively. The electrical properties of the films (resistivity ρ, and breakdown field E_B) were obtained by measuring the I-V characteristics of the metal-insulator-metal (MIM) capacitor structures. MIM devices were fabricated as follows: firstly, the Si wafers were coated with a layer of 20nm of Ti and 150nm of Au by e-beam evaporation. Then 100nm SiN was deposited on the top of Ti/Au layer. Finally, Ti/Au squares were evaporated through a photo resist mask by e-beam evaporation to define the top electrodes. In order to separate individual capacitors, SiN films lying outside electrode areas were etched away by RIE etching. For room temperature deposition, the breakdown field E_B, ~3-4x10^{6}V/cm has been obtained, which was defined at the field at which the MIM current is 1μA/cm^2. Considering if the SiN films lying outside electrode areas were not etched away, the actual breakdown field E_B of the SiN films might be higher than that we measured, because the breakdown may occurs through the air beneath the two electrodes. The films having higher value of E_B contain less hydrogen inside. The relation between E_B and the presence of hydrogen in the PECVD SiN films was already suggested [15]. The stress of the films, directly related with the presence/absence of hydrogen, may play some specific role in the understanding of breakdown properties of SiN films. The detailed results of electronic properties of the SiN films on Si, Si/Ge and III-V devices will be presented in other papers.

Infrared transmission spectra of SiN films deposited on Si substrates were obtained with an infrared spectrometer in the midinfrared region (400-4000cm^{-1}). Since the Si wafers used for deposition were not double side polished, SiN films could only be deposited on the polished side. Therefore, after SiN deposition, the unpolished Si surface will be oxidized in air, which will results in the absorption peak related to Si-O bond in infrared spectra. The composition, hydrogen content and bond configuration of the films were deduced with infrared transmission spectra. Absorption peaks due to Si-N, Si-H and Si-Si bonds are observed at ~850cm^{-1}, ~2160cm^{-1} and ~610cm^{-1} for all SiN films deposited at different conditions by ICP CVD. But we have not observed the absorption peaks due to N-H bonds (~1200cm^{-1}, ~2160 and ~610cm^{-1}) within the detectable limit of the spectrometer. However, this result is similar to that reported by Mito et al [8]. Detailed spectroscopic analysis of the SiN films deposited on Si substrates will be presented in other papers.

Conclusions

High quality ammonia SiN films have been deposited on Si and GaAs substrates at temperature range from 20^{o}C to 200^{o}C using SiH_4 and N_2 plasma at pressures lower than 10mT. The ratio of SiH_4:N_2 was adjusted to give refractive index in the range of 1.95 – 2.05. Both the lowest tensile stress 2.7x10^{8}dyne/cm^2 and compressive stress 2.5x10^{8}dyne/cm^2 have been obtained at room temperature deposition without using RF power on the lower electrode. We noticed that if the lower electrode with 5W RF power on it, the stress can be as high as 1.36x10^{10}dyne/cm^2 compressive. We also discovered that the best film quality could be achieved at low ICP powers and low pressures, probably due to reduced deposition rate. At room temperature, ICP power of 100-150W and pressure 4-7mTorr, it is possible to obtain an acceptable deposition rate of 12-17nm/min, with good film quality and reasonable uniformity typically between ±4% and ±7% across a 4” wafer. The dielectric strength is 3-4x10^{6}V/cm. The composition, hydrogen content and bond configuration of the films were deduced with infrared transmission spectra.

Acknowledgements

We wish to thank Dr A. Glidle for doing the infrared measurements. We would also like to thank Mr. Dave Clifton, Colin Roberts and Ronnie Roger for their help in the Dry Etch Laboratory.

Flames Control by Means of Non-Equilibrium Low-Temperature Nanosecond Silent Gas Discharge Plasma

E.I.Mintoussov, A.Yu.Starikovskii

Department of Physical Mechanics, Moscow Institute of Physics and Technology, Dolgoprudny, Russia

Abstract

The influence of pulsed nanosecond silent (or barrier) discharge on the flame velocity was investigated for propane/air mixture in a wide range of equivalence ratios at atmospheric pressure. It was experimentally obtained that blow-off flow rates are more than twice increased as compared to the system without silent discharge. Discharge energy input is less then 1% of burner power. This effect is explained by the formation of atomic oxygen in silent discharge followed by acceleration of limiting chemical reactions.

1. Introduction

The effect of an electric field on a flame first was discovered by Brande in 1814. In his work [1] he reported that flame behavior changes greatly if the candle is placed between two electrodes. The interaction of electric fields and discharges with flames has been studied widely and extensively all over the world since than. The main idea of the most of these studies is the possibility to apply electric fields or discharges for stabilization of flames, production of active particles which reduce carbon and NOx formation, extending flammability limits or increasing flame luminosity. The problem of determining fundamental mechanisms by which it's possible to control the flame stability is of interest as well.

The works aimed at applying electric discharge to increase flame velocity (for example, [2]) form a separate group of studies. Faster burning means the possibility to practice combustion of mixtures with low fuel content followed by reducing the formation of NOx oxides. Therefore, the problem of an effective controlling the flame stability is actual nowadays. The goal of the present work is to find mechanisms of flame control.

The easiest way to influence a gas mixture by means of electric discharge is well-known to all motor-car enthusiasts, and this is a spark plug. But in this case spark discharge current is rather large, so mixture ignition is caused by thermal heating of gas. That’s why mechanisms with energy input in flame which is low or insufficient for mixture heating up to spontaneous ignition temperature has special significance.

Flame can be treated as a low-temperature plasma with charged particles energy approximately of 0.1 eV, which mainly consists of molecules and radicals as well as electrons and positively charged ions caused by chemi- and thermo-dissociation. So, besides joule heating, which was mentioned above, there are two main mechanisms which are suggested for the influence of electric field on flame velocity. In weak fields (about couple of hundred volts per centimeter), where field energy is insufficient to excite mixture components, the ionic wind is a determining factor. Under its influence redistribution of charged particles in the combustion zone as well as neutral particles involved in motion by resonance recharging process takes place. It was shown in a classical book of Lawton and Weinberg [3] that such electric forces acting in flame can as more as two hundred times exceed convectional forces. The influence of ionic wind is especially considerable in the case of diffusion flames, where velocities are much lower than in premixed flames [2].

In strong fields processes of chemical kinetics, which are being changed under field influence, play an important role in flame. In this case particles energy should be great enough for electronic and vibrational excitation of molecules, so we mostly imply electrical discharges (corona discharge, streamer discharge and so on).

The method of acceleration of combustion by means of non-equilibrium excitation of gas mixture components allows to change chemical kinetics processes; so it is seemed to be the most promising nowadays. Such excitation can be achieved by using corona discharge. Short (nanosecond) pulses should be used to provide high-performance electronic excitation. Pulsed barrier discharge was selected to avoid the transition of the streamer discharge to the spark form (dielectric barrier limits the maximum current). The form of discharge is non-equilibrium – electron’s temperature is quite high (about 4-5 eV), whereas temperature of heavy particles is near to room temperature. Thus there is no any gas heating by the discharge, and energy is put into the vibrational and electronic degrees of freedom of the mixture.

2. Experimental set-up

A set-up consisted of burner, pulse high-voltage power supply, gas supply system and diagnostic system has been used to settle the problem (fig.1).

The burner body is made of glass. The exit section is a rectangle with 30mm x 2mm dimensions, so flame basis is long enough to work in a 1D geometry. Multipoint brass plate with rectangle section 1mm x 28mm is used as a high-voltage electrode and placed into the nozzle parallel to its walls. Low-voltage electrodes are made of copper foil, placed into the quartz tubes and positioned near the burner nozzle. The distances between high voltage electrode and quartz tubes can be varied.

One of the advantages of such construction is the fact that voltage and discharge power are limited from above only by high-voltage generator intrinsic properties; the transition from streamer phase to spark form is impossible because of dielectric barrier.

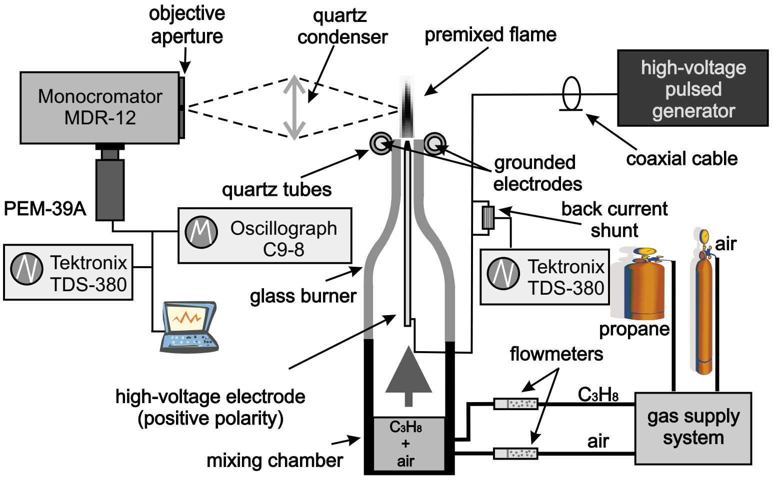

Figure 1. Experimental set-up

High voltage pulses are produced by pulsed high-voltage generator assembled according to rotating interrupter scheme. Characteristics of the single pulse are the following: amplitude up to 25 kV, time of front grow is 10±2 ns, pulse duration on the half-height is 77±5 ns, pulse repetition rate is 1200 Hz. The polarity of pulses could be varied, as well as voltage type: direct or pulse. Pulse's current and voltage was measured during the experiment; this allowed to obtain the value of energy input.

A blow-off flow rate was chosen as a macroscopic parameter which determines the efficiency of barrier discharge influence on the flame. Blow-off rate is directly connected with rates of chemical processes. Consumptions of mixture's components were measured to determine blow-off flow rate.

The investigation on active particles in flame was carried out by optical methods using an emission spectroscopy technique.

So, such set-up makes it possible to study burning of premixed gases in a wide range of equivalence ratios (propane-butane mixture used as a fuel and air used as an oxidizer) and generate the non-equilibrium plasma ahead the flame front.

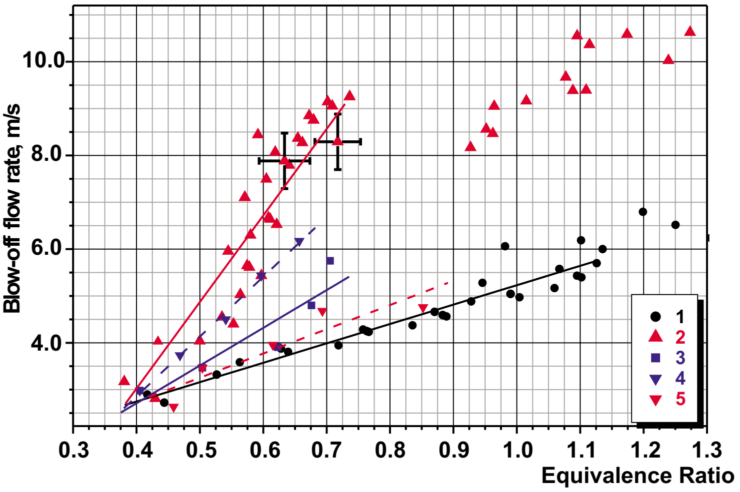

Fig.2 The comparative analysis of discharge influence on flame acceleration: **1** – without discharge; **2** – pulse 25 kV voltage of positive polarity; **3** – pulse 25 kV voltage of negative polarity; **4** – direct 25kV voltage of negative polarity and **5** – direct 25kV voltage of positive polarity.

3. Experimental results

It has been found out that influence of the barrier discharge on the flame leads to increase in blow-off flow rate, which is proportional to the discharge power. Nevertheless, the discharge energy input is less then 1% of burner power. Four different cases were studied: direct 25 kV voltage of positive polarity, direct 25 kV voltage of negative polarity, 25kV voltage pulses of positive polarity and 25kV voltage pulses of negative polarity. The comparative analysis of these effects and their influence on blow-off rates is represented on figure 2. It was found out that the pulse 25kV voltage of positive polarity is most effective. It is more efficient than the pulse discharge of negative polarity because cathode-directed streamer is more saturated with active particles than the anode-directed one. On the contrary, negative voltage is more effective in the case of direct voltage discharge (cathode is a good emitter of electrons and corona appears on it). Positive polarity of direct discharge doesn't provide any significant result.

For pulse voltage, which is the most effective for flame velocity increase, the change of blow-off flow rate was studied in a wide range of equivalence ratios (0.5-5); see fig.2. It's clear that the most strong influence of discharge takes place in the area of ϕ=0.65-0.75. The change in blow-off flow rate in the system with barrier discharge exceeds 100%.

Pulse voltage monitoring was performed to evaluate the energy inputted into the gas mixture. The energy of one pulse is 8 mJ, and this value corresponds to the mean power approx. of 9 watts. This is less than 1% of chemical power of propane/air mixture burning.

The diagnostic of active particles in flame was fulfilled by means of emission spectroscopy. The results are shown in fig.3: the barrier discharge spectrum in a propane/air mixture (ϕ=1, U=22kV), premixed propane/air flame spectrum (ϕ=0.6) and the spectrum of premixed propane/air flame in the presence the barrier discharge (ϕ=0.6, U=22kV). Spectra were read within the range of 200-600 nm.

Emission bands in these spectra are identified easily. Bands of 2^+ system of nitrogen (290-550 nm) are seen well in a barrier discharge. There can be also found γ-bands of NO oxide (220-260 nm) and 1^- nitrogen system band (391.4). Bands of CH, CN, NO, NH, C_2 are existed as well as emission line of $0 \rightarrow 0$ vibrational transition of $A^2\Sigma^+ \rightarrow X^2\Pi$ electronic transition (306.4 nm) in the flame spectrum. When discharge is on, an emission line of OH $3 \rightarrow 2$ vibrational transition appears in flame (294.5 nm). The main mechanisms of OH formation in reaction zone are:

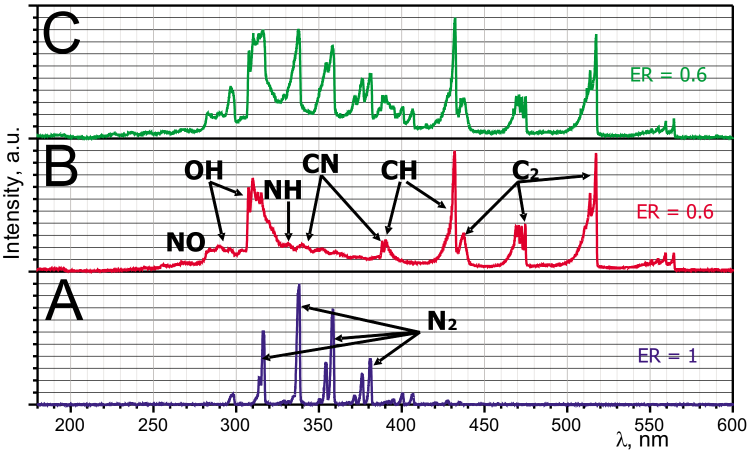

Fig. 3. A – the barrier discharge spectrum in a propane/air mixture (ϕ=1, U=22kV); B – premixed propane/air flame spectrum (ϕ=0.6) and C – the spectrum of premixed propane/air flame in the presence the barrier discharge.

$$CH + O_2 \rightarrow OH^* + CO \tag{1}$$
$$H + O \rightarrow OH^*. \tag{2}$$

OH radical plays an important role in combustion and mainly determines reaction rate as well as normal flame velocity.

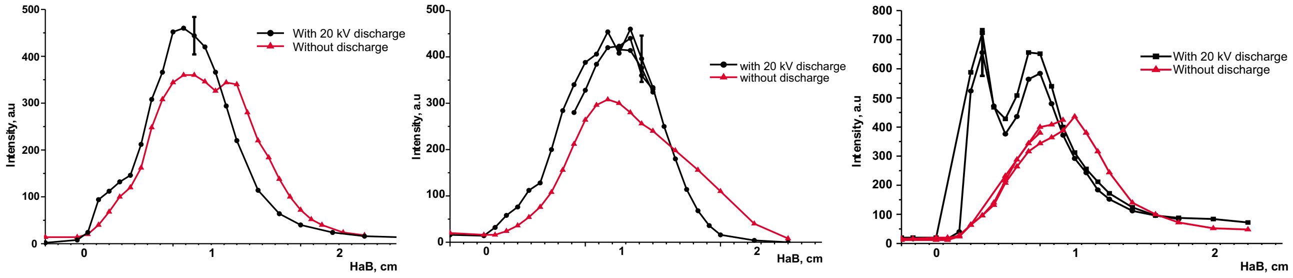

Fig.4 CH (ϕ=1, λ=431.5) , C_2 (ϕ=1, λ=517.8) and OH (ϕ=1.3, λ=306.4) emission profiles.

Emission profiles of C_2, CH and OH particles are shown in fig.4. It's distinctly seen that emission intensity maximum increases, and profile becomes narrower and moves toward the nozzle in the presence of barrier discharge due to the intensification of the combustion and acceleration of reaction rates. A second emission peak appears near the burner nozzle in the case of OH radical profile due to OH formation in discharge. Such OH behavior confirms importance of OH radical role in the combustion processes. In fig.5 you can see the OH emission dependence upon the height above burner for different gas consumption in the presence of barrier discharge. Equivalence ratio is constant and equals 0.6. With flow rate increase OH emission profile changes into the curve with two peaks. This is connected with radicals' formation and the creation of secondary reaction zone in front of the main flame. This region is characterized by strongly non-equilibrium concentration of active particles produced by electron impact in the discharge zone.

4. Discussion

It is necessary to determine the role of plasmochemical processes taking place in the pre-combustion zone to find the mechanisms of flame acceleration by electrical non-equilibrium discharge. Authors assume that barrier discharge influence on flame velocity is the result of excitation of initial gas mixture and formation of active particles before the reaction front. It's well-known that reagents' excitation as well as increasing of number of radicals leads to burning acceleration.

In a general case, electric field distribution in a discharge gap is non-uniform and rather difficult for precise description. We can use voltage between electrodes and the gap's length to get a rough estimate of the reduced electric field. Such estimation gives us the value of 330 Td. Another method of determining reduced field lie in measuring the emission intensity ratio of electronic-vibrational nitrogen transition (detailed description of this technique can be found in [4]). Overestimated value of reduced field obtained by means of this method is equal to 570 Td.

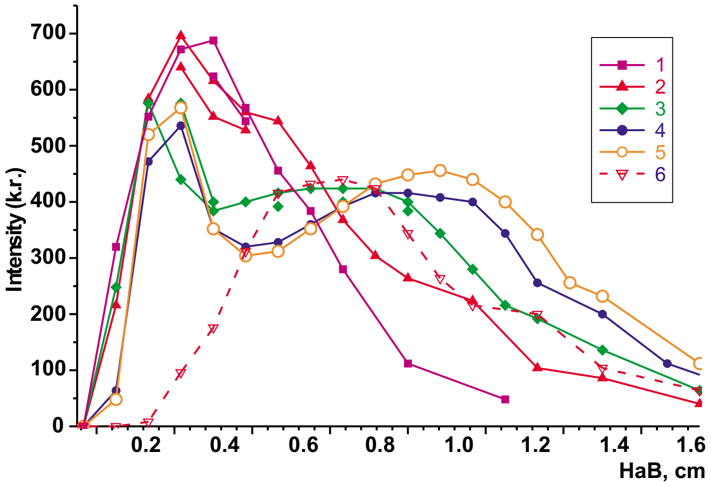

Fig. 5 OH emission for different consumptions in the presence of 25 kV barrier discharge, equivalence ratio is 0.6. **1** – 2.9 m/s, **2** – 4.0 m/s, **3** – 4.7 m/s, **4**- 5.4 m/s, **5** – 6.1 m/s, **6** – 4.0 m/s without discharge.

We'll consider 1D stationary task as an approach. In this case kinetics of plasmochemical process taking place in the pre-combustion zone in the presence of discharge can be divided into three spatially-separated parts: excitation of molecules by electron impact in the barrier discharge, kinetics of excited states and combustion processes. Of course, these areas can intersect each other and it's worth taking into account state-to-state kinetics as well as the influence of excited particles on the combustion. Unfortunately, the majority of constants of such processes are unknown, that's why authors state problem to build qualitative model describing burning acceleration by silent discharge.

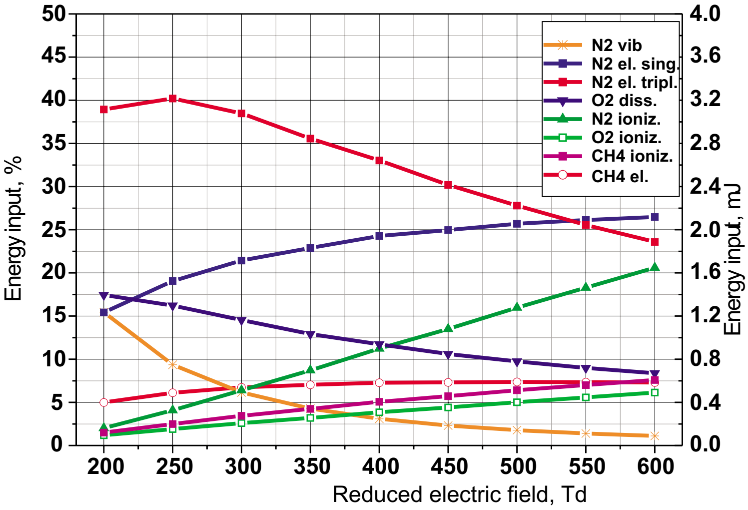

Fig. 6. Energy branching to the elementary processes in methane due to electron impact (calculation is performed using "BOLSIG" package)

On the first stage formation of excited particles by the electron impact takes place. Streamer starts from the high-voltage electrode in the presence of high-voltage pulse (about 100 ns). High-energy electrons are generated in streamer head (5-6 eV at the maximum of EEDF). In 5-7 ns streamer overlaps the gap. Only a streamer head (which is quite small) produces excited species as a rule, but the regime exists when high electric field within the total gap interval is reached. This mode takes places after overlapping and lasts until the spark breakdown. In the case of barrier discharge spark channel can't appear because of dielectric barrier limits electric current in the circuit. It's important that in this case field in the gap is a linear function of the length and generation of electrically excited particles occurs along the full length of the interelectrode space quite uniformly. So it's worth expecting the increase of number of excited species in the gap during the overlap regime because of their additional formation in the streamer channel. The main processes taking place during the electron impact are given below:

- Elastic collisions of electrons with molecules;
- Vibrational and electronic excitation of molecules;
- Dissociation;
- Ionization.

The analysis of high-voltage pulse energy branching to the processes given above whithin the range of our interest (300-600 Td) was performed using a "BolSig" package; results are shown in figure 6. The main part of energy is put into the electronic excitation of molecules (especially N_2) as well as dissociation, and into the nitrogen ionization in the case of strong fields.

After high voltage being turned off, electric field in the gap rapidly decreases and high-voltage electrons in channel disappear. Ionic-molecular reaction practically finishes.

On the second stage that lasts tens of microseconds processes with participation of formed excited particles as well as atomic-molecular reactions take place. Let's consider the main of them:

- Quenching of electronically excited states of nitrogen molecules. The main channels of their quenching are:

$$N_2^* + O_2 \rightarrow N_2 + O + O. \tag{3}$$

- Emission of electronically excited singlet states of nitrogen molecules.
- Dissociation of oxygen molecule through its electronically-excited states.

$$O_2^* \rightarrow O(^3P) + O(^3P) \tag{4}$$
$$O_2^* \rightarrow O(^3P) + O(^1D) \tag{5}$$

According to energy levels diagram, reaction (5) goes trough $O_2(B^3\Sigma^-)$ state, and reaction(4) goes through $O_2(A^3\Sigma^+)$ state. The number of O atoms formed in reaction (5) is three times greater than that in (4), so about a half of all atoms are in $O(^1D)$ state. This fact explains appearance of electronically-vibrationally excited OH in the presence of barrier discharge on wavelength which equals 294.5 nm

- Ionization of mixture's components (N_2 mainly). The main ions – N_2^+ and O_2^+ – quite quickly transform into the O_2 molecule through N_4^+ and O_4^+ ions
- Translational relaxation of vibrationally excited states of reagents. This is the way the gas heating occurs.

Authors draw a conclusion that at the mentioned times electronic and vibration excitation relaxes into translational movement as well as oxygen dissociation. About 40% of total energy goes to oxygen dissociation. Thus, the third stage can be treated as combustion of new mixture formed at the burner exit as a result of barrier discharge influence.

Calculation gives that concentration of atomic oxygen due to barrier discharge influence is quite high (0.13%); this explains such significant combustion acceleration.

A numerical modeling of combustion and propagation of 1D premixed methane-air flame is performed with the aid of "PREMIX" subprogram of "CHEMKIN" package. This program allows to take into account diffusion of components, thermo diffusion, and heat transfer. The main equations are: the equation of mass conservation, the heat transfer equation, the mass transfer equation and the equation of state. All forward rate coefficients are supposed to satisfy Arrhenius law, and each reaction proceeds according to the law of mass action. Kinetic scheme consists of 17 components and 58 reactions.

The results of modeling are represented on figure 7. Let's examine modification of the concentration profile of OH radical. It's distinctly seen that reaction zone becomes narrower with the increase of initial concentration of oxygen atoms. This means that combustion rate is increased too. The main particles taking part in reactions are O, H, and OH. Oxygen atoms that formed at the burner exit participate in reaction of chain branching. If the temperature is low (there is now gas heating by the discharge), rate of chain breaking is greater than chain branching rate, so initial oxygen concentration isn't enough to mixture inflammation. Nevertheless, temperature increase happens due to chemical reactions and heat flow from the reaction zone to the nozzle. Temperature rise depends on the atomic oxygen concentration, so flame velocity goes up with oxygen concentration increase.

If concentration of oxygen exceeds some critical (about 0.12%), the model gives an infinity value of flame velocity. This result should be interpreted by the following way. At certain concentration a temperature at which rate of chain branching becomes equal to the rate of chain breaking is achieved due to chemical reaction. The initial oxygen concentration in this case is enough to inflammation, so flame velocity is equal to infinity formally. For every flow rate combustion will be supported. But this situation demands to sustain the critical oxygen concentration at burner exit permanently, and this, in turn, demands infinite discharge power. So in practice critical concentration achieved, than flow rate increases and number of O atoms drops. As a result burning decelerates and, if flow rate is fast enough, can't sustain temperature gradient required for flame stabilization. The flame velocity increase is determined by the discharge power and is equal to 20% at maximum subcritical oxygen concentration.

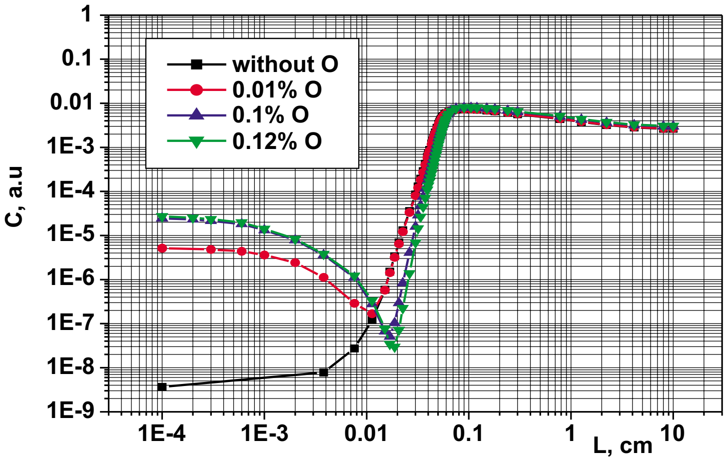

Fig.7. Results of OH profile calculations

Conclusions

The mechanisms of influence of non-equilibrium discharges on the propagation of premixed propane-air flame have been investigated in the present work. Here are the main results of experimental work and numerical simulation:

- Premixed flame acceleration in the presence of different types of discharges has been studied. A comparative analysis of discarges influence on burning rate was performed.
- Changing in premixed flame velocity in the presence of nanosecond pulse silent discharge has been investigated. With energy input less then 1% of burner' power a combustion of mixtures with fuel content half as great in comparison with system without barrier discharge accomplished. A two times increase in flame velocity has been obtained.
- As a primary mechanism of flame blow-off velocity increase we assume acceleration of limiting reaction followed by excitation of fuel mixture components (i.e. N2) by means of silent discharge.
- A numerical model has been built. The results obtained are in a good agreement with the experimental ones. The combustion acceleration occurs due to the formation of atomix oxygen in front of the reaction zone. It's well known that excitation of reagents increases the rates of many reactions, so excitation of O_2 molecule leads to increase in combustion rate on the whole. Additional heat release in this region and radicals production lead to the blow-off flow rate growth.

The work was supported in part by RFBR (grants 02-02-06523, 02-03-33376), ISTC 1474 and CRDF MO-011-0.

References

[1] W.T. Brande – Phil. Trans. Roy. Soc. **104**, 51 (1814).

[2] E.I. Mintoussov, S.V.Pancheshnyi, A.Yu.Starikovskii - Propane-Air Flame Control by Nanosecond Pulsed Streamer Discharge. 17th International Symposium on Gas Kinetics. University of Essen, Essen, Germany. CP24 (2002).

[3] Lawton, J. and Weinberg, F. - Electrical Aspects of Combustion, Clarendon Press, Oxford. (1969).

[4] S.V.Pancheshnyi, S.V. Sobakin, S.M.Starikovskaia, A.Yu.Starikovskii. – Discharge dynamics and active particles formation in a cathode-directed streamer. Plasma Physics,. **26.** N.12. p. 1126-1138. (2000).

Compared properties of Organosilicon films induced by RF and Microwave organosilicon/O_2 plasmas and afterglows

A. Mackova[1], V. Perina[1], V. Hnatowicz[1], P. Supiot[2], C. Vivien[2],
A. Bousquet[3], A. Granier[3], F. Boufayed[4], D. Escaich[4], P. Raynaud[4], Y. Segui[4],
G. Dennler[5], M. Wertheimer[5], Z. Stryhal [6] and J. Pavlik [6]

[1] *Nuclear Physics Institute of AS CR, Rez near PRAGUE, 25068, Czech Republicy*
[2] *Laboratoire de Génie des procédés d'interactions fluides Réactifs matériaux USTL, Cit Scientifique ,*
59655 VILLENEUVE D'ASCQ, cedex, France
[3] *Laboratoire des plasmas et des couches minces , Institut des matériaux Jean Rouxel, 2 rue de la houssinière, BP 32229, 44322 NANTES cedex 3, Fr ance.*
[4] *Laboratoire de Génie Electrique de Toulouse (LGET), Université Paul Sabatier,*
118 route de Narbonne, 31062 TOULOUSE CEDEX, France.
[5] *Groupe des Couches Minces (GCM) and Department of Engineering Physics and Materials Engineering, Ecole Polytechnique, C.P. 6079, Station Centre-Ville, MONTRÉAL, QC H3C 3A7, Canada.*
[6] *J.E. Purkyne University, Department of Physics, Ceske mladeze 8, USTI NAD LABEM, Czech Republic*

Abstract:
We presently show the influence of plasma processes (RF helicon, microwave DECR, Microwave Induced Remote Nitrogen Afterglow) on the film properties (surface energy, composition, ageing, roughness…) obtained from organosilicon monomers on Polypropylene and silicon substrates. Composition (by RBS, ERDA, XPS), morphology (by SEM and AFM) and optical properties (by Ellipsometry) of the different films have been analysed. A general set of physical and chemical films properties is presented in connection with the nature of the substrate.

1. Introduction

Plasma technologies are good candidates to synthesise material with specific electrical, optical, barrier properties in thin layers. Different ways are available to make organosilicon plasma polymer. Among them low-pressure PECVD deposition reactors (DECR [1]), RF inductively Coupled Reactor [2] are widely encountered because of the good thickness homogeneity required for application dealing with micro- and opto-electronics and optics. These are chosen for the present study, for comparison of the typical films obtained with each process. Nevertheless, these kinds of low pressure plasmas cannot perform high deposition rates as high as several tens or hundreds of angstroms per second which be obtained by a PACVD involving a Microwave Induced N_2 plasma Remote Afterglow (MIRA) [3]. The expected difference of such a method is a large porosity of the film due to a lower cross-linking of polymer chains than for previously mentioned ones. Deposit's chemical composition is the basic information. This contribution gather different results providing arguments to compare properties of plasma assisted organosilicon polymers. The influence of oxygen addition with the monomer on the film properties is studied. Thin films (100, 500 and/or 1000 nm thickness) are deposited to discuss material growth modes. A general set of physical and chemical films properties is presented.

Polypropylene (PP) and silicon are used as substrate materials. Such a difference for substrates is motivated by the differences~~,~~ which may appear in film's adhesion properties through the different approaches due to stress appearance. One of the difficulties in chemical analysis is the hydrogen content determination. The elemental composition is presently looked by Rutherford Backscattering Spectroscopy (RBS) and Elastic Recoil Detection Analysis (ERDA). This latter allows propose a global formula for deposits including hydrogen. The relevance of the results is discussed for both substrate types. Additionally, morphological differences are also expected to appear between samples obtained by the different processes. In this aim, Atomic Force Microscopy (AFM) is particularly sensitive to surface topology changes and is applied to put into relief the specificity of each film. Ellipsometry measurements allowed us to compared the optical properties of the films as consequences of both composition and density.

2. Experimental

- Reactors, substrates and Film deposition

PECVD deposits are prepared in low pressure discharges in pure HMDSO. Besides, PACVD-MIRA coatings are obtained from polymerisation of TMDSO premixed with oxygen induced in a nitrogen plasma afterglow. Details about the three plasma reactors can be found in previous publications (PECVD-RFICP [1] - DECR [2], PACVD-MIRA [3]). A thin layer (100 nm) and thicker ones (0.5 and 1 μm) obtained from Hexamethyledidiloxane (HMDSO)- and Tetramethyledisiloxane (TMDSO) compounds are considered to evaluate the resulting polymer film quality in term of growth and sensitivity to the process type. Substrates are made of Silicon (100) (Si) and of polypropylene (Po) (GoodFellow). Deposition by RFICP and DECR processes were operated either in pure HMDSO or in (10%HMDSO-90% O_2) mixtures . PACVD-MIRA coatings are obtained from polymerisation of TMDSO premixed with a gas vector (GV) (either nitrogen or oxygen) with 17%TMDSO-83% GV proportions. Nitrogen as GV is used in order to ensure the same flow conditions. Table 1 summarise the experimental conditions used for this work.

Table 1: General deposition parameters for each reactor (*: With both N_2 and O_2 as GV, the flow rates are 5 sccm/25 sccm for TMDSO/GV mixture, respectively)

Reactor type	DECR (2.45 GHz)		RF-ICP (13.6 MHz)		MIRA	
Pressure/Flow-rate	1 mTorr	2 mTorr	2 mTorr	3 mTorr	4.3 Torr N_2 /1800sccm	
Composition HMDSO / O2	100/-	10/90	100/-	10/ 90	100/-*	17/83*
Power	400 W	300 W	600W			
Sample position	post discharge		Diffusion plasma		post discharge	
Substrate potential	<8eV		<10eV		-	
Growth rate (nm/min)	33	10	30	10	840	300

- RBS-ERDA measurements

The RBS and ERDA analyses of prepared samples were performed in vacuum target chambers at the ion beam 2.745 MeV alpha particles and 2.4 MeV protons. The RBS and ERDA techniques enabled us to determine content and depth profiles of C, H, O and Si elements with the sensitivity from 10^{11}- 10^{15}at.cm-2.The depth profiles could be determined non-destructively to the depth of a few mm with a typical depth resolution of 10-50 nm by RBS and ERDA, respectively. The RBS spectra measurement of back-scattered 2.4MeV protons is useful for the determination of the light elements C, O, N due to the resonant backscattering cross section on the other hand the depth resolution is lower in this case Fig. 1b. The background of backscattered protons in polypropylene substrate sample spectra is practically removed and we are able to evaluate more precisely the amount of C, O and to confirm the occurrence of nitrogen in the very low amount about 0.4 atomic % (Fig. 1a). The accuracy of RBS analysis is in the range of 5 atomic % due to the substrate background. The RBS spectra were evaluated by GISA3 code [4]. The ERDA measurement enables to evaluate the hydrogen content. The accuracy of the hydrogen determination is about 8 atomic % in the case of thin layers (100 nm), but is better for thick layers. The ERDA measurement results was evaluated by SIMNRA5.0 code [5].

- Ellipsometry

The films were analysed by mean of JY UV-Visible phase modulated ellipsometer (UVSEL). Both refractive index and extinction coefficients are were determined from 250 to 800 nm.

- AFM-measurements

The surface topography and roughness were measured by Atomic Force Microscopy (AFM) - Metris-2001A-NC, manufactured by Burleigh Instruments Inc. The measurements were carried out in the contact mode. A commercially available pyramidal probe of silicon nitride (Si_3N_4) was used. All AFM measurements were made at the ambient atmosphere and at room temperature.

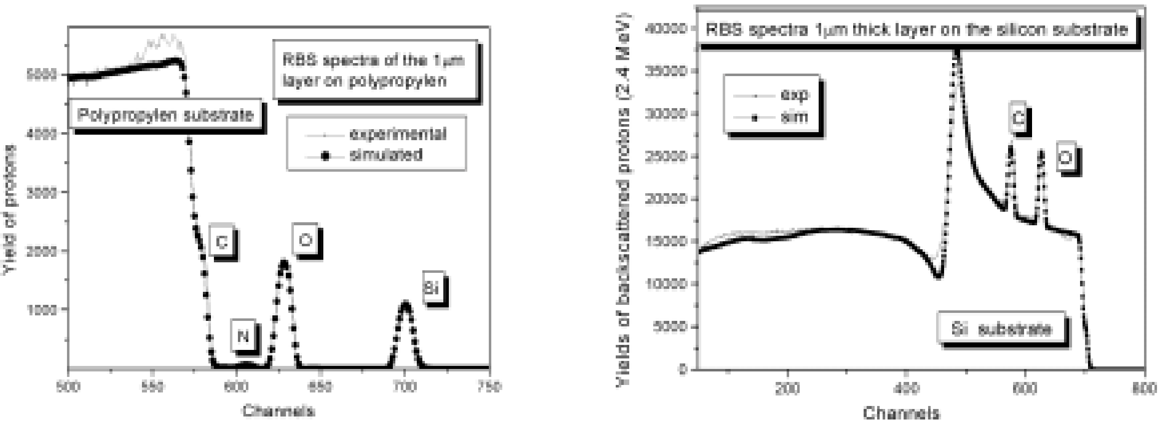

Fig. 1: RBS spectra (measured with 2.4 MeV proton beam) of the 1 µm thick HMSDO layer on a) polypropylene and b) silicon substrate.

3. Results and discussion

- Composition

The composition was investigated by RBS and ERDA technique. It was also possible to probe the depth profiles of the elements in the deposited layers.

Table. 2. Thickness and Atomic percentages of Si, O and C deduced from RBS and percentage of H determined from ERDA. The chemical composition of the corresponding polymer pattern is compared with the Polydimethylsiloxane (PDMSO) taken as reference (* :The hydrogen was not homogeneous, the concentration in the layer with thickness 6500 at.10^{15}/cm^2 was 51% and in the second layer 2500at. 10^{15}/cm^2 thick was 38% of hydrogen, ** : These composition take account of the presence of 2 % nitrogen in the film).

Sample	Thickness (RBS)	Composition (atomic %) Si	O	C	H	Polymer pattern $Si_xO_yC_zH_t$
	atoms.10^{15}/cm	at %	at %	at %	at.% / thickness	
			HMDSO			
RFICP-Si-100 nm	790	14	16	22	50	$Si_5O_6C_8H_{19}$
RECR-Si-100 nm	1200	15	12	28	45	$Si_6O_5C_{11}H_{18}$
RFICP-Si-1000 nm	8000	13	11	24	52	$Si_6O_5C_{11}H_{23}$
RECR-Si-1000 nm	9000	13	10	26	51/ 6500*	$Si_6O_5C_{11}H_{23}$
					38/ 2500	
			TMDSO			
MIRA-Si-730 nm	1900	17	19	31	31	$Si_5O_6C_9H_9N_1$**
MIRA-Si-1300 nm	5500	18	27	31	22	$Si_5O_7C_9H_7N_1$**
			HMDSO/ O_2			
RECR-Si-50 nm	500	24	63	10	3	$Si_5O_{14}C_2H_1$
RECR-Si-260 nm	1900	26	57	13	4/800*	$Si_5O_{12}C_3H_1$
		27	58	14	1.4/1200	
			TMDSO/ O_2			
MIRA-Si-100 nm	950	15	21	21	43	$Si_5O_7C_7H_{14}$
MIRA-Si-1000 nm	7800	13	18	20	49	$Si_5O_7C_8H_{19}$
PMDSO	-	10	10	20	60	$Si_6O_6C_{12}H_{36}$

The main goal of the RBS and ERDA measurements was to characterise the composition and to determine the depth profiles of the elements in the deposited layers. Two sets of the samples Si or Po were measured and the composition was obtained from RBS and ERDA spectra evaluation. The results are summarised in the Table 2 for the Si case for the three considered processes. The description of the samples in the first column includes the reactor type as well as the given deposit thickness. The composition is evaluated in atomic % and thickness of the layer in atoms/cm^2. Table 2 firstly shows that the deposition processes lead to only slightly different film composition according to precision RBS and ERDA techniques for low pressure processes in pure HMDSO. The hydrogen content is quite high in all samples around 50 atomic %. In the case of the sample DECR-Si-1000 nm sample the hydrogen is non-homogeneously distributed. Comparison of compositions of the films with that of the equivalent pattern of the polydimethylsiloxane (with 5 or 6 Si atoms) taken as reference shows a strong depletion of H content in plasma deposited organosilicon polymers. Besides the MIRA deposit from pure TMDSO exhibits a strong decrease of both carbon and hydrogen. This result probably comes from a strong fragmentation of the monomer and some nitrogen inclusion within the material (~2%) which probably leads to a smaller crosslinking of the chains.

When oxygen is add to the monomer for the DECR deposited film, the RBS and ERDA spectra essentially show a silica-like composition with some trace of carbon and hydrogen. For MIRA deposits for which oxygen is premixed with the monomer the films do not present any strongly different Si/O ratio when compared with the case of pure monomer process. The role of oxygen is then to ease to polymerisation process as ascribed by the large remaining amount of carbon and hydrogen. The deposit composition is then close to that of the low pressure processes in pure monomer discharges. The absence of nitrogen in the MIRA samples is then consistent with previous studies showing depletion of NH groups detected by IRTF spectroscopy [3]. The hydrogen amount is very difficult to determine in the case of polypropylene substrate and thin deposited layer (100 nm). The evaluation difficulties are caused by the high hydrogen amount in the polypropylene substrate. No information could often be obtain for this substrates because of either too low adhesion of the film (DECR, RFICP) or to low signal from the deposit for the MIRA films due to low films densities.

- Morphology

The second goal was to combine the RBS and ERDA measurements with AFM studies. Figure 2 shows some of the AFM images concerning deposits grown (1000 nm thick) on Si. One can see despite differences in the grain sizes that RFICP and DECR films shows similar growth types. Additionally their morphologies strongly contrast with that the MIRA film. This one presents small and oriented lines and seems to be more porous. Such a structure is consistent with the additional smooth etching by oxygen mentioned through RBS analysis in MIRA case and with some linear arrangement of moderately large polymeric chains. Both RFICP and DECR film look dense, but the DECR sample exhibits some columnar features resulting in a larger roughness.

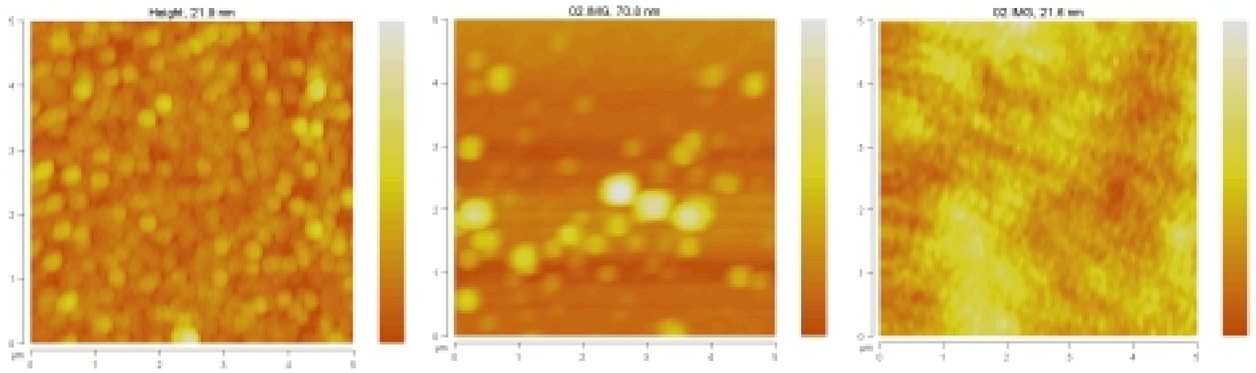

RFICP (Rq=1.7 nm) **DECR(Rq=9.1 nm)** **MIRA(Rq=2.3 nm)**

Fig. 2. AFM scans (5µmx5µm) of 1000 nm thick films obtained on Si from processes a) RFICP, b) DECR and c) MIRA% Average roughness Rq is also indicated on the bottom of images

- Optical properties

The results of optical measurements are gathered in Table 3. The values of the refractive index, *n,* and of the extinction coefficient, *k,* of the films obtained in the DECR and RF-ICP reactor appear to be quasi constant whatever the thickness of the deposit. This is not the case for the films deposited in the high pressure MIRA reactor: In TMDSO/O$_2$ mixtures, *k* value drastically changes with the thickness. This can be explained by the growing mode which changes during the deposition process creating an interface with properties different than the upper layer or by an artefact due to the measurement protocol. This particular point needs to be analysed. As a general trend the carbon amount in the films can explained the value of k which increase when the amount of carbon increases. At high pressure and high deposition rate *n* reaches very low values closed to 1.1. This is compatible with the low density value obtained for these films from both ellipsometry and RBS. A very surprise result is the low k value of the MIRA film obtained in presence of O_2 despite a large amount of carbon. This point is not clear at present.

Table. 3. Film thickness, refractive index and extinction coefficients (two wavelength) for the different deposits (* : thickness is given as indicative value, no measurement is available)

Samples	Thickness (nm)/ Substrate	*n* (620 nm)	*k* (620 nm)	*k* (250 nm)
DECR - HMDSO/O_2	51	1.46	9.8E-08	2.2E-06
DECR - HMDSO/O_2	264	1.46	9.5E-08	2.1E-06
RFICP - HMDSO/O_2	960	1.46	1.6E-08	2.0E-08
RFICP - HMDSO/O_2	528	1.45	1.2E-08	1.6E-08
RFICP - HMDSO/O_2	103	1.45	1.2E-08	1.8E-08
MIRA - TMDSO/O_2	100*	1.39	1.0E-03	1.0E-03
MIRA - TMDSO/O_2	1000*	1.39	6.2E-08	2.3E-06
DECR - HMDSO	100*	1.55	8.1E-04	3.0E-02
DECR - HMDSO	1000*	1.50	1.0E-03	1.0E-03
RFICP - HMDSO	100*	1.50	4.4E-04	1.6E-02
RFICP - HMDSO	1000*	1.47	6.0E-04	2.3E-02
MIRA - TMDSO	96	1.26	1.4E-02	1.3E-02
MIRA - TMDSO	730	1.14	4.1E-03	2.5E-03
MIRA - TMDSO	1352	1.15	4.1E-03	4.1E-03

4. Conclusion

This paper gathers different results providing elements to compare plasma assisted organosilicon polymers. RBS, ERDA, AFM and ellipsometry techniques are used to determine composition, morphologies and optical properties of the 100, 500 and 1000 nm thick films deposited either on silicon. A strong difference of the films properties is observed between the low pressure processes and the MIRA one: the carbon contents, density of the films then the optical properties show opposite trends. for results about polypropylene, we should emphasise the difficulty in studying the films on such substrates. Work is still in progress on that subject. Work is in progress to complete this comparative work.

References :

[1] P.Raynaud, Y. Segui, G. Balmer, A. Boulanger, R. Burke, J. Phys.D - Applied Physics :.**30**, L23, L27 (1997)

[2] K. Aumaille, C. Vallée, A. Granier, A. Goullet, F. Gaboriau and G. Turban, Thin Solid Films **359**, 188-196 (2000)

[3] F. Callebert, P. Supiot, K. Asfardjani, O. Dessaux, P. Goudmand, P. Dhamelincourt and J. Laureyns, *J.* Appl. Polym. Sci.*,* **52**, 1595 (1994)

[4] J. Saarilahti and E. Rauhala - Interactive personal-computer data analysis of ion backscattering spectra, Nucl. Instrum. And Methods in Physics Research **B64**, 734-738, (1992)

[5] Mayer M, SIMNRA User`s Guide, Inst. für Plasmaphysik, Forschunscentrum Julich ,1998

Acknowledgement: The authors are grateful to the European Community for support in the ease of exchanges between partner within the COST 527 program.

EFFECT OF METHANE ADDITION ON FILM PROPERTIES IN LOW PRESSURE HEXAMETHYLDISILOXANE DISCHARGES

G. Borvon, X. Mellhaoui, A. Goullet, A. Granier

Laboratoire des plasmas et des couches minces , Institut des matériaux Jean Rouxel, 2 rue de la Houssinière,
CNRS-Université de Nantes BP 32229, 44322 NANTES cedex 3, France.

Abstract

Thin polymeric films are deposited on Si substrates at ambient temperature in pure HMDSO plasma or HMDSO mixed with methane. The plasma source is operated at 2 mTorr, 300 W rf power. The plasma composition and film properties are studied as function of the additional methane fraction X_{CH4}, which is varied from 0 to 100% in the plasma. The $SiO_xC_yH_z$ layers are analysed by in situ ellipsometry, ex situ quantitative Fourier Transform Infrared spectroscopy (FTIR) and electrically by MIS structures. The intensity of CH*, H_β, Si*, SiH* and SiO* emissions are measured by optical emission spectroscopy to control film growth. In addition, correlations between the film composition and dielectric constant are investigated.

1. Introduction

Organosilicon plasma-polymerized thin films have been demonstrated to be a material with excellent properties and have high potential for many important industrial applications, for example as protective films on hard disks, lenses, as biomedical implants or insulating layers in microelectronic devices [1]. This is mainly due to the fact that important properties of these films can be varied widely by suitable choice of source monomer and deposition parameters. In particular, the effects of adding hexamethyldisiloxane (HMDSO) to CH_4 plasmas on the adhesion, antireflective, mechanical properties and thermomechanical stability of diamond-like carbon films (DLC/Si) have been recently studied [2-4].
This paper is focused on the study of organosilicon polymer-like films deposited in pure hexamethyldisiloxane and HMDSO/ methane plasma in an inductive PECVD reactor. After a brief description of the helicon reactor, results obtained from different diagnostics in pure HMDSO and CH_4/HMDSO plasmas will be presented and compared. The low-pressure rf helicon reactor is equipped with a UV-visible spectroscopic ellipsometer which allows to analyse the film thickness and its optical properties. In addition, the film composition has been investigated by ex situ Fourier transform infrared spectroscopy (FTIR). The relation between the film structure, particularly the number of Si-(CH_3) and Si-O-Si bonds, and its electrical properties will be discussed.

2. Experimental set-up and diagnostics

2.1 Deposition conditions

The plasma polymer films were deposited on silicon substrates in a PECVD system. It consists of a source made of a pyrex tube surrounded by a helicon antenna and, below it, the diffusion chamber, where the substrate holder is located. The radio-frequency (RF, 13.56 MHz) plasma is inductively coupled in the source. The magnetic field (60 G) inside the source is generated using an electromagnet coil around the antenna. Methane is introduced at the top of the source, while the HMDSO vapour is injected via dispersal ring 8 cm above the substrate. The pressure (before plasma ignition), total gas flow rate and power are fixed at 16 sccm and 300 W, respectively. The organosilicon flow rate is mixed to methane and the methane fraction, X_{CH4}, deduced from the methane to organosilicon partial pressures, is varied from zero to 100%. The silicon substrates are at the floating potential and their surface temperature is less than 70°C [5].

2.2 Plasma and film characterisation

The diffusion plasma is analysed by optical emission spectroscopy (OES), in the 180-850 nm spectral range using a JY HR460 monochromator.

The diffusion chamber is equipped with a phase modulated spectroscopic UV-visible ellipsometer (1.5-5 eV) which enables in situ real time monitoring of the film growth. The thickness, the refractive index n and the extinction coefficient k_e of the films are deduced from the analysis of the in situ spectra recorded, after the film deposition. The Cauchy formalism is used to describe the dielectric $SiO_xC_yH_z$ films [6].

The substrates are weighed before and after the deposition using a microbalance (±10µg) and the precision on the film density of the is estimated to be ±0.2 g.cm^{-3}.

The chemical nature of the bonds in 500nm thick films is determined by Fourier transform infrared (FTIR) spectroscopy in the frequency range of 400-4000 cm^{-1}.

The dielectric constant is obtained by capacitance-voltage (C-V) measurements at 1 MHz using Al/film/c-Si (MIS) structures. The dielectric losses are evaluated by resistance-frequency (R-f) measurements at 5 V. Electrical properties such as leakage current and breakdown voltage of the MIS are measured using current-voltage (I-V) characteristics. All these electrical measurements are carried out at room temperature. To achieve electrical measurements, a 100 nm thick film is first deposited on a 2-inch Si wafer, which is cleaned in diluted hydrofluoric acid (HF) before deposition. The resistivity of the n-type (100) Si wafer is 1-5 Ω.cm. Then, MIS structures are patterned by standard photolithography and submitted to a post-metallisation anneal (PMA) in N_2 atmosphere at 390°C for 30 min. The Al electrode area (S) is 4.1×10^{-3} cm^2.

In addition, the variation in the film structure, optical and electrical properties upon ageing will be investigated.

3. Results and discussion

3.1 pure HMDSO plasma

The main atomic and molecular emission lines detected in pure HMDSO plasmas [7] are reported in Table 1 and 2. The main radiative species are CH, H_2 and H. However, weaker emissions from Si containing species (Si, SiO or SiH) are also detected, suggesting that some HMDSO molecules are completely dissociated in the plasma.

Atom	Symbol	Transition	System name	Spectral range
H	H_α, H_β, H_γ, H_δ	n > 2 → n=2	Balmer lines	656.3, 486.1, 434.0, 410.0
C		$2s\ ^1S_0 - 3s\ ^1P_1$		247.9
Si		$4s\ ^1P^0 - 3p^2\ ^1D$		288.1

Table 1: Atomic lines identified in pure HMDSO plasma in the spectral range 180-850 nm.

Molecule	Transition	System name	Spectral range
H_2	$^3\Sigma_g - {}^3\Sigma_u$ $G^1\Sigma_g^+ - B^1\Sigma_u^+$ $d^3\Pi_u - a^3\Sigma_g^+$	Primary system G → B Fulcher - α	200-320 453-464 580-650
C_2	$A^3\Pi - X^3\Pi$	Swan system	512.9 516.5
SiO	$A^1\Pi - X^1\Sigma$		216.0-292.5
SiH	$A^2\Delta - X^2\Pi$	414.2 nm system	414.2
CH	$C^2\Sigma^+ - X^2\Pi$ $B^2\Sigma - X^2\Pi$ $A^2\Delta - X^2\Pi$	310 nm system 390 nm system 430 nm system	314.5 387.1, 388.9 431.4

Table 2: Molecular emissions observed in pure HMDSO plasma in the spectral range 180-850 nm.

Fig.1 shows the FTIR spectrum of a 100 nm thick film prepared in a pure HMDSO plasma, denoted ppHMDSO film. The position and attribution of the absorption peaks, which are characteristic of the ppHMDSO film, have been previously identified by several authors [8-9].

The absorption band between 2340 and 2360 cm^{-1} corresponds to stretching asymmetric vibrations of gaseous CO_2 trace, which are present in the FTIR spectrometer.

The strong stretching mode of Si-O-Si in the range 1000-1150 cm^{-1} is observed. The other absorption peaks identified are the following: (1) C-H symmetric and asymmetric stretching in CH_3 at 2900 and 2960 cm^{-1}, (2) CH_3 rocking in $Si(CH_3)_2$ and $Si(CH_3)_3$ at 800 and 840 cm^{-1}, (3) symmetric CH_3 bending in

$Si(CH_3)_x$ at 1260 cm^{-1}, (4) CH_2 bending in Si-CH_2-Si and Si-$(CH_2)_2$-Si at 1355 and 1400 cm^{-1}, respectively. The peak centered at 2133 cm^{-1} is assigned to Si-H stretching. The ppHMDSO film infrared spectrum is very close to the one of polydimethylsiloxane (PDMS) [8].
The refractive index and the extinction coefficient at 1.96 eV are 1.5 and 2 10^{-3}, respectively. The deposition rate of ppHMDSO is 35 nm/min while its density is low and close to 1 $g.cm^{-3}$.
For a 1.2 µm thick ppHMDSO film, the hardness is near 0.5 GPa and its Young modulus close to 25 GPa for a 400 nm penetration depth which corresponds to a charge of 20 nN. Hence, this kind of film presents a low hardness, an elastic behaviour and a weak plastic deformation [10].
The ppHMDSO films have a weak leakage current density up to 1 MV/cm; their critical and breakdown electric fields are equal to ≈1 MV/cm and 6 MV/cm, respectively. In addition, the dielectric constant and dielectric losses of the ppHMDSO film are low too : $k \approx 3$ and $\tan\delta \approx 4\ 10^{-3}$.

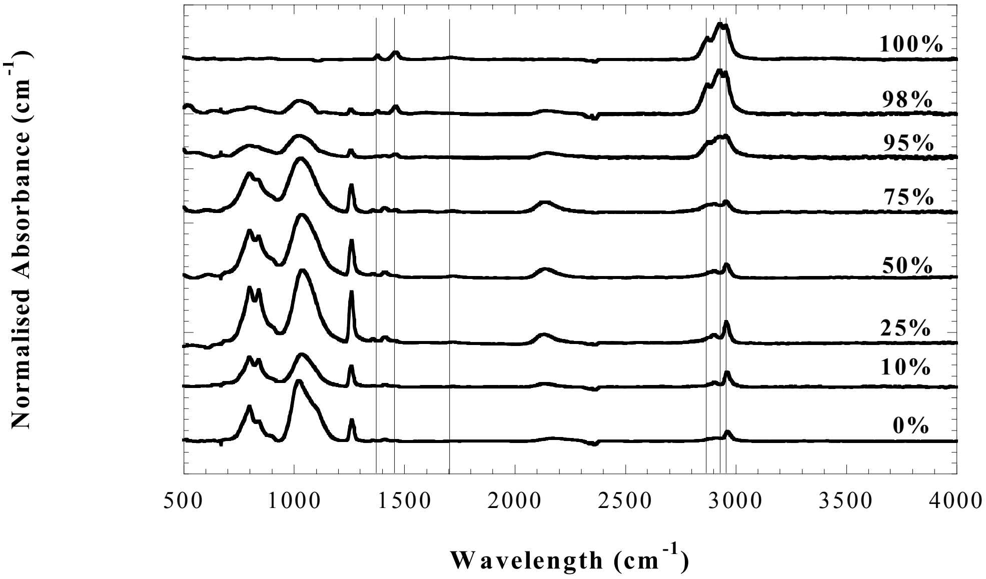

Fig.1: FTIR transmission spectra of 500 nm thick ppHMDSO(CH_4) films prepared in different HMDSO/CH_4 plasmas.

3.2 CH_4/HMDSO plasmas

Plasma analysis by OES : For semi quantitative OES analysis, 5% Ar is added to the CH_4/HMDSO mixture. Variation of the intensities emitted by excited Ar, H_2 (379.7nm), H_β, CH, C_2, Si, SiO and SiH are monitored as functions of X_{CH4}. Intensities are divided by the 750 nm argon line intensity in order to partly get free from the variation of the electron density and temperature and are plotted as functions of X_{CH4} in Fig. 2. Intensities of SiO*, SiH* and Si* slightly increase up to X_{CH4}=25% and then decrease and cancel in CH_4 plasma. This behaviour is consistent with the variations of the HMDSO monomer fraction. As expected, CH, H and H_2 emissions are important whatever the mixture composition. The variations of H and H_2 emissions are opposite, which is likely to indicate that H and H_2 concentrations have opposite variations. In addition, C_2 emission seems to decrease as CH_4 is replacing HMDSO. Further analysis, for instance by mass spectrometry are necessary to conclude on the variations of the normalized intensity of CH, H, C_2 and H_2.

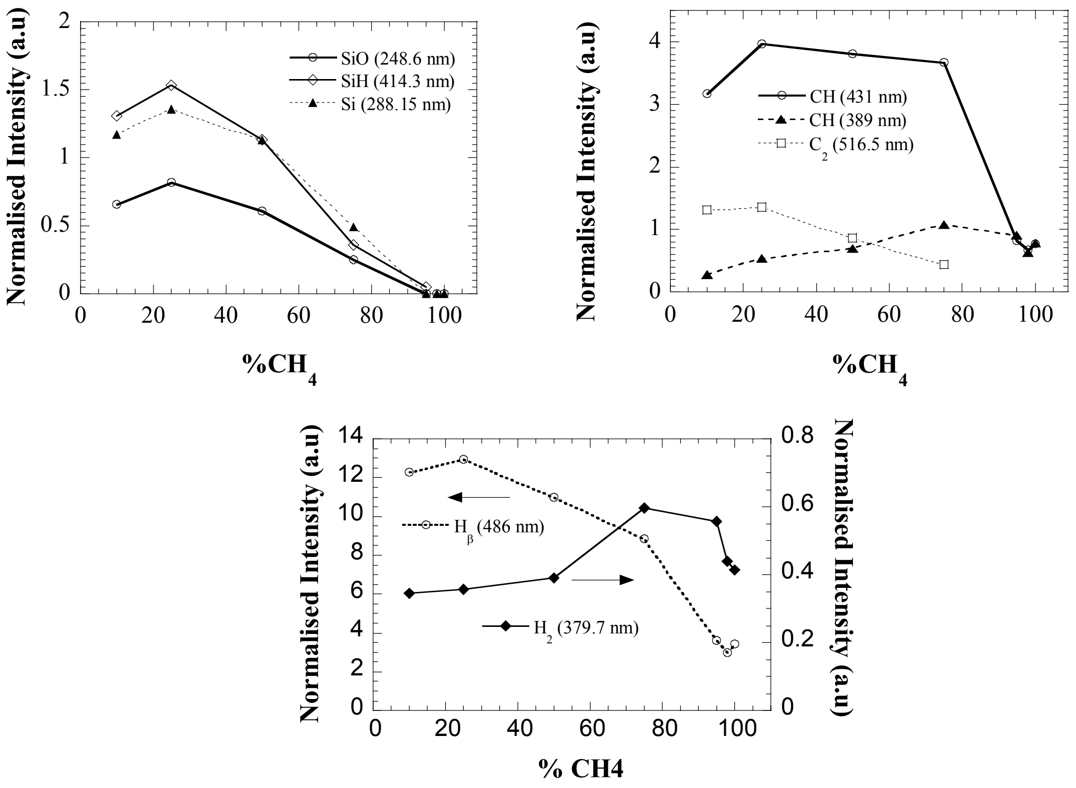

Fig.2: Evolution of (SiO, SiH, Si), (H_β, H_2), CH and C_2 emissions intensity as function of the CH_4 fraction in the gas mixture.

*Film structure :*Fig.1 shows the FTIR spectra of different films deposited in HMDSO/CH_4 plasmas, denoted ppHMDSO(CH_4). These spectra were measured on freshly deposited film, namely a few days after their deposition. The FTIR spectra of the films prepared in HMDSO-rich plasmas are very similar to the one of ppHMDSO. As X_{CH4} is greater than 50%, we can identify the C-H symmetric stretching in CH_2 at 2867 cm^{-1}. As X_{CH4} is increased above 75%, all the absorption peaks related to Si containing bonds decrease and completely disappear in the case of the a-C:H-like film deposited in pure CH_4 plasma. The spectrum of the a-C:H film deposited in the CH_4 plasma, exhibits different absorption peaks characteristic of C-H stretching attributed to sp^3 CH_2 (sym.) at 2867 cm^{-1}, sp^3 CH_2 (asym.) at 2922 cm^{-1}, sp^3 CH_3 (asym.) at 2955 cm^{-1} and the CH_3 symmetric and asymmetric bending at 1377 and 1455 cm^{-1}, respectively. In addition, C=O stretching at 1711 cm^{-1} is identified in the films prepared for $X_{CH4}>50\%$. C=O is likely to be formed after venting by reaction of the film with oxygen and/or water vapour.

Up to X_{CH4}=75%, the deposition rate is close to 30 nm/min, n increases from 1.49 to 1.58 and k_e from 0.5 10^{-3} to 1.3 10^{-3} at 1.96 eV. For $X_{CH4}\geq$ 95%, n decreases from 1.58 to 1.51 and k stands at 2.4 10^{-3}. We have plotted in Fig.3 the Lorentz-Lorenz formula which relates the density ρ and n, provided the composition of sample under study is basically constant : $\rho = K\left(n^2-1\right)/\left(n^2+2\right)$, where K is a constant. For HMDSO rich mixtures, the values of ρ are close to those of ppHMDSO film whereas ρ increases as X_{CH4} increases. For CH_4 rich mixtures, ρ decreases as X_{CH4} increases. Two linear relationships are obtained : the first one is observed as long as X_{CH4} is less than 75%, and the second for $X_{CH4}\geq$ 95%. These relations show that, up to X_{CH4}=75%, the structure of ppHMDSO(CH_4) films are very similar to the one of ppHMDSO, and that, from X_{CH4}=95%, the film composition changes from $SiO_xC_yH_z$ to a-C:H films, as previously shown by the infrared spectra.

Electrical properties : For X_{CH4}=25%, the critical and breakdown fields are close to those of the ppHMDSO film, the dielectric constant is equal to 2,8 and the dielectric losses at 1 kHz are equal to 2 10^{-3}. As X_{CH4} is further increased the electrical properties of the ppHMDSO(CH_4) films are affected : the dielectric constant, dielectric losses and leakage current density increase while the breakdown electric field decreases [11]. In order to relate the dielectric constant of the film to its composition, we have carried out a quantitative analysis of the infrared spectra. The integrated intensities of the Si-(CH_3)$_x$

absorption band at 1260 cm^{-1} and the Si-O-Si stretching peak at 1030 cm^{-1} have been calculated. Then, the dielectric constant is plotted as a function of the Si-$(CH_3)_x$ to Si-O-Si integrated intensity ratio, denoted R hereafter (see Fig. 4). This figure clearly demonstrates that the dielectric constant decreases as R increases. The minimum value of the dielectric constant is reached for X_{CH4}=25%.

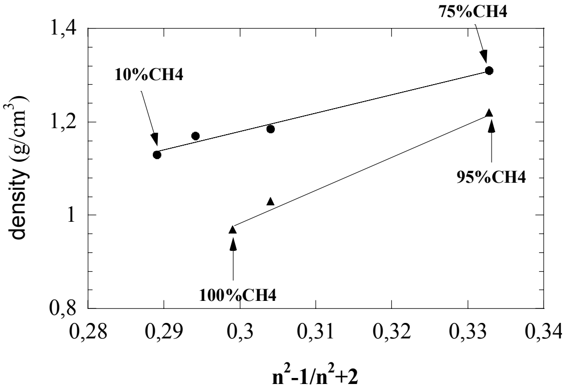

Fig.3: Lorentz-Lorenz plot of ppHMDSO(CH_4) film density for various CH_4 fractions

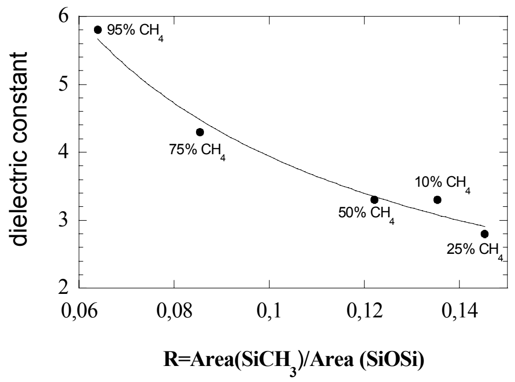

Fig. 4 : Dielectric constant of ppHMDSO(CH_4) films versus $SiCH_3$ to SiOSi integrated infrared peaks ratio

Film ageing : These films were stored in the atmosphere during eight months and analysed by FTIR and ellipsometry after that. The ppHMDSO FTIR spectra and optical properties were shown to be almost unchanged upon air storage. In addition, its electrical properties, namely its dielectric constant, leakage current, breakdown electric field were unaffected. This is consistent with the results obtained by Gengenbach et al who have studied the ageing of ppHMDSO films upon 3 years [9]. In contrast, significant modifications appear upon ageing in the case of ppHMDSO(CH_4) films. The infrared spectra clearly indicate that the intensity of the C=O peak at 1700 cm^{-1} increases, a wide OH absorption band appears while the CH peak intensity decreases. The FTIR spectra of the freshly deposited and aged a-C:H film deposited in CH_4 plasma are displayed in Fig. 5. The analysis of the aged films by ellipsometry shows a decrease in the extinction coefficient, which is consistent with a loss of CH_x groups. Hence, the reaction of ppHMDSO(CH_4) films with water vapour enhances the formation of C=O bonds and loss of hydrocarbon groups upon ageing. In addition, the C-V and I-V characteristics measured after 8-month storage, clearly show that all electrical properties are affected by the ageing : both the dielectric constant and the leakage current significantly increase. The evolution upon air storage is all the more important as the CH_4 fraction is high.

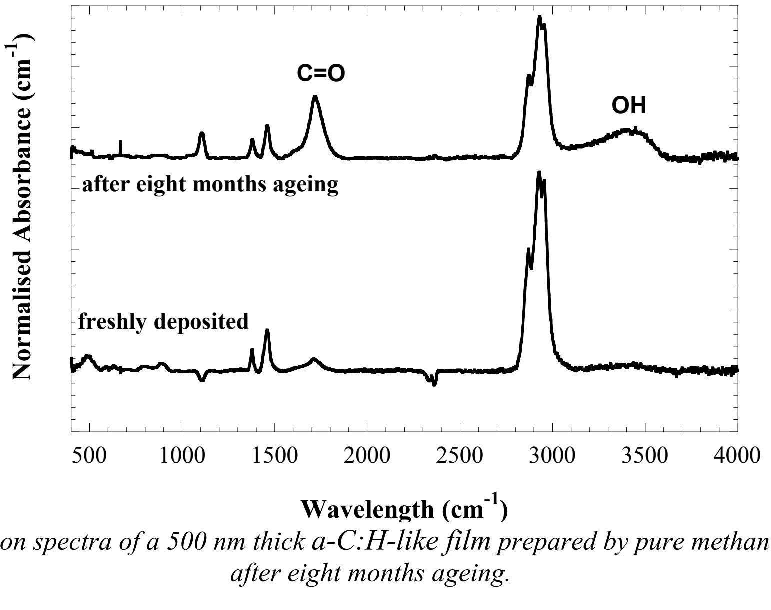

Fig.5: FTIR transmission spectra of a 500 nm thick a-C:H-like film prepared by pure methane plasma before and after eight months ageing.

4. Conclusion

Polymer-like films, ppHMDSO(CH_4) films, have been prepared by PECVD using HMDSO/CH_4 gas mixtures. Their structure and electrical properties have been investigated and compared to those of a ppHMDSO film prepared with pure HMDSO plasma. ppHMDSO(CH_4) films have been demonstrated to be low-k dielectric films ($k \leq 3$) compatible with intermetallic dielectric requirements : high critical and breakdown electric field and stability up to 400°C, provided the CH_4 fraction in the gas mixture is low ($\leq 25\%$). The low dielectric constant of these films is due to the methyl groups containing in the films. However, we have shown that these films become unstable upon ageing when the CH_4 fraction in the gas mixture is increased. In further experiments, we plan to investigate the effects of a rf bias voltage applied to the substrate during deposition in order to improve the quality of the films.

References :

[1] J.H. Lee, D.S. Kim, Y.H. Lee, B. Farouk, *Thin Solid Films* **280**, 204 (1996).

[2] Liang-Yih Chen, Franklin Chau-Nan Hong, *Diamond and related Materials*, **10**, 1058 (2001).

[3] V. Bursikova, P. Slavek, P. St'ahel, L. Zajickova, *J. Non-Cryst. Solids*, **299-302**, 1147 (2002).

[4] V. Bursikova, V. Navratil, L. Zajickova and J. Janca, *Mat. Sci. Eng.* **A324,** 251 (2002)

[5] D. Goghero, Ph. D., Propriétés structurales et électriques de couches d'oxydes de silicium élaborées par plasma basse temperature d'oxygène/tétraéthoxysilane sur des alliages silicum-germanium. Nantes Université 2001.

[6] C. Vallée, A. Goullet, A. Granier, A. Van der Lee, J. Durand, C. Marlière, *J. Non-Cryst. Solids* **272**, 163 (2000).

[7] A. Granier, M. Vervloet, K. Aumaille and C. Vallée, *Plasma Sources Sci. Technol.* **12**, 89-96 (2003).

[8] C. Rau, W. Kulish, *Thin Solid Films*, **249**, 28 (1994).

[9] M.P. Bonnar, J.I.B. Wilson, B.M. Burnside, R.L. Reuben, T.R. Gengenbach, H.J. Griesser, G. Beamson, *J. Mat. Sci.*, **33**, 4843 (1998).

[10] L. Zajíčková, V. Buršíková, G. Borvon, A. Goullet, A. Granier, V. Peřina, A. Macková, ISPC16, Taormina (2003)

[11] G. Borvon, A. Goullet, X. Mellhaoui, N. Charrouf, A. Granier, *Materials Science in semiconductor* **5**, (2-3), 279-284 (2002).

Ammonia RF-plasma treatment for anchoring biomolecules to improve the surface interaction of ePTFE vascular prostheses with blood and cells

P. Chevallier[1], M. Crombez[1], R. Janvier[1], G. Laroche[1,2] and D. Mantovani[1,2]

1.Bioengineering & Biotechnology Unit, Research Center St. François d'Assise Hospital, Quebec City, Qc, Canada
2. Department of Mining, Metallurgy and Materials, Laval University, Québec, Qc, Canada

Abstract

We developed a strategy to improve the biocompatibility and hemocompatibility of ePTFE prostheses in order to modulate the tissue/biomaterial interface interaction by modifying the PTFE surface properties. Ammonia RF-plasma treatment was first used to introduce amino groups on the polymer surface which were then used to covalently conjugate specific molecules onto the surface. In this context, phosphorylcholine (PRC) has been chosen for its properties to improve the surface hemocompatibilty. In the same manner, Vascular Endothelial Growth Factor (VEGF) was conjugated on the PTFE surface to improve endothelial cell proliferation.

1. Introduction

Synthetic vascular prostheses, made of Dacron™ (polyethyleneterephthalate, or PET) or microporous Teflon™ (expanded polytetrafluoroethylene, or ePTFE), are clinically used since the 60's as arterial bypasses in the case of vascular occlusive diseases such as aneurysms and acute renal failures. These diseases are the cause of 38% of the deaths in North America [1]. On the other hand, approximately 350 000 synthetic vascular prostheses are implanted each year in Western countries and Japan [2]. These data clearly indicate the importance of synthetic vascular devices from a social and economical point of view. Nevertheless, graft failures due to thromboses, pseudo-aneurysms, and intimal hyperplasia often occur with ePTFE vascular grafts when used as medium and small-diameter bypasses (< 8 mm) [3]. In a study reported on 398 ePTFE vascular prostheses implanted as medium-diameter bypasses and retrieved following complications, it was found that 65 % of them were explanted due to thrombosis in the 10 years following the implantation [4]. Clinically, improving the tissue/synthetic grafts interaction should lead to a better life time of prosthetic devices. In the last 20 years, many efforts have been put forward in the field of prosthesis hemocompatibility improvement. The common idea is to increase the blood/biomaterial surface interaction without modifying the physical and mechanical graft properties; it has been shown in many instances that surface modification through plasma treatment is one of the most promising techniques [5]. Low pressure plasma surface treatments are particularly advantageous in the design and development of new biocompatible materials, since they allow surface modifications without altering the bulk of the materials' properties [2]. Moreover, plasma treatment can be used to graft reactive functional groups on the surface of polymers: these moieties may be subsequently used to covalently attach various specific molecules trough appropriate synthesis strategies.

Strategy to improve the ePTFE prostheses surface interaction with blood and cells

We have developed a cylindrically RF plasma to modify the internal surface of ePTFE prostheses [6]. Plasma treatments were performed with gaseous ammonia that allows to introduce amino groups on the polymer surface [7-9]. Amino groups are often used in organic synthesis as they readily react with several other chemical functional groups [10], allowing the attachment of specific molecules strongly enough to prevent the removal by the blood stream. Using appropriate experimental conditions, the amine surface concentration can be controlled as probed through surface derivatization experiments [7, 9, 11, 12]. It turns out that the surface concentration of molecules to be conjugated can be precisely tuned; this is of paramount importance when dose/response effects are expected.

Molecules to be grafted onto the plasma-treated surface are chosen depending on their specific biological properties. For example, phosphorylcholine (PRC) mimic the outer surface of erythrocyte, a natural hemocompatible surface [13, 14] while Vascular Endothelial Growth Factor (VEGF) is known to improve the proliferation of endothelial cell which naturally cover blood vessels [15, 16]. On one hand, PRC was covalently grafted onto the PTFE plasma-treated surface through appropriate activation scheme (Fig. 1). On the other hand, VEGF requires to be internalized within the cell for promoting cell proliferation and therefore, it has been immobilized on the surface through Coulombic interactions using an intermediate charged matrix to fill the gap between VEGF and the polymer surface. For instance, we have chosen Human Serum Albumin (HSA), grafted trough glutaric anhydride onto plasma-treated PTFE surfaces to play the role of this intermediate matrix. The negative charges onto the HSA structure were introduced by reacting cis-aconitic anhydride on the protein surface to enable the electrostatic attachment of the growth factor (Fig. 1).

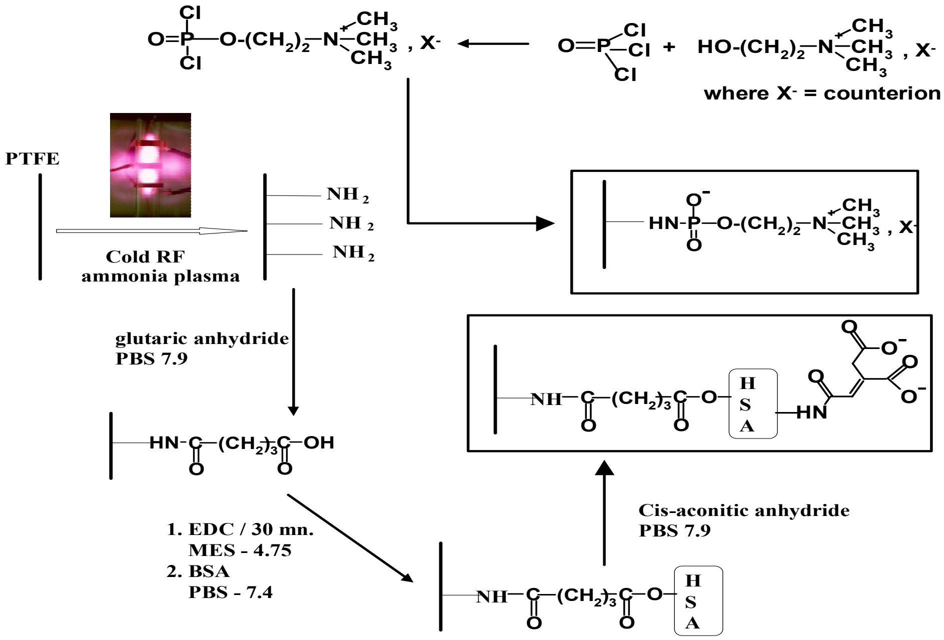

Figure 1 : Phosphorylcholine and VEGF matrix grafting onto PTFE surfaces pretreated by ammonia plasma

In order to verify the hemocompatibility and non-thrombogenicity of the PRC grafted vascular prostheses, various *in vitro* tests such as platelets quantification, neutrophils adsorption, and clotting time have been performed. The VEGF binding was validated by immunodetection (ELISA test). Following PRC or VEGF/HSA immobilization, cells cultures were performed in order to verify the influence of the molecule grafting on cell adhesion and proliferation.

2. Materials and methods

Materials

Microporous 10 mm I.D. ePTFE vascular prostheses were purchased from Gore and Associates. Chloroform, phosphorus oxychloride, and choline chloride, were purchased from Sigma-Aldrich and used without further purification. Glutaric and cis-aconitic anhydride, HSA, 1-Ethyl-3-(3-dimethyl aminopropyl) carbodiimide hydrochloride (EDC) and 2-(N-morpholino)-ethanesulfonic acid (MES) buffer were purchased from Sigma-Aldrich. Phosphate-buffer-saline (PBS, pH 7,4) and phosphate buffer were purchased from VWR and prepared in deionised water at 0.2M. Recombinant human vascular endothelial growth factor 165 (VEGF) was obtained from R&D Systems Inc.. Goat anti-humanVEGF, rabbit anti-goat IgG-Alkaline phosphatase conjugate (AP), diethanolamine buffer (DEA) and 4-Methyl umbelliferyl phosphate (MUP) were obtained from Sigma-Aldrich.

Methods

Surface treatment of the prostheses for PRC grafting

Plasma treatment : All plasma treatments were performed in a cylindrical plasma reactor under 300 mTorr of high purity ammonia with 20 W of RF power at a frequency of 13.56 MHz during 250s. Experimental procedures and configurations have been already described and published elsewhere [6, 9].

Molecule grafting : the dichloro derivative of PRC was synthesized by the addition of phosphoryl chloride ($POCl_3$) in chloroform solution to a chloroform solution containing choline under dry nitrogen stream. The mixture was then stirred at room temperature overnight to allow the reaction to proceed. Then the 3 cm-long plasma treated prostheses were immersed at room temperature in the above mentioned reaction mixture and agitation was continued for an additional 2 hours. Thereafter, prostheses were washed several times in water. The prostheses were then dried under vacuum overnight and then placed into a sealed sterilization bag and sterilized in an autoclave at 120ºC and 15 psi during 20 min.

Surface treatment of the PTFE films for VEGF matrix binding

Pieces of PTFE films were cut (3 x 3 cm) from a 250 µm-thick commercial film (Goodfellow), successively washed in an ultra-sonic bath with acetone and methanol, and then dried overnight under vacuum.

Plasma treatment : All plasma treatments were performed as previously described for prostheses whereas for films the plasma duration was 100s.

VEGF matrix grafting : the plasma-treated films were immersed in phosphate buffer pH=7.9 and glutaric anhydride was added every 20 minutes during one hour to reach a final concentration of 50 ± 5 mg/mL. The films were then washed many times with water and vacuum-dried overnight at 40°C. The carboxylic group grafted on PTFE was activated in MES buffer (0,1 M, pH=4,75) by adding EDC (30 ± 5 mg/ml) every 10 minutes, during 30 minutes, at room temperature and under stirring. The films, previously rinsed by MES buffer were immersed in HSA solution (1 mg/mL) in PBS pH 7.4 under stirring for 3 hours. These samples were then repeatedly washed with water, vacuum-dried at room temperature, and immersed in PBS solution pH 7.4 containing cis-aconitic anhydride that was added in 3 times for one hour under stirring to reach a final concentration of (30 mg/mL). Finally, the films were washed with water and vacuum-dried overnight at room temperature.

Surface analyses by X-Ray Photoelectron Spectroscopy (XPS) : The efficacy of surface modifications was ascertained using a PHI 5600-CI XPS spectrometer (Physical Electronics) with the Al kα radiation (1486.6eV) at 200 W while detecting the emitted photoelectrons at 45^o with respect to the surface normal.

Vascular endothelial growth factor (VEGF) seeding and detection

Triplicata were performed for each of the VEGF-seeded concentrations (0.01, 0.03, 0.1, 0.3, 1 and 3 µg/mL), for the HSA and negatively charged HSA treated films. VEGF immobilisation on PTFE was allowed to proceed between 30 minutes and 1 hour at room temperature. The films were thereafter rinsed twice with PBS. Each VEGF-seeded film as well as various controls were deposited into a 48-well microplate (Falcon). Non-specific sites were blocked with 1% casein in PBS at 37°C for 1 hour. The primary antibody, goat anti-human VEGF, was added at 1/500 dilution in 1% of casein in PBS and the plate was incubated overnight at 4°C. It was then shaken out and repeatedly washed with buffer. The secondary antibody, rabbit anti-goat IgG-AP, was added at 1/200 dilution in 1% of casein in PBS, incubated for 1 hour at 37°C and repeatedly washed with buffer. The substrate solution (MUP at 10^{-4} M in DEA buffer at 0.03 M, pH=9.8) was then added for conversion into a fluorescent product for which the concentration is related to the amount of analyte bound during the initial reaction. After approximately 30 minutes of reaction, the fluorimetric measurements were performed using a FL600 Microplate Fluorescence Reader (Bio-Tek) with excitation and emission wavelengths of 360 nm and 470nm, respectively. The results were analyzed with a standard curve expressed by $f = a/(1+\exp(-(-x-x0)/b))$, where fluorescence values were plotted as a function of the concentration of the secondary antibody.

In vitro tests for prostheses grafted by PRC : All hemocompatibility tests were carried out in triplicate using the blood of six healthy human volunteers.

Quantification of neutrophils and platelets adsorption : after centrifugation of human blood, platelet-rich suspension ($5 * 10^4$ platelets / µl) and leukocyte-rich suspension were extracted and labeled with 300 µCi of ^{51}Cr and 300 µCi of ^{111}In respectively. 1 mL of each suspension were placed on the surface for 2 hours at 37 °C. The prostheses, washed 3 times with PBS, were then analyzed with gamma scintillation counter adjusted to 260-480keV in order to quantify the number of adherent neutrophils and 270-370keV for platelets adsorption. SEM analyses were also performed to assess the activation and aggregation of blood platelets on prostheses.

Clotting time : one mL of human blood sample was deposited onto the surface of the prosthesis right after collection. The clotting time corresponds to the period required for the blood fluidity to disappear.

Cell cultures : cell cultures were done either with fibroblasts or endothelial cells (HUVEC) by incubation at 37ºC for 3 to 7 days with culture media. The cells proliferation, adhesion and morphology were assessed by fluorescence (Hoescht and rhodamine-phalloïdine staining for nuclei and actine filaments) and SEM analyses.

3. Results and discussion

Molecules grafting

XPS analyses and chemical derivatization reaction with chlorobenzaldehyde were performed with the aim of quantifying the amount of amino groups created onto the surface. For a plasma treatment of 250s, at 300mToor and 20W, 5 to 6% of amines were obtained onto ePTFE prostheses. The 4% phosphorus surface concentration detected after PRC grafting therefore indicates an almost complete reaction with the surface amino groups (Fig. 2). Glutaric anhydride was also quantitatively anchored as calculations similar to those performed for derivatization experiments allowed to predict a theoretical oxygen surface concentration of 10.7%, in perfect agreement with the experimental value (Fig. 2). This result is further confirmed through titration of the surface acidic charges with Ag^+ where the silver XPS signal allowed reaching identical conclusions (not shown).

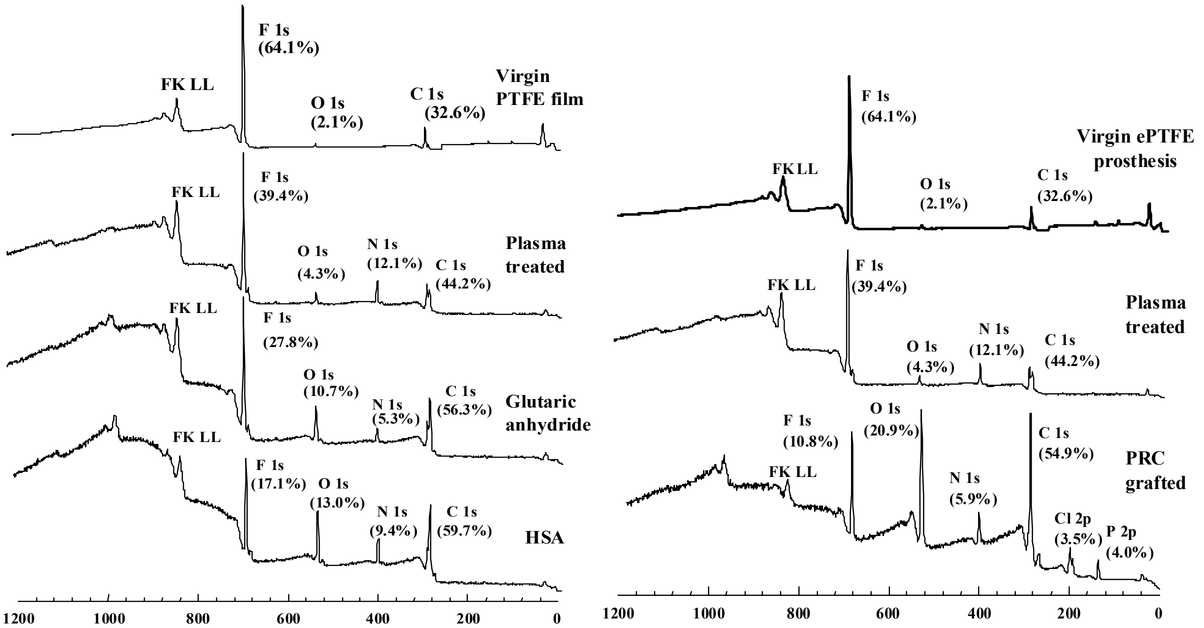

(a) **(b)**

Figure 2 : Survey spectra in XPS of each step of : - PTFE films grafted by glutaric anhydride/ HSA as VEGF matrix (a) and ePTFE prostheses grafted by PRC (b).

Following the successful grafting of glutaric anhydride, the acidic functionalities were activated using EDC to further react with the HSA amino groups. As may be seen on the XPS survey spectra depicted in figure 2, HSA was successfully grafted as an increase of the nitrogen surface concentration was clearly observed with along with a decrease of the fluorine content. Because the cis-aconitic anhydride grafting is difficult to ascertain, similar reaction was performed using trichloroacetic acid easily detected through XPS using the chlorine signal.

In vitro characterization of the treated ePTFE arterial prostheses

After the sterilization step where PRC grafting was found to be stable, the hemocompatibility of the treated prostheses was assessed using various tests such as clotting time, neutrophils quantification and blood platelet quantification and activation. Moreover, cell cultures were performed to verify the ability of the treated surface to act as a viable substrate for the adsorption and spreading of cells that are necessary for the development of an endothelium.

Clotting times were significantly longer on PRC-grafted prostheses for each volunteer with a minimum increase of 2 % and a maximum of 167 %. Thus, it appears that the treated prosthesis is less thrombogenic when compared to the virgin prosthesis. The results of platelets quantification on prostheses did not allowed to conclude whether the virgin or PRC-grafted prostheses were less thrombogenic, the results spanning from a decrease of the platelet adsorption of -30% to an increase of +32% upon surface modification with PRC. However, for all volunteers, SEM analyses clearly revealed that the virgin prosthesis lead to a significantly greater aggregation and activation of platelets than the treated prosthesis (Fig. 3) therefore pointing toward a less thrombogenic behavior upon surface modification with PRC.

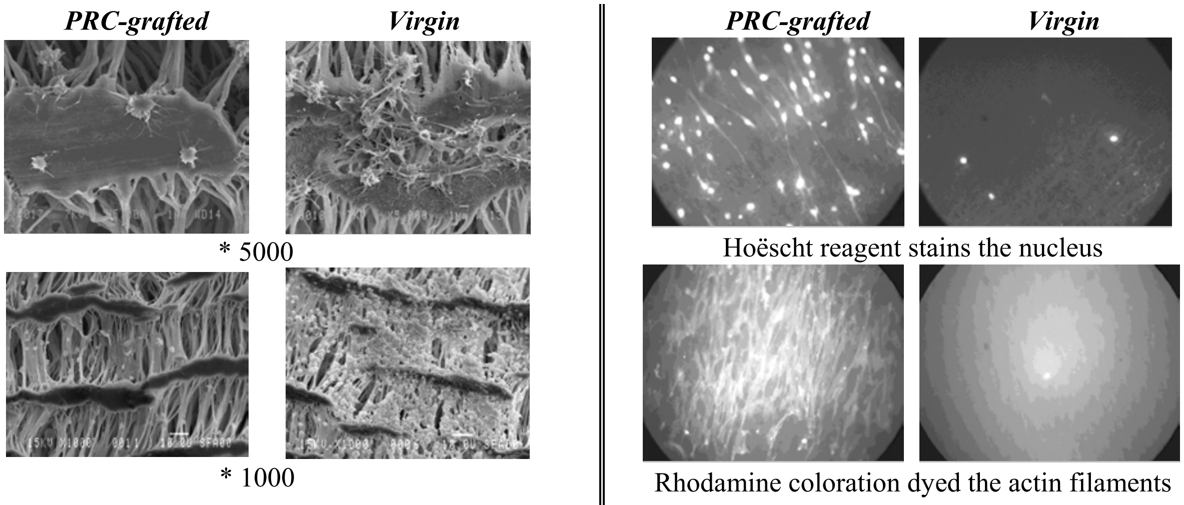

(a) SEM photos showing the degree of accumulation of blood platelets within a PRC-grafted prosthesis and virgin prosthesis for 2 different donors

(b) Microscopic slides of the growth of fibroblasts within a PRC-grafted prosthesis and virgin prosthesis after 7 days of incubation (* 20)

Figure 3 : Photos showing the effect of PRC surface modification on the accumulation of blood platelets (**a**) and growth of fibroblasts **(b)** on the PTFE prosthesis surface

The inflammatory response towards both virgin and PRC-treated prostheses was assess through the quantification of the adherent neutrophils using the blood of eight volunteers. For each of them, les adherent neutrophils were observed on the PRC-grafted prosthesis than on the virgin (decrease from 36 to 86 %). Therefore, these results indicate that the PRC surface-modified prostheses may be less prone to promote inflammatory reactions. In addition, our data evidenced that the PRC-treated ePTFE prostheses support fibroblast adhesion and proliferation as depicted in figure 3b. Similar observations were made with of endothelial cells after 3 days of incubation (results not shown).

VEGF loading and detection

Immunodetection tests were performed to verify that the protocol described above lead to the immobilization of VEGF on the PTFE film surfaces (Fig. 4a) and to quantify its relative concentration for various experimental conditions. First, a standard curve reporting the fluorescence intensity versus anti-IgG concentrations was constructed; these data demonstrated a dynamic range from 0.1 to 1 µg/mL. Then, the fluorescence rates obtained for the films loaded with VEGF were reported to the standard curve and correlated to the Anti-IgG dilution factor. Finally, the Anti-IgG dilution factor, which was directly related to the amount of VEGF seeded onto the surface, was plotted as a function of the VEGF initial concentrations (Fig. 4b).

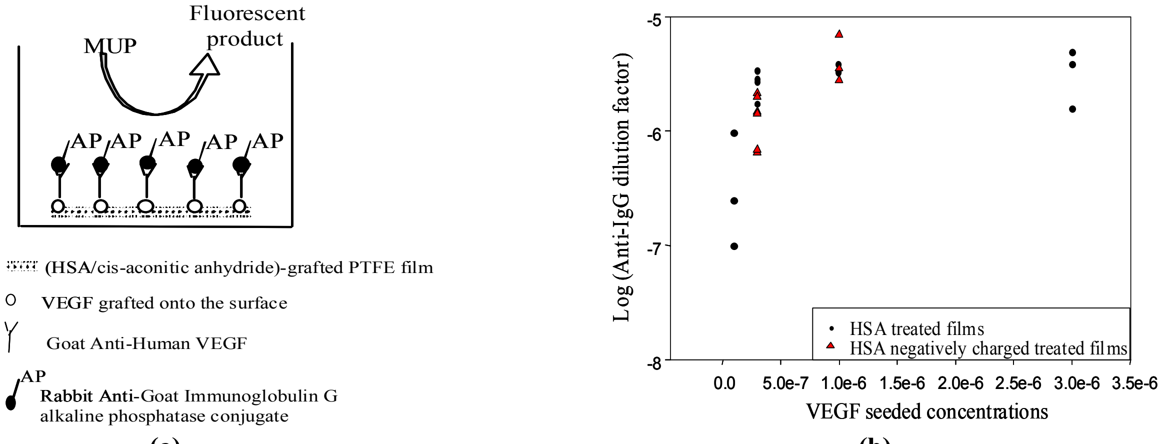

(a)

(b)

Figure 4 : Immunodetection method (**a**), and Anti-IgG dilution factor as a function of the initial VEGF-concentrations (**b**)

Figure 4b shows that an equal amount of VEGF was loaded onto surfaces whether the binding matrix was loaded with negative charges or not. Therefore it seems that the electrostatic interactions are not of prime importance for the grafting of VEGF. However, these data clearly indicates that it is possible to modulate the number of growth factor molecules per surface unit by seeding more or less VEGF on the surface. This result is of paramount importance for future dose-response reactions between VEGF surface concentrations and endothelial cell proliferation. Preliminary endothelial cell seeding tests for HSA/VEGF and HAS-cis-aconitic anhydride/VEGF complexes conjugated onto plasma treated PTFE films did not demonstrate any improvement of the endothelial cell spreading. Two reasons may be taken into account to explain this result. First, the VEGF surface concentration may have been too high, therefore causing an opposite effect to that expected. Indeed, one of the characteristics of the VEGF regulatory pathway is a cellular down-regulation in response to an excess of the growth factor. Second, VEGF, which is proliferation signal, may require a prior adhesion signal to exert its effects.

4. Conclusion

The reaction of the PRC activated derivative with the amines on the ammonia plasma treated PTFE prostheses surface was successfully performed. The PRC grafting is homogeneous and stable to sterilization. *In vitro* tests demonstrated that the PRC grafted prostheses are potentially more hemocompatible and support cell adhesion and proliferation. On the other hand, VEGF was successfully grafted on ammonia plasma-treated PTFE film first conjugated with either HSA of HSA loaded with negative charges. Immunodetection tests demonstrated that VEGF-seeded concentrations did not depend on the presence of negative charges onto the binding matrix. The ability to adequately monitor and control the amount of VEGF grafted onto the surface of a biomaterials will no doubt be of paramount importance in future research dealing with the dose-response behaviour between VEGF surface concentrations and endothelial cell proliferation. In addition, VEGF, which induces a proliferative signal, may require an additional cell triggering event through an adhesion signal. This hypothesis will be verified in a near future. Other binding matrices, such as other glycosaminoglycans, modified heparin or heparin sulphate will also be investigated in future studies.

References

[1] F. G. Fowkes, E. Housley, E. H. Cawood, *et al*., *International Journal of Epidemiology,* **20**, 384 (1991).
[2] B. D. Ratner, *"Biomaterials science : an introduction to materials in medicine"*, A. S. H. B. D. Ratner, F. J. Schoen, J. E. Lemons, Academic Press, San Diego, 1996, p. 1.
[3] M. H. Criqui, *American Journal of Cardiology,* **88**, 43 (2001).
[4] R. Guidoin, N. Chakfé, S. Maurel, *et al*., *Biomaterials,* **14**, 678 (1993).
[5] B. D. Ratner, *Journal of Biomedical Materials Research,* **27**, 837 (1993).
[6] D. Mantovani, M. Castonguay, J. Pageau, *et al*., *Plasma and Polymers,* **4**, 207 (1999).
[7] P. Favia, M. Stendardo, and R. d'Agostino, *Plasmas and Polymers,* **1**, 91 (1996).
[8] R. Sipehia, G. Martucci, M. Barbarosie, *et al*., *Biomaterials, Artificial Cells & Immobilisation Biotechnology,* **21**, 455 (1993).
[9] P. Chevallier, M. Castonguay, S. Turgeon, *et al*., *Journal of Physical Chemistry - Part B,* **105**, 12490 (2001).
[10] G. T. Hermanson, "*Bioconjugate Techniques*" Academic Press, San Diego (1996).
[11] C. Batich, *Applied Surface Science,* **32**, 57 (1988).
[12] J. Hammond, *Polymer Preprints,* **21**, 149 (1980).
[13] R. F. Zwaal, P. Comfurius, and L. L. M. Van Deenen, *Nature,* **268**, 358 (1977).
[14] J. A. Hayward and D. Chapman, *Biomaterials,* **5**, 135 (1984).
[15] E. Tischer, R. Mitchell, T. T Hartman, *et al*., *Journal of Biological Chemistry,* **266**, 11947 (1991).
[16] M. S. Pepper, N. Ferrara, L. Orci, *et al*., *Biochemical and Biophysical Research Communications,* **189**, 824 (1992).

Investigations of dielectric-barrier atmospheric-pressure glow discharges in helium-gas mixtures

Laxminarayan L. Raja, Xiaohui Yuan, and Jichul Shin

THE UNIVERSITY OF TEXAS AT AUSTIN

Large-volume atmospheric-pressure glow (APG) discharges are emerging as an important new class of glow discharges with several potential novel applications in processing of materials surfaces and in the processing of gas streams. APG discharges operate in a previously inaccessible regime of plasma parameter space and have properties that resemble classical low-pressure glow discharges, but at atmospheric or near-atmospheric pressures. For example, APG discharges are known to produce copious amounts of highly reactive radical species at room-temperature conditions. In addition to the obvious advantages of atmospheric-pressure operation, APG discharge plasmas have other advantages associated with extremely low power requirements and unique properties associated with fundamentally different plasma reaction pathways under high-pressure and low-temperature conditions.

Widespread use of APG discharge technologies are currently limited by a lack of fundamental understanding of the physical and chemical properties of these discharges. While some progress has been achieved recently through experimental and modeling studies, important questions on the structure, stability, and breakdown mechanisms of APG discharges remain. This study attempts to address some of these questions through detailed modeling and experiments. In particular we study dielectric-barrier controlled APG discharges in helium and helium-reactive gas mixtures. The modeling approach provides a description of physical and chemical phenomena in APG discharges through use of multiple species continuity, electron energy transport, and the Poisson equation for the electrostatic potential. Important surface interaction effects such as secondary electron emission are included. The role of plasma impurities in pure helium is specified through use of a model impurity species. The experimental studies are performed to validate the model. Principal diagnostics include voltage-current waveforms for the discharge and time-resolved spectral data.

The study reveals insights into the pulsed glow structure of pure helium dielectric-barrier controlled APG discharges. The mechanisms of pulse glow formation and extinction and the plasma characteristics during the interpulse period are discussed. While previous studies by others have stressed the importance of impurity species in pure noble gas dielectric-barrier APG discharges, we show that impurities in fact play a relatively minor role in the plasma dynamics of these discharges. Our study reveals that it is the secondary electron emission which controls discharge plasma properties, thereby stressing the importance of plasma-surface interactions in these systems. The modification of discharge structure in the presence of helium-gas mixtures is reported and the implications for materials processing is discussed. Directed ion impact energies at surfaces are expected to be negligible for atmospheric-pressure systems. Here we report on relatively high ion impact energy for APG discharges and the relevance of these ion impact energies for in situ material processing is discussed.

Oxidation of n-hexane in stoichiometric mixtures with air and oxygen under nanosecond discharge at high overvoltage condition

S.V. Pancheshny, N.B. Anikin, S.M. Starikovskaia, A.Yu. Starikovskii

Moscow Institute of Physics and Technology, Dolgoprudny, Moscow region, Russia.

Abstract

In this work we have investigated slow oxidation of methane in fast ionization wave (FIW) under low-pressure condition. Time-resolved (in nanosecond and second ranges) profiles of $OH(A^2\ \Sigma)$, $CH(A^2\Delta)$ radicals and molecules $N_2(C^3\Pi)$, $N_2(B^3\Pi)$, $CO(B^1\Sigma)$, $CO_2^+(B^2\Sigma)$, $N_2^+(B^2\Sigma)$ emission intensity, electrical parameters such as, dynamics of electric field, energy consumption per pulse, current were measured. As results we obtain kinetic curves of set of active particles and full set of electrical parameters of discharge.

List of References

[1] Vasilyak L.M., Kostyuchenko S.V., Kudryavtsev N.N., Filyugin I.V // *Physics – Uspekhi*, 1994 V.37 N.3 p 247.

[2] S.M. Starikovskaia, A.Yu. Starikovskii and S.A. Bozhenkov // ESCAMPIG 16-th, ICRP 5-th Joint Conference (2002) V1. p.313.

[3] S.M. Starikovskaia, A.Yu. Starikovskii and D.V. Zatsepin // *Combust. Theory Modeling.*, 5 (2001) p.97.

[4] N.B.Anikin, S.M. Starikovskaia, A.Yu. Starikovskii *J.Phys. D: Appl.Phys.*, 34(2001) p.177.

[5] N.B. Anikin, S.M. Starikovskaia, A. Yu. Starikovskii // Gas Discharge and Their Applications, Liverpool, 2002, V 2, p 52.

1. Introduction

In a case of high overvoltage on the discharge gap nanosecond breakdown develops in a form of so-called fast ionization wave (FIW) [1]. Efficiency of ignition of combustible mixture under non-equilibrium uniform plasma conditions, which were obtained after FIW development in the combustion cell, has been shown experimentally in [2]. Therefore, study of hydro-carbons-air and hydrocarbons-oxygen mixtures is important for the plasma-assisted combustion application.

In this paper kinetics of $N_2 + O_2 + C_6H_{14} = 71.5 : 19 : 9.5$ and $O_2 + C_6H_{14} = 67 : 33$ mixtures in 0.8-12 Torr total pressure range excited by nanosecond uniform discharge at high overvoltage was experimentally studied.

2. Experimental setup

Uniform discharge was initiated in discharge cell with 500 cm^3 volume at pressure of mixture 1-12Torr. The electric pulse was 25 ns half-width, 11 kV amplitude, 60mJ pulse energy and 40 Hz repetition rate. The discharge cell [3] consists of thin-walled quartz tube with 20 cm length and 5 cm inner diameter, which is

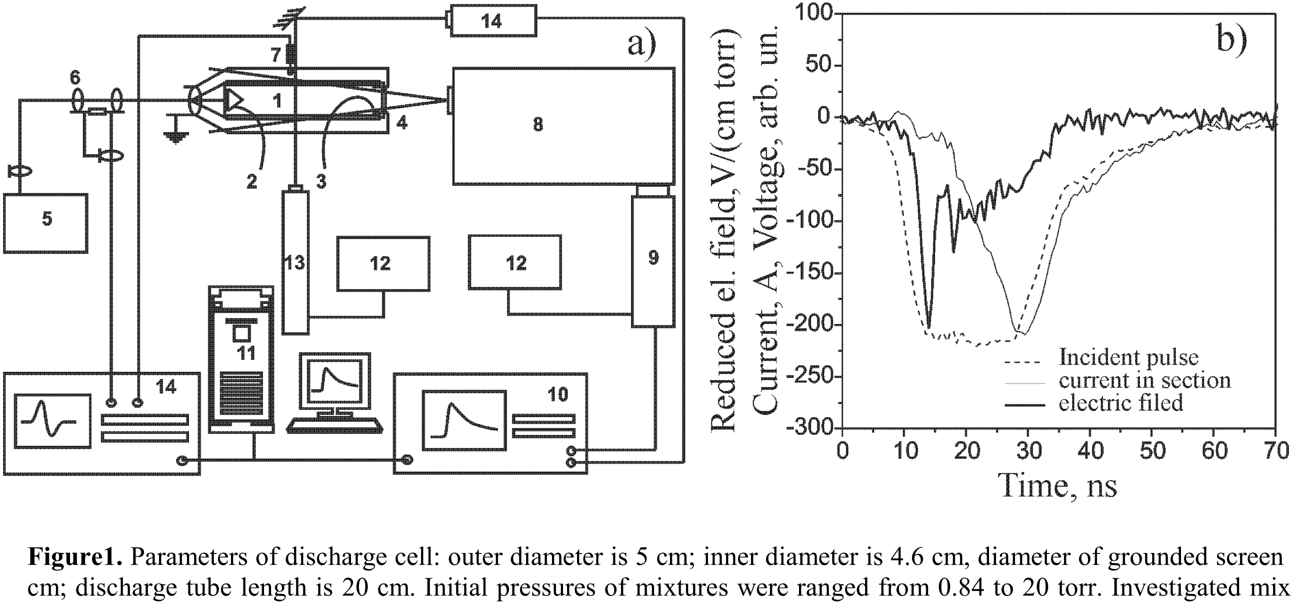

Figure1. Parameters of discharge cell: outer diameter is 5 cm; inner diameter is 4.6 cm, diameter of grounded screen is 14 cm; discharge tube length is 20 cm. Initial pressures of mixtures were ranged from 0.84 to 20 torr. Investigated mixtures were stochiometric ($N_2 + O_2 + C_6H_{14} = 80:18.1:1.9$ and $O_2 + C_6H_{14} = 90.5:9.5$). Parameters of high voltage pulses: amplitude is 11kV; halfwidth is 25 ns; repetition frequency is 40 Hz.

surrounded by 14 cm diameter metallic screen.

Pressure change of chemical reactive mixture during oxidation process was measured by the mechanotron gauge MDHX4S. Time of breakdown, which developed as the fast ionization wave [1], was measured by a capacitive gauge [4] and gave about 3—10 ns in the whole range of experimental condition. Velocity of fast ionization wave and spatial-temporal dynamics of longitudinal electric field were measured with the capacitive gauge.

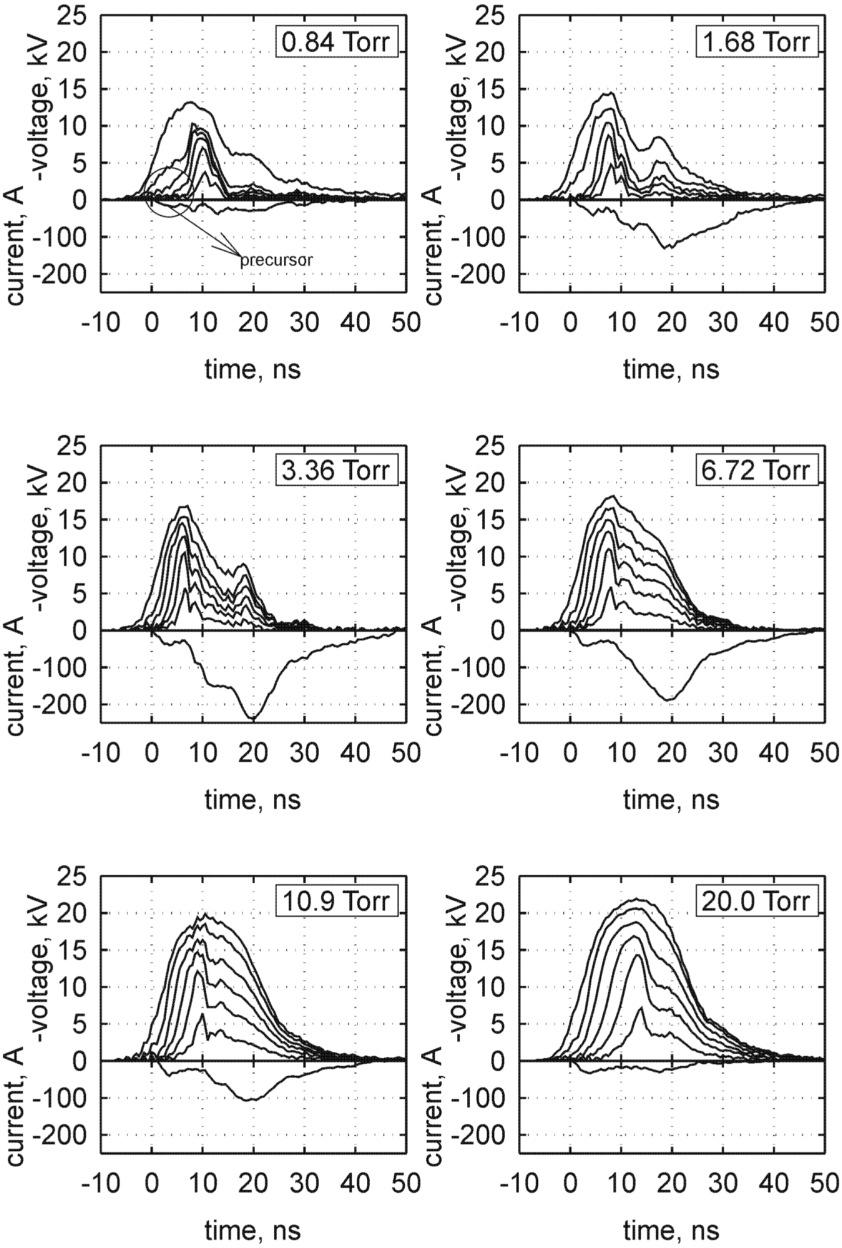

Figure 2. Potential distribution along the discharge tube (upper graphic, here, as amplitude decreases, are represented measurements in points x=0.0; 3.6; 7.2; 10.8; 14.4; 18.0) and current through the cathode (bottom graphic) in the first electric pulse.

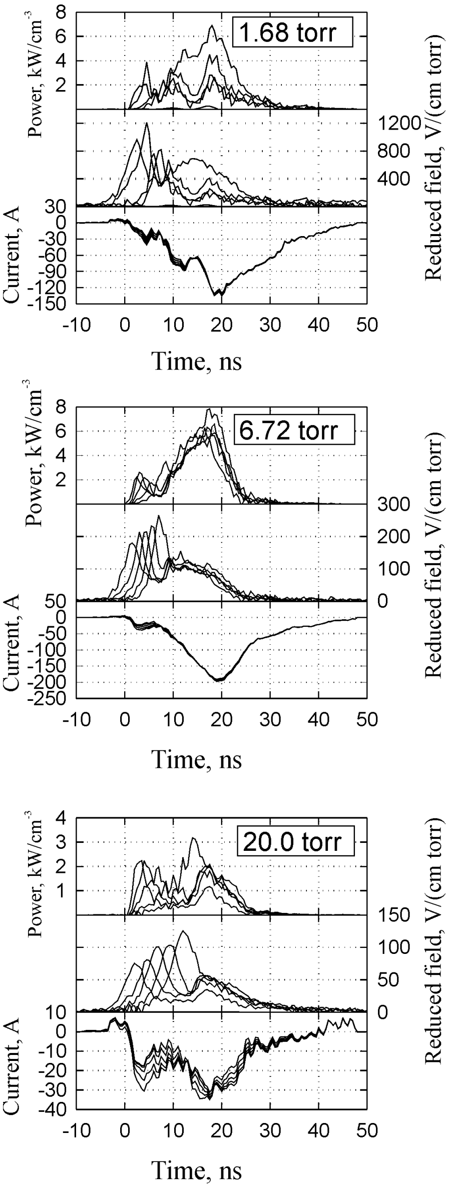

Figure 3. Reduced electric field, current and power per unit volume in sections x=1.8; 5.4; 9.0; 12.6; 16.2 cm. Peaks of field shifted with time corresponds to the FIW front moving.

3.Electrodynamics characteristics of the discharge

Therewith, that diameter of discharge cell screen is similar to its length, electrodynamical situation of the discharge is complicated and essential differ from a situation in a long tube [4]. Experimental investigation of electrical parameter of discharge was performed by experimental methods based on measurements by capacitive gauges and back current shunts. These methods have been described in our works in details (for example [4]). Energy consumption was calculated from the signals of back current shunt, which averaged on interval 4 s just after discharge on, and after conversion of mixture. Difference of energy consumption of these values is not large at the considerable range of initial pressures. Under the circumstances it is capable to use spatio-temporal distributions of longitudinal component of electric field and current measured in converted mixture. Distributions of potential, current and longitudinal component of electric field along the tube have been shown on figures 2 and 3.

On these figures, when the initial pressure of mixture was 0.84 torr, it is emphasized precursor – ionization wave, which developed under condition of high cathode fall of potential. This wave is characterized by weak emission current and relatively great polarization current [4]. Under the higher pressure condition the precursor practically unregistered on the background of the fast started main wave.

The high cathode fall of potential after moment when main wave was started is characteristic feature of the discharge under low-pressure condition. In a long discharge tube a main wave start causes sharp growth of current through the cathode and neutralization space positive charge in cathode layer. To the contrary, in this installation the main wave start causes not full neutralization of the positive charge under low-pressure condition and fall of the cathode potential continues to be essential after main wave start - it is clearly seen on the figures 2 and 3 with pressure lower than 3 torr.

Breakdown in this discharge tube is accompanied by series of forward and backward wave of electric field. Amplitudes of waves greatly decrease with number, thus only first pare of wave (first incident and first reflected) is important. Ionization wave leads to smoothing of electric field in the discharge tube. After the lapse of wave process in the discharge tube uniform electric field has been established. The value of the electric field decreases with time quasi-stationary on this stage of discharge by the action of slow growth of current through the tube, which caused by electron concentration growth.

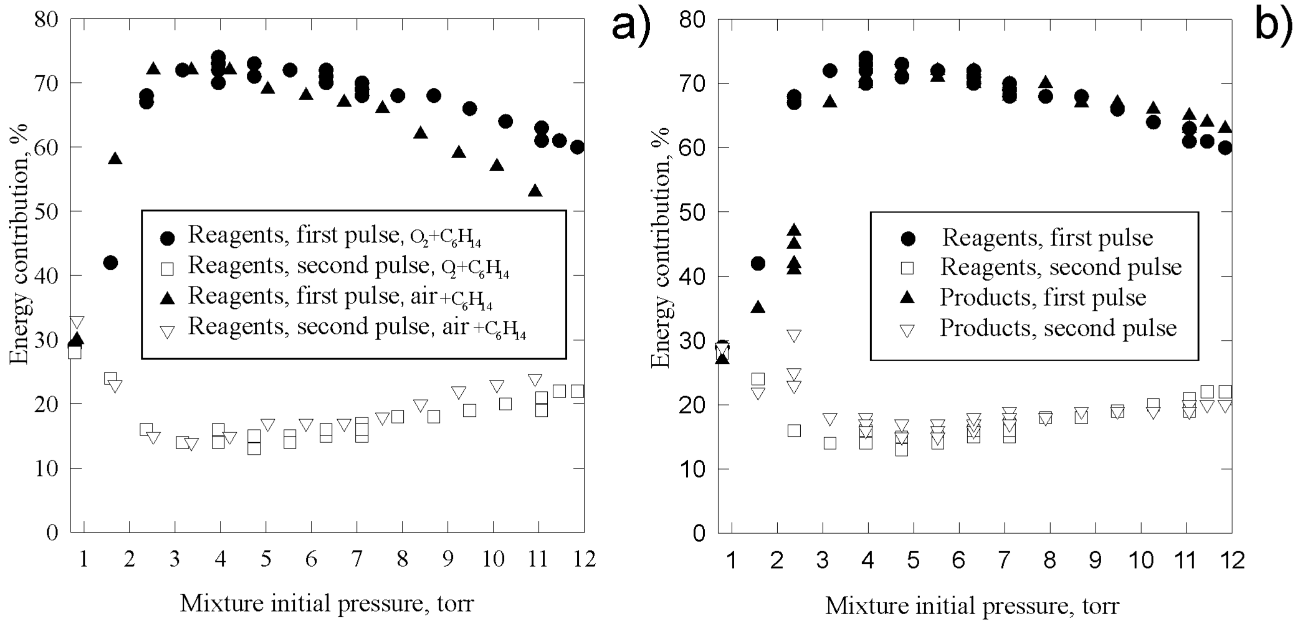

Figures 4-5. The energy contribution in gas discharge cell in the first and the second high-voltage pulses has been shown on figure 4 in reagents (for mixtures C_6H_{14}+O_2 and C_6H_{14}+air) and on the figure 5 in products and reagents (for mixtures C_6H_{14}+O_2).

Under low-pressure condition discharge is characterized by presence of re-breakdown stage. On the figure 2 peak of potential at the moment t=20 ns corresponds to the stage. Re-breakdown occurs on the background of linear distribution of potential in the distance of the cathode and caused by growth of electric field near the cathode. Intensive ionization of gas in the main part of tube leads to sharp growth of conductivity in the discharge, at the same time emission from the cathode occurs insufficient to support the same growth of conductivity of the cathode layer and so electric field decreases in main part of discharge cell and increases in the cathode layer - when electric field in the cathode layer reaches some critical value, wave of re-breakdown starts. Re-breakdown smoothing out the electric field near cathode. Discharge is over with the high-voltage pulse end, but potential and electric field drops faster than current, which is explained by finitesimal value of high-voltage source resistance. In our case this value is equal to impedance of the leading-in coaxial cable (R_s=50 Ohm).

After the uniform field establishing, current through the cell increases from a few Ampere to maximum value (~200 A in our case), and electric field decreases to zero. Maximal part of energy is contributed on this interval. Full energy of high-voltage pulse was about 60 mJ.

Incident high-voltage pulse reflects partially from the discharge cell due to inconsistence of impedances of the discharge cell and the coaxial cable. After that, reflected part of the pulse returns to the high-voltage generator. Greater part of this pulse reflects from the generator and returns to the discharge cell. Up to 90% of the total energy is contributed to discharge cell for the first pair of pulses. From the figure 4 it is clearly seen, that the energy contribution as in first, so in second pulses weakly depends on degree of conversion of mixture.

4.N-hexane oxidation process and emission of molecular bands

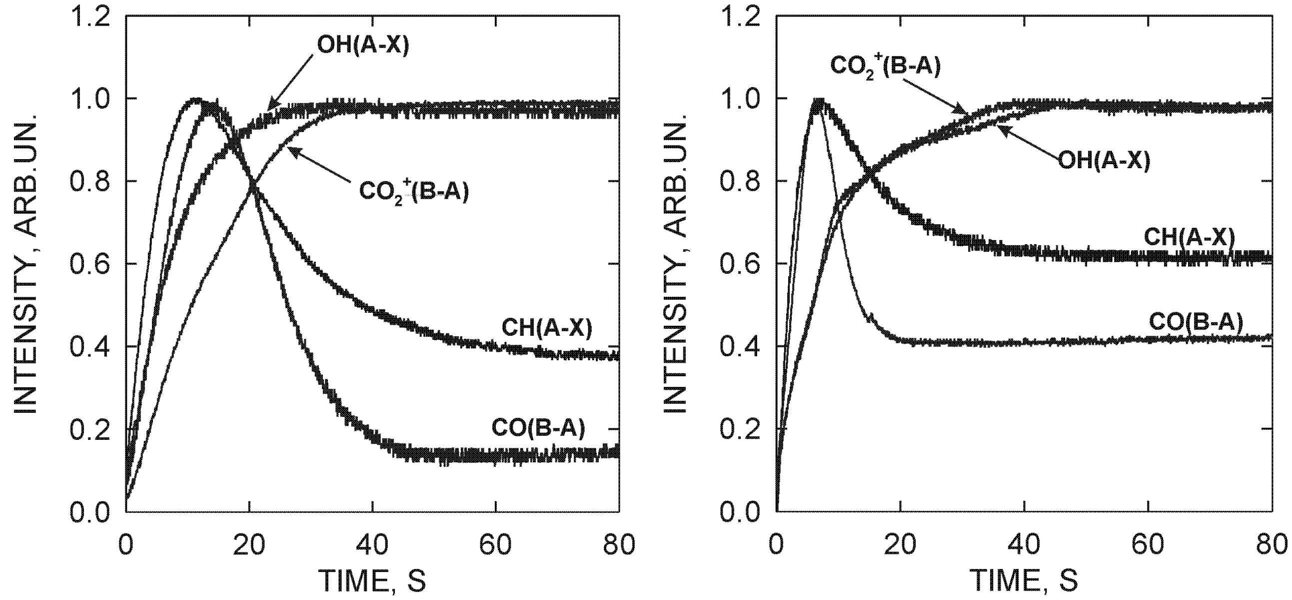

Figure6-7. Dynamics of emission intensities of electronic excited molecules at second resolution range. On the a) mixture is C_6H_{14}+O_2 and on the b) mixture is C_6H_{14}+air. Initial pressure of mixtures is 4.8 torr.

To investigate kinetics of hexane oxidation in stochiometric air-hexane and O_2-hexane mixtures under action of nanosecond uniform discharge, emission intensities of exited radicals $OH(A^2\Delta)$, $CH(A^2\Delta)$ and molecules $CO(B^1)$, $CO_2^+(B^2)$, $N_2(B^3)$, $N_2(C^3)$, $N_2(B^2)$, NO(A) were measured in time resolved (with nanosecond resolution) and integral ranges (with second resolution). Measurements were performed on the 0.8-12 torr initial pressure range. From the experimental data lifetimes and integral quenching constants in the initial and converted mixtures has been obtained. Integral measurements were used for determination rates of the mixture components. It is necessary to note that, for first at all due to the changing of quenching constants with transfer from reagents to products, emission intensities of electronically excited states produced from non-reactive components (N_2) changed. Characteristic times of emission intensities changes of these states depended on initial pressure mixture by the same way as in the states of reactive molecules cases.

In the previous work [5] we have shown that the characteristic time of methane loss with experimental accuracy was equal to the characteristic time of intensity emission drop of CH(A-X) band (figure 8). Residual emission intensity of CH(A-X) band was low than its maximal value by the two order of magnitude. It is necessary to note that the maximal value of this band intensity was reached practically at the moment of the discharge switching on.

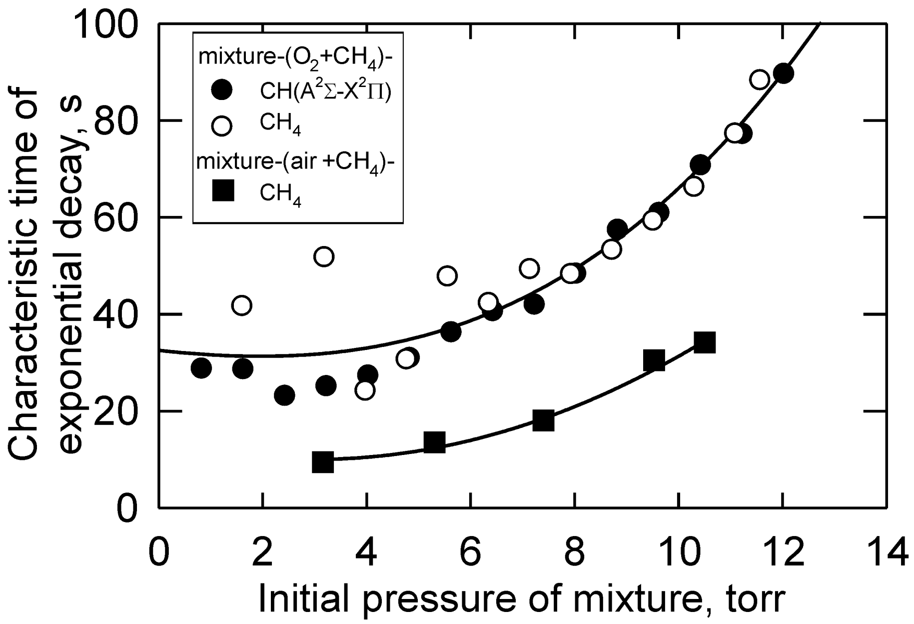

Figure 8. Times of exponential drop of methane concentration and the CH(A-X) emission intensity.

In this work characteristic time of n-hexane oxidation was determined by the drop of intensity of the radical CH(A). From the figures 6-7 you can see, that the intensity on the wavelength of the band grown at first 5-10 s from the moment of the discharge switching on, after that the intensity dropped to the constant value. As time resolved measurements shown (figure 9) the residual emission belonged to ion of dioxide of carbon bands. It is clearly seen on the figure, that the emission in products belonged to the states with lifetime, which essentially smaller than lifetime of CH(A).

In the paper [5] it has been shown, that a characteristic time of various band of different molecules and radicals emission changes measured in processes of oxidation of methane under nanosecond discharge action are same to each other with experimental accuracy. The changes of intensities in time can be described by exponential dependencies with the good accuracy.

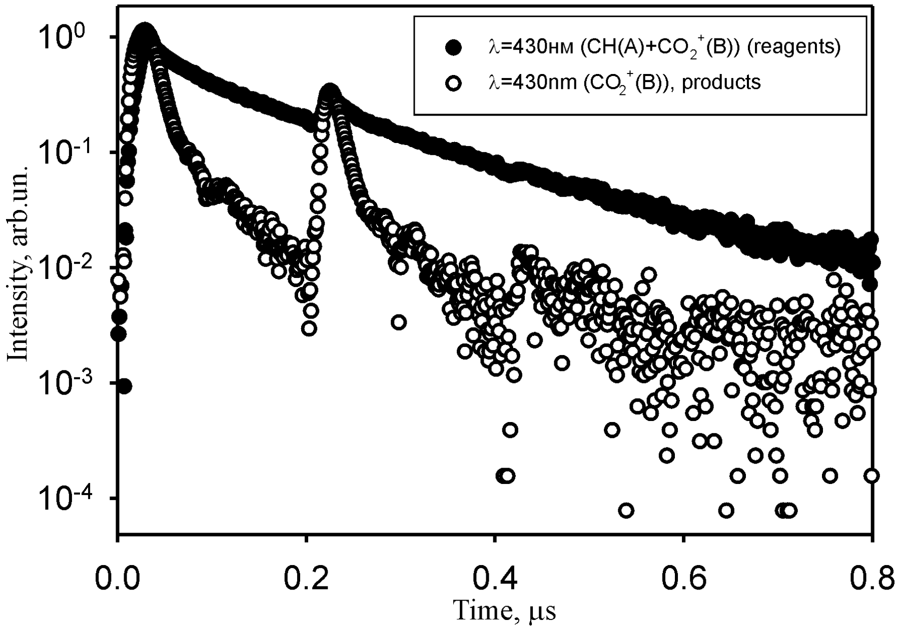

Figure 9. Time resolved emission intensity on the 430 nm wavelength. Initial pressure of mixture 4.8 torr.

In the hexane-oxidation process dynamics of integral emission of components essentially more complex (figures 6-7) than one in the methane oxidation process, that probably is explained by more complex kinetics. So on figure 10 it has been shown characteristic times of intensity changes of CH(A) radical and CO(B) molecule. From the figure it is clearly seen, that the intensity of CO(B) emission achieve the constant value faster than the one of CH(A) approximately by two times.

Because of complex behavior of kinetic curves question of choice of single transition as indicator of degree oxidation need subsequent analysis, however, the $CO(B^1-A^1)$ looks more perspective, because of this transition directly conducted with important intermediate CO. CH(A-X) is less informative, therefore it originates from all intermediate hydrocarbons with very different effectiveness by electron impact.

Comparison of figures 8 and 10 shows, that characteristic time of alkanes in pulsed nanosecond discharge decreases with the its mass and with transition from methane to hexane is diminished by about 4 times. It is necessary to note, that with this transition energy characteristics of discharge changes insignificantly.

5.Conclusions

In this work, processes of n-hexane oxidation in hexane-air, hexane-oxygen mixtures including some radicals and intermediates kinetics have been investigated experimentally. On the basis of this result further it will assumed to create a kinetic model, the same as model for hydrogen oxidation [3], of hydrocarbons oxidation in hydrocarbons-air and hydrocarbons-oxygen under action of nanosecond periodic discharge.

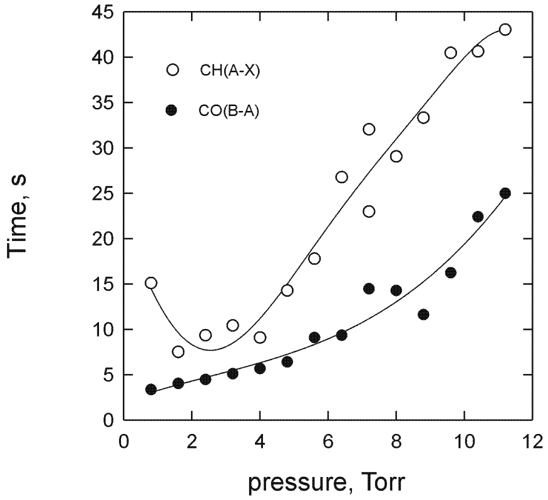

Figure 10. Time of exponential drop of emission intensity of CH(A-X) and CO(B-A) transitions. The mixture is hexane-oxygen, stochiometric .

Improved calibration procedure of an RF plasma impedance probe

V. Kudrle[1], L. Zajíčková[1], K. Wiesemann

Ruhr-Universität Bochum, Experimentalphysik insbes. Gaselektronik, D-44780 Bochum, Germany
[1]*Department of Physical Electronics, Masaryk University, Kotlářská 2, CZ-61137 Brno, Czech Republic*

Abstract

Rather precise electrical measurements are needed for calculation of such fundamental macroscopic quantities like the absorbed power in the radiofrequency discharge or the plasma impedance. All voltage or current probes introduce an error into the measurements. Such error must be compensated. In this paper we present calibration procedure with improved precision in comparison with standard 3 impedances method.

Introduction

For obtaining the macroscopic electrical properties of radio-frequency (RF) discharges the electrical measurements on the RF line are necessary. Such experiments are, for example, used for calculating the absorbed power and the plasma impedance or to study the harmonic frequencies production.

In capacitively coupled discharges stray impedances of the plasma reactor constitute a serious problem for these measurements. They are often of the same magnitude as the plasma impedance and thus rather precise measurements are necessary. In pulsed discharges the static methods (e.g. [1]) are not usable and therefore direct measurement by current and voltage probes is necessary.

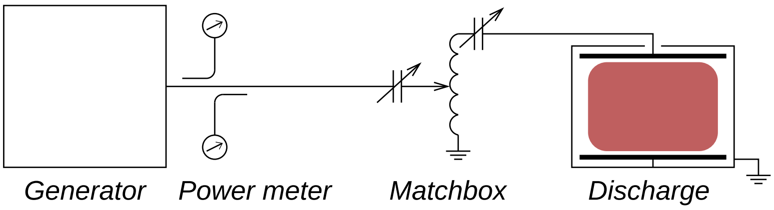

Figure 1: Example of a typical arrangement of the capacitively coupled plasma device.

In absorbed power measurements, the direct measurement of RF current and voltage on RF line as close to plasma as possible is also preferred. In typical arrangement (see Fig.1) there is certain loss of RF power in the matchbox. This loss can easily reach tens of percents and therefore the measurement of absorbed power by a subtraction of the forward and the reflected powers may be seriously flawed. A placement of the powermeter between the matchbox and the plasma is unfortunately out of question, too.

Results and discussion

Voltage and current measurements on the RF line are complicated by the fact that the measuring probes introduce a substantial error. It might seem that errors in the range of several percents (as stated by many manufacturers) are not so important. That is true for amplitude errors. But phase error of several percents is extremely important when the voltage and the current are $\pi/2$ out of phase, as found is the case of nearly all capacitively coupled plasma reactors.

A graphical representation of the errors in RF current and voltage measurements is given in Fig.2. For each test impedance Z ($+$ in the graph) we measured the voltage and current on a 13.56 MHz line terminated by this impedance. From this current and voltage we calculate Z_m, the apparent impedance value (represented by $\times$ in Fig.2), which strongly deviates from the actual value.

However, we can compensate for this systematic error if the probe system is properly calibrated. The probe system may be abstracted as a two port linear device, where the measured (output) and correct (input) values

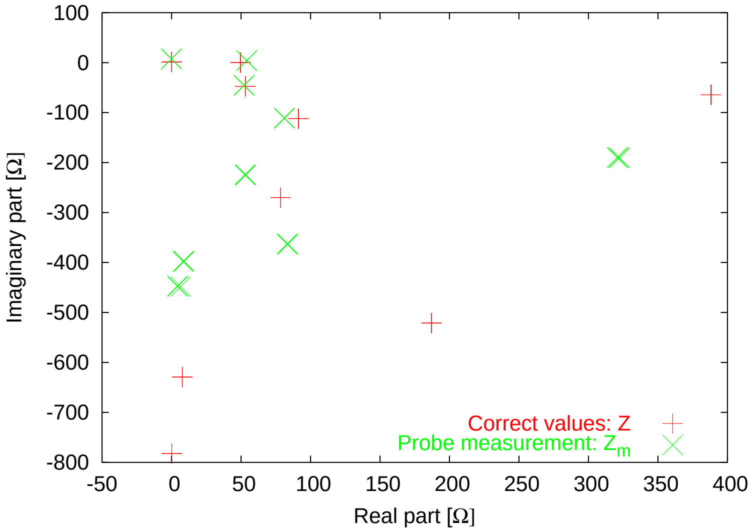

Figure 2: Test impedances Z and values Z_m, measured by our probe system, are plotted in Gauss plane. The differences between correct and measured values are great due to errors introduced by probes.

are related by

$$\begin{pmatrix} U_\mathrm{m} \\ I_\mathrm{m} \end{pmatrix} = \begin{pmatrix} a_{11} & a_{12} \\ a_{21} & a_{22} \end{pmatrix} \begin{pmatrix} U \\ I \end{pmatrix}$$

where all quantities are complex. Such expression includes not only amplitude or phase errors but also such subtle effects like capacitive coupling between the current probe and the RF line. If the coefficients of transformation matrix are known, measured complex amplitudes U_m, I_m may be transformed back to correct values U, I.

The coefficients of the transformation matrix must be determined by a calibration process. Widely used method is to terminate the RF line successively by three known impedances (often Z_1=0, Z_2=Z_0 and Z_3=∞) and to measure corresponding apparent impedances (complex voltage and current ratio). It is also needed for one of these impedances (Z_0 choice is apparent) measure the correct and apparent power. From these four equations (for Z_1, Z_2, Z_3 and P) the four unknown quantities a_{11}, a_{12}, a_{21}, a_{22} may be determined.

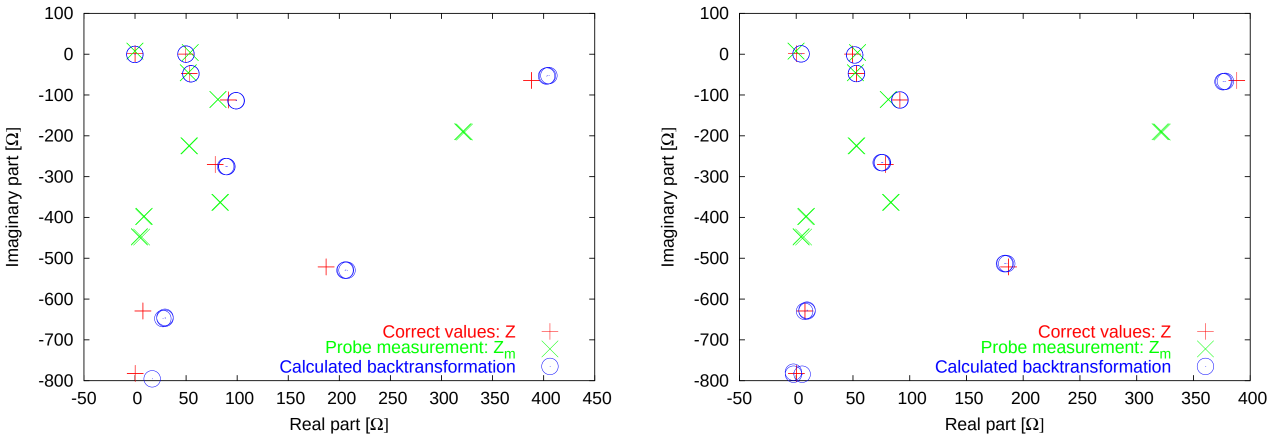

Figure 3: Examples of non-optimal direct calculation of matrix coefficients from three known impedances. The left and right figures differ only in the choice of these three known impedances.

Usually not more than three calibration impedances are used. The problem is that the results differ when using more than three impedances and calculating the transformation matrices from different triplets [2] (see

Fig.3). This means that such a calibration is not optimal and the following measurements of plasma parameters may be erroneous.

Therefore we propose to use a greater number (approximately ten) of carefully selected impedances and then to find that transformation matrix, which is the best fit for all of them. As most suitable fitting method appears the least squares procedure on quasilinearised system

$$\begin{pmatrix} -1 & Z_1 Z_{m1} & Z_{m1} \\ -1 & Z_2 Z_{m2} & Z_{m2} \\ -1 & Z_3 Z_{m3} & Z_{m3} \\ \vdots & \vdots & \vdots \end{pmatrix} \begin{pmatrix} c_1 \\ c_2 \\ c_3 \end{pmatrix} = \begin{pmatrix} Z_1 \\ Z_2 \\ Z_3 \\ \vdots \end{pmatrix}$$

where $c_1 = a_{12}/a_{11}$, $c_2 = a_{21}/a_{11}$ and $c_3 = a_{22}/a_{11}$ are sought parameters.

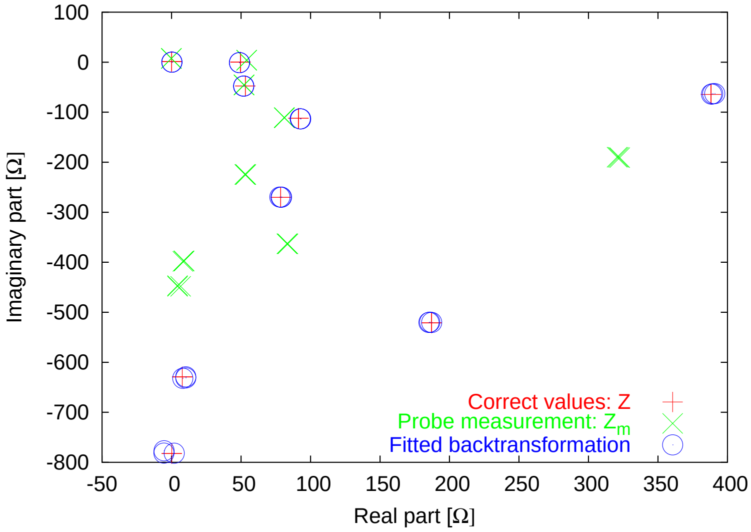

Figure 4: Example of calibration process, using nine test impedances.

A graphical representation of the successful calibration process is given in Fig.4. For each test impedance Z we measured by our probes the value Z_{m}. Then we evaluated by a least square fit the estimation of the transformation matrix coefficients. That matrix then should transform the apparent impedances back to the real ones. Indeed the transformed (indicated by $\circ$) and true impedance values coincide well – see Fig.4.

Conclusion

From these experiments it is evident that our procedure gives generally much better results than the traditional three impedances calibration. This better accuracy is then usable e.g. to separate plasma impedance from stray impedances.

References

[1] L. P. Bakker, G. M. W. Kroesen, F. J. de Hoog: *IEEE Trans. on Plasma Sci.* **27** 3 (1999)

[2] S. Lichtenberg: *Experimentelle Untersuchungen zur Bestimmung des Ersatzschaltbildes eines Lichtbogens mittels RF-Impedanzmessungen und Simulationen*, diploma thesis, Ruhr Universität Bochum (2000)

Study of reaction between HMDSO and O atoms in afterglow

V. Kudrle, V. Doležal, A. Tálský, J. Janča

Department of Physical Electronics, Masaryk University,
Kotlářská 2, CZ-61137 Brno, Czech Republic

Abstract

In this work the kinetics of the reaction between atomic oxygen and HMDSO was studied, in continuation of our previous works [1, 2]. Rate constant was calculated from the loss of O atoms. Atomic oxygen density was measured by means of the electron paramagnetic resonance spectroscopy.

1. Introduction

Hexamethyldisiloxane (HMDSO, see Fig.1) is often used for plasma enhanced chemical vapour deposition (PECVD) of the silicon containing films. By varying an amount of oxygen in the discharge it is possible to prepare the films with properties ranging from the organic (polymer-like) to the inorganic (SiO_x-like). It is caused by a fact that monoatomic oxygen acts as radical scavenger, decreasing the polymerisation rate of organic radicals, increases conversion and fragmentation of monomer, and removes parts of the organic fraction of the film by means of gas–surface reactions (see [3]). Better understanding of the processes involved is needed for the optimisation and modelling of the deposition reactors.

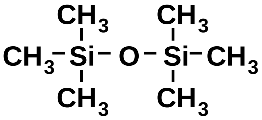

$$CH_3-Si(CH_3)_2-O-Si(CH_3)_2-CH_3$$

Figure 1: Molecule of hexamethyldisiloxane (HMDSO).

In the present study we determined the rate constant of HMDSO+O reaction. Oxygen atoms produced in the discharge are recombining slowly and thus their density in the flowing afterglow is relatively high. When the HMDSO vapour is injected into the afterglow, due to HMDSO+O reaction the concentration of O decreases. From this decrease the rate constant was calculated. Absolute density of atomic oxygen was measured by means of the electron paramagnetic resonance (EPR) spectroscopy (for detailed description, see [4, 5]).

2. Experiment

Schematic drawing of the experimental apparatus is presented in Fig.2. A radiofrequency electrodeless discharge was sustained in the quartz tube with inner diameter of 37 mm by RF generator working at 13.56 MHz. Relatively low power (25 W) was fed into the plasma to maintain the discharge within the cavity; this prevents possible presence (due to backdiffusion) of HMDSO vapours in the active discharge. Main gas (99.995% oxygen) was fed from a standard gas bottle through a reduction valve and a mass flow controller. In the discharge the oxygen was partially atomised and passed through the right–angle bend into afterglow tube and further to a measuring resonator (X–band) of the EPR spectrometer Zeiss ER9. The density of O atoms in the distance of 35 cm from the discharge reached 10^{15} cm^{-3}.

Between the discharge and the measuring resonator the HMDSO vapour was injected into the flux of partially atomised oxygen via small-diameter tube. The vapour flow rate (order of tenths of sccm) was measured and controlled by special flow-controller. The distance between the injector and the EPR resonator could be varied over a limited range from 10 to 30 cm. Because of the fact that the distance from the discharge was as much as 10 times higher than the tube diameter, the back diffusion could be neglected. The total pressure in the EPR resonator during all measurements was maintained at 100 Pa (it corresponds to O_2 flow rate of 7 sccm). This relatively low pressure was maintained because the HMDSO flow-controller needs sufficient pressure drop between inlet and outlet.

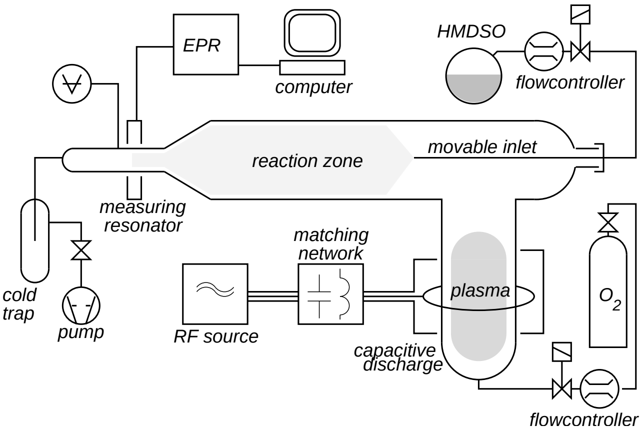

Figure 2: Experimental setup.

The EPR spectrometer was calibrated with molecular oxygen as described in [4]. All measurements were carried out in a flow regime.

3. Measurements and results

EPR measurements provided absolute values of atomic oxygen concentration [O] and the correction for the loss of [O] by processes that were first order in [O] and independent of [HMDSO], such as diffusion followed by wall recombination.

The reaction HMDSO+O is second order reaction but can be transformed into first order reaction when HMDSO is greatly abundant. In our case there was more [O] than [HMDSO] but the results gave clearly first order behaviour (ln([O])∝-[HMDSO]). Therefore it is clear that oxygen reacts also with products and fragments of the first HMDSO+O reaction. The first step of HMDSO+O reaction generally involves CH_3, CH, SiO etc. abstraction from stable HMDSO molecule.

Monitoring of O–atom loss as a function of time (residential time) and HMDSO flow was the basis of this experiment. Correction for the [O] loss due to the wall recombination is achieved by recording [O] at each position x downstream from the injector both with (“on”) and without (“off”) flowing HMDSO.

For the case without flowing HMDSO we can write for the O–atom concentration

$$\frac{\mathrm{d}[\mathrm{O}]_{\mathrm{off}}}{\mathrm{d}t} = -k_{\mathrm{loss}} \cdot [\mathrm{O}]_{\mathrm{off}} \tag{1}$$

where k_{loss} is the wall recombination coefficient (second–order reactions were not considered because of their insignificant role in our experimental conditions).

From this equation we get

$$[\mathrm{O}]_{\mathrm{off}} \cdot \frac{[\mathrm{O}_2]_0}{[\mathrm{O}_2]_x} = C_1 \cdot \exp(-k_{\mathrm{loss}}t) \tag{2}$$

where C_1 is a constant depending on the experimental arrangement and the term $[\mathrm{O}_2]_0/[\mathrm{O}_2]_x$ compensates the O–atom concentration decrease due to pressure decrease along the tube.

For the case with flowing HMDSO

$$\frac{\mathrm{d}[\mathrm{O}]_{\mathrm{on}}}{\mathrm{d}t} = -(k_{\mathrm{loss}} + k \cdot [\mathrm{HMDSO}]) \cdot [\mathrm{O}]_{\mathrm{on}} \tag{3}$$

where k is the coefficient of the reaction O + HMDSO.

We obtain

$$[\mathrm{O}]_{\mathrm{on}} \cdot \frac{[\mathrm{O}_2]_0}{[\mathrm{O}_2]_x} = C_2 \cdot \exp\Big(-(k_{\mathrm{loss}} + k \cdot [\mathrm{HMDSO}]) \cdot t\Big) \tag{4}$$

where C_2 is constant given by experimental conditions.

By dividing (4) and (2) and taking the logarithm of both sides we have

$$\ln\left(\frac{[\mathrm{O}]_{\mathrm{on}}}{[\mathrm{O}]_{\mathrm{off}}}\right) = C_3 - k\cdot[\mathrm{HMDSO}]\cdot t \tag{5}$$

Time of residence t may be determined from known pressure, flow rate and discharge tube diameter. Therefore, principally two types of experiment may be carried out:

- keeping [HMDSO] constant and moving the injector (varying t)
- residence time t fixed, varying HMDSO flow rate

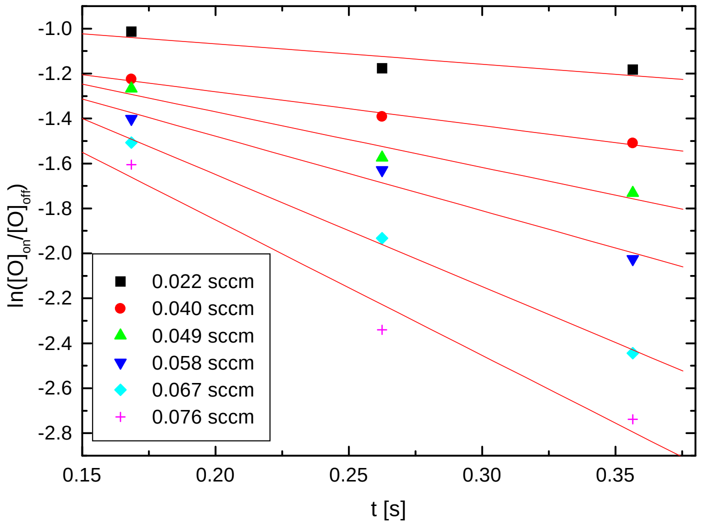

Figure 3: Dependence of O–atom loss (in logarithmic scale) on the reaction time for several HMDSO flows.

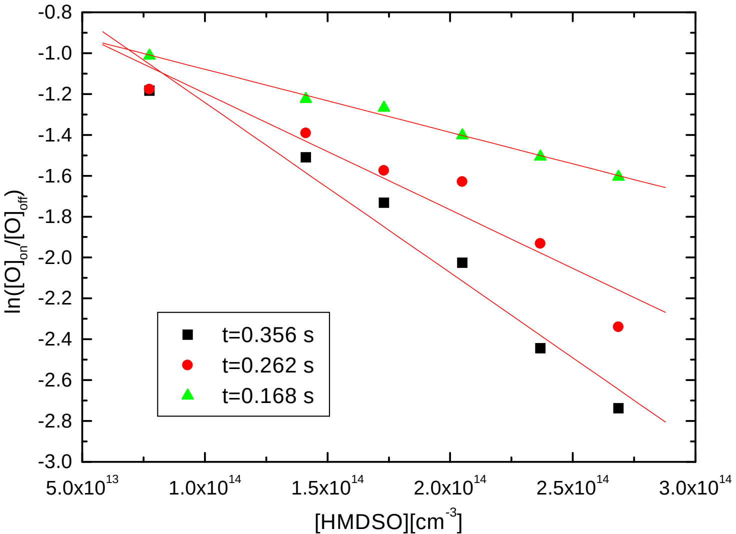

Figure 4: Dependence of O–atom loss (in logarithmic scale) on the HMDSO flow for several reaction times.

In our apparatus, uncertainty in t may arise because there is a change in diameter of the tube. In such region the flow is irregular and simple relation between flow, diameter and velocity does not hold. This can be circumvented by “differential” measurement, where for two injector positions x the function $[\mathrm{O}]=f_x([\mathrm{HMDSO}])$

is measured. From these functions a new function [O]=$f_{\Delta x}$([HMDSO]) is constructed. In this form, only Δt plays a role and not actual value of t. A disadvantage of such calculation is higher statistical error due to subtraction of close numbers.

We have performed both principal types of measurement (see Figures 3 and 4). It is evident that the curves are linear and thus our quasi-first order solution is correct. Moreover if difference methods (above explained for Δt, but it can be done also for Δ[HMDSO]) are applied, the resulting rate constants are quite close to those calculated by non-difference methods.

Using all four methods (constant t, constant [HMDSO], difference Δt and difference Δ[HMDSO]) and the relation (5) we obtain

$$k = (2.4 \pm 0.7) \cdot 10^{-14} \mathrm{cm}^3 \mathrm{s}^{-1}$$

4. Conclusion

The rate coefficient for the reaction of HMDSO with atomic oxygen was measured by means of the flowing afterglow and the EPR technique. These experiments yield the total rate coefficient of the reaction O + HMDSO (and its fragments) around $2.4 \cdot 10^{-14}$ cm^{3}s^{-1}.

Acknowledgements

This work was supported by Czech Ministry of Education under contract MSM 143100003, by Grant Agency of Czech Republic, contract GACR 202/01/P106 and by COST 527.20.

References

[1] J. Janča, A. Tálský, V. Zvoníček: *Plasma Chemistry and Plasma Processing* **16** (1996), 187–194
[2] M. Janča, V. Kudrle, V. Křápek, A. Tálský, J. Janča: *Proceedings of 13.SAPP, Tále, Slovakia* (2001), 100
[3] F. Fracassi, R. d'Agostino, P. Favia: *J. Electrochem. Soc.* **139** (1992), 2636
[4] A. A. Westenberg, N. de Haas: *J. Chem. Phys.* **40** (1964), 3087–3098
[5] A. A. Westenberg: *Prog. React. Kinet.* **7** (1973), 23–82

Structural analysis of hydrogenated carbon films deposited by rf (13.56MHz) methane gas plasma

M.Ouchabane[1], M.Aoucher[2], A.Sekkal[1], K.Henda[1] and H.Lahmar[1]
[1]Centre de Développement des Technologies Avancées
Laboratoire des plasmas
Cité du 20 Août 1956, BP 17, Baba Hassan, Alger, Algérie
[2]Laboratoire de physique des matériaux,
Equipe couches minces et semiconducteurs
Faculté de Physique, USTHB, BP32, El Alia,
16111 Bab-ezzouar, Alger, Algérie

Abstract

Diamond-like carbon films (DLC) were deposited on silicon wafers in both diode and triode plasma enhanced chemical vapour deposition (PECVD) reactor using hollow cathode. It is well known that properties of DLC films are determined by the amount of sp^3/sp^2 hybridization ratio. For structural analysis the films were characterized by X-ray auger electron spectroscopy (XAES) in either N(E) and dN(E)/dE to assess the sp^2/sp^3 ratio of the DLC films. Also the electron energy loss (EELS) spectra are registered to show features corresponding to plasmon and core loss energies. In comparison with an evaporated amorphous carbon films (a-C) and graphite specimen spectra the results show a higher sp^3 bonds in the DLC films in both XAES and EELS analysis.

Keywords: Diamond-like carbon, Hollow cathode, XAES, EELS

1. Introduction

Hydrogenated amorphous carbon films a-C: H and diamond-like carbon films (DLC) have received much attention of any authors [1,2,3] relating to their interesting properties such as extreme hardness [4], chemical inertness [5], high electrical resistivity [5], low IR absorption [6,7], their unique characteristic in wear durability [8] and biocompatibility [9,10]. They have been prepared by RF plasma decomposition of hydrocarbon (CH_4) gas [11,12] and dilution of hydrocarbon species such as CH_4 in H_2 and Argon [13]. The plasma is produced between two parallel electrodes by a 13.56 MHz generator with using a multihole cathode. Although some of their mechanical, physical optical and electrical properties appear to be determined by the relative amount of sp^3/sp^2 hybridisation ratio. This is the reason why the assessment of this ratio is important. This is done through the use of different characterization techniques. In this work we present some results of structural characterization of hydrogenated carbon films by X-ray auger electron spectroscopy (XAES) and by electron energy loss spectroscopy (EELS).

2. Experimental procedure

2.1 Deposition apparatus

The films were deposited in an apparatus consisting with stainless steel vacuum discharge chamber of 23 cm diameter and 25 cm height with two electrodes (Figure 1). Around its lateral wall, 12 lines of ferrite magnets with reversed polarity are disposed in order to produce a multicusp magnetic field of about 100 G. The discharge is created between the multihole cathode (upper electrode) and the electrode substrate holder (lower electrode). The multihole cathode shown in figure 1 allows both an increase of the discharge efficiency and a decrease of electrode sputtering. This electrode is a metallic disc (stainless steel) of 12.6 cm diameter and 5 cm height with 7 holes throughout of 4 cm diameter. It is capacitively coupled to the rf power supply output via matching network.

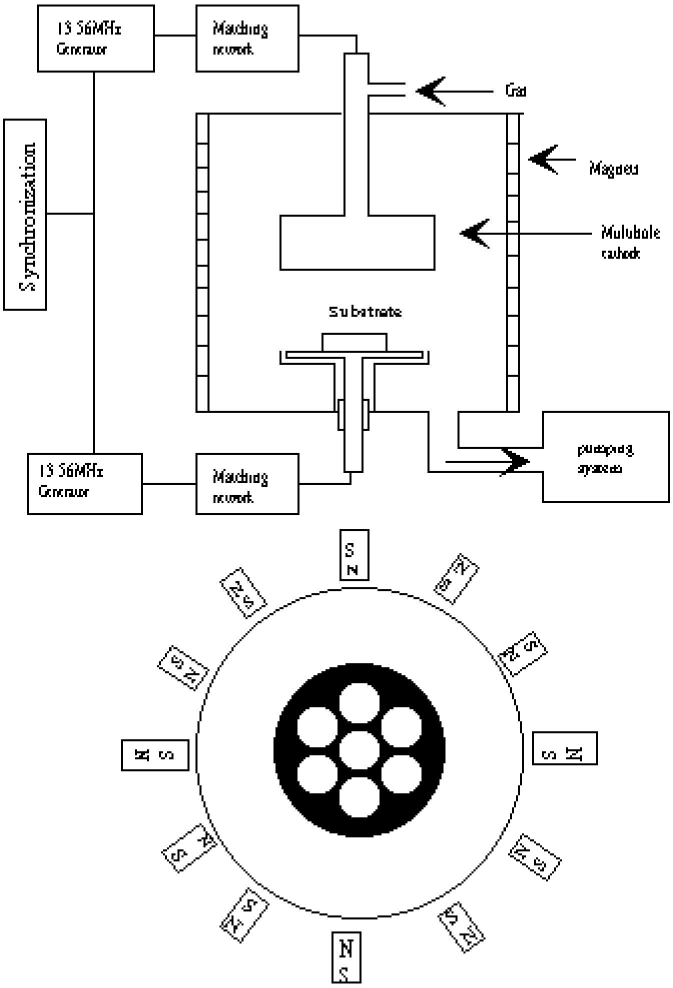

Figure.1. Deposition chamber apparatus

Triode mode is obtained by an RF (13.56 MHz) polarization of the sample holder. Prior deposition, the plasma chamber is evacuated until a residual base pressure of 10^{-5} mbar. Before introducing gas, the pressure was adjusted to 10^{-4} mbar. Methane gas (99.5 %) was used as the feedstock into the plasma region through an orifice along the hollow cathode. For triode system, the two generators are driven by the same oscillator in order to avoid the signal beat at the bottom, which receives relatively less power than the upper one. In this case and for all the experiments, the reflected power was adjusted nearly zero. The upper electrode self-bias potential V_{dcu} and the lower self-bias potential V_{dcl} were measured with a voltmeter through a low pass filter. Before deposition, the Si substrates were cleaned from contamination in an argon RF discharge at –400 V self-bias potential.

2.2. Experimental conditions

The carbon films were deposited by PECVD using methane gas plasma excited at 13.56MHz. During all the experiments of deposition in triode or diode, the substrate was always negatively polarized. The experimental deposition conditions are given in table I.

Table I: Experimental conditions of deposited films

Sample	Mode	P_s (Torr)	V_{dcl} (Volts)	D (Å/min)
DLC1	Diode	0.1	200	100
DLC2	Triode	0.06	240	90
DLC3	Diode	0.04	210	73
DLC4	Triode	0.06	50	33

3. Results and discussions

3.1. X-ray Auger electron spectroscopy (XAES)

The *XAES* is a technique, which has an advantage so that it does not damage the films under investigation. In figures 2, the C KLL spectra for all the samples in either integral *N(E)* or derivative form *dN/dE* are shown and compared to that of graphite structure. The kinetic energy of the main feature in all *N(E)* ranges from 250 to 280eV. It is reported [14] that the main feature for graphite occurs at 269eV, and those for diamond occur at 262eV, and it occurs at 260 for DLC films. One can see that the *N(E)* spectra of DLC films are the same for all the samples indicating that their structures are the same. The C KLL transition observed for graphite is especially broadened due to the high number of possible Auger transitions in graphite [15]. In the DLC samples, it is generally observed to be narrower, which may be indicative of mixed sp^3-sp^2 hybridisation states of the C-C bonds. However, differences between the structures are pronounced when the data were smoothed and differentiated for comparing the energy difference between the maximum and minimum values (D parameter), see figure 2(b).

Table II: Results of D values and sp^3/sp^2 ratio

Sample	D (Initial value)	D (After Ar^+ sputtering)	sp^2%	sp^3%	sp^3/sp^2
DLC1	14.9	19.2	11.3	88.7	7.8
DLC2	16.1	22.6	30.6	69.4	2.2
DLC3	15.6	21.3	22.6	77.4	3.4
DLC4	15.9	19.9	27.4	72.6	2.6
Graphite	**20.4**		Not measured		
Diamond	**14.2**		Not measured		

D is correlated to C-C bonding configuration, being 14.3eV in diamond (100% sp^3) [16] and 20.4eV for graphite (100% sp^2) (It was estimated from the measured spectrum and it is smaller than usual). The D values for the DLC films are given in table II together with those of diamond and graphite references. This energy (D) indicates the state of hybridisation of carbon in sp^2 or sp^3 [16-18]. From these values (14.9 to 16), the assumption that we can make here is that the DLC films are consisted of sp^3 (diamond) and sp^2 (graphite) hybridisations with different proportions with neglecting sp^1 bonds and H content.

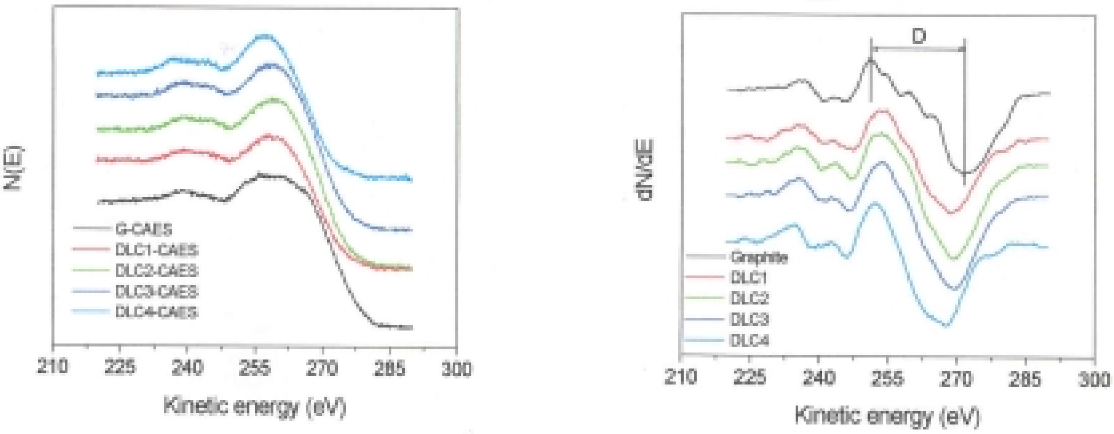

Fig.2. Typical (a) *N(E)* and (b) *dN/dE* spectra of DLC films studied by XAES.

According to Lascovich et al [18] the sp^2 percentage is evaluated by the relation:

$$sp^2\% = \left(\frac{D_{DLC} - D_{diamond}}{D_{graphite} - D_{diamond}}\right) x\ 100 \qquad (1)$$

Where D_{DLC}, $D_{diamond}$ and $D_{graphite}$ are the D values of DLC films, diamond, and graphite respectively. From XAES studies we find that the sp^2 percentages are 11.3 and 22.6 for diode system and 30.6 and 27.4 in case of triode excitation. It is evident that when the substrate holder is polarized enhancing ion bombardment the DLC films exhibit more diamond-like behaviour with high sp^3 percentages of 88.7, 69.4, 77.4 and 72.6. In diode or triode system, and according to the results of Zhang and co-workers [19] the negative self-bias voltage has an effect on the sp^3 fraction; it increases when increasing bias voltage until a certain value and it decreases at extreme self-bias voltages. This behaviour is in good agreement with our results and other works [16,17] when the deposit is bombarded with Ar^+ ions inducing disorder on the DLC films by the formation of sp^2 hybridisations, which indicates a tendency towards a graphitic nature. However in diode system, one can see that coatings are more diamond-like (7.8,3.4) than those obtained in triode system although the bias voltage are not very different (210, 200). This is due certainly to the assumption that all of the deposition processes, including ion bombardment, are at the vicinity of the substrate, which is not the case when samples are coated in triode system. Also when increasing pressure the deposit tends to have DLC behaviour with sp^3/sp^2 ratio of 7.8 in DLC1 and 3.4 in DLC3. Lascovich et al [16] have reported this effect of pressure.

3.2 Electron energy loss spectroscopy (EELS)

EELS is a sensitive surface technique, which can provide reliable information about the bond structure in graphite, diamond and a variety of diamond-like carbon films [19]. The EELS analyses were performed in the low-loss or plasmon region and the core loss region characteristic of the atomic elements in the specimen. Figure 3 shows low energy loss spectra from 0 to 50eV. The low-loss spectra for graphite display two loss features attributed to π and $\sigma+\pi$ plasmon. The former appears at 7eV and is due to π electrons alone and the latter appears at 26.5eV due to all the valence electrons [20]. In figure 4, in comparison with graphite structure, all the samples present a slight response of plasmon energy near 7eV indicating a higher content of the sp^3 bonding in the films [21].

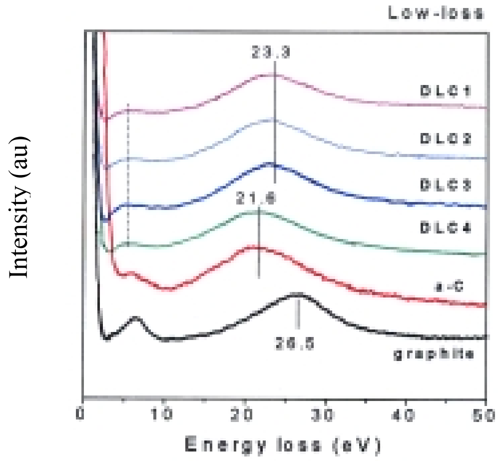

Fig.3. Low-loss EELS spectra of DLC films

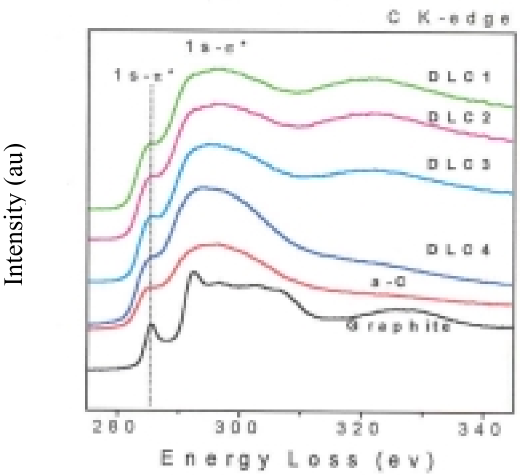

Fig.4. Core loss EELS spectra of DLC films

However, samples 1, 2 and 3 exhibit plasmon energy at 23.3eV, being different of sample 4 where plasmon energy appears at 21.6eV. These shifts in the $\sigma+\pi$ plasmon peak at a reduced energy is due to the lower atomic density of our samples with respect to graphite [22]. This indicates also that sample 4 has a lower density of free electrons compared to the others according to Riedo et al [22]. These results have an effect on the electronic properties of thin films. Also the magnitude of the electron-energy loss due to $\sigma+\pi$ is related to the deposition temperature [23]. It is evident that too high bias voltage creates too high temperatures like in samples 1, 2 and 3. Figure 4 depicts typical EELS spectra at the C K-edge for all the specimens after removal from the background. The spectra for an evaporated amorphous carbon films (a-C) and graphite specimen are also included for comparison. The main features are the two extremes values at ~285.5eV and 295eV corresponding to the 1s-π^* and 1s-σ^* transitions, respectively, observed in graphite. In comparison with graphite, all the samples and a-C spectra do not present the 1s-π^* peak so enhanced and the 1s-σ^* appears merged indicating higher sp^3 bonds. These signatures are typical of amorphous and nanocristalline materials

[24,25]. The spectra for all the coatings look very similar, only sample 4 resulted slight different. The spectrum for this sample resembles more to an evaporated amorphous carbon film than the others.

Conclusion

Diamond-like carbon films have been carried out in diode and triode rf reactor. We have studied the structural states of DLC films from XAES and EELS characterizations. In summary, we have shown that films deposited, in both diode or triode reactor, contain high percentages of sp^3 bond fraction with little differences possibly due to deposition conditions and deposition mode. Moreover the application of a negative self-bias voltage to the substrate has an important effect in modifying films structure and electronic properties.

Acknowledgements

The authors are grateful to J.C.Sánchez-López for his helpful discussions and for EELS and XAES characterizations.

References

[1] D.L.Pappas and J.Hopwood, J.Vac.Sci.Technol. **A12(4),** 1576(1994).
[2] G.J.Vendentop, M.Kawasaki, R.M.Mix, I.G.Brown, M.Salmeron, and G.A.Samorjai, Physical review B.**41(5),** 3200(1990).
[3] P.Couderc and Y.Catherine, Thin solid films. **146,** 93(1987).
[4] P.Couderc, Dépôt par plasma de couches minces de carbone amorphe hydrogéné. Thèse de Doctorat 3éme cycle, Nantes (1986).
[5] W.J.Varhue, K.A.Pandelisev, and B.S.Shinseki, J.Apply.Phys.**67(8),** 3835(1990).
[6] Y.Kokaku, M.Kohno, S.Fujimaki, and M.Kitoh, J.Vac. Sci. Technol **A9(3),** 1162(1991).
[7] P.A.Stenman and H.E.Hinterman, J.vac.Sci.Technol. **A3,** 2934(1985).
[8] M.R.Wertheimer and J.Klember.Sapiena, Thin Solid Films. **115,** 109(1984).
[9] A.Mattnews, S.S.Eskildsen, Dia.Relat.Mater. **43**, 902(1994).
[10] L.J.Yu, X.Wang, and X.H.liu, Surf.Coat.Technol. **128-129,** 484(2000).
[11] Junegie Hong, Antoine Goullet and Guy Turban, Thin Solid Films. **364**, 144(1999).
[12] Alanazi Ali, Kenji Hirakuri and Gernot Friedbacher, Vacuum. **51(3),** 363(1998).
[13] J.B.Cul and R.C. Fang, J.Phys.D:Apply.phys. **29**, 2759(1996).
[14] D.Sarangi and al, J.Vac.Sci.Technol. **A18(5),** 2302(2000).
[15] D.Ramaker, J.Vac.Sci.Technol. **A7,** 1614(1989).
[16] J.C.Lascovish, R.Giorgi, S.Scaglione, Apply.Surf.Sci. **47,** 17(1991).
[17] Y. Mizokawa, T. Miyasato, S. Nakamura, K. M. Geib, and C. W. Wilm-sen, J. Vac. Sci. Technol. **A5**, 2809 (1987).
[18] Y. Mizokawa, T. Miyasato, S. Nakamura, K. M. Geib, and C. W. Wilm-sen, Surf. Sci. **182**,431(1987)
[19] S.Zhang, X.T.Zeng, H.Xie and P.Hing, Sur.Coat.Technol. **123,** 256(2000).
[20] P.Kovarik,E.B.D.Bourdon, R.H.Prince, Phys.Rev. **B 48,** 12123 (1993).
[21] Y.Fan, A.G.Fitzgerald, P.jhon, C.E.troupe and J.I.Wilson, Surf.Interface .Anal. **34,** 703(2002).
[22] E.Riedo, E.Magnano, S.Rubini, M.Sancrotti, E.Barborini, P.Piseri and P.Milani, Solid State Communication. **116,** 287(2000).
[23] M.A.Capano, N.TmcDevitt, R.Ksingh and F.Gian, J.Vac.sci.Technol. **A14(2),** 431(1996).
[24] J.C.Sánchez-López, C.Donnet, A.Erdemir, T.C.Rojas, Surf.Coat.technol. **163-164,** 444(2003).
[25] S.D.berger, D.R.Mckenzie, P.J.Martin, Phil.Mat. 285(1988)

Application of quadrupole mass spectrometry and gas chromatography for analysis of neutral species of processing plasma

J. Pavlik[1], M. Maly[1], J. Matousek[1], Z. Stryhal[1], S. Novak[1], J. Rejnek[2], J. Skoda[2] and P. Hedbavny[3]

[1] *Department of Physics, J. E. Purkyne University, Usti nad Labem, Czech Republic*
[2] *Department of Chemistry, J. E. Purkyne University, Usti nad Labem, Czech Republic*
[3] *Vakuum Praha spol. s r. o., Prague, Czech Republic*

Abstract

For a number of applications of plasma surface processing it is helpful to know the nature of the neutral species present in the plasma. In our experiment the influence of the plasma gas composition on the plasma oxidation process in oxygen and oxygen/argon plasma was studied. The plasma gas phase reaction by-products were determined by using quadrupole mass spectrometry (QMS) and gas chromatography (GC) methods.

1. Introduction

Plasma parameters during plasma assisted processes are often characterized by optical emission spectroscopy and by Langmuir electrostatic probe. The analysis of Langmuir probe characteristics is complicated if the plasma impurities are present. These impurities can originate from interactions between plasma and experimental system walls. The plasma gas phase reaction by-products were determined by using quadrupole mass spectrometry and gas chromatography methods. The analysis of neutral plasma gas phase composition provides an information on changes in the plasma gas composition during the plasma oxidation of thin metal films and consequently on the stability and reproducibility of the plasma process.

2. Experimental apparatus

The experiments were carried out in the system for plasma-chemical surface modification of thin films [1], see Fig. 1. Tin metal films first were evaporated in UHV chamber from Mo boat on Pyrex glass, aluminium, and SiO_2 substrates. The pressure in the UHV chamber during thin tin film evaporation was 1×10^{-5} mbar, whereas the base pressure prior to the evaporation was better than 1×10^{-9} mbar. The tin oxide films were then obtained by in situ plasma oxidation in the flowing post-discharge. The RF discharge (13.56 MHz) was applied in oxygen or oxygen/argon mixture (purity: argon 99.9999 %, oxygen 99.995 % or 99.9999 %). Argon and oxygen gas flows were controlled by independent flow meters. Flow rates were adjusted in order to attain a total mixture pressure of 0.2 mbar – 1 mbar which was found experimentally to be the optimum pressure for the plasma ignition (oxygen/argon mixture – 5:3 and RF power 35 W). The substrate was held on the plasma floating potential during plasma oxidation (oxidation time 30 – 50 min).

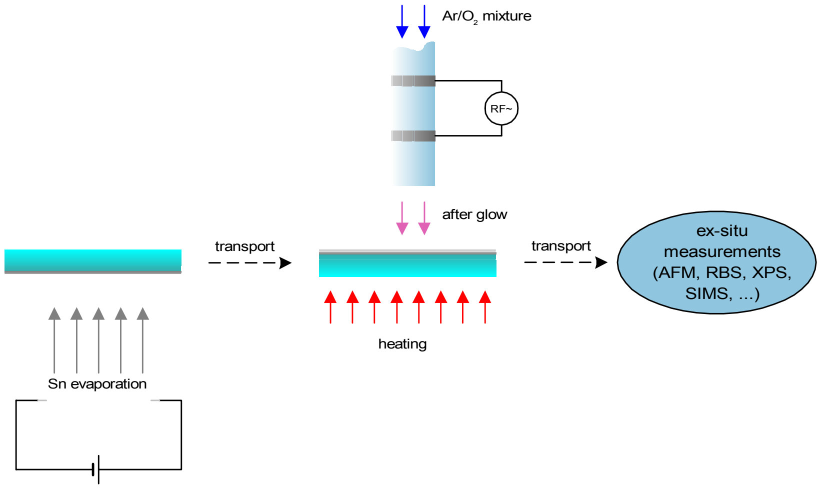

Fig. 1: The schematic layout of experimental set-up for plasma oxidation of thin metal films

2.1. Mass spectrometry analysis of neutral species

The QMS analysis of plasma composition was performed on-line during plasma oxidation of thin tin layers. That plasma oxidation process occurs in a pressure range from 0.5 mbar to 1.5 mbar, therefore a pressure reduction system was needed. A small amount of the process gas was extracted from the active plasma zone and transported through the pressure reduction system to the QMS sampling cell, see the schematic Fig. 2.

The details about the experimental apparatus with the sampling system are given in [2]. Here we can summarize the main features of the apparatus only.

The sampling gas system consists of a stainless steel tube (length 110 cm, I.D. = 4 mm) ending in the plasma zone, sapphire dosing valve and a closed sampling cell around the ion source of the quadrupole mass spectrometer. Using a small rotary pump a laminar flow of process gas is diverted from the plasma zone through the tube to dosing valve. The pressure at the exit of the tube and at the input of the dosing valve is about 0.1 mbar. A small part of this flow is introduced through the dosing valve into the sampling cell. The QMS measures the composition of sampled process gas with a relatively short response time due to high conductivity of the sampling system tube (about 10^{-2} l.s^{-1}). The neutral species of process gas are analysed in sampling cell at the typical pressure 10^{-7} mbar or less. The signal-to-noise ratio (dosing valve closed) is in this way increased overall by a factor of 1000 or more.

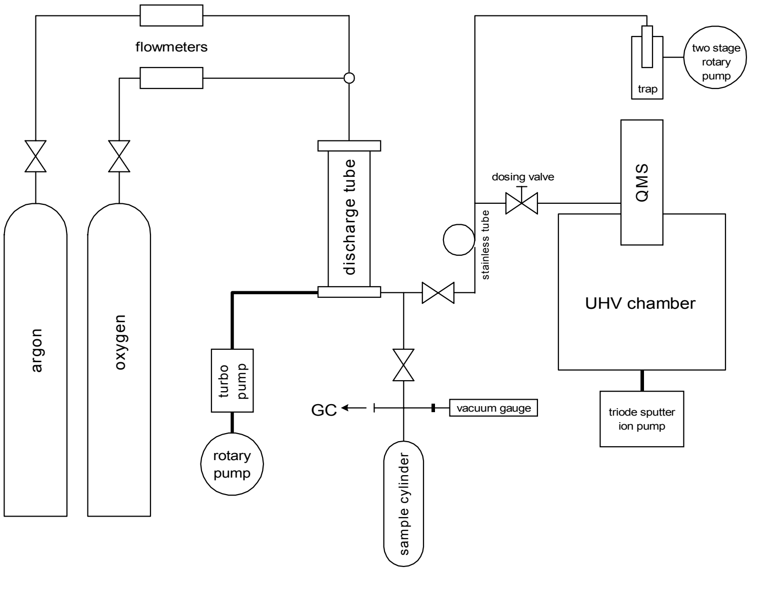

Fig.2: The schematic layout of the sampling gas system

The software for mass spectra analysis developed in our laboratory [3] was used for the mass spectra evaluation. The analysis of spectra assumes that the spectrum of every mixture of gases is the same as found by linear superposition of the spectra of the individual gases. The software was successfully tested on random generated spectra and used for analysis of some measured spectra.

2. 2. Gas chromatography

In addition to the comparative study of the process gas phase composition the method of gas chromatography was used. Analyses were performed on a Hewlett–Packard gas chromatograph (Model HP 5890 Series II) equipped with an electron capture detector (ECD). The temperature of the detector was 300 ºC. The separation was performed using column HP-5 Crosslinked 5 % PH ME Siloxane (30 m × 0.53 mm × 2.65 μm). The temperature program began at 60 ºC for 5 min; increased 6 ºC/min up to 240 ºC and was held on this value until termination (40 min). High purity nitrogen (99.999 %), filtered through the oxygen trap was used as the carrier gas with a column head pressure of 276 mbar.

The direct coupling and sample injection to the gas chromatograph was not possible in our experimental set-up. Therefore a portable sampling system was used. The system was connected to the experimental apparatus, evacuated during the bake out and filled by sample of the process gas phase. After addition of the high purity nitrogen (99.9999 %) to the sample of process gas the value of pressure in the system increased above the value of the column head pressure of the chromatograph carrier gas. The sampling system was separated and transported to another laboratory with GC analyser.

The gas-tight syringe was used to transfer the sample gas from the stainless steel vessel of transportable sampling system and its injection through injection port into the column head. As the sample is transferred from the vessel to the injection port, some of it may be lost because of the pressure differences between the vessel and ambient atmosphere. Therefore we tested the system for reproducibility. The results of these tests indicate an acceptable degree of reproducibility.

3. Results and discussion

3.1. Mass spectrometry measurements

We carried out the residual gas analyse (RGA) measurements of the sampling cell before each set of process gas QMS measurements. In our case the detection of residual gas traces of the sampling cell is neglected due to high contributions of the process gas sample, see Fig. 3, Fig. 4, Fig. 5, and Fig. 6.

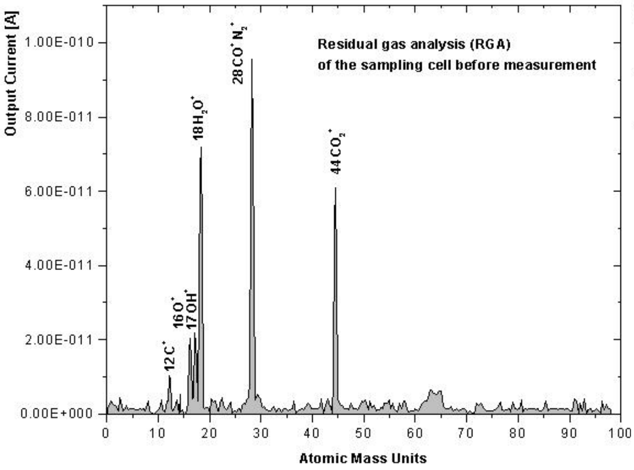

Fig. 2: Residual gas analysis mass spectrum of the sampling cell before measurements (p = 3 × 10^{-9} mbar).

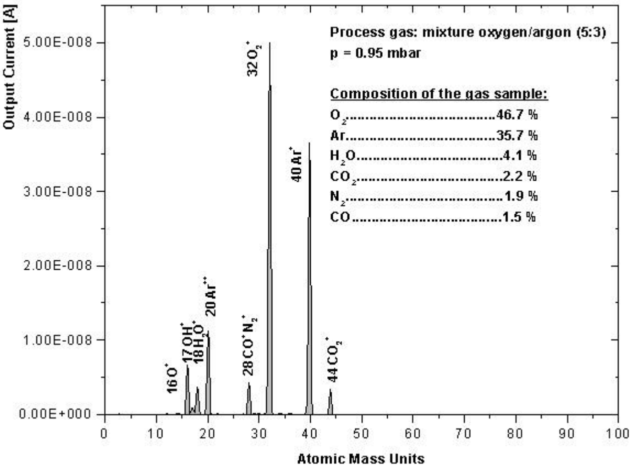

Fig. 3: Mass spectrum of neutral species sampled from process chamber when the discharge was OFF (mixture oxygen/argon – 5:3)

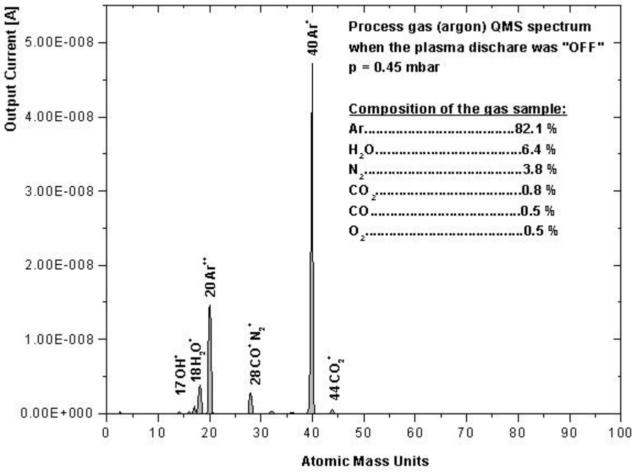

Fig. 4: Mass spectrum of neutral species sampled from process chamber when the discharge was OFF (argon)

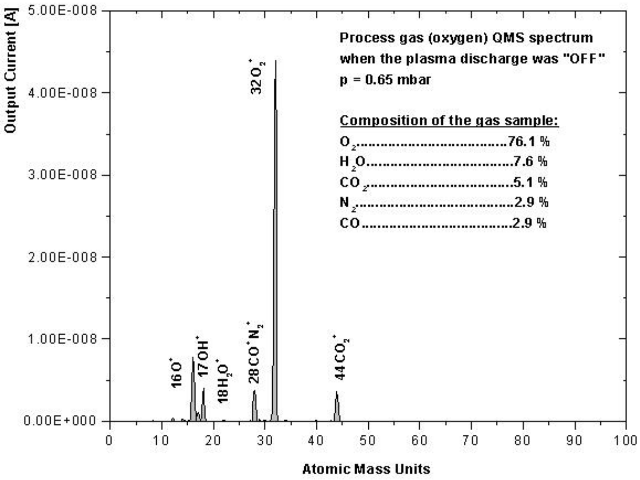

Fig. 5: Mass spectrum of neutral species sampled from process chamber when the discharge was OFF (oxygen)

The peaks representing the process gases dominate in these mass spectra. There may still be observed some signals from process gas impurities in which the water signal was dominant. These impurities can origin as results of gas desorption from inlet system.

The QMS analysis of neutral species sampled from process chamber during plasma oxidation give us information about the formation and variation of neutral species resulting from interactions between plasma and process chamber walls or sample surfaces. For a sample of mass spectrum of neutral species sampled from process chamber when the oxygen discharge was used, see Fig. 6.

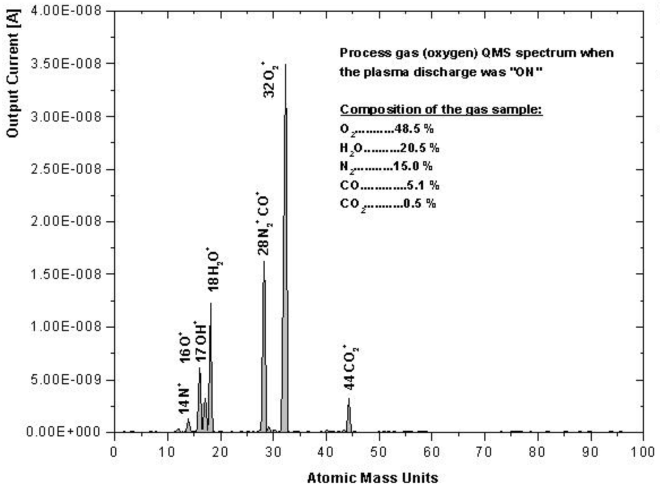

Fig. 6: Mass spectrum of neutral species sampled from process chamber when the discharge was ON (oxygen), p = 0.2 mbar

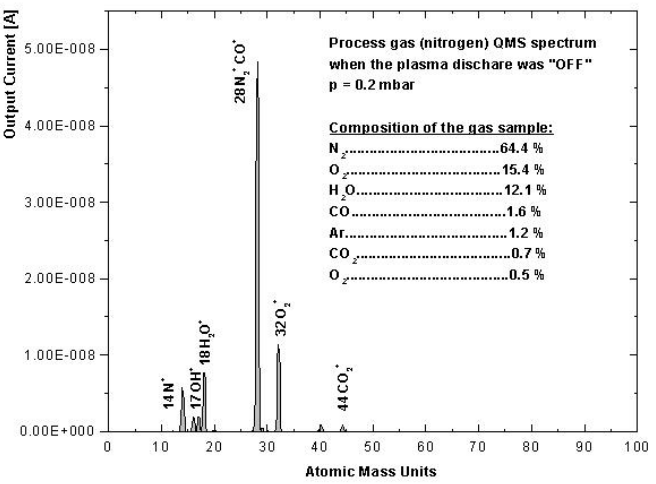

Fig. 7: Mass spectrum of neutral species sampled from process chamber when the discharge was OFF (nitrogen), p = 0.2 mbar

In order to study sample of process gas by gas chromatography method we used some addition of nitrogen to increase the sample pressure in transportable vessel. The mass spectrum of neutral species sampled for nitrogen indicates the possible admixtures, which can influence the gas chromatography analysis, see Fig. 7.

3.2. Gas chromatography measurements

The neutral species of process gas samples were analysed qualitatively by gas chromatography, too. The possible admixture of nitrogen observed in QMS spectra can not be in chromatograms detected since the nitrogen was used as the chromatograph carrier gas. The detection of argon was not possible either since we used the ECD detector. However, the sensitivity for oxygen and other electronegative gas species is very high in this case.

Fig. 8 shows the chromatogram of pure oxygen (99.9999 %) measured in the case that the vessel was filled with oxygen (pressure 10^3 mbar) only.

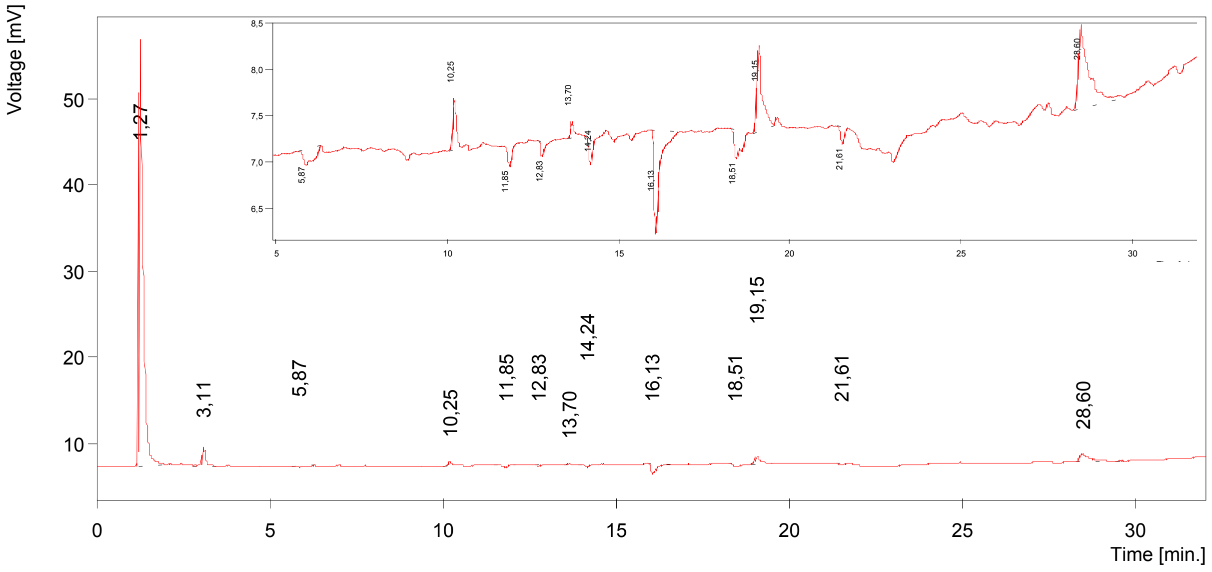

Fig. 8: Chromatogram of pure oxygen 99.9999 % (the vessel filled with oxygen only, p = 10^3 mbar).

Fig. 9 shows the chromatogram of pure oxygen sample (p = 0.2 mbar, purity: 99.9999 %) measured in the case that the vessel was filled with nitrogen (final pressure 10^3 mbar).

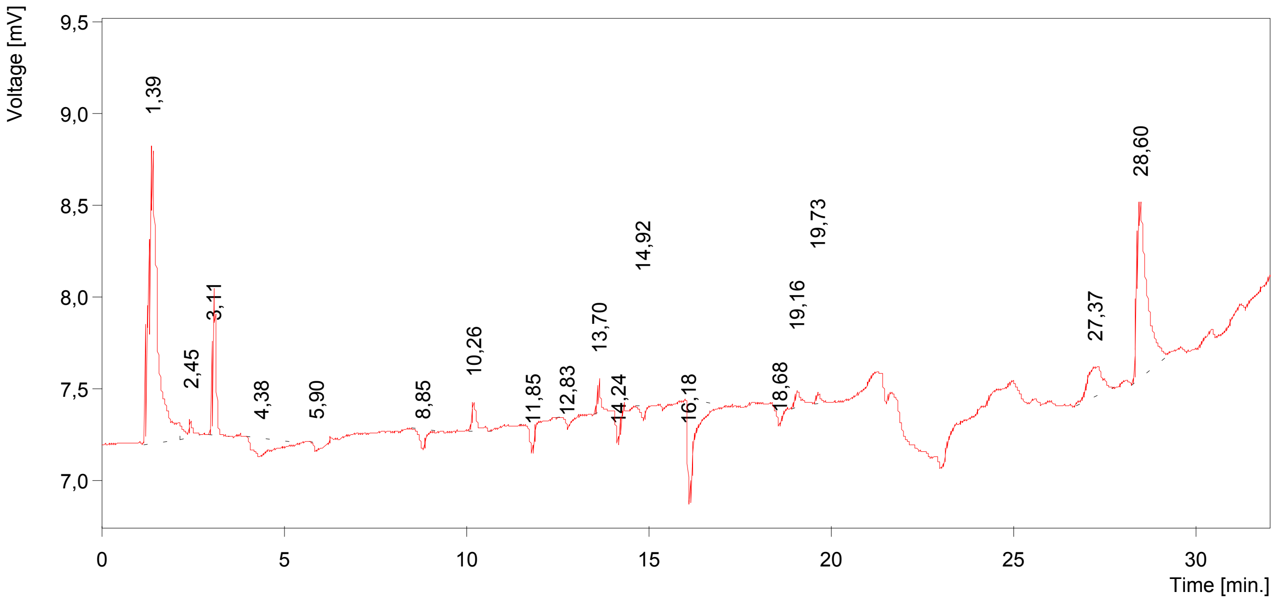

Fig. 9: Chromatogram of pure oxygen sample, p = 0.2 mbar (the vessel was filled with nitrogen, p = 10^3 mbar).

For both these chromatograms is typical a peak with retention time 1.39 min. The area value (mV.s) of this peak is dependent on the pressure, i.e. concentration of oxygen sample. Other peaks at higher retention times represent probably trace amount of the other admixtures of tested gas sample, like carbon monoxide, carbon dioxide and other impurities like water, halogens and hydrocarbons.

Fig. 10 shows the chromatogram of neutral species of process gas (p = 0.2 mbar) sampled from oxygen plasma and measured in the case that the vessel was filled with nitrogen (final pressure 10^3 mbar).

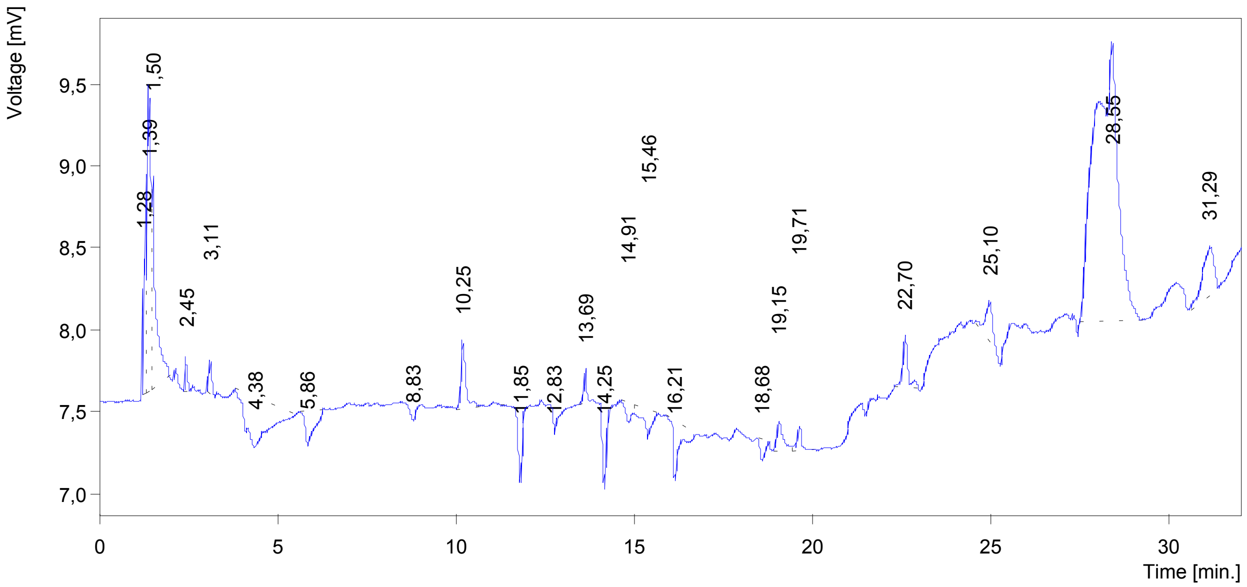

Fig. 10: Chromatogram of neutral species of process gas sampled from oxygen plasma, p = 0.2 mbar (the vessel was filled with nitrogen, p = 10^3 mbar).

Comparing these chromatograms we can observe the changes in area values of some peaks as results of plasma influence, especially in the case of peak with retention time 28.55 min.

4. Conclusion

The first results of measurements with GC and QMS are very promising. Both methods have sufficient selectivity and low detection limit for identification of all impurity species of investigated process gas even in low concentrations. Several problems with GC determination of all different components in a process gas sample should be overcome with a future calibration of the gas chromatograph with reference gases like CO, CO_2, and impurities as H_2O and C_nH_m. All these species could result from gas bottle impurities.

We would like to focus our effort on improvement of sample gas injection into the chromatograph column in future, too, in order to prevent misrepresentation of results and to enhance reproducibility of GC measurements.

In summary, the analysis of process gases is necessary to monitor and control purity of the investigated plasma process. The complex QMS and GC analysis provides not only a basic information on the neutral species of process gas composition, but it helps us to grow up our knowledge of the plasma processes and of chemical composition of plasma.

5. Acknowledgements

This work was supported by the Ministry of Education of Czech Republic (Projects COST 527.50, COST 527.30 and Research Intent MSM 1343 00001).

References

[1] J.Pavlik, R. Hrach, P. Hedbavny, P. Stovicek –Superficies Y Vacio. **9**, Diciembre (1999), pp. 131 - 134

[2] J. Pavlík, P. Hedbavny, M. Maly, Z. Stryhal, V.Kleger, R. Basta - Le Vide: science, technique et application **56** (2001), No. 300 – suppl., pp. 186 - 188

[3] J. Pavlik, M. Maly, Z. Stryhal, S. Novak – Symposium Proc. of 13th SAPP – Symposium on Application of Plasma Processes, Tále, Low Tatras, Slovakia, (2001) , pp.124 – 125

Comparison of two r.f. PECVD processes in oxygen/HMDSO mixtures

L. Zajíčková[1], V. Buršíková[1], G. Borvon[2], A. Goullet[2], A. Granier[2], V. Peřina[3] , A. Macková[3]

[1]*Department of Physical Electronics, Masaryk University, Kotlářská 2, 611 37 Brno, Czech Republic*
[2] *Institut des Materiaux Jean Rouxel, CNRS-Université de Nantes, Nantes, France*
[3] *Institute of Nuclear Physics, Czech Academy of Science, Řež, Czech Republic*

Abstract

Two different low pressure r.f. plasmas, both operated at the frequency 13.56 MHz, have been compared as concern plasma enhanced chemical vapour deposition (PECVD). Namely, a helicon reactor operated in the inductively coupled mode (ICP) and capacitively coupled discharge (CCP) in oxygen/hexamethyldisiloxane (HMDSO) gas feeds have been applied to the deposition of thin organosilicon and SiO_2-like films. The films were compared as concern their optical and mechanical properties, structure and composition.

1. Introduction

The present paper deals with plasma enhanced chemical vapour deposition (PECVD) of thin films containing silicon using hexamethyldisiloxane monomer ($C_6H_{18}Si_2O$ - HMDSO). The use of organosilicon precursor instead of silane (SiH_4), whenever a source of silicon atoms is needed, is often motivated by high flammability of the latter. Organosilicon-oxygen mixtures can be used for PECVD of inorganic silicon dioxide films (SiO_x) as was shown many times for tetraethoxysiloxane (TEOS) monomers [1, 2] as well as for HMDSO [3]. Moreover, the inorganic character of deposits can be changed fluently to the organic one simply by a variation of oxygen-to-monomer ratio [4]. It takes advantage when some multilayer system or a graded layer are demanded for a particular application. The films that are prepared without any oxidising gas, i. e., from pure monomer or with addition of an inert gas like argon, are then often referred as plasma polymers due to their high organic content [5]. The plasma deposition from HMDSO mixed with argon or oxygen has been tested already in 60-ties and early 70-ties [6]. At the moment a great deal of applicative work can be found in the field of protective anti-scratch coatings on plastic substrates [7, 8], barrier films for food and pharmaceutical packaging, corrosion protection layers [9], coatings for biocompatible materials and low-k dielectric layers for microelectronic applications [10, 11]. Either silicon oxide or organosilicon polymer films are prepared in a variety of discharges and plasma reactors. Therefore it is necessary to find some general rules between different film properties and it is of course interesting to compare the effects of different reactor conditions.

2. Experimental

Thin organosilicon and SiO_2-like films have been deposited in two different low pressure r.f. plasmas, both operated at the frequency 13.56 MHz, using oxygen/hexamethyldisiloxane (HMDSO) gas feeds. Namely, a helicon reactor operated in the inductively coupled mode (ICP) [12] and capacitively coupled discharge (CCP) [8] have been used for the comparison. In each reactor, the fraction of HMDSO was varied from 2 to 100 %.

The CCP discharge was produced in a stainless steel parallel plate reactor. The bottom electrode, 420 mm in diameter, was r.f. powered and due to the asymmetric coupling and different mobility of electrons and ions the negative self-bias was superimposed to the r.f. voltage. This electrode was used as a holder of substrates in order to allow the ion bombardment of the growing films. The gases were fed into the chamber through an upper grounded showerhead electrode, 380 mm in diameter. The distance between the electrodes was 55 mm. R.f. power (P) varied from 100 to 450 W. Corresponding total pressures were in the range 1.2–43 Pa. Silicon and glass were used as substrates.

The helicon reactor used to create plasmas in O_2/HMDSO mixtures is described in detail by Granier *et al.* [13]. Briefly, it is made of two parts: the helicon source where the r.f. power is coupled via the external helicon antenna and the stainless steel diffusion chamber where the helicon plasma diffuses. The oxygen was introduced from the top of the helicon source whereas the HMDSO vapours were injected into the diffusion chamber via a dispersal ring placed 80 mm above the substrate. The discharge was operated at 0.4 Pa and

300 W with a fixed total gas flow rate of 16 sccm. Under these conditions the plasma was inductively coupled. The substrate holder was at the floating potential and the substrate temperature was less than 80 °C. Silicon and glass were used as substrates.

The optical, mechanical and electrical properties as well as the composition and structure of the deposited films were investigated. The films deposited on silicon substrates in ICP discharge were characterised by in-situ Jobin-Yvon spectroscopic ellipsometer at the fixed angle of incidence 72° before and after the chamber venting. All the films, i.e. deposited in both, ICP and CCP discharges, were studied by variable-angle spectroscopic ellipsometry (VASE) with ex-situ Jobin-Yvon ellipsometer. The angle of incidence varied from 55° to 75°. The wavelength range in both cases, in-situ and ex-situ measurements, was 240–800 nm (1.5–5.0 eV). The refractive index n and extinction coefficient k of the films in the UV-visible range as well as their thickness were derived from the ellipsometry measurements.

The mechanical properties such as plastic hardness, elastic modulus and fracture toughness are deduced from the depth sensing indentations by means of Fischerscope tester. The electrical properties, namely the dielectric constant, the breakdown electric field, the leakage current and dielectric losses, are derived from C/V and I/V measurements achieved on Si/film/Al MIS structures [10]. RBS, ERDA, XPS and FTIR analyses are applied in order to asses the composition and the structure of the films.

3. Results and Discussion

We have compared the films deposited in the same gas mixtures using CCP and ICP discharges. Namely, the films prepared in oxygen-rich (2 % HMDSO, 98 % O_2) and pure HMDSO plasmas were investigated. The films deposited in oxygen-rich plasma had very low extinction coefficients and the refractive index was closed to that of fused silica. Supported also by the infrared spectra and atomic composition (see below) these films can be denoted as SiO_2-like. The films deposited from pure HMDSO plasma or from HMDSO plasma without only small addition of oxygen can be called HMDSO plasma polymers (PP-HMDSO) because they contain large amount of carbon and hydrogen.

In Fig. 1, the refractive indices obtained from the in-situ single angle spectroscopic ellipsometry and ex-situ VASE on the SiO_2-like ICP film are compared. We have to note that the as-deposited SiO_2-like ICP film has identical optical properties after exposure to the atmosphere which is confirmed by in-situ ellipsometry before and after the chamber venting. However, there is a small difference between n obtained by in-situ ellipsometry and ex-situ VASE. This is probably caused by the fact that VASE gives extended information due to the variability of incidence angle and slightly different alignment of the sample. Anyway, the difference in n is only about 0.002 which is not significant when we want to compare films which differ by the values of one order higher. This is for example the case of the SiO_2-like films deposited in ICP and CCP discharges at the r.f. power of 300 W, both. The refractive indices of these films are compared in Fig. 1 too. The film deposited in CCP discharge has n very closed to the SiO_2 tabulated values. The dispersions of n for the ICP film look

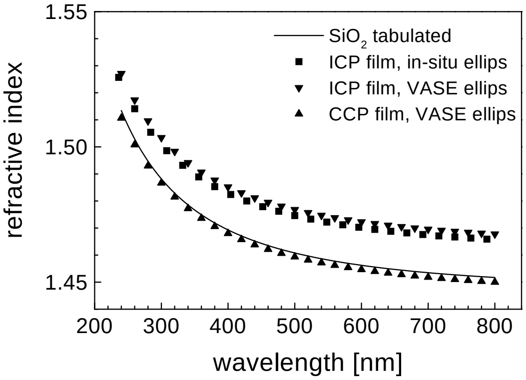

Figure 1: Comparison of the refractive index for the films deposited in 2% HMDSO mixed with oxygen, CCP and ICP discharges at the r.f. power of 300 W.

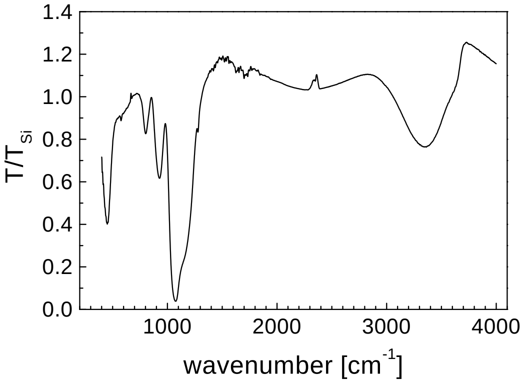

Figure 2: Infrared transmission spectra of the CCP film (for deposition conditions see Fig. 1). The film thickness is 1.59 μm.

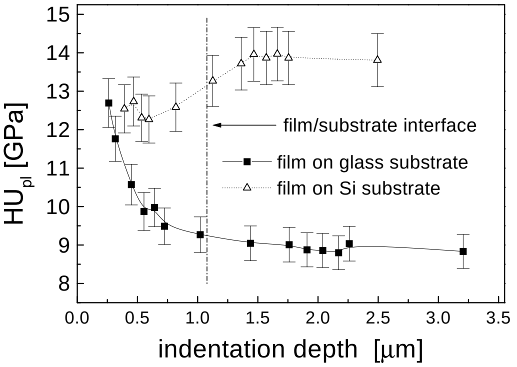

Figure 3: Plastic hardness dependence on the applied load for the ICP film deposited in the mixture of 2% HMDSO and 98% O_2 on silicon and glass substrates.

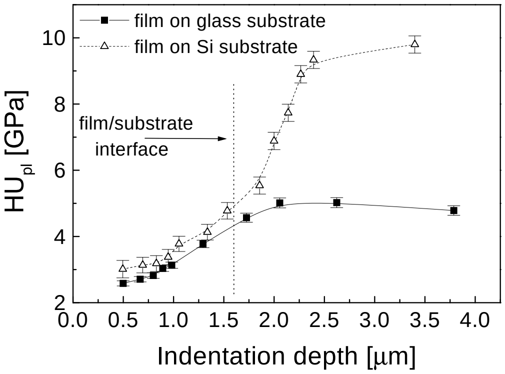

Figure 4: Plastic hardness dependence on the applied load for the CCP film deposited in the mixture of 2% HMDSO and 98% O_2 on silicon and glass substrates.

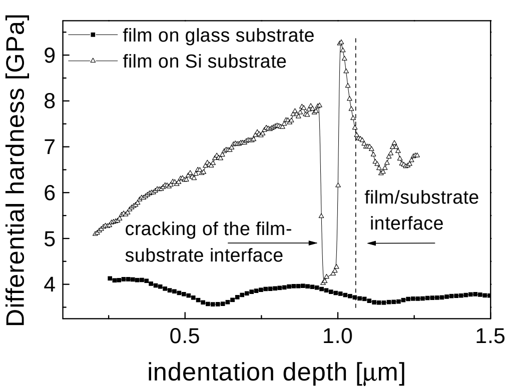

Figure 5: Differential hardness dependence on the indentation depth for the ICP SiO_2-like films on glass and silicon substrate (for deposition conditions see Fig. 3).

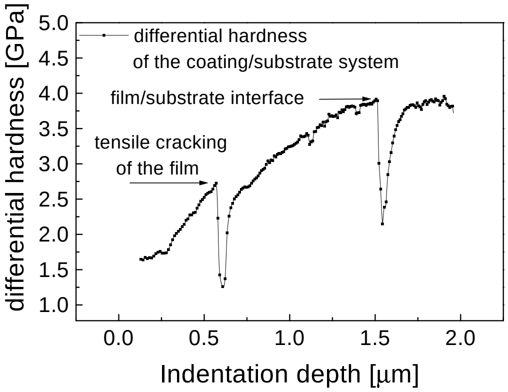

Figure 6: Differential hardness dependence on the indentation depth for the CCP SiO_2-like film on glass substrate. (for deposition conditions see Fig. 4).

similar but the values are shifted to higher values by 0.016–0.018.

The composition and the density of the film deposited in oxygen rich plasma in ICP are close to pure SiO_2, the carbon content is below the detection limit of XPS and the hydrogen content was very low. The films deposited in CCP still contain small amount of carbon (5–8 at. %) and 20–40 at. % of hydrogen even for the lowest HMDSO fraction. The density is smaller than that of quartz, 1.55 g.cm^{-3}. The infrared transmission spectra confirm that both the films show three characteristic peaks of SiO_2 network vibrations around 1070 cm^{-1} (stretching), 810 cm^{-1} (bending), and 450 cm^{-1} (rocking). Besides, there were spectral features correlated with -OH functional groups: relatively strong broad bands centered at 3450 cm^{-1} and 3650 cm^{-1} (H-OH or Si-OH, respectively [14]) and a peak at 930 cm^{-1} associated with Si-OH stretch [15]. The typical FTIR spectrum for 1.59 μm thick film deposited in CCP is shown in Fig. 2. Here, we can see really high amount of OH groups which cause also lower density of the film as compared with 2.2 g.cm^{-3} of the fused silica [16]. The density of the ICP film, on the other hand, is about 2.3 g.cm^{-3}, i.e. higher. Although it is not clear up to now why the refractive index of the CCP film agrees so well with the fused silica the higher refractive index of the ICP film can be explained by the slightly higher film density. It is known that the refractive index n and film density ρ are related by the formula [17]

$$\frac{dn}{d\rho} = 0.20\ \mathrm{cm}^3\mathrm{g}^{-1}. \tag{1}$$

According to Eq. (1) an increase of the density by 0.1 g.cm^{-3} should correspond to an increase of the refractive

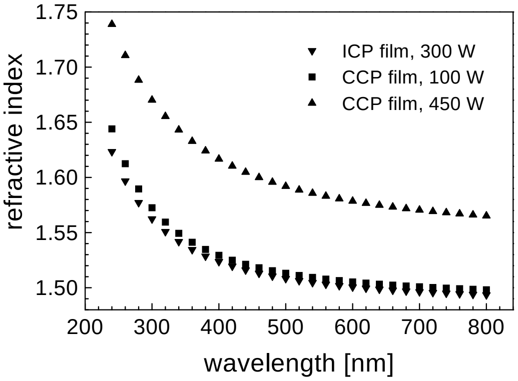

Figure 7: Refractive index compared for the films from pure HMDSO deposited in ICP and CCP discharges with the r.f. power given in figure legend.

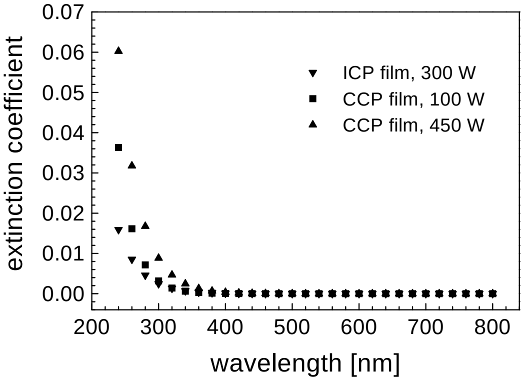

Figure 8: Extinction coefficient compared for the films from pure HMDSO deposited in ICP and CCP discharges with the r.f. power given in figure legend.

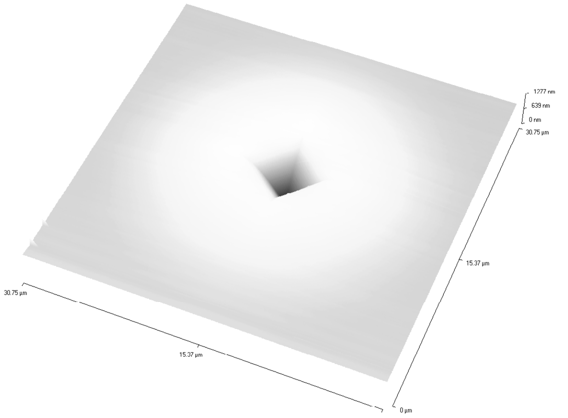

Figure 9: AFM micrograph of the indentation induced buckling around the indentation print.

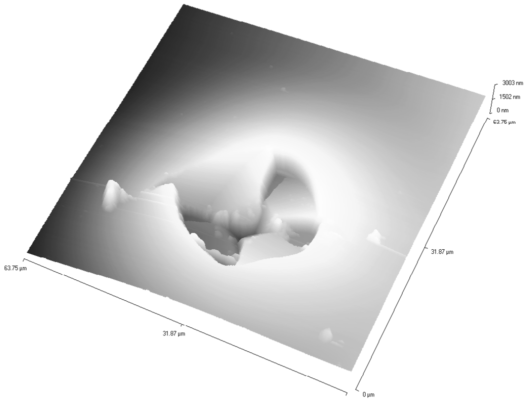

Figure 10: AFM micrograph of the indentation induced delamination around the indentation print.

index by 0.02 which is in relative good agreement with the observation.

The relatively high density of the ICP deposited oxygen-rich films revealed oneself also on the mechanical characteristics mainly in enhanced hardness (12.5 GPa) compared to the fused silica (approx. 10 GPa). In general the hardness of the plasma deposited SiO_2-like films varies between 1 to 9 GPa. As it is shown in Fig. 3 the coatings deposited either on glass or silicon substrate exhibited hardness of about 12.5 GPa. This hardness value was obtained for indentation depths up to 0.25 μm, which is more than 20 % of the coating thickness (see Fig. 3. This extremely high hardness value could be explained pointing out the fact, that the coatings exhibit high compressive stress. On the other hand, the coatings prepared from the same deposition feed composition by CCP exhibited rather tensile intrinsic stress. For increased hardness of coatings prepared by CCP plays important role the negative self bias voltage. In the case of the studied coatings the bias voltage was relatively low, so the obtained hardness value was 2.7 GPa as it is shown in Fig. 4. This hardness value was obtained for indentation depths up to 0.25 μm, which is more than 20 % of the coating thickness. The depth sensing indentation test is sensitive to cracking events. The indentation induced crack initiation in coatings or at the coating-substrate interface appears on the load-penetration curves as a jump. This effect could be nicely visualized by the derivative $\partial L/\partial h^2$ (so called "differential hardness") of the loading curve. In Fig. 5 the differential hardness dependencies on the indentation depth for the ICP deposited SiO_2-like coatings on two different substrates are shown. Even if the coating exhibits compressive stress as it was mentioned above, the coating deposited on glass shows very high resistance against delamination because of high interfacial strength. In the case of the glass substrate there is no elastic mismatch, i. e., the elastic modulus of the substrate and the coating was almost the same (78 GPa), which resulted in the case of the high adhesive bonding also high

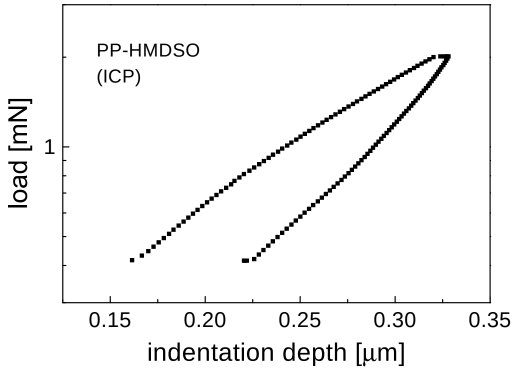

Figure 11: Load/penetration curve for coating prepared from pure HMDSO in ICP-300 W.

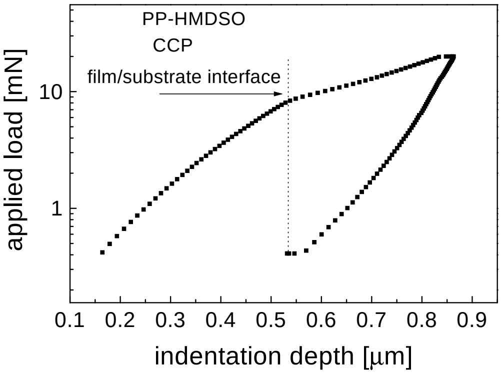

Figure 12: Load/penetration curve for coating deposited from pure HMDSO in CCP-100 W.

interfacial fracture toughness. In the case of the silicon substrate the elastic mismatch was high (the elastic modulus of the substrate is 160 GPa). Even in this case the coating was very resistant against delamination. The interfacial cracking appeared till the indenter almost reached the coating/substrate interface as it is shown in Fig. 5. On the other hand, the SiO_2-like coating deposited by CCP had lower elastic modulus (42 GPa), than the glass substrate and exhibited tensile stress. In the case of the tensile stress the coating tends to crack itself in the case of low film fracture toughness. The tensile cracking of the CCP deposited SiO_2-like coating begun for indentation depth of about 6 μm as it is shown in Fig. 6. The film delamination begun when the indenter reached the coating substrate interface. The AFM images illustrate the effect of the compressive stress on the indentation induced delamination. The compressive stress resulted in buckling of the film around the indentation print (Fig. 9) followed by delamination (Fig. 10) at higher than critical applied loads.

In Fig. 7 and 8 there are compared optical properties of the films deposited from pure HMDSO. We can see the refractive index is always higher than for a fused silica. Although in the visible the extinction coefficient of the films from pure HMDSO was very low it increased abruptly from 310 nm. This is a second difference between these films and a fused silica that is transparent in the whole range under investigation. The values reported for plasma polymerized HMDSO films (PP-HMDSO), i. e., for the films deposited from pure HMDSO or from a mixture of HMDSO with argon, differ all over the various discharges and deposition conditions like applied power or admixture of argon. Lower reported values of n for wavelength of 632.8 nm are that of Tien *et al.* [6] for HMDSO/Ar mixture ($n = 1.488$) and Poll *et al.* [18] for pure HMDSO in closed reactor ($n = 1.44$ at the beginning of deposition and $n = 1.49$ at the end of the deposition phase in which still some monomer remains in the chamber). In some other papers the refractive index in case of pure HMDSO feed was found higher than 1.5, namely $n = 1.51$ for a 40 kHz capacitive discharge [19] and $n = 1.59$ for a microwave distributed electron cyclotron resonance discharge [19]. Mota *et al.* [20] studied a change of optical parameters for pure HMDSO plasma polymerized films as a function of applied power. He found an increase of n from 1.46 to 1.55 with applied power but these values are given at higher wavelength of 1240 nm and therefore they may be slightly higher at 600 nm. For our conditions of plasma polymerization the refractive index at 632.8 nm was 1.498, 1.504 and 1.576 for ICP 300 W, CCP 100 W and CCP 450 W, respectively. All the values lay in the range reported for PP-HMDSO films.

The summing formulae of PP-HMDSO films are $SiO_{0.9}C_{1.8}H_{4.0}$, $SiO_{1.0}C_{1.5}H_{6.4}$ and $SiO_{1.7}C_{1.5}H_{4.8}$ for ICP 300 W, CCP 100 W and CCP 450 W, respectively. The density of these films is between 1.1 and 1.5 $g.cm^{-3}$ depending on the deposition conditions. The PP-HMDSO coatings prepared by ICP as well as by CCP show similar viscoelasto-plastic behaviour. The load-penetration curves for both types of the coatings are shown in Figs. 11 and 12. We can see a significant creep effect, i. e., time dependent plastic deformation at maximum load kept 5 s constant. The hardness and the elastic modulus of the films are about 0.6 GPa and 10 GPa, respectively. The coatings do not exhibit cracking, only piles-ups around the indentation print due to the low hardness compared with the substrates used.

4. Conclusion

The films deposited in oxygen-rich discharges exhibited properties similar to silicon oxides. However, we have observed the difference between the CCP and ICP discharges as concern the carbon and hydrogen impurities. The ICP film was very closed to the SiO_2 with low hydrogen content and slightly higher density. The increased density caused higher refractive index and hardness of the film as compared to the fused silica. The PP-HMDSO films contained high amount of carbon and hydrogen, they had higher refractive indices and were absorbing in UV. The films deposited in ICP-300 W and CCP-100 W had similar optical and mechanical properties but their atomic composition was not the same. Namely, the first film contained more carbon and the latter more hydrogen.

Acknowledgement

The present work was supported by the bilateral Barrande project and by the Ministry of Education of the Czech Republic, contracts MSM143100003, COST 527.20 and ME489.

References

[1] C.-P. Chang C. S. Pai - J. Appl. Phys. **68(2)** 793 (1990).

[2] S. K. Lahiri N. B. Chakrabarti S. K. Ray, C. K. Maiti - J. Vac. Sci. Technol. B **10(3)** 1139 (1992).

[3] K. Ebihara, T. Fujishima, D. Kojyo, M. Murata - Plasma Sources Sci. Technol. **2** 14 (1993).

[4] C. Valée, A. Goullet, A. Granier, A. van der Lee, J. Durand, Marlière - J. Non-Cryst. Solids **272** 163 (2000).

[5] A. M. Wrobel, M. R. Wertheimer, Plasma-polymerized organosilicones and organometallics, In R. d'Agostino, editor, *Plasma Deposition, Treatment and Etching of Polymers* pp. 163–268, Academic Press, New York 1990.

[6] P. K. Tien, G. Smolinsky, R. J. Martin - Applied Optics **11(3)** 637 (1972).

[7] G. Benz, G. Mutshler, G. Schneider - Germany Patent DE 3413019 (1985).

[8] L. Zajíčková, V. Buršíková, V. Peřina, Macková, D. Subedi, J. Janča, S. Smirnov - Surf. Coat. Technol. **142-144** 449 (2001).

[9] H. P. Schreiber, M. R. Wertheimer, A. M. Wrobel - Thin Solid Films **72** 487 (1980).

[10] G. Borvon, A. Goullet, A. Granier, G. Turban - Plasmas and Polymers **7(4)** 341 (2002).

[11] G. Borvon, A. Goullet, X. Mellhaoui, N. Charrouf, A. Granier - Mater. Sci. Semicond. Process. **5** 279 (2003).

[12] K. Aumaille, C. Vallée, A. Granier, A. Goullet, F. Gaboriau, G. Turban - Thin Solid Films **359** 188 (2000).

[13] A. Granier, D. Berhomieu, J. P. Deville, M. Ducarroir, J. Durand, A. Goullet, P. Leprince, C. Marlière, P. Raynaud, Y. Ségui, G. Turban, V. Vervloet - In *Proc. CIP'97, 11th Int. Colloq. on Plasma Processes* p. 318 (1997).

[14] J. D. Chapple-Sokol R. Carruthers K. Olsen W. J. Patric, G. C. Schwartz - J. Electrochem. Soc. **139(9)** 2604 (1992).

[15] D. E. Ibbotson D. L. Flamm N. Selamoglu, J. A. Mucha, - J. Vac. Sci. Technol. B **7(6)** 1345 (1989).

[16] W. A. Weyl, E. C. Marbone, *The Constitution of Glasses*, Wiley-Interscience, New York 1964.

[17] R. A. B. Devine - Trans. Mater. Res. Soc. Jpn. **8** 165 (1992).

[18] H.-U. Poll, J. Meichsner, M. Artz, M. Friedrich, R. Rochotzki, E. Kreyssig - Surf. Coat. Technol. **59** 365 (1993).

[19] C. Vallée, A. Goullet, A. Granier, C. Marlière, A. Van der Lee, J. Durand, P. Raynaud, J. P. Deville - In *Proc. CIP'97, 11th Int. Colloq. on Plasma Processes* p. 326 (1997).

[20] R. P. Mota, D. Galvao, S. F. Durrant, M. A. Bica de Moraes, S. de Oliviera Dantas, M. Cantao - Thin Solid Films **270** 109 (1995).

Plasma spraying of capillary-porous coatings:
Experiments, modeling and applications

V. Kalita[1], A. Gnedovets[1]

[1] *Baikov Institute of Metallurgy, Russian Academy of Sciences, Moscow, Russia*

Novel technology of plasma spraying of three-dimensional capillary – porous (TCP) coatings with principally new structure consisting of ridges and cavities has been developed. Ridges and cavities represent a macrostructure of TCP coatings. The ridges form the solid structure and the cavities – the porous structure of TCP coatings.

The process of fabrication of TCP coatings is performed under a sharp incidence angle of the particle-laden plasma flow to the substrate. This method of spraying is based on the hypothesis that behind the particles already deposited to the substrate, the "shaded zones" may appear, and new forthcoming particles can not reach these zones. Solidified deposited particles accessible for forthcoming particles form the ridges of TCP coating. The cavities of the TCP coating "consist" of the shaded zones.

The width of cavities may be regulated by an angle of impact of spraying particles with a substrate and particles size. The ratio of the width of cavities to the sum of widths of a cavity and a ridge determines the value of a porosity, which may reach ~60%. The width of the cavities of TCP coatings may be regulated over a wide range from 5 up to 2000 µm, and the width of ridges – from 200 to 2700 µm. The walls of ridges may have micro-rough structure. The smaller sized pores (capillary tubes) are arranged in the walls and within internal volume of the ridges. The small porosity (2-10 %) of the internal volume of the ridges allows reaching the values of adhesion and cohesion close to the values of initial (dense) sprayed materials.

Methods of direct numerical simulation have been developed for modeling of the process of TCP coating growth in 2D and 3D geometries. Fig.1 compares the results of plasma spraying experiment and 3D numerical simulation of titanium coating deposition at the surface of cylindrical sample.

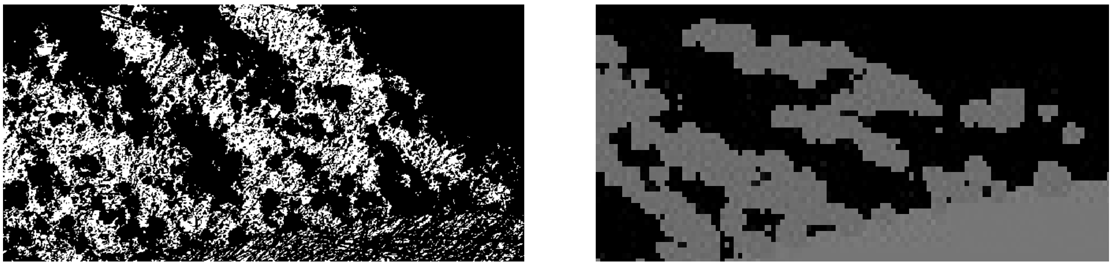

Fig. 1. Cross-section (fragment 1600 × 800 µm) of plasma sprayed Ti TCP coating deposited at the surface of cylyndrical substrate (experiment – left; 3D numerical modeling – right). Particle-laden plasma flow is directed horizontally from left to right.

The technology of plasma deposition of porous coatings is of great significance for biomedical applications. For example, a connection of a bone skeleton with the help of artificial implants remains an important problem of medicine and material science. Osteal tissue should easily grow into the surface layer of an implant ensuring strong connection. High values of porosity and surface area are favorable for fastening of the connection of an osteal tissue with an implant. After growing bone tissue fills the cavities, and new composite material "TCP coating - bone tissue" is expected to have very high strength properties This value of shear strength may be 5 times higher than the values of shear strength for conventional titanium porous coatings for implants.

Development of Meter-Scale Large-Area Inductively Coupled Plasma Source with Multiple Low-Inductance Internal Antenna Units

A. Ebe[1] , Y. Setsuhara[2] , N. Yamamoto[3] , S. Baba[1] , H. Inami[1] , T. Shoji[4] , S. Miyake[1, 3]

[1] *New Techno-Venture Oriented Research and Development, Japan Science and Technology Corporation,*
2-1 Yamada-oka, Suita, Osaka 565-0871, Japan
[2] *Department of Aeronautics and Astronautics, Kyoto University, Yoshida-honmachi, Sakyo-ku, Kyoto 606-8501, Japan*
[3] *Joining and Welding Research Institute, Osaka University, 11-1 Mihogaoka, Ibaraki, Osaka 567-0047, Japan*
[4] *Department of Energy Engineering and Science, Nagoya University, Furo-cho, Chikusa-ku, Nagoya 464-8603, Japan*
e-mail:ebe@crcast.osaka-u.ac.jp

Abstract

Large-area inductively coupled plasma (ICP) source has been developed for plasma enhanced chemical vapor deposition. An internal-antenna configuration with multiple low-inductance antenna (LIA) units is demonstrated for production of meter-scale large-area ICPs. This novel type of the source configuration can provide low-voltage operation of ICPs, where the electrostatic coupling can be effectively suppressed and results in low plasma potentials while maintaining high-density plasma production by inductive coupling.

1. Introduction

Development of large-volume plasma sources with high density and uniform plasma parameters is one of the demands for the microelectronics device fabrications toward the size enlargement of substrates in flat panel displays, for instance, in these years. However, in conventional inductively coupled plasmas (ICP) sources with supply of discharge power from an antenna located on an insulator in the open air, the scale-up of the plasma source causes various problems such as degradation of the source efficiency and increase of an antenna inductance.

The plasma source composed of an internal antenna is effective to solve these problems. Even in the internal antenna configurations, however, it is essential to minimize the electrostatic coupling of an RF energy to the plasma.

In our previous work [1], suppression of the electrostatic coupling was obtained by attaining low-voltage operations of the internal antenna, based on the reduction of the antenna inductance and the dielectric isolation of the antenna conductor. This plasma source could be operated stably to attain high densities. In argon, hydrogen and nitrogen gases the plasma density reached to an order of $10^{11}\sim10^{12}$ cm^{-3} in this ICP source having a vacuum chamber of 300 mm inner diameter and 435 mm height excited by a unit with four internal antennas [2,3].

In the present work, we demonstrated a new antenna configuration consisting of multiple internal antenna units with low-inductance to produce rectangular large-scale and high-density plasma. Plasma properties in a meter-scale chamber with argon and hydrogen gases are reported to exhibit capability of various applications of large area high-density plasmas.

2. Experimental

The ICP source studied in the present study is employed with low-inductance antenna (LIA) units, schematically illustrated in Fig. 1. The LIA unit consists of a U-shaped antenna conductor with a scale length of 150-400 mm, which is fully covered with dielectric tubing for complete isolation from the plasma. This structure enables the low voltage operation of the RF antenna while maintaining primarily inductive coupling, and the electrostatic coupling to the plasma is decreased.

Figure 2 shows a schematic illustration of the meter-scale plasma source for depositing films on a substrate with a size of 680×880mm. The ICP source consists of four sections mounted on each of the sidewall flange of the

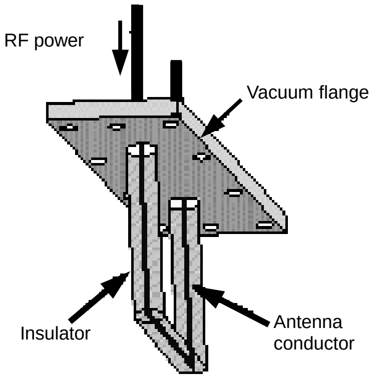

Fig. 1. Schematic illustration of an LIA unit.

discharge chamber. Each section consists of three or four LIA units, which are connected in parallel to a 5-kW RF power generator at 13.56 MHz via a matching network. Each antenna is terminated directly to the grounded electrode.

The discharge chamber has an internal area of 1030×1230 mm and a height of 445mm. In the present work, the X, Y and Z-axes are taken to be along the axes of the discharge system as described in Fig. 2. In the X-Y plane, the position X = 0 and Y = 0 corresponds to the center of the discharge chamber. While in Z direction, the position Z = 0 lies in the same plane as the top flange inner surface of the discharge chamber and the positive Z direction are taken from top to bottom direction.

The base pressure of the discharge system, evacuated with a turbo molecular pump, was 3.7×10^{-4} Pa and the plasmas were produced in argon and/or hydrogen gas at a pressure of 1.33 Pa. Plasma parameters are measured using two cylindrical Langmuir probes.

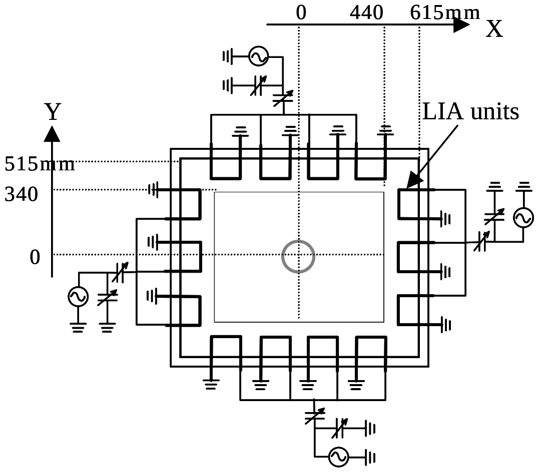

Fig. 2. Schematic illustration of the plasma source equipped with multiple LIA units.

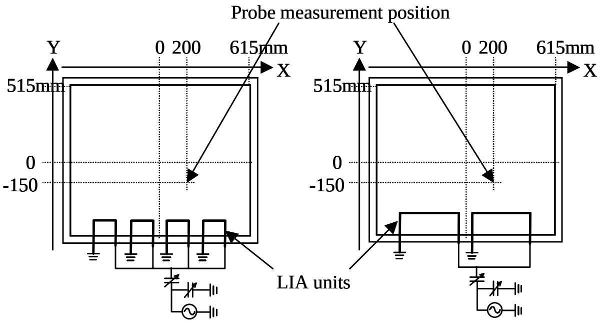

(a) 105×150mm 4antennas (b) 150×400mm 2antennas

Fig. 3. Schematic illustration of LIA units arrangement and probe measurement position

3.Results and Discussion

3.1 Influence of antenna size variation on plasma parameters

The plasma parameters were measured when four antennas or two antenna 150mm×400mm of 105×150mm was connected with one RF power supply as shown in Fig. 3. The position where the probe is measured is X=200mm, Y=-150mm, and z=190 mm, which is the same as the antenna plane.

Figure 4 shows the power dependence of the plasma parameters in argon. The electron density by four antennas of 105×150mm is higher than that by two antennas of 150×400mm(Fig.4(a)). On the other hand, the electron temperature(Fig.4(b)), the floating potential(Fig.4(c)), and the plasma potential(Fig.4(d)) by four antennas of 105×150mm are decreased. These results show that an increase in the voltage of the antenna due to an increase of the antenna inductance modify the plasma

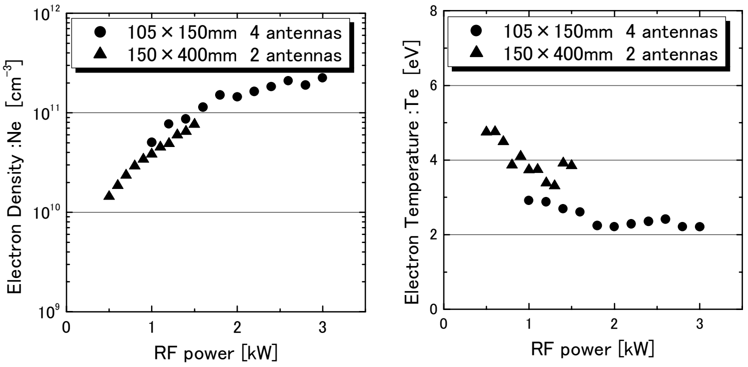

(a) Electron Density :Ne (b) Electron Temperature:Te

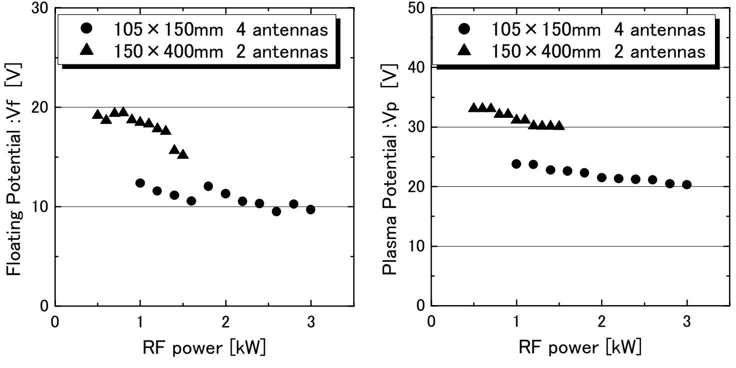

(c) Floating Potential :Vf (d) Plasma Potential :Vp

Fig. 4. Variation of plasma parameters by difference of antenna size

parameter remarkably, and the method to connect many LIA units enable us to achieve high density and low plasma potential simultaneously, which is especially important in a large area plasma source.

3.2. Plasma characteristic in a meter-scale plasma source with multiple LIA Units

Figure. 5(a) shows the RF power dependence of plasma parameters in the case of using four RF power supplies in Ar (100sccm) gas at a pressure of 1.33 Pa. It is found that the electron density, Ne increases almost lenearly with increasing the RF power and reaches to a value of 1.8x10^{11} cm^{-3} at an RF power of 8 kW (2 kW x 4). On the other hand, plasma potential, Vp and electron temperature, Te does not significantly depend on the RF power and Vp is about 15V with Te of about 2eV. The change in the plasma parameters is similar even in the case of the hydrogen plasma as shown in Fig.5(b), and these results indicate that the plasma density can be controlled in proportion to the RF power keeping low plasma potential and electron temperature. This feature of the low potential formation is considered to be very significant for CVD preparation of high-quality films with less plasma damage, such as in the case with polycrystalline silicon film formation. Additionally it is considered that higher deposition rate can also be feasible without suffering significant degradation of the film quality due to high energy ion damage.

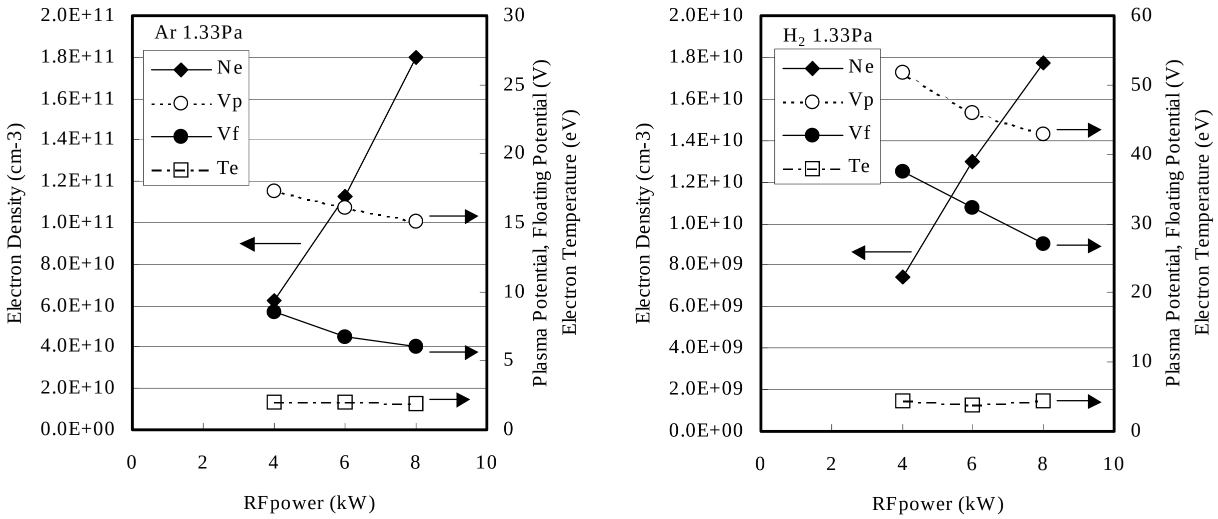

(a) Argon gas plasma (1.3Pa) (b)Hydrogen gas plasma (1.3Pa)

Fig.5. Plasma characteristic as function of RF power in meter-scale plasma source with multiple LIA Units (Measured position : X = 0 mm, Y = 0 mm, Z = 180 mm)

The uniformity of the plasma parameters in a hydrogen plasma is shown in Fig. 6. We can clearly see the electron density in the plasma is almost uniform over the whole area of the chamber. On the other hand, the plasma potential increases slightly in the vicinity of the antenna, for which it is suggested that the plasma potential will be influenced by the voltage of the RF antenna. To obtain uniform distributions for all plasma parameters, further studies are necessary. We demonstrate, however, the plasma production by newly designed low-inductance internal antennas are very promising in obtaining a large-area uniform plasma advance for varieties of plasma processing. These result indicate that the new plasma source which we had proposed can generate the high density and uniformity plasma within the range of one meter or more.

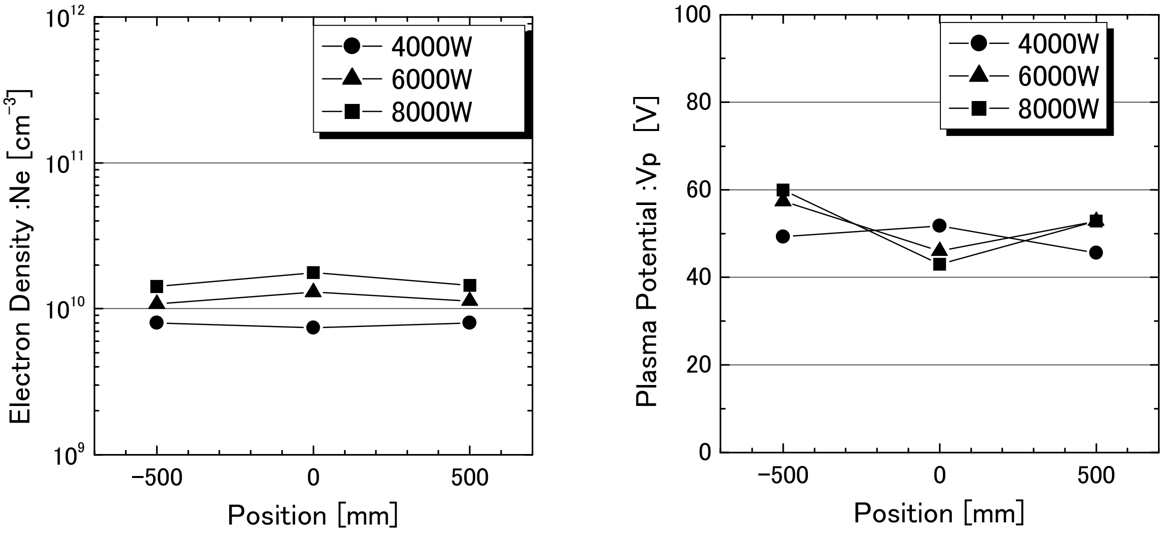

(a) Electron density:Ne

(b) Plasma potential:Vp

Fig. 6. The uniformity of the plasma characteristic in the hydrogen plasma (1.3Pa)

4. Summary

We investigated the production of meter-scale large-area high density plasma by using multiple low-inductance internal antenna units. It is effective to an increase in the density of plasma and the decrease of plasma potential and electron temperature to reduce low inductance of an internal antenna. A new plasma source consisting of multiple internal antenna units with low-inductance can generate the high density and meter-scale large area plasma.

5. References

[1] Y. Setsuhara, S. Miyake, Y. Sakawa and T. Shoji: Jpn. J. Appl. Phy. , **38** (1999) 4263

[2] Y. Setsuhara, T. Shoji, Y. Sakawa and S. Miyake: Proceedings of 25th ICPIG, **1** (2001) 19

[3] Y. Setsuhara, T. Shoji, Y. Sakawa and S. Miyake: Proceedings of PSS-2001/SPP-18, (2001) 317

Kinetic simulation of plasma-surface interaction and its 3D-visualization

G.I. Zmievskaya[1] and V.V. Savchenko[2]

[1] *Keldysh Institute of Applied Mathematics, Moscow, Russia*
[2] *Hoscey University, Tokyo, Japan*

Abstract

Plasma-surface interaction problem can be inspected as the dusty plasma computer simulation problem, which treats of the origin and the charging of liquid metal droplets into near electrode space. Its influence on plasma flux is investigated. For modelling of thin (close to 1000 Debye lengths from electrode) dusty plasma layer had been used kinetic simulation code. The screening electrode processes depend on the distribution function of droplets versus its sizes (charges) and kinetic distribution function of plasma particles, accounting the self-consistent electrostatic fields in conformity with non-equilibrium plasma behaviour. Volumetric visualization of results allows to recognize the "cavity" or the "contraction" structures of plasma, it can reveal the instabilities in plasma fluxes. The same tomography-like aproach to data processing is able to be used in future kinetic simulation of dusty plasma structures formation.

1 Introduction

The principal problem in kinetic plasma computer simulation, which have been study (last three decade) using the both kinetic theory of non-linear plasma description and its computer simulation methods are shown in monography [1]. New approaches to visualization of results are concerned with plasma strong Langmuir turbulence, plasma-beam or plasma-laser pulse interaction, dusty plasma kinetics and other problems. These results were revealed from precisions calculation of non-equilibrium DF, of spectral plasma characteristics, of plasma phase space projection in dynamics of presentation, using new method of wavelet-analysis and etc.

Object-oriented plasma (OOP) kinetic code **SUR** [1, 2] put forward ten years ago. One of the first in the world [2] highly optimized version OOP plasma kinetic computer simulation model have been modified to the dusty plasma code **SUR-Dust** by Yu.S. Sigov, V.D. Levchenko and L.V. In'kov, [1, 5, 6]. For plasma-like media (gaseous pores into lattice, clusters or liquid charged droplets near surfaces) kinetic simulation or stochastic simulation model (SSM) were put forward earlier [3, 4] and it was applied to problem of plasma-surface interaction [12, 8]. The pictoral show of effects (in plasma chemistry) to improve understanding of molecule sputtering from surface mechanisms [7] of high energy bombardment of thin organic film. Tomographic-like visualization of the results, presented here, is important for non-destructive quality control of materials embedded by plasma beam or such as control of dusty clouds of technological devices. The kinetic simulation of the blistering-phenomena [8, 10] as well the liquid metal cluster formation [3, 12, 11]examination can be investigated by such way. But here we put attention on simulations of low-temperature dusty plasma near electrodes.

Using of a kinetic plasma code is a challenge; this kind of modeling consists of several preliminary stages, including combined computation techniques with different approximation levels. Study of dusty plasma is aimed to elucidation of main mechanisms controlling plasma interaction with charged dust and providing the quantitative estimates for the dust impact on electrode erosion and there is as a consequence dust grains origin.

2 Kinetic approach to problem

Charged particles phase coordinates : three components of velocities, V_x, V_y, V_z, and three components of coordinates $\vec{r}$ or (x, y, z), are characterised by $f_\alpha = f_{i,e}(\vec{V}, \vec{r}, t)$; the dust grains sizes g (and its charges) is described by kinetic equation for distribution functions /DF/ versus sizes and coordinates

$f_d(g,\vec{r},t)$. The Vlasov-Poisson equations have been formulated for dusty plasma

$$\frac{\partial f_\alpha}{\partial t} + \vec{V}_\alpha \frac{\partial f_\alpha}{\partial \vec{r}} + eZ_\alpha \frac{\partial \varphi}{\partial \vec{r}} \frac{\partial f_\alpha}{\partial \vec{V}} = 0,$$

$$\Delta\varphi = -4\pi\Big(\sum_\alpha \rho_\alpha + \rho_d\Big), \qquad \rho_\alpha = eZ_\alpha \int f_\alpha \, d\vec{V},$$

where index α referes to species of plasma particles, while index d referes to dust grains.

To solve plasma equations system we use particle-in-cell (PIC) method. Just a couple of words to remind, what is PIC. In this method, a number of plasma particles of one species is aggregated in a coarse modeling particle with the same ratio of $\frac{e}{m}$. Due to this fact, the set of equations for the modeling particle will be exactly the same as for an individual plasma particle:

$$\frac{d\vec{r}^{\,i}_\alpha}{dt} = \vec{V}^i_\alpha, \qquad \frac{d\vec{V}^i_\alpha}{dt} = \frac{eZ_\alpha}{m_\alpha}\vec{E}, \qquad \vec{E} = \nabla\varphi.$$

The potential φ can be found from Poisson equation on the mesh:

$$\Delta\varphi^j = -4\pi\Big(\sum_\alpha \rho^j_\alpha + \rho^j_d\Big), \qquad \rho^j_\alpha = eZ_\alpha \sum_i S_\alpha(X^i_\alpha, X^j_\alpha).$$

From the last equation it can be seen, that the modeling particle isn't pointwise. The particle is represented by the charged cloud with formfactor $S_\alpha(X^i_\alpha, X^j)$, where X^i_α is the location of this particle of species α with the number i, and X^j is the mesh nod number j. This is an ordinary technique of noise reduction for PIC method.

In our model both electrons and ions are represented by rectangular shaped clouds. The modeling 3-D region is periodic across two coordinates (x and y). Across the third coordinate (axis z): on top the region contacts with reservoir of undisturbed plasma, while on bottom we have partial absorption/rejection from the metal wall. The equation of motion for grains:

$$\frac{d\vec{r}^{\,i}_d}{dt} = \vec{V}^i_d, \qquad \frac{\Delta(m^i_d \vec{V}^i_d)}{\Delta t} = \sum_{\alpha,k} m_\alpha \vec{V}^k_\alpha + q^i_d \vec{E}.$$

The dust grain size fluctuations is due to processes of attachment as well evaporation of metal vapor particles. SSM of non-equilibrium plasma-chemical and phase conversion processes modelling [4] is based on the Leontovich (or Kolmogorov) equation solution. In fluctuation limit this equation has form of Fokker-Planck-Kolmogorov equation /FPK/. The Fol'mer–Zel'dovich problem of first order phase conversion at fluctuation stage is formulated for liquid metal charged droplets formation from vapore of the surface sputtering material.

The first results of plasma and fluctuation of dust size common calculations were presented in [13].

Condensation as well as many of the physical phenomena, which exhibit the probability nature, can be described by

$$\frac{\partial f}{\partial t} = \mathcal{L}(f), \tag{1}$$

where $\mathcal{L}$ is the nonlinear integro-differential operator. In the kinetic theory, the subject of study is kinetic DF f, which is function of the phase coordinates and time t. In case of phase transition of first order (namely metal vapor condensation) we are using $f(\vec{r}, g, t)$, where g is determined abow.

We use the Îto stochastic differential equation (SDE) as equations for the analogs of physical phenomena which are of collisional or fluctuation nature. We write down the Îto SDE for the variable cluster size g and here we are investigating expanding vapores. The spatial coordinate r will be determined from stochastic equation of uniform vapore expandind; both quantities depend on time t.

For construction of the volumetric images of internal cavities, which appear into plasma volume as result of charged dusty particles screening effect we are using the computer simulated information of rang up of some benchmark points (i.e. microscopic DF of plasma). It will allowed to generate a set of approximate planes on a which a picture is saved.

Computer plasma physics simulation[1, 5, 6] put forward to study of dusty plasma model with parameters of low dust grain concentration near electrode. Other problem concerning to dusty plasma modelling is the fluctuation stage of metal droplets formation. This process is able to be modeled by SSM [4, 3]. The results of screening electrode effect of metal cluster formation on the plasma temperature, density and heat flow near plate of divertor was estimated earlier [11, 12]

Here by means of hybrid kinetic model (code **SUR-dust** with supplement SSM methodics), diferent to foregoing, the DF of ions and electrons were investigated in plasma space near surface with the scale close to 1000 Debye length. DF metal droplets versus sizes and charges using plasma parameters is calculated as well. We start from a model of an "open" physical system with main initial parameters of the physical transition (temperature, pressure, and super-saturation of vapor) taken constant for the stage of calculation of nucleus size. For our problem statement, they are consistent with parameters of plasma flow establishing near surface of electrode or collector plate[9]. Note here that the result, revised by code **SUR-Dust** without assumption about Maxwellian character of DF versus velocities as well coordinates. The contact of charged grain with plasma disturbs initial equilibrium state. Accounting of charging processes on the surface of dusty particles is required the hight accuracy of calculation of electrostatic fields in plasma [6] and screening effect of charged particles, and influence of this phenomena on plasma behavior. The comparison calculated data of DF visualization have some principal problems related with absence for experimental probes such level of detalization etc. So, computer experiment is real possibility of prediction of dusty plasma behaviour near electrode.

3 Dusty plasma modeling.

The dusty plasma behavior near surface put forward the set of questions concerning plasma flow interaction with dust charged particles, the contribution to sheet potential formation and energy transport in plasma with metal particles appearance. It is known that kinetic approach is very important in describing of plasma including charged clusters of sizes close to Debye length.

The parameters of kinetic PIC code: 3D3V object–oriented code **SUR-Dust** for electron–ion plasma in this case of dusty plasma model , is represented by PIC method, each dust droplet is modeled by particle with spherical shaped cloud with Gaussian smooth function(tabulated), that allows precise self–consistent field calculation nearby the droplet. Some set of models work out for charge and momentum transmission to droplet surface. There is kinetic code **SUR-Dust** for small number of dust grains(10-100) in plasma volume, code includes some grid and up to 8 million plasma particles. This permits us to carry out full scale computation of kinetic plasma effects related with metal cluster presence near surfaces. The results which received by PDK code let us investigate role of accounting such phenomena as:
—long range repulsion of dust particle,
—attraction due to bombardments by plasma particles,
—attraction due to the Coulomb scattering of plasma flows.
We can evaluate the both role and contribution to surface screening effect.

Stochastic simulation of dust particles arising. We start modeling the phase conversion (such as condensation) by numerical approach, using the model of stochastic Markovs process in a phase space $\{\mathbf{G}\}$ with size g of condensing metallic droplets: $\{g(t), t > 0\}$. Here the size g means the number of unit volumes of condensing substance in the nucleus (however, it is possible also to consider the radii R of spherical droplets). The maximum of R is determined by stability of a liquid metal droplet. Note that conditions for droplet merging or splitting can be formulated in the terminology of jump-like random processes [9] in a way similar to approach of chemical reaction modeling (reaction controlled by inelastic collisions)[14, 15, 4]. But this problem is beyond of consideration here.

For plasma which contain super-saturated expanding vapores of metal we are used the model of phase conversion such as coagulation process at the fluctuation stage [3, 12]. Fluctuation instability in coagulating vapors is described by the Îto stochastic differential equations in Stratonovich form. We are able to investigate out–of–equilibrium DF of metal clusters versus its sizes at instant time moments. As a result of kinetic stochastic model phase conversion gives us a distribution of liquid metal droplets on their sizes that corresponds to calculated parameters of expanding metal vapor, calculated by stochastic equation $\frac{d\vec{v}_i}{dt} = -\frac{1}{t}\vec{v}_i$ with known velocity $v\ T_e^{0-1/2}$ of expanding.

FPK equation for metal droplet formation process. Kolmogorov equation (FPK) for diffusion in phase space of cluster sizes(Fol'mer-Zel'dovich problem) is formulated

$$\frac{\partial f_r(g,t)}{\partial t} = \frac{\partial}{\partial g}[D(g,t)\frac{\partial f_r(g,t)}{\partial g}] + \frac{1}{kT}\frac{\partial}{\partial g}[D(g,t)f_r(g,t)\frac{\partial}{\partial g}\{\Delta\Phi(g,t)\}], \tag{1}$$

where $f_r(g,t)dg$ is number of clusters g into sizes interval $[g, g+\Delta g]$ in unit of volume V, $f_r(g,t)$ is normalized that: in V here is even if one cluster, consisting non less, then two particles. The coefficient $D(g,t)$ is determined in space of cluster sizes and can be represented by formula
$D(g,t) = g^{2/3}\alpha(T)\nu_l^{2/3}n_\nu V_\nu$. $\alpha(T)$ is known as accomodation coefficient, n and V are plasma parameters, connected with metal vapor pressure and temperature. $\Delta\Phi(g,t,p,T)$ is thermodynamic potential or free Gibbs energy of liquid cluster formation. $\Delta\Phi(g,t,p,T) = N\varphi_G + N^-(\varphi_L + 4\pi\sigma R^2 + W + Q^2/2R)$ is consist of the work of neutral drop creation, energy of interphase interaction and workfunktion. This model is applied to metal cluster formation(without accounting of entropie consideration). There φ_L, φ_G -thermodynamic potentials of liquid and gas per unit particle, its differense is proportional to $\sim gkTlnP/P_\infty$. Inter phase interaction $\sim 4\pi\sigma R^2$, where σ- surface tension, R -is radius of cluster, this value is proportional to ν_l-unit volun per molecule of liquid phase. W is workfunction, $Q^2/2R$ can be accounting as $Z_d q\nu_l^{-1/3}g^{-1/3}$where Z_d is the charge of dust grain.. Let us formulate SDE Îto-Stratonovich for Markov process $g(t), t > 0, g > 2$, related with FPK for $f(g,t)$

$$\left\{ \begin{array}{l} \frac{\partial g}{\partial t} = -\frac{1}{kT}\frac{\partial\Delta\Phi(g,t)}{\partial g} - \frac{1}{2}\frac{\partial D(g,t)}{\partial g} + \sqrt{D(g,t)}\tilde{\xi}(t), \\ t_0 \le t \le T_k,\ g(t_0) = g_0,\ t \in [t_0, T_k],\ g(t) > 2 \end{array} \right. \tag{1}$$

Initial stage of metal droplet formation is caracterized by time period, wich is equal to dimensionless $100 \sim 1000\tau$, comparable with plasma description time. Note, that every simulation run is made for a constant negative charge of all droplets ($Zd \sim 10^3 \div 10^5$ of charge units), but charge of dusty grains have to be presized from kinetic simulation of dusty plasma model.

Thus, we consider here the sizes DF evolution of metal tungsten at fluctuation stage at a constant temperature of 0.2 eV. The process of formation of charged nuclei for spherical metallic droplets is studied. According to the chosen model for Gibbs energy of nucleation with a high and constant negative charge of droplets, we observe a decline in the average nucleus size with the growth of total amount of nuclei (Fig.1)

Volumetric visualization. The problem of three dimensional-images processing arise in a lot of technical applications such as analysis of internal cavities for industrial and medical purposes, robotics movement control etc. Method of three dimensional-image construction and the corresponding information processing algorithms depend on specific data of computer experiment in field of plasma physics. Solution of kinetic equations put attention on non-equilibrium plasma behavior under influence dusty component into volume. Since the purpose of this simulation is to study the electrostatic (in case of dusty plasma) response of plasma, there is phenomena of nanosec time period registration. The volumetric model can be formed in a kind of set of surface (or planes) in phase space. A full set of these surfaces has to correspond to a volumetric picture. As a rule having been constructed the volumetric surface model is recorded in computer memory as coordinates of space points with factor having significance 1 if point is on cavity surfaces and significance 0 otherwise. Because exact coordinates are known from computer experiment for visualization we need in definition of the distance to the point of investigated surface from "virtual TV-camera"(point of view of visualization). The examination of a complex surface (i.e. disturbed plasma structure) one needs to transfer a "ranging scanning system" processing with the recalculation of built volumetric fragments to the unit coordinate system. The space model is formed as a set of planes crossing bench mark points. This fact permits to add new bench mark points and specify volumetric model. Development of algorithm of approximation permits to obtain the threedimensional models by given object. Similar approximation will presumably allow to find algorithm of revealing of abnormal areas of surface. Program simulates the view process by model including model of “TV- camera round-up” from some distance and under different angles. Input is a certain collection (xi,yi,zi) for some points on the surface z=g(x,y). The frame of the part of the surface built and is shown on the screen. Then the surface z= g(x,y) is shown on the screen. One can obtain it under the different angles.

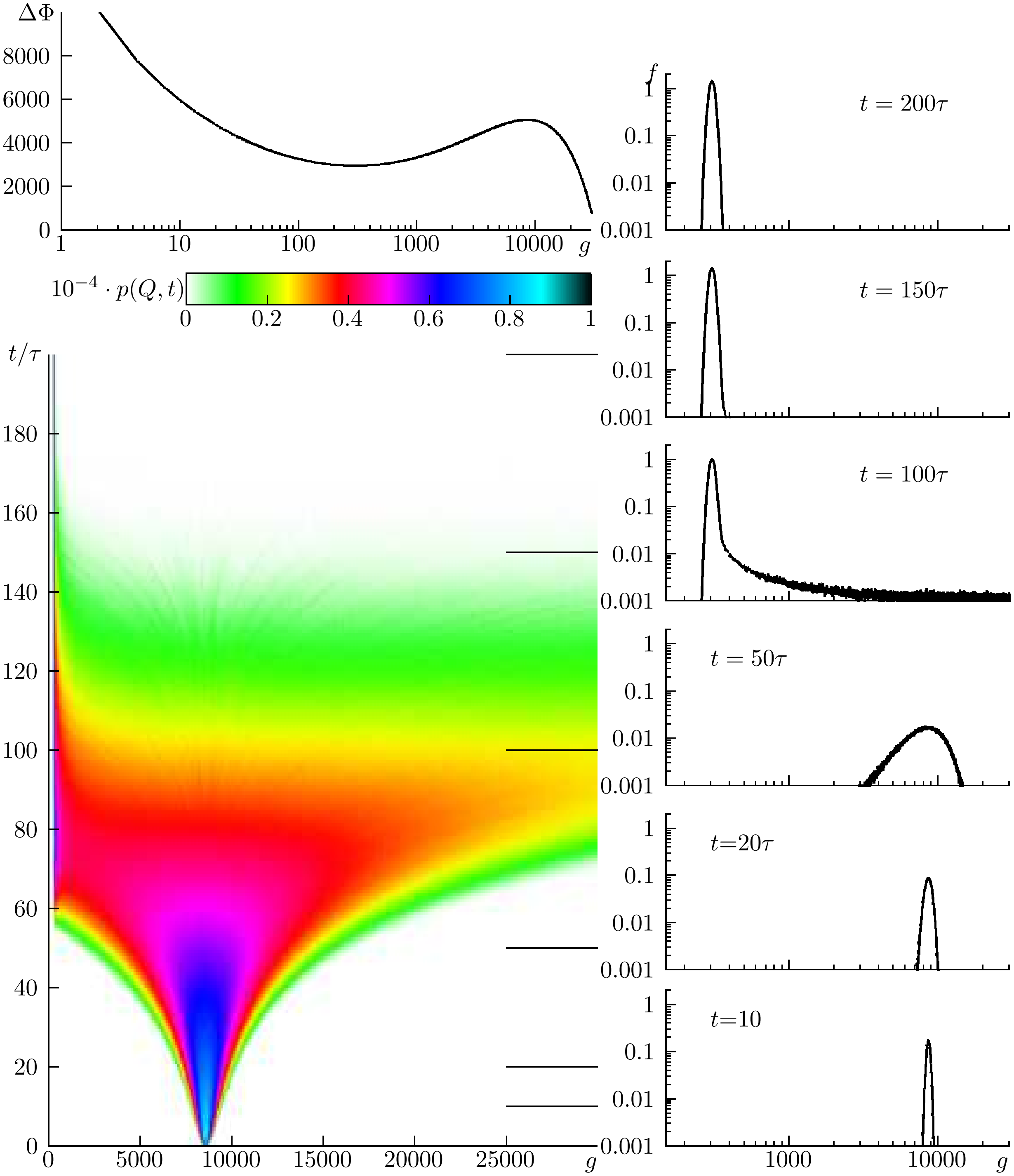

4 Conclusion

We are presenting here the results of kinetic simulation of cluster formation influence on the plasma flow parameters for the conditions characteristic for low-temperature near electrode plasma: upstream plasma density $10^{14} - 5 \cdot 10^{14}$ cm^{-3} , upstream temperature 0.2-5 eV. Initial cluster density was $3 \cdot 10^5$cm^{-3}. The results of numerical simulation are presented on Fig.1. On Fig.1 (similar to [12]) we can see the map of two dimensional DF surface $f(g, t)$, there are:left– phase space “cluster sizes – time” evolution of metal cluster formation under initial condition $g|_{t=0} = 100$ (the needed constants concerning tungstain data is done from [17]) and on right side of Fig.1 there are cross-sections of DF map for time instants 10, 50, 100, 175, 250τ, $\tau = t(\frac{3v_l}{4\pi})^{2/3} n\sqrt{\frac{kT}{2\pi m}}$, where ν_l volume relates to Wigner-Zeits radii, n is concentration of vapour and T is equal to 0.2 eV, vapour saturation $S = \frac{n}{n_\infty} = 1$, where n_∞ corresponds to metal vapour pressure of saturation.

Acknolegment. We are grateful to Dr. V.D. Levchenko for collaboration and valuable help. This work is partially supported by Grants N 02-01-01004 of Russian Foundation of Basic Researches and by Russian Academy of Sciences Programme “Nanoparticles and nanotechnology” .

Bibliography

[1] Yu.S. Sigov, Computer Simulation: The link between past and future of plasma physics. Selected works,//composed by V.D. Levchenko and G.I. Zmievskaya.–Fizmatlit (Physics and Mathematics publisher, IAPC “Nauka”),Moscow.– 2001, 288 p. (in rus.)

[2] V.D. Levchenko and Yu.S. Sigov, in book “Dynamics of transport in plasmas and charged beams”,// G. Maino and M. Ottaviani, Eds., Singapore-London, Publishing Co. Pte. Ltd. World Scientific.–1996, p.55.

[3] G.I. Zmievskaya, ibide, p.84.

[4] G.I. Zmievskaya,//Plasma Phys.Rep., Vol.23, No.4,–1997, p.368.

[5] L.V. In’kov, V.D. Levchenko and Yu.S. Sigov,// Prikladnaya physica (Applied physics).Vol.3,–2000, p.138 (in rus.).

[6] L.V. In’kov,//Matematicheskoe modelirovanie (Math. modeling).–2003 (in print).

[7] B.J. Garrison, A. Delcorte, K.D. Krantzman,// Acts. Chem. Res., 33,–2000, p.69.

[8] A.L. Bondareva and G.I. Zmievskaya,// Applied Physics, No.3,–2000, p.122(in rus.).

[9] G.I. Zmievskaya, V.D. Levchenko, T.V. Levchenko and T.K. Soboleva,// presented to 16th ISPC, Taormine, Italy,–2003.

[10] A.L. Bondareva and G.I. Zmievskaya,// presented to 16th ISPC, Taormine,Italy,–2003.

[11] G.I.Zmievskaya, T.V.Levchenko and T.K.Soboleva, //Proc. of 15th Symp. on Plasma Chemistry, Vol.VII, Ed. by A. Bouchoule et al., Orleans (France).– 2001, p.2793.

[12] G.I. Zmievskaya, T.V. Levchenko and T.K. Soboleva, //Thermophysics and Aeromechanics,v.9, No.4,–2002, p.633.

[13] A.L. Bondareva, L.V. In’kov, V.D. Levchenko, T.V.Levchenko and G.I.Zmievskaya, //Proc. of XXV*Int.Conf. on Phenomena in Ionized Gases*, Nagoya, Japan, Toshio Goto, Ed., Nagoya Univ.–2001, p.119.

[14] G.I. Zmievskaya, — Proc. of XVII*Int.Conf. on Phenomena in Ionized Gases*, Bakos, J.S and Sorlei,Z.,Eds., Budapest, 1985, p. 296.

[15] G.I. Zmievskaya,—Proc. of XIX*Int.Conf. on Phenomena in Ionized Gases*, Labat, J.M., Ed., Belgrade:Univ.of Belgrade, 1989, p.540.

[16] V.N. Tsytovich,//Plasma Phys.Rep., Vol.28, No.8,–2002, p.675.

[17] B.M. Smirnov,*Cluster plasma*, Physics of Our Dayes (UPhN), Vol.170, No.5.–2000, p.495.

Surface screening by thin layer of charged metal clusters

G.I. Zmievskaya[1], T.V. Levchenko[2], V.D. Levchenko[1], T.K. Soboleva[3]
[1]*Keldysh Institute of Applied Mathematics, Moscow, Russia*
[2]*VNII Geosistem, Moscow, Russia*
[3]*ICN, UNAM, Mexico City, Mexico, INF RSC Kurchatov Institute, Moscow, Russia*

Abstract

Complex plasma is investigated via kinetic multi-dimensional computer simulation code SUR-Dust. Screening electrode effect is depend not only to the dust grains (or liquid metal clusters) size and its volume concentration, but especially it depends on dust grain charging. Plasma particles, moved near dust grain, deviate from its trajectories by screenig field, which appear into the Debye length of dust grain surface. The plasma-dust interaction modeling allows to examine the non-equilibrium behavior of plasma.

1 Introduction

The physical conditions of near-wall plasma are revealed also in a setup for surface plasma treatment (where the condensed phase above the electrodes is a common phenomenon). The applications of dusty plasma for technical purposes were considered in review [1].

Numerical experiment for dust plasma is a very complex problem: the processes have very different time scales and are nonlinear. Phase and plasma-chemical conversions, collision processes, self-consistent fields are to be modeled with consideration of their nonequilibrium. For example, kinetic numerical experiments [2] for non-linear plasma and plasma-similar media were performed without assumption about the Maxwellian distribution for ions and electrons velocity. Particles interacting with charged dust was done mainly due to high requirements to accuracy of calculation of electrostatic fields in plasma (this accuracy in calculations depends on the process of dust particle charging, etc.) [3].

Those charged dusty grains near the electrode create instability in the plasma flow (in turn, this is responsible for nonlinear mechanisms of self-organization in dust plasma). Solution of that kind of problem is impossible without development of a comprehensive multi-dimensional (3D3V) kinetic computer simulation code that considers the plasma dynamics in the framework of Vlasov–Poisson equations. Using the theory and experience of numerical experiments in plasma physics developed by Yu.S. Sigovs school [6], and applying the new approaches and techniques of programming, the numerical model and object-oriented kinetic code SUR-Dust for dusty plasma (written in C++). had been developed [3]. The code was used for analysis of non-equilibrium phenomena in a low-density dusty plasma. The effect influence of the processes of charging the particles on the parameters of the discharge plasma, made simulation analysis of nonequilibrium velocity distributions for ions and electrons as a function of parameters of dusty layer and plasma flow and it was used to calculate heat and particle flows towards the electrode for preset upstream values of the heat flux and plasma density characteristic.

Recently in the paper [4, 5] we presented the results on dust screening effect obtained with help of 1D MHD steady-state code. The code was used to calculate heat and particle flows towards the divertor plate. Plasma temperature in the vicinity of target surfaces still may be enough to melt or evaporate metallic surfaces. Characteristic size of the condensed from metal vapor liquid droplets was obtained using stochastic code based on kinetic stochastic model [7] of non-linear stage of first kind of phase conversion, based on stochastic Markov process [10]. This model was used to account for dust screening effect, calculated by MHD code [4, 5], as well as by kinetic code [8].

Now we are able to use the effective computer simulation method [3, 9] for deep investigation of screening electrode phenomena nature. The analysis of computer simulated (experimental) cross-sections of dusty plasma is realized. Kinetic calculations of particle and heat flow, decrease (for the initial electron temperature $T_e = 0.2 \div 1eV$ and plasma density $n_e = 10^{14}cm^{-3}$) have shown high efficiency of the electrode screening by dust particles of small size $(0.1 \div 1mkm)$ of low volume concentration with distance between particles about of $5 \div 100mkm$. New results developed on the base of the kinetic code SUR-Dust show that screening effect is related not only geometrical as well dust grains density factors, but effects of non-steady state charging of grains, accounted in kinetic model.

2 Kinetic plasma simulation: model assumptions and main parameters

This 3-D object-oriented model of dusty plasma is based on follows methods and assumptions:

- PIC method for electron-ion plasma [6];
- dust grains are represented by PIC method with spherical shaped clouds that allows precise field calculation nearby the grain [3];
- two spatial scales for the calculation of the force acting on plasma particle(“particle-dust” nearby the dusty grain, and “particle-mesh” if the particle is far from grain) [9];
- two time scales: large time step for the motion of particles far from grains, and small time step for the motion of particles close to a grain;
- quasi-stationary problem: plasma comes to an equilibrium with dust grains, whereupon the grains are moved in the direction their momentum and so on;
- the injection of plasma particles is realized over the volume or through the surface;
- first model of dust charging may be named as “electron and ions collection from ambient plasma” [11].

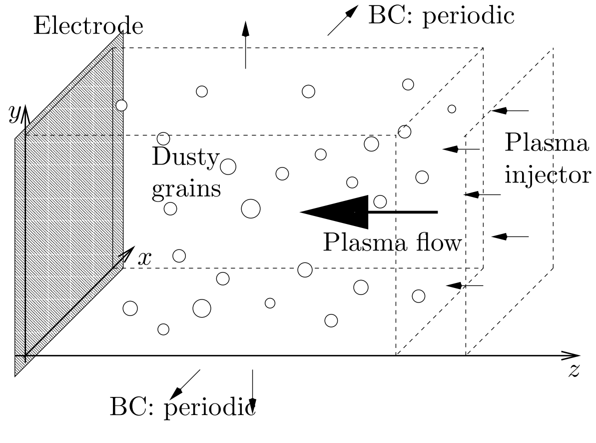

Figure 1: The scheme of numerical experiment

The modeling 3-D region (Fig. 1) is periodic across two coordinates (x and y). Across the third coordinate (axis z): on top the region contacts with reservoir of undisturbed plasma, while on bottom we have partial absorption/rejection from the metal wall. Both electrons and ions are represented by rectangular shaped clouds.

Dust grain representation. Dust particles are represented by PIC method with a spherical shaped cloud. Formfactor can be gaussian or any other smooth enough function. The complexity of formfactor doesn't influence the performance of the code, because all the required spatial integrals are tabulated before computations.

Two spatial scales. In order to describe the motion of particles nearby the grain adequately, different methods of force calculation are used for different spatial regions: if the particle is far from grains, the force is calculated on the basis of field values in the nearest grid points; if the particle is close to some grain, this force should be corrected. Because of spherical shape of the cloud, representing the grain, the correcting term is nonzero only inside the sphere.

Two time scales. In order to calculate the attractive force between the grains accounted, for example, for the coulomb scattering of ion flows, we should describe the motion of ions nearby the grain in great details. On the other hand, detailed tracking of particle trajectories far from grains is too expansive. Therefore two time scales are used: large time step for particles which are far from grains (this time step is limited by stability condition) and small time step for particles close to grains.

Quasi-stationary problem. The velocity of dust grains in plasma crystal experiments was about several cm/s, that is much less than electron thermal velocity. Therefore, the time of grains coming to equilibrium is much greater than the time step which has an order of $1/\omega_p$. To overcome this difficulty we solve quasistationary problem. First, plasma comes to equilibrium with dust grains, after which each grain is displaced in the direction of its velocity and so on. It may occur that this approach will be of particular use in plasma etching problem.

The injection. On the grain surface continual recombination of electrons and ions takes place. Thus we need to provide the injection of plasma particles. It can be done both through the surface of the region and throughout its volume.

Some other aproaches to numerical simulation of dusty plasma can be found in [13, 14, 15]. The simplest attempt of calculation is [16].

Electron-ion plasma representation. We are solving the set of Vlasov-Poisson equations:

$$\frac{\partial f_\alpha}{\partial t} + \vec{V}_\alpha \frac{\partial f_\alpha}{\partial \vec{r}} + eZ_\alpha \frac{\partial \varphi}{\partial \vec{r}} \frac{\partial f_\alpha}{\partial \vec{V}} = 0,$$

$$\Delta\varphi = -4\pi\Big(\sum_\alpha \rho_\alpha + \rho_d\Big), \qquad \rho_\alpha = eZ_\alpha \int f_\alpha \, d\vec{V},$$

where index α referes to species of plasma particles, while index d referes to dust grains.

To solve this system we use particle-in-cell (PIC) method. Just a couple of words to remind, what is PIC. In this method, a number of plasma particles of one species is aggregated in a coarse modeling particle with the same ratio of $\frac{e}{m}$. Due to this fact, the set of equations for the modeling particle will be exactly the same as for an individual plasma particle:

$$\frac{d\vec{r}^{\,i}_\alpha}{dt} = \vec{V}^i_\alpha, \qquad \frac{d\vec{V}^i_\alpha}{dt} = \frac{eZ_\alpha}{m_\alpha}\vec{E}, \qquad \vec{E} = \nabla\varphi.$$

The potential φ can be found from Poisson equation on the mesh:

$$\Delta\varphi^j = -4\pi\Big(\sum_\alpha \rho^j_\alpha + \rho^j_d\Big), \qquad \rho^j_\alpha = eZ_\alpha \sum_i S_\alpha(X^i_\alpha, X^j_\alpha).$$

From the last equation it can be seen, that the modeling particle isn't pointwise. The particle is represented by the charged cloud with formfactor $S_\alpha(X^i_\alpha, X^j)$, where X^i_α is the location of this particle of species α with the number i, and X^j is the mesh nod number j. This is an ordinary technique of noise reduction for PIC method.

In our model both electrons and ions are represented by rectangular shaped clouds. The modeling 3-D region is periodic across two coordinates (x and y). Across the third coordinate (axis z): on top the region contacts with reservoir of undisturbed plasma, while on bottom we have partial absorption/rejection from the metal wall. The equation of motion for grains:

$$\frac{d\vec{r}^{\,i}_d}{dt} = \vec{V}^i_d, \qquad \frac{\Delta(m^i_d \vec{V}^i_d)}{\Delta t} = \sum_{\alpha,k} m_\alpha \vec{V}^k_\alpha + q^i_d \vec{E}.$$

Collisions. The collision takes place when the distance between the particle and the grain is less than some critical value. Conventionally this value can be refered to as the radius of the grain.

We consider a spherical grain immersed in a plasma of ionsH^+ and electrons, assume that the main charge mechanism come from the fluxes of this particles. Secondary emission of electrons becomes important at the electron energy of order $300eV$. We neglect here also the secondary emission due to ion impact, but the reflection and back-scattering of particles in electrostatic fields are taking into account. Since the purpose of these computer experiments is the study of dust-plasma interaction, i.e. electrostatic charging of dust grain of low concentration under influence of special plasma injection into 3D vol near electrode with purpose to dicusse general mechanisms of screning electrode by dusty plasma presence near surface. Note here, that next step of model development will be stochastic simulation of photoelectric, secondary electrons and ions thermoionic as well as electric field emission. Chemical reaction on the grain surface such as Auger-neutralisation and non-resonance charge exchange (tipical for divertor processes) naturally can be included to kinetic model of dusty plasma by method of stochastic analogue of non-equilibrium processes, used in [10].

3 Result of screening effect investigation

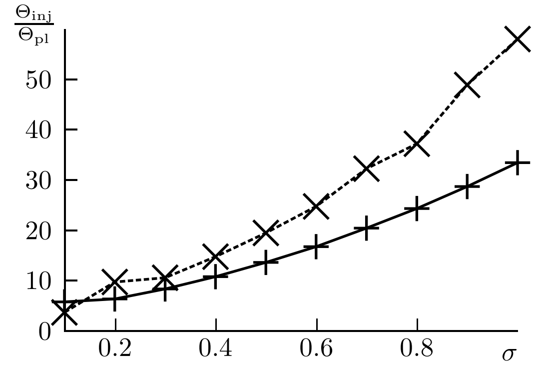

Figure 2: Relative decrease of heat (+) and particle (×) fluxes versus crossection equal to σ_{exp}, calculated by MHD 1D code.

Let l_d is thinckness plate matherial, which creat the grain layer L_d and R_d is characterful grain size. Then the concentration of grains is $n_d = \frac{3}{4\pi R_d^3}\frac{l_d}{L_d}$. The geometrical crossection ratio of grains layer will be $\sigma_{geom} = n_d L_d \pi R_d^2$. Here λ_D is the Debye length and the crossection due to Debye screening of each grain will be $\sigma_{scr} = n_d L_d \pi \lambda_D^2 = \sigma_{geom}(\frac{\lambda_D}{R_d})^2$. The parameters of crossections is follow

$$\sigma_{geom} < \sigma_{exp} < \sigma_{scr}.$$

Note, that σ_{exp} is divided on unit of surface square, this value has been calculated by kinetic code.

Let us to introduce the decrease of plasma fluxe p as

$$\frac{dp}{dz} = \sigma_{exp}/L_d \cdot p, \quad \text{or else} \quad p(z) = p_0 e^{-\sigma_{exp}(L_d - z)/L_d},$$

here z is distance from electrode and p_0 is plasma fluxe without dust grain layer. The amount of sputtered material was related to the resulting heat flux and temperature at the target surface. We will compared screening effect, calculated by kinetic code SUR-Dust and other way.

1D MHD-calculations of particle and heat flow decrease for the initial electron temperature $T_e = 3eV$ and density of electrons $n_e = 10^{14} cm^{-3}$ (neutral gas of density $n_H = 0.1 n_e$) have shown high efficiency of the divertor plate screening by thin dust particles layer of size $L_d = 10cm$ with dust density convenient with kinetic model calculation (Fig. 2). Gas puffing into divertor, which is accounted in MHD plasma model, is used to decrease the heat loads towards the electrode plate due to ionization, charge-exchange and other inelastic processes. But this information is not available for mechanisms of screening explication.

The results of kinetic simulation, presented here, were obtained under follows conditions: $R_d/\lambda_D = 0.2$, $\sigma_{scr} = 2.5$, $L_D/\lambda_D = 420$, $n_d \cdot \lambda_D = 0.002$, $l_d/\lambda_D = 0.008$. Initial distribution function of injected plasma is Maxwellian, as well $T_e = T_i$, and neutral gas is not acounted in kinetic dusty plasma model. Note, that the case, when dust grain size is about λ_D is not simple for calculation as well for interpretation. We are not known about the same calculations of non-equilibrium state of plasma (general assumption in dusty plasma calculation put forward under assumption about equilibrium of distribution functions). Necessary to add, that Molecular Dynamic simulation combined with Monte-Carlo code as a rule have not requared accuracy of self-consistent electrostatic field determination. Our results, presented on the Figs.3-5, confirm the deviation plasma state from equilibrium state. All moment characteristics, such as fluxes of particles, momentum, energy, had been calculated by integrating of distribution function, demonstrated in the paper. Due to charging of dust grain electron

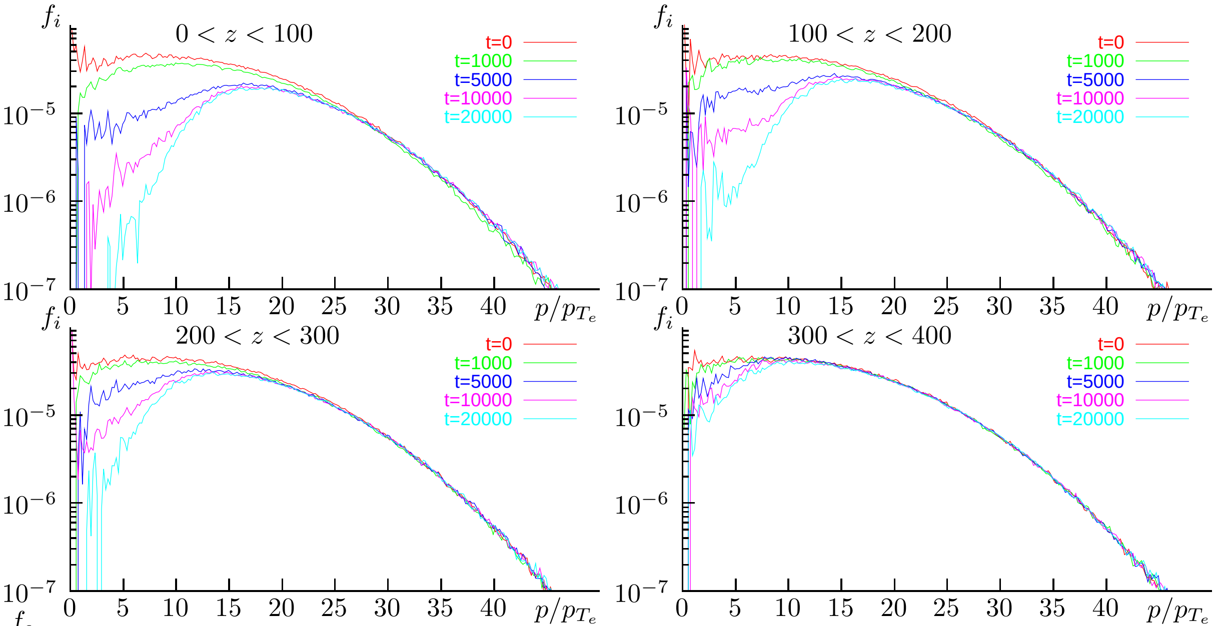

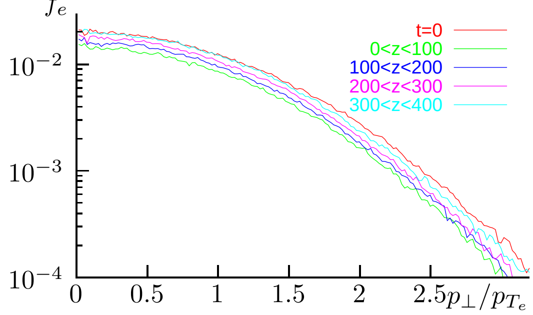

Figure 3: Kinetic ion distribution function (logarithmic scale) subject to absolute value of ion momentum for four space subregions of Z mesured in λ_D at consecutive $(0 \div 20000)$ time.

Figure 4: Kinetic electron distribution function (logarithmic scale) depending on transversal momentum for four space subregions at steady-state behaviour of fluxes. For comparision it is shown initial value of distribution function.

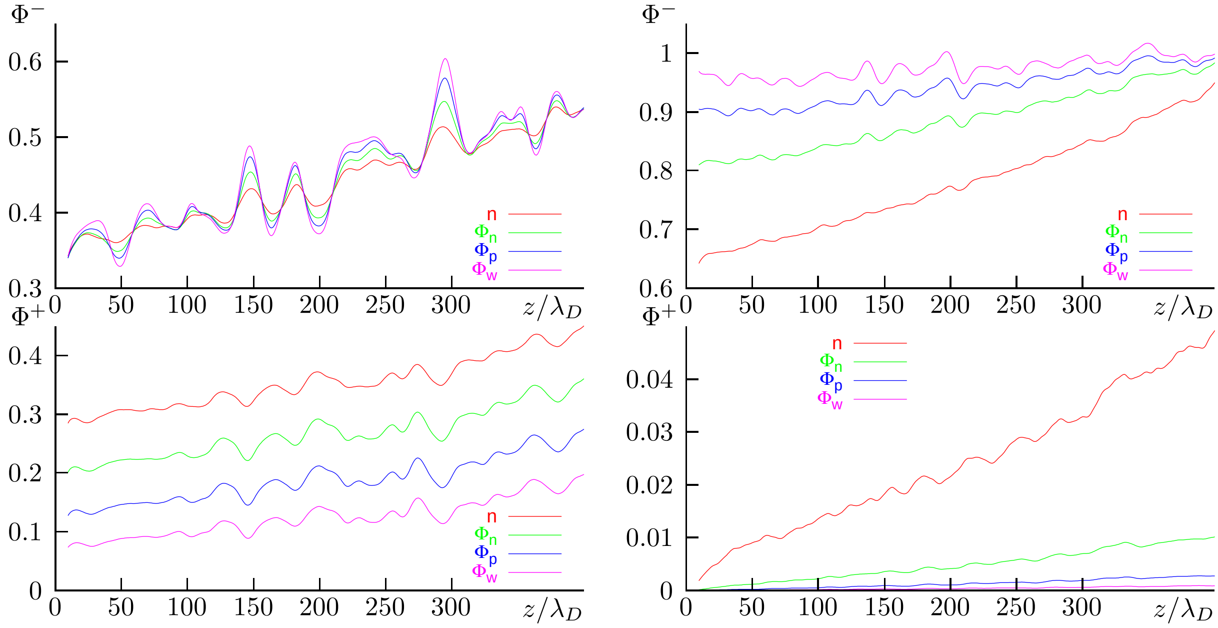

Figure 5: Calculated by SUR-Dust dependence of electrons (left) and ions (right) particle density n, fluxes of particles Φ_n, momentum Φ_p and energy Φ_W versus distance to electrode. The fluxes of particles, moving to plate are shown on top picture, reversal fluxes on the bottom one.

distribution function lose its “tails”, and on the contrary, ions distribution lose slow part. Average velocity of ions decrease and the temperature of ions increase due to transformation of longitudional momentum component to transversal ones. We can see reversal fluxes on the pictures, this fact is very important for applications.

Acknowledgments

This work partially supported by Russian Foundation for Basic Research, grants N 02-01-01004 and by Department of Mathematical Sciences RAS, program of basic research, 2003.

Bibliography

[1] L. Boufendy and A. Bouchoule //Plasma Sources Sci. Tech., 2002, vol.11, No.3A, P.A211-218.

[2] Yu.S. Sigov, Computer Simulation: The link between past and future of plasma physics. Selected works //composed by V.D. Levchenko and G.I. Zmievskaya.–Fizmatlit (Physics and Mathematics publisher, IAPC “Nauka”),Moscow.– 2001, 288 p. (in rus.)

[3] L.V. In’kov, V.D. Levchenko, Yu.S. Sigov // Prikladnaya physica (Applied physics).–2000, Vol.3, P.138-145 (in rus.).

[4] G.I.Zmievskaya, T.V.Levchenko, T.K.Soboleva //Proc. of 15th Symp. on Plasma Chemistry, Vol.VII, Ed. by A. Bouchoule et al., Orleans (France).– 2001, P.2793-2798.

[5] G.I. Zmievskaya, T.V. Levchenko, T.K. Soboleva //Thermophysics and Aeromechanics, 2002, vol.9, N4, p.633-646.

[6] V.D.Levchenko, Yu.S.Sigov //Eds. G.Maino and M.Ottaviani , Singapore-London, Publishing Co.Pte.Ltd. World Scientific.–1996,p.55-69. pp.84-98.

[7] G.I. Zmievskaya //Eds. G.Maino and M.Ottaviani, Singapore-London, Publishing Co.Pte.Ltd. World Scientific.–1996, pp.84-98.

[8] A.L. Bondareva, L.V. In’kov, V.D. Levchenko, T.V.Levchenko and G.I.Zmievskaya. //Proc. of XXV ICPIG, Nagoya, Japan, Vol.2, Ed. by Toshio Goto, Nagoya Univ.– 2001, P.119-120.

[9] L.V. In’kov //Matematicheskoe modelirovanie (Math. modeling).–2003 (in print).

[10] G.I. Zmievskaya //Plasma Phys.Rep.–1997, Vol.23, No.4, P.368-382.

[11] V.N. Tsytovich //Plasma Phys.Rep.–2002, Vol.28, No.8,P.675-707.

[12] V.N.Tsytovich // Physics of Our Days, N 1, 57 (1997)

[13] F.Melandso, J.Goree // J.Vac.Sci.Technol. A, 14, 511 (1996)

[14] N.Otani, A.Bhattacharjee // Phys.Rev.Lett. 78 1468 (1997)

[15] D.Winske, M.Murillo, G.Selwyn // Bull.Amer.Phys.Soc. (1997)

[16] Ya.K.Khodataev, R.Bingham, V.N.Tsytovich // Plasma Physics Reports, 22(11), 932 (1996)

Temperature distribution modeling for a hemispherical bowl-shaped vessel during plasma source ion implantation

Chengsen Liu and Dezhen Wang

State Key Laboratory of Materials Modification by Laser, Electron, and Ion Beam,
Department of Physics, Dalian University of Technology, Dalian 116023, People's Republic of China

Plasma source ion implantation (PSII) is a versatile method for surface modification. Ion implantation is used to improve the wear, corrosion, and fatigue resistance of metals and in the fabrication of semiconductors. Because the power incident on the implanted objects can be large during the PSII process, the target temperatures can be quite high. The target temperature during PSII of metals and semiconductors is crucial as it affects the resultant surface properties and structures. Therefore, target temperature prediction can be quite useful. In our work, a two-dimensional (2-D) model for a hemispherical bowl-shaped vessel has been described. This model combines the plasma fluid model with the no steady-state heat transfer equation. The ion flux is calculated using the fluid model and input into the heat transfer equation to derive the temperature distribution in the target. In the model we take into account the influence of shape factor of the bowl on the radiation heat transfer from the target to the chamber. A time-dependent temperature distribution of a hemispherical bowl-shaped vessel can be obtained. Using this model, the effects of the implantation voltage, pulse duration, pulsing frequency, as well as density on the target temperature can be determined.

On the Absorption of Microwave by a multiform Plasma Slab

WU Bin, LIN Lie, WU Cheng-Kang, PAN Wen-Xia

Institute of Mechanics, Chinese Academy of Sciences, Beijing 100080, China

Abstract

This contribution gives impedance method to calculate the absorption of microwave by a stratified plasma layer with a kind of distribution of electron number density. The effects of wavelength, incident angle and maximum electron number density with parabolic profile on the absorbed power coefficient are also investigated. It is found that the absorption coefficient is nearly the same when the incident angle is less than 30^0

1. Introduction

Interest in the absorption of microwave in plasma has been sustained for many years as a result of applications of such studies as the microwave torches, the microwave diagnosis, and atmosphere and ionosphere propagation [2]. The geometric optical method is widely used to calculate the power of reflection, transmission and absorption of microwave. In this paper, we introduce the impedance method for the calculation of the absorption, in the second part. And the third part discusses some numerical results.

2. The model for the calculation

In this work we consider a plasma slab, which is modeled as adjacent, homogeneous sub-slaps that approximate a kind of distribution, such as linear or parabolic profile. It was assumed that a plane microwave is incident on the layer at some arbitrary angle.

2.1 The coefficients of reflection, transmission and absorption

The general geometry of the problem is shown in Fig. 1. The plasma layer is separated into (n-1) sub-layers, which are numbered in 2,3,4,⋯,n-1. Out of the plasma layer, are semi-infinite air layers in atmosphere pressure, which we enumerate by 1 and (n+1). The thickness of the plasma sub-layers are d_2, d_3, $\cdots d_n$, respectively. The microwave is incident on the boundary of the last layer at an arbitrary angle θ_{n+1}.

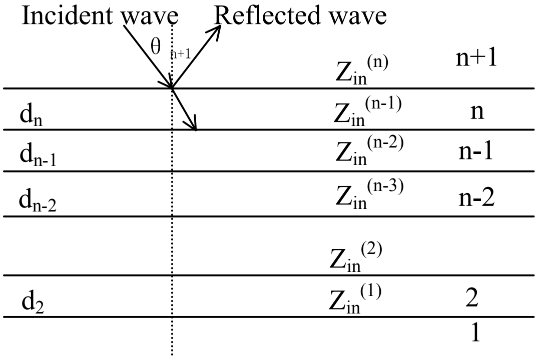

Fig. 1. Determination of absorption coefficient of a set of plasma layers

The theoretical method to analyze the propagation of the wave is based on the impedance of the sub-layers. We have included multiple reflections between sub-slab interfaces in the model.

For determination of the reflection coefficient [1], the required input impedance of the system is determined by the formula

$$Z_{in}^{(n)} = [(Z_{in}^{(n-1)} - iZ_n \tan k_{nz} d_n) / (Z_n - iZ_n^{(n-1)} \tan k_{nz} d_n)] Z_n \tag{1}$$

$Z_{in}^{(n)}$ is the "input impedance" of the boundary of sub-layer n and n+1, which is in explicit form. Where, we denote the impedance of the sub-layer n and (n-1) boundary by Z_n, and the wave number by k.

The reflection coefficient by the formula

$$V = (Z_{in}^{(n)} - Z_{n+1}) / (Z_{in}^{(n)} + Z_{n+1}) \tag{2}$$

And the transmission coefficients

$$t = \prod_{j=1}^{n} (Z_{in}^{(j)} + Z_j) / (Z_{in}^{(j)} + Z_{j+1}) e^{i\phi_j} \tag{3}$$

Then, the power coefficient of absorption is determined by

$$A = 1 - |V|^2 - |t|^2 \tag{4}$$

The influent of plasma parameter, such as electron density, temperature and gas temperature, on the absorption characteristics is expressed in Z_j and k.

$Z_j = 1/(n_j \cos\theta_j)$ for TE wave, $j=1,2,\ldots,n+1$ (5)
$Z_j = (\cos\theta_j)/n_j$ for TM wave, $j=1,2,\ldots,n+1$

For further interest, one can check it on ref. [1].

2.2 Typical result of the power coefficients of absorption, reflection and transmission

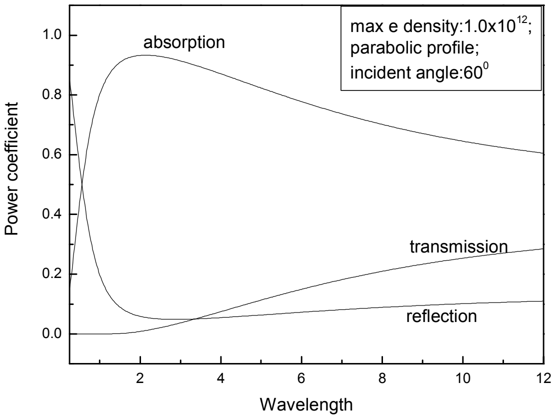

Fig. 2. Absorbed, reflected and transmission power per unit incident power versus wavelength, with parabolic electron density profile ($n_{max} = 1.0 \times 10^{12} cm^{-3}$) at incident angle $\theta = 60^0$

Figure 2 shows the absorption, attenuation and reflection coefficients versus wavelength. The maximum electron density of the plasma layer is $1.0\times 10^{12}\mathrm{cm}^{-3}$, and the incident angle 60^0.

It is found that the power coefficient of transmission will be greater with the increase of wavelength. The absorption coefficient increases with the wavelength, but decrease when the wavelength is greater than 2cm. The reflection coefficient decreases rapidly with the wavelength, but increases smoothly when the wavelength is bigger than 2cm.

3. Results and discussion

The condition for the calculation is as followed:

The thickness of the plasma d is 4cm, the electron temperature 1eV and the gas temperature 2000K. The electron density is parabolic profile with the max number density being in the center and without electron on the boundary.

Figure 3 to figure 6 are numerical result. They show the power coefficient of absorption by a particular plasma layer. It was showed that the wavelength, incident angle and the max electron density are main factors, which lead to the change of absorption coefficient.

3.1 The influent of wavelength on the power coefficient of absorption

Figure 3 shows the power coefficient of absorption versus wavelength for different maximum electron density at incident angle of 60^0. The absorption coefficient increases with the wavelength in short wavelength, but decrease in long wavelength. It has a maximum absorption coefficient for the same electron density, but the corresponding wavelength is different. The maximum absorption can be reach when the electron density is $1.0\times 10^{12}\mathrm{cm}^{-3}$ for a 2cm microwave, $1.0\times 10^{13}\mathrm{cm}^{-3}$ for 5mm, and $5.0\times 10^{12}\mathrm{cm}^{-3}$ for 3cm when the incident angle is 60^0.

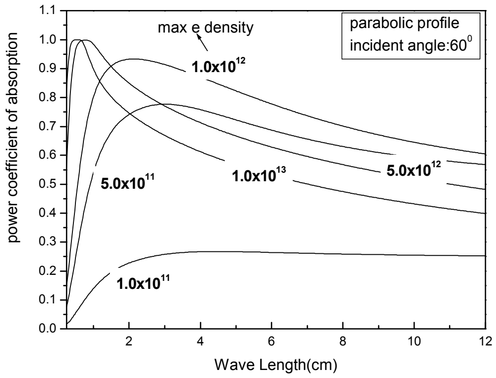

Fig. 3. The power coefficient of absorption versus wavelength at different electron density

It can be seen from Figure 4 that the maximum absorption coefficient is not sensitive to the incident angle. That is to say, the maximum absorption exists almost in the same wavelength for different incident angle.

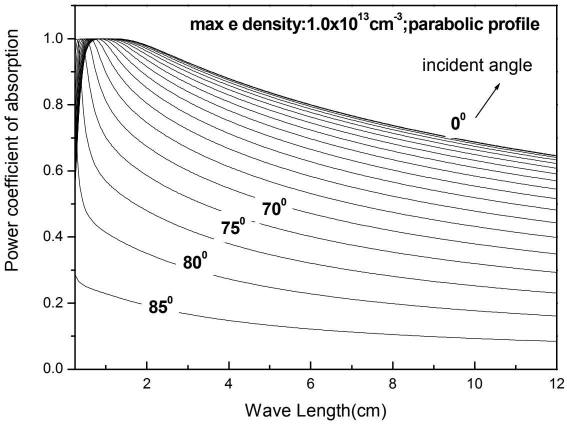

Fig. 4. The power coefficient of absorption versus wavelength at different incident angle

3.2 The influent of incident angle on the power coefficient of absorption

For the same wavelength, the incident angle does influent the absorption coefficient. Figure 5 shows the power coefficient of absorption versus incident angle for 3cm microwave with different maximum electron density. This influent occur when the incident angle is big enough, especially when the angle is bigger than 60^0. But the absorption coefficient is almost the same when the incident angle is less than 30^0. This characteristic is very convenient when we use microwave to diagnosis plasma density. We do not need to care much about the accuracy of the incident angle. Further more, we can regard microwave with a small incident angle as a vertical wave, without losing much accuracy.

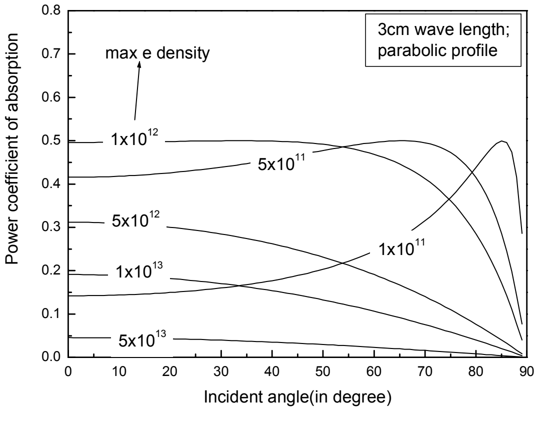

Fig. 5. The power coefficient of absorption versus incident angle for different max electron density

3.3 The influent of max electron density on the power coefficient of absorption

Figure 6 cares about the power coefficient of absorption versus max electron density. Both parabolic and line profile have a maximum absorption for different electron density. It is near 1.0×10^{12} cm^{-3} for incident 60^0 and 3cm microwave. The results are familiar with figure 3, but clearer than it.

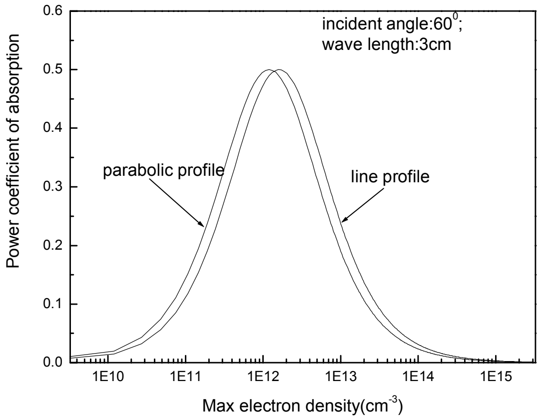

Fig. 6. The power coefficient of absorption versus max electron density with line and parabolic profile (incident angle: 60^0, wavelength: 3cm)

4. Conclusion

Impedance method for the calculation of absorption of microwave at an arbitrary angle by a stratified plasma layer is better in accuracy and convenience than geometric optical method [3].

The absorption coefficient is nearly the same when the incident angle is less than 30^0. We can regard microwave with a small incident angle as a vertical wave, without losing much accuracy.

Also, the max electron density is almost the same with both parabolic and line profile, when the maximum absorption occur. It is near 1.0×10^{12} cm^{-3} for incident 60^0 and 3cm microwave.

5. Acknowledgments

This work is supported by National Nature Science Foundation of China №. 90205026.

6. References

[1] L.M. Brekhovskikh, Wave in layered media, second edition translated by Robert T Beyer, Academic press. P15-26 (1980)

[2] Mounir Laroussi, *IEEE Trans. Plasma Science,* Vol. 21, NO. 4, Jun. 1993

[3] Wu Bin, Lin Lie and Wu Cheng-kang, "The Effect of Electron Density Profile on the Reflection, Absorption and Transmission of Microwave by a Plasma Slab", *Joint International Plasma Symposium of 6th APCPST, 15th SPSM, OS2002 and 11th KAPRA,* July 1-4,2002 Jeju Island, Korea.

Temperature and Radiant Power emitted from DC Horizontal Short Free Arc Discharge mixed with Tungsten Vapor near 50A

T. Iwao[1], Y. Inoue[2], and T. Inaba[3]

[1] JSPS Research Fellow, University of Minnesota and Chuo University, Minneapolis, USA
[2] Graduate Course of Electrical Engineering, Chuo University, Tokyo, Japan
[3] Department of Electrical Engineering, Chuo University, Tokyo, Japan

Abstract

The radiant power emitted from a high temperature medium is useful for lighting and treatment of hazardous wastes, because it has a highly intense radiation. In this paper, the relation between radiant power, temperature, and radius is discussed. The total radiant power density is estimated to be about 10^9W/(m^3sr) at 6,000 - 10,000K, 300 nm - 30 μm in wavelength region. The radiant power density with continuous and line spectrum emitted from tungsten is higher than nitrogen and oxygen. The radiant power, Φ(W)(300nm-30μm), in the case of the point light source of radiant power emitted from DC horizontal short free arc discharge mixed tungsten vapor as a function of current, I, is 1,480W(50A), and increases in proportion to the 1.06th power of the current. The radiant energy Φ_E(kJ)(300 nm – 30 μm) in the same condition as a function of in-put energy is 35 kJ(45 kJ), and increases in proportion to the 1.06th power of the in-put energy. The radiant efficiency is extremely high level about 80% as white light. This value is considered as a champion data, because it is double than gases only. The temperature of free arc mixed with tungsten is estimated about 9,000 K(30, 50 A) and 6,400 K(70A) by using line pair method. These temperatures are almost same value when the current is 30, 50 A. The radiant power density of 9,000 K and 6,400 K is almost same value. When the current increases, the effect of arc expanse to radius direction is stronger than increment of temperature in the case of free arc. It is considered that the energy of arc brings about the increment of radius, because there is no influence of the wall and the gases can move for radius. Because the free arc doesn't have the restriction of radius, the radius expands to radius direction. The arc radius increases in proportion to the square root of the current in the case of constant of current density. The theoretical radiant power is expressed such as $\Phi \propto I^{1.0}$. This result is very close to the result of current power parameter, 1.06, in this experiment.

1. Introduction

The characteristics of the arc discharge have the high temperature and highly intense radiation. Therefore, the arc discharge is used to a lot of application[1] such as plasma torches[2] and lighting. The radiant power emitted from a high temperature medium is useful for lighting and treatment of hazardous wastes, because it has a highly intense radiation, especially UV and IR rays. However, there is few application of radiant power source for hazardous wastes. Therefore, in this paper, we calculate and measure the radiant power emitted from dc free arc to know the relation between radiant power, temperature, and radius and to apply for the hazardous wastes. Concretely, the number densities of the tungsten, nitrogen and oxygen are calculated. The temperature of the arc discharge in air was measured by the spectrometer and the radiant power of the DC horizontal free arc between tungsten electrodes was measured with a spectroscopy and a radiant power meter at 20-70A in the arc current, 0.1MPa in pressure. Then, we discuss the relation of them.

Table 1 Dissociated and ionized voltages(energy).

Status				Voltage(energy)	
W I	$\Longleftrightarrow$	W Ⅱ	(W^+)	7.98 eV	(1.28×10^{-18} J)
W Ⅱ	$\Longleftrightarrow$	W Ⅲ	(W^{2+})	17.7 eV	(2.84×10^{-18} J)
N_2	$\Longleftrightarrow$	N I	(N)	9.8 eV	(1.57×10^{-18} J)
N I	$\Longleftrightarrow$	N Ⅱ	(N^+)	14.54 eV	(2.33×10^{-18} J)
O_2	$\Longleftrightarrow$	O I	(O)	8.00 eV	(1.28×10^{-18} J)
O I	$\Longleftrightarrow$	O Ⅱ	(O^+)	13.614 eV	(2.18×10^{-18} J)

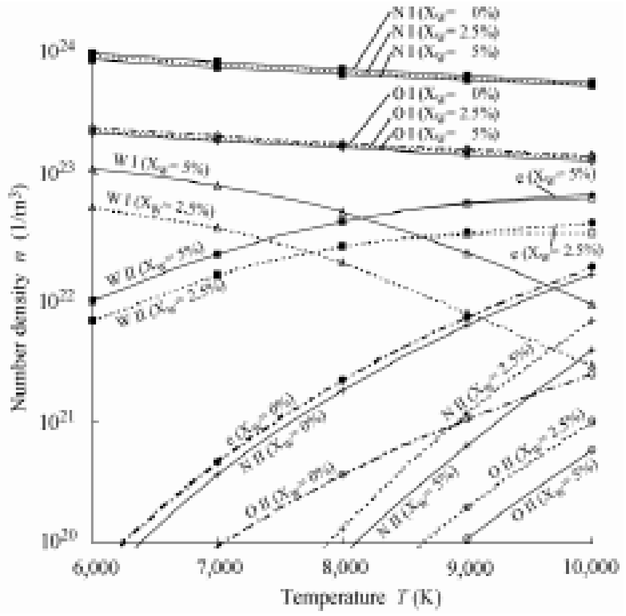

Fig.1 Number density of high temperature gases mixed with tungsten in air

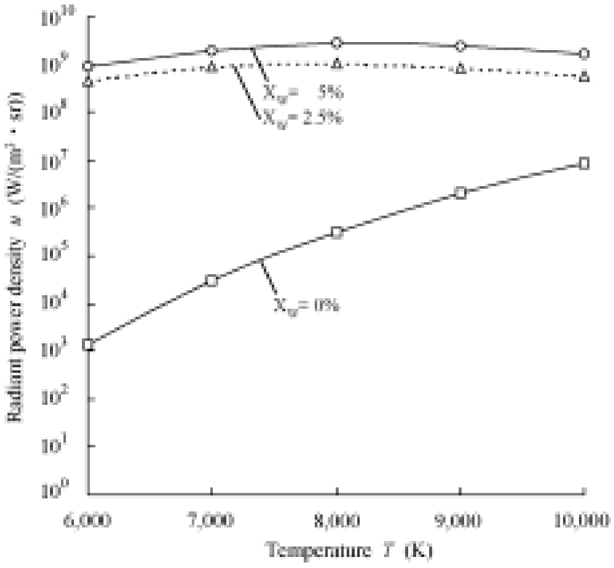

Fig.2 Radiant power density in air

2. Number Density of High Temperature Gases mixed with Tungsten

The number density of high temperature gases mixed with tungsten in air was calculated to know the radiant power density. In this paper, the ten species such as W I, W II, W III, N_2, N I, N II, O_2, O I, O II, e and 6 chemical reactions as shown in Table 1 are calculated. And, it is assumed that the temperature region of this calculation is 6,000-10,000 K which is generated by a free arc at 50 A[3]. Then, the mol mixture ratio of high temperature gases mixed with tungsten is assumed as a free arc. It is assumed that the mixed ratio is W I : 0, 2.5, 5 %, N_2 : 80, 78, 76 %, O_2 : 20, 19.5, 19 %, respectively. Each of dissociated and ionized voltage of species is shown in Table 1. Subscript Z is described as ionized status(Z=I:base). The simultaneous equations such as dissociation equation, Saha equation, equation of state, neutral equation of electron, equation of mol mixture ratio of nitrogen, oxygen, is calculated by using the Newton-Raphson method. This program is written by C language, and the compiler is Microsoft C/C^{++}, and the program is running on Windows XP.

The number density of high temperature gases mixed with tungsten is shown in Fig. 1. The number density of W I is more than about 5×10^{22} m^{-3} at 6,000 K. However, it decreases with temperature, and it is cross with W II around 7,750 K(X_W = 2.5 %), 8,100K(X_w = 5 %). After this, W II is bigger than W I. N_2 and O_2 of about 99.9 % has already dissociated to N I and O I at 6,000 K. As the temperature increases from 6,000 K, the dissociated ratio of N_2 and O_2 increases. The number densities of N II, O II are about 7×10^{21} m^{-3}, 1×10^{21} m^{-3} at 10,000 K, X_W = 2.5 %, respectively. They barely exert an influence on total electron density at 10,000 K. Therefore, the number density of electron is almost same as W II, and the ionization from W I is dominant. It can be confirmed by Fig. 1. This phenomenon is explained because the increment of ionized voltage is W I＜O I＜N I as shown in Table 1.

3. Radiant Power Density of High Temperature Gases mixed with Tungsten

The radiant power density with continuous and line spectrum of high temperature gases mixed with tungsten, u (W/(m^3 sr)), is calculated by using the result of the number density of high temperature gases mixed with tungsten[4]. In this paper, It is assumed that the region of wavelength is 300nm - 30μm[3]. The radiant power density (300nm - 30μm) of high temperature gases mixed with tungsten in air is shown in Fig.2. The total radiant power density is estimated to be about 1.07×10^{9} (X_w = 2.5%), 2.7×10^{9} (X_w = 5 %), and 3.16×10^{5} (X_W = 0%) W/(m^3 sr) at 8,000 K, 300 nm - 30 μm in wavelength region. The radiant power emitted from high temperature gases mixed with tungsten in air is extremely 1,000 - 10,000 times as high as pure air without tungsten. The tungsten has an excellent effect for radiation even if the relatively low temperature near several thousand K and small mixture ratio up to 5 %.

4. Experimental arrangement

The experimental arrangement is shown in Fig.3. The free arc is generated by DC Power supply. And it is measured by a spectroscopy to estimate the temperature of the free arc and by a power meter to know the radiant power emitted from the free arc. The experiment of the radiant power, radiant energy, radiant efficiency and temperature emitted from the free arc was held to know the characteristics of DC horizontal short free arc mixed with tungsten vapor near 50 A. In this experiment, the measurement was held in the case of the tungsten electrodes, the distance *L* between electrodes at 1 cm, and the current *I* at 30, 50, 70 A. The radiant power emitted from the DC horizontal short free arc mixed with tungsten vapor near 50A between tungsten electrodes in an atmospheric air was measured by using power meter[3]. The power meter can measure the radiation in the wavelength from 300nm-30μm, and the sensitivity of it is flat on wavelength. The radiant power emitted from the free arc is not constant in wavelength. But this power meter can measure the wide wavelength. So, there is little disturbance due to wavelength. While the radiant power emitted from W I and W II exists from 200 - 400 nm [5][6], this experimental result is from 300 nm to 30 μm, because the power meter can measure from 300 nm-30 μm. The radiant power ϕ measured by using power meter is the value at X=5 m from the free arc, and the diameter of sensor area is d_p = 0.015 m. Each value was recorded by digital oscilloscope. In same time, the spectrum emitted from the DC horizontal short free arc discharge mixed tungsten vapor near 50A between tungsten electrodes in an atmospheric air was measured [3]. In this experiment, the spectrum from N I doesn't make sure, because there are a lot of the spectrums from W I [3]. So, the temperature was estimated by using spectrum from W I from 450 - 480 nm.

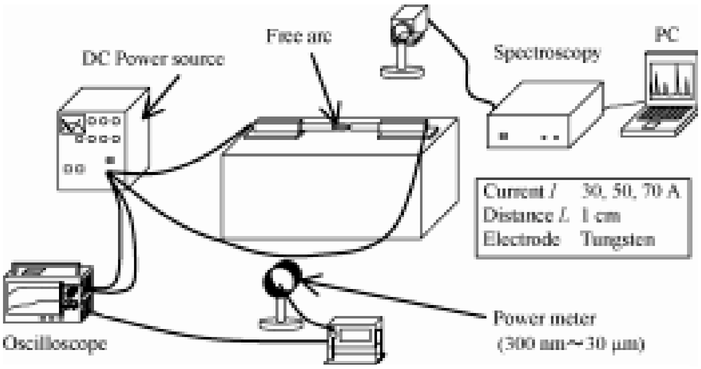

Fig.3 Experimental arrangement

5. Experiment of Radiant Energy and Temperature

5.1 Temperature of free arc

The temperature of DC horizontal free arc between the tungsten electrodes was measured with a spectroscopy at 30-70A of the current in atmospheric air. The arc discharge in the case of LTE status consists of Boltzmann distribution between excited atoms. The arc temperature was measured at the middle point between electrodes, and then calculated according to Line Pair Method under a condition of LTE. When the x-axis is energy $E_{mi\mathrm{N}}$, the y-axis is the intensity of spectrum area, the slope of this plots becomes the straight line. The arc temperature, T, is derived from the slope. The distribution of spectrum of free arc was measured by spectroscopy at center point between electrodes [3][7]. According to this distribution and the radiant power density [3], the radiant power emitted from WI is dominant. Therefore, the arc temperature is calculated by line spectrum from W I. The W I was dominant in this wavelength. Figure 4 shows the temperature of the free arc. The line spectra were determined at 5 points (455.184 nm, 457.067 nm, 458.875 nm, 465.744 nm,

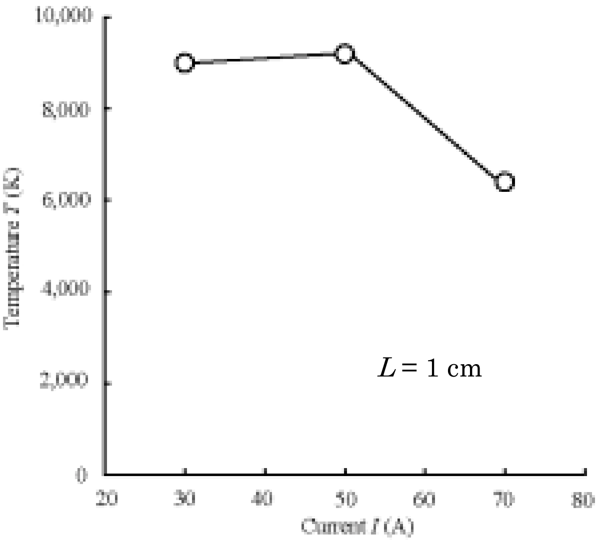

Fig.4 Temperature of the free arc in air

469.373 nm, 475.754 nm), because it was clear to recognize W I line. The arc temperature is measured to be about 9,000 K at 30 - 50 A and 6,400 K at 70 A in current, 0.01 m in plasma length by the line pair method [3][7]. The arc temperature was same value in different currents such as 30 and 50 A, even if the radius of the free arc at 50 A could be bigger than that at 30 A [3]. Therefore, the arc temperature for the electrode erosion would be almost same value at both case. The arc temperature at 70 A is lower than those at 30 and 50 A. This is the reason why the radius could be extremely expanded than the case of 30 and 50A. It is assumed that this temperature is the average temperature in the arc column.

5.2 Radiant power

Figure 5 shows the radiant power Φ (W)(300 nm-30 μm) in the case of the point light source of radiant power emitted from DC horizontal short free arc discharge mixed with tungsten vapor as a function of current[3]. The radiant power is 860 W (30 A), 1,480 W (50 A), 2,100 W (70 A), and increases in proportion to the 1.06th power of the current. The arc temperature was same value in different currents, even if the radius of free arc at 50 A could be bigger than it at 30 A. The logarithmic power, 1.06, of the current for the radiant power was lower than it in the case of the wall-stabilized model and torch plasma, because the radiant power depended on the bigger radius and lower temperature of the free arc. According to calculation of radiant power emitted from the wall-stabilized arc model fixed by the arc radius, the radiant power increases in proportion to the 2.0th power of the several tens of the current, to the 1.7th power of the several hundreds of the current, to the 1.2nd power of the several thousands of the current, in other words fully ionized region. And these calculated value is close to measured value in stabilized arcs. But in this free arc, the radiant power increases in proportion to the 1.06th power of the several tens of the current. This value is almost half of the wall-stabilized arc. Therefore, the radiant power of the free arc doesn't increase so sharply, but softly with current. This is different between the free arc and the wall-stabilized arc.

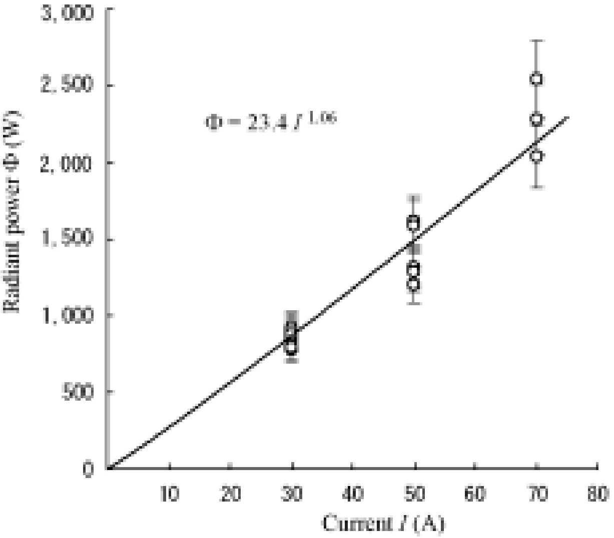

Fig.5 Radiant power as a function of current

6. Radiant power as functions of current and in-put energy

Each of the electrical in-put energy to the arc column, Q_{in} (kJ), and radiant energy from the arc, Φ_E(kJ) (t_1=0s, t_2=30s), is calculated such as the time integral of arc power to be current times arc voltage and measured as shown in Fig.6. The radiant energy increases in proportion to the 1.06th power of the in-put energy. This value is almost same when the current changes, because the arc voltage between the electrodes is almost constant. The radiant energy Φ_E (kJ)(300 nm- 30 μm) in the case of the point light source of radiant power emitted from DC horizontal short free arc discharge mixed tungsten vapor as a function of in-put energy is 27 kJ (35 kJ), 35 kJ (45 kJ), 43 kJ (55 kJ), and increases in proportion to the 1.06th power of the in-put power. The radiant efficiency was extremely high level, to be about 80 % as white light as shown in Fig.6. While, so far, it is considered about 40 - 50 % at a pure air arc or gaseous arcs[2][3]. This

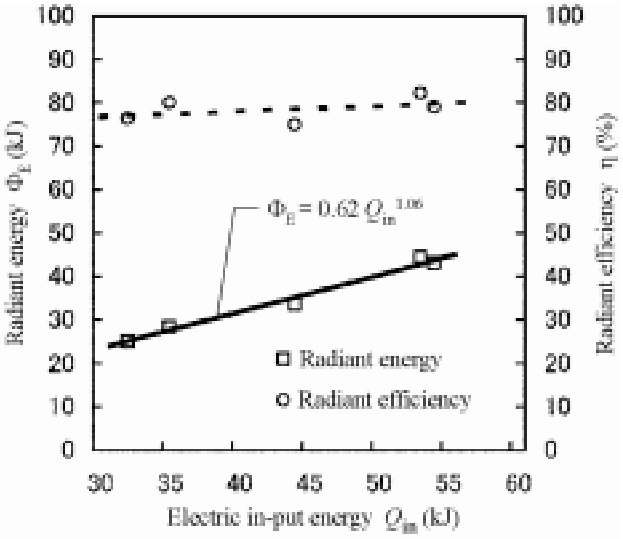

Fig. 6 Radiant energy and radiant efficiency of the arc as a function of electric in-put energy

value is considered as a champion data. It is doubly higher than gases only. The reasons of this high value of radiant efficiency are partially due to the mixed condition with tungsten vapor from electrodes and partially due to the radiation emitted from the electrodes. The mixed gases with metallic vapor should be chosen to increase the radiant power.

7. Relation Between Radiant Power and Temperature of Free Arc considered by Arc Radius

The result between the number density of high temperature gases mixed with tungsten, measured radiant power, and temperature from the line spectrum method is compared to know relation between the radiant power and temperature of free arc considered by arc radius.

7.1 Relation between arc radius and temperature of free arc

The temperature of free arc in air mixed with tungsten is estimated about 9,000 K at 30 A and 50 A, and 6,400 K at 70 A as shown in Fig.4. In the case of the wall-stabilized arc, the arc temperature increases with the current. The arc radius in the case can't expand because the wall exists even if the current increases. So, the arc temperature increases because the current density or current/radius ratio increases. But, in the case of free arc, the arc radius can increase when the current increases. So, the current density doesn't increase or so, and the temperature also doesn't increase or so. Therefore, in a free arc, the current density doesn't increase and the temperature also doesn’t increase in comparison with the wall-stabilized arc. In other words, when the current increases, the effect of arc expanse to radius direction is stronger than increment of temperature in the case of free arc. For example, the average current density, J, is expressed as $J = I / (\pi R^2)$ (R:arc radius). If the current density, J, is constant, the arc radius is expected to increase in proportion to the square root of current and the arc temperature and also the radiant power density, u, will be kept almost constant. These characteristics conduct the radiant power $\Phi \propto u\pi R^2 \propto R^2 \propto I$ as shown in Fig.5. However, in the case of 70 A, this relation is explained by different reason. Because the radius is extremely expanded, the arc temperature decreases. However, as the calculation result of radiant power density, radiant power densities of 9,000 K and 6,400 K are same value in the tungsten mixture range of X_W = 2.5 - 5%. If $X_W \approx 0\%$, the Φ should be disappeared. Fig. 5 shows the actual X_W should be 2.5 - 5%..

7.2 Relation between arc radius and radiant power

According to the radiant power theory of the wall-stabilized arc in the case of the same radius, the radiant power increases in proportion to the 2.0th power of the current at several tens ampere of the current as mentioned above. And the measured value and the theory value is almost same. But the radiant power increases in proportion to the 1.06th power of the current in this experiment. This value is about half of the wall-stabilized arc. So, the radiant power of the free arc doesn't increase with the current so sharply such as wall-stabilized arc. Because the free arc doesn't have the restriction of radius, the radius increases to expand to radius direction. So, the increment of current density is not occurred so much, and then the temperature also doesn't increase up to 50A. In the case of 70A, while the radius is extremely expanded, the radiant power density is almost same value. So, the result of relation between the radiation power and the current in the range of 30, 50, and 70 A could be same. Therefore, the radiant power density doesn't increase such as the wall-stabilized arc. In this case, the radiant power increases to expand the cross-section due to increment of arc radius. For example, the arc radius increases in proportion to the square root of the current in the case of constant current density. The radiant power is assumed that it has "radiant power $\propto$ cross-section of arc x radiant power density (almost constant) $\propto$(arc radius)^2 $\propto$ current". Therefore, the radiant power is expressed such as $\Phi \propto I^{1.0}$. This result is very close to the result of current parameter, 1.06, in this experiment.

8. Summary

In this paper, the number density and the radiant power density as a function of the temperature emitted from the DC horizontal short free arc discharge in air mixed tungsten vapor near 50A is calculated, and also, the radiant power, the radiant efficiency, the radiant energy, temperature, radius of free arc are measured and discussed by using a radiant power meter and a spectroscopy. The result is indicated below:

(1) It was calculated that the radiant power density with continuous and line spectrum of W I was more than 100

times as big as it of nitrogen and oxygen when the temperature was less than 10,000K. The total radiant power density in the tungsten mixture range up to 5 % is estimated to be about 3×10^9 W/(m^3 sr) at 6,000 - 10,000 K in temperature, 300 nm - 30 μm in wavelength region.

(2) The radiant power, Φ (W)(300 nm-30 μm), in the case of the point light source of radiant power emitted from DC horizontal short free arc discharge mixed tungsten vapor as a function of current was measured to be 860 W (30 A), 1,480 W (50 A), 2,100 W (70 A), and increases in proportion to the 1.06th power of the current.

(3) The radiant energy Φ_E (kJ)(300 nm-30 μm) in the case of the point light source of radiant power emitted from DC horizontal short free arc discharge mixed tungsten vapor as a function of electrical in-put energy is 27 kJ (35 kJ), 35 kJ (45 kJ), 43 kJ (55 kJ), and increase in proportion to the 1.06th power of the in-put power.

(4) The radiant efficiency is extremely high level to be about 80 % as white light. This value is considered as a champion data, because it is doubly higher than gases only.

(5) The temperature of free arc mixed tungsten is estimated about 9,000 K at 30 - 50 A and 6,400 K at 70 A by using line pair method. However, the radiant power density of them is same value due to the calculation.

(6) When the current increases, the effect of arc expanse to radius direction is stronger than increment of temperature in the case of free arc. It is considered that the energy increment of arc becomes the increment of radius, because there is no limitation of the wall for radius.

(7) The radiant power increases in proportion to the 1.06th power of the current. This power value of 1.06 is about half of that of the wall-stabilized arc. Because the free arc doesn't have the restriction of radius, the radius increases to expand when the current increases.

(8) The arc radius increases in proportion to the square root of the current in the case of constant current density. The radiant power is expressed such as $\Phi \propto I^{1.0}$. This power result of 1.0 is very close to the result of current parameter, 1.06, in this experiment.

(9) In the case of 70A, while the radius is extremely expanded, the radiant power density is same value at the smaller current up to 50 A. Therefore, the result of relation between the radiation and the current in the range of 30, 50, and 70 A could be same.

In the future, we will research the effect of the radiant power in the high current region, in various gases, and also the degradation of materials due to radiant power and the application for hazardous wastes.

Acknowledgements

The authors thank Prof. I.Miyachi of Aichi Institute of Technology, Prof. Y. Yokomizu of Nagoya University, Prof. Y. Tanaka of Kanazawa University, Mr. K. Ikeda and Dr. M. Iwata of CRIEPI for his fruitful suggestions and Mr. J. Mizuno, Y. Yamaguchi, Y. Uenishi, and K. Kanda belonging to the High Current, Power and Energy Laboratory of Chuo University for their experimental efforts. This research was supported by High-Tec Project on High Temperature Plasma by The Institute of Science & Engineering of CHUO University, and Japan Society for Promotion of Science.

Reference

[1] T. Inaba, T. Iwao, Trans.IEEE-DEI, Vol.7, No.5, pp.684-692, 2000.
[2] T. Iwao, H. Miyazaki, T. Hayashi, T. Hirano, T. Inaba, Vacuum 59, pp.88-97, 2000.
[3] T. Iwao, H. Miyazaki, Y. Kanazawa, H. Yoshida, T. Inaba, IEEJ, GID-01-10, 2000
[4] T. Matsumura, Y. Yokomizu, Y. Tanaka, Journal of IAPS, Vol. 5, pp.10-16, 1997
[5] National Institute of Standards and Technology, U.S.A, http://physics.nist.gov/, 1999
[6] CfA AMP Atomic and Molecular,
http://cfa-www.harvard.edu/amdata/ampdata/ampdb.shtml, 2000
[7] Y. Liu, Y. Kanazawa, T. Iwao, H. Yoshida, H. Aoki, H. Shindo, T. Inaba, Trans. MRSJ, Vol.25, pp.381-384, 2000

Treatment of Hazardous Wastes by DC High Temperature Arc

T. Inaba[1], Y. kubo[1], Y. Liu[1], N. Furuta[2], and T. Iwao[3]

[1] *Department of Electrical, Electronic, and Communication Engineering, Chuo University, Tokyo, Japan*
[2] *Department of Applied Chemical Engineering, Chuo University, Tokyo, Japan*
[3] *JSPS Research Fellow, University of Minnesota and Chuo University, Minneapolis, USA*

Abstract

The temperature of the DC thermal plasma arc discharge is discussed, and examples of the waste treatment for the inorganic compounds such as fly ash, asbestos, and for the organic compounds such as the toxic Dioxins and benzene gas by using the DC plasma arc discharge are shown. In addition, the plasma treatment by using a radiant power emitted from the DC plasma arc discharge is also shown as another new kind of ones.

1. Introduction

The problem of the disposal of hazardous wastes has become very important in recent years. Plasma treatment is being developed and tested for incinerator ash, low level radioactive wastes, industrial and biomedical wastes, etc. by industrial companies and municipalities over the world. The high current plasma arc can generate ultrahigh temperatures, highly intense radiation, and high heating power. The plasma torch is one of the very effective heating devices. The plasma arc heating technology is very appropriate and essential for plasma treatment to protect the environment and keep human health[1-3]. In this paper, the principles are discussed about the temperature of the plasma arc evaluated by the calculation and the Line Pair Method, and then examples are shown about waste treatment such as asbestos, fly ash, toxic Dioxins, and Benzene by using DC high temperature arc.

2. DC Plasma Arc Discharge

2.1 Plasma Torch of Transfer Type

The radial temperature distribution of a transfer type of plasma torch is shown in Fig.1[4]. It is estimated that the central temperature T_0 is more than 14,500 K at plasma current I=150 A, gas flow-rate F=12 L/min(Normal), appearance plasma length L_a=5cm and appearance plasma position X_a=0[5,6]. T_0 decreases with the appearance plasma position, X_a, and decreases with the radius *R(T).* At any appearance plasma position, the radial temperature, *T(r),* decreases with the radius, r, because the radial temperature gradient is owing inversely to the radius times the thermal conductivity.

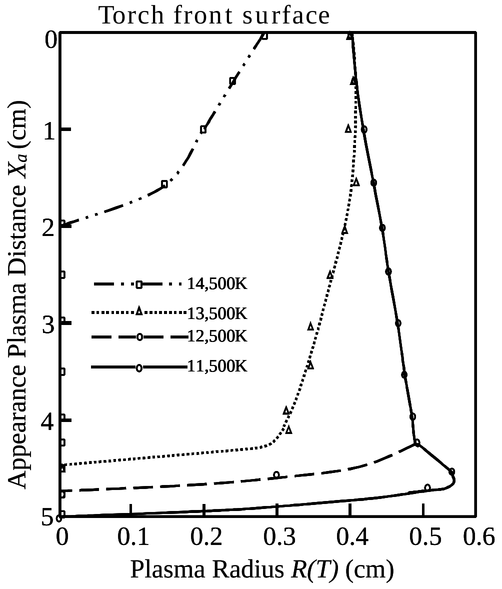

Fig.1 Axial and Radial Temperature Distribution of Torch Plasma (La=5cm)

2.2 Plasma Torch with Hollow Cathode

The plasma torch with a hollow cathode is shown in Fig.2. The temperature of the DC thermal plasma arc discharge with the hollow cathode of 50~150A in current and 0.02~0.1 MPa in pressure in the argon is measured to be higher than 8,000K at the middle point between electrodes according to Line Pair Method [7,8] as shown in Fig.3. The gap length between the electrodes was 5mm. The figure of the plasma is changed with the current and the pressure of the working gas. In argon gas, the radius of the plasma was thicker, if the pressure was lower.

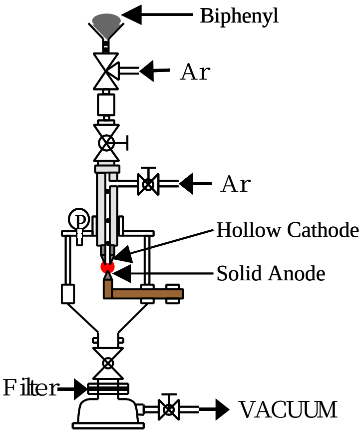

Fig.2 Hollow Cathode Torch

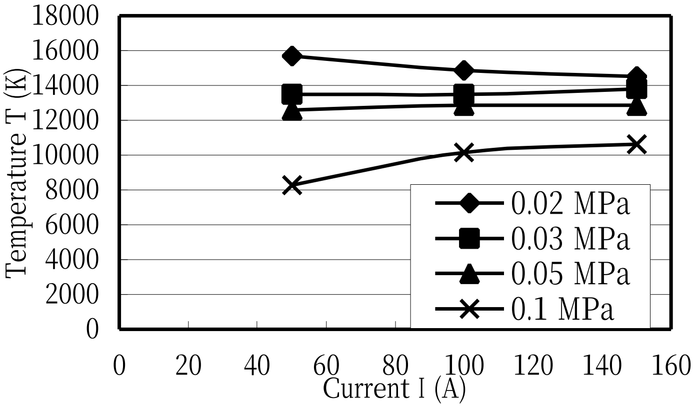

Fig.3 Plasma Temperature

3. Plasma Treatment for Inorganic Compound

3.1 Asbestos

The Environmental Protection Agency has declared the asbestos fibers to be a known human carcinogen, which can cause cancer. Consequently, the asbestos fiber thermal insulators are being replaced by non-hazardous fibers as shown in Fig.4. Million of tons of replaced original asbestos fiber thermal insulators as shown in Fig.5 are in storage. The plasma treatment of the asbestos results in the formation of a hard coating on the surface. The surface of the molten asbestos becomes a hard shell in 6 Mohs without needlelike fibers. Therefore, the asbestos can be transformed into safe materials for human health.

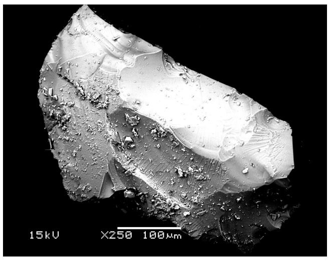

Fig.4 Plasma Molten Slag treated from Asbestos

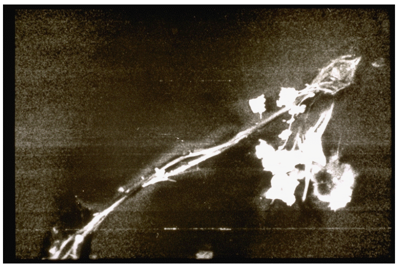

Fig.5 Original Asbestos

3.2 Fly Ash

Figure 6 shows the DC thermal plasma arc discharge generated by the plasma torch of the transferred type. Figure 7 shows the appearance of non-treatment fly ash and molten slag obtained by cooling in a still atmosphere after plasma treatment. By DC arc plasma, the molten slag from the fly ash protects the environment from heavy metal pollution. However, if the slag will be buried in the ground it will be exposed in an acid rain in the future. The heavy metal elements may ooze out again into the soil. In this experiment, solubility test of the molten slag by changing pH at 1,4,7 and 9 by using a nitric acid was investigated. The slag ground under 0.1mm in diameter was compared with original fly ash[9]. Then, the effects of the particle diameter on the solubility is investigated. The test was examined at pH1. The solubility test was examined in 6 hours stirring a solution. The solubility condition was 10ml/g. The analysis method was ICP-MS and ICP-AES. The plasma torch of the transfer type was used in this experiment to generate the DC thermal plasma arc discharge. Atmosphere in the furnace is argon at 0.1MPa. Figure 8 shows pH dependency of the solubility test result. The ground slag prevents to be dissolved in water rather than the original fly ash. The acid rain's pH value is about 4.5 in Japan now. However, the acid fog’s pH will be expected more severe or smaller number of pH than that. Our result was safe enough in pH4 compared with drainage standards by the Prime Minister’s Office in Japan. It is a little bit safer for the Environment Recommendation Values: ERV. The effect of the particle diameter can be expected for the ground slag. The surface area facing to the solution increases, if the slag is ground, or even if its weight is still held. Therefore, the solubility will increase if the particle diameter decreases, when the hazardous components are contained uniformly in the slag. However, when the hazardous components are accumulated only on the surface of the slag, the solubility level is not changed for grinding the slag. Concretely the lithophile elements (A) such as Cr are the former and the chalcophile ones (B) such as Pb are the latter in our experiment as shown in Fig.9, which indicates the particle diameter should be not less than 5mm but larger than 8mm in case of pH1 in order to satisfy the drainage standards.

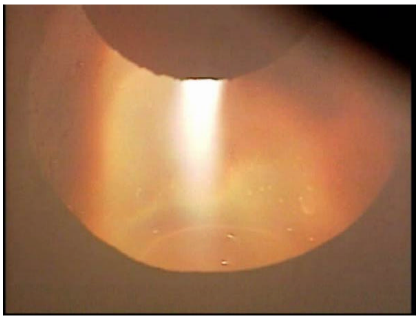

Fig.6 DC Thermal Plasma Arc Discharge

Fig.7 Appearance of Non-treatment Fly Ash (left), and Molten Slag obtained by Cooling in a still Atmosphere after Plasma Treatment (right).

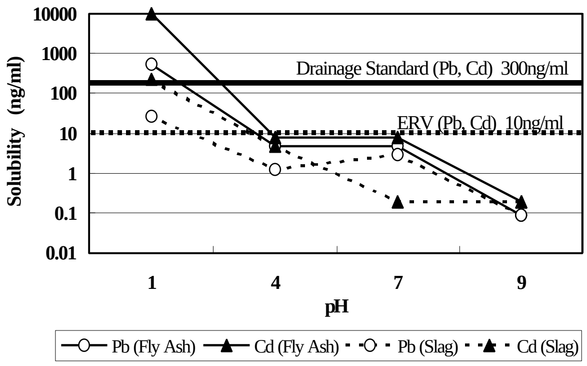

Fig.8 pH dependency of Solubility test result

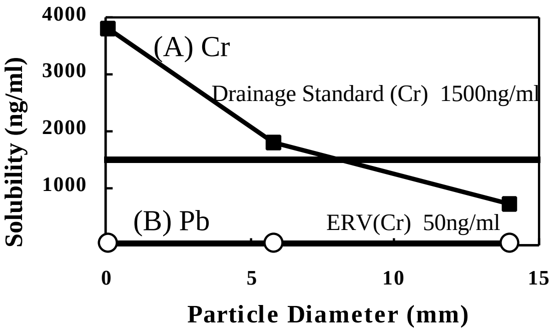

Fig.9 Influence of diameter of ground slag on solubility at pH1

4. Plasma Treatment for Organic Compound

4.1 Dioxins

The Dioxins are the most terrible toxic chemicals in the world. They are very stable to acid through alkalis. The half-lives of the Dioxins in environment are very long. Nevertheless, the Dioxins can be easily decomposed under temperature higher than 1,000K[10]. The Biphenyl was selected as the test chemical, because it has two aromatic rings as same as the toxic Dioxins. The pictures of decomposed Biphenyl are shown in Fig.10. The residue was collected with a filter during the experiment. The filter was analyzed by Laser-Raman-Spectrometry. Amorphous-carbon, the most possible decomposing product from the biphenyl, was detected as shown in Fig.11. The amorphous-carbon proved that the DC thermal plasma arc discharge with the hollow cathode could destroy the aromatic ring. Therefore, the method can be applied to decompose the kind of the Dioxins. The temperature and fluid conditions in the chamber are calculated and the effect of decomposing a particle through the plasma region is recognized[8].

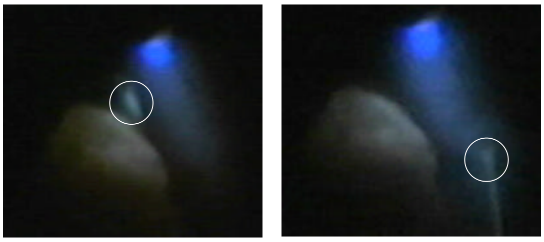

(1) 0ms (2) 2ms

Fig.10 Decomposed Biphenyl

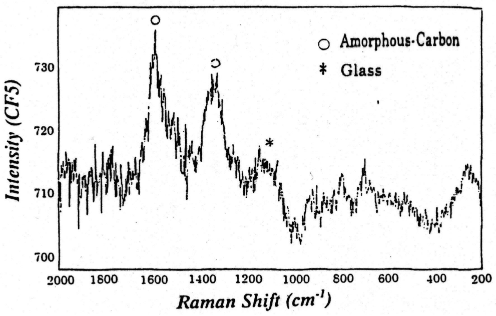

Fig.11. Laser-Raman Spectrometry

4.2 TBT

The tri butyl tin compound (TBT) as shown in Fig.12 was used at the painting of surface of the ships to avoid some shellfish in Japan since the middle 1950's. Nowadays, the TBT is prohibited to paint it because the TBT has the toxic chemicals in Japan. However, there are some countries using TBT even now. In this experiment, the biphenyl was decomposed by the dc plasma torch of the transfer type. And also, the biphenyl in a paint that has alkyd resin was decomposed. It is close to a ship's bottom paint. As a result, the biphenyl is decomposed about 99.995%[11,12] as shown in Fig.13 and Table 1, and a metal oxidation substance appeared . Therefore, it could be separated into carbon and tin.

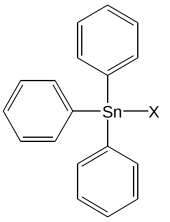

Fig.12 TBT

Table 1 Detection of Biphenyl

Substance	Amount (µg/g)
Biphenyl	35

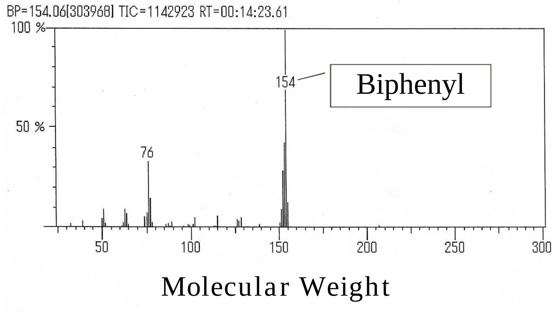

Fig.13 Detection of Biphenyl

4.3 Benzene and Chlorobenzene Gas

Benzene and Chlorobenzene gas can be treated by using free arc. It is possible to analyze the treated Benzene(100%=1,000,000ppm) after the experiment in a closed chamber in condition of 50A in current, 500s in duration and ca. 0.1MPa in pressure. Even the non-conducting materials can be decomposed in high performance by using the tungsten electrodes. The Benzene and Chlorobenzene gas GC/MS Chromatograms are shown in Figs. 14 and 15. The apparent 45.9% of benzene gas can be decomposed. After decomposition of benzene gas, many compounds such as the methane, the acetylene, the ethylene, the ethane, and the propylene are generated. The apparent 93.6% of chlorobenzene gas can be decomposed. After decomposition of chlorobenzene gas, the benzene and the methane are generated. The aromatic compounds are decreased, because the air is contaminated in the free arc equipment in the closed furnace. The recombination of the treated gases may not be made due to the almost constant pressure in the chamber after the experiment[12].

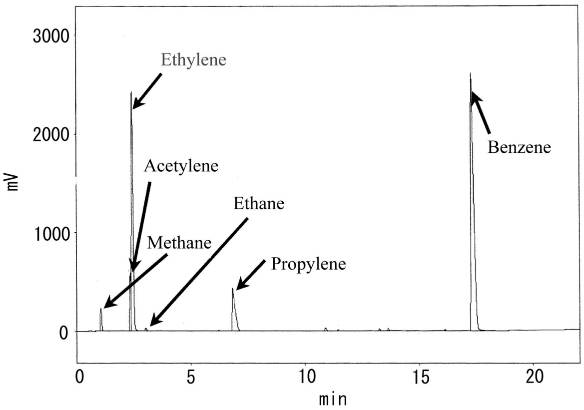

Fig. 14 Benzene Gas GC/MS Chromatogram

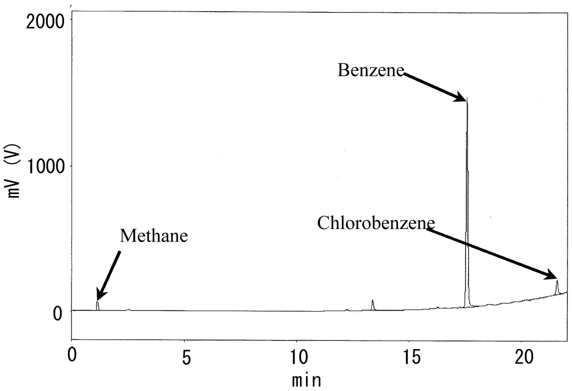

Fig. 15 Chlorobenzene Gas GC/MS Chromatogram

4.4 Plasma Treatment by Radiant Power

The DC plasma arc discharge has mainly two kinds of energies, heat and radiation. It is considered that the radiant power is about 50% of the in-put electric power at the plasma torch of transfer type at 150A[13]. It is considered as a loss, so far, because the heating and melting technology is not so important for the radiant power. However, the radiant power emitted from the DC thermal plasma arc discharge is always generated when the DC plasma arc is generated. Therefore, the radiant characteristic should be used as well as the heating one. Figure 16 shows the paints treated by a radiant power at 100A, for about 1 minute and by a gas burner for 5 minutes. Figure 17 shows the radiant power of the high temperature air with tungsten(5%) at 6,000K[14]. It has a lot of UV rays. Therefore, it could be used to treat the hazardous wastes with UV and IR rays.

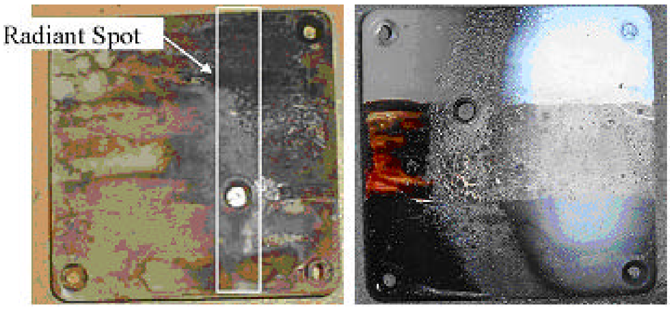

(1) By Radiant Power (2) By Gas Burner

Fig.16 Treatment for Paint

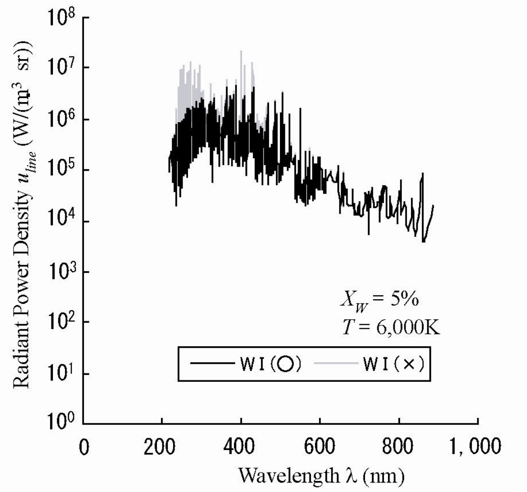

Fig.17 Radiant Power with Tungsten(5%) Air

5. Summary

(1) The radial temperature distribution in the torch plasma becomes flatter and reaches a radially constant temperature model with increment of the appearance plasma position toward the opposite flat electrode. The temperature of the surrounding surface of the torch plasma is thousands of degrees and it forms a distinct boundary of the temperature.
(2) The temperature of the hollow cathode argon plasma of 50~150A in current and 0.02~0.1 MPa in pressure is measured to be higher than 8,000K at the middle point between electrodes according to Line Pair Method.
(3) The plasma molten slag from fly ash buried under ground keeps excellent water tightness even if it is exposed to the acid rain near pH index of 4.
(4) The surface of the molten asbestos becomes a very hard shell in 6 Mohs without needlelike fibers. Therefore asbestos can be transformed into safe materials for human health by the plasma.
(5) The amorphous-carbon captured with the filter settled at the outlet proved that the hollow cathode plasma could destroy the aromatic rings. Therefore, the method can be applied to decompose Dioxins.
(6) The benzene and chlorobenzene gas of 100%(1,000,000ppm) is decomposed to 45% and 99% respectively by using free arc at 50A in current and 600s in duration time.
(7) The radiant power can treat the paint and has a lot of UV rays. Therefore, it could be used to the hazardous wastes with UV and IR rays.

Acknowledgments

The authors wish to thank Prof. M. Endo, Dr. M. Ohata, Mr. Y. Watanabe, Mr. M. Nagano, Mr. T. Hosoi, Mr. K. Morita, Mr. H. Miyazaki, Mr. Y. Kanazawa, Ms. Y. Kaneko, Mr. Y. Yamaguchi, Ms. Y. Inoue, Mr. Y. Honsho, Mr. J. Ishii, Mr. J. Mizuno, and Mr. T. Beppu of Chuo University for their fruitful suggestion and cooperation. This research was supported as a High-Tech Project on the “Plasma Treatment for the hazardous wastes by using Ultra High Temperature” by the Institute of Science and Engineering of Chuo University and Japanese Ministry of Education, and Japan Society for Promotion of Science.

References

[1] T. Inaba, T. Iwao, IEEE, Trans. DEI, **7**(2000), 684-692
[2] T. Inaba, M. Nagano, M. Endo, Trans. IEEJ, **117-D**(1997), 831-838 (Japanese), or Electrical Engineering in Japan, **126**(1999), 73-82
[3] T. Iwao, Y. Liu, N. Furuta, T. Inaba, Proc. of ISPC 15, Vol.V, Orleans, France, July, 2001, 2037-2043
[4] T. Iwao, T. Inaba, Vacuum, **65**(2002), 299-304
[5] T. Iwao, T. Ishida, T. Hayashi, M. Endo, T. Inaba, Proc. of ISPC 14, Prague, August, 1999, 373-378
[6] T. Iwao, H. Miyazaki, T. Ishida, Y. Liu, T. Inaba, Trans. ISIJ, **40**(2000), 275-279
[7] Y. Liu, Y. Kanazawa, T. Iwao, H. Yoshida, H. Aoki, H. Shindo, T. Inaba, Trans .MRSJ, **25**(2000), 381-384
[8] Y.Liu, H.Qi, T.Iwao, H.Shindo, T.Inaba; Vacuum, **65**(2002), 463-468
[9] N. Furuta, T. Hosoi, M. Ohata, T. Inaba, Int. Workshop on Use of Incinerator Ash, Dundee, U.K., March, 2000, 67-75,
[10] M. Hiraoka, S. Okajima, Kankyo newspaper publishing Co., 1998 (Japanese)
[11] Y. Yamaguchi, Y. Honsho, T. Iwao, T. Inaba, Proc. of IEEJ National Convention, 1-151, March, 2001 (Japanese)
[12] Y. Yamaguchi, T. Iwao, T. Inaba, Trans. IEEJ, **122-A**(2002), 544-550 (Japanese)
[13] T. Iwao, H. Miyazaki, T. Hayashi, T. Hirano, T. Inaba, Vacuum, **59**(2000), 88-97
[14] T. Iwao, Y. Inoue, Y. Yamaguchi, J. Mizuno, T. Inaba, Technical Meeting of IEEJ, ED-02-44&SP-02-10&FTE-02-16, June, 2002 (Japanese)

Emission Spectroscopy of a Supersonic Plasma Jet with Secondary Discharge during Deposition of c-BN

Eric Runde[1], Jami McLaren[1], J.V.R. Heberlein[1]

[1]*Department of Mechanical Engineering, University of Minnesota, Minneapolis, Minnesota, U.S.A.*

Abstract

An emission spectroscopy set-up has been used to qualitatively study the reactant mixing and the plasma jet chemistry during deposition of h-BN/c-BN. Two-dimensional images have been produced showing spatial distributions of the relative emission line intensities of the possible growth precursors of boron nitride. These distributions have been studied to better understand the effect of mixing in the jet and in the boundary layer in front of the substrate on the quality and growth rate of the produced boron nitride films.

1. Introduction

Cubic boron nitride (c-BN) is the second hardest intrinsic material to diamond, with a Vicker's hardness of 50-70 GPa. However, unlike diamond, c-BN remains stable in air to extremely high temperatures when used with ferrous materials. Therefore, considerable interest lays in the future development of c-BN as a machine tool coating or optical device thin film. Cubic boron nitride thin films have been produced with both physical and chemical vapor deposition techniques using different precursors including B_2H_6, BCl_3, TMB, and BF_3 [3-5].

Optical emission spectroscopy is a powerful plasma diagnostic that can non-intrusively gather a large amount of information about the plasma. The optical emission lines of various species in a plasma originate from the electronically excited states of these species. To conclude from atomic line emissions on the densities of atomic species would require making assumptions on the thermodynamic state or knowing the excitation rates [1]. Because the supersonic plasma jet is far from equilibrium, we qualitatively determine the relative concentration of species in the jet by measuring the emission line intensities of various species.

In this work, thin films containing a mixture of hexagonal boron nitride (h-BN) and c-BN have been deposited at high rates on silicon substrates by dissociation of boron trifluoride (BF_3), hydrogen (H_2), and nitrogen (N_2) in a supersonic d.c. plasma jet. An arc-produced Ar-N_2 plasma has been expanded through a supersonic nozzle into a chamber kept at a relatively low pressure (see Fig. 1). Boron trifluoride and H_2 are injected into the Ar-N_2 plasma in the expansion portion of the converging-diverging nozzle. Optical emission spectroscopy was used to study the degree of mixing of the reactants within the supersonic arcjet. In particular, atomic hydrogen and nitrogen concentrations were observed and compared to the location of deposits on the substrate.

2. Experimental details

The film deposition is performed within a low-pressure vacuum chamber pumped by a 6,000 l/min, two-stage mechanical pump. The chamber pressure can be maintained at 0.26-0.39 kPa (2-3 Torr) during deposition. An Ar-N_2 d.c. plasma jet is generated using a radiation-cooled torch developed by NASA Lewis for space propulsion. Figure 1 shows a schematic of the convergent-divergent nozzle that generates a supersonic jet. The d.c. arc strikes between the cathode and thoriated tungsten nozzle, which serves as the anode. The plasma then passes through

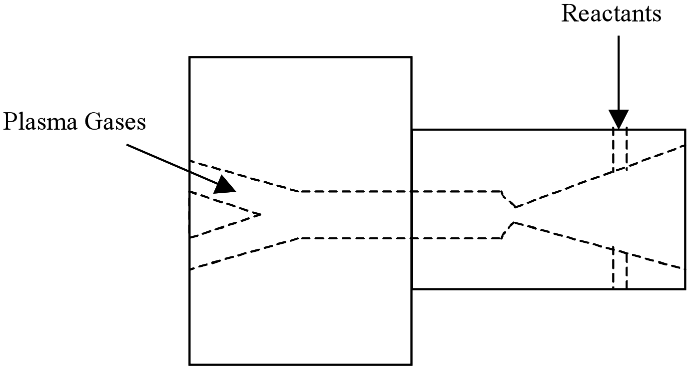

Figure 1: Schematic of convergent-divergent nozzle

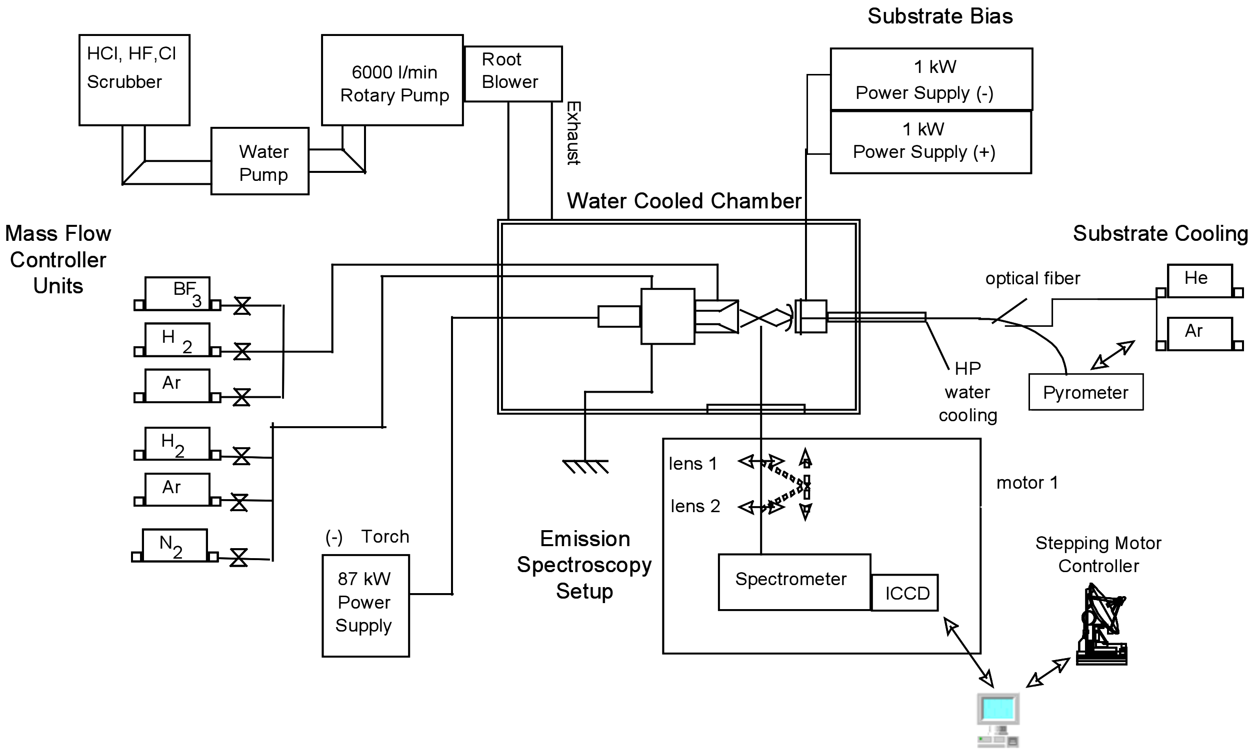

Figure 2: Experimental set-up

the converging-diverging portion of the nozzle, expanding in the vacuum chamber to supersonic speeds. The reactant gases (BF_3 and H_2) are injected in two locations, from above and below, through 200 µm holes in the expansion zone of the nozzle. Figure 2 describes the set-up, while Table 1 shows typical deposition conditions used during these experiments.

Films were deposited on 25 mm Si (100) wafers mounted on a water-cooled Cu substrate holder. The backside substrate temperature was measured with a quartz optical fiber connected to a pyrometer using 950 nm radiation. A He/Ar gas mixture flowing between the substrate and the substrate holder was varied to maintain the substrate temperature within 10 °C during deposition. A secondary discharge is established between the substrate and the grounded torch by applying either a positive or negative bias to the Si wafer. The bias is applied by using two high-voltage DC power supplies in conjunction with a bipolar pulser and function generator that allows for constant or pulsed DC biasing.

Transmission Fourier infrared spectroscopy (FTIR) has been used to determine the nature of the bonds present in the films. A Nicolet Series II Magna-IR System 750 with Omnic software is used for analysis. The background is taken with a 25 mm Si (100) wafer subjected to similar experimental conditions without deposition. For h-BN, two different frequencies are observed within the fingerprint region at 1380 cm^{-1} and 780 cm^{-1}. The former is known to represent the in-plane transverse optical (TO) mode, while the latter represents the out-of-plane TO modes. Cubic boron nitride, on the other hand, has an absorption band (TO mode) located at or around 1065 cm^{-1}. Further analysis has taken place using micro x-ray diffraction to analyze the crystalline nature of the film and scanning electron microscopy to observe the top and cross-section morphology.

Table 1. Deposition conditions for BN

Power (kW)	3-5
Pressure (kPa)	0.26-0.39
Ar (slm)	13
N_2 (slm)	0.25-1.3
BF_3(sccm)	5-30
H_2 (sccm)	5-60
Substrate Temperature (°C)	700-950
Negative bias (V)	Pulsed or DC

Emission spectroscopy measurements were performed using a Jobin-Yvon ISA 0.32m spectrometer with an 1800 groove/mm grating and a Princeton Instruments ICCD or TE/CCD detector to collect spectra. Two collimating lenses project an image of the plasma jet, reduced 0.33 times and oriented perpendicular to the entrance slit, onto the entrance slit of the spectrometer. The CCD array allows us to measure a radial profile with a resolution of approximately 0.10 mm/pixel. The entire system is mounted on a table that may be moved by a stepper motor allowing measurement of different sections of the plasma jet in the axial direction. With an entrance slit of 25 μm and a stepper motor resolution of 5 μm, we have a spatial resolution of 85 μm in the axial direction.

To determine the relative concentration of different chemical species in the plasma jet the intensities of desired spectral lines are determined at each radial location and the continuum is subtracted. The integrated intensities of the emission lines in question are then divided by the integrated intensity of a specific Ar line to qualitatively determine the relative intensity of the species at each radial and axial position of interest.

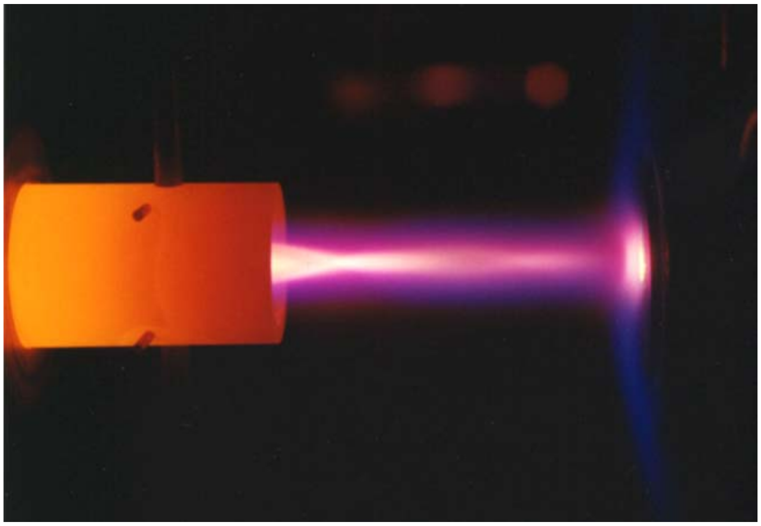

Figure 3: Image of plasma jet in operation

Table 2. Optical emission lines used in relative intensity calculations

Species	$E_i - E_j$ (cm^{-1})	Peak Position (nm)
Ar	93144 – 106237	763.51
Ar	10560 – 125220	506.01
N		496.4
H_α	82260 – 97492	656.3

3. Results and discussion

The convergent – divergent nozzle used in this experiment allows for supersonic flow (M=2-5) conditions that will strongly influence the mixing and eventual growth in this chemical vapor deposition process. As Fig. 3 demonstrates, the plasma jet is made up of several diamond shock waves where compression lines cause a large increase in thermal energy followed by a subsonic region. Then, in the boundary layer, a bow shock develops where a sudden decrease in velocity from supersonic to subsonic flow causes sharp increases in temperature and pressure. This sharp increase in temperature and pressure works to compress the boundary layer, causing sharper chemical and thermal gradients resulting in stronger diffusion to the substrate surface.

Table 2 shows the optical emission lines we used to characterize our plasma. Figure 4 shows an

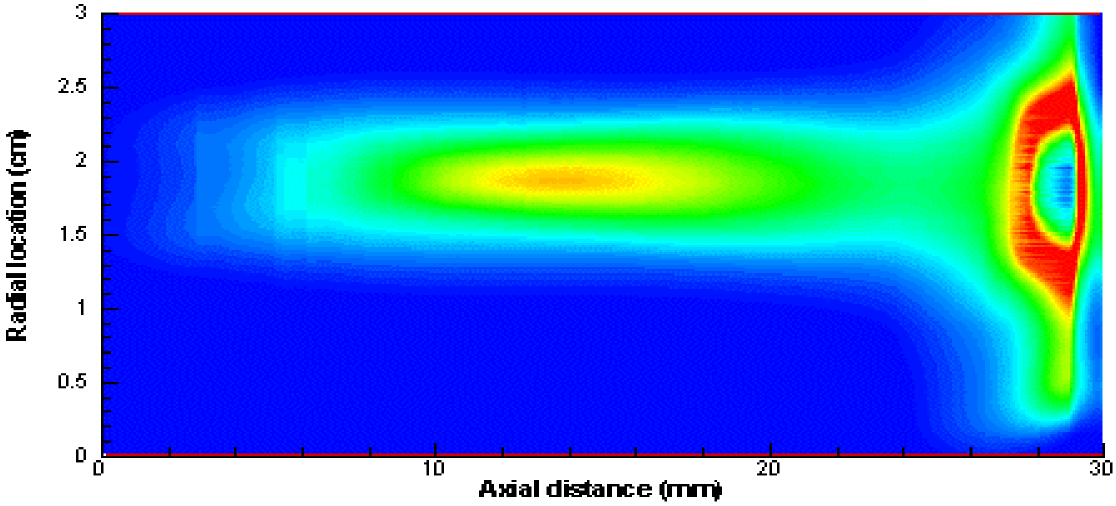

Figure 4: Integrated intensity plot of Ar (763.51): Torch operating at 2.8kW, 14 slm Ar.

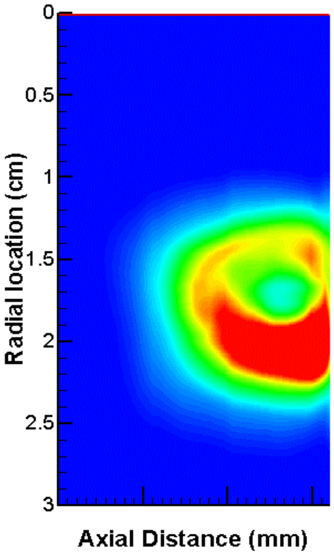

Figure 5: Relative integrated intensity plot of H_α/Ar: Torch operating at 2.8 kW 12 sccm H_2, 14 slm Ar.

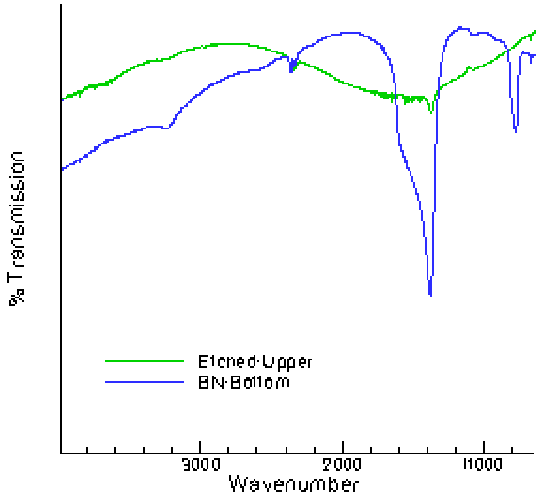

Figure 6: FTIR spectra showing etched/deposited areas

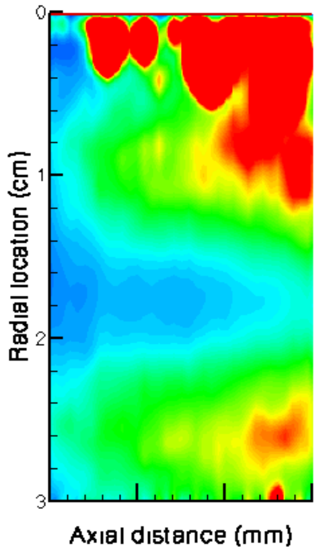

Figure 7: Relative integrated intensity plot of N/Ar: Torch operating at 4 kW, 1.25 slm N_2, 13 slm Ar.

integrated 2-D plot of the radial intensity of the 763.51 nm Ar line as a function of axial distance. From low to high axial displacement, the areas of higher intensity represent higher temperature and pressure characteristic of diamond shock waves in the jet and the boundary layer shock zone, respectively.

Figure 5 shows the intensity of the H_α line over the 763.51 nm Ar line shown in Fig. 4 in the boundary layer. This plot reveals a greater relative concentration of atomic H in the boundary layer near the bottom of the substrate. This distribution is consistent with the appearance of the deposited film from the experiment in question as the film is etched in the upper region where a smaller relative amount of atomic hydrogen is assumed. Therefore, these results would agree with thermodynamic calculations stating that solid BN cannot be deposited in an Ar-N_2-BF_3 environment. Only when H_2 is present does the following reaction become preferred [6]:

$$2BF_3 + N_2 + 3H_2 \rightarrow 2BN + 6HF$$

The FTIR results shown in Fig. 6 demonstrate a BN deposition in the lower portion of the substrate with only bare/etched Si in the upper portion. Judging from these results, we can assume that there was more F present, due to a lack of H, on the upper portion of the substrate resulting in an etched area without deposition. These results agree with previous reports of no film deposition without H_2 added [4].

Spectra taken with lower torch power (2.7 kW) and lower N_2 flow rates (0.25 slm) indicate a relatively large amount of N_2 and no detectable atomic N. However, spectra taken with higher torch power (4 kW) and N_2 flow rates (1.25 slm) did reveal atomic N emission, confirming that the degree of molecular nitrogen dissociation is higher under these conditions. Figure 7 shows the integrated intensity of the 496.4 nm N line over the 506.01 nm Ar line. This plot reveals that the relative concentration of atomic N, an essential precursor in the formation of BN, is higher in the outer regions of the plasma jet. The thickness of the deposited film in this experiment is larger around the edges of the substrate, a result consistent with the

N concentration in Fig. 7. However, we cannot be certain whether this was caused by more atomic N present or less F present allowing for a decreased amount of etching.

Comparing the relatively uneven intensities of both H and N emission spectra within the jet, it appears that the high velocities result in stratified layers preventing even mixing of the reactants. This finding would agree with our previous work examining the relative reactant concentration during boron carbide deposition [2]. However, further work is needed to determine why atomic N/Ar relative concentrations are asymmetric when N_2 is injected together with Ar upstream of the supersonic nozzle.

4. Conclusions

Using optical emission spectroscopy, we analyzed the relative integrated intensities of atomic hydrogen and nitrogen during deposition of BN thin films. The emission data pointed to poor mixing conditions present in the supersonic plasma jet, which are consistent with uneven film deposition and etching likely due to low localized atomic hydrogen content. These findings show that two-dimensional spatially resolved emission spectroscopy is useful in examining the mixing quality within a supersonic plasma jet during a chemical vapor deposition process.

5. Acknowledgments

This work was supported by the U.S. Department of Energy, Basic Energy Sciences, grant no. DE-FG02-85ER-13433, and by the NSF IGERT program on Nanoparticle Science and Technology, grant no. 0114372.

References

[1] Y. Liao, C.H. Li, Z.Y. Ye, C. Chang, G.Z. Wang, R.C. Fang. *Diamond and Rel. Mat.* **9** (2000) 1716-1721.
[2] O. Postel, J.V.R. Heberlein. *IEEE Transactions on Plasma Science* **27** (1999) 100-101.
[3] T. Yoshida. *Diamond and Related Materials* **5** (1996) 501-507.
[4] W.J. Zhang. S. Matsumoto. *Chemical Physics Letters* **330** (2000) 243-248.
[5] S. Khizroev, D. Litinov. *Applied Physics Letters* **73** (2001) 353-355.
[6] W. Kalss, R. Haubner, B. Lux, *Diamond and Rel. Mat.* **7** (1998) 369-375.

Single shot time resolved spectroscopy on the low voltage vacuum arc

G. Pavelescu[1], C. Fleurier[2], D. Hong[2], V. Braic[1], F. Gherendi[3],
M. Braic[1], D. Pavelescu[4], J.P. Bauchire[2], M. Balaceanu[1], G. Dumitrescu[5]

[1.] National Institute for Optoelectronics, Bucharest-Magurele, Romania
[2.] GREMI , Université d'Orléans, Orléans, France
[3.] National Institute for Lasers, Plasma and Radiation Physics, Bucharest-Magurele, Romania
[4] "Politehnica" University of Bucharest, Romania
[5.] Electrotechnical Institute, ICPE, Bucharest, Romania

Abstract

Single shot time resolved spectroscopy around current zero on partial unsuccessful interruption of the low voltage circuit breaker was used to analyze the evolution of the vacuum arc plasma. Plasma temperature and electron density were measured during the arcing in order to provide information on the arc reignition phenomena.

1. Introduction

The circuit breaker is an important part of any electrical distribution network, providing protection in the case of a fault. This action involves a set of macroscopic and microscopic processes, essentially based on the separation of contacts parts in which the current to be interrupted circulate. Together with this separation of contacts, an electric arc is created, which must be quickly switched off.

There are several models that describe the arc ignition in vacuum [1]. The most accepted model states that in the moment of the contact separation a melted metal bridge is formed by Joule heating. The heating continues and in the vapour stage, when the voltage is sufficient to initiate the metal vapour breakdown, discharge channels occur. In vacuum, this discharge channels induce explosive vaporization of the cathode, resulting in the formation of the cathode spots. The increase of the current leads to the formation of many discharge channels that attract each other in the middle of the arc column (by electromagnetic force) and repulse each others (by electrostatic force) at the arc roots. If the current increase continues the division of the cathode spots begins and the discharge channels multiply. The reciprocal electromagnetic forces increase and at higher currents the discharge channels get in contact. This is the column mode foot point arc, one of the constricted arc forms. At even higher current (> 10 kA) the column and the foot points are submitted to the pinch effect and the arc goes through the anode spots regime to the intense regime when we have uniform, thin arc column with unique anode and cathode spots.

In the most of low voltage circuit breakers, arc reignition is one of the most critical phenomenon that prevents the devices from performing an efficient short circuit current interruption operation. The aim of this paper is to apply the time resolved spectroscopy method to study the evolution of the arc plasma during the interruption process in a low voltage vacuum circuit breaker. The study presented concerns the behavior of the plasma parameters around current zero (C.Z) in an unsuccessful interruption process.

2. Experimental

The short-circuit current was produced in a special high power installation in order to reproduce exactly the short-circuit regimes developing in low voltage distribution network. The tests were performed for different current values in the range 5 ÷ 50 kA $_{\mathrm{rms}}$, voltage being varied between 200 and 1000 $V_{\mathrm{c.a.}}$. As an experimental model of interrupter a stainless steel vacuum chamber with Cu-Cr electrodes was used (fig.1). In this structure, a strong axial magnetic field was applied, which allows the diffuse arc mode to be maintained even in the case of high currents.

The emission spectroscopy set-up, using an Acton spectrograph and an intensified CCD camera, allowed the spatial and time-resolved investigation of spectra emitted by the vacuum arc plasma. Time resolved spectra were taken at different moments of the arc evolution with the micro-channel plate (MCP) gate of 500 μs.

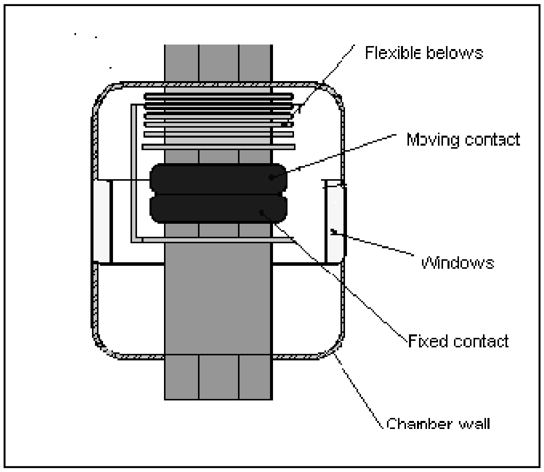

Fig.1 Experimental setup

A number of 16 gates were recorded on a single shot. The gate width was chosen to assure sufficient photon number and to guarantee a correct spectroscopic statistic, taking into account that the measurements are performed in single shot. We assume that changes in arc voltage and current during 1 ms (500 µs gate, 500 µs pause) can be neglected. Since we are not looking at the cathode spots that have lifetime of about few ns we also take for granted that there is no significant evolution in the plasma columns in 1 ms time.

3. Results and discussion

Study of the arc interruption process was applied to the arc regime corresponding to the constricted column mode. This regime, when the anode becomes active during discharge, appears for current values that exceed 15 kA. This mode is undesired for vacuum interruption, due to the strong contact erosion. However, in some critical situations this regime is unavoidable and the functioning of the circuit breaker should not present any failure in such case. In this range of testing currents, unsuccessful interruptions could occur. We will focus in this paper on the partial unsuccessful interruptions (PUI) that was accomplished for current intensity up to 19 kA. In our experiments, the transient recovery voltage slope is 0.28 kV/µs. From the electric arc energy formula: $W_a = \int_0^{t_1} uidt$ we got for the first halfperiod a value of, W_a=8.47 kWs, higher than was obtained in successful interruption [2].

Using single shot time resolved spectroscopy we analyzed the evolution of the arc emission in 16 time sequences, 500 us exposures at 1ms time slices. An example of 15 recorded spectra covering the first and the second half-period of the current arcing time, including the passage through C.Z., is shown in fig 2. The spectrum taken in the moment of CZ is highlited in fig. 2, track 14, where the copper species are also indicated. Time resolved spectroscopy correlates the changes in plasma density with the changes in the arc current. The arc constriction leads to higher plasma densities that can be seen in sequential spectra acquired during the arc development. As a result, the emitted lines are broadened and become again thin after the current maximum, when the plasma is in the expansion phase.

The emitted lines were identified using a code sequence taken from the “SimSpec” program [3], developed for the study of the diffuse vacuum arc emission spectra. However, the code itself could not be used to compute the plasma temperature, because of the important Stark broadening that “SimSpec” does not take into account. Modifications of the code are under work to allow Monte-Carlo simulation fit [3] of such spectra with important Stark broadenings and shifts.

The evolution of some Cu and Cr atomic lines intensities are presented in fig. 3. The intensities confer, in the first quarter of period, an approximate measure of the density evolution, as we shall see later when presenting the plasma temperature calculations (fig.5). For a real density calculation, an absolute calibration of the measure chain is necessary, but impossible to perform due to specific measurement conditions.

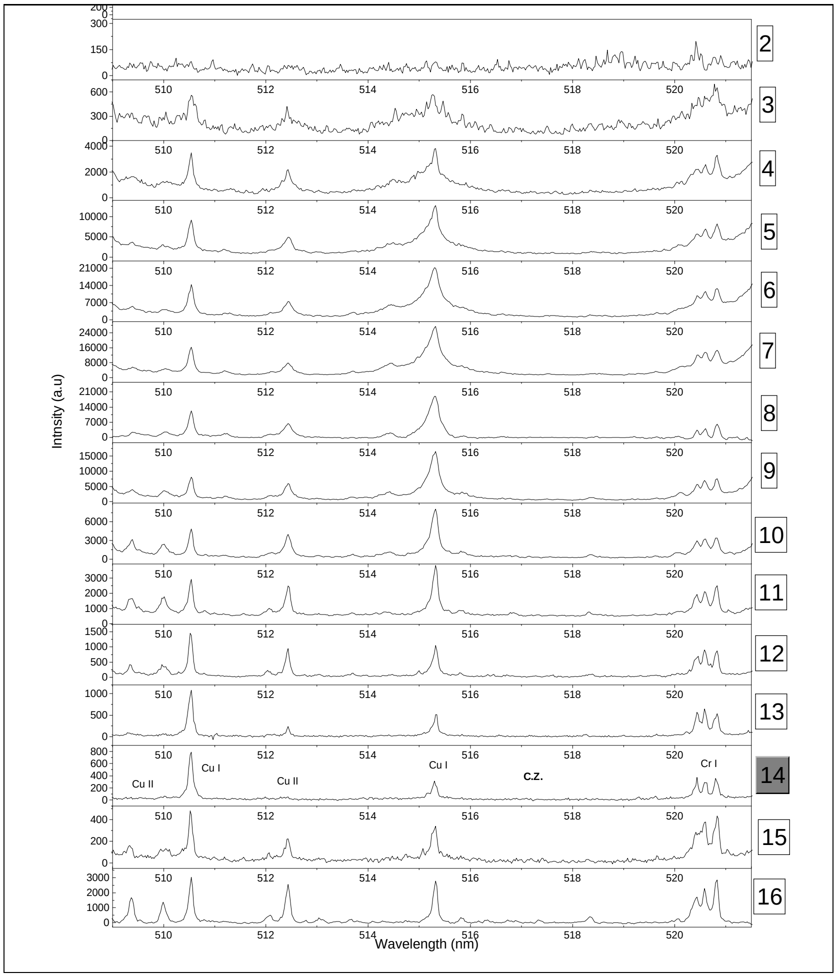

Fig. 2 Time resolved spectra

During the arcing atomic Cu lines (510.55 and 515.32 nm) and atomic Cr lines (520.45, 520.60 and 520.84 nm) are present in all the sequence of spectra. These particular CrI lines belong to an upper level of about 3.38 eV, which is much lower than the thermal movement energy. Some other lines, e.g. Cr atoms (510.35, 515.75, 516.30 and 518.45 nm) or Cu atoms (514.22, 514.41, 515.83 and 520.08 nm) randomly appeared and disappeared during the arc evolution. These lines are either emitted from excited energy levels close to the ionization potential (such being the case of CrI with a ionisation potential of 6.77eV), or disappear because of ionization (mainly in the case of Cu I).

Together with Cu and Cr atomic lines, a lot of Cu ion lines, more than the ones emitted by Cr ions, are present in spectra. The time dependence of the intensities corresponding to the Cr and Cu ionic lines is exemplified in fig. 4. Cu ions were the only ions evidenced after the arc reignition in this spectral region, despite the fact that the electrodes are composed by 50%Cu - 50%Cr alloy. These lead to the supposition that the presence of copper ions, near the C.Z, is responsible for the arc reignition, more than the presence of the Cr ions. This fact is even more obvious when thinking of the relatively low ionization potential for CrI.

The increase of Cu ions lines intensities after CZ indicates that the Cu ions were already present in the electrode gap in the moment of the reignition. The increase of the Cu ions concentration around CZ could be induced by the late charge transfer from ionized stages of Cr (acting like a catalyser for copper ionization). This mechanism is the lowering of the Cu ionization potential in interaction with Cr ions.

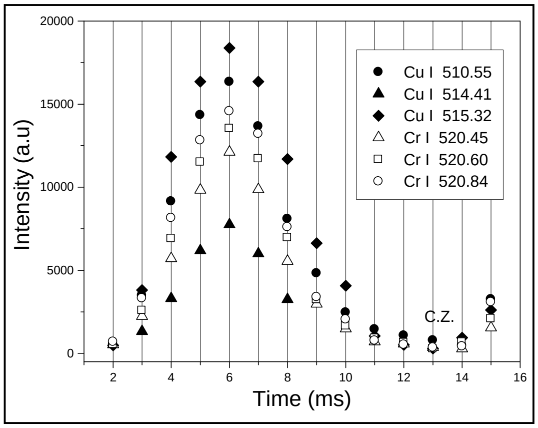

Fig. 3 Intensities of the atomic species vs. time

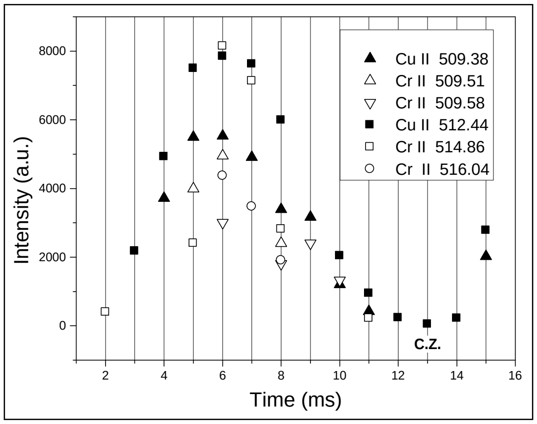

Fig.4 Intensities of the ionic species vs. time

The determination of the arc plasma temperature was based on the Boltzmann graph method, with the assumption of local thermodynamic equilibrium-LTE. The temperature time dependence follows, as expected, the current evolution during the arcing. In the first quarter of period, the temperature increases and it is slightly higher than the temperature in the second quarter period. This is due to the fact that, in the first quarter of period the plasma column develops itself in the interelectrode gap, while after the current maximum it expands in the quenching chamber. The expansion produces an adiabatic component of the plasma cooling that does not exist while the plasma columns are constricted. This can be observed by the slope of the temperature decrease after the current maximum. Plasma temperature value higher than 5800^0K, that was obtained in C.Z., provides a sufficiently excited state to create the conditions for ionization with a lower energy per particle consumption. This can be one of the mechanisms that lead to the arc reignition. Another reignition cause is the higher plasma density in the interelectrode gap in comparison with the case of successful interruption, providing an appropriate breakdown medium.

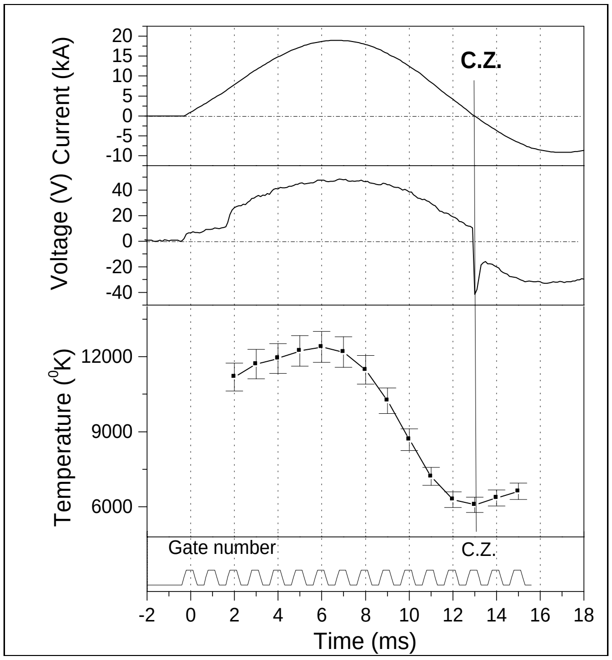

Fig.5 Time dependence of the arc current, voltage and temperature.

The line profiles observed in spectra from figure 2 are lorentzian. Considering that the vacuum arc plasma is neither strongly collisional, nor very dense, we can assume that Van der Waals (pressure) broadening and ion impact component of the lorentzian line profile can be neglected. Thus, we assume that the spectral lines are broadened only by electron interaction and we have a quadratic Stark effect.

According to Griem [6], in LTE conditions, if one knows the line broadening $\Delta\lambda_0$ for a given isolated line at a certain temperature T and electron density N_{e0}, then the electron density depends linearly on the Stark broadening: $N_e = N_{e0} \cdot \frac{\Delta\lambda}{\Delta\lambda_0}$. There is a lack in literature for Stark broadening data of Cu lines; however data exists both for neutral and ionised Cr lines [7].

For determining the electron density, we used a theoretical model for the Cu II lines, and semi-empirical model or the CrI lines, both inspired from the COSSAM astrophysical spectra simulation code [8] which uses the calculations of Gonzales (1995) [7].

According to this model, the quadratic Stark broadening of a line has the semi-empirical form

$$\Delta\lambda = \Delta\lambda_0 + 10^{E_{ldp1} - \frac{2}{3}\log(C4)} \qquad (1)$$

When the quadratic Stark broadening parameter C4 is known

$$\Delta\lambda = \Delta\lambda_0 + 10^{E_{ldp2} + \log\_C4[8]} \qquad (2)$$

as a theoretical model for ions only lines, with a logarithmic quadratic Stark parameter given by

$$\log\_C4 = \log\left(\frac{N_{lo}^2 + N_{up}^2}{Z^2}\right) \qquad (3)$$

In (3), N_{lo} and N_{up} are the populations of the lower, respectively upper energy level of the transition and Z is the ion charge. Eldp1 and Eldp2 (formulas 4 and 5) are the measured, respectively theoretical logarithm of the electron impact de-populations, both depending on the electron density Ne and weakly depending on the electron temperature.

$$E_{ldp1} = 7.7621 + \log(N_e kT) + \frac{5}{6}\log\left(\frac{5040}{T}\right) \qquad (4)$$

$$E_{ldp2} = \log(6 \cdot 10^{-6}\frac{N_e}{\sqrt{T}}) \qquad (5)$$

Because we were using a model that was only tested on astrophysical interest spectra, we took 3 lines into account: CrI 520.8419 (line with known Stark broadening parameter), CuII 512.480 and CuII 509.381 (lines without any known broadening data, but isolated, implying that the theoretical broadening model from eq. 2 should be valid). The electron densities determined for the 3 lines, as well as a polynomial fit of the averaged electron densities (versus time) are presented in figure 6.

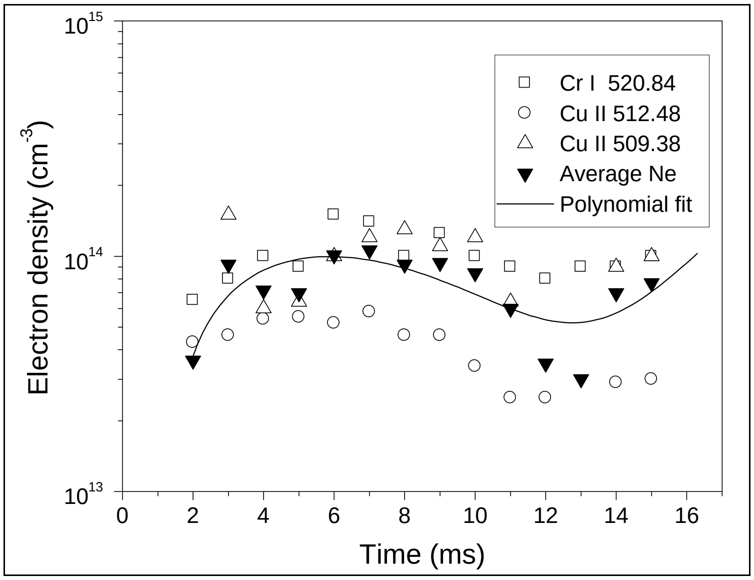

Fig.6 Time evolution of the electron density determined from Stark broadening

As one can see from Fig.6, the errors are less than 50%, and most of them can be caused by an imprecise determination of the apparatus function of the spectrograph-CCD chain. The electron density has a similar time evolution with the ion densities (fig.4). As an observation, non-zero electron density is present in the moment of CZ, proving that we still have ionized plasma in the electrodes gap, appropriate medium for reignition.

4. Conclusions

Single shot time resolved spectroscopy proved to be a well suited method to investigate interruption process in vacuum circuit breakers.

The time evolution of ion lines evidenced that charge transfer ionisation also occurs in anodic regime of the vacuum arc. CuII was found to be one of the responsible factors for the arc reignition.

Quadratic Stark broadening effect was investigated using theoretical and semi-empirical models, proving that the electron density is also high enough in the moment of the current zero to favorize the arc reignition. The electron density is in the order of 10^{14} cm^{-3}, following the arc current in the same manner as the ion densities and the plasma temperature. This value of the electron density is suitable for a LTE plasma according to Griem [6], but near the lower limit.

Acknowledgement

The financial support for this work comes from NATO-SfP-974083 LOVARC and CORINT-Romania projects. Also, the present research was partially supported from European Community–Access to Research Infrastructure Action of the Improving Human Potential Programme.

References

[1] EDF Club “Arc Electrique”: “L’arc electrique et ses applications”, Tome 1, “Etude physique de l’arc electrique”, Editions CNRS, Paris (1984)

[2] D.Pavelescu, V.Braic, G.Dumitrescu, F.Gherendi, M.Braic, G.Pavelescu, P.Anghelita, M. Stefan, Proc. XX-th Int. Symp. On Discharges and Electrical Insulation in Vacuum, 2002, France, p.170-173

[3] F.Gherendi: “*Study of the transition from a diffuse mode to anode mode of the vacuum circuit breaker arc*”, PhD thesis, GREMI, University of Orleans (2002)

[4] A.Anders, S.Anders, J.Phys.D: Appl. Phys. **24**, 1986 (1991)

[5] P.Malkin, J.Phys.D:Appl.Phys.**22,** 1005 (1989)

[6] H.R.Griem: “*Spectral lines broadening by plasma*” Acad. Press, NewYork, MacGraw-Hill (1974)

[7] J.-F.Gonzales, F.LeBlanc, M.-C.Artru, G.Michaud, Astronomy and Astrophysics (ISSN 0004-6361), **297**, no. 1, 223-236 (1995)

[8] COSSAM: COdice per la Sintesi Spettrale nelle Atmosfere Magnetiche, Vienna University, Astrophysics Laboratory, online documentation and ADA language source code at http://fedelma.astro.univie.ac.at/web/cossam_public

Stimulation by laser plasma-chemical processes on a surface of vitreous materials

V.A. Stepanov, I.V. Terehin, A.B. Yastrebkov

Departament of Physics, University of S.A.Esenin, Ryazan, Russia

In papers [1,2] a possibility of local laser plasma-chemical precipitation of metal-containing chemical compounds on a surface of glass without its preliminary heating are discussed.

Here we consider the plasma-chemical precipitation mechanisms of various oxides of metals from a solid phase on a surface of a glass by action of IR laser. There defined threshold values of power density of laser radiation at which a change of plasma-chemical reactions occurring on glass surface takes place defined.

On the basis of cw CO_2 laser (output power of radiation up to 100 W) we developed a laser technological complex which allows to investigate physical processes of interaction laser radiation with matter in a wide range of power (from 10 up to 100 W). Experiments carried out with the chemical compounds of copper and cobalt. As a damping substance silicate of lead was selected which also allowed to hold safely the chemical compounds of copper and cobalt on a surface of vitreous materials.

Laser irradiation of glass surface covered will Cu salts has revealed the following facts. Threshold value of the power density of laser radiation at which we observe a changing of the type of the surface reaction (color of the substance changes from green to light brown), depends on the velocity of the ray movement. At low speeds of movement and low values of power density the thermal mechanism plasma-chemical precipitation (color of precipitated substance is green) predominates. In this case laser heating to low temperatures realizes synthesis of complex compound $CuSiO_3$. This complex compound is known as chrizokolla and has light green colouring. Threshold value of the power density of laser radiation at which there is a changing of the type of the surface reaction, is equal to $(1\text{-}2).10^7$ W/m^2 at velocity of the ray movement ~5mm/sec. The increasing of velocity of the ray movement and the increasing of the power density of laser radiation changes the character of plasma-chemical precipitation (the substance of light brown color precipitates). It was supposed, that changing of the type of the surface reaction may be determined both by the local thermal overheat of glass surface and the quasi-resonance laser excitation up to a level of initiation of chemical reaction [2,3].

The experimental researches of conditions of an irradiation were represented as a three-dimensional file. The basic parameters, determining a kind of precipitated substance, were the followings: 1) diameter of a beam in focal spot of a lens; 2) placement of a lens focus in relation to a surface of a sample; 3) diameter of aperture limiting a laser beam.

The analysis of results has allowed making some conclusion.

The area of formation gemioxide copper is displaced to the lower speeds of input of radiation and apertures with a smaller diameter at the movement of a focus of lens into surface of a material.

The visual researches of samples show, that under certain conditions within the limits of one line made by laser radiation, the type of received substance on a surface depends on distance up to an axis of symmetry. At the center is formed gemioxide, and on border chrizokolla. Such distribution is explained by distinction of a level of power density at the center and at border of section of a laser beam.

Thus the carried out researches create necessary conditions for the development of new methods of plasma-chemical processing of materials by a cw IR laser radiation with flexible choice of a type of plasma-chemical process.

[1] V.A. Stepanov, I.V. Terehin, A.B. Yastrebkov. Precipitating in the glass of various metals and oxide metals by action of cw CO_2 laser radiation. Proceedings of XIII International Symposium on Gas Flow & Chemical Lasers and High Power Laser Conference, 18-22 September 2000, Florence, Italy.

[2] V.A. Stepanov, I.V. Terehin, A.B. Yastrebkov. Initiation by laser radiation plasma-chemical processes on a surface of vitreous materials. Proceedings of SPIE (in printing).

[3] Laser-induced chemical processes, Edited by Jeffrey I. Steinfeld, Massachusetts Institute of Technology Cambridge, Massachusetts. Plenum Press, New York and London, 1981.

A Numerical Analysis of rf Discharges and Particle Transport in the Sheath and Microstructures on the Substrate

Y. Osano, T. Nomura, K. Miki, and K. Ono

Department of Aeronautics and Astronautics, Graduate School of Engineering, Kyoto University, Kyoto, Japan

Abstract

An analysis of asymmetric parallel-plate rf discharges in Ar and the particle transport in the sheath and microstructures on the substrate has been carried out using two-dimensional Particle-in-cell/Monte Carlo method. The simulation self-consistently provided the dc self-bias voltages on the powered electrode by including an external circuit in the model. The feature profile evolution of SiO_2 substrates on the electrode is also simulated, including the surface charging and forward ion scattering.

1. Introduction

Parallel-plate rf discharges have been widely used for materials processing in industry. However, the behavior of rf discharges is not fully understood; in particular, the particle transport onto the substrate through the sheath then in microstructures on the substrates is considerably difficult to understand along with the reaction process in microstructures, owing to a number of physical and chemical effects that occurs. Thus, a self-consistent analysis is required for the particle transport in the plasma, sheath, and microstructural features, to gain a better understanding of the physics and chemistry underlying the processing and then to achieve a more precise and efficient processing.

This paper presents a numerical analysis of parallel-plate rf discharges in Ar and the transport of ions and electrons in the sheath and microstructures on the substrates. The numerical model consists of two parts: a simulation of rf discharges including the sheath, and a simulation of the transport of ions and electrons in microstructures. The feature profile evolution is also simulated assuming purely physical sputtering by ion bombardment.

The plasma simulation employs two-dimensional Particle-in-cell/Monte Carlo (PIC/MC) method. An asymmetric cell geometry, or a large difference in size between rf-powered and grounded electrodes, is considered, including an external electric circuit containing a blocking capacitor and an rf power supply. Thus, the present model self-consistently gives the dc self-bias voltages that occur on powered electrodes, and the characteristics of incident ions and electrons onto the surfaces thereat such as the energy and angular distribution of incident fluxes.

The transport of ions and electrons in microstructures on the substrates is then analysed also by the two-dimensional particle simulation, assuming that the substrate being etched is an insulating dielectric such as SiO_2 with an insulating photoresist mask thereon. The model gives self-consistently the trajectory of ions and electrons in microstructural features, along with the electrostatic potential distribution therein and on the feature surfaces. In practice, the microstructural feature surfaces of insulating materials are differentially charged up, owing to the difference in velocity distribution of ions and electrons incident on the substrate and then into microstructures thereat, which results in the deflection of ion trajectories in microstructures. In addition, some of incident ions scatter inelastically on feature surfaces along with being neutralized. These effects lead to the nonuniformity of ion fluxes onto the feature surfaces, and thus to the profile anomalies such as notching, bowing, and microtrenching, depending on the conditions of rf plasma discharges and pattern feature sizes of interest.

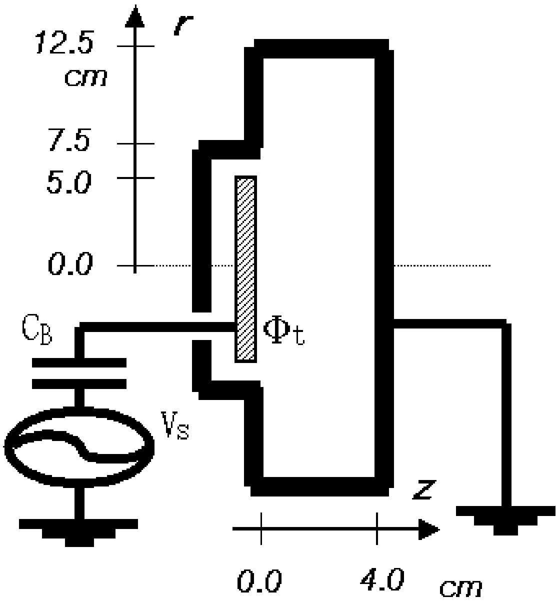

Fig. 1. Schematic of the asymmetric rf discharge system presently simulated, and the cylindrical coordinates in the simulation.

2. Plasma Simulation of rf Discharges

The simulation of rf discharges was performed in a reactor as shown in Fig. 1. The cell geometry is a simple cylinder 25 cm in diameter and 4 cm long. The rf-powered electrode 10 cm in diameter is located at one end of the cylinder, and the other cylinder walls are grounded. Hence, there is a large difference in size between the rf-powered and grounded electrodes, or the discharge system is asymmetric. The model includes ion-neutral and electron-neutral collisions in the gas phase, which are described by the null-collision method [1], and also secondary electron emissions through ion bombardment on electrode surfaces. Note that the ion-neutral collisions consist of elastic scattering and charge exchange collision, while the electron-neutral collisions consist of elastic scattering, excitation, and ionisation. The neutrals were assumed to be thermalized and uniformly distributed throughout the discharge region. The gas pressure was 200 mTorr, and the time-varying rf source voltage was taken as $V_s(t) = V_0 \sin(2\pi f t)$ with $V_0 = 200$ V and $f = 13.56$ MHz.

The electric field in the discharge is derived from the axially symmetric Poisson's equation in the cylindrical coordinates:

$$\frac{\partial^2\Phi}{\partial r^2}+\frac{1}{r}\frac{\partial\Phi}{\partial r}+\frac{\partial^2\Phi}{\partial z^2}=-\frac{\rho}{\varepsilon_0}, \qquad (1)$$

where Φ is the potential, ρ is the charge density, and ε_0 is the permittivity of vacuum. The equation is solved by the Fourier-Analysis and Cyclic Reduction (FACR) method [2]. To obtain the dc self-bias voltages that occur at the rf-powered electrode, the model includes external electric circuit [3], and the following equations are also solved at each time step: the circuit equation

$$\frac{\int_0^t I dt}{C_B}=V_s(t)+\Phi_t, \qquad (2)$$

charge conservation law

$$A\frac{\partial\sigma}{\partial t}=J_{\mathrm{cond}}+I, \qquad (3)$$

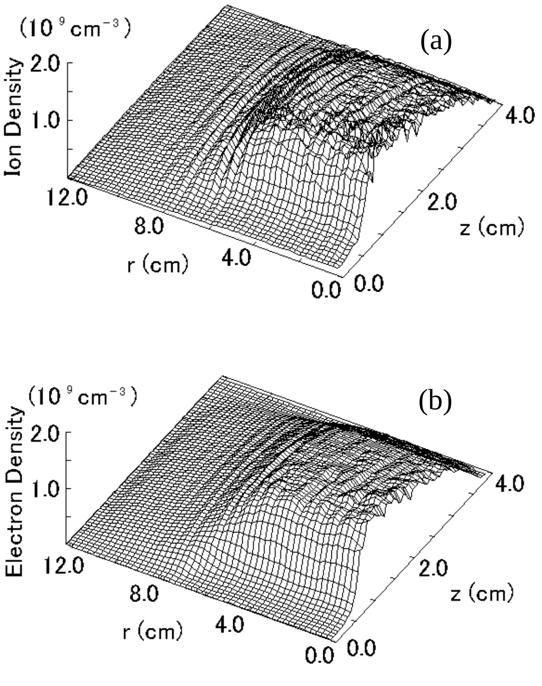

Fig. 2. Two-dimensional distribution of the (a) ion and (b) electron density averaged over one rf cycle.

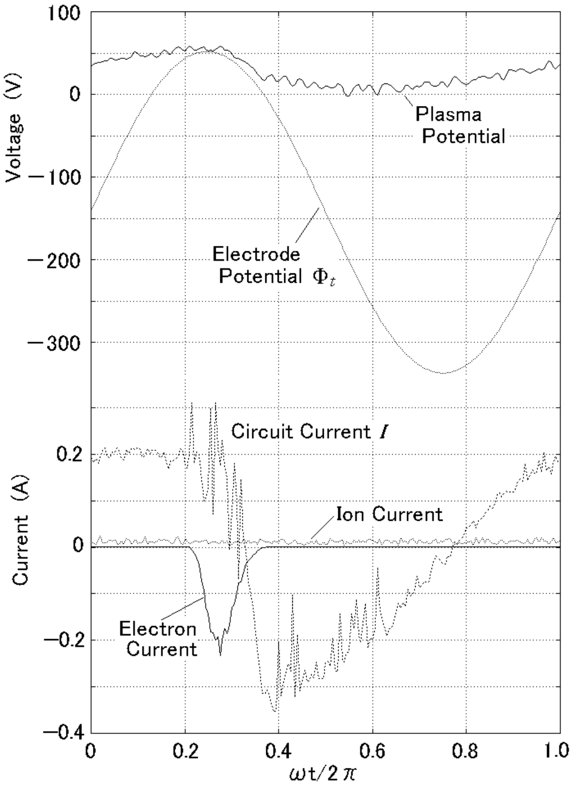

Fig. 3. Time-varying behavior of the rf-powered electrode potential Φ_t, potential at r = 0.0 and z = 1.0 cm, circuit current I, and flow of ions and electrons into the rf-powered electrode.

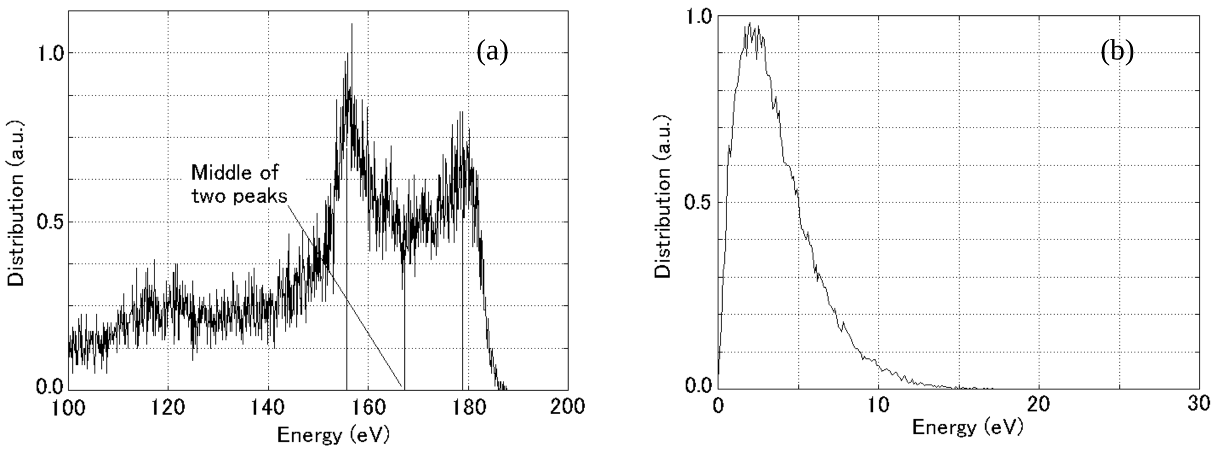

Fig. 4. Energy distribution of (a) ions and (b) electrons incident onto the powered electrode surfaces.

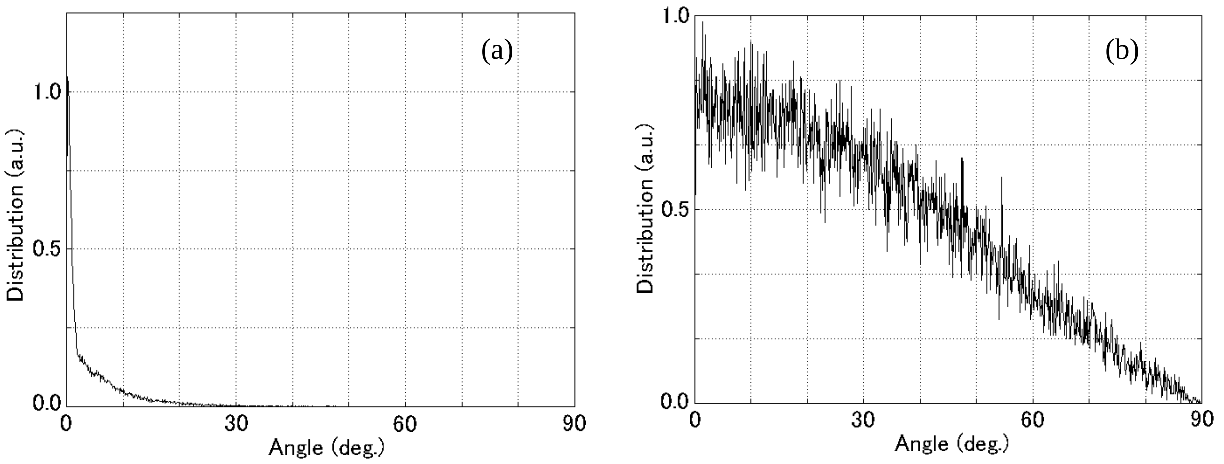

Fig. 5. Angular distribution of incident (a) ions and (b) electrons onto the powered electrode surfaces.

and surface charge relation

$$\sigma = \varepsilon_0 E = -\varepsilon_0 \frac{\partial \Phi_t}{\partial z}, \tag{4}$$

where I is the circuit current, C_B = 500 pF the capacitance of the blocking condenser, Φ_t the potential of the powered electrode, A the surface area of the electrode, and σ the surface charge density on the electrode. The conduction current J_{cond} consists of the flow of ions and electrons from the plasma into electrodes and the flow of secondary electrons emitted from the electrodes.

Figure 2 shows the two-dimensional distribution of the ion and electron density averaged over one rf cycle, indicating a significant sheath that is formed around the rf-powered electrode. Figure 3 shows the time-varying behavior of the circuit current I and the flow of ions and electrons into the powered electrode, together with that of the potential Φ_t of the powered electrode and the plasma potential at r = 0.0 and z = 1.0 cm. We can see that the dc self-bias voltage V —140 V occurs on the powered electrode. It is further noted that the flow of ions and electrons are much smaller than the circuit current, except the period when the electrode potential Φ_t reaches its peak. These results imply that the circuit current consists mainly of the displacement current generated at the electrode.

Figures 4(a) and 4(b) show the energy distribution function of ions (IEDF) and electrons (EEDF) incident on the powered electrode, respectively, averaged over one rf cycle. The IEDF has two peaks at around 155 and 180 eV; the middle (～165 eV) of these two values agrees with the results shown in Fig. 3, in terms of incident ions whose average energy is the difference between the average plasma potential and the dc self-bias voltage on the powered electrode. The corresponding angular distribution function of ions (IADF) and

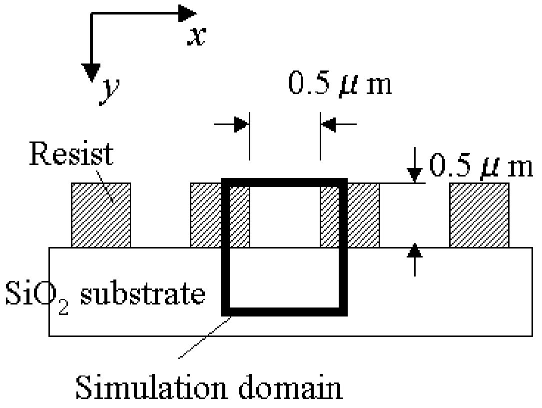

Fig. 6. Schematic illustration of the simulation domain.

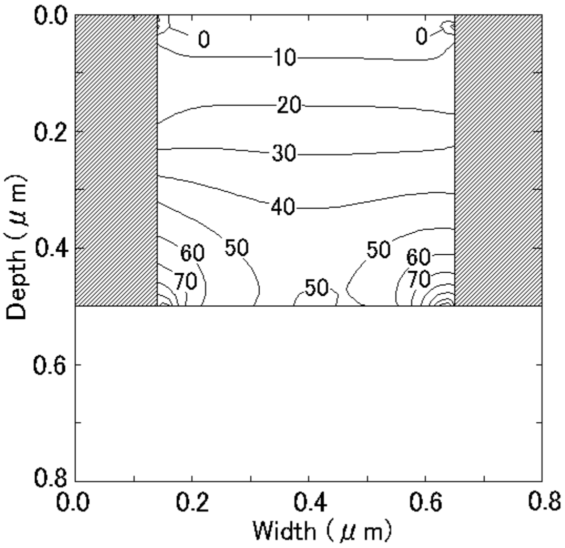

Fig. 7. Potential contour map in microstructures at a steady state of charging. The numerals along solid curves give the relative potentials in volts.

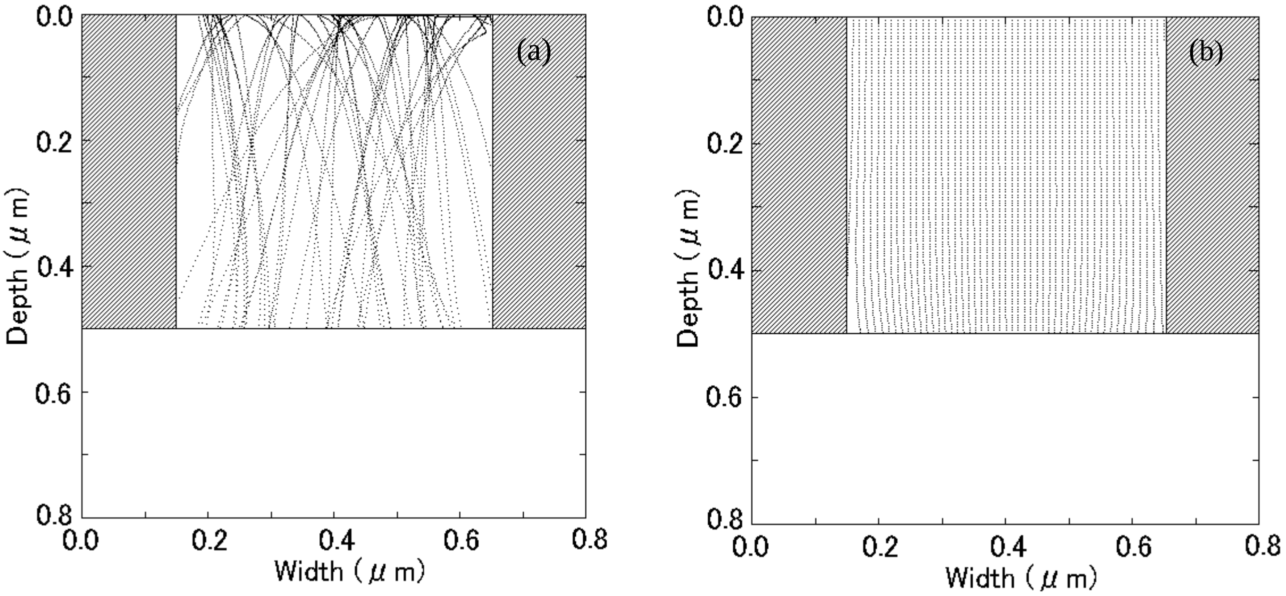

Fig. 8. Particle trajectories in microstructural pattern features at steady state of charging for (a) randomly incoming electrons and (b) perpendicularly incoming ions with an initial kinetic energy 155 eV.

electrons (EADF) is shown in Figs. 5(a) and Fig. 5(b), respectively. The IADF has a significant peak at an incident angle of 0 deg. from the surface normal of the electrodes, implying that a large part of ions impact almost perpendicularly onto the powered electrode after being accelerated through the sheath.

3 Simulation of the Particle Transport in Microstructures and Surface Evolution

The two-dimensional PIC/MC simulation was also performed in an infinitely long trench of line-and-space pattern features. As shown in Fig 6, the simulation domain consists of insulating SiO_2 substrates with a photoresist mask thereon, which is 0.5 μm wide and 0.5 μm thick, each separated by 0.5 μm space.

3.1 Particle transport and surface charging

The transport of ions and electrons in microstructure is analysed by integrating the equation of motion under the electrostatic field Φ:

$$m\frac{d^2x}{dt^2} = -\frac{q}{\varepsilon_0}\frac{\partial\Phi}{\partial x}, \quad m\frac{d^2y}{dt^2} = -\frac{q}{\varepsilon_0}\frac{\partial\Phi}{\partial y} \tag{5}$$

where m and q are the mass and charge of the particle, respectively. These particles were taken to be initially positioned at the upper boundary of the simulation domain (and randomly allocated in the x direction), and their incoming velocity vectors were given by randomly sampling the particle energy and angular distribution through the sheath onto the substrate obtained in the plasma simulation. The ions and electrons incident on feature surfaces of insulating dielectric materials were taken to transfer their charges to the surface, where the charges were assumed to stay at the surface position on incidence. Solving the Poisson equation

$$\nabla^2 \Phi = -\frac{\rho}{\varepsilon_0}, \tag{6}$$

where ρ is the charge density including the surface charging at interfaces, gives the localized potential distribution, thus resulting in the deflection of ion and electron trajectories.

The model also includes the ion reflection on feature surfaces in microstructures. The probability and energy loss rate of the reflection rely on the incident energy and angle of ions, which were taken from the result of molecular dynamics simulation by Helmer and Graves [4]. The ions that approach the surface are neutralized, so no influence of the electric field occurs after reflection; in addition, the reflection angle is generally larger than the incident angle, since the particle momentum along the tangent direction of the surface is conserved in spite of energy loss.

At the initial stage of simulation, the incident fluxes on microstructural feature surfaces are different between ions and electrons, owing to the difference in angular distribution of their incoming fluxes at the upper boundary of the simulation domain. In more detail, most of ions enter the microstructure with nearly perpendicular incoming angles, and thus reach the bottom surfaces of the feature; on the other hand, a large part of randomly incoming electrons tend to reach the feature sidewalls. Such imbalance of incident ion and electron fluxes results in surface charging of microstructural pattern features. In practice, the potential distribution reaches a steady state with time, since the surface charging causes the ions and electrons to be deflected so that their incident fluxes are equal at each position on feature surfaces. Figure 7 shows the potential distribution in microstructural features at a steady state of charging, where the potential increases deeper into microstructures. It is noted here that considerable positive charging occurs around the corner of the feature bottom, along with strong potential peaks, since the randomly incoming electrons hardly reach there.

Figure 8(a) shows the trajectories of randomly incoming electrons in microstructures at a steady state of charging, indicating that most of incoming electrons are accelerated toward the bottom of the feature, owing to the large Coulomb force between ions and electrons. Figure 8(b) shows the trajectories of perpendicularly incoming ions with an initial kinetic energy of 155 eV at which the IEDF has its peak as shown in Fig. 4. It is noted that although the ions are less influenced by the Coulomb force owing to their large mass and kinetic energy, the ions are slightly deflected around the corner of the feature bottom owing to the strong positive charging thereon.

3.2 Feature profile evolution

The time scale of the feature profile evolution is much longer than that of surface charging, and so the profile evolution was assumed to make progress under equilibrium conditions or at steady states of surface charging obtained in the previous section. The profile of insulating materials of interest was divided by a regular two-dimensional array of cells, where each cell is removed when a finite amount of etch yield is accumulated by the successive ion bombardment (cell removal model [5]). Experiments exhibited that the etch yield Y by ion bombardment relies on the incident kinetic energy E_i and incident angle θ from the surface normal:

$$Y(E_i, \theta) = (\sqrt{E_i} - \sqrt{E_{\mathrm{th}}})\, f(\theta), \tag{7}$$

where E_{th} is an energy threshold for etching [6]. The angular dependence $f(\theta)$ was taken from the interpolation of the result of Lee's experiments [7] for Ar/SiO_2. To take into account changes of the potential distribution during feature profile evolution, the simulation was stopped every 2.0×10^{2} s, when the charging model previously discussed was invoked for the feature surfaces concerned.

Figure 9 shows the feature profile evolution of SiO_2 surfaces every 1.0×10^{3} s. At the initial stage of evolution, the etch depth near the corner of the bottom surfaces is larger than that in the central region; this profile anomaly is referred as microtrenching, being caused by concentration of the flux of high-energy neutrals generated at the reflection of ions on sidewalls. As the profile evolution proceeds, the central region of bottom surfaces is etched faster. This is a consequence of the slight deflection of ions, illustrated in Fig 8(b), which tends to concentrate the ion flux on the bottom central.

4 Summary

A two-dimensional PIC/MC simulation has been performed for parallel-plate rf discharges in Ar and also for the transport of ions and electrons in the sheath and microstructures on the substrate, to self-consistently analyse the feature profile evolution in micro fabrication. The energy and angular distribution of incident ions and electrons on the electrodes, obtained from the simulation of rf discharges, was given to the simulation of particle transport in microstructures, so that the profile evolution can be self-consistently analysed in terms of plasma parameters and reactor configurations of interest.

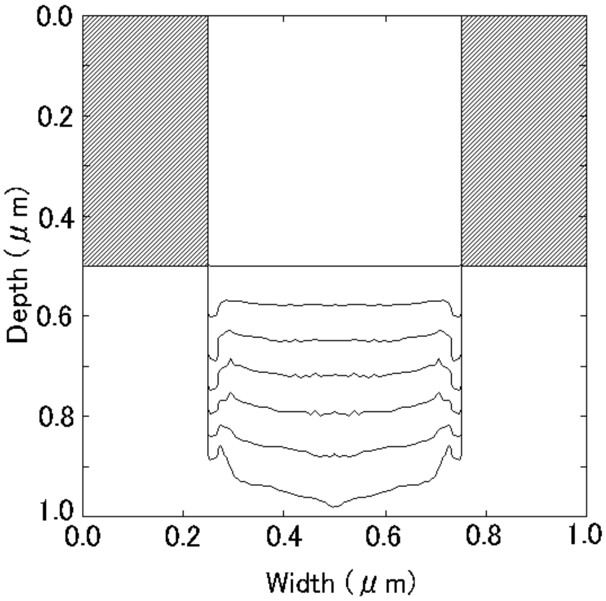

Fig. 9. Feature profile evolution every 1.0 × 10^3 s under the same conditions of Figs. 7 and 8.

References

[1] V. Vahedi and M. Surenda: Comput. Phys. Communications **87**, 179 (1995).

[2] *Numerical Recipes in Fortran77*, ed. W. H. Press *et al*. (Cambridge, 1992).

[3] J. P. Verboncoeur, M.V. Alves, V. Vahedi, and C.K. Birdsall: J. Comput. Phys. **104**, 321 (1993).

[4] B. A. Helmer, D.B. Graves: J. Vac. Sci. Technol. A **16**, 3502 (1998).

[5] Y. Hirai, S. Tomida, K. Ikeda, M. Sasago, M. Endo, S. Hayama, and N. Nomura: IEEE Trans. Comput. Aided Des. **10,** 802 (1991).

[6] C. Steinbruchel: Appl. Phys. Lett. **55**, 1960 (1989).

[7] R. E. Lee: J. Vac. Sci. Technol. **16**, 164 (1979).

Kinetics of decontamination of steel surfaces using DBDs and He-O_2 at atmospheric pressure

E. Michel[1], E. Silberberg[2], P. Choquet[3] and F. Reniers[1]

[1] Service de Chimie Analytique et Chimie des Interfaces, Université Libre de Bruxelles, Brussels, Belgium
[2] Arcelor Group, RDCS, Liège, Belgium
[3] Arcelor Group, IRSID, Maizières–les-metz, France
email: freniers@ulb.ac.be, fax:+32-2-6502934, tel:+32-2-6503116

Steel surfaces covered by an organic oil originating from Tinnol N200 were treated using DBD high pressure He-O_2 plasmas.
The kinetics of decontamination was followed by Infrared reflection-absorption spectroscopy (IRRAS) and by Auger electron spectroscopy (AES). Complete elimination of the organic layer could be reached, and a pseudo-order 1 kinetic law was established.

Introduction

The degreasing of steel surfaces is an important step in the manufacture of advanced coated steel for automotive applications. The removal of the organic oil layer, usually a few microns thick is usually done using wet chemical processes. The use of environmental friendly plasma techniques has a large interest in this respect. The dielectric barrier discharge (DBD) allows to initiate high pressure plasma (up to atmospheric pressure), far away from thermodynamic equilibrium. Reactive species created in such discharges can be used for surface treatments. The oxygen active species present in mixed He-O_2 plasmas can be used for the combustion of the organic layer. Carbon dioxide and water produced in such discharges are evacuated by flowing. Moreover, the mechanical properties of steel are preserved thanks to the characteristics of the homogeneous glow discharge obtained in helium ("cold" plasma). The advantage of high pressure plasmas which do not need expensive high vacuum systems has to be taken into account.

Experimental

The DBD is obtained between two parallel metal electrodes, one of which being covered by a dielectric [1]. The discharge works using a sinusoidal high voltage (up to 4 kV), at middle frequency (around 100 kHz). The dielectric is made of alumina. Figure 1 shows the experimental setup, and a scheme of the discharge is presented in Figure 2.

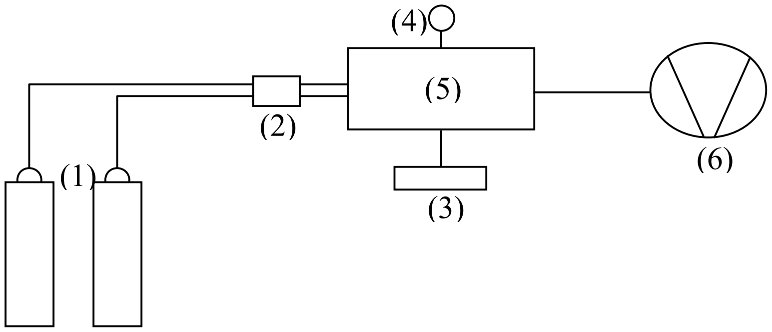

Figure 1 : Experimental setup; (1) He and O_2 cylinders, (2) gas flow meters, (3) cooling system, (4) pressure gauge, (5) discharge system, (6) primary rotary pump used for flowing.

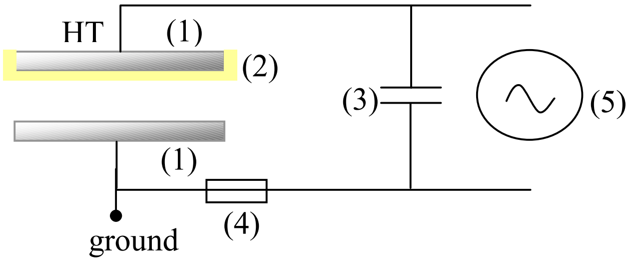

Figure 2: Scheme of the discharge system. (1) electrodes; (2) dielectric material, alumina; (3) condenser; (4) current probe; (5) AC generator.

The samples used are steel plates covered by controlled amounts of industrial organic oil (Tinnol N200). The organic film is deposited by dipping the steel foil into an oil bath and its thickness is measured by a FTIR – IRRAS analysis of the CH signal at 2920 cm^{-1} after calibration. The instrument used is a Nicolet FTIR 710 equipped with variable angle Spectratech accessories. The resolution is 16 cm^{-1}, the angle of incidence is 80°, and the number of scans is 50. Figure 3 presents the standardisation curved of the IRRAS signal, for various oil thicknesses.

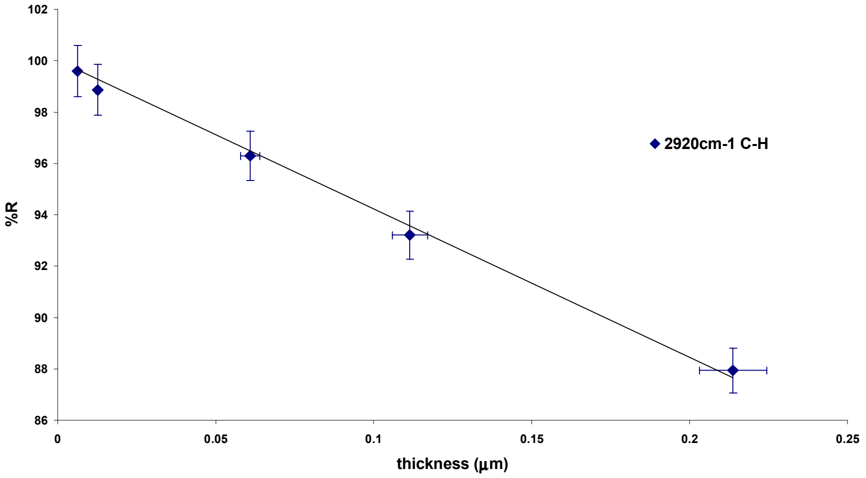

Figure 3: Standardisation curve for infrared spectroscopy

After plasma treatment, the samples are characterized by FTIR-IRRAS and by Auger electron spectroscopy. The instrument used is a Physical Electronics, PHI 590 scanning Auger system, with a primary beam energy of 3 keV. The kinetics of decontamination, for low organics contamination, is followed by the intensity of the Auger peaks of C (273 eV), Fe (652 eV) and O (510 eV). Molar fractions are extracted from the usual Auger equation (1):

$$X_i = \frac{I_i / S_{(i/Fe)}}{I_{Fe} + I_C / S_{(C/Fe)} + I_O / S_{(O/Fe)}} \quad (1)$$

with the following sensitivity coefficients, extracted from the Auger Handbook [2]:
$S_{(Fe/Fe)} = 1$, $S_{(C/Fe)} = 1$ et $S_{(O/Fe)} = 2.5$.

Properties of the DBD for the treatment of organic contaminants

The stability of the discharge depends on many parameters such as the gas composition, the total pressure, the frequency used and the value of the high voltage [3]. Most often, Helium is used to stabilize the homogeneous glow discharges at high pressure, because of its metastable state He ($^3S_1$), which has an energy of 19.8 eV and a lifetime of 7900 s in interstellar vacuum [4].
The plasma gas reactions involved are summarized hereafter:

$He + e^- \rightarrow He\,(^3S_1) + e^-$ (2) [5]
$He\,(^3S_1) + He\,(^3S_1) \rightarrow He^+ + e^- + He$ (3) [5]

The introduction of oxygen into the plasma induces the creation of oxygen active species according to the following reactions:

$He\,(^3S_1) + O_2 \rightarrow He + O_2^+ + e^-$ (4) [6]
$He\,(^3S_1) + O_2 \rightarrow He + O^+ + O + e^-$ (5) [6]

The oxygen active species (O*) can then interact with the contaminated surface in order to remove organics according to the global reaction (6):

$$5nO^* + [\text{-}CH_2\text{-}CH_2\text{-}]_n \rightarrow nCO_2 + nCO + 2nH_2O \quad (6)$$

Above a content of 5 % oxygen partial pressure, the metastable atoms of helium are eliminated and the homogeneous glow discharge is destabilized into a filamentary one.

Results

The remaining thickness of the organic layer, after plasma treatment is determined from the intensity of the C-H stretch in IRRAS-FTIR. Figure 4 shows the typical evolution of this C-H stretch for different treatment time in He – O_2 plasmas.

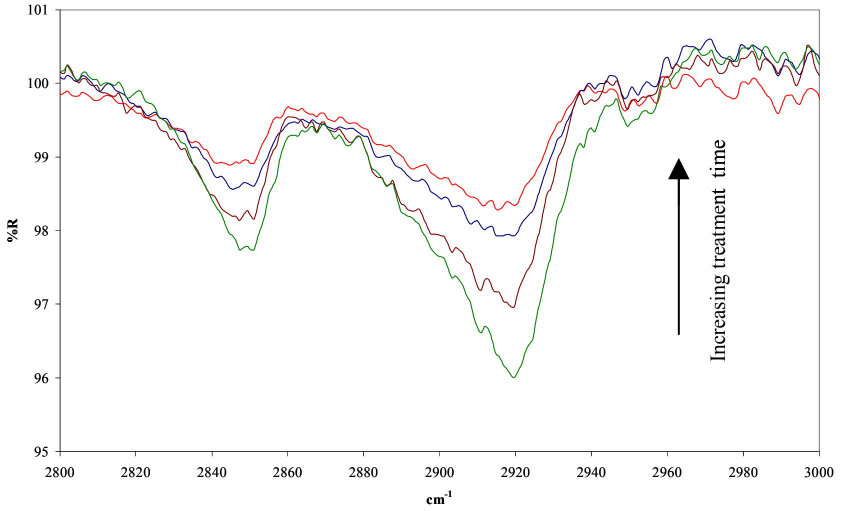

Figure 4: Typical decrease of the IR C-H stretch at 2920 cm-1 as a function of plasma treatment time.

When the remaining organic layer becomes too thin, AES is used to follow the efficiency of the treatment. From the Auger peak-to-peak heights it is possible to determine the molar fractions using equation (1). After the He – O_2 plasma treatment, the surface of the steel foil is oxidized and the molar fractions of iron and oxygen respectively worth 0.46 and 0.54, which correspond to an intermediate composition between FeO and Fe_2O_3, in agreement with the literature [7].

Figures 5-7 show the evolution of the molar fractions of C, Fe and O versus the plasma treatment time for different oxygen partial pressures in helium. For all the results presented hereunder, the initial thickness of the Tinnol oil was 0.13 µm. In these conditions, the only peak detected by AES is the carbon one.

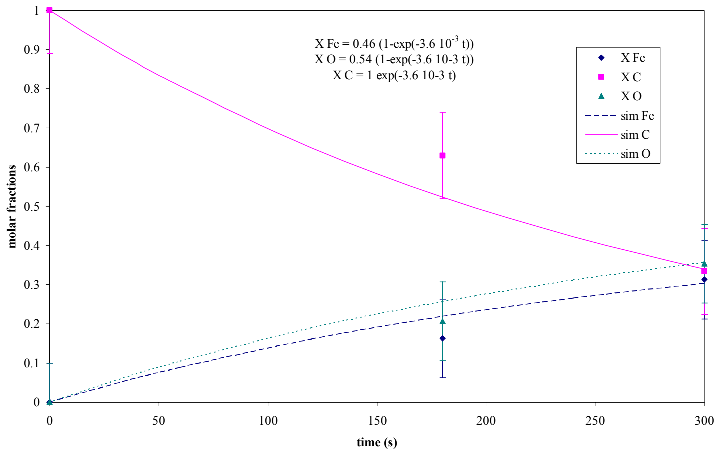

Figure 5: Evolution of the molar fractions of C, Fe and O versus plasma treatment time at 600 mbar. 2% O_2 - He (12 mbar of O_2).

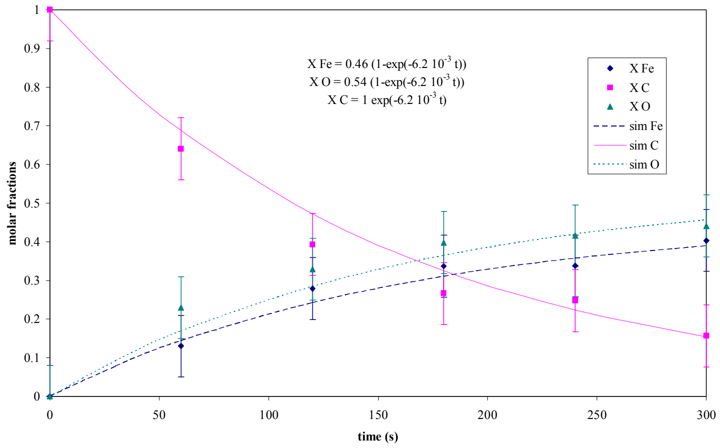

Figure 6: Evolution of the molar fractions of C, Fe and O versus plasma treatment time at 800 mbar. 2% O_2 - He (16 mbar of O_2).

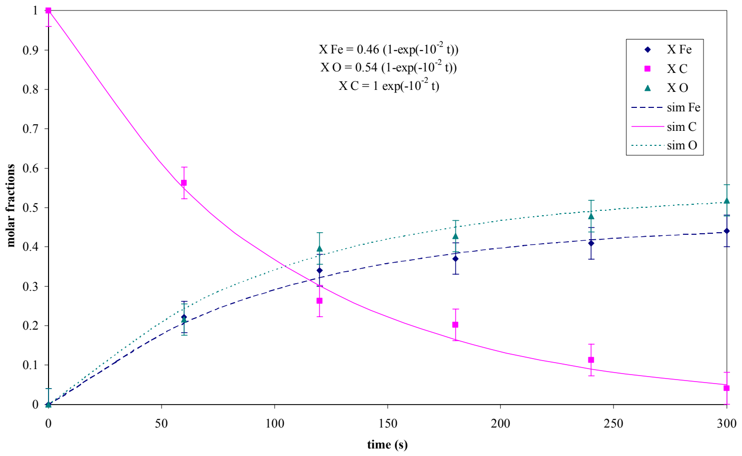

Figure 7: Evolution of the molar fractions of C, Fe and O versus plasma treatment time at 1000 mbar. 2% O_2 - He (20 mbar of O_2).

The decrease of the carbon peak is concomitant with the increase of the oxygen and iron peaks.

The analysis of the decrease of the C-H stretch followed by infrared, as well as the analysis of the decrease of the carbon molar fraction (X_C) calculated from the AES experimental data versus the He – O_2 plasma treatment time reveal an apparent first order kinetic law as shown in Figure 8.

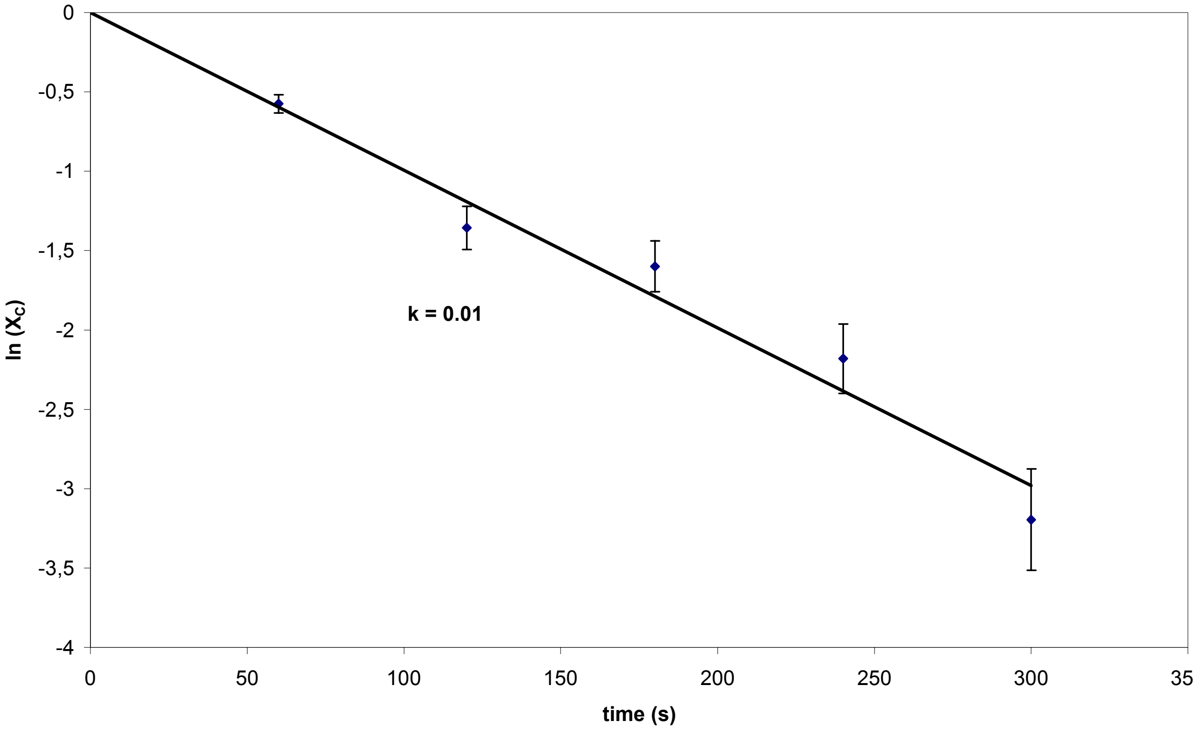

Figure 8: Determination of the kinetic order law and of the kinetic constant for a He-2% O_2 plasma at atmospheric pressure.

For an apparent first order kinetic law, the evolution of the molar fractions of carbon, iron and oxygen versus treatment time are given by:

$$X_C = \exp(-kt) \quad (7)$$

$$X_{Fe} = 0.46\,[1 - \exp(-kt)] \quad (8)$$

$$X_O = 0.54\,[1 - \exp(-kt)] (9)$$

Simulations have been performed using equations 7-9. As shown in Figures 5-7 obtained for different oxygen partial pressure in helium, equations 7-9 fit correctly the experimental observations concerning the evolution of the carbon, iron and oxygen molar fractions versus treatment time. Moreover, equations 7-9 allow to determine the time needed to reach completion of the cleaning process, depending on the experimental conditions.

Table 1 gives the apparent kinetic constants extracted from the experimental data presented in Figures 5-7.

conditions	**P_{eff}**	**k (s^{-1})**
p_{total} = 600 mbar – 2% O_2 in He (12 mbar of O_2)	146 ± 5 W	$3.6\ 10^{-3}$
p_{total} = 800 mbar – 2% O_2 in He (16 mbar of O_2)	146 ± 5 W	$6.2\ 10^{-3}$
p_{total} = 1000 mbar – 2% O_2 in He (20 mbar of O_2)	146 ± 5 W	$1.0\ 10^{-2}$

Table 1

As shown in Table 1, an increase of the oxygen total pressure present in helium increases the apparent kinetic constant.

Conclusions

The potentialities of dielectric barrier discharges initiated at high pressure in helium – oxygen mixtures for the removal of the oil present on steel were studied. The analysis of the experimental data reveals an apparent first order kinetic law. This order is apparent since the kinetic constant k depends also on the oxygen total pressure. Indeed, the higher the oxygen partial pressure in the He-O_2 mixture, the higher the kinetic constant k. It should also be reminded that the partial pressure in oxygen should not be higher than 5% in order to keep the characteristics of a homogeneous glow discharge, so that the oxygen partial pressure cannot be increased indefinitely.

References

[1] Okazaki S, Kogoma M, Uehara M, Kimura Y., *J. Appl. Phys*. **23** (1990) 1125-1128.
[2] Lawrence E.Davis, Noel C.MacDonald, Paul W.Palmberg, Gerald E.Riach, Roand E.Weber, *Handbook of Auger electron spectroscopy*. Physical Electronics Idustries, Inc, (1976).
[3] Massines F, Gouda G, *J. Appl. Phys*. **31** (1998) 3411-3420.
[4] Massines F, Messaoudi R, Mayoux C, *Plasmas and Polymers*, **3**(1) (1998) 43-59.
[5] Ségur P, Massines F, Rabehi A, Bordage M, *Theorical and experimental analysis of high pressure glow discharge controlled by a dielectric barrier*. Proceedings of the Gazeous dielectric conference (1998).
[6] Ricard A, *Plasmas réactifs*, SFV editions (1995).
[7] J. Wanbach, A. Wokaun, A. Hiltpold, *Surf.Interface.Anal*. **34** (2002) 164-170.

CO_2 and N_2 plasma modification of LDPE, HDPE and PP surfaces. XPS, contact angle, AFM and OES study

N. Vandencasteele[1], E. Michel[1], F. Reniers[1]

[1] Analytical and interfacial Chemistry CP 255, Faculty of sciences, Univeristé Libre de Bruxelles, Bld Triomphe, B-1050 Bruxelles, Belgium. Tel : +32-2-6503116 ; Fax +32-2-6502934 ; E-mail : freniers@ulb.ac.be (corresponding author)

Abstract

We study the modification of high and low density polyethylene (HDPE, LDPE) and polypropylene (PP) by N_2 and CO_2 RF plasma. Contact angle measurements showed that the surface energy of the samples increased after plasma treatment. XPS analysis of the surface showed that after plasma treatment new functionalities are grafted onto the polymer surface. The chemical nature and the amount of the grafted species depend on the plasma parameters such as plasma power, treatment time and processing gas. AFM measurements showed a decrease of the samples roughness.

Introduction

Plasma treatments are a convenient way to increase the surface energy of polymers, to modify their adhesion properties, as well as the chemical composition of the surface [1-4]. Contrary to traditional wet chemistry, the plasma techniques are environmental friendly as there is no toxic waste. Plasma modifications only affects the surface of the polymers and don't change the bulk properties. However, due to the numerous energetic species created inside the plasma, the surface modification is often non selective, and poorly controlled. We undertook a global research project in order to better understand the role of the different species created in a plasma on the surface modifications of selected polymers [5], and this paper will focus on the effect of (mostly) neutral species created in N_2 and CO_2 plasma on the surface of polymers. More general results about other plasma species (ions, electrons) are presented in a different paper of this meeting [6].

Experimental

SAMPLES

Additive free low density polyethylene film (LDPE), high density polyethylene sheet (HDPE) and polypropylene films are supplied by Goodfellow. Before treatment they are ultrasonically cleaned in methanol (Acros 99.8%) and ethanol (Merck 99.8%) and then dried by N_2 flux.

PLASMA

Samples are treated using a Hüttinger PFG 300RF generator and a PFM 1500A matching box. Before plasma treatment the chamber is pumped down to a base pressure of $2x10^{-6}$ torr with a turbomolecular pump. The chamber then is backfilled with ultra pure N_2 (alphagaz 2, 99.9999%) or CO_2 (alphagaz 99.9998%) to a pressure of $5x10^{-2}$ torr. In order to avoid contamination of the plasma, the gases are continuously introduced and pumped out (dynamic regime).

The samples are placed outside the plasma, just above the anode made of metallic grid. The anode can be grounded or biased, in order to selectively filter out charged species. A detailed description of the plasma setup can be found in [5]. The plasmas are characterized by optical emission spectroscopy using a Sofie instrument (SCM350 Monochromator Unit). Figure 1 shows the relative intensity of the 391.4 nm N_2^+ to the 315.85 nm N_2 lines in the dark space, in the negative glow and in the positive column at various plasma powers. As expected from the theory of RF plasmas, positive ions are mostly located close to the cathode (dark space and negative glow).

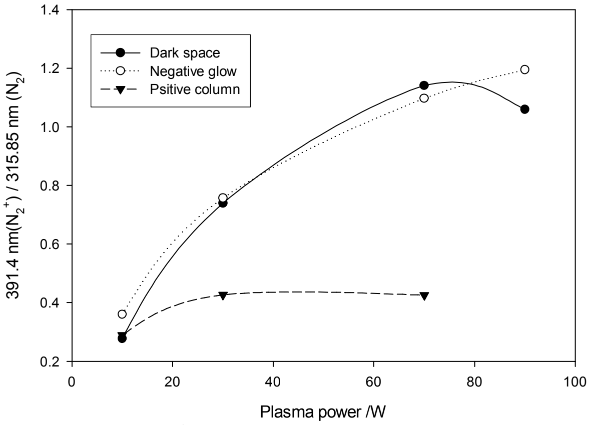

Fig.1: OES analysis of a N_2 plasma ($p=5x10^{-2}$ torr). Ratio of the N_2^+ band (391.4 nm) to the N_2 band (315.85 nm) in the different regions of the discharge.

X-RAY PHOTOELECTRON SPECTROSCOPY:

After plasma treatment, the samples are transferred into the XPS introduction chamber at atmospheric pressure. The analyses are made in a UHV chamber equipped with a VG-CLAM2 analyser and a dual anode (Al/Mg) source. The Mg K_α (1253.6 eV) radiation is used (operating at 300 W, 20 mA, 15kV). Full survey scans were recorded at 100 eV pass energy, 1 eV/step, 30 scans. Elemental regions (C 1s, N 1s) were recorded at 50 eV pass energy, 0.5 eV/step, 30 scans. Deconvolutions are made with a FWHM of 2.7 eV for C 1s peak (determined on clean LDPE) and 2.54 eV for N 1s peak (determined in previous studies [5]). The lineshape for fitting was a 30/70 Laurentzian – Gaussian envelope. The composition in the surface region was calculated using the following sensitivity factors: O 1s: 0.711; N 1s: 0.477; C 1s: 0.296.

CONTACT ANGLE:

Static contact angle measurements are made with a CCD camera mounted on a magnifying optics. For each sample, ten drops of water, deposited with a syringe, were analyzed. The patterns are then analyzed by image treatment software. All the measurements are made with milli-Q water in a climatized room (22°C).

ATOMIC FORCE MICROSCOPY:

Some of the samples have been analyzed by atomic force microscopy using a Topometrix Explorer instrument. The samples are analyzed under water conditions to avoid charging effects, and in contact mode (Park Scientific cantilever, 0.4nN/µm).

Results and discussion:

SURFACE ENERGY:

All the samples showed a decrease of their contact angle (i.e. an increase of their surface energy) after the plasma treatment. Results for N_2 and CO_2 plasmas as a function of time and power, for the different polymers investigated are presented in Figures 2 and 3.

For all the samples, the same behaviour is observed: a sharp increase of the surface energy at low exposure times, or low plasma powers, followed by a plateau regime where the surface energy reaches a limit. For low exposure times, the slope for the surface energy increase depends on the plasma power.

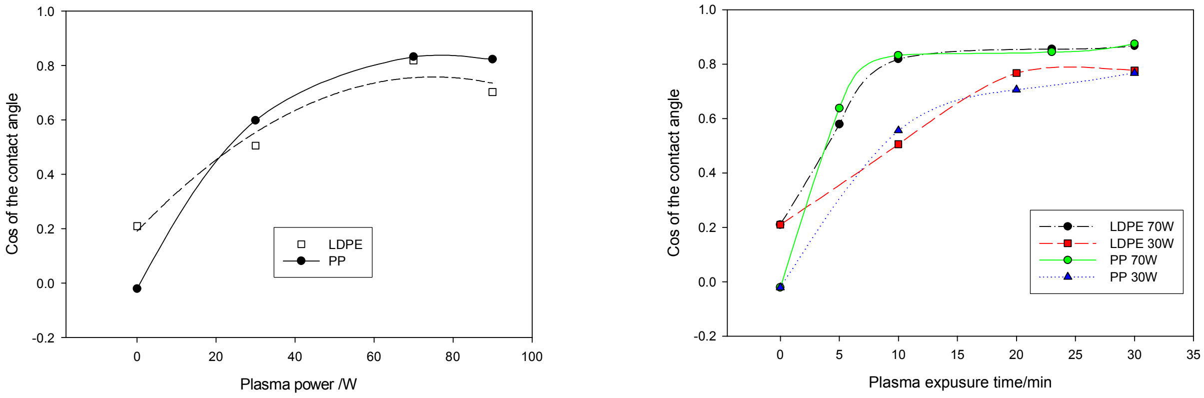

Figure 2: surface energy of the polymer samples treated by a Nitrogen plasma ($5x10^{-2}$ torr). Left: effect of the power at constant exposure time (10 min); right: effect of the exposure time.

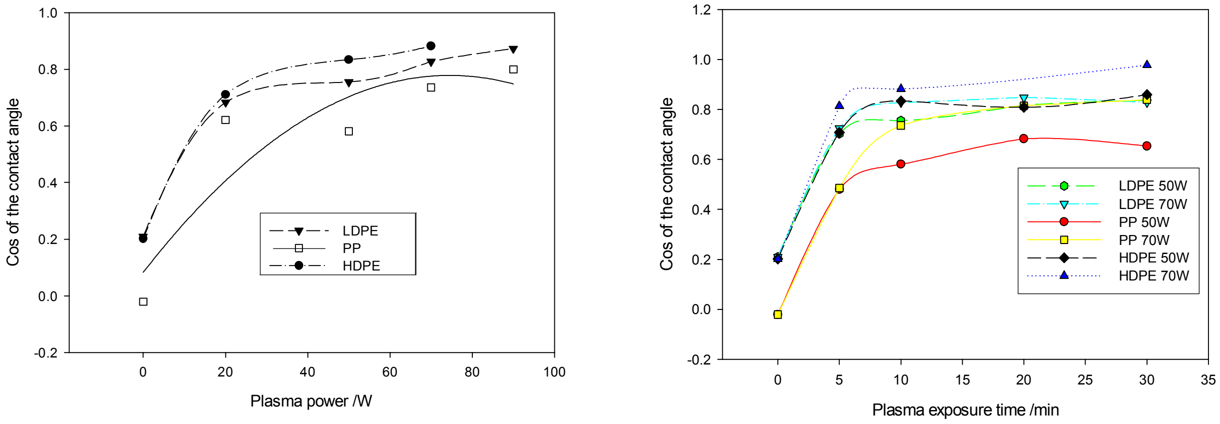

Figure 3: surface energy of the polymer samples treated by a CO_2 plasma. ($5x10^{-2}$ torr). Left: effect of the power at constant exposure time (10 min); right: effect of the exposure time.

SURFACE COMPOSITION:

The changes in surface energy have been correlated to changes in the surface composition, as determined by XPS. After N_2 plasma treatments, the XPS survey shows the presence of the N1s (around 400 eV) and O1s (around 530 eV) peaks. Oxygen is a natural contaminant of polymer, and can only be removed from "clean" untreated PE and PP by ion sputtering under UHV. Moreover, as the sample must be transferred in air after plasma treatment to undergo the XPS analysis, the following reaction, already reported [7], occurs:

$$\text{R-C=NH} + H_2O\ (g) \rightarrow \text{R-CH=O} + NH_3\ (g)$$

Figure 4 shows the evolution of the N+O surface content as a function of the treatment time. An excellent similarity is observed between the curve shapes for surface energy (Fig.2), and the total concentration of polar groups on the surface (Fig.4).

The CO_2 treatment of polymer sample induces an uptake of oxygen, as presented in Figure 5. In this case also, a first sharp increase is observed, followed by a plateau at long exposure times. In this case also, a good similarity between the behaviour of the surface energy curves and the oxygen surface concentration curve is observed.

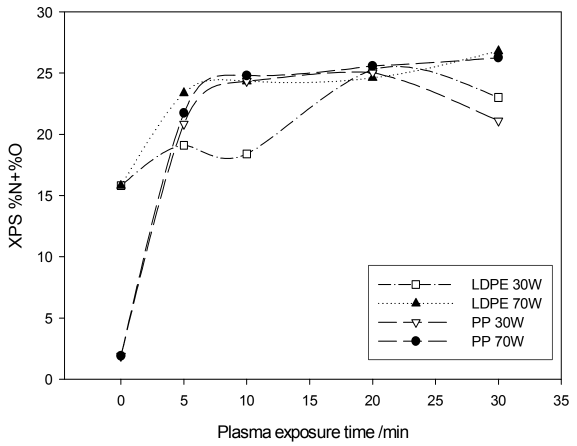

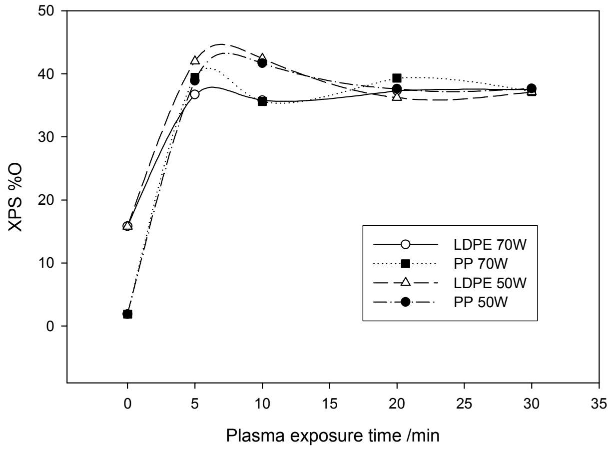

In order to determine the nature of the functionalities grafted during the plasma treatment, the spectral envelope of the N1s peak (for N_2 plasmas) and the C1s peak (for CO_2 plasmas) were studied. In both cases, the plasma treatment induces a broadening of the photoelectron lines, and a change in symmetry of the peak, due to the apparition of new functionalities at higher binding energies. This is illustrated in Figures 6 (CO_2) and 7 (N_2). Figure 7 also shows that the relative distribution of the functionalities changes with time.

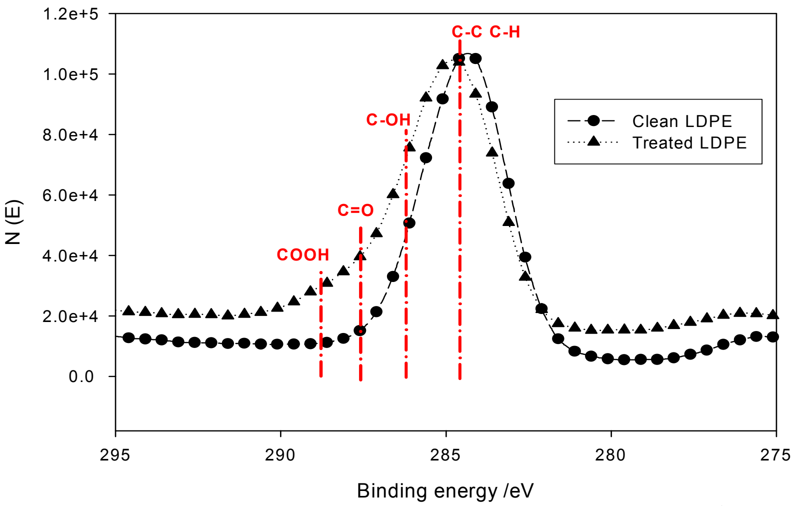

Fig.6: C 1s peak of clean LDPE and plasma treated LDPE. CO_2 plasma, p=5x10^{-2} torr P=70W, t=30min. The vertical lines indicate the energy position of the functionalities indexed following the literature [8]

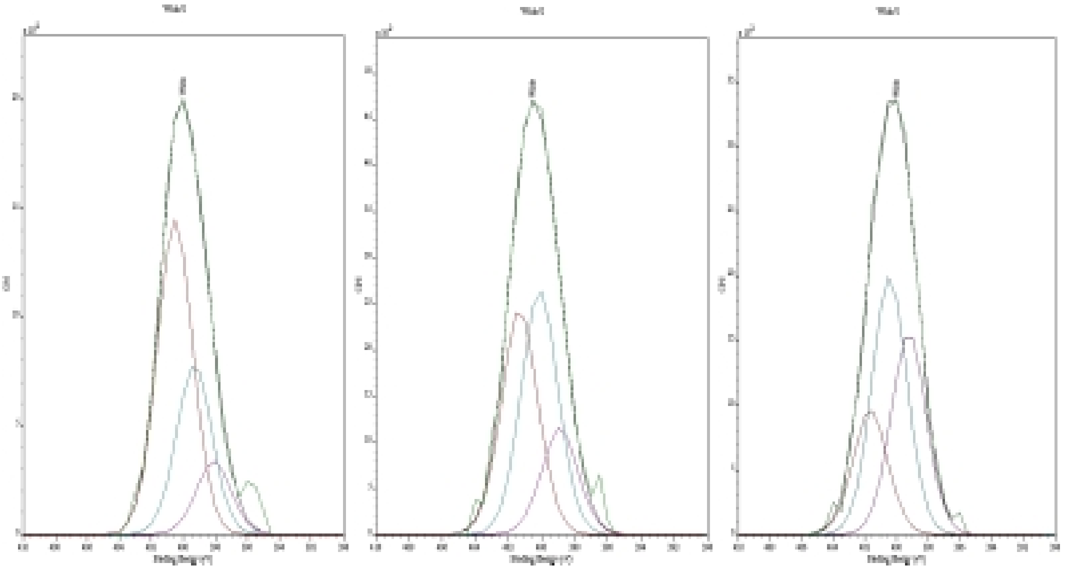

Fig.7: Deconvolution of the N 1s peak for plasma treated LDPE (N_2 plasma p=5x10^{-2} torr, P=30W). From the left: 5, 20 and 30 minutes of treatment. Green: experimental peak, Red: C≡N or (C=O)NH_2, Blue: C=N, Purple: C-N

A summary of the results obtained is presented in Tables 1 and 2, where a progressive functionalisation sequence is evidenced.

N_2 plasma	**Species**
30 W 5 min	C≡N,(C=O)NH_2 > C=N > C-N
30 W 20 min	C≡N,(C=O)NH_2 ≈ C=N > C-N
30 W 30 min	C=N > C-N > C≡N,(C=O)NH_2
70 W 5 min	C=N > C-N > C≡N,(C=O)NH_2

Table 1: Results for the N 1s peak deconvolution

CO_2 plasma	**Species**
20 W 5 min	C-C > C-OH > C=O > COOH
50 W 5 min	C-C > C-OH > C=O > COOH
50 W 10 min	C-C ≈ C-OH > COOH > C=O

Table 2: Results for the C 1s peak deconvolution

SURFACE ROUGHNESS:

After plasma treatment the surface structure of LDPE and PP has changed, as illustrated in Fig. 8 for polypropylene. The roughness values are presented in Table 3. The decrease in surface roughness is not common for plasma treated samples, where generally an increase of roughness after treatment is observed. This is probably due to the peculiar positioning of the sample, located outside the plasma, and therefore far away from the energetic charged molecules, well known to create strong surface damage. This decrease in surface roughness also reveals that the increase in surface energy is in our case mostly due to a surface composition change, and not to a surface structure change.

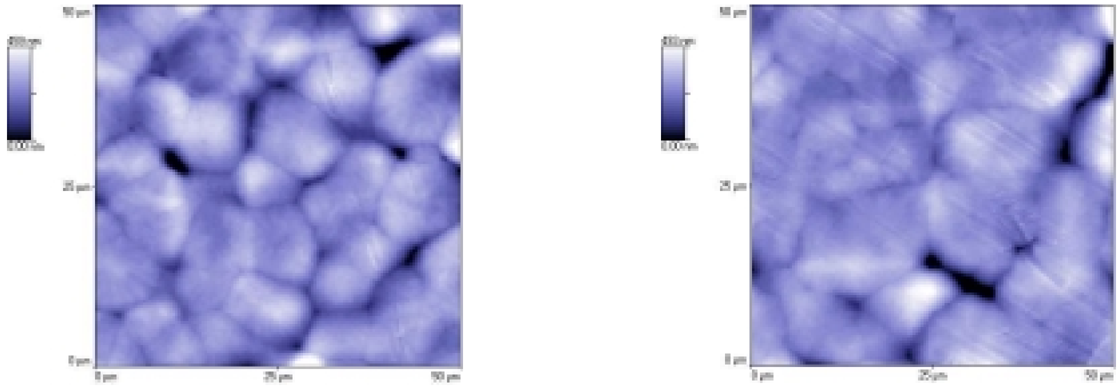

Figure 8: AFM contact mode topography image of a polypropylene sample before (left) and after (right) exposure to a CO_2 plasma (P=70W, t=30min, p=5x10^{-2} torr)

		Untreated samples	**Plasma treated samples**
PP	2500 μm^2	264,5174	188,4183
PP	400 μm^2	160,2822	111,7102
LDPE	2500 μm^2	214,7287	109,8541
LDPE	400 μm^2	88,7352	37,2441

Table 3: Roughness (Ra coefficient) of PP and LDPE before and after plasma treatment (CO_2, P=70W, t=30min, p=5x10^{-2} torr).

Conclusions

The treatment of PE and PP surfaces by RF N_2 and CO_2 plasmas, with the samples positioned above the anode, induce a selected grafting of functionalities, which depends on the treatment time, the plasma power and the gas. The surface energy is increased, while the surface roughness decreases.

References

[1] Vallon, S.; Hofrichter, A.; Drévillon, B.; Klemberg-Sapieha, J. E.; Martinu, L.; Poncin-Epaillard, F. *Thin Solid Film* **1996**, *290-291*, 68-73.

[2] Aumann, T.; Theirich, D.; Engemann, J. *Surface and Coatings Technology* **2001**, *142-144*, 169-174.

[3] Poncin-Epaillard, F.; Chevet, B.; Brosse, J.-C. *Makomolecular Chemistry* **1991**, *192*, 1589-1599.

[4] Sprang, N.; Theirich, D.; Engemann, J. *Surface and Coatings Technology* **1995**, *74-75*, 689-695.

[5] Wagner, A. J.; Fairbrother, D. H.; Reniers, F. *Plasma and polymers* **2003**, *Under Press*.

[6] Wagner, A.; Vandencasteele, N.; Michel, E.; Fairbrother, D. H.; Reniers, F., *see these proceedings*.

[7] L. J. Gerenser, J. Adh. Sci. Technol. **7** (10), 1019 (1993).

[8] Wagner, C. D.; Riggs, W. M.; Davis, L. E.; Moulder, J. F.; Muilenberg, G. E. *Handbook of X-ray photoelectron spectroscopy*; Perkin-Elmer: Eden Prairie, 1979.

Ackowledgments

We wish to thank T. Matzelle (ULB- Physical Chemistry of Materials, prof. N. Kruse) for AFM measurements. This work is part of a INT NSF collaboration (#9985372) with prof. D.H. Fairbrother (J. Hopkins University – Baltimore USA).

Selected effect of ions and neutrals in the nitrogen plasma modification of PE surfaces. A XPS, contact angle, and OES study

A. Wagner[1], N. Vandencasteele[2] , E. Michel[2], D.H. Fairbrother[1] and F. Reniers[2]

[1] Department of chemistry, The Johns Hopkins University, Baltimore, Maryland, USA
[2] Service de Chimie Analytique et Chimie des Interfaces, Université Libre de Bruxelles, Brussels, Belgium
email: freniers@ulb.ac.be ; tel:+32-2-6503116; fax:+32-2-6502934

Abstract

Model PE samples were modified by the various constituents of a nitrogen plasma: nitrogen ions, nitrogen neutrals and electrons. The polymer was either exposed to an ion gun or to a modified RF plasma allowing the filtering of the ions. It is shown that the concentration of nitrogen grafted on the surface, as well as the nature of the functionalities grafted (C≡N, O=CN, C=N, C-N) depend on the nature of the incoming particle (ion or neutral), the treatment time and the energy of the plasma

Introduction

The modification of polymer surfaces is of enormous importance in today's chemical industry. Compared to traditional wet chemistry, plasma treatments are surface sensitive and environmental friendly. Moreover, "cold" plasmas do not modify the bulk properties of the polymers such as elasticity, strain. Many studies have been published these last years about the use of such plasmas to modify polymer surfaces [1-3]. However due to the variety of the excited species created in a plasma (ions, neutrals, electrons, UV), the understanding of the chemical mechanisms involved in the plasma treatment of polymers is not trivial. This paper presents the first results of a NSF-funded collaboration [4]. We have undertaken a model study where PE samples are separately bombarded by ions generated in an ion gun or neutrals generated in a RF nitrogen plasma.

Experimental

HDPE samples (Mc-Master-Carr, technical grade, amorphous), and LDPE (Goodfellow) were cut to size and washed using methanol and isooctane. Samples were introduced into either (1) an ultra-high vacuum (UHV) chamber and exposed to N_2^+/N^+ ions generated by an ion gun or (2) a plasma chamber and exposed to the neutral reactive nitrogen species generated from a N_2 RF plasma.
Figure 1 presents a schematic of the experimental setup for the ion treatment of the samples.
The samples are introduced into a PHI 5400 UHV chamber equipped with the PHI 04-303 ion gun, aligned at 45° with respect to the sample normal, a PHI 04-500 dual anode X-ray source (Mg Kα anode, 1253.6 eV radiation, 15 kV and 300 W operating conditions) and a PHI 10-360 hemispherical analyzer. The samples are exposed to ions which could be accelerated from 0.5 to 4 keV. After exposure, the samples are analyzed in situ by XPS.

Figure 2 shows a schematic of the experimental setup for the plasma treatment. The PE samples are mounted on a magnetically coupled translator housed behind a PE shield in a stainless steel – pyrex chamber equipped with a turbomolecular pump. The base pressure is 1*10-6 torr. Experiments were initiated by filling the chamber with Nitrogen (99.999%) up to a pressure of 2 10-1 torr. To minimize contamination from background gases, a dynamic flow was used. A RF plasma was initiated between the cathode (SiO_2 covered stainless steel disk) and a stainless steel grid anode, located 3 cm above the cathode. The anode can be positively biased at +10 V using an external voltage source in order to filter electrons from the plasma and to repel positive ions. The RF generator consists either in a Huttinger PFG 600 coupled to a PFM 3000 A matching unit or a Huttinger PFG 300 coupled to a PFM 1500 A matching unit.

In this configuration, the ions generated in the plasma remain mostly located close to the cathode. The plasma is characterized by optical emission spectrometry using a Sofie spectrometer (SCM350 Monochromator Unit). Spectra between 200 and 900 nm are recorded. Table 1 shows the ratio of the intensities of the N_2 and N_2^+ transitions at 357.69 nm and 391.44 nm measured above the cathode, below the anode, and between the anode and the sample. At this last probe position, the N_2^+ lines have almost completely disappeared, contrary to the N_2 lines. After treatment, the samples are transferred in air into a XPS chamber equipped with a dual Mg/Al anode (Mg Kα radiation at 1253.6 eV was used, 15 kV and 300 W operating conditions) and a VG CLAM2 analyser. Some measurements were also performed using a PHI 5500 XPS system.

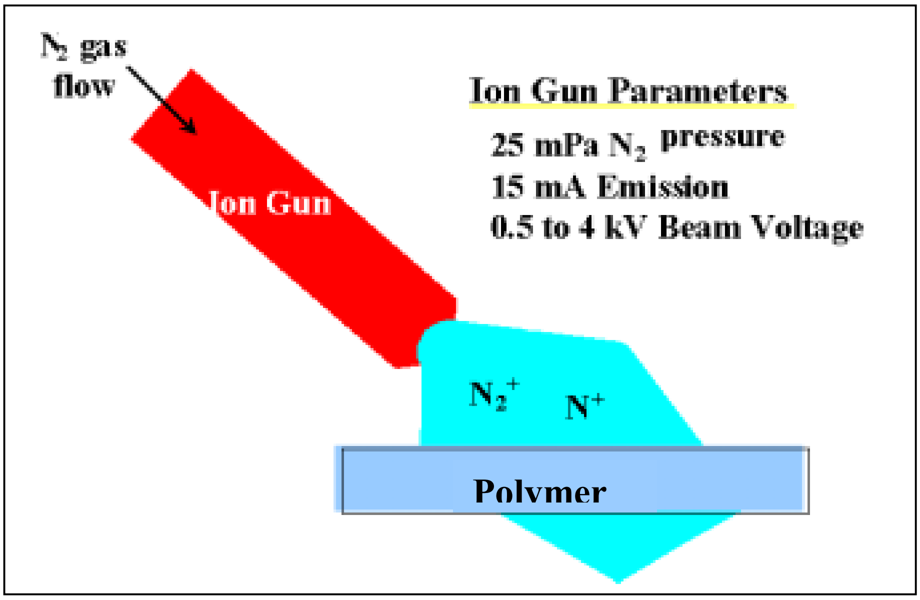

Figure 1: Schematic of the treatment of polymers by ion gun, with the experimental conditions.

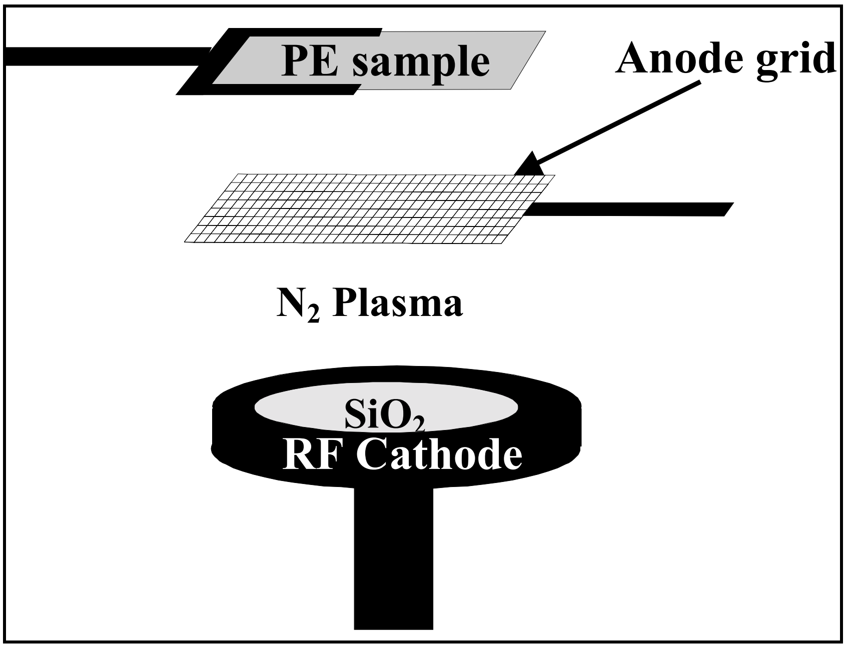

Figure 2: experimental setup for the modified RF plasma system. The anode grid is connected to a voltage generator or can be grounded.

OES fibre optic location	N_2^+(391.44)/N_2(357.69) intensities
Above cathode	0.53
Below anode	0.19
Between anode and polymer surface	0.02

Table 1 relative intensity of the N_2^+(391.44)/N_2(357.69) lines as a function of the optical probe position in the plasma chamber. The plasma power was 50 W, the anode was grounded.

Results and discussion:

Due to the peculiar positioning of the sample above the anode, only a limited amount of ions can reach the polymer surface, as qualitatively confirmed by Table 1. Therefore, the modifications induced on the PE surface mostly result from the action of neutrals (molecules, atoms), and electrons. On the other hand, only ions reach the PE surface for the samples exposed to the ion gun. Figure 3 shows the difference in the surface composition, determined by XPS for samples exposed to nitrogen ions and to neutrals.

Figure 4 shows the difference in the N 1s peak shape for both sets of experiments. The acquisition conditions of the N 1s spectra, and the deconvolution procedure can be found in [5]

The main information which can be extracted from these results is that the amount of nitrogen grafted on the PE surface is lower in the case of ions exposure and that the nature of the functionalities grafted are different. After ion exposure, the main functions grafted are amine groups, which is not the case for the exposure to neutrals, where a more complex, time dependent, behaviour is observed. Indeed, the shape of the N 1s peak, is not modified by the exposure time for the experiments carried on with the ion gun, but the relative distribution of the functionalities grafted changes with time for the RF plasma experiments, as shown in the right part of Figure 4.

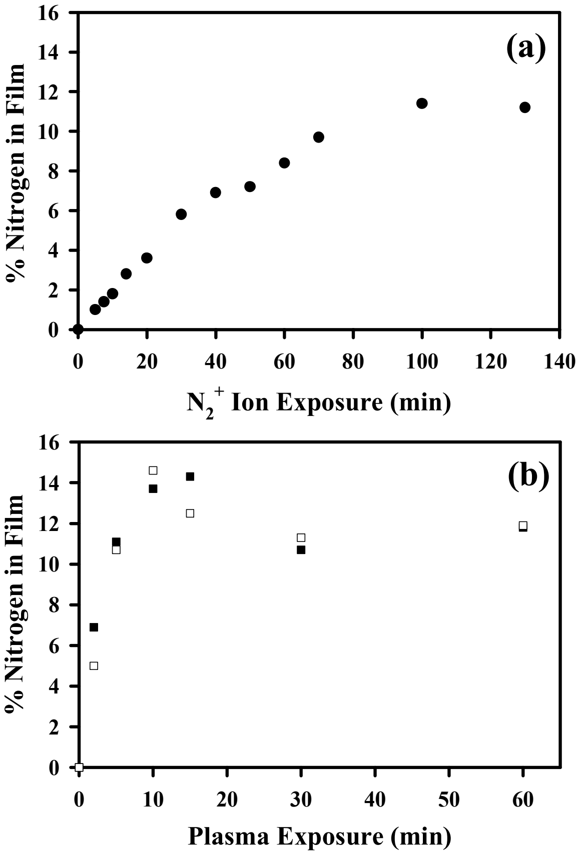

Figure 3: Nitrogen molar fraction at the surface of HDPE samples submitted to 4 keV ion exposures (top) and 50 W N_2 RF plasma (bottom), with (□) and without (■) anode +10 V bias.

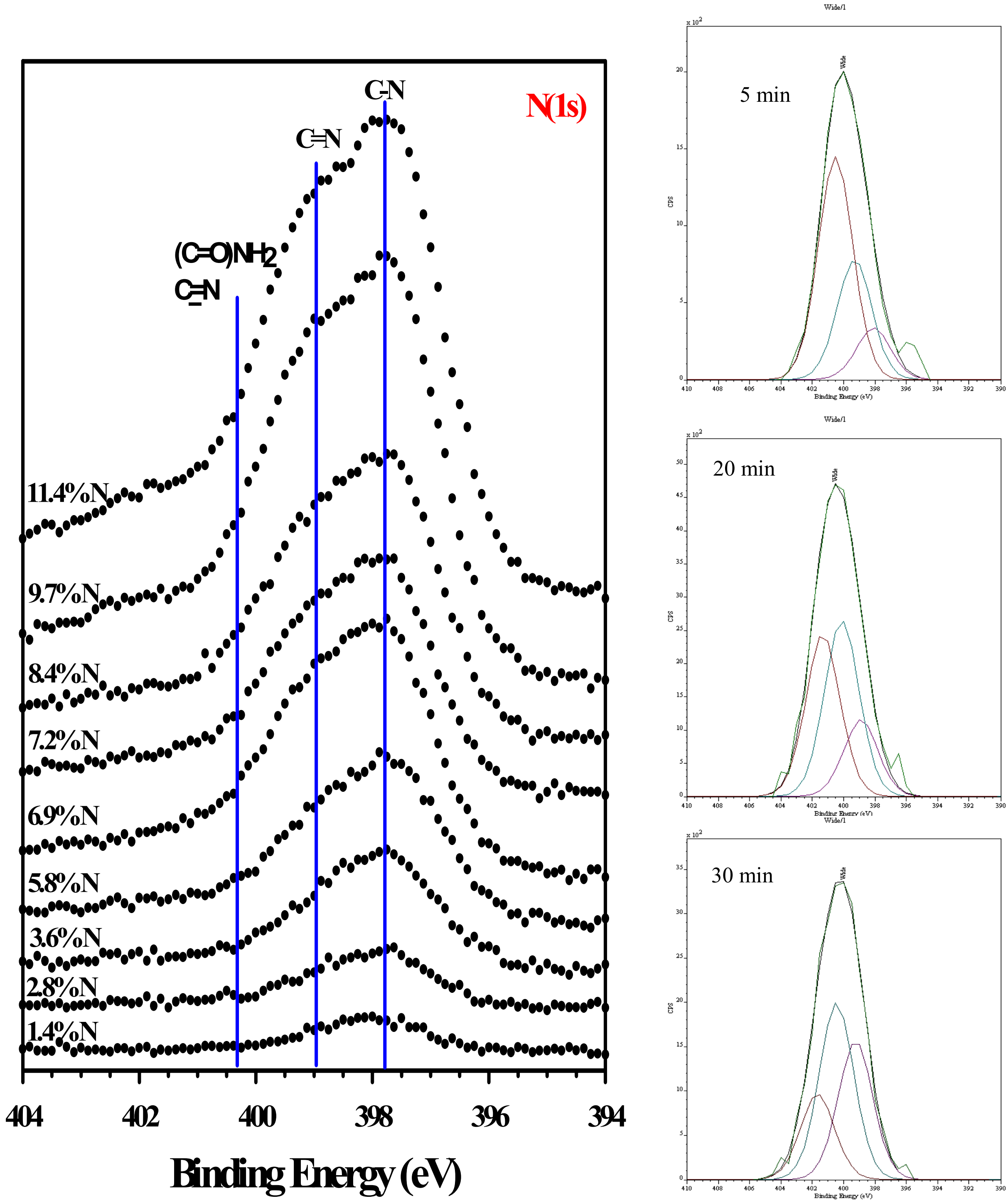

Figure 4: Left : N1s peak shape evolution as a function of the exposure time for a PE sample exposed to the N_2^+/N^+ ion gun ; Right :N 1s peak shape evolution as a function of the exposure time for a PE sample exposed to a RF N_2 plasma. Green: experimental peak, Red: C≡N or (C=O)NH_2, Blue: C=N, Purple: C-N

However, care must be taken for the comparisons between the two sets of experiments. As the plasma treated polymers are transfered in air before the XPS analysis, the hydrolysis of imine groups, reported by Gerenser [2] may occur:

$$R\text{-}CH{=}NH + H_2O \rightarrow R\text{-}CH{=}O + NH_3 \qquad (1)$$

XPS results indeed show an increase of the oxygen concentration after plasma treatment.

Consequently, the surface concentration in nitrogen reported in figure 3 (bottom) is probably underestimated. The presence of oxygen at the polymer surface makes the deconvolution of the C1s peak doubtful, as too many possible combinations (C-N, C-O) exist. For this reason, the study of the chemical bonding was performed on the N1s peak. In this last case, the assignment of the high energy (401 eV) contribution is still subject to controversy in the literature.

The increase in the relative concentration of amine groups produced during ion beam treatment compared to the modified nitrogen plasma treatment (Figure 4) is postulated to arise from the fact that ion beam bombardment is expected to induce significant C-H bond cleavage in PE. The atomic hydrogen liberated from such a process can then react with unsaturated carbon-nitrogen linkages. For example:

$$C{=}NH + H^{\bullet} \rightarrow\rightarrow C\text{-}NH_2 \qquad (2)$$

It should also be noted that amine species are the dominant species obtained when a NH_3 plasma, containing atomic hydrogen rather than N_2, is used to modify PE [7, 8]

The surface thermodynamics was studied by water contact angle. As shown in Figure 5, the contact angle for plasma treated HDPE samples decreases when the exposure time increases. Two contributions have been evidenced: an increase in the surface concentration of polar groups [6], and a separate effect of the electrons. Indeed when the anode is biased, the electron flow on the sample strongly decreases, as shown in [5].

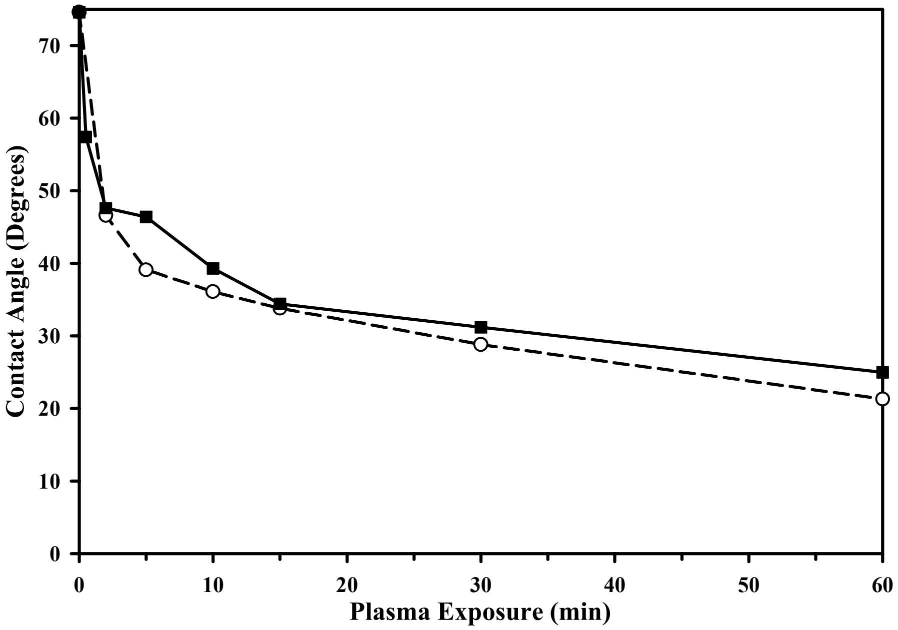

Figure 5: Variation in the static water contact angle for the modified nitrogen plasma treated PE substrates as a function of exposure time for both a grounded (o) and a +10V biased (■) anode. Each data point corresponds to the average of 10 drop measurements

Conclusions

We have undertaken a systematic study of the effect of the constituents of a plasma on the surface modification of polymers. The results presented here show that nitrogen ions and neutrals interacting with a polyethylene surface do not create the same surface functionalities. A progressive functionalisation sequence has been evidenced for the samples submitted to neutrals, which is not present in the case of ion bombardment. The static water contact angle depends on the increase of the number of polar groups on the surface, and on the electron impact.

References

[1] R. Foerch, *Journal of Applied Polymer Science : Applied Polymer Symposium* **46**, 415 (1990).
[2]L.J. Gerenser, *J. Adh. Sci. Technol.* **7**, 1019 (1993)
[3] S. O'Kell, T. Henshaw, G. Farrow, M. Aindow, ,C. Jones, *Surf. Interface Anal.* **23**, 319 (1995)
[4] D.H. Fairbrother, F. Reniers, International Supplement to NSF award (D.H.F. #9985372)
[5] A.J. Wagner, D.H. Fairbrother, F. Reniers, *Plasma and Polymers*, under press (2003).
[6] N. Vandencasteele, E. Michel, F. Reniers, *see these proceedings*.
[7] J. E. Klemberg-Sapieha, O. M. Kuttel, L. Martinu and M. R. Wertheimer, J. Vac. Sci. Technol. A 9 (6), 2975 (1991).
[8] R. Favia, M. Stendardo and R. d'Agostino, Plasmas and Polymers 1 (2), 91 (1996)

Acknowledgements

Support for thiss research was provided by an International Supplement to a National Science Foundation CAREER award (# 9985372). The authors would like to acknowledge the use of the surface analysis laboratory at Johns Hopkins, part of the Materials Research Science and Engineering Center, funded through the National Science Foundation. The authors would also like to acknowledge Prof. J. Vereecken, from the Vrije Universiteit Brussel (Belgium), Department of Metallurgy, Electrochemistry and Materials science for providing access to the PHI 5500 XPS, and Arcelor, for OES measurements.

Time-resolved cavity ring-down spectroscopic study of the surface reactivity of Si and SiH_3 plasma radicals

J.P.M. Hoefnagels, Y.Barrell, W.M.M. Kessels and M.C.M. van de Sanden
Department of Applied Physics, Eindhoven University of Technology,
P.O. Box 513, 5600 MB Eindhoven, The Netherlands

Abstract

The gas phase and surface loss rates of Si and SiH_3 radicals during plasma deposition of hydrogenated amorphous silicon have been measured by time-resolved cavity ringdown absorption measurements. It is shown that Si reacts with SiH_4 with a reaction rate $k_r=(3.0\pm1.3)\times10^{-16}$ $m^{-3}s^{-1}$, while SiH_3 is unreactive in the gas phase. The surface reaction probability β of SiH_3 is independent of the substrate temperature and has an averaged value of $\beta_{SiH3}=0.30\pm0.03$, while $0.9<\beta_{Si}\leq1$.

Introduction

For basic understanding and modeling of plasma deposition processes, information on the density as well as the surface reactivity of the plasma species is essential. Often the surface reaction probability β of the species has been obtained indirectly [1] or under process conditions different from the actual plasma deposition process, *e.g.*, from a molecular beam scattering experiment [2] or by time-resolved density measurements in an afterglow plasma [3,4]. In this work, time-resolved cavity ringdown spectroscopy (τ-CRDS) is used to obtain β *during* plasma deposition: the highly sensitive cavity ring-down spectroscopy (CRDS) method [5] is used to map an increased radical density due to a pulsed rf bias to the substrate in addition to the continuously operated remote SiH_4 plasma. Although time-resolved CRDS has been employed previously to obtain gas phase loss rates of radicals [6,7], in this work the technique has been extended to measurements of the surface loss rates of the radicals [8,9]. This simultaneously yields information on the surface reaction probability β and the density of the radicals under the specific plasma conditions, here particularly for the case of high rate deposition of hydrogenated amorphous silicon (a-Si:H) [10]. Using this method, it is shown that Si is mainly lost in the gas phase to SiH_4, whereas SiH_3 is only lost via diffusion to and reactions at the surface. Moreover, β of Si and SiH_3 are determined and it is shown that β_{SiH3} is independent of the substrate temperature.

The τ-CRDS experiment

In the expanding thermal plasma (ETP) technique [Fig. 1(a)] a remote expanding Ar-H_2-SiH_4 plasma is created. To detect (low-density) radicals such as SiH_3 and Si the CRDS technique has previously been employed; SiH_3 has been identified at the $\tilde{A}\,{}^2A_1{}' \leftarrow \tilde{X}\,{}^2A_1$ broadband transition ranging from ~200 to ~260 nm [11], whereas Si radicals have been probed at the 4s ${}^3P_{0,1,2}\leftarrow 3p^2\,{}^3P_{0,1,2}$ transition around 251 nm [12]. In the time-resolved CRDS (τ-CRDS) measurements, a minor periodic modulation of the radical densities is produced by applying 5 Hz, 2.5% duty cycle rf pulses to the substrate in addition to the continuously operating ETP [9]. The additional absorption A_{rf} due to the radicals generated by the rf pulse is obtained from the difference in absorption at some point Δt in the rf afterglow and at a point long after the influence of the rf pulse has extinguished [see Fig. 1(b)]. Every CRDS trace is handled separately by means of a 'state-of-

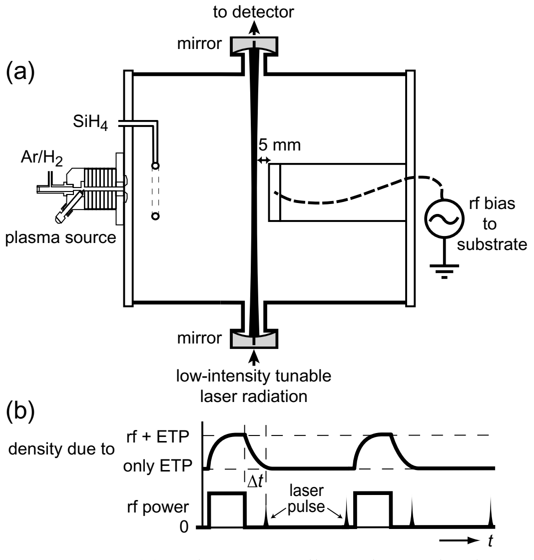

Figure 1: (a) The expanding thermal plasma (ETP) setup equipped with the cavity ringdown spectroscopic setup and an rf power supply for pulsed bias voltage application to the substrate. (b) Schematic time diagram illustrating the modulation of the radical density and the synchronization of the CRDS laser pulses.

the-art' 100MHz, 12 bit data acquisition system [13] and an averaged A_{rf} is obtained as a function of time Δt in the afterglow of the rf pulse.

A typical τ-CRDS measurement for Si and SiH_3 is shown in Fig. 2. A duty cycle of 2.5 % has carefully been chosen in order to obtain a good signal-to-noise ratio in the additional Si and SiH_3 absorption, while possible powder formation due to the 'anion confining' rf plasma sheath is suppressed [14]. Fig. 2 shows that both Si and SiH_3 decrease single exponentially, which is expected from the radicals' mass balance [15]. The corresponding loss rate τ^{-1} depends linearly on the gas phase loss on one hand and the loss due to diffusion to and reactions at the surface on the other hand [15]:

$$\tau^{-1} = k_r n_x + \frac{D}{\Lambda^2}. \tag{1}$$

In this equation, k_r is the gas phase reaction rate with species x with density n_x, D is the diffusion coefficient for the specific radical in the Ar-H_2-SiH_4 mixture [16], and Λ is the effective diffusion length of the radical. The latter depends on diffusion geometry and on the radical's surface reaction probability β [15].

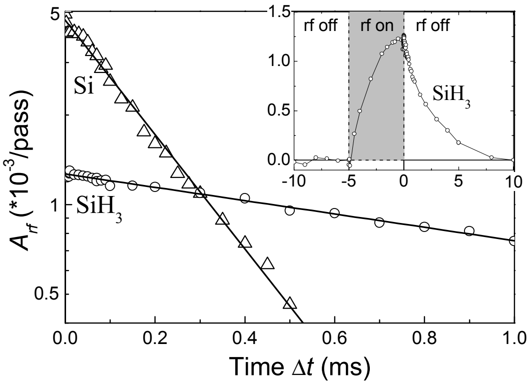

Figure 2: Typical semi-logaritmic plot of the additional absorption A_{rf} of Si and SiH_3 during the rf afterglow showing a single exponential decay with a loss time of (0.226±0.006) ms and (1.93±0.05) ms for Si and SiH_3, respectively. Every data point is an average of 128 CRDS traces. The inset shows a linear plot of the A_{rf} of SiH_3 for the complete rf pulse of 5 ms.

Si temperature and saturation measurements

As will be shown below, the gas temperature T_{gas} is necessary to calculate the density of SiH_4 via the ideal gas law, while T_{gas} is also needed to calculate the diffusion term in Eq. (1) for 6 different substrate temperatures T_{sub}. Therefore, T_{gas} has been measured from the Doppler broadning of the Si 4s $^3P_2 \leftarrow 3p^2\,^3P_1$ atomic line. To do so, first optical saturation of the Si profile has been excluded. Optical saturation has been checked from a measurement of the area and width of the Si profile as a function of the light intensity I in the cavity (Fig. 3). Fig. 3 shows that for $I>2\times10^{-4}$ lm the Si peak flattens off, i.e., the Si transition gets optically saturated. To ensure no optical saturation of Si (and SiH_3), all further measurements have been done at $I=5\times10^{-5}$ lm. Moreover, it has been checked that the Si atoms are thermalized, such that the temperature of Si can be taken equal to T_{gas} [9]. Subsequently, T_{gas} has been measured as a function of T_{sub}, see Fig. 4. It is found for SiH_4-flow=1, used for all β measurements, that $T_{gas}\approx1500$K, while the measurements of SiH_4-flow=0.5 sccs, used for its high Si density and thus good signal-to-noise ratio, show that T_{gas} is independent of T_{sub}.

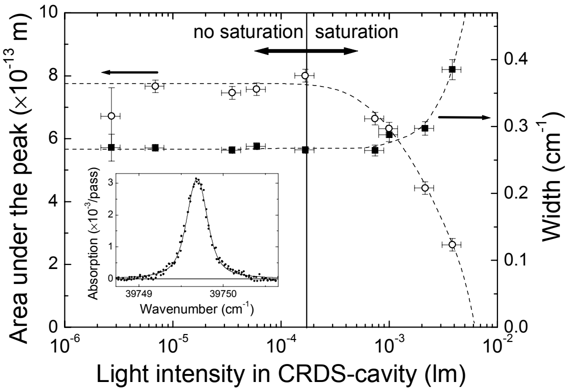

Figure 3: the area and the width of the Si 4s $^3P_2 \leftarrow 3p^2$ $^3P_1$ absorption profiles as a function of the light intensity inside the CRDS-cavity. The vertical solid line indicates the transition between saturation and no saturation, whereas the dashed lines are guides to the eye. The area and width of the peak are obtained from the profiles by means of a Voigt fit. A typical example *of a profile with Voigt fit is shown in the inset.*

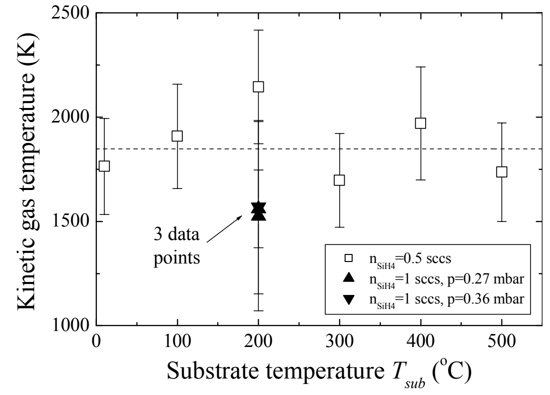

Figure 4: the kinetic gas temperature T_{gas} as obtained from Doppler profile measurements of a Si transition as a function of the substrate temperature T_{sub}. The dashed line depicts a fit of the measurements of SiH_4-flow=0.5 sccs. Additional measurements have been performed at T_{sub}=200 °C for *SiH_4-flow=1 sccs (solid symbols). and show an average temperature of T_{gas}≈1500K.*

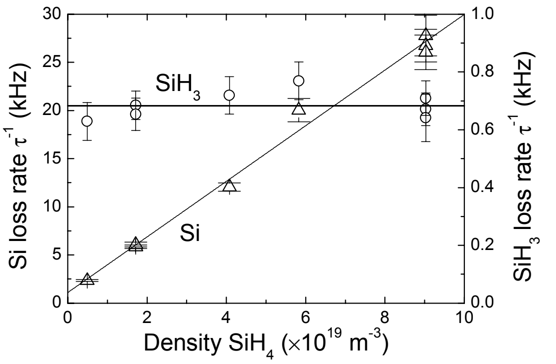

Figure 5: The loss rate of Si and SiH_3 as a function of the SiH_4 density keeping the total

Gas phase loss of Si and SiH_3

From Eq. (1) it is seen that the gas phase loss processes need to be considered first before surface loss rates of the radicals can be deduced. For Si and SiH_3 in the ETP plasma the only candidate for a significant gas phase loss is SiH_4 [16]. Therefore the loss rate of Si and SiH_3 has been obtained as a function of the SiH_4 density (Fig. 5) keeping the pressure and thus the diffusion term in Eq. (1) nearly constant. The SiH_4 density has been calculated from the SiH_4 partial pressure using T_{gas}=1500K including a correction for the local SiH_4 consumption [9]. The loss rate of SiH_3 in Fig. 5 is independent of the SiH_4 density, which indicates no gas phase loss of SiH_3, while the loss rate of Si increases linear with the SiH_4 density. The slope reveals a reaction rate constant of Si(^{3}P) with SiH_4 of k_r=(3.0±1.3)×10^{-16} $m^{-3}s^{-1}$. This value corresponds well with literature values [8,9].

Surface reaction probability of Si and SiH_3

To deduce the surface reaction probability β of Si and SiH_3 from Eq. (1), a semi-empirical expression with radial and axial diffusion length *R* and *H*, as proposed by Chantry [15], has been assumed for the cylinder symmetrical diffusion geometry of the ETP reactor. Then, for SiH_3 (no gas phase loss) the loss time τ in Eq. (1) depends linear on the pressure with a slope depending on *R*, *H*, and T_{gas} and an offset depending on *R*, *H*, T_{gas}, and β. After careful consideration it has been assumed that the diffusion of the radicals in radial direction can be neglected in respect to the diffusion in axial direction, i.e., $R \rightarrow \infty$ [8]. Subsequently, *H* can be obtained from the pressure dependence of the loss time of SiH_3. Therefore, the loss time of SiH_3 has been measured as a function of the pressure for 6 different substrate temperatures, see Fig. 6. In Ref. [9] it is shown that based on the independence of T_{gas} on T_{sub} all the individual data set of Fig. 6 can be fitted simultaneously with a shared slope to Eq. (1) to obtain better accuracy in *H*, see Fig. 6. Then, from the 6 offsets in Fig. 6 the surface reaction probability β can be obtained as a function of T_{sub} (Fig. 7). No clear dependence of β_{SiH3} on T_{sub} is seen. Apparently, all values of β_{SiH3} can be averaged, yielding β_{SiH3}=0.30±0.03. This value is in good agreement with estimated values of β_{SiH3} for 3 different T_{sub} as obtained previously with the indirect method of 'aperture-well assembly' applied under similar conditions in the same setup [1]. The value also corresponds to β_{SiH3}=0.28±0.03 at T_{sub}=300 °C as determined by Perrin *et al.* using time-resolved threshold ionization mass spectrometry in an rf plasma with a 100% on-off modulation [3].

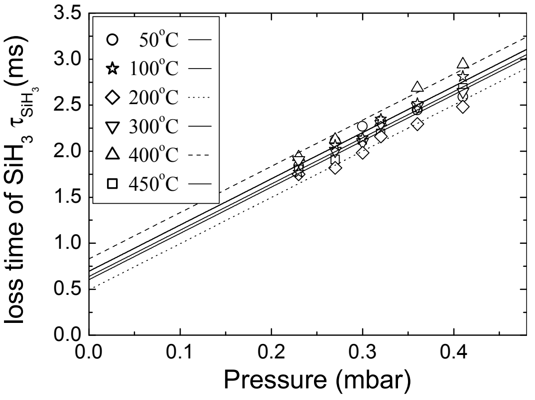

Figure 6: *The decay time of SiH_3 as a function of the total pressure for 6 different substrate temperatures and for a constant SiH_4 flow.*

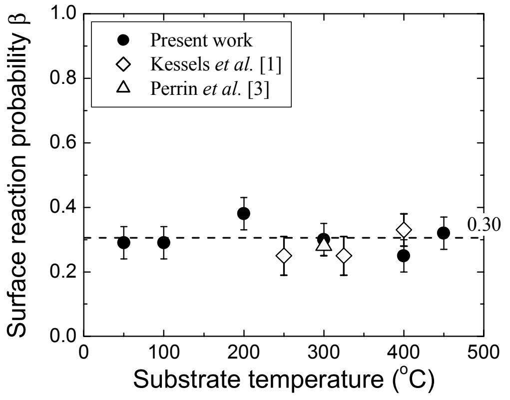

Figure 7: *the surface reaction probability β of SiH_3 as deduced from the offsets of Fig. 6 as a function of T_{sub}. Also shown are values of β from literature, Refs. [1,3].*

For Si also the loss time has been measured as a function of the pressure (not shown here). Assuming the same diffusion geometry for Si as for SiH_3, while taking into account the gas phase loss to SiH_4, a lower limit of 0.9 has been obtained for β of Si, yielding therefore $0.9<\beta_{Si}\leq1$. Although this is the first direct experimental evidence for a nearly unity surface reaction probability of Si, a β of ~1 is generally assumed for the Si radical on the basis of its hydrogen deficiency [4].

Based on (estimates of) the densities of all plasma species, combined with their β, it is found that SiH_3 has the main contribution to the a-Si:H film growth [9]. Furthermore, the independence of the β_{SiH3} on T_{sub} seems remarkable, because the surface structure depends strongly on T_{sub} [17]. The implications of these observations on the growth mechanism of a-Si:H will be discussed in [17].

Conclusions

It has been shown that the time-resolved cavity ring-down experiment applied on a remote plasma is capable of obtaining radical loss rates during the actual plasma deposition process. From partial and total pressure series, it has been shown that Si is highly reactive in the gas phase with SiH_4 whereas its surface reaction probability β_{Si} is $0.9<\beta_{Si}\leq1$. SiH_3 on the other hand is unreactive with SiH_4 and has a surface reaction probability of β_{SiH3}=0.30±0.03 in good agreement with previously reported values. Furthermore, β_{SiH3} is independent of the substrate temperature.

Acknowledgments

The authors acknowledge the Technical Laboratory Automation group of the Eindhoven University of Technology and the technical assistance by M.J.F. van de Sande, J.F.C. Jansen, H.M.M. de Jong, and A.B.M. Hüsken. This research was supported by The Netherlands Foundation for Fundamental Research on Matter (FOM: 98PR1781 and 99PSI03) and the Royal Netherlands Academy of Sciences and Arts (KNAW) by the fellowship of one of the authors (W. K.).

References

[1] See *e.g.*, W.M.M. Kessels, M.C.M. van de Sanden, R.J. Severens, and D.C. Schram, J. Appl. Phys., **87** 3313 (2000) and references therein.

[2] P.R McCurdy, K.H.A. Bogart, N.F. Dalleska, and E.R. Fisher, Rev. Sci. Instrum., **68,** 1684 (1997).

[3] J. Perrin, M. Shiratani, P. Kae-Nune, H. Videlot, J. Jolly, and J. Guillon, J. Vac. Sci. Technol. A, **16,** 278 (1998).

[4] P. Kae-Nune, J. Perrin, J. Guillon, and J. Jolly, Plasma Sources Sci. Technol., **4,** 250 (1995).
[5] K.W. Busch and M.A. Busch, Cavity-Ringdown Spectroscopy, Am. Chem. Soc., Wash. DC, (1999).
[6] D.B. Atkinson and J.W. Hudgens, J. Phys. Chem. A, **101,** 3901 (1997) and references therein.
[7] A. P. Yalin, R. N. Zare, C. O. Laux, C. H. Kruger, Appl. Phys. Lett., **81**, 1409 (2002).
[8] J.P.M. Hoefnagels, A.A.E. Stevens, M.G.H. Boogaarts, W.M.M. Kessels, and M.C.M. van de Sanden, Chem. Phys. Lett., **360,** 189 (2002).
[9] J.P.M. Hoefnagels, Y. Barrell, M.C.M. van de Sanden, W.M.M Kessels, to be published.
[10] W. M. M. Kessels, R. J. Severens, A. H. M. Smets, B. A. Korevaar, G. J. Adriaenssens, D. C. Schram, and M. C. M. van de Sanden, J. Appl. Phys., **89,** 2404 (2001).
[11] W.M.M. Kessels, A. Leroux, M.G.H. Boogaarts, J.P.M. Hoefnagels, M.C.M. van de Sanden, and D.C. Schram, J. Vac. Sci. Technol. A., **19,** 467 (2001).
[12] W.M.M. Kessels, J.P.M. Hoefnagels, M.G.H. Boogaarts, D.C. Schram, and M.C.M. van de Sanden, J. Appl. Phys., **89,** 2065 (2001).
[13] Technical Laboratory Automation Group, Eindhoven University of Technology, Den Dolech 2, 5600 MB Eindhoven, The Netherlands.
[14] C. Courteille, J.L. Dorier, C. Hollenstein, L. Sansonnens, and A.A. Howling, Plasma Sources Sci. Technol., **5,** 210 (1996).
[15] P.J. Chantry, J. Appl. Phys., **62,** 1141 (1987).
[16] J. Perrin, O. Leroy, and M.C. Bordage, Contrib. Plasma. Phys., **36,** 1 (1996).
[17] W.M.M. Kessels, J.P.M. Hoefnagels, P.J. van de Oever, M.C.M. van de Sanden, to be published.

CH_4 Reforming with CO_2 Using Microwave Plasma Technique

H.Nagazoe[1], H.Naito[1], M.Kobayashi[1], T.Yamaguchi[1], H.Kimuro[2], K.Onoe[1]
[1]*Department of Industrial Chemistry, Faculty of Engineering, Chiba Institute of Technology, Narashino, Japan*
[2]*Ishikawajima-Harima Heavy Industry Co., Yokohama, Japan*

Abstract

Using microwave irradiated CH_4/CO_2 plasma (2.45 GHz), a direct conversion technology of CH_4 into synthesis gas (H_2/CO) was developed under reduced pressure (6.5 kPa). Microwave irradiated power was controlled in the range from 10 to 300 W. CO_2 molar ratio was adjusted from 0 to 100%. At 100 W irradiation and CO_2 molar ratio was supplied at 50%, dehydrogenative coupling of CH_4 and reduction of CO_2 were progressed simultaneously. However, at 300W irradiation, partial oxidation of CH_4 to CO was observed.

1. Introduction

Synthesis gas (H_2/CO) is a suitable material in the production of low-molecular hydrocarbons by the Fischer-Tropsch reaction and GTL (Gas to Liquid) processes such as the synthesis of alcohol and aldehyde (Fig.1). Usually synthesis gas is obtained by reforming of CH_4 adding oxidizer (CO_2, H_2O). However, the plant cost of synthesis gas production is occupying up to 60% in GTL process [1], thus the cost reduction by the achievement of the efficient production of synthesis gas is one of serious problems.

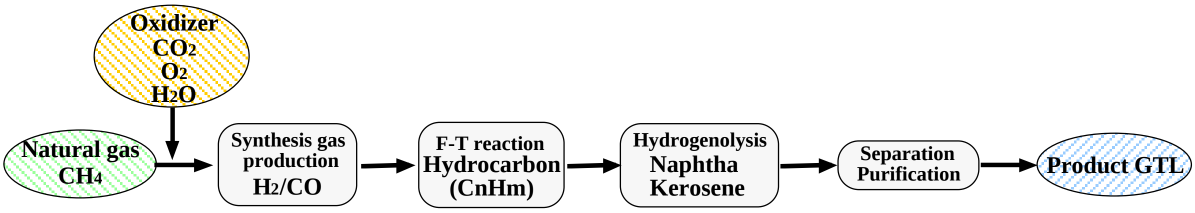

Fig.1 Flow-chart of GTL (Gas toLiquid) process

From the lowering in environmental loading, CO_2 utilization as an oxidizer of CH_4 is suitable. However, in the CH_4 reforming with CO_2 using catalyst, there are some problems with carbon deposition from decomposition of CH_4 and degradation of catalytic activity by the sintering. Recently, in the case of non-catalytic reaction, dielectric barrier discharge and corona discharge methods in order to reform CH_4/CO_2 mixed gas have been reported [2,3]. The authors have been developed with a partial oxidation of CH_4 to CO using O_2 plasma reactions [4].

In this study, reforming of CH_4 using non-catalytic microwave plasma technique is examined [5]. Both effects of microwave irradiated power and CO_2 molar ratio on the conversions of CH_4 and CO_2 and product yield are discussed.

2. Experimental

2.1 Apparatus

The experimental apparatus using microwave plasma technique is shown in Fig.2. The apparatus consists of four sections (gas supply, microwave generator, reactor and gas analysis). A cylindrical quartz tube in 25 mm i.d. with 300 mm length was used as the reactor. Microwaves (2.45GHz) were irradiated into the vertically held reactor through a waveguide. The reactor was connected to a vacuum line for feeding gaseous reactants. CH_4/CO_2 mixture gas was fed continuously in the downward flow.

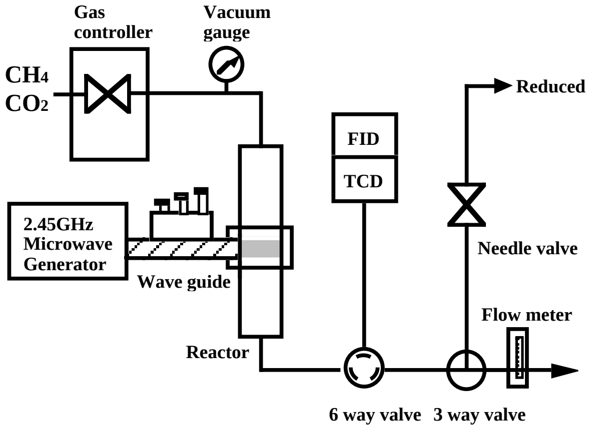

Fig.2 Experimental apparatus for microwave plasma reaction

2.2 Procedure

Experimental conditions were summarized in Table 1. Initial pressure was controlled by a gas regulator at 6.5 kPa. Microwave power was adjusted from 10 to 300 W. Total feed rate was controlled at 2.08 mmol/min. Feed gas was passed through the irradiated zone at the center of the reactor. After microwave irradiation had been applied for 60 s in the plasma state, the outlet gas was analyzed by use of a gas chromatography.

Table 1 Experimental conditions

Feed gas	
System	CH_4, CH_4/CO_2
Total feed rate	2.08 mmol/min
Linear velocity	27.0 mm/s
Initial pressure	6.5 kPa
Reactor	
Material	Quartz glass tube
Size	25 mmϕ × 300 mmL
Microwave	
Frequency	2.45 GHz
Wave guide	54.6 mm × 109.2 mm
Power	10-300 W
Products analysis	TCD , FID gas chromatograph

3. Results and Discussion

3.1 Effect of microwave irradiated power on dehydrogenation of methane

Figures 3 and 4 show the CH_4 conversion and carbon selectivity of product, respectively. The CH_4 conversion increased with increasing microwave power, and the selectivity of C_2H_2 was still as high as over 92 % in the range from 100 to 300 W. However, it was observed that further increase of microwave power (over 300 W) gave the deposition of carbonaceous matter on the wall of the reactor. Consequently, over 70 % yield of C_2H_2 from CH_4 was achieved in the range from 200 to 300 W incident power level.

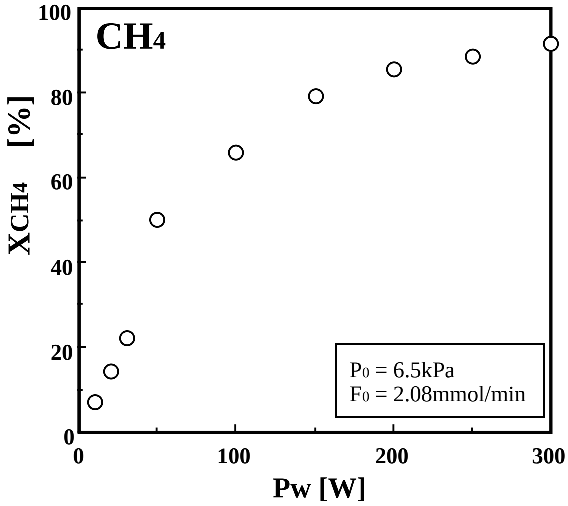

Fig. 3 Relation between microwave power and methane conversion

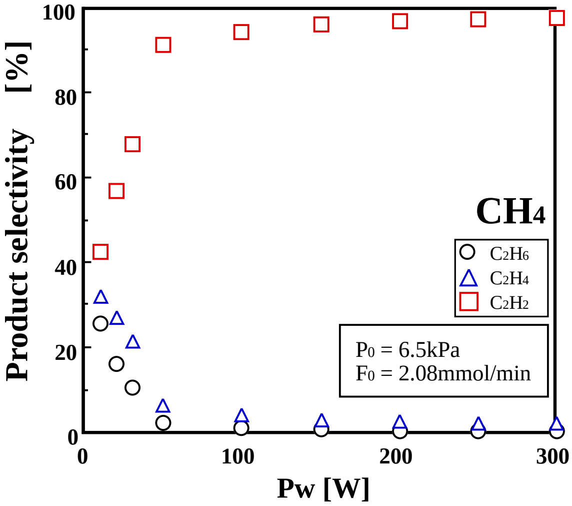

Fig.4 Relation between microwave power and product selectivity

From these results, when CH_4 was reacted in the plasma state under microwave irradiation, the following dehydrogenation may occur (Fig.5). At first the methyl radical is formed, and consecutive dehydrogenation progresses by passing methylene and methine radicals. Finally, the C_2H_2 is formed by the coupling of methine radicals.

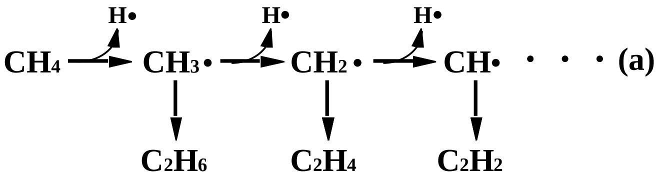

Fig.5 Assumed mechanism for methane plasma reactions

3.2 Effect of CO_2 molar ratio on CH_4 and CO_2 conversions

Figures 6 and 7 show the results of CH_4 and CO_2 conversions by varying CO_2 ratio from 20 to 100 %, when the initial pressure of feed gas was constant at 6.5 kPa.

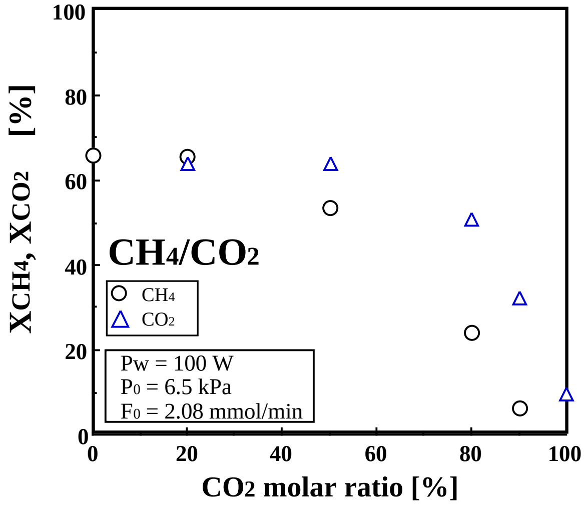

Fig.6 Relation between carbon dioxide molar ratio and feed conversions (100 W)

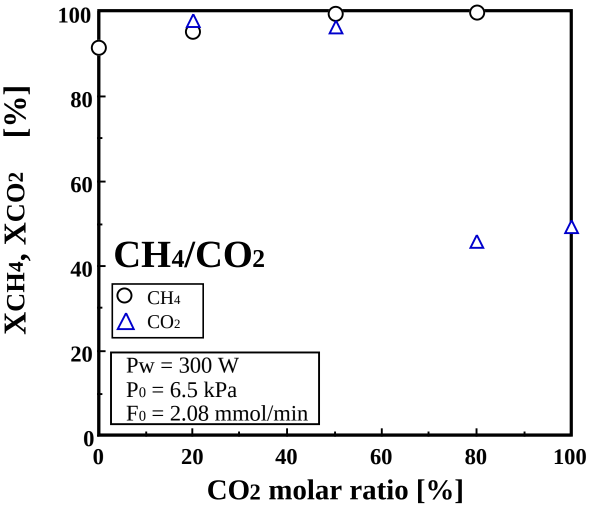

Fig.7 Relation between carbon dioxide molar ratio and feed conversions (300 W)

At 100 W incident power level (Fig.6), it was cleared that both conversions of CH_4 and CO_2 were decreased with increasing CO_2 moral ratio. When pure CO_2 was supplied, CO_2 conversion was 9.8 %. It was assumed that much microwave irradiated power was consumed in decomposition of CO_2, and both conversions of CH_4 and CO_2 were decreased. Meanwhile, at 300 W incident power level (Fig.7), both conversions of CH_4 and CO_2 were over 90 % in the range of CO_2 molar ratio below 50 %. When CO_2 molar ratio was over 50 %, CO_2 conversion was decreased. These results indicate that a sufficient energy was supplied for the decomposition of CO_2 at 300 W incident power level, and decomposition of CH_4 was progressed. We have obtained from preliminary experiment in H_2/CO_2 plasma reactions that CO_2 conversion was increases with increasing microwave incident power level. Thus the reduction of CO_2 may be promoted by the hydrogen active species generated from CH_4 decomposition.

3.3 Effect of CO_2 molar ratio on product selectivity with regard to C-mol of CH_4

Figure.8 and 9 show the relation between CO_2 molar ratio and product selectivity based on C-mol of feed CH_4. C_2 hydrocarbons, H_2 and CO were main products.

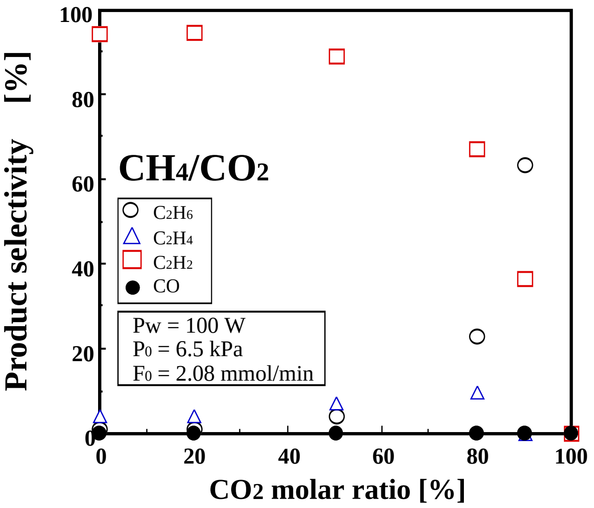

Fig. 8 Relation between carbon dioxide molar ratio and product selectivity from methane (100 W)

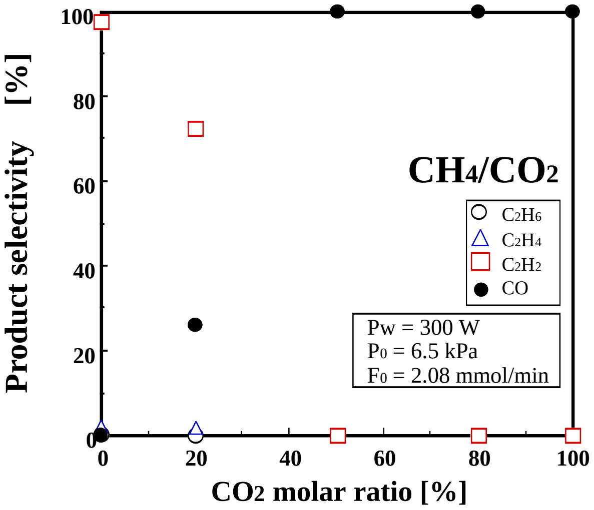

Fig.9 Relation between carbon dioxide molar ratio and product selectivity from methane (300 W)

At 100 W incident power level (Fig.8), C_2H_2 was obtained mainly when CO_2 molar ratio was up to 80 %, and C_2H_6 selectivity was remarkably increased at the range over 80 % CO_2 molar ratio. It was indicated that no partial oxidation of CH_4 into CO was occurred judging from the converted moles of CO_2 are almost equal to the produced moles of CO. However, at 300 W incident power level (Fig.9), CO selectivity was increased with increasing CO_2 molar ratio. Especially, when CO_2 molar ratio was over 50 %, CO selectivity was near 100 %. Under these conditions, the partial oxidation of CH_4 into CO was progressed stoichiometly. Consequently, at 100 W incident power level, both reaction of (a) and (b) were occurred. Meanwhile, the incident power level was up to 300 W, partial oxidation of methine radical (c) was progressed by the absence to activated oxygen radical.

Fig.10 Assumed reaction mechanism for CO formation

3.4 Comparison of the produced moles of H_2 and CO

Figures11 and 12 show the relation between CO_2 molar ratio and produced moles of synthesis gas, where both produced moles of H_2 and CO were calculated in the assumption that the supplied CH_4/CO_2 mole number is 1.

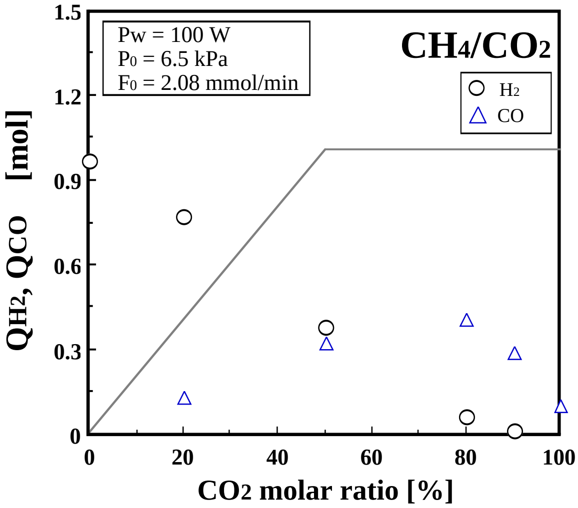

Fig. 11 Relation between carbon dioxide molar ratio and producted hydrogen, carbon monoxide (100 W)

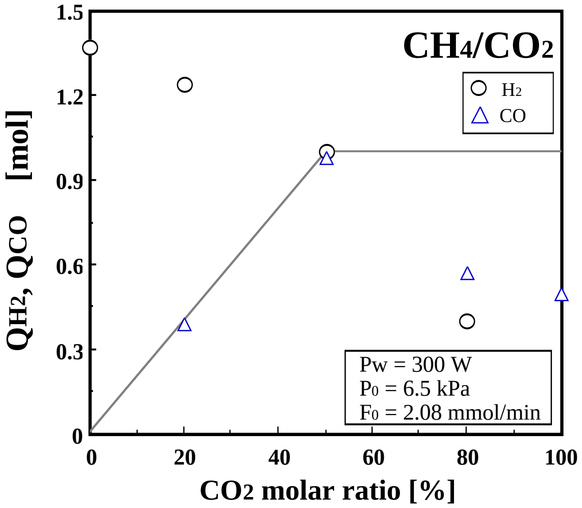

Fig.12 Relation between carbon dioxide molar ratio and producted hydrogen, carbon monoxide (300 W)

At 100 W incident power level, the produced CO mole was shown the maximal value at 80 % of CO molar ratio. However, at 300 W incident power level, the maximal value was observed when CO molar ratio is 50 %. It is cleared that the produced H_2 mole was decreased with increasing CO_2 molar ratio regardless of incident power level. The dotted line in Figs.11 and 12 reveals the two-type of assumed CO mole by varying CO_2 molar ratio: I. CO_2 molar ratio is below 50%, and CH_4 molar ratio surpasses CO_2. In this case, the dissociated oxygen from CO_2 combines with the carbon which constitutes CH_4, and CO is formed. II. CO_2 molar ratio is over 50%; and molar fraction of CH_4 is insufficient. If the both supplied gases (CH_4 and CO_2) perfectly convert to CO, the formed mole of CO becomes constant at 1. From the results in Fig.12, both partial oxidation of CH_4 and decomposition of CO_2 into CO were progressed efficiently when CO_2 molar ratio is below 50%.

3.5 Effect of CO_2 molar ratio on H_2/CO

Figures13 and 14 show the relation between CO_2 molar ratio and H_2/CO. It is cleared that H_2/CO was decreased with increasing CO_2 molar ratio. When 50 % of CO_2 molar ratio was noticed, H_2/CO ratio was shown near 1 regardless of incident power level. Especially at 300 W, the oxidation of the methine radical produced in the dehydrogenation of the CH_4 easily progresses, and hydrogen active species which simultaneously occurred in the dehydrogenation of the CH_4 promotes the reduction of the CO_2.

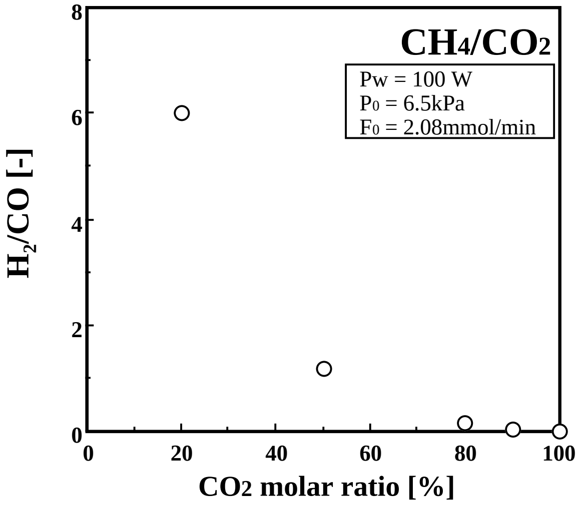

Fig.13 Relation between carbon dioxide molar ratio and hydrogen/carbon monoxide ratio (100 W)

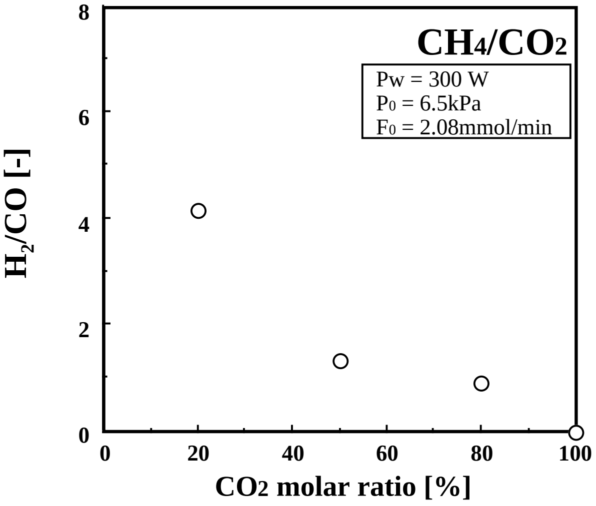

Fig.14 Relation between carbon dioxide molar ratio and hydrogen/carbon monoxide ratio (300 W)

4. Conclusion

Non-catalytic CH_4 reforming with CO_2 using microwave plasma technique was developed, and the following results were obtained.

a) Dehydrogenation of CH_4 and decomposition of CO_2 was progressed independently.

b) Partial oxidation of CH_4 was progressed at 300 W incident power level.

c) Main products were H_2 and CO, and C_2 hydrocarbons (mainly C_2H_2) were obtained as a by-product.

d) Higher yield of H_2/CO (molar ratio is near 1) was achieved when molar ratio of CO_2 was equal to that of CH_4.

5. References

[1] R.Nielsen, Catalysis Today, 71, 243 (2002).
[2] S.Kado, K.Urasaki, Y.Sekine, K.Fujimoto, Chem. Commun, 5, 415 (2001).
[3] X.Zhang, B.Dai, A.Zhu, W.Gong, C.Liu, Catalysis Today, 72, 223 (2002) .
[4] K.Onoe, H.Naito, T.Narita, H.Nagazoe, M.Kobayashi, T.Yamaguchi, H.Kimuro, 67th Annual Meeting of The Society of Chemical Engineers, Japan, Abst. K209 (2002).
[5] K.Onoe, A.Fujie, T,Yamaguchi, Y,Hatano Fuel, 76, 281 (1997).

Biomass Decomposition under Microwave Plasma State

K.Konno, M.Kobayashi, K.Onoe, T.Yamaguchi
Department of chemistry, Faculty of Engineering, Chiba Institute of technology, Narashino, Japan

1. Introduction

Natural organic resource is classified roughly into two types-depletion and regenerative. The representative of the depletion type resources is coal and petroleum, and biomass is mentioned as a regenerative resource. The unused biomass richly exists in the fields of agriculture, forestry, fishery and livestock industry. Ogi *et al.* [1] reported that biomass produced in agriculture or forestry was handled as a plant biomass. Mainly plant biomass was composed of cellulose and lignin, and cellulose content was higher than lignin. Recently, considerable attention has been paid for effective utilization of plant biomass with regard to higher content of cellulose[2]. Miura *at el.* [3] studied the conversion from cellulose into chemical raw materials. Here, element ratio of cellulose is noticed, O/C ratio is 1 and H/C ratio is nearly 2. Then it is possible to obtain synthesis gas (H_2/CO) when cellulose gasification is perfectly progressed. However, in the thermal decomposition of the cellulose, carbon dioxide and steam are often formed as vice-product [4-8]. In this study, a direct conversion technique from biomass into synthesis gas was developed under microwave plasma state. Four kinds of material were selected as the solid reactant, and effect of microwave irradiation time on conversion and product yield was examined in detail.

2. Experimental

2.1 Raw material

A marketing grade argon was used as the supplying gas. Cellulose (Merck Co. 200 mesh under) and lignin (Kanto Kagaku Co. 200 mesh under) are selected as the standard material which constitutes plant biomass. Furthermore, sugarcane (Okinawa. 16 mesh under) and cedar sawdust (Alaska 16 mesh under) are used as the raw material. Table 1 shows physical property of each material. Ash content in lignin was measured by JIS M8812. The content of cellulose and lignin within raw material were measured by chlorite and sulfuric acid method, respectively. Each sample was dried at 380 K for 3 h under argon supplying.

Table 1 Physical properties of biomass

		Proximate analysis (d.b)			Elemental analysis (d.a.f)				Molar ratio		component [wt%] (d.b.)		
		[wt%]			[wt%]				[-]				
	district	VM	Ash	FC	C	H	N	O(diff)	H/C	O/C	oily component***	chlorite method	sulfuric acid method
cellulose	reagent*	95.5	0.0	4.5	42.6	6.2	0.0	51.2	1.7_5	0.9_0	0.7	99.3	0.0
sugarcane (bagasse)	Okinawa	82.5	4.5	13.0	47.6	6.1	0.3	46.0	1.5_4	0.7_2	3.0	73.8	23.2
cedar (sawdust)	Alaska	79.7	1.2	9.1	48.5	6.4	0.0	45.1	1.5_8	0.7_0	2.6	70.0	27.4
lignin	reagent**	46.6	17.8	35.6	65.7	5.4	0.1	28.8	0.9_9	0.3_3	1.5	—	98.5

VM:Volatile matter FC:Fixed carbon d.a.f:dry ash free d.b.:dry base *Merck Co. **Kanto Chemical Co.

*** benzene/ethanol soluble

2.2 Apparatus

Figure 1 shows the experimental apparatus for biomass decomposition using microwave plasma. The desiccated sample (1.5 g) was set in the middle of a cylindrial quartz tube reactor (25 mm inside diameter, 2 mm thickness, and 500 mm length). The layer length of packed cellulose or lignin was 5 mm, meanwhile that of sugarcane or cedar sawdust was 20 mm because the packed density is comparatively small. The upper level of sample layer was held in the middle of wave guide.

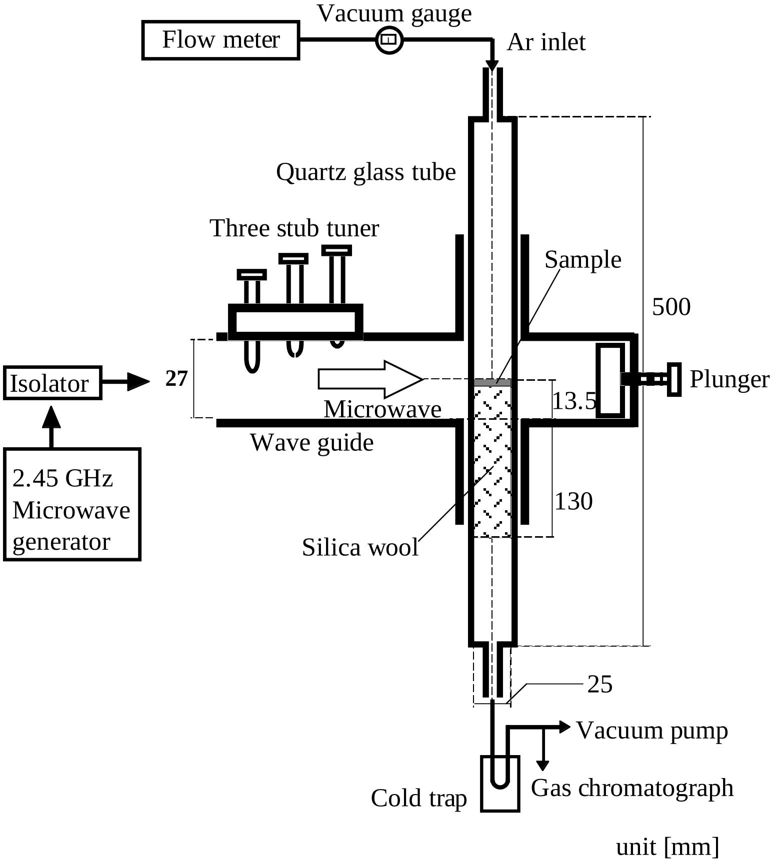

Fig.1 Elemental apparatus by microwave plasma technique

2.3 Procedure

Table 2 shows the experimental conditions. The procedure for the calculation of conversion (X) and product yield of gaseous (Y_{gas}) and oily (Y_{oil}) was as follows: After microwaves were irradiated for a given time, the reactor was removed off the line, and yield of gaseous product was calculated by weight difference between before and after reaction. The oil products remaining within the reactor and condensed in cold trap were separately extracted using benzene as a solvent at 298 K for 48 h. The residue was obtained by employing vacuum drying at 333 K for 1 h and normal pressure drying at 380 K for 1 h, and yield of oily product was calculated by weight difference between before and after extraction. The values of conversion and product yield were revealed on the basis of dry ash free, where only the ash content of lignin was measured by the ignition residue method.

Table 2 Experimental conditions of microwave plasma technique

Sample	cellulose, lignin (200 mesh pass)
	cedar, sugarcane (8.6 mesh pass)
Weight	1.5 g
Feed gas	
System	Ar
Feed rate	0.89 mmol/min
Initial pressure	4.0 kPa
Reactor	
Material	Quartz glass tube
Size	25 mm ϕ ×500 mm L
Microwave	
Frequency	2.45 GHz
Power	300 W
Irradiation time	0.5 − 10 min

2.4 Product analysis

Gaseous products were analyzed using a Shimadzu GC-14B gas chromatograph. A thermal conductivity detector (TCD) was used to determine the molar fraction of inorganic compound including in outlet gas using SHINCARBON-T column. Oily products were analyzed using another Shimadzu GC-14B gas chromatograph equipped with a flame ionization detector (FID) and UA-DX30 column (Carborane-Silioxane 60 m × 0.25 mm × 0.15 μm). Furthermore, FI-IR measurement was employed for oily products.

3. Results and discussion

3.1 Effect of irradiation time on conversion and product yield during cellulose or lignin decomposition

When cellulose or lignin was packed within the reactor, the time change of conversion and yield of gaseous and oily product were shown in Fig.2. At 1 min irradiation, cellulose conversion (40.1 wt%) slightly showed higher value with lignin (37.2 wt%). After 2 min irradiation, cellulose conversion was increased with an increase of microwave irradiation time, and reached 90% in 5 min. But the lignin conversion remained near 53 wt% after 2 min. The reason why lignin conversion does not increase seems to cause higher carbon content of lignin, even if the exposure time is lengthened. With regard to the change of oxygen and hydrogen element mole during lignin decmposition, higher conversions of oxygen (93.5 %) and hydrogen (83.3 %) were obtained at 10 min irradiation. In the case of cellulose decomposition at 10 min irradiation, oxygen (99.1 %) and hydrogen (99.6 %) hardly remain for the residue. From these results, when the C/O ratio of the material is higher than 1, limitation of conversion exists. For lignin decomposition, the conversion limitation seems to be 55-60 wt%.

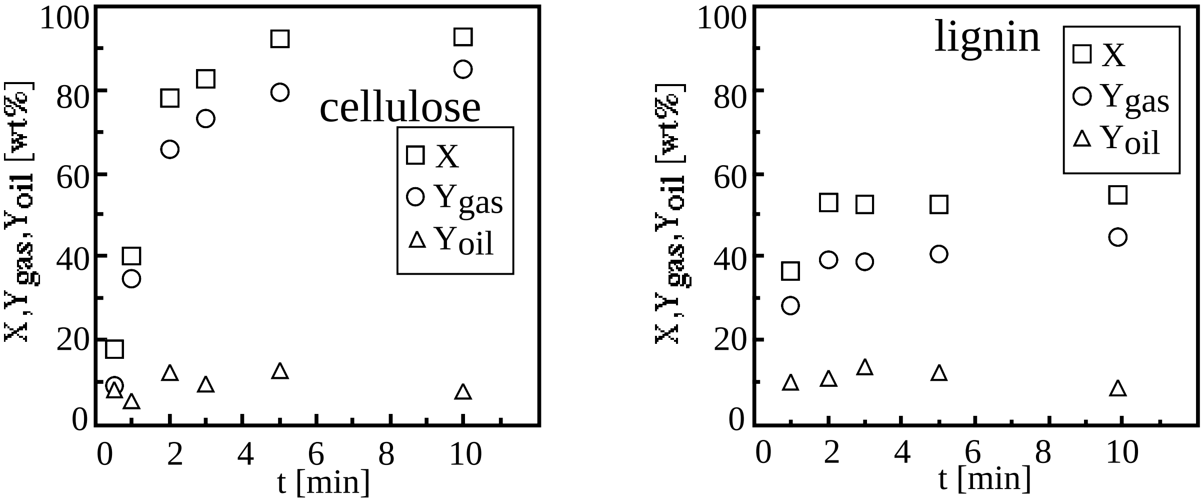

Fig.2 Time change of conversion and product yield (cellulose, lignin)

3.2 Characteristic of gaseous product during cellulose or lignin decomposition

Figure 3 shows the time change of accumulation of gaseous product obtained by cellulose or lignin decomposition. Carbon monoxide and hydrogen were major products, and carbon dioxide and steam were slightly formed under these conditions. It was cleared that molar fraction of carbon monoxide and hydrogen were almost constant independent on irradiation time. The produced H_2/CO ratio during cellulose decomposition was lower (0.7) compared with lignin decomposition (1.35). As for wheat decomposition by TG-FTIR measurement, Bassilakis *et el.*[10] reported that CO_2 (10 wt%) and steam (23 wt%) were produced. Meanwhile, Kamei *et al.*[11] obtained H_2 and CO during Yalluron coal decomposition by microwave plasma technique. These facts indicate that synthesis gas formation is peculiar phenomenon observed in microwave plasma reactions.

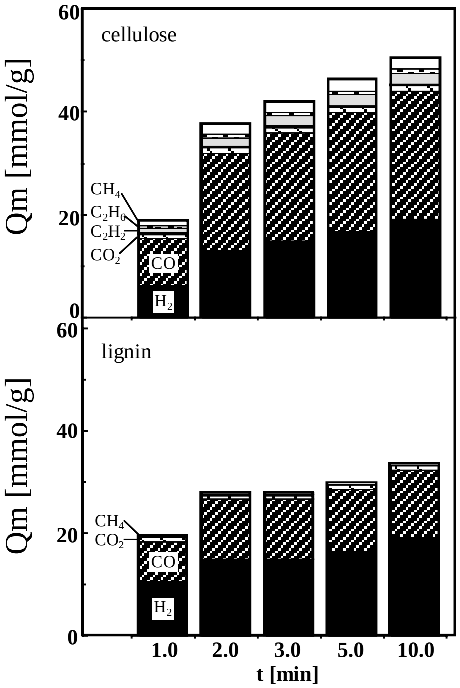

Fig.3 Time change of gaseous product (cellulose, lignin)

3.3 Effect of irradiation time on conversion and product yield during cedar or sugarcane decomposition

Figure 4 shows the time change of conversion, oily and gaseous yields when either sugarcane or ceder sawdust was packed within the reactor. The curves in the figures show the calculated value on the assumption that cellulose and lignin in the material individually decomposed. The experimental values exceed the calculated line within 3 min irradiation, which indicates that the intermediate produced from lignin in the initial stage accelerates the decomposition of the cellulose.

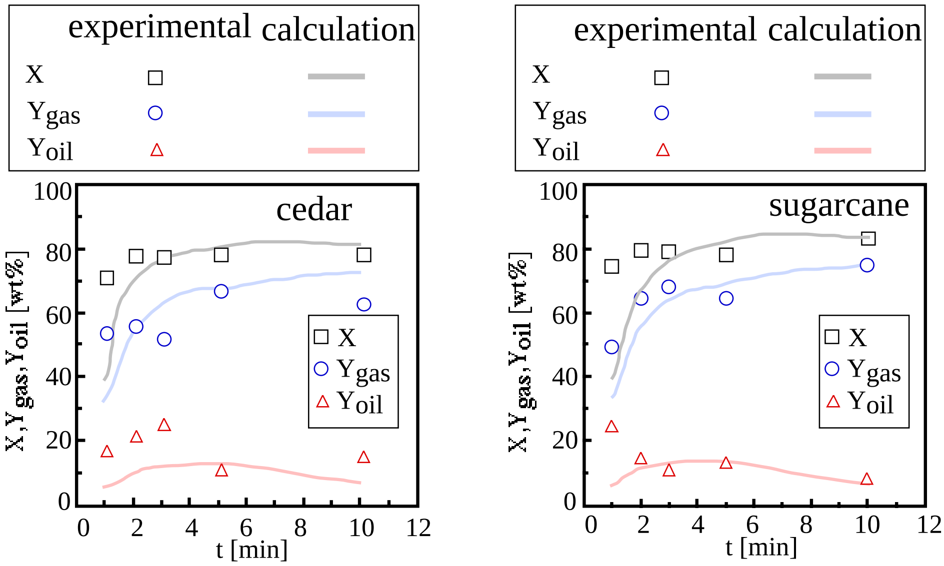

Fig.4 Time change of conversion and product yield (cedar, sugarcane)

3.4 Characteristic of gaseous products during sugarcane or cedar decomposition

Figure 5 shows the time change of accumulation of gaseous product during sugarcane or cedar decomposition. Similar to the cellulose and lignin decomposition, the constant ratio of carbon monoxide with hydrogen was produced independent on irradiation time. The total amount of carbon monoxide and hydrogen produced from sugarcane was higher compared with cedar.

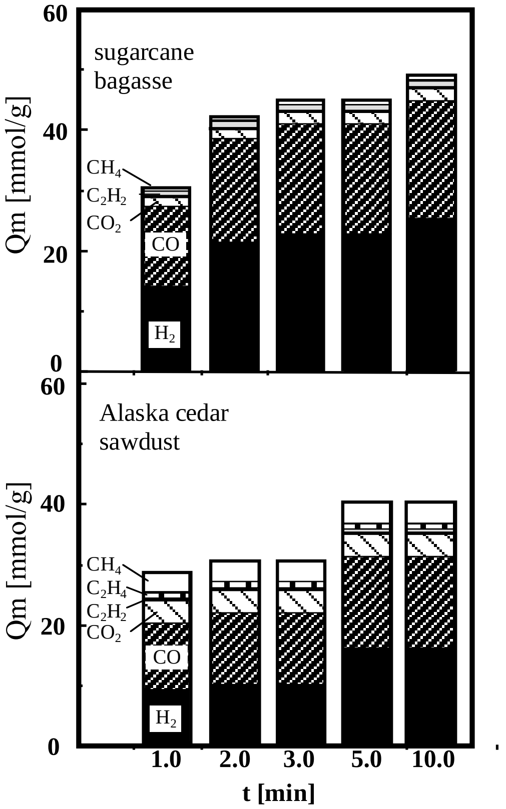

Fig.5 Time change of gaseous product (cedar, sugarcane)

3.5 Characteristic of oily products

Figure 6 shows chromatogram of oily product at 1 min microwave irradiation. The molecular weight distribution of oil derived from cellulose or lignin showed a bimodality. As for oil derived from sugarcane and cedar, aliphatic compounds in the carbon range from C_{10} to C_{30} were mainly produced

Figures 7 and 8 show FT-IR spectra of oil derived from each material at 1 min microwave irradiation. The cellulose-derived oil had spectra of methyl (2960 cm^{-1}), epoxy (1260, 800 cm^{-1}), ether (1100 cm^{-1}) and cycropropane (1030 cm^{-1}). The lignin-derived oil had characteristic spectra of hydroxy (3400 cm^{-1}), carbonic acid (1700 cm^{-1}). In addition, sugarcane- and cedar-derived oil was observed for strong spectra of methyl (2920 cm^{-1}, 2849 cm^{-1}) and carbonic acid (1730 cm^{-1}).

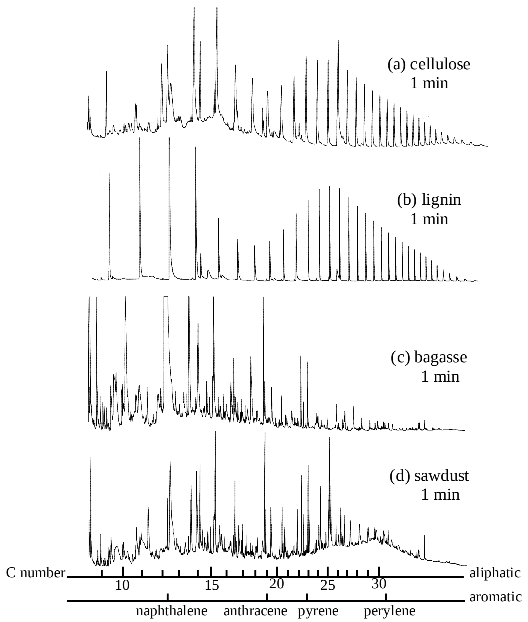

Fig.6 Gas Chromatogram of benzene soluble compounds (t = 1 min)

Column : UA-DX30 Carborane-Silioxane 60 m × 0.25 mm × 0.15 μm
Carrier : He 270 kPa
Oven : Temperature program 323 K (5 min) to 648 K at 5 K/min
Injection : 623 K, 0.5 μl
Detector : FID, 648 K
Standard sample : nonane, undecane, tridecane, icosan, paraffin 122P
naphthalene, anthracene, pyrene, perylene

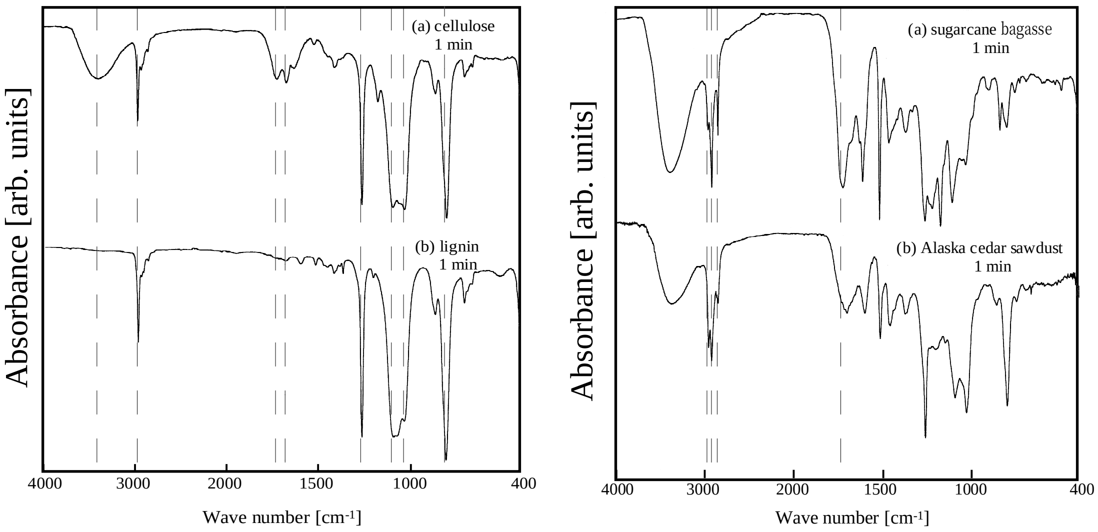

Fig.7 Comparison of FT-IR spectra of benzene soluble compounds (t=1 min)

4. Conclusions

Decomposition of plant-based biomass (sugarcane and cedar) and base compounds (cellulose and lignin) by the microwave plasma process was developed and the following results were obtained.

1) Cellulose showed a greater conversion and a higher yield of gases than lignin.
2) Both cellulose and lignin produced hydrogen and carbon monoxide as main gases.
3) Compared to cellulose and lignin, sugarcane and cedar initially showed a higher conversion and produced high amounts of hydrogen and carbon monoxide.

Reference

[1] Ogi, T., *Nihon Enerugi Gakkaishi*, **78** (4), 232 (1999).
[2] Saka. S., "Baiomass · Energy · Environment," Industrial Publishing & Inc., Tokyo p262 (2001).
[3] Hajaligol, M., Waymack, B., Kellogg. D., *Fuel*, **80**, 1799 (2001).
[4] Okuo. H., Kojima. T., Inaba. A., *Nihon Enerugi Gakkaishi*, **76** (9), 879 (1997).
[5] Minowa. T., Ogi. T., *Sekiyu Gakkaishi (J. Jpn. Petrol. Inst.)*, **41** (1), 11 (1998).
[6] Ando. H., Kokusho. T., Sasaki. T., Shibata. M., Uemura. Y., Hatate. Y., *Ind. Eng. Chem. Res.*, **39** (10), 3688 (2000).
[7] Mae. K., Miwa. M., Nakagawa. H., Miura. K., The Preprint of 10th Annual Meeting of the Japan Institute of Energy, Japan, No.5-4 (2001).
[8] Tanaka. K., Eguchi. H., Sakai. M., The Preprint of 10th Annual Meeting of the Japan Institute of Energy, Japan, No.5-7 (2001).
[9] Bassilakis. R., Carangelo. R.M., Wójtowicz. M.A., *Fuel*, **80**, 1765 (2001).
[10] Bassilkis. R., Carangelo. R.M., Wójtowicz, *Fuel*, **80**, 1765 (2001).
[11] Kamei. O., Sudoh. H., Onoe. K., Yamaguchi. T., The Preprint of 74th Annual Meeting of the Chemical Engineers, Japan, No.2F114 (1998).

Positive Streamer Discharge Investigations: Experimental Measurements and Direct Numerical Simulations

S V Pancheshnyi and A Yu Starikovskii

Physics of Nonequilibrium Systems Laboratory
Moscow Institute of Physics and Technology, Moscow, Russia

1 Experimental Setup

Discharge section comprises cube chamber 20x20x20 cm. There is a possibility to pump up to 10^{-2} torr and to heat the chamber. Special optical windows made of quartz to register optical emission in a wavelength range of 190-3200 nm.

A rotating-interrupter generator was used as a pulsed voltage supply. The high-voltage pulses were fed through a coaxial electric cable to the high-voltage connector of the discharge system. Repetitive frequency of the high-voltage pulses was 1.2 kHz, voltage amplitude in the cable was 11 kV, high voltage pulse on the half-height was 75 ns. A calibrated back-current shunt placed in the break of the shield of the feeding coaxial cable was used to control electrical parameters of the pulses.

The emission spectroscopy technique was used to analyze a cathode-directed streamer discharge. The densities of excited molecules was determined, and the reduced electric field in the streamer head was estimated. The emission from the discharge was selected by the quartz lens and slits, monochromator MDR-12 and measured by photomultipliers FEY-100 and SNFT3. The dynamics of the linear density of excited particles in the discharge gap was studied using time-resolved measurements with the use of a set of 5-mm-high diaphragms. A micrometer mechanism provided the positioning of the diaphragms with high accuracy.

1.1 Spectral and Electrical Measurements

It has been obtained that the character of emission depends significantly upon the degree of closure of the discharge gap. Integral spectra for short-closing gap (interelectrode distance 10 mm) and streamer breakdown without shorting the circuit are represented in Fig.1. Analysis performed has proved that in the regime of partially closed circuit the temperature of the streamer channel increases (and, consequently, the intensity of the continuous part of spectrum rises), the main channels of an energy distribution change essentially and production of atoms and radicals increases.

Volt-second characteristics of the discharges were obtained for gap lengths from 0 to 60 mm, the following parameters were obtained: voltage on the discharge gap; current through the high-voltage electrode; total energy input in the discharge gap during high voltage pulse. These values for two interelectrode gaps are represented in Fig.2-3.

Fig.4 represents the dependencies of the peak (corresponding to the instant the streamer head passes through the given cross section of the gap) linear densities of the different excited states versus the distance from the high-voltage electrode for different interelectrode distances. The results obtained show that, at distances up to $l = 6$ mm from the high-voltage electrode (anode), the streamer corona is formed. In this stage, the glow front propagation is determined by the local electric field near the high-voltage electrode and depends only slightly on the distance from the low-voltage electrode (i.e., on the average field in the gap). In this region, the linear densities of excited particles reach their maximums. For small interelectrode distances, when the streamer channel bridges the gap, the linear densities of active particles created in the discharge change slightly along the discharge gap. For long gaps, the linear densities of active particles drop sharply beyond the zone where the streamer is formed. As is seen from the Figure, the longer the gap (at the same electrode voltage), the shorter the effective length of the region where active particles are produced.

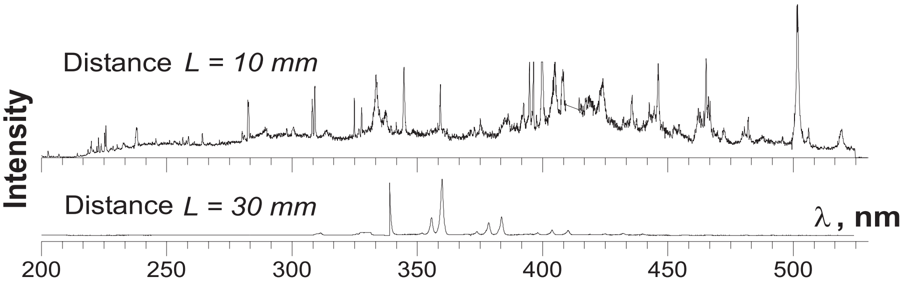

Figure 1: Spectra for different length of discharge gap in spark and streamer regime.

1.2 Electric Field Determination

The reduced electric field can be estimated by analyzing the population rates of the electronically excited states of molecular nitrogen. The populations of the $N_2(C^3\Pi_u, v = 0)$ and $N_2^+(B^2\Sigma_u^+, v = 0)$ excited states are determined by the processes of direct electron impact excitation from the ground state of nitrogen, radiative depopulation, quenching in collisions with heavy particles and associative conversion of the nitrogen ions to N_4^+ ion. Detailed procedure is described in paper [1]. To estimate the electric field, we consider the ratio between the population rate constants of the levels.

A typical longitudinal profile of the reduced electric field E/N in the streamer head corresponding to the maximum rate of the production of electronically excited N_2 molecules is presented in Fig.5 for the gap length 24 mm. The reduced electric field reaches its maximum ($\sim 10^3$Td) near the high-voltage electrode. At a distance of 7 mm from the electrode, the formation of the streamer channel is completed and the electric field decreases to 400 Td. As the streamer head approaches the low-voltage electrode, the reduced electric field increases to 500 Td. For longer discharge gaps, at distances from the high-voltage electrode of up to 10 mm, the electric field profiles are nearly the same as in the Figure. For very long gaps, at distances from the high-voltage electrode of longer than 12 mm, the emission intensity of the first negative nitrogen system becomes so weak that it does not allow accurate absolute measurements of the population rate of the $N_2^+(B^2\Sigma_u^+, v = 0)$ state.

2 Numerical Model

We numerically investigated individual cathode-directed streamer discharges for the conditions of our experiments. The numerical model includes the following balance equations for charged particles [2]:

$$\frac{\partial n_e}{\partial t} + \text{div}\,(\vec{v}_e \cdot n_e) = S_{ion} + S_{photo} - S_{att} - S_{rec}^{ei} \tag{1}$$

$$\frac{\partial n_p}{\partial t} = S_{ion} + S_{photo} - S_{rec}^{ei} - S_{rec}^{ii} \tag{2}$$

$$\frac{\partial n_n}{\partial t} = S_{att} - S_{rec}^{ii} \tag{3}$$

Here, n_e is the electron density; n_p and n_n are the concentrations of positively and negatively charged ions; $\vec{v_e}$ is the drift velocity in a local electric field $\vec{E}$; and S_{ion}, S_{photo}, S_{rec}, and S_{att} are, respectively, the rates of ionization, photoionization, electron–ion and ion–ion recombination, and electron attachment. The electric field $\vec{E}$ in the discharge gap is described in terms of the potential φ, whose distribution over the gap was determined by solving Poisson's equation:

$$\vec{E} = -\nabla\varphi \tag{4}$$

$$\Delta\varphi = -\frac{e}{\varepsilon_0}\,(n_p - n_e - n_n) \tag{5}$$

The set of equations (1-5) was solved numerically by difference schemes employing the finite-volume method on an adaptive space–time grid. The difference schemes were constructed using the integro-interpolation method.

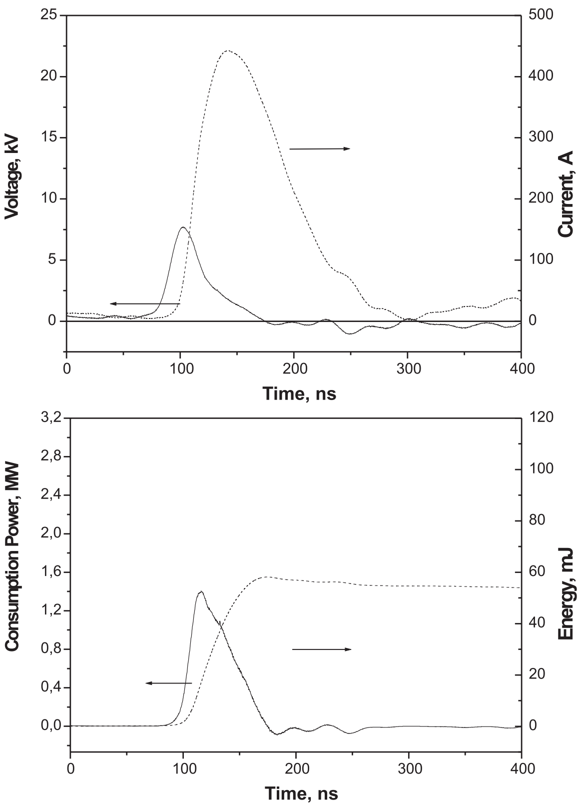

Figure 2: Time-resolved voltage, current, power and energy input. Interelectrode distance is $L = 3$ mm. Air.

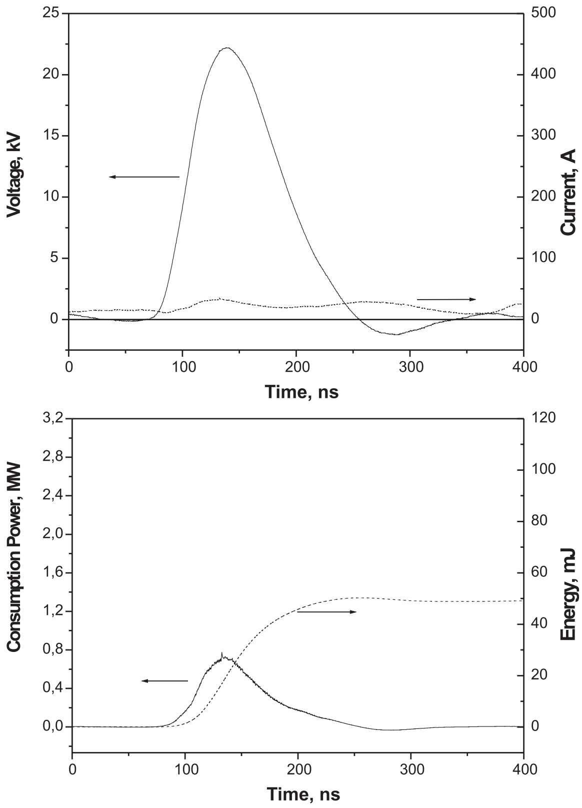

Figure 3: Time-resolved voltage, current, power and energy input. Interelectrode distance is $L = 60$ mm. Air.

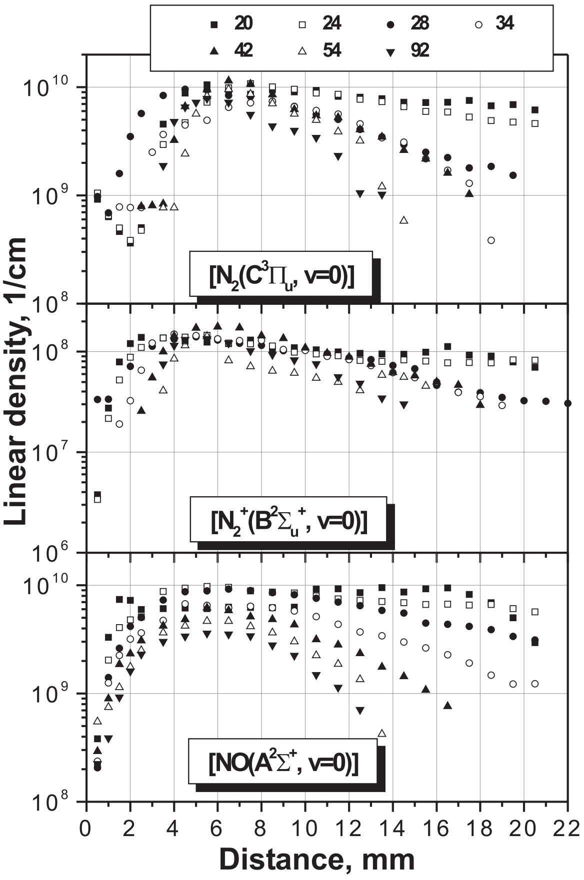

Figure 4: Peak densities of excited states in the streamer head *vs* the distance from the high-voltage electrode for different interelectrode distances, indicated in mm in the upper part of the figure near the symbols.

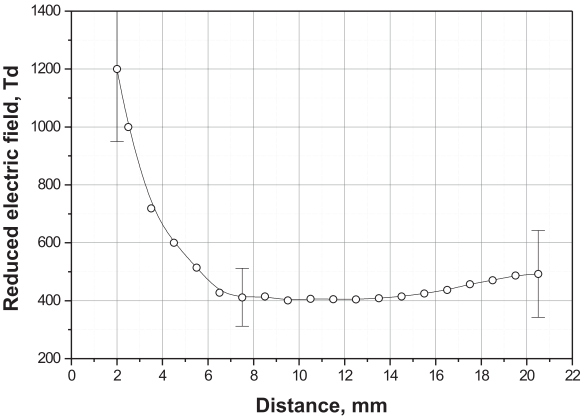

Figure 5: Reduced electric field in the streamer head *vs* the distance from the high-voltage electrode for L = 24 mm.

Figure 6: Surfaces of the space charge (top) and electric field (bottom) at the time 0.1 ns.

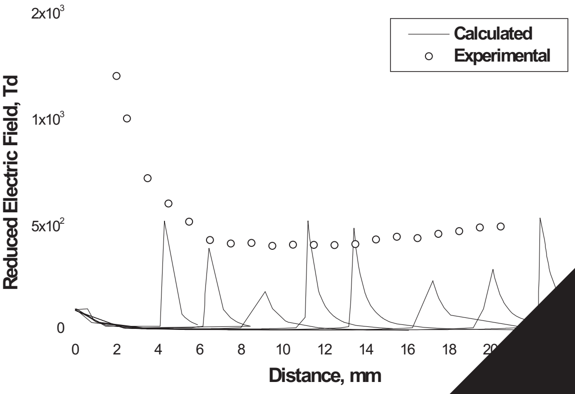

Figure 7: Peak electric field propagation. Comparison of experimental data and calculations. Numerical profiles are represented for time moments $t = 28 - 78$ ns with a time step $\Delta t = 5$ ns.

It is assumed that heavy particles are immobile throughout the streamer discharge. At the initial time, the gas in the gap is assumed to be quasineutral. The onset of the streamer channel is modeled by specifying the electron density at a certain preionization level in the immediate vicinity of the anode. The rate of gas photoionization, S_{photo}, is described in the same manner as in [3]:

$$S_{photo} = \frac{1}{4\pi} \cdot \frac{p_q}{p + p_q} \int\limits_V \mathrm{d}^3 \vec{r}_1 \frac{S_{ion}(\vec{r}_1)}{|\vec{r} - \vec{r}_1|^2} \Psi(|\vec{r} - \vec{r}_1| \cdot p) \qquad (6)$$

where $1/4\pi$ is the normalizing constant, p is the gas pressure, p_q is the quenching pressure of the emitting states, and $\Psi(|\vec{r} - \vec{r}_1| \cdot p)$ is the coefficient of absorption of the ionizing radiation in the medium.

3 Comparison with Experiment

Some time after a high-voltage pulse has been applied to the anode (a delayed onset), a narrow channel with a pronounced region of strong electric fields at the leading edge originates from the high-voltage electrode and extends toward the low-voltage electrode (Fig.6).

The comparison of experimental and calculated peak reduced electric fields along a discharge axis is represented in Fig.7. In the region of relatively weak electric field (up to 600 Td) we obtain a quite good coincidence. At small distances (less than 4-5 mm) difference may be explained by the fact that two-term approximation of the Boltzmann equation is not valid in this region because of strong electric fields near the electrode.

To compare with the experimentally studied intensities of emission of 2^+ and 1^- nitrogen systems the dynamics of population of $\mathrm{N_2(C^3\Pi_u}, v = 0)$ and $\mathrm{N_2^+(B^2\Sigma_u^+}, v = 0)$ excited states was calculated by calculated electron density, reduced electric field and known radiative lifetime and collisional quenching rate. Dependencies of production of $\mathrm{N_2(C^3\Pi_u}, v = 0)$ and $\mathrm{N_2^+(B^2\Sigma_u^+}, v = 0)$ per unit length of the channel – states along a discharge gap integrated in time is represented in Fig.8-9.

4 Streamer Development in Long Discharge Gap

The main results presented below were obtained in experiments with streamer discharges in an N_2-O_2 (9:1) mixture at a pressure of 760 torr, the voltage at the anode being held constant, $U = 100$ kV. According to the experiments carried out in [4], this regime is characterized by a streamer flash consisting of five to ten individual streamer channels, having no considerable tendency to branch.

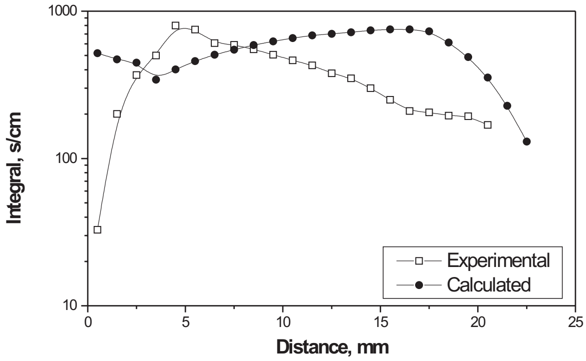

Figure 8: Density of $N_2(C^3\Pi_u, v = 0)$ per unit length along a discharge axis.

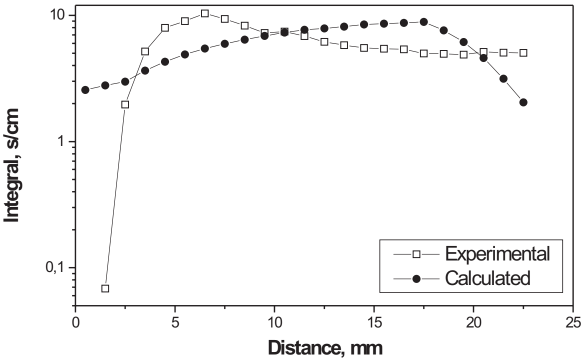

Figure 9: Density of $N_2^+(B^2\Sigma_u^+, v = 0)$ per unit length along a discharge axis.

In order to determine the extent to which the modeling of plasmochemical conversion processes in the streamer plasma should be complete, we carried out two series of simulations. In the first series, we took into account only direct electron impact processes, and, in the second series, we tried to simplify the complete kinetic scheme developed in [6] for N_2-O_2 mixtures to the ultimate possible extent [7]. In the first series of simulations, we ignored the electron loss processes. In the second series, we took into account the processes in which charged particle are lost but neglected the secondary processes in which charged particles are produced — such as associative ionization and electron detachment from negative ions. Hence, these two approaches yielded the upper and lower estimates of the electron density in the streamer channel and of the global discharge parameters.

The dynamics of the development shows that on time scales of 30-40 ns and longer, the streamer propagation velocity calculated with allowance for plasma kinetic processes in the streamer channel differs markedly from that calculated without allowance for the plasma kinetics. It was shown that, on time scales of up to 100 ns, electron-ion recombination processes reduce the electron density in the streamer channel by a factor of three (Fig.10). We have also obtained that, when the electron loss processes are neglected, the discharge dynamics changes insignificantly: the electric field in the streamer head changes by less than 1% and the streamer propagation velocity changes by 7%, while the anode current and the electric field in the streamer channel change by a factor of about two.

The main results of our numerical simulations of an individual streamer discharge are summarized in the Table 1. In both cases, the numerical results on the rate of development of the discharge and its geometric parameters agree well with those measured experimentally. The calculated anode current is

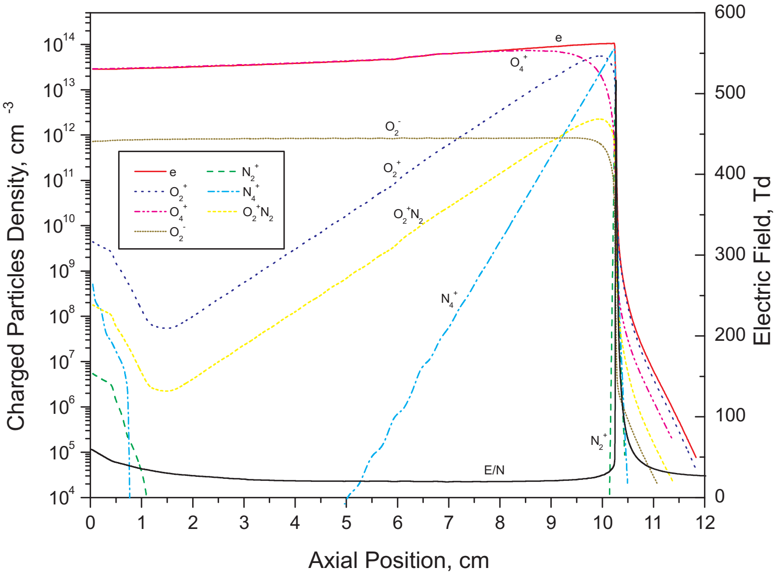

Figure 10: Profiles of the electric field and the density of charged particles along the discharge axis at the time 80 ns, at which the streamer head is at a distance of 10 cm from the high-voltage electrode.

Table 1: Comparison of the calculated parameter values with the experimental data.

	Calculations		Measurements
	with kinetics	without kinetics	[4]
Streamer velocity, cm/s:	1.4×10^8	1.5×10^8	1.4×10^8
Channel radius, mm:	0.8 - 1.3	0.8 - 1.6	0.5 - 1.5
Maximum electric current, A:	0.28	0.48	$\sim (0.2 - 0.4)^*$
Maximum reduced electric field, Td:	550	550	—
Electron density in the channel, cm^{-3}:	$(0.3 - 1.0) \times 10^{14}$	10^{14}	—

* Note: estimates for a single channel from electrodynamic measurements and high-speed shutter photography.

found to coincide with the experimental one only when kinetic processes in the streamer channel are taken into account. Previous analytical and direct numerical modeling studies of a streamer discharge in a short gap [2] showed that the streamer parameters are determined exclusively by the processes in the streamer head and are uniquely related to its electric potential. A decrease in the electron density in the recombination processes leads to an increase in the electric field in the streamer channel, which, in turn, results in a higher potential drop between the anode and the streamer head and, accordingly, in a lower propagation velocity and smaller streamer radius.

5 Conclusions

At this work complex study of positive streamer development has been performed. Experimental measurements of streamer discharge dynamics in N_2/O_2 mixtures at different pressure have been compared with direct numerical simulation within the scope of 2D hydrodynamics approach.

This work was supported in part by the “Energiya–Kompleks” Scientific and Technology Center, the Russian Foundation for Basic Research (project nos. 01-02-17785 and 02-03-33376), the Ministry of Education of the Russian Federation (project no. E 02-3.2-98), and the International Science and Technology Center (project no. 1474).

References

[1] S. V. Pancheshnyi, S. V. Sobakin, S. M. Starikovskaia, and A. Yu. Starikovskii *Discharge Dynamics and the Production of Active Particles in a Cathode-Directed Streamer* // Plasma Physics Reports. **26** (2000) 1054.

[2] Pancheshnyi S.V., Starikovskaia S.M., Starikovskii A.Yu. *Role of Photoionization Processes in Propagation of Cathode-Directed Streamer* // J.Phys.D.: Appl.Phys. **34** (2001) 105.

[3] M. B. Zheleznyak, A. Kh. Mnatsakanyan, and S. V. Sizykh *Photoionization of Nitrogen–Oxygen Mixtures by Emission from a Gas Discharge* // Teplofiz. Vys. Temp. **20** (1982) 423.

[4] Won J.Yi., Williams P.F. *Experimental study of streamers in pure* N_2 *and* N_2/O_2 *mixtures and a* $\simeq$ *13 cm gap* // J.Phys.D.: Appl.Phys. **35** (2002) 205.

[5] Aleksandrov N.L., Bazelyan E.M. *Ionization processes in spark discharge plasmas* // J. Phys. D: Appl. Phys. **8** (1999) 285.

[6] Kossyi I.A., Kostinsky A.Yu., Matveyev A.A., Silakov V.P. *Kinetic scheme oh the non-equilibrium discharge in nitrogen-oxygen mixtures* // Plasma Sources Sci. Technol. **1** (1992) 207.

[7] S V Pancheshnyi, A Yu Starikovskii *Two-Dimensional Numerical Modeling of the Cathode-Directed Streamer Development in a Long Gap at High Voltage* // J.Phys.D.: Appl.Phys. *will be published in 2003*

Dynamics of Multiple Needles Pulsed Discharge for Plasma Chemistry Application

G.P. Berezina, Ju.V. Bunchikov, V.I. Mirny, I.N. Onishchenko, V.S. Us

National Science Center "Kharkov Institute of Physics & Technology"
Academic St. 1, Kharkov, 61108, Ukraine
E-mail: onish@kipt.kharkov.ua

The behaviour of the pulsed discharge at atmospheric pressure between multiple needles-plane electrode has been investigated. This type of discharge has been used in our experiments as a suitable tool for plasma chemistry of CO_x, NO_x and SO_x, i.e. for effective decomposition of these radicals. The main advantage of it concludes to a phenomenon of spark jumping from one needle to another over whole volume of treated gas. The object of the presentation is the investigation of the dynamics of the discharge between a set of needles and plane that is used in experiments on plasma-chemistry [1].

The behavior of the pulsed discharge of such type has been studied with use of the optical registration method of discharge for each needle. The applied noncontact method of recording of the discharges in an interelectrode gap has allowed to register synchronous sequences of electrical impulses relevant to light radiation from each needle, and to compare them. We can conclude, that for long time of observation all gaps in the configuration of electrodes: set of needles - plane are being broken down by spark with almost equal probability.

[1] G.P.Berezina, I.N.Onishchenko, V.S.Us - Prikladnaja Fizika (rus) **2**, 34-44 (2002).

Experimental Investigations of Non-Equilibrium Radiation and Physical-Chemical Processes in Earths and Mars Atmosphere under Strong Excitation

S.V.Pancheshnyi, V.E.Sych, A. Yu. Starikovskii

Physics of Nonequilibrium Systems Laboratory
Moscow Institute of Physics and Technology, Dolgoprudny, Russia

Abstract

The spectra from gas mixtures corresponded to Earth and Mars atmospheres were analyzed using different types of excitation. The results obtained about non-equilibrium radiation in different types of the gas discharges (glow, microwave and pulsed high-voltage) allow to analyze the main spectral regions of energy transfer. It was found that emitting chemical species in Mars atmosphere differ sensibly from those found in Earth plasmas.

1. Introduction

The significant progress in development of hypersonic aerodynamics is recently observed in connection with achievements of spacecraft, creation of aerospace vehicles, shuttles and other high-speed space-rocket systems moving in rarefied atmosphere. Under the conditions of high flight velocities in rarefied gas the orders of the characteristic times of gasdynamic, chemical and relaxation processes become close to each other, and it means that they are necessary to be considered jointly. Thus, the key characteristics of a hypersonic flow depend directly on kinetics of both surface chemical reactions in a gas phase and the relaxation processes.

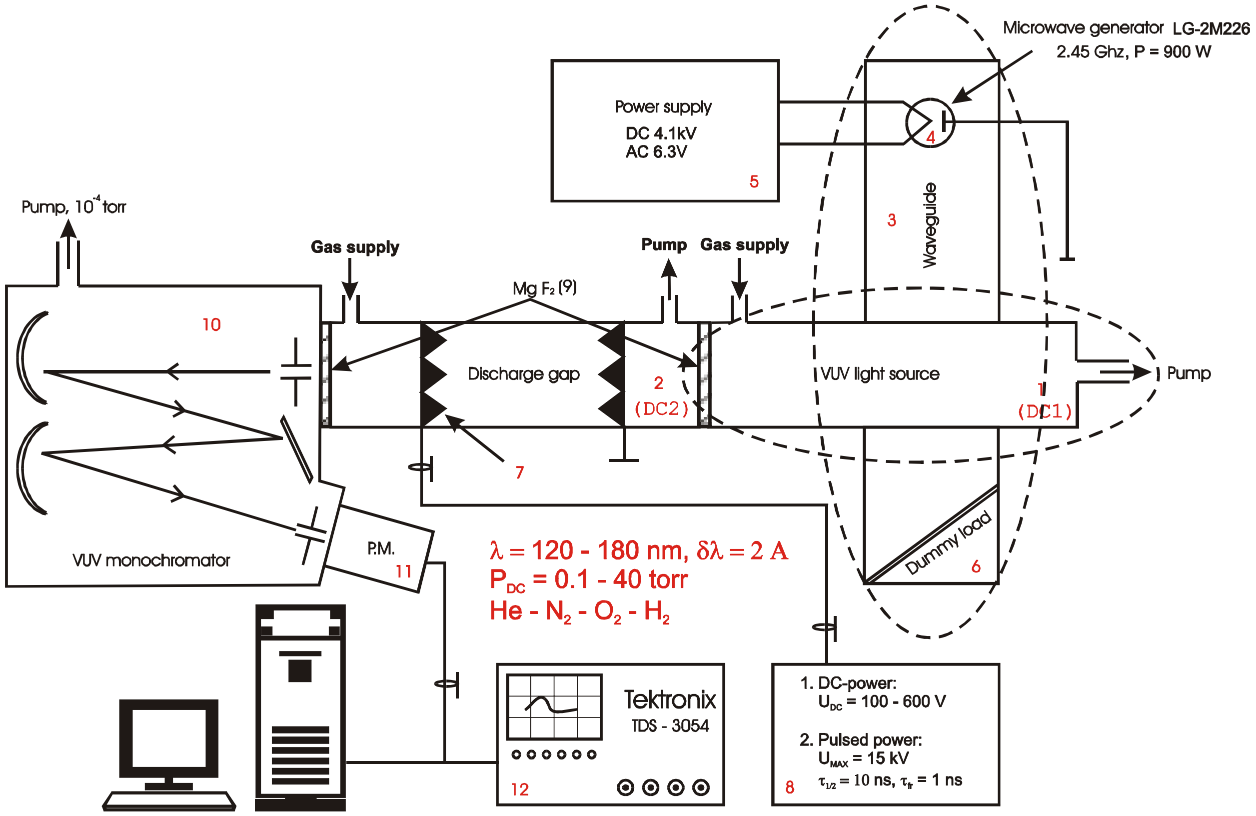

Figure 1. Experimental set-up for VUV-radiation measurements in different types of electric discharges. 1 – Discharge chamber of VUV light source (DC1).2 – Discharge chamber (DC2).3 – Waveguide. 4 – Magnetron 2.45 GHz.5 – Power supply for magnetron.6 – Microwave dummy load.7 – High-voltage electrodes.8 – High-voltage pulsed generator.9 – Optical windows (MgF_2).10 – VUV monochromator.11 – Photomultiplier (PM - 181).

The investigation of the radiative heat transfer for the supersonic flow along solid bodies is very important due to the high impact on the design of space vehicles. Radiation of the created plasma can account for up to

50% of the heat fluxes endured by a space vehicle shield. Plasma radiation in front of the vehicle (mainly UV) is important for heat-shield design. Plasma created behind the hypersonic shock wave is optically thin, characterized by small ionization rate and chemical and thermodynamic non-equilibrium [1].

The Venus and Mars atmospheres consist mainly of carbon dioxide impure with minor species – nitrogen, argon, hydrogen and others. The influence of formation of electronically and vibrational excited particles on characteristics of the radiative heat transfer should be investigated to estimate the heat flux.

In the mixture corresponded to Mars atmosphere we identify CO_2, C_2 Swan, CN(Violet), CN(Red), CO(4^+), $N_2(1^+)$, $N_2(2^+)$, $N_2^+(1^-)$, O_2(S-R), NO(β), NO(γ), Ar, Ar^+, C, C^+, N, N^+, O and O^+ lines. The chemical reactions involving carbon, oxygen and nitrogen atoms play main role in the processes of chemical relaxation in the CO_2-N_2 mixtures plasma.

In our research we compare the spectra from gas mixtures corresponded to Earth and Mars atmospheres. The results obtained about non-equilibrium radiation in the Earth and Mars atmospheres in different types of the gas discharges (glow, microwave and pulsed high-voltage) allow to analyze the main spectral regions of energy transfer.

Experimental setup

Fast ionization wave was initiated by voltage pulses of negative polarity, 11-15 kV in amplitude, 25 ns half-width and 2-3 ns rise time with repetition frequency of 40-100 Hz. Discharge setup is represented schematically in Fig.1. It consists of two separate chambers.

Microwave discharge (2.45 GHz) is organized in the first one. We use it as an effective source of radiation in VUV-region of spectra.

Fast ionization wave is ignited in the second chamber. This is quartz tube of 29 mm inner diameter, 32 mm outer diameter and 250 mm in length. Brass hollow electrodes of special shape to initiate discharge start are placed at the ends of the tube.

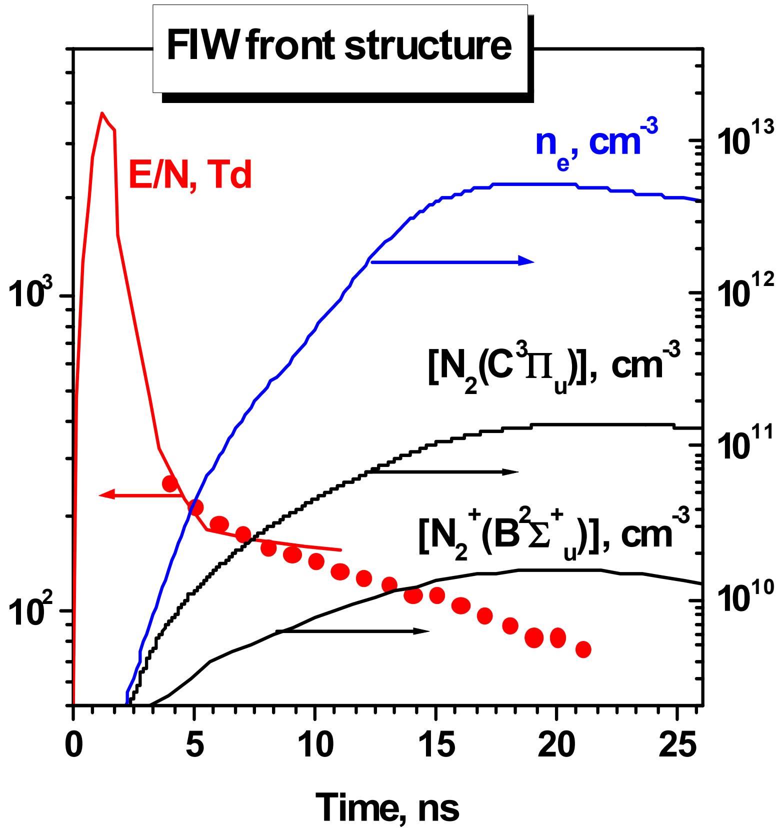

Figure 2. Temporal evolution of the electric field, $N_2(C^3\Pi_u$, v'=0) and $N_2^+(B^2\Sigma^+_u$, v'=0) densities and electron concentration. The electric field, represented by full curves, is determined from the electrical measurements; the electric field represented by the symbols is from spectroscopy. Air, P = 4 Torr.

Emission was measured with the help of optical system, which includes vacuum monochromator and photomultiplier FEU-181(sensitivity region is 112-830 nm) with a typical spectral resolution 1.5-5.0 A. To separate monochromator and discharge tube we used MgF_2 optical windows. Signals were registered be Tektronix TDS3054 (500 MHz) oscilloscope and LA-70M4 ADC card (13 kHz).

Discharge parameters were controlled with the help of calibrated back current shunt, capacitive gauges and independently with the help of emission spectroscopy technique in visible and UV regions of spectra with nanosecond temporal resolution.

Measurements of emission spectra were performed in synthetic air (N_2:O_2=4:1) spectral purity at pressures from 0.1 Torr to 20 Torr and synthetic Mars atmosphere (CO_2:N_2=97:3). Microwave discharge was realized in flowing mixture at pressure ranged from 4 Torr to 20 Torr. For analysis of E/n influence glow discharge in some mixtures was used. Vacuum system allows to pump chambers separately up to pressure 10^{-2} Torr and to regulate work pressure and gas flow.

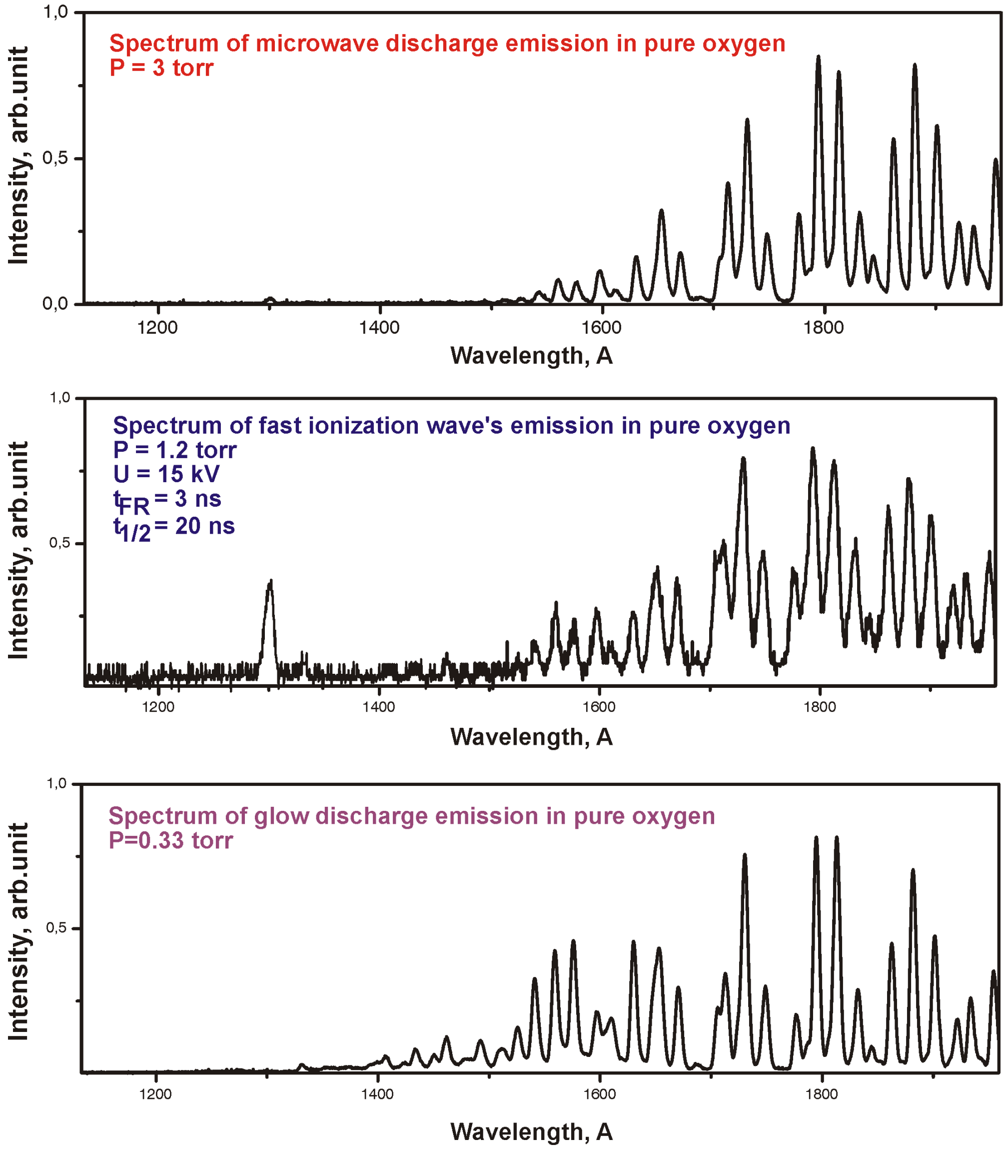

Figure 3. Vacuum ultraviolet emission spectrum of microwave discharge (1), fast ionization wave (2), and glow discharge (3).

Structure of the discharge

Structure of the fast ionization wave has been obtained experimentally [2,3]. Fig. 2 shows temporal evolution of electric field and population of $N_2(C^3\Pi_u$, v'=0) and $N_2^+(B^2\Sigma^+_u$, v'=0) levels in the fast ionization wave.

As clearly seen from the Figure, an active population of excited states begins behind the FIW front. The time moments when "electric" and "light" fronts arrive at the measuring cross-section are significantly separated. In the same figure the structure of a streamer front taken from numerical calculations16 in air for atmospheric pressure is represented for comparison. The most significant distinction between these two types of nanosecond discharge lies in the fact that high energy electrons which are produced in the front of ionization wave, where reduced electric field reaches value up to kTd, lead to uniform gas preionization on a scale comparative with the front length, and, consequently, to the discharge uniformity.

It was found that the longitudinal component of the electric field has a sharp (2-3 ns) maximum and that the electrons and excited particles are produced preferentially behind the front in relatively weak electric fields. The peak field value was close to or even stronger than the threshold for the generation of runaway electrons in a steady-state uniform electric field. An analysis based on absolute time-resolved measurements of the spectrum of two molecular bands showed that, behind the breakdown front, the EEDF should be substantially overpopulated with high-energy electrons. Energy branching in the discharge was analyzed.

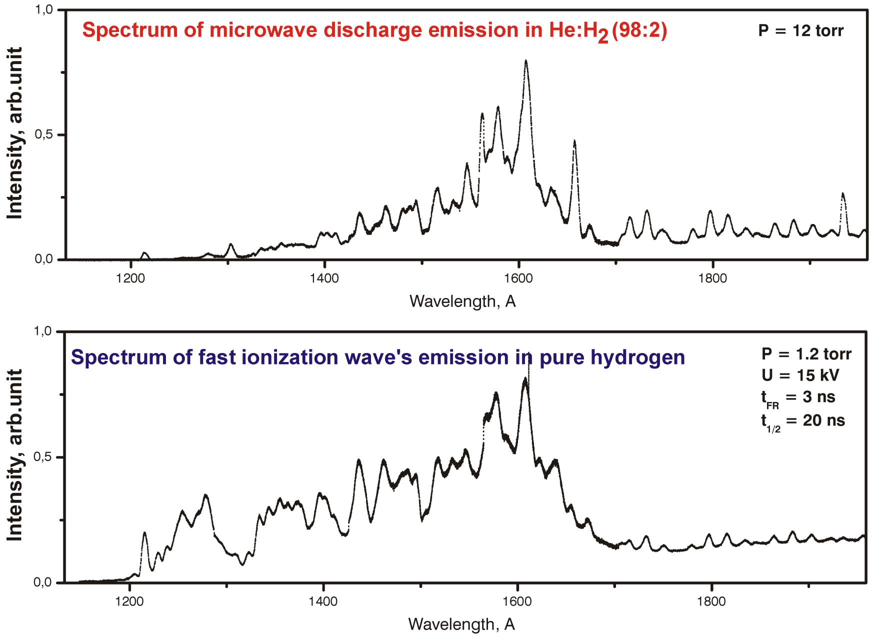

Figure 4. Vacuum ultraviolet emission spectrum of (1) – microwave discharge. He-H_2 = 98:2, P = 12 Torr; (2) – FIW, pure hydrogen, P = 1.2 Torr

Emission of gas discharges in VUV spectral range – influence of the reduced electric field value

As a reference light source of VUV emission we used microwave discharge in mixtures of He with 5% admixtures of O_2 and H_2 at pressures ranged in 1-30 Torr. Emission spectra for this discharge in VUV range are represented in Fig.3.1. From the emission spectra it is seen that microwave discharge in given conditions can be used as a proper source of emission at the atomic lines of dilution gas. The most intensive is triplet emission O($^3S_1$) -> O($^3P_{0,1,2}$) at $\lambda = 130.5$ nm in He:O_2 = 95:5 mixture.

Spectra of nanosecond pulsed gas discharge in the form of fast ionization wave in VUV region has an intensity maximum in vacuum ultraviolet region, that proves the fact that one of the most distinctive features of the fast ionization wave is quite high energy of electrons [4].

Spectra of nanosecond pulsed gas discharge in the form of fast ionization wave and of microwave discharge in VUV region for hydrogen plasma are represented in Figs. 4.1 and 4.2. It follows form the comparison that in nanosecond discharge intensity maximum is shifted to the ultraviolet region in comparison with microwave discharge (Figure 5).

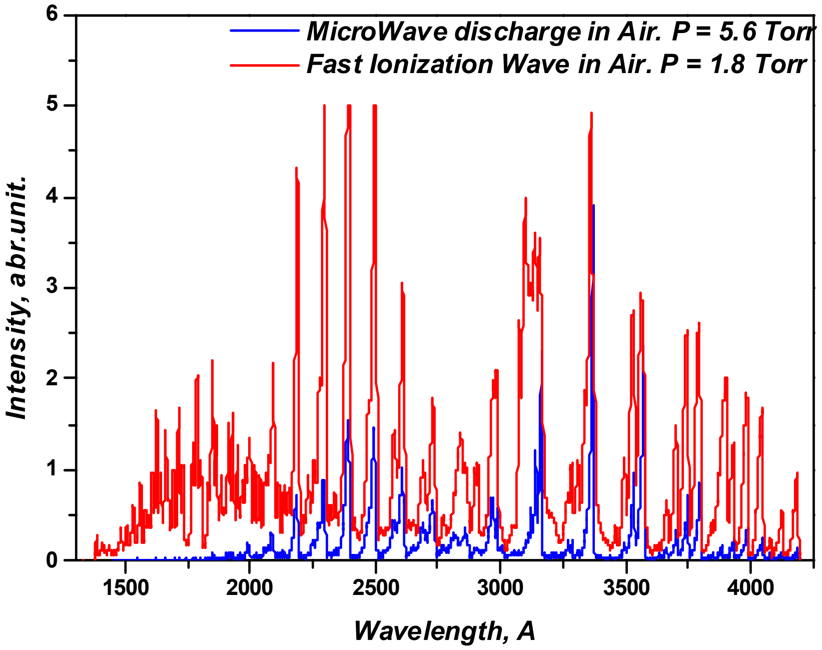

Figure 5. Vacuum ultraviolet emission spectrum of gas discharge in air. Dependence on the reduced electric field value.

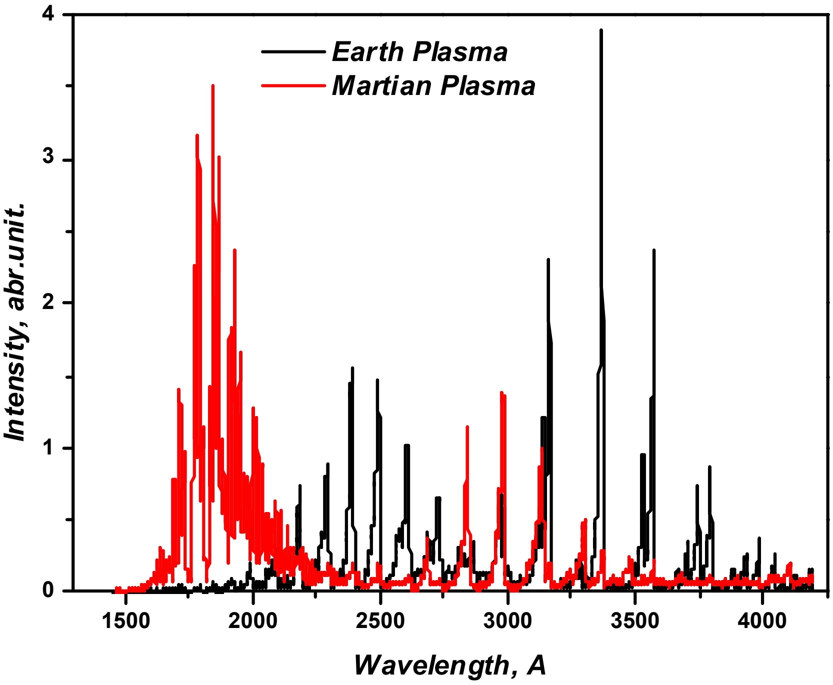

Figure 6. Comparison of the emission spectra from Martian and Earth atmosphere plasma. Microwave discharge. P = 5.6 Torr. Mars: CO_2-N_2 = 97:3. Earth: N_2-O_2 = 4:1

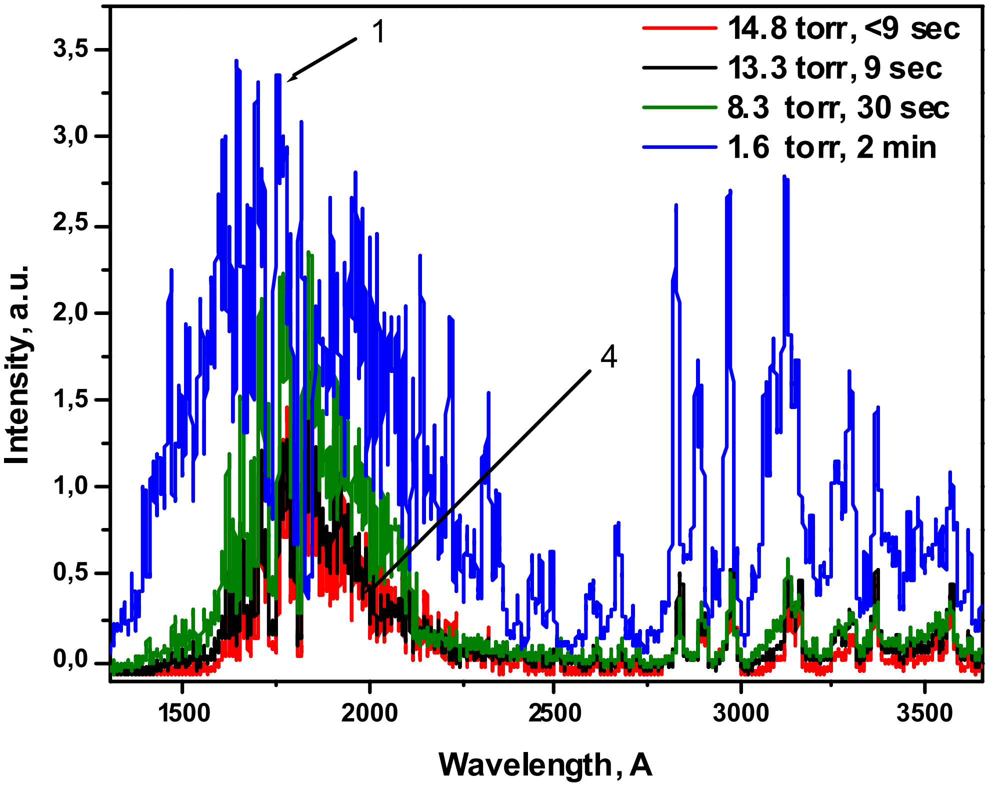

Figure 7. Martian plasma emission in VUV region. Excitation by fast ionization wave.

In our research we compare the spectra from gas mixtures corresponded to Earth and Mars atmospheres (Figures 6, 7). The results obtained about non-equilibrium radiation in the Earth and Mars atmospheres in different types of the gas discharges (glow, microwave and pulsed high-voltage) allow to analyze the main spectral regions of energy transfer. In the mixture corresponded to Mars atmosphere we identify CO_2, C_2 Swan, CN(Violet), CN(Red), CO(4^+), $N_2(1^+)$, $N_2(2^+)$, $N_2^+(1^-)$, O_2(S-R), NO(β), NO(γ), Ar, Ar^+, C, C^+, N, N^+, O and O^+ lines.

It is shown that the main energy flux in the Mars atmosphere corresponds to the VUV and near-UV spectral regions (Figure 7).

Acknowledgements

The work was supported in part by RFBR (grants 01-02-17785, 02-03-33376), ISTC Project 1440 and CRDF Award MO-011-0.

References

[1] R.N.Gupta, K.P.Lee, An Aerothermal Study of MESUR Pathfinder Aeroshell, AIAA Paper 94-2025, 1994

[2] S.V.Pancheshnyi, S.M.Starikovskaia, A.Yu.Starikovskii, Population of nitrogen molecule electron states and structure of the fast ionization wave, J.Phys.D.: Appl.Phys., v. 32, pp. 2219-2227, 1999.

[3] S.M.Starikovskaia, N.B.Anikin, S.V.Pancheshnyi, D.V.Zatsepin, A.Yu.Starikovskii, Pulsed breakdown at high overvoltage: development, propagation and energy branching, Plasma Sources Sci. Technol. v. 10, pp. 344-355, 2001.

[4] S.M. Starikovskaia, N.B. Anikin, S.V. Pancheshnyi, A.Yu. Starikovskii Time resolved emission spectroscopy and its applications to study of pulsed nanosecond high-voltage discharge. Proceedings of SPIE, 2002. V. 4460, pp. 63-73.

Effects of O_2 and Ar-plasma treatments on hydrogen and helium evolution in implanted silicon wafer during annealing.

L. D'Urso[1], L. Gozzo[1], A .Scandurra[2], O. Puglisi[1]

[1] *Department of Chemistry, University of Catania, Catania, Italy*
[2] *SUPERLAB-CCR, Stradale Primosole c/o ST-Microelectronics, Catania, Italy*

Abstract

Surface blistering and exfoliation phenomena induced by thermal treatments on H^+ and He^+ implanted silicon wafers, suitable for SOI fabrication were investigated. For the blistering experiments single-crystal silicon implanted with 30 keV He^+ and 24 keV H^+ singly, or in combination, with doses ranging from 1×10^{16} to 3×10^{16} cm^{-2} were used. The attention was focused on the influence that O_2 and Ar-plasma treatments, performed during surface cleaning, have on gas evolution in implanted silicon wafer.

References

[1] Q.-Y. Tong and U. Gösele, Semiconductor Wafer Bonding, An Electrochemical Society Monograph, John Wiley & Sons, New York (1999);

[2] S. N. Farrens, J. R. Dekker, J. K. Smith, and B. E. Roberts,, J. Electrochem. Soc., 142 (1995) 3949;

[3] P. Armirfeiz, S. Bengtsson, M. Bergh, E. Zanghellini and L. Börjesson 147 (2000) 2693;

[4] M. K. Weldon, Y. J. Chabal, D. R. Hamann, S. B. Christman, and E. E. Chaban, J. Vac. Sci. Technol. B, 14 (1996) 3095;

[5] Q.-Y. Tong , E. Schmidt, U. Gösele , and M. Reiche, Appl. Phys. Lett. 64(5), 31 Jan 1994, pp 625-627

[6] K. Ljunberg, A. Söderbärg, and Y. Bäcklund, "Spontaneous bonding of hydrophobic silicon surfaces", Appl. Phys. Lett., 62, 1362 (1993).

1. Introduction

Silicon on silicon direct bonded substrates are an ideal replacement to epitaxial deposition in the field of silicon on insulator (SOI) for the fabrication of microelectromechanical devices. The direct wafer bonding has made possible to manufacture in a single step highly uniform SOI structures ("Smart Cut Process"). The method is based on H^+, or H^+ and He^+ ion implantation of a silicon wafer, subsequently bonded, at room temperature, to an other wafer, acting as mechanical substrate. In direct wafer bonding either hydrophobic or hydrophilic surfaces on the bulk wafer can be employed. Si wafers with a hydrophilic surface can bond spontaneously at room temperature. For certain applications of wafer bonding, such as SOI preparation, the native oxide presents no obstacle for the resultant structures; for some applications, such as replacement of epitaxial growth, the removal of the surface native oxide is essential. In this last case, bonding energies at room temperature are often lower than those obtained for hydrophilic surfaces.

To enhance the bonding, wafers pairs are usually thermally treated. In most cases the bonding procedure involves annealing temperatures around 1000°C, while in many application high-temperature steps are unacceptable. The knowledge of mechanism that explain the increase in bonding energy as a function of temperature and time allowed the development of a low-temperature bonding technology which is essential for bonding of wafers that contain temperature sensitive structures or of wafers of dissimilar materials. In this context, it has been reported that strong hydrophilic bonding with Si can be achieved at low temperature (~400°C) by exposing the wafers to a low pressure plasma before the bonding process [1-3]. The plasma of various gases, including O_2 and Ar, have been found to give similar results. Infrared spectroscopic measurements have confirmed that the bond strengthening in hydrophilic bonding of Si is due to the formation of covalent siloxane bonds (Si-O-Si) at the bonded interface[3, 4]. Farrens et al. have suggested that the increased oxidation rate (Si-O-Si) bond formation) at the bonded interface is due to the plasma induced surface charge [2]. Amirfeiz et al. found no evidence to substantiate this hypothesis [3]. They suggested that plasma treatment creates a porous surface structure which enhances the diffusivity of water molecules from the bonded interface. This different assumptions and experimental results suggest that the effects of plasma activation are not fully clarified yet.

Upon annealing the two wafers become chemically bonded and the implanted wafer is ion-cut at the point of highest ions concentration, leaving the desired SOI film. The thin film separation process is based on the observation that ion-implantation induces blistering and exfoliation on the surface of semiconductors. It is generally, accepted that the thin film separation process proceeds by chemical interaction (bond breaking and internal surface passivation) and physical interaction (gas coalescence, pressure raise and fracture of implanted ions in the silicon substrate). However, gas blisters are frequently generated during annealing. The understanding of the origin of the temperature dependent gas bubbles at the bonding interface allowed the development of procedures suitable to prevent their formation [1]. The quality of the bonding interface is one of the most important factors in determining the performance of these structures. Depending on the pre-bond cleaning or other surface treatment, various impurities may be incorporated at the interface, which can diffuse out into the active layers during the bond anneal or subsequent processing, and influence the electrical characteristics. Since annealing temperature required to form hydrogen and helium optically detectable blisters is a measure of ion-cut performance, blistering phenomena on the co-implanted unbonded silicon wafers with various hydrogen and helium doses were studied at various temperatures ranging between 300°C and 700°C. The observation of these surface blisters is a convenient way of investigating the hydrogen and helium agglomeration process as a function of implantation dose and annealing temperature.

This paper discusses physical and chemical processes occurring during annealing on the implanted silicon surface, as a function of cleaning and activation surface processes. The paper is focused on the practical surface preparation approaches which can meet the requirements of surface cleanliness and reactivity of polished silicon wafer.

2. Experimental

In order to investigate the influence of O_2 and Ar-plasma surface cleaning treatments on the gas evolution in implanted silicon wafers, p-type 1.7-2.5 Ωcm (100) single-crystal silicon wafers implanted with helium and hydrogen ions were employed in our studies. Silicon wafers were implanted at room temperature with helium ions at 30 keV with doses of $1\cdot10^{16}\div3\cdot10^{16}$ cm^{-2} and successively implanted with hydrogen ions at 24 keV with doses of $1e10^{16}\div3e10^{16}$ cm^{-2}.

In order to obtain contamination free wafer surfaces (particulate, organic and metallic species), H/He co-implanted samples were cleaned by both wet and dry chemical procedure, commonly used in the semiconductor industry. In the wet cleaning procedures samples were rinsed in ethanol and acetone in ultrasonic bath for 3 minutes. After wet cleaning wafers were rinsed in de-ionized water. HF solution 1% was then employed to remove the native oxide layer (2÷10 Å thick) which may trap traces of impurities. Samples were dipped in the HF solution for 30 sec and then dried with nitrogen. It should be noted that in order to avoid the roughening of the silicon surface during the HF dip, very diluted aqueous solutions (≤1%) was used for a short time (< 5 min) at room temperature. This procedure, performed for all samples, was followed by an O_2 or Ar plasma treatments, in order to remove residual organic species, oxidize and activate the silicon surface. A Plasmod plasma reactor (March) with Barrel configuration was used at 75 W for times ranging from 1 to 100 minutes. After plasma treatments samples were dipped in 1% HF solution for 30 sec to obtain hydrophobic wafer surfaces. Contact angle measurement by using the sessile drop method were performed with a Contact-Angle Meter Kernco Instrument Co., Inc. (Model VCA-2000). In our studies water was employed as measure liquid.

Two mating Si wafers are then brought together face to face in air at room temperature manually. As reported in literature [5] the interface energy of bonded silicon wafer pairs increases with time at a given temperature. Therefore, bonded samples were stored in a furnace at 300°C for 20 h under a vacuum of 10^{-3} torr. A further heating step was subsequently performed at temperature of 450°C for 1 h under a vacuum of 10^{-5} torr. During the annealing the implanted wafer bonded to the handle wafer is split from the handle wafer and a thin layer (of thickness depending on the implant energy) is transferred by ion-cutting. In our work a layer of ~250 nm was transferred. Silicon surfaces obtained after cleaning procedures were characterized by XPS. XPS spectra were performed with an AXIS HS Spectrometer by Kratos using Mg X-ray source ($Mg\text{-}k_{\alpha\,1,2}$).

The blistering phenomena and the transferred layer were observed with an Atomic Force Microscopy (AFM-Digital Instrument Nanoscope, model III) and by an optical microscope (Nikon, model ECLIPSE-ME 600).

3. Results

XPS analysis of as implanted as well as treated surface reveal the signals of carbon, oxygen and silicon. Fig.1 shows the XPS Si2p regions for O_2 and Ar-plasma samples as an example. The spectrum of as implanted sample exhibit two components: the main peak centred at 99 eV of binding energy, due to elemental silicon and a second peak at binding energy about 103.5-104 eV, due to Si^{4+} species (SiO_x). After plasma treatments and HF cleaning, the component due to SiO_x disappears indicating the removal of the silicon oxide from the surface.

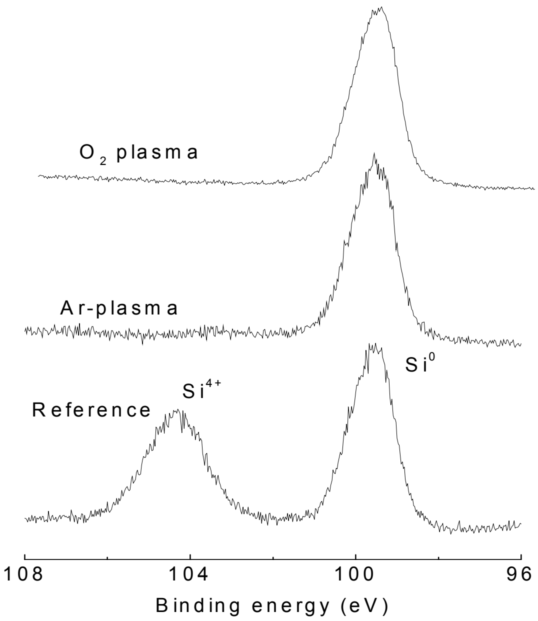

Fig.1. XPS Si2p regions of reference, Ar and O_2 plasma treated samples.

In Tab.1 the surface atomic compositions of these samples are reported. The carbon content of about 60% found for the reference silicon co-implanted samples, mainly due to hydrocarbon contaminations, is reduced respectively to about 4% for silicon surfaces treated with O_2 plasma and to about 8% for Ar plasma treatment.

	C 1s (%)	**Si 2p(%)**	**O (%)**
As implanted	63.7	13.8	22.5
O_2-Plasma	3.7	90.8	5.5
Ar-Plasma	7.5	76.3	16.2

Tab.1- Surface atomic compositions obtained by XPS measurements

Cleaned surface wettability was evaluated by contact angle measurements. It was found that after treatments with Ar or O_2 plasma performed at 75 W for 10 min, contact angle θ of the silicon surface was about 10°. By dipping wafers, after plasma cleaning, in a 1% HF solution for 30 sec, silicon surface became highly hydrophobic with a contact angle of ~70°. It has been reported that Si surfaces prepared by a dip in diluted HF show a room temperature-bonding performance similar to that of the hydrophilic surfaces [6]. This is generally ascribed to that the silicon surface after the HF process is terminated mostly by hydrogen (Si-H) and also by a small amount of fluorine (Si-F) [1].

Fig.2 reports image obtained by optical microscope measure of silicon sample co-implanted with He and H ions at dose of 1E16 cm^{-2}, obtained after a plasma treatment with O_2 performed at 75W for 10 min and annealed at 450°C for 1h under a vacuum of 10^{-5} mbar.

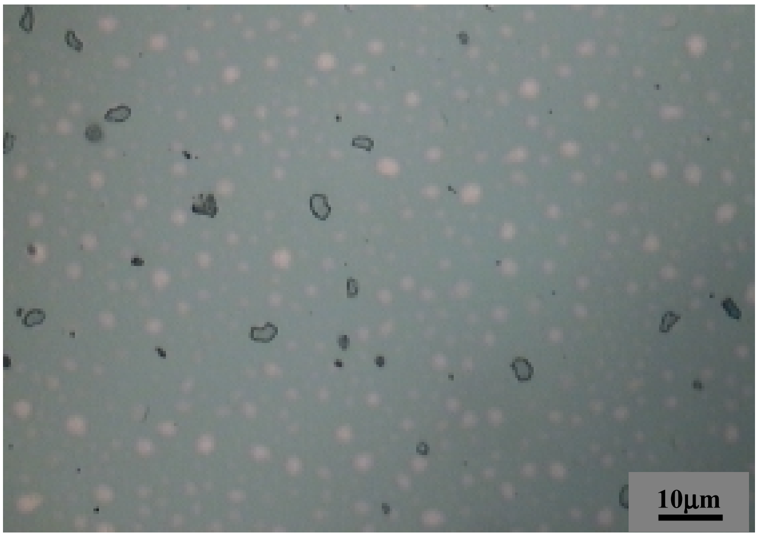

Fig.2- Optical microscope image of a silicon sample co-implanted with He and H ions at dose of 1E16 cm^{-2} after a plasma treatment with O_2 performed at 75W for 10 min and annealed at 450°C for 1h under a vacuum of 10^{-5} mbar.

The image evidences the blisters formed on the surface, some of them resulting evolved into craters due to the exfoliation of the surface cap. The blisters section is 2 to 15 µm^2, and the size seems to be independent of annealing temperature The circular base and shape is clearly due to the gas evolution of implanted species. By increasing annealing temperature exfoliation phenomena increase up to a temperature of ~600°C (see fig.3a), while no exfoliation (as well as gas evolution) was detected at temperatures lower than 300°C. In fig.3a exfoliation behaviour as function of annealing temperature for silicon wafers co-implanted with a larger dose ($3\cdot10^{16}$ cm^{-2}) is also reported. As clearly visible, the increased dose enhances blisters formation and decreases the annealing temperature at which the largest number of blisters is detectable. Since the temperature required to form hydrogen and helium-induced optically detectable blisters is a measure of the required splitting temperature in the layers transfer, the decreased exfoliation temperature at highest dose of implanted species allows to realise low-temperature silicon layer–splitting in all devices temperature-sensitive. In order to study the influence of plasma treatment on blisters formation both time and nature of plasma was varied. Fig.3b shows exfoliation behaviour as a function of annealing temperature for silicon wafers treated with O_2-plasma at different times 1, 10 and 100 min at a power of 75 W. Results show that 1 min of plasma treatment promote a higher amount of blisters on the silicon surface even though these treatment conditions are not enough to remove totally organic impurities, then the minimum time possible to realise both a perfectly surface contaminations-free and blistering was detected at 10 min. Surface cleaning treatments were realised also using an Ar-plasma (see fig.3c), performed at a power of 75 W for 10 min. As showed in figure treatments with Ar-plasma negatively affect exfoliation phenomena increasing the temperature of blistering and decreasing the bubbles amount.

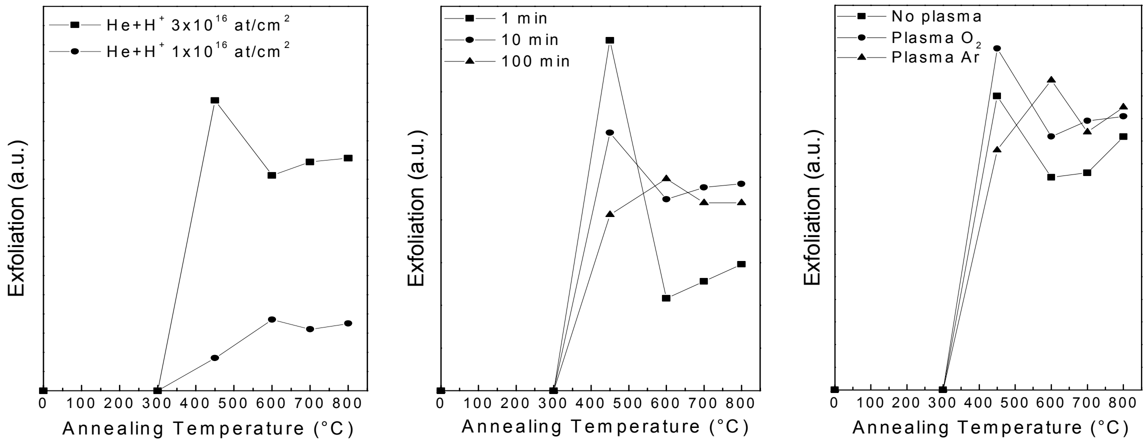

Fig.3 (a,b,c)- Exfoliation behaviour (number of craters/cm^2) as a function of annealing temperature for silicon wafers: co-implanted at different doses and annealed after an O_2-plasma treatment performed at 75 W for 10 min and followed by an HF cleaning (3a), subjected to an O_2-plasma treatment performed at 75 W for different times (1, 10, 100 min) (3b), and no-plasma, Ar, O_2 -plasma treated at 75 W for 10 min and cleaned with an HF solution (3c).

Results above discussed show that in order to realise the Si-to-Si bonding the best solution is an H and He implantation dose in silicon wafers of $3\cdot10^{16}$ cm^{-2} and an O_2-plasma surface treatment performed at 75 W for 10 minutes followed by an HF cleaning. After cleaning step, two mating Si wafers are then brought together face to face in air at room temperature manually and stored in a furnace at 300°C for 20 h under a vacuum of 10^{-3} torr. A further thermal treatment was then performed at temperature of 450°C for 1 h under a vacuum of 10^{-5} torr. During annealing the hydrogen and helium-implanted layer bonded to the handle wafer is split off from the device wafer around the mean ions penetration depth. In fig.4 the transferred layer after annealing is shown. The layer thickness is of ~250 nm and perfectly corresponding with mean ions penetration depth.

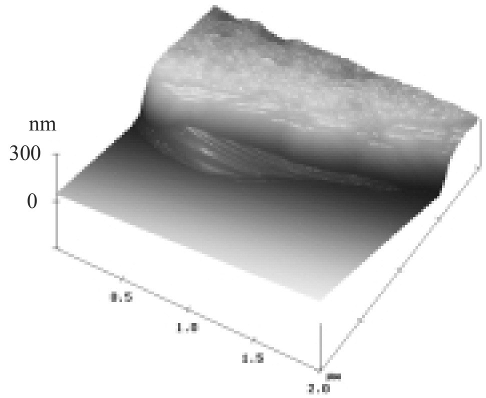

Fig.4 – AFM micrograph of a transferred layer obtained after 1h annealing at 450°C.

4. Conclusions

It has been shown that for Si-to-Si hydrophobic wafer bonding, the O_2-suface plasma treatment, performed at 75 W for 10 min, is the optimal choice both as cleaning surface method and to made the bonding very spontaneous at room temperature. An H- and He-induced layer splitting in bonded silicon wafers at implantation dose of $3\cdot10^{16}$ cm^{-2} with an high bond-strength was then obtained by annealing at temperature of ~ 450°C for 1h.

Acknowledgments: The authors wish to acknowledge Prof. G. Ottaviani for hydrogen and helium implanted silicon wafers. MIUR (Cofin) is gratefully acknowledged for financial support

Cleaning of metallic foils by dielectric barrier discharges under unipolar excitation conditions

G. Bauville[1], P. Choquet[2], B. Lacour[1], E. Michel[3], V. Puech[1], E. Silberberg[4]

[1] Laboratoire de Physique des Gaz et des Plasmas, Université Paris-Sud, 91405 Orsay Cedex, France
[2] IRSID (Centre de Recherche Arcelor), 57214 Maizières les Metz, France
[3] Service de Chimie Analytique, Université Libre de Bruxelles, Campus Plaine, B-1050 Bruxelles, Belgique
[4] RDCS / Cockerill-Sambre / Usinor, B-4400 Ivoz-Ramet (F300), Belgique

Abstract

An atmospheric pressure dielectric barrier discharge excited under pulsed unipolar conditions has been used in pure oxygen to remove oil contamination from metallic surfaces. Surface diagnostics through FTIR, XPS and SEM techniques point out that a good cleaning quality can be achieved with the pulsed-DBD plasma technique with treatment times short enough to allow an on-line industrial application.

1. Introduction

Nowadays dielectric barrier discharges (DBD) at atmospheric pressures are commonly used to produce transient non thermal plasmas usable for many industrial applications such as ozone production, flue gas treatment or surface modification [1-6]. Usually the DBD are powered by applying an alternating sine wave potential of several kV with a frequency of a few kHz between two electrodes, at least one of which being covered by a dielectric. For most excitation conditions, the discharge consists of numerous filaments randomly distributed over the electrode surface, and the discharge current consists of many spikes appearing during each half period. However for some specific conditions [5] the discharge can be homogeneous (it is the so-called atmospheric pressure glow discharges: APGD), which could be more advantageous for applications devoted to surface treatment. The surface modification of metallic foils usually involves two successive steps: first, a cleaning of the surface to remove oil contamination by an oxygen-rich plasma, and second, the deposition of a thin film with the required functionality. Thus, an efficient on-line treatment of metallic surfaces will require both a plasma with a high oxygen concentration and very high discharge frequencies, two conditions for which APGD cannot be obtained. On the other hand, Baravian et al previously showed [6] that an homogenous cleaning of metallic foils can be achieved by driving DBD in oxygen with a pulsed power supply. Unfortunately, the treatment time were too long, up to ten minutes, to allow an implantation of the plasma cleaning process on an industrial production line. Thus the present investigation has been devoted to an optimization of the pulsed BDB technique, in such a way that the treatment time have been reduced by two orders of magnitude.

2. Experimental set-up

The DBD reactor used in the present work mainly consists of two electrodes (20.5x2.8 cm^2), one of which being covered by a dielectric plate, while the other consists of the metallic foil to be decontaminated. A dip-coating technique was used to uniformly covered the foil with an oil layer of a controlled thickness in the range 5-200 nm before its introduction into the reactor. The inter-electrode gap was continuously swept with an oxygen flow at atmospheric pressure. The DBD, for which an equivalent electric circuit is given in Fig 1, is driven by an home-made high-voltage pulse generator able to produce unipolar pulses with a maximum voltage of about 20 kV and a rise time of 200 ns. Pulse repetition frequency as high as 100 kHz can be achieved with a maximum transferred energy of 30 mJ per pulse. The applied voltage $V_m(t)$ and the total current $I_m(t)$ are respectively measured with a Lecroy voltage probe and a current viewing resistor (R=0.2 ohm) connected to a fast digitizing oscilloscope (Lecroy LT264: 350 mHz, 1 GS/s). Plasma diagnostics are performed through time resolved optical emission spectroscopy (Chromex spectrograph and Princeton Instrument intensified CCD camera) and the spatio-temporal evolution of the discharge filaments in the inter-electrode gap is monitored by a second intensified CCD camera. The opening gates of the spectroscopic and imaging cameras, which can be as short as 5 ns, are synchronized with an adjustable delay time generator to the onset of the discharge current. Typical waveforms are shown in figure 2.

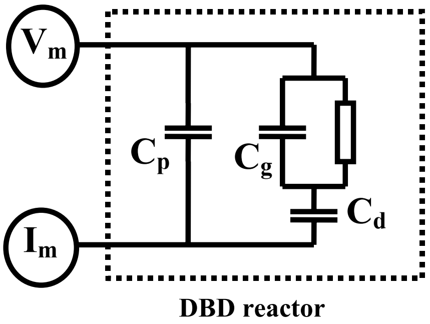

Figure 1: Equivalent electrical circuit of the DBD reactor.

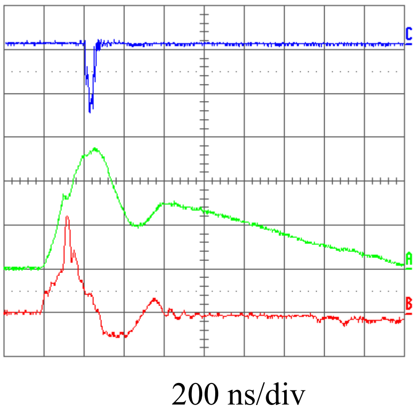

Figure 2: typical waveforms. Blue = opening gate of the CCD cameras; green = applied voltage (5 kV/div); red = total current (5A/div).

To characterize the efficiency of the plasma cleaning technique, we mainly used IRRAS FTIR spectroscopy of the surface layer by following the evolution of the reflectance of the CH bands near 2800 cm^{-1}. Before analysing plasma-cleaned metallic foils, a calibration curve has been established (Fig. 3) from the reflectance of foils contaminated with a known quantity of oil. As shown in Fig.4 this IRRAS technique allows to measure a residual contamination as low as 10 mg/m^2.

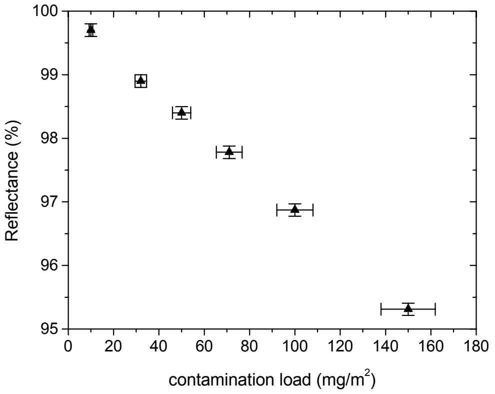

Figure 3: Evolution of the reflectance at 2920 cm^{-1} versus the contamination load.

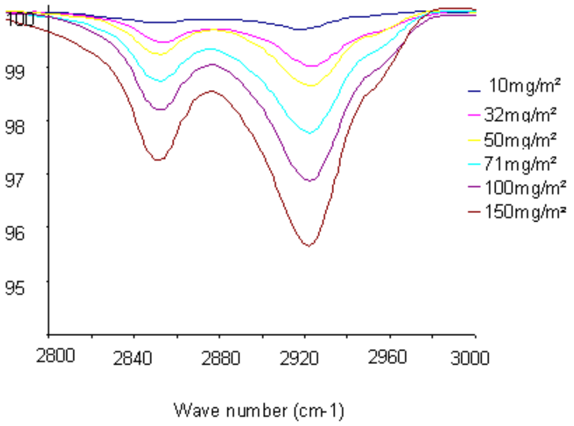

Figure 4: : FTIR spectra of metallic foils contaminated with calibrated oil load

3. Results and discussion

3-1. Energy deposition

As in most plasma-chemical processes, a comprehensive knowledge of the energy deposition into the plasma is essential to optimize the process effectiveness. The temporal evolution of the plasma voltage, $V_p(t)$, and plasma current, $I_p(t)$, can be obtained by applying the Kirchoff laws to the equivalent electrical circuit of the DBD reactor shown in Fig.1. They are related to the measured voltage, $V_m(t)$, and current, $I_m(t)$, by the relations:

$$I_p(t) = \frac{C_g + C_d}{C_d}\left[I_m(t) - \left(\frac{C_g C_d}{C_g + C_d} + C_p\right)\frac{dV_m(t)}{dt}\right] \qquad (1)$$

$$V_p(t) = \frac{C_d}{C_g + C_d} V_m(t) - \frac{1}{C_g + C_d} \int I_m(t)\, dt \qquad (2)$$

where C_d, C_g and C_p are respectively the capacitance of the dielectric, of the inter-electrode gap and the stray capacitance between the high-voltage electrode and the reactor which is usually of the same order of value as the equivalent DBD capacitance given by $C_gC_d/(C_g+C_d)$. For an alumina dielectric 3 mm thick, an inter-electrode gap of 2 mm, and a DBD running under pure oxygen at atmospheric pressure, the temporal evolution of voltages and currents are respectively plotted in figures 5 and 6, which clearly point out large differences between the measured electrical parameters, $V_m(t)$ and $I_m(t)$, and those, $V_p(t)$ and $I_p(t)$, controlling the energy which is actually deposited into the plasma: $E_p = \int V_p(t).I_p(t)dt$. The BDB ignites when the applied voltage reaches 8.5 kV. Then the plasma voltage remains approximately constant, 7± 1 kV during the current flow, whereas the applied voltage continuously increases up to 16 kV. Before DBD ignition, the measured current is a pure displacement current corresponding to the charging of the DBD and stray capacitances. Thus, the knowledge of C_d and C_g from the characteristic of the DBD reactor (discharge geometry and dielectric permittivity) allows to determine from eq.1 the value of Cp: Cp=17 pF. This value is then used to calculate (eq.1) the plasma current during all the pulse duration. Fig 6 points out that after discharge breakdown, the plasma current sharply increases to reach 20 A in less than 8 ns. The plasma current is characterized by a first spike whose duration at half maximum is less than 20 ns, while after this spike, a slower decay can be observed. At 400 ns there is a reversal of the plasma current, and a negative current pulse is then observed during about 100 ns. However, the ratio between the positive peak and the negative one is about 10. A second negative current pulse can also be observed between 1.2 and 1.8 µs which is connected to the saturation of the magnetic core of the output transformer of the power supply. As a result, an additional 20% of energy is deposited in the plasma in this second pulse as shown in Figure 7. This figure also points out that, because of an impedance mismatch, the plasma cannot absorb the totality

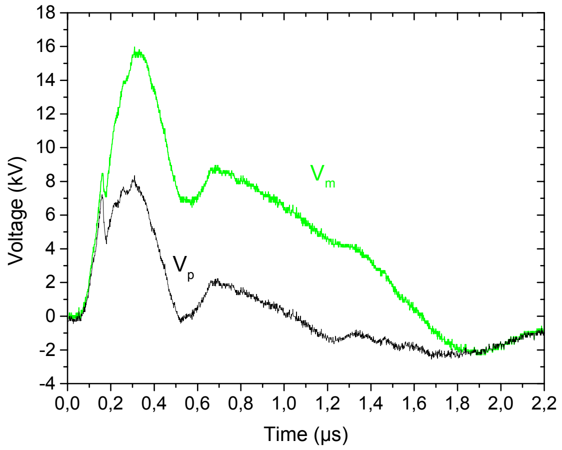

Figure 5: temporal evolution of the voltage measured across the DBD electrodes (green) and of the plasma voltage (black).

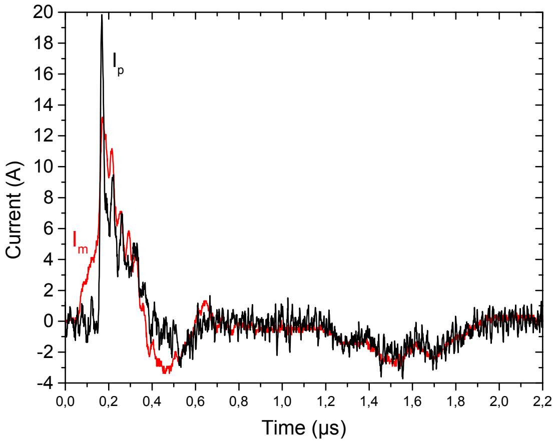

Figure 6: temporal evolution of the measured total current (red) and of the plasma current (black).

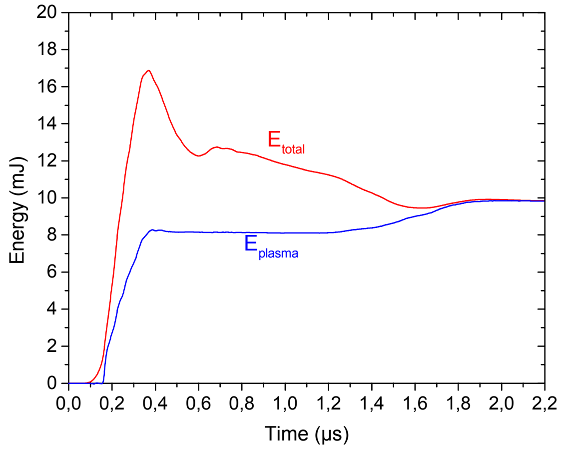

Figure 7: temporal evolution of the total energy provided by the pulsed power supply (red) and of the energy dissipated in the plasma (blue).

of the energy provided by the power supply. In the operating conditions of Fig.5-7, only 10 mJ are deposited in the plasma while up to 17 mJ are available from the power supply.

3-2. Surface cleaning

For a DBD running at 100 kHz with a deposited energy of about 0.15 mJ/cm^2, the evolution, versus the treatment time, of the oil contamination is plotted in figures 8 and 9 for two different initial oil loadings, 53 mg/m^2 and 100 mg/m^2 corresponding respectively to oil layers of 61 and 115 nm in thickness. These figures shows that for these two initial contaminations, the oil amount decreases exponentially versus time, with a time constant which slightly depends on the initial concentration: 1.3 s at 53 mg/m^2 and 1.8 s at 100 mg/m^2. Such a behavior is very similar to that previously reported by Behnke at al [4] for the decontamination of aluminium plates and results both from the statistical nature of the treatment by numerous filaments of tiny impact area and from a polymerisation effect. However, Fig 8-9 shows that a complete removal of the oil layer can be obtained for treatment times of a few seconds which are compatible with an industrial on-line application.

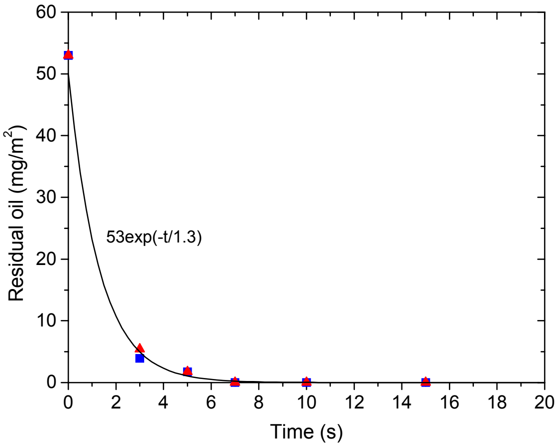

Figure 8: evolution, versus time, of the oil contamination for an initial load of 53 mg/m^2.

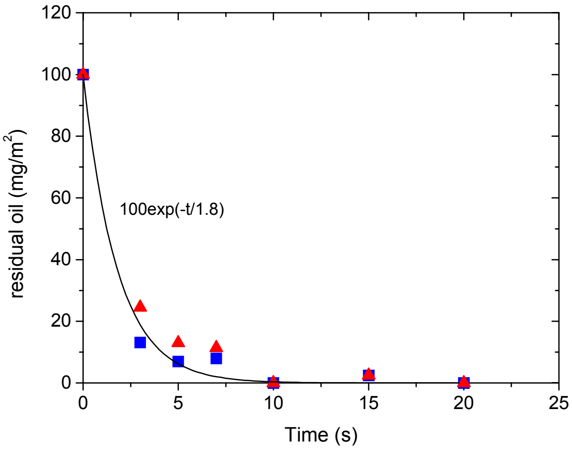

Figure 9: evolution, versus time, of the oil contamination for an initial load of 100 mg/m^2.

While IRRAS FTIR spectroscopy has been proved a very efficient technique to study the removal kinetic, it has a detection sensibility limited to about 10 mg/m^2 as shown in Fig.2. Therefore, complementary measurements have be performed to assess the quality of the plasma-cleaning and to compare its performance to the classical cleaning by liquid solvents. For that purpose, we used XPS analysis. Typical XPS spectra are shown in Fig. 10. Before cleaning (Fig. 10a) the spectrum is dominated by a carbon line and no iron line can be detected. On the other hand, Fig. 10b and 10c point out that chemical cleaning and plasma cleaning give rise to quite similar spectra with the appearance of many iron lines, indicating that if any contamination remains, the corresponding layer thickness is of order of one molecular layer, which is a cleaning quality good enough for application of subsequent coating. Moreover, analysis of the surface morphology has been performed through scanning electron microscopy. Figure 11 shows that the plasma cleaning (Fig 11c) is better than a chemical cleaning performed only by liquid solvent immersion and gives results quite comparable to those obtained by the combination of liquid solvent and ultra-sonic action.

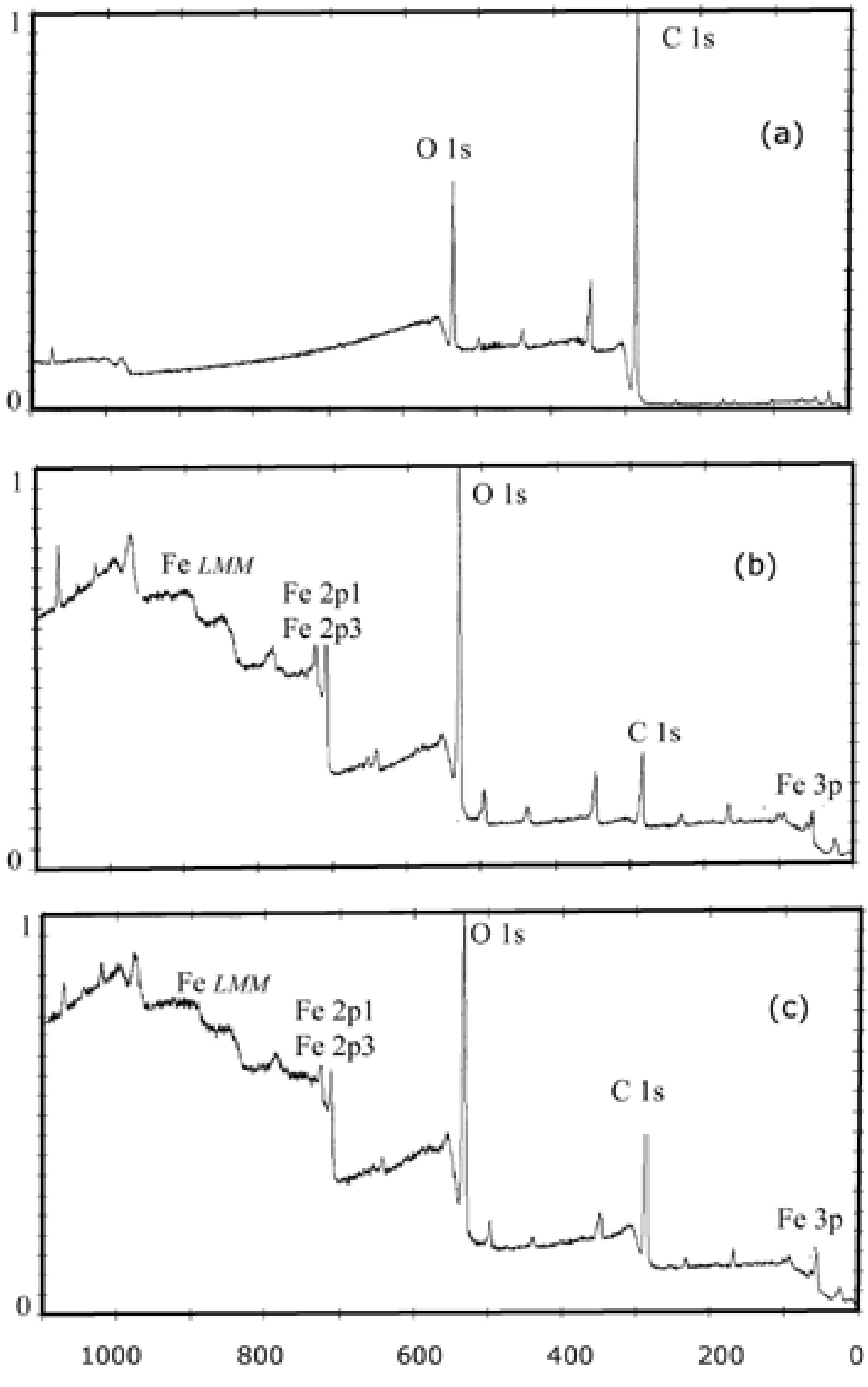

Figure 10: X-ray photoelectron spectra of : (a) a metallic plate oil-contaminated, (b) an oil contaminated plate after a cleaning procedure combining liquid solvent and ultra-sonic action, (c) an oil contaminated plate after plasma cleaning.

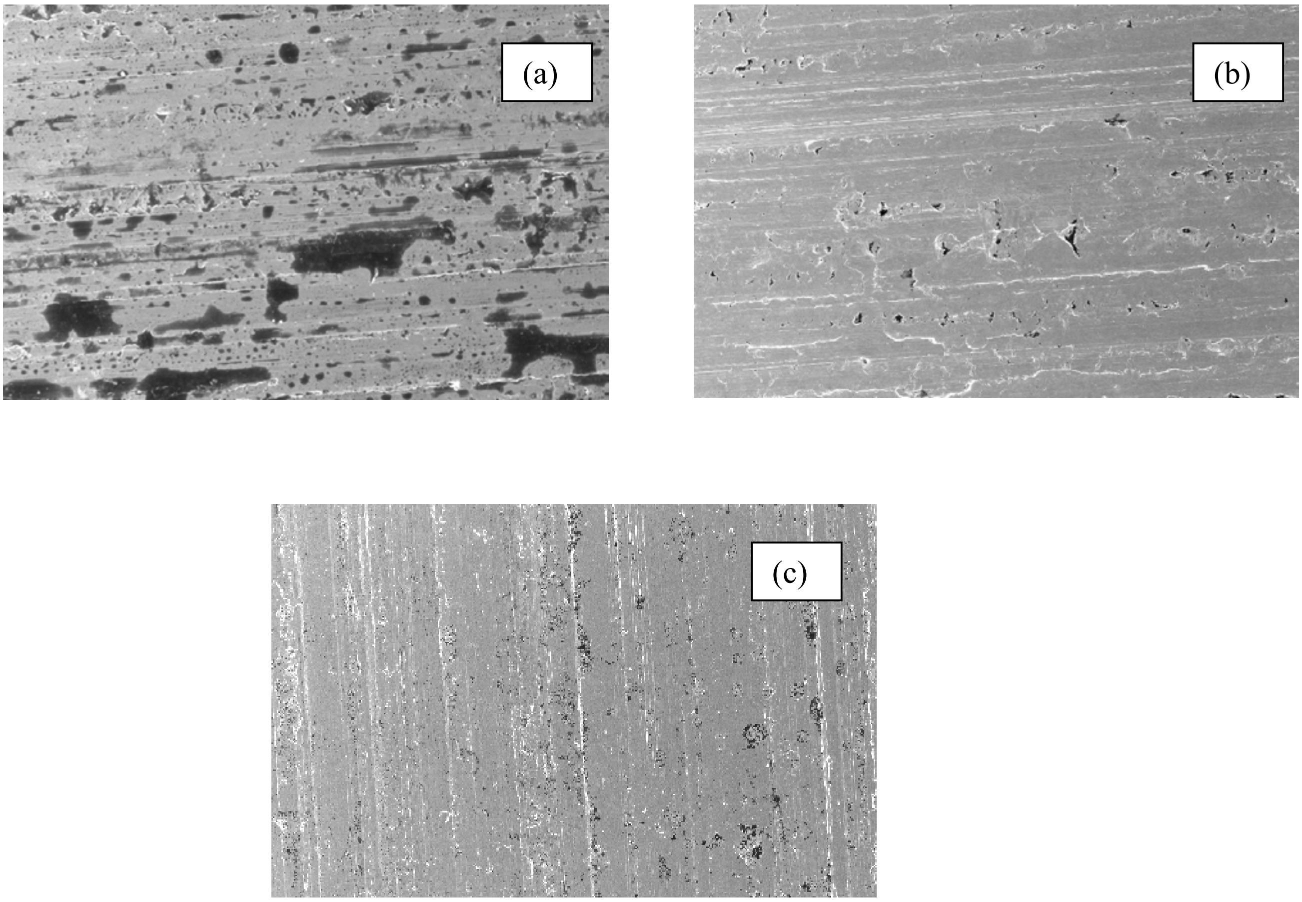

Figure 11: scanning electron micoscope pictures of: (a) metallic plates cleaned by immersion in a liquid solvent,
(b) metallic plates cleaned by immersion in a liquid solvent and ultrasonic bath,
(c) metallic plates cleaned by plasma treatment.

References

[1] U. Kogelschatz, B. Eliasson, W. Egli, J. Physique IV C4, **7**, 47 (1997)
[2] K. Pochner, W. Neff, R. Lebert, Surf. Coat. Technol., **74-75**, 394 (1995)
[3] J. Salge, Surf. Coat. Technol., **80**, 1 (1996)
[4] J.F. Behnke, H. Steffen, A. sonnenfeld, R. Foest, V. Lebedev, R. Hippler, Hahone VIII, Puhajärve (Estonia), July 21-25, 2002, p 414
[5] N. Gherardi, F. Massines, IEEE Trans. Plasma Sci, **29**, 536 (2001)
[6] G. Baravian, D. Chaleix, P. Choquet, P.L. Nauche, V. Puech, M. Rozoy, Surf. Coat. Technol., **115**, 66 (1999)

Low Noise Vacuum Arc Ion Source

E.Oks
High Current Electronics Institute, Tomsk,Russia

I. Litovko
Institute For Nuclear Research, Kiev, Ukraine

The influence of a pair of electrostatic meshes on beam parameters of ion source was investigated. The meshes were placed in the expansion zone of vacuum arc plasma. This mode of operation provides significant control over the ion charge state distribution of the extracted beam. The results of simulations of the processes involved are in good agreement with experimental results. In this article we report on the result of some investigations of the space charge limited mode of operation of the ion source, particularly as relevant to its possible application in the heavy ion fusion research program.

System identification and control of a non-transferred plasma torch for thermal plasma spray processes

C. M. Lee[1], M. R. Kim, K. S. Kim, T. H. Hwang, and S. H. Hong

[1] *Department of Nuclear Engineering, Seoul National University, Seoul 151-742, Korea*

Abstract

A simple feedback control system for the uniform output power of a non-transferred thermal plasma torches is developed by using the system identification technique and linear control theory. A mathematical model of the plasma torch system is first created on the basis of the ARX (Auto Regressive with eXogenous input) model. A control system for producing the uniform output power of the plasma torch is designed and developed by a control simulation using this mathematical model. Finally, the performances of the control system are experimentally tested and compared with the simulation results.

1. Introduction

Thermal plasma spraying is a well-established commercial process in a variety of high-performance coating applications. However, the plasma spray process features complex plasma-particle interactions that can result in significant process variations leading to limitations on reliability and reproducibility of the present techniques [1]-[2]. These limitations mainly come from several input perturbations, such as non-uniformity of electric power supply, irregularity of gas inflow and mixture, and electrode wear. To overcome these limitations, considerable efforts have been in progress to develop the completely automated system of plasma torch operation. At present, the automated control on the plasma spray system is carried out mostly by an open-loop control based on the database of input/output parameters accumulated through experiments, in which there is no feedback compensation of input parameters such as arc current, gas flow rate, and so on.

Recently, rapid progresses have been made in the real time diagnostics technology used for characterizing plasma jets, plasma-particle interactions, and particle-substrate interactions [3], and a few studies is carried out about the real-time feedback control of plasma spray process [1], [4]-[5]. In this work, a simple feedback control system is developed for producing the uniform output power of a non-transferred thermal plasma torch. The primary object is to build a mathematical model of the plasma torch system using the system identification technique by examining the experimental input and output data. The second is to design and develop the control system based on the mathematical model. Finally, some performance test results of the control system are presented for step response, set point tracking and disturbance rejection.

2. Experimental setup and procedures

Fig. 1 shows an experimental setup for plasma torch operation and its control. It consists of a DC non-transferred plasma torch, a 100 kW DC power supply, a gas supply unit, data acquisition devices, and a personal computer. The plasma forming gas is a mixture of argon and hydrogen, and supplied by mass flow controllers. The data acquisition devices acquire the analog output signals of operating current and voltage from the power supply as well as gas flow rates from the mass flow controllers, and generate the analog voltage command signals for manipulating the current and gas flow rates. A personal computer monitors the operating conditions by input signal processing, issues a command for the generation of command signals, and writes the operating history on a storage device with real time. In addition, the personal computer determines the correct values of operating variables to issue the command in the control process.

The first step for the development of control system is to collect experimental datasets of input and output variables. In this study, the output variable is the torch output power, of which control is achieved by manipulating the operating electric current. Then, the control system of this study employs a single input/single output (SISO) model. Based on the measured input and output data, a mathematical model of plasma torch system is formulated by introducing a system identification technique. This technique is used for building the mathematical model of dynamic systems by adjusting parameters in the formulated model

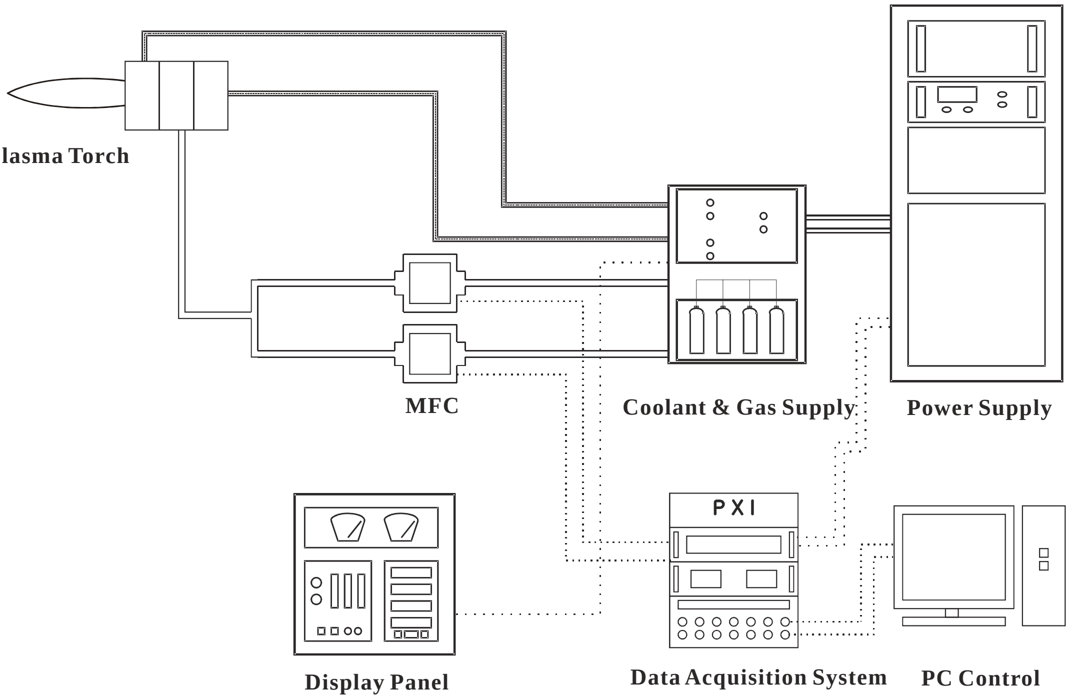

Fig. 1. Experimental setup of a plasma torch operation and control system

until its output value coincides with the measured output one as well as possible. If the mathematical model is good enough for describing the dynamic model of the plasma torch system, it is applied to the numerical simulation for finding the appropriate parameters required for an optimum design of the compensator for feedback control. Lastly, the performance of the control system is verified by some operation tests for step response, set point tracking, and disturbance rejection.

3. System identification

In the system identification, most commonly used models are difference equations descriptions, like an ARX (Auto Regressive with eXogenous input) model described as [6]

$$y(t) + a_1 y(t-1) + \ldots + a_{n_a} y(t-n_a) = b_1 u(t-n_k) + \ldots + b_{n_b} u(t-n_k-n_b+1) . \qquad (1)$$

This equation relates a measured output $y(t)$ to a finite number of past outputs $y(t-k)$ and inputs $u(t-k)$. The structure is thus entirely defined by the three integers n_a, n_b, and n_k. The number n_a of past outputs is equal to the number of poles, and the number $n_b - 1$ of past inputs is the number of zeros, while n_k is the pure time-delay (the dead-time) in the system. To build a mathematical model of dynamic system, the parameters a_i should be determined by using least squares method [6]. In most cases, outputs are also affected by other signals from external disturbances except the prescribed inputs. In the plasma torch system, for example, it could be electrodes wear and measurement noises. In this study, the mathematical model includes such unexpected inputs of disturbance signals or noise.

Since frequency-rich input signals are, in general, required for creating good mathematical models, pseudo-random, binary signals (PRBS) are commonly used as input signals in the system identification process [6]. The PRBS are sequences of rectangle pulse, modulated in width, which approximate a discrete-time white noise and have a spectral rich content in frequency. In this study, the PRBS is selected as an input electric current signal of 200 A ~ 500 A in the normal operation range. Because the rising time of the torch output power is about 0.03 sec, a sampling time of 0.005 sec is chosen for reliable identification and the input and output signals are measured during 2 sec. The half of the measured data is used for estimation process, and the other half is used for validation process of the created mathematical model by comparing the model’s outputs with the measured outputs. The input current signal and the corresponding output power signal used in this work are plotted in Fig. 2. The parameter estimation algorithms are implemented by using the MATLAB program, and the following mathematical model is created:

$$\begin{aligned} y(t) = {} & 0.4662y(t-0.005) - 0.1134y(t-0.01) - 0.008737y(t-0.015) + 0.07004y(t-0.02) \\ & -0.1043y(t-0.025) + 0.1285y(t-0.03) - 0.05215(t-0.035) + 0.009602u(t-0.01) \\ & +0.01474u(t-0.015) - 0.002531u(t-0.02) \end{aligned} \tag{2}$$

The mathematical model's output powers obtained from Eq. (2) is compared with the measured output powers in Fig. 3(a). For the system identification, the mean values are removed in each value. The simulated outputs show a quite satisfactory agreement with the measured ones. A little discrepancy is partly observed between two signals due to the signal noise and system non-linearity, but it can be compensated in the feedback control process. A similar feature also appears in Fig. 3(b) for the step response of the mathematical model and the torch system. When the input current jumps from 200 A to 500 A, the step responses of both the simulation model and the measured system show quite similar characteristics in the rising time and step height.

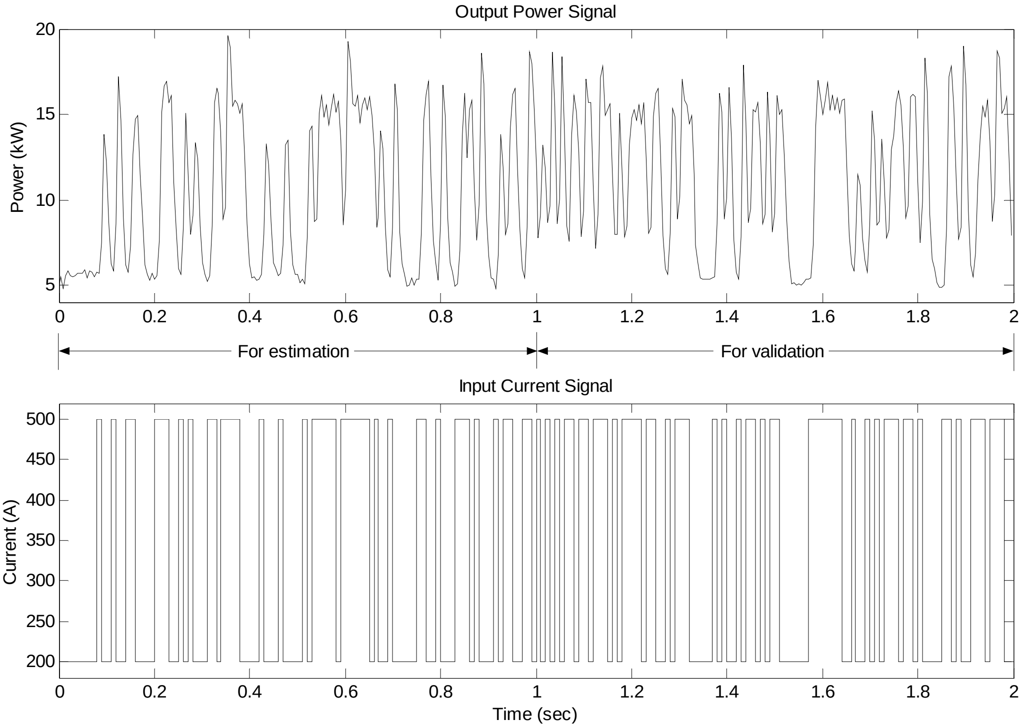

Fig. 2. Input current signal and corresponding output power signal used for the system identification.

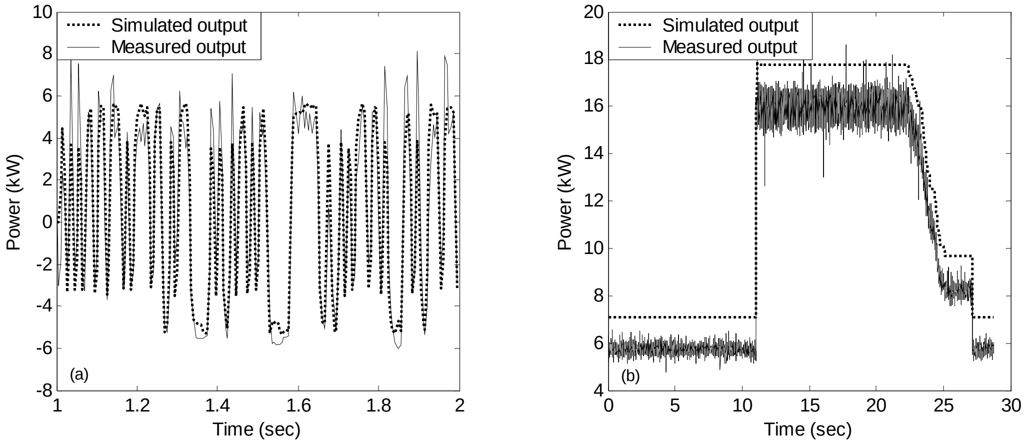

Fig. 3. Comparison between the measured and simulated outputs for the validity of the mathematical model; (a) input pulse signal responses, and (b) step responses

4. Feedback control

A block diagram of the feedback control system considered is depicted in Fig. 4. The transfer function G denotes the dynamic properties of the system, i.e., how the output is formed from the input, and it is transformed from the mathematical model in the system identification process. The compensator (i.e., controller) C determines the correct input values to compensate the differences between the command values and the output values. Since the dynamic property is determined in the system identification process, the controller is to be designed by simulation. The PID (Proportional-plus-Integral-plus-Derivative) controller, the most commonly used scheme in the control application, is employed in this study. With the controller input $e(t)$ and output $m(t)$, the PID controller is defined as [7]

$$m(t) = K_p e(t) + K_i \int_0^t e(\tau)d\tau + K_d \frac{de(t)}{dt} \qquad (3)$$

where K_p, K_i, and K_d are the proportional, integral, and derivative gains, respectively. The proportional control element is a pure gain as an inevitably used element, and the integral element is used for no steady-state errors. The derivative element improves the transient response, but in case of noisy input signal the system may be unstable. Therefore, the derivative control element is not used in this study. To determine the values of K_p and K_i, various analytical approaches are available in Ref.[6]. The determined values are K_p=5.90 and K_i=237.92. A relationship of the controller between the differences and input values is represented in the form of a discrete transfer function with a sampling interval of 0.01 sec as follows:

$$m(t) = m(t-0.01) + 5.90e(t) - 3.52e(t-0.01) \qquad (4)$$

With the determined values in the controller design, a control system of the plasma torch is manufactured.

The performance test of the manufactured control system applied to the plasma torch operation is carried out for the step response, set-point tracking and disturbance rejection, and the test results are presented in Figs. 5-7. In Fig. 5, the measured step response for a command from 9 to 18 kW is in a good agreement with the simulation result. The settling time is about 0.48 sec without showing an overshoot and a steady state is attained in 0.75 sec. In this case, to compensate the differences, the input current is raised from 300 A to 550 A and changed in succession. Figure 6 shows the experimental test results of the set-point tracking compared with the simulation results. When the commands from 9 to 18 kW and vice versa are repeatedly given, quite similar output powers are resulted from both the measurement and simulation.

Finally, the control process results of the disturbance rejection test shown in Fig. 7 indicate that a constant command output power of the plasma torch is achievable by the feedback control system developed in this work even though the operating conditions are disturbed. In this test, the hydrogen gas inflow of 2 lpm is assumed as a disturbance. As shown in Fig. 7(a) for a case of no control process, the output power changes according to the disturbed shape of gas flow rate due to the voltage increase with the hydrogen flow rate in the plasma torch. On the other hand, in case of the control process shown in Fig. 7(b), the input current is regulated to keep the output power with a command level. This control feature is similarly applicable when the flow rate of hydrogen is decreased.

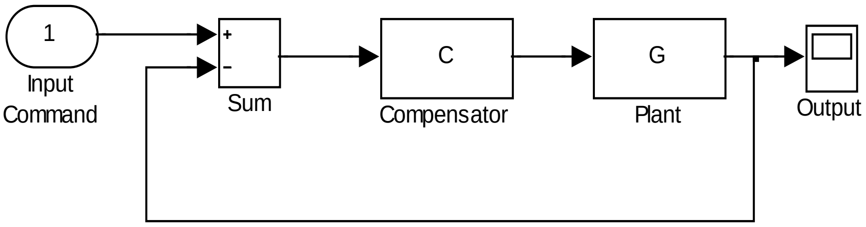

Fig. 4. Block diagram of a feedback control system considered for the automated operation of plasma torch system.

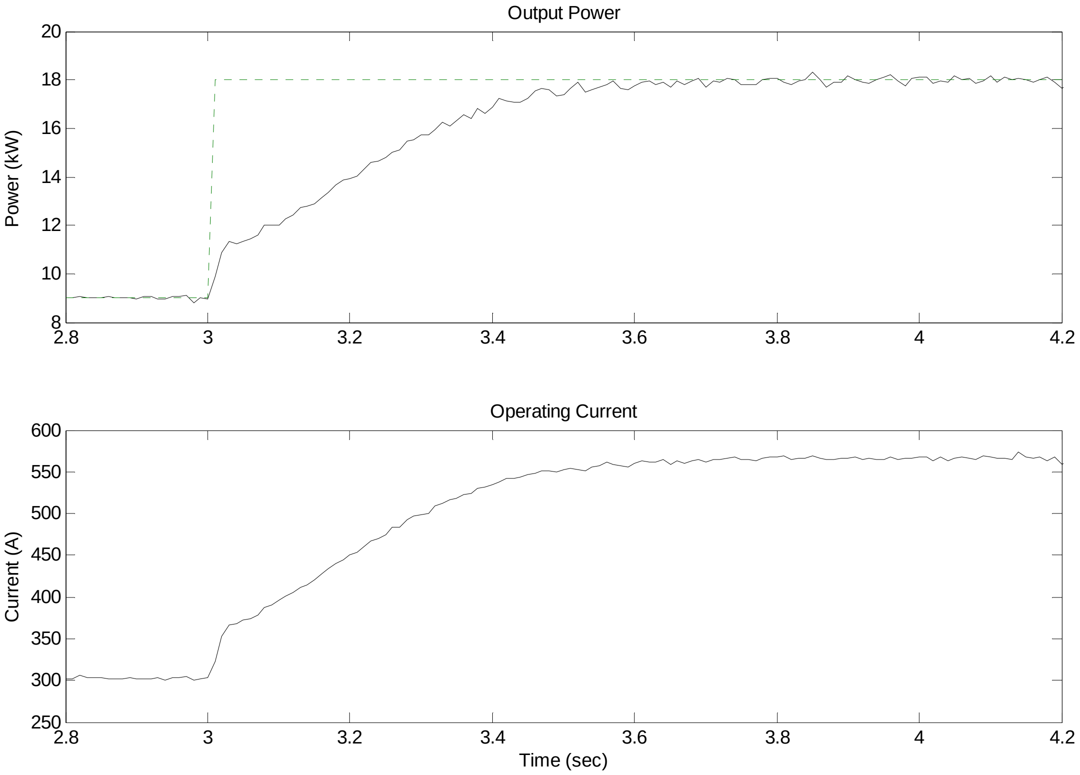

Fig. 5. Step responses of the plasma torch system operated in the feedback control process (solid line measured by experiment, and dashed line predicted by simulation)

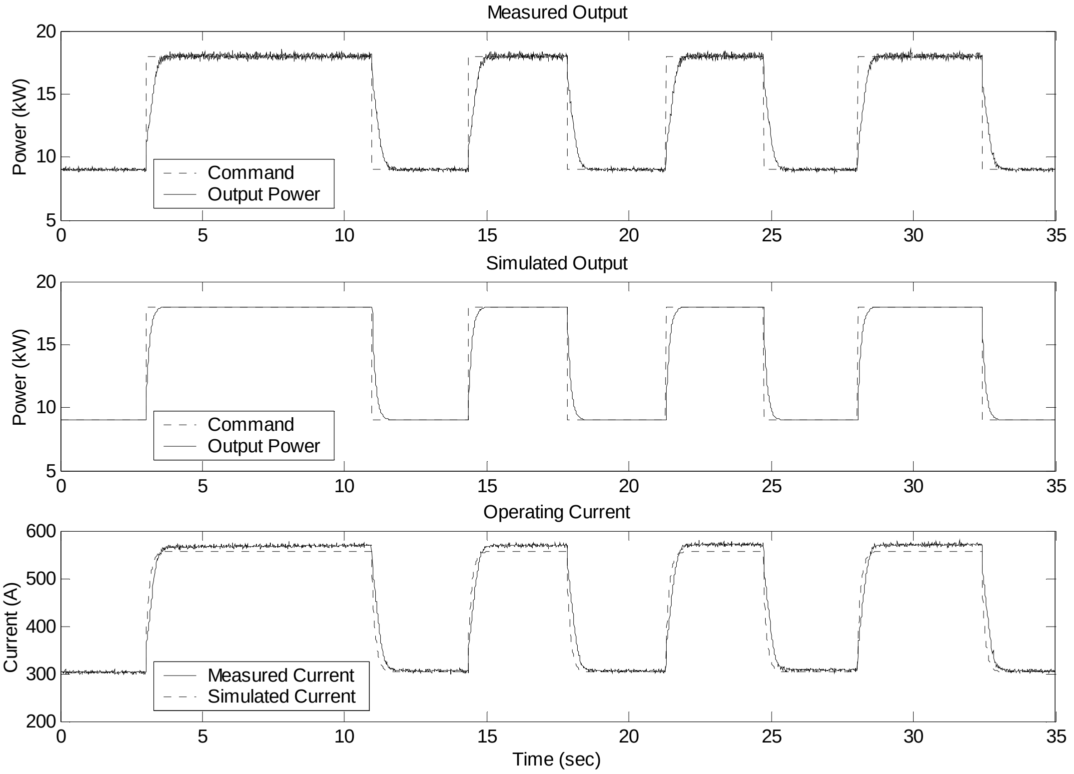

Fig. 6. Comparison between the measured and simulated results of set point tracking response for the plasma torch system in the feedback control process.

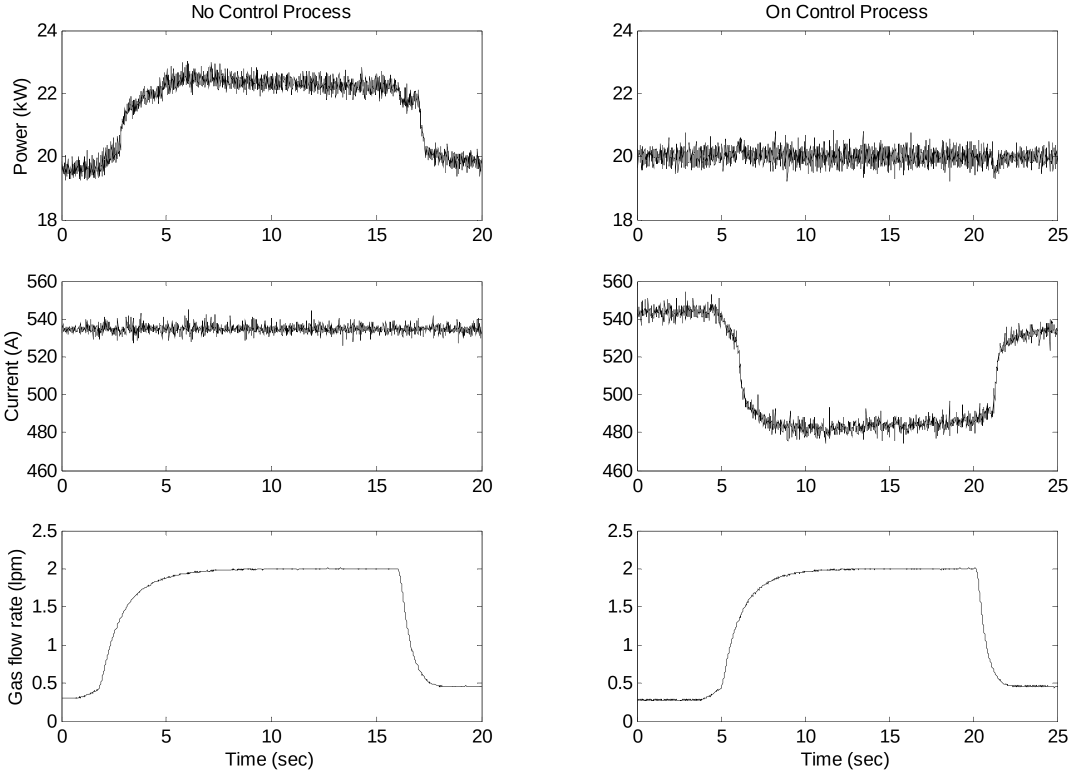

Fig. 7. Feedback control test results for the disturbance rejection on hydrogen gas inflow to maintain the constant output power of the plasma torch by regulating the electric current.

5. Conclusion

The thermal plasma spray process features significant process variations because of complex plasma characteristics and disturbances. These variations lead to limitations on the plasma torch performance, which requires the feedback control to overcome this drawback. In this study, the simple feedback control system of the plasma torch is developed by using the system identification technique and linear control theory. With the system identification technique, the mathematical model of the plasma torch system can be built and the design of the control system is possible through the simulation taking advantage of the mathematical model. The feedback control system successfully performs the command as tracking the set point command and rejecting the disturbances. These control test results imply that the system identification technique and feedback control process will be of great help for developing the optimal intelligent control system of the plasma process system.

References

[1] J. R. Fincke, W. D. Swank, R. L. Bewley, D. C. Haggard, M. Gevelber, D. Wroblewski, *Surface and Coatings Technology*. **146-147**, 537 (2001)

[2] M. I. Boulos, P. Fauchais, E. Pfender, Thermal Plasmas, Vol. 1, Plenum Press, N.Y. (1994)

[3] M. Vardelle, P. Fauchais, *Pure Appl. Chem*. **71**, 1909 (1999)

[4] L. Beall, Z. Duan, J. Schein, M. Stachowica, M. P. Planche, J. Heberlein, *Proc. 15th Int. Therm. Spray Conf.* 815 (1998)

[5] H. Nishiyama, T. Sato, D. Kato, *Proc. 15th Int. Symp. Plasma Chem.* Ⅰ, 155 (2001)

[6] Ljung L., System Identification - Theory for the User, Prentice Hall, Upper Saddle River, N.J. 2nd edition (1999)

[7] C. L. Phillips, R. D. Harbor, Feedback Control Systems, Prentice Hall, Englewood Cliffs, N.J. (1991)

Destruction of Ozone-Depleting Substances by Thermal Plasmas – Technologies, Chemistry and Modelling

A. B. Murphy

CSIRO Telecommunications and Industrial Physics, P.O. Box 218, Lindfield NSW 2070, Australia

Abstract

Plasma technologies for the destruction of ozone-depleting substances are briefly reviewed. The results of thermochemical, chemical kinetic and fluid dynamic modelling of the destruction of ozone-depleting substances in the PLASCON process, based on an argon plasma produced by a dc plasma torch, are presented. The usefulness of the mixing temperature and the feed rate to plasma power ratio concepts, and the importance of interconversion of different ozone-depleting substances in the plasma, are demonstrated.

1. Introduction

The production of most ozone-depleting substances (ODS), such as halons and chlorofluorocarbons (CFCs), has been prohibited in developed countries since the mid 1990s by the Montreal Protocol and its revisions. Many countries have destroyed or are planning to destroy their stockpiles of ODS. Thermal plasmas are well suited to this task. The high temperatures that are available ensure that destruction to the 99.99% level required by the Montreal Protocol is easily achievable, even at high feed rates. Plasma destruction is economically competitive with incineration, particularly since the high fluorine content of ODS can lead to damage by HF to incinerator equipment, severely limiting the ODS feed rate.

The recent Report of the Task Force on Destruction Technologies of the United Nations Environment Programme [1] recommended eleven technologies for the destruction of CFCs, and five for the destruction of halons. Four of the technologies recommended for CFC destruction utilise thermal plasmas; two of these were also recommended for halon destruction. The plasma technologies are described briefly in Section 2. One of these technologies, the PLASCON process, is described in more detail in Section 3. The chemical and physical processes occurring in the PLASCON process have been studied using thermochemical, chemical kinetic, and fluid-dynamic modelling, as well as through extensive experimental trials. The respective modelling procedures, their importance in understanding the phenomena occurring in PLASCON, and their usefulness in process design, are discussed in Sections 4 to 6.

2. Plasma Technologies for ODS Destruction

The Task Force on Destruction Technologies of the United Nations Environment Programme recently considered all available technologies for ODS destruction [1], recommending eleven technologies for the destruction of CFCs and five for the destruction of halons. Recommendation required that the technology had been demonstrated to destroy CFC and/or halon on at least a pilot or demonstration scale (defined as 1.0 kg h^{-1} or more) with destruction and removal efficiency (DRE) of at least 99.99%, and with dioxin and furan, acid gas and halogen, particulate, and carbon monoxide emissions in the exhaust gas below defined upper limits. The plasma technologies recommended for CFC destruction were argon arc, inductively-coupled radio-frequency plasma, nitrogen arc, and microwave plasma; the first two were also recommended for halon destruction. The argon arc technology is the PLASCON process, which is described in Section 3.

The inductively-coupled radio-frequency plasma technology uses a 185 kW rf plasma torch to destroy gaseous ODS mixed with steam. Destruction and removal efficiencies exceeding 99.99% have been obtained for CFC feed rates of 50 to 80 kg h^{-1}. The technology was developed in Japan by a consortium of industrial concerns under the auspices of the Ministry of International Trade and Industry. A commercial plant has operated since 1995, and over 300 t of CFCs, HCFCs (hydrochlorofluorocarbons) and HFCs (hydrofluorocarbons) had been destroyed by 2001.

The nitrogen arc technology, which is similar to the PLASCON argon arc process, uses a dc non-transferred plasma torch, but with nitrogen as the plasma gas. The torch power is around 15 kW. CFCs, HCFCs or HFCs are fed into the nitrogen plasma jet at a rate of 10 kg h^{-1}. The plasma gas is then fed into an oxidation tube in which HCFCs and HFCs are reacted with steam and then air. Five units, produced by ShinMaywa Auto Engineering, are currently being used commercially in Japan, and have destroyed more than 90 t of CFCs, HCFCs and HFCs.

The microwave plasma technology was developed by Mitsubishi Heavy Industries, Ltd, and launched commercially in 2000. An atmospheric-pressure thermal plasma is generated by 2.45 GHz microwaves in a coaxial cavity. Argon is used to initiate the plasma, but otherwise the plasma operates on a mixture of CFCs with steam. DREs exceeding 99.99% have been reported for a CFC feed rate of 2 kg h^{-1}.

Other thermal plasma technologies, such as an ac process designed by Scientific Utilization International, and a CO_2 arc process developed by Kinectrics and Plasma Environmental Technologies of Toronto, Canada, have been proposed for the destruction of ODS, but had not been demonstrated on a commercial scale. Non-thermal technologies have also been researched, but reported DREs are well below 99.99%.

3. The PLASCON Process

The PLASCON process, developed by CSIRO and SRL Plasma Ltd, is based on a dc non-transferred arc plasma torch, with argon as the plasma gas. A schematic diagram of the process is shown in Figure 1. An argon plasma jet is produced using a 150 kW plasma torch. The liquid or gaseous waste is co-injected with an oxidising gas through an injection manifold towards the end of the plasma torch. The resulting mixture of hot gases passes through a flight tube, whose purpose is to ensure that residence times are sufficient for thorough conversion of the hazardous waste into benign substances. The mixture is then rapidly quenched by a liquid spray, before passing through a NaOH scrubber to remove acid gases and halogens. The waste products for ODS destruction are argon, carbon dioxide, and sodium halides.

Four 150 kW PLASCON systems are now operating on a commercial basis in Australia, destroying the liquid waste stream from the production of the herbicide 2,4D, PCB contaminated oils, and ODS. DREs for ODS exceed 99.9998% for halon feed rates of 100 kg h^{-1} and CFC feed rates of 50 kg h^{-1}. The process has been used to destroy Australia's and New Zealand's stockpiles of halons and CFCs since late 1995. Over 1000 t of halon and 200 t of CFC have been destroyed to date. A facility using the PLASCON technology has recently been constructed by DASCEM Europe to destroy European halon stockpiles.

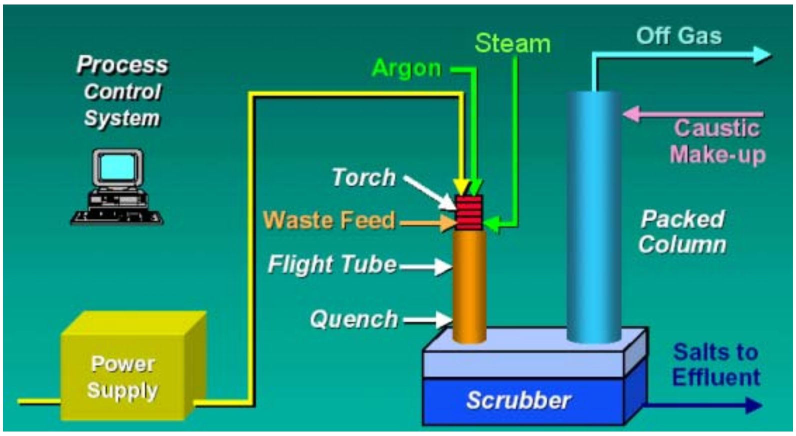

Figure 1. Schematic of the PLASCON process.

4. Thermochemical Calculations

Thermochemical calculations are based on the assumption that reaction rates are large relative to residence times, so that chemical equilibrium is attained. This has some validity in PLASCON, particularly in the plasma torch and injection manifold regions, where temperatures and hence reaction rates are largest. A particularly useful parameter is the mixing temperature, defined as the temperature at chemical equilibrium of a given gas mixture for a given energy input. For PLASCON, the mixing temperature is the temperature to which the mixture consisting of the plasma gas, the substance to be destroyed and the oxidising gas is heated by the plasma torch. A good correlation has been demonstrated between the calculated mixing temperature and the measured destruction performance for a wide range of substances, including PCBs, the 2,4D waste liquid, and ODS [2,3]. Mixing temperatures of around 3000°C are associated with DREs of 99.9999%, and mixing temperatures of around 2000°C with DREs of 99.99%. Figure 2 shows mixing temperatures for C_6ClH_5 (chlorobenzene) and CF_2Cl_2 (CFC-12) for two different oxidising gases, oxygen and steam. The mixing temperature for chlorobenzene is substantially higher when oxygen is used. Mixing temperatures above 3000°C are calculated, and hence better than 99.9999% destruction is expected, when the feed to

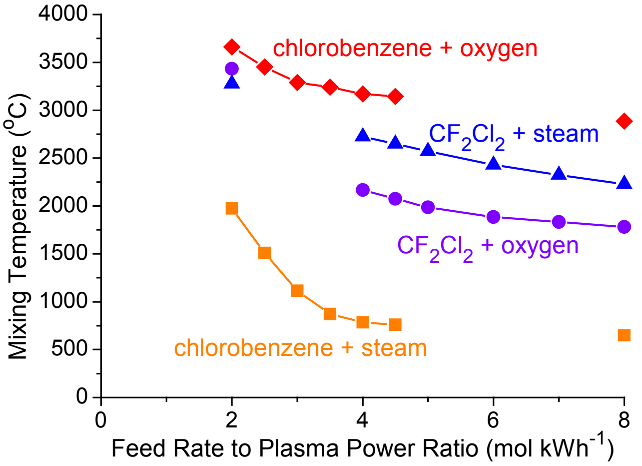

Figure 2. Mixing temperatures for chlorobenzene and dichlorodifluoromethane as a function of feed rate normalised to the plasma power. Results are given for steam and oxygen as oxidising gases. The plasma power was 75 kW.

plasma power ratio is below about 5 mol (kWh)$^{-1}$. In contrast, mixing temperatures for CF_2Cl_2 are larger when the oxidising gas is steam. The mixing temperatures for CF_2Cl_2 with steam are lower than those for chlorobenzene with oxygen, indicating that destruction will be less complete for a given feed rate. However, DREs of 99.99% are sufficient for ODS; the corresponding mixing temperature of 2000°C is obtained for feed rates of more than 8 mol (kWh)$^{-1}$.

5. Chemical Kinetic Calculations

Departures from chemical equilibrium often occur, particularly in the flight tube region. Chemical kinetic calculations are then required to model the destruction process. A chemical kinetic scheme for the destruction of the halons CF_2ClBr and CF_3Br in the presence of steam, which considers 47 species and 139 reactions, has been developed [4]. Schemes for the destruction of CF_2Cl_2 in the presence of steam, and for the destruction of all three ODSs in the presence of oxygen, are subsets of the full scheme.

Initial experimental tests of ODS destruction were performed with oxygen as the oxidising gas. Figure 3 shows a summary of results obtained for the destruction of CF_2Cl_2 in a 50 kW research reactor. The mole fractions of CF_2Cl_2, CF_3Cl and CF_4 are shown as functions of the CF_2Cl_2 feed rate normalised to the plasma power. The CF_2Cl_2 residual was below 10 ppm for feed rates up to 14 mol (kWh)$^{-1}$. This may be compared to the Montreal Protocol limit of 100 ppm (which corresponds to a DRE of 99.99%). However, for feed rates greater than 6 mol (kWh)$^{-1}$, the CF_3Cl concentration in the stack gas was greater than 0.1%. Since CF_3Cl has the same stratospheric ozone depletion potential as CF_2Cl_2, the feed rate for CF_2Cl_2 must be kept below

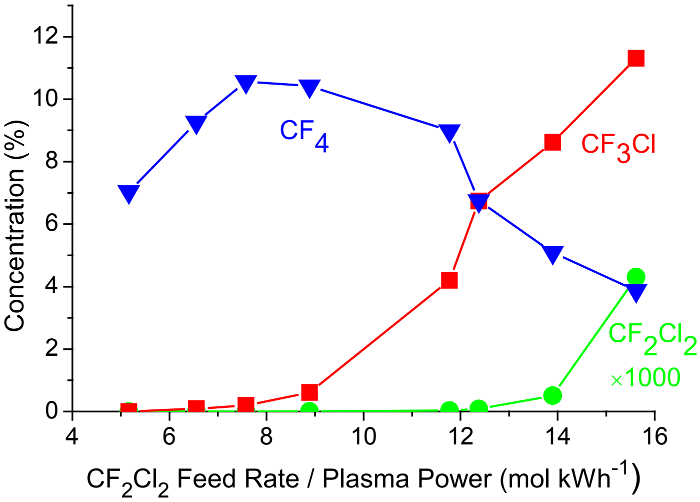

Figure 3. Measured concentrations of CF_2Cl_2, CF_3Cl and CF_4 in the exhaust gas as a function of CF_2Cl_2 feed rate normalised to the plasma power, with oxygen as the oxidising gas. The argon plasma gas input rate was 42 L min^{-1}, the CF_2Cl_2 feed rate ranged from 13.6 to 42.8 L min^{-1}, and the plasma power ranged from 7.1 to 7.3 kW

6 mol $(kWh)^{-1}$ to maintain compliance with the Montreal Protocol requirements. A further problem shown in Figure 3 is that CF_4, a strong greenhouse gas, is produced at concentrations of around 10%.

Use of steam rather than oxygen as the oxidising gas resulted in a substantial decrease in the production of both CF_3Cl and CF_4. Table I gives concentrations of ODSs and CF_4 in the exhaust gas for the destruction of CF_2Cl_2 with both oxygen and steam co-injection. The total ODS concentration, weighted for ozone depletion potential, is also given. It can be seen that steam in stoichiometric quantities (H_2O / CF_2Cl_2 mole ratio of 2) eliminated the formation of CF_4 and greatly reduced the level of ODS in the exhaust gas, to well below the level of 28 ppmv that in this case corresponds to the DRE of 99.99% required by the Montreal Protocol.

Table I. Concentrations of ozone-depleting substances and other halogenated hydrocarbons detected in the exhaust gases from the decomposition of CF_2Cl_2 in an argon plasma with co-injection of steam or oxygen for a feed to plasma power ratio of 6.5 mol $(kWh)^{-1}$. For oxygen co-injection, plasma power = 7 kW, CF_2Cl_2 feed rate = 19 L min^{-1}. For steam co-injection, plasma power = 15 kW, CF_2Cl_2 feed rate = 40 L min^{-1}. Ar flow rate = 42 L min^{-1}.

O_2 / CF_2Cl_2 mole ratio	H_2O / CF_2Cl_2 mole ratio	Measured concentration (ppmv)						
		CF_4	CF_3Cl	CF_2Cl_2	$CHCl_3$	CCl_4	C_2Cl_4	Total ODS[1]
1.0	0.0	92600	924	0.3	—[2]	—[2]	—[2]	799
0.0	2.0	0[3]	0[3]	0[3]	10	5	30	7
0.0	1.5	0[3]	760	1	10	5	30	665

[1] Total ozone-depleting substance concentration, weighted for ozone depletion potential on a mole basis (1.0 for CF_2Cl_2, 0.86 for CF_3Cl, 1.4 for CCl_4, 0 for other substances). Note that ozone depletion potentials are normally quoted on a mass basis.

[2] Concentrations of these substances were not measured in this experiment.

[3] Detection limits are 0.1 ppmv for CF_2Cl_2 and 10 ppmv for CF_4 and CF_3Cl.

Table II gives results of chemical kinetic calculations of the destruction of CF_2Cl_2 in the presence of oxygen and steam. The temperature–time profile was derived from the two-dimensional fluid dynamic model described in Section 6 [4]. The results are in reasonable accord with those given in Figure 3 and Table I. In particular, the total ODS concentration is greatly decreased, and CF_2Cl_2, CF_3Cl and CF_4 are eliminated, by the use of steam at stoichiometric levels. The calculations indicate that the H_2O / CF_2Cl_2 mole ratio has to be reduced below 1.5 before ODS and CF_4 levels become significant, while the measurements show this already occurs at a ratio of 1.5.

Table II. Concentrations of ozone-depleting substances and other halogenated hydrocarbons in the exhaust gas, calculated using the chemical kinetic scheme for the decomposition of CF_2Cl_2 in an argon arc plasma with co-injection of oxygen or steam. Plasma power =15 kW, CF_2Cl_2 feed rate = 40 L min^{-1}, Ar flow rate = 42 L min^{-1}.

O_2 / CF_2Cl_2 mole ratio	H_2O / CF_2Cl_2 mole ratio	Concentration (ppmv)			
		CF_4	CF_3Cl	CF_2 Cl_2	Total ODS[1]
1.0	0.0	16190	586	6.4	513
0.0	2.0	0.0	0.0	0.0	0
0.0	1.5	1.1	0.0	0.0	0
0.0	1.0	120	34970	184800	215000

[1] Total ozone-depleting substance concentration, weighted for ozone depletion potential on a mole basis (1.0 for CF_2Cl_2, 0.86 for CF_3Cl, 1.4 for CCl_4, 0 for other substances). Note that ozone depletion potentials are normally quoted on a mass basis.

Measurements were also performed for the destruction of the halon CF_2ClBr (commonly known as BCF) in the 50 kW research reactor, with steam as the oxidising gas. Figure 4 shows measurements of the CF_2ClBr concentration in the exhaust gas for a range of feed rate to plasma power ratios. The concentration is below 10 ppmv until the feed to plasma power ratio reaches 9 to 10 mol $(kWh)^{-1}$. In the measurements, the steam was at or close to stoichiometric levels. Some interconversion of CF_2ClBr to CF_3Cl was detected, but the CF_3Cl concentration was well below that of CF_2ClBr in all cases [4].

Chemical kinetic simulations of the destruction of CF_2ClBr with co-injection of steam were performed for a range of plasma powers [4]. Significant conversion to CF_3Br (around 3% of the final ODS concentration by

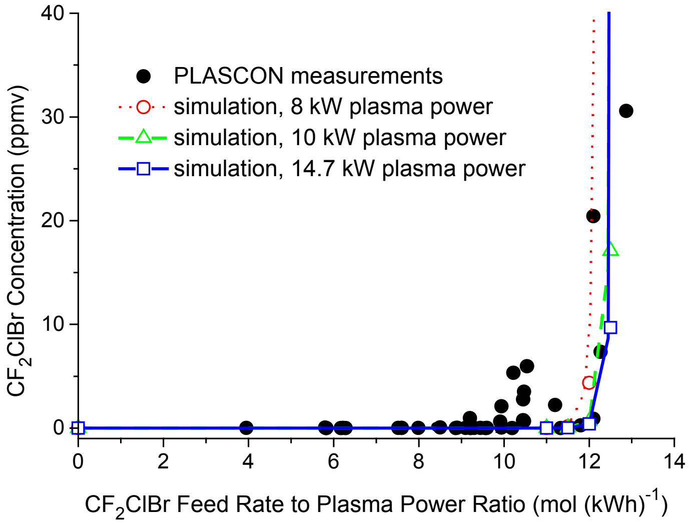

Figure 4. Comparison of measured and calculated concentrations of CF_2ClBr in the exhaust gas as a function of its feed rate, normalised to the plasma power, with steam as the oxidising gas. The solid circles show experimental results for CF_2ClBr destruction in PLASCON. The argon plasma gas input rate was 42 L min^{-1}, the CF_2ClBr feed rate ranged from 22.5 to 67.2 L min^{-1}, and the plasma power ranged from 7.6 to 16.4 kW. The steam to CF_2ClBr molar input ratio was above 1.5, and in most cases above 2.0. The curves and open shapes show the results of simulations of CF_2ClBr destruction for three different plasma powers, with steam to CF_2ClBr molar input ratio of 2.0.

volume), CF_3Cl (around 10% by volume) and CF_2Cl_2 (around 25% by volume) was predicted. Of these, CF_3Br is the most significant, since its ozone-depleting potential is 3.0 times that of CF_2ClBr, 12.3 times that of CF_2Cl_2, and 14.2 times that of CF_3Cl, on a mole basis. CF_3Br was not measured in the experiments, while significant conversion to CF_2Cl_2 was not observed. Results of the simulations are shown in Figure 4. The results closely follow the trend displayed in the experimental observations, showing a sharp increase in ODS residual towards or above the Montreal Protocol limit at feed rate to plasma power ratios of between 12.5 and 13 mol (kWh)$^{-1}$ for the higher plasma powers, and 12 to 12.5 mol (kWh)$^{-1}$ for 8 kW plasma power. These feed to plasma power ratios are associated with mixing temperatures of approximately 2170 K.

6. Fluid Dynamic Modelling

The chemical kinetic calculations described in Section 5 were one-dimensional, based on average temperature–time profiles, and did not take into account diffusion or recirculating flows. A two-dimensional computational model of the plasma torch, injection manifold and flight tube was developed to obtain a more complete description of the phenomena occurring in PLASCON for the destruction of CF_2Cl_2. The model takes into account electromagnetic, fluid dynamic and chemical kinetic processes [5]. The coupled partial differential equations describing mass continuity, conservation of momentum in axial, radial and azimuthal directions, conservation of energy, conservation of mass of the individual chemical species, electric charge continuity and turbulent phenomena (using the two equation K–ε model) were solved numerically in axisymmetric geometry using the control-volume method of Patankar [6]. Solution took place in two stages. In the first, the fluid dynamic and temperature equations were solved, with the composition calculated by invoking local chemical equilibrium, except that a one-step kinetic scheme was used to model the initial dissociation reaction $CF_2Cl_2 + M \rightarrow CF_2Cl + Cl + M$. In the second stage, an extended kinetic scheme, involving 23 species and 42 reactions [7] was solved to calculate the concentration fields of all chemical species considered, using the temperature and flow fields calculated from the first stage.

Figure 5 shows temperatures and concentrations of CF_2Cl_2 and CF_3Cl calculated by the model for the destruction of CF_2Cl_2, with oxygen as the oxidising gas. The temperature of the argon plasma gas within the plasma torch reaches 27 000 K, falling to 13 000 K on axis at the injection manifold. The influx of the cold CFC and oxygen leads to rapid cooling, so that the temperature is between 1000 K and 2000 K in most of the flight tube. The injected CF_2Cl_2 is rapidly dissociated, its mass fraction falling to below 10^{-9} about 350 mm downstream of the injection manifold. However, CF_3Cl is formed with mass fraction greater than 0.01 in a small region close to the injection manifold. The CF_3Cl dissociates less rapidly than the CF_2Cl_2, so that its mass fraction is between 10^{-5} and 10^{-4} at the end of the flight tube. Increasing the CF_2Cl_2 feed rate, or decreasing the plasma power, leads to a decrease in temperature in the flight tube and less rapid decomposition of the CF_3Cl.

The model has been validated by comparison with measurements of exhaust gas composition and laser-scattering measurements of temperature in the reaction tube [5,7].

7. Conclusions

Ozone-depleting substances have been successfully destroyed by a number of thermal plasma processes to the 99.99% level required by the Montreal Protocol. The PLASCON dc argon jet process has already been used to destroy over 1200 t of CFCs and halons in Australia, and a further plant has been constructed in the UK.

Extensive thermochemical, chemical kinetic and fluid dynamic modelling of the destruction of ODS in PLASCON has yielded an extensive understanding of the chemistry and physics of the process. In particular, it has been found that the mixing temperature and the feed rate to plasma power ratio can be used to predict destruction. Chemical kinetic calculations have been used to model the observed phenomenon of interconversion of ODS in the reactor. The use of steam as the oxidising gas has been shown to improve destruction performance, both through increasing the mixing temperature and through minimising interconversion.

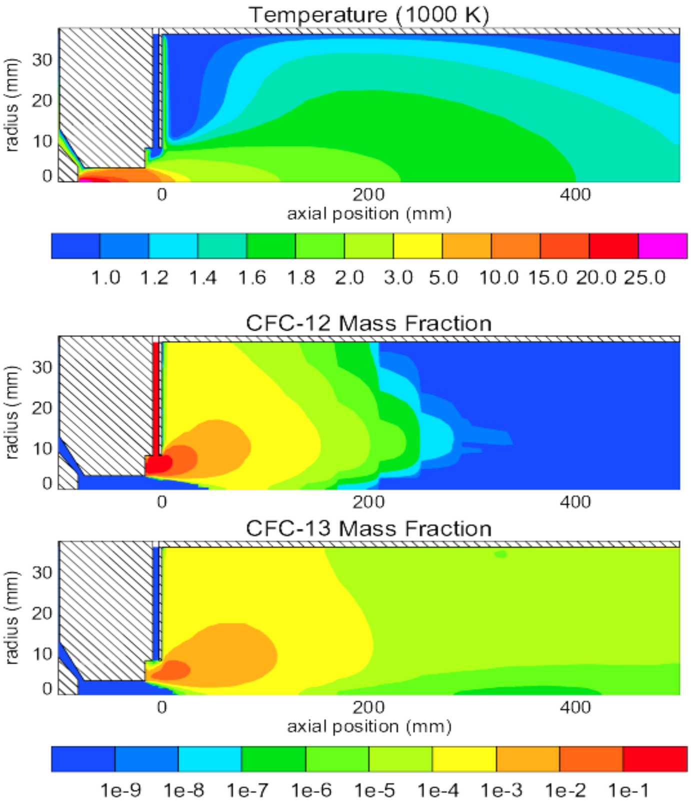

Figure 5. Isotherms and mass fraction contours of CF_2Cl_2 (CFC-12) and CF_3Cl (CFC-13) calculated for typical conditions in a laboratory-scale PLASCON reactor (15.0 kW arc power, 42 L min^{-1} argon plasma gas flow, and injection of a mixture of 40 L min^{-1} each of CF_2Cl_2 and oxygen). The plasma torch extends from axial position z = –100 to –16.4 mm, the injection manifold from z = –16.4 to 0 mm, and the reaction tube from 0 to 500 mm.

Acknowledgments

Most of chemical kinetic calculations described here were performed by Dr T. McAllister of CSIRO. Those contributing to the laboratory tests included Dr A. J. D. Farmer, Ms E. C. Horrigan, Dr L. M. Besley, Dr A. R. Dayal, Dr R. T. Deam, Mr R. J. Western, Mr A. E. Munday, Mr P. Zemancheff and Dr S. Ramakrishnan of CSIRO, and Mr M. Lane of SRL Plasma. The financial support of SRL Plasma, and useful discussions with Mr M. Krynen and Mr R. Hawkes of SRL Plasma, are gratefully acknowledged

References

[1] Report of the UNEP Technology and Assessment Panel, Vol. 3B, Report of the Task Force on Destruction Technologies, United Nations Environment Programme, April 2002. Available at http://www.teap.org.

[2] T. McAllister, The relative efficiencies of oxidants used in plasma processing, *Proc. 13th International Symposium on Plasma Chemistry, Beijing, 1997*, Peking University Press, Beijing, 1997, Vol. 4, p. 1780.

[3] A. B. Murphy and T. McAllister, Modeling of the physics and chemistry of thermal plasma waste destruction, *Phys. Plasmas* **8**, 2565 (2001).

[4] A. B. Murphy, A. J. D. Farmer, E. C. Horrigan, T. McAllister, Plasma destruction of ozone depleting substances, *Plasma Chem. Plasma Process.* **22**, 371 (2002).

[5] A. B. Murphy, T. McAllister, Destruction of ozone-depleting substances in a thermal plasma reactor, *Appl. Phys. Lett.* **73**, 459 (1998).

[6] S. V. Patankar, 'Numerical Heat Transfer and Fluid Flow', Hemisphere, Washington DC (1980).

[7] A. B. Murphy, Plasma destruction of gaseous and liquid wastes, *Ann. N. Y. Acad. Sci.* **891**, 106 (1999).

Why Thomson Scattering Measurements of Thermal Plasma Electron Temperatures are Unreliable

A. B. Murphy

CSIRO Telecommunications and Industrial Physics, P.O. Box 218, Lindfield NSW 2070, Australia

Abstract

Electron heating leads to major difficulties in Thomson scattering measurements of thermal plasmas. The standard procedure of linearly extrapolating electron temperature versus laser pulse energy data to zero pulse energy is flawed, due to the electron temperature dependence of absorption, and collisional and radiative cooling. Further, the derivation of a temperature from the spectrum of radiation scattered by electrons undergoing heating is problematical, as are measurements using an expanded laser beam to minimise heating.

1. Introduction

In high-temperature low-density plasmas, such as those used in magnetically-confined fusion experiments, Thomson scattering is regarded as the most reliable technique for the measurement of electron temperature. However, strong doubts have emerged about the reliability of Thomson scattering as a diagnostic technique in thermal plasmas. Thomson scattering measurements of free-burning arcs and plasma jets [1,2,3,4] have indicated that the electron temperature is several thousand kelvin higher than the ion excitation temperatures. These results are difficult to reconcile with theoretical considerations. The high collision frequency indicates that the electrons and ions should be at a similar temperature. Furthermore, measurements performed using spectroscopic and laser scattering techniques [5] indicate that the bulk of the plasma is in local thermodynamic equilibrium (LTE), and therefore the electron, ion and excitation temperatures should be equal.

Significant efforts have been made to determine the source of the anomalously high electron temperatures. Gregori *et al.* [6] noted a dependence of the measured electron temperature on the scattering angle for a laser wavelength of 532 nm. They ascribed this to the large density gradients within the scattering volume, which affect the description of the electron density fluctuations in the theoretical treatment of the scattering process. However, Snyder *et al.* [7] demonstrated that there was no scattering angle dependence for a laser wavelength of 355 nm. They instead hypothesised that the scattering angle dependence was due to plasma resistivity. Terasaki *et al.* [8] supported this result by showing that there is no scattering angle dependence in a helium arc. Gregori *et al.* [9] recently questioned the standard method of deriving the electron temperature from the frequency spectrum of the scattered signal on the basis of the low Debye number. They showed that a memory function method can yield electron temperatures close to ion and excitation temperatures.

In this paper, I investigate difficulties with the application of Thomson scattering to thermal plasmas that are related to the heating of the electrons by the laser beam. To account for this heating, workers have measured the electron temperature as a function of laser pulse energy, and extrapolated the line of best fit to zero pulse energy to obtain the initial electron temperature. This procedure is invalid, since the laser light absorption depends on electron temperature, and the electrons lose energy by collisions and radiation during the laser pulse, leading to a nonlinear dependence of the electron temperature increase on pulse energy [10]. The laser heating of the electrons also means that, over the duration of the laser pulse, scattering occurs from electrons at a range of temperatures. This causes difficulties in the derivation of an electron temperature from the resulting spectrum of scattered radiation. The accuracy of Thomson scattering measurements that use an expanded laser beam to minimise the electron heating is also examined. The defocusing of the laser beam, combined with the large temperature gradients that occur in thermal plasmas, again leads to scattering from electrons at a range of temperatures, giving rise to overestimates of the electron temperature.

2. Laser Heating of Electrons

The measurement of electron temperature from the spectral profile of the Thomson-scattered signal requires that there is sufficient scattered radiation relative to the background radiation from the plasma, necessitating the use of a high-power pulsed laser. Typically, a frequency-doubled Nd-YAG laser, with wavelength 532 nm, is used. The interaction of the laser beam with the plasma heats the electrons by linear inverse bremsstrahlung [11]. To take this effect into account, workers have measured electron temperature as a function of laser pulse energy. A straight line has then been fitted to the results, and extrapolated to zero pulse energy to obtain the electron temperature free of influence from laser heating.

The use of a straight-line fit has been justified [1,2,4,6] by reference to Hughes [11]. Hughes, however, gives the following expression for the coefficient of absorption of laser light by a plasma:

$$\alpha = \frac{n_e n_i Z^2 e^6 \left[1 - \exp\left(-\hbar\omega / k_B T_e\right)\right]}{6\pi\varepsilon_0^3 c\hbar\omega^3 m_e^2} \left(\frac{m_e}{2\pi k_B T_e}\right)^{1/2} \frac{\pi}{3}\bar{g} \qquad (1)$$

In Equation (1), n_e and n_i are respectively the electron and ion number densities, T_e is the electron temperature, Z is the average ionisation level of the plasma, ω is the laser frequency, and the constants e, m_e, $\hbar$, k_B and c are respectively the electron charge and mass, Planck's constant, Boltzmann's constant, and the speed of light in vacuum. It is clear from Equation (1) that the absorption coefficient depends on the electron temperature, the electron density, and the ion density, both directly and through the average Gaunt factor $\bar{g}$. Since the electrons are heated during a laser pulse, the absorption coefficient will therefore vary with time during the pulse, and the total absorbed energy will have a nonlinear dependence on the laser pulse energy.

3. Fluid Dynamic Modelling of Laser Heating

The heating of the electrons through absorption of laser radiation is balanced by cooling of the electrons through collisional and radiative processes. The former can be separated into three particular types of interaction: collisions with other electrons (or electron thermal conduction), elastic collisions with heavy particles, and inelastic collisions with heavy particles (or electron-impact ionisation). The heating and cooling of electrons during a laser pulse can be described by a one-dimensional equation in polar geometry:

$$\frac{\partial}{\partial t}\left(\frac{5}{2} k_B n_e T_e\right) = \frac{1}{r}\frac{\partial}{\partial r}\left(r k_e \frac{\partial T_e}{\partial r}\right) + \frac{\alpha E_p}{A\tau_p} - W_{eh} - \sum_{i=1}^{2} R_i E_i - U \qquad (2)$$

where r is the radial coordinate; the centre of the laser beam cross-section corresponds to $r = 0$. A is the cross-sectional area of the laser beam and t is time; E_p and τ_p are respectively the laser pulse energy and duration; k_e and U are respectively the electron thermal conductivity and the radiative emission coefficient, W_{eh} is the rate of transfer of energy from electrons to heavy particles through inelastic collisions, R_i is the rate of ith ionisation of argon, and E_i is the ith ionisation energy of argon. The electron density n_e was calculated as a function of time using the ionisation rates R_i, for which the data of Almeida *et al.* [12] were used.

Equation (2) was solved numerically, using the finite-difference method of Patankar [13]. A Gaussian laser beam profile and square pulse shape were used. It was assumed that the ion and electron temperatures were initially equal. Consistent with Thomson scattering measurements [1], it was assumed that the ion temperature remained constant. The laser beam diameter (FWHM) and the laser pulse duration were chosen to be 200 μm and 7 ns, respectively, in accordance with the experimental parameters [1,2]. The calculation region extended over a radius of 350 μm, with a 1 μm grid. The time step used was 0.1 ns. Doubling the time and grid resolution and the extent of the calculation region resulted in a less than 0.1% change in the results.

Figure 1 shows typical results for the evolution of the electron temperature during the laser pulse. The rate of temperature increase is greatest in the early part of the pulse, decreasing rapidly with time. Figure 1 also shows that the rate of absorption of laser energy decreases rapidly in the first nanoseconds of the pulse. This is predominantly a result of the electron temperature increase. The absorption increases slightly towards the end of the pulse, because of the influence of the electron density increase, which at this stage more than compensates for the relatively slow increase in electron temperature. The rate of energy loss through each of the four cooling processes increases during the pulse. Energy transfer to heavy particles through electron impact ionisation is the dominant electron cooling process; electron thermal conduction is also significant.

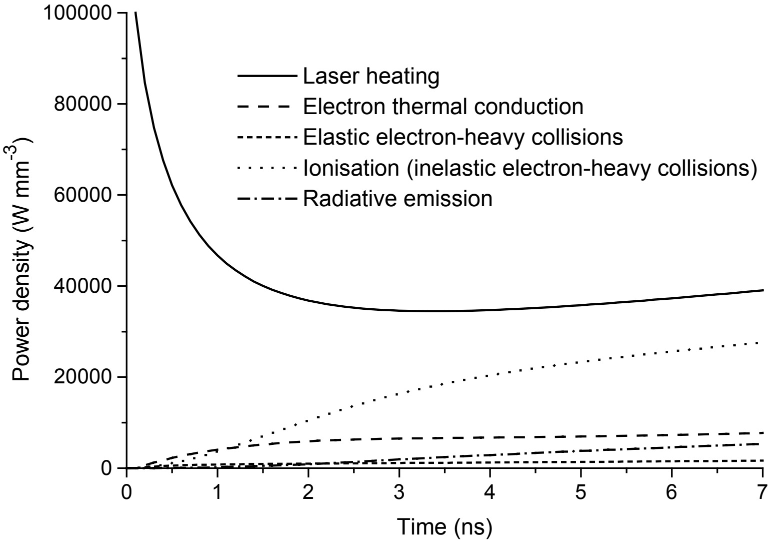

Figure 1. Evolution of the laser heating and the four cooling processes at the centre point of the laser beam. The initial temperature is 17 000 K, the pulse energy is 100 mJ, and the beam radius is 100 μm.

The electron temperatures calculated from the fluid dynamic model were compared with the measured electron temperatures as follows. For each set of measured electron temperature and pulse energy data, a least-squares fitting routine was used to find the values of the initial temperature T_{e0}, and a constant C by which the absorption coefficient α was multiplied, that give electron temperatures closest to the experimental values. Deviations from $C = 1$ were required to take into account experimental uncertainties in the laser beam's spatial profile and diameter, in the time dependence of the laser pulse energy, and in the spatial and time averaging of the electron temperature. An electron temperature was obtained from the fluid dynamic model for a given pulse energy using a simple time average over the duration of the laser pulse, and a spatial average over the laser beam diameter, weighted according to the Gaussian laser beam intensity profile. The question of determining an average electron temperature is discussed further in Section 4.

Figure 2 compares least-squares linear fits to the measurements of Snyder *et al.* [1] and Bentley [2] with least-square fits to solutions of Equation (2). The least-squares best fit to the measurements of Snyder *et al.* shown in Figure 2(a) is obtained for T_{e0} = 15 200 K and C = 1.05. This may be compared with the ion temperature measured by Thomson scattering of 14 200 ± 700 K [14]. As a measure of the sensitivity of the least-squares fit, fits for which the standard deviation is 25% greater than the minimum were calculated; the deviation in T_{e0} is around 1000 K. The least-squares best fit to the measurements of Bentley shown in

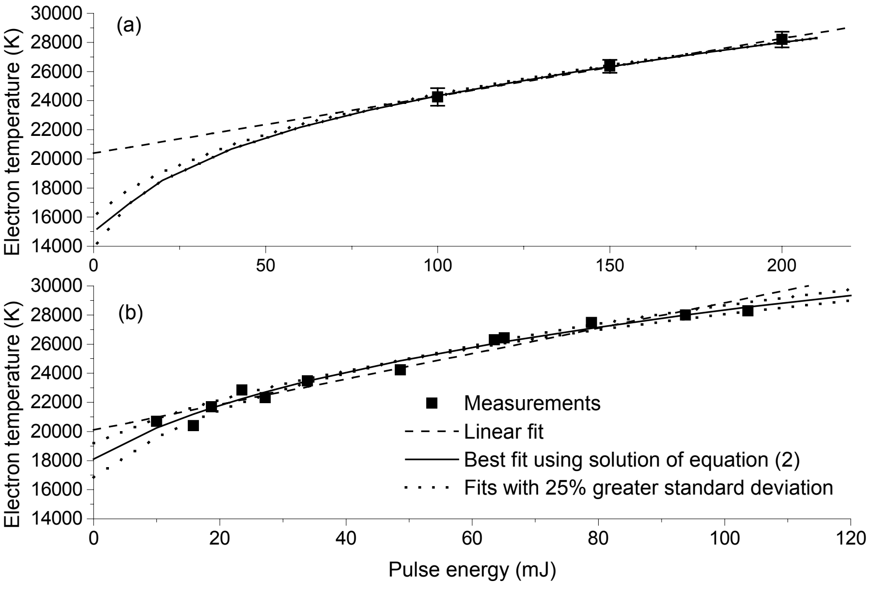

Figure 2. Comparison between the best fit obtained using a solution to Equation (2) and the line of best fit, to the measured data of (a) Snyder *et al.* [1] and (b) Bentley [2]. Also shown are fits obtained using solutions to Equation (2) for which the standard deviation from the experimental points is 25% greater than for the best fit.

Figure 2(b) is obtained with T_{e0} = 18 100 K and C = 1.455. The deviation in T_{e0} corresponding to a 25% increase in standard deviation is in this case 1300 K. The excitation temperature, and the ion temperature measured by laser scattering, were around 16 600 K for the same conditions [5]. The values of T_{e0} calculated using best fits to the solution of Equation (2) are thus between 2000 K and 6000 K lower than those obtained using a linear fit, and are within 1500 K of the ion temperature and excitation temperature.

The use of the one-dimensional fluid dynamic model significantly improves the accuracy of the electron temperatures derived from the measurements. There are nevertheless significant uncertainties that remain. These include uncertainties in the transport and rate data used in the calculations, the fact that results of calculations using a wide range of values of T_{e0} fit the measured data almost equally well, and the possibility that different values of T_{e0} may be obtained if the assumption that the initial electron temperature was equal to the ion temperature was not used.

4. Derivation of Temperature from the Spectrum of Thomson-scattered Radiation

The heating of electrons by the laser pulse causes a further complication in Thomson scattering measurements. In the measurements, the electron temperature is derived from the spectrum of the scattered light collected over the duration of the laser pulse, and across the full cross-section of the laser beam. The temperatures present cover a wide range; for the conditions of Figure 1, for example, they range from 17 000 K to 33 800 K. The spectrum of the Thomson-scattered radiation is a complicated function of electron temperature and density. Sample spectra are shown in Figure 3. The measured scattered signal will be an average of the frequency spectra over the range of temperatures present. The derivation of a single electron temperature from the average spectrum is clearly a procedure of dubious validity, and this alone casts significant doubt on the reported electron temperature measurements.

For temperatures above about 17 000 K, the plasma is essentially fully-ionised, and as shown in Figure 3, the main effect of a temperature increase is a broadening of the Thomson-scattering peak, so the temperature derived from the average spectrum is likely to fall within the range of the temperatures that are represented. If electron temperatures lower than around 17 000 K are present in the laser beam cross-section, the position of the peak in the Thomson spectrum can shift significantly as electron temperature changes, with the result that the average spectrum has a broader peak than the spectrum of any of the temperatures that are represented; this can lead to a significant overestimate of the temperature. This is demonstrated in Section 5.

5. Measurements Performed with an Expanded Laser Beam

In some Thomson scattering measurements of plasma jets [6,9], an expanded laser beam diameter of 2 mm was used, with pulse energies from 50 mJ to 400 mJ and a pulse length of 10 ns. The aim was to avoid laser heating of the electrons. The electron temperatures and densities derived from the scattered signals using standard Thomson scattering theory were 18 000 K and 1.17 × 10^{23} m^{-3} [6], and 20 000 K and 0.68 × 10^{23} m^{-3} [9] respectively. These values are similar to those obtained by Snyder *et al.* [4] in their Thomson scattering

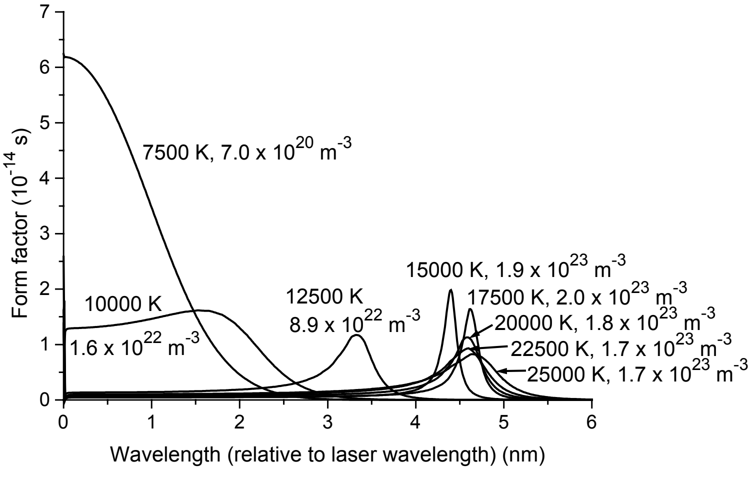

Figure 3. Spectral distribution of the Thomson scattering electron feature for different temperatures in an LTE plasma. The electron density is shown in each case. The wavelength of the peak in the spectrum increases as the electron density increases. At temperatures above about 17 500 K, the electron density is roughly constant, and the main effect of increasing temperature is a broadening of the peak.

measurements of electron temperatures in plasma jets.

A problem with the use of an expanded laser beam is that, because of the steep gradients of temperature and density in plasmas, a range of temperatures and densities are present within the beam cross-section. To examine the influence of this gradient, I have simulated the heating of the electrons for the conditions used in the expanded laser beam measurements. As an initial electron and ion temperature profile, I used an approximation of the ion and spectroscopic temperatures measured by Snyder *et al.* [4] for similar plasma jet parameters; a central temperature of 14 000 K, decreasing linearly to 12 500 K at a radius of 1 mm, then to 10 000 K at 2 mm and 5000 K at 3 mm. (Note that, owing to the one-dimensional geometry, it is assumed that this profile is axisymmetric. The results are nonetheless expected to be reasonably representative of those for a two-dimensional simulation.) The central electron temperature was calculated to reach 17 680 K for a laser pulse energy of 400 mJ, and 16 130 K for a pulse energy of 200 mJ.

As noted in Section 4, the electron temperature is derived in the experiments by averaging the Thomson-scattered spectrum over all temperatures present, and by calculating a temperature from this average spectrum. This procedure was simulated by calculating such an average Thomson-scattered spectrum, and using a least-squares fitting routine to derive an electron temperature and density from the average spectrum. The average spectrum, and the best-fit Thomson spectrum, are shown in Figure 4. The electron temperature derived by this method was 18 230 K for a pulse energy of 400 mJ, and 17 620 K for a pulse energy of 200 mJ. The electron density was 1.04×10^{23} m^{-3} in both cases. These calculated electron temperature values are significantly higher than the electron temperatures present anywhere in the plasma. This is the result of the artificial broadening of the average spectrum due to the presence of a range of temperatures and electron densities. This effect is important for plasmas at relatively low temperatures (below about 15 000 K for a plasma in LTE) when the electron density is below its maximum of around 2×10^{23} m^{-3}, since as shown in Figure 3, the spectral position of the Thomson peak depends strongly on the electron density.

The calculation demonstrates that, at least for the relatively low temperatures present in a plasma jet, the use of an expanded laser beam leads to significant distortion of the measured Thomson line shape, which leads to the derivation of anomalously high electron temperatures from this lineshape.

6. Conclusions

A number of flaws in previous measurements of electron temperature by Thomson scattering in thermal plasmas have been demonstrated. The first, arising from the heating of the electrons by the laser beam, is that the spectral distribution of the scattered radiation is a spatial average over the cross-sectional area of the laser beam and a time average over the duration of the laser pulse. The "electron temperature" derived from this average scattered signal is a complicated function of the electron temperatures present within the cross-sectional area of the laser beam during the laser pulse. This leads to significant uncertainty in electron temperatures measured in fully-ionised plasmas. For partially-ionised plasmas, such as those present in

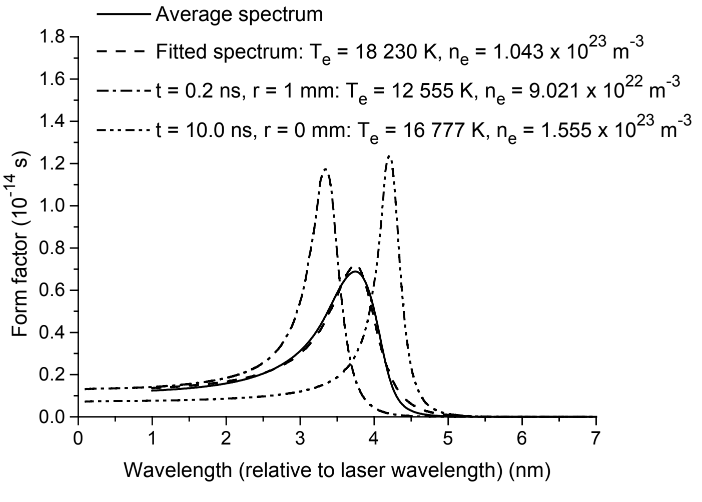

Figure 4. Average Thomson spectrum calculated for expanded laser beam measurement of a plasma jet (pulse energy = 400 mJ, pulse length = 10 ns, beam radius = 1 mm, initial central electron temperature = 14 000 K), and the least-squares best-fit spectrum. Also shown are spectra for the electron temperatures and densities present at two times and positions during the laser pulse.

plasma jets, the measured ‘electron temperature’ can be significantly greater than the temperature anywhere in the scattering region.

A second problem is that the method, used in the previous measurements, of deriving an unperturbed electron temperature by linearly extrapolating measurements of electron temperature as a function of laser pulse energy, is physically invalid. The dependence of the absorption of laser energy, and the cooling of the heated electrons by thermal conduction, by elastic and inelastic collisions with heavy particles, and by radiation, must all be considered. We have used a one-dimensional fluid dynamic model of the electron heating and cooling to show that these effects are substantial, and that electron temperatures are 2000 to 6000 K lower than those given by the linear extrapolation. Large uncertainties remain even when the heating and cooling effects are taken into account.

Finally, it has been demonstrated that the use of an expanded or defocused laser beam to decrease the heating of electrons can also lead to inaccurate values of electron temperatures. The steep temperature and density gradients in plasmas, and the large laser beam cross-section, mean that light is scattered from regions at a range of temperatures. The “electron temperature” derived from the average scattered signal has been shown, at least for the partially-ionised plasmas present in plasma jets, to be substantially greater than the temperature anywhere within the laser beam cross-section.

The heating of electrons by the laser in Thomson scattering measurements of thermal plasmas makes the measurement of electron temperature highly problematic. The uncertainties that are introduced lead to the conclusion that Thomson scattering is not a reliable electron temperature diagnostic in thermal plasmas.

References

[1] S. C. Snyder, G. D. Lassahn, L. D. Reynolds, Direct evidence of departure from local thermodynamic equilibrium in a free-burning arc discharge, *Phys. Rev. E* **48**, 4124 (1993).

[2] R. E. Bentley, A departure from local thermodynamic equilibrium within a freely burning arc and asymmetrical Thomson electron features, *J. Phys. D: Appl. Phys.* **30**, 2880 (1997).

[3] M. Tanaka, M. Ushio, Plasma state in free-burning argon arc and its effect on anode heat transfer, *J. Phys. D: Appl. Phys.* **32**, 1153 (1999).

[4] S. C. Snyder, L. D. Reynolds, J. R. Fincke, G. D. Lassahn, J. D. Grandy, T. E. Repetti, Electron-temperature and electron-density profiles in an atmospheric-pressure argon plasma jet, *Phys. Rev. E* **50**, 519 (1994).

[5] A. B. Murphy, A. J. D. Farmer, J. Haidar, Laser-scattering measurement of temperature profiles of a free-burning arc, *Appl. Phys. Lett.* **60**, 1304 (1992).

[6] G. Gregori, J. Schein, P. Schwendinger, U. Kortshagen, J. Heberlein, E. Pfender, Thomson scattering measurements in atmospheric plasma jets, *Phys. Rev. E* **59**, 2286 (1999).

[7] S. C. Snyder, D. M. Crawford, J. R. Fincke, Dependence on the scattering angle of the electron temperature and electron density in Thomson-scattering measurements of an atmospheric-pressure plasma jet, *Phys. Rev. E* **61**, 1920 (2000).

[8] H. Terasaki, M. Tanaka, M. Ushio, Effects of metal vapor on electron temperature in helium gas tungsten arcs, *Metall. Mater. Trans.* **33A**, 1183 (2002).

[9] G. Gregori, U. Kortshagen, J. Heberlein and E. Pfender, Analysis of Thomson scattered light from an arc plasma jet, *Phys. Rev. E* **65**, 046411-1 (2002).

[10] A. B. Murphy, Electron heating in the measurement of electron temperature by Thomson scattering: Are thermal plasmas thermal? *Phys. Rev. Lett.* **89**, 025002-1 (2002).

[11] T. P. Hughes, ‘Plasmas and Laser Light’, Adam Hilger, Bristol (1975), ch. 2.

[12] R. M. S. Almeida, M. S. Benilov, G. V. Naidis, Simulation of the layer of non-equilibrium ionization in a high-pressure argon plasma with multiply-charged ions, *J. Phys. D: Appl. Phys.* **33**, 960 (2000).

[13] S. V. Patankar, ‘Numerical Heat Transfer and Fluid Flow’, Hemisphere, Washington DC (1980).

[14] S. C. Snyder, L. D. Reynolds, G. D. Lassahn, J. R. Fincke, C. B. Shaw Jr, R. J. Kearney, Determination of gas-temperature and velocity profiles in an argon thermal-plasma jet by laser-light scattering, *Phys. Rev. E* **47**, 1996 (1993).

Modelling of Titanium Particle Formation from a Titanium Tetrachloride Plasma

A. B. Murphy

CSIRO Telecommunications and Industrial Physics, P.O. Box 218, Lindfield NSW 2070, Australia

Abstract

The formation of titanium particles from plasmas in mixtures of titanium tetrachloride, argon and hydrogen is examined using chemical kinetics and a moment model of nucleation. The results indicate that yields approaching 100% are possible for sufficiently large residence times at high temperature, and sufficiently rapid quench rates. The residence time and quench rate conditions are less stringent for high argon to $TiCl_4$ ratios. Adding hydrogen leads to less stringent residence time, but more stringent quench rate, conditions.

1. Introduction

The method generally used for the production of metallic titanium from titanium ores such as rutile is a complicated and expensive process. The first step involves chlorination of the ore to form titanium tetrachloride, which is a liquid and can be purified by fractional distillation. The next stage, known as the Kroll process, requires heating of the titanium tetrachloride with magnesium ingots to form a mixture of titanium sponge, magnesium chloride and unreacted magnesium. The mixture is dug out of the reactor, crushed, and leached to separate titanium granules, which are compacted and welded together to form electrodes. The electrodes are then melted in a vacuum arc to form titanium briquettes.

The batch nature and high energy costs of this process have led to many attempts to develop processes to produce titanium metal directly from titanium tetrachloride. Many of these have involved thermal plasma technology [1,2]. Some successes have been reported, such as the rapid quenching of a plasma jet in argon, hydrogen and titanium tetrachloride to form titanium powder [3].

In this paper, simulations are presented of the production of titanium particles in an atmospheric-pressure thermal plasma containing argon, hydrogen and titanium tetrachloride. The simulations take into account chemical reactions and the nucleation of titanium metal. A chemical kinetic scheme for the dissociation of titanium tetrachloride, largely taken from the literature, is presented. Nucleation and condensation are modelled using the moment approach of Friedlander [4], with the nucleation rate calculated using the self-consistent expression derived by Girshick [5,6].

Results indicating the effects on the titanium yield of parameters such as the plasma temperature and residence time, the quench rate and initial titanium tetrachloride concentration are presented. The influence of the addition of hydrogen to the plasma is also investigated.

2. Equilibrium Calculations

Calculations of the equilibrium composition of mixtures of titanium tetrachloride and argon, and titanium tetrachloride and hydrogen, indicate that no solid titanium is formed, irrespective of the relative titanium tetrachloride concentration [7]. However, at temperatures above about 2000 K, atomic titanium is present in the gas phase.

Figure 1 shows the fraction of the input titanium atoms present as atomic titanium for different mixtures of titanium tetrachloride with argon or hydrogen. Calculations were performed using thermochemical data from the JANAF tables [8], using the method of Gibbs free energy minimisation. Large excesses of argon or hydrogen favour the formation of atomic titanium, with hydrogen more effective than argon. To obtain large percentages of atomic titanium requires temperatures from 3000 K to 5000 K, depending on the composition of the mixture. Titanium is also present as gaseous TiCl, $TiCl_2$, $TiCl_3$ and $TiCl_4$, and as solid $TiCl_3$ [7].

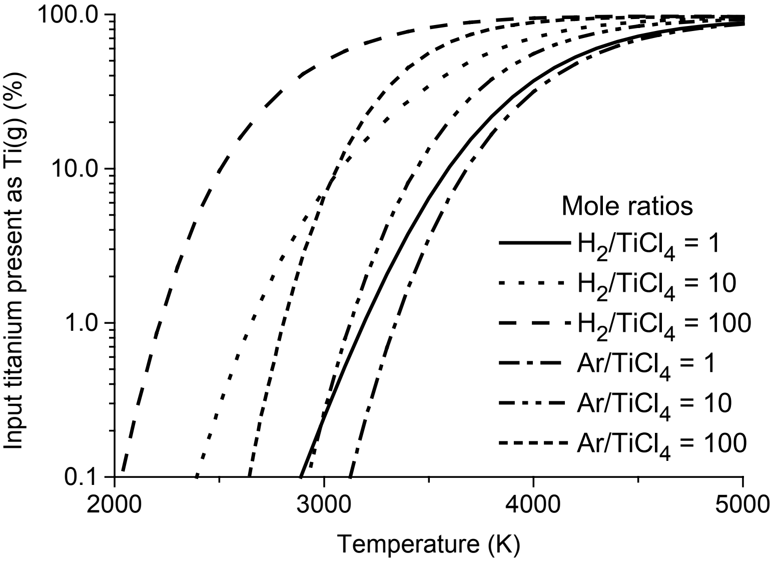

Figure 1. Temperature dependence of the percentage of titanium present as gaseous atomic titanium. Results are presented for different mixtures of titanium tetrachloride and hydrogen, and titanium tetrachloride and argon, calculated assuming chemical equilibrium.

3. Chemical Kinetic Calculations

Since no solid titanium is formed from mixtures of titanium tetrachloride and argon or hydrogen under chemical equilibrium conditions, it can be concluded that production of solid titanium from such mixtures requires non-equilibrium conditions. These can be provided, for example, by rapidly quenching the hot gas mixture. The formation of titanium powder under such conditions has been demonstrated experimentally [3]. Modelling of such non-equilibrium processes requires the consideration of chemical kinetic effects.

Rate coefficients for most of the reactions of interest are given by Teyssandier and Allendorf [9]. The rate coefficients for the reaction $\mathrm{TiCl} + \mathrm{M} \rightarrow \mathrm{Ti} + \mathrm{Cl} + \mathrm{M}$ were obtained from those given for the analogous reaction for the decomposition of SnCl [10], with the binding energy calculated using thermodynamic considerations. Rate coefficient data are given in Table I. Reverse reaction rates were calculated using equilibrium coefficients.

Table I. Rate coefficients expressed in the form $AT^b \exp(-E_a/RT)$. The activation energies E_a are in kJ mol^{-1}. The units of A are s^{-1}, cm^{3}mol^{-1}s^{-1} and cm^{6}mol^{-2}s^{-1} for unimolecular, bimolecular and trimolecular reactions respectively.

Reaction	A	b	E_a
$\mathrm{TiCl_4} \rightarrow \mathrm{TiCl_3} + \mathrm{Cl}$	7.76×10^{43}	-8.56	424.9
$\mathrm{TiCl_3} \rightarrow \mathrm{TiCl_2} + \mathrm{Cl}$	2.12×10^{34}	-5.88	447.9
$\mathrm{TiCl_2} \rightarrow \mathrm{TiCl} + \mathrm{Cl}$	5.41×10^{-4}	4.08	431.6
$\mathrm{TiCl} + \mathrm{M} \rightarrow \mathrm{Ti} + \mathrm{Cl} + \mathrm{M}$	1.90×10^{14}	0	439.5
$\mathrm{TiCl_4} + \mathrm{H} \rightarrow \mathrm{TiCl_3} + \mathrm{HCl}$	5.11×10^{6}	2.5	12.6
$\mathrm{TiCl_3} + \mathrm{H} \rightarrow \mathrm{TiCl_2} + \mathrm{HCl}$	1.11×10^{6}	2.5	33.5
$\mathrm{TiCl_2} + \mathrm{H} \rightarrow \mathrm{TiCl} + \mathrm{HCl}$	3.05×10^{6}	2.5	145.2
$\mathrm{TiCl} + \mathrm{H} \rightarrow \mathrm{Ti} + \mathrm{HCl}$	4.09×10^{5}	2.5	24.7
$\mathrm{H} + \mathrm{Cl} + \mathrm{M} \rightarrow \mathrm{HCl} + \mathrm{M}$	7.20×10^{21}	-2.0	0.0
$\mathrm{Cl} + \mathrm{Cl} + \mathrm{M} \rightarrow \mathrm{Cl_2} + \mathrm{M}$	2.00×10^{14}	0	-7.5
$\mathrm{H} + \mathrm{HCl} \rightarrow \mathrm{Cl} + \mathrm{H_2}$	1.69×10^{13}	0	17.2
$\mathrm{Cl_2} + \mathrm{H} \rightarrow \mathrm{Cl} + \mathrm{HCl}$	8.60×10^{13}	0	5.0
$\mathrm{H} + \mathrm{H} + \mathrm{H_2} \rightarrow \mathrm{H_2} + \mathrm{H_2}$	9.70×10^{16}	-0.6	0.0
$\mathrm{H_2} + \mathrm{M} \rightarrow \mathrm{H} + \mathrm{H} + \mathrm{M}$	2.20×10^{14}	0	402.1

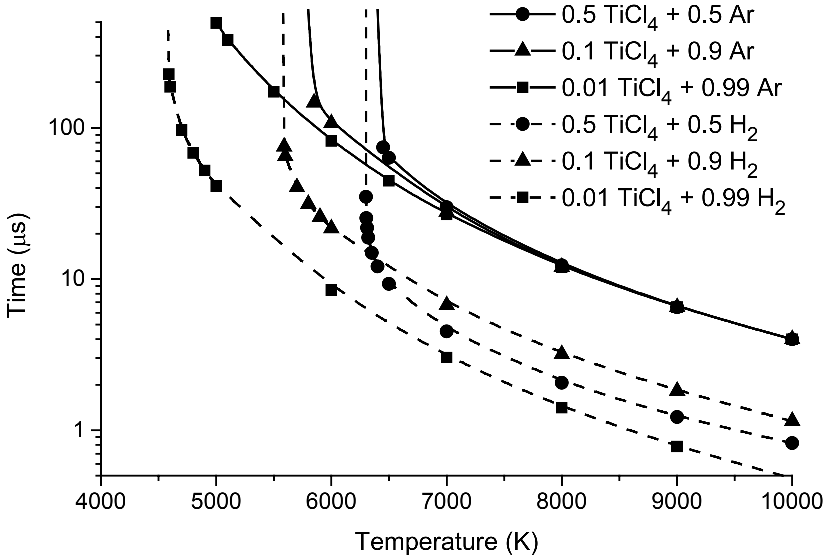

Figure 2. Dependence on temperature of the time required for titanium tetrachloride to be 99% dissociated to form atomic titanium, for different mixtures of titanium tetrachloride and argon or hydrogen, at atmospheric pressure.

To maximise the yield of solid titanium, it is desirable that the titanium tetrachloride is fully dissociated in the plasma. Figure 2 shows the time required for 99% dissociation of titanium tetrachloride to atomic titanium to occur. For mixtures of titanium tetrachloride and argon, temperatures greater than 8000 K are required for dissociation to occur within 10 μs. For mixtures of titanium tetrachloride and hydrogen, temperatures between 6000 K and 7000 K are sufficient. In general, the greater the dilution of titanium tetrachloride, the lower the temperature required for thorough dissociation.

4. Nucleation Calculations

An expression for the nucleation rate J (the number of particles formed per unit volume per unit time) from an ideal supersaturated vapour has been derived by Girshick and Chiu [11]:

$$J = v_1 \left(\frac{2\sigma}{\pi m_1} \right)^{1/2} n_s^2 S \exp\left[\Theta - \frac{4\Theta^3}{27(\ln S)^2} \right] \tag{1}$$

where v_1 and m_1 are respectively the volume and mass of the monomer (in this case a titanium atom), σ is the surface tension (under the capillarity approximation that droplet properties are similar to those of the material in the bulk phase), n_s is the equilibrium monomer number density for the saturated vapour (calculated using the Clausius–Clapeyron equation), $S = n_1/n_s$ is the supersaturation of the vapour, n_1 being the monomer number density, and $\Theta = \sigma s_1/k_B T$ is the dimensionless surface energy, s_1 being the surface area of the monomer, k_B Boltzmann's constant and T the temperature. The approach used by Girshick and Chiu is based on classical theories of nucleation, in that it uses the assumption that the physical properties of the clusters are the same as those of the bulk material. However, a correction factor of $\exp(\Theta)/S$ arises from an improved treatment of evaporation.

The following material data were used for titanium: surface tension $\sigma = 1.51\ \mathrm{N\,m^{-1}}$ [12], heat of vaporisation = 451 kJ mol^{-1}, boiling temperature = 3533 K, mass density = 4500 kg m^{-3}. The critical particle diameter, above which particles are stable, corresponds to the equilibrium particle diameter, given by [4]

$$d^* = \frac{4\sigma v_1}{k_B T \ln S} \tag{2}$$

The moment model derived by Friedlander [4] is used to calculate the production of titanium particles from titanium atoms in the plasma. The conservation equation for the number density of titanium atoms n_1 takes into account the balance between formation by the chemical reactions given in Table I, nucleation to form particles of the critical size, and condensation onto previously-nucleated particles

$$\frac{\partial n_1}{\partial t} = R - Jk^* - \left(S-1\right)\frac{b_1 A}{2v_1} \tag{3}$$

Here *R* is the rate of production of titanium atoms by chemical reaction, *k** is the number of atoms in a critical particle, and $b_1 = 2n_s v_1\sqrt{kT/2\pi m_1}$, where m_1 is the mass of a titanium atom. The following three equations describe the particle properties:

$$\frac{dA}{dt} = Jk^{*2/3} s_1 + 2\pi b_1 \left(S-1\right) m_1 \tag{4}$$

$$\frac{dM}{dt} = Jd^* + \left(S-1\right) b_1 N \tag{5}$$

$$\frac{dN}{dt} = J \tag{6}$$

Here $A = \int_{d^*}^{\infty} \pi d_p^2 n\left(d_p\right) d\left(d_p\right)$ is the total surface area of particles per unit volume, $M = \int_{d^*}^{\infty} d_p n\left(d_p\right) d\left(d_p\right)$ is the first moment of the particle diameter, and $N = \int_{d^*}^{\infty} n\left(d_p\right) d\left(d_p\right)$ is the particle number density; d_p is the particle diameter.

Equations (3) to (6), together with the production rate equations for the other gaseous species, form an initial value problem. This is solved using the ordinary differential equation solver DVODE [13] for a given initial composition, with $n_1\left(0\right) = A\left(0\right) = M\left(0\right) = N\left(0\right) = 0$. The pressure is assumed to be constant at 1 atm, and the temperature changes as a function of time.

Figure 3 shows typical results for an atmospheric-pressure plasma with initial mole fractions $x\left(\mathrm{TiCl_4}\right) = 0.01$ and $x\left(\mathrm{Ar}\right) = 0.99$. The temperature is maintained at 6500 K for 0.1 ms to ensure complete dissociation of the $TiCl_4$, followed by a rapid quench, with $dT/dt = -10^7$ K s^{-1} . Nucleation commences when temperature falls below 2450 K, at which point the supersaturation level increases above about 10. Initially, titanium particles are formed by nucleation; at later times, condensation onto existing particles dominates, and the average particle diameter increases above the critical particle diameter. Approximately 95% of the input titanium is converted to solid titanium particles.

Figure 4 shows the titanium yield, defined as the percentage of input titanium converted to solid titanium particles, for different quench rates and different initial compositions. The mean particle diameter, given by $\left\langle d_p \right\rangle = M/N$, is also shown. In each case, a high initial temperature was maintained for sufficiently long to ensure complete dissociation of the $TiCl_4$ to Ti.

Increasing the quench rate increases the titanium yield, since a rapid decrease in temperature increases the supersaturation, favouring nucleation and condensation processes over the gas phase reactions that lead to the reaction of Ti atoms with Cl atoms to form $TiCl_x$. The titanium yield is increased by greater dilution of the $TiCl_4$ by argon and hydrogen. The presence of hydrogen can increase the yield for high quench rates, but has the effect of decreasing the yield for lower quench rates. This is a result of the competing influences of

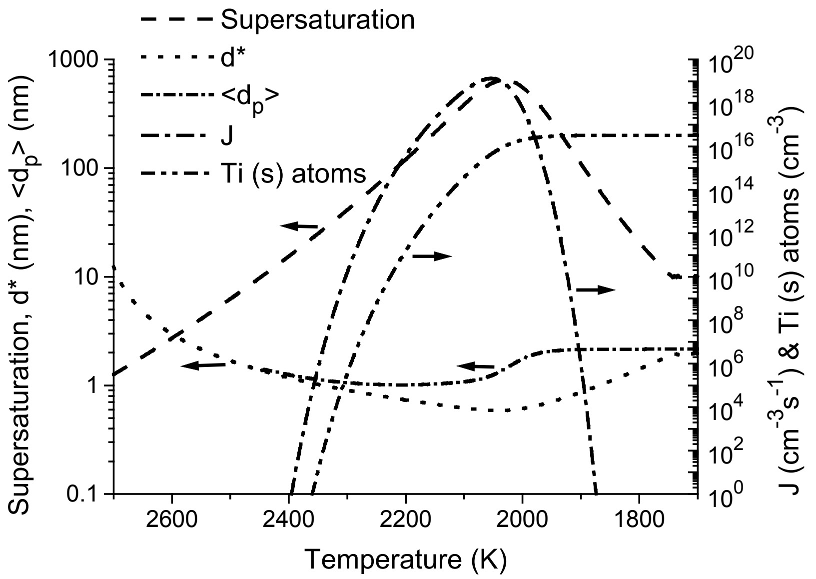

Figure 3. Parameters during the quenching of a plasma with initial composition of 0.99 Ar and 0.01 $TiCl_4$ by mole fraction. The quench rate is –10 K μs^{-1}. The parameters shown are the supersaturation *S*, the critical particle diameter *d**, the mean particle diameter $\langle d_p \rangle$, the nucleation rate of titanium particles *J*, and the number of titanium atoms in solid form.

two effects that occur in the presence of hydrogen. The first, which favours higher titanium yields, is that the reactions $\mathrm{H} + \mathrm{Cl} + \mathrm{M} \rightarrow \mathrm{HCl} + \mathrm{M}$ and $\mathrm{H}_2 + \mathrm{Cl} \rightarrow \mathrm{HCl} + \mathrm{H}$ decrease the concentration of atomic chlorine, therefore decreasing the reaction of titanium with chlorine through the reaction $\mathrm{Ti} + \mathrm{Cl} + \mathrm{M} \rightarrow \mathrm{TiCl} + \mathrm{M}$. The second, which favours lower titanium yields, is that the reaction $\mathrm{Ti} + \mathrm{HCl} \rightarrow \mathrm{TiCl} + \mathrm{H}$ leads to reaction of titanium atoms to form $TiCl_x$. As the quench rate increases, the concentration of HCl decreases, so the latter effect becomes less important.

Figure 4 also shows that mean titanium particle diameter depends strongly on the quench rate and the initial gas composition. When the titanium yield is above about 50%, the particle size decreases as the quench rate increases. This is because the rapid temperature decrease increases the supersaturation, leading to enhanced nucleation, and hence the formation of more, smaller, particles. However, for low titanium yields, the

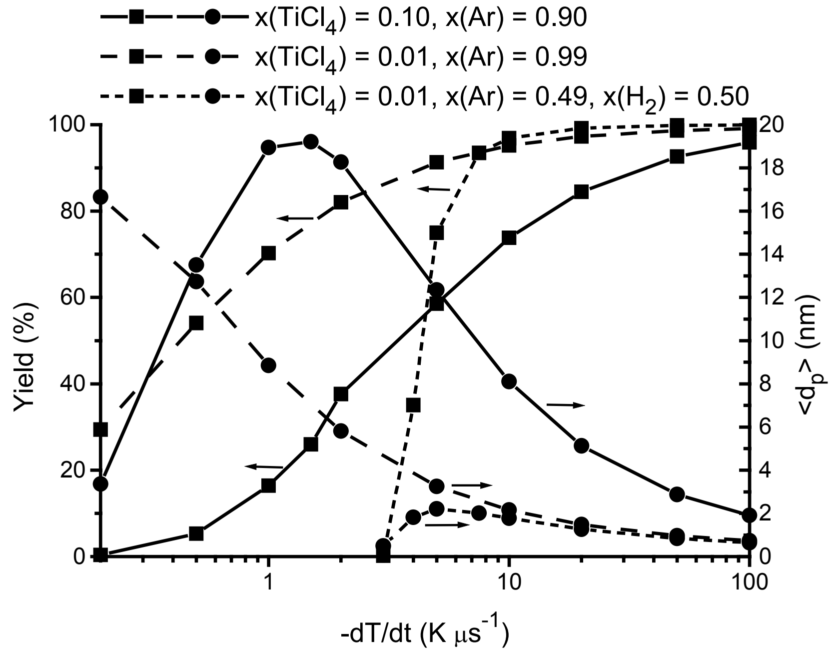

Figure 4. Dependence of titanium yield (squares, left axis) and mean particle diameter (circles, right axis) on quench rate, for different initial mixtures of titanium tetrachloride, argon and hydrogen.

particle size increases as the quench rate increases. This effect results from the competition between Ti reactions with Cl and HCl, and condensation of Ti onto existing particles. For the conditions under which the yield is low (i.e., slow quench rates), recombination reactions dominate, leading to relatively small particle size.

5. Conclusions

The formation of titanium particles from plasmas in mixtures of titanium tetrachloride, argon and hydrogen has been modelled using coupled chemical kinetic and nucleation equations. The results indicate that yields approaching 100% are possible if the titanium tetrachloride is fully dissociated to atomic titanium in the plasma, and the hot gas mixture is rapidly quenched.

The temperature and residence time required for full dissociation can be reduced by decreasing the concentration of titanium tetrachloride relative to argon in the gas mixture, and by the addition of hydrogen. The quench rate required for high conversion percentages of gaseous titanium atoms to titanium particles can be reduced by decreasing the concentration of titanium tetrachloride relative to argon in the gas mixture. The presence of hydrogen interferes with the conversion of gaseous titanium atoms to titanium particles at low to moderate quench rates. At high quench rates, the presence of hydrogen is advantageous.

It can be concluded that dilution of the titanium tetrachloride by argon favours high titanium yields. Hydrogen addition can either favour or hinder high titanium yields, depending on the process parameters.

Acknowledgements

The author thanks Dr T. McAllister for calculating the rate coefficients for the decomposition of SnCl.

References

[1] K. A. Bunting, Sodium and titanium tetrachloride feed systems for a plasma route to titanium, Proc. ISPC-6, Montreal, 1983, p. 193.

[2] P. G. Tsantrizos, L. T. Mavropoulos, M. I. Boulos, J. Jurewicz, K. Chen, The reactive spray forming production of titanium aluminides in the tail flame of a d.c. plasma torch, Proc. ISPC-10, Bochum, 1991, paper 1.4–2.

[3] S. G. Hutchison, C. M. Wai, J. Dong, R. J. Kearney, Titanium production in a plasma reactor – a feasibility investigation, *Plasma Chem. Plasma Process.* **15**, 353 (1995).

[4] S. K. Friedlander, Dynamics of aerosol formation by chemical reaction, *Ann. N. Y. Acad. Sci.* **404**, 354 (1983)

[5] S. L. Girshick, C.-P. Chiu, P. H. McMurry, Modelling particle formation and growth in a plasma synthesis reactor, *Plasma Chem. Plasma Process.* **8**, 145 (1988).

[6] S. L. Girshick, C.-P. Chiu, Numerical study of MgO powder synthesis by thermal plasma, *J. Aerosol Sci.* **21**, 641 (1990).

[7] A. B. Murphy, M. Bing, Equilibrium calculations of the reduction of titanium tetrachloride by aluminium and hydrogen, *High Temp. Chem. Process.* **3**, 365 (1994).

[8] M. W. Chase, Jr, C. A. Davies, J. R. Downey, Jr, D. J. Frurip, R. A. McDonald, A. N. Syverud, JANAF thermochemical tables, *J. Phys. Chem. Ref. Data* **14**, Suppl. 1 (1985).

[9] F. Teyssandier, M. D. Allendorf, Thermodynamics and kinetics of gas-phase reactions in the Ti-Cl-H system, *J. Electrochem. Soc.* **145**, 2167 (1998).

[10] K. Takahashi, A. Kunz, D. Woiki, D. Roth, Thermal decomposition of tin tetrachloride based on Cl^- and Sn^- concentration measurements, *J. Phys. Chem. A* **104**, 5246 (2000).

[11] S. L. Girshick, C.-P. Chiu, Kinetic nucleation theory: A new expression for the rate of homogeneous nucleation from an ideal supersaturated vapor, *J. Chem. Phys.* **93**, 1273 (1990).

[12] F. D. Richardson, Physical Chemistry of Melts in Metallurgy, Academic Press, London (1974), p. 427.

[13] P. N. Brown, G. D. Byrne, A. C. Hindmarsh, VODE: A Variable Coefficient ODE Solver,"SIAM J. Sci. Stat. Comput. **10**, 1038 (1989).

High-Voltage Power Line Corona Discharges: Production, Transport And Possible Health Effects Of Ions

A. B. Murphy[1], R. Morrow[1,2], P. Espel[1,3] and A. J. Medlin[1]

[1] CSIRO Telecommunications and Industrial Physics, P.O. Box 218, Lindfield NSW 2070, Australia
[2] Morrow Corona Solutions International Research and Applications Pty Ltd,
P.O. Box 1970, Macquarie Centre NSW 2113, Australia
[3]Current address: Laboratoire National d'Essais, 33 av. du General Leclerc, 92260 Fontenay-aux-Roses, France

Abstract

Initial results of an investigation of charge production and transport near high-voltage power lines are presented. Two-dimensional modelling of the corona production of ions and convective, diffusive and conductive ion transport indicates that the ion distribution around a model dc power line is strongly modified by a crosswind. Measurements of the ion density near a model dc power line support this conclusion. Initial measurements did not reveal significant ion densities near an ac power line under windless conditions.

1. Introduction

It is well established that fine aerosol particles have significant negative health effects. A recent major study [1] demonstrated a 4% increased risk of all-cause mortality, a 6% increased risk of cardiopulmonary mortality, and an 8% increased risk of lung cancer mortality, for every 10 μg m^{-3} increase in fine particulate air pollution. Mean fine particulate levels are typically of order 20 μg m^{-3} in metropolitan areas. Fine particulates are defined as suspended particles measuring less than 2.5 μm in diameter, this is often abbreviated as PM$_{2.5}$. Coarse particles (those between 2.5 μm and 15 μm) were not found to be consistently associated with mortality.

The peak in the number distribution of particulate air pollution occurs in the approximate range 20–200 nm [2]. These ultrafine particles are able to penetrate deeply into the lung when inhaled, and as such are postulated to be of major significance in both cardiovascular and respiratory illnesses associated with particulate air pollution. Experiments using a model lung have demonstrated that electrically-charged ultrafine particles of 20 nm and 125 nm diameter are five to six times more likely to be retained in the lung than uncharged particles [3], suggesting that charging of such particles significantly increases the associated health risk.

Measurements of dc electric fields close to high voltage power lines (or transmission lines) have shown significant levels of space charge up to 1 km downwind of the power lines [4,5]. The space charge is almost certainly due to charging of aerosol particles by the corona ions emitted from the high-voltage power lines. It has been proposed [4,5], on the basis of the established human health effects of fine particles, and the demonstrated increase in lung deposition due to charging, that charging of aerosols by power lines is likely to affect the health of humans in the vicinity of the power lines.

In this contribution, we present initial results of theoretical and experimental studies aimed at assessing this hypothesis. In Section 2, we give results of a theoretical study that predicts the distribution of ions emitted from a high-voltage power line, taking into account the influence of a crosswind that convect the ions away from the line. In Section 3, we consider atmospheric ion evolution and the transfer of charge from ions to aerosol particles. In Section 4, we compare the results of the theoretical studies with laboratory measurements of ion densities performed with a Gerdien ion counter. The results of initial outdoor measurements of the ion densities near ac power lines are discussed in Section 5.

2. Numerical Modelling of Corona Ion Production and Ion Transport

We have calculated the steady-state electrical potential and space charge density distributions around a high-voltage dc power line in the presence of a crosswind by self-consistent solution of Poisson's equation

$$\nabla^2\phi + \rho/\varepsilon_0 = 0 \tag{1}$$

where ϕ is the electrical potential, ρ is the ionic space charge density, and ε_0 is the permittivity of free space, and the time-dependent current continuity equation

$$\partial\rho/\partial t + \nabla\cdot\boldsymbol{J} = 0 \tag{2}$$

The current density $\boldsymbol{J}$ can be written

$$\boldsymbol{J} = \rho\left(\boldsymbol{V} - ks\nabla\phi\right) - D\nabla\rho \tag{3}$$

where $\boldsymbol{V}$ is the background gas velocity, k is the ion mobility, s is the sign of the ions (+1 for positive and –1 for negative ions), and D is the diffusion coefficent. This form allows ion conduction, convection and diffusion to be taken into account.

A pseudo-transient technique was used to iteratively solve Equations (1) and (2) until a steady state solution was obtained. An artificial time-dependent term was introduced into the Poisson equation to aid convergence to the steady state. The charge density at the power line was determined by forcing the electric field at the surface to be equal to the field given by the modified Peek's formula [6]

$$E_{\text{Peek}} = A + BR^{-\frac{1}{2}} \tag{4}$$

where $A = 32.3\times10^5$ V m^{-1} and $B = 0.846\times10^5$ V m^{-1} for air at standard temperature and pressure, and R is the power line radius in metres.

The technique has previously been applied to the phenomenon of unipolar electrical corona in an electrostatic precipitator with the inclusion of a background gas velocity field [7]. The technique allows the effect of crosswinds blowing ions away from the power line to be calculated [8].

The computational domain and the power line geometry used in the calculations are shown in Figure 1. For the case presented here $H = 1.56$ m, $L = 30$ m and $R = 3$ mm. The gas is air at 1 atm and 300 K. The ion mobility was set at $k = 1.3\times10^{-4}$ m^{2}V^{-1}s^{-1}, and the diffusion constant was set at $D = 0.1$ m^{2}s^{-1}.

In Figure 2, results are shown for the conditions of the experimental measurements described in Section 4. The power line voltage was 150 kV and the crosswind speed was chosen as either zero or 3 m s^{-1}. The figure demonstrates the strong influence of the wind on the charge distribution; there are similar effects on the electrical potential. The maximum electric field is less than 100 kV m^{-1}, so the drift velocity is below 13 m s^{-1}, and therefore of the same order as the wind speed. Even greater distortions of the charge distribution are calculated for larger wind speeds.

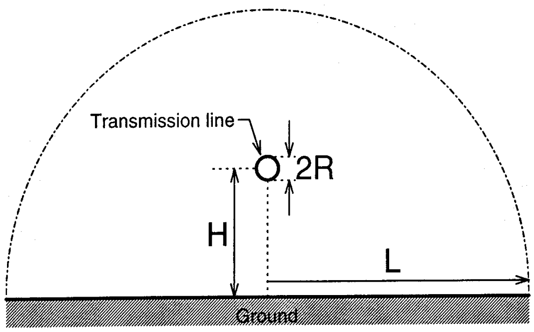

Figure 1. Computational domain and power line geometry.

Figure 2 indicates that, in the presence of a 3 m s^{-1} crosswind, the charge density is 6×10^{10} ions m^{-3} at a distance 25 m downwind of the power line. Calculations with a larger computational domain ($L = 60$ m) indicate that the charge density falls to about 2×10^{10} ions m^{-3} at a distance of 60 m downwind. These results are consistent with the

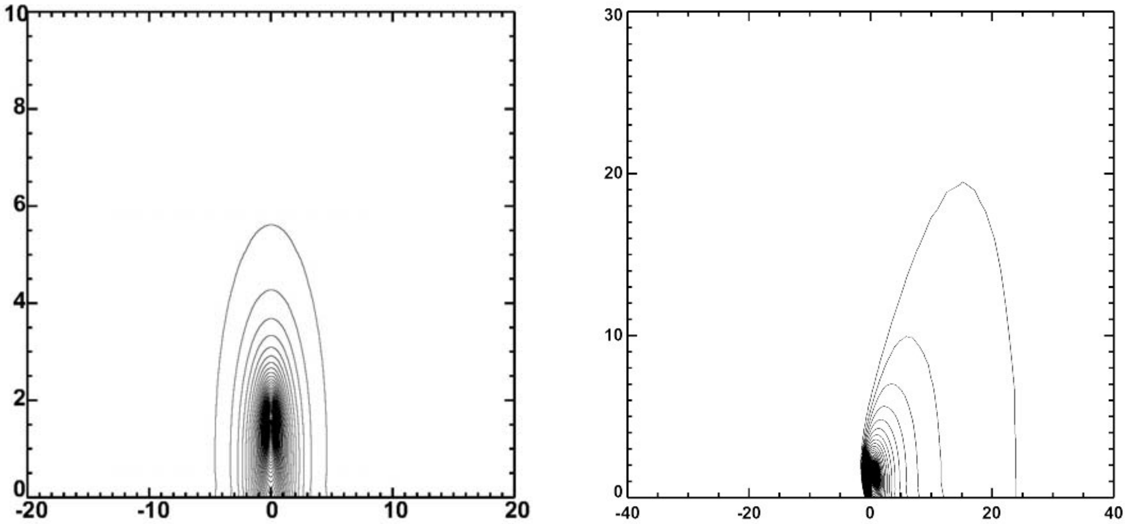

Figure 2. Calculated charge distribution near a 6 mm diameter model transmission line at 150 kV, at a height of 1.56 m above an earthed plane. The ion mobility is assumed to be $1.33\times10^{-4}\ \mathrm{m^2V^{-1}s^{-1}}$. Left: no crosswind; right: with a uniform $3\ \mathrm{m\,s^{-1}}$ crosswind. Spatial dimensions are in metres (note the different scales on the two graphs), and the outer contours, and the contour spacing, are both 6×10^{10} ions $\mathrm{m^{-3}}$.

measurements of Fews *et al.* [4,5], who, on the basis of dc electric field measurements, estimated a lower limit of the space charge of around 3×10^{9} ions $\mathrm{m^{-3}}$ for distances of 50 to 100 m from 132 kV ac power lines with crosswinds of order $3\ \mathrm{m\,s^{-1}}$. However, it is important to point out that the model is not expected to accurately simulate the experimental conditions, owing to (i) the fact that measurements were performed on ac power lines, and some neutralisation between positive and negative charge clouds is expected to occur, and (ii), the model does not take into account the complex ion reactions and ion-particle interactions that occur in the atmosphere. These latter phenomena are considered in Section 3.

3. Ion Evolution and Attachment of Ions to Particles

Air ions such as O_2^- and O_2^+ produced by corona discharges rapidly bind to water molecules or trace pollutant gases to form cluster ions, following reaction pathways exemplified by [9]

$$\begin{aligned}O_2^- &\xrightarrow{10^{-10}\mathrm{s}} O_2^-(H_2O) \xrightarrow{10^{-9}\mathrm{s}} O_2^-(H_2O)_2 \xrightarrow{10^{-8}\mathrm{s}} O_2^-(H_2O)_3 \xrightarrow{10^{-7}\mathrm{s}} O_2^-(H_2O)_4 \\ &\xrightarrow{1\ \mathrm{s}} CO_3^-(H_2O)_4 \xrightarrow{\text{etc.}}\end{aligned} \tag{5}$$

$$\begin{aligned}O_2^+ &\xrightarrow{10^{-10}\mathrm{s}} O_2^+(H_2O) \xrightarrow{10^{-9}\mathrm{s}} O_2^+(H_2O)_2 \xrightarrow{10^{-8}\mathrm{s}} H_3O^+(H_2O)_4 \xrightarrow{10^{-6}\mathrm{s}} H_3O^+(H_2O)_5 \\ &\xrightarrow{10^{-5}\mathrm{s}} H_3O^+(H_2O)_6 \xrightarrow{1\ \mathrm{s}} NH_4^+(H_2O)_3 \xrightarrow{\text{etc.}}\end{aligned} \tag{6}$$

Mobility measurements of ions generated in laboratory air by various ionisation sources at room temperature and atmospheric pressure give average mobility values of $k=1.33\times10^{-4}\ \mathrm{m^2V^{-1}s^{-1}}$ for positive ions, and $k=1.84\times10^{-4}\ \mathrm{m^2V^{-1}s^{-1}}$ for negative ions [10]. Hence the ion mobility used in the calculations of Section 2 is representative of positive ions; the corresponding ion mass and diameter are around 200 amu and 1 nm respectively.

The cluster ions attach to ultrafine aerosol particles (diameters up to 100 nm) on a time scale of 10 to 100 s [5,11]. In equilibrium, particles of order 50 nm or less are more likely to be uncharged than charged [11]; hence the charging of these particles by corona ions significantly affects the charge distribution. Further, the lifetime of the charged particle states is of the order 3 to 30 min [5]. Clearly the model presented in Section 2 does not take into account of these phenomena. To do so would require the solution of an equation of the form

$$\frac{\partial n_i}{\partial t} + \nabla\bullet\left\{n_i\left[\boldsymbol{V} - Z_i k_i \boldsymbol{E_0}\sin\left(\omega t\right)\right]\right\} - \nabla\bullet\left(D_i \nabla n_i\right) = S_i \qquad (7)$$

for each type of ion or charged particle. In Equation (7), n_i, Z_i, k_i and D_i are respectively the number density, charge number, electrical mobility and diffusion coefficient of species *i*, $\boldsymbol{V}$ is the wind velocity, and E_0 and ω are respectively the amplitude and frequency of the electric field. S_i is a source term for species *i*, which, depending on the species, takes into account production of ions by the corona discharge, reactions between ions, and reactions between ions and charged particles.

4. Laboratory Measurements of Ion Distributions

A Gerdien ion counter, in which air is drawn through a coaxial electrode arrangement, has been constructed for the measurement of the density of atmospheric ions. The inner electrode is connected to a Keithley 6514A electrometer, which measures currents from 10 aA (i.e. 10^{-5} pA) to 21 mA. A positive or negative voltage is applied to the outside electrode. The design of the ion counter is shown in Figure 3. The threshold mobility of the Gerdien ion counter was $2.9 \times 10^{-5}\ \mathrm{m^2V^{-1}s^{-1}}$, which is sufficiently low that all the small and large cluster ions, with diameters less than about 2 nm, can be detected.

Several measurements were carried out with a positive voltage applied to the outside electrode. The temperature was between 19°C and 22°C, and the relative humidity between 56% and 64%. The laboratory was electrically screened by earthed mesh on all sides and was not, therefore, subject to the vertical potential gradient of the Earth. All metal surfaces and components within the laboratory were earthed.

Measurements showed that the background positive air ion density fluctuated between 4.6×10^8 ions $\mathrm{m^{-3}}$ and 7.5×10^8 ions $\mathrm{m^{-3}}$. Experiments were carried out for a line conductor to plane gap. The line conductor was 6 mm in diameter and was supported by an insulator. The dc high voltage source and the line conductor were connected using flexible aluminium tubes of 220 mm diameter, to avoid corona originating from locations other than the line conductor. For the same reason, the top of the insulator was capped by a 150 mm diameter sphere. The height of the line conductor was 1.56 m.

Measurements of ion densities were performed for applied voltages from 100 kV to 250 kV. Values of the ion density for positive voltages with no crosswind are presented in Figure 4. In all cases, the ion density is many orders of magnitude above the background (zero voltage) density. The densities were steady in time for an applied voltage of 200 kV, whereas there was a large variation at 100 kV. This is due to the fact that, at 100 kV, the maximum electric field on the conductor line is only $3.7\ \mathrm{kV\ mm^{-1}}$, which is just above the critical field in air ($3\ \mathrm{kV\ mm^{-1}}$). The result is that corona discharges occur infrequently and can develop everywhere on the conductor. The corona discharge repetition rate increases with increasing voltage, and corona develops all along the conductor, leading to steadier ion densities. Figure 4 shows that the ion density increases rapidly with voltage, and decreases rapidly with distance from the power line. The rate of decrease is similar to that predicted by the model. The voltage at a horizontal distance of 3 m from the 150 kV power line is measured to have a value approximately

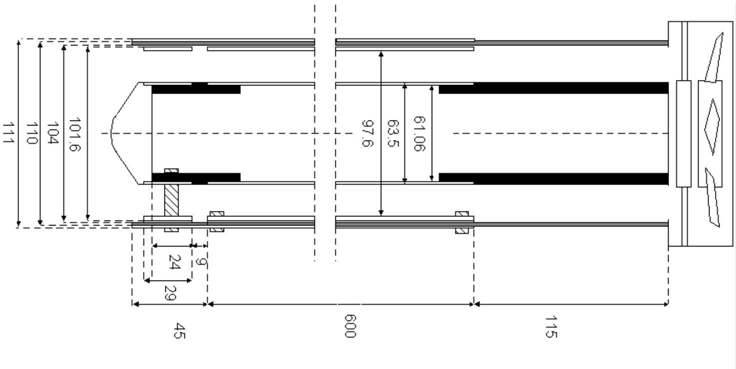

Figure 3. The Gerdien ion counter. The outer diameter is 111 mm.

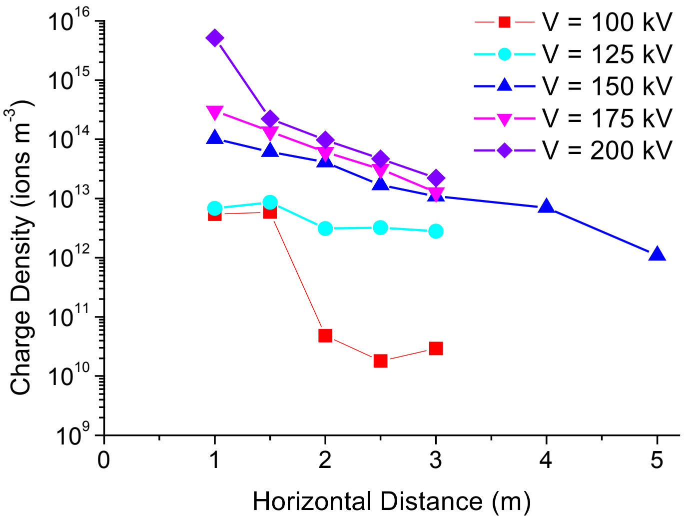

Figure 4. Charge density as a function of horizontal distance from the conductor, for different applied voltages, with no crosswind. (Without corona, the charge density is around 6×10^8 ions m^{-3}.)

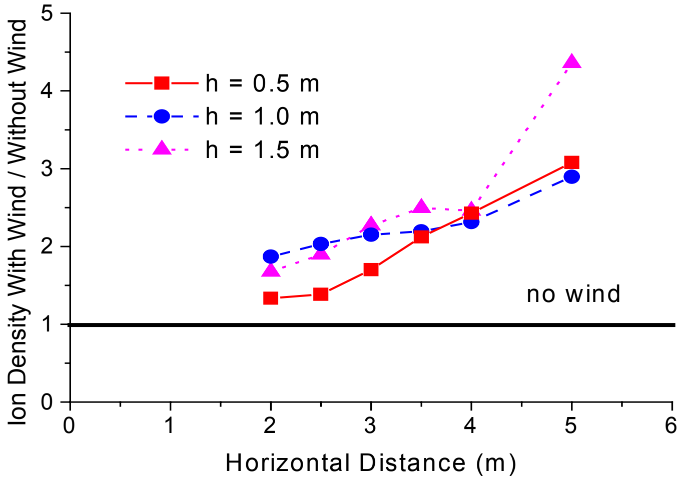

Figure 5. Effect of a 3 m/s crosswind on the positive ion density at different heights, for the conditions of Figure 4, with an applied voltage of 150 kV.

50 times larger than that predicted by the model, suggesting the the model underestimates the ion production rate.

Figure 5 shows that an applied crosswind of 3 m s^{-1} has a significant effect on ion concentration. The relative increases are larger at greater distances from the power line. The model predicts charge density enhancements due to the crosswind of factors 1.5, 2.3 and 4.2 at horizontal distances of 2, 3 and 4 m respectively from the power line. The enhancement factors follow the same trend and are of similar magnitude to the measured factors.

5. Outdoor Measurements of Ion Densities

We have performed preliminary measurements of ion densities in the vicinity of ac high-voltage power lines. We performed measurements for 132 kV, 220 kV and 500 kV 50 Hz lines under windless conditions on fine, low humidity days. We measured only minor enhancements, of factors in the range 1 to 2, in the charge density compared to background values. Reasons for the differences between these ac measurements and the dc laboratory measurements are as follows:

- Our calculations and laboratory measurements, and the dc electric field measurements of Fews *et al.* [4,5] show that the space charge density is larger under windy conditions.
- Alternating-current voltages produce ions of both polarities. In the absence of wind to separate the ion clouds, these ions will tend to neutralise each other. Hence the influence of wind is expected to be greater for ac power lines.

- The Gerdien ion counter used in our measurements detects only small, high mobility, ions. The ac power lines are much higher than the model dc power line used in our laboratory experiments. It is likely that the ions produced by the power lines have combined with larger particles by the time they reach ground level [4]; the resulting charged particles would not be detected.

6. Conclusions

Research in the UK has indicated significant space charge is present near high-voltage power lines, particularly under windy conditions. Based on the established negative health effects of fine particulates, and the enhancement in lung deposition due to particle charging, it has been hypothesised that the charging of particles by high-voltage power lines could affect the health of humans in the vicinity of the power lines. We have initiated a programme of research to investigate these findings.

We have developed a numerical model that predicts the ion densitiy distribution around high-voltage conductors. The model indicates that an imposed convective flow increases the ion density downwind of the conductor. The ion densities predicted by the model are consistent with the charge concentrations derived from the measurements of Fews *et al.* [5]. However, the model does not take into account the complex set of ion and charge-transfer reactions that occur in the atmosphere.

Measurements of the ion density distribution near a model dc power line show that significant ion densities are produced by corona discharges, and that an imposed convective flow increases the density downwind of the conductor by factors consistent with those predicted by the model.

Our initial measurements of the ion densities near ac power lines found only low levels on windless days. Limitations in our apparatus mean we are not able to draw any firm conclusions from these measurements. Further measurements on windy days, and using apparatus capable of detecting larger charged particles, will be required to draw more definite conclusions.

References

[1] C. A. Pope III, R. T. Burnett, M. J. Thun, E. E. Calle, D. Krewski, K. Ito, G. D. Thurston, Lung cancer, cardiopulmonary mortality, and long-term exposure to fine particulate air pollution, *J. Am. Med. Ass.* **287**, 1132 (2002).

[2] R. M. Harrison, J. P. Shi, S. Xi, A. Khan, M. R. Kinnersley, J. Yin, Measurement of number, mass and size distribution of particles in the atmosphere — ultrafine particles in the atmosphere, *Philos. Trans. Roy. Soc.* **358**, 2567 (2000).

[3] B. S. Cohen, J. Q. Xiong, C.-P. Fang, W. Li, Deposition of charged particles on lung airways, *Health Phys.* **74**, 554 (1998).

[4] A. P. Fews, D. L. Henshaw, R. J. Wilding, P. A. Keitch, Corona ions from power lines and increased exposure to pollutant aerosols, *Int. J. Radiat. Biol.* **75**, 1523 (1999).

[5] A. P. Fews, R. J. Wilding, P. A. Keitch, N. K. Holden, D. L. Henshaw, Modification of atmospheric DC fields by space charge from high-voltage power lines, *Atmosph. Res.* **63**, 271 (2002).

[6] M. Abdel-Salam, D. Wiitanen, Calculation of corona onset voltage for duct-type precipitators, *IEEE Trans. Ind. Appl.* **18**, 54 (1982).

[7] A. J. Medlin, C. A. J. Fletcher, R. Morrow, A pseudotransient approach to steady state solution of electric field-space charge coupled problems, *J. Electrostatics* **43**, 39 (1998).

[8] A. J. Medlin, R. Morrow and C. A. J. Fletcher, Calculation of monopolar corona at a high voltage DC transmission line with crosswinds, *J. Electrostatics* **43**, 61 (1998).

[9] A. Luts, Evolution of small negative ions at enhanced ionization, *J. Geophys. Res.D* **100**, 1487 (1995).

[10] G. P. Reischl, J. M. Mäkelä, R. Karch, J. Necid, Bipolar charging of ultrafine particles in the size range below 10 nm, *J. Aerosol Sci.* **27**, 931 (1996).

[11] W. A. Hoppel, G. M. Frick, Ion–aerosol attachment coefficients and the steady-state charge distribution on aerosols in a bipolar ion environment, *Aerosol Sci. Tech.* **5**, 1 (1986).

Vacuum Arc Cleaning of Metal Surface Covered with Organic Contaminant

M. Sugimoto, H. Takahashi and K. Takeda

Faculty of Systems Science and Technology, Akita Prefectural University, Akita, Japan

Abstract

Arc discharge in vacuum is applied for cleaning of metal surface covered with organic contaminant. In this method, the cleaning metal is served as a cathode in discharge circuit. Generated some small arc spots move on the cathode surface and remove the contaminant. Although cleaning area per second decreases with the contaminant thickness, total weight of removed organic contaminant increases inversely. Additionally, removed contaminant per discharge current is improved with discharge current.

1. Introduction

Surface cleaning is the most fundamental and important in metal surface treatments. Residual contaminants, which are cumulated on surface by natural or artificial processes, often give the bulk damage. For example, since some acid or alkaline residue on metal surface causes erosion of the bulk of metal, it must be removed completely.

Metal surface treatments such as painting or coating are usually processed for almost metal products in order to protect the surface from damage and add strength, endurance to them. Since metal surface is much activated and has a tendency to connect with other kind matter in general, it is hardly seen that pure metal surface is exposed to air. This feature usually causes its oxide layer formation on pure metal surface. It is harmful for metal surface treatments because adhesions of the painting or coating layers are prevented, and hence the surface cleaning is necessary as the pretreatment of those processes.

What should be removed are not only the oxides. When metal products are machined or polished, various kinds of grease are used so much. After these processes, degrease treatment is indispensable. In many cases, those metal products are cleaned by wet process with organic solvent or chemical agent. However, there are some problems in degrease by wet treatment. This cleaning method needs washing process of the cleaner solvent and drying after that. In addition, the cleaner solvent is often toxic and harmful for human body and natural environment.

Authors have been studying about application of arc discharge in vacuum for metal surface cleaning. It is well known that small bright spots appear and move rapidly on the cathode surface in vacuum arc discharge [1,2]. Current is concentrated in those small spots and thus they have enormous energy density, which is estimated at 10^{10}~10^{14} W/m^2. Therefore the cathode spot heats everything on the cathode surface to very high temperature and enables impurity on the surface to vanish in a moment. Actually, it has been shown that this method is very effective for removal of oxide layer on metal surface [3].

This method is also expected to be applicable for degrease of metal surface. Our previous experiment qualitatively suggests that it is promising for removal of organic compound on metal surface [4,5]. The cleaning mechanism of organic compound is considered as follows. Liquid or solid state organic compound on metal surface is decomposed to simpler hydrocarbon compound or lighter gaseous matter such as CO_2, H_2, CO and so on by high energy density of cathode spots. Since these gaseous compounds can be evacuated from the vacuum chamber by pump, there is no possibility of recontamination on metal surface. It may be able to change toxic contaminant into harmless matter. This cleaning method does not need drying process different from wet treatment with chemical agent or organic solvent, which shortens the time for cleaning process. Because of the treatment in vacuum, it is easy to preserve the cleaned surface from exposure to air and keep the highly activated state, which is a big advantage for the following surface treatments.

In the present study, removal of organic compound on metal surface is quantitatively investigated. Experimental results show that the removal efficiency is not constant and depends on the surface density of the liquid paraffin and the discharge current.

2. Experimental Setup

Apparatus for this experiment is shown in Fig. 1. A vacuum chamber shaped like a cup, whose inner dimensions are 50 mm in diameter and 70 mm in height, is equipped a water-cooled copper anode inside.

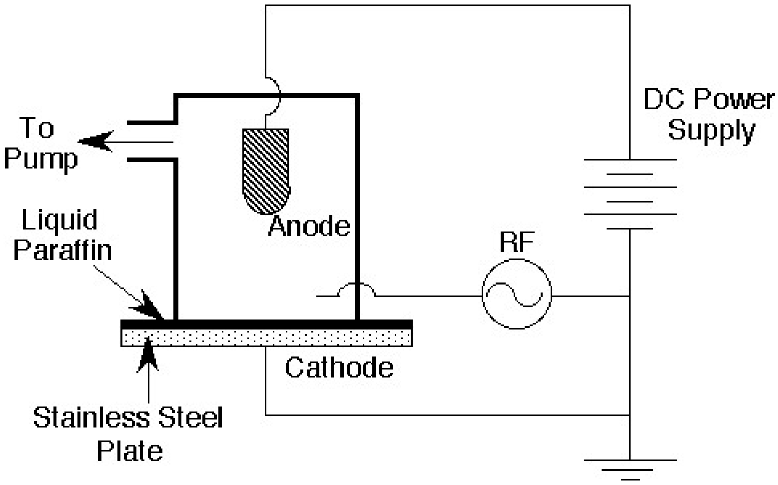

Fig. 1 Schematic view of experimental apparatus.

This chamber caps on a test piece and is evacuated to 50 Pa by rotary pump before discharge. Test piece is a stainless steel (SUS430) plate of 100 mm×100 mm and 3 mm thick, which is negatively polarized. The surface of test piece is covered with liquid paraffin as organic contaminant. Liquid paraffin is a mixture of alkane C_nH_{2n+2}, in which the values of "n" are near 15. Arc discharge starts with high frequency voltage and is sustained by dc power supply. The discharge current is controllable up to 120 A, while the voltage is almost fixed between 40 V and 50 V automatically.

In this experiment, liquid paraffin is selected as contaminant because it is handy and the chemical structure is simple. However, it is not so easy to remove this hydrocarbon compound from metal surface. That is because it hardly solves in water and alkali is also useless since sponification does not occur. In order to spread liquid paraffin over the surface uniformly, stainless steel plate is dipped into the pooled liquid paraffin diluted with petroleum benzine and then dried until almost petroleum benzine on the surface diffuses into air. The dilution ratio is varied between 20 and 120 cm^3 liquid paraffin to 100 cm^3 petroleum benzine. The weight of stainless steel plate is measured before the dip in the paraffin pool and the cleaning. From the difference of these values, the weight and the surface density of liquid paraffin on plate are calculated. The amount of

Fig. 2 Photograph of uncompletedly cleaned surface of test piece. The residual liquid paraffin is wiped up in order to show cathode spot track.

liquid paraffin, therefore its surface density on the test piece can be controlled to some extent by tuning the mixture of liquid paraffin and petroleum benzine. The surface density of liquid paraffin in this experiment is changed from 4 μg to 36 μg per 1mm^2. Since the density of liquid paraffin is about 0.9 g/cm^3 at 20 centigrade, the thickness of liquid paraffin layer on the test piece surface is estimated from 4 μm to 40 μm.

3. Experimental Results and Discussion

Although the inside of the vacuum chamber can not be observed during the discharge, it is acceptable to explain that some small cathode spots are moving on the test piece in random manner and liquid paraffin is gradually removed from the surface. Figure 2 is a picture of the treated surface of test piece, which is not cleaned entirely and the residual liquid paraffin is wiped up in order to show cathode spot track. In this photograph, the region eroded by cathode spots looks dark compared with the original surface. A lot of thin lines whose width are a few of 0.1 mm form a filament structure in the periphery of the treated surface. These lines are possibly the track of individual cathode spot and the filament structure shows that they are moving disorderly.

In many cases, the region where liquid paraffin is completely eliminated tends to expand toward the periphery and looks bright white, while uncompleted cleaning area is brown because the liquid paraffin turns color right after the arc starts [5]. In the present study, the widths of completely cleaned region are measured in several points and the cleaning area is estimated numerically assuming that it has an equal area of a circle whose diameter is same as the average of measured widths.

Figure 3 shows relation between surface density of liquid paraffin and surface removal rate when the discharge currents are 50 A and 100 A. “Surface removal rate” means completely cleaned area in a second, here. In both cases, surface removal rate decreases with the surface density of contaminant. It also shows that lager discharge current leads to rapid finish of surface cleaning.

On the contrary, Fig. 4 is a plot of weight removal rate for various surface density of liquid paraffin. “Weight removal rate” means weight of removed liquid paraffin in a second, here. Despite the longer cleaning time is necessary for the higher density contamination, removal rate in weight of contaminant increases with its surface density, as shown in Fig. 4. In addition, weight removal rate much increases with the surface density of liquid paraffin when the arc discharge current is larger.

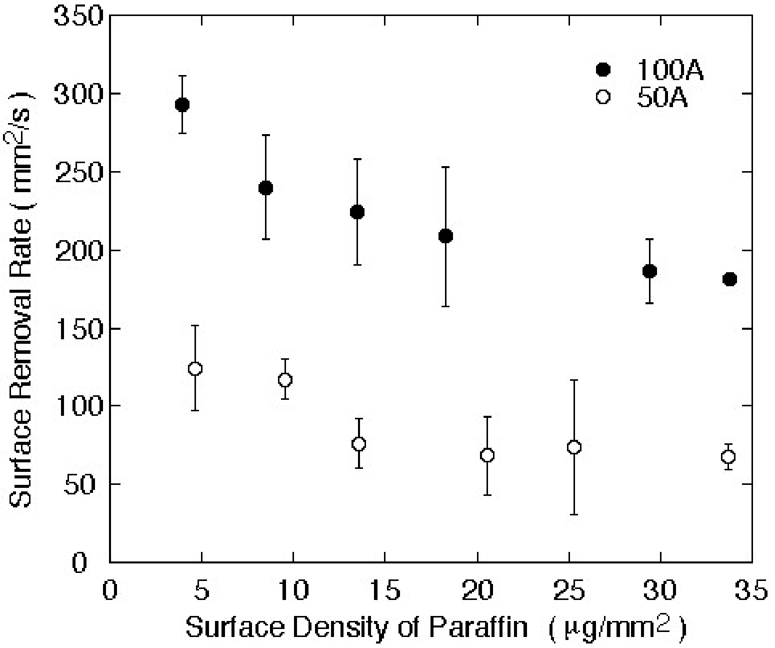

Fig. 3 Dependence of surface removal rate on surface density of liquid paraffin for different discharge current. Open and closed circles stand for cases of 50 A and 100 A arc discharge, respectively.

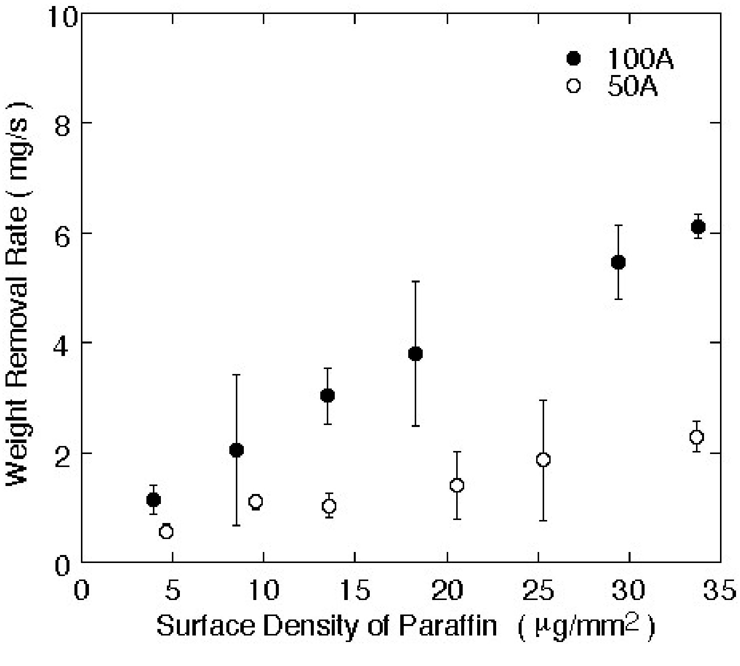

Fig. 4 Dependence of weight removal rate on surface density of liquid paraffin for different discharge current. Open and closed circles represent cases of 50 A and 100 A arc discharge, respectively.

Judging from this result, removal rate of liquid paraffin also seems to depend on arc discharge current. Figure 5 is the dependence of weight removal rate on the discharge current. The weight removal rate drastically increases with the current in the case of thick contaminant layer on the surface, while little dependence can be seen with small surface density of liquid paraffin. This result can be explained as follows. Removal capacity of vacuum arc cleaning whose current is more than 50 A is so large that the weight removal rate is saturated because the surface density of 4.5 μg/mm^2 liquid paraffin is too small. Therefore, under the condition of rich liquid paraffin on the surface, that is 33.7 μg/mm^2 in Fig. 5, the weight removal rate increases with the discharge current.

Figure 6 shows the current dependence of efficiency for different surface density of liquid paraffin. Here, “efficiency” is calculated from weight removal rate divided by its own discharge current. In this result, efficiency is improved as the discharge current increases when the surface density of liquid paraffin is enough. Authors have no idea about it at present. According to the previous study of arc spot on cathode surface with oxide layer, current in one spot is almost constant and the number of spots is nearly proportional to discharge current. Even if it is also correct for this case, it is difficult to explain this result only with it. Although the mechanism has not been clarified yet, our recent research about vacuum arc cleaning of oxide layer reveals that cathode spots sometimes behave in another style under the different surface condition. Higher current density and more rapid moving of cathode spots are often observed when some organic compound or chemical agent is on the oxide layer. If the same phenomenon occurs in the present experiment, it may be possible to understand the result in Fig. 6.

In order to evaluate the energy efficiency of this cleaning method, necessary power for decomposition of liquid paraffin on the surface of test piece is compared with actual input power by arc discharge. For convenience to estimate, the values of weight removal rate of liquid paraffin, discharge current and voltage are fixed to 6 mg/s, 100 A and 50 V.

As mentioned in the second section, liquid paraffin consists of some kinds of alkane C_nH_{2n+2} whose values of “n” are around 15. Assuming that “n” is just equal to 15 in the liquid paraffin used in this experiment, the numbers of C-C and C-H bond in this case are 14 and 32, respectively. Since the bond energies of C-C and C-H are 324 kJ/mol and 410 kJ/mol, total required energy for entire decomposition of the liquid paraffin can be calculated at 17656 kJ/mol. On the other hand, the amount of removed liquid paraffin in a second is estimated at ~ 2.8 $*10^{-5}$ mol/s because the molecular weight of C_nH_{2n+2} is 212 in the case of n=15. Therefore, the necessary power for complete decomposition of liquid paraffin on the test piece can be estimated at ~ 500 W. Actual input power of arc discharge is nearly 5000 W at 100 A because of 50 V discharge voltage, and thus it can be concluded that about 10 % of total input power is used to remove the liquid paraffin on the

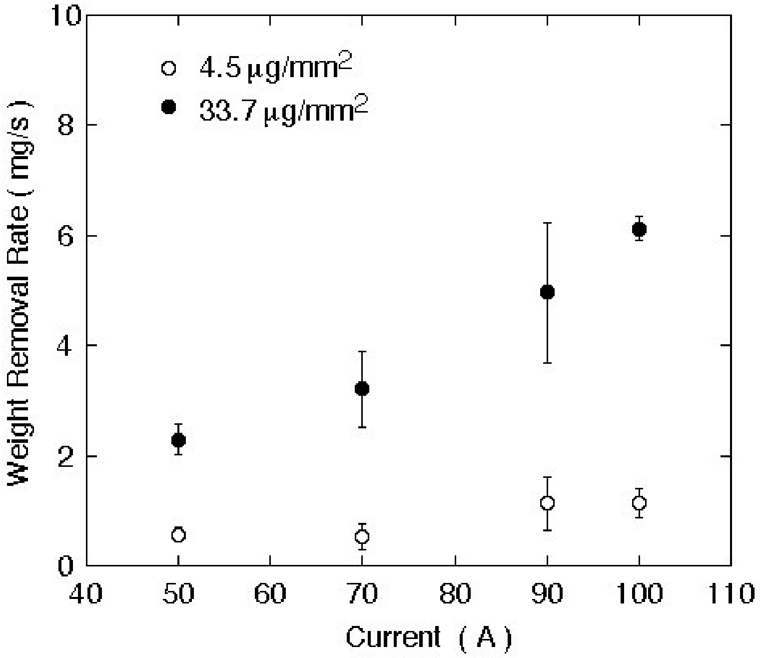

Fig. 5 Current dependence of weight removal rate for different surface density of liquid paraffin. Open and closed circles stand for cases of 4.5 μg/mm^2 and 33.7 μg/mm^2, respectively.

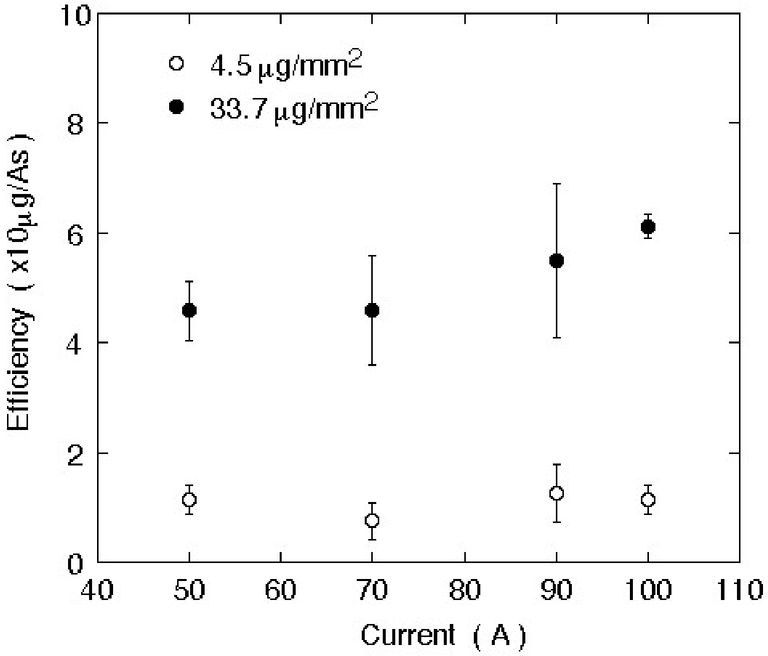

Fig. 6 Current variation of efficiency for different surface density of liquid paraffin. Open and closed circles represent cases of 4.5 μg/mm^2 and 33.7 μg/mm^2, respectively.

cathode surface if all of removed liquid paraffin is decomposed. It can be supposed that actual situation is not far from this estimation because contamination with liquid paraffin is never seen on the surface of test piece and wall of chamber. Instead, a little dust like carbon is watched when the liquid paraffin layer is thick. This estimation, therefore, suggests that it is an efficient process, taking into account that a large part of the input power usually goes into anode in arc discharge.

During the treatment, cathode spot that has enormous energy density not only remove the contaminant on the surface but also melt and quench the surface of sample, and thus the surface roughness increases. There is no removing contaminant completely without erosion of the surface by cathode spot. Metal surface cleaning by arc in vacuum may be inadequate if the smooth surface is necessary for the following treatment. However, the increase of surface roughness leads to the increase of surface area, which possibly helps painting or coating layer to adhere fast to the metal surface.

In this method, cleaning process tends to finish earlier around the center of treatment area. As the arc discharge continues, cathode spots spend long time in the central region where the cleaning is completed and the cleaning in the periphery proceeds slowly. This problem has to be solved because it means the waste of input electric power. Although some modifications such as tuning of the distance between electrodes are expected to lead improvements, those are future works.

4. Conclusion

Vacuum arc cleaning of metal surface covered with organic contaminant is experimentally investigated. Test piece is stainless steel plate with liquid paraffin as organic contaminant. As the surface density of liquid paraffin increases, completely cleaned area on the surface in the same discharge duration becomes small. However, the weight of removed liquid paraffin increases proportionally to the surface density of liquid paraffin. The weight removal rate of liquid paraffin drastically increases with discharge current. In particular, it is revealed that weight removal rate per discharge current improves as the current increases. It is estimated that about 10 % of total input power is consumed for decomposition and removal of liquid paraffin.

This research has been supported by Grant-in Aid for Scientific Research (B) from the Ministry of Education, Culture, Sports Science and Technology in Japan.

References

[1]J. M. Lafferty-Vacuum Arcs, A Wiley-Interscience Publication, 120(1980).
[2]R. L. Boxman, P. J. Martin and D. M. Sanders-Handbook of Vacuum Arc Science and Technology, Noyes Pubications, 73(1995).
[3]K. Takeda and S. Takeuchi-Materials Transactions, JIM **38**, 636(1997).
[4]K. Takeda and M. Sugimoto-IEEE Transactions on Plasma Science **29**-5, 718(2001).
[5]M. Sugimoto, K. Takeda and T. Inaba-Journal of High Temperature Society **28**-2, 84(2002).

Physico-chemical modifications of the DBD and UV irradiation treatments on the PET and PET+TiO_2 films

N. Dumitraşcu[1], I. Topală[1], C. Miheşan[1], M. Craus[2], G. Popa[1]

[1]*Plasma Physics Department, "Al. I. Cuza" University, Iasi – 6600, Romania*
[2]*TechnicalPhysics Institute, Iasi-6600, Romania*

Abstract

Treatments by a dielectric barrier discharge (DBD) in helium and UV irradiation were used for obtaining controlled effects of functionalization and crosslinking on the surface of PET and PET+TiO_2 films. Morphology of PET and PET+TiO_2 films investigated by AFM is modified and surface energy and its polarity are increased after the DBD and UV treatments. The efficiency of DBD treatment is proved for less than 10sec, functionalization and crosslinking at the surface of PET and PET+TiO_2, being initiated by DBD in a few seconds. In air environments wettability decays in time but the DBD treatments may be effective in keeping the stability of surface properties. Crystalline structure of the films investigated by XRD showed a polycrystalline phase of the films with a higher crystallinity factor after the DBD treatments. Chemical structure of the films investigated by FTIR-ATR is not affected by the DBD treatments but UV irradiation provokes a degradation of the surface. Concerning the duration of DBD treatments, the first seconds appear to be essential in the subsequent dynamic of the surface modifications.

1. Introduction

Usually, treatments by electrical discharges and UV irradiation have various effects on the polymer surfaces, such as cleaning, functionalization, crosslinking and chemical modifications including the surface degradation. These phenomena can occur in a few monolayers of the polymer and they generate physico-chemical modifications in surface properties such as wettability, polarity, chemical structure etc., but keeping the bulk properties unchanged [1, 2, 3]. One of the techniques to modify and, in particular, to improve the wettability, printability, bondability and biocompatibility of polymer surfaces is the dielectric barrier discharge (DBD) [4, 5]. In this work we present, comparatively, the effects of DBD treatments and UV irradiation on some surface properties of the poly(ethylene terephthalate-PET) and PET and titanium dioxide (PET + TiO_2) films.

PET is linear semicrystalline polyester, with hydrophobic characteristics and biggest stretch strength of all thermoplastics. This polymer is used as magnetic video and industrial tape, packing foils, suture filaments and for medical devices such as vascular grafts, too [2, 3].

It is known that after exposure to air or/and aggressive environments the surface properties of polymers are modifying in time and this process is considered as ageing of polymers. For this reason, it is necessary to improve the surface stabilization by adding additives such as ultraviolet absorbers, thermal stabilizers, hydrophylization agents etc. Unfortunately, some of these additives may migrate to the surface and properties are changing and the surface becomes instable. TiO_2 is one of the most important additives as hydrophilic colorless material, with n-type semiconductivity, resistant to corrosion, with photo-catalytic effects and biological good performance. Alloys with Ti are used in orthopedic and dental prostheses because it gives has good biocompatibility and a longer clotting time, less amounts of adherent platelets etc. TiO_2 is a pigment capable to achieve desired properties such as brightness, whiteness and opacity to any commercial product, for ex., plastics for food and pharmaceutical packing industry and many applications in visor, antireflective and protective optical coatings, automobile industry, gas barrier coatings. In mixtures it is important to know the optimum percentage of TiO_2 which may give a maximum dispersion. Few percentages of TiO_2 incorporated in the matrix of PET improve certain mechanical, physical and chemical properties of this composite, favorable in many applications [6]. For ex., in order to improve the stabilizing effects of TiO_2 by the UV absorption, sometimes levels of up to10% are desirable, even at these levels physical properties are mainly unaffected [7].

We treated surfaces of PET and PET+TiO_2 films with a dielectric barrier discharge (DBD) and UV irradiation and certain differences in the effects of functionalization are established and discussed. An increasing of adhesion properties and crosslinking at the surface were observed. Characterization of the surfaces was made by AFM, contact angle measurements, XRD, ellipsometry and ATR-FTIR.

2. Experimental

We used PET (Goodfellow Co.) and PET+4%TiO_2 films (industrial Romanian product, produced in the form of biaxially stretched). PET and PET+TiO_2 films (sheets with 1.5cmx1.5cm) were washed in ethanol and deionized water for some minutes.

TiO_2 is known in the anatase, rutile and brookite crystal phases, with remarkable characteristics, such as chemical stability, a high refractive index, and good transmittance in the visible and infrared region. In our experiments the TiO_2 rutile form was included in the matrix of PET, because the rutile form gives a more stability of surface properties whereas the anatase crystal form is very reactive and can initiate polymer degradation.

Treatments by DBD were performed at atmospheric pressure in helium (spectral purity 99.99%), selected as the most efficient inert gas in the functionalization and crosslinking of the polymer surface. Discharge configuration consists of two electrodes separated by a dielectric barrier of glass plate, the distance between electrodes was 3cm and the discharge is driven by a pulsed high voltage (28kV peak-to-peak), with a frequency of 13.5kHz and a total electric power of 40W was dissipated on the discharge. Both discharge voltage and current intensity are measured and time evolution is simultaneously monitored with a METRIX oscilloscope and an acquisition system type IEE488 [4, 5].

The films were exposed to UV irradiation from a high pressure Hg lamp (ELECTROLUX, 80W) with a distance lamp to film of 5cm. We used several treatments time were, i. e., 1, 3, 5, 7, 10, and 30sec, for DBD treatments and 10s, 1min, 10min, 30min and 1h, for UV irradiation.

The AFM technique has been used to visualize the surface topography working in the taping mode. We used a standard silicon nitride cantilever (NSC21), with a force constant of 17.5N/m, 250kHz resonance frequency and tip radius less than 7nm. The roughness of samples is verified by statistic AFM estimations. In our experiments the image covers various area, from 70μm x 70μm to 1μm x 1μm and AFM measurements are extended to different sites of the sample and are repeated in same conditions at room temperature and ambient atmosphere.

The contact angles of bidistillated water and formaldehyde were measured by the sessile drop method, at room temperature and controlled humidity, immediately after the treatments, after one day and 10 days.

The crystalline structure of thin films was analyzed by X-ray diffraction (XRD) using a DRON 2.0 diffractometer with a Co Kα radiation ($\lambda = 1.79$ Å) and a data acquisition system. The amorphous component was separated by the method presented in ref. [8] and the range of the diffraction angle was from 20^0 to 40^0 , this range covering the dominant spectrum peaks of PET.

Optical properties of surfaces were obtained using a EL X-01R ellipsometer, which permit to evaluate the refraction index and the absorption coefficient of the films. We analyzed the ellipsometric response in two perpendicular directions taking into account the optical anisotropy of biaxilly drawn PET films which is depending on the molecule orientation at interface. Slides of SiO_2 are used as substrates, each substrate having 1cm wide and 1cm long.

FTIR-ATR spectroscopy was performed to control the chemical structure before and after the treatments. We used a Bommen IR spectrophotometer with a source of KBr laser and a Ge ATR crystal and the spectra were recorded from 500-4000cm^{-1} with a resolution of 2cm^{-1}.

3. Results and discussions

It is known that plasma treatments may initiate on the surface of different materials a complex of reactions between the free energetic species produced within the plasma volume and the species presented and/or created on the surface. In these complicated reactions it must include also the photons coming from the plasma. Moreover after treatments some reactions may continue in atmospheric air and many other processes are possible. In these methods of treatments, i. e. DBD and UV irradiation, the energies dissipated on the surface are sufficient to break all the bonds existing in the polymer chains. Nevertheless, the effects are very different, giving us a motivation to emphasize that the time parameter is much more important than values energy in this complicated system which is plasma-surface. Starting from this point of view, we analyzed the most important effect of treatments, i. e. the surface functionalization. This effect is compulsory condition to improve the adhesion properties and to initiate reactions of deposition and grafting at the surface. Functionalization is strongly dependent on the methods and time of treatment. We analyzed the surface polarity as a measure of the surface functionalization vs time of treatment for DBD and UV irradiation. The surface polarity is defined by the ratio between the polar component (γ_{SV}^{p}) of surface free energy and the surface free energy ($\gamma_{SV} = \gamma_{SV}^{p} + \gamma_{SV}^{d}$). So, the surface polarity is increased in both methods of treatment but the DBD treatment is evidently more favorable to maximize the functionalization in very short time (a few seconds) (Figs. 1 and 2). These results may suggest that the most important parameter in functionalization is not the duration of treatment and the level of energy but the duration of interaction at the level of particles and photons. In the case of DBD there are interactions as photons-surface and particles-surface. So, in the DBD we have collisions between the species from the plasma and the macromolecules, free radicals, atoms etc. and the duration of interaction is comparable with the duration of physico-chemical reactions on the surface. But in UV treatment there are exclusively photons, which has a very short duration of interaction with particles at the surface. To conclude, for a maximum transfer of energy from external source of excitation to the surface, it is necessary to have approximately the same duration of interaction. Moreover at the polymers surface the dynamic of processes are significantly different from the bulk.

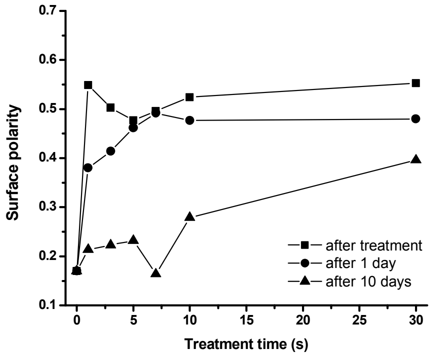

Fig.1.a. Surface polarity of PET films treated by DBD.

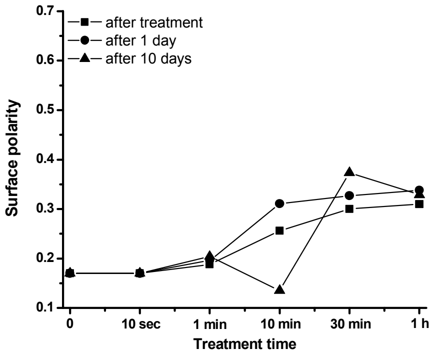

Fig.1.b. Surface polarity of PET films treated by UV.

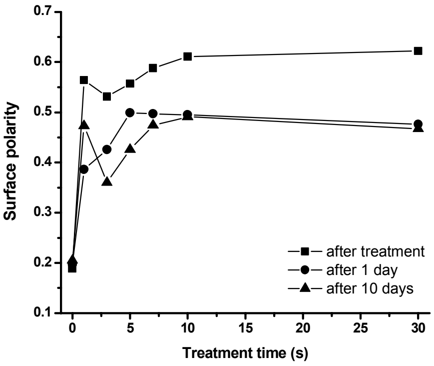

Fig.2.a. Surface polarity of PET+TiO_2 films treated by DBD.

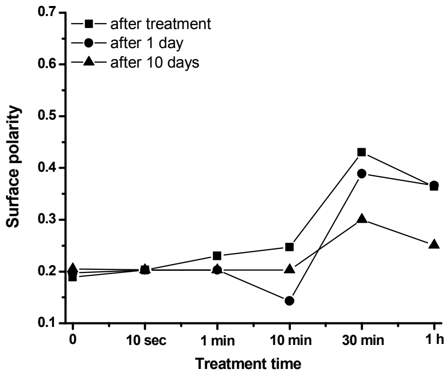

Fig.2.b. Surface polarity of PET+TiO_2 films treated by UV.

One of the functionalization effects is the improving of adhesion properties at the surface. Work of adhesion as a measure of the surface wettability and adhesion properties is increased after the DBD and UV treatments in all types of films, i.e., in the case of PET films (Figs. 3.a. and 3.b.) and PET+TiO_2 (Figs. 4.a. and 4.b.), too. In DBD treatments the maximum values of adhesion is achieved in a few seconds of treatments in comparison with the UV irradiation where 1h of treatment is necessary to obtain a similar effect, that in spite of the fact that DBD power was of the order of 40W while the UV mercury lamp had 80W.

Similar results are presented in ref. [1], where adhesion significant processes are completed within some seconds. Introduction of functional groups, a reorientation of mobile chains near the surface and their optimum arrangement along the interface may explain this increasing of the adhesion properties in the both methods of treatments. This is possible because the polymer chains have more free volume at the surface than in the bulk and a high degree of freedom and various orientations are expected.

The time evolution of adhesion properties and surface polarity (ageing phenomena) are considered and the differences are observed, the subsequent surface dynamics being different in the two methods of treatments (Figs. 1 - 4). So, the PET and PET+TiO_2 films treated by DBD kept a high wettability and surface polarity even 10 days. A comparison of the effects provoked by DBD and UV irradiation and their time evolution suggests that it is less probable that UV radiation from DBD to action as a stabilizer of surface properties and more important could be the excited and free radicals species from the plasma.

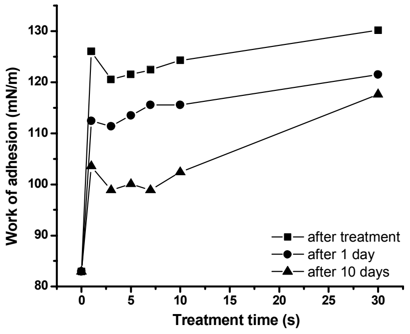

Fig.3.a. Adhesion work of distillated water on PET films treated by DBD.

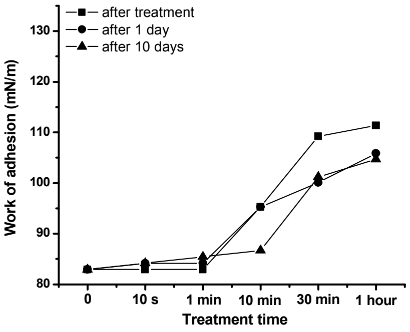

Fig.3.b. Adhesion work of distillated water on PET films treated by UV.

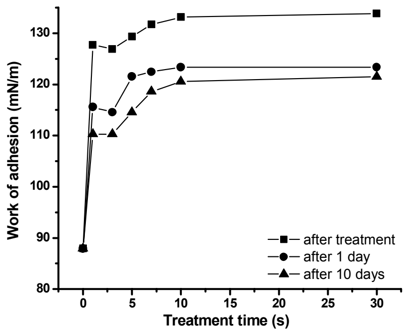

Fig.4.a. Adhesion work of distillated water on PET+TiO_2 films treated by DBD.

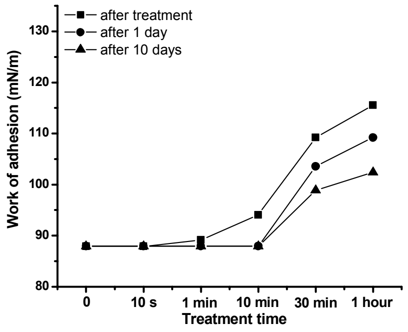

Fig.4.b. Adhesion work of distillated water on PET+TiO_2 films treated by UV.

Another consequence of surface functionalization is the crosslinking reaction initiated by the plasma treatments; it is observed that the index of crystallinity is maximum after some seconds of DBD treatments (Table 1). UV irradiation does not initiate a crosslinking reaction at the surface. These higher crosslinked layers created by DBD treatments can restrict the molecular chain mobility and the diffusion of free radicals, assuring stabilization in time of surface properties (see Figs. 3.a. and 4.a.).

Sample	**2θ**	**d_{hkl} (Å)**	**f_c**
Untreated PET	29.46	3.475	0.64
Untreated PET+TiO_2	29.73	3.489	0.56
PET 10s DBD treated	29.96	3.463	0.66
PET+TiO_2 10s DBD treated	29.86	3.474	0.63
PET 1h UV treated	30.15	3.441	0.64
PET+TiO_2 1h UV treated	30.07	3.450	0.56

Table 1. The variations of structural parameters of treated and untreated PET and PET+TiO_2 films.

Surface functionalization may give not only new adhesion properties and crystalline structure of polymers but also it can to generate chemical reaction, and for this reason the surface chemistry were evaluated.

In our opinion the chemical processes and formation of new products are not dominant at the interface. We worked in helium and less reactive chemical groups are expected on the surface. A high mobility of the functional groups, their rearrangement and bonds between neighboring polymer chains are more probable than chain scission. By FTIR-ATR it has investigated the characteristics peaks in of PET IR absorbency: free OH at (3650-3590cm^{-1}), CH_2 (2855-2925cm^{-1}), C=O (1705-1720cm^{-1}), C-O (1240-1400cm^{-1}) and C-H from aromatic ring (720-760cm^{-1}) and new functional groups were not identified in the DBD treatments and within the limits of measurement error of the intensities. It is interesting to emphasize that OH free groups are not increased after the treatments, probably other hydrophilic functional groups such CO (Figs. 5.a and 5.b.) are important in the mechanism of hydrophylization and crosslinking.

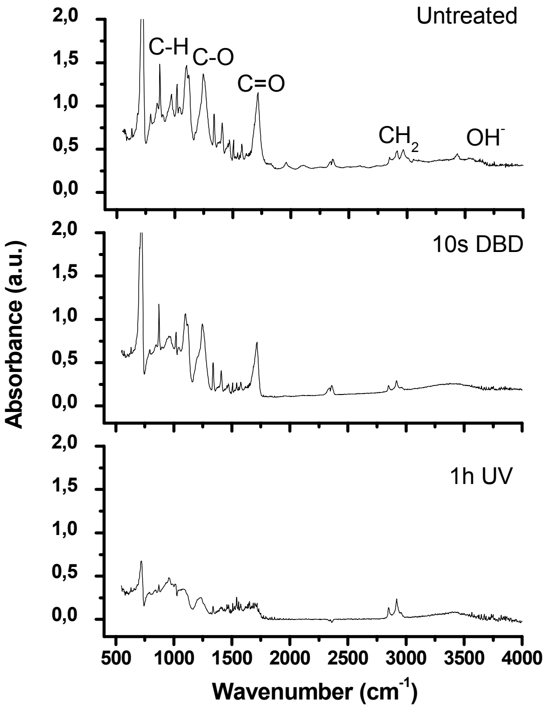

Fig.5.a. ATR-FTIR spectra of PET films.

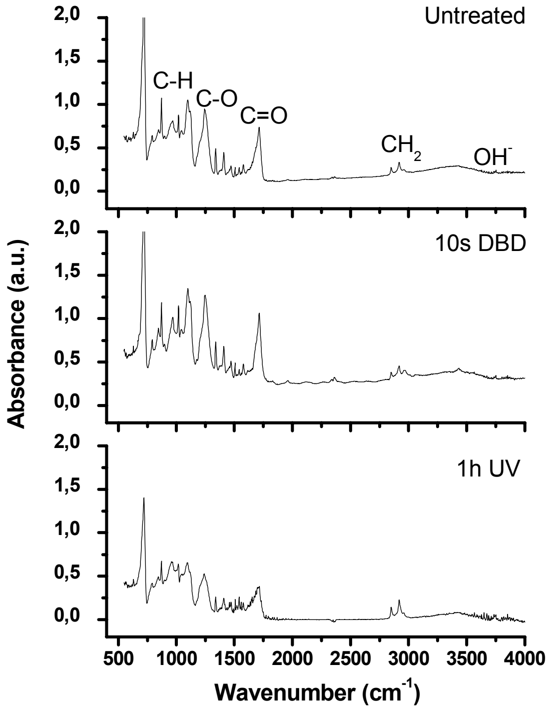

Fig.5.b. ATR-FTIR spectra of PET+TiO_2 films.

In the case of UV treatments a chemical photodegradation process is very clear and probably this degradation is promote by carboxyl group formation and the presence of TiO_2 in PET+TiO_2 films; when TiO_2 is exposed to UV in its crystal lattice more positive holes are created and a mechanism of photodegradation could be initiated [7].

Reactions with oxygen from a variety of sources (atmospheric air, excited molecules etc) are possible after the treatments and the humidity of the environment could be an essential ingredient of the degradation/oxidation processes [9].

Finally we show the effects of DBD and UV irradiation on the optical properties (preliminary results) of the PET and PET+ TiO_2 films. We made measurements at two samples orientations taking into account that biaxially drawn films have different optical anisotropy and molecular orientation. The results are presented in the Table 2 and show a decreasing in refraction index and in the surface anisotropy, proved by less differences when we change the orientation (parallel and normal) of the surface in the incidence plane of laser light. The results presented in Table 2 are an average of then measurements taken from different points on the surface.

Sample	**n**		**k**	
	parallel	*normal*	*parallel*	*normal*
Untreated PET	1.732	2.235	0.661	0.565
10s DBD treated PET	1.537	1.608	1.039	0.789
Untreated PET+TiO_2	1.982	1.933	0.385	0.513
10s DBD treated PET+TiO_2	1.625	1.873	0.431	0.222

Table 2. The variations of optical properties of treated and untreated PET and PET+TiO_2 films.

The surface morphology studied by AFM showed a new distribution and size of the grains, the roughness of the surface being modified. R_{rms} (root mean square roughness) is strongly dependent of time exposure by DBD and UV irradiation. Nevertheless, a regular structure was not detected after the both methods of treatments. It is possible to have more nanometer size particles, but this aspect has not been considered. Table 3 present values of R_{rms} before and after the DBD treatments.

Sample	**R_{rms} (nm)** *Untreated*	**R_{rms} (nm)** *10s DBD Treated*
PET	6.7	7.8
PET+TiO_2	3.5	3.3

Table 3. The root mean square roughness (R_{rms}) of PET and PET+TiO_2 films before and after the DBD treatments.

3. Conclusions

The DBD treatment needs of few seconds to provoke certain surface modifications on the PET and PET+TiO_2 films and for obtaining similar effects by UV irradiation we need a treatment duration more than 1h. The treatment effects at the surface can be understood as a dynamic and competitive equilibrium between the functionalization, crosslinking and degradation processes.

- *Morphology* of PET and PET+TiO_2 films is modified after both the DBD and UV treatments; it shows a new distribution and size of the grains and the roughness of the surface was modified.
- *Surface energy* and its *polarity* are increased after the both methods of treatment. Wettability decays in time but the treatment by DBD is more effective in keeping the surface properties; thus wettability is stabilized even 10 days after the DBD treatments. Storing for a long time in air conditions the surfaces treated by DBD remain more wettable and stabilized probably due to a crosslinked structure.
- *Crystalline structure* of the films investigated by XRD showed a polycrystalline phase of the films. The crystallinity factor is higher after DBD treatments and an increase of the lattice constant is observed after the both methods of treatment.
- *Chemical structure* of the films investigated by FTIR-ATR does not show new functional groups. It showed that OH bonds are not affected by the DBD treatments, but in the case of UV treatments a chemical photodegradation process is initiated.

Effects of *functionalization* and *crosslinking* on the surfaces of PET and PET+TiO_2, are initiated by DBD treatments in helium in a few seconds of treatments. That is why the DBD treatments could be a simple and faster technique for functionalization and crosslinking, with low production costs and good efficiency.

References

[1] J. F. Friedrich, *Plasma modification of polymers* in *Polymer-Solid interfaces*, IOP Publishing Ltd, 1992.

[2] *Biomaterials Science, An introduction to Materials in Medicine*, Eds B. D. Ratner et al., Academic Press, San Diego, 1996.

[3] K. J. Pratt, S. K. Williams, B. E. Jarrell, J. Biomed. Mat. Res. **23**, 1131 (1989).

[4] N. Dumitrascu et al., Materials Chemistry and Physics **65,** 339 (2000).

[5] N. Dumitrascu, G. Borcia, N. Apetroaei, G. Popa, Plasma Sci. Technol. **11**, 1 (2002).

[6] T. Miyamae, H. Nozoye, J. Photochemistry and Photobiology **A145**, 93 (2001).

[7] G. J. M. Fechine, M. S. Rabello, R, M. Souto-Maior, Polymer Degradation and Stability **75**, 153 (2002).

[8] S. Polizzi, G. Fagherazzi, A. Benedetti, M. Battagliarin, T. Asano, J. Appl. Cryst. **23,** 359 (1990).

[9] J. M. Pochan, L. J. Gerenser, J. F. Elman, Polymer **27**, 1058 (1986).

Enthalpy probe measurements of nitrogen thermal plasma characteristics depending on anode nozzle geometry of non-transferred torch for materials processing

T. H. Hwang[1], J. H. Seo, D. U. Kim, S. S. Choi, J. S. Nam, and S. H. Hong

[1] *Department of Nuclear Engineering, Seoul National University, Seoul 151-742, Korea*

The enthalpy probe measurements are made to find the spatial distributions of enthalpy and velocity in the nitrogen thermal plasmas generated in the atmospheric-pressure condition by the DC non-transferred plasma torches with different anode geometries of tubular and stepped nozzles, respectively. And the radial distributions of plasma temperature and density are calculated from the measured plasma enthalpies on the basis of the assumption of local thermodynamic equilibrium (LTE). The nitrogen thermal plasma properties produced with different types and diameters of the anode nozzle are compared. From these comparative studies on the effects of anode nozzle geometry on the nitrogen thermal plasma characteristics, the optimum design conditions of nozzle type and geometry can be determined for the non-transferred plasma torches to be used for materials processing, such as plasma spraying, synthesis, CVD and so on.

Self-consistent modelling of an atmospheric argon plasma jet sustained by microwave power

V. K. Liau, C. F. Pau, M. T. C. Fang and J. D. Yan

Department of Electrical Engineering and Electronics, University of Liverpool

Abstract

A two-dimensional, axisymmetric, two-temperature argon plasma jet sustained by microwave power at 2.45GHz with 6l/min gas flow rate and 500W source power was modelled theoretically. Conservation and Maxwell's equations are solved in a self-consistent manner. The plasma jet consists of an active zone where there is a strong interaction between the microwave field and the plasma and a weakly illuminating tail. From the simulation results, the electron temperature in the active zone is above 10000K, the plasma density above $1.0\times10^{22}/m^3$ and the highest heavy particle temperature around 3500K.

1. Introduction

Recently, atmospheric microwave plasma has been increasingly used in industrial applications, especially in surface spraying, wielding and coating [1]. The electrodeless design of the plasma makes it suitable for use in processing non-metallic material as well as metallic materials. Moreover, compared with low-pressure plasma, atmospheric microwave plasma does not require a containment vessel which makes it cost-effective. Over the past few decades, various atmospheric microwave plasma systems have been developed [2-3]. The current waveguide-based microwave plasma system developed at Liverpool University is far simpler and cheaper than the existing microwave plasma systems [4]. A schematic diagram of the microwave plasma system is shown in Figure 1.

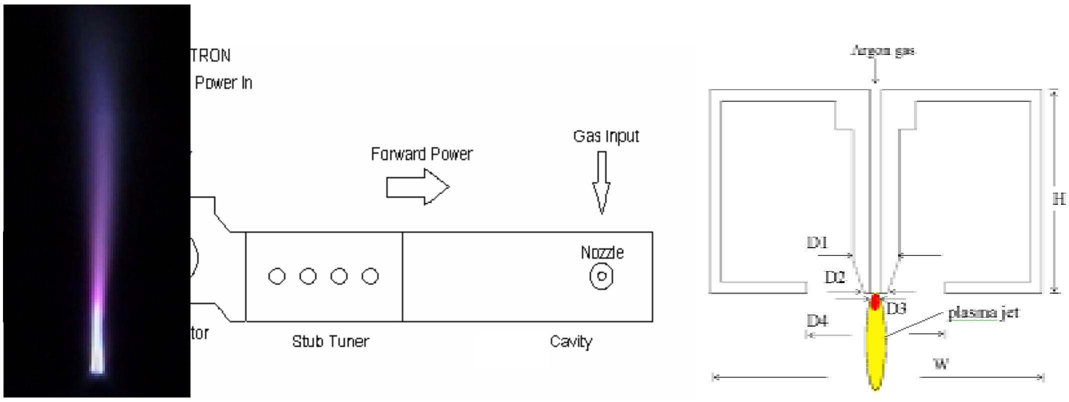

(a) (b) (c)

Figure 1. Schematic diagram for the microwave system (1a), schematic diagram for the cavity and nozzle (1b), and photo showing the plasma jet (1c). Dimensions in mm H=43, W=86, D1=8, D2=3, D3=1.2, D4=50

The axis of the nozzle in Figure 1 is located a quarter wavelength away from the short circuited end of the waveguide. High speed argon gas is fed into the nozzle. In the absence of the metallic nozzle, TE10 mode is excited in the waveguide. A circular hole (known as the aperture) is drilled at the bottom plate of the waveguide. The microwave energy leaking out from the aperture interacts with the metallic nozzle to produce a high electric field around the nozzle tip. Breakdown is initiated by placing a sharp pin close to the nozzle tip, which is subsequently removed. After the breakdown, the rate of ionisation builds up rapidly which subsequently increases the electrical conductivity in the breakdown region. Due to the presence of the high electrical conductivity region, the microwave field tends to be guided along the surface of the highly conducting core. A steady state plasma jet is maintained when the electric field along the surface of the plasma jet is such that the power input from the microwave field balances the energy loss processes. Proper design of the nozzle shape, the aperture size and the gap between the nozzle exit and the bottom plate of the waveguide is important to produce a stable and energy-efficient plasma jet.

Recent spectroscopic measurements [5] show that the plasma is not in local thermal equilibrium (LTE). The electron temperature has been found higher than the heavy particle temperature inside the active zone. The objective of the present investigation is to establish a two-temperature plasma model to elucidate the coupling between the plasma and microwave fields. In Section 2, the governing equations and an outline of the solution methodology are given. This is followed by a presentation of the computational results together with a comparison with the available experimental results. Attention is given to the case where the microwave source power is set at 500W and the argon gas flow rate at 6l/m. Finally, appropriate conclusions are drawn.

2. Theoretical Model

In the present calculation, the plasma jet is assumed to be laminar, axisymmetric and consists of electrons, singly ionised argon ions and argon neutrals. Since the argon plasma jet is at atmospheric pressure, frequent collisions between electrons and heavy particles ensure that the macroscopic motion of the electrons is locked with that of heavy particles. Thus, the movement of the plasma jet is described by the overall mass and momentum conservation equations:

$$\frac{\partial \rho}{\partial t} + \nabla \cdot \left(\rho \vec{V}\right) = 0 \tag{1}$$

$$\frac{\partial}{\partial \mathrm{t}}(\rho \mathrm{v}) + \nabla \cdot (\rho \vec{\mathrm{V}} \mathrm{v}) - \nabla \cdot [\mu_l \nabla \mathrm{v}] = -\frac{\partial P}{\partial r} + \frac{1}{r}\frac{\partial}{\partial r}[r\mu_l \frac{\partial v}{\partial r}] + \frac{\partial}{\partial z}[\mu_l \frac{\partial w}{\partial r}] - \frac{2}{3}\frac{\partial}{\partial r}[\mu_l \frac{1}{r}\frac{\partial}{\partial r}(rv) + \mu_l \frac{\partial w}{\partial z}] - \frac{2\mu_l v}{r^2} \tag{2}$$

$$\frac{\partial}{\partial \mathrm{t}}(\rho w) + \nabla \cdot (\rho \vec{\mathrm{V}} \mathrm{w}) - \nabla \cdot [\mu_l \nabla w] = -\frac{\partial P}{\partial z} + \frac{1}{r}\frac{\partial}{\partial r}[r\mu_l \frac{\partial v}{\partial z}] + \frac{\partial}{\partial z}[\mu_l \frac{\partial w}{\partial z}] - \frac{2}{3}\frac{\partial}{\partial z}[\mu_l \frac{1}{r}\frac{\partial}{\partial r}(rv) + \mu_l \frac{\partial w}{\partial z} \tag{3}$$

where v and w are respectively the mass averaged radial and axial component of the velocity, P the pressure, ρ the density, μ_l the viscosity and $\vec{V}$ is the mass-averaged velocity of the plasma particles. The mass density is determined from

$$\rho = m_e n_e + m_a(n_i + n_a) \cong m_a(n_a + n_e) \tag{4}$$

where m_e is the electron mass, m_a the atomic mass of argon, n_e the electron number density which is equal to n_i, the ion number density and n_a the atom number density.

The conservation equation for electron number density reads as

$$\frac{\partial}{\partial t}(n_e) + \nabla \cdot \left[n_e \vec{V} + \vec{g}\right] = \alpha n_a \left[S(T_e) - \frac{n_e^2}{n_a}\right] \tag{5}$$

where $\vec{g}$ is the electron diffusion flux, α the recombination coefficient, $S(T_e)$ the LTE ratio for ionisation equilibrium and T_e the electron temperature. α can be written as [6,7]

$$\alpha = \begin{cases} 1.29\times10^{-44}(\dfrac{135300}{T_e} + 2)\exp(\dfrac{47800}{T_e})n_e & ,T_e > 3000K \\ 1.09\times10^{-20} n_e T_e^{-9/2} & ,T_e < 3000K \end{cases} \tag{6}$$

The ratio for ionisation equilibrium $S(T_e)$ is defined as:

$$S(T_e) = \frac{2Z_i(T_e)}{Z_a(T_e)}\frac{(2\pi m_e k_b T_e)^{3/2}}{h^3}\exp\left(-\frac{E_i}{k_b T_e}\right) \tag{7}$$

where Z_i and Z_a are the partition functions of argon ions and atoms respectively, E_i the ionisation energy of argon atoms at ground state, k_b the Boltzmann's constant and h the Planck constant.

The electron diffusion flux, $\vec{g}$ is dominated by ambipolar diffusion due to density gradient.

$$\vec{g} = -\frac{(n_a + 2n_e)^2 m_a}{\rho} D_A \nabla\left(\frac{n_e}{n_a + 2n_e}\right) \tag{8}$$

where D_A is the ambipolar diffusion coefficient [8].

The energy conservation equation for electrons reads

$$\begin{aligned} &\frac{\partial}{\partial t}\left(\frac{5}{2}k_b n_e T_e\right) + \nabla\cdot\left\{\left(\frac{5}{2}k_b n_e T\right)\vec{V} - k_{el}\nabla T_e + \frac{5}{2}\vec{g}k_b T_e\right\} \\ &= \operatorname{Re}\langle\sigma\rangle\left(\vec{E}\cdot\vec{E}^*\right) - \frac{3m_e}{m_a}k_b(T_e - T_h)n_e\gamma_{eh} - \gamma_1 E_i - S_{exc} \end{aligned} \tag{9}$$

where T_h is the heavy particles temperature, k_{el} the electron thermal conductivity, γ_{eh} the momentum transfer collision frequency between one electron and heavy particles (ions and atoms), S_{exc} the energy loss due to excitation, Re<σ> the real part of electrical conductivity, * denotes complex conjugate and $\vec{E}$ is the electric field. The terms on the left hand side represent, respectively, the time dependent term, energy transport terms by convection, thermal conduction and diffusion. On the right hand side, the terms account respectively Ohmic heating, energy transfer to heavy particles due to elastic collisions, ionisation and excitation (S_{exc}) losses. An accurate account of the excitation loss needs to consider the population of all relevant excitation levels of argon atoms and ions, which is beyond the scope of the present investigation. It is assumed that excitation losses accounts for 80% of the total power input to the plasma jet as indicated from the work of Ferreira [9]. Radiation has been found negligible.

The energy conservation equation for heavy particles is given by

$$\frac{\partial}{\partial t}\left(\frac{5}{2m_a}\rho k_b T_h\right) + \nabla\cdot\left[\vec{V}\left(\frac{5}{2m_a}\rho k_b T_h\right) - \frac{k_{hl}}{c_{pa}}\nabla\left(\frac{5}{2m_a}k_b T_h\right)\right] = \frac{3m_e}{m_a}k_b(T_e - T_h)n_e\gamma_{eh} \tag{10}$$

where k_{hl} is the heavy particles thermal conductivity and c_{pa} is the specific heat capacity at constant pressure.

The electric conductivity of the plasma is given by

$$\sigma = \frac{e^2 n_e}{m_e}\frac{1}{\gamma_{eh} + j\omega} \tag{11}$$

where ω is the angular frequency of the applied microwave field.

Since $\varepsilon_p = 1 - j\dfrac{\sigma}{\omega\varepsilon_0}$, we readily arrive at the corresponding relative plasma permittivity

$$\varepsilon_p = \left(1 - \frac{\omega_p^2}{\omega^2 + \gamma_{eh}^2}\right) - j\left(\frac{\gamma_{eh}}{\omega}\frac{\omega_p^2}{\omega^2 + \gamma_{eh}^2}\right) = \varepsilon_{pr} + j\varepsilon_{pi} \tag{12}$$

where ε_{pr} and ε_{pi} are respectively the real and imaginary part of the relative plasma permittivity and ω_p the electron plasma frequency.

The coupling between the plasma and microwave fields is through Ohmic heating and the plasma permittivity which can be written as follow:

$$\nabla\left(\nabla \cdot \vec{E}\right) - \nabla^2 \vec{E} = \varepsilon_{pr} \frac{\omega^2}{c^2} \vec{E} + j\varepsilon_{pi} \frac{\omega^2}{c^2} \vec{E} \tag{13}$$

Equation (13) is solved for the axial and radial components. Each component is further decomposed to real and imaginary parts.

The equation of state is given by

$$P = n_e k_b T_e + (n_i + n_a) k_b T_h \tag{14}$$

Solutions to the above equations are subjected to the appropriate boundary conditions for axisymmetric plasma jet. The radial velocity and the radial component of electric field and the radial derivatives of all other relevant quantities should vanish on the axis. The axial and radial derivatives of all quantities are set zero far away from the plasma jet.

The boundary conditions for the real part of the axial electric field need special consideration. The discharge is first initiated in a small region close to the nozzle exit. The rapid increase in the electron number density in this region affects the field distribution. The increased electrical conductivity tends to guide the microwave along the surface of this active region. A steady state is reached when the electric field along the surface of this active zone is just sufficient to maintain the energy balance of the electrons as well as the ionisation equilibrium. The field along this boundary is computed by Concerto [10] assuming a known distribution of electric conductivity of the region occupied by the plasma jet. It was found that the radial component is negligible. This initial electric field is taken as boundary conditions. With the field boundary conditions so specified, the governing equations as well as the field equation are solved simultaneously by PHOENICS [11]. The updated plasma conductivity is input to CONCERTO to obtain improved electric field boundary conditions and the whole process repeats until satisfactory solutions are obtained.

3. Simulation Results

Attention is focused on the case for which the power from the source generator is 500W and the argon flow rate of 6l/min. The nozzle exit diameter is 1.2mm. It has been found that the reflected power to the source is less than 5% of the incident power. Thus, 475W accounts for the power consumed in the plasma jet, radiated to the surroundings and losses in the waveguide system.

Figure 2(a) and 2(b) show the calculated electron and heavy particle temperature profiles respectively. The active zone of the plasma jet is about 5mm in length, starting from 2.5mm to 7mm below nozzle exit. The electron temperature is above 10000K inside the active zone. The maximum heavy particle temperature is 3500K which is located away from the active zone. Inside the active zone, the heavy particle temperature increases rapidly due to the large difference between electron and heavy particle temperatures. Since there are insufficient collisions for energy transfer from electrons to heavy particles, the plasma jet is far from thermal equilibrium. Outside the active zone, the heating of electrons by microwave is negligible and electrons are rapidly thermalised with heavy particles to attain a single temperature of around 3000K. The computed electron and heavy particle temperatures along the axis are given in figure 3(a) together with the experimentally measured electron temperature, which shows an agreement within the measurement errors.

The calculated electron number density is shown in figure 2(c), with the maximum value of $1.4\times10^{22}\text{m}^{-3}$ off the axis showing the skin effect. The electron number density is lower than that of the plasma under LTE at the same electron temperature and total pressure, thus indicating the over population of the ground level of argon atoms. Away from the active zone, the electron number density reduces rapidly to the value of the order of 10^{20}m^{-3}. The electron number density on the axis, together with experiment measurement are plotted in figure 3(b), which shows good agreement. The jet velocity is mainly determined by the cold gas emerging from the nozzle. The highest velocity of 152m/s^{-1} is attained inside the active zone as shown in figure 2(d) and the subsequent expansion of the jet reduces the axis velocity close to the axis velocity of the cold argon jet. To generate the required flow acceleration in the active zone, the required pressure gradient is rather small and the pressure is near atmospheric for the whole jet.

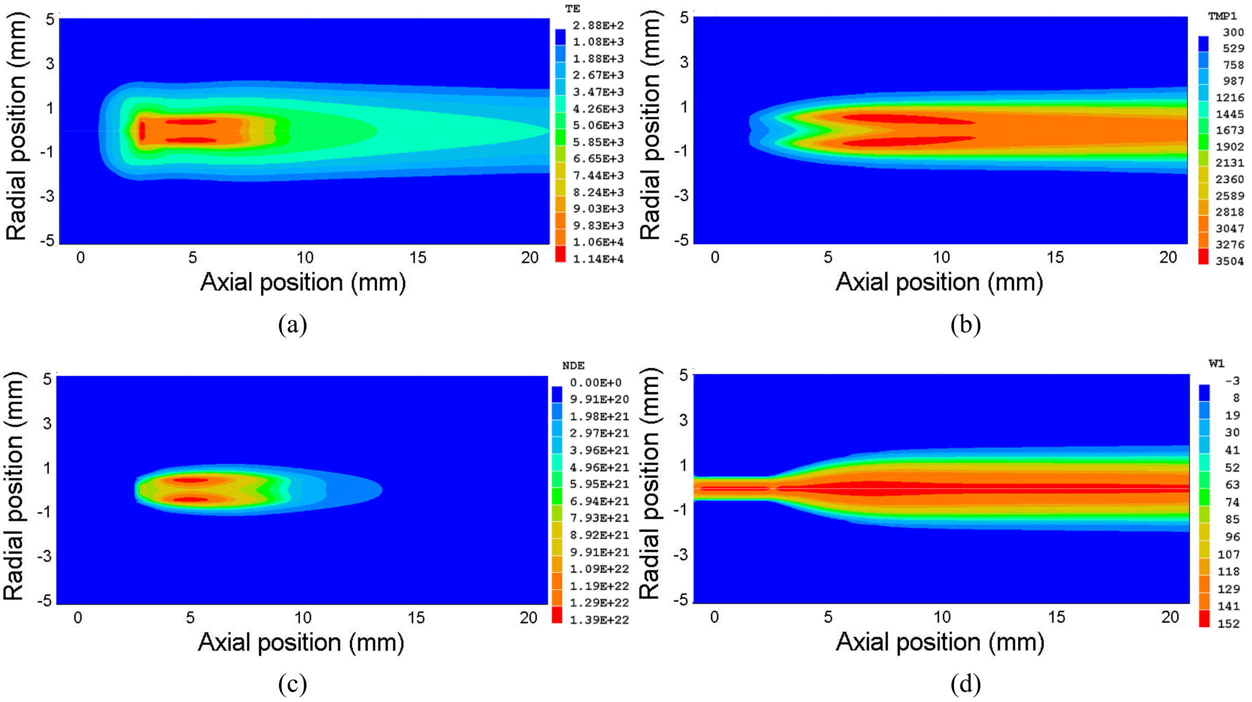

(a) (b)

(c) (d)

Figure 2 Results of an argon plasma jet at 2.45GHz with gas flow rate of 6l/min and microwave source power of 500W for (a) electron temperature, (b) heavy particle temperature, (c) electron number density and (d) axial velocity profiles.

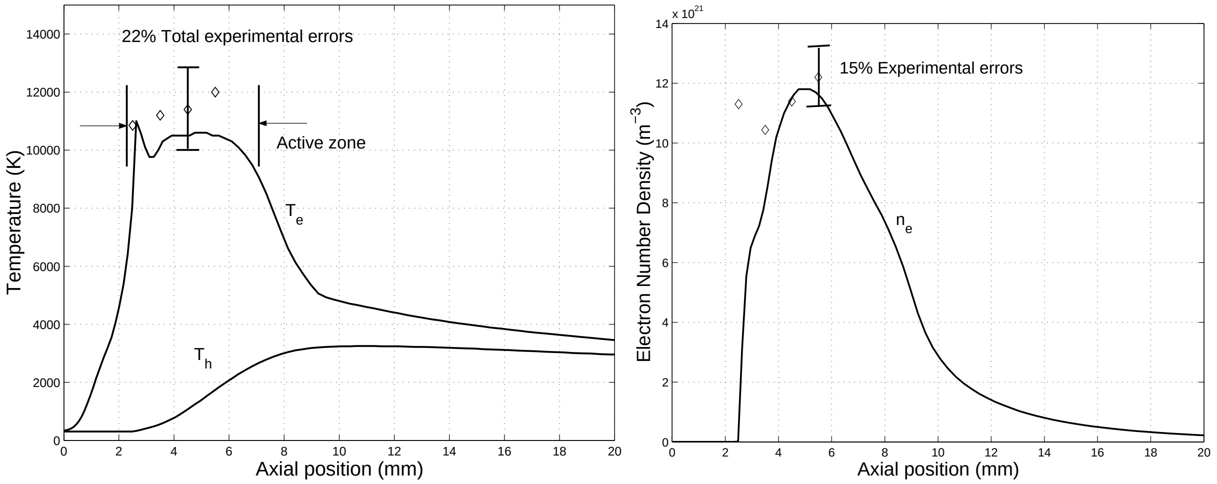

(a) (b)

Figure 3 (a) Comparison of electron and heavy particle temperatures and, (b) profile of electron number density on axis together with experimental results from [5] for an argon plasma jet at 2.45GHz with gas flow rate of 6l/min and microwave source power of 500W.

The axial and radial electric field distributions are shown in figure 4(a) and 4(b) respectively. It is obvious that the radial electric field is smaller than the axial electric field. Nevertheless, the radial electric field need to be included in the calculation since the first term on the left hand side of equation (13), i.e. $\nabla(\nabla\cdot\vec{E})$ can not be neglected. Skin effects could be clearly observed in figure 4(a). Because of the skin effect, the maximum electron number density and electron temperature are off the axis as shown in figures 2(b) to (c). The maintenance electric field is around 25kVm^{-1}. The total power dissipated inside the plasma jet has been found to be 455W.

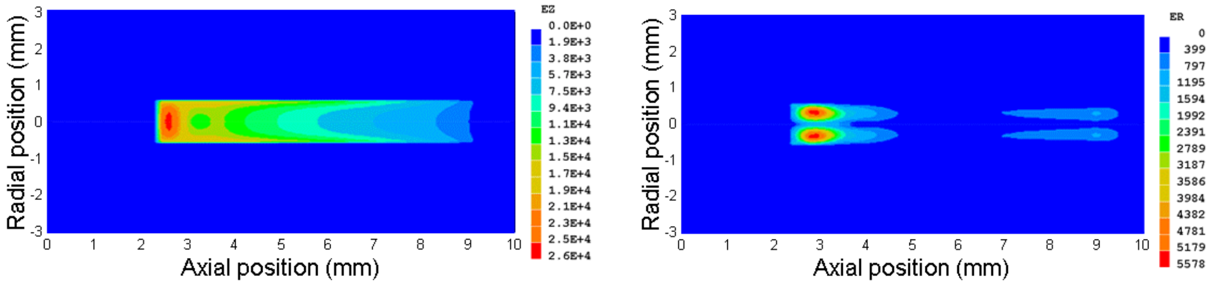

(a) (b)

Figure 4 (a) Axial component and (b) radial component of the electric field distribution of an argon plasma jet at 2.45GHz with gas flow rate of 6l/min and microwave source power of 500W.

4. Conclusions

A two-temperature plasma model has been developed for the simulation of an atmospheric microwave argon plasma jet operating at 2.45GHz with microwave source power setting of 500W and gas flow rate of 6l/min. Electromagnetic field radiated from the aperture propagates along the surface of the core of high electrical conductivity. It attenuates fairly rapidly due to the power absorbed by the plasma in the active zone. In general, the electron temperature is above 10,000K, plasma density above $1.0\times10^{22}/m^3$ and the highest heavy particle temperature around 3500K. The main electron energy loss process is by inelastic collisions with argon atoms, mainly due to excitation processes, which is around 80% of the input power into the plasma jet. A more accurate account of the energy loss due to excitation would require the use of collisional radiative model, which is beyond the scope of the present investigation. The power density inside the active zone is around $10^{11}Wm^{-3}$. Outside of the active zone, power input is negligible and electrons and heavy particles are rapidly thermalised to attain a single temperature around 3000K.

5. Acknowledgement

The research forms part of a programme supported by the EPSRC of the UK. Two authors (VKL and CFP) thank Lee Foundation for financial support.

References

[1] H. Conrads and M. Schmidt, Plasma Sources Sci. Technol., 9, 441 (2000)
[2] M. Moisan, G. Sauve, Z. Zakrzewski and J. Hubert, Plasma Sources Sci. Technol., 3, 584 (1994)
[3] Y. Arate, S. Miyake, S. Takeuchi and Kobayashi, Transactions of JWRI, 4, 31 (1975)
[4] A. I. Al-Shamma'a, S. Wylie and J. Lucas, J. Phys D., 34, 2734 (2001)
[5] C. F. Pau, Microwave Generated Plasma Jet for Material Processing, Phd Thesis, University of Liverpool (2000)
[6] M. I. Hoffert and H. Lien, Phys. Fluids, 10, 1769 (1967)
[7] M. Mitchner and C. H. Kruger, Partially Ionized Gases, John Wiley and Sons, New York (1973)
[8] R. S. Devoto, Phys. Fluids, 10, 354 (1967)
[9] C. M. Ferreira and M. Moisan, Microwave Exited Plasmas (Plasma Technology) (Amsterdam: Elsevier), edited by M. Moisan and J. Pelletier, 63 (1992)
[10] Concerto is supplied by Vector Field Ltd which is based at 24 Bankside, Kidlington, Oxford,OX5 1JE, UK.
[11] Phoenics is supplied by CHAM which is based at Bakery House, 40 High Street, Wimbledon Village, London SW19 5AU, UK.

Enthalpy probe analysis on thermal plasma characteristics of DC-RF hybrid plasma jets

J.H. Seo, T.H. Hwang, J.S.Nam, S.I.Choi And S.H.Hong

Department of Nuclear Engineering, Seoul National University, Seoul 151-742, Korea

Abstract

Enthalpy probe measurements are carried out in order to investigate the effects of operating and design parameters, such as swirl in sheath gas flow, DC gas flow rate, DC input power, and anode nozzle diameter, on the characteristics of the DC-RF hybrid plasma for various industrial applications. From the results of measurements, it is especially found that the sheath gas flow rate with a swirl has significant effects on the radial temperature profile of hybrid plasma and the reheating process of central arc column as well as the expansion of the stagnation region of axial mass flux near the DC torch exit. It is concluded from this experimental work that the unique features of hybrid plasma in temperature and velocity fields are controllable by these operating and design parameters.

1. Introduction

The unique characteristics of DC-RF hybrid plasma in temperature and velocity fields have been well known from the results of numerical analyses and utilized in many practical applications such as materials synthesis, thermal plasma CVD process and thermal plasma spray coating. A numerical characterization of DC-RF hybrid plasma was reported by T. Yoshida et al [1], who predicted that the hybrid plasma had two temperature peaks in a coil inlet region, one located on the axis and the other placed off axis towards the confinement tube wall. And, as the hybrid plasma was passing through the coil region, this two-peak radial temperature profile had gradually changed into the temperature profiles with a single off-axis profile. This temperature profile change was caused by the radial heat conduction from RF induction region to a central DC arc column but it was not so effective to heat up the DC arc column completely due to the shortness of the induction coil and the fast transit time of the DC arc column. So that, the gas emerging from the coil in a central DC arc column was reheated up from outer RF induction region at the exit of the coil region. This reheating process experienced by the central arc column was considered to be a feasible phenomenon for actual applications requiring an effective heating of axially injected reagents. Moreover, a relatively insensitive character of the exit plasma enthalpy to the RF input power was also introduced as a prominent feature of hybrid plasma because it is able to offer higher efficiencies in input power for practical applications using the central channel.

Based on the above-mentioned useful features of hybrid plasma, an application of DC-RF hybrid torch in the preparation of Si_3N_4 was also reported by T. Yoshida et al [1], and recently, R. Shimpo et al used it for the fabrication of Ni-YSZ cermet electrode for SOFC (Solid Oxide Fuel Cell) [2]. In addition to the numerical characterization by T. Yoshida et al, the advantage of hybrid plasma for materials synthesis and plasma spraying have been numerically investigated by J.W. McKelliget et al [3] and S.W. Nam et al [4], respectively.

However, there are lack of experimental data for the hybrid plasma characteristics created under the various design and operating conditions, which are essential in actual design and applications of hybrid plasma torch systems. Therefore, it is of importance to investigate the effects of these conditions experimentally on the flow fields and overall energy distributions of hybrid plasma, which are needed for optimal design and applications of DC-RF hybrid plasma torches. For this purpose, the temperature and velocity distributions of hybrid plasma obtained from the enthalpy probe measurements are presented with the variations of design and operation parameters, such as sheath gas flow rate with a swirl, anode nozzle diameter of the DC torch, DC gas flow rate and DC current, and they are discussed together with the overall heat conduction distributions in the hybrid plasma.

2. Experimental Setup

An experimental system layout and a DC-RF hybrid torch used in the present measurement study are shown in Fig.1 and Fig.2, respectively. Experimental apparatus in Fig. 1 consists of a hybrid torch mounted on a discharge chamber, DC and RF power supplies, gas and coolant supplies, and an impedance matching box for an effective transport of RF power to the torch.

A DC torch with a nozzle diameter of 6 mm (or 8mm) is attached on the top of an RF torch with an inner diameter of 50 mm and a 4-turn induction coil, molded in acryl structure by epoxy, which is connected to a 25 kW, 4 MHz RF power supply. The principal dimensions of the hybrid torch shown in Fig. 2 are given in Table 1.

An enthalpy probe with an outer diameter of 4.8mm and an inner diameter of 1.5mm is placed at the torch exit for measurements of temperature and velocity distributions. It is made of three concentric stainless steel tubes with different radii, and connected to the coolant supply and gas sampling systems.

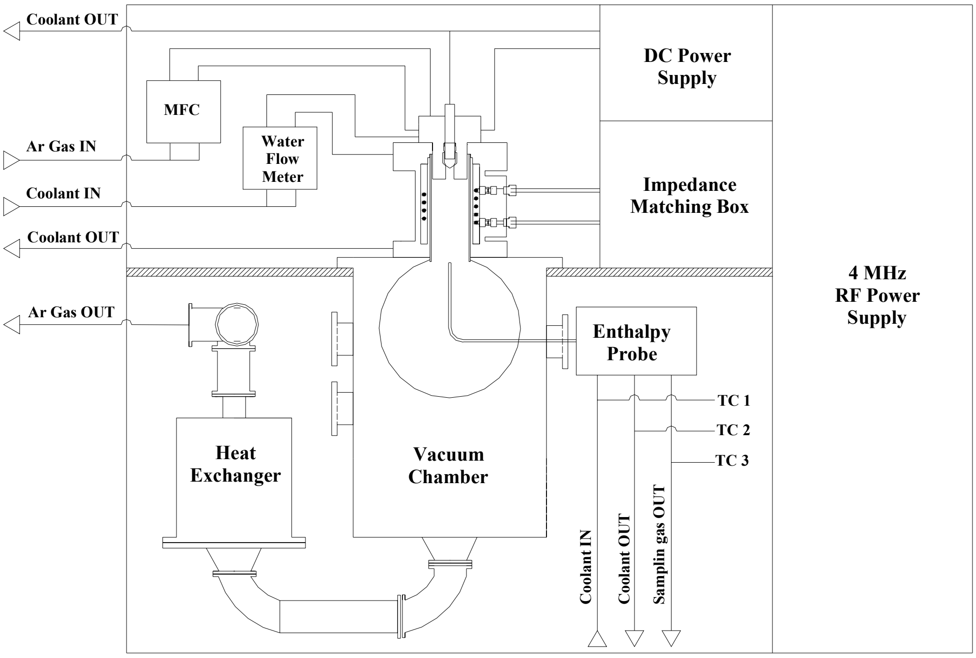

Fig.1 Schematic diagram of experimental setup for enthalpy probe measurements on the DC-RF hybrid thermal plasma characteristics.

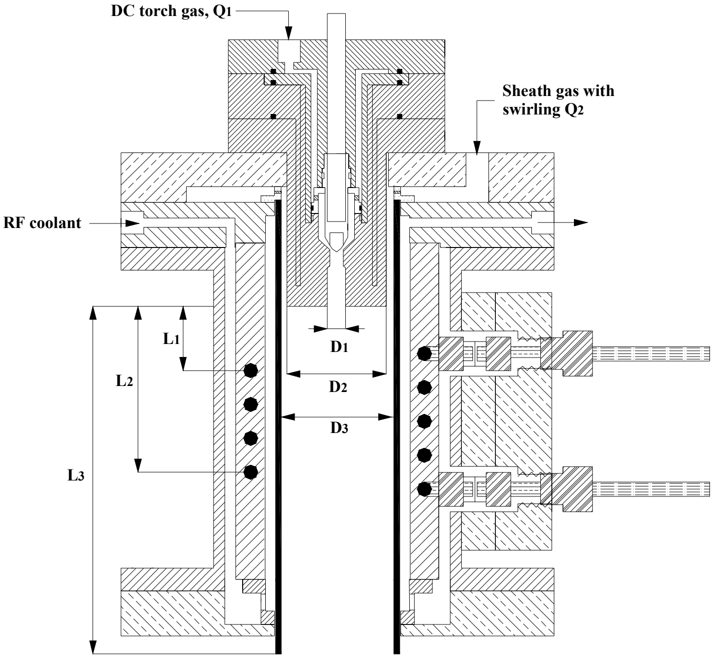

Fig 2. Cross-sectional view of a DC-RF hybrid plasma torch

Table 1. Principal dimensions of the DC-RF hybrid plasma torch shown in Fig. 2.

D_1 [mm]	6 and 8
D_2 [mm]	44
D_3 [mm]	50
L_1 [mm]	30
L_2 [mm]	75
L_3 [mm]	154

Table 2. Operating conditions of the DC-RF hybrid plasma torch shown in Fig. 2.

DC torch gas flow rate, Q_1 [lpm]	10 and 20
Sheath gas flow rate, Q_2 [lpm]	50, 60 and 70
DC current, I_{DC} [A]	70 and 110
RF input power, P_{RF} [kW]	8
Operating pressure, P_a [Torr]	760

The temperature difference between inlet and outlet coolant of the enthalpy probe is measured using K-type thermocouples, and the measured data are processed in a data acquisition and control system consisting of PC, SCXI, and PXI devices.

The hybrid torch is operated with Ar as a DC torch plasma gas and an RF sheath gas, which are injected to the DC torch and through an annular tube formed between the DC torch and RF confinement tube, respectively, as shown in Fig 2. Sheath gas is introduced into the hybrid torch with an azimuthal component of gas flow velocity, which is proportional to the sheath gas flow rate supplied by a gas distributor. For example, the azimuthal velocity is designed to have values of 65 m/s, 78 m/s and 91 m/s for the sheath gas flow rates of 50, 60 and 70 lpm, correspondingly. Experiments have been conducted with the combination of operating conditions presented in Table 2 for finding the effects of operating conditions on the profiles of hybrid plasma temperature and velocity.

3. Results and Discussion

The plasma temperature and velocity profiles at the hybrid torch exit plane are measured along with the power distributions by heat conduction to the hybrid torch under the operating conditions given in Table 2. Fig 3 shows the measured results for the hybrid plasmas generated with different sheath gas flow rates, Q_2 = 50, 60 and 70 lpm, at atmospheric pressure when a DC torch uses an anode nozzle of 8mm in diameter. It is seen in Fig 3 (a) that the temperature profiles for Q_2 = 60 and 70 lpm have two peaks at the axis and off-axis, one of which seems to be attributed to the DC arc jet flame and the other to the RF induction plasma. However, in case of Q_2 = 50 lpm, the plasma temperature and velocity have relatively uniform distributions.

Such a two-peak feature in temperature profiles was appeared at the coil inlet in the numerical results by T. Yoshida et al [1], and was explained as the result of a low efficiency of convective heat transfer from the RF induction region to the central channel due to the presence of stagnation region in the axial mass flux around the DC torch exit. They also predicted that the concave temperature profile region would be heated only by radial heat conduction, and suggested that such a tendency is the feature of hybrid plasma appearing in the low RF power input. In addition, it was also shown that the temperature profiles change in their shape to only one off-axis maximum temperature with a reheating process of the DC arc jet column in the coil region.

It is, however, interesting from the present measurements shown in Fig. 3(a) that the temperature profiles with two peaks appear at the torch exit for Q_2 = 60 and 70 lpm (accordingly azimuthal velocities of 78 m/s and 91 m/s at the torch inlet, respectively) under the relatively high RF input power of 8 kW. These measured results seem to come from the effects of swirl on flow and temperature profiles of hybrid plasma. Boulos et al [6] reported from their numerical work that in the RF plasma with a swirl, the centreline plasma velocity decreases in the downstream of the coil region and the circulation eddy in the plasma fire ball moves outwards closer to the confinement tube wall compared with the RF plasma without a swirl. And, the heat flux to the wall in the upstream of the coil region was predicted to increase with rise in the swirl intensity. Considering that the sheath gas flow is responsible mainly for the formation of RF induction region in the DC-RF hybrid plasma, the effect of swirl on hybrid plasma may be explained like the case of RF plasma as follows:

The increase in sheath gas flow rate with a swirl seems to cause the plasma velocity to slow down in the region close to the central arc column with relatively high velocity, and to expand the stagnation region of axial mass flux under the DC torch exit just like the extended circulation eddy appeared in the RF plasma. Then, the reduced velocity in the central region may be ineffective for heat transfer between the arc column and the RF induction region so that the unique shape of temperature profile in the coil inlet region remains almost unchanged up to the hybrid torch exit. It is seen in Fig 3 (a) that the central velocities decrease with the swirl intensity, and the low pressure zone measured by the enthalpy probe expands with increase in the sheath gas flow rate.

The expansion of the stagnation region of axial mass flux around the DC torch exit may result in heating the greater part of sheath gas flow by RF input power, flattening the concave region between two peak temperatures, and transferring more heat to the DC torch anode by conduction. These effects of swirl on the heat transfer are shown in Figs. 3 (a) and (b), where a more flattened temperature profile is obtained for Q_2 = 70 lpm compared with that for Q_2 = 60 lpm (Fig 3 (a)), and the heat removed by the DC torch coolant increases as the sheath gas flow rate is higher (Fig 3 (b)).

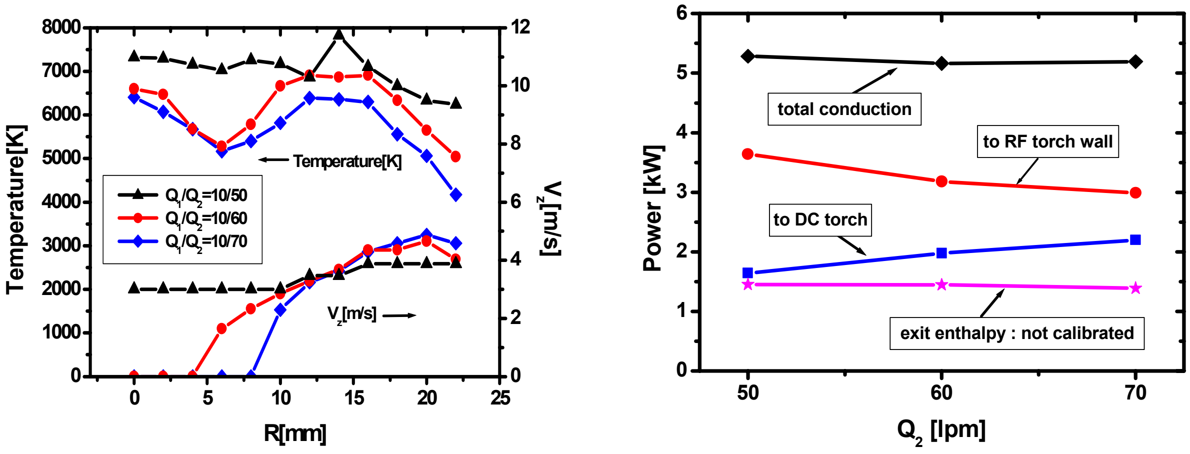

(a) (b)

Fig 3. (a) Radial profiles of the hybrid plasma temperature and velocity at the torch exit, and (b) the overall conduction heat distributions depending on the sheath gas flow rate for P_{RF} = 8 kW, I_{DC} = 70 A, and anode nozzle diameter = 8 mm.

Figures 4 and 5 show the effects of DC gas flow rate Q_1 and anode nozzle diameter D_1 on the profiles of temperature and velocity for a DC current of 70 A and an RF input power of 8 kW. The radial profiles of temperature and velocity are plotted in Fig 4 for Q_1 = 10, 20 lpm with the conditions of Q_2 = 60 (Fig 4 (a))or 70 lpm(Fig 4 (b)). An increase in the DC gas flow rate leads to a decrease in the central temperature, of which difference between the two cases of Q_1 = 10 and 20 lpm is 628 K under Q_2 = 60 lpm (Fig 4 (a)) and 1133 K under Q_2 = 70 lpm (Fig 4 (b)). But, the central velocity increases with rise in the DC gas flow rate. Similar tendency is found in the experiments conducted with two different anode nozzle diameters under the same DC and sheath gas flow rates as seen in Figs. 5 (a) and 5 (b).

The central temperatures have not varied so much (about 200 K) in the cases of Q_1 = 10 lpm for each condition while they show the relatively large differences (from 660 K to 1100 K) in the case of Q_1 = 20 lpm and D_1 = 6 mm for each experiment depending on sheath gas flow rate. These results may come from the reheating process of central arc column by the radial conduction from the RF induction region under the given sheath gas flow rate. In addition, it is noticed that the total heat conduction to the DC and RF torch coolant is larger in the case of smaller D_1 = 6 mm. The amount of heat conduction to the DC torch is not relatively so much, but the heat conduction power to the RF torch increase more rapidly in the case of D1 = 6 mm with decrease in the sheath gas flow rate as shown in Fig 6.

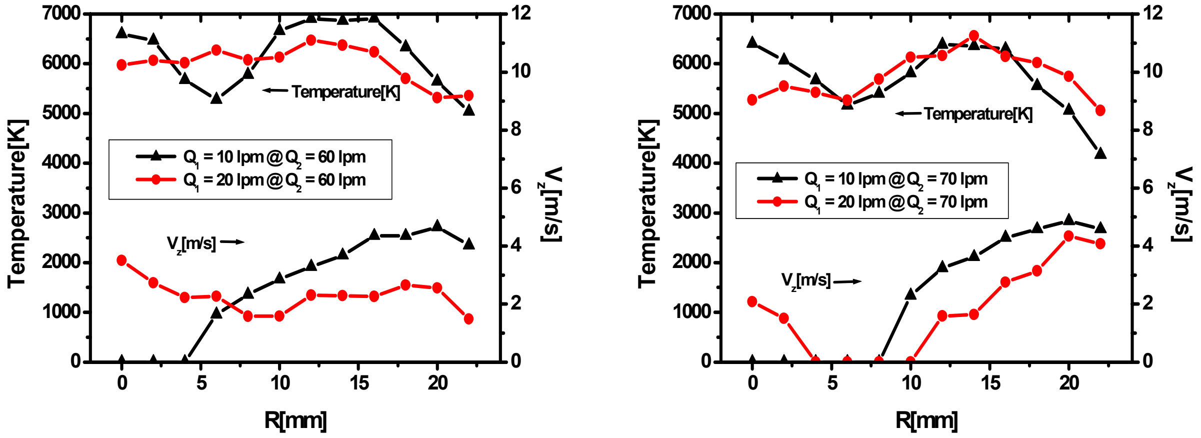

(a) (b)

Fig 4. Radial profiles of the hybrid plasma temperature and velocity at the torch exit measured with the different ratios of DC gas flow rate Q_1 to sheath gas flow rate of Q_2 for P_{RF} = 8 kW, I_{DC} = 70 A, and anode nozzle diameter = 8 mm; (a) Q_2 = 60 lpm and (b) Q_2 =70 lpm.

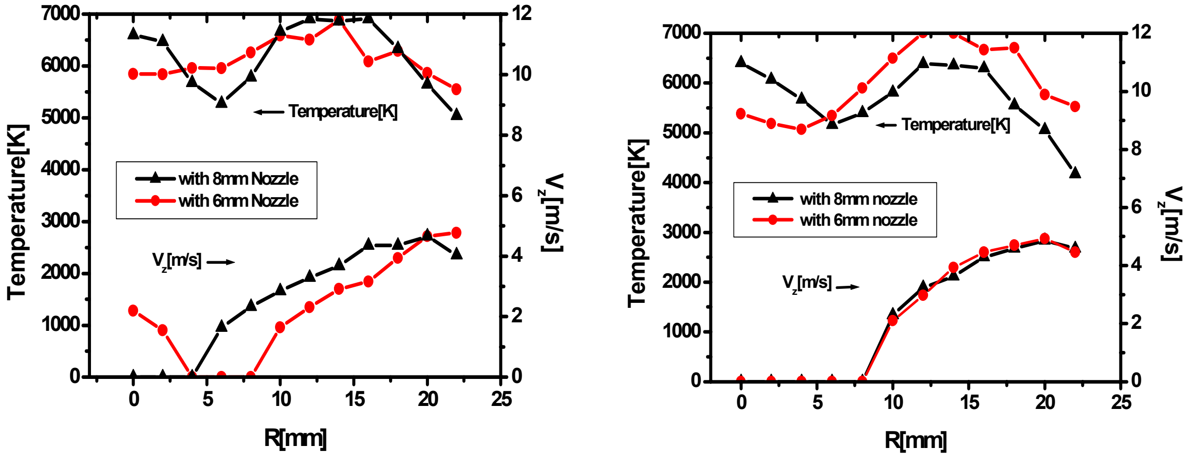

(a) (b)

Fig 5. Radial profiles of the hybrid plasma temperature and velocity at the torch exit measured with the different diameters of anode nozzle for P_{RF} = 8 kW, I_{DC} = 70 A, and Q_1 = 10 lpm; (a) Q_2 = 60 lpm and (b) Q_2 =70 lpm.

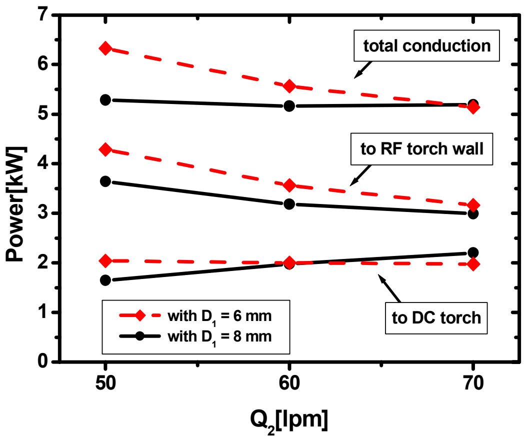

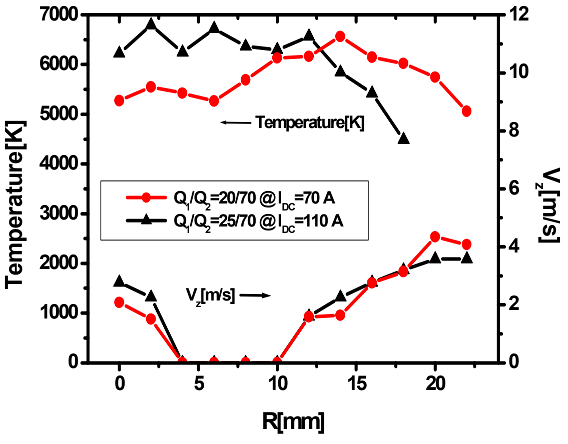

Fig 6. Overall conduction heat distributions measured with different diameters of anode nozzle for P_{RF} = 8 kW and I_{DC} = 70 A.

Fig 7. Radial profiles of the hybrid plasma temperature and velocity at the torch exit measured with different DC powers for P_{RF} = 8 kW and anode nozzle diameter, D_1 = 8 mm.

Figure 7 is presented for the profiles of temperature and velocity at the hybrid torch exit measured with two different DC powers. The higher DC current raises the temperatures in the central region as expected, but the temperature distributions show relatively rapid falling in the peripheral region outside of R = 12 mm. The axial velocity distributions obtained with different DC powers are not so different even for the higher flow rate of DC gas. Therefore, the change in the DC current has an effect mainly on the temperature profile, but not considerably on the velocity profile.

4. Conclusion

The profiles of hybrid plasma temperature and velocity at the torch exit have been measured using the enthalpy probe method for finding the effects of design and operating parameters, such as swirling, DC gas flow rate, anode nozzle diameter, and DC current. From the measured results in this work, the following conclusions are obtained.

(1) The sheath gas flow rate with a swirl seems to have significant effects on the radial temperature profile of hybrid plasma and the reheating process of central arc column by reducing the axial velocities in central region as well as the expansion of the stagnation region of axial mass flux near the DC torch exit.

(2) Increase in the sheath gas flow rate with a swirl enhances the heat conduction to the DC torch from the hybrid plasma as a result of expansion of the stagnation region under the DC torch anode nozzle, and also affects the radial heat conduction between the DC arc column and the RF induction region near the coil inlet. This phenomenon may be important in the design of hybrid torch for a high power operation with swirling.

(3) Increase in the DC gas flow rate and decrease in the anode nozzle diameter cause the axial gas velocity (the central temperature) to increase (decrease), and the degrees of their changes depend on the sheath gas flow rate. Therefore, it will be possible to control the shape of radial temperature profiles and the reheating process in the hybrid plasma by selecting these operating parameters appropriately.

(4) Finally, a further study is required for the comparison between the measured and numerical results for a complete understanding of the effects of design and operating parameters on the hybrid plasma characteristics, especially for clarifying the effect of swirl flow on the radial temperature profiles and the axial mass flux near the DC torch exit. This may be the subject of future work

Acknowledgements

Financial support from the Ministry of Science and Technology of Korea is gratefully acknowledged.

References

[1] T.Yoshida, T,Tani, H.Nishimura, K.Akashi, "Characterization of a hybrid plasma and its application to a chemical synthesis", J.Appl.Phys. 54, 640 (1983)

[2] J.W.McKelliget, N.El-Kaddah, "Computer aided design of hybrid plasma reactors for use in materials synthesis", in Metallurgical Processes for the Year 2000 and Beyond, Ed. H. Y. Sohn and E.S. Geskin, T.M.S, 169 (1989)

[3] S.W.Nam, H.Nishiyama, Shini.I.Kamiyama, "Numerical analysis on plasma spraying in a DC-RF hubrid plasma reactor", JSME Inter.J. Series B. 39, 134 (1996)

[4] R.Shimpo, Y.Uehara, T.Yoshida, "Fabrication of Ni-YSZ Cermet Electrode for SOFC by Hybrid Plasma Spraying and its electrical characterization", Proceedings of ISPC 14, Prague, 4, 2115 (1999)

[5] M.I.Boulos, R.Gagne, R.M.Barns, "Effect of swirl and confinement on the flow and temperature fileds in an inductively coupled r.f. plasma", Can. J. Chem. Eng., 58, 367 (1980)

Hardening of metal surface in a vacuum arc cleaning

K.Takeda and M.Sugimoto

Department of Machine Intelligence and System Engineering, Akita Prefectural University, Hon-jo, Japan

Abstract

The cathode spots of a vacuum arc have been used for cleaning of metal surface such as oxide removal and degreasing. In this work, the authors focused the research on the hardening effect of the metal surface during the arc cleaning. Drastic increase in the hardness of surface layer was obtained after the removal of oxide layer on a steel surface. X-ray analysis revealed that considerable amount of tensional stress existed in the resolidified layer under the surface.

1. Introduction

A vacuum arc is characterized by (1) presence of multiple arc spots on a negative electrode, which is called “cathode spots”, (2) violent evaporation of cathode material due to the extremely intense power density at the spot, and (3) the random motion of the spots over the cathode surface[1].

Recently, cathode spots of a vacuum arc have been used to remove thick oxides on a metallic surface[2]. It is well known that the pretreatment of cleaning or activating a surface is essentially important to obtain good coating over the metallic substrate. Conventionally, oxide layer on a surface is removed by pickling in a strong acid bath and chemical compounds such as grease is eliminated by washing in a bath of alkaline solution or organic solvent. Such chemical treatments are not friendly to environment. Grit blasting is another cleaning method often used. This mechanical treatment is also not friendly to workers, because of the emission of loud noise and heavy dust. In either case, the treated surface looks clean but in fact residual chemicals or grits contaminate the work piece. As the vacuum arc process is completely clean and dry, it is quite friendly to environment and workers. The principle of the arc cleaning is the vaporization of the surface materials. In a cleaning action, the cathode spots behave as a smart heat source. They detect oxides on a surface and attack the oxides preferentially to the metal and remove them from the surface selectively. Not only oxides but also carbides or nitrides have the priority over metals in the removal by the cathode spot. The mechanism of the preferential removal of the non-metallic materials such as oxides has not been cleared but it is likely to be attributed to their lower work functions than those of metals. Observation of the eroded tracks of the cathode spot revealed that the energy flux at the cathode spot has a high value of 10^{10} W/m^2 or more[2] . Owing to the high energy density and fast movement of the cathode spot, thin surface layer of the metal under the cathode spot is melted and resolidified rapidly. Therefore it is expected that the cleaning action of the cathode spot results in the increase of surface hardness by quenching.

The objective of the present work is to investigate the hardening effect in the vacuum arc cleaning.

2. Experiment

To investigate the hardening effect in the vacuum arc cleaning, we used steel as test material. After the vacuum arc treatment, the changes of surface structure and hardness were examined.

(1) Test piece:

As the test materials, three kinds of hot rolled steel with different carbon contents were used in the present experiment. The chemical compositions are shown in Table 1. The size of the test pieces was 100 x 100 x 15 ^{t} in mm. The surfaces of them were covered with scale (oxide) whose thickness was 20-30 μm. Some of the experiments were carried out for the test pieces whose surface had been grinded to remove the oxide layer beforehand .

Table 1　Chemical composition of test pieces used for the experiment (weight %)

	Fe	C	Si	Mn	P	S	Cr
Machine structural carbon steel　(S45C)	balance	0.45	0.25	0.75	0.018	0.016	-
Rolled steel for general structure (SS400)	Balance	0.22	0.09	0.64	0.021	0.005	0.02
Fire resistance steel (FR490)	balance	0.11	0.20	1.29	0.006	0.005	0.02

(2) Vacuum arc treatment:

Test pieces were treated by using a vacuum arc cleaner as shown in Fig.1. They were connected to the negative polarity of the arc power supply.　A cup type cleaner was put on the test piece and the arc was ignited after the evacuation of air inside the cup at a pressure less than 50 Pa. The inner diameter of the cup was 50 mm. The arc was operated in a constant current mode. Typical current was 100 A. In the arc operation, several cathode spots ran on the surface of the test piece in a random manner to remove the oxide inside the cup.　It took about 40 seconds to remove such a thick surface oxide of the hot rolled steel.

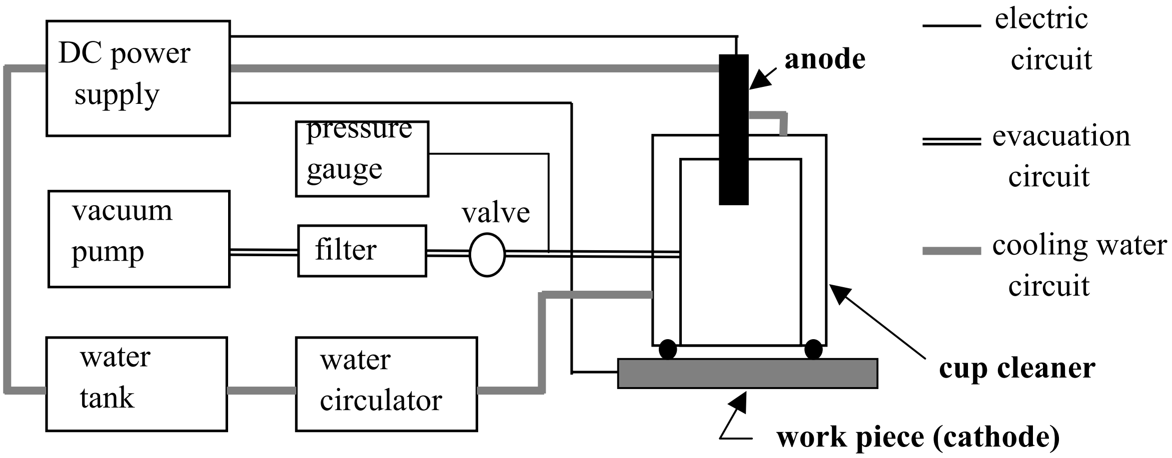

Fig.1　Schematic illustration of a vacuum arc cleaner

(3) Grit blasting:

To compare the hardening effect by the arc treatment with that by a conventional cleaning method, the oxide layer of some hot rolled steel pieces were removed by grit blasting where sharp angular abrasive particles of white alumina were projected with the air stream at the pressure of 3kgf/cm^2.

(4) Analyses of surface morphology and structure :

The surfaces treated by the vacuum arc, and those by grit blasting were observed by using SEM (JEOL, model TSM-T20) and a laser microscope (Laser-tech, model 1LM15). A profilometer (Mitsutoyo, model Surftest 401) was used for the measurement of surface roughness.

After polishing and etching, resolidified layer and heat affected layer were observed over the cross-section of the test piece by SEM.

(5) X-ray analysis:

X-ray diffraction by using Co-Kα was utilized to measure the lattice constant of material. By the comparison of the lattice constants between initial state and that after the vacuum arc treatment, residual stress in the resolidified surface layer was evaluated.

(6) Hardness measurement:

Hardness change by the vacuum arc treatment was measured by a Vickers micro-hardness tester (Shimazu, Model DUH-W201). In the measurement, test force and loading speed were 300 mN and 70.6 mN/sec respectively. Duration of the test force was 5 sec.

3. Experimetal Results

As mentioned above, the cathode spots of the vacuum arc attack and remove the oxide on the steel surface preferentially to the metal. Fig.2 represents the surface change before and after the vacuum arc treatment. As shown in the figure, the oxide layer inside the cup cleaner was completely removed by the arc treatment.

（a） （b）

Fig.2 Descaling of hot rolled steel (SS400): (a) initial surface covered with oxide and (b) surface after vacuum arc cleaning

The cross sections of the test pieces were observed after polishing and etching. The SEM images without and with arc treatment are shown in Fig. 3 (a) and (b), respectively. Thick oxide layer of 20-30 μm is observed in the initial hot rolled steel piece in Fig.3 (a).

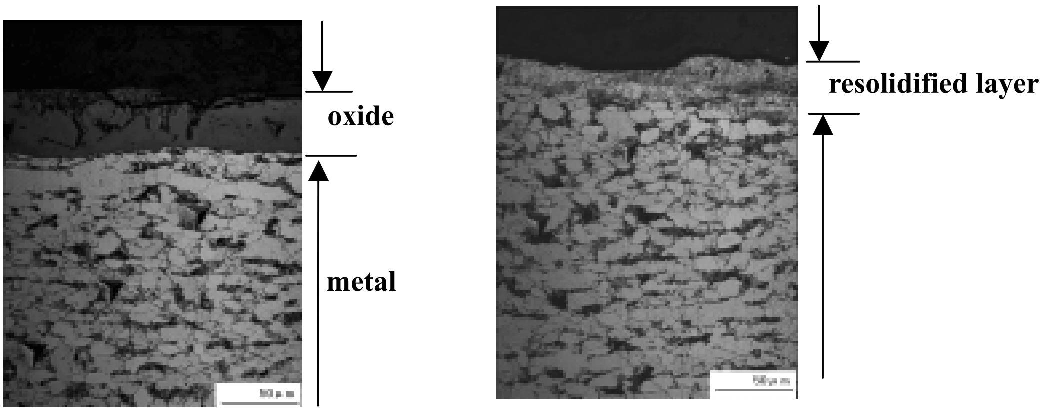

(a) **(b)**

Fig.3 Change of cross sections: (a) initial test piece with oxide layer and (b) after arc treatment. Materials: SS400

In Fig.4, the variation of Vickers hardness with a distance from the surface is illustrated where open circles and closed circles represent hardness without and with the arc treatment, respectively. For the initial test piece, distance zero corresponds to the interface between oxide layer and steel substrate. Remarkable increase in hardness was obtained in a resolidified layer after the removal of oxide layer. Similar increase was observed in other types of steel as shown in Fig.5.

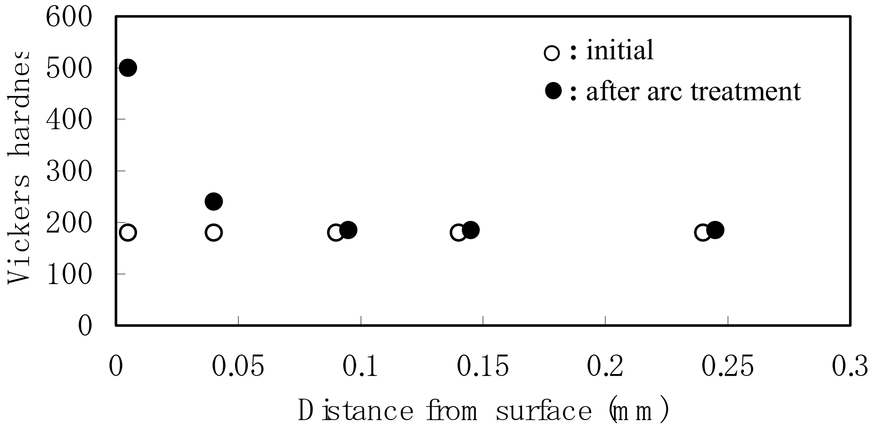

Fig.4 Hardness distribution (Material is SS400.)

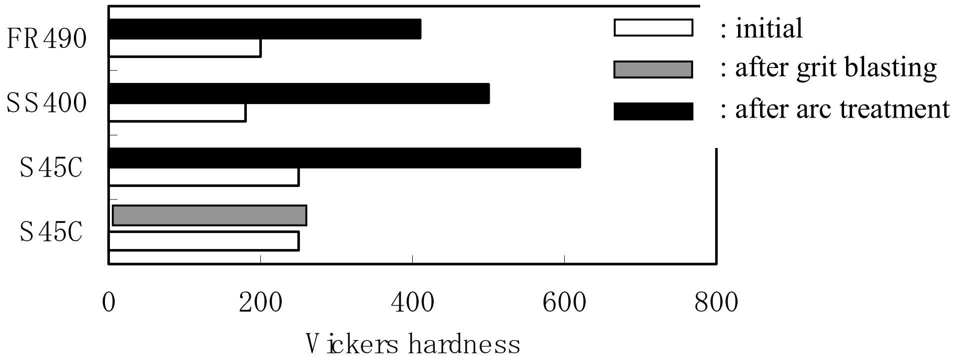

Fig.5 Surface hardening effect by arc treatment and grit blasting for various types of steel.

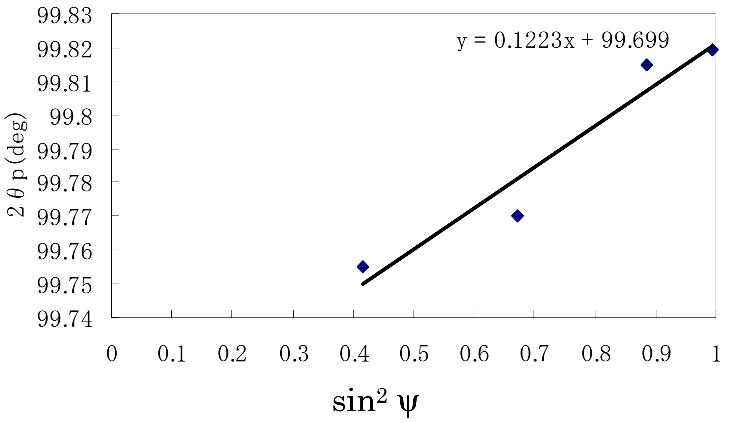

Fig.6 X-ray diffraction angle for arc treated SS400.

The relation between incident angle and diffraction angle of the X-ray as shown in Fig. 6 revealed that the vacuum arc treatment resulted in considerable amount of residual stress in a thin surface layer. The stress was tension. For SS400 steel, it was evaluated to be 16 kg/mm^2.

4. Discussion

The vacuum arc cleaning always follows heating and melting of thin metal layer under the cathode spots. Because of the rapid movement of the spots, the molten metal is quenched at a high rate of cooling, which results in the hardening of metal surface. In this section, the authors will make order-estimation on the cooling rate at the instant when the molten metal starts to resolidify. Based on the modeling of the arc cleaning process [2,3], we assume that a cathode spot stays at a certain point and remove the oxide. When all the oxide under the cathode spot evaporates after the time interval τ, the spot moves on a new oxide surface, as shown in Fig.7. During the evaporation of oxide, molten pool of metal grows under the oxide. As the cathode spot is easy to exist on the oxide rather than on the metal, it moves to other oxide surface at a time τ. Then the molten metal starts to quench.

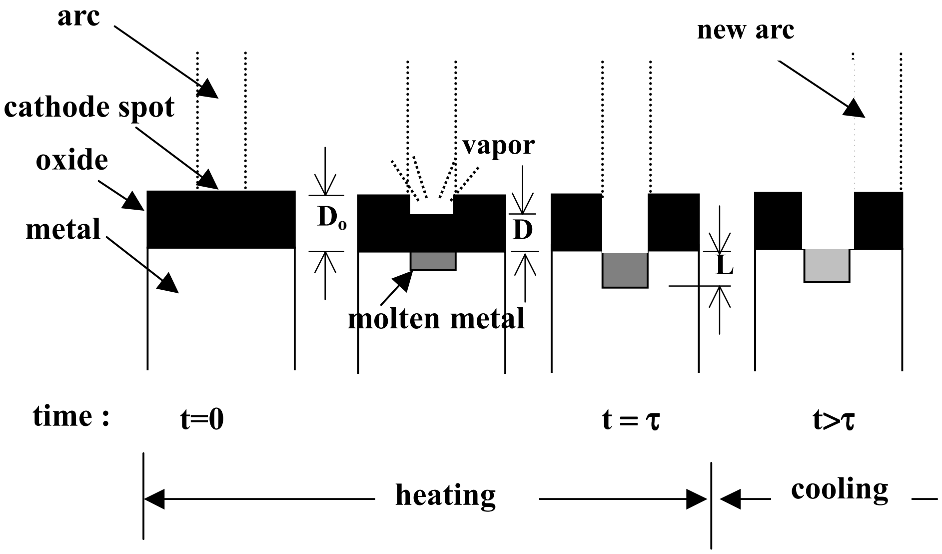

Fig. 7 Schematic illustration of rapid heating and rapid cooling of surface layer

Under the assumption of one dimensional heat conduction without any phase change, temperature distribution *T(x)* under the cathode spot was given by the following equation[3];

$$T(x) = T_v \,\mathrm{erfc}\left(\frac{x}{\sqrt{4\alpha\tau}}\right). \tag{1}$$

Where x denotes the distance from the surface, T_v and α represent boiling temperature of the oxide and thermal diffusivity, respectively. As the oxide thickness is expressed in the following equation

$$D(t) = D_o - \left[Et - \left(\frac{2\kappa T_v}{\sqrt{\pi\alpha}}\sqrt{t}\right)\right], \tag{2}$$

the time τ is obtained by putting D(t)=0. Where E is the power density at the cathode spot and k is thermal conductivity. At $t = \tau$, the depth of molten metal pool, L, is approximated from the following relation,

$$T_m = T_v \operatorname{erfc}\left(\frac{L}{\sqrt{4\alpha\tau}}\right). \tag{3}$$

T_m represents the melting temperature of the metal. By introducing a representative temperature T^* of the molten metal, the average cooling rate of the surface layer can be estimated as

$$\frac{dT^*}{dt} = \frac{\alpha}{L}\left(\frac{dT}{dx}\right)_{x=L} \tag{4}$$

Since L and $dT/dx)_{x=L}$ are the functions of the power density of the cathode spot, the cooling rate, dT^*/dt strongly depends on it. Fig.7 shows the predicted relation between the cooling rate and the power density at the cathode spot. As power density of the cathode spot was estimated to be 10^{10} W/m^2 or more in a previous experiment[2], predicted cooling rate is in the order of 10^6 - 10^7 K/sec. Taking the roughness of many simplifications adopted here into account, the real cooling rate might be different from the theoretical rate obtained above by one order. Even though it is enough high rate to harden steel surface by quenching.

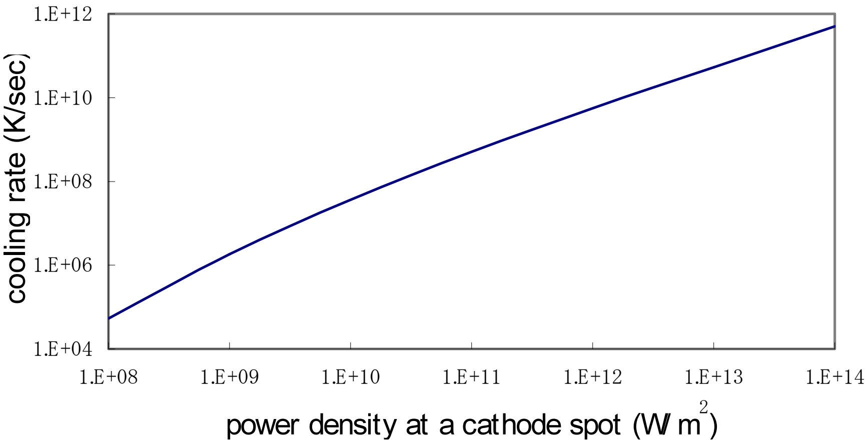

Fig. 7 Predicted cooling rate of molten steel layer as a function of power density at the cathode spot.

5. Conclusions

Vacuum arc treatment has been known as a clean process to provide a fresh and activated surface. In this work, the authors focused the investigation to a quenching effect. Surface analyses reveal that the cleaning action by cathode spots of a vacuum arc follows the remarkable increase of surface hardness. Molten metal under the cathode spot resolidifies very rapidly. Quenching rate is estimated to be 10^6 K/sec or more.

6. Acknowledgements

This work has been supported by Grant-in Aid for Scientific Research (B) from the Ministry of Education, Culture, Sports Science and Technology in Japan. The authors would like to thank Miss E. Chida for her participation to this work.

References

[1] J. M. Lafferty: “Vacuum Arcs”, A Wieley-Interscience Publication, JHON WILET & SONS, New York, (1979), p120

[2] K.Takeda and S.Takeuchi: Materials Transactions, JIM, 38 (1997), 636-642

[3] K.Takeda and S.Takeuchi: Thin solid films, 407 (2002), 163-168

Experimental investigation on interaction of wire vapor plasma With polyethylene wall

Rahmani bouabdallah[1], Yasuoka Kouiti[2] and Ishii shozo[2]

1- Institute of Electronics, University of Sciences and Technology
of Oran (U.S.T.O), B.P.1505 Mnaouer, Oran, ALGERIA
Email:brrahmani@caramail.com
2- Department of Electrical and Electronic Engineering
Tokyo Institute of Technology (T.I.T)
2-12-1 O-Okayama, Meguro-ku, Tokyo, JAPAN

Abstract

A simple experimental method is proposed to investigate the radiation emitted from the boundary layer, which is formed near the insulator wall. This method consists of a fast-pulsed exploding aluminum wire set on the Low-Density PolyEthylene (LDPE) flat wall. Two phases have been observed in the intensity shape of the aluminum and the carbon atoms lines showing an enhancement during the collisionless interaction regime. The photoablation of LDPE wall was occurred during the plateau as observed in the temporal behavior of the intensity of the carbon atom line, which agree with the observed peak value in the UV radiation emission.

1.Introduction

The interaction of supersonic hydrogen plasma stream with flat metal target leads to the formation of a boundary layer near the surface of metal [1]. The intensity of the observed hydrogen lines shows a peak value near the surface of this metal target. However, the analysis of spectra emitted from this boundary layer shows no emitted lines from the target. In the visible and ultra-violet wavelength range, an enhancement of spectral efficiency of dynamic plasma discharge was achieved by an axial and radial limitation of the free expansion of plasma [2]. The formation of plane, spherical and reflected shock waves were responsible in the enhancement of the time dependent behavior of emitted radiation, which reveals some peak values.

The interaction of jet capillary plasma with an insulator tube wall in an electrothermal launcher [3] leads to the formation of a boundary layer adjacent to the surface wall, where a large gradient of the temperature and the density was observed. The insulator tube wall was ablated by the processes of convection and radiation loss energy of plasma source [3]. The inflow of ablated particles into the formed boundary layer increases the thickness of this layer, which shields the insulator surface from the heat flux of plasma source.

The ablation of Teflon (PTFE) tube wall was dominated by the process of emitted radiation from the column arc plasma occurred in the circuit breaker [4]. The inflow of ablated particles into the column arc plasma reduces the time of extinction of the arc in the circuit breaker [4], where the most effective ablated processes occur around the maximum temperature, since the ablation rate scales as the fourth power of temperature [5]. The major fraction of the arc power [5] have been dissipated to the PTFE wall by heating, melting, evaporation and ionization processes. The occurred processes in the boundary layer are complicated and affected by the properties of the plasma source as well as by the type of the wall surface. Some processes involved in the plasma-wall interaction are illustrated in Fig.1.

In this paper we present the visible and ultraviolet radiation emitted from the boundary layer, which is formed near the LDPE wall surface by interaction with a metal vapor plasma. These experimental data have been obtained by a simple method, which consists of pulsed electrical exploding aluminum wire plasma set initially on a flat LDPE wall.

2. Experimental and Diagnostic setup

The exploding wire plasmas are generated by swiching on an ignitron in order to transfer the storaged energy from a capacitor bank of 4.45 uF into an aluminum wire with a length of 1 cm and a diameter of 100 um. The wire is set between two electrodes of copper in a chamber evacuated at a pressure of 5.0 10^{-4} Torr.

The discharge current in the load was measured by Rogowski coil. The LDPE surface was carefully cleaned with ethanol and set near the wire at a distance between 50 um to 100 um.

The electrical circuit, the views of sample and the diagnostics setup are given in Fig. 2 (a),(b),(c) respectively. The monochromator was coupled to the exploding wire by an optical fiber with a length of 10 m mounted approximately at 30 cm from the axis of the wire, viewing the discharge radially through the glass window. A lens on the optical fiber head, viewing a limited area between copper electrodes, focused the emission of radiation. The observing point was fixed at a distance of 1.5 mm far from the LDPE wall surface and at the center between electrodes in order to study the radiation emitted from the formed boundary layer near the surface. The UV intensity of the radiation emitted from the free expansion of aluminum metal vapor plasma was recorded by a photomultipier, which has a gain band between 160 nm, and 320 nm with the highest value of gain is reached at 190 nm. The UV radiation provides information on the time range of the photoablation of LDPE wall, since the C-C and C-H binding energies are 4.2 and 3.47 eV respectively which require a threshold wavelength of 300 nm for the photodegradation mechanism.

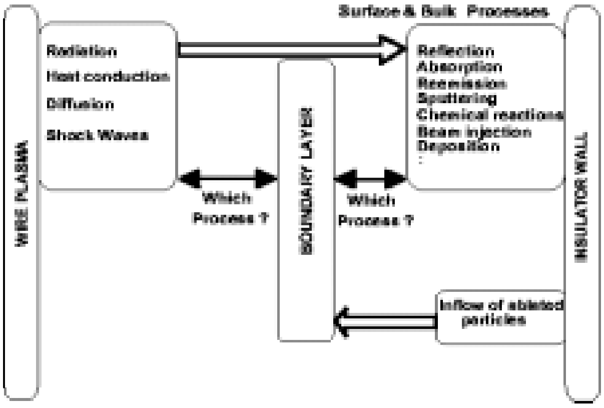

Fig.1: Some interaction processes between plasma and wall.

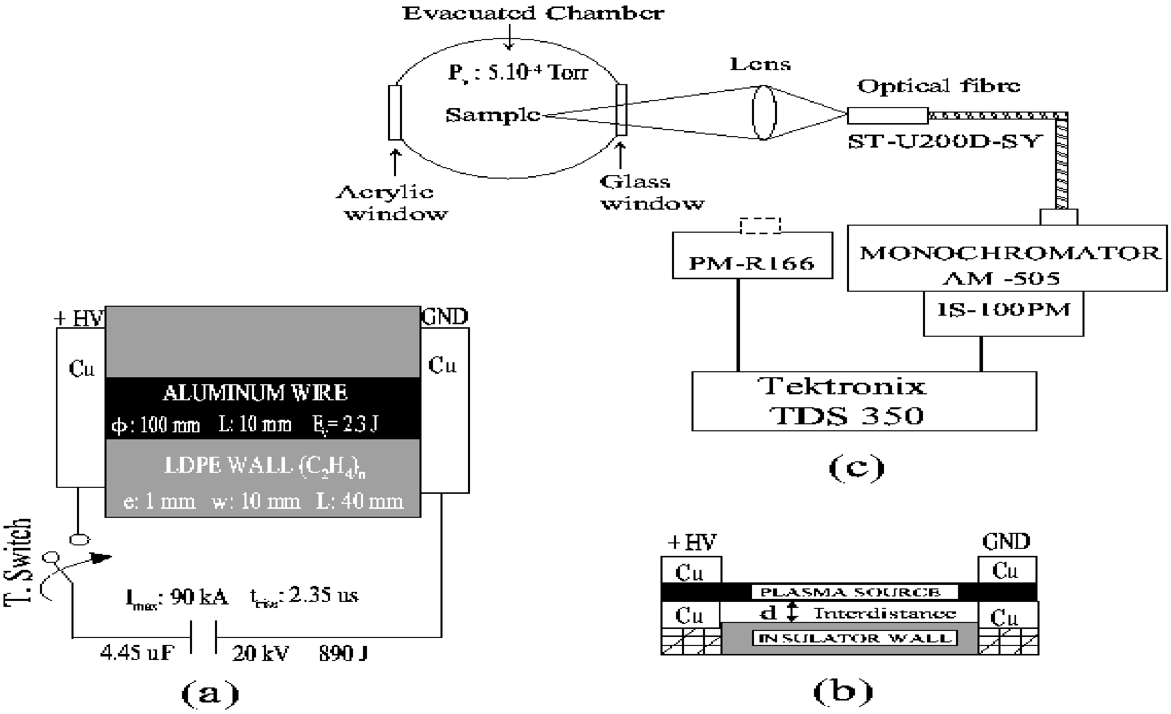

Fig.2: A schematic view of the experiment and diagnostic setup.
(a) Electrical circuit and top view of the sample, (b) side view of the sample, (c) diagnostic setup

3. Results and discussion

The discharge current in the circuit measured by a Rogowski coil is given in Fig.3. The total discharge current reaches 90 kA in a rise time of 2.34 us. The drop in the current waveform has not been observed which is due to the fast rise time (t_r) of the electrical discharge (2.3 us) and a high averaged field strength (20 kV/cm). This drop has been observed for exploding aluminum wire in atmosphere [6] at 4 kV/cm with a rise time of 7.5 us. Furthermore, the storage bank energy of 890 J is greatly exceeded the calculated evaporation energy of the aluminum wire 2.3 J. The observed oscillating form in the current waveform is essentially due to the low resistance of the wire.

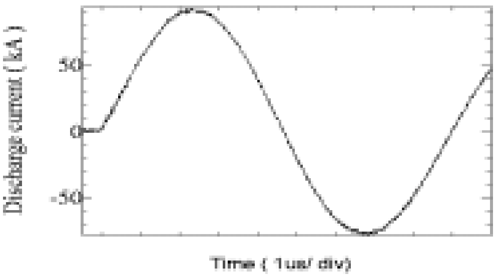

Fig.3: Electrical discharges current waveform.

The ablation of LDPE surface by the photons of 300 nm emitted from the aluminum vapor plasma is expected to occur during the first 2 us from the beginning of the discharge as shown by the peak value in the UV radiation given in Fig.4.

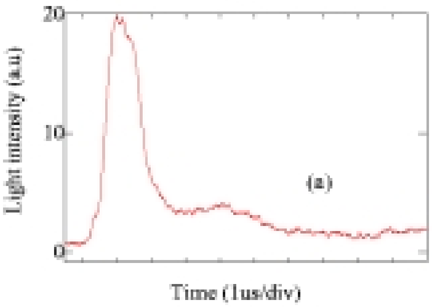

Fig.4: Ultra violet radiation emitted from the free expansion of aluminum vapor plasma (a).

ATOMS	E_i (eV)	E_k (eV)	A_{ki} (10^7 s^{-1})	λ_{ki} (Å)
Aluminum	0.01	3.14	9.8	3961.52
Carbon	7.68	10.59	0.032	4268.99

Table 1: Atomic data for the aluminum and the carbon atom lines. The lower and upper energy levels of transition i to k are indicated by E_i and E_k respectively, A_{ki} refers to the transition probabilities coefficient and λ_{ki} to the wavelength of line.

The radiation emitted from the aluminum vapor plasma has been observed [6] to be strongly dependent on the background gas, pressure, and bank energy ,which affect the amount of ablated particles and the interaction processes. The ionization, thermal and kinetic energies components of the internal energy of the layer are enhanced by self-absorption of the emitted radiation from the aluminum vapor plasma. Furthermore, the impact of incoming electrons from the vapor plasma source with the layer particles increases the internal energy of this layer. The diagnostic method was based on the aluminum and the carbon atoms lines with their atomic data [8] are listed in Table 1. The observed resonance line of aluminum atom, given in Fig.5a,b, shows a significant change in the intensity shape between the free expansion of aluminum vapor plasma (a) and when this vapor strike the LDPE surface (b). In case of the free expansion (a), the intensity shape shows a peak which appears near the maximal value of the discharge current I_M. The delay of its appearance, is due to the optical thickness of plasma, which is enhanced by the self-absorption of radiation as, observed elsewhere [6,9]. This enhancement in the radiation transport of aluminum vapor plasma is expected to occur around the current value I_M where the optical thickness of radiation is reduced in consequences. After the peak current value I_M, the temperature of aluminum vapor plasma goes down according to the decrease in the input energy.

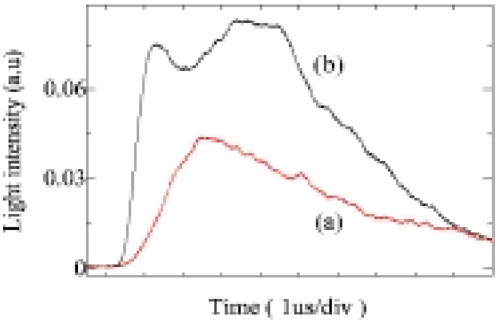

Fig.5: Temporal behavior of the intensity of aluminum line when the aluminum vapor plasma strike with the LDPE wall (b). For (a) refers to Fig.4.

When the expansion of the aluminum vapor plasma strike the LDPE wall surface (Fig.5 b), the emitted intensity of resonance line of aluminum atom is enhanced and its temporal behavior shows two peaks with a fast slope at the beginning of the discharge for the first one. This enhancement provides that a part of the internal energy of the plasma source lost by radiation is improved by the presence of the wall.

The first peak, which appears before the current value I_M and near the peak value of the UV radiation emission, is enhanced by 1.5 times. Its appearance provides that the particles of aluminum, during the crucial pre-explosion and explosion phases, are further heated when the insulator wall radially reflects the free expansion. The heating transfer flux to both aluminum and insulator particles depend on the free expansion velocity, on physical and thermal properties of the insulator wall. It was observed [1,2,10,11] that the radial limitation of a jet plasma by the wall leads to an improvement in the conversion rate of the kinetic energy into radiation.

As, the released input energy increases; the density of the formed boundary layer is enhanced by recombination of the incoming aluminum particles with the inflow of ablated particles from the insulator wall. Therefore, the self-absorption of lines is enhanced by some broadening processes [12]. Thus, a decrease of the intensity by 13 percent near I_M was observed. However, it was observed that near the metal target, the intensities of hydrogen atom lines (Ref.7 Fig.2) increase proportionally to the increase in the density of neutrals in the boundary layer. It is due to the absence of the inflow of target particles in the boundary layer [1], which increase the optical thickness of radiation emission. A gradual increase in the intensity until appearance of another intense peak has been observed after the current I_M. This enhancement is due to the expansion of the compressed aluminum vapor plasma between the outgoing shock wave and the wall body. It was observed that the distribution of the radiation power in the far ultra-violet wavelength range consists of peaks where the intense one appears after the maximal value of the discharge current [2]. Also, the streak data analysis has been shown that the relative intensification near the flat target is more pronounced in the collisionless regime [11].

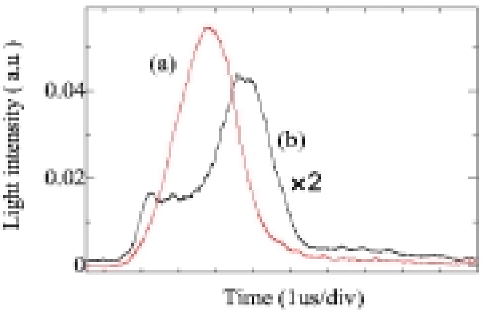

Fig.6: Temporal behavior of the intensity of carbon line. For (a) and (b) refer to Fig.5.

The observed line of carbon atom, given in Fig.6 a,b, show a change in the intensity shape between the free expansion of aluminum vapor plasma and when this vapor strike the LDPE wall. Without insulator wall (Fig.6a), the residual atoms of carbon initially in the chamber and surrounding initially the wire are excited by impact of incoming electrons during the free expansion of aluminum vapor plasma. The intensity reaches a maximal value at the current peak where the kinetic energy of incoming electron is enhanced. Furthermore, the initial reduced amount of carbon particles reduces the heat away from the wire and the absorption of radiation emission.

When the expansion of aluminum vapor plasma strikes the LDPE wall (Fig.6b), the line of carbon atoms shows an appearance of a plateau followed by a peak in the intensity shape. The photoablation was the violent process responsible in the degradation of the Teflon wall [4]. For polyethylene wall, this process occurs during the plateau as shown by the temporal behavior of the ultra-violet radiation given in Fig.4. Furthermore, the spectral distribution of the optical absorption for polyethylene [13] shows an exponential increase in the wavelength range from 200 nm to 300 nm. This plateau provides that the inflow of photo-ablated wall particles in the boundary layer enhance the self-absorption of the radiation emission by the layer itself. The observed peak value of the carbon atom line is due to an enhancement in the ionization and other atomic processes in the boundary layer, which reduce the opacity effect on this line.

4. Conclusion

The UV emitted radiation and the temporal behavior of the aluminum and the carbon atoms line emitted near the insulator wall has been experimentally studied.

The interaction of the expansion of the aluminum vapor plasma with the insulator wall improves the conversion rate of the kinetic energy into radiation. The photoablation phase of LDPE wall surface has been shown both by the emitted ultra-violet radiation and by the plateau observed in the intensity shape of the carbon line.

An enhancement in the conversion rate of the kinetic energy into radiation can improves the extinction ability in circuit breaker and the damping of high power wire electrical fuse. However, further investigation on the radiation emission should be studied such lines of some ions for both the plasma and the wall particles. Because, the emtted radiation and other interaction processes are dependent on some factors such insulator type and its physical and thermal properties, wire's dimension, background gas and pressure. Using a high speed camera in streak and framing modes in order to record the visible light emitted from the boundary layer should follow this work.

Acknowledgment

The Ministry of Education, Science, Culture and Sports of JAPAN supported this work. I want to thank Tokyo Institute of Technology and the University of Sciences and Technology of Oran in Algeria, which have allowed this collaboration.

References

[1] P.A. Demchenko and L. I. Krupnik , Sov. Phys. Tech. Phys. 21, 1382 (1976)

[2] A.S. Kamrukov, G.N. Kashnikov, N.P. Kozlov, V.A. Malashchenko, V.K. Orlo, and Yu.S. Protasov , Sov. Tech. Phys.Lett. 2, 66 (1977)
[3] J. Gilligan, O. Auciello, M. Bourham, O. Hankins,
B. Wehring, D. Hahn, R. Mohanti , and J. Stock, Fusion Technology 15, 522 (1989)
[4] J.G. Gilligan, and R.B. Mohanti, IEEE. Tr. Plasma. Sci. 18, 190 (1990)
[5] Ruchti C.B., Niemeyer L., IEEE Trans. Plasma. Sci, PS-14,no.4, 423, 1986
[6] N. Graneau, P.W. Smith , IEE coll. on "Pulsed Power" 95, 4/1-4, 50, 1995
[7] A.E. Vlastos, J. Appl. Phys. 38, 4993 (1967)
[8] W.L. Wiese, M.W. Smith, and B.M. Glennon, NSRDS-NBS 4, Vol. I, Washington 1966
[9] C. Christou, IEEE Trans. Magn. 31, 689 (1995)
[10] P.A. Demchenko and L.I. Krupnik and E.S. Lyangner , Sov. Phys. Tech. Phys. 21, 1377 (1976)
[11] P.A. Demchenko and L.I. Krupnik , Sov. Phys. Tech. Phys. 21, 1374 (1976)
[12] H.Griem , Spectral line broadening by plasma, Academic press, New-York,London(1974)
[13] M.E. Kassem, A.A. Higazy, Materials Letters 16, 236 (1993)

Control of cathode spot behavior in vacuum arc cleaning

T. Nakamura, H. Takahashi, K. Takeda and M. Sugimoto

Department of Machine Intelligence and System Engineering, Akita Prefectural University,
Honjo, Akita, 015-0055, Japan

Abstract

Recently the cathode spots of a vacuum arc have been used to remove the oxide on the metal surface. The authors found the presence of two different types of cathode spots in vacuum arc cleaning process. The cathode spots of "type 2" removed oxide more quickly than those of "type 1". Application of polyethylene glycol (PEG) to the steel surface enhanced the probability in appearance of "type 2" cathode spots. Without PEG almost all cathode spots belonged to "type 1".

1. Introduction

It is well known that degreasing and oxide removal are the essential pretreatment for various surface processing such as plating, coating, painting and any other surface modifications. Conventianally, mechanical treatment by grit blasting has been widely used. And chemical treatments by using acids, alkalis or organic solvents are also popular. However both treatments are not friendly to the environment. In mechanical treatment, emmissions of loud noise and fine dust are severe problem. Disposal of harmful sludge and waste liquid are another problem in chemical treatment. Vacuum arc cleaning is completely clean process to solve these problems. Vacuum arc is characterazed by scattering a multitude of arc spots on the cathode,which are called "cathode spots". The vapor of a cathode material is emitted at the cathode spots due to the extremely intense power density. And the cathode spots moves rapidly over the cathode surface in a random manner [1]. The following unique properties are advangtageous for the removal of oxide on the metal surface [2];

(1) Cathode spot detects oxides on the surface by itself.
(2) Cathode spot attacks oxides preferentially and remove them selectively.
(3) Arc voltage raise by few volt when all the oxide removed from the surface. The arc notifies the completion of cleaning by the increase of arc voltage.

The purpose of this research is to improve the rate of the oxide removal and to reduce the surface roughness. In previous work the authors had investigated the effects of alkali metal elements on the cleaning actions of a vacuum arc. Remarkable improvement on the removal rate had been obtained by the application of aqueous solution of KOH or NaOH with a suitable concentration [3]. As was expected from the theoretical consideration, the increase in the rate of oxide removal was followed by the reduction of surface roughness. However these chemicals are not favorable for practical processing because of their strong corrosive properties against metals. In the previous research the similar improvements had been found in the application of some organic chemicals [4]. In present work, authors also applied various kinds of polyethylene glycol (PEG) to the steel test piece whose surface was covered with thick oxide. Precise observation was carried out on the cleaning action by the cathode spots of vacuum arc.

The rate of oxide removal and the surface roughness reach to more than 300 % increase and to 65 % decrease, respectively. Observation by using a high-speed video camera reveals that there exist two different types of cathode spot (type 1 spot and type 2 spot). Type 2 spot which moves faster than the other contributes to the increase of the removal rate and to the reduction of surface roughness. Almost all cathode spots generated on a oxide surface without any additional chemicals belong to type 1. If PEG is applied to the surface, type 2 spots appear at higher probability. The probability depends on the molecular weight of PEG and the amount of its application.

In the present work, the investigation is focused on the difference between two types of cathode spot.

2. Experimental Set-up

As shown in Fig. 1, the experimental set-up is composed of: a vacuum chamber with electrodes inside (gap length between two electrodes is 55 mm); a DC power supply for the arc; an evacuation system with a rotary pump; and a water circulation system to cool the anode. Test pieces are made of hot rolled stainless steel (SUS430). The surfaces of test pieces are covered with an oxide layer of 5 - 10 μm in thickness. The dimensions are 100mm × 100mm wide, and 3mm thick.

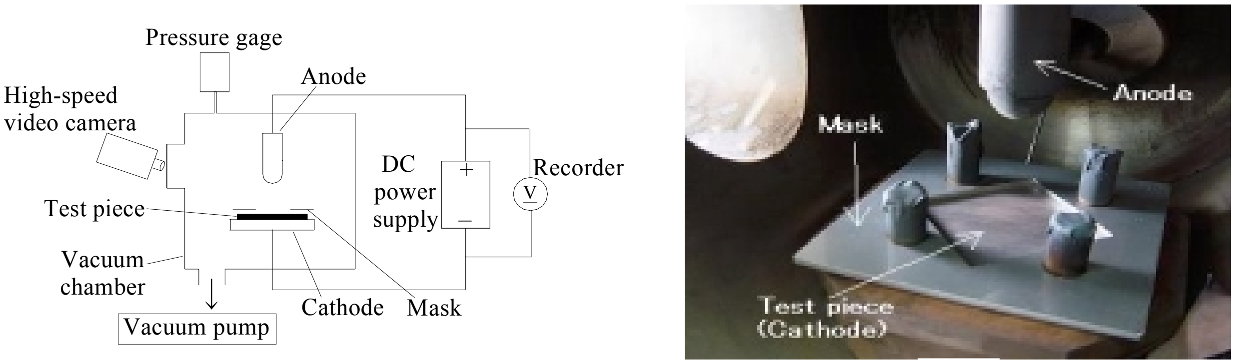

(a) (b)

Fig. 1. Schematic illustration of experimental set-up (a); and the arrangement of the electrodes inside the vacuum chamber (b).

Experimental conditions are sumarized in Table 1. The arc is generated at a constant current mode. The arc current is adjusted at 50 A or 100 A. Various kinds of polyethylene glycol (PEG) with different molecular weights are applied to the surface of SUS430. Amount of application is also changed as shown in the table. In every condition, same experiments are repeated 5 or 6 times. Experiments without any application of polyethylene are also carried out.

Table 1. Condition of test piece

Substance name	Polyethylene glycol (PEG)				
Molecular formula	H (OCH$_2$CH$_2$)$_n$OH				
Average of molecular weight	200	300	400	600	1000
Amount of application [mg]	0, 1, 5, 10, 40, 100				
Specific gravity	1.13				
State at room temperature	liquid	liquid	liquid	liquid	solid
Arc current [A]	50, 100				

After applying a cirtain amount of PEG on the surface SUS430 uniformly, the test piece is connected to the negative polarity of the power supply in the vacuum chamber. By putting a mask on the test piece, the area to be exposed to the arc is restricted to be 40.96 cm^2. Before the arc ignition, the chamber is evacuated up to 5 Pa. For solid PEG whose molecular weight is 1000, it is melted by heating and apply it uniformly to the surface. Its weight on the test piece is determined by measuring the weight of the test piece before and after the application.

The movement of cathode spots is visually observed through the window of the chamber by a high-speed video camera (FHOTRON FASTCAM-Net C) whose time resolution is 56 msec. The arc voltage is recorded by a data logger (NEC DC5200). After the oxide removel, the surface roughness of the test piece is measured by using a profile meter (MITUTOYO Surftest 401) with a stylus tip of diamond whose radius is 5 µm.

The rate of oxide removal, V, is expressed by:

$$V = \frac{40.96\ [\mathrm{cm}^2]}{t\ [\mathrm{sec}]} \tag{1}$$

where t represents a time necessary to complete the oxide removal. The time is determined by the visual observation of the cathode spot movement together with the observation of the arc voltage change.

3. Results and Discussions

3.1. Rate of oxide removal

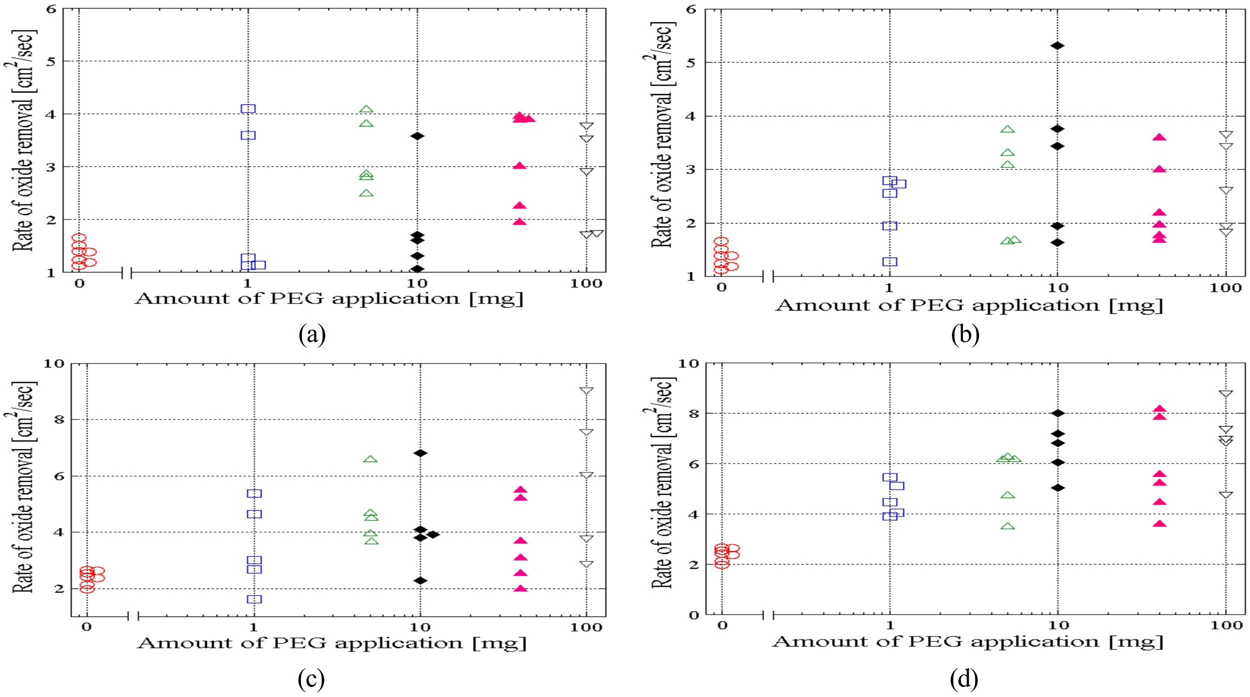

Fig.2. Variation of the rate of oxide removal with amount of PEG application: (a) arc current 50A, moleculer weight 200; (b) current 50A, moleculer weight 1000; (c) current 100A, moleculer weight 200; (d) current 100A, moleculer weight 1000.

Typical changes in the oxide removal rate with the amount of PEG application are shown in Fig. 2, where (a) and (b) are the results obtained at an arc current of 50 A. On the other hand, (c) and (d) are those at an arc current of 100 A. In (a) and (c), the moleculer weight is 200. In (b) and (d), it is 1000. On average, the application of PEG results in the increase of the oxide removal rate. In a case of no application of PEG, the removal rates do not disperse so much. But if PEG is applied, the removal rates disperse in a wide range. Maximaum increase of the removal rate reaches to more than 300 % compared to those without PEG application. On the other hand, the minimum removal rates with PEG application are almost same as those without PEG application. The removal rate increases proportionally with the increase of the arc current.

3.2. Observation of cathode spot behavior

The behavior of the cathode spots is observed by a high speed video camera under various conditions. Much attention is paid to the differnce between the spot behavior at a low rimoval rate and that at a high removal rate. As mentioned below, the observation reveals that there exist two different types of cathode spot. The movement of cathode spots on the surface without PEG is shown at a time interval of 0.1second in Fig.3- (a), (b) and (c). As is shown in these three pictures, the cathode spots of this type move slowly. Not only on the surface without PEG but also on the surface with PEG, the cathode spots of this type appear. Because of the slow movement of the cathode spots, the rate of oxide removal is small. The movement of the other type of cathode spots is shown in Fig. 4-(a), (b) and (c). They move fast and, as the result, they remove the oxide at higher rate. Herein after, the former type is called “type 1” and the latter “type 2”. The latter spots are brighter than the former ones. During the removal of oxide, some cathode spots often change the type from one to the other suddenly.

The removal rate depends on the type of the cathode spots on the surface. The more the cathode spots belong to type 2, the faster the oxide layer is removed. At minimum removal rate, cathode spots of type 1 always appear on the surface, and at muximum removal rate, almost all cathode spots belong to type 2. Between minimum and maximum rate, two types are mixed. Mixing ratio changes the removal rate.

(a) (b) (c)

Fig. 3. Movement of cathode spots with low velocity on the oxide at a time interval of 0.1 sec.

(a) (b) (c)

Fig. 4. Movement of cathode spots with high velocity on the oxide at a time interval of 0.1 sec.

3.3. Tracks of cathode spot movement

The vacuum arcs are operated in a short duration for 3 seconds at a current of 100A, then the tracks of cathode spot movement are observed. Fig.5 (a) shows the tracks of type 1 cathode spots which are obtained on the surface with PEG of molecular weight 600. Fig.5 (b) shows the tracks of type 2 cathode spots on the surface with PEG of molecular weight 200. There are big differences between them. The tracks produced by type 1 cathode spots are wider than those by type 2. It is expected that the diameter of type 2 cathode spot is smaller than that of type 1 cathode spot.

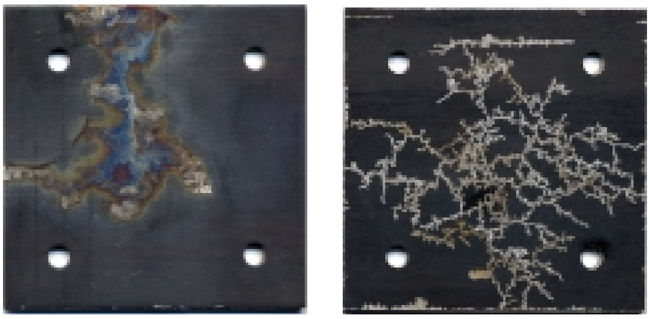

(a) (b)

Fig. 5. Comparison of cathode spot-trace in two types: (a) the type of low-rate of removeal; (b) the type of high-rate of removeal.

As for the length of tracks formed for 3 seconds operation, that of type 2 is much larger than that of type1.

3.4. Vriation in number of cathode spot

The authors examine the difference of current per one cathode spots between two types. The number of cathode spot are measured under various conditions. On the surface without PEG, 3 to 5 spots are found at a arc current of 50 A, and 5 to 7 spots at 100 A. When PEG was applied on surface of the test pieces, experimental results are classified into 3 cases. In one case almost all cahode spots belong to type 1, in another case, only type 2 spots appear, and in the third case, two types are mixed. Totally 250 test pieces are examined after the appication of PEG. Half of them are used for experiments at the arc current of 50 A, and the others are at 100 A. In each experiment, number of the cathode spots on the surface is measured and the type of cathode spots are classified. The numbers of the test pieces are listed in the matrix between the number of cathode spots and types of cathode spots. During the removal of oxide, the number and the type change with time. The location in the matrix of Table 2 is determined for the time intreval of 5 seconds after the arc ignition. Table 2 (a) represents the results at the current of 50 A and (b) at the current of 100 A. At the arc current of 50 A, the average numbers of cathode spots are calculated to be 3.2 and 2.4 for type 1 and type 2 , respectively. And at the current of 100 A, they are 6.3 and 4.9 for type 1 and type 2, respectively. In average, the number of the cathode spots is proportional to the arc current. It is clear that one cathode spot of type 2 carries more current than that of type 1.

Table 2. The number of cathode spot on the surface with the PEG

(a) Arc current 50 [A]

		Number of test piece		
		Type 1	Mixed type	Type 2
Number of cathode spot	1 – 2	0	0	12
	2 – 3	20	27	16
	2 – 4	3	2	2
	3 – 4	20	14	6
	3 – 5	3	1	0
	4 – 5	3	0	0

(b) Arc current 100 [A]

		Number of test piece		
		Type 1	Mixed type	Type 2
Number of cathode spot	3 – 4	0	2	2
	3 – 5	0	2	2
	4 – 5	1	0	19
	4 – 6	0	5	4
	5 – 6	6	25	16
	6 – 7	14	10	0
	6 – 8	3	6	0
	7 – 8	2	1	0

3.5. Surface roughness

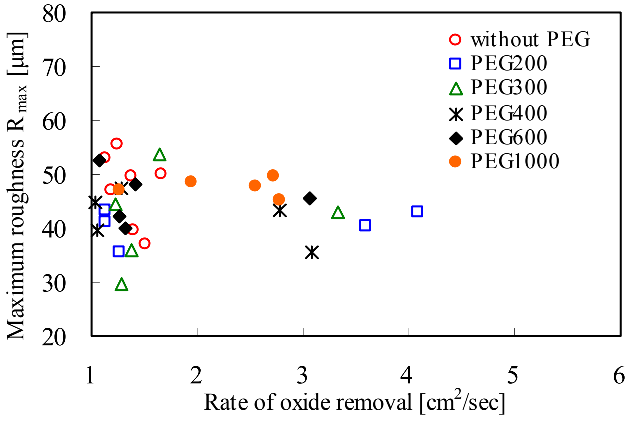

(a)

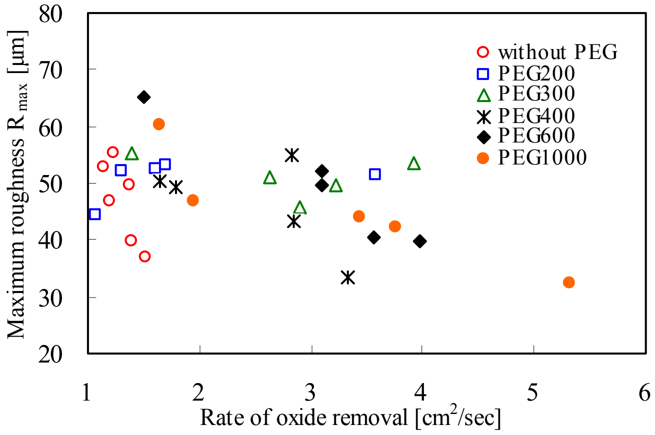

(b)

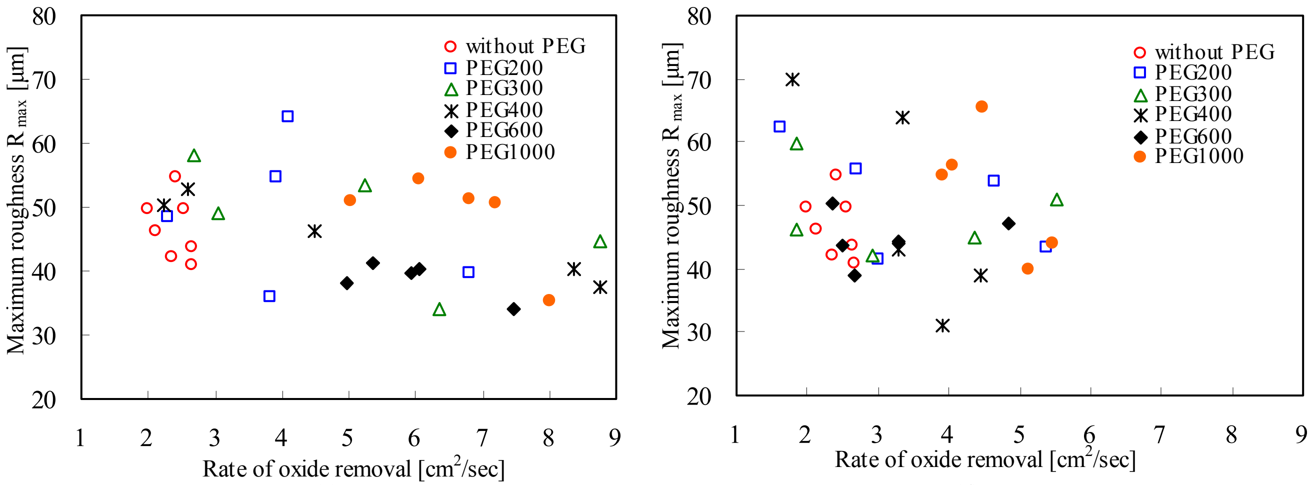

(c) (d)

Fig. 6. Variation of the maximum roughness R_{max} with the rate of oxide removal: (a) Arc current is 50A,and amount of application is 1mg; (b) the current is 50A, and amount of application is 10mg; (c) the current is100A, and amount of application is 1mg; (d) the current is 100A, amount of application is 10mg.

Vacuum arc cleaning roughens the surface. Typical changes in surface roughness (R_{max}) are shown in Fig. 6 where (a) and (b) represent the results at an arc current of 50 A, (c) and (d) are those at 100 A. Roughly saying, the surface roughness decreeases with the increase of oxide removal rate. It could be said that the appearance of type 2 cathode spots contributes to reduce the surface roughness.

4. Concluding remarks

The authors invstigate the effect of PEG application on the oxide removal action of the cathode spots. Experimental observations reveals that cathode spots are classified into two types, type 1 and type 2. Compared to type 1 cathode spots, characteristic features of type 1 cathode spots are summarised as;

(1) They (type 2 cathode spots) carries more electric current than the others (type 1 cathode spots).
(2) They move faster than the others.
(3) They have larger diameter than the others.
(4) They remove oxide more quickly than the others.
(5) They provide smoother surface than the others.

The application of PEG enhances the proberbility of the presence of type 2 cathode spots.

5. Aknowledgement

This work has been supported by Grant-in Aid for Scientific Research (B) from the Ministry of Education, Culture, Sports, Science and Technology in Japan.

References

[1] K. Takeda, S. Takeuchi - Thin Solid Films. 407, (2002) , 163-168
[2] K. Takeda, S. Takeuchi - J. Japan Inst. Metals. **63**, 1, (1999), 41-47
[3] K. Takeda, S. Pozharov, A. Mirkarimov and M. Sugimoto – "Efeects of active elements on oxide removal by avacuum arc", in Proc. XXth ISDEIV, Tours (France), (2002), 107-110
[4] Z. Kondo, K. Takeda, S. Takeuchi - Patent application, JP N 8-243630, (1996)

Gas phase nucleation of diamond in non-thermal fluorocarbon dusty plasmas

Kazuo Takahashi[1], Kouichi Ono[1], Yuichi Setsuhara[1], Tetsuyuki Okano[2], Takashi Kouzaki[2]

[1] *Department of Aeronautics and Astronautics, Kyoto University,*
Yoshida-Honmachi, Sakyo-ku, Kyoto 606-8501, Japan
[2] *Matsushita Technoresearch, Inc.,*
3-1-1, Yagumo-Nakamachi, Moriguchi, Osaka, 570-8501, Japan

Abstract

Nanometer-scale nuclei of dust have been precisely observed with high resolution transmission electron microscope, which are synthesized and grow to the micrometer-sized dusts in gas phase of room temperature fluorocarbon plasmas. The many crystalline grains were confirmed in the view of the microscope, corresponding to diamond and graphite structures. The present study shows that nanostructured crystal of diamond can be synthesized even at low pressure of 250 mTorr and at room temperature.

1. Introduction

Dust formation in plasmas has been very attractive in exploring the origin of solid matters as well as for purification of processing plasmas for microelectronics device fabrication. We reported the dust formation in fluorocarbon plasmas used as a tool of silicon dioxide etching and thin film deposition [1, 2, 3]. In the fluorocarbon plasmas, large polymerized molecules of nanometer-scale are produced in gas phase and grow to micrometer-sized dusts [1]. The polymerized molecules working as dust nuclei have not been specified in atomic structure. Nanostructured matters such as the polymerized molecules stimulate curiosity which are synthesized in a non-thermal-equilibrium circumstance of plasma, since nanometer-scale materials of fullerene, nanotube and diamond may be formed in conditions such as high pressure and high temperature and not in gas phase. Burden et al. confirmed the formation of fullerene and nanotube in a room temperature plasma, then they hypothesized that these products were synthesized in gas phase rather than on surface of electrodes [4]. Frenklach et al. reported the homogeneous nucleation of diamond power under high pressure of 10 Torr or higher [5]. The diamond nucleus has also been discovered in other conditions at high temperature, detonations [6], meteorites [7] and a low pressure high density plasma heated up to 500 °C [8]. In this paper we present that the nanometer-scale molecules have atomic orders, which are synthesized in gas phase of fluorocarbon plasmas generated at low pressure of 250 mTorr and at room temperature.

2. Experimental

A conventional parallel-plate type reactor was used, whose schematic was described in Ref. 3. The rf powered electrode at the upper side was a plate of 15 cm in diameter, surrounded by grounded metal shield. The other electrode was grounded and set 3 cm below the rf electrode. A capacitively coupled plasma was generated by a 13.56 MHz rf power source with a p-type matching network. The discharge power was measured at the output of the generator, so that the losses in the matching network and cables not taken into account. The nominal value of the power density was maintained at 0.15 W/cm^2 corresponding to the total power of 30 W. The source gas molecule of octafluorocyclobutane (C_4F_8) was supplied by a mass flow controller through the upper shower-head electrode. The flow rate was 1.7 sccm. In this configuration, the residence time of the source gas molecule was long being of the order of a few minutes. This condition was preferable for the dust production [2].

Si wafers were rinsed by a solvent to remove the impurities such as house dust before the plasma treatment. A wafer was mounted on the lower electrode and exposed to the discharge for 15 min. Thin film of fluorinated amorphous carbon was deposited on the wafer, and dusts fell down from the trapped region near the plasma-sheath boundary to the surface during the discharge. The dusts were found to be agglomerates composed of micrometer-sized spherical particles in the observation by scanning electron microscope. Since the dusts were identified to be white or yellow powder by naked eyes, we could pick up only the dust particles. The dusts seemed to be covered with the thin film deposited on surface. Nevertheless there is great difference in molecular composition between the dusts and the thin film [1]. Therefore it is not hindered from understanding that the thin film coating the dusts did not affect the composition of the dusts.

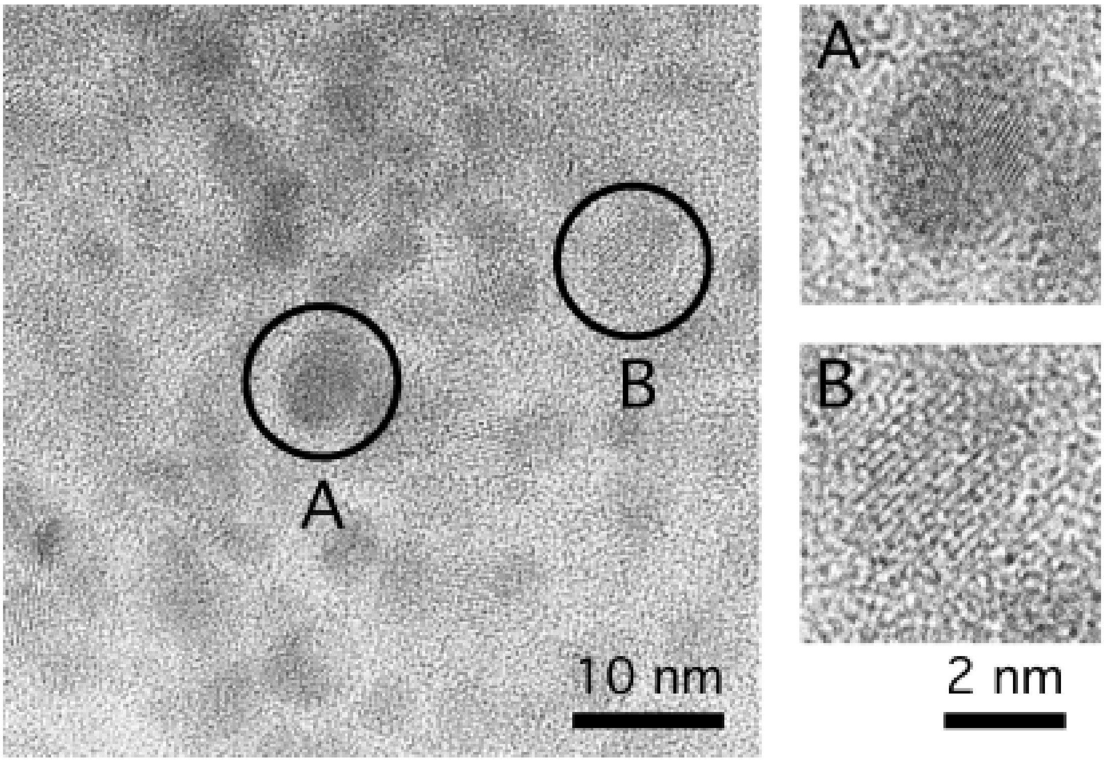

Fig. 1 Typical photograph of view of the HRTEM. The parts enclosed by the circles A and B show the crystalline domains of diamond and graphite, respectively, corresponding to the magnified views in the right side.

The corrected white or yellow colored powder were dissolved in a small quantity of tetrahydrofuran (THF). Then the solution was spread on a holey carbon support film of a copper electron microscopy finder grid. The nanostructure of the soluble molecules were analyzed by using a JEOL JEM-4000EX high resolution trasmission electron microscope (HRTEM) operated at 400 kV with a filament.

3. Results and discussion

In the former study, deposited films and dust particles were observed, produced in the fluorocarbon plasmas in the pressure range from 23 to 250 mTorr. In the whole tested range, amorphous fluorocarbon film was deposited irrespective of the surface condition. The dust particles, however, were observed only at the pressure higher than 50 mTorr. Whose diameter measured in scanning electron microscope observation ranged between 0.5 and 2.3 μm [2]. Chemical characterization of the dust particles was performed with gel permeation chromatography (GPC) and x-ray photoelectron spectroscopy (XPS). From the GPC results, it became clear that the dust particles produced in gas phase contained polymers of ultrahigh mass around 100,000. In addition, species with molecular weight less than 2,000 were also found in an extract from the dust particles as in the case of the deposited film. In the first XPS measurement, the XPS spectrum of the dust particles was almost the same as that of the film, because the dust particles were possibly covered with the fluorocarbon films after dropping on the surface. In order to remove the film on the dust particles, Ar ion sputtering was done in the XPS system using a low energy ion beam so as to avoid the transformation of the chemical composition. The XPS spectrum of the dust particles obtained in such way was obviously different from that of the film. The content of C-CF_x bond component in the dust particles was more than from that of the film. This result indicated that the branching of carbon network was promoted in the precursor molecules composing the dust particles.

The ultrahigh mass polymer as the precursor of the dust particle is 9.7 nm in geometrical dimension, estimated for the molecular weight of 100,000. The polymer was tried to be observed with HRTEM, which was extracted by the THF solution process. We could find many crystalline grains in a view of HRTEM (Fig. 1). There were two types of structure in the atomic order. The electron beam diffraction pattern indicated that the structures were the diamond (111) planes (0.206 nm) and the graphite (002) planes (0.336 nm), shown by the circles A and B, respectively, in Fig. 1. It is predicted from the XPS results that these grains seemed to be terminated by fluorine atoms on the surface. On the other hand, dusts of a few hundreds nanometers could be obtained by the discharge for short time of 1 min. The surface on the dust was observed by using TEM and found to be covered with amorphous layer. Hence the crystal structure of nanometer-scale did not continue to epitaxially grow on the nucleus surface.

It is possible that the crystallization is caused in nanometer-scale regime exposed by heat flux from electrons and ions. Stoffels et al. have reported that micrometer-sized particles in plasmas can be heated higher than 100 °C [9]. Since heat capacitance of nanometer-sized matter become small, temperature of the matter may reach to a few hundreds degrees or higher. Furthermore in nanostructured carbon, heat of formation for diamond is lower than that for graphite [10]. These facts may support our experimental results that nanometer-sized crystalline grains were obtained in gas phase of room temperature plasmas at low pressure of 250 mTorr.

4. Conclusions

From the point of view of material science, it is interesting that a crystalline structure is synthesized in the non-thermal (non-equilibrium) plasmas at low pressure of 250 mTorr. In gas phase, the reactions excited by energetic electrons of a few electron volts and bombarding ions may cause the crystallization, and the fact that heat of formation for diamond is lower than that for graphite in a nanometer-scale regime may explain essentially the mechanism of the diamond nucleation in the non-thermal fluorocarbon plasmas.

References

[1] K. Takahashi and K. Tachibana, J. Appl. Phys. **89**, 893 (2001).
[2] K. Takahashi and K. Tachibana, J. Vac. Sci. Technol. A **19**, 2055 (2001).
[3] K. Takahashi and K. Tachibana, J. Vac. Sci. Technol. A **20**, 305 (2002).
[4] A. P. Burden and S. R. P. Silva, Appl. Phys. Lett. **73**, 3082 (1998).
[5] M. Frenklach, R. Kematick, D. Huang, W. Howard and K. E. Spear, J. Appl. Phys. **66**, 395 (1989).
[6] N. R. Greiner, D. S. Phillips, J. D. Johnson and F. Volk, Nature **333**, 440 (1988).
[7] R. S. Lewis, T. Ming, J. F. Wacker, E. Anders and E. Steel, Nature **326**, 160 (1987).
[8] K. Teii and T. Yoshida, J. Appl. Phys. **85**, 1864 (1999).
[9] E. Stoffels, W. W. Stoffels, H. Kersten, G. H. P. M. Swinkels and G. M. W. Kroesen, Phys. Scr. T **89**, 168 (2001).
[10] P. Badziag, W. S. Verwoerd, W. P. Ellis and N. R. Greiner, Nature **343**, 244 (1990).

16th International Symposium on Plasma Chemistry

PAPER SUBMI SSION FORM

Author Contacting Details

Mr. (X) Ms. ( )

*Family Name	TAKAHASHI		
*First Name	KAZUO		
*Title	DR.		
*Institute /Company	KYOTO UNIVERSITY		
*Address	YOSHIDA-HONMACHI, SAKYO-KU		
*Zip Code	606-8501		
*City	KYOTO	*Country	JAPAN
Phone	+81-75-753-5798		
§E-mail	TAKAHASHI@KUAERO.KYOTO-U.AC.JP		
§Fax	+81-75-753-5980		

Contribution Details

Abstract File Code	**ISPC- 505**		
*Paper Title	GAS PHASE NUCLEATION OF DIAMOND IN NON-THERMAL FLUOROCARBON DUSTY PLASMAS		
*Presenting author	Kazuo Takahashi		
*Key Words	Diamond	Nanoparticle	Dusty plasma

*E-mail or fax required

*Required fields

Please check the above information and fill in the blank fields and return this form along with the Full-Paper before March 30th, 2003 to

ISPC-16 Scientific Secretariat
Dipartimento di Chimica – Università di Bari
Via Orabona 4, 70126 Bari Italy
e-mail: info@ispc16.org

TRANSFER OF COPYRIGHT

To be signed by the author or, in the case of multiple authorship, by at least one of the authors who agrees to inform the others, or, in the case of a work made for hire, by the employer. The signed statement must be received by the Editor before the manuscript can be accepted for publication.

Copyright to the article by ………………………………………………………………………
Kazuo Takahashi, Kouichi Ono, Yuichi Setsuhara, Tetsuyuki Okano and Takashi Kouzaki
....
submitted under the title ....……...............................
Gas phase nucleation of diamond in non-thermal fluorocarbon dusty plasmas
....

is hereby transferred to the International Plasma Chemistry Society for publication in the

PROCEEDINGS OF THE 16th INTERNATIONAL SYMPOSIUM ON PLASMA CHEMISTRY.

The authors explicitly reserve the following rights:

All proprietary rights other than copyright, such as patent rights.

The right to use all or part of this article in future works of their own, such as lectures, reviews, textbooks, or reprint books.

The right to make copies for the authors' own teaching use.

The right to use figures and tables in future publications, provided explicit acknowledgment is made of their initial appearances in the proceedings.

....	....
Signature	Signature
Kazuo Takahashi	
....	....
Name (print)	Name (print)
Kazuo Takahashi	
....	....
Date	Date
24 Mar. 2003	

Influence of the incident angle of energetic carbon ions on the properties of tetrahedral amorphous carbon (ta-C) films

Dongping Liu[1], Günther Benstetter[1], Edgar Lodermeier[1], and Johann Vancea[2]

[1]University of Applied Sciences Deggendorf, Deggendorf 94469, Germany
[2]University of Regensburg, Institute of experimental and applied physics 93040 Regensburg Germany
Dongping.liu@fh-deggendorf.de
Guenther.benstetter@fh-deggendorf.de
Edgar.lodermeier@fh-deggendorf.de
Johann.Vancea@physik.uni-regensburg.de

Tetrahedral amorphous carbon (ta-C) films have been deposited on Ar^+-beam-cleaned Si substrates by changing incident angle of energetic carbon ions produced in the plasma of cathodic arc discharge. Their composition, surface roughness, tribological and mechanical properties as a function of the incident angle of energetic carbon ions are reported. The substrate holder is rotated and an angle of deposition is defined as an angle of the ion flux with respect to the substrate surface. Nanoscale atomic force microscopy (AFM) (tapping mode) surface roughness analysis is carried out on these films. The films with lowest root-mean-square (RMS) roughness (0.10 nm) are obtained at the deposition angle of 59° - 77°. The film deposited at the deposition angle of 90° shows RMS roughness of 0.16 nm. While the deposition angle is varied from 59° to 20°, RMS roughness increases from 0.10 to 0.50 nm. Nanoindentation and nanowear measurements are carried out by using the atomic force microscope and a diamond-tipped cantilever. The pyramidal diamond tip (tip radius lower than 50 nm) mounted on a stainless-steel cantilever is used to generate indentation impressions and wear marks. The loading force acting on the tip is calculated by multiplying the tip displacement with its spring constant. AFM tapping mode is used to image the surface after the indentation using the diamond tip with no additional damage to the surface. The hardness is defined as the ratio of the indentation force to the projected area of the residual indentation. While the deposition angle increases from 20° to 59°, the film hardness increases greatly from 30 to 100 GPa, but turns to decrease when the deposition angle is more than 77°. The variation correlates well with the one of RMS roughness with the deposition angle. Wear tests are conducted by scanning a 500nm×500nm area at a given load of 33 μN. AFM images of the resulting wear craters are obtained for an increasing number of wear cycles. The wear tests show the soft layers existing at the surfaces of the DLC films and their thickness increases from 0.38 to 3.2 nm while the deposition angle is varied from 90° to 30°. The change is accompanied by the decrease of the sp^3 contents determined by X-ray photoelectron spectra (XPS). The sp^3 content proportionally varies from 38% to 72% with the deposition angle increasing from 30° to 77°. Thickness of graphite-like surface layers can have great effect on the sp^3 contents determined by XPS. Nanoscale friction coefficient measurements from lateral force microscope (LFM) are performed with the AFM system. A V-shaped Si_3N_4 cantilever with tip radius of approximately 20 nm is used for these measurements. The friction coefficient shows an increase from 0.78 to 0.95 with the deposition angle increasing from 30° to 77°. The low friction coefficient of these films can be attributed to their graphite-like surface structure. We propose a film deposition processes where surface roughness, thickness of graphite-like surface layers and mechanical properties are determined by the deposition angle. It is assumed that the growth and coalescence of adsorbed species via surface diffusion could lead to formation of rough and graphite-like surface layers while ion subplantation process could give a quenched-in density increase and cause the etching of the soft surface layer.

Deposition of thin organosilicon polymer films in atmospheric pressure glow discharge

Z. Navrátil, L. Zajíčková, P. Sťahel, V. Buršíková, J. Čech, Z. Kučerová, D. Trunec

Department of Physical Electronics, Masaryk University, Kotlářská 2, 611 37 Brno, Czech Republic

Abstract

The atmospheric pressure glow discharge in nitrogen with small admixture of different organosilicons compounds such as hexamethyldisilazane or hexamethyldisiloxane was studied by means of emission spectroscopy and electrical measurements. The deposited films were characterised by ellipsometry, depth sensing indentation technique, contact angle and infrared transmission measurements.

1. Introduction

Owing to their suitability for industrial processes, especially because of atmospheric pressure processing and the possibility of on-line treatment, dielectric barrier discharges (DBD) are widely used for industrial purposes such as modification of polymer surface properties, e.g. wettability or adhesion. Even though this treatment is very useful, it has at least two drawbacks, namely the lack of uniformity and the limitation of surface transformation. This is due to the fact that, at atmospheric pressure, the discharge is normally, a filamentary discharge. Moreover, the reproducibility and the control are limited due to the filamentary nature of the discharge. Because of these drawbacks an effort to homogenise DBD discharges as well as their effect on a surface has been made, for instance, by increasing the number of statistically distributed micro-discharges. Another possibility is the homogenisation of the discharge itself that is the case of an atmospheric pressure glow discharge (APG).

The plasma enhanced chemical vapour deposition (PECVD) methods enable to prepare coatings with wide range of properties changing, e.g. wetting and sticking behaviour, mechanical, optical or electrical properties. The disadvantage of the low pressure PECVD techniques is their demand of expensive vacuum pumping systems. Moreover, the difficulties to arrange the deposition system for large area depositions has to be overcome. Recently plasma deposition at atmospheric pressure becomes a promising technology due to its economical and ecological advantages.

The APG discharges can be easily generated in various pure gases [1, 2, 3, 4]. However, in nitrogen which is from the technological point of view the most suitable gas, the small admixture of impurities such as oxygen can lead to the generation of filamentary DBD instead of APG [4]. Therefore it is important to study the influence of monomer admixture and its concentration on the character of the barrier discharge. In the present paper we have studied the APG discharges in nitrogen with small admixture of two different organosilicons compounds, hexamethyldisilazane ($C_6H_{19}Si_2N$ - HMDSZ) and hexamethyldisiloxane ($C_6H_{18}Si_2O$ - HMDSO), which can be used for the deposition of thin films with desired surface energy, permeability, optical and mechanical properties [5, 6, 7].

2. Experimental

The atmospheric pressure glow discharge was generated between two plane metal electrodes covered with a dielectric barrier (glass). The space between the electrodes was 1 mm. High voltage with the frequency 6 kHz was used for discharge generation. The type of discharge as concern a filamentary or glow mode was determined from the current-voltage measurements. The power density 10W/cm^3 was kept in all experiments presented in this study. Configuration of the reactor is drawn on the Fig. 1.

The films were deposited from different mixtures of organosilicons (HMDSZ, HMDSO) with nitrogen. The pure nitrogen was mixed with nitrogen driven through glass bottle containing monomer. Thin polymer-like layers were deposited on a thin glass substrate of 25 x 60 x 0.3 mm size, for ellipsometry and FTIR analysis the silicon wafer of 10 cm in diameter was used.

The total surface energy of the films was investigated by means of the sessile drop technique using the Surface Energy Evaluation System (SEE System) developed in our lab [8]. The contact angles were measured directly from the observation of the solid-liquid meniscus. The liquid drop set on the solid was taken with CCD

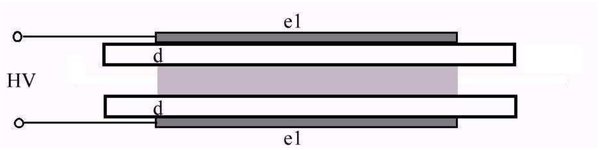

Figure 1: Configuration of the reactor used for generation of APGD. El – electrodes, d – dielectric barrier (glass), HV – high voltage.

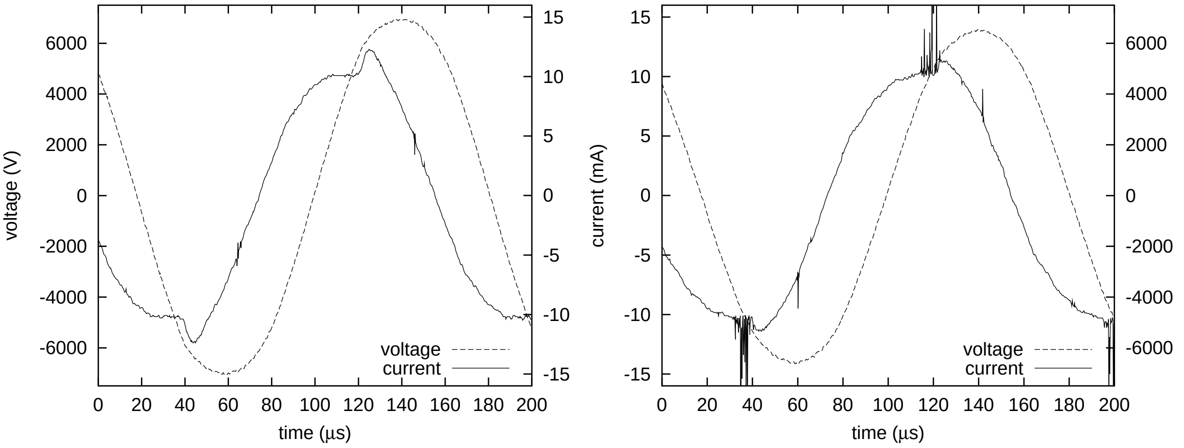

Figure 2: Time variation of current and applied voltage of APG discharge (a) and filamentary discharge (b).

camera. For the determination of total free surface energy from the contact angle measurement the so-called ”acid-base” theory we used. This theory [9] enables to determine polar and apolar part of free surface energy and the electron-acceptor and electron-donor parameters of the surface tension.

The composition of the film was determined by Fourier Transform Infrared Spectroscopy (FTIR) using NICOLET Impact 400 spectrometer. The bare silicon substrate was taken as a reference. The resolution of the spectrometer was set as 0.96 cm^{-1}. In the ultraviolet-visible range, the optical properties of the films on the silicon substrates were investigated by ellipsometry. The UVISEL Jobin Yvon ellipsometer was used to measure the ellipsometric parameters at five angles of incidence (55°–75°) in the spectral range 240–830 nm. The films were only slightly absorbing in the UV/VIS and the elipsometric measurements could be fitted using a simple Cauchy formula for film refractive index n and an exponential form for film extinction coefficient k (λ is wavelength):

$$n = a + b/\lambda^2 + c/\lambda^4, \qquad k = \alpha.e^{-\beta\lambda} \tag{1}$$

where a, b, c, α and β are dispersion parameters.

The morphology of the deposited films was studied by Atomic Force Microscopy (AFM). The mechanical properties were studied by means of the depth sensing indentation technique using a Fischerscope H100 tester. The discharge was studied by means of the optical emission spectroscopy. The spectra emitted by the discharge were recorded with the Jobin-Yvon TRIAX 550 monochromator, with the CCD detector.

3. Results and discussion

The first part of the results is devoted to the diagnostics of the discharge itself. This is in particular important in order to observe the transition between the filamentary and glow modes of DBD and understanding of the chemistry in the discharge. The second part of the results describes the properties of the deposited films which are important from the application point of view.

3.1 Discharge diagnostics

The characteristic course of APGD voltage and current is presented in Fig. 2a. Whereas applied voltage is

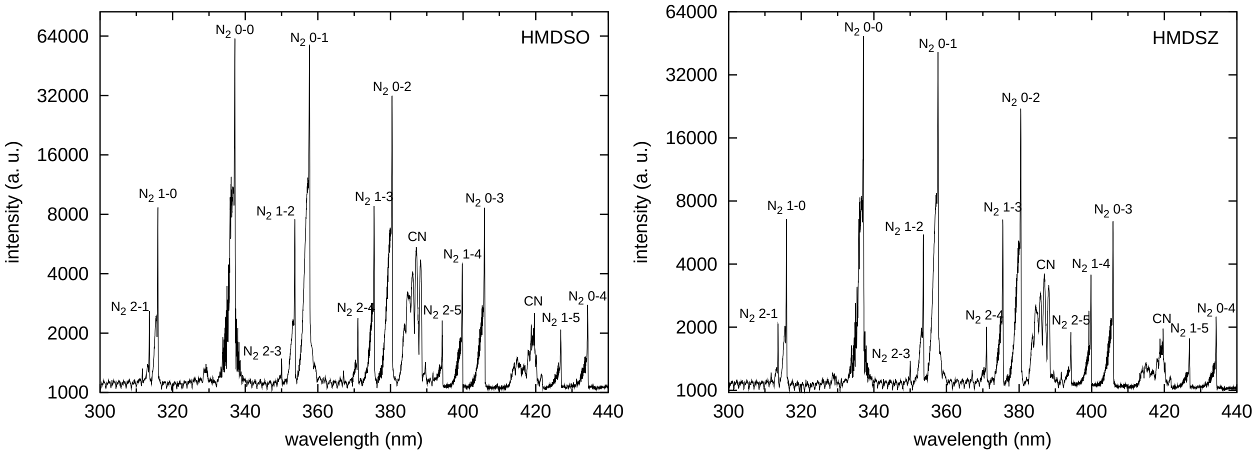

Figure 3: Emission spectra of APGD in nitrogen with organosilicon. Flow rate of organosilicon vapours was 0.8 lmin^{-1} in both cases.

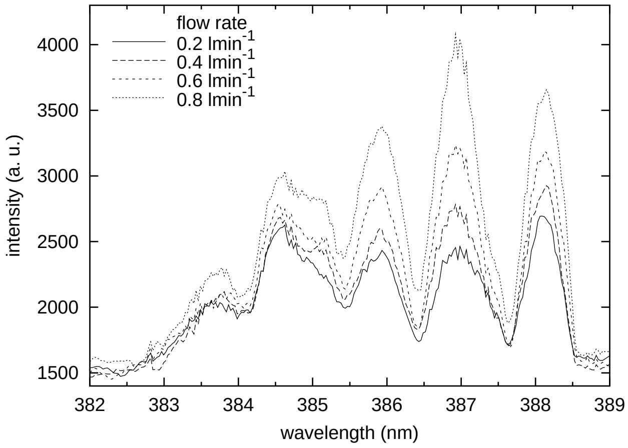

Figure 4: Structure and intensity variation of the CN band at 388 nm with the flow rate of HMDSZ.

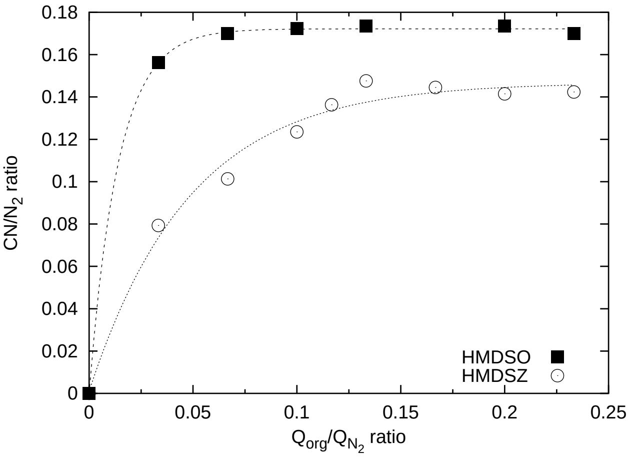

Figure 5: Ratio of integrated intensities of CN 388.3 nm band and N_2 system vs. concentration of organosilicon.

sinusoidal, the current consists of two parts. The sinusoidal current course corresponds to capacitive current, the small peak represents the current of the APG discharge. In case of high concentration of monomer the character of the discharge changes to filamentary discharge (see Fig. 2b).

Fig. 3 shows typical emission spectra of the APG discharge in nitrogen containing organosilicon vapours. The spectra were recorded in the range of 300 – 800 nm, but above 450 nm only the second spectral order was registered. Spectra of the discharges containing HMDSO or HMDSZ are very similar. Spectra consist of the molecular bands of second positive system of nitrogen ($C\,^3\Pi_u \rightarrow B\,^3\Pi_g$). In the case of the monomer admixture to nitrogen two intensive bands of CN violet system (($^2\Pi \rightarrow {}^2\Sigma$) appear at 388 nm and 422 nm. In Fig. 4 the structure and intensity variation of CN band for different concentrations of organosilicon is plotted. Since not only the intensity of CN band but also the intensity of N_2 system depends on the flow rate of the organosilicon, ratio of the integrated intensities of CN band and N_2 system was calculated. The CN/N_2 ratio exponentially increases with increasing concentration of HMDSO or HMDSZ (see Fig. 5).

The bands of second positive system of nitrogen N_2 0-2, N_2 1-3 and N_2 2-4 were used to calculate vibrational temperature. Determined vibrational temperature is at about 1710 ± 20 K in case of HMDSO, 1760 ± 30 K in case of HMDSZ and does not change with the variation of the flow rate of organosilicon.

3.2 Film characterisation

The optical properties, refractive index and extinction coefficient in the ultraviolet-visible range (UV-VIS) for

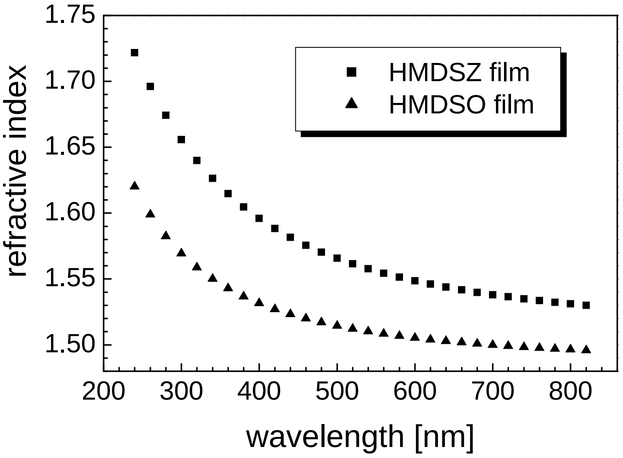

Figure 6: Refractive index of the films deposited from HMDSO/N_2 and HMDSZ/N_2 gas feeds. The flow rates of monomer and N_2 were 0.2 and 6 slm, respectively.

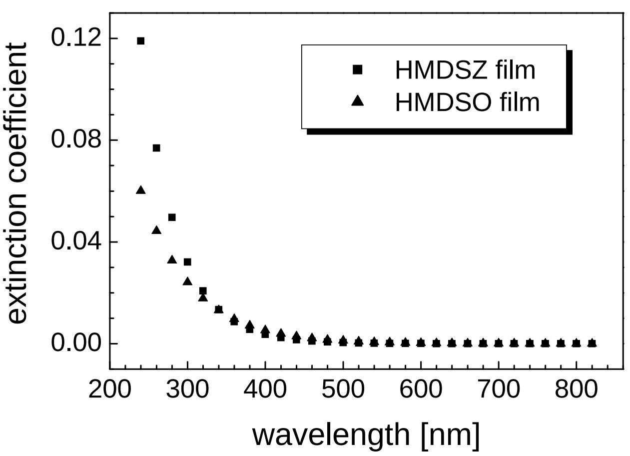

Figure 7: Extinction coefficient of the films deposited from HMDSO/N_2 and HMDSZ/N_2 gas feeds. The flow rates of monomer and N_2 were 0.2 and 6 slm, respectively.

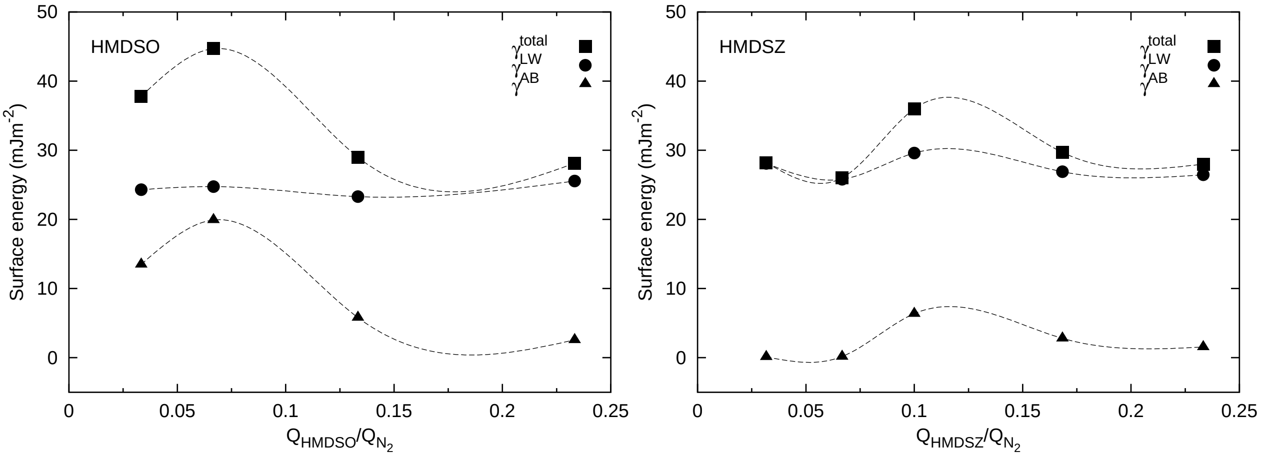

Figure 8: Components of the surface free energy as a functions of relative flow rate of HMDSO and HMDSZ. Q_{org} denotes the flow rate of organosilicon vapours, $Q_{\mathrm{N_2}}$ denotes the flow rate of pure nitrogen. Dashed lines serve only as a guide of eyes.

films deposited from both monomers are given in Figs. 6 and 7. The refractive indices are higher than for silicon oxides but lower than for silicon nitrides. Although both mentioned materials are fully transparent the polymers deposited exhibit absorption especially in UV.

The total, polar and apolar surface free energies as a function of monomer concentration in nitrogen are shown in Fig. 8. Acidic and basic components of the polar part are not displayed to keep the clarity of the plot. In case of the films deposited from HMDSO the apolar part does not change with the concentration of monomer, but the polar part decreases with increasing concentration. Total surface free energy of the films deposited from HMDSZ and its polar and apolar parts depend only slightly on the concentration of HMDSZ.

The chemical structure of the films deposited from HMDSZ and HMDSO was investigated by means of FTIR spectroscopy. The characteristic spectra are shown in Figs. 9 and 10, respectively. Three absorption peaks characteristic of silicon oxide films [11] can be assigned for both monomers around 1040 cm^{-1} (Si-O-Si stretching), 800 cm^{-1} (Si-O-Si bending), and 450 cm^{-1} (Si-O-Si rocking). This fact suggests that oxygen was also present in the deposition process due to the atmospheric pressure conditions. However, we can see that the peak at 450 cm^{-1} that is associated solely with the Si-O-Si network is much more intensive for HMDSO. The other two peaks are probably overlaped with the vibrations of the organic structures like Si-CH_2-Si (1020–

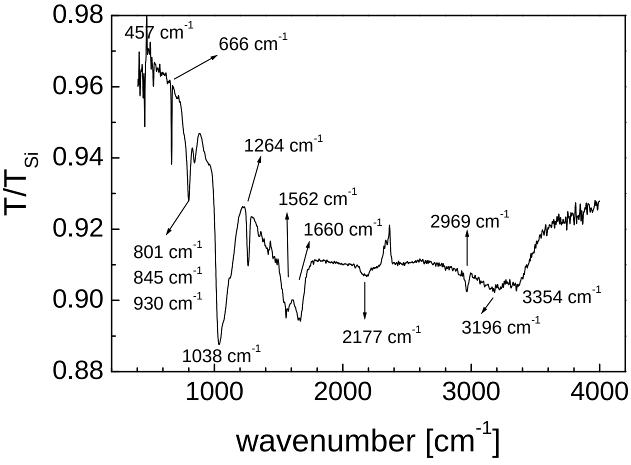

Figure 9: Typical infrared spectra of the film deposited from HMDSZ/N_2 gas feed.

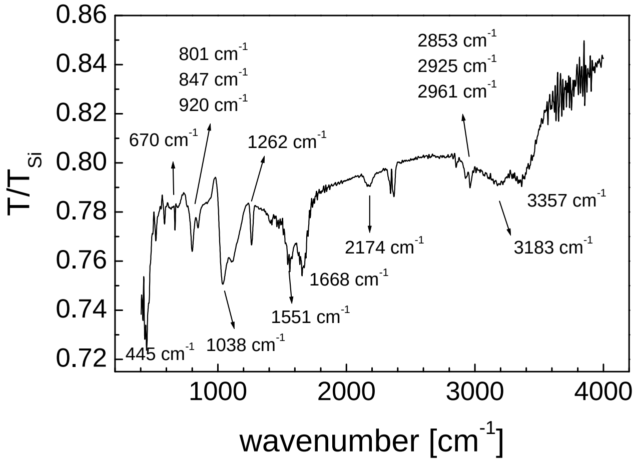

Figure 10: Typical infrared spectra of the film deposited from HMDSO/N_2 gas feed.

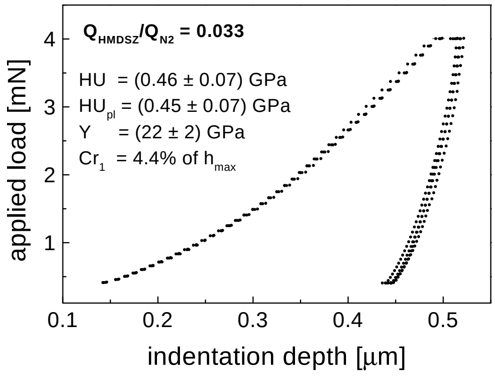

Figure 11: Load/penetration curve for coating deposited on glass substrate from mixture of HMDSZ and nitrogen.

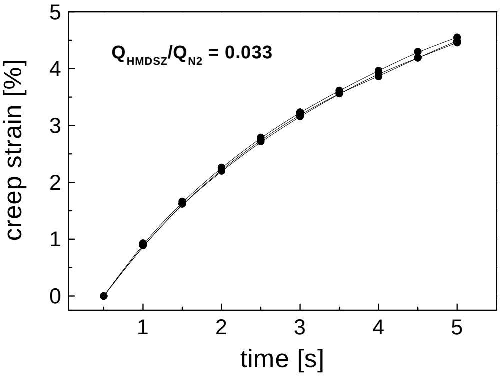

Figure 12: Creep curves measured at constant load of 4 mN for coating deposited on glass substrate from mixture of HMDSZ and nitrogen.

1090 cm^{-1}), Si-CH_3 (980–990 cm^{-1}), Si-$(CH_3)_3$ (840 cm^{-1}), Si-CH_x or Si-$(CH_3)_2$ (around 800 cm^{-1}) [12, 13]. The organic structure is revealed also by the peak at 1260 cm^{-1} that can be assigned to Si-CH_3 vibrations and by the C-H stretch absorption bands from 2850 to 2970 cm^{-1}. It is interesting to notice that although the HMDSZ film shows only absorption at 2969 cm^{-1} associated to sp^3CH_3 configuration the C-H stretch band of HMDSO film composes from three distinguished peaks at 2853, 2925 and 2961 cm^{-1} related to sp^3CH_2 (symmetric deformation), sp^3CH_2 (asymmetric deformation) and sp^3CH_3 configurations, respectively [14]. The peak observed at 2170–2180 cm^{-1} can be assigned to Si-H vibrations. The presence of water and OH groups is revealed by the peaks at 930, 1560, 1660, 3190 and 3350 cm^{-1}.

The coatings exhibited good abrasion resistance and the microhardness of the films deposited from organosilicon/nitrogen mixtures (measured on films deposited on thin glass and polycarbonate plates) was about 0.1 – 0.6 GPa. The elastic modulus ranged from 10 to 25 GPa. The film exhibited polymer-like visco-plastic behaviour. A typical load-penetration dependence is shown in Fig. 11. The creep (time dependent plastic deformation at constant applied load) behaviour of the coatings was also studied. In Fig. 12 the time dependence of the creep strain is illustrated for coating prepared from mixture of HMDSZ and nitrogen. The flow rate ratio Q_{HMDSZ}/Q_{N2} was 0.033.

4. Conclusion

A new deposition technique based on atmospheric pressure glow discharge was studied. Homogeneous layers transparent in the visible with good mechanical properties were deposited from mixtures of organosilicon monomers with nitrogen. The free surface energy of deposited coatings was in the range of 30–45 mJm^{-2} (HMDSO+N$_2$) and 26–40 mJm^{-2} (HMDSZ+N$_2$) depending on the conditions of the deposition. The FTIR spectra showed organic structure of the films, incorporated oxygen in the silicon oxide network and a presence of water and OH groups.

Acknowledgement

The present work was supported by the Grant Agency of the Czech Republic, contracts No. 202/02/0880 and 202/02/D097 and by the Ministry of Education of the Czech Republic, contracts MSM143100003, COST 527.20, ME489 and FRVŠ 2003/601.

References

[1] S. Kanazawa, M. Kogoma, T. Moriwaki, S. Okazaki – J. Phys. D: Appl Phys. **21**, 838 (1988).

[2] N. Gherardi, G. Gouda, E. Gat, A. Ricard, F. Massines – Plasma Sources Sci. Technol. **9**, 340 (2000).

[3] D. Trunec, A. Brablec, J. Buchta – J. Phys. D: Appl. Phys. **34**, 1697 (2001).

[4] R. Brandenburg, K. V. Kozlov, F. Massines, P. Michel, H.-E. Wagner – Proceedings of HAKONE VII. Greifswald 10-13 Sept. 2000. **1**, 93 (2000).

[5] A. M. Wrobel, M. R. Wertheimer, Plasma-polymerized organosilicones and organometallics, In R. d'Agostino, editor, *Plasma Deposition, Treatment and Etching of Polymers* pp. 163–268, Academic Press, New York 1990.

[6] L. Zajíčková, V. Buršíková, V. Peřina, A. Macková, D. Subedi, J. Janča, S. Smirnov – Surf. Coat. Technol.**142-144**, 449 (2001).

[7] A. Sonnenfeld, T.M. Tun, L. Zajíčková, K.V. Kozlov, H.-E. Wagner, J.F. Behnke, R. Hippler – Plasma and Polymers. **6**, 266 (2001).

[8] SeeSystems – Surface Energy Evaluation System. [On-line]. http://www.seesystem.wz.cz.

[9] R.J. Good – Contact Angle, Wettability and Adhesion ed. K.L. Mittal 3 (1993).

[10] P. Sťahel, V. Buršíková, Z. Navrátil, A. Zahoranová, J. Janča, J. Buršík – *ibid.*

[11] N. Selamoglu, J. A. Mucha, D. E. Ibbotson, D. L. Flamm – J. Vac. Sci. Technol. B **7**, 1345 (1989).

[12] M. T. Kim – Thin Solid Films **311**, 157 (1997).

[13] R. Lamendola, R. d'Agostino, F. Fracasi – Plasmas and Polymers **2**, 147 (1997).

[14] B. Dischler, A.Bubenzer, P. Koidl – Solid State Communications **48**, 105 (1983).

Numerical calculation of stability limit of diffuse discharge on thermionic cathodes

M. S. Benilov and M. D. Cunha

Departamento de Física, Universidade da Madeira
Largo do Município, 9000 Funchal, Portugal

Abstract

An approach is developed and calculations performed of bifurcation points positioned on the diffuse and axially symmetric modes of current transfer to axially symmetric thermionic cathodes. In particular, the first bifurcation point of the diffuse mode is calculated, and thus the current value at which the diffuse discharge becomes unstable. The effect of variation of control parameters on the limit of stability of the diffuse discharge is analysed.

1. Introduction

Advances achieved recently in the theory of current transfer to refractory cathodes of high-pressure arc discharges (see, e.g., review [1]) have been attained by means of the model of nonlinear surface heating.

In particular, it has been proved that multiple solutions may exist for a given set of input conditions, some of these solutions describing the diffuse mode of cathode operation and the others describing spot modes. In the case of an axially symmetric cathode, the diffuse mode is described by a two-dimensional (2 D) axially symmetric solution, while spot modes are described by 2 D or 3 D solutions. At present, 2 D solutions describing both diffuse and spot modes have been studied relatively well [2–4].

An important question arising in problems with multiple solutions is whether these solutions branch off from (join) one another, or, in other terms, whether bifurcations occur. As far as the model of nonlinear surface heating is concerned, this question has been studied [5] by means of the bifurcation theory for the case of cathodes having the form of a right cylinder with an insulating lateral surface. The solution describing the diffuse mode is 1 D in this case. It was found that 2 D and 3 D solutions describing spot modes branch off from the 1 D diffuse-mode solution. This prediction has been confirmed, in the part concerning branching of 2 D spot-mode solutions from the 1 D diffuse-mode solution, by the modelling [4].

As far as cathodes with current-collecting lateral surface are concerned, the two-dimensional numerical modelling [2,4] has revealed no bifurcations, i.e., the spot- and diffuse-mode solutions do not join. This is not surprising since the diffuse-mode solution is 2 D for such cathodes, as well the spot-mode solutions calculated in [2, 4], and one would not expect to encounter bifurcations if breaking of symmetry does not occur. On the other hand, one would not exclude the possibility of 3 D solutions describing spot modes to branch off from 2 D solutions describing the diffuse mode (and maybe also spot modes).

In the present work, an approach is developed to finding bifurcation points in which 3 D solutions describing spot modes branch off from 2 D solutions describing diffuse or spot modes. Apart from being of theoretical interest, this may be also of considerable technological interest due to the following. In many applications, the diffuse mode of operation of a high-pressure arc cathode is preferred. The experiment indicates that the diffuse mode is stable at large values of the arc current (e.g., [6, 7]). As the current decreases, the diffuse discharge becomes unstable. One can expect, in accord to [8], that the loss of stability occurs at the first bifurcation point, at which a 3 D solution describing the first spot mode branches off from the diffuse-mode solution.

Thus, the current value corresponding to the first bifurcation point is likely to represent the limit of stability of the diffuse discharge, i.e., the current below which the diffuse discharge becomes unstable.

It should be emphasized that numerical calculations required for finding bifurcation points at which 3 D solutions branch off from 2 D solutions are two- (rather than three-) dimensional. Thus, the approach developed in this work for calculation of the stability limit of the diffuse discharge is not computationally intense and can be easily realized on a PC, thus being suitable for engineering practice.

2. The model

We consider an axially symmetric cathode made of a substance with the thermal conductivity κ which is a known function of the temperature, $\kappa = \kappa(T)$. The base of the cathode Γ_c is maintained at a fixed temperature T_c by external cooling; the rest of the cathode surface Γ_h is in contact with the plasma or the cold gas and can exchange energy with it. We introduce cylindrical coordinates r, φ, z with the origin at the center of the front surface of the cathode and with the z-axis directed from the front surface into the cathode body. Neglecting the Joule heat production inside the cathode body, a steady-state temperature distribution in the cathode is determined by the nonlinear boundary-value problem for the Laplace equation,

$$\frac{\partial^2\psi}{\partial r^2} + \frac{1}{r}\frac{\partial\psi}{\partial r} + \frac{1}{r^2}\frac{\partial^2\psi}{\partial\varphi^2} + \frac{\partial^2\psi}{\partial z^2} = 0, \tag{1}$$

$$\Gamma_h: \quad \frac{\partial\psi}{\partial n} = q(\psi_w, U), \qquad \Gamma_c: \quad \psi = 0. \tag{2}$$

Here n is a direction locally orthogonal to the heated surface Γ_h and directed outside the cathode, the function $\psi = \psi(T)$ is the heat flux potential related to the temperature by the equation $\psi(T) = \int_{T_c}^{T} \kappa(T)\, dT$. $q = q(\psi_w, U)$ is the density of the net energy flux from the plasma to the cathode surface which is considered as a known function of the local temperature T_w of the cathode surface (or, which is equivalent, of the respective value ψ_w of the heat flux potential) and of the near-cathode voltage drop U (which is assumed to be constant along the cathode surface). The function $q(\psi_w, U)$ is calculated by means of the approach [3].

3. Calculation of bifurcation points

The aim of this section is to determine bifurcation points in which 3 D solutions branch off from (or join) axisymmetric solutions. Let $\psi_0(r, z; U)$ be an axisymmetric solution. Designate by U_i the value of the voltage drop corresponding to a bifurcation point in which 3 D solutions branch off. All solutions in the vicinity of this point (i.e., for U close to U_i) are sought in the form of a series $\psi(r, \varphi, z; U) = \psi_0(r, z; U_i) + \varepsilon\psi_1(r, \varphi, z) + \dots$, where ε is a small parameter related to $U - U_i$. The problem governing function ψ_1 may be obtained by differentiating Eqs. (1) and (2) with respect to ε and setting $\varepsilon = 0$:

$$\frac{\partial^2\psi_1}{\partial r^2} + \frac{1}{r}\frac{\partial\psi_1}{\partial r} + \frac{1}{r^2}\frac{\partial^2\psi_1}{\partial\varphi^2} + \frac{\partial^2\psi_1}{\partial z^2} = 0, \tag{3}$$

$$\Gamma_h: \quad \frac{\partial\psi_1}{\partial n} - \frac{\partial q}{\partial\psi_w}\psi_1 = \frac{\partial q}{\partial U}\alpha_1, \qquad \Gamma_c: \quad \psi_1 = 0. \tag{4}$$

Here and further derivatives of $q\left(\psi_w, U\right)$ at each point of the surface Γ_h are evaluated at the local surface temperature evaluated at the bifurcation point and at $U = U_i$.

Since a bifurcation occurs in the point considered, the (linear inhomogeneuos) problem (3), (4) must have non-unique solutions. The respective homogeneous problem [which is obtained by dropping $\frac{\partial q}{\partial U}\alpha_1$ on the right-hand side of the first boundary condition (4)] must have a non-trivial solution. In other words, one should consider the homogeneous problem as an eigenvalue one, the role of an eigenvalue parameter being played by the voltage drop U_i, which is the only control parameter of the homogeneous problem.

The above-described homogeneous problem allows one to separate the azimuthal variable, i.e., it admits solutions in the form $\psi_1\left(r,\varphi,z\right) = f(\varphi)\ F(r,z)$. Functions $f\left(\phi\right)$ and $F(r,z)$ satisfy

$$\frac{d^2 f}{d\varphi^2} + k^2 f = 0, \tag{5}$$

$$\frac{\partial^2 F}{\partial r^2} + \frac{1}{r}\frac{\partial F}{\partial r} - \frac{k^2}{r^2}F + \frac{\partial^2 F}{\partial z^2} = 0, \tag{6}$$

$$\gamma_h : \quad \frac{\partial F}{\partial n_1} - \frac{\partial q}{\partial \psi_w}F = 0, \qquad \gamma_c : \quad F = 0. \tag{7}$$

where k^2 is a separation constant, γ_h and γ_c are generatrixes of the revolution surfaces Γ_h and Γ_c, respectively, and n_1 is a direction in the plane (r,z) locally orthogonal to γ_h and directed outside the cathode.

In order that the function $f(\varphi)$ [and, consequently, $\psi_1\left(r,\varphi,z\right)$] be single-valued, k must be integer or, without loosing the generality, natural. Thus, finding bifurcation points of the original problem is reduced to solving the eigenvalue problem (6), (7) for $k = 0, 1, 2, \ldots$, the role of an eigenvalue parameter again being played by the voltage drop U_i. Different values of k correspond to branching of solutions describing different modes of current transfer: one should expect that solutions branching off in bifurcation points with $k = 0$ are axially symmetric and solutions branching off in bifurcation points with $k = 1$ or with $k = 2$ describe an off-center spot or, respectively, a system of two spots positioned opposite each other.

The uniqueness of a solution is violated not only in branching points, at which essentially different solutions join (brach off from) one another, but also at turning points, at which a solution reaches the limit of its existence region and then turns back. The latter situation occurs in the problem considered when the current-voltage characteristic (CVC), $U = U\left(I\right)$, of a certain mode passes through an extremum.

It follows that the above-described procedure of finding bifurcation points must predict bifurcations with $k = 0$ at every extremum of the CVC of any axially symmetric mode, however, no solutions branch off here.

The axially symmetric linear eigenvalue problem (6), (7) has been solved by using a finite-difference numerical scheme; the grid equations were solved by means of a variant of LU decomposition.

4. Numerical results

Calculations described in this work have been performed for a cylindrical cathode. Bifurcation points corresponding to $k = 0, 1, 2$ were sought in the range of values of the near-cathode voltage drop of up to 40 V. Control parameters of the model are the cathode radius R, the cathode height h, the cathode material, the plasma pressure p, and species of the plasma-producing gas.

In Fig. 1, current-voltage characteristics (CVC's) are shown of the diffuse mode and of the axially symmetric spot mode obtained by means of numerical calculations [4], as well as bifurcation points detected on the respective solutions by means of the numerical calculations of the present work. There is one bifurcation point with each value of k on both solutions.

Bifurcation points with $k = 0$ found for each solution coincide with the point of minimum of the respective CVC. This conforms to what has been said in the end of the preceeding section, and no branching occurs at this points.

Calculations have been performed also for a cathode with an electrically and thermally insulating lateral surface. Calculation results are shown in Fig. 2. (Most of the low-voltage branch of the CVC of the spot mode in this figure coincides, to the graphical accuracy, with the CVC of the diffuse mode; there is a point at which the two solutions coincide exactly.) Bifurcation points positioned on the diffuse mode may be calculated analytically for this model [5]; identical results may be obtained also by separating variables in the problem (6), (7). The analytical results coincide with those obtained by means of numerical calculations. In contrast to the case of a cathode with the active lateral surface, there are two bifurcation points with $k = 0$ on the diffuse mode, the one coinciding with the minimum point, at which no branching occurs, and another one, at which the axially symmetric spot mode branches off from the diffuse mode (in other words, at which the two modes coincide). No bifurcations with $k = 1$ has been detected on the axially symmetric spot mode, while a bifurcation point with $k = 2$ is undistinguishable from the point of minimum of the CVC, the latter again representing a bifurcation point with $k = 0$.

The above results confirm the hypothesis that for axially symmetric cathodes 3 D solutions describing spot modes branch off from axially symmetric solutions describing the diffuse mode. In fact, 3 D spot-mode solutions branch off also from axially symmeric spot-mode solution, and the general structure of steady-state solutions is rather complex. The latter is consistent with the experimental fact that spot modes are difficult to reproduce in the experiment.

A result of the present modelling which is probably most imporant for applications is a position of the bifurcation point with $k = 1$ which belongs to the diffuse mode: as is discussed in the Introduction, the corresponding current value is likely to represent the limit of stability of the diffuse discharge, i.e., the current below which the diffuse discharge becomes unstable. In the rest of this section, this stability limit is calculated for different values of control parameters.

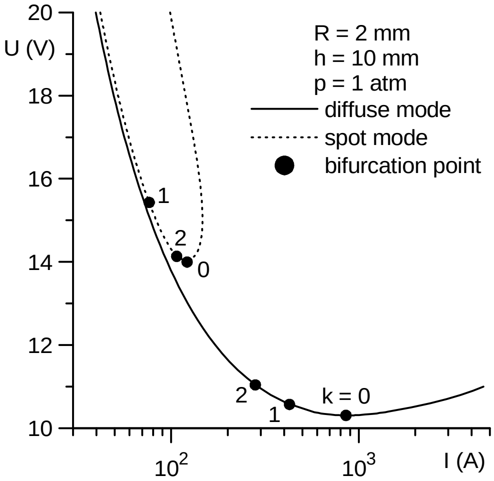

Fig. 1. CVC's and bifurcation points. Tungsten cathode, argon plasma.

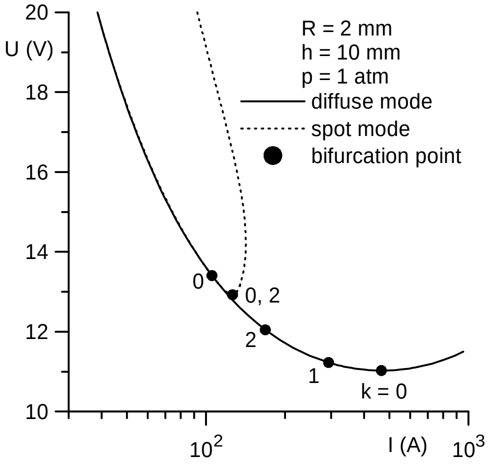

Fig. 2. CVC's and bifurcation points. Tungsten cathode with an insulated lateral surface, argon plasma.

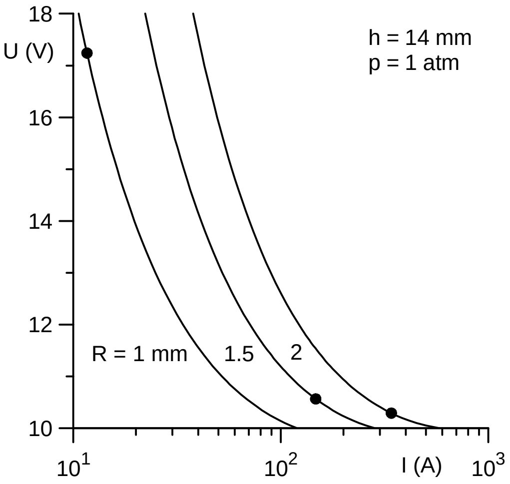

Fig. 3. CVC's and bifurcation points.
Tungsten cathode, argon plasma.

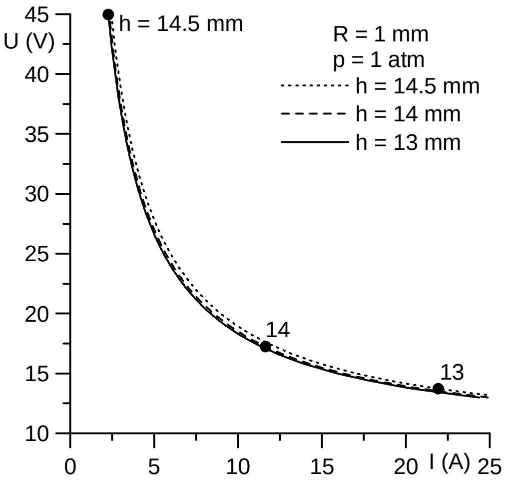

Fig. 4. CVC's and bifurcation points.
Tungsten cathode, argon plasma.

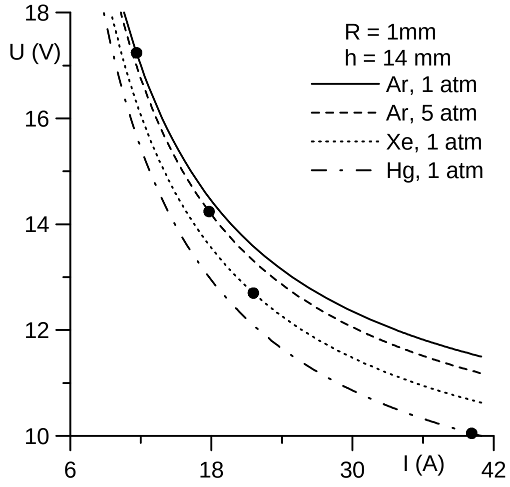

Fig. 5. CVC's and bifurcation points.
Tungsten cathode.

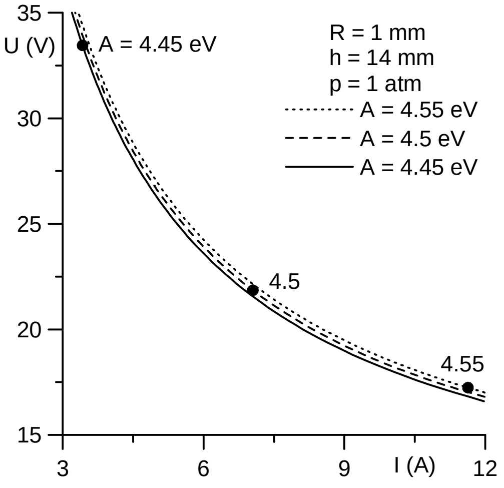

Fig. 6. CVC's and bifurcation points.
Tungsten cathode, argon plasma.

The effect of the cathode geometry is illustrated by Figs. 3 and 4. One can see from Fig. 3 that the stability limit decreases rapidly with a decrease of the cathode radius.

Fig. 4 shows that an increased height of the cathode results in a decrease of the stability limit. On the other hand, the stability limit is much more sensitive to a variation of the cathode height than, e.g., the current-voltage characteristic. Indeed, the CVC's shown in Fig. 4 for different h are quite similar, which seems to be natural given the smallness of variation of h. However, the stability limit suffers dramatic changes: as h increases, the limit of stability is shifted to lower values of the current very rapidly.

Fig. 5 illustrates effects of the plasma pressure and composition. An increase of the argon pressure results in a appreciable increase of the stability limit, while an effect produced on the CVC is rather weak (the CVC is shifted weakly in the direction of lower voltages). The changes from argon to xenon and from xenon to mercury result in an increase of the stability limit. Again, the effect produced on the stability limit is much stronger than that produced on the current-voltage characteristic (which are weakly shifted in the direction of lower voltages).

Fig. 6 illustrates an effect of A the work function of the cathode material. Note that the value $A = 4.55$ eV, which is usually assumed to be appropriate for cathodes made of pure tungsten, was used in all the above-described calculations. A small decrease of the work function originates a weak shift of the current-voltage characteristic in the direction of lower voltages and a strong decrease of the stability limit. Effects produced on the stability limit by the above-described variations of control parameters agree with trends observed in the experiment [6].

5. Conclusion

An approach has been developed to calculation of bifurcation points positioned on diffuse and axially symmetric spot modes of current transfer to axially symmetric thermionic cathodes. A complex structure of a general pattern of CVC's of various modes on axially symmetric thermionic cathodes has been found. Extensive data on the limit of stability of the diffuse mode are given. The effect of variation of control parameters (cathode dimensions, plasma gas, cathode material, plasma species and pressure) on the limit of stability is analysed and found to agree with trends observed experimentally. It is found that the stability limit is much more sensitive to variations of control parameters than the current-voltage characteristic, the strongest effect being produced by the cathode dimensions and the work function of the cathode material. The approach developed in this work for calculation of the stability limit of the diffuse discharge is not computationally intense and can be easily realized on a PC, thus being suitable for engineering practice.

Acknowledgments The work was performed within activities of the project *Theory and modelling of plasma-cathode interaction in high-pressure arc discharges* of the program POCTI of Fundação para a Ciência e a Tecnologia and FEDER and of the project *NumeLiTe* of the 5th Framework programme ENERGIE of the EC.

References

[1] Jüttner, B. *J. Phys. D: Appl. Phys.* **34**(17), R103–123 (2001).

[2] Bötticher, R. and Bötticher, W. *J. Phys. D: Appl. Phys.* **33**(4), 367–374 (2000).

[3] Benilov, M. S. and Cunha, M. D. *J. Phys. D: Appl. Phys.* **35**(14), 1736–1750 (2002).

[4] Benilov, M. S. and Cunha, M. D. *J. Phys. D: Appl. Phys.* **36**(6), 603–614 (2003).

[5] Benilov, M. S. *Phys. Rev. E* **58**(5), 6480–6494 (1998).

[6] Neumann, W. *The Mechanism of the Thermoemitting Arc Cathode.* Akademie-Verlag, Berlin, (1987).

[7] Lichtenberg, S., Nandelstädt, D., Dabringhausen, L., Redwitz, M., Luhmann, J., and Mentel, J. *J. Phys. D: Appl. Phys.* **35**(14), 1648–1656 (2002).

[8] Benilov, M. S. and Pisannaya, N. V. *Sov. Phys. - Tech. Phys.* **33**(11), 1260–1266 (1988).

Oxygen plasma modification of Polyhedral Oligomeric Silsesquioxanes (POSS-copolymers) for Nanolithographic applications

E. Gogolides[1], E. Tegou[1], N. Vourdas[1], V. Bellas[1], O. Brani, P. Argitis[1], A. Tserepi[1]
D. Eon[2], G. Cartry[2], C. Cardinaud

[1] *Institute of Microelectronics, NCSR "Demokritos", Aghia Paraskevi, 15310 Athens, Greece*
[2] *Laboratoire des Plasmas et des Couches Minces, Institut des Materiaux, BP 32229, 44322, Nantes, France*

Abstract

Polyhedral oligomeric silsesquioxanes (POSS) represent a novel class of well-defined nano materials that consist of a silicon-based inorganic cage (Si_8O_{12}) surrounded by eight organic corner groups. In this work plasma etching studies of POSS-containing polymers in Oxygen plasmas are reported. As for most silicon-containing resists, the etch resistance of the POSS polymers is primarily related to their silicon content. The POSS content required for sufficient etch resistance is 30 wt % (i.e. the silicon content is 9 %). Surface roughness is monitored after various etch times with the aid of atomic force microscopy and scanning electron microscopy. Surface roughness depends on Silicon content, type of organic group of the POSS moiety, type of reactor (ICP or RIE) and temperature of the wafer. Both smooth and very rough surfaces can be obtained by changing the material, the reactor, and the temperature.

1. Introduction and experimental conditions

Next generation microelectronics cirquits require minimum characteristic dimensions below 90 nm, a task achievable through the employment of 157 nm lithography and, in the future, through EUV (13.4 nm) lithography. However, the high absorbance values of carbon-based polymers at both wavelengths force to thin, yet etch-resistant, films. Bilayer lithography fulfills these needs and is regarded as the method of choice by many research groups [1]. In such a lithographic scheme, a pattern is imaged on a thin (~100 nm) silicon-containing photosensitive film (top layer) lying over a thick carbon-based polymer (underlayer) and is subsequently transferred to the bottom layer through plasma etching. Pattern transfer schemes using silicon-containing polymers can also find applications in micro and nano fabrication in general for example in microfluidics and lab on chip device fabrication [2].

Polyhedral oligomeric silsesquioxanes (POSS) represent a novel class of well-defined materials that consist of a silicon-based inorganic cage (Si_8O_{12}) surrounded by eight organic corner groups. Typically, a variety of inert substituents can be attached at the seven corner positions around the cage, while the remaining position is occupied by a reactive polymerizable group. A variety of POSS-containing copolymers have been synthesized in this manner in our group in Athens. The use of these hybrid materials as potential photoresists for bilayer lithography has recently been explored and their resolution capabilities have been demonstrated [3, 4]. The POSS polymers can have numerous other applications in nanotechnology as evidenced in the international conference devoted to these materials [5].
The purpose of this work is to do plasma etching studies in POSS-containing polymers in O_2 plasmas. The main issues we will address are the etching rate and the surface roughness induced by the plasma treatment, parameters affecting the quality of the structures fabricated using such polymers. The organic corner group R is mostly the ethyl group, although the cyclopentyl group was also compared. Comparison with polydimethyl siloxane (PDMS) and polymethylsilsesquioxane (PMSQ) a ladder rather than polyhedral silsesquioxane is done. Table I shows the various polymers used in this study

Plasma etching is done in an inductively coupled plasma reactor (Alcatel MET system) both in Athens and Nantes. Oxygen plasma at 600-800W source power and 0 or 100 V bias at a pressure of 10-15mTorr and a flowrate of 100sccm, are typically the conditions used in both laboratories. Comparison with RIE etching is also done in Athens. Etching rate is monitored with laser interferometry in Athens and in situ spectroscopic ellispsometry (Woolam M88 system) in Nantes.

Surface roughness is measured with a Topometrix TMX 200 AFM in the contact mode in Athens. FTIR measurements are done in Athens, and in situ XPS in Nantes.

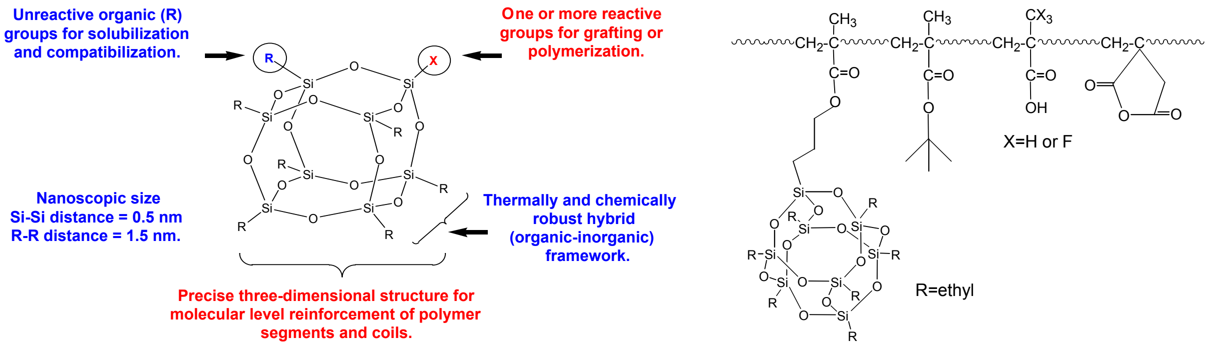

Figure 1. Schematic of the 3-D structure of a POSS monomer (left), and of a typical POSS copolymer (right). The X unit is a methacrylic unit, permitting copolymerization with other monomers.

Table I: Polymers and copolymers used for this study

Name of polymer	*S41*	*S48*	*S53*	*S47*	*S69*	*S71*	*S61*	*S83*	*S79*	*S43*	*S52*	*PMSQ*	*PDMS*
Ethyl POSS content per weight	*100 e-POSS*	*60*	*40*	*40*	*30*	*30*	*30*	*30*	*30*	*20*	*100 cyclopentyl POSS, cp-POSS*	*-*	*-*
Si content per weight	*30*	*18*	*12*	*12*	*9*	*9*	*9*	*9*	*9*	*6*	*21.8*	*41.8*	*37.8*

2. Etching of POSS copolymers in Oxygen plasmas

The etching of POSS copolymers containing various contents of POSS monomer, and hence various Silicon contents was studied with in situ spectroscopic ellipsometry and laser interferometry. A series of POSS copolymers containing 100% to 20% w/w ethyl-POSS was etched and compared with methylsilsesquioxane (a ladder polymer), and crosslinked PDMS (polydimethylsiloxane). Figure 2a shows that all polymers exhibit a very fast initial thickness loss (large etching rate), followed by a much slower etching rate (see Figure 2b). Although for methylsilsequioxane and 100%POSS the etching rate seems to stabilize to constant values (constant slope in the figure), for smaller POSS contents the etching rate is higher and constantly decreases, i.e. it does not stabilize.

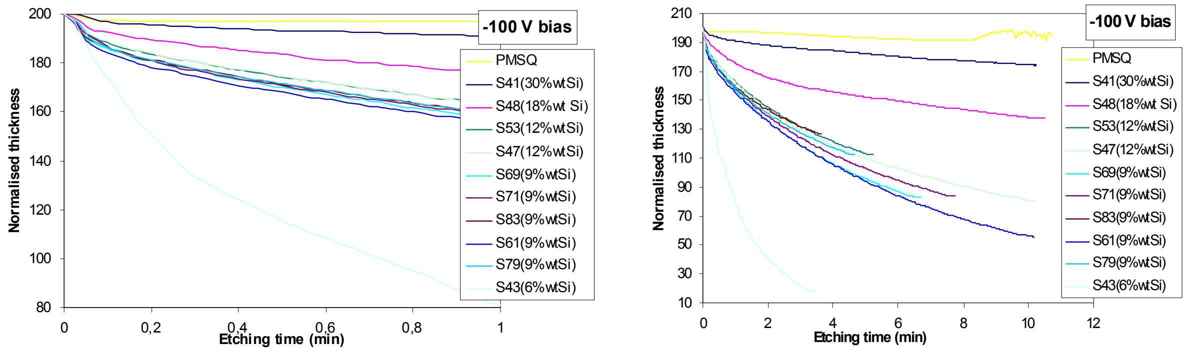

Figure 2. Normalized thickness loss from ellipsometry for the various POSS copolymers and PMSQ

S43 copolymer (20% e-POSS or 6%w/w Si) is not resistant to the oxygen plasma as shown in Figure 2. All copolymers with 30% e-POSS (9%w/w Si) show adequate etching resistance and similar thickness loss. Laser interferometry data confirm the ellispometric results and reveal that for sufficient film resistance more than 20% ethyl-POSS content is required.

The thickness loss is a strong function of the POSS content and decreases as the POSS content increases as shown in Figure 3.

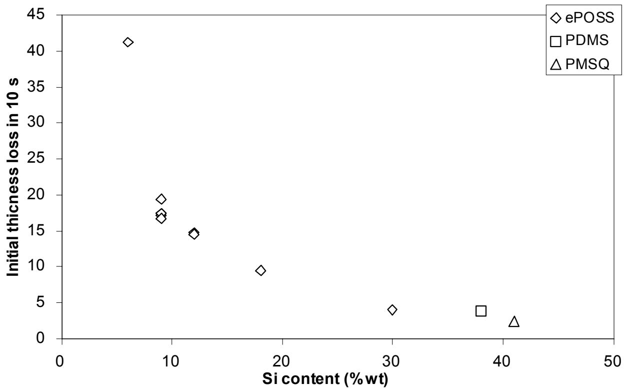

Figure 3 Thickness Loss versus silicon content, after 10s of etching in ICP oxygen plasma with 100V bias.

The first fast thickness loss is attributed to etching of the organic groups from the surface of the film, while the subsequent etching rate reduction is attributed to oxide formation. A similar mechanism has been proposed by our team for PDMS [6], however more studies are necessary to determine the surface oxide layer thickness for POSS materials.

FTIR spectroscopy has also been used for understanding the mechanism of etching. Figure 4 shows the FTIR spectra of one POSS copolymer containing 30% POSS (S69) before etching and after 150s of etching with 100V bias.

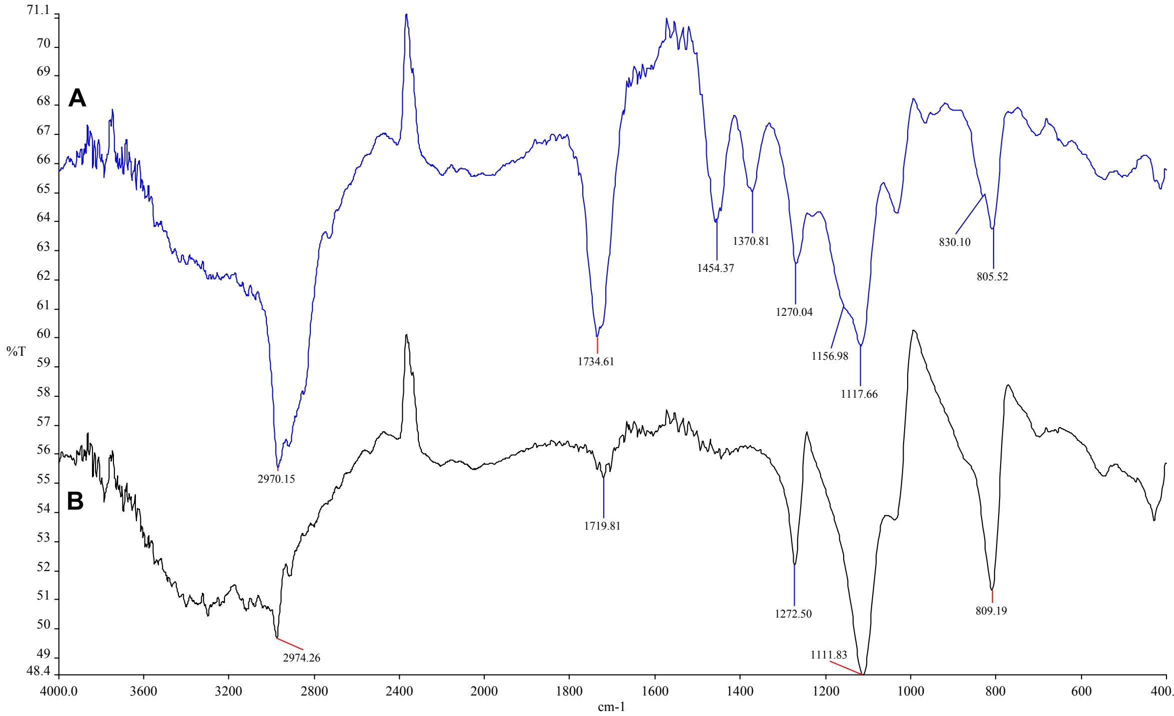

Figure 4. FTIR spectra of POSS copolymer before and after 150s etching in Oxygen plasma: **A:** S69 a copolymer consisting of ethyl POSS-TBMA-MA-IA before plasma etching (film thickness :147nm on 350nm hard baked novolac; the novolac spectrum has been subtracted) **B**: S69 copolymer after 150s oxygen plasma etching (film thickness:70 nm)

The following peaks exist in spectrum A and get smaller in spectrum B:
2970 cm^{-1}: C-H stretch, 1454, 1371 cm^{-1}: C-H bend, 1734 cm^{-1}: C=O stretch, =1156 cm^{-1}: C-O stretch
The following peaks are predominant in spectrum B: 1272 cm^{-1}: Si-C stretch, =1112 cm^{-1}: Si-O-Si stretch. These data point to a strong oxidation of the POSS layer and formation of an oxide-like surface.

3. Surface Roughness of POSS polymers after plasma treatment

Surface roughness is an issue of great concern for application of these materials to micro or nano fabrication. In general silicon polymers when treated in plasmas can give very rough surfaces, especially when the silicon content is low and etch resistance is not appropriate. In addition surface roughness can be greatly enhanced by high wafer temperature during etching [7].
Figure 5 shows the surface roughness (rms value) for a series of e-POSS copolymers and one cyclopentyl-POSS (cp-POSS) polymer treated for 2min in the oxygen plasma at 100V bias. The electrode and wafer temperature were 15 C. He-backside cooling of the wafer maintains a constant wafer temperature. The e-POSS copolymers shown contain at least 30% POSS, i.e. they can withstand the oxygen plasma and form a protective oxide film on too. While all e-POSS polymers exhibit very smooth surfaces, the cp-POSS polymer surface is very rough. This interesting observation reveals that bulky POSS organic corner groups can greatly hinder the surface oxide formation in the plasma and result in very rough surfaces. Table II above shows that all surfaces are indeed smooth with the exception of the cp-POSS, which shows high roughness.

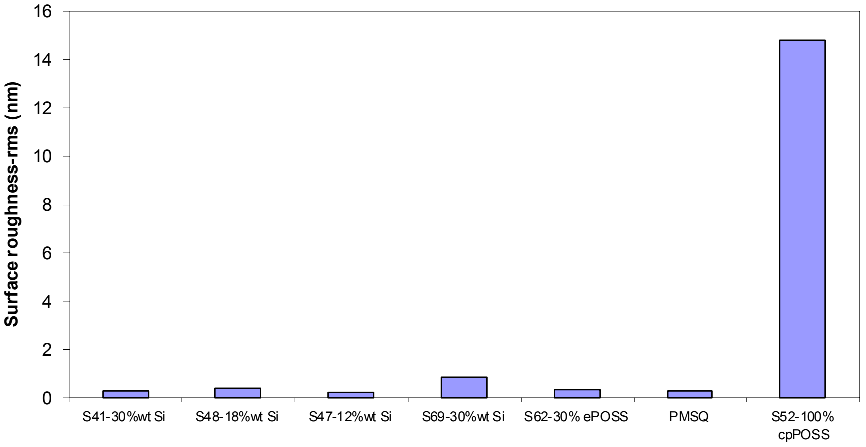

Figure 5. Surface roughnes of various POSS copolymers after 2min oxygen plasma treatment. Comparison with PMSQ.

Table II. AFM images of various POSS copolymer surfaces after 2min oxygen plasma treatment.

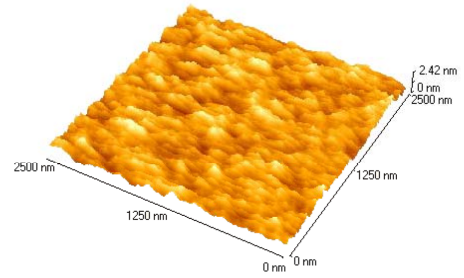 S41	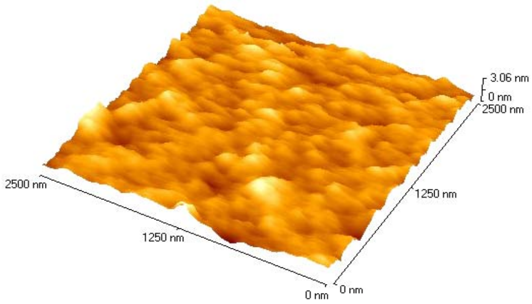 S48

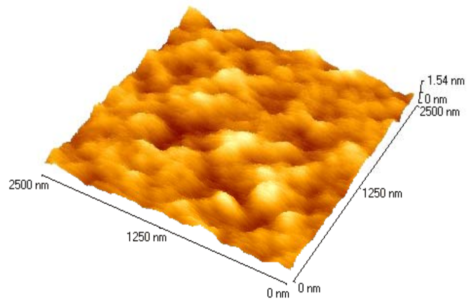

S47

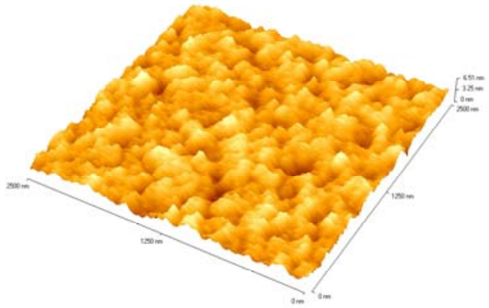

S69

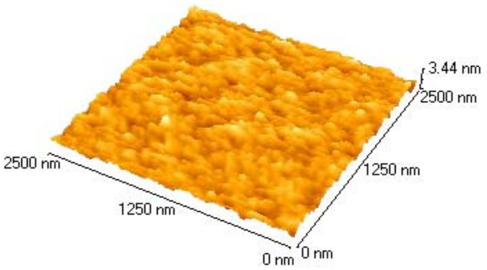

S62

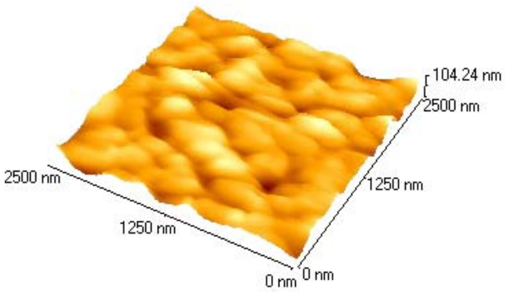

S52

Next we examined the effect of etching time at constant etching conditions for S69 a polymer containing 30% e-POSS and S41 a polymer containing 100% e-POSS. Polymers were post apply baked at 160 C, i.e. above the glass transition temperature of S69, or at 120 C. Notice that both polymers are smooth at short plasma etching times, while roughness increases for long etching times for the 30% POSS polymer, due to erosion of the film. Notice also that the 100% POSS film shows no roughness even at long etching times. This is due to the higher silicon content of the polymer (see also figures 2 and 3). The difference between the post apply bake temperatures for S69 may reflect differences in the packing of the film and the reduction of the free volume as in one case it is baked above while in the other below the Tg (143 C).

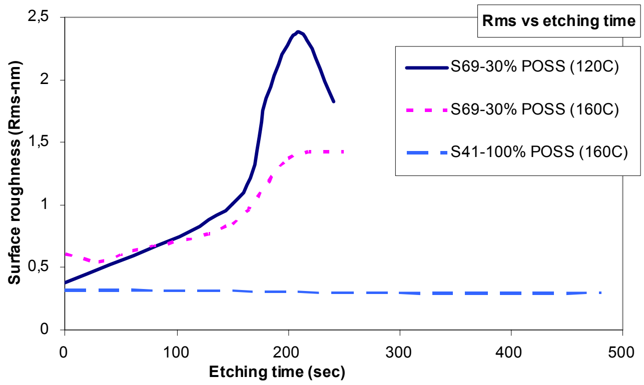

Figure 6 Surface Roughness versus etching time in ICP reactor, oxygen plasma, 100V bias.

While e-POSS surfaces look smooth after ICP etching, they look very rough after RIE etching when etched at the same pressure and electrode bias potential. The wafers in the RIE reactor are not cooled with He in the wafer backside, thus the temperature during etching rises to approximately 120 C. As a result the oxide is formed at a high temperature. During cooling to ambient temperature the oxide is compressed due to much smaller thermal expansion coefficient compared to the polymer, and buckles forming rough surfaces [7]. This temperature-reactor effect is shown in Figure 7 and Table III below.

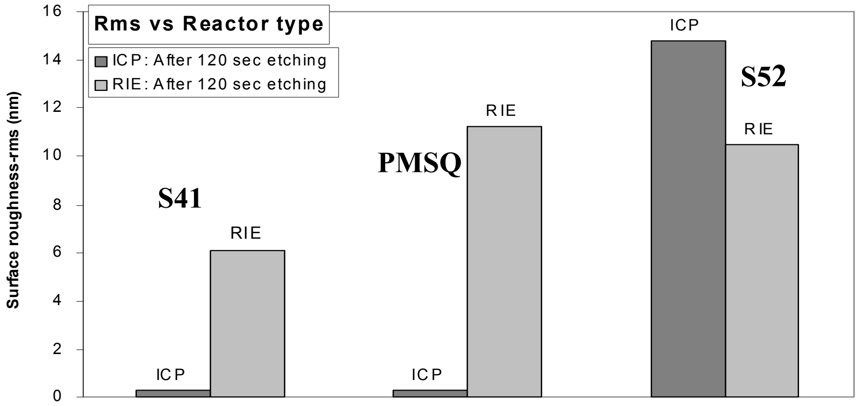

Figure 7. Surface roughness for RIE and ICP etching after 2min etching in Oxygen plasma at 100V bias. In the RIE reactor the wafer temperature can reach 120 C within two minutes of etching. In the ICP reactor the wafer is cooled with He backside cooling and maintains a constant temperature 15C.

Table III. Surface roughness and topography in RIE and ICP reactors

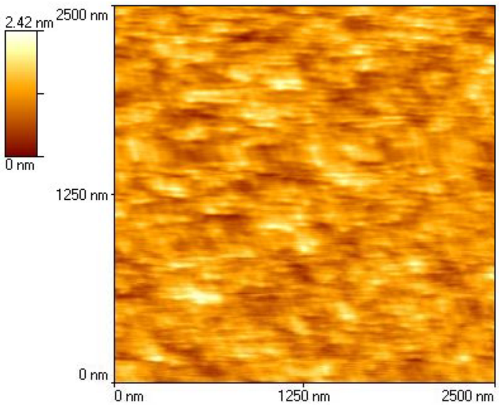 RMS roughness of S41 in ICP after 2min etching is 0.31nm	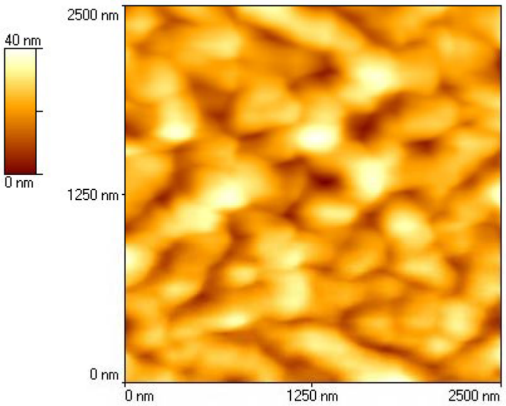 RMS roughness of S41 in RIE after 2min is 6.05nm

4. Conclusions

The behaviour of POSS polymers under treatment in oxygen plasmas was studied. Etching rates and surface roughness depend on the amount of POSS and the organic corner group of the POSS monomer. Ethyl POSS copolymers can resist oxygen plasma etching by forming surface oxide, and produce smooth surfaces in ICP reactors when the POSS content is higher than 20%. Wafer heating in RIE reactors and/or the presence of cyclopentyl corner groups on POSS monomers result in rough surfaces.

Acknowledgments: The European Union IST project 157 CRISPIES supported this work.

References

[1] S. Miyoshi, T. Furukawa, H. Watanabe, S. Irie and T. Itani, Proc. SPIE **4690**, 221 (2002)
[2] H. Becker, L.E. Locascio, Talanta, 56 (2002), 267-87
[3] V. Bellas, E. Tegou, I. Raptis, E. Gogolides, P. Argitis, H. Iatrou, N. Hadjichristidis , E. Sarantopoulou, A.C. Cefalas, J. Vac. Sci. Technol. B, to appear
[4] E. Tegou, V. Bellas, E. Gogolides, P. Argitis, E. Sarantopoulou, A.C. Cefalas, K. Dean, Proc. of SPIE, 2003, to appear
[5] R. Gonzalvez, POSS Nanotechnology Conference, CA-USA (2002), pp. 155 – 177.
[6] A. Tserepi, G. Cordoyiannis, G.P. Patsis, V. Constantoudis, E. Gogolides, E.S. Valamontes, D. Eon, M.C. Peignon, G. Cartry, Ch. Cardinaud, G. Turban, J. Vac. Sci. Technol. B **21(1)** (2003), pp. 174 – 182
[7] A. Tserepi, E. Gogolides, V. Constantoudis, G. Cordoyiannis and I. Raptis and E.S. Valamontes, Journal of Adhesion Science and Technology (accepted for publication 2003).

Atmospheric pressure barrier glow discharge for ozone generation

Z Buntat, J.E.Harry and I.R.Smith

Department of Electronic and Electrical Engineering, Loughborough University, UK

Abstract

A barrier glow discharge for ozone generation is investigated theoretically in air at atmospheric pressure, using a disc/plane electrode configuration with and without a barrier and wire mesh. The effects of the thickness and relative permittivity of different dielectric barriers, the gap distance, supply voltage, disc thickness and separation. are all determined. The disc electrode shows great potential for ozone generation and the optimum operating conditions for ozone generation are suggested.

1. Introduction

Ozone can be used as a pollution-free oxidant in a wide range of applications, including deodorisation, decolourisation, disinfection, sterilisation, bleaching processes, gas treatment, medical treatment and chemical synthesis, and in all of these, ozone requires less energy than does the alternative chlorination process[1,2]. The consequent interest in the use of ozone has brought about the need for a technique that can generate high quantities of ozone in air at a rate greater than 150 g/kWh and concentrations higher than 6% by weight. To fulfil these demands, extensive research has been undertaken in recent years on different configuration and discharge techniques.

Glow discharges at atmospheric pressure show great potential for ozone production and have been extensively studied [3-6]. Their advantages include the production of a homogeneous discharge over a large volume, low breakdown voltage, a high electron temperature capable of dissociating gas molecules, low temperature and high concentrations of both ions and radicals [7]. Existing evidence suggests that the optimum design of the discharge gap, together with the correct selection of dielectric barrier materials, input voltage and frequency, as well as the gas flow rate, should enable a homogeneous discharge to be obtained, even with the use of air or oxygen [3-8]. The discharge produced would fill the entire discharge volume and the technique would have other advantages over existing methods such as a higher production efficiency and a greater ozone concentration.

The ionization rate in the discharge depends on the local electric field strength [9]. Wire/cylinder configurations are commonly used for ozone generation, and it has been reported that the diameter of the wire electrode influences the ozone production [2]. The smaller the diameter, the higher is the production of ozone (g/kWh). In this study a disc electrode was used, with the effect of the disc thickness and separation on the electric field strength being studied and analyzed with and without a dielectric barrier and wire mesh.

The present paper investigates theoretically the effect of several parameters such as relative permittivity, dielectric thickness, gap distance and magnitude of input voltage on the electric field strength within the discharge volume. The use of a disc electrode in a disc/plane configuration, with and without a dielectric barrier and wire mesh is investigated, and compared to the wire/plane configuration. The optimum operating condition and optimum value of each parameter when the disc electrode is used are related to the electric field strength (MV/m) and the average electron energy (eV) is determined.

2. Model of electrode arrangement

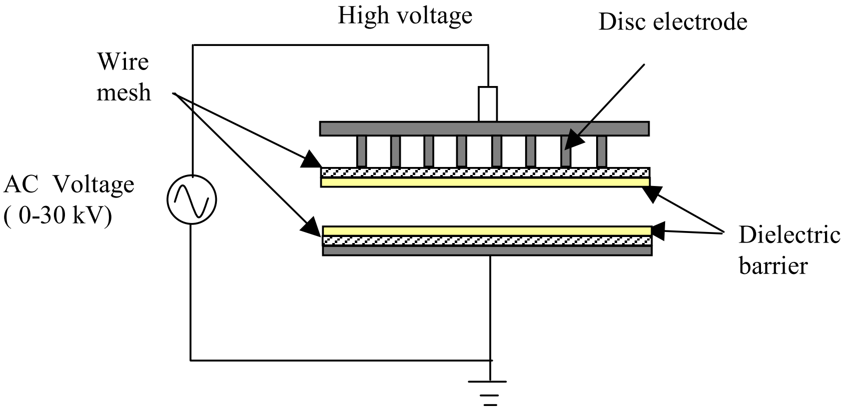

Figure 1 : Disc/plane electrode configuration.

The electrode configuration used for the simulation is shown in Figure 1. The disc thickness was varied between 0.05 mm and 1 mm and the disc separation between 0.5 mm to 6 mm, to enable their effects on the electric field strength with and a without barrier and wire mesh to be studied. The gap distance was varied from 0.5 mm to 3 mm. Three different barrier material were used: :Al_2O_3 ($\varepsilon_r = 9.8$), mica ($\varepsilon_r = 6$) and quartz glass ($\varepsilon_r = 3.78$). The barrier thickness was varied between 0.05 mm to 2 mm and the input voltage between 5 kV to 30 kV.

3. Result and discussion

Figure 2 a) and b) below show an example of the 2-D simulation of the electric field strength and distribution, obtained using an Ansoft-Maxwell 2D program. Two different type of discharge configuration were studied, with and without a dielectric barrier and wire mesh,. The results in figure 2 b) can be used to compare the effect of the disc electrode on the electric field strength, by relating the electric field strength (V/m) and the average electron energy (eV) to the electrode geometry and the optimum value of parameters for ozone generation for an atmospheric pressure barrier glow discharge.

Ozone is produced through two different mechanisms [10,11] :

$$e + O_2 \rightarrow e + O_2(A\,^3\textstyle\sum_U^+) \qquad \text{at 6 eV}$$
$$\rightarrow e + O(^3P) + O(^3P)$$
$$\rightarrow O_2 + O(^3P) \rightarrow O_3. \qquad (1)$$

$$e + O_2 \rightarrow e + O_2(B^3\textstyle\sum_U^+) \qquad \text{at 8.4 eV}$$
$$\rightarrow e + O(^3P) + O(^3D)$$
$$\rightarrow O_2 + O(^3P) \rightarrow O_3. \qquad (2)$$

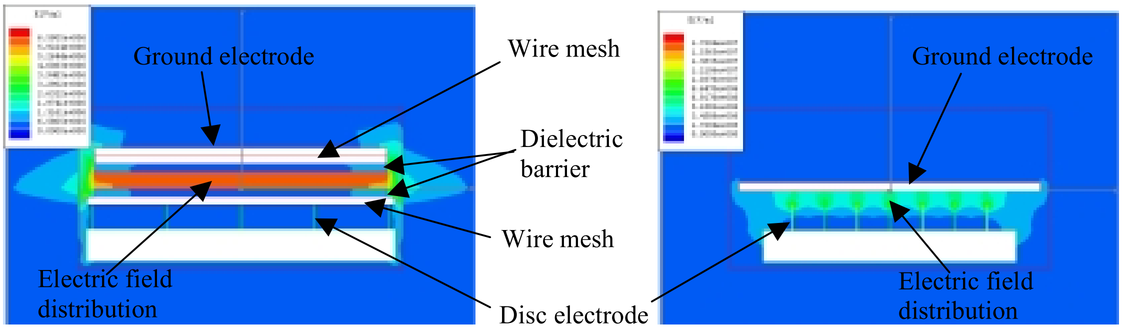

a) b)

Figure 2: Two-dimensional simulation of electric field strength and distribution using Ansoft-Maxwell 2D program.

a) Disc with dielectric barrier and wire mesh. Configuration : gap distance, 1 mm, relative permittivity, ε_r = 9.8, disc thickness, 0.05 mm, disc separation, 4.5 mm, dielectric thickness, 0.5 mm and input voltage, 7 kV.

b) Disc without dielectric barrier and wire mesh. Configuration : gap distance, 1 mm, disc thickness, 0.05 mm, disc separation, 2 mm and input voltage, 7 kV.

Ozone can be generated at a slow rate by reaction (1), or generated by both reactions (1) and (2) afterwards. Thus, in principle, electrons with an energy of about 6–9 eV would be ideal for ozone generation, which corresponds to reduced electric fields of about 150–350 Td (1 Townsend (Td) = 10^{-21}Vm^2) and an electric field strength of about 5–10MV/m. To increase the ozone concentration and production and minimize any losses of energy due to temperature rise, the operation should be carried out around this range. Operating the system too much above this condition results in a decreased ozone production due to ozone decomposition by electron bombardment, and this range is therefore referred to as the optimum operating condition for ozone generation.

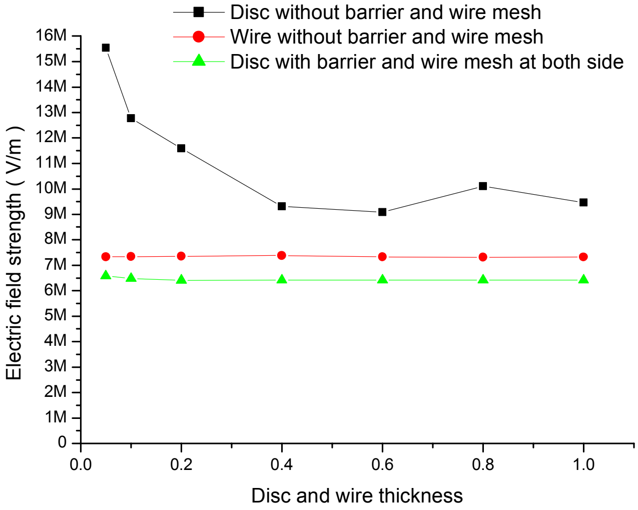

Figure 3 : The effect of different disc and wire thickness on electric field strength.
Disc and wire thickness (0.05 to 1.0 mm), gap distance, 1 mm, disc separation, 4.5 mm, dielectric material (Al_2O_3), dielectric thickness, 0.5 mm and input voltage, 7 kV.

The effect of the disc thickness and wire diameter on the electric field strength are clear from Figure 3. In the configuration without the dielectric barrier and wire mesh the result show that the wire diameter does not have much influence on the electric field strength. Varying the wire diameter results in almost the same strength of electric field for all thicknesses, even down to a wire diameter of 0.05 mm The electric field strength was around 7MV/m, which corresponds to an average electron energy of 7.2 eV. The disc-plane configuration results in a higher electric field strength, especially at a disc thickness of 0.05 mm (15.5 MV/m), which corresponds to an average electron energy of 12.3 eV. This indicates that the disc electrode shows promise for a higher concentration and production of ozone in future.

In the configuration in which the disc electrode is covered with dielectric material and wire mesh, the electric field is slightly lower. The highest electric field strength is at a disc thickness of 0.05 mm, and at about 6.5 MV/m, corresponding to an average electron energy of 6.9 eV. However increasing the thickness above 0.05 mm i.e from 0.2 mm to 1.0 mm, reduces the electric field strength to a constant value of about 6 MV/m, corresponds this time to an average electron energy of 6.6 eV at an input voltage of 7 kV. To increase the average electron energy to a higher rate of ozone generation, that is to the optimum operating condition, requires a higher input voltage.

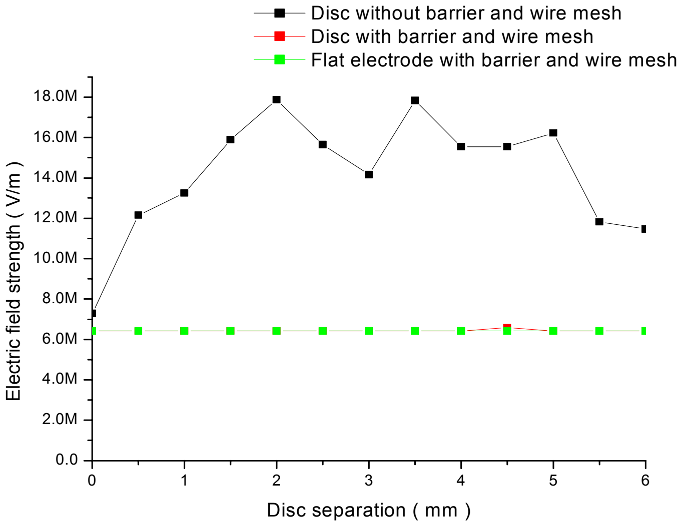

Figure 4: The effect of disc separation on electric field strength with and without dielectric barrier. Configuration : disc separation, (0.5 to 6 mm), gap distance, 1 mm, disc thickness, 0.05 mm, dielectric material, Al_2O_3 ($\varepsilon_r = 9.8$), dielectric thickness, 0.5 mm and input voltage, 7 kV.

The effect of disc separation on electric field strength was analyzed using a disc thickness of 0.05 mm, as shown in Figure 4 below. The results establish that, in the configuration without a dielectric barrier and wire mesh, at a disc separation of 2.0 mm and 3.5 mm, the highest electric field strength was obtained at about 18MV/m, which corresponds to an average electron energy of 13.8 eV . The reason that the highest electric field strength was achieved at the above two disc separations remains unclear and will be investigated in future experimental work. The results however indicates that at a disc thickness of 0.05 mm and a disc separation of 2.0 mm or 3.5 mm, the highest electric field strength can be generated at a lower input voltage of about 7 kV. The average electron energy of 13.8 eV produced is sufficient to generate ozone at a high rate[10,11].

In the configuration with a barrier and wire mesh, the electric field was approximately constant at about 6MV/m and increased slightly at a disc separation of 4.5 mm, to nealy 6.3 MV/m. As expected, the existence of a barrier and wire mesh in front of the disc electrode results in almost the same electric field strength as generated by flat electrode cover with a barrier and wire mesh, see Figure 4.

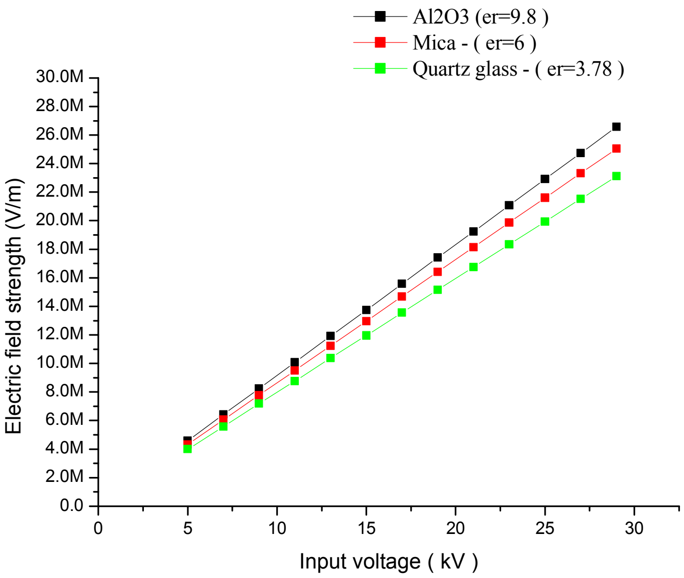

Figure 5 : The effect of relative permittivity on electric field strength at different input voltage. Configuration : different dielectric material, Al_2O_3 (ε_r=9.8), mica (ε_r=6.0), and quartz glass (ε_r=3.78), disc separation, 4.5 mm, gap distance, 1 mm, disc thickness, 0.05 mm, dielectric thickness, 0.5 mm and input voltage, 5 -30 kV.

The dielectric material was found to play an important role in determining the nature of the discharge and also to avoid any arc discharge leading to a thermal plasma. The effect of material of a different relative permittivity on electric field strength at different input voltage in a dielectric barrier and wire mesh configuration is shown in Figure 5. This confirms that different dielectric material with different values of relative permittivity result in different electric field strengths. High purity alumina (Al_2O_3) with relative permittivity, ε_r=9.8 results in a higher electric field strength than mica (ε_r=6.0) and quartz glass (ε_r=3.78). The higher the value of relative permittivitty the higher is the electric field strength in the discharge gap. The result also show that an increase in input voltage will also increase the electric field strength. It can also be seen that the optimum operating condition can be achieved when operating at an input voltage of about 11–13 kV, which will generate an electric field strength between 10–12 MV/m, corresponding to an average electron energy of about 9–10.2 eV.

Figure 6 below shows the effect of the dielectric thickness(Al_2O_3) on the electric field strength at different input voltage. The highest electric field strength occurs at 0.2 mm dielectric thickness. Increasing the thickness results, as expected, in a lower electric field strength for any range of input voltage. The use of very thin (< 0.2 mm) dielectric material in the discharge configuration can cause failure of the material during handling and installation, as well as during operation. A thickness of 0.5 mm has been proposed and results show that at an input voltages of 11 and 13 kV, the electric field strength is about 10 and 12 MV/m, which, corresponding to average electron energies of 9 and 10.2 eV, can be produced at optimum operating conditions.

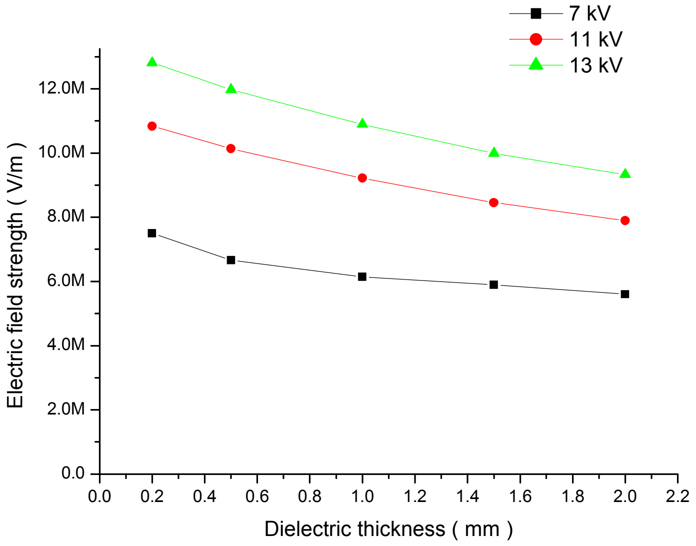

Figure 6 : The effect of dielectric thickness on electric field strength. Configuration : different dielectric thickness (0.2 to 2.0 mm), disc separation, 4.5 mm, gap distance, 1 mm, disc thickness, 0.05 mm, dielectric material (Al_2O_3) and input voltage, 7–13 kV.

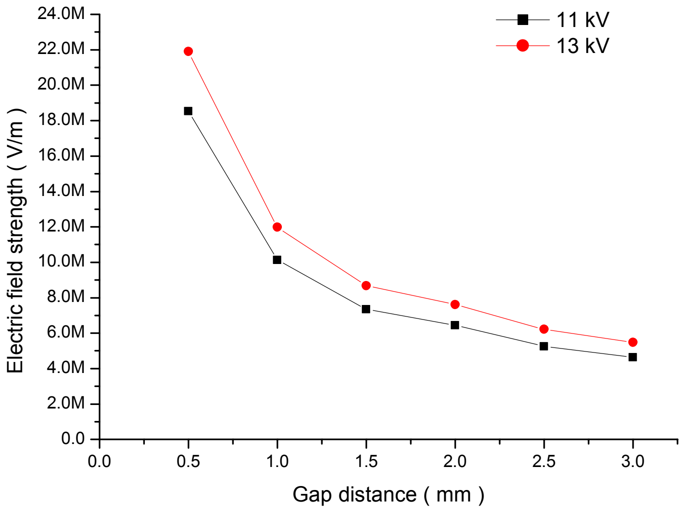

Figure 7 : The effect of gap distance on electric field strength with and without dielectric barrier and wire mesh. Configuration : gap distance, (0.5 mm to 3 mm), dielectric thickness, 0.5 mm, disc separation, 4.5 mm, disc thickness, 0.05 mm, dielectric material (Al_2O_3) and input voltage, 7 kV

The effect of varying the gap distance on the electric field strength at two different input voltages, with a dielectric barrier and wire mesh, is shown in figure 7. Both curves shows clearly that, as expected, an increase in gap distance reduces the electric field strength. These results suggest that a narrow gap distance should be used in order to obtain a higher electric field, if a higher ozone concentration and production are required. The optimum operating condition was achieved at a gap distance of 1.0 mm, with an input voltage of about 11 and 13 kV, producing an electric field strength of about 10 MV/m and 12 MV/m and an average electron energy of about 9 eV and 10.2 eV respectively.

4. Conclusion

The effect of using a disc electrode in a configuration with and without a dielectric barrier and wire mesh has been studied theoretically, to obtain the optimum operating condition of ozone generation in an atmospheric pressure barrier glow discharge. The results obtained can be summarized as follows:

i) The disc electrode produced a higher electric field strength compared to a single-wire electrode, in a configuration without a dielectric barrier and wire mesh.

ii) A combination of a disc thickness of 0.05 mm and a disc separation of 4.5 mm generated a high electric field strength, in a configuration with a dielectric barrier and wire mesh.

iii) The optimum operating condition for ozone generation in a dielectric barrier and wire mesh configuration was obtained with a disc thickness of 0.05 mm, separation of 4.5 mm, relative permittivity of 9.8 (Al_2O_3), dielectric thickness of 0.5 mm, gap distance of 1 mm and an input voltage of 11-13 kV.

iv) The disc discharge electrode has a great potential for ozone generation, with a proper selection of disc thickness and disc separation generating a high electric field strength.

References

[1] Samaranayake W J M, Miyahara Y, Namihira T, Katsuki S, Hackam R and Akiyama H, "Pulsed Streamer Discharge Characteristics of Ozone Production in Dry Air". IEEE Trans. on Dielectrics and Electrical Insulation, Vol. 7 No. 2, (2000), pp.254-260.

[2] Chalmers I D, Zanella L,. and MacGregor S J, "Ozone Generation by Pulsed Corona Discharge in a Wire Cylinder Arrangement.", IEE Colloquium Digest No.229, (1994), pp.1-4.

[3] Kogoma M and Okazaki S," Raising of ozone formation efficiency in a homogeneous glow discharge plasma at atmospheric pressure", J.Phys. D : Appl.Phys., Vol 27, (1994), pp.1985-1987,.

[4] Trunec D, Brablec A and Buchta J, " Efficiency of ozone production in atmospheric pressure glow and silent discharges", Proc. of Int. Symp. on High Pressure, Low Temperature Plasma Chemistry, Hakone VII, Greifwald, Germany, (2000), pp.313-317.

[5] Tepper J and Lindmayer M, " Investigations on two different kinds of homogeneous barrier discharges at atmospheric pressure", Proc. of Int. Symp. on High Pressure, Low Temperature Plasma Chemistry, Hakone VII, Greifwald, Germany, (2000),pp.38-43.

[6] Okazaki S, Kogoma M, Uehara M and Kimura Y., "Appearance of stable glow discharge in air, argon, oxygen and nitrogen at atmospheric pressure using a 50Hz source", J.Phys. D: Appl.Phys., Vol 26, (1993), pp.889-892.

[7] Yokoyama T, Kogoma M, Moriwaki T and Okazaki S," The mechanism of the stabilisation of glow plasma at atmospheric pressure", J.Phys. D : Appl.Phys., Vol 23, (1990), pp.1125-1128.

[8] Kanazawa S, Kogoma M, Moriwaki T and Okazaki S, “ Stable glow plasma at atmospheric pressure”, J.Phys. D :Appl.Phys., Vol 21, (1988), pp.838-840.

[9] I.Muller, C.Punset, E.Ammelt, H.G.Purwins and J.P.Boeuf, “ Self-organized Filaments in dielectric barrier glow discharge”, IEEE Trans. on Plasma Science, Vol.27, No.20, (1999).

[10] B.Eliasson, M.Hirth and U.Kogelschatz, “Ozone synthesis from oxygen in dielectric barrier discharges”, J. Phys. D: Appl. Phys., Vol.20, No. 11, (1987), pp.1421-1437.

[11] B.Eliasson and U.Kogelschatz, “ Nonnequilibrium Volume Plasma Chemical Processing”, IEEE Trans. On Plasma Science, Vol 19, No.6, (1991), pp 1063-1077.

Pulsed plasma treatment of wear- resistant coatings.

V.Astashynski[1], Yu.Chivel[1], A.Ilyuschenko[2],V.Okovity[2], A.Shevtsov[2].

[1] *Institute of Molecular and Atomic Physics, Minsk, Belarus*
[2] *Institute of Powder Metallurgy, Minsk, Belarus*

Abstract

The object of the work are wear resistant coatings manufactured by plasma spraying of powder composites with the following additional treatment by pulsed plasma flows.

Investigated are plasma impulse processing parameters of coatings, sprayed with NiCr--Fe+Cr_3C_2 powders.. The obtained results may be used to increase service life of machine parts, which operate in conditions of intensive friction and wear – out.

1.Introduction

Pulsed plasma flow as an energy source has its own peculiarities and advantages when treating a part's surface:

o high concentration of the fed energy and locality enable to treat only the surface area of the material without heating the rest bulk and distorting its structure and properties, that results in minimum part's buckling;

o high concentration of the fed energy enables to heat and to cool the treated bulk of the material with high rates, the effect period being small. As a result it is possible to make unique structures and properties of the treated surface;

o possibility to control the parameters of impulse-plasma effect enables a structure regulation of the surface layer, its hardness, roughness, wear-resistance, geometrical sizes of the treated areas etc.

Therefore, when treating protective coatings the plasma flow impulse enables to make layers with the needed operational properties. To solve the problem success fully investigations of the plasma flow impulse effect are necessaryTo make investigations there is chosen a common methodic approach, envisaging with the analysis of coating's structures resulting therewith, as indication of their quality. The validity of such approach is confirmed by practice of coating's spraying, which testifies that operational properties of the sprayed materials greatly depend on their structure.

Investigations are made on samples from steel 45(1.0503), which were plasma sprayed with NiCr-Fe+Cr_3C_2. Spraying was made on «Plasma-Technik» (Switzerland) unit. The two stage quasi-stationary high- current plasma accelerator (QHPA) with coaxial system of electrodes served as a source of impulse effect on coatings.

2. Experimental Unit to Produce Pulsed Plasma Flows

The unit for investigations was a quasi-stationary high- current plasma accelerator (QHPA) in a vacuum chamber [1]. The latter is formed by two rectangular compartments forming a singular space, sizes 0,8x0,8x0,4m. Systems of vacuum pumping-out and operating gas supply (hydrogen nitrogen),sectional accumulators of energy to feed the first and the second stages of the accelerator and systems of impulse-valve gas leading-in are envisaged by the design. The energy accumulator of the first stage with total energy content 40kJ consists of four capacitor sections. Each section discharges on its inlet ionization chamber (ICh) of a small size. To accumulate the energy in systems of impulse functioning of valves for gas leaking-in in ICh a capacitor battery 5,4kJ is used. The energy accumulator of the second stage (the main discharge) with total energy content 150kJ consists of eight capacitor sections. Impulse plasma flow formation was made in an electrode QHPA system under discharge of capacity energy accumulators between its electrodes. Discharge device consists of an inlet ionization block, anode and cathode units, separating insulators. Scheme of the discharge device are shown in Fig.1. The inlet ionization block consists of four ICh, disposed on a common flange symmetrically along the circumference diameter 390mm.Anode unit is formed from 16 copper rods ,length 1200mm, disposed symmetrically along the circumference diameter 500mm.

The cathode unit is disposed on the axis of the discharge device. It consists of two coaxial cylinders separated with insolators,16 copper tubes, forming an ellipsoid of rotation with the maximum diameter 280mm and the length 500mm. Copper needles disposed in the space between the tubes serve as cathodes. Design of the cathode unit enables to shift it relatively the inlet ionization block and to change sizes of the rotation ellipsoid. Therewith the length of a drift channel and a profile of an accelerating one are varied.

The peculiarity of the ICh design is that the insulator with the developed surface is located in a pocket of the carrying flange, and an operating cone part of the inner electrode is situated on a considerable distance from it, the inner electrode is made like a truncated cone with an axis opening and the outer electrode makes by itself a cylinder formed with copper rods located symmetrically along the circumference with diameter 50mm. Such ICh design excludes a possibility of displacement of the ionization zone in the insulator direction. The operating gas supply in the interelectrode ICh gap is made with a circular impulse (electrodynamic) valve. To stop the gas spreading in radial direction the discharge device is surrounded with a casing from organic glass. Eighteen openings for gas leaking-in are located symmetrically along the circumference disposed between the outer 1Ch electrode and the casing , thereby ensuring the operating gas supply in the interelectrode gap from the anode direction, that contributes to stability of the going out plasma flow.

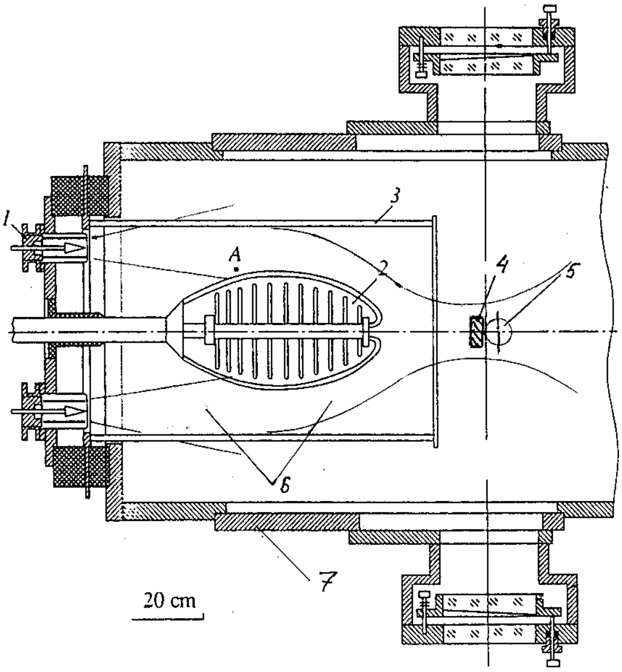

Figure 1: Discharge device of QHPA:1 – ICh, 2-cathode unit,
3 – anode unite, 4 – sample , 5 – sample holder, 6 – plasma flow, 7 – vacuum chamber.

3.InvestigationMethodics

At preparation is samples on a substrate from steel 45(1.0503) realized plasma spraying in the air of investigated coatings. The modes of spraying of NiCr – Fe + 50(80)% Cr_3C_2 coatings are: current of an arc of a plasmatron – 300-350A; distance of spraying -120mm; flow rate of plasmaforming gas – nitrogen – 50 l/min; flow rate of transporting gas – nitrogen – 10 l/min.
The sizes of sprayed powder particles were in limits ~ 40-100µm. To increase a adhesive strength of wear-resistant coatings on a steel substrate beforehand deposited a underlayer of an adhesive NiCr. Width of underlayer NiCr is 0,05mm.
The coatings NiCr-Fe+50(80)%Cr_3C_2 deposited by plasma spraying are processed in conditions of vacuum at residual chamber pressure 10^{-1}-10^{-2}Pa by pulsed plasma flow on unit considered in the previous partition. The main factors of high-energy action of pulsed plasma flow, responsible for material modification, include high–speed heating and cooling, the shock-wave processes accompanying supersonic plasma flow incidence on a surface

The parameters of a compression plasma flow are: length ~ 0,5m, diameter in the field of maximal compression - 0.03m, rate of flow-(1-2)x10^5m/sec, temperature of plasma 3x10^4K. The action of plasma flow was conducted in pulsed-periodic regime [2] with pulse duration-200µs, period – 15-30s and pulsed number in series 2-10. Pulsed periodic regime was used to reduced the shielding level and to increase the exposure duration. The power density on sample was 10^5 -10^6 W/cm^2. The pressure on target surface in retardation point was 2--3MPa.

As have shown preliminary experiments, macrogeometry of a processed surface of a coating and width of the transformed surface layer are depend from distance between a back of an external electrode of the discharge device of quasi-stationary high-current plasma accelerator (QHPA) and sample (distance of effect) from an amount of impulses (at multiple effect) of plasma flow action. In view of results of preliminary experiments a research and optimisation of impulse processing were carried out at a variation of a distance of effect and amount of impulses. The measure of optimisation was served required structure of processed coatings. We analyse structure of a coating with width 0.3- 0.4 mm deposited on one of backs cylindrical samples with diameter 10 mm and height 12 mm. Structure of coatings studied on microsections of it's cross-section, at which preparation executed following operations:

o - Grinding by an abrasive paper with silicon carbide with a speckle 180, 240, 320,600 unities;

o - Rough polishing on a nylon coating "dp-cloths" with adding of diamond pastes ACM 7/5, 5/3, 2/1 and fluid "metadi fluid" of "Buehler" Corp.(Switzerland);

o - Final polishing on velour "microcloths" with adamant (α-Al_2O_3) with speckle 0.3μm in distilled water;

o - Etching by reagent containing H_3PO_4 -10 ml, HC1-10ml; HNO_3-30ml, CH_3COOH - 50ml.

A research of microsections of a cross-section of coatings conducted on a metallographic microscope "MeF-3" of "Reichert" Corp. (Austria) at magnification x200, x500 and on a semi-automatic image analyser MOP-AMO3, on which obtained the generalised quantitative information about porosity of the deposited materials and hard particles of carbide phase crumbled at preparation of microsections. This information was used at an estimation of effectiveness of impulse plasma processing for increase of a density and strength in volume of sprayed materials, that is especially actual at forming wear-resistant coatings NiCr-Fe+50(80)%Cr_3C_2.

The research of microsections of coatings containing carbide phase was accompanied with measuring of a microhardness on width of sprayed materials. The measurings were carried out in five belts on length of a cross-section of coatings with application of a microhardness gauge "Micromet-II" of the corporation "Buehler" (Switzerland) with a load 100g on indentor. The values of a microhardness were used for an estimation of uniform of allocation of carbide phase describing serviceability of wear-resistant coatings. Alongside with the metallographic analysis of samples studied phase composition of the deposited materials. The comparison of phase composition to similar already known data for deposited powders allowed to estimate correlation between parameters of starting and finally processed materials. The phase analysis executed on a computer-assisted X-ray diffractometer of common assignment DRON-3 in monochrome CuKa radiation. Qualitative analysis of phases was conducted under the program "PDWIN". By its results executed a quantitative analysis of a content of selected phases under the program "X-RAY". The researches on installation DRON-3 conducted at continuous motion of the counter in an interval of angles from 20 to 120 through 0,1°. The shot of the X-raygram of diffusion lines at major angles 120-160° was conducted in a scanning mode. The decryption of phase composition was carried out with aid of a card-catalogue of the American Society of a Test of Materials "ASTM".

4. Results of Investigations

The intensity and aggregate energy of thermal and dynamic effects on coatings at a variation of a distance of processing and amount of multiple impulses have been varied. Thus we have gained different microgeometry of a surface of coatings, varying depth of fusion and degree of heat of melted layer.At processing wear-resistant coatings the measure of optimisation of its modes was obtain dense, sweated structure on whole width of sprayed material. The obtain of such structure ensures a increase of cohesive and adhesion strength of sprayed coating, that, in turn, increases its resistant ability to mechanical destruction during process of friction. The researches have shown, that the required structure can be received at multiple pulse-plasma effects. Also it is established that at an optimal distance of processing an amount of impulses for vitrification on whole width of sprayed material (0,4 mm) at coatings NiCr--Fe+50%Cr_3C_2, NiCr-Fe+80%Cr_3C_2 are attuned and equal to 5.

As noted the distance of processing operate on an amount of a thermal energy transmitted by impulse. For increase of an amount of a transmitted energy and decrease of an aggregate amount of impulses before complete vitrification of wear-resistant coatings the decrease of a distance of processing is expedient. At the same time at a distance 0,3m a destruction of sprayed materials takes place by alms of kinetic head of a compression plasma flow. On base received data the optimal distance of pulse-plasma processing for coatings NiCr-Fe+50%Cr_3C_2, NiCr-Fe+80%Cr_3C_2 is 0,38 m. The measured power density in this point in optimal regime was $5 \cdot 10^5 W/cm^2$.

In this case the vitrification of a surface and underlying layers on whole width of sprayed material is reached. After processing the generalised index of porosity and crumbled hard particles of carbide phase at preparation microsections has decreased (Table 1).

The tabulated data testify that the density and cohesive strength of sprayed materials after pulse-plasma effects has increased. At the same time residual porosity and crumbled hard particles of carbide phase take place that apparently is bounded with fugacity of thermal and dynamic impulse effects. At short-term effects with a high level of its localisation and density of an evolved energy the thin layers of sprayed materials heated up to temperature, which is more than melting point of elements of composition coatings. The first impulse sweat thin surface layer. At repeated impulse the heat transfer through layer is facilitated, and the thermal energy concentrates in following layer on width of a coating, which, in turn, sweated, etc. before complete vitrification of a coating. For an estimation of uniform of allocation of carbide phase describing serviceability of wear-resistant coatings, the metallographic analysis of sample is supplemented with measures of a microhardness of sprayed and sweated at optimal mode of materials.

Table 1

Coating	Generalised index of porosity and crumbled hard particles off carbide phase at preparation microsections, %	
	Before processing of coating	After processing of coating
NiCr-Fe+50%Cr_3C_2	5,3 – 7,9	4,4 – 6,5
NiCr-Fe+80%Cr_3C_2	7,1 – 10,0	6,4 – 9,1

Concerning a microhardness it is necessary also to note that its medial values after pulse-plasma effects increase in comparison with sprayed and unfinished material on 20-35%.

In figure 2 the characteristic graph of a microhardness on width of processed coatings is shown.As is visible from the figure2 graph is characterised with a maximum of a microhardness shifted deep into of layer. The obtained effects of increase of microhardness and allocation of its maximum apparently are linked with accrued at microhardness and allocation of its maxima apparently are linked with accrued at multiple pulse-plasma effects thermal and structural stresses, dislocations. However this assertion requires more accurate researches.

In Fig.3 the typical X-raygram of coatings NiCr-Fe+50(80)%Cr_3C_2 is shown.

The collation of the X-raygrams displays that an essential modification of phase composition of deposited powder materials during deriving coatings does not happen. At the same time the modification of the carbide phase is observed. For example, after impulse processing only the carbides Cr_3C_2 is detected and junction Cr_7C_3 is absent, which income into phase composition of a starting powder

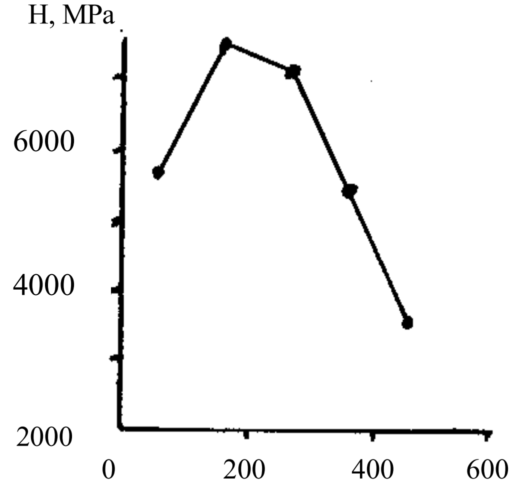

Figure 2 Graph of microhardness on width of coating NiCr-Fe+50%Cr_3C_2 after pulse-plasma processing.

.Fi
c

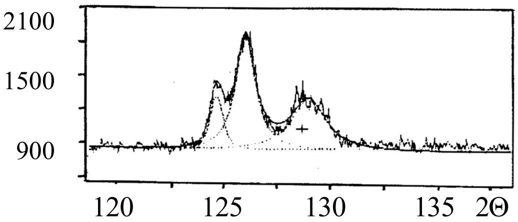

Figure 3.X-raygrams of sprayed wear-resistant composite coating NiCr-Fe+50%Cr_3C_2 after pulsed-plasma processing

It is explained with followed: in conditions of short-term pulse-plasma effect with local vitrification and superfast cooling of the sprayed material in a chrome-carbon system a phase Cr_3C_2 is stable.

In sprayed and processed materials takes place amorphisation of phases,the presence halo on the X-raygrams argumentatives about that, Fig.3. The increased presence of amorphous and microcrystalline phases is explained with super fast cooling of layers of coatings after pulse-plasma effects. Amorphisation of structure promotes a increase of its wear-resistance [3].

5. Conclusion

The researches of effect of impulses of a pulsed plasma flows on wear-resistant coatings obtained by plasma spraying are carried out.

At a research of coatings NiCr+50(80)%Cr_3C_2 is established, that the optimal distance of pulse-plasma effect is 0,38 m($q = 5\ 10^5 W/cm^2$), optimal amount of impulses is 5. Thus the vitrification of a surface and underlying layers on whole width of sprayed materials is reached. The density and cohesive strength of sprayed materials are rises, decrease on 15--20% its a generalised index of porosity and crumbled hard particles of carbide phase is argumentatives about that. Such transformation of structure promotes resistance of a coatings against mechanical destruction during friction. At the same time residual porosity and crumbled hard particles of carbide phase take place, that is apparently linked with fugacity of thermal and dynamic impulse effects (~200 µsec).

The comparison of the X-raygrams of starting powders and coatings after impulse effects displays that an essential modification of phase composition does not happen. However intensive heat by impulse of plasma with local vitrification and superfast cooling of layer of sprayed material causes modification of carbide phase and increase of presence of amorphous phases, which, as is known, create premises of wear-resistance of coatings.

References

[1].Astashinski V.M., Man'kovski A.A., Min'ko L.Ya., Morozov A.I. J.Plasma Physics. **18**, 47 (1992)

[2].AstashinskiV.M.,Min'ko L.Ya., Moukhin Yu.V., Chivel Yu.A. Proceedings 24th International Conference IEPC95. Moscow, P.395. (1995)

[3]. Ilyuschenko A. , Ivashko V.,Shevtsov A., ,Okovity V. ,Buykus K., Chivel Yu., Steinhauser S. Proceedings International Conference "Balttrib-99". Kaunas, . P.305 (1999).

ICP treatment of Titania, two-phase Tungsten Carbide and permanent magnetic NdFeB powders

P. Linke, K. Sittig, K.-H. Weiß, G. Nutsch

Fachgebiet Plasma- und Oberflächentechnik, Technische Universität Ilmenau, Ilmenau, Germany

Abstract:
Due to its advantages the electrode-less radio frequency inductively coupled plasma is used for powder remelting, cleaning and modification. Oxide powders such as alumina or titania are treated under atmospheric conditions, the other materials, which are sensitive to oxygen have to be treated in an inert gas atmosphere. The aim of the studies was to achieve a particular material composition of the powder by the plasma treating. The composition is examined by XRD and EDX, the morphology by SEM, and the magnetic properties by vibrating sample magnetometer.

1. Introduction

The application of the thermal radio frequency inductively coupled plasma (RF ICP) has become more important in the last years. The ICP is used in numerous laboratories [1-8], and more recently also in industrial scale in thermal spraying (e.g. [9]), and also in powder treatment processes, especially the in-flight spheroidization. The ICP in-flight powder treatment of refractory materials is characterized by extreme high heating temperature (about 5 –10 kK) and correspondingly, by very high heating and cooling rates (up to 10^6 K/s) of the rapidly moving particles [10]. It has been successfully applied to the spheroidization of several refractory materials by rapid solidification from partially or completely molten particles [11Bou]. The processing of advanced powder materials for the spraying industry is one of the most promising applications of the thermal RF ICP. Selecting the feedstock carefully and adjusting the RF plasma parameters unique materials can achieve with a high quality. Powders injected in the hot plasma core emerge with modified shapes, morphology, crystal structure and chemical composition.

Due to its electrode-less operation, the ICP can be generated with nearly all gases, also with oxygen. Oxidic powders such as Al_2O_3, ZrO_2, and SiO_2 are spheroidized with a high spheroidization rate [12,13].

The relatively long dwell times of powder particles within the ICP of about 10 milliseconds enable also chemical reactions of the feedstock with the plasma forming gases.

Using hydrogen as additional gas the in-flight reduction of oxide powders such as Fe_2O_3, Cr_2O_3, TiO_2 can be carried out in the ICP whereby the utilization efficiency of hydrogen was always higher than the estimated value by thermodynamic equilibrium [14].

Based on the studies of plasma treatment of oxide powders, the ICP is applied for the manufacturing of two-phase tungsten carbide spherical powders. Due to the high oxygen sensitivity of the tungsten carbide powders the process has to carry out under inert gas atmosphere. The plasma processing of the highly oxygen sensitive hard magnetic $Nd_2Fe_{14}B$ powders require a special handling, and still more important, a non-oxidizing environment [15].

In the following, the conditions of the powder treatment processes of varying materials are given. The particularities and the obtained results of this study such as spheroidization rate, morphology and treated powder composition are described.

2. Experimental set-up

The experimental study is carried out in the arrangement consisting on the RF generator (f = 3.75 MHz), the TU Ilmenau plasma torch (Fig. 1), and the reactor for ensuring the desired gas atmosphere. More details of the experimental set-up have been described in previous papers [12,13]. The operating conditions of the experiments performed are listed in Table 1. The both molecular gases nitrogen or hydrogen are introduced as an addition to the sheath gas argon. The feedstock is injected by water-cooled injection probe located in high of the first turn of the induction coil.

Quartz glass tubes for the plasma confining tube as well as for the central gas tube, which make possible to watch the plasma plume and the powder trajectories, characterize the TU Ilmenau ICP torch.

Table 1: **Parameters used**

Plate power	kW	12 -28
Coil diameter	mm	47
Sheath gas flow Ar	slpm	15 - 45
Sheath gas flow N_2	slpm	2. - 6
Sheath gas flow H_2	slpm	2 - 10
Sheath gas flow O_2	slpm	5 - 20
Central gas Ar	slpm	15 - 30
Carrier gas Ar	slpm	0.5 - 2
Powder feeding rate of: crashed TiO_2 spray dried, agglom. WC / C melt spun $Nd_2Fe_{14}B$	 g / min g / min g / min	 2 – 10 < 45 2 - 6

Fig. 1: ICP torch (type TU Ilmenau) consisting of two concentric quartz glass tubes for watching plasma plume and powder trajectories

3. Treatment of Titania Powders

3.1 Properties of Titania

The TiO_2 is the most important oxide in the Ti-O phase diagram [16, 17], but it exists in several modifications. The most stable modification is the rutile; the other is anatase, which transforms irreversibly into rutile by heating. So-called titanium sub-oxides are formed in the range of lower oxygen content: difficultly identifiable phases exist in the range of oxygen content x_o between 1.9 and 2.0, which do have not so industrial importance.

Table 2: Titanium oxides and their properties [19]

Index n	Phase	Composition	Oxygen Deficiency [wt%]	Structure	JCPDS number
-	TiO_2 (Rutile)	$TiO_{2.00}$	-	tetragonal	21-1276
-	TiO_2 (Anatase)	$TiO_{2.00}$	-	tetragonal	21-1272
-	TiO_2 (Brookite)	$TiO_{2.00}$	-	orthorhombic	76-1937
10	$Ti_{10}O_{19}$	$TiO_{1.9}$	2.00	triclinic	11-474
9	Ti_9O_{17}	$TiO_{1.89}$	2.23	triclinic	18-1405
8	Ti_8O_{15}	$TiO_{1.88}$	2.5	triclinic	18-1404
7	Ti_7O_{13}	$TiO_{1.86}$	2.96	triclinic	18-1403
6	Ti_6O_{11}	$TiO_{1.83}$	3.34	triclinic	18-1401
5	Ti_5O_9	$TiO_{1.80}$	4.01	triclinic	11-193
4	Ti_4O_7	$TiO_{1.75}$	5.01	triclinic	18-1402
-	α-Ti_3O_5	$TiO_{1.67}$	6.68	monoclinic	23-606
-	β-Ti_3O_5	$TiO_{1.67}$	6.68	monoclinic	11-217
-	γ-Ti_3O_5	$TiO_{1.67}$	6.68	monoclinic	40-806

The so-called Magnéli phases with oxygen content between 1.75 and 1.9 can be described by the general formula Ti_nO_{2n-1} [18] for $4 \leq n \leq 10$. Further phases are the Ti_3O_5, Ti_2O_3 and TiO. Especially, the Magnéli phases are of particularly industrial interest due to their mechanical and electrical properties: The lower the oxygen content the higher is the electrical conductivity. So, the electrical conductivity of Ti_4O_7 is comparable with those of graphite [19]. The microhardness also depends on the oxygen content. Table 2 [20] gives an overview on the composition, oxygen deficiency, and structures of the most important titanium oxides. Also, changes in the crystalline structure influence the colors of the titania powders, the oxygen deficit leads to color changes from white via yellow and gray-blue up to black.

3.2 ICP treatment of Titania powder

Because of the industrial demand on titanium sub-oxides it is of interest to investigate the material composition of plasma treated titania powder at varying ICP operation conditions. First results are shown in the following. The feedstock is titanium oxide obtained as commercial plasma spray powder (GTV mbH, Luckenbach, D; MEDICOAT AG, Mägenwil, CH) with a grain size of 45 - 90 µm, molten and crashed, with a composition of 99.8% TiO_2. The gray-black color demonstrates that non-stoichiometric titanium oxide phases exist shown in Figure 2. The ICP treated powder shown in Figure 3 is manufactured with the sheath gas flow of 15 slpm Argon with an addition of oxygen, the argon central gas flow rate of 25slpm, and a powder feeding rate of 10 g/min. The particles are spheroidized with a rate higher than 95%. The particles have a light gray color caused by the in-flight oxidation of the powder particles.

Fig.2: The black color of the feedstock

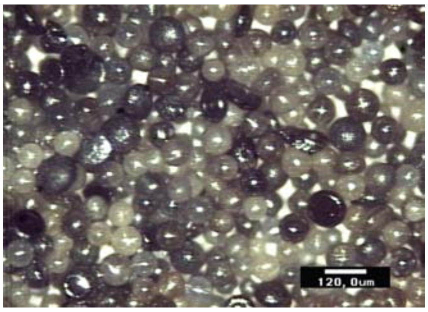

Fig.3: light gray colored plasma treated powder particles

Fig.4 shows the corresponding X-Ray-Diffractometry (XRD) diagrams. The untreated powder has the best accordance with the Ti_9O_{17} peaks. The diffuse underground comes from the $Ti_{10}O_{19}$, but the corresponding peaks are not indicated. Also, an amorphous phase exists as is shown in the range $15° < 2\vartheta < 23°$. The inert gas treated powder with argon as well as an argon/nitrogen gas mixture as sheath gas shows no significant phase changes. Oxygen has to be added to the sheath gas in order to enhance the oxygen content of the powder and to initiate phase modifications: The higher the oxygen content in the sheath gas the more stoichiometric phases are obtained.

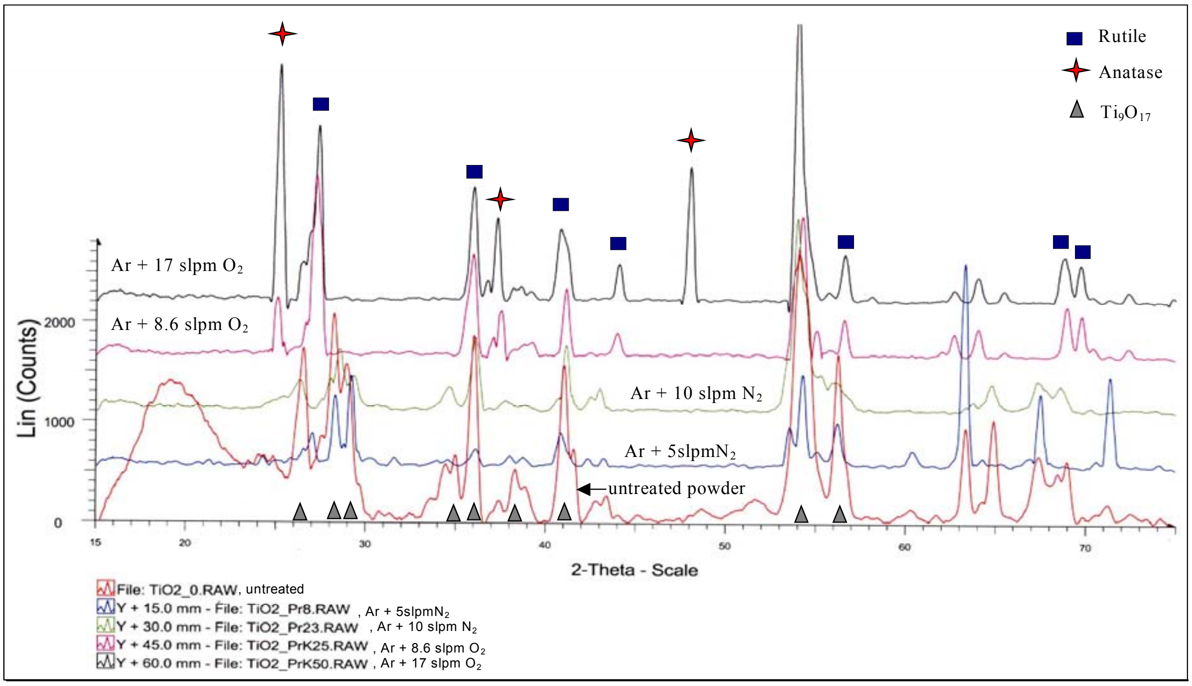

Fig. 4: XRD diagram of the titanium dioxide ICP treated with varying working gas mixtures

The XRD diagram of the oxygen treated powder shows clearly the peaks of the both pure TiO_2 phases, rutile and anatase. However, the phase changes happen incompletely. Further investigations have to be done.

Scanning electron microscope pictures made from the surface of the single particles are shown in Figure 5. The enhanced surface area and roughness due to the dendritic patterns are of interest as catalyst supports in the chemical industry for vapor-phase processes as well as for liquid-phase processes because the pore sizes amounts to about 1 µm. Work is in progress to establish the conditions for the formation of dendrites and pores.

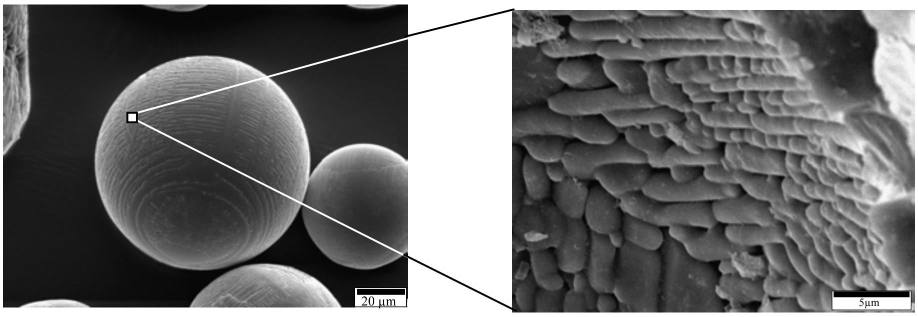

Fig.5: SEM pictures of the particle surface

4. Manufacturing two-phase tungsten carbide spheroids

4.1 Properties of the tungsten carbide

Spherical tungsten carbide particles can be manufactured with various techniques. Due to its uniform shape and low surface energy, spherical powder particles made from the composition of W_2C + WC has for many years a widespread use in cases where wear resistance and hardness are primary requirements. At present, well-known production technologies supply still no satisfying results in the desired grain size range of 40 until 150 µm. The ICP technique is well suited for processing of such refractory metals. The parameters of the given ICP for manufacturing the two-phase tungsten carbide are optimized in relation to high powder feeding rate and high spheroidization rate. First coatings using the spheroidized powder are prepared by HVOF spraying [20].

From the phase diagram [21] follows: Eutectic W + W_2C is formed at the temperature of 2710°C and W_2C + β-WC at a temperature of 2670°C. The β-WC is stable at temperatures above 2525°C and exists between W_2C and α-WC. At temperatures below 2525°C, the β-WC decomposes in a eutectoid reaction to forming the phase W_2C + α-WC. The last one decomposes at temperatures of 2755°C with the formation of C and β-WC, so that β-WC transforms to W_2C under forming of carbon, which has been oxidized to volatile carbon mono-oxide. The W_2C melts congruently at 2760-2776°C.

Those tungsten carbides are of particular interest consisting of a mixture from W_2C and WC with a carbon concentration of 3.8 – 4.3 wt%. This carbon content corresponds to a composition of approx. 73 – 80 wt% W_2C and 20 – 27 wt% WC. This two-phase compound is a metastable phase. By fast cooling after the ICP treatment this special phase has been frozen, and the desired pearlitic-type microstructure is achieved. The parameters used for the remelting process are given also in Table 1.

4.2 Two-phase tungsten carbide spheroids manufacturing

The raw material consists of free W and WC particles with a grain size of about 2 µm. For spray drying the particles are agglomerated with an organic binder. The spray-dried raw material is shown in Figure 6.

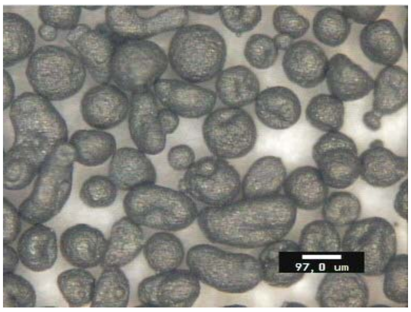

Fig.6: Spray dried W-WC agglomerates

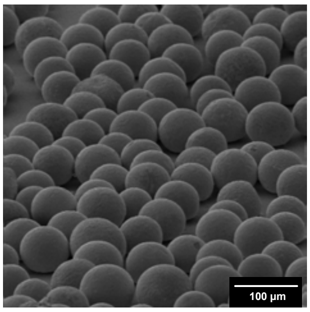

Fig.7: Spheroidized WC-W_2C powder

Therefore, the powder has a low cohesion, and the porosity of the powder particle amounts to approximately 50 %. The powder size used for the ICP treatment ranges from 100 µm to 125 µm. The small variety in the size distribution guarantees a uniform plasma treatment of all particles. The powder shown in Figure 7 is ICP treated with a spheroidization rate higher than 95% using the parameters given in table 1.

By fast quenching of the powder particles immediately after passing the plasma, the needle-like structure of the hard W_2C phase is obtained embedded into the tougher WC matrix as shown in Figure 8. That is the desired microstructure of the two-phase powder particles, which is very interesting for abrasive applications.

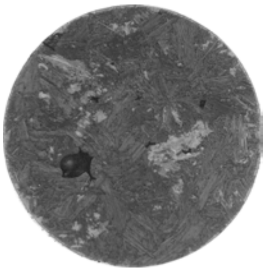

Fig. 8: Cross Section of ICP treated Tungsten Carbide Powder (diameter = 100 µm)

The XRD studies show evidently that the free tungsten of the raw material reacts completely with the carbon and forms W_2C because only carbide phases are verifiable in the plasma treated powder. Unwanted phases of oxides or nitrides cannot be proven. The carbon content of the powder particles is in the expected range of 3.8 –4.3 wt. %, measured with a LECO device. The powder particles have a hardness $HV_{0.1} > 3500$.

5. Treatment of hard magnetic powders

5.1 Properties of $Nd_2Fe_{14}B$ powders used

Intermetallic compounds, based on rare earth metals, transition metals, and boron show superior properties as the samarium-cobalt-based permanent magnets. Known as third generation of Rare Earth magnets, Neodymium-Iron-Boron (NdFeB) based magnets are the most powerful and advanced commercialised permanent magnets today. Since they are made from Neodymium, one of the most plentiful rare earth elements, and inexpensive iron, NdFeB magnets offer the best value in cost and performance. The $Nd_2Fe_{14}B$ compound has the record energy product, which makes it interesting for applications in the automotive industry. The physical properties such as saturation magnetization and the coercive force are the most important factors for obtaining its high performance rivaling Sm-Co magnets. Their disadvantages are the low working temperature (<200^{0}C) and their tendency to oxidize more than any other magnet alloy. Excellent Nd-Fe-B based permanent magnets are produced in a variety of technologies such as the conventional powder processing technology and the rapid solidification method.

The MQP-B powder used is manufactured by melt spinning from the Magnequench Inc., USA. The properties of this powder generally used for manufacturing of bonded magnets are given in table 3 and the morphology is shown in Figure 9.

Table 3: Physical Properties of the MQP-B powder

	$Nd_2Fe_{14}B$
Residual Induction B_r	0.840 – 0.895 T
Coercive Force H_c	640 - 800 kA/m
Energy Product	111-126 kJ/m^3
Curie Temperature T_C	360 °C
Density (theoretical)	7.64 g/cm^3
Apparent density	2.7 g/cm^3
Powder size	< 0,1% > 420 µm < 15% < 44 µm

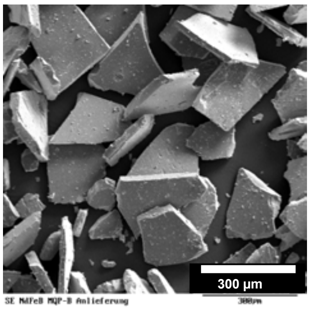

Fig.9: Melt-spun MQP-B powder

The powders have to wet milled for six up to nine hours in order to achieve the desired powder particle size of +40 – 60 µm used for ICP treatment.

5.2 ICP powder treatment

The important parameter of the NdFeB powder treatment is the residual oxygen content in the reactor chamber. The chamber has to be carefully rinse some times with argon before the treatment process can be start. Also, an addition of hydrogen is useful for adhering the oxygen. By using the additional quench gas the cooling rate increases and the oxidation is prevented. The as-treated powders show the hard magnetic phase verified by the X-Ray Diffraction in the 2-Θ-Scale range from 30° up to 60° (Fig. 11). The powder is well spheroidized shown in Figure 10.

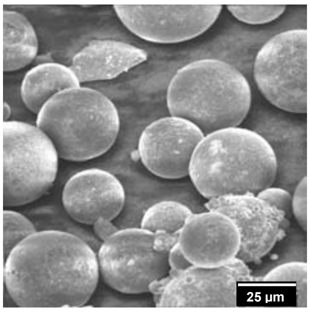

Fig.10: SEM picture of the spheroidized NdFeB powder particles

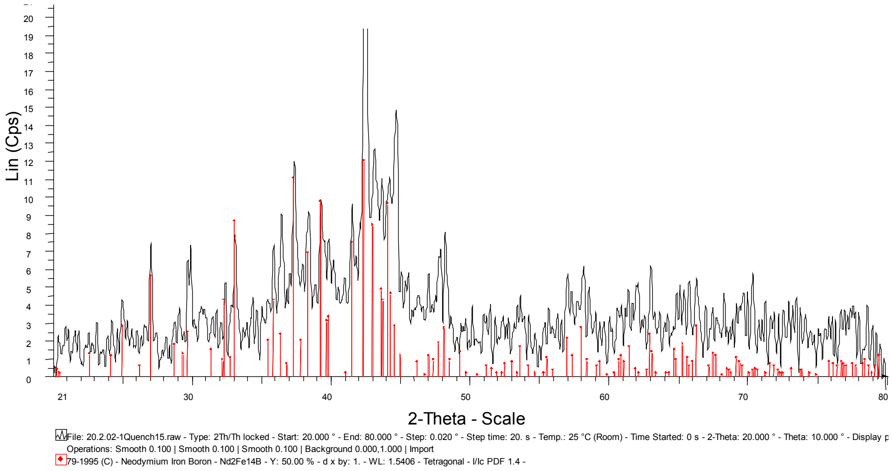

Fig.11: XRD diagram of the plasma treated powder

6. Conclusion

Using the thermal inductively coupled plasma powder particles are well spheroidized. Due to the long dwell times of the particles in-flight chemical reactions can occur using additionally injected reactive gases such as hydrogen or oxygen: Titania sub-oxide powder can be oxidized to thermodynamic stable phases. The dendritic surface of the titania particles is well suited for catalytic applications. Two phase tungsten carbide particles can be manufactured Also, hard magnetic powder particles such as $Nd_2Fe_{14}B$ powder can be well treated by the ICP.

References

[1] M.I.Boulos, High Temp. Mat. Proc. **1**(1997), 17-39
[2] M.F. Besser et al., J. Mat. Synthesis and Processing **3** (1995), 223-230
[3] N.M. Dignard et al. Proc. ISPC 13, Bejing, 1997, 1031-1036
[4] Z. Karoly et al., Powder Technology **110** (2000), 169-178
[5] J.M. McKelliget, in: Thermal Plasma Appl. in Materials and Metallurgical Processing, Ed.: N. El-Kaddah, MMM Society, 1992
[6] N.N. Novikova et al., Ogneupory, 1992, number 11-12, pp. 4-9
[7] Y.L. Li et al., Chemistry of Materials, **13** (2001), 1577-1584
[8] N.A. Klinskaya-Rudenskaya et al., High temperature **37** (1990), pp. 22-26
[9] P. Rödhammer, PLANSEE Seminar
[10] M. Boulos et al., Thermal Plasma, Vol. 1, Plenum Press, New York, 1994
[11] Boulos + Gitzhofer
[12].G. Nutsch, Inv. Lecture on TPP7, 2002, Strasbourg, France,
[13] P. Linke et al., Proc. ISPC 15 (2001), Orleans, France, vol. IV, 2603-2608
[14] T. Kitamura et al., ISIJ International, **33** (1993), pp. 1150-1158
[15] P. Linke et al., Workshop Plasmatechnology 2002, TU Ilmenau, pp. 44-51
[16] J. Murray et al., Bull. Alloy Phase Diagrams, 8(1987), 2, pp.148-165
[17] P.G. Wahlbeck et al., J. Am. Ceram. Soc. 49 (1966),4, pp.180
[18] S. Anderson et al., Acta Chem. Scand., 11(1957)10, pp. 1641-1652
[19] M. Zweynert et al., Chem.-Ing. Technik 70(1998), 7, pp. 827-841 (in German)
[20] G. Nutsch et al., Proc. 47th IWK TU Ilmenau, 2002, (in German), pp.
[21] R. W. Sara, J. Am. Ceram. Soc. 48 (1965), pp 251

Investigations of turbulence in thermal plasma jets by CCD camera image analysis

J. Hlína, V. Něnička, J. Šonský

Institute of Electrical Engineering, Academy of Sciences of the Czech Republic, Prague, Czech Republic

Abstract

Turbulent structures in a thermal plasma jet were detected by a method based on subtraction of subsequent images in picture sequences acquired by a CCD camera. This method leads to visualisation of regions characterised by positive or negative change of optical emission between the succeeding pictures. The regions move downstream along the gas flow. The evaluation yields results showing the increase of the mean number of structures and decrease of their average size with the gas flow rate. These quantities reflect the turbulence scale in the plasma jet.

1. Introduction

Turbulence in thermal plasma jets is very important for their applications because the turbulent phenomena influence the thermal transport that plays a crucial role in the involved technological processes. At the same time, plasma turbulence is one of the most difficult phenomena to understand in plasma physics. Contrary to turbulence in neutral fluids, there is still relatively little experimental evidence about the space-time structure of turbulence in thermal plasma flows. Previous results of the analysis of CCD camera images [1] have shown that methods based on the comparison of recorded plasma jet radiation intensities for the pictures succeeding in a recorded sequence may be very suitable for investigations of the plasma jet dynamics. The most simple of these methods is the subtraction of matrices representing intensities of plasma jet optical radiation in two succeeding pictures (referred-to as the difference method). The resulting series of differential matrices show regions characterised by high differences of recorded radiation intensities moving along the gas flow. These regions are connected with vortex structures responsible for changes of the plasma temperature and density, which make these structures detectable. Important tools for quantitative evaluations of spatial structures in spatial statistics are Minkowski functionals which include the volume, surface, mean curvature and Euler characteristic of the structures [2]. Our recent studies deal with evaluations of some quantities related to Minkowski functionals (especially the structure sizes) in a thermal plasma jet by the difference method applied to the series of images acquired by a CCD camera. Records of a sufficient number of images may yield data also for the statistical evaluation of the structure numbers and sizes. According to the results, the average number of structures and their average size depend on the gas flow rate. It has been shown [3] that the departure of corresponding distribution functions from the Gaussian distribution is an important measure of turbulence scales.

2.Experimental arrangement

In our experiments (Fig.1), the argon plasma jet was generated by a d.c. fed plasma torch equipped with a cylindrical nozzle with diameter 8 mm. The arc current was 150 A and arc voltage 30-40 V for gas flow rates 10-60 slm. The fast shutter CCD camera in the regime of multiple exposures was adapted for acquisition of image sequences by inserting of a rotating mirror between the CCD chip and objective lens and was able to record 8 pictures of the jet with exposure time 1 μs and 10 μs interval between the pictures.

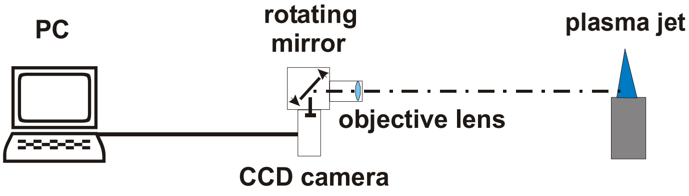

Fig.1. Experimental arrangement

3.Results

The evaluation of CCD camera records of the plasma jet was based on the comparison of changes of recorded plasma jet radiation intensities for the succeeding pictures in the sequence. The most simple method for evaluating the plasma jet dynamics consists in the subtraction of the two succeeding images of the jet represented by matrices $\{a_k(i,j)\}$. The intensity value of each pixel in the differential matrix is computed as a difference of intensities in corresponding pixels of original matrices

$$\{b_k(i,j)\}=\{a_{k+1}(i,j)\}-\{a_k(i,j)\}.$$

The resulting series of differential matrices shows then regions characterised by different values of recorded radiation intensities in succeeding pictures.

The quantity and shapes of turbulent structures detected by the method described above vary not only depending on the operating parameters but the results show also a high variability for non-changing operating conditions. The examples of results in Figs. 2-5 for gas flow rates 20, 30, 40 and 60 slm, respectively, show the images of the plasma jet (a), the difference images (b) and evolutions of chosen structures characterised by positive values of the differences ("red " structures – (c)) or by negative values of differences ("blue" structures – (d)). Bar diagrams on the right-hand side in Figs. (c) and (d) show the evolution of sizes of the highlighted structures. The average values of the number of structures and their average size as functions of the gas flow rate evaluated from 30 sequences acquired in stable operating conditions are in Fig. 6. Examples of histograms showing occurrence of various numbers of detected structures for the gas flow rates 20 and 60 slm are in Fig.7. The red curves show the corresponding Gaussian distributions fitted to the data by the least squares method.

4.Conclusion

The method using the subtraction of the succeeding images in a sequence for the detection of regions characterised by decreasing or increasing luminosity is suitable for the evaluation of turbulence in thermal plasma jets. The regions of decreasing luminosity (blue in our representation) are probably connected with turbulent structures cooled by the entrainment of the surrounding air. These areas are carried by the gas flow downstream along with hotter regions between them (red in the presented figures). Shifts of these structures between succeeding pictures may yield their velocities. Velocity values acquired in this way are mostly similar to those acquired by methods based on the FFT of local radiation records (the results have been shown e.g. in [4,5]) but in some cases these velocities may substantially differ. An essential reason for this may be sought in the different time intervals used for the velocity evaluation: while the FFT principally requires the application to long data series and its results thus reflect the mean plasma velocity, in the method utilizing camera images it is possible to evaluate the instantaneous velocity values from plasma jet images acquired in a very short time interval. The results based on evaluations of many records show that the number and average size of the detected structures depend significantly on the gas flow rate. The number of the structures increases with the gas flow rate up to 30 slm, while the average size of the structures at the same time decreases. The changes of these quantities for the gas flow rates over 30 slm are small. This is connected with the rising vorticity leading to the formation of smaller and more frequent turbulent structures in the range of gas flow rates up to 30 slm and stabilisation of the conditions for vortex generation at higher flow rates. According to the results, this type of quantitative evaluation of CCD camera images is suitable for the detection of turbulence level in plasma jets including measurements of evolution, velocity and size of characteristic turbulent structures. The results show high variations of the evaluated quantities for steady operating conditions. The conclusions concerning the coincidence of statistical distributions of the numbers and sizes of the structures with the Gaussian distribution will require evaluations of more experimental data. In the analysis of CCD camera pictures we have not applied the Abel inversion

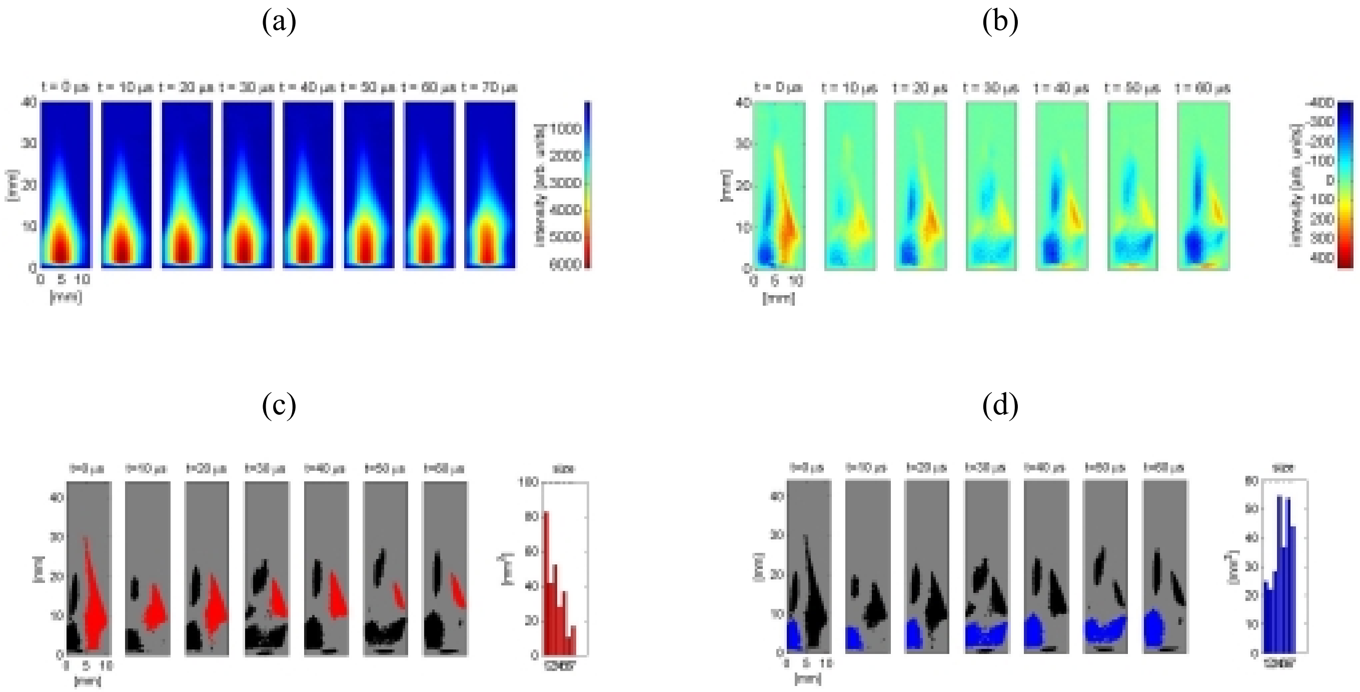

Fig.2. Sequence of plasma jet images (a), image differences (b), evolution of a structure characterized by a positive value of the difference (c) and evolution of a structure characterized by a negative value of the difference (d) along with their sizes at right. Gas flow rate 20 slm.

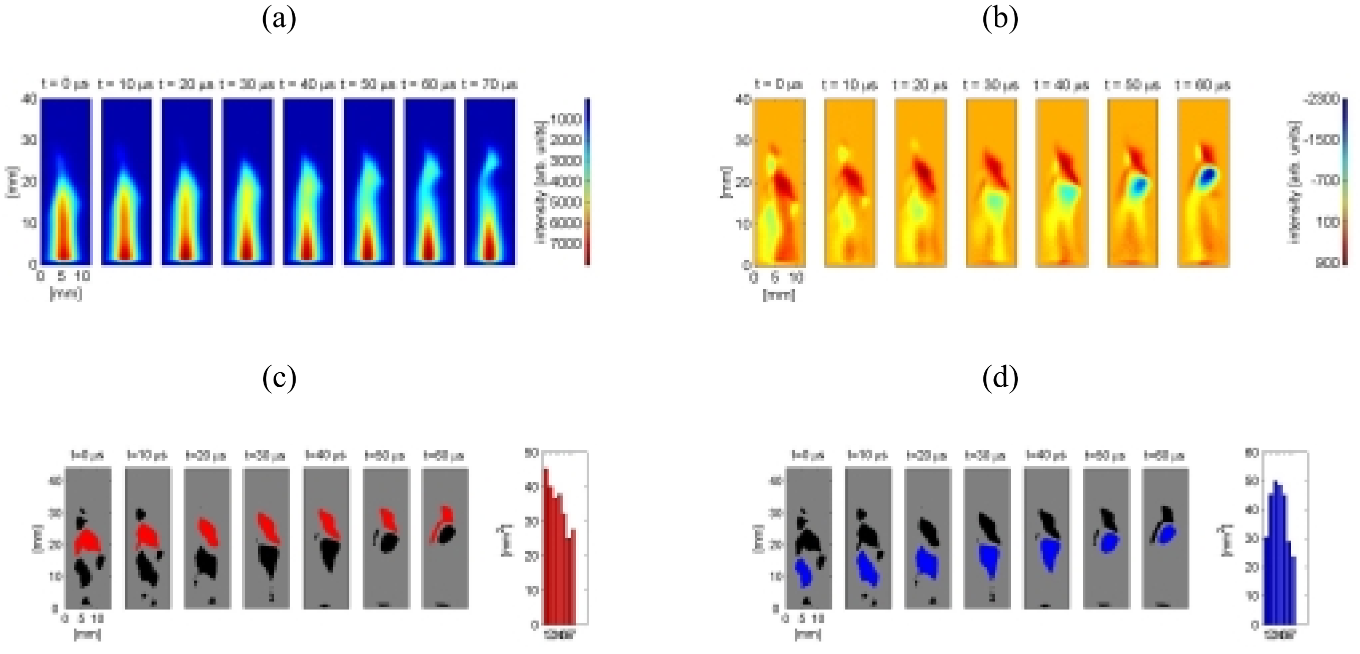

Fig.3. Sequence of plasma jet images (a), image differences (b), evolution of a structure characterized by a positive value of the difference (c) and evolution of a structure characterized by a negative value of the difference (d) along with their sizes at right. Gas flow rate 30 slm.

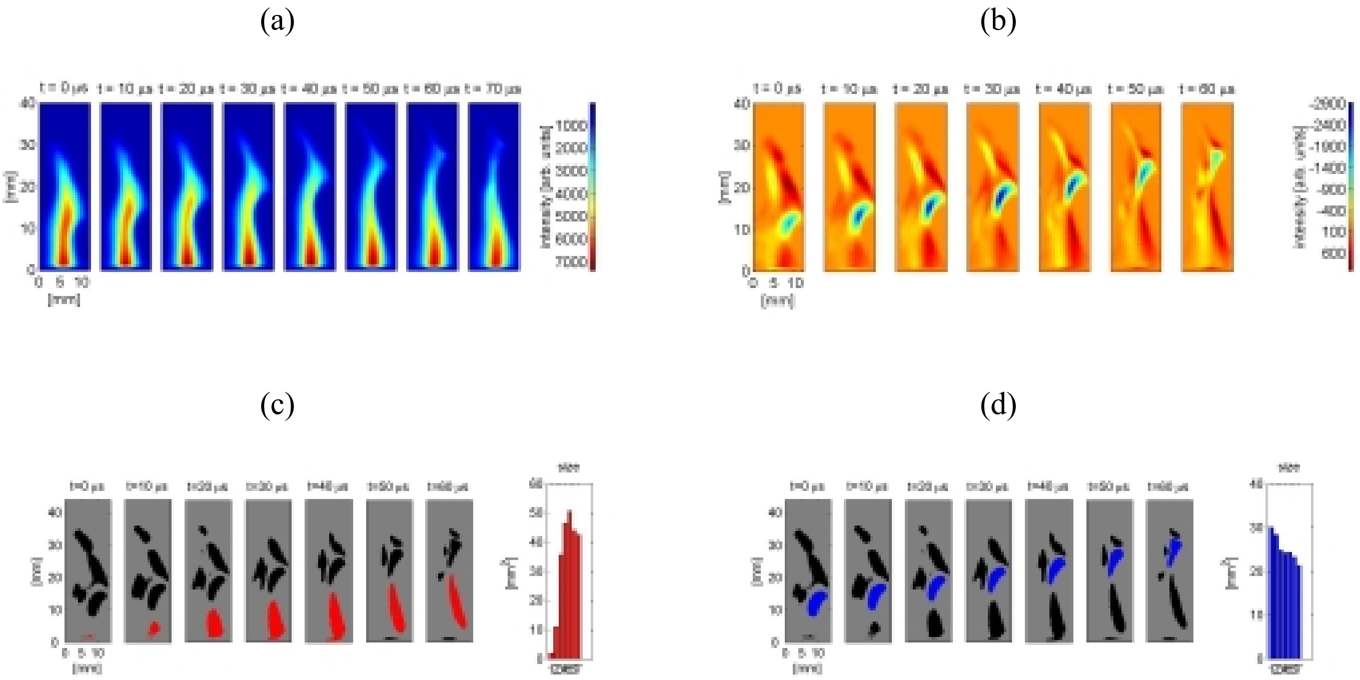

Fig.4. Sequence of plasma jet images (a), image differences (b), evolution of a structure characterized by a positive value of the difference (c) and evolution of a structure characterized by a negative value of the difference (d) along with their sizes at right. Gas flow rate 40 slm.

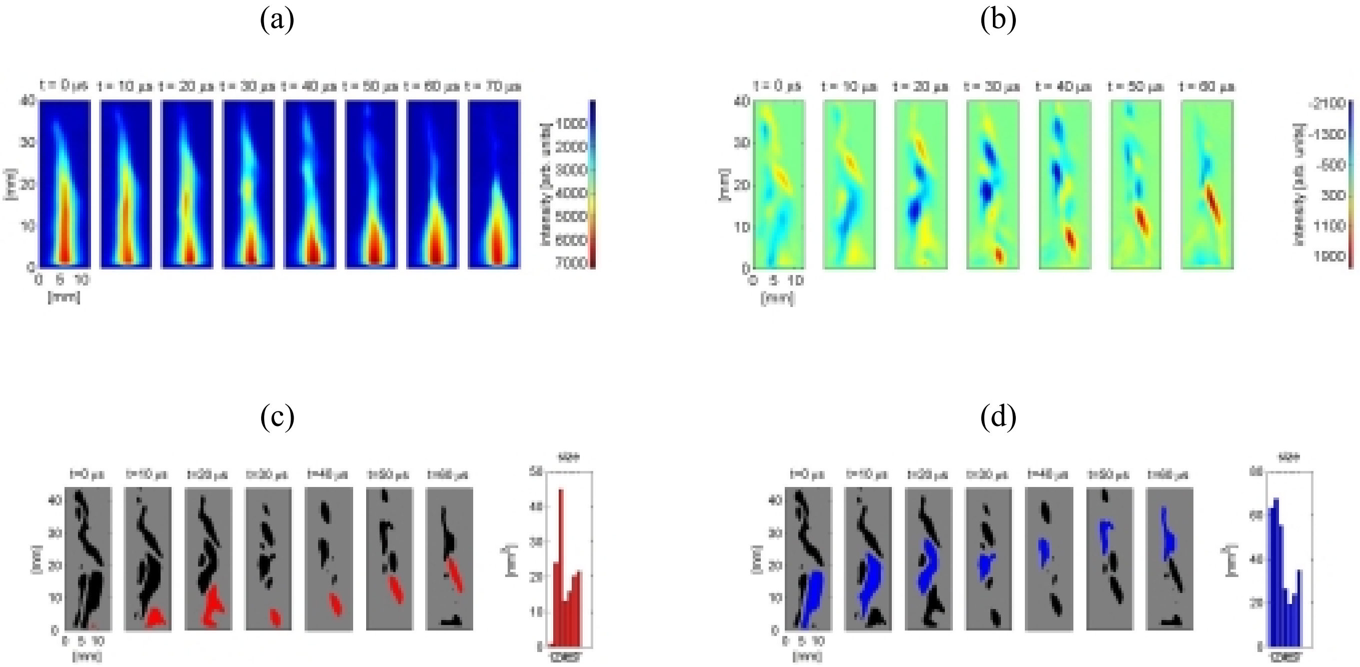

Fig.5. Sequence of plasma jet images (a), image differences (b), evolution of a structure characterized by a positive value of the difference (c) and evolution of a structure characterized by a negative value of the difference (d) along with their sizes at right. Gas flow rate 60 slm.

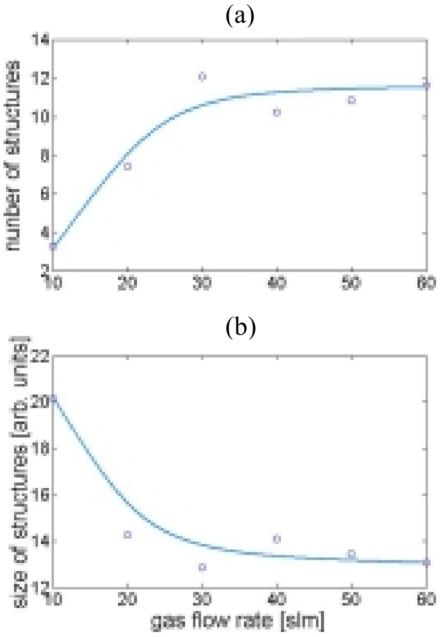

Fig.6. Average values of the number (a) and size (b) of structures detected in CCD camera images as functions of the gas flow rate.

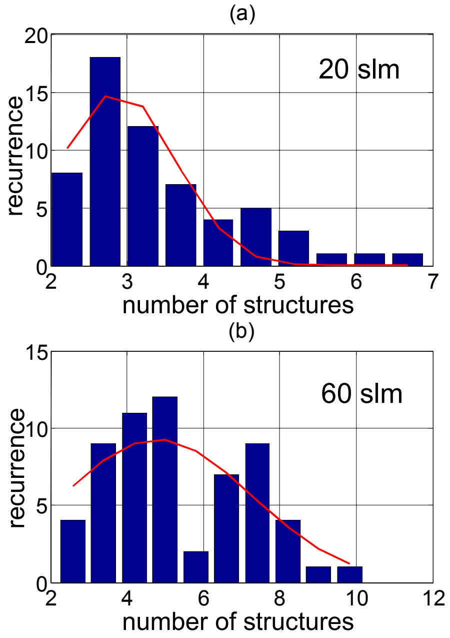

Fig.7. Recurrence of structure quantities for 20 slm (a) and 60 slm (b) compared to the Gaussian distribution (red curves).

of the acquired images (which is obviously used to derive the radial distribution from the „side-on“ records) because of the lack of cylindrical symmetry in the plasma jet pictures. This holds also for the structures detected in the flow. Their shapes are often irregular and even records showing the jet from two directions would be insufficient for their exact spatial (3-dimensinal) identification. Therefore we have to be careful interpreting the results. In spite of that even in the case of "one-direction" observations the method is able to detect unambiguously the z-axis motion (and consequently the axial velocity) and evolution of the shape and number of the structures. The analysis of "red and "blue" regions in difference images shows a certain level of fractal segmentation of the structure borders. The sizes of these interface instabilities depend on the flow rate and can be observed well especially for the flow rates 20 and 30 slm. The exact evaluation of these effects is difficult due to relatively low space resolution of our images (each of 8 images in the sequence includes approx. 140x400 pixels). The influence of dissipative processes on the evolution of fractal characteristics as a source of information about self-similarity degree in the system will be investigated in the future. It is possible to study dynamic dissipation in plasma jets as a result of shear layer strains in pre-turbulent regimes using similar methods as authors in [6]. Such approach would correspond to the results of the dynamic system theory applied to evaluations of the fractal dimension by methods mentioned in [7].

Acknowledgement. The experimental data were acquired in the laboratory of the Institute of Thermomechanics AS CR. This opportunity is greatly acknowledged. The authors also thank for the financial support of the Grant Agency of the Academy of Sciences of the Czech Republic under the contracts IAA1057202 and IAA1057001/00.

References

[1] V. Něnička, J. Hlína, J. Šonský: *Identification of dynamic patterns in CCD camera records of thermal plasma jets*, Symposium TPP 7 Thermal Plasma Processes, Strasbourg, June 18-21, 2002, to be published in Progress in Plasma Processing of Materials 2002, ed. P.Fauchais, Begell House

[2] Statistical Physics and Spatial Statistics, eds. K. R. Mecke and D. Stoyan, Springer 2000

[3] L. Sorriso-Valvo, V. Carbone, P. Giuliani, P. Veltri, R. Bruno, V. Antoni, E. Martines: *Intermittency in plasma turbulence*, Planetary and Space Science **49**, 1193-1200 (2001)

[4] N. Singh, M. Razafinimanana, J. Hlína: *Determination of plasma velocity from light fluctuations* J. Phys.D: Appl. Phys. 33, 275-279 (2000)

[5] J. Hlína, V. Něnička, J. Šlechta, L. Krejčí , V. Dolínek: *Influence of plasma torch characteristics on temperatures and velocities in a plasma jet,* 14th Int. Symposium on Plasma Chemistry, Aug 2-6, Prague, Symp. Proc. Vol. I, 367-372 (2000)

[6] A. Agrawal, A.K. Prasad: *Properties of vortices in the self-similar turbulent jet*, Exp. Fluids **33**, 565-577 (2002)

[7] R.C. Hilborn: *Chaos and nonlinear dynamics*, Oxford University Press, 1994

Plasma processing of Si and glass before electroless metallization by a tin-free catalytic method

M. Charbonnier, Y. Goepfert, M. Romand

Laboratoire de Sciences et Ingénierie des Surfaces, Université Claude Bernard - Lyon 1, 69622 Villeurbanne, France

Abstract

The tin-free process developed in our laboratory in the recent years for electroless metallization of polymers has shown it could be extended to silicon, SiO_2 / silicon or glass substrates, on condition to coat these substrates with an ultra-thin layer of an adequate material able to play the role of a bridge between substrate and metal film. Indeed, the massive presence of oxygen in SiO_2 or glass substrates as well as the omnipresence of a thin native SiO_2 layer on any silicon substrate hinder the grafting, by plasma-treatment, of nitrogenated functionalities necessary to the attachment of Pd species able to catalyse the electroless reaction initiation. The simplest solution consists in depositing by plasma polymerization (PACVD): (i) an amorphous hydrogenated carbon film (a-C:H) from CH_4 and in functionalizing it through a short NH_3 plasma, (ii) an amorphous hydrogenated carbonitride film (a-CN_x:H) from a CH_4 / NH_3 mixture or from a volatile organic precursor containing both carbon and nitrogen in its formula. After an activation treatment in a dilute $PdCl_2$ solution to make their surface catalytic, the different substrates were metallized in a low-phosphorus commercial Ni bath for various times. Adhesion of Ni films was estimated as a function of their thickness using the Scotch®-tape test. Ni films up to 4 µm in thickness passed this test without presenting the least adhesion failure.

1. Introduction

Metallization of silicon and SiO_2 / silicon wafers on the one hand, of glasses on the other hand, is of a great interest for many industrial applications. For example, this technology is widely used in the microelectronics industry in the fabrication of chip-level interconnects, ohmic contacts, printed circuit boards …

Unfortunately, deposition of thick (a few µm) well-adherent metal films on oxygen-rich compounds presenting a very smooth surface is not very easy. The difficulty is mainly due to the large mechanical mismatch between the metal film and brittle substrate which induces strong interfacial stresses responsible for spontaneous peelings off.

Metallization of insulating materials can be performed either by physical vapour deposition (PVD) in vacuum (deposition of very thin films), or by chemical vapour deposition (CVD), or by the electroless process (deposition of thick films). The latter method consists in an autocatalytic redox reaction, performed in aqueous solution, between metal ions (generally Cu^{+2} or Ni^{+2}) and an adequate reducer. This reaction which proceeds by itself, needs, to be initiated, the presence of a catalyst (Pd) which must be chemisorbed on the surface to be metallized. The conventional process developed many years ago [1-4] to metallize insulating materials needs both Sn and Pd species to attach active Pd entities on a chemically etched surface, that is to say on a strongly oxidised surface.

Electroless plating of glasses was studied by different authors who used various methods to attach palladium species on the substrate. Among these methods, let us cite the deposition before the electroless plating itself (i) of an aminosilane able to chemisorb Pd species, (ii) of a Pd film by evaporation under vacuum, (iii) of a Pd organometallic precursor further reduced by laser irradiation, (iv) of a Pd-doped diamond-like film.

Our works developed for polymer metallization [5-9] have also allowed to chemisorb Pd species without the help of tin species as it is the case with the conventional method. For that, the surface to be metallized must carry nitrogenated groups (brought up, for example, by NH_3 plasma treatment) on which Pd^{2+} ions (from a dilute $PdCl_2$ solution) chemisorb strongly [6] allowing an efficient and well-adherent Ni or Cu metallization.

The aim of the present work is to extend this tin-free process to other insulating materials and particularly to silicon, SiO_2 / silicon and glass substrates. As the surfaces of SiO_2 / silicon and glass substrates are strongly oxidised ([O] ~ 60 at. %), they will be here considered as equivalent and no difference will be done between them. As, for chemical reasons, nitrogen cannot be strongly attached on very oxygenated surfaces, the problem was solved by the deposition of an ultra-thin film able to play the role of a strong bridge between the oxygen atoms of the substrate and the nitrogen atoms necessary to chemisorb Pd species [10-11]. A carbon film, which is able to strongly adhere to the substrate via the formation of covalent C-O bonds and to be grafted with nitrogenated groups, fulfils these conditions. Different ways were explored to deposit suitable films. All are based on plasma polymerization either from methane (the film obtained having to be further functionalized by NH_3 plasma), or from precursors containing nitrogen atoms in order to avoid a post-functionalization. Under these conditions, an appropriate gas mixture (CH_4 / NH_3) or a volatile liquid organic precursor (allylamine, acetonitrile …) were used.

2. Experimental

The substrates used in this work consisted of silicon, thermally grown SiO_2 on silicon and of glass slides for microscopy. Before any plasma treatment, these substrates were ultrasonically cleaned in ethanol. All plasma treatments were operated in a RF reactor (RIE 80 from Plasma Technology). Surface treatments were performed with different gases (O_2, NH_3, Ar, H_2) in the following conditions (100 mTorr, 100 sccm, 0.5 W cm^{-2}, various times). Plasma polymerized films were deposited by Plasma Assisted Chemical Vapour Deposition (PACVD) from CH_4 or from different CH_4 / NH_3 gas mixtures (50 sccm for CH_4 and different flow-rates for NH_3, 100 mTorr, 0.5 W cm^{-2}). When volatile liquid organic precursors (allylamine (AA), acetonitrile (AN)) were used, they were introduced into the reactor on exhaustion and pressure fixed at 30 mTorr with a needle valve in order to regulate their flow rate. After stabilization, the working pressure was adjusted at 100 mTorr and film deposition realized at 0.5 W cm^{-2} for 2 min.

Catalytic conditioning of the surfaces was performed by immersion for 2 min in a 0.1 $g.l^{-1}$ $PdCl_2$ solution. After water rinsing, the reduction of Pd^{+2} ions chemisorbed on nitrogenated groups was initiated by a 3 min treatment at 85°C in a 10 $g.l^{-1}$ $H_2PO_2^-$ solution. This step was made necessary to easily start the metal deposition from the very stable industrial bath working at 65°C (Enplate Ni 426 supplied by Enthone-OMI, France).

XPS analyses were carried out with a Riber SIA 200 spectrometer using a non-monochromatic AlK_α source and a take-off angle of 65° with respect to the specimen surface. All spectra were referenced to the C 1s peak from C-C and C-H bonds at 285 eV.

Adhesion evaluation was performed using the standard Scotch®-tape test. Adhesion scale ranges from 5 (no film area removed by the tape) to 0 (more than 65 % removed).

3. Results

3.1. Treatment of substrates by NH_3 plasma

* Glass and SiO_2/silicon substrates

A 1 min NH_3 plasma treatment leads to non-reproducible results concerning grafting of nitrogenated groups. Nitrogen concentrations were in the range 2 to 5 at. % and no trace of Pd was detected by XPS after the usual treatment in the $PdCl_2$ solution, solution in which nitrogenated species, which are not strongly bonded to the oxygen-rich surface, are partly dragged.

* Silicon substrates

Reasoning by analogy with C which has the same external electronic structure as Si, we can infer that a NH_3 plasma treatment will graft nitrogenated groups as well on graphite and silicon substrates. Similar plasma treatments were realized simultaneously on silicon wafers, which present a very thin oxide layer on their surface (cf. Si 2p XPS spectrum in Fig. 1) and on graphite samples whose surface oxygen concentration was only 0.3 at. %. After only 5 s of NH_3 plasma, significant nitrogen grafting was observed on both substrates (Table 1) and particularly on silicon, despite its strongly oxidised surface. In both cases, longer plasma treatments result in a decrease of nitrogen and an increase of oxygen concentrations. The latter is mainly due to a post-oxidation in air after the plasma treatment, oxidation being all the more significant as the plasma treatment is long, therefore as the number of very reactive free radicals created capable to fix atmospheric oxygen is large. Palladium activation performed immediately after plasma treatment leads to a very significant palladium grafting on graphite while, surprisingly, no palladium was detected on silicon substrates, despite the presence of nitrogen after the $PdCl_2$ treatment. To explain this phenomenon, we must consider the possible bonds which could establish on both substrates during plasma treatment and post-plasma oxidation (Fig. 2).

In the case of graphite (Fig. 2 (a)), nitrogen grafting does not create any significant polarisation and nitrogen atoms can give easily their lone pair of electrons to palladium according to the mechanism previously described [6]. In other respects, Pd species which chemisorb in large proportions (5.5 at. % cf. Table 1) are partly reduced to Pd(0) at the time of their chemisorption (Fig. 3) thanks to the C reducing power and Ni plating proceeds immediately in the industrial bath without any additional reducing step.

The case of the silicon substrate which is coated with a natural oxide layer estimated at 2 or 3 nm from the Si 2p XPS spectrum (Fig. 1), is more complex. Indeed, NH_3 plasma, which grafts, among them, amino groups, breaks simultaneously Si-O bonds and liberates oxygen atoms. Under these conditions, amino groups graft on Si atoms which are more or less oxygen-surrounded (Fig. 2 (b), (c)). The corresponding N 1s peak for a plasma treatment of 5 s (Fig. 4 (a)) is mainly due to amine groups bonded to Si atoms. When the plasma treatment is prolonged, more oxygen is introduced on the surface, by post-oxidation in air, and particularly in the close surrounding of N atoms (Fig. 2 (d), (e)). In these configurations, there is a strong inductive effect exerted by the very electronegative oxygen atoms which withdraw electronic charge from nitrogen atoms. This results in a chemical shift of the N 1s peak to higher binding energies, associated with the appearance of new components (Fig. 4 (b) (c)). As a result of the strong inductive effect, nitrogen atoms tend to strongly attract their lone pair of electrons which prevents Pd chemisorption.

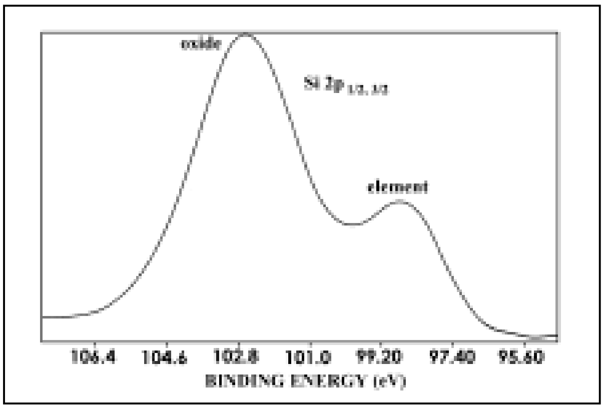

Figure 1: Si 2p core-level spectrum of an ethanol-cleaned Si wafer.

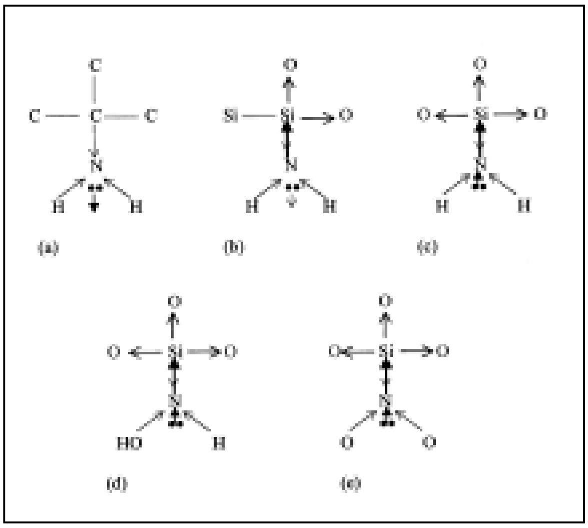

Figure 2: Scheme of bonds susceptible of being formed on graphite (a) and silicon (b to e) substrates after NH_3 plasma treatment. Bold type arrows indicate the direction of the inductive effect.

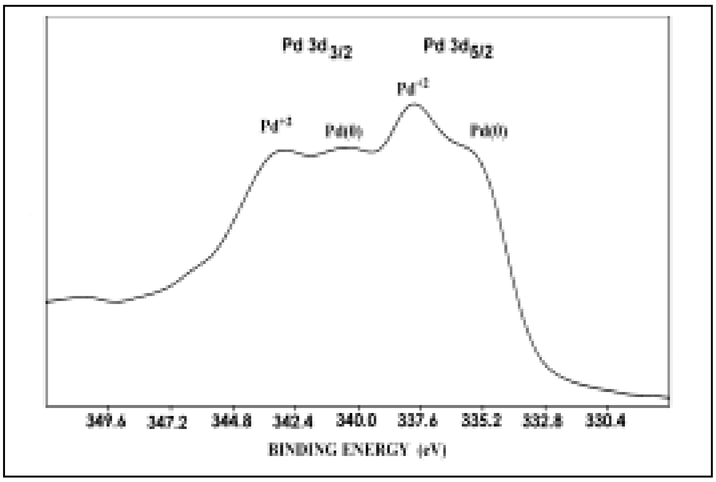

Figure 3: Pd 3d core-level spectrum obtained on graphite after NH_3 plasma (30 s) and activation (2 min) by $PdCl_2$.

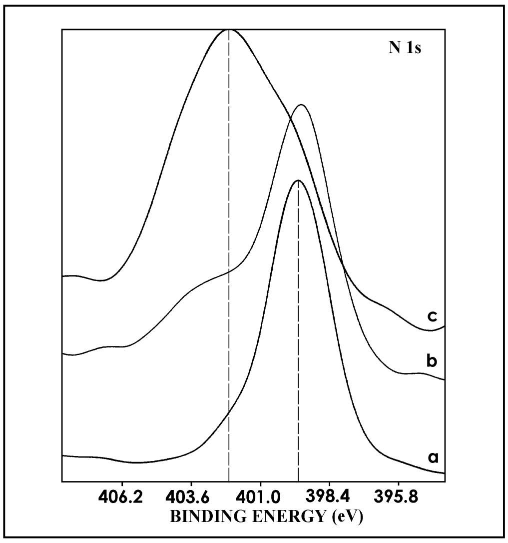

Figure 4: N 1s core-level spectra obtained on a silicon substrate after NH_3 plasma for 5 s (a), 1 min (b), 5 min (c).

In the aim of eliminating the SiO_2 thin layer present on silicon substrates which is detrimental to palladium grafting, various plasma treatments were tried up: (i) H_2 or Ar plasma (5 s to 5 min) immediately followed by NH_3 plasma for 5 s, (ii) [H_2 (50 sccm) + NH_3 (50 sccm)] plasma (5 s to 5 min). Whatever the treatment performed, the same trends were observed: the longer the plasma treatment, the higher the oxygen and the lower the nitrogen surface concentrations measured by XPS. From these experiments, it appears that it is quasi-impossible, by a simple plasma treatment, to get rid of oxygen present on silicon wafer surfaces.

Table 1 - Atomic concentrations (%) of O, N and Pd measured by XPS on graphite and silicon after various treatments

	Graphite			Si		
Surface treatment	[O]	[N]	[Pd]	[O]	[N]	[Pd]
Ethanol cleaning	0.3			52.5		
5 s NH_3 pl.	3.8	10.8		36.6	13.4	
5 s NH_3 pl. + 2 min $PdCl_2$	13.4	5.7	5.5	33.3	7.9	0
1 min NH_3 pl.	7.5	7.6		38.9	8.9	
1 min NH_3 pl. + 2 min $PdCl_2$	11.1	7.4	3.7	32.9	3.1	0

In conclusion, to hold back nitrogenated groups and beyond, to graft palladium on very oxidised surfaces, it is necessary to interpose between substrate and metal film an ultra-thin layer of a material containing no electronegative element. Such a layer, should strongly bind to the oxidised substrate through covalent bonds and be easily functionalised by NH_3 plasma to graft nitrogenated groups. An ultra-thin carbon layer deposited by plasma polymerization (PACVD) in the same reactor as that used for plasma treatments satisfies these conditions. Such a treatment will be performed on all the substrates considered in this work: silicon, silicon coated with thermally grown SiO_2 and glass.

3.2 - Deposition of carbon films carrying nitrogenated groups

Such films were obtained by plasma polymerization from various precursors after a systematic cleaning O_2 plasma treatment.

- The simplest way explored, supported by previous works [11, 12], consisted in a 2 min CH_4 plasma leading to the formation of a thin amorphous hydrogenated carbon film (a-C:H) which was immediately functionalized by NH_3 plasma for 5 s in the same reactor. Surface composition, determined by XPS after plasma and after Pd activation is given in Table 2.
- Another way aiming at decreasing the number of operations consisted in depositing, in a single experiment, a-CN_x:H films from CH_4 / NH_3 gas mixtures [10, 11]. As NH_3 presents significant etching properties [11, 12], it was first required to determine the CH_4 and NH_3 flow-rates which allow to obtain films of convenient composition. Details concerning this study can be found in [11]. The most efficient films for palladium grafting were obtained with a CH_4 / NH_3 = 50 sccm/10 sccm flow-rate ratio. Surface composition of such films, before and after Pd activation, is given in Table 2. These results compared to those obtained in the previous case show lower N and Pd surface concentrations. The films deposited by this way are ultra-thin since the presence of Si characteristic of the substrate is detected by XPS. Their thickness is estimated between 6 and 8 nm. Obviously, concentrations given by XPS concern, either the elements as Pd which are only present at the top surface of the samples, or, as in the case of "carbon nitride" films, elements as nitrogen which are distributed within the whole film thickness probed by XPS. For the purpose of the present work, it is nitrogen concentration in the first monolayer that it would be necessary to know and to increase in order to reach a high density of grafting sites for Pd. As it is difficult to check up the top surface nitrogen concentration, we have increased it by performing a functionalization of the "carbon nitride" films in the course of the same operation. For that, after the film deposition, CH_4 introduction was stopped, working pressure of NH_3 adjusted again at 100 mTorr and a short plasma (5 s) carried out. A significant increase of N and correlatively Pd surface concentration was observed (Table 2).
- The last way investigated to deposit a "carbon nitride" film consisted in a 2 min plasma polymerization from a volatile organic precursor. Two precursors were used: allylamine (AA) and acetonitrile (AN) which possess, in their formula, nitrogen under two very different chemical forms. Before introducing the precursor into the reactor, the flask containing it, gas circuit and reactor were thoroughly purged by an Ar flow in order to eliminate any oxygen trace which could compete with film deposition and hinder it. With both precursors, the resulting films deposited for 2 min were thicker than those obtained in the previous case since no Si signal, characteristic of the substrate, was detected by XPS. Large nitrogen concentrations were detected: 17.4 and 23.9 at. % for AA and AN plasma polymers respectively (Table 2). Correlatively, Pd species were grafted in large concentration (1.7 and 1.4 at. %). More Pd was grafted on the AA polymer whose nitrogen concentration is less than that of the AN polymer. This behaviour is to be compared to the fact, already mentioned [9], that amine groups are more active toward Pd chemisorption than other nitrogenated groups.

All "carbon" and "carbon nitride" thin and ultra-thin films deposited according to the above-mentioned methods were subjected to the Scotch®-tape test and no debonding was observed. This test constitutes the first essential step before any metallization attempt aiming at obtaining a subsequent strong adhesion of the metallic films on their substrate.

Table 2 - Surface atomic composition (%) of various films obtained by PACVD and submitted or not to $PdCl_2$ activation

Plasma treatment	[C]	[N]	[O]	[Si]	[Pd]	[Cl]
CH_4 pl. (2min) + NH_3 pl. (5 s)	79.3	13.3	7.4			
CH_4 pl. (2min) + NH_3 pl. (5 s) + $PdCl_2$ (2 min)	73.2	10.2	12.1	2.4	1.1	1.0
CH_4 / NH_3 = 50/10 pl. (2 min)	72.7	7.6	15.4	4.3		
CH_4 / NH_3 = 50/10 pl. (2 min) + $PdCl_2$ (2 min)	70.4	7.3	16.3	4.3	0.8	1.0
CH_4 / NH_3 = 50/10 pl. (2 min) + NH_3 pl. (5 s)	50.2	12.2	27.8	9.8		
CH_4 / NH_3 = 50/10 pl. (2 min) + NH_3 pl. (5 s) + $PdCl_2$ (2 min)	54.3	21.6	22.5	8.4	1.9	1.3
AA pl. polymer (2 min)	73.5	17.4	9.1			
AA pl. polymer (2 min) + $PdCl_2$ (2 min)	68.0	14.4	13.9		1.7	2.0
AN pl. polymer (2 min)	64.4	23.9	11.8			
AN pl. polymer (2 min) + $PdCl_2$ (2 min)	70.1	13.5	14.0		1.4	1.0

3.3 - Ni metallization of "carbon" and "carbon nitride" films by the tin-free simplified process

After deposition of the different layers on glass and on more or less oxidised silicon, samples were immersed for 2 min in the $PdCl_2$ solution, water rinsed, submitted to the reduction pretreatment for 3 min in the hypophosphite solution at 85°C, then immersed in the Ni plating bath for various times in order to obtain Ni coatings of different thicknesses. The latter were determined by XRFS through the measurement of the Ni K_α radiation intensity which was converted into thickness using a calibration curve obtained by gravimetry.

As already mentioned, account being taken of the similarity of the surface chemical composition of glass and oxidised silicon, results obtained with one substrate can be extrapolated to the other one. Table 3 gives some results obtained with the three surface preparations described in the previous chapter. These results correspond to average values obtained from 4 to 6 samples per Ni film deposit.

Films obtained from organic precursors have a very different behaviour with respect to metallization according to the chemical surrounding of nitrogen atoms introduced in the corresponding "carbon nitride" layer. Indeed, AA plasma polymers metallize easily and uniformly after an induction time of about 10 s, while AN plasma polymers, when they metallize, need an initiation time of 20 to 120 s. The longer the induction time, the worst the Ni deposit. The latter, when it happens, is always heterogeneous, either limited to very localized areas, or needing a few minutes to extend to the whole surface.

Table 3 - Adhesion results of Ni films deposited on silicon or glass after various surface preparations

Surface preparation before Ni plating	Ni thickness (µm)	Scotch® test results
CH_4 pl. (2 min) + NH_3 pl. (5 s) / silicon	4.2	5
	6.3	2-3
CH_4 pl. (2 min) + NH_3 pl. (5 s) / glass	2.6	5
	4.7	4
(CH_4 / NH_3 = 50/10) pl. (2 min) / glass	2.3	5
(CH_4 / NH_3 = 50/10) pl. (2 min) + NH_3 pl. (5 s) / glass	2.8	5
	3.4	5
AA pl. polymer (2 min) / glass	3.9	5
AN pl. polymer (2 min) / glass	~ 0.7	5
	~ 1.8	0

4. Discussion

Deposition of a carbon-nitrogen-based layer to realize an interphase between an oxidised substrate and a metal layer needing, to get deposited, the presence of catalytic Pd species at the interface, is right in its principle. Indeed, in most cases experienced in this work, metallization using the low-phosphorus Ni-426 Enthone plating bath was possible by the tin-free process and led to satisfying adhesion results. However, the same surface preparations associated with a high-phosphorus plating bath gave less satisfying results [11]. The thickest Ni films obtained with these solutions and passing the Scotch® test reached, in the best cases, about 0.5 µm. This is due to stresses which are particularly significant in Ni films containing a large proportion of P (7 to 8 wt. %). For a specific plating bath, adhesion is very likely governed by nitrogen concentration on the surface to be metallized and beyond by Pd sites density.

When nitrogen in the amine form is present in the bulk at a concentration less than 10 at. %, its surface concentration is necessarily lower. Even though it allows Pd species chemisorption, Pd sites density is relatively low and adhesion of thick films is not very satisfying. It is the case of "carbon nitride" films deposited from the CH_4 / NH_3 gas mixture for which the maximal Ni thickness allowing to pass the Scotch$^{®}$ test is about 2 µm.

When nitrogen is chemisorbed in the amine form and when its surface concentration is at least 10 at. %, Pd concentration is in the range 1-1.9 at. % (Table 2) which allows to deposit adhering thick Ni films. It is the case of "carbon" or "carbon nitride" films post-functionalized by a short NH_3 plasma and of AA plasma polymers. For all these films, 3 to 4 µm thick Ni layers pass the Scotch$^{®}$ test.

However, when N in the "carbon nitride" films is present, even at a large concentration, but not in an amine form, metallization, when it happens, progresses slowly and with difficulty as if the electroless reaction catalysis was little-active. It is the case of the AN plasma polymers. To try and understand the reasons of such a behaviour compared to that of the AA plasma polymers, XPS analyses were performed. Palladium concentrations and chemical state, which are the key factors of metallization, were particularly examined on both AA and AN plasma polymers after the reduction pretreatment. Surprisingly, in both cases, the relatively high Pd concentrations indicated in Table 2 after $PdCl_2$ treatment were conserved and a similar partial reduction of Pd^{+2} ions sufficient to initiate Ni plating, observed. For the time being, no explanation can be given to this experimental fact.

5. Conclusion

By choosing an appropriate Ni plating bath (low-phosphorus bath) we have shown it is possible to minimize the mechanical stresses which develop in films and at the interface film / substrate and by that to deposit well-adhering Ni films on highly-oxidised mineral substrates (SiO_2 in the present case). The general method proposed to deposit metal films by the electroless process using a tin-free surface preparation consists to coat the SiO_2 surface by plasma polymerization, with a "carbon" or "carbon nitride" film which plays the role of an interphase and to functionalize or not its surface by a NH_3 plasma. The three processes studied here namely: (i) plasma polymerization of a "carbon" film from CH_4 followed by a short NH_3 plasma, (ii) plasma polymerization of a "carbon nitride" film, either from a CH_4 / NH_3 gas mixture, followed or not by a short NH_3 plasma or from an organic precursor (allylamine (AA) or acetonitrile (AN)), are pertinent and all allow, except the AN plasma polymer, to deposit well-adhering, thick Ni films (up to 4 µm in the best cases). The final choice of a surface preparation process before plating is based on its simplicity, rapidity and easiness of use. It appears that a process using commercial compressed gases whose flow-rate can easily be checked is of easier use than a process using a volatile liquid organic precursor whose flow-rate is more difficult to control. In fine, our choice turns to the simplest process described, namely a CH_4 plasma followed by a short NH_3 plasma, process which offers enough Pd sites to develop well-adhering Ni films.

References

[1] R. Sard - J. Electrochem. Soc. **117**, 864 (1970).
[2] D.J. Sharp - Plating **58**, 786 (1971).
[3] R.L. Meek - J. Electrochem. Soc. **122**, 1478 (1975).
[4] I. Kiflawi, M. Schlesinger - J. Electrochem. Soc. **130**, 872 (1983).
[5] M. Alami, M. Charbonnier, M. Romand - Proc. 9th International Colloquium on Plasma Processes (CIP 93), Antibes (France), June 6-11, 1993, pp. 392-401.
[6] M. Charbonnier, M. Alami, M. Romand - J. Electrochem. Soc. **143**, 472 (1996).
[7] M. Alami, M. Charbonnier, M. Romand - Polymers and Plasmas **1**, 113 (1996).
[8] M. Charbonnier, M. Alami, M. Romand - J. Appl. Electrochem. **28**, 449 (1998).
[9] M. Charbonnier, M. Romand, M. Alami - In "Polymer Surface Modification: Relevance to Adhesion", Vol. 2, K.L. Mittal, Ed., VSP, Utrecht, The Netherlands, 2000, pp. 29-43.
[10] E. Touchais-Papet, M. Alami, M. Charbonnier, M. Romand, A. Mikou - Proc. 22nd Annual Meeting of the Adhesion Society, D.R. Speth Ed., The Adhesion Society Inc., Blacksburg, VA, 1999, p. 48.
[11] M. Charbonnier, M. Romand - Surf. Coat. Technol. **162**, 19 (2002).
[12] L. Deshayes, M. Charbonnier, N.S. Prakash, M. Romand - J. Adhesion **43** (1993) 209.

Kinetic and spectroscopic study of rare gas based hollow cathode luminescent discharges :
Application to the lifetime enhancement of mercury-free signs

E. Robert[1], H. Sarroukh[1,2], C. Cachoncinlle[1], R. Viladrosa[1] and J.M. Pouvesle[1]

[1]GREMI-IPO, 14 rue d'Issoudun, BP 6744, 45067 Orléans Cedex 02, France
[2]Present address : OSRAM, Nonnendammallee 44-61, 13629 Berlin, Germany

This paper reports on the development and potentialities of mercury free low pressure discharge tubes for their application in signs industry. Experimental and simulation studies performed in CPAT and GREMI laboratories have been initiated by the AUPEM-SEFLI company together with the support of LEGRAND and A2E Technologies industrial partners. This research program is devoted to the development of mercury free signs and of their specific electronic ballast. Critical issues such as illuminance (Lm), cathode fall, cathode erosion, lifetime, electrical input (duty cycle, waveform, frequency, voltage and current amplitude), efficiency (Lm/W), phosphor nature, etc… have been investigated. In this paper, much details will concern the positive column radiative properties while keeping in mind that the development of the new environmentally friendly signs is a highly cross-correlated problem.

The experimental set-up consists in a gas handling system, a discharge tube mounted with two electrodes and an evacuation port, a high voltage power supply and the diagnostics tools. The discharge tube is evacuated and heated up to a few hundreds of degrees using a neon tube bombarder device before being filled with high purity gases at a pressure ranging from a few hundreds of mtorr to a few tens of torr. The discharge vessel is a commercial glass tube having its inside surface coated with four different phosphors and equipped with an evacuation port allowing VUV-UV-Visible spectroscopic measurement and imaging experiments from 110 nm to 900 nm. Both electronic ballasts and a parametric high voltage power supply have been used for discharge production with voltage ranging from 1 to 10 kV, current amplitude from 10 to 200 mA and excitation frequency from 50 Hz to 100 kHz.

A detailed spectroscopic analysis of pure rare gases and their mixtures [1] has been performed from the VUV spectral range in which the resonance lines are emitted to the visible in which both the plasma column and the phosphors are producing light. It has been measured that the best conditions for phosphors excitation correspond to the optimization of the rare gas resonance line emission. The population of the resonance lines upper levels at the lowest pressures, the production of highly excited molecular states and the resonance line self absorption in the higher pressure conditions have been measured and optimized to extract the highest VUV photon flux from the positive column.

The excitation of rare gas based mixtures in combination with the use of phosphors developed for PDP technology appears to be a viable solution for the design of mercury free signs. Taking into consideration the results on cathode fall measurement [2], activation product and cathode nature [3], cathode ablation processes and the positive column radiative properties [1] leads to the development of a mercury free product whose characteristics are in agreement with most of the signs requirements.

The highest illuminance have been obtained in some Ne/Xe mixtures but ageing studies on signs filled with such mixtures exhibit typical lifetime as low as a few tens of minutes. The selective trapping of xenon atom in both the electrodes in hollow cathode geometry and in the glass tube appears as a catastrophic features. Fortunately the excitation of Ne/Xe mixtures in different experimental conditions or of mixtures of three or four constituents including Ne and Xe allows to obtain slightly less efficient discharges but presenting a lifetime higher than 12000 hours. The kinetic processes between ionic and neutral species of various weight appears of peculiar importance for the lifetime enhancement of low pressure high voltage discharge tubes. Spectral analysis has been performed in mixtures of two to four constituents during days to measure the kinetic evolution of the different constituent population and to optimize the discharge tube lifetime and stability. Successful ageing studies including spectral analysis, illuminance and chromatic coordinates measurement have been performed on a significant number of signs sealed by the AUPEM SEFLI company.

[1] H. Sarroukh, E. Robert, C. Cachoncinlle, R. Viladrosa and J.M.Pouvesle, ISPC 15, **II**, 561-566, 2001.
[2] H. Capdeville, Ph. Guillot, L.C. Pitchford, J. Galy and H. Brunet, ICPIG XXIV Proc., **III**, 5, 1999.
[3] G. Auday, H. Capdeville, Ph. Guillot, J. Galy and H. Brunet, ICPIG XXIV Proc., **III**, 25, 1999.

Air + freon plasma diagnosis in the range 2000 K < T < 6000 K using UV OH band spectrum.

Jean-Philippe Sarrette[1], Saker Saloum[2] and Anne-Marie Gomès[1].

[1] *Centre de Physique des Plasmas & Applications de Toulouse, Université Paul Sabatier, 118 route de Narbonne, 31062 Toulouse cedex, France.*
[2] *Atomic Energy Commission of Syria Physics Department BP 6091, Damascus, Syria.*

Abstract.

The conditions of use of the partially resolved OH UV band A-X (0-0) for accurate temperature determination in air-based plasmas were investigated. Some methods are proposed founded on a simulation of the absolute intensity of the spectra accounting with non-thermal equilibrium and with the characteristics of the experimental set-up. The more suitable structures were identified and the results compared to local temperatures obtained from alternative emission spectroscopic methods in air and air + CCl_2F_2 plasmas.

1. Introduction.

Variable water concentrations C_{H2O} (about 1%) are naturally present in atmospheric air and the emission of the OH UV band A-X (0-0) is particularly strong in air plasma at atmospheric pressure even for low C_{H2O} or moderate temperature values. The OH band exhibit weak interferences with prominent other molecular air structures. For these reasons it is often used for temperature estimation of air plasmas.

In the recent works of Pellerin [1] and de Izarra [2] some groups of rotational lines G_i of the partially resolved spectra were selected. It was shown that, for definite experimental conditions, the ratio of the emission coefficients of these particular groups are sufficiently sensitive to the plasma temperature to allow rough characterisation of plasma sources.

The existent methods are not suitable for rapid and precise diagnosis of a RF air torch at atmospheric pressure seeded with halogenic compounds in the range 2000-6000 K. Their use, when non negligible and unknown quantities of reactive pollutants as chlorine and fluorine are added to air, is questionable and needs improvement.

2. Purposes and conditions of the study

As in the previous works, the diagnosis methods investigated are founded on a careful simulation of the absolute intensity of the spectra [3-7]. From these synthetic spectra, the requisite experimental conditions and the groups G_i the most sensitive to the temperature and the less affected by the apparatus function of the detection set up were selected.

The main advantage of the OH band resides in the fact that it allows a lowering of the inferior limit for the measured temperature values. It can be used for the diagnosis of areas where the local emission coefficients $\mathbf{J_Y}$ for the other bands are too weak to be recorded in good conditions.

In this work, the effects on the recorded spectra of non negligible quantities of reactive chlorinated or/and fluorinated molecules were also analyzed. The freon 12 CCl_2F_2 has been chosen as test molecule.

The proposed methods does not require the knowledge of the water concentration C_{H2O} and remain valid even when a weak thermal non equilibrium exists. Particularly, we have considered the normal temperature T_n of the UV OH spectra for it allows simple calibration of the measured temperatures.

The measured temperatures were compared to the one obtained from other optical emission spectroscopic methods [8, 9] using the alternative air bands, given in Table 1, in the areas where they can be recorded.

Table 1. Emission systems used for air and air + freon plasma diagnosis. The temperatures obtained in air plasma are presented Fig. 6.

Species	Emission system	Band (v'- v '')	λ (nm) band head
NO	$A^2\Sigma^+$-$X^2\Pi$ (Gamma)	(0-1)	236.271
OH	$A^2\Sigma^+$-$X^2\Pi_i$	(0-0)	306.450
NH	$A^3\Pi$-$X^3\Sigma$	(0-0)	336.000
Cu	$^2P_{3/2} - {}^2S_{1/2}$	Atomic line	324.754

3. OH molecular spectra simulation.

3. 1. Plasma composition.

First of all, the compositions of mixtures air + x.H_2O + y.CCl_2F_2 (0<(x, y)<4%) were calculated for dithermal plasmas. The kinetic temperatures are T_g for the gas particles and T_e for the electrons; the thermal non equilibrium was characterised by the ratio $X=T_e/T_g$. The total number densities $N_Y(T_e,T_g)$ of the Y species were calculated for different couples (T_g , X) with (1<X<1.2).

The emission coefficient of a spectral line λ due to a transition |n',v',J'>→|n",v",J"> between two rotational states is given by:

$$\varepsilon_{n'',v'',J''}^{n',v',J'} = N_Y^{n',v',J'} \;.\, A_{n'',v'',J''}^{n',v',J'} .hc/(4\pi\lambda)\ (W.m^{-3}.sr^{-1}) \qquad (1)$$

where $N_Y^{n',v',J'}$ is the number of emitting molecules in the initial state of the transition, h is the Plank constant and $A_{n'',v'',J''}^{n',v',J'}$ is the transition probability.

The main hypothesis concerns the excitation temperatures assigned to the different modes of energy storage. According to previous studies [10, 11] the excitation temperatures T_{exc}, T_{vib}, T_{rot} for the electronic, vibrational and rotational molecular state were chosen as follow:

$$T_{exc} = T_g;\quad T_{rot} = T_g \quad \text{and} \quad T_{vib} = T_e. \qquad (2)$$

The number of emitting molecules were calculated with these hypothesis:

$$N_Y^{n',v',J'}(T_e,T_g) = \frac{N_Y(T_e,T_g)}{Q_{int}^{Y}(T_e,T_g)}\, g_{n'} \exp(-\frac{E_e(n')}{k_B T_g}) \exp(-\frac{G(v')}{k_B T_e})\,(2J'+1)\exp(-\frac{F_V'(J')}{k_B T_g})$$

$Q_{int}^{Y}(T_e,T_g)$ is the internal partition function of the Y species, $g_{n'}$ is the statistic weight of the electronic configuration n' of the emitting level of energy E_e. The quantities (v', J') and (G(v'), Fv(J')) are respectively the quantum numbers and the energies of the vibrational and rotational molecular states.

3-2 Numerical simulation of the OH UV spectrum.

Using the physical parameters of the rotational OH spectrum given by Dieke and Crosswhite [3] the spectra were computed for λ = 306- 313 nm as a function of T_g and X.

The agreement between experimental and calculated spectra was largely improved by multiplying the transition probabilities $A_{n'',v'',J''}^{n',v',J'}$ of relation (1) by the coefficient FCM(J'). This multiplier, calculated by Chidsey and Crosley [6], was introduced by Levin et al [7] to account for rotation distortions in the vibrational states. This coefficient is lower than unity and is particularly important for high J' values.

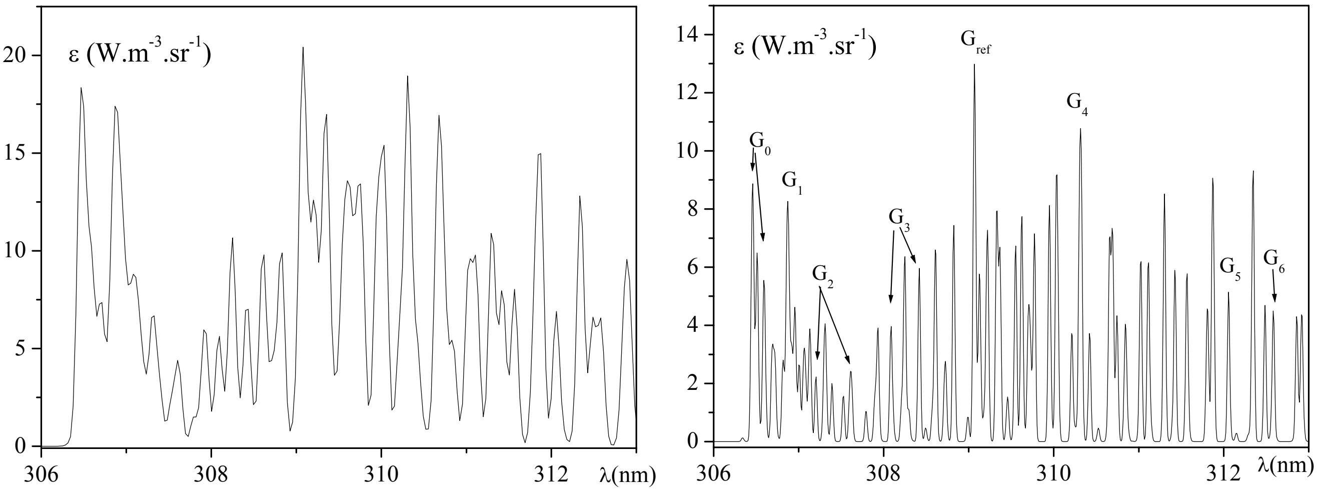

Figures 1 a and b: OH spectrum between 306 and 313 nm for T_g=4500 K and X=1.
a -Grating 1200 lines.mm^{-1}; b- Grating 3600 lines.mm^{-1}.

The full width at half maximum (FWHM) of the Gaussian optical apparatus function $\Delta\lambda_{app}$ was introduced to account for the characteristics of the experimental set up (monochromator and intensified UV photodiode array). It can be writen:

$$\Delta\lambda_{app} = \text{FWHM}.\ \Delta\lambda_p \qquad \text{with} \qquad \Delta\lambda_p = D^{-1}(\lambda).\ w_p$$

where w_p is the width of each pixel and D^{-1} the reciprocal dispersion of the monochromator. In the above relation $\Delta\lambda_p$ is the spectral interval recorded by pixel p of the photodiode; FWHM is expressed in terms of number of pixels, it depends on the width of the entrance width w_e and on the grating.

Two holographic grating with respectively 1200 lines.mm^{-1} ($\Delta\lambda_p = 3.130\ 10^{-2}$ nm/pixel) (Figure1-a) and 3600 lines.mm^{-1} ($\Delta\lambda_p = 8.34.10^{-3}$nm/pixel) (Figure 1-b) were successively used.

With the 1200 lines.mm^{-1} grating, the calculated emission coefficients were found strongly FWHM dependant, introducing a dramatic loss of sensitivity in temperature determination. For this reason, the measured values were obtained using the 3600 lines mm^{-1} grating.

4. Selection of the groups of rotational lines.

The groups of lines G_i studied in this work are given in Table 2. Some of them have been already investigated in references [1] and [2]. In this work, others groups were added as they appeared particularly well isolated and/or temperature dependent.

Table 2 : Groups of rotational lines studied in this work and by other workers (cf Figure 1-b).

G_0	G_1	G_2	G_3	G_4	G_5	G_6	G_{ref}
G01 306.47 nm	306.86	G21 307.22 nm	G31 308.10	310.34 nm	312.09 nm	312.61 nm	309.09 nm
G02 306.60 nm		G22 307.54 nm	G32 308.43 nm				

Table 3 : Ratios of emission coefficients investigated in this work [*] and by other workers.

Ratio	$\varepsilon_{01}/\varepsilon_{31}$	$\varepsilon_{01}/\varepsilon_{32}$	$\varepsilon_{02}/\varepsilon_{31}$	$\varepsilon_{02}/\varepsilon_{32}$	$\varepsilon_{22}/\varepsilon_{21}$	$\varepsilon_1/\varepsilon_{ref}$	$\varepsilon_4/\varepsilon_{ref}$	$\varepsilon_5/\varepsilon_{ref}$	$\varepsilon_6/\varepsilon_{ref}$	$\varepsilon_4/\varepsilon_5$
Reference	[1], [*]	[1], [*]	[1], [*]	[1], [*]	[2], [*]	[2], [*]	[*]	[*]	[*]	[*]

The temperature dependence of the emission coefficient ε_i of some of the groups studied in this work is presented on Figure 2. In pure air and with the hypothesis (2), the temperature T_n of the maximum of the emission coefficient is independent on X and on the water concentration C_{H2O}. It depends on the studied structure, moving slowly towards higher temperatures as J' increases. In the studied λ interval, T_n remains close to 4000 K; it allows in air an easy and simple calibration of the data recorded for the other emitting bands. Though the ε_i calculated for each group G_i depends, in addition to T_g , on X, on the apparatus function FWHM and on the water and freon concentrations, the calculated ratios $\varepsilon_i/\varepsilon_j$ depend only on T_g and, for some of them, strongly on the apparatus function. The ratios studied in this work are given in Table 3; their dependence with X is shown on Figure 3 and that with the FWHM on Figures 4.a and b. From this set of curves it is shown that the ratio $\varepsilon_5/\varepsilon_{ref}$ exhibits low dependence with FWHM.

5. Temperature determination.

5. 1. Measurements using Tn calibration.

The normal temperature allows simple calibration of the emission coefficient $\mathbf{J}_i(r)$ deduced, for a group G_j, with Abel Transformation (AT) from the measured intensities. The local temperature $T_g(r)$ was obtained from the comparison between the calculated $\varepsilon_i(T_g)$ and measured $\mathbf{J}_i(r)$ emission coefficients using the relation:

$$\mathbf{J}_i(r)/\mathbf{J}_i(r_n) = \varepsilon_i(T_g)/\varepsilon_i(T_n) \qquad (3)$$

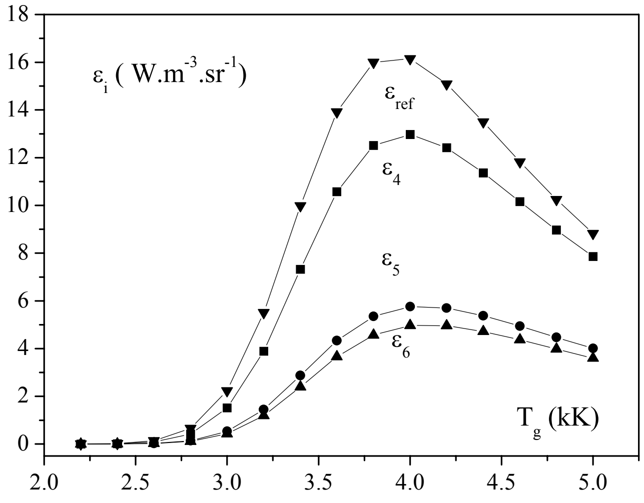

Figure 2. Calculated (X=1) emission coefficients in air plasma for the groups particularly studied in this work.

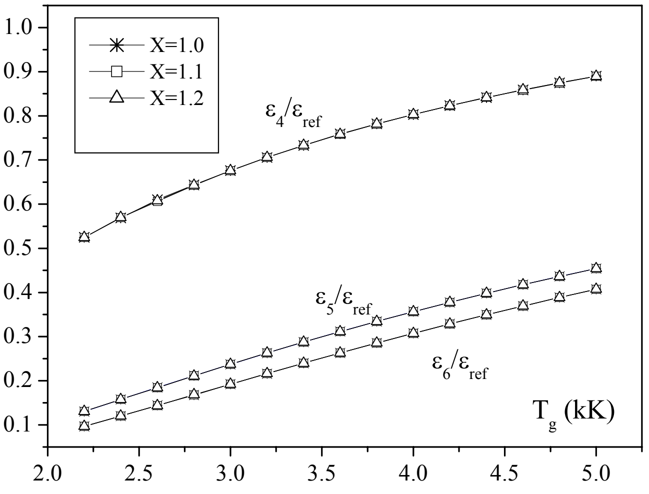

Figure 3. Evolution of the ratios $\varepsilon_i/\varepsilon_{ref}$ with the temperature for X= 1.0, 1.1 and 1.2 .

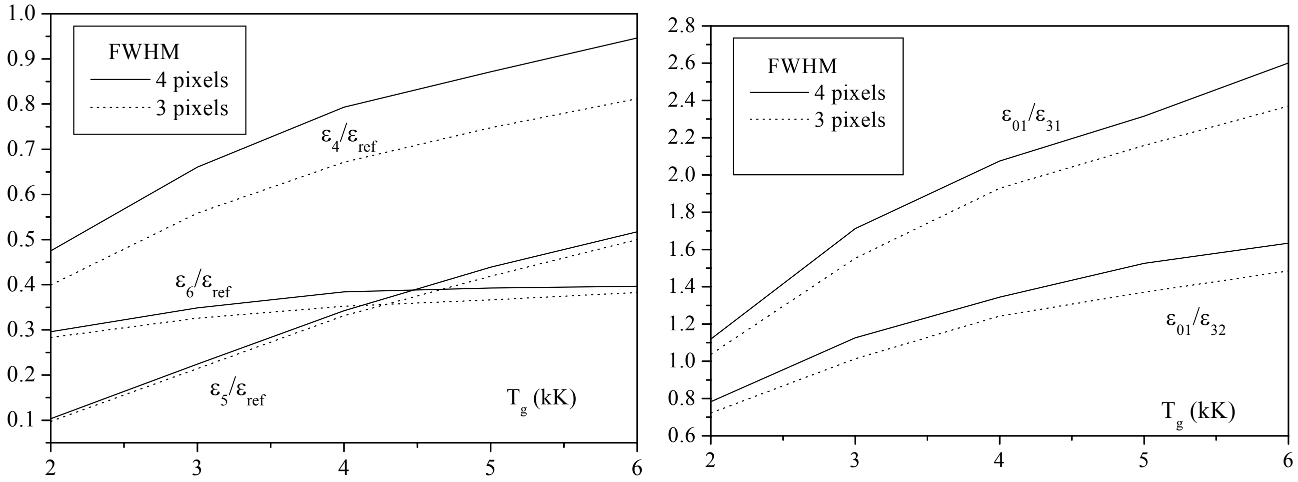

Figures 4 a and b: Incidence of the apparatus function on the calculated values of $\varepsilon_i/\varepsilon$.

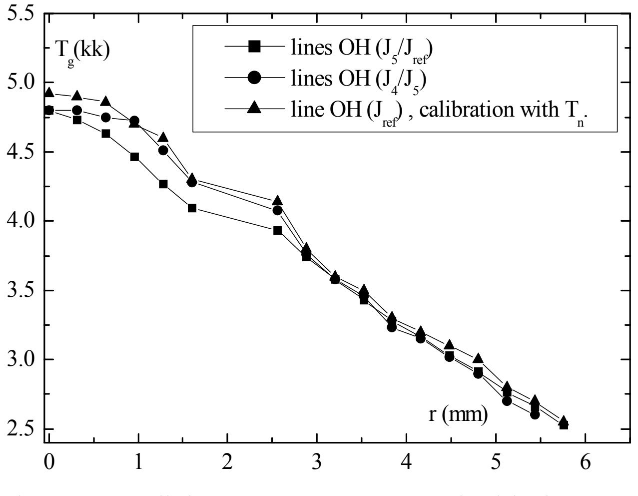

Figure 5. Radial temperature measured with the OH band.

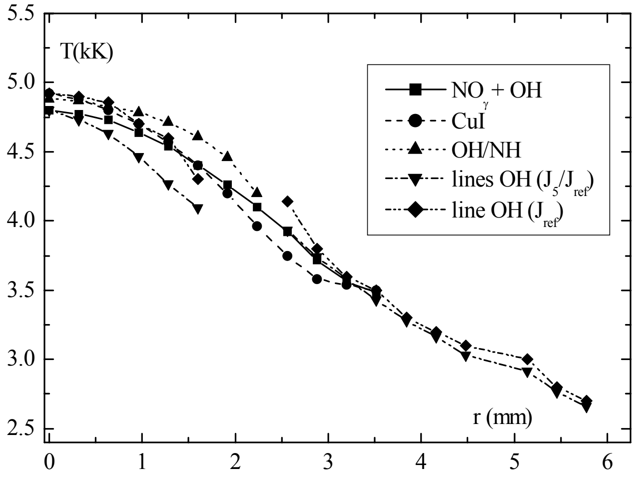

Figure 6. Radial temperature measured with the OH band and with other air bands.

The position r_n of the out of axis maximum of $J_i(r)$ is associated with the temperature T_n and allows the calibration of the measured values. This method gives satisfying results in so far as the ratios $\varepsilon_i(T_g)/\varepsilon_i(T_n)$ are largely independent of X. As it can be seen on Figures 4 and 5, the sensitivity of the method is low around T_n but the OH band allows the extension of the measurements down to 2500 K, whereas 3500 K is the lower limit when the other bands were used (Figure 5).

Absolute calibration of the OH band head and of a pertinent O_2 rotationnal line of the $B^3\Sigma$, $0 \rightarrow X^3\Sigma$, 14 band allows to deduce the emission coefficient ε_j from the measured local values $\mathbf{J_j}$. From this calibration, the concentration C_{H2O} and the X factor were calculated. A value X~ 1.1 and a concentration $C_{H2O} \sim 0.7\%$ were obtained.

5. 2. Measurements from the ratios $\varepsilon_i/\varepsilon_j$

The measured ratios $\mathbf{J_i}(r)/\mathbf{J_j}(r)$ were directly compared to the calculated ratios $\varepsilon_i(T_g)/\varepsilon_j(T_g)$. The implementing of this method exhibits a discrepancy between the temperatures obtained from some of the ratios and those deduced from other bands mentioned on Table 1. For example, the values of Table 4 have to be compared with the value T_g= 4850K of Figure 6.

Some of these ratios as $\varepsilon_4/\varepsilon_5$ (Figure 5) leads to values in good agreement with this temperature, provided that the FWHM was chosen with precaution. In these conditions, the determination of the position r_n associated to T_n may, if necessary, improve the calibration of the ratio.

Table 4. Axial temperatures, measured in the centre of the inductor of the RF discharges, deduced from the different ratios. A value 4850 ± 50 K was obtained from the emission of other systems (Figure 6).

Ratio	$\varepsilon_{01}/\varepsilon_{31}$	$\varepsilon_{01}/\varepsilon_{32}$	$\varepsilon_{02}/\varepsilon_{31}$	$\varepsilon_{02}/\varepsilon_{32}$	$\varepsilon_{01}/\varepsilon_{ref}$	$\varepsilon_4/\varepsilon_{ref}$	$\varepsilon_5/\varepsilon_{ref}$	$\varepsilon_4/\varepsilon_5$	$\varepsilon_6/\varepsilon_{ref}$
T_g (kK)	4.5	>5	>6	>6	>6.0	>6.0	4.8	4.8	4.8

5. 3. Measurement of the axial temperature $T_g(r=0, z)$ from integrated intensities

The axial temperatures $T_g(r=0, z)$ obtained in the coils area (0< z< 15 mm) and in the post discharge (15< z< 85 mm) with and without AT are compared on Figure 7.

In the colder areas of the post discharge, the optical signal becomes too weak to allow radial analysis. In this situation, the measured intensities I(0,z), integrated along a diameter, were substituted to the local values $\mathbf{J}(r=0, z)$ in relation (3):

$$I(0, z) / I(0, z_0) = \varepsilon(T_g)/ \varepsilon(T_g^0)$$

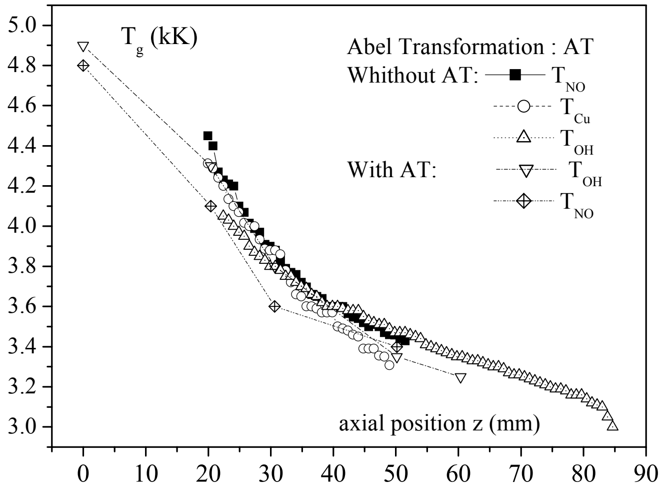

Figure 7. Axial temperatures measured from OH band and from other air bands with and without AT.

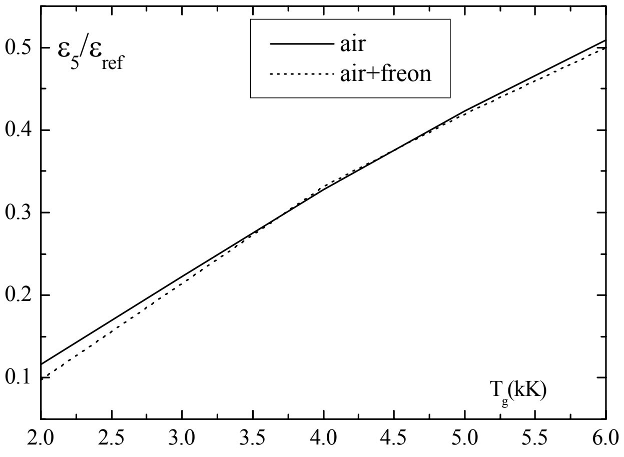

Figure 8. Ratios of the calculated emission coefficients with and without CCl_2F_2 (2%).

The axial temperature $T_g(r=0, z)$ was obtained with a relatively good appreciation without AT, provided that the temperature T_g^0 has a value appreciably lower than T_n ; T_g^0 was a temperature previously obtained with AT for a selected position $r = 0$ and $z = z_0$. For example, if T_g^0=3 800 K, a systematic error ΔT_g of about 100 K was introduced by this approximation.

6. Incidence of the freon concentration on T_g measurements.

The population of the OH emitting levels is heavily modified by the injection of freon in the discharge even for concentrations lower than 2%. It was shown [8] that the normal temperature T_n moves towards higher values as the concentration C_{CCl2F2} increases. This effect is of particular importance when a precise T_n value is needed for calibration purpose. It can be experimentally observed when freon was added to air: the out of axis maximum of **J** moves towards the axis and vanishes as a consequence of both a weak cooling of the gaz and of the shifting of T_n toward higher values.

But, as is shown on Figure 8, for low C_{CCl2F2} values, the ratio $\varepsilon_5/\varepsilon_{ref}$ is not affected. If C_{CCl2F2} is lower than 4%, freon can be neglected for the determination of T_g from this ratio.

7. Conclusions.

The UV OH band was employed to extend the diagnosis of air and air + freon RF discharges towards low temperatures. Below 3500 K when all the optical signals become too weak, this band allows a precise temperature determination in the colder peripheral areas and in the post discharge down to 2500 K. The more interesting groups of rotational lines for this purpose lie between 310 and 312 nm.

Two methods were developed. One of them is a calibration of the emission coefficient **J**(r) of a well identified group of lines G_{ref} by its value **J**(r_n) measured at the position of the out of axis maximum. This method gives results largely independents on X and on C_{H2O} with a good sensitivity but is not valid even for low C_{CCl2F2} values. Another method compares the calculated and the measured ratios of two groups of lines. As the temperature dependence of these ratios is low in the frame 2000-6000 K, the calculation of the synthetic OH band is critical and the groups of structures of rotational lines have to be selected carefully.

In this case, a comparison with complementary methods is needed. In pure air, the position of the normal temperature can supply valuable complementary inquiries. Some couples of lines were dismissed. The source can be an unsatisfactory synthetic spectra. Interferences with other spectra can also be invoked. The main advantage of this second method is that, for low C_{CCl2F2} values, the ratios are independent of the freon concentration.

It was also shown that, below 3800 K, a very good appreciation of the axial temperature T(r=0, z) can be obtained, without Abel Transformation, directly from the intensities integrated along a diameter.

References :

1- S. Pellerin, J M Cormier, F Richard, K Musiol and J Chapelle, J.Phys.D, **29** (1996), 726-739.
2- C. de. Izarra, J.Phys.D: App.Phys, **3** (2000), 1697-1704..
3- G.H. Dieke and H. M. Crosswhite, J. Quant. Spectrosc. Radiat. Transfer, **2** (1962), 97.
4- J. Luque and D.R. Crosley, J.Chem.Phys, **109** (1998), 439-448.
5- J. Luque and D.R. Crosley, SRI International report MP99-009, (1999).
6- I.L. Chidsey and D. Crosley, J.Quant. Spectrosc. Radiat. Transfer, **23** (1980), 187-199.
7- D .A. Levin, C.O. Laux and C.H. Kruger, J.Quant. Spectrosc. Radiat. Transfer, **61** (1999), 377-391.
8- A-M. Gomès, J.P. Sarrette and S. Saloum, High Temp. Material Processes, **5** (2001), 169-180.
9- P. Teulet, J. P. Sarrette and A. M. Gomès; J. Quant. Spectrosc. Radiat. Transfer, **70** (2001) 159-187.
10- C. J. Park, thermodynam; Heat transfer, **3** (2001), 159-187.
11- A-M. Gomès, J.P. Sarrette, L. Madon and A. Epifanie, J. Analytical Atom. Spectrom., **10** (1995), 923-928.

Water cleaning in a heterogeneous pulsed corona reactor

L. Grabowski [1], E.M. van Veldhuizen[1], A.J.M. Pemen[2], W.R. Rutgers[1]

[1] *Department of Physics ,Technische Universiteit Eindhoven (TU/e),The Netherlands*
[2] *Department of Electrical Engeneering ,Technische Universiteit Eindhoven (TU/e),The Netherlands*

Abstract

This article discusses a water cleaning reactor in a heterogeneous medium, called CAW (corona above water). The pulsed corona discharge is created on a wire above a thin water layer. In order to obtain sufficient power input in the corona pulses a power supply with a transmission line transformer is used which gives ~100 mJ/pulse. The ozone concentration above the water is measured to show the efficiency of the discharge. Preliminary measurements show that phenol is decomposed succesfully and PEG samples show significant increase of BOD/COD demand already at very low energy consumption.

Introduction

Although the Earth is covered in 75% by water, most of it is useless for people. Resources of potable water are shrinking in hectic pace. With the growing commitment to improve water quality, there is a need for new processes for environmental cleanup. Discovery of those processes is necessary for both existing and ongoing wastes. Studies of plasma processing of waste water have shown good possibilities for more effective treatment and for lower treatment cost especially of persistent organic molecules at low concentrations.

Plasmas created in corona discharges are used nowadays for many purposes.[1,2] Its oldest application is probably ozone generation. Water and gas cleaning experiments started in 1980's and are becoming the biggest part of using plasma in environmental objectives. Gas and water cleaning using corona discharges make use of the radicals created during discharges and are similar in principle to ozone generation. Existing applications concern removal of NO_x, SO_2 and various VOC's from flue gases. Water cleaning is also an option but is reported less frequent [3].

Recently a European project on corona discharge gas and water cleaning, called **ytriD**, has started [4]. Within this project two different techniques for water cleaning will be studied. An aerosol reactor build by Soreq Israel will be compared with the CAW reactor from TU/e Eindhoven. Optimisation and upscaling the system for water cleaning by pulsed corona discharges will be studied. This implies a parametric study of a reactor module and testing a large reactor system with a continuous water flow.

1. Wastewater treatment with the Corona Above the Water Reactor

Initially the discharge creates ions, radicals and photons. These products are relatively short-lived and up to now it is unknown which part of them will diffuse into the water.
Indirect products with larger lifetime are O_3 and H_2O_2. It is shown that O_3 is present in large amounts in a CAW reactor [5]. The ozone will diffuse into the water where it can directly attack hydrocarbons or it can react with water to form H_2O_2. This hydrogen peroxide is in dissociation equilibrium with OH-radicals that can also oxidise hydrocarbons. This equilibrium can be influenced by additives in order to enhance the efficiency. Additions of H_2O_2 , Fe^{2+} , and NaOH have been applied succesfully [7,11].

In our study we use phenol as a model compound. This is because it is an important precursor in organic chemical synthesis and also a persistent molecules in waste water which is difficult to treat with biological methods. Another advantage of phenol is that many studies on degradation of phenol are published with which our results can be compared. Other substances, such as PolyEthyleneGlycol (PEG), are being tested using BOD/COD ratio as determining parameter. This parameter is of importance since it is often used in legislation.

2. CAW treatment system

The main elements of CAW treatment unit are:

A) a rectangular reactor made of Perspex with the system of electrodes,
B) a high-voltage pulse generator
C) a diagnostic system.

A) Reactor

The reactor is an hermetic sealed construction, to prevent the corona products from escape. The reactor is made of Perspex where inside dimensions are 80x55x380 mm^3. The side wall thickness is 10 mm and the bottom is 4 mm. The four electrodes, 0.2 mm in diameter, are placed in cover of the reactor. The cathode is placed outside the reactor, at the bottom side.

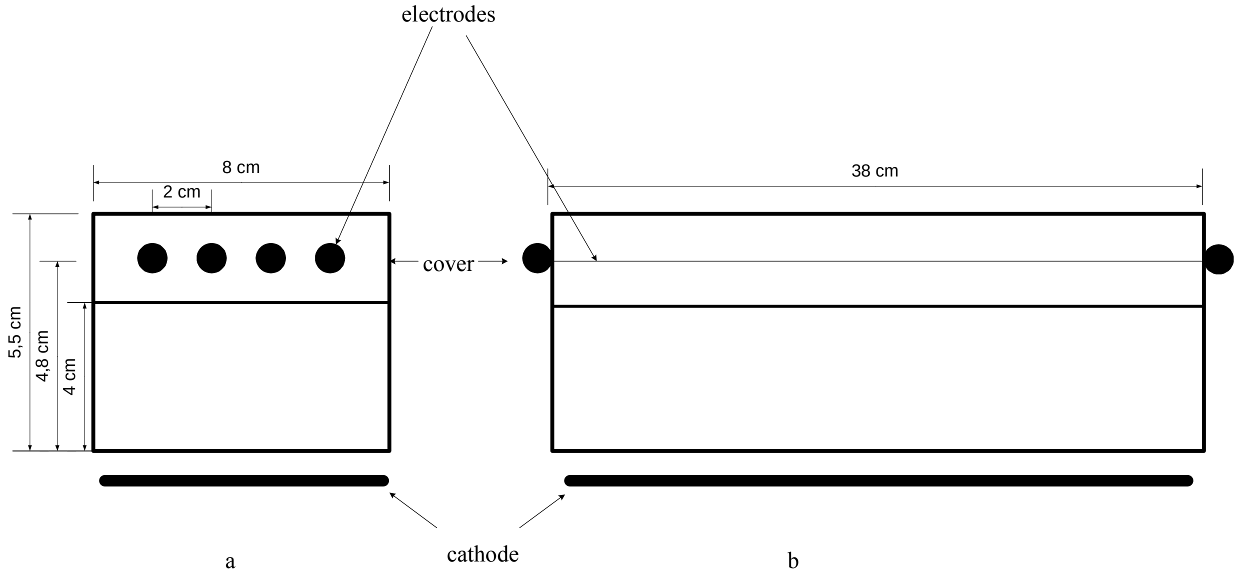

Fig. 1.Reactor view (with a system of electrodes): a-side view, b- front side view

The horizontal distance between the electrodes is 20 mm. The gap between cathode and anodes is 45 mm. Water volume used for all test was 250 ml, therefore the water layer thickness is about 10 mm.

B) Electric circuit

Repetitive pulsed power generators are the enabling technology for successful industrial applications of pulsed corona discharges. Prototypes of efficient nanosecond pulse generators are available and have been demonstrated in laboratory and in field trials [2]. These generators employ a heavy-duty spark-gap switch combined with a transmission-line-transformer. Lifetime and reliability are adequate for industrial demonstrations. Treatment of gas flows up to 100.000 Nm^3/hr is possible. We expect to reach an average corona output power of 100 kW within the year 2004 [9].

During the firsts tests the very basic circuit shown in Fig.2 was used. The power supply works at maximum pulse voltage of 40 kV with repetition rate from 1 up to 50Hz. The DC current at 50 Hz was about 200 μA. Although this circuit has been used succesfully in previous studies [3, 5], it turned out that in this larger reactor at 40 kV there was almost no real corona current. The energy per pulse was estimated very roughly at ≈1 mJ. This is insufficient to obtain the desired treatment time and to determine accurately the consumed energy.

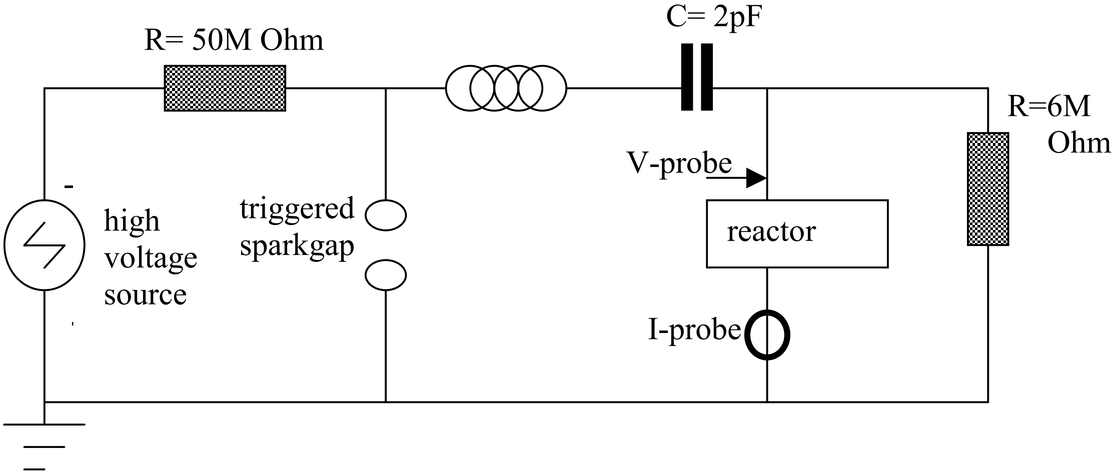

Fig 2. Basic high voltage circuit to generate positive corona discharges as used in the first tests.

For these reasons a second pulsed power generator is tested in this work, its diagram is shown in fig. 3. Its voltage, current, power and energy waveshapes are given in Fig. 4. The capacitor C is discharged over a transmission-line-transformer (TLT) via a sparkgap switch, with a repetition rate up to about 100 pps. Detailed descriptions of a TLT are given in [1,10]. The TLT used here consists of four 50 ohm coaxial cables of 2 m length. At the generator-side, the lines are connected in parallel, thus providing a low discharge impedance for the capacitor (12.5 ohm). At the reactor-side, the lines are connected in series. This output impedance of 200 ohm provides better matching with the corona reactor. In addition, the output voltage is increased. The main functions of the TLT are: (i) impedance transformation for faster switching and for better matching with a corona reactor, (ii) increase the output voltage, and (iii) protection of the switch against short-circuits and breakdowns. The performance of a TLT depends to a large extent on the choice of magnetic cores. For this work, no magnetic cores were used. As a result, the low secondary mode impedance limits the voltage transformation (about 2 instead of 4) and oscillations on the voltage occur (Fig. 4). Due to these oscillations, a second, negative corona discharge will occur after about 200 ns. For the coming experiments, Metglas cores with a microgap will be added to the TLT. This will significantly increase the voltage (upto about 50 kV) and will prevent the oscillations.

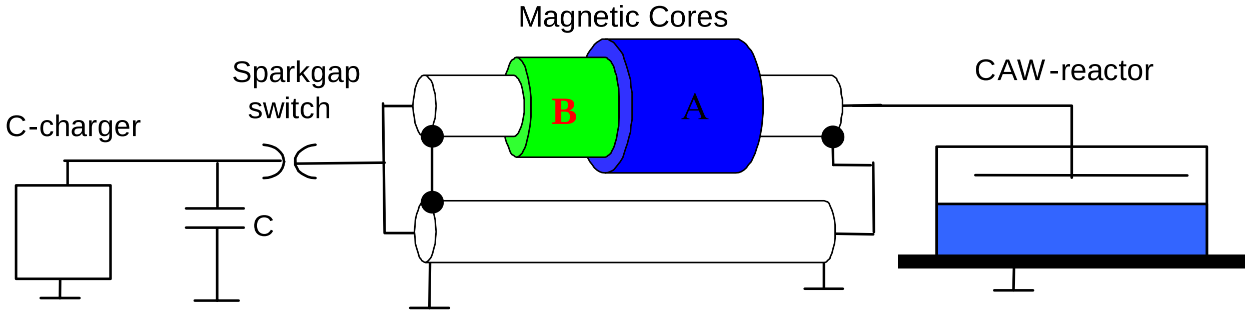

Fig.3. Schematic diagram of the pulsed power generator using coax cables as transmission line transformer.

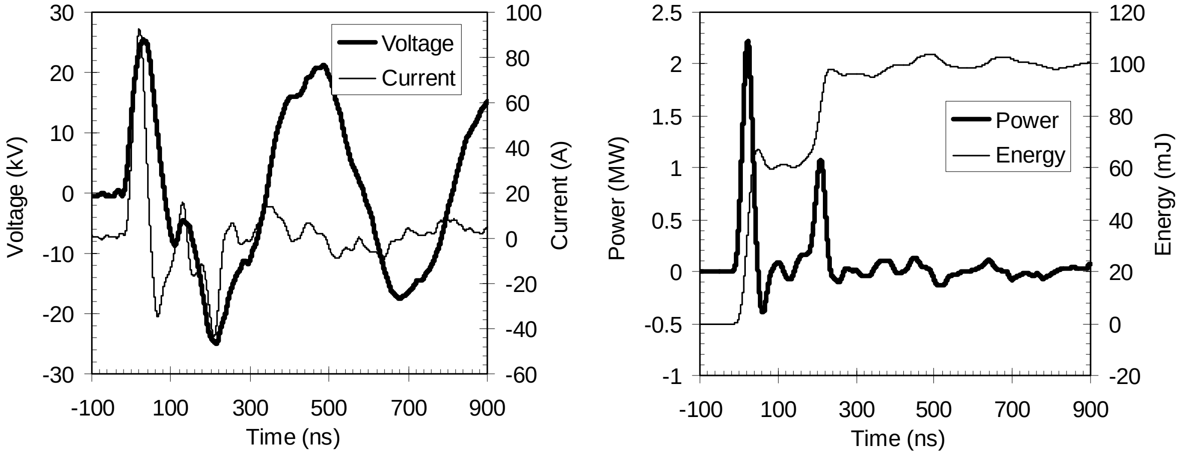

Fig.4. Pulse voltage, current, power and energy of the TLT pulsed power supply.

From fig. 4 it is seen that an energy input of ~100 mJ/pulse is now obtained due to the better matching of the impedances of the source and the reactor. The circuit of fig. 3 is similar to the one used in large systems and can have wall plug efficiencies of more than 80% [2].

C) Diagnostics

To measure the reactor efficiency an on-line diagnostics system, similar as in [5] and [6] , has been installed.

For concentration measurements of the model compounds a new LIF setup is constructed using a Quantel Brilliant Ultra YAG laser with 4 mJ/pulse output at 266 nm and an Ocean Optics HR2000 spectrometer. This system is tested with phenol and polyethyleenglycol (PEG), see fig.5.

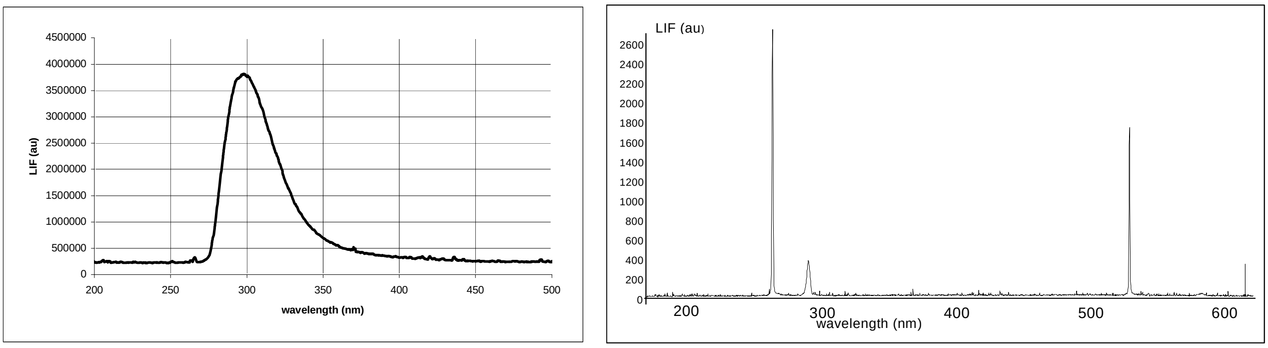

Fig. 5: First examples of LIF spectra of solutions of 1mM phenol (left) and 0.1% PEG (right) in water.

These results show that sufficient signal is readily obtained to determine the reduction of these target compounds. The spectrum of phenol is obtained from a 1mM solution, this shows that can be detected down to very low concentrations with this method (<~10^{-3} M).

In the case of PEG flourescence is observed just below 300 nm but also an even stronger signal is seen at the laser wavelength of 266 nm. This light is also seen at the double wavelength in the second order of spectrometer. This signal is probably due to Raylight scattering of the large PEG molecules. Further tests are required to check if this signal can be used to monitor the PEG concentration.

Ozone concentration in air is measured by absorption of UV light using the spectrometer and a deuterium lamp (Heraeus Fiberlight). In the near future the ozone concentration in water will also be measured.

4. Obtained results

To study the reactor ozone creation efficiency several tests were performed. Absorption technique, using the deuterium lamp, was applied at wavelengths between 250 and 300 nm. The first results, obtained in a dry reactor, are shown in fig.6.

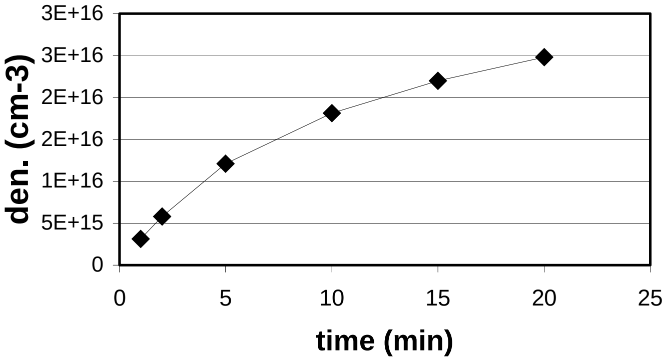

Fig. 6. Ozone density measured in a dry reactor using the deuterium lamp.

This figure shows that the ozone concentration increase rapidly during first 10 min, than the concentration becomes stationary. The ozone concentration rises to several times 10^{16} cm^{-3}. These results are similar to studies performed earlier [5], despite the fact that here the corona energy input, using the power supply of fig. 2, was very limited.

Reactor functioning tests were performed using different compounds. Phenol, PEG, waste water from textile industry and from mattress industry.

All CAW treatments were realized with the DC supply voltage at 35-40 kV, leading to a DC current from 100-200 µA. The estimated energy going into the corona discharge was ~0.1W. For different times of treatment the changes in efficiency were noticed.

Both industrial waste water used in tests, are characterised by small BOD/COD ratio, unpleasent odour and intensive colour. The main task of treatment was to decrease the level of colour and increase BOD/COD ratio. Decoloration was obtained in both samples and, although it was not complete, also the BOD/COD ratio of the samples was increased. This means that after corona treatment those waste waters can be easier decomposed in biological reactors and natural environment.

The PEG sample treatment shows the increase in BOD/COD ratio from starting 0.053 to 0.37 after 30 min corona discharge treatment with a total energy consumption of only ~0.01 kWh/ltr.

In the near future a chemical model will be set up. It will help to find the speed-limiting step of the conversion and to obtain rules for optimization and up-scaling.

4. Conclusions

A new corona reactor is build and tested for operation in a heterogeneous medium. It uses a wire-plate electrode configuration with four wires of 38 cm length. This technique is suitable for treatment of different kinds of water wastes. The tests were started with a pulsed power supply that switches a capacitot with a spark gap. This supply gave almost no power into the reactor (≈1 mJ/pulse). The second power supply tested uses a transmission line transformer with four coax cables. In this way the spark gap discharges the capacitor into a 12.5 Ohm load and the transformer has an output impedance of 200 Ohm as the source for the reactor. This leads to a much better impedance matching of the source to the load and in this way pulses of ~100 mJ are achieved. Further improvements to this supply are expected from the use of ferrites.

The setup has been in first tests used for treatment of phenol and PEG contaminated water and also for cleaning chemical wastes from different types of industries. Measurements using LIF spectroscopy and UV light absorption have been shown to be suitable for in-situ detection of the model compounds decomposition and ozone creation.

Performed tests confirm the efficiency of CAW technique. The BOD/COD ratio of PEG increased significantly and decoloration of the industrial samples is demonstrated, although not complete. Tests will be continued using the TLT supply.

Further optimization of reactor conditions, such as residence time of treated wastes, electrode configurations, additives is required to obtain information on how to scale up the process for industrial applications.

References:

[1] E.M. van Veldhuizen (editor)- Electrical Discharges for Environmental Purposes: Fundamentals and Applications, Nova Science Publishers, New York, 1999, ISBN 1-56072-743-8, 420 pages.
[2] Keping Yan- Corona Plasma Generation, PhD thesis TU/e, nov. 2001.
[3] W.F.L.M Hoeben, E.M. van Veldhuizen, W.R. Rutgers, G.M.W. Kroesen-J.Phys.D:Appl.Phys. **32**(1999)L133-L137.
[4] www.phys.tue.nl/EPG/YTRID
[5] W.F.L.M. Hoeben, E.M. van Veldhuizen, W.R. Rutgers, C.A.M.G. Cramers, G.M.W. Kroesen- Plasma Sources Sci. Technol. **9**(2000)361-369.
[6] Daiyu Hayashi, Wilfred Hoeben, Geert Dooms, Eddie van Veldhuizen, Wijnand Rutgers, Gerrit Kroesen- Applied Optics LP **40**(2001)986-993.
[7] N.Sano, T. Kawashima, J. Fujikawa, T.Fujimoto, K. Takaaki, T. Kanki, A. Toyoda, Ind. Eng. Chem. Res. **41**(2002)5906.
[8] N.A. Yavorovski, S.S. Peltsman, J.I. Kornev, Yu.V. Volkov- Technology of water treatment using pulsed electric discharges.
[9] K. Yan, E.J.M. van Heesch, A.J.M. Pemen, S.A. Nair, P.A.A.F. Wouters, "Transmission line transformers for up to 100 kW pulsed power generation", Proc. of the 25th IEEE Int. Power Modulator Symposium, June 2002, pp. 420-423.
[10] P.W. Smith, "Transient electronics; pulsed circuit technology", John Wiley & Sons, UK, 2002, ISBN 0-471-97773-X.
[11] B.R. Locke, B.Srinivasan, "Optimisation of continous pulsed corona reactor", Ch.E.Science 56 (2001) 1035-1039.

The influence of inner nozzle contour on the plasma torch performance for atmospheric plasma spraying

A. Schwenk[1], H. Gruner[2],S. Zimmermann[3], K. Landes[3], G. Nutsch[1]

[1] Technische Universität Ilmenau, Fachgebiet Plasma- und Oberflächentechnik, Germany;
[2] MEDICOAT AG, Mägenwil, Switzerland;
[3] Universität der Bundeswehr, München-Neubiberg, Grundgebiete der Elektrotechnik, Germany

Abstract

Derived from previous investigation [1], a new convergent-divergent nozzle with a de Laval-like inner contour is designed and used for atmospheric plasma spraying. Experimental studies regarding the measurement of powder particle trajectories and their velocities, the plasma jet velocity and plasma jet temperature are done by Laser Doppler Anemometry and enthalpy probe measurements. These results are compared with measurements obtained with the standard nozzle. Especially, the deposition efficiency rises enormously.

1. Introduction

Industrial DC atmospheric plasma spraying (APS) torches generally utilize anode nozzles characterized by a convergent entrance near the cathode followed by a cylindrical shape in the exiting part, in the following **c**onvergent-**c**ylindrical **n**ozzles (CCN). High intensity current arcs generated between the cathode and this CCN nozzle show more or less a re-striking behaviour, especially when molecular gases are used. The re-strikes cause voltage fluctuations and therefore, power fluctuations. The re-strikes are also responsible for the strong noise. The cylindrical nozzle with a diameter of 6 mm leads to high velocities of plasma jet emanating from the nozzle and therefore, to a strong cold ambient air entrainment into the jet shortly after the nozzle exit. The cold gas entrainment is the reason for the rapid cooling down and deceleration of the plasma jet. So, the plasma jet emanating from the CCN is characterized by a narrow hot core and steep radial and axial temperature and velocity gradients. That makes the powder injection sensitive to changes of all spray parameters.

Therefore, a wide plasma jet with lower temperature and velocity gradients is more preferable for plasma spraying. The divergent end part of a nozzle commonly used for the vacuum plasma spraying (VPS) wides the hot plasma core, which leads to low velocity and temperature gradients of the emanating plasma jet and reduces the interactions with the ambient cold air.

For some applications, a conical end part is used. The more specific nozzle design is obtained by calculations done after Foelsch's [13] characteristic method. [2-4]. Such **c**onvergent-**d**ivergent **n**ozzles (CDN) used for the VPS are mostly derived from the CCNs by a simple prolongation of the cylindrical part by divergent ending. In the last years, these CDNs were also tested for APS conditions [2-5]. It has been shown that the hot plasma jet core extends as expected, and lower temperature and velocity gradients are also obtained. However, these studies are done mostly with low power levels and with the use of Argon / Helium gas mixtures and powder sizes (+5 – 22 µm) such as usually applied in VPS [2-4].

Our studies are done with Argon / Hydrogen gas mixtures (12Vol.% H_2), power levels of 36 up to 45 kW, current intensities of 600 to 800 amperes, and alumina as feedstock with a grain size in the range of +22 – 45 µm. Using these parameters we also found that turbulences could be minimized, the hot jet core extended, the deposition efficiency increased up to 50%, and the coating quality was well improved [1].

Based on these results, a new nozzle contour is designed and tested under atmospheric conditions. The aim is to enhance the torch performance without any torch and powder injection changes. That is a highly practical advantage for industrial applications. The design and some of the results obtained are demonstrated in the paper.

2. Experimental Set-up

2.1 Torch design and parameters used

The APS system of the MEDICOAT AG, Switzerland, is used for studies of the influence of various nozzle designs for the atmospheric plasma spraying process. The used MC-60 DC-Plasma torch consists of the finger-tipped thoriated tungsten cathode surrounded concentrically by the copper anode nozzle with a tungsten inlet, described in previous paper [1]. The DC arc with 600 – 900 A, corresponding to a plasma torch power of 32 - 45 kW is operating between these two water-cooled electrodes. An Ar/H_2 plasma gas mixture (12 vol. % H_2) with a total gas flow rate of 50 slpm is injected with a swirl angle of 45°. Argon is used as carrier gas with a gas flow rate of 4.5 slpm. Alumina powder in the α–phase with a grain size of +22 - 45 µm and a purity of >99.6 % is injected perpendicularly to the plasma jet from above with a powder feed rate of 12 g/min. The powder injection tube of 1.8 mm in diameter is mounted externally on the torch. S235 steel substrates are used at the substrate temperature of 300 °C for all samples. Coatings with a layer thickness of 300 µm are produced at varying spray distances.

2.2 LDA – Laser Doppler Anemometry

Important parameters of plasma spraying are the particle velocity and the particle trajectories. The velocities, trajectories, and the flux density of the particles can be determined using the Laser Doppler Anemometry (LDA) as an approved and reliable diagnostic method as described in numerous papers, e.g. [19,20]. The LDA is a scanning system where in the measuring volume single measurement points are located. In the modified LDA system used for measurements in this study, transmitting and receiving elements are combined in a single unit as is schematically shown in Figure 1 along with the other used equipment. This combination and the compact measurement set-up give more flexibility and make easier the system adjustment. No photo-detector has to be optically adjusted relative to the measurement volume. The sensor head can be moved without torch moving for an in-flight determination of particle parameters. Particularly, this LDA measurement set-up can be also applied for vertically arranged plasma spray systems.

2.3 Enthalpy Probe Measurements

In thermal DC and RF plasmas, the enthalpy probe system is successfully used since the earlier sixties [17] for the determination of enthalpy-, temperature- and velocity profiles. In this study, the measure device made by TEKNA Plasma Systems Inc., Sherbrooke, Canada, is used combined with a mass spectrometer for gas composition measurement as described in [18]. The local specific enthalpy (h_∞) of the plasma flow is calorimetrically measured and determined from the energy balance on the cooling water circuit in two-steps: the tare measurement is done as a Pitot tube without a gas flow through the probe and for the stagnation pressure p_0 measurement, and the gas sampling measurement for the temperature determination as is written in Figure 1. The velocity is derived from the Pitot tube measurement.

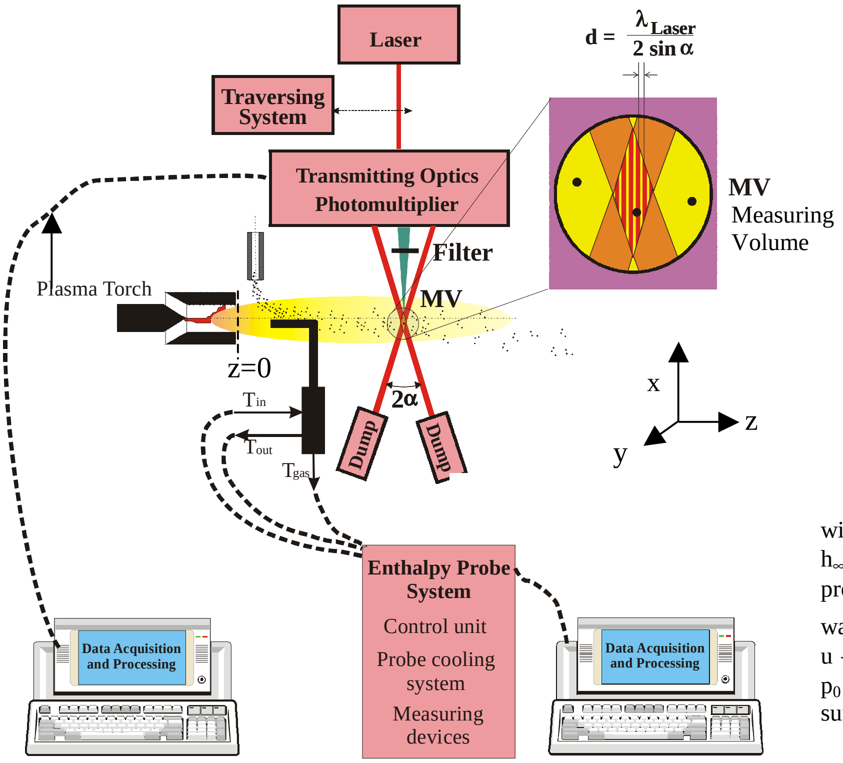

For T and u determination:

$$h_\infty = h_{exit} + \frac{\dot{m}_w}{\dot{m}_g} \cdot c_P \cdot \left(\Delta T_{sample} - \Delta T_{tare}\right)$$

$$u = \sqrt{\frac{2 \cdot (p_0 - p_\infty)}{\rho_\infty}}$$

with
h_∞, h_{exit} – enthalpies of the plasma and of the probe exit, $\dot{m}_g, \dot{m}_w$ - mass flow rates of water and gas, c_p – specific heat capacity, u – axial velocity, ρ_∞ - plasma mass density, p_0 - stagnation pressure, p_∞ - chamber pressure

Fig.1: Schematic of the measure arrangements

3. Preliminary studies

3.1 with the standard Convergent-Cylindrical Nozzle (CCN)

The MC-60 DC Plasma torch usually applies the standard CCN (V0s) shown in Figure 2 under atmospheric conditions. The hydrodynamic and self-magnetic forces move the anodic arc root within the cylindrical part whereby the local overheating and the erosion of the anode inner wall can be prevented. It is known that the movement of the anodic arc root causes voltage fluctuations. Particularly, using molecular gases instead of inert gases saw tooth-like voltage fluctuations are obtained (Fig.3). Such re-striking behaviour causes also very strong noises with approximately 120 dB at frequencies of about 4 - 5 kHz [1].

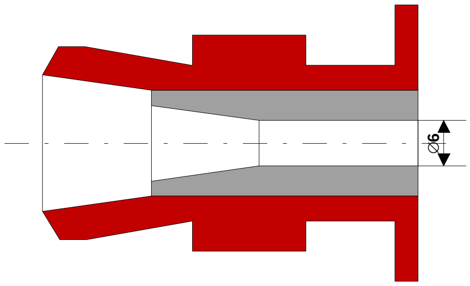

Fig.2: Schematic of the standard CCN V0s

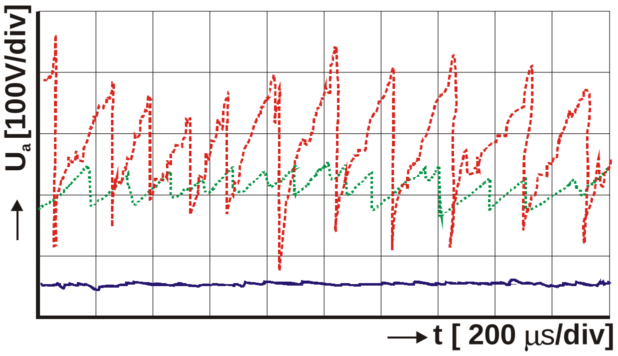

Fig.3: Voltage fluctuations with varying working gases [6]
—— Argon, ········ Nitrogen, - - - - Hydrogen

Similar results to Fig.3 are also obtained when gas mixtures are used: More than 1 Vol.% of hydrogen in an argon plasmas leads already to saw tooth voltage fluctuations. Due to the high thermal conductivity of the hydrogen, the arc as well as the anodic arc root are constricted. Therefore, self-magnetic and hydrodynamic forces affect the arc behaviour in much stronger way than the diffuse argon arc and its anode attachment. Using hydrogen / argon gas mixtures and CCNs the arc root shows partially strong movements. The arc behaviour switches from the so-called re-strike mode up to the take-over mode [1, 16].

As mentioned above, these voltage fluctuations lead to power fluctuations that influence the plasma jet emanating the torch [7]. Spray powders in general injected externally and vertically to the plasma flow direction are sensitive to these power fluctuations, because the trajectories of the powder particles and the heating up of the powder particles are strongly influenced. Therefore, the deposition efficiency of alumina powder under industrial conditions is limited to 50 –60%. The mean plasma jet velocity at the nozzle exit yields 1500 m s^{-1}. The high velocity of the plasma jet exiting into the surroundings interacts very strongly with the ambient air. Due to this interaction, a strong air entrainment into the plasma jet is obtained [8, 9]. This is the reason for the strong axial and radial temperature and velocity gradients [9, 10] with a narrow and short hot arc core. The optimisation of the powder particles injection into the hot core has to be done very carefully. The injection parameters such as powder size, mass density, carrier gas flow rate, injection nozzle diameter, distance from the torch exit, as well the torch parameters such as the current intensity, gas composition, gas flow rate have to be taken into account.

3.2 with the Convergent-Divergent Nozzles (CDN) usually used

In recent years, the torch nozzle design is improved, especially for applications at low pressures with supersonic flow conditions [2-5, 11,12]. The divergent end part of these nozzles is designed by Henne [2] using the characteristic method and the assumptions of isentropic flow, thermodynamic equilibrium and the absence of a boundary layer based on the paper of [13]. Characteristic values of the nozzles are the diameter relation of the throat and the exit, the nozzle length, and the Mach number at the nozzle exit. Calculations are done for cold gas flows of pure argon and air.

The divergent end step is designed as prolongation to the cylindrical nozzle. In this way, the CDNs are the longer the higher the Mach number is chosen [4,12]. The longer the prolongation the lower will be the thermal efficiency of the torch, but the hot core is more extended.

In previous studies [1,14], the **Mach-2 nozzle** named after [2] (Fig.4) is tested under atmospheric conditions with the alumina powder as feedstock as described above. It has to be mentioned, that at atmospheric pressure no supersonic conditions prevail and that with the divergent end part the velocity of the emanating plasma jet will be reduced to a subsonic one. Because of that and the fact that the de-Laval-like nozzle contour with the desired Mach number is calculated for cold gas flows the nozzles are named as *so-called* Mach 2 nozzle.

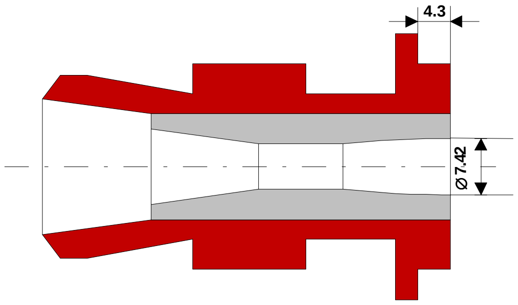

Fig.4: Schematic of the Mach-2-nozzle

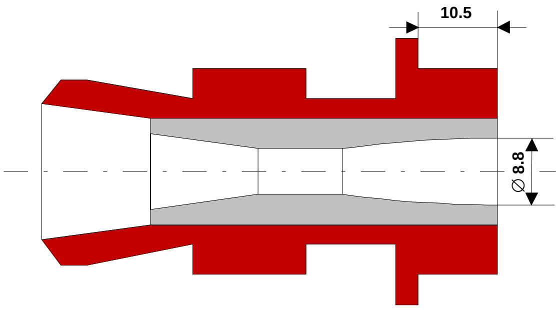

Fig.5: Schematic of the Mach-2.5-nozzle

As already reported in [1], excellent deposition and coating qualities are obtained with the parameters given above. The reason for that are the extended hot core of the plasma jet, the lower jet velocity and therefore, the longer dwell times of the powder particles inside the hot core. Moreover, the entrainment of the cold gas is reduced proofed by oxygen content measurements inside the jet with the enthalpy probe combined with the mass spectrometer. The most important advantage is the increase of the deposition efficiency up to more than 150% related to the standard nozzle at the same parameters.

The results obtained with the so-called Mach-2.5 nozzle (Fig. 4) at the same operating parameters have shown that the plasma jet is wider than in the case of Mach-2 nozzle [15]. However, the deposition efficiency is lower, the temperature and velocity gradients in axial directions are steeper, and the oxygen content at the substrate distance is much higher. That means that the cold gas entrainment from the surrounding air is enhanced with this nozzle contour.

Calculations with the FLUENT Software package [14] show that under atmospheric conditions the gas flow is already shocked inside this divergent nozzle part, and the flow is separated from the nozzle wall. That is the reason for the strong air entrainment into both the nozzle and the plasma jet. It is the aim of further studies to reduce the air entrainment by improved inner nozzle contours.

4. Results obtained with new CDN design

4.1 Nozzle properties

The new nozzle design is calculated by Fluent software as mentioned above for the gas mixture of argon/hydrogen (88/12 vol.%) with the total flow rate of 50 slpm, the heat capacity ratio as a function of the temperature and the desired Mach number of 2.5. The modelling has been described more in detail in [14, 16]. The new CDN is named V70. The shortening of the cylindrical part has reduced the total nozzle length (Fig.6). The electrical arc behaviour is characterized by a very smooth voltage plot related to the one of the standard CCN shown in Figure 7.

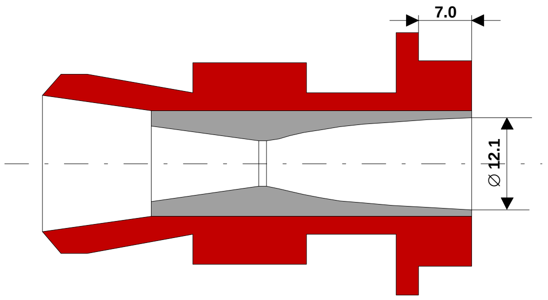

Fig. 6: New CDN (V70)

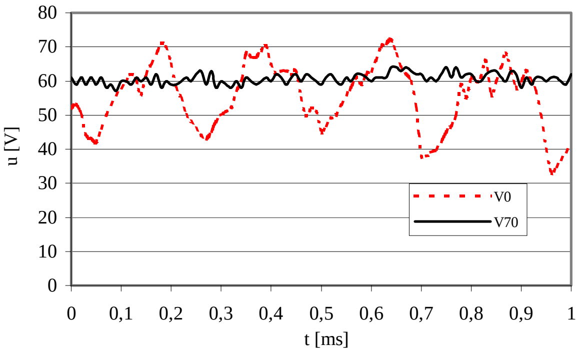

Fig.7: Voltage plots of the standard CCN (V0s) and the new CDN (V70)

The smaller voltage fluctuations with the new CDN are connected with an extremely low noise [14, 16], which improves the operating conditions in workshops. Especially, fluctuations in the highly bothering frequency range of 4 – 5 kHz do not longer exist. The thermal efficiency of the torch is in the same range of the standard CCN.

4.2 Plasma jet properties

The velocity and temperature distribution obtained from the enthalpy probe measurements within the plasma jet using the CCN (V0s) and new CDN (V70) are shown in Figures 8 and 9. The minimum measure distance from the nozzle exit amounts to 32 mm due to the high heat flux of the argon-hydrogen gas mixture to the probe tip close to the nozzle exit. As written above, the divergent end part of the V70 nozzle leads at atmospheric conditions to lower axial velocities of the plasma jet compared with the commonly used cylindrical end part of the V0s nozzle. The expansion of the plasma flow results in an extended hot core of the plasma jet and a reduced cold air entrainment from the surrounding.

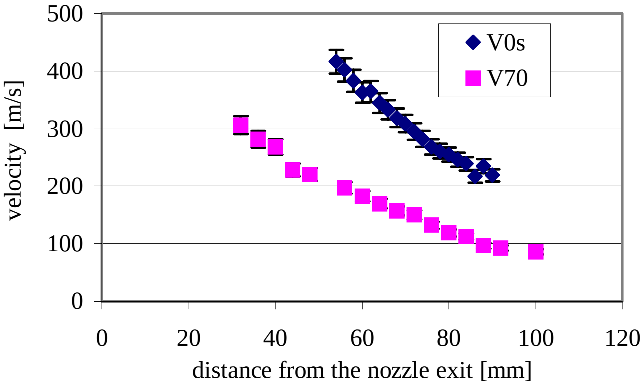

Fig. 8: Velocities in the centreline of the plasma jet using CCN (V0s) and CDN (V70)

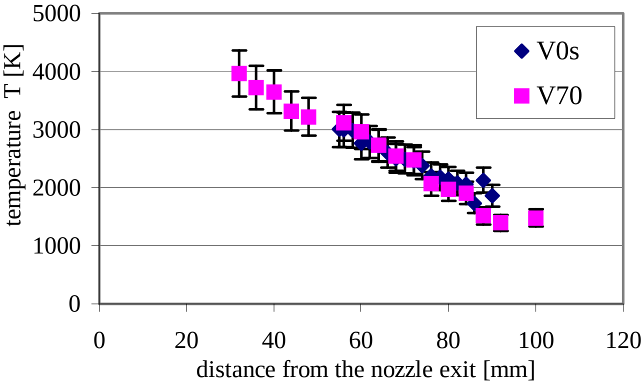

Fig.9: Temperatures in the plasma jet axis using CCN (V0s) and CDN (V70)

4.3 Particle behaviour

The results of the LDA measurements confirm the enthalpy probe results. Figure 10 shows for example the velocity isocontours of the injected powder particles within the plasma jet for both the CCN V0s the CDN V70 at nozzle exit distances of 45 mm and 38 mm, respectively. The results are well comparable because the acceleration of the injected particles has been almost completed at this distance, and the mean particle velocities keep nearly constant in flow direction as shown in Figure 11.

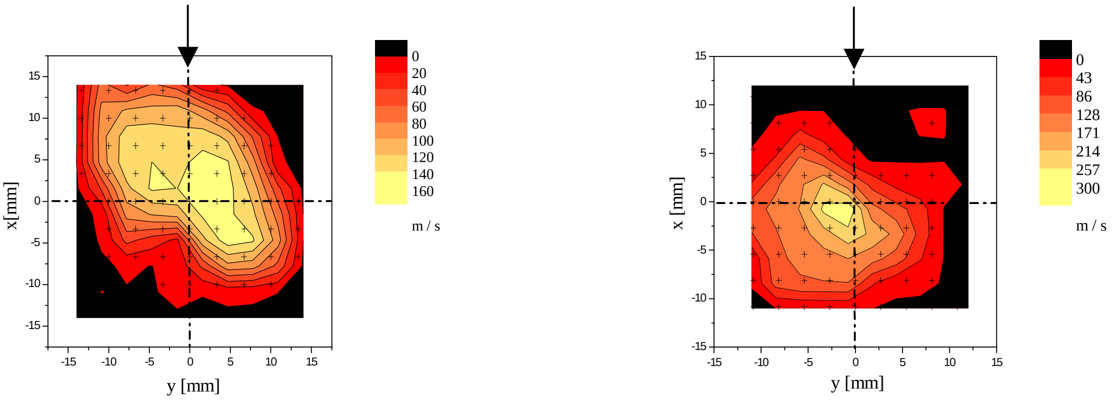

Fig.10: Particle velocity isocontours for the CDN (V70) left and the CCN (V0s) right
arrows mark the particle injection direction

The high plasma jet velocity of the standard CCN (V0s) leads inevitably to the high acceleration of the powder particles, and therefore, to high particle velocities. On the other hand, the extended plasma jet results also in a wide uniform velocity area in the centre. Due to their low velocities using CDN (V70) the particles have long dwell times within the enlarged plasma jet, which results in a strong increase of the deposition effiefficiency as it is shown in Figure 12. For example, with the current intensity of 600 amps, the deposition efficiency using the CDN (V70) is enhanced up to more than 200% though the percentage of hydrogen in the gas mixture has been reduced by 40 percent related to commonly used spray parameters using CCNs (V0s).

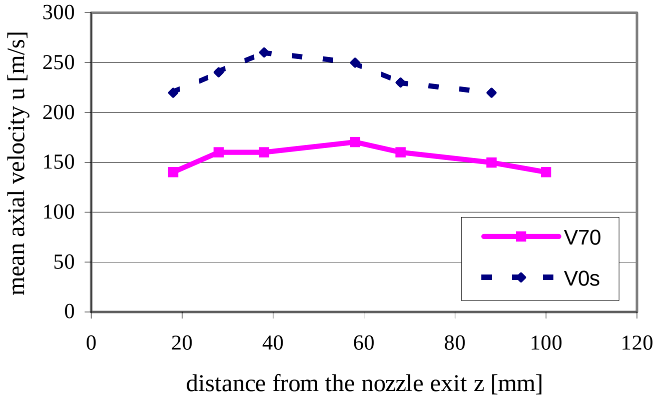

Fig.11: Mean particle velocity versus the spray distance

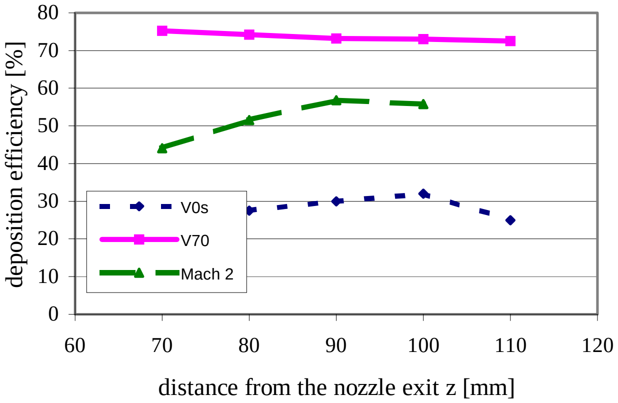

Fig.12: Deposition efficiency at varying spray distances

5. Conclusion

First results are represented using the new convergent-divergent nozzle (V70). Because of the relatively short prolongation the thermal efficiency of the plasma torch is nearly the same as the CCN (V0s). Using this new CDN (V70), the noise is extremely reduced, the plasma jet has been widen, so that the injection of particles is not so sensitive to injection parameter changes. The particles posses high dwell times, which enhance the particle melting process. The deposition efficiency of alumina has been enormously increased.

References

[1] A. Schwenk, H. Gruner, G. Nutsch, Proc. ITSC 2002, Essen,510-514
[2] R. Henne, W. Mayr, A. Reusch, M. Rahmane, G. Soucy, M. Boulos, Proc. TPP’94, 1994, Aachen
[3] R. Henne, V. Borck, W. Mayr, K. Landes, A. Reusch, Proc. 8th Nat.Thermal Spray Conf., 1995, Houston
[4] R.Henne, E. Boyer, V. Borck, G. Schiller, Proc. ITSC 2001, Singapore
[5] O. Betoule, G. Soucy, M. Vardelle, P. Fauchais, Proc. ITSC, Orlando, USA, 1992, 773-779
[6] G. Nutsch et al., Proc. TPP’94, 1994, Aachen
[7] E. Pfender, W.L.T. Chen, R. Spores, Proc. 3rd Nat. Therm. Spray Conf., 1990, Long Beach, California,
[8] E. Pfender, J.R. Fincke, R. Spores; Plasma Chem. & Plasma Proc. **11**(1991) 529-543
[9] G. Nutsch, Habil. Thesis, TU Ilmenau, 1995, pp.
[10] P. Fauchais, E. Boudrin, J.-F.Coudert, Plasma Chemistry IV, Akademie-Verlag, Berlin, 1983, pp59-183
[11] M. Cao et al., Plasma Sources Sci. Techn. **6** (1997) 39-45
[12] M. Rahmane et al., J. Thermal Spray Techn. **7** (1998) 349-356
[13] A. Foelsch, J. Aeronautical Sciences, (1949), 161-167
[14] A. Schwenk, H. Gruner, G. Nutsch, Proc. ITSC 2003, Orlando, USA
[15] A. Schwenk, Diploma Thesis, 2001, TU Ilmenau (in German)
[16] A. Schwenk, H. Gruner, G. Nutsch, Proc. 10th Workshop Plasmatechnik, 2002, TU Ilmenau
[17] J. Grey, ISA Transactions 4 (1965), pp 102-115
[18] M. Rahmane, G. Soucy, M.I. Boulos et al., Rev. Sci. Instr. **66** (1995) pp.3424-3431
[19] W. Mayr, K. Landes, A. Reusch, Proc. of the TS 93, Aachen, March 1993
[20] S. Zimmermann, K. Landes, Proc. 11th Bundesdeutsche Fachtagung Plasmatechnologie, 2003, Ilmenau,

KINETIC MODEL FOR PLASMA CHEMICAL PRODUCTION OF ACTIVATED WATER

B.F.Gordiets*, A.G.Sokolskiy**, A.B.Zaika**, V.V.Kuznetsov**

P.N.Lebedev Physical Institute of Russian Academy of Sciences, Moscow;
*** Russian firm "Technosystema-ECO", Moscow*
E-mail: a-sokolsky@mtu-net.ru

The modern technology is the activation of aqueous solutions water by plasma chemical method with use the electric discharge in the water vapors and following absorption of the plasma chemical products by liquid water. Such activated water has unique specific properties and is already used in the different areas: in medicine; in an agriculture and industry (for example, for cleaning of waste products, whiting of fabrics (materials), extracting of precious metals from ore and so on) and solves many ecological problems. Recently for production of the activated water it was proposed to use the non-independent decaying discharge in the special plasma chemical reactor. This reactor (production of *"Technosystema-ECO")* has the vertical coaxial electrodes (inside –anode, outside – cathode) and liquid water cover of cathode and flows down. The discharge in the water vapors is pulsed and developed due to series of very short (~ 10^{-8} sec) high voltage (~10^{4} volt) pulses, which create the free plasma electrons. The low voltage (~500 volt) pulses exist more long time (10^{-4}–10^{-3} sec) and are responsible for the discharge current in the decaying plasma.

The present paper gives the description of such type of discharge and kinetic processes in the non-equilibrium plasma in the water vapors. The following processes are included into model: *a)* ionization, dissociation, attachment (including dissociative attachment) and vibrational excitation of H_2O molecules by plasma electrons; *b)* ion-molecular reactions, processes of electron-ion and ion-ion recombination, electron attachment to small admixtures; *c)* vibrational relaxation of H_2O molecules; *d)* mobility of electron and ions; *f)* gas heating due to absorption of electric energy and cooling due to thermo conductivity; *g)* dissociation of H_2O molecules by energetic ions in the cathode layer. The fluxes of gas phase chemical species to liquid water, which is in contact with plasma, are calculated for some variants of activation. These species are absorbed by liquid water and provide its activation.

This work was supported by Russian Foundation for Basic Researches.

Generation of a Stable Atmospheric Glow in a DBD Configuration

E. Aldea[1], C.P.G. Schrauwen [2], M.C.M van de Sanden [1],

[1] Eindhoven University of Technology, Dept. of Applied Physics, Eindhoven, The Netherlands
P.O Box 513, 5600 MB Eindhoven, The Netherlands, e-mail m.c.m.v.d.sanden@tue.nl
[2] TNO- TPD, Division Models and Processes, Eindhoven, The Netherlands

Abstract

In this paper the generation mechanism of an atmospheric glow plasma is discussed. The plasma was generated in Ar, N_2 and air between two electrodes (electrode gap 0.3- 10 mm) covered by a dielectric. It is concluded that the atmospheric glow generation is unlikely to be attributed to a preionization mechanism involving metastables but rather to a mechanism involving the dielectric surface.

1. Introduction

Due to their promise for low-cost applications atmospheric glow plasmas received in the last years a considerable attention. Conventional wisdom attributes their generation to gas preionization, which is related to ions [1] or to electron generation by metastable-metastable and metastable-surface collisions [2-4]. However there is not yet unambiguous experimental evidence, which can prove the validity of either of the proposed mechanisms. In several papers dedicated to modeling of atmospheric glows [3-5] the generation mechanism is assumed to be similar to that occurring in the low-pressure glows. However in these models the calculations are made starting with a uniform density of seed electrons in the reactor of at least $10^5/cm^3$. The mechanism for the generation of this uniform density of seed electrons is not considered and the difficulties of glow generation and its notorious instability are not explained. Considering all these arguments to our opinion the physical basis of the atmospheric glow remains an open and challenging issue. In this paper we analyse the basic conditions needed for homogenous glow generations. It is concluded that metastables formation is rather the problem of atmospheric glow than the solution. Also it will be argued that the ion trapping cannot explain the atmospheric glow generation. Our experiments suggest that in fact the surface of the dielectric plays a key role in the generation of atmospheric glow plasmas.

2. Atmospheric glow generation. Why it is difficult?

To generate a glow plasma one must first have a uniform breakdown and secondly one must maintain it. In both of these steps major instabilities like streamer breakdown for the breakdown phase and filamentation due to glow to arc transition in the post-breakdown phase can occur. To generate a homogenous glow both instabilities must be avoided.

Streamer breakdown is the usual breakdown mechanism of atmospheric plasmas. The streamer breakdown occurs when the charge density in the avalanche is so high that near the avalanche tip the electric field reaches the breakdown value. This happens when the product between first Townsend ionization coefficient α and the interelectrodic gap d is around 18-19. If the streamer breakdown occurs plasma will be filamentary because the streamers repel each other due to the space charge of their tips and cannot superpose. Strikingly most of the atmospheric glow plasmas reported in the literature are ignited at electric fields and gaps much lower than those required for streamer breakdown [2,3,6]. For our system the αd product at the breakdown is around 3. It is clear than that the breakdown mechanism of atmospheric glow is not a streamer breakdown. Assuming that the breakdown mechanism is a classic Townsend breakdown ($\gamma * \exp(\alpha d) = 1$) a value of secondary ionization coefficient γ around 0.1 can be obtained. Such a value is highly unusual for other types of cold atmospheric plasmas like corona's and silent discharges. Because the ion energy is very small and most of the photons are adsorbed near the avalanche γ is usually very small in these discharges in the range of 10^{-3}. In fact it is the low value of γ which allows a Townsend breakdown at relatively large value of αd product making more probable that a Townsend breakdown occurs rather than a streamer breakdown. Thus it is likely that in fact in atmospheric glow the streamer breakdown is avoided due to some physical mechanism which results in a higher than usual secondary ionization coefficient.

Filamentation due to glow to arc transition

Plasmas at atmospheric pressures are very unstable and will tend to go into a spark in a short time after the breakdown. Any random local increase in the current density will tend to grow rather than to be damped and plasma will be constricted in a high current density filament. For example a local increase of electron density will increase the ionization probability via the generation of strong electric fields due to space charge. Furthermore the ionization probability will increase due to the increase in density of excited species, which can contribute to the ionization via stepwise ionization or photoionization. Of course, any plasma has its own negative feedback to deviations from the equilibrium but the rate of negative feedback is determined by the diffusion of ions or metastables in neighboring regions. At atmospheric pressure the diffusion speed is negligible so the speed of negative feedback is only in the range of a millisecond. On the contrary the rate of increase of perturbation is in the range of tens of nanoseconds. In this respect it appears there are no solutions for preventing glow to arc transition and the atmospheric glow plasma appears to be a “miracle”. In this respect it is clear that the explanation of atmospheric glow must be related to some physical mechanism, which avoids the glow to arc transition. The presumed metastable abundance of atmospheric glow [2,5] cannot be the explanation, because as a consequence of their generation the stepwise ionization probability will increase significantly and thus any random perturbation will increase even faster. The large probability of metastable formation in molecular gases is probably the reason why the atmospheric glow is difficult to generate in such gases [2,6].

3. Importance of preionization

The preionization was proposed [2-3,7-8] as a way to generate many electron avalanches in the same time superposing then the space charge and suppressing the streamers breakdown mechanism. Experiments with an external preionization source (UV, secondary discharge, X rays) shown indeed that the density of streamers can increase but there is no clear proof that glow plasma can be generated in this way. A significant preionization current on order of $\mu A/cm^2$ is required in order to generate concomitant avalanches in order to suppress streamers. In [1-4] the atmospheric glow generation was explained as a consequence of streamer suppression due to ion-atom, ion-molecule or to electron generation by metastable-metastable and metastable-surface collisions [2-4]. Even if presently the glow formation is attributed to a preionization mechanism involving either metastables or ions it is obviously that neither the metastables nor the ions are present <u>during the first ignition of the plasma</u>. Thus a preionization based on metastables or ions cannot explain why the breakdown mechanism is not a streamer breakdown. In fact the real problem is the glow to arc transition. During the plasma breakdown the high electric field generated by the avalanche space charge is a major risk for glow to arc transition. Preionization of the plasma could be than indeed a solution for reducing the space charge by superposing the avalanches. A detailed evaluation of this mechanism is given in the following section. Note that if the problem is to avoid glow to arc transition at breakdown and not to suppress streamers the preionization current must be of only a few nA/cm^2 because the time scale of the glow to arc transition is hundreds of nanosecond and not few nanoseconds like in the case of streamer formation. However preionization is just <u>one of the solutions</u> to reduce the risk of glow to arc transition at breakdown. A significant secondary emission will also decrease αd product and thus the space charge and the risk of glow to arc transition at breakdown.

4. Experimental

The plasma was generated in Ar, N_2 and air between two electrodes (electrode gap 0.3-5 mm) covered by a dielectric. The electrodes are mounted in a gas tight cabinet. In order to simulate an industrial-like treatment (mobile dielectric surface) the bottom electrode can be translated along a rail. The high voltage (1-10 kV, 0.1-30 kHz) was applied to the electrodes using a system consisting of a computer controlled pulse generator, an amplifier and high voltage transformers. Two type of pulses were applied, sine waveform (Fig. 2a), and an sequence of sinusoidal pulses with a delay between them (Fig. 2b). The current, voltage and plasma emission pulses were recorded through a computer controlled TDS 3034 B TEKTRONIX oscilloscope (sampling resolution 1 ns, bandwidth 350 MHz). Current probes (Tektronix CT-1 and TCP 202) were used for current measurements. Due to the capacitive coupling beside the plasma current component the current measured by the current probes has also a component due to the displacement current. The displacement current component was determined separately by measuring the current through a capacitor in parallel with plasma reactor and subtracted subsequently from the total current. This procedure allows a very precise determination of the plasma current component. The light emitted from the plasma is measured by an optical system consisting of a 10 cm focal length lens and an optical fiber (200-900 nm), which is attached to the input slit of an ORIEL ¼ m monochromator (maximum resolution 0.03 nm, 280-900 nm). The light intensity spatial distribution was monitored using a DALSA Eclipse fast CCD camera (integration time 13μs). At the exit slit of the monochromator a photomultiplier and a fast current amplifier are connected. The temporal resolution of the spectral system is 5 ns. The emissions of the N_2 (C-B), OH (B-X) and CN (B-X) spectral systems were used to calculate the rotational and vibrational temperatures.

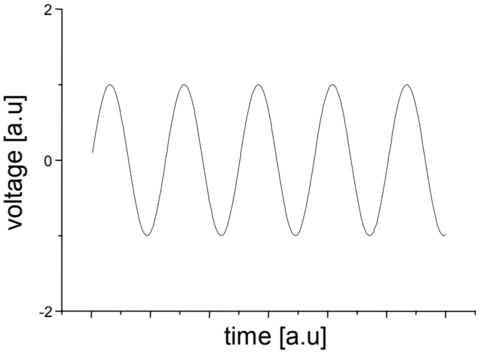

Fig. 1a. Pulse type A
Sinusoidal function, frequency 0.1-30 kHz

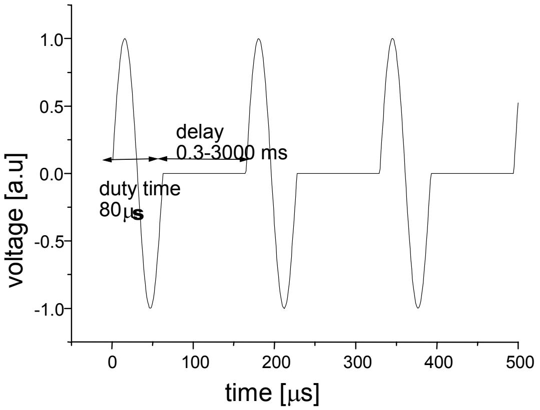

Fig. 1b. Pulse type B
Delayed sinusoidal pulses, duty time 80 μs

4. Contribution of metastables to glow generation mechanism

In [2-4] is proposed that the preionization by metastables occurs through following processes:

$$A^* + B \rightarrow A + B^+ + e \tag{1}$$

$$A^* + A^* \rightarrow A^+ + A + e \tag{2}$$

$$A^* + e(\text{surface}) \rightarrow A^+ + e \tag{3}$$

Reaction (1) is the main channel in a He plasma in which B are impurities species and reaction (3) is the dominant channel in an N_2 plasma. We made a estimation of the minimal density required for preionization metastables by taking in account the maximum reaction rate of 10^{-11} cm^{-3}/s reported in literature [4,5] for reactions (1) and (2) and respectively a diffusion speed of 1 cm/s and a degree of coverage of surface by charge of 10^{-4} for reaction (3). In the case that one needs to suppress the streamers a huge density of metastables of at least $10^{13}cm^{-3}$ is required in order to generate the required preionization through reactions (1) and (2) of $10^{15}cm^{-3}$ through reaction (3). Such densities are highly improbable in a discharge in which the electron density is in the range of 10^{10} cm^{-3} and the probability of collisional quenching of metastables is so large. But if the real issue is only the glow to arc transition then the required preionization and the required metastable density will drop with two orders of magnitude. Still metastable density of 10^{11} cm^{-3} (for reactions 1 and 2) and 10^{13} cm^{-3} for reaction (3) are considerable and such an abundance of metastables should be detectable experimentally. We have tried to detect the metastable presence using the breakdown voltage, which is a sensitive parameter to metastable presence. A considerable amount of metastables will generate a drop of the breakdown voltage after the first pulse due to the increased of probability by means of stepwise ionization. Within the limit of experimental uncertainty of 2% of the breakdown voltage we did not detect any notable decrease of the breakdown voltage after the first pulse. Another signature of metastables can be obtained by studying the temporal dependence of current and plasma emission. The presence of the high-energy metastables could generate a notable plasma emission (afterglow) after the end of the electron generation (marked temporally by the end of the current pulse). Thus when compared with the current pulse the plasma emission will have a "tail". We could not detect any afterglow in plasma emission for any lines or bands. An example is shown in Fig.2a for Ar (4p-4s) line in a Ar plasma and in Fig. 2b for N_2 (C-B) emission in a N_2 plasma.

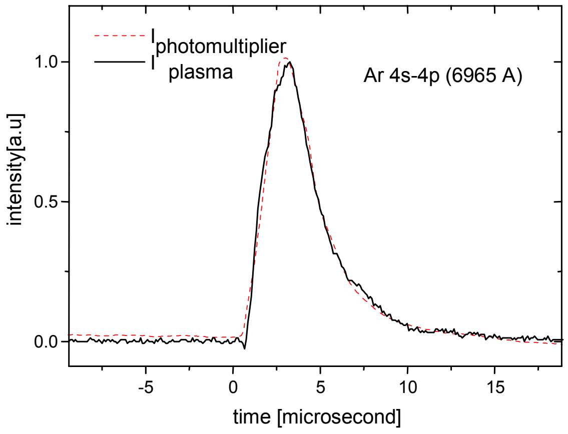

Fig.2a The correlation between Ar emission and the current pulse (Ar, d=1mm, f=13 KHz)

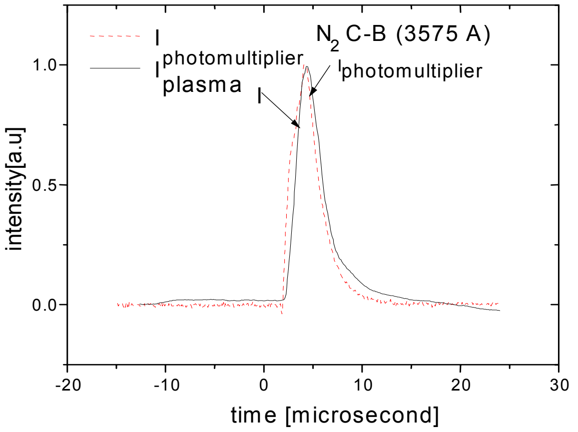

Fig.2b The correlation between N_2 (C-B)-emission and the current pulse (N_2, d=1 mm, f=13 KHz)

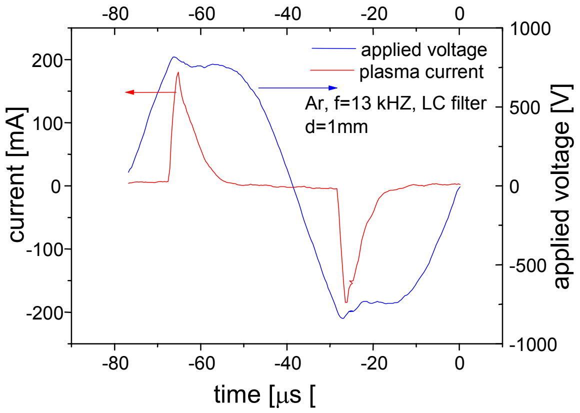

Fig.3 Absence of afterglow in the current pulse (Ar , d=1mm, f=13 KHz)

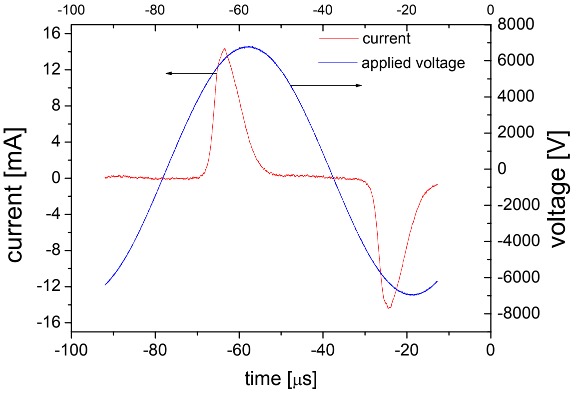

Fig.4 Absence of afterglow in the current pulse (N_2 , d=1mm, f=13 KHz)

Also in disagreement with the results reported in Refs [2,3] no long tail of the current pulse, which could indicate the presence of an afterglow preionization, was detected (see Fig. 3 and Fig. 4). This disagreement n could be related to differences in the procedures for subtracting the displacement current. In the experiment presented here the displacement current is not fitted with a sine but is measured directly through a capacitor in parallel with the plasma reactor. It is debatable anyway that the current afterglow reported in [3] can be attributed to electrons because no afterglow tail in plasma emission was observed. It could be related to ions that have a smaller mobility and a longer time of order of 10 µs is required to remove them from the discharge area.

But apart form the difficulty to detect the large amount of metastables required for suppressing the streamers or the glow to arc transition, there are solid arguments that the metastables cannot be the key to a uniform glow. It is clear that at the first breakdown there is not any preionization due to metastables and ions and thus the first breakdown must always be filamentary. So a mechanism allowing the transition from filamentary variety to arc must exist. In Refs [2,3] it is considered that the metastables are diffusing from the initial area of avalanches so finally due to superposition of the diffusion “clouds” a uniform preionization will be generated in all the volume of the reactor. But due to the limited diffusion speed the metastables lifetime must be very long in the order of seconds to support such a mechanism. For example even in a second the metastables will diffuse about 1 cm from the place of avalanche formation. It is highly improbable to find metastables of such a long lifetime. At atmospheric pressure due to collision de-excitation the lifetime of most of metastables is very short in the range of μs. Similar arguments hold also for ion-atom or ion-molecule pre-ionization. The diffusion speed of ions is also very low and they are removed form the reactor by the electric field in few microseconds so they cannot be either candidates for the superposition of diffusion clouds of avalanches or the transition from filament to glow. Having in view all these arguments to our opinion a preionization mechanism based on ions or metastables cannot provide a consistent explanation for the atmospheric glow formation.

6. The role of dielectric surface

For some dielectric surfaces we found that atmospheric glow plasma can be generated already from the first pulse when no metastables or ions are present in the discharge area. Also using type B pulses with variable delay we did not observe filamentation even when the delay between pulses was increased in to the second range. Thus any lifetime effect of metastables can be excluded. An example of current–voltage waveforms during the first pulses for an Ar plasma is shown in Fig. 5. The non-glow character is indicated by the absence of random high-intensity and short current pulses that are typical for a filamentary plasma and by the fast camera images of plasma. For other types of dielectric surface these sharp current pulses signaling a filamentary plasma can be clearly noted (see Fig. 6, 7). The current oscillations observed in Fig. 6 are due to the strong EM waves emitted by the filamentary plasma. It appears then that the glow generation mechanism cannot have anything to do with the metastables but has to do with the surface. The explanation of this surface effect could be related to the contribution of the dielectric surface to the secondary ionization. As was discussed in the previous section a high secondary emission at the surface can explain the suppression of the streamer formation and glow to arc transition.

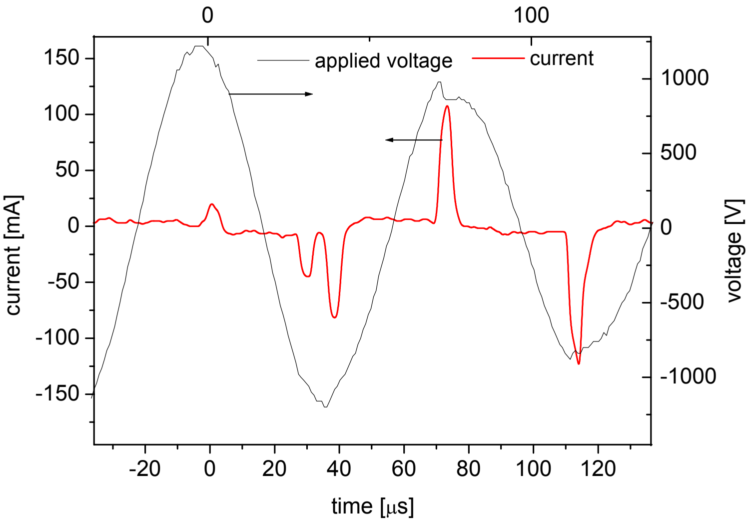

Fig.5 Glow generation from the first pulse
(Dielectric material type A, Ar d=1 mm, f=11.8 kHz)

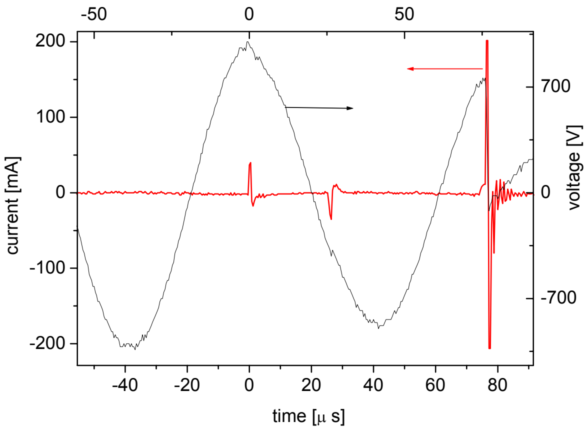

Fig.6 Filamentary plasma variety during the first pulses (Dielectric material type B, Ar d=1 mm, f=12.6 kHz)

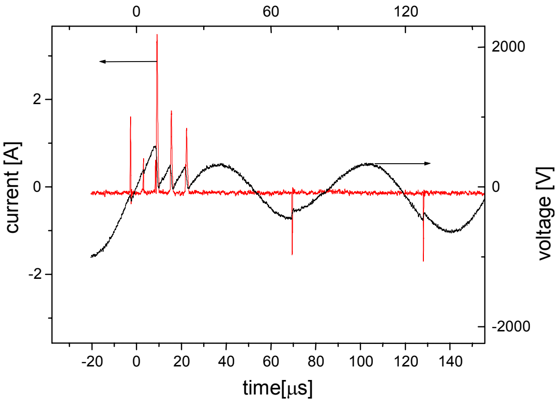

Fig.7 Filamentary plasma during the first pulses (Dielectric material type C, Ar d=1 mm, f=12.6 kHz)

Conclusions

A simple analysis of the glow generation basis indicates that it is extremely improbable that the metastables or ions can have a significant contribution to glow generation via a pre-ionization mechanism. The low diffusion rate of ions and metastables excludes any mechanism of streamers or electron avalanches superposition. The ions or metastables cannot also explain why the standard breakdown mechanism of atmospheric plasma streamer breakdown does not occur.

Besides the theoretical arguments no evidence was found in the current-voltage characteristics, plasma emission or breakdown voltage suggesting a significant preionization or even the presence of a large amount of metastables.

It was concluded that the major problem in generation of atmospheric plasma is glow to arc transition. In this respect metastables are rather the problem for a stable plasma generation because their presence increases the probability of stepwise ionization and glow to arc transition. The experimental data suggests that the surface of the dielectrics plays a major role in glow generation. The surface effect is probably due to a high secondary emission at the surface.

References

[1] J.R. Roth, P.P.Tsai, C. Liu, C. Wadsworth, P.D.Spence, US Patent 5403 453 (1995)

[2] N. Gherardi, G. Gouda, E. Gat, A. Ricard, F. Massines, Plasma Sources Sci. Technol. **9,** 340 (2000).

[3] F. Massines, A. Rabehi, P. Decomps, R. Ben Gadri, P. Segur, J.Appl.Phys, **83**, 2950 (1998).

[4] Yu.B. Golubovskii, V.A. Maiorov, J. Behnke, J.F. Behnke, J. Phys. D: Appl. Phys. **35,** 751(2002)

[5] Yu.B. Golubovskii, V.S.Egorov, I.B. Mekhov, J. Behnke, A.Sonnenfeld, Hakone VII, Greisfwald (2000) , http://www.physik.uni-greifswald.de/hakone7/

[6] S. F. Miralaï, E. Monette, R. Bartnikas, G. Czeremuszkin, M. Latrèche , M. R. Wertheimer, Plasmas and Pol. **5**, 2, 62, (2000)

[7] H.D. Park and S. Dhali, Appl. Phys. Lett. **77**, 2112, (2000)

[8] A.K. Laflamme , Rev.Sci Instrum **41,** 1578 (1970)

MOLECULAR SPECTROSCOPY DIAGNOSTIC OF AQUEOUS SOLUTIONS ACTIVATED BY LOWTEMPERATURE PLASMA

A.G.Sokolskiy*, V.V.Kuznetsov*, A.V.Kraiskii**, N.N.Melnic**, T.A.Babushkina***,
Z.S.Klemencova***, B.V.Lokshin***, N.M.Sergeyev****, V.N.Torocheshnikov****

* *Russian firm "Technosystema-ECO", Moscow*
** *P.N.Lebedev Physical Institute of Russian Academy of Sciences, Moscow*
*** *A.N.Nesmeynov Institute of Organoelement Compounds of Russian Academy of Sciences, Moscow*
**** *Chemistry Department of Moscow State University*
E-mail: a-sokolsky@mtu-net.ru

The paper contents the description of experimental results of comparative diagnostics of lowtemperature plasma activated aqueous solutions (and original solutions) by the molecular spectroscopy methods. It were used raman spectroscopy, infrared spectroscopy and spectroscopy of nuclear magnetic resonance. It was proved that the main reason - big activity of ions H_3O^+ and ions in which H_3O^+ is as a main their part. This is in agreement one with others and with theoretical results of kinetic model for plasma chemical production of activated aqueous, parallels created. The paper contents many color illustrations of spectrums.

This work was supported by grant of *Russian Foundation for Basic Researches*.

Mapping of the internal plasma parameters of an unbalanced magnetron DC discharge

S. Kvasnica[1,2], P. Adámek[3] P. Špatenka[3,4]

[1]*Institute of Industrial Electronics and Material Science, TU-Vienna, Austria*
[2]*Boltzmann Institute of Biomedical Microtechnology, Vienna, Austria*
[3]*Department of Physics, University of South Bohemia, Czech Republic*
[4]*Department of Material Engineering, Technical University of Liberec, Czech Republic*

Abstract

Langmuir probe diagnostics using thin cold cylindrical probe has been performed in r-z plane of a DC unbalanced magnetron discharge in argon at 0.5 and 2.5 Pa. Important plasma parameters as the electron density, plasma and floating potential have been extracted from the measured characteristics and its second derivative. We present typical probe characteristics at selected locations of the discharge as well as complete spatial distributions of extracted plasma parameters. Comparison with results of recent PIC/MCC simulation is discussed.

1. Introduction

Unbalanced magnetron [5] is an interesting tool for deposition of new materials under increased ion bombardment. In contrast to the conventional balanced magnetron characterized with good magnetic confinement of plasma resulting in negligible charged particle fluxes to the substrate, in case of unbalanced magnetron the unbalanced magnetic fluxes of the inner and outer magnetic poles ('leaky' magnetic circuit) lead to increased ion/electron bombardment of the growing film. Recently spatial discharge structure and electron transport processes in such magnetron configuration has been the subject of study in Ref. [1–4]. First qualitatively correct results were also obtained with PIC/MCC model in [6]. Aim of this work is to present a comprehensive set of plasma parameters measured by the Langmuir probe technique to verify the simulation results. The obtained data will also be loaded to achieve faster the steady state of the simulation.

2. Experimental

The experiments were carried out in 20 l viton-sealed cylindrical vacuum chamber pumped out by turbomolecular pump and rotary vane pump with base pressure 5×10^{-4} Pa. The working gas (Ar) was introduced through a mass flow controller. Pressure was adjusted by a throttle valve installed between the chamber and the turbomolecular pump. Magnetron of unbalanced type with $\varnothing$ 80 mm polycrystalline Ti target (99.6% purity) cathode was installed in up-side-down position (Fig. 1). Detailed description of the magnetron geometry and the FEM model of the magnetic field along with the PIC/MCC plasma simulation results were discussed elsewhere [6].

Probe tip was made from tungsten wire of 50 µm diameter inserted in copper and glass capillaries. The outer glass capillary was about 2.5 mm longer than the inner copper capillary as shown in Fig. 1. Active part of the wire was 5 mm long. This construction avoids shortening of the probe tip with the grounded probe holder due to deposition of the conductive layer. However, the measured plasma densities can be still affected by probe area growth due to the deposition. Thus quick measurement and replacement of probe tips was important especially during measurements in the vicinity of the target. Other plasma parameters (V_{pl}, V_{fl}, T_{eff}) are not affected. Probe positioning was achieved by rotation and axial movement of the probe holder in the feedthrough as depicted in Fig. 1, where also the coordinate system is defined. In this configuration the probe tip is always perpendicular to the magnetic field lines as follows from the symmetry. Such arrangement minimizes the effect of magnetic field on the space-charge deformation around the probe. Further, the lower limit of the Larmor radius $r_{\mathrm{L}} = 80\,\mu\mathrm{m}$ estimated at 1 eV and maximum magnetic field near the target 40 mT is still larger that the probe diameter. Langmuir probe measurements in magnetron discharges can be additionally affected by significant $\mathbf{E} \times \mathbf{B}$ drift which shifts the EEDF [7]. This effect is also minimized in used configuration since the probe tip is (anti)parallel with drift within the limit of 15°. Due to the cylindrical symmetry of the magnetron

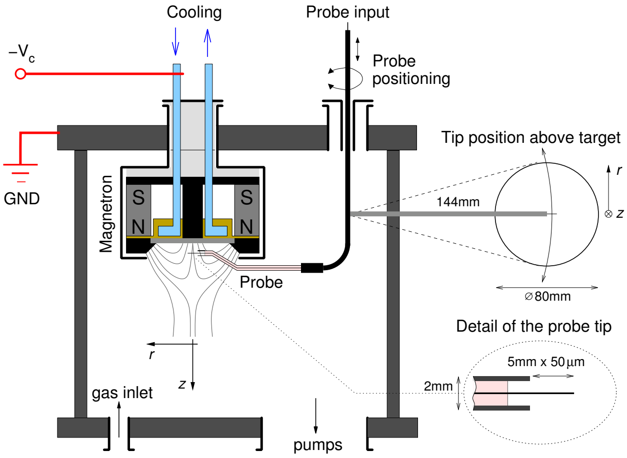

Fig. 1: Schematic diagram of the experimental set-up showing the orientation of the probe with respect to magnetron during the positioning and detail of the probe tip.

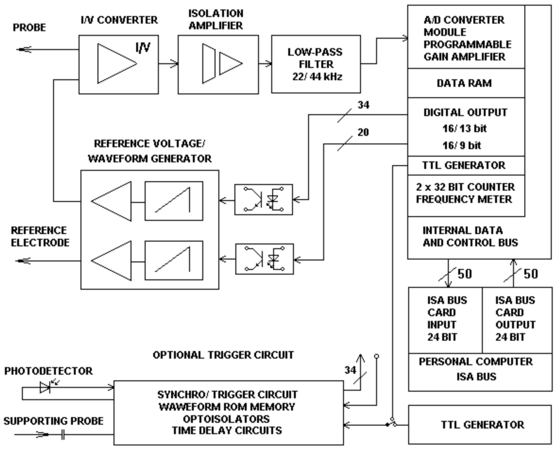

Fig. 2: Block diagram of the probe electronics

discharge measurements of the area $(0,60)\times(4,52)$ mm in the r-z plane would be sufficient to perform volume resolved measurements but for sake of higher confidence this area was extended to $(-60,60)\times(4,52)$ mm. The positioning resolution in r and z coordinates was typically 5 mm. In regions with higher gradients the resolution of z coordinate was enhanced to 2 mm.

The block diagram of the measurement electronics is shown in Fig. 2 [8]. The offset voltage was set by a 8-bit D/A converter. The probe voltage span of 50 V was swept in 1024 steps over at 20 kHz by the second 12-bit D/A converter. 400 measurements were sampled by 12-bit A/D converter and averaged for each characteristic. In very low plasma density areas outside of the plasma beam and the confined region the resolution of the probe electronics was insufficient for estimation of the correct position of the zero crossing of the probe characteristic. In this region we used voltmeter (*Keithley 196*) to measure the floating potential of a floating probe.

Plasma was generated using the *Advanced Energy Pinnacle Plus 5K* DC power source operating in constant current mode. First set of measurements was performed at $p = 0.5$ Pa (3 sccm Ar), at discharge current $I_c = 0.4$ A and cathode voltage $V_c = 328$ V. During the second set of measurements the pressure was $p = 2.5$ Pa (10 sccm Ar), $I_c = 0.4$ A and cathode voltage $V_c = 266$ V.

3. Data processing

Since the EEDF is generally expected to be non-Maxwellian [3, 9–11] at low pressure and in presence of the magnetic field, the Druyvesteyn method was applied. The first and second derivatives were numerically computed from the probe current using the centered difference. To reduce the noise smoothing was performed on the probe characteristic and its first derivative. We used 2 × repeated running averages with length of 4 points (≈ 0.2 eV) on the data measured outside of the confined region and in the beam of plasma far from the target. Approaching the confined region with higher plasma density, the smoothing procedure was successively increased to 8 × 14 points (≈ 0.7 eV) average due to higher noise.

The plasma potential V_{pl} was determined from the maximum of the first derivative of the retarding probe current. EEDF (g_e) can be expressed in terms of the computed values of second derivative:

$$g_e(\mathcal{E}) = \frac{2m}{e^2 A}\sqrt{\frac{2e\mathcal{E}}{m}}\frac{\mathrm{d}^2 I_e}{\mathrm{d}\mathcal{E}^2} \qquad (1) \qquad\qquad n_e = \int_0^\infty g_e(\mathcal{E})\mathrm{d}\mathcal{E} \qquad (2)$$

where $A = \pi \cdot d \cdot l$ is probe area of cylindrical probe of length l and diameter d, $\mathcal{E} = V_{\mathrm{pl}} - V_{\mathrm{probe}}$ is energy in eV [12]. The electron density $n_e$was numerically computed as integral of g_e (2).

$$\mathrm{T}_{\mathrm{eff}} = \frac{2}{3}\langle\mathcal{E}\rangle = \frac{2}{3}\frac{1}{n_e}\int_0^\infty \mathcal{E} g_e(\mathcal{E})\mathrm{d}\mathcal{E} \qquad (3) \qquad\qquad g_p(\mathcal{E}) = \frac{1}{\sqrt{\mathcal{E}}} g_e(\mathcal{E}) \qquad (4)$$

The effective electron temperature $\mathrm{T}_{\mathrm{eff}}$ was computed according to (3). Further we estimated the drift velocity $v_d = \mathbf{E}\times\mathbf{B}/B^2$ and the drift current $j_H = e \cdot v_d \cdot n_e$ perpendicular to the r-z plane using the gradient of the measured plasma potential and the modelled magnetic field and the measured electron density. As the electron energy probability function g_p (EEPF) (proportional to the second derivative) defined in (4) is linear with $\mathcal{E}$ in the semilogarithmic plot for Maxwellian distribution, the linear regression was applied to determine the electron temperature where appropriate.

4. Results and discussion

Figures 3 and 4 show 2d images of extracted plasma parameters at 0.5 Pa and 2.5 Pa visualized using the *OpenDX Data Explorer* [13]. Electron density in Fig. 3a, 4a ranges from $10^{14}\,\mathrm{m^{-3}}$ to more than $10^{17}\,\mathrm{m^{-3}}$. The discharge can be divided into 3 main parts: area with the highest density up to 30 mm from target (referred to as the confined region), plasma beam emerging from the area of contraction of the confined region and the surrounding background area characterized by afterglow plasma with densities around $10^{14}\,\mathrm{m^{-3}}$. In the fact a 4th area near the center of the target enclosed by the confined region with fast secondary electrons present but low plasma densities can be defined. At lower pressure the confined region and the beam are more sharply delimited whereas at higher pressure we observed more diffuse distribution due to increased collisional frequency. The values of the electron density are similar in the both cases, however at 0.5 Pa the discharge power was 130 W while at 2.5 Pa only 106 W. For positive values of r (where probe is oriented anti-parallel to the drift) we measured up to 20 % higher densities than in the opposite half-plane. Because this effect remained after rotating the magnetron, but was reversed by swapping the orientation of permanent magnets, we can conclude, that the 2 mm glass capillary holding the probe tip was somewhat shadowing the drifting electrons when oriented parallel with the drift velocity.

As already predicted by PIC/MCC modell in [6] negative values of plasma potential were measured in the confined region (Fig. 3b, 4b). This effect is more pronounced at low pressure (with potentials up to -18 V), while potentials only up to -8 V were measured at 2.5 Pa. Similar results were presented recently in [2,4]. The plasma potential lies around zero in the plasma beam while the floating potential still remains negative up to -17 V (Fig. 3c, 4c). This effect can be explained by a group of fast secondary electrons present in the beam and is important for increased ion bombardment of the substrate.

Maps of the drift velocities in Fig. 3d, 4d computed from the measured plasma potential and the modelled magnetic field indicate that the drift velocity should be below 10^5 m/s which would correspond to ~ 0.03 eV. This means that the probe characteristics should not be significantly distorted even if the probe was not exactly aligned in the drift direction. Integration of the drift current density in Fig. 3e, 4e over the discharge area results in total Hall current 0.16 A at 0.5 Pa and 0.09 A at 2.5 Pa.

Fig. 3d, 4d show effective temperature distribution in the discharge. Lower effective temperatures and lower difference in temperature of confined region and the beam were found at higher pressure.

Detailed EEPF at selected locations of the discharge for 0.5 Pa and 2.5 Pa is shown in Fig. 5, 6. In the background region we found Maxwellian distribution with temperatures around 0.3 eV, slightly increasing towards the target. In the plasma beam a bi-Maxwellian distribution with a low-energy part temperature around 1 eV and a high-energy part temperature around 8 eV at 0.5 Pa and 4 eV at 2.5 Pa indicating group of fast secondary electrons was found. Both temperatures as well as the ratio of high/low energy part contribution increase while approaching the confined region. In Fig. 5f still present disappearing low-energy part and non-Maxwellian part appearing in confined region can be observed. In the confined region we generally observed non-Maxwellian distributions (Fig. 5g, 6c) with larger distinction from Maxwellian distribution at lower pressure.

5. Conclusions

Mappings of the electron density, plasma and floating potentials, drift velocities and effective temperature in unbalanced magnetron DC discharge at 0.5 Pa and 2.5 Pa were obtained by means of Langmuir probe diagnostics. These mappings along with the detailed EEDF characteristics present a comprehensive set of data important for further development of the PIC/MCC model. We observed variations of the plasma density within 3 orders of magnitude. This indicates that current superparticle ratio used in the PIC/MCC simulation has to be decreased. Measurements confirmed existence of negative plasma potential in the confined region as well as the presence of fast secondaries in the plasma beam. However, simulation gives more negative potentials, which is probably caused by insufficient grid resolution near the target. Non-Maxwellian EEDF in the confined region was observed.

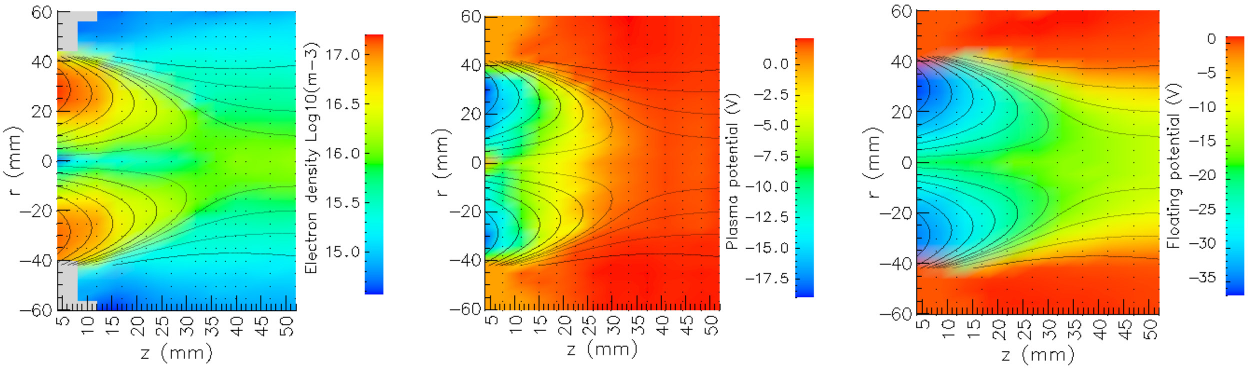

(a) Electron density n_e **(b)** Plasma potential V_{pl} **(c)** Floating potential V_{fl}

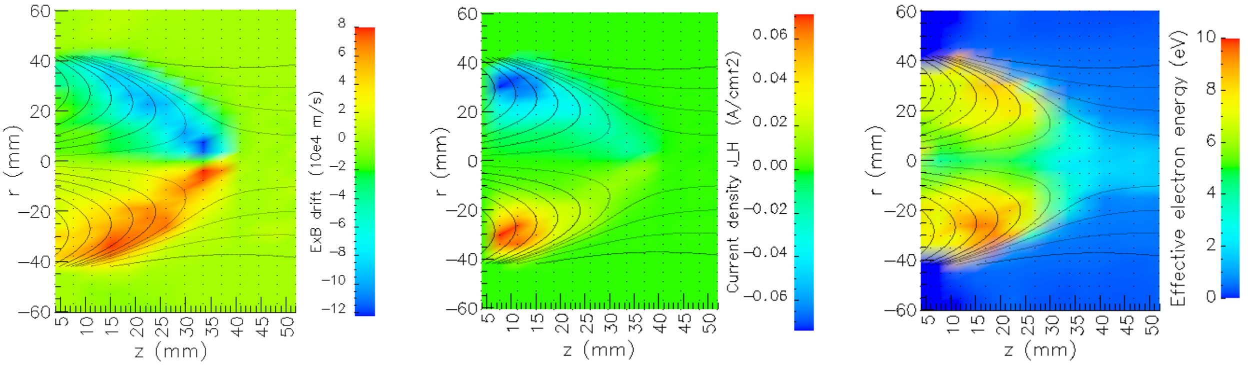

(d) Drift $v_d = -\nabla V_{pl} \times \mathbf{B}/B^2$ **(e)** Drift current $j_H = e \cdot v_d \cdot n_e$ **(f)** Effective electron energy

Fig. 3: Spatial distribution of extracted plasma parameters in r-z plane for discharge at 0.5 Pa; black curves represent the shape of the magnetic field, black points the measurement locations

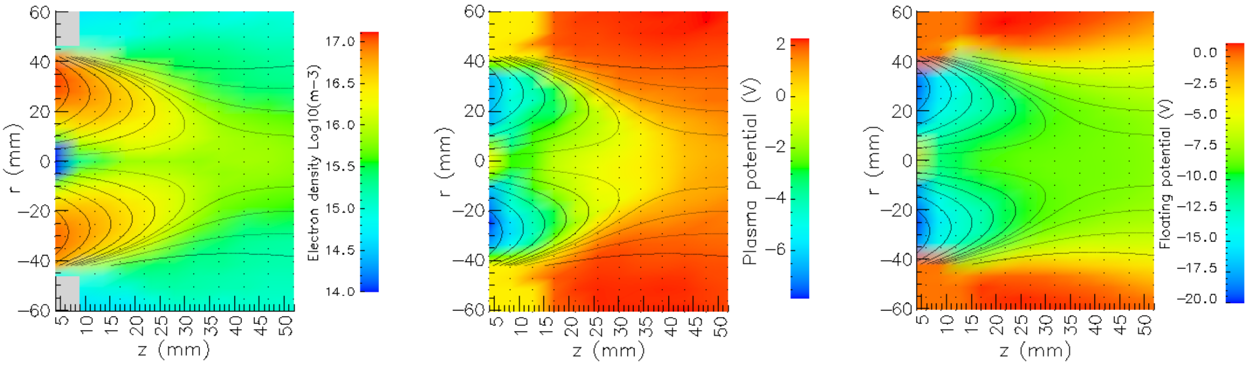

(a) Plasma density n_e **(b)** Plasma potential V_{pl} **(c)** Floating potential V_{fl}

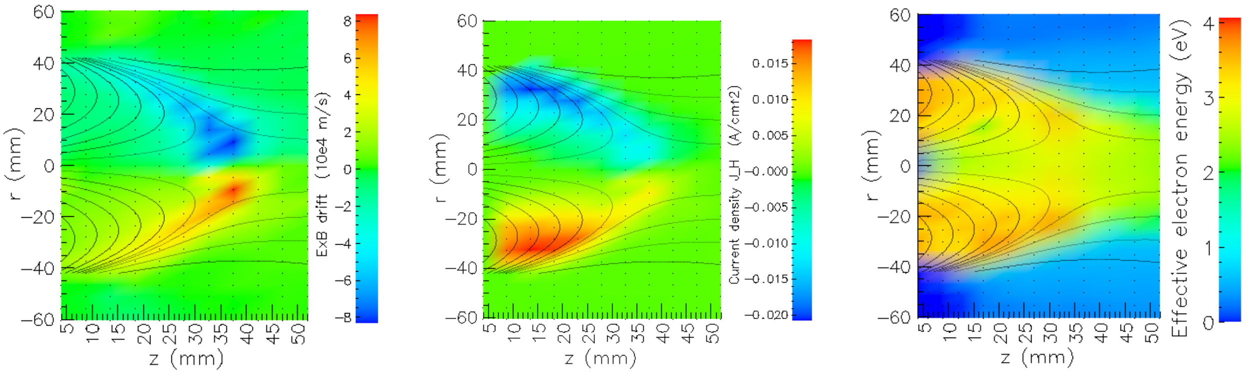

(d) Drift $v_d = -\nabla V_{pl} \times \mathbf{B}/B^2$ **(e)** Drift current $j_H = e \cdot v_d \cdot n_e$ **(f)** Effective electron energy

Fig. 4: Spatial distribution of extracted plasma parameters in r-z plane for discharge at 2.5 Pa; black curves represent the shape of the magnetic field, black points the measurement locations

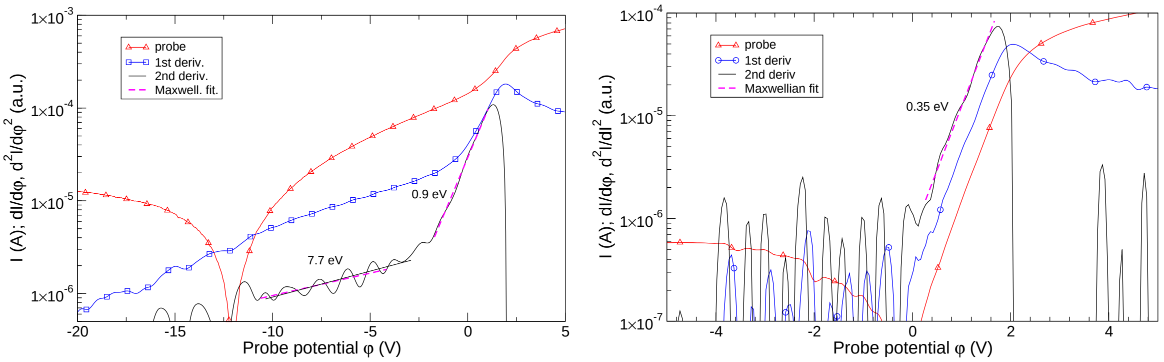

(a) $z = 52\,\mathrm{mm}$, $r = -10\,\mathrm{mm}$: in the plasma beam

(b) $z = 38\,\mathrm{mm}$, $r = -40\,\mathrm{mm}$: background

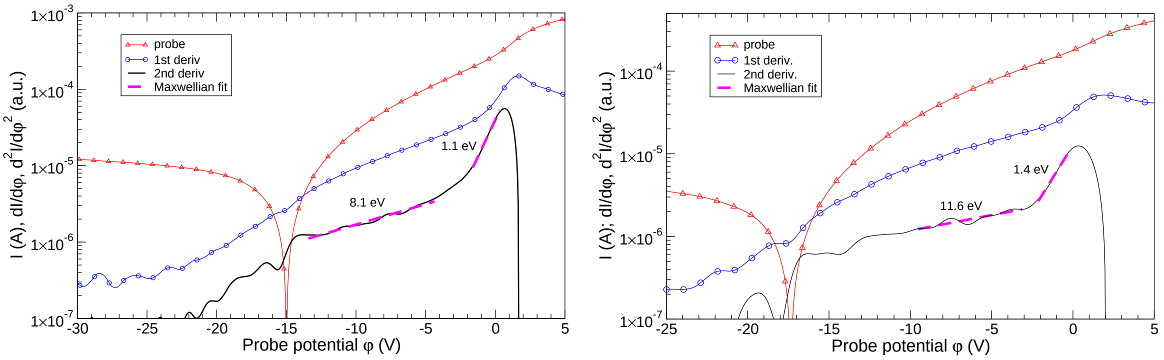

(c) $z = 38\,\mathrm{mm}$, $r = -5\,\mathrm{mm}$: centre near the confined region where the plasma beam begins

(d) $z = 22\,\mathrm{mm}$, $r = -35\,\mathrm{mm}$: edge of the confined region

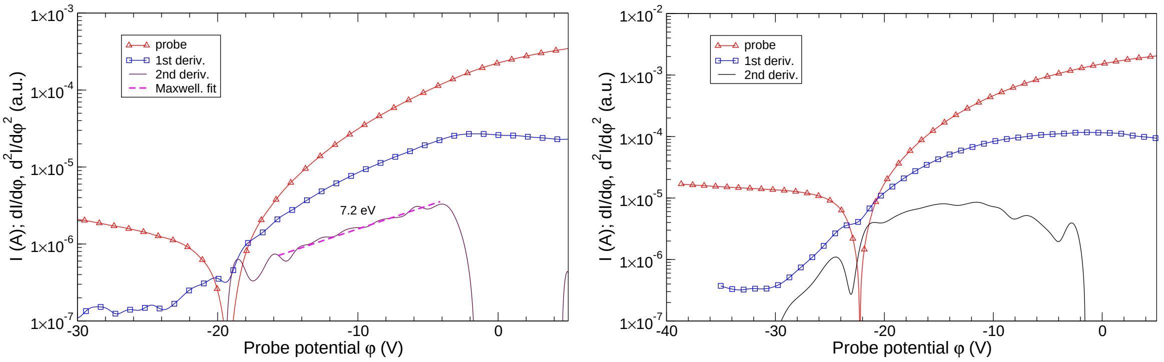

(e) $z = 22\,\mathrm{mm}$, $r = 0\,\mathrm{mm}$: centre inside of the confined region

(f) $z = 22\,\mathrm{mm}$, $r = 30\,\mathrm{mm}$: in the confined region

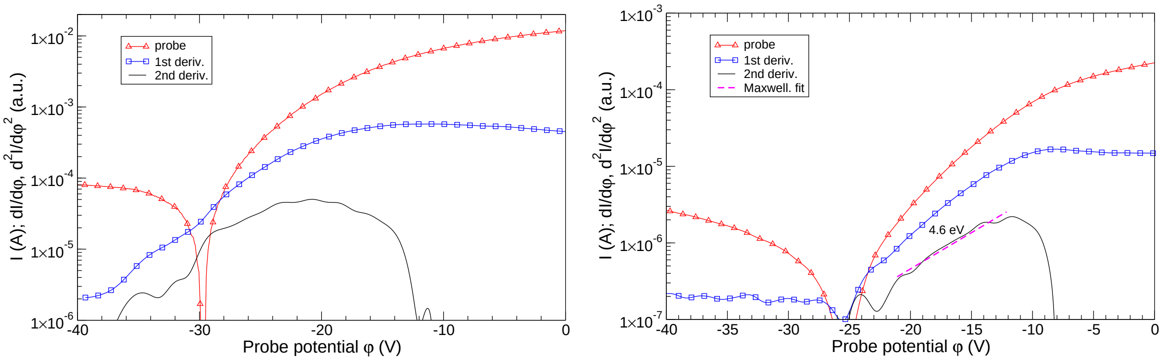

(g) $z = 12\,\mathrm{mm}$, $r = 25\,\mathrm{mm}$: in the confined region

(h) $z = 8\,\mathrm{mm}$, $r = 0\,\mathrm{mm}$: outside of the confined region near the target center

Fig. 5: Semilogarithmic plots of probe characteristic at 0.5 Pa including first and second derivatives and Maxwellian fits where appropriate

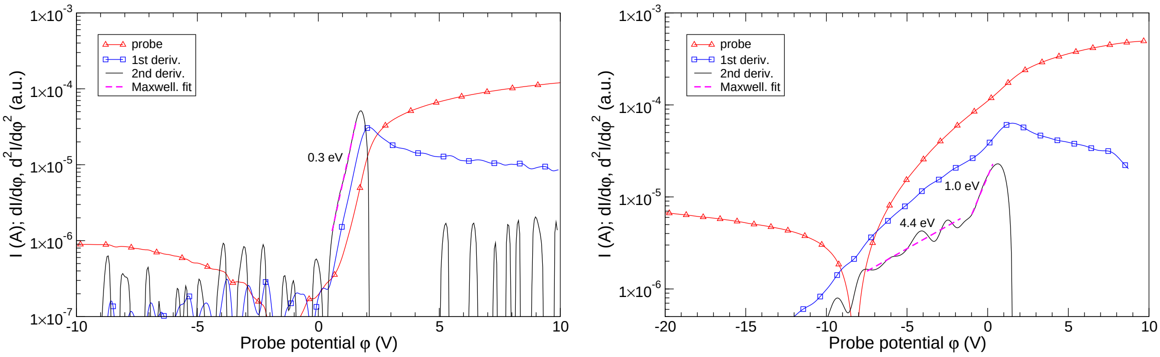

(a) $z = 52$ mm, $r = -60$ mm: background **(b)** $z = 52$ mm, $r = -15$ mm: in the plasma beam

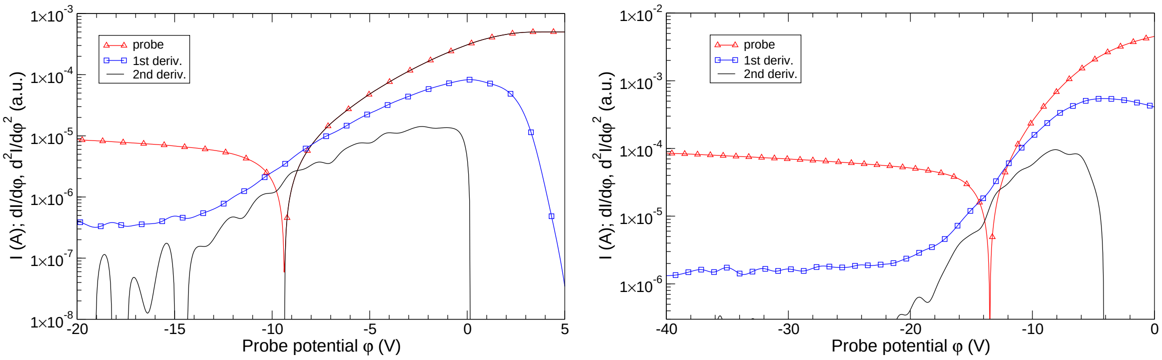

(c) $z = 37$ mm, $r = -5$ mm: centre of the confined region where the plasma beam begins **(d)** $z = 12$ mm, $r = -30$ mm: in the confined region

Fig. 6: Semilogarithmic plots of probe characteristic at 2.5 Pa including first and second derivatives and Maxwellian fits

Acknowledgments

This work was financially supported by *COST 527 / OC 527.60* project. We are also grateful for partial support from the *Ministry of Education, Youth and Sports of the Czech Republic*, research project *MSM 124100004*.

References

[1] P. Špatenka, J. Vlček, J. Blažek, Vacuum 55 (1999) 165–170.

[2] P. Špatenka, I. Leipner, J. Vlček, J. Musil, Plasma Sources Sci. Technol. 6 (1997) 46–52.

[3] J. Bradley, R. Arnell, D. Armour, Surf. Coat. Technol. 97 (1997) 538–543.

[4] J. Bradley, S. Thompson, Y. Gonzalvo, Plasma Sources Sci. Technol. 10 (2001) 490–501.

[5] B. Window, N. Savvides, J. Vac. Sci. Technol. A 4 (3) (1986) 453–456.

[6] S. Kvasnica, R. Fasching, Modeling of unbalanced planar magnetron DC discharge, in: ISPC 15 Proceedings, Orléans, 2001.

[7] T. E. Sheridan, J. Goree, Phys. Rev. E 50 (4) (1994) 2991–2996.

[8] P. Adámek, Measuring system for the Langmuir probe diagnostics of the plasma, in: CO-MAT-TECH Proceedings, Trnava, Vol. I, 2001, pp. 11–16.

[9] I. Ivanov, S. Statev, V. Orlinov, Vacuum 43 (8) (1992) 837–842.

[10] I. D. Sudit, R. C. Woods, Rev. Sci. Instrum. 64 (9) (1993) 2440–2448.

[11] V. Godyak, R. Piejak, B. Alexandrovich, J. Appl. Phys. 73 (8) (1993) 3657–3663.

[12] M. Lieberman, A. Lichtenberg, Principles of Plasma Discharges and Materials Processing, John Wiley & Sons, Inc., 1994.

[13] Open source version of IBM's visualization data explorer. URL `http://www.opendx.org`

PLASMA POLYMERIZATION ON POWDERS FOR NEW REINFORCING FILLERS

E. Vidal-Escales[2], S.K. Lee[1], S. Borros[2], W.J. van Ooij*[1]

[1]Department of Materials Science &Engineering, University of Cincinnati,
Cincinnati (OH) 45221-0012 USA vanooiwj@email.uc.edu
[2] Material Science Lab., GEM-IQS, Universitat Ramon Llull, Barcelona (Spain).

ABSTRACT

Fine particles of inexpensive nanosize fillers have been coated uniformly with thin organic films, thus modifying the properties of the powder in terms of surface energy, reactivity, adsorption power, etc., without affecting the bulk properties of the particles. The plasma polymerization has been performed in order to produce new reinforcing fillers from inexpensive inorganic materials.

INTRODUCTION

For many years carbon black has been the main reinforcing filler in rubber goods. The particular structure, morphology and surface from carbon black are parameters that make this filler the best reinforcing agent. Between others, silica has been the best substitute of carbon black as high performance filler. The use of this filler needs a coupling agent to disperse and better interact with the polymer matrix. However, silica is expensive and the coupling agent increases highly the price of this substitution and reduces dramatically the application field.

For these reasons, in the present work clay has been selected as an inorganic inexpensive material in order to perform as high reinforcing filler. This material has been use previously in the rubber industry, but the low reinforcing properties make it a non-adequate filler. To increase the interaction between the filler and the polymer in the composite, the use of nanosize clay particles is a interesting opportunity. Working in the nanosize field many properties improve just due to the size range.

Nevertheless, as in the case of silica it is necessary the use of a chemical that modifies the hydrophilic surface to a hydrophobic surface compatible with the polymer. In literature could be found some works that chemically modify nanoclay [1-3].

The surface modification of fine particulate matter (powders) by plasma treatment was considered a novel process in 1998 and there was very few literature references on this topic [4]. The reason is that handling of powders in a vacuum environment is extremely difficult. In the present moment many attempts have been performed obtaining interesting and successful results in the lab scale. For example, the surface plasma polymerization of rubber accelerator powders can change their dispersion and reactivity [5]. Also inorganic products as ZnO have been plasma treated to modify the surface hydrophobic properties [6], as well as fillers like mica and silica [7,8]. Concretely, plasma polymerization process allows the generation of polymeric organic homogeneous films on the particles. Even funcionalized surfaces with acidic groups or double bonds between others can be obtained depending on the monomer used and plasma reactor conditions. In our target, this fact present the advantage that an adequate functional group can be a anchor to cross-link the filler surface with the rubber polymer.

Therefore, as plasma polymerization can be performed at industrial scale and it is economically viable for this application, in the present project nanoclay particles will be modified by plasma polymerization in order to develop new reinforcing filler that can be chemically cross-linked with the rubber.

EXPERIMENTAL PART

Ball clay has been dried at 110ºC and introduced inside the down stream plasma reactor. It has been treated by cold plasma polymerization at the following conditions. The plasma has been generated by RF power of 13.56 MHz.

Substrate	Ball Clay	Ball Clay	Ball Clay
Monomer	Pyrrole	Acetylene	Acetylene
Power	40W	30W	60W
Monomer pressure	250 mtorr	370 mtorr	200 mtorr
Treatment time	1 hour	2 hours	2 hours

Table 1. Ball clay sample has been treated at different down stream plasma reactor conditions.

Vulcanization reactions were performed as described in a previous paper [9]. The mixture used is presented in Table 2.

INGREDIENTS	AMOUNT (PHR)
Squalene	100
Carbon black / clay	10
CBS	1.2
Sulfur	2
Zinc oxide	5
Stearic acid	2

Table 2. Vulcanization mixture composition.

After the plasma treatment and vulcanization reaction, the clay particles were examined by using Time-of-Flight Secondary Mass Spectrometry (TOFSIMS) and High Performance Size Exclusion Chromatography (HPSEC).

The TOFSIMS analyses were performed on an ION-TOF Model IV instrument. The HPSEC analyses

RESULTS AND DISCUSSION

As discussed in the introduction, the objective of this project is to obtain a reinforcing filler using nanoclays. In a first attempt it has been decided to work with nanosize particles that are aggregated in microsize clusters because it will be studied the plasma surface modification and the substrate size will not be important in this step of the project.

After treatment, treated and untreated clay particles were analyzed by SEM. Result show that the plasma treatment had not affected the clay structure. The surface was analyzed by SIMSTOF observing clear differences due to characteristic fragments coming from the polymeric film generated on the surface. Then, while the structure had not been modified, the clay surface has changed its nature.

To better understand the nature of the new surface chemistry and performance in contact with vulcanization agents and rubber, model compound vulcanization was performed using squalene as model molecule of natural rubber. After the vulcanization, the filler was washed gently with organic solvent and only adsorption products remain on the surface. Figure 1 shows a negative ions TOFSIMS analysis of cleaned carbon black surface after 45 minutes of vulcanization in squalene. It can be observed a high intensity peak at 134 a.m.u. that confirms the adsorption of accelerator or accelerator by-products on the filler surface. This adsorption behavior has been also observed in the other studied fillers.

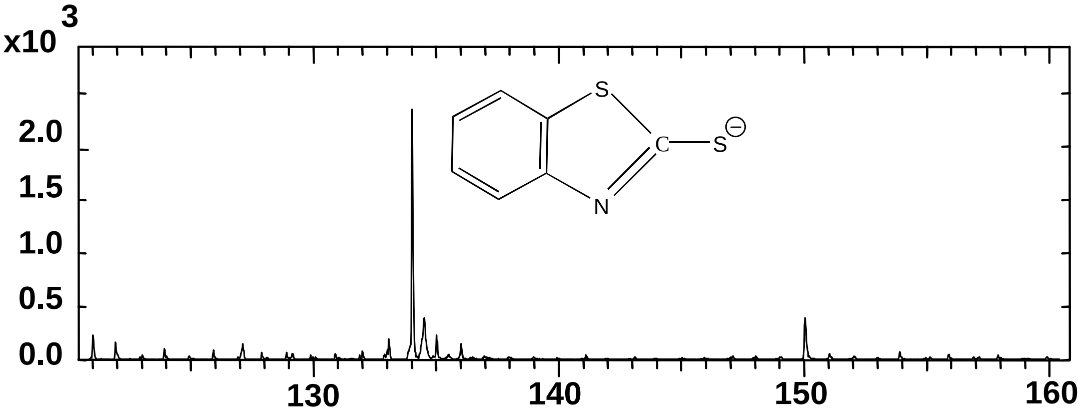

Figure 1. Negative TOFSIMS spectra of carbon black surface after 45 minutes of vulcanization reaction. 134 peak corresponds to the accelerator fragment presented.

When the intensity of this peak is plotted during vulcanization time for carbon black and clay, clear differences in the behaviour are observed. Then, this behaviour related with adsorption and other kinds of interactions of the filler surface with vulcanization chemicals will be use as a characteristic to direct the design of following plasma polymerized polymers. Then the first step will be to have the behaviour closer to carbon black when clay is used.

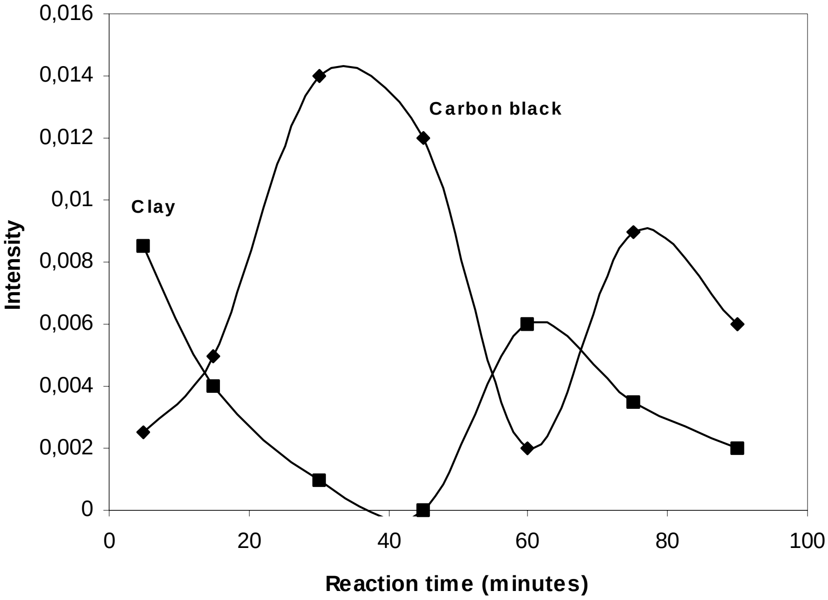

Figure 2. The evolution of the accelerator fragment on carbon black surface and clay is completly different.

For example, in the following figure it could be observed that the behaviour working with 30W acetylene treated clay is closer to carbon black than untreated clay. In addition, it could be understood how the plasma conditions could affect the final polymer obtained. While working at 30W it was obtained a reactive surface, at 60W the accelerator fragment profile has changed clearly due to a less reactivity and interaction. The higher RF power, the lower functional groups on the surface is obtained for these monomers.

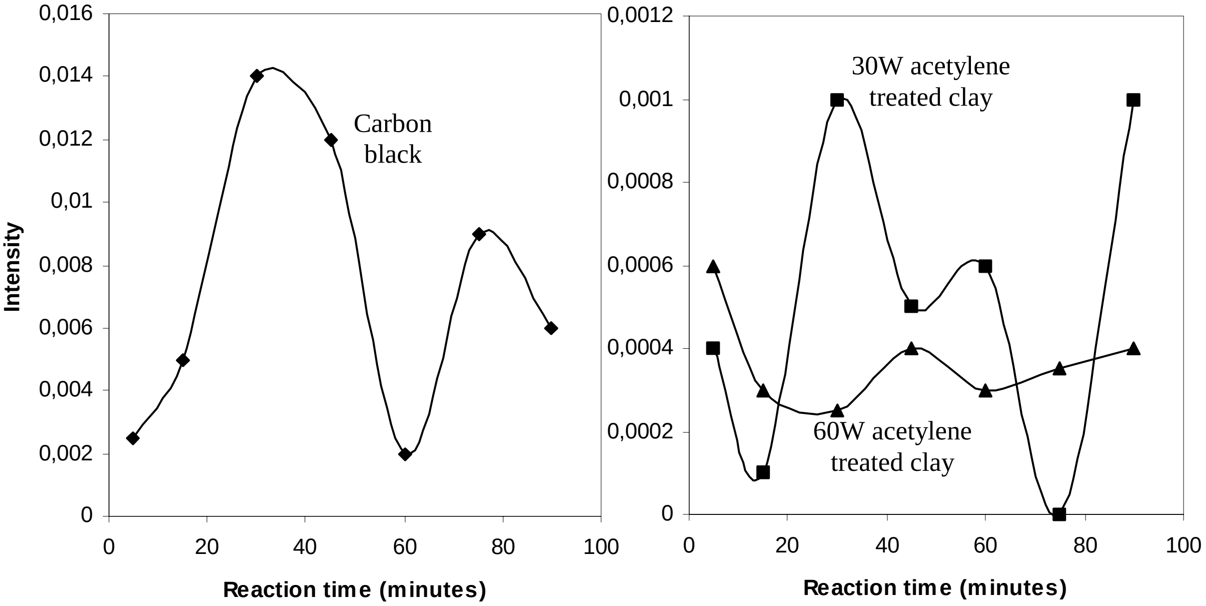

Figure 3. Despite the accelerator adsorption is much higher for carbon black, the most reactive surface generated (30W, acetylene) has a closer behaviour to carbon black.

Studying the effect of the plasma treatment on the vulcanization mixture, it can be observed some differences as in the previous example. HPSEC chromatography allows following the cross-linked and modified structure of squalene during the vulcanization. Concerning to cross-linked squalene (figure 4), the results show a fast vulcanization due to the presence of clay in the reaction mixture. It accelerates the process due to the high polar component of the inorganic filler [10] compared with carbon black. Carbon black has a lower reactivity related with the start of cross-linking. However, cross-linked squalene reaches a higher concentration than working with clay as filler. The plasma treated clays have different behaviors. The ones less reactive (pyrrole and acetylene at 60W) have a similar behavior to carbon black but the cross-link concentration is lower than for carbon black. The most reactive, acetylene treated clay (30W), has a behaviour between clay and carbon black. This behavior is due to two effects: First, the treatment avoids the effect of clay on vulcanization (less reactive). Second, the double bonds formed on the new surface (from acetylene) activate the vulcanization. The last treatment discussed seems to be the best treatment presented in this work.

Another parameter used in this application is the modified squalene evolution. In figure 5, the modified squalene increases in all cases reaching the same value for all the fillers. First is reached by the clay, and the last one by the carbon black. All the plasma treated clays react between clay and carbon black as discussed for the cross-linking.

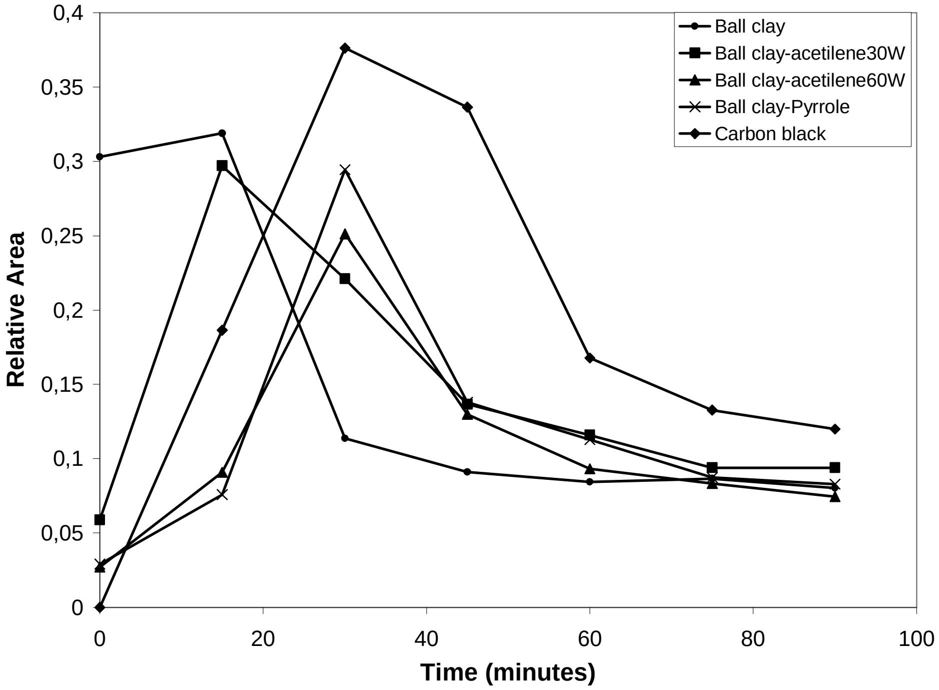

Figure 4. Following the vulcanization of squalene, HPSEC results show that the cross-linked squalene formation depends on the filler and also on the plasma treatment.

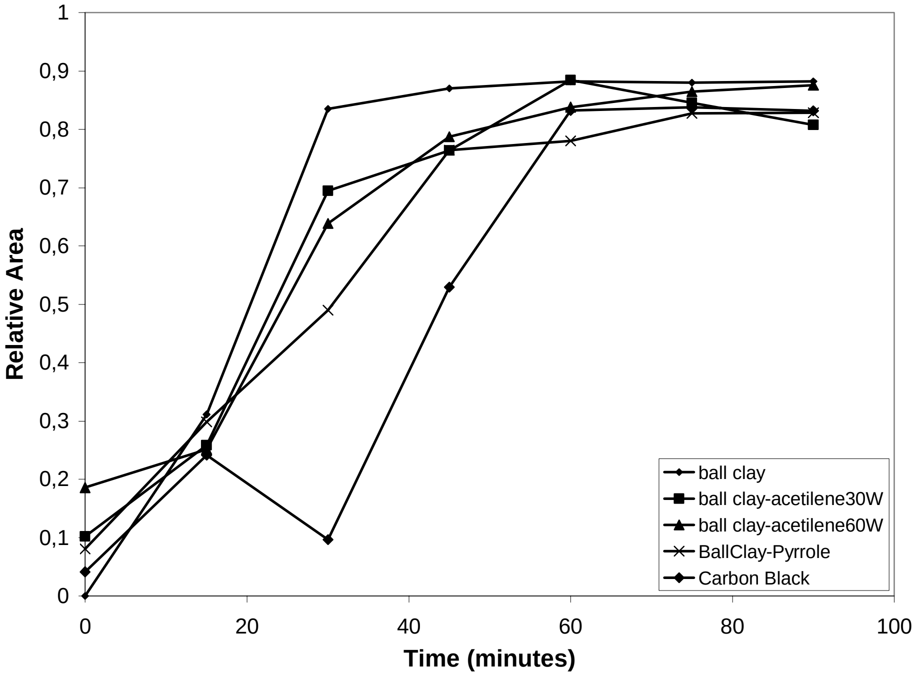

Figure 5. Modified squalene is followed in reaction time. Treated clays have a behaviour between clay and carbon black.

CONCLUSIONS

The treatment of clay by plasma polymerization with a down stream plasma reactor and the study focused on the effect on vulcanization and accelerator adsorption on the filler surface shows the possibility of modifying the surface of inexpensive fillers in order to create a new concept of reinforcing fillers. The change of plasma reactor parameters as monomer of RF power and consequent changes in the polymer film reactivity ensures the future improvement of this fillers.

REFERENCES

[1] A. Oya, Y. Kurokawa and H. Yasuda, Journal of Materials Science, 35(5), 1045 (2000)
[2] M. Laus, M. Camerani, M. Lelli, K. Sparnacci, F. Sandrolini and O. Francescangeli, Journal of Materials Science, 33(11), 2883 (1998)
[3] Y. Li, G-X. Wei and H-J. Sue, Journal of Materials Science, 37(12), 2447 (2002)
[4] W.J. van Ooij, Ning Zhang, Sheyu Guo and Shijian Luo, Presented in the “Functional Fillers and fibers for plastics 98” meeting, Beijing (China) 1998
[5] E. Vidal, S. Borrós, N. Agulló and W.J. van Ooij, Gummi Fasern Kunststoffe, 54(5) 330 (2001)
[6] D. Shi, P. He, J. Lian, L. Wang, W.J. van Ooij, submitted to J. Mat. Res. (2002)
[7] A. Bialski, R. Manley, M. Wertheimer and H. Schreiber, Polymer Prints, 16, 70 (1975)
[8] H. Schreiber, M. Wertheimer and M. Lamba, J. Appl. Polym. Sci., 27, 2269 (1982)
[9] S. Borros, E. Vidal, N. Agullo and W.J. van Ooij, Kautschuk Gummi Kunststoffe, 53(12), 711-715 (2000)
[10] E. Vidal-Escales, PhD thesis, Universitat Ramon Llull, Barcelona, Spain (2003)

SOME NEW PROBLEMS ASSOCIATED WITH PLASMA CHEMISRY OF ACTIVATED AQUEOUS SOLUTIONS

E.V.Ihsanov*, V.V.Kuznetsov**, S.V.Medvedev***, A.V.Prihodko***, A.G.Sokolskiy**

* *Atirau Engineering-Humanistic Institute, Kazahstan*
** *Russian firm "Technosystema-ECO", Moscow*
*** *Moscow State Aviation Institute*
E-mail: a-sokolsky@mtu-net.ru

During the solving of problems of the results of plasma activation of aqueous solutions there is a deficiency of computer mathematical models (theories), which quantitative describe proper objects, simultaneously for methods of diagnostic and for models of structure of the final product.

This paper contents the description of two new nonlinear "mechanistic" models, using nonlinear dynamics methods in nonstationary problems of plasmachemical activation of aqueous solutions:

1) for the motion of molecular H_2O_2 in outer force field induced by cluster environment of H_2O molecules (on the base of hamiltonian approach - [4,5]); the formation of H_2O_2 from H_2O we proved on the base of spectral experiments.
2) in form of the nonautonomous resonance hamiltonian system for the phenomena of nuclear magnetic resonance used for diagnostic of plasma activated aqueous solutions; main idea - the nonlinear generalization of F.Bloch equations [1] and using modern nonlinear theory of parametric resonance [1] and its computer realization [2,3].

Main references:

1. A.Abragam. The Principles of Nuclear Magnetism.//Oxford Press, 1961.
2. A.P.Ivanov, A.G.Sokolsky (in Russian). //J. of Applied Mathem. and Mech.,1980, vol.44, No 5, pp.811-822 and No 6, pp.963-970.
3. I.I.Shevchenco, A.G.Sokolsky. //Computer Physics Com., 1993, v.77, p.11-18.
4. A.G.Sokolsky. //Cel. Mech., 1978, v.17, p.373-394.
5. I.G.Wittenburg. Dynamics of Systems of Rigid Bodies. //B.G.Teurner, Stutgart, 1977.

This work was supported by Russian Foundation for Basic Researches.

On the possible mechanisms of enzymes activation changes at their pulsed X-ray irradiation

A.V. Dubrovsky[1], I.G. Gazaryan[2], V.A. Gribkov[1&3], O.A. Kost[2], M.A. Orlova[2], N.N. Troshina[2]

[1]*Institute for Theoretical and Experimental Physics, B. Cheremushkinskaya 25,* *adubrov@mail.ru*
[2]*M.V. Lomonosov Moscow State University, Leninsky Gory, 119899, Moscow,* *orlova@radio.chem.msu.ru*
[3]*Institute of Plasma Physics and Laser Microfusion, 00-908 Warsaw, Poland,* *gribkovv@comail.ru*

Abstract

Dense Plasma Focus with a miniature chamber is a new source of X-ray radiation of extremely high brightness. It can produce an irradiation of the whole volume during a characteristic time of chemical reactions. The irradiation of biological objects by ionizing radiation, primarily by X-ray photons with low dose but high dose power, i.e., high power flux density, can result in synergetic effects - activation of enzymes at a very low absolute value of the dose. The hypothesis on a possible explanation of the effect is based on a saturation effect.

1. Introduction

Dense Plasma Focus (DPF) devices with miniature chambers became available recently [1]. This apparatus belongs to a class of gas-discharge devices of the Z-pinch type. It can generate X-rays (both soft and hard – SXR and HXR), plasma jets, fast ion and electron beams, and neutrons as well.

The present report relates to a DPF-based source of soft and hard X-ray radiation, basically to sources suitable for X-ray pulsed radiobiology. It also can be utilized in medicine and semiconductor industry.

At this time for the above applications mainly two classes of sources are discussed as potential candidates for the industrial usage – the multi-beam synchrotron radiation source and the single-beam sources of certain types. The first one operating alone with about 20 workplaces and having excellent beam characteristics yet has several disadvantages in comparison with the second one. At first it is very expensive. Also it belongs to a class of low power X-ray sources, thus having its own niche in the radiobiology.

Between pulsed one-beam devices for X-ray generation (X-ray tubes, higher laser harmonic generation, X-ray lasers, laser produced plasma, pinch devices, high-current accelerators, e.g. of the Febetron or Angara types, and so called ‘laser synchrotron source’) namely Dense Plasma Focus at present moment looks to be the most attractive one. It can be small and cheap and has higher efficiency in a soft X-ray production in comparison with laser-produced plasma. It has small radiation source size and its design is more compact if compared with the pinches of various types. This device generates X-ray photons of wide energy range – from a hundred eV up to a few MeV. These features coupled with a wide spectrum of radiation distinguish the DPF from the “Febetron” type facilities [2], which are currently used in radiation chemistry and biology.

On the level of circa 1 kJ the DPF is rather compact, the X-ray source is small enough, and the DPF chamber can be easily attached to the auxiliary apparatus. A high repetition rate mode of operation can be organized here. The miniature chambers deliver an opportunity to approach the source of the above radiation very close (circa 1 cm). And these small DPF may demonstrate the highest possible efficiency, which can be in principle above 10% for soft and about 1% for hard X-ray correspondingly [1,3]. Taking into consideration also, that the pulse duration of the radiation is a few nanoseconds, all these characteristics give a possibility to reach a very high power flux density at an irradiated sample. Their constructions easily can be fitted to goals of radiobiology, as well as for microlithography and micromachining.

Attempts to increase its X-ray yield by increasing of an energy storage system will result in the cumbersome design of its chambers. They will also increase a size of them thus increasing a distance attainable for sample positioning. Thus DPF capacitor bank energy storage from 0.1 through several kJ is optimal for the applications of our interest.

Classical radiation biology, the radiation treatment of patients, and even “pulsed radiation chemistry” [4, 5] usually deals with “weak” beams of radiation (low power flux density) and operates by terms of “doses” (D). In this case only the *absolute number of ionizing particles or photons* interacting with the object is important. The primary assumption is that each fast particle or hard photon interacts with the object independently from the others. But as for ideal conditions, pulsed radiation biology should operate with “instantaneous” flashes of radiation. However, it is physically impossible to produce instantaneous pulses. Strictly speaking the term “flash radiation biology” would be applicable to the interaction of the beams with objects, provided that the time of this interaction (the beam pulse duration) is *short compared with the duration of a corresponding specific biological process*. As a result, we must take into account a dose power ($P \sim D/\Delta t$, where Δt is a pulse duration) as well.

We shall operate now with beam energy and power flux density of the irradiating beam at the target, which are the physical characteristics of a source. Taking into consideration mean free path of the X-ray beam photons within a biological tissue, we shall eventually discuss the problem in terms of a concentration of fast particles within the biological object during the irradiation process. In other words, we shall analyze the beam’s influence in terms of absorbed dose and dose power simultaneously, which are the ‘chemical’ characteristics of the source.

We shall show that under certain conditions the effect of short-pulsed irradiation of an object will have the essentially non-diffusive character on initial stages, and it may be accompanied by synergetic (collective) effects. The final result will be formed by 2 stages – this “instant” volumetric creation of active products of water radiolysis and their subsequent classical transformation and diffusion.

The most important point is that during irradiation, a concentration of “effective interaction volumes” (spurs and blobs) with characteristic size about one mean free path of active particles should be sufficiently dense to allow micro-volumes to overlap each other. And as it was mentioned above, this condition should be realized *during a time interval* (radiation pulse duration)*, which is less compared with the corresponding biochemical process*.

The non-stationary development of biochemical processes has to be counted as an intrinsic feature of perfect flash radiation biology. For the above conditions two issues become important. Do these photons or fast particles, when compressed in time and space to the proper degree, result in a mutual *collective* action? Will this condition result in catastrophic consequences for the object at an overall dose much lower than the upper classical allowable limit? In this work we resume our previous investigations of enzyme activation/inactivation by pulsed ionizing radiation [6] produced with the Dense Plasma Focus device.

2. Apparatus

The transportable source PF-2 (2 kJ) comprises of the following main parts – a capacitor bank, a charger, pseudo-spark switches (PSS), a master trigger (NMS), two pumps, cooling system and a DPF chamber. The device PF-0.2 (0.2 kJ) has the same but more miniature systems making the source portable (~15 kg).

Master trigger switches, based on pseudo-spark gaps, have its rise-time and jitter less than electromagnetic transit time between capacitors and the discharge breakdown time. It ensures the initial phase of the breakdown in the DPF chamber more symmetrical and provides the safeguard for the capacitors. The DPF chamber (Fig. 1, all dimensions in mm) works with D_2 and noble gases filling (Ne, Ar etc.) separately or in a mixture. Both its electrodes are water-cooled. It provides a possibility to work with a rep rate more than 3 Hz and prevents a destruction of the electrodes by plasma, electron and X-ray beams, as well as by high current. Functioning with different initial gas pressures – below a certain limit and above that limit - delivers two distinct DPF chamber regimes. The first one in case of neon is characterized by the SXR radiation source having a shape of a single bright X-ray spot with the dimension less than 10 micrometers. In case of D_2 filling an output of hard X-rays is strongly increased. The second regime demonstrates a pinch-like structure of the diameter about 300 micrometers for neon and 1 mm for deuterium. The above features of the DPF design provide an increase of the X-ray yield by 1-2 orders of the magnitude in comparison with the conventional DP Foci in both cases. These features ensure the source to be sufficient for goals of pulsed radiobiology in the above defined sense.

For different experiments in radiobiology one needs different wavelengths of the X-ray radiation. In the soft and medium X-ray energy range it will be mostly ruled by the working gas used and by a central anode insert. Ne gives a luminescence with soft X-ray photons energy mostly concentrated near 1 keV [3], whereas Ar gives the 0.4 nm-centred radiations [1]. Some metals as well as alloys and pseudo-alloys demonstrated good operation being used for the anode central insert. E.g. copper can help to produce strong K_α radiation with photon energy around 9 keV with efficiency up to 1%.

Numerous tests of both devices have shown the following advantages, which are important for radiation biology:

- very short pulse duration of the soft as well as hard X-ray radiation (Fig. 2) lying in the range of several ns;

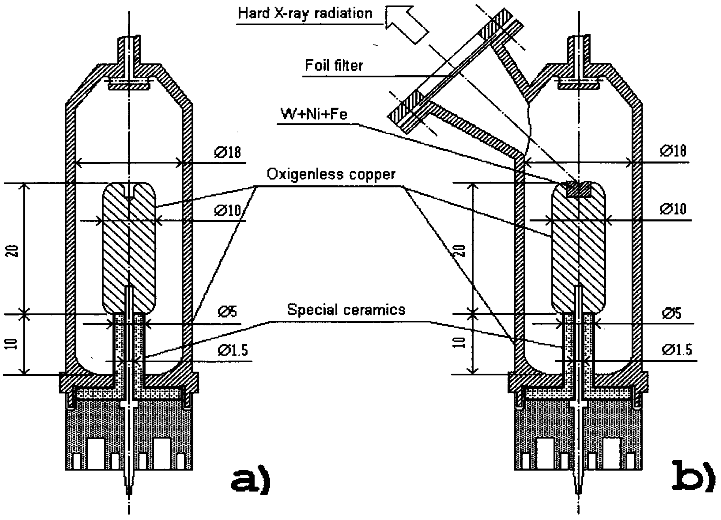

Fig. 1. Miniature chambers of 0.2 kJ DPF: a) HXR/n source with a copper anode and b) same with an alloy insert

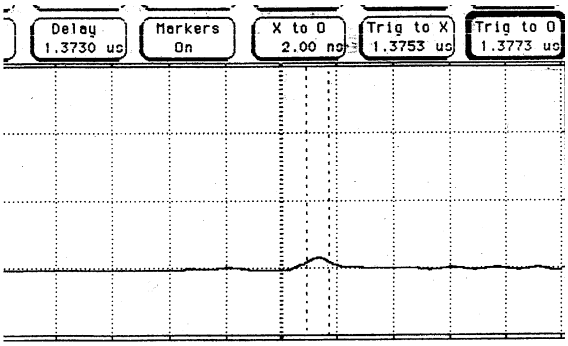

Fig. 2. Oscilloscope trace of SXR+HXR signal from PF-0.2

- in the low pressure mode of operation the SXR source is a bright point with dimensions less than 10 μm, whereas at the high pressure mode there is a pinch with the diameter of about 300 μm;
- with D_2 our PF-0.2 device produces high enough yield (up to 0.2 J) in HXR (9 keV of Cu K_α plus ~50 keV).

3. Materials and experiment

The search for an optimal ratio between dose and dose power in the field of radiation biology is important because of the possible applications of the DPF in medicine. Indeed, for safety reasons, a high dose power device at low absolute dose such as a DPF might be used for X-ray diagnostics. In the opposite case, such a device can be exploited for low-dose radiotherapy. Now we'll describe our experiments on irradiation of several types of enzymes *in vitro* using several sources of hard radiation with differing dose, dose power and spectrum. These experiments are a continuation of our previous work [6].

3.1 *ACE* We irradiated an isolated and purified electrophoretically homogeneous ACE (MW 180 kDa) from bovine lungs. The enzyme contained circa 98% of active molecules as determined by stoichiometric titration with a specific competitive inhibitor. ACE enzymatic activity was determined with 10^{-5} M carbobenzoxy-L-phenilalanyl-L-histidyl-L-leucine (Cbz-Phe-His-Leu) (Serva) as a substrate in 0.05 M phosphate buffer, pH 7.5, containing 0.15 M NaCl, 25°C, using o-phthalaldehyde modification of His-Leu as a reaction product.

3.2 *Peroxidases* Native horseradish peroxidase C (HPR, MW 44 kDa) purchased from Biozyme, and recombinant wild-type HRP (MW 34 kDa) produced from *Escherichia coli* inclusion bodies by the method developed by us earlier (see ref. in [6]). The measurements of peroxidase activity performed with 2.2`-azinobis(3-ethylbenzothiazoline-6-sulfonate) (ABTS) as substrate using Shimadzu UV 120-02 spectrophotometer (Japan) at 25°C by the following method:

0.05 mL of ABTS solution (8 mg/mL) and aliquot of the enzyme were added to 2 mL of 0.1 M Na-acetate buffer (pH 5.0); the reaction was initiated by the addition of 0.1 mL of hydrogen peroxide (100 mM). A molar absorptivity of ABTS oxidation product was taken equal to 36800 L/mol/cm at 405 nm.

3.3 *Irradiation* We have used several sources of X-ray radiation in the dose range 10^{-6} through 10^{2} Gy within dose power limits 10^{-2} … 10^{6} Gy/s, determined by an exposure time (isotopes) or a number of shots (DPF):

- *Standard γ-source ^{137}Cs*: $E_{h\nu,\, max}$ = 662 keV, D = 0.1…200 Gy, $P_D = 5\times10^{-2}$ Gy/s (from seconds till hours)
- *Standard medical X-ray tube* working in 3 regimes: U_{tube} = 50.0, 60.0 and 90.0 keV, $E_{h\nu,\, max} \leq$ 35.0, 40.0 and 60 keV correspondingly, pulse duration ~ 0.1...1.0 s, number of pulses at a séance – 1…10, $D = 10^{-4} - 10^{-1}$ Gy
- *Isotope calibration β-source* of DRG3-01 (Sr-Y) with the X-ray energy spectrum in the range of 8…2000 KeV at various time periods lasting from minutes till hours; its dose power is much less than 10^{-3} Gy/s
- *Miniature DPF device "PF-0.2"*: energy storage - 100 J, $E_{h\nu,\, max} \geq$ 0.1…100 keV, X-ray pulse duration – 2 ns, X-ray yield ~ 0.1…1.0 J/shot, $D = 10^{-6} - 10^{-3}$ Gy/shot, neutron yield ~ 10^{6} n/pulse (E_n = 2.45 MeV)
- *Medium-size DPF device "PF-2.0"*: energy storage - 2.0 kJ, $E_{h\nu,\, max} \geq$0.1…200 keV, X-ray pulse duration ~ 10 ns, X-ray yield ~ 1.0…10.0 J/shot, $D = 10^{-5} - 10^{-2}$ Gy/shot, neutron yield ~ 10^{8} n/pulse (E_n = 2.45 MeV)

Both DPF sources were used at various distances and with one to 100 times irradiation ('shots') per séance for a specimen, with two types of X-rays filters – Al and Cu foils, and with two types of *n/γ* filters – transparent for X-rays and opaque for neutrons or – in contrary – transparent for neutrons and opaque for X-rays.

The irradiation was performed at 18-20ºC. The absorbed dose was determined by thermo-luminescent detectors based on LiF activated with Mg, Cu, and P with a help of analyzer Harshaw TLD system-4000. X-ray spectrum of sources and its pulse shape in the case of DPF were monitored by filter method [7, 8]. Detectors in these measurements were a Roentgen-γ dosimeter 27040 (Germany), calibrated X-ray films, photomultipliers SNFT (Russia) with plastic scintillators (2-ns time resolution), and individual dosimeters (gas-ionizing chambers).

4. Results

Typical results of radiation-induced changes in enzyme activity are illustrated in Fig. 3. Because of the broad energy range of the experiments, we present only the most representative points taken from the original curves and subsequent experiments. In two cases – irradiation by ^{137}Cs and DPF sources – we have registered activation and inactivation of enzymes as well. When irradiated by X-ray tube, a small inactivation of enzyme have been found in two séances only in one regime, namely when we have used the lowest voltage on the tube (50 kV). Our experiments with *β*-active isotope source have given negative results (no change in enzyme activity) in spite of the fact that we have overlapped the range of doses $10^{-5} - 10^{-2}$ Gy. In all regimes, the activity changes appeared to be irreversible – at least for several days. The main differences between changes in activity of the enzymes irradiated by isotope ^{137}Cs γ-sources (a&b) and the ones illuminated by PF-0.2 (c) are as follows:

- Although the amplitudes of the activity changes are about the same in all cases, the changes are measurable in the Cs-source case only at doses above 1.0 Gy. In the DPF case, however, irradiation is registered at a dose less than five or six orders of magnitude. But the dose power in this case was 4-5 orders higher.
- When the dose was decreased below the above 2 critical levels (isotope – lower than 10^{-1} Gy, and DPF – lower than 10^{-5} Gy) no changes in enzyme activity were detected.
- As expected, an increase of dose in the case of isotope irradiation was resulted in the complete enzyme inactivation. Contrary to that, the dose increase under the DPF irradiation during one shot – by 1…2 orders of magnitude – shows that the activity of both enzymes does not change, i.e. became the initial one.

To clarify the situation, we have undertaken several additional experiments. At first, we checked the influence of neutrons on the results by using of special filter. This did not show any appreciable effect of neutrons on the activity of enzymes in this case. Second, in case of the use of classical X-ray tubes for irradiation in the dose range of 10^{-5} through 10^{-1} Gy the only exception was found when we have made irradiation at the lowest voltage at the X-ray tube (50 kV). In this case in two experiments we have found the weak peak of the same character. Third, we changed the X-ray dose from the DPF source in ten times by increasing the distance from the source (PF-2.0 in this case) to the specimen (likewise for the dose power as the pulse duration was not changed). At the same time we increased a number of shots. However, the effect appears at a dose of 100 times greater – not 10 times higher as it was expected (at about 2×10^{-4} Gy) than in the case of higher dose power. Finally we have found that at changing the Cu filter into the Al one all attempts to repeat the above results have been failed.

a) **b)**

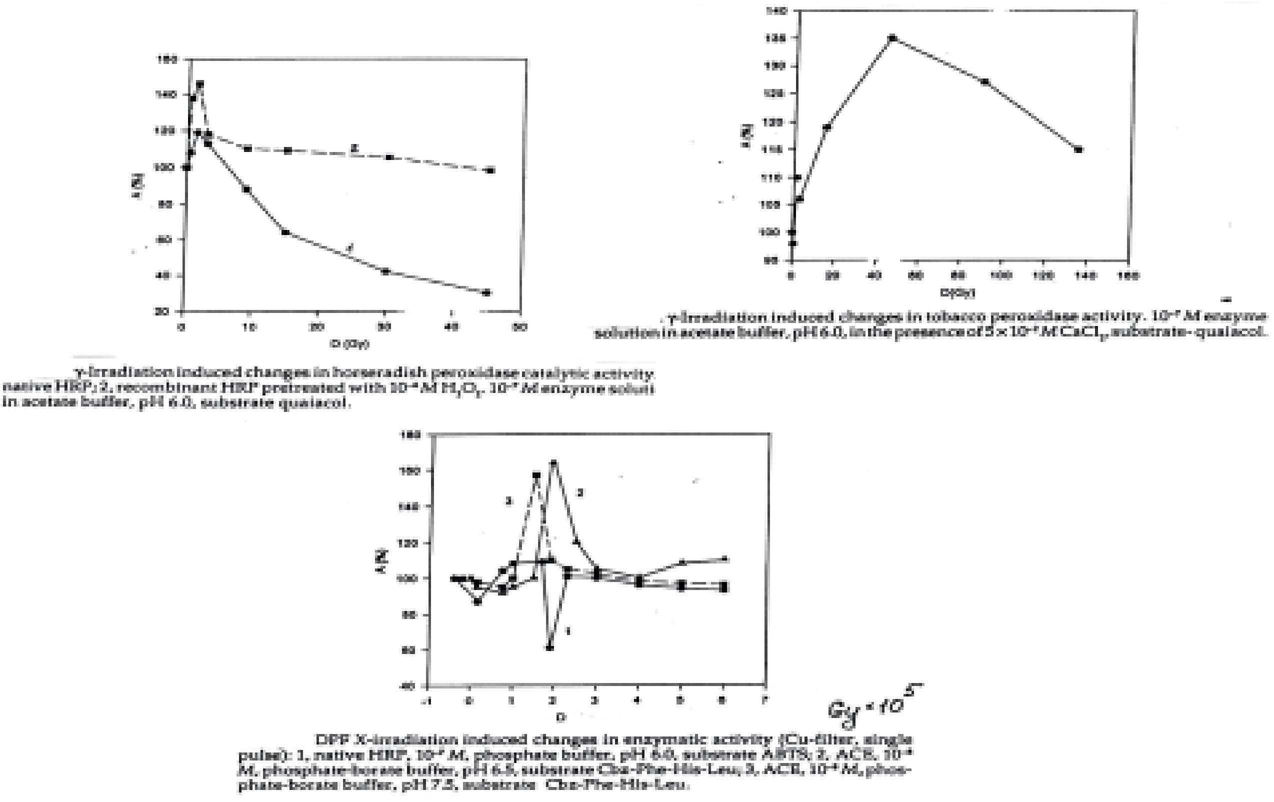

c)

Fig. 3. Low dose high power X-ray enzyme activation [5].

5. Discussion

To deduce any conclusions we must take into consideration a number of important conditions of our experiments. The overall spectrum of X-rays, generated by accelerated electrons at their dissipation on the anode, in our case of relatively thick foils at the output window, consists of two parts. The first is a bremsstrahlung (a high energy component with a peak near 30 keV). Its spectrum has a power-like law decreasing in the high-energy wing. It possesses quite low efficiency (circa 0.1%). The second one has a peak with the efficiency of ~1% near the photon's energy of 9 keV. The highest brilliance is represented here by Cu K_α line [7]. The difference in the radiation spectra in the two cases – Al-foil filter and Cu-foil filter – is due to the Cu foil having a "window of transparency" – *K*-edge – at circa 9 keV in a scale of photon energies. The Al filter contributes nothing in this low-energy wing, whereas it is about the same in the range above 18 keV.

The enzymes with the strongest activation/inactivation effects had atoms of Zn or Fe in their structure. The spectral absorption curves of Zn and Fe atoms overlap with the Cu *K*-edge curve. Therefore it is reasonable to suppose that a presence of an atom of Zn in *ACE* and of Fe in *HRP* might favor the above activity oscillation. However it is not all. The thickness of the enzyme solution layer under irradiation (3 mm) was about the mean free path of the 9 keV photons (~1 mm). But it is considerably lower than the mean free path of 30-keV photons (peak of the high-energy component) and much lower than the 662-keV X-ray photons from the ^{137}Cs source. As it is well known [4], X-rays below 1 MeV spend almost all its energy on the creation of spurs (size about 10 nm) and blobs (about 100 nm). For X-ray photons below about the 5-keV limit mainly blobs are produced.

Electrons produced by X-ray photons in cases of the isotope source (662 keV) and the DPF's hard component (30-100 keV) are of the Compton nature. The 9 keV photons produce primarily photoelectrons. When these electrons penetrate water solutions they never create δ-electrons with the energy more than 1 keV (main part of them has energy of the order of the ionization potential of the water molecules) [4]. It is easy to estimate the mean distance between blobs (in the case of 9 keV photons) and spurs (in the cases of hard component of DPF and isotope γ-quanta). In the case of the copper foil this distance is equal or less than the blob size. This implies that our ionization zones are overlapped. Furthermore, this overlapping takes place during the pulse duration, which is on the order of the time intervals (10^{-12} – 10^{-8} s [4]) of the creation of water radiolysis products. However, it is much less than the end of reaction with radicals (10^{-6} s [4]).

Therefore *all the products instantly* start to diffuse and interact predominantly with the *exited giant* enzyme molecules (not with each other). The interaction of the above products likely must result in conformation changes of the molecule.

Just opposite situation takes place in the case of hard X-ray components. It is extremely unlikely that a very long pulse of low intensity could produce an excitation of these Zn or Fe atoms when an individual track of a fast electron crosses a site of an enzyme molecule in a presence of a radical in the vicinity of it. That is why we need much higher dose (much larger statistics) in this case to reach the necessary coincidence.

The most difficult phenomenon to understand is the disappearance of the effect with an increase in dose, which takes place at high-power irradiation. It is particularly interesting to plot the data of Fig. 3 in dependence of the parameter *PD*. It appears that in such a graph all our peaks for pulsed sources having low energy X-ray component will be collected around $PD \approx 10^{-2}$ Gy^2/s. Just contrary to it ^{137}Cs isotope-based source will produce the effect only at this parameter of two orders of magnitude larger. Given that a well-documented explanation of the low-dose effect is currently absent, the authors wish to propose the following hypothesis.

It seems clear that for the effects presented in Fig. 3c) from one side and 3a), b) from the other side the main difference lies in the dose power. It is quite possible that any dose increase above a certain critical level will result in an effect known in laser physics as the saturation effect of a two-level system at its high photon pumping [9]. We suppose that a large number of possible conformation states of the initial enzyme molecule exist in chemical equilibrium that has numerous experimental confirmations. Under irradiation, a shift of equilibrium might take place, particularly in the direction of a super active state. At the high-power source (DPF), with the power increase, the balance between activation and inactivation processes might be reached. This will result in the saturation of conformation changes and eventually in the insensitivity to a low-dose radiation. In the case of a low power source such as ^{137}Cs, this effect is impossible. But prolonged irradiation increases the dose, what finally leads to a complete destruction of the molecule. Only in the case of an ‘intermediate’ dose and within a certain (high!) dose power range – shall we have such an effect. It is clear that to verify or refute this hypothesis many experiments should be conducted.

References

[1] V.A. Gribkov, E.P. Bogoljubov, A.V. Dubrovsky, Yu.P. Ivanov, P. Lee, S. Lee, M. Liu, V.A. Samarin – Proc. of the IAEA International Conference on Research in Use of Small Fusion Devices, Cheng-do, P.R. of China (2001) (to be published)

[2] S. Karolczak, D.C. Walker, Radiat. Phys. and Chem., **10** (1977) 139-150

[3] S. Lee, P. Lee, G. Zhang, X. Feng, V.A. Gribkov, M. Liu, A. Serban, and T.K.S. Wong - IEEE Transactions on PLASMA SCIENCE **26**, 4 (1998) 1119-1126

[4] A.K. Pikaev, Modern Radiation Chemistry, **v.1**, Moscow, Nauka (1985) 201-236, *in Russian*

[5] a) N.V. Timofeev-Resovskij, A.V. Savich, M.I. Shal'nov, Introduction to Molecular Radiobiology, Medizina, Moscow (1981), *in Russian*

b) A.V. Agafonov, Application of accelerators in medicine, Priroda, No. 12 (1996) 65-77, *in Russian*

[6] M.A. Orlova, O.A. Kost, V.A. Gribkov, I.G. Gazaryan, A.V. Dubrovsky, V.A. Egorov, Applied Biochemistry and Biotechnology, **88** (2000) 243-255

[7] G.W.C. Kaye, T.H. Laby, "Tables of Physical and Chemical Constants and some Mathematical Functions", Longman, London and New York (1986)

[8] N.G. Basov, V.A. Boiko, V.A. Gribkov, O.N. Krokhin, G.V. Sklizkov, ZhETP Letters, **9** (1969) 520-524

[9] K.N. Drabovich, Saturation effect, Encyclopedia of Physics, ed. by A.M. Prokhorov, Moscow, Bolshaja Rossijskaja Enciklopedia (1992) 249-250, *in Russian*

Modification of elastomer surfaces by plasma treatments

J. Tyczkowski[1], I. Krawczyk[1], B. Woźniak[2]

[1] *Faculty of Process and Environmental Engineering, Technical University of Lodz,*
Wolczanska 213, 93-005 Lodz, Poland
[2] *Leather Research Institute, Zgierska 73, 91-462 Lodz, Poland*

Abstract

Modification of the surface of a styrene–butadiene elastomer (Finaprene 435) by plasma treatment was studied. The process was performed in rf (13.56 MHz) glow discharge utilizing a plate reactor fed by the following precursors: $CHCl_3$, CCl_4, CO_2, and O_2. The elastomer surfaces were investigated by T-peel test, contact angle measurements and FTIR spectroscopy. More detailed analysis was performed for the CO_2 plasma treatment. It was found that an especially important role is played by the duration of the treatment.

1. Introduction

The gluing of elastomers (such as styrene–butadiene copolymers) to other materials makes an especially important problem in diverse branches of industry. It is obvious that the adhesive strength depends in great part on the chemical structure of the elastomer surfaces and, therefore, can be controlled by various chemical treatments. One of the common methods to improve their adhesion to polyurethane adhesives is the chlorination performed by means of active halogen derivatives such as trichloroisocyanuric acid (TCI) feeding in an organic solvent (e.g. butanone). On the basis of numerous studies it has been found that the chlorination process creates C–Cl and C–O polar groups on the elastomer surfaces, which are responsible for the improvement in adhesion. Unfortunately, both the vaporizing flammable solvent and educed gaseous chlorine are very toxic and hazardous substances for the environment [1-4].

Recently, an attempt has been undertaken to replace the wet chemical chlorination of styrene–butadiene rubbers with the plasma technique [5-7]. This is provoked by the fact that the plasma treatment enables the realization of various surface modifications by a much more clean, energy-saving and environmentally compatible way in comparison with the classical chemical methods. The surface modification by N_2 and O_2 rf plasma [5] as well as using rf and af plasmas generated in various reactive mixtures containing chlorine moieties [6,7], has been investigated. Other alternative techniques to the conventional chemical processes, for example as corona discharge and ultraviolet radiation treatments, have been also applied to that end [8,9].

The present work aims at testing the surface modification of a model styrene–butadiene elastomer by rf plasma implanting chlorine and oxygen functionalities. The chlorination has been performed using $CHCl_3$ and CCl_4 as precursors, whereas O_2 and CO_2 have been employed to create hydroxyl, carbonyl and carboxyl groups.

2. Experimental

Thermoplastic elastomer of a radial type styrene–butadiene block copolymer (Finaprene 435), provided by Atofina S.A. (Belgium), was used in this work. The copolymer did not contain any ingredients such as oils, plasticisers or fillers. A butadiene-to-styrene ratio was 69–31 wt.%. The samples were obtained by injecting the copolymer into a heater mould at 420 K, where plates of 120 mm width and 150 mm length were formed. To further tests, the samples of 10 mm width and 75 mm length cutting from the plates were used.

The plasma treatment was carried out in a parallel plate reactor with a radio frequency (rf, 13.56 MHz) glow discharge. As precursors, trichloromethane ($CHCl_3$), tetrachloromethane (CCl_4), carbon dioxide (CO_2), and oxygen (O_2) were used. These compounds were supplied to the reactor as pure agents (without a carrier gas). A typical flow rate was approx. 3.5 sccm for $CHCl_3$ and CCl_4 vapors and 7.5 sccm for CO_2 and O_2 gases, whereas an initial pressure of approximately 13 Pa was attained in all these cases. The power of glow discharge was changed from 10 to 80 W and the plasma treatment of the samples lasted from 15 s to 20 min.

To determine the adhesion strength of the elastomer surface, T-peel tests were carried out. Adhesive joints were made using the elastomer samples with the surface mechanically roughed before the modifying treatments and strips of standard leather (box cow, chrome tanned, non-pigmented). The one-component solvent-born polyurethane adhesive, based on hexandiol, was spread on each adherend and dried for 15 min. The dry adhesive film on the elastomer was reactivated at 353 K and the surfaces were placed in contact immediately under a pressure of 0.4 MPa for 10 s. Adhesive joints were conditioned for 48 h at room conditions. The T-peel strength measurements were performed using an Instron 5566 test instrument (peeling rate = 1.67×10^{-3} m/s).

The elastomer surfaces was also characterized using contact angle measurements (water, 298 K) and Fourier transforms infrared (FTIR) spectroscopy. A NRL model 100 Contact Angle Goniometer (Rame-Hart) equipped with a digital camera and a programmable system was utilized for the contact angle records. FTIR spectra were recorded using a Bio-Rad model 175C spectrometer equipped with an IRS microscopy system (Harrick Scientific), working in a reflection mode. Signal accumulation from 20 scans was taken with the resolution of 4 cm^{-1}.

3. Results and discussion

The most important feature of the elastomer surfaces, from the point of view of their applications, is the peel strength of adhesive joints formed between the elastomer and another material. The main attention in this paper is paid therefore to the T-peel test investigations. In Fig. 1 such results are presented for the F435 samples treated by various plasmas. The $CHCl_3$, CCl_4, CO_2, and O_2 plasmas with discharge powers of 10, 20, 50, and 80 W were tested. In all these cases the plasma treatment was performed by 5 min. For comparison, T-peel test result for non-treated samples is also shown.

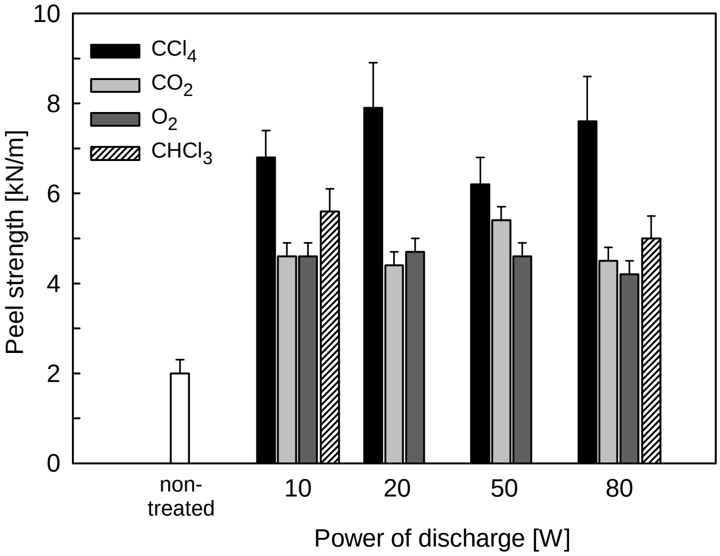

Fig. 1. Measurements of the T-peel strength for F435 elastomer after treatment by various plasmas at various glow discharge powers. Time of treatment – 5 min.

Two general conclusions emerge from the results presented above. Firstly, the all treatments give a considerable improvement in the adhesion properties of the elastomer. The greatest increase in the peel strength, about 4 times compared with the non-treated samples, is observed for CCl_4 plasma used as a modifier. And secondly, the peel strength values for a given plasma treatment are only weakly and non-systematically dependent on the discharge power in the investigated range. For example, the use of CO_2 plasma generated at 10 and 80 W gives the samples with the same value of the peel strength, whereas some increase in this value is observed for the plasma at 50 W. On the other hand, the samples treated by O_2 plasma reveal the same values of the peel strength (in the limit of error) for all used discharge powers.

The second important parameter (besides the discharge power) describing the plasma treatment process is the duration of the plasma action. It has been investigated in details for the CO_2 plasma treatment. T-peel strength test values obtained for elastomer F435 after such a modification at different times between 15 s and 20 min, and different powers (from 10 to 80 W), are given in Fig. 2. In general, we can distinguish three regions in relation to the treatment time: (*1*) the region of evident increases in the peel strength values at the beginning of the process (the peel strength for non-treated samples is about 2 kN/m), then (*2*) the reduction of these values, and finally (*3*) their growing at times longer than 10 min.

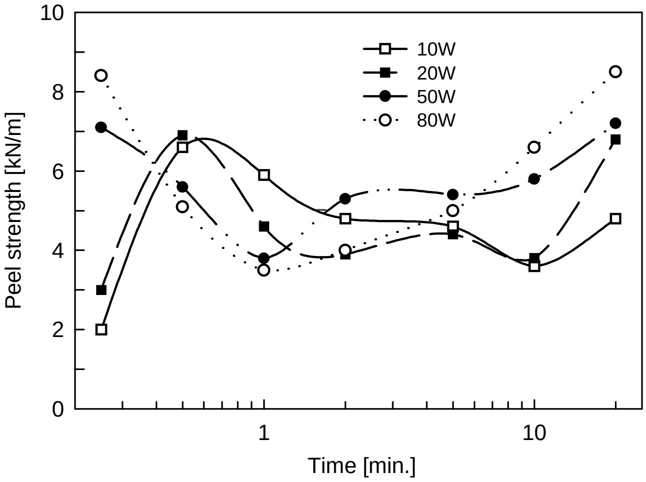

Fig. 2. Measurements of the T-peel strength for F435 elastomer after treatment by CO_2 plasma as a function of the exposure time and the discharge power.

The position of peel strength maximum that is disclosed at the beginning of the treatment process depends on the power. If the power is higher, the maximum occurs for shorter times. For 50 and 80 W it lies below 15 s. Taking into account the FTIR measurements, we can connect the peel strength changes in the first period of the treatment with a chemical modification of the elastomer surface. In Fig. 3 we can see bands at about 1548 and 1711 cm^{-1} appearing already for the 15-s-treatment at the glow discharge power of 50 W. Identical results we also obtain for the treatment by the 80 W plasma, however, for plasma of 10 W we can see these bands only after treatment time equal at least 0.5 min. The bands are attributed to carboxyl groups created by CO_2 plasma on the conventional polymer surfaces [10]. As one can see in Fig. 3, intensities of the bands (normalized to a band at 1493 cm^{-1} that is characteristic for styrene–butadiene copolymers [11]) are practically identical for longer times of the treatment (up to 20 min.). This suggests that more complex effects must be responsible for the observed changes in the peel strength. It seems that some active centers (not typical carboxyl groups) can play a crucial role in chemical bonding of the polyurethane adhesive to the elastomer surface. At the beginning of the treatment process the center density drastically

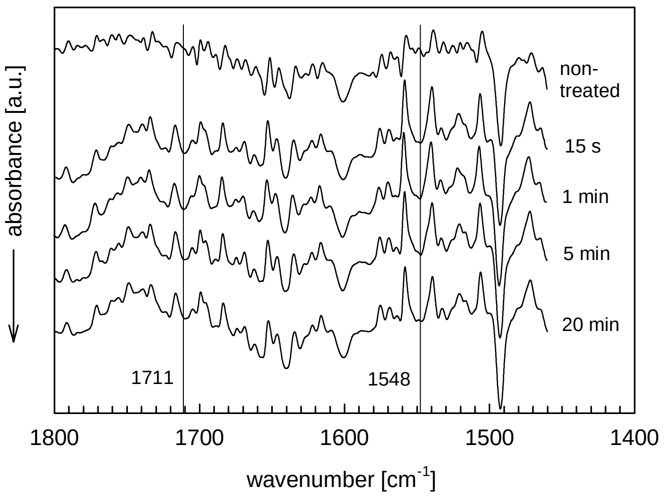

Fig. 3. FTIR spectra of F435 samples treated by CO_2 plasma for different times of the treatment. Discharge power – 50 W.

increases, but for times longer than 0.5 min it is reduced, for example by plasma etching. Continuing the treatment process we should expect a surface microroughening [8]. It can be response for the increase in the peel strength for times longer than 10 min.

Investigations of the contact angle supply arguments to support the conception discussed above. Fig. 4 presents the results of contact angle measurements performed for F435 samples treated by CO_2 plasma at different times between 15 s and 20 min, and different powers (from 10 to 80 W). We can notice a coincidence of these results and those shown in Fig. 2. For the power of 10 and 20 W, we can see at the beginning of the treatment process simultaneous increase of the peel strength (attaining the maximum at about 0.5 min) and decrease of the contact angle down to practically constant values for the times longer than 0.5 min. On the other hand, for 50 and 80 W we observe only constant values of the contact angle. However, these values are distinctly lower than that for the non-treated sample. It implies that the decrease in the contact angle had to occur in these cases for the treatment times shorter than 15 s. Similarly, Fig. 2 suggests that the maxima of the peel strength for the power of 50 and 80 W lie also below 15 s.

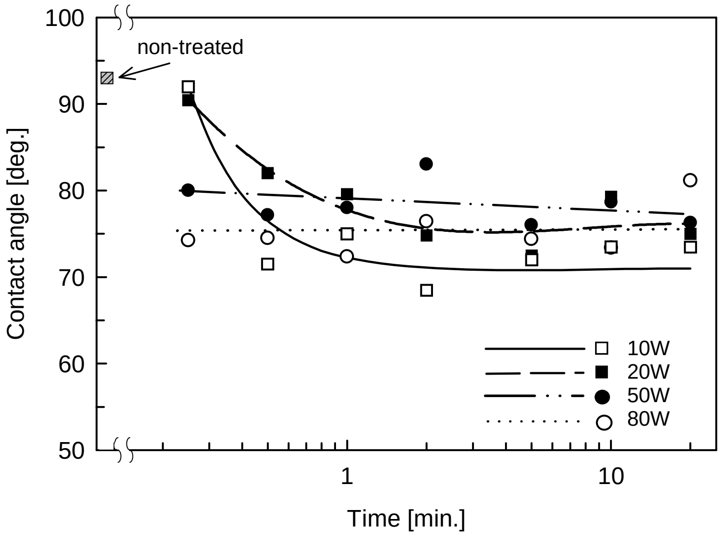

Fig. 4. Measurements of the water contact angle for F435 elastomer after treatment by CO_2 plasma as a function of the exposure time and the discharge power.

Although the increase in the peel strength at the beginning of the process can be connected with the decrease in the contact angle, the next stage, namely the lowering of the peel strength after passing the maximum does not reveal any correlation between these parameters. It suggests that the adhesion between the elastomer surface and the polyurethane adhesive originates from some active centers that do not have a visible share in the surface energy. Similarly, for the treatment times longer than 10 min, we see an increase in the peel strength, but the contact angle values remain constant. Perhaps, in this case a surface microroughening, as it has been mentioned above, begins to play a role in the adhesion properties of the elastomer.

Further investigations will be aimed at obtaining more information about the chemical structure and microstructure of the elastomer surface and determining the nature of the active centers responsible for the adhesion properties of the plasma treatment styrene–butadiene elastomers.

4. Conclusion

The presented investigations indicate that the plasma treatment is a very promising method to improve the adhesion properties of styrene–butadiene elastomers. Both plasma implanting chlorine functionalities (by plasma of $CHCl_3$ and CCl_4) and oxygen functionalities (CO_2 and O_2 plasmas) have turned out to be an effective technique for the surface modification. In this paper more detailed studies have been discussed for CO_2 plasma. Taking into account two parameters characterizing the plasma process, namely the power of the glow discharge and the duration of the treatment, it has been found that first of all the plasma treatment time has an especially important influence on the treatment process. Only the duration of the treatment from a few to over a dozen seconds is enough for obtaining a maximal value of the peel strength (independently of the power in the range of 10–80 W). For longer times we observe a decrease in the peel strength, and then, from about 10 min the next increase. At this stage of investigations it is difficult to explain the observed improvement of adhesion from the molecular point of view. It has been found, however, that the adhesion between the elastomer surface and the polyurethane adhesive originates from some kind of active centers created by plasma. These centers are not typical carboxyl groups (although such groups are identified by FTIR on the surface treated by CO_2 plasma) and also do not have a visible share in the surface energy (which is shown by measurements of the contact angle). We plan further investigations on the chemical nature of these centers.

Acknowledgements

This work is supported by the Polish Committee for Scientific Studies under project code 7 T09B 097 21. The authors are grateful to Prof. W. Rzymski from Chemistry Faculty of TU Lodz for the FTIR measurements as well as Prof. S. Slomkowski and Dr. Sosnowski from CMMS PAS for their help in the contact angle measurements.

References

[1] J.M. Martin-Martinez, J.C. Fernández-Garcia, A.C. Orgilés-Barceló, J. Adhes. Sci. Technol. **6**, 1091 (1992).
[2] D. Oldtield, T.E.F. Symes, J. Adhes. **39**, 91 (1992).
[3] M.M. Pastor-Blas, R. Torregrosa-Marciá, J.M. Martin-Martinez, J.G. Dillard, Int. J. Adhes. Adhes. **17**, 133 (1997).
[4] M.D. Romero-Sánchez, M.M. Pastor-Blas, T. del Pilar Ferrándiz-Gómez, J.M. Martin-Martinez, Int. J. Adhes. Adhes. **21**, 101 (2001).
[5] A.B. Ortiz-Magán, M.M. Pastor-Blas, T.P. Ferrándiz-Gómez, C. Morant-Zacarés, J.M. Martin-Martinez, Plasmas and Polym. **6**, 81 (2001).
[6] J. Tyczkowski, I. Krawczyk, B. Woźniak, Acta Agrophys. **80**, 231 (2002).
[7] J. Tyczkowski, I. Krawczyk, B. Woźniak, Surf. Coat. Technol. in press (2003).
[8] M.D. Romero-Sánchez, M.M. Pastor-Blas, J.M. Martin-Martinez, P.A. Zhdan, J.F. Watts, J. Mater. Sci. **36**, 5789 (2001).
[9] M. Staeger, E. Finot, C.H. Brachais, S. Auguste, H. Durand, Appl. Surf. Sci. **185**, 231 (2002).
[10] J. Gancarz, G. Poźniak, M. Bryjak, Europ. Polym. J. **35**, 1419 (1999).
[11] G. Bador, Structural Investigations of Polymers, Ellis Hordwood, New York 1991, Sect. 8.1.

Experimental study of pattern formation in dielectric barrier discharge at atmospheric pressure

Lifang Dong[1], Zengqian Yin[1], Yafeng He[1], Zhifang Chai[1], Xuechen Li[1], Long Wang[2]

[1]*College of Physics Science & Technology, Hebei University, Baoding 071002, China*
[2]*Institute of Physics, Chinese Academy of Sciences, Beijing 100080, China*

Abstract

The traveling hexagon and square pattern have been observed in dielectric barrier Air/Ar gas discharge in streamer discharge. It's found that the appearance of these patterns is very sensitive to air concentration and applied voltage. The applied voltage for obtaining the hexagon (square) pattern increases with increasing air concentration. The drifting velocity as well as spatial frequency of hexagon (square) pattern increases with increasing air concentration.

1. Introduction

Pattern formation is a well known self-organization phenomenon. It has been studied in many different systems such as in convecting fluid, liquid crystals, optical systems and chemistry. In recent years, pattern formation in dielectric barrier discharge (DBD) has attracted much attention.[1-4] DBD is a typical non-equilibrium gas discharge. Its experimental device generally consists of two parallel electrodes covered with thin dielectric layer. It can operate in AC discharge. The discharge type mainly depends on product *pd* of gas pressure *p* and gas gap width *d*. For a low *pd* value, the discharge operates in Townsend breakdown and appears in uniform transient glow discharge. For a high *pd*, the discharge operates in a streamer regime leading to the formation of narrow discharge filaments. Under appropriate conditions, patterns can take place in two discharge regimes. Some periodic patterns such as hexagon and stripe structure have been observed in DBD at low *pd* (less than 10 Torr cm) by many researchers.[1,2] However, there is rare report on the observation of pattern formation in DBD at high *pd* because it is difficult to obtain the pattern at high *pd* due to the limitation of conventional DBD device. Recently, we obtained a rich variety of pattern formations in DBD at high *pd* (not less than 70 Torr cm) by using a pair of water electrodes. In this paper, we report the observations of hexagon pattern and square pattern in DBD.

2. Experimental Setup

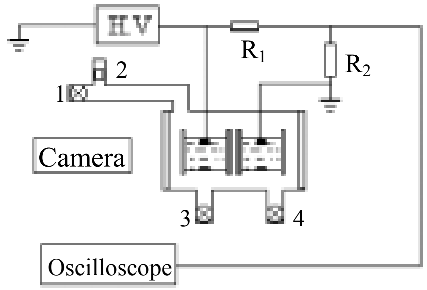

Fig.1 Schematic diagram of experimental setup. (1: gas source, 2: flowmeter, 3: manometer, 4: pump, R_1=200MΩ, R_2=1.5MΩ)

The experimental device is shown in Fig.1. Two cylindrical containers with diameter of 4.67 cm filled with ordinary water are used as electrodes. The metallic rings connected with power supply are immersed in the water for conducting current. The parallel glass with thickness 1.5 mm served as dielectric end walls of the containers. The gas gap width between the dielectric layers can be adjusted with the micrometer caliper. The water is also served as coolant and transparent media for observation. The overall structure is put into a chamber, which is connected with the mechanical pump and inlet chamber. A sinusoidal ac voltage (with the frequency 10-42 kHz) is applied to the electrodes. Resistors are used to monitor the applied voltage. A digital camera (Canon Powershot G1) is used to take the picture of patterns. The gas is Air/Ar mixture.

3. Results and Discussions

Hexagon pattern and square pattern have been observed in dielectric barrier Air/Ar gas discharge at high pd (not less than 70 Torr cm) in our experiment. They are generally time-dependent. They sometimes drift in a certain direction and sometimes rotate. Fig.2 gives the snapshots of square pattern and hexagon pattern. It is worth pointing out that the *pd* product of gas pressure and gas gap width in present experiment is about 70 Torr cm, which is much larger than that in previous works.[1-2] That is to say that the discharge type in present experiments is streamer regime, not Townsend discharge. It is found that the appearance of hexagon and square patterns is very sensitive to experiment parameters such as air concentration in gas mixture and applied voltage. The hexagon pattern and square pattern can appear if the air concentration is not larger than about 25%. The applied voltage for obtaining hexagon pattern (or square pattern) increases with the increasing air concentration in gas mixture. For example, the applied voltage for obtaining square pattern is 2.8kV if air concentration is 0.5% (see also Fig.2(a)), while it is 4.8kV if air concentration is 10% (see also Fig.3(a)).

Fig.3 gives two pictures of square pattern with different exposure time. It can be clearly seen that the square pattern drifts in a certain direction by comparing the filament trace length in two pictures. It is shown that the filaments leave traces after long exposure time due to the square pattern drifting. Fig.4 gives picture of traveling hexagon with the same air concentration as in Fig.3. The drifting velocity can be estimated by dividing the filament trace length by exposure time. It is found that the drifting velocity increases generally with increasing air concentration and the drifting velocity of hexagon pattern is larger than that of square pattern.

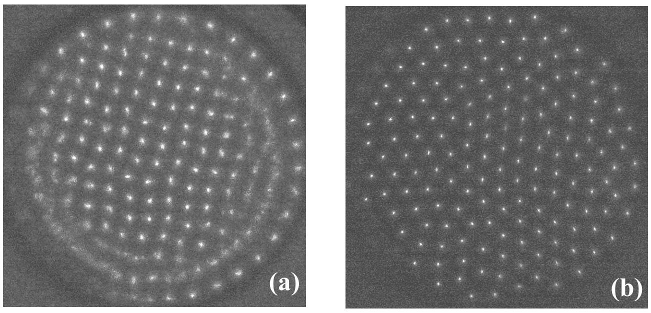

Fig.2 The pictures of square pattern (a) and hexagon pattern (b) under the conditions: air concentration = 0.5%, gas gap width = 1.0 mm. The other parameters are: (a) applied voltage = 2.8 kV, the exposure time 125 ms. (b) applied voltage = 2.6 kV, the exposure time 4 ms.

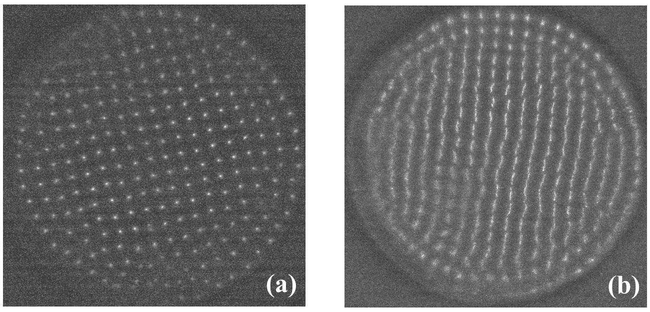

Fig.3 The pictures of square pattern with different exposure time: 5 ms in (a) and 80 ms in (b). The other parameters are: air concentration = 10%, the gas gap width = 1.0 mm, the applied voltage = 4.8 kV.

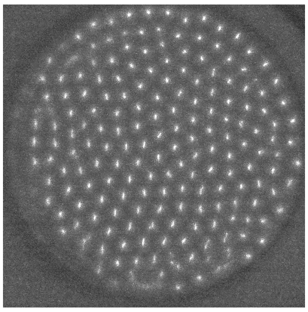

Fig.4 The picture of hexagon pattern under the conditions: air concentration = 10%, gas gap width = 1.0 mm, the applied voltage = 4.1 kV, the exposure time 8 ms.

In our experiments, it is also found that the spatial frequency of pattern increases with increasing air concentration, which can be clearly seen by comparing Fig.2(a) with Fig.3(a).

In conclusion, the traveling hexagon and square pattern have been observed in dielectric barrier Air/Ar gas discharge in streamer discharge. The appearance of these patterns is very sensitive to air concentration and applied voltage. The applied voltage for obtaining the hexagon (square) pattern increases with increasing air concentration. The drifting velocity as well as spatial frequency of hexagon (square) pattern increases with increasing air concentration.

The further work is going on.

Acknowledgement: This work is supported by Ministry of Education, China under Grant No. 02020 and Committee of Science and Technology, Hebei Province, China under Grant No. 01212180.

References

[1] I. Müller, C. Punset, E. Ammelt, H. –G. Purwins, and J. P. Boeuf, IEEE Trans. on Plasma Sci. **27**, 1 (1999) 20

[2] W. Breazcal, K. M. Flynn and E. G. Gwinn, Phys. Rev. E **52,** 2 (1995) 1503

[3] M. Klein, N. Miller, and M. Walhout, Phys. Rev. E **64** (2001) 026402

[4] L. F. Dong, Z. Q. Yin, X. C. Li et al., 6th APCPST, (invited talk), I-O3, Jeju, Korea, (July, 2002), Thin solid films (in press)

Chemical kinetics of SO_2 removal from air with dielectric barrier discharges

A. B. Saveliev, A. R. Murtazin, G. J. Pietsch

Gas Discharge Technology, RWTH Aachen University, Aachen, Germany

Abstract

One of the possibilities to control the SO_2 contamination of flue gases is treating it with dielectric barrier discharges (DBDs). The non-thermal plasma of DBDs provides a chemical active medium able to oxidise SO_2 to SO_3, which easily can be removed by scrubbing. The mechanism of SO_2 conversion is proposed based on a simplified and extended set of reactions and exploiting the knowledge about ozone synthesis. The role of temperature, nitrogen oxides and humidity on this mechanism is highlighted.

1. Introduction

Conventionally sulphur dioxide (SO_2), which causes acid rain, is treated with calcium-based sorbents. An alternative method is based on the use of dielectric barrier discharges (DBDs). DBDs provide non-thermal plasmas, which contain energetic electrons with energies of some eV in air. By electron collisions with heavy particles, excitation and dissociation processes take place, which result in chemical active media able to initiate chemical processes.

In order to remove SO_2 from air in DBDs, SO_2 must be oxidised. Subsequently gaseous SO_3 can be scrubbed easily. As atomic oxygen is necessary to oxidise SO_2 it must be provided by DBDs. In air apart from SO_2-oxidation other processes require atomic oxygen as well. Ozone synthesis is the most important process consuming oxygen atoms. As the SO_2 concentration in air is relatively small in general, the number of oxygen atoms available is mainly determined by the reaction scheme, which governs ozone generation in air. That is why the mechanisms of ozone synthesis is considered at first. Afterwards a simplified and an extended reaction scheme is used to describe SO_2 conversion. Finally the influence of NO_x and of humidity on SO_2 removal is discussed.

2. Mechanism of ozone synthesis

DBDs in electronegative gases at about ambient conditions consist of numerous microdischarges temporally and spatially distributed in the discharge gap. Typical values of the transferred charge and dissipated energy are some nC and some μJ per microdischarge, respectively. Only a certain part of this energy is consumed by electron drift (depending on gas mixture and other boundary conditions).

More than hundred elementary reactions between electrons, ions and neutrals in the ground and excited states are involved in ozone generation from air. Some of the most important reactions in air polluted with SO_2 are given in Table 1. Ozone synthesis can be divided into two stages, oxygen dissociation and ozone formation.

The first stage comprises the generation of oxygen atoms in microdischarges. Its duration is in the order of the lifetime of microdischarges (~ 100 ns). The direct impact of electrons on oxygen molecules (R1, Table 1), on ozone (if its concentration is high enough, R2) and on nitrogen molecules via a metastable excited state of nitrogen (R3, R4) yield atomic oxygen. The number of oxygen atoms depends linearly on discharge energy as long as the boundary conditions remain unchanged like chemical composition, pressure, temperature and discharge character. It is assumed that this linearity is uninfluenced by temperature change, gas impurities and components of low concentration like ozone and nitrogen oxides.

In the second stage the atoms generated in microdischarges are consumed. Nearly all oxygen atoms will be converted to ozone (R5) during some 10 μs if the energy density (energy per unit volume) is low. The ozone concentration increases linearly with the specific energy at this condition. Additionally atomic nitrogen is converted to different nitrogen oxides of low concentration. (The number of nitrogen atoms generated in microdischarges is about 100 times smaller than that of oxygen atoms.) Ozone destruction (R6) occurs simultaneously. It is of importance at elevated ozone concentrations.

Table 1. Some important reactions in non-thermal air plasmas containing SO_2 admixtures

$O_2 + e^- \rightarrow O\cdot + O\cdot + e^-$	$k_1 = f_1(E/n)$	[1]	(R1)
$O_3 + e^- \rightarrow O_2 + O\cdot + e^-$	$k_2 = f_2(E/n)$	[1]	(R2)
$N_2 + e^- \rightarrow N_2(A^3\Sigma^+_u) + e^-$	$k_3 = f_3(E/n)$	[1]	(R3)
$N_2(A^3\Sigma^+_u) + O_2 \rightarrow N_2 + 2\,O\cdot$	$k_4 = 2.54 \cdot 10^{-12}$	[1]	(R4)
$O\cdot + O_2 + M \rightarrow O_3 + M$	$k_{5a} = 6.9\cdot10^{-34} \cdot(300/T)^{1.25}$ $(M = O_2)$ $k_{5b} = 6.2\cdot10^{-34} \cdot (300/T)^2$ $(M = N_2)$	[1] [1]	(R5)
$O\cdot + O_3 \rightarrow O_2 + O_2$	$k_6 = 2 \cdot10^{-11} \cdot \exp(-2300/T)$	[1]	(R6)
$O\cdot + SO_2 + M \rightarrow SO_3 + M$	$k_7 = 4.0\cdot10^{-32} \cdot \exp(-1000/T)$	[2]	(R7)
$O\cdot + SO_3 \rightarrow SO_2 + O_2$	$k_8 = 4.59 \cdot 10^{-17}$	[3]	(R8)
$N\cdot + SO_3 \rightarrow SO_2 + NO$	$k_9 = 5.1 \cdot 10^{-16}$	[3]	(R9)
$O\cdot + NO_2 \rightarrow NO + O_2$	$k_{10} = 1.13 \cdot 10^{-11} \cdot (T/1000)^{0.18}$	[1]	(R10)
$O\cdot + NO_2 + M \rightarrow NO_3 + M$	k_{11}	[1]	(R11)

rate coefficients k_i in $cm^{-3}\cdot s^{-1}$ or in $cm^{-6}\cdot s^{-1}$, temperature T in K

At high energy density the concentration of nitrogen oxides rises and the reaction rate of R10 increases. That is why oxygen atoms mainly are consumed by nitrogen oxides (R10) instead of ozone synthesis (R5). Moreover, ozone can be destroyed by catalytic reaction chains with nitrogen oxides [4] so that its concentration may even drop to zero.

3. Treatment of SO_2 in DBDs

The sulphur dioxide concentrations considered here are in the order of up to a few 1000 ppm. There exists no detailed information about the direct dissociation of sulphur dioxide by electron collisions at low electron energy (< 10 eV). Dissociative electron attachment is known as process, which reduces the SO_2 concentration to SO, SO^-, S and S^- [5]. However, as the final product should be SO_3, these processes finally do not facilitate SO_2 conversion. In any case dissociative attachment plays not a crucial role because of the low SO_2 concentrations under consideration. The main part plays sulphur dioxide oxidation by atomic oxygen leading to sulphur trioxide (R7). Reaction R7 is competitive to ozone synthesis (R5). That is why the kinetics of SO_2 conversion can be treated in analogy to ozone synthesis.

Back reactions to SO_2 take place as well (R8 and R9). If there is no lack on free available oxygen and nitrogen atoms, the equilibrium between the direct (R7) and the back reactions can be calculated. From this equilibrium follows that the maximum SO_2 conversion degree is theoretically 99.99 % at the concentration ratio between the oxygen and nitrogen atoms of 100:1. However, this value has not been reached experimentally in dry air [7]. The situation is much more complicated because heterogeneous processes (with the liquid and solid state of SO_3) are involved.

The maximum number of oxygen atoms, which are provided by DBDs in air can be estimated from the maximum efficiency of ozone production, reached at small energy densities ($Y_{O3} \approx 100$ g/kWh in air [4]). At this condition practically all oxygen atoms are converted to ozone. Therefore, the number of oxygen atoms per Wh, η_O, can be determined (N_A is the Avogadro number and $M(O_3)$ the mole mass of ozone):

$$\eta_O = \frac{Y_{O3}}{M(O_3)} \cdot N_A = \frac{100\,[\mathrm{g/kWh}]}{48\,[\mathrm{g/mol}]} \cdot 6.02 \cdot 10^{23}\left[\mathrm{mol}^{-1}\right] = 1.25 \cdot 10^{24}\left[\mathrm{kWh}^{-1}\right] = 1.25 \cdot 10^{21}\left[\mathrm{Wh}^{-1}\right] \qquad \text{(E1)}$$

If the amount of energy W will be deposited in the discharge, $W\cdot \eta_O$ oxygen atoms will be available for further reactions. Other components of small concentrations like O_3, NO_x and SO_x will not change this number remarkably. It is assumed that these components will not influence the number of oxygen atoms.

The reduction of the SO_2 concentration by oxidation processes (R7) is influenced by competing reactions consuming oxygen atoms. The main are ozone synthesis (R5) and nitrogen dioxide reduction and oxidation

(R10 and R11, respectively). Reactions with ozone, NO and NO_3 are less important. From this follows for the concentration reduction (the back reactions R8 and R9 are neglected because of their small rate coefficients):

$$\begin{aligned} -d[\mathrm{SO_2}] &= \frac{dN(\mathrm{O})}{V}\cdot\frac{w_7}{w_7+w_5+w_{10}+w_{11}+\ldots}\approx \\ &\approx d\left(\frac{W}{V}\right)\cdot\eta_{\mathrm{O}}\cdot\frac{k_7\cdot[\mathrm{SO_2}]\cdot[\mathrm{M}]}{k_7\cdot[\mathrm{SO_2}]\cdot[\mathrm{M}]+(k_{5a}\cdot 0.2+k_{5b}\cdot 0.8)\cdot[\mathrm{O_2}]\cdot[\mathrm{M}]+(k_{10}+k_{11}\cdot[\mathrm{M}])\cdot[\mathrm{NO_2}]} \end{aligned} \qquad \text{(E2)}$$

[X] means a concentration (particle number per volume unit), M collision partner, N(O) number of oxygen atoms, V volume and w_i reaction rate.

The reaction rate of R7 is much smaller than that of R5 at low SO_2 concentrations (~ 1000 ppm). At ambient temperature w_7 is equal to w_5 at an SO_2 concentration of about 92,000 ppm. From this follows that the reaction rate w_7 in the denominator of E2 can be neglected. With constant $[O_2]$, $[NO_2]$ and temperature follows:

$$[\mathrm{SO_2}]=[\mathrm{SO_2}]_0\exp\left(-\frac{W}{V}\cdot\frac{1}{\beta}\right)\quad\text{with}\quad \beta=\frac{(k_{5a}\cdot 0.2+k_{5b}\cdot 0.8)\cdot[\mathrm{O_2}]\cdot[\mathrm{M}]+(k_{10}+k_{11}\cdot[\mathrm{M}])\cdot[\mathrm{NO_2}]}{\eta_{\mathrm{O}}\cdot k_7\cdot[\mathrm{M}]} \qquad \text{(E3)}$$

β is the energy efficiency factor, which determines the amount of energy necessary to reduce the sulphur dioxide concentration by a factor of 2.71.

4. Extended reaction scheme

If a more sophisticated reaction scheme for SO_2 conversion is used, the equation system cannot be solved any longer analytically. The following assumptions and boundary conditions were taken solving the system:

- Zero-dimensionality (the concentration of each component is independent on location),
- the calculation begins after each discharge pulse with initial concentrations of oxygen and nitrogen atoms (in the ground state) given in [1],
- reactions between non-charged and non-excited particles are considered only, (the reaction set is taken from [1] plus N_2O_5 decomposition (from [2]) and SO_2 conversion (R7, R8, R9)).

The results are given in Fig. 1. As the initial concentration of oxygen atoms is rather low, the SO_2 concentration seems to be uninfluenced. The SO_2 conversion is only detectable by the increase of the SO_3 concentration. The temporal behaviour of SO_3 and O_3 is similar corresponding to the competing reactions R5 and R7. SO_2 is converted as long as oxygen atoms are available.

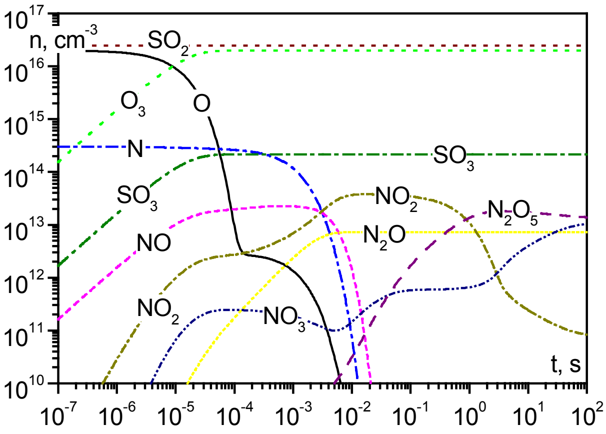

Fig. 1. Temporal development of particle densities after a discharge pulse at 25 °C (initial conditions dry air at 1 bar with $[SO_2]_0 = 1000$ ppm, $[O]_0 = 2\cdot10^{16}$ cm^{-3}, $[N]_0 = 3\cdot10^{14}$ cm^{-3}, $[N_2]_0 : [O_2]_0 = 4 : 1$).

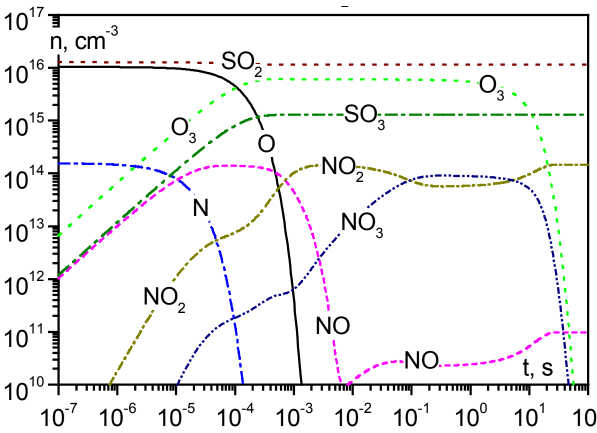

Fig. 2. Temporal development of particle densities after a discharge pulse at 300 °C, other conditions like in Fig. 1.

At elevated temperature the rate coefficient of ozone generation (R5) decreases and as consequence the lifetime of oxygen atoms increases (compare Fig. 1 with Fig. 2). The rate coefficient of SO_2 conversion (R7) increases as well. As result the concentration of SO_3 rises.

Ozone is unstable at high temperature [6]. The thermal destruction of ozone in the gaseous space delivers additional oxygen atoms. This process may increase the SO_2 conversion efficiency. If however ozone is destroyed at hot surfaces of the reactor, additional oxygen atoms do not appear. The thermal destruction of ozone is not taken into account.

The energy efficiency factor β can be derived from E3:

$$\delta[SO_2] = -\delta[SO_3] = -[SO_2]_0 \cdot \frac{1}{\beta} \cdot \delta(W/V) \qquad \Rightarrow \qquad \beta = \frac{[SO_2]_0 \cdot \delta(W/V)}{\delta[SO_3]} \tag{E4}$$

The values of β in Fig. 3 belong to energy densities at low NO_x concentrations. They are calculated with E4 ($\delta[SO_3]$ was determined with the extended reaction scheme, the specific energy values $\delta(W/V)$ result from the ozone concentration level reached in Fig. 1 and Y_{O3} was taken as 100 g/kWh). The dependence of β on temperature calculated with E3 and with the extended reaction scheme using E4 are shown in Fig. 3 as full line and circles, respectively. They are nearly identical.

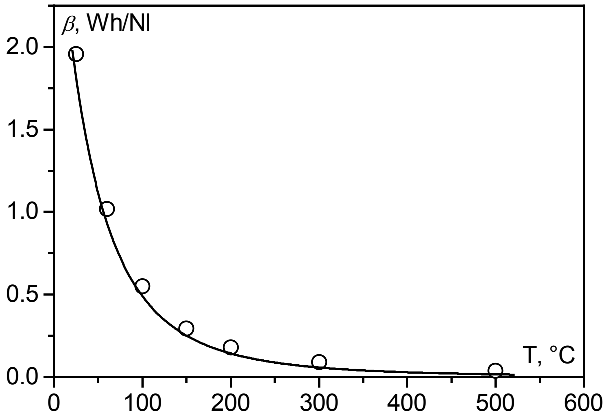

Fig. 3. Dependence of the energy efficiency factor of SO_2 conversion β on temperature at negligible NO_x concentrations for dry air at atmospheric pressure and an initial SO_2 concentration of 1000 ppm (solid line calculated with E3 – simplified reaction scheme; circles calculated with E4 - extended reaction scheme).

5. Influence of nitrogen oxides

Up to now the reaction scheme was solved for small atomic oxygen numbers, i. e. for negligible NO_x concentrations. However, in air during long DBD activity a remarkable amount of NO_x appears [4]. In the presence of NO_x the lifetime of oxygen atoms is reduced (Fig. 4). This leads to a decrease of the SO_3 concentration and reduced SO_2 conversion (compare with Fig. 1). The dependence of the energy efficiency of SO_2 conversion on the admixtures NO_2, NO and O_3 is shown in Fig. 5. In the presence of NO_2 the energy consumption is essential higher. The influence of NO is smaller, while ozone has nearly no influence on the energy efficiency factor β (if thermal destruction of ozone is not considered).

From the results follows that on one hand temperature improves the energy efficiency of SO_2 conversion, on the other hand nitrogen oxides (NO_2, NO_3, NO) have the contrary effect. As a rule, nitrogen oxides in atmospheric DBDs appear in form of N_2O_5 at ambient temperature. N_2O_5 has no strong influence on the lifetime of oxygen atoms and do not disturb SO_2 conversion. At higher temperature N_2O_5 becomes unstable, and the nitrogen oxides appear mainly as NO_2, NO_3 and NO, which reduce SO_2 conversion. The appearance of these nitrogen oxides counteracts the positive temperature effect, which follows from the temperature dependency of k_5 and k_7.

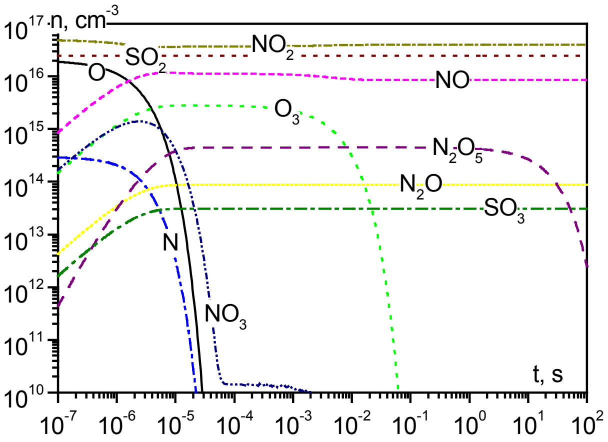

Fig. 4. Temporal development of particle densities after a discharge pulse at 25 °C (initial conditions like in Fig. 1, except $[NO_2]_0 = 2000$ ppm).

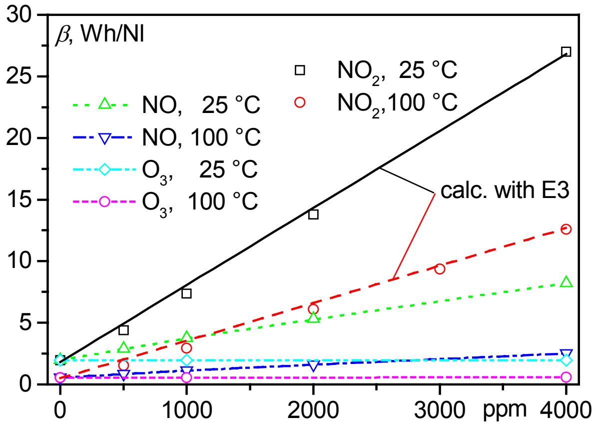

Fig. 5. Calculated dependence of the energy efficiency factor of SO_2 conversion β on the initial concentration of the nitrogen oxides NO_2, NO and ozone (without thermal destruction) at 25 and 100 °C.

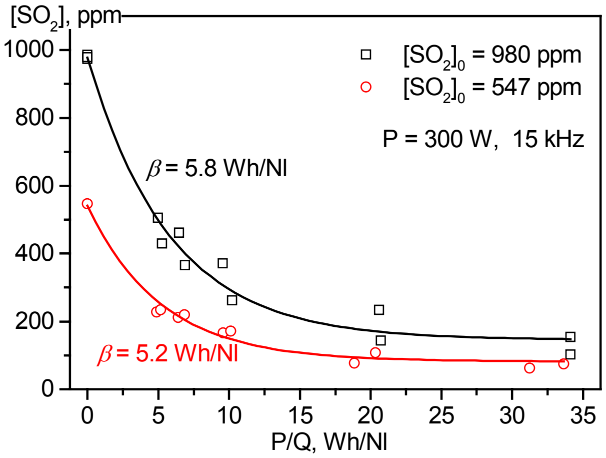

Fig. 6. Measured kinetic curves of SO_2 conversion in DBDs at different initial concentrations.

In Fig. 6 experimental values of SO_2 degradation in a DBD reactor for two different initial SO_2 concentrations are given over the energy density W/V = P/Q (P is the power and Q the flow rate). The process temperature was about 75 °C. Approximately 4000 ppm NO and 400 ppm NO_2 have been detected. The energy efficiency factor β was determined for both curves and is equal to 5.8 and 5.2 Wh/Nl for the initial

SO_2 concentration 980 and 547 ppm, respectively. Theoretically β should be about 0.7 Wh/Nl at 75 °C according to Fig. 3. However, the high concentrations of NO_2 and NO deteriorates this value (Fig. 5). If they are taken as initial condition a value of $\beta = 5.5$ Wh/Nl follows at a temperature of 75 °C.

DBD experiments show only a weak dependence of the energy efficiency factor β on temperature [7]. This can be explained with the appearance of NO_2 and NO in the reaction area at evaluated temperature.

6. Influence of humidity

In humid gases OH radicals appear in non-thermal discharges [8, 9]. OH radicals can oxidise sulphur dioxide effectively:

$SO_2 + OH\cdot + M \rightarrow HOSO_2 + M$	k_{12}	[2]	(R12)
$HOSO_2 + O_2 \rightarrow SO_3 + HO_2$	k_{13}	[2]	(R13)

With this second fast channel of SO_2 oxidation the conversion efficiency rises remarkably. Further reactions with water, its radicals and nitrogen oxides may improve SO_2 conversion additionally by reducing the nitrogen oxide concentrations (which decrease the lifetime of atomic oxygen).

In [7] it is shown experimentally that the efficiency of SO_2 conversion in humid air strongly depends on temperature, namely the conversion rate rises with temperature. This can be explained as follows: Temperature affects R7 ($SO_2 + O + M \rightarrow SO_3 + M$) positively and R12 negatively. In dry air the positive effect of temperature on SO_2 conversion is counteracted by rising NO_x concentrations. In humid air the observed rise of the conversion rate with temperature can be explained by a decrease of nitrogen oxide concentrations.

7. Conclusions

A mechanism of oxidative conversion of sulphur dioxide in dry and humid air with DBDs is proposed. Atomic oxygen is the main channel of this mechanism. The SO_2 oxidation process is competitive to ozone synthesis. In dry air the positive effect of temperature is reduced by an increased concentration of nitrogen oxides (NO_2, NO_3, NO). In humid air a second channel of SO_2 removal with OH radicals may be of importance. At rising temperature the observed improvement of SO_2 conversion is believed to result from a reduction of nitrogen oxide concentrations.

References

[1] I.A. Kossyi, A.Yu. Kostinsky, A.A. Matveyev, V.P. Silakov - Plasma Sources Sci. Technol. **1**, 207-220 (1992).

[2] R. Atkinson, D. L. Baulch, R. A. Cox , J. N. Crowley , R. F. Hampson Jr , J.A. Kerr, M.J. Rossi, J. Troe - Summary of Evaluated Kinetic and Photochemical Data for Atmospheric Chemistry - IUPAC Subcommittee on Gas Kinetic Data Evaluation for Atmospheric Chemistry, Web Version (2002).

[3] A. Jacob, C.A. Winkler - J. Chem. Soc. Faraday Trans. **68**, 2077-82 (1972).

[4] D. Braun, U. Küchler, G. Pietsch – Pure & Appl. Chem. **60**, 741-746 (1988).

[5] I.M. Čadež, V.M. Pejčev, M.V. Kurepa - J. Phys. D: Appl. Phys. **16**, 305-314 (1983).

[6] V.V. Lunin, M.P. Popovich, S.N. Tkachenko, Physical Chemistry of Ozone, Moscow State University Press (in Russian) (1998).

[7] A.R. Murtazin, A.B. Saveliev, G.J. Pietsch – Proc. 16th Int. Symp. on Plasma Chem., Taormina, Italy (2003).

[8] R. Peyrous, P. Pignolet, B. Held - J. Phys. D: Appl. Phys. **22**, 1568-1667 (1989).

[9] F. Fresnet, G. Baravian, L. Magne, S. Pasquiers, C. Postel, V. Puech, A. Rousseau - Proc. XIVth Int. Conf. on Gas Disch. and their Appl., Liverpool, UK, **2,** 40-43 (2002).

Acknowledgement

The authors gratefully acknowledge the funding of these investigations by the European Community under the “Competitive and Sustainable Growth” programme (Project No. G1ST-CT-2001-50138, project coordinator: Ecozone Technologies, Israel).

Experimental investigation of SO_2 removal from air with dielectric barrier discharges

A. R. Murtazin, G. J. Pietsch, A. B. Saveliev

Gas Discharge Technology, RWTH Aachen University, Aachen, Germany

Abstract

A dielectric barrier discharge reactor has been used to study SO_2 removal from polluted air. The performance of the reactor depends on reactor design parameters and operating conditions like frequency of applied voltage, energy density, gas temperature and humidity. SO_2 destruction removal efficiencies of more than 98 % have been reached.

1. Introduction

Sulphur dioxide (SO_2) is an air pollutant present e. g. in exhaust gases of coal-fired power and iron-ore plants. In big plants it is removed by scrubbing the off-gases with a lime solution. There is a need for alternative and simple desulphurisation methods especially for smaller gas flows. Non-thermal atmospheric pressure plasmas have been shown to be promising for this purpose [1]. One of the most effective sources of non-thermal plasmas are dielectric barrier discharges (DBDs).

DBDs consist of a multitude of microdischarges in gas gaps and on the surface of dielectric barriers. In microdischarges high energetic electrons collide with molecules producing chemical active particles, viz. radicals, molecules and atoms in excited states. The number of these active particles generated in the unit of volume is proportional to the electric energy dissipated in this volume. The particles react with pollutants reducing their concentration.

The SO_2 removal is determined by the specific power (or energy density) of the discharges P/Q with P the power and Q the gas flow rate. Assuming that sulphur dioxide removal is governed by first-order chemical reactions, it can be described by:

$$[SO_2] = [SO_2]_\infty + ([SO_2]_0 - [SO_2]_\infty) \cdot \exp\left(-\frac{1}{\beta} \cdot P/Q\right) \tag{1}$$

with β a factor describing the energy efficiency or consumption (the amount of energy per volume unit, which is needed to get a reduction of 63 % of the SO_2 concentration related to the initial one), $[SO_2]_0$ the initial and $[SO_2]_\infty$ the minimum reachable concentration. The percentage of SO_2 removed is determined by the maximum destruction removal efficiency (DRE). The DRE is defined as $100\,\% \cdot ([SO_2]_0 - [SO_2]_\infty)/[SO_2]_0$. β and DRE are figures of merit, which are useful to describe the effectiveness of different reactor designs and operation conditions. They depend apart from others on power, frequency, amplitude of the applied voltage, gas composition and temperature, on reactor design parameters like thickness and kind of dielectric, gap distance between the electrodes.

2. Experimental set-up

The experimental set-up used to determine the features of the DBD reactor is presented in Fig. 1. A gas mixture prepared from synthetic air (20.5 % O_2 in N_2) and 980 ppm SO_2 in synthetic air was used. If necessary water vapour was added by passing the gas stream through a home-made humidifier provided with a digital hygrometer. All gas streams are determined by mass flow controllers. The outlet gas is analysed on-line by an FTIR spectrometer equipped with a 10 cm single-pass or a 2 m multi-pass absorption cell.

In order to avoid overheating of the reactor, an internal oil flow was used to cool it. It should be mentioned that gas flow variation influences cooling conditions remarkably. The temperature was measured by three thermocouples in the gas in- and outlet chambers (T_{in}, T_{out}) and in the oil cooling system within the reactor (T_{int}). The thermocouples are embedded in grounded stainless steel mantles to avoid electrical interferences from the discharge. The mean value of T_{in} and T_{out} during the concentration measurements was defined as gas temperature within the reactor.

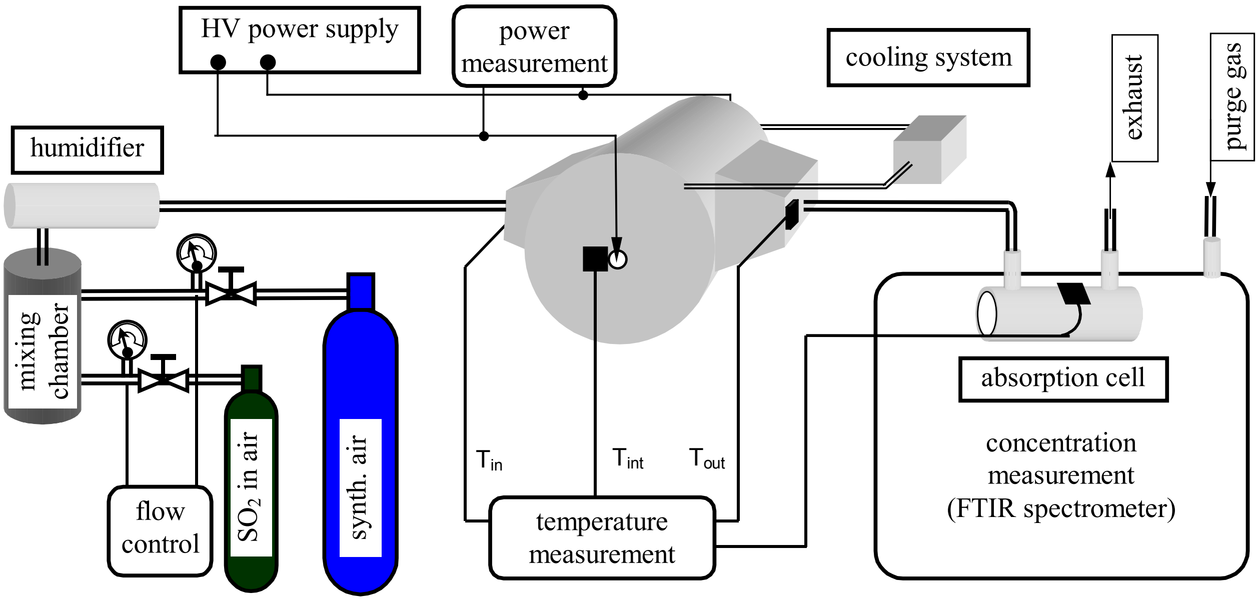

Fig. 1. Experimental set-up.

High voltage (HV) was supplied by a frequency converter in combination with a HV transformer. Two sources were used covering the frequency range from about 400 Hz to 1000 Hz (up to 50 kV peak voltage) and 10 kHz to 20 kHz (up to 15 kV peak), respectively. The power was determined with the well-known Lissajous figure method, the voltage with a HV probe and the charge with a measuring capacitor of 1 µF. All measurement devices connected to the reactor were protected by fast suppressor diodes.

Additionally to concentration measurements the discharge structure was controlled with an intensified CCD camera.

3. Results

3.1 Reactor contamination

During continuous operation of the reactor a drift of the SO_2 concentration was observed. This drift starts after switching on the reactor and lasts for 5 to 30 minutes (Fig. 2). After that the SO_2 concentration remains nearly constant for a long time (in the order of a day). If the operation is interrupted for some minutes, the SO_2 concentration even exceeds the initial one before it decreases again. The concentration decrease lasts then for 5 to10 minutes, that is considerable longer than the decay time at the beginning of the measurement (Fig. 2).

Looking at the electrodes of the reactor after long time operation, a layer of residua has been found on the surface of the electrodes. In contact with atmospheric moisture this layer causes droplets of sulphuric acid within some minutes. Operating the contaminated reactor with pure nitrogen (N_2 5.0 grade) a considerable SO_2 concentration is detected again, which decreases later on exponentially. From this follows that the contamination of the reactor consists mainly of SO_2 oxidation products, i. e. SO_3 and H_2SO_4.

In pure air a high number of microdischarges were observed stochastically distributed in the discharge gap. Adding SO_2 the discharge structure changes. A smaller number of microdischarges is now observable and their location is mostly fixed (Fig. 3). This situation remains unchanged even if sulphur dioxide is not any longer present in the gas stream. After cleaning the electrodes by a washing procedure the initial discharge behaviour returned.

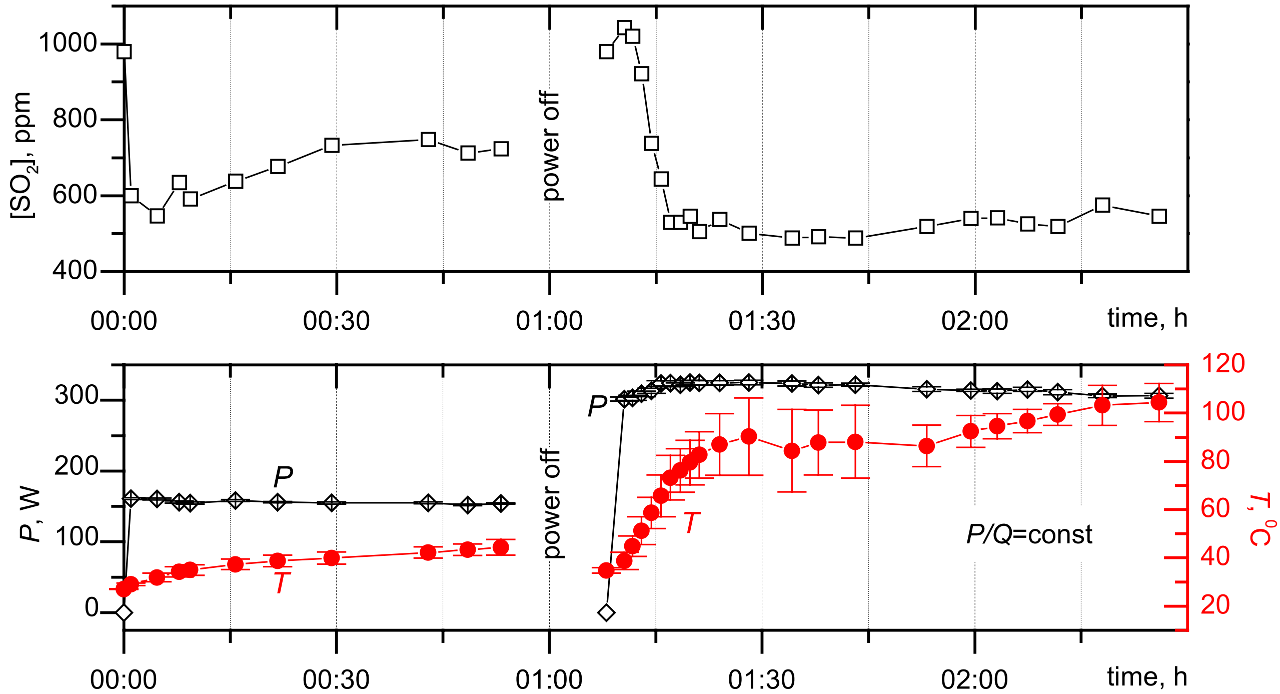

Fig. 2. SO_2 concentration, temperature and power versus time (the operation of the reactor was interrupted after about 55 minutes for 15 minutes).

The removal efficiency of the clean reactor is about two times higher than that of the contaminated one. As the transition of the performance between the clean and contaminated reactor is not reproducible all measurements were carried out with the contaminated and warmed-up reactor (after about half an hour of operation).

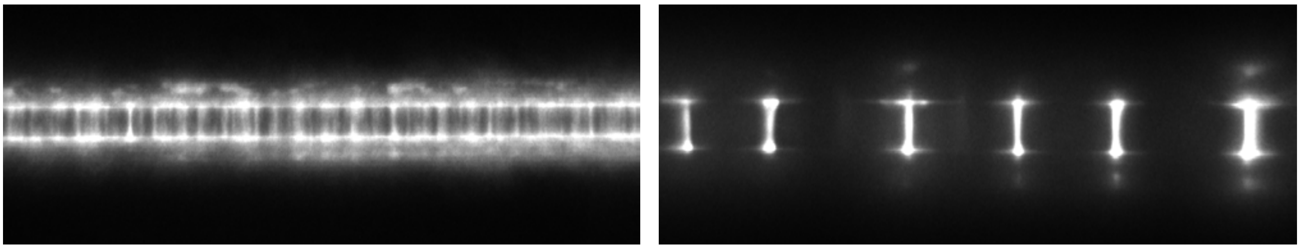

Fig. 3. Discharge structure (left) in dry air and (right) in humid air polluted with SO_2 (CCD images, exposure time 660 µs, H_20 2 % vol.).

3.2 Influence of initial SO_2 concentration

The experimental results for three different initial SO_2 concentrations are presented in Fig. 4. The concentration decreases exponentially. The destruction removal efficiency DRE and the energy efficiency factor β are nearly independent on the initial concentration (Table 1). This confirms that the SO_2 removal can be described by equation (1).

Table 1. Parameters of the kinetic curves of Fig. 4 calculated with equation (1).

$[SO_2]_0$, ppm	$[SO_2]_\infty$, ppm	DRE, %	β, Wh/Nl
980	146	85	5.8
547	82	85	5.2
111*	47	58	1.4
* The data belonging to this concentration are not reliable because of measurements nearby the detection limit.			

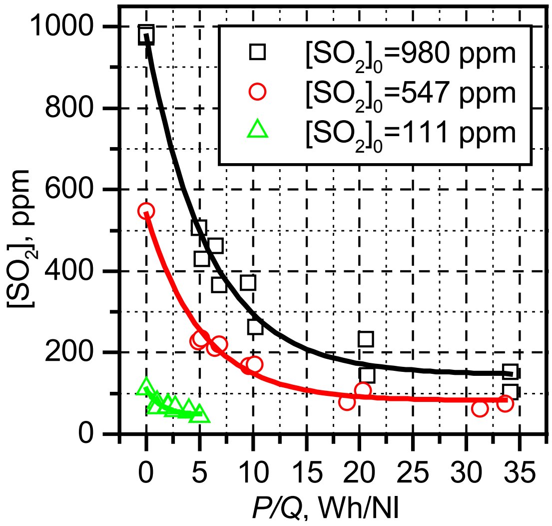

Fig. 4. Kinetic curves of SO_2 removal in dry air (15 kHz, 300 W).

3.3 Influence of temperature and humidity

Changing the gas temperature by varying the cooling conditions the residual SO_2 concentrations have been measured in dry and humid air (Fig. 5 and 6). All other boundary and operating conditions have been fixed as far as possible.

From Fig. 5 follows that in dry air temperature has nearly no influence on the SO_2 concentration in the range of 60 to 100 ^{0}C and on the energy efficiency factor β as well as the destruction removal efficiency DRE.

At a humidity of about 20,000 ppm (2 % vol.) the situation changes (Fig. 6). The SO_2 concentration drops drastically in the temperature range from 20 to 100 ^{0}C. This is explained in [2] by a reduction of nitrogen oxides in the presence of water vapour.

In general temperature influences the structure of the discharge. At elevated temperature the discharge looks more homogeneous (diffuse) both in dry and humid air, with and without SO_2 admixtures.

.

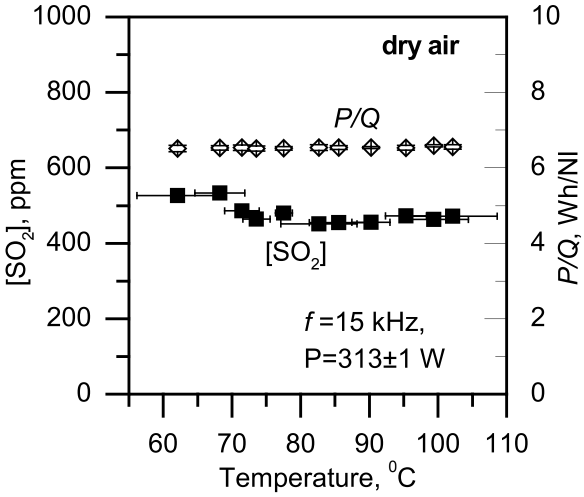

Fig. 5. SO_2 concentration versus temperature in dry air.

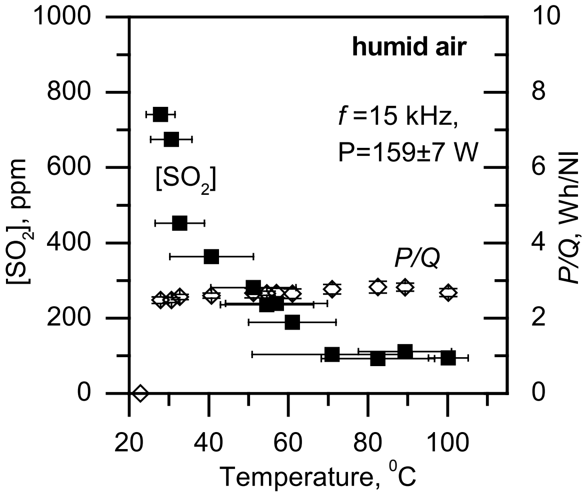

Fig. 6. SO$_2$ concentration versus temperature in humid air (2 % vol. H$_2$O).

The kinetic curves of SO$_2$ removal in dry and humid air are presented in Fig. 7. The curve for humid air was obtained at approximately constant temperature (about 40 ^{0}C). The presence of water vapour strongly influences the reactor performance. At the given temperature the minimum reachable sulphur dioxide concentration $[SO_2]_\infty$ is drastically improved even at significantly lower values of the specific power.

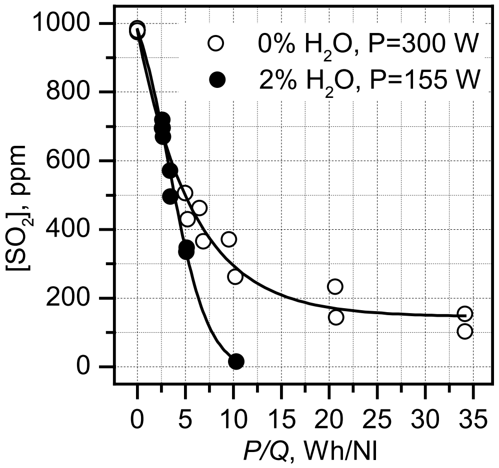

Fig. 7. Kinetic curves of SO$_2$ removal in dry and humid air (15 kHz).

3.4 Power supply and reactor design

The parameters of the power supply, i. e. voltage amplitude, frequency and power cannot be changed independently. Changing the power means changing either frequency and/or voltage amplitude. In general the experiments were performed with a frequency of 15 kHz in the power range from 100 to 400 W (8 to 15 kV). No systematic influence of the power value on the energy efficiency factor β has been found. The minimum sulphur dioxide concentration $[SO_2]_\infty$ has been reached at a power value of about 300 W with all reactor designs under investigation.

Changing the frequency (with the same reactor design) leads to differences in the reactor performance (Table 2, No. 1 and 2). At 15 kHz the value of $[SO_2]_\infty$ is considerable lower than that at 1 kHz. At the lower frequency β is higher, however, with a larger scatter. The discharge structure does not change remarkably if the lower frequency is applied.

The reactor design was changed with respect to the thickness and kind of dielectric as well as the width of the discharge gap. Changing the thickness of the dielectric (No. 1 and 3 of Table 2) no pronounced difference in the performance has been found. Replacing glass by quartz (No. 3 and 4) a certain improvement was observed. In all cases the discharge structure did not change.

Table 2. Energy efficiency factor β and minimum sulphur dioxide concentration $[SO_2]_\infty$ for different reactor designs ($[SO_2]_0$ = 980 ppm).

No.	Dielectric		Gap, mm	f, kHz	β, Wh/Nl	$[SO_2]_\infty$, ppm
	thickness	material				
1	1.0 mm	glass	2	15	5.1±1.3	254±75
2	1.0 mm	glass	2	1	7.5±3.4	502±14
3	1.5 mm	glass	2	15	6.2±1.6	241±76
4	1.4 mm	quartz	2	15	4.0±0.5	197±178
5	1.5 mm	glass	4	15	5.3±0.9	114±58

Increasing the discharge gap from 2 to 4 mm (No. 3 and 5) the value of $[SO_2]_\infty$ is about halved. Looking at the structure of the discharge a change was observed with the 4 mm gap. A lower number of channels are observed, which happen always at the same position like in Fig. 2 (right).

From the data presented it follows that mainly the discharge gap influences the performance of the reactor. The kind of the dielectric is of less and its thickness of no importance. Enlarging the discharge gap from 2 to 4 mm the SO_2 conversion is improved considerably.

4. Conclusion

The dielectric barrier discharge has been proved to be an effective tool to remove SO_2 pollution from air. The destruction removal efficiency reaches values of more than 98 %. The reactor performance depends mainly on operating frequency, discharge gap distance and especially gas temperature in combination with humidity. Increasing these values desulphurisation is more effective. High efficiency has been reached although the reactor was contaminated by SO_2 oxidation products.

References

[1] B.M. Penetrante, S.E. Schultheis (Eds.) – NATO ASI Series G: Ecological Sciences **34**, Part A (1993).
[2] A.B. Saveliev, A.r. Murtazin, G.J. Pietsch – Proc. 16th Int. Symp. On Plasma Chem., Toarmina, Italy (2003).

Acknowledgement

The authors gratefully acknowledge the funding of these investigations by the European Community under the “Competitive and Sustainable Growth” programme (Project No. G1ST-CT-2001-50138, project coordinator: Ecozone Technologies, Israel).

The Behaviour of Metal Bath in the Laboratory Plasma Furnace with Ceramic Crucible

M. Rozpondek, J. Siwka

Technical University of Częstochowa, Department of Metallurgy and Material Engineering, Poland

Introduction

The knowledge of distribution of the temperature and the movement of metal in crucible during heating with transferred plasma is indispensable for the description of thermodynamic phenomena and chemical reactions occurring at the liquid metal – slag – gas (plasma) interface. The present study reports the results the measurements the temperature on the surface of liquid metal.

On the base of the experiments date we were carried out the calculation of the distribution of the temperature and the velocity in the metal bath by commercial computer program FLUENT v. 6.0.

The present study reports the results obtained from tests carried out in a laboratory plasma furnace at the Extraction Department of the Technical University of Częstochowa.

1. Methodology of the measurements

Temperature measurements were taken by means the two-colour optical pyrometer (Integrated Ratio Pyrometer MR1F) by RAYTECK with a measurement range of 1000 – 3000°C. Measurements were executed after switching off the plasma arc (an electrical system for operating the shutter) and in the presence of the plasma beam (using an optical filter that modifies the radiation characteristics) [1].

2. Conclusions

The surface temperature is influenced mainly by the type of metal being melted and the level of heating the metal baths and the furnace working space. The effects of the electrical parameters of the plasma arc, the flow rate of the plasma-generating gas, and the pressure within the furnace, on the other hand, are much lesser [2]. The heat transfer in the metal bath is proceed mainly by the conductivity and in less degree through the convection. The temperatures gradient on the surface of liquid metal may reach 200 °C and it causes the Marangoni flow of the metal bath. The Marangoni effect may be a main force decided about a movement of liquid metal in the plasma melting. The temperatures of the liquid steel surface (anode spot) were in the range 2000 ÷ 2600 K.

References

[1] Rozpondek M., Siwka J., 14th Int. Symp. on Plasma Chemistry, Vol. 4, Prague, Czech Republic, 1999
[2] Rozpondek M., Siwka J., EMRS 2000 (Thermal Plasma Processes 6), Strasbourg, Francja, 2000
[3] Erochin A.A.: Zakonomiernosti plazmienno-dugowogo legirowanija i rafinirowanija metallow, Nauka, Moskwa, 1984, s. 20-23, 98-112

Silicon trench etch for Shallow Trench Isolation in 0,18 µm and below Flash Memory technology

Roberto Colombo[1], Simone Alba[1], Francesco Ciovacco[1], Chiara Savardi[1]

[1] *ST Microelectronics, Agrate Brianza, Italy*

Abstract

STI has become the method of choice for the isolation of devices in advanced CMOS processing. STI is typically 100÷400 nm deep for 0.18 µm technologies and below. The requirements for this etch process include good control of critical dimensions of active area, of etch depth uniformity, of trench slope angle and of the shape of Nitride layer. Top and bottom rounding of the trench are also applied to reduce the possibility of stress-induced defects from oxidation of the trench.

[1] S. Alba, F. Ciovacco, R. Colombo, C. Savardi, R. Patrick, D. Schaefer, M. Stendardo – In situ sub-0.18 µm Silicon trench etch – European Semiconductor, June 2002
[2] R. Patrick, S. Baldwin, N. Williams – Application of direct bias control in high-density inductively coupled plasma etching equipment – J. Vac. Sci. Technology A18(2), Mar/Apr 2000
[3] M. Ohkuni, S. Kugo, T. Sasaki, K. Tateiwa, H. Nikoh, T. Matsuo, M. Kubota – High performance etching process for organic films – The Institute of Electrical Engineers of Japan, Proceedings of symposium on dry process, November 12-14, 1997 Tokyo.
[4] S. J. Ullal, H. Singh, J. Daugherty, V. Vahedi, E. S. Aydil – Maintaining reproducible plasma reactor wall conditions: SF6 plasma cleaning of films deposited on chamber walls during Cl2/O2 plasma etching of Si - J. Vac. Sci. Technology A20(4), Jul/Aug 2002

Introduction

The Shallow Trench Isolation (STI) has become the most popular choice for the field isolation of Flash Memory. STI is typically 100÷400 nm deep for 0.18 µm and below technologies. The requirements for this etch process include good control of etch depth uniformity (from 5 to 10 %), control of trench slope angle, top and bottom rounding of the trench.

The STI is obtained by dry plasma etching processes, giving the chance to develop it with different characteristics: vertical and tapered STI, and also the application of top corner rounding at STI itself. In the results presented in this paper, equipments used for this application are inductively coupled plasma etchers. Critical parameters to keep under control are: the iso/dense microloading (due to the different pattern density) and shapes of isolated trenches respect of matrix areas.

The film stack to be etched in order to obtain a STI feature is patterned by lithographic photoresists (DUV lithography, 248 or 193 nm) which act as mask for the following etch steps; from top to bottom layers the stack is usually composed by organic bottom anti-reflecting coating (BARC), Silicon Nitride, Silicon Dioxide (Pad Oxide) and Silicon (in which the STI will be etched). In some cases the configuration could be different due to the presence of an hard mask layer (usually Silicon Dioxide) at the top of the Nitride layer (Fig.1).

The resulting etch recipe is quite complicated because of the shape of STI has an impact on electrical behaviour of memory cells, built on this isolation structure.

Equipment

The etch recipes for STI applications are developed on Lam TCP9400 PTX or DFM tools. They are inductively coupled plasma etchers consisting of a flat spiral transformer plasma coil that couples power inductively into the chamber. Two generators – locked in phase – drive power to the plasma and to the wafer chuck. The radio frequency power at 13,56 MHz is used for both the inductive source and wafer bias. The gas injection is from central top for DFM tools and from bottom side for PTX tools. A voltage sensor is attached immediately below the chuck to monitor the voltage applied to the wafer: this allows to set directly in the recipe the desired voltage bias (Fig.2).

Interferometry, optical emission spectroscopy and monochromator channels are used to detect endpoints.

Typical ranges of parameters involved in recipes are: RF power between 200 and 800W, chamber pressure between 5 and 80 mtorr, total gas flow between 100 and 400 sccm.

In order to maintain reproducible chamber conditions, after every processed wafer is applied a cleaning recipe without wafers inside the chamber. This recipe, named Waferless AutoClean, guarantees to remove organic and inorganic byproducts deposited on chamber walls.

Process definition

The photoresist is patterned by lithographic tools and acts as mask for the layers below. The choice about which photoresist to apply (DUV at 248 or 193 nm) is dependent from various issues: feature dimensions and density, overlaying to previous mask levels. From the etching point of view this choice is not negligible, due to the extremely different etch resistance of the two photoresist generations. Both the vertical and lateral consumption of the resist during the etch are very important. The vertical consumption must be low in order to preserve the film stack during all the recipe steps. The lateral consumption causes a progressive change in the dimensions of photoresist features during the etch and this doesn't allow to obtain vertical profiles of the layers below. The photoresist of 193nm lithography has poor etch performances, specifically for STI process, that is highly resist consuming (Fig.3).

The first etched layer is the BARC (60÷80nm thick) and the step has implications related to defectivity and, mainly, to the Critical Dimensions (CD) performance of STI process. Several chemistry mixtures are able to etch the BARC layer: Cl_2/O_2, HBr/O_2, CF_4 are the usual etching agents. They differ for CD performance, iso/dense microloading and selectivity to the underlying layers. Specifically the Cl_2/O_2 mixture has good endpoint detection but poor microloading performance, the HBr/O_2 has high selectivity to Silicon Nitride but high CD loss and CF_4 has good CD performance but high iso/dense microloading. About CD performance, thanks to a new STMicroelectronics solution (patent pending), it's possible to manage the resulting CD of features, obtaining variation up to 60nm of the after-lithography dimension. Contrary of resist trimming, the solution "reduces" the dimensions of the exposed features, allowing the etching of smaller trenches in the layers below the BARC.

The following step of etching Silicon Nitride (100÷160nm thick) is one of the most critical because the shape and the dimensions of Nitride features have a great impact on the performances of memory cell built on STI. The Nitride profiles can be vertical or at specified slope: the plasma etching is typically based on $HBr/CF_4/O_2$ mixture and varying this mixture in accordance with the power applied to the wafer is possible to tune the angle of the profile. It's also critical to guarantee that the Silicon Nitride is completely removed from areas exposed to etch: if not, it acts as mask for the following etch steps, preventing the correct formation of the trench. The etching of Nitride is a high resist consumption step and there must be a concern about this: the ideal shape of Nitride after etch must not show any faceting of the upper corners of features. The following steps for defining the memory cell would be heavily affected by a "bad" Nitride. The faceting is a result coming from the consuming of the photoresist: so the process recipe has, at the same time, to etch the layer and to save photoresist thickness. To find the right balance is not a trivial work (Fig.4).

The Pad Oxide (13÷16nm thick) acts as buffer layer between the Si_3N_4 and the Si bulk; this step doesn't present any specific problem during the standard STI etch. The small thickness of the layer allows to etch it by a short step at fixed time (Fig.5a). But if the device is designed with the application of top corner rounding (TCR; fig. 5b), the simple Pad Oxide step (simply named Breakthrough) is substituted with a more complex step that applies the characteristics of the gas mixture CF_4/CH_2F_2 (the latter can also be CHF_3) to create a shoulder at the beginning of the trench. The reason for the application of TCR derives from the need to avoid an abrupt transition from active area region (under the Nitride) and the sidewall of the trench: a smoother bending should reduce dislocations in the Silicon below.

The presence of TCR has a great impact on the shape of the trench, etched just after TCR step. In fact, TCR shoulders are created by polymer formation on the sidewall of photoresist, BARC and Nitride. During the following trench etch step, this polymerization modifies the etching conditions, giving birth to bowed profiles instead of the wanted straight profiles, clearly seen in the case of sloped profiles, that are obtained by

polymerizing etch step. The shape of TCR depends on the gas mixture, and the dimension on the time duration of the step. Very different TCR shoulders can be obtained by tuning the two parameters (Fig.5).
The trench step gives the chance to obtain a number of different shapes of the Silicon trench: usually sidewalls have straight profiles, vertical or at specified angle (the so called tapered trench). Vertical or near vertical sidewalls are the simplest solution because the etching is almost independent from the TCR (if any) step. The tapered trench is obtained by a polymerizing etch using HBr/O_2 mixture: the trench is tuned to have a not-zero deposition rate and depending from this rate it is possible to etch the trench at specified angle.
The choice to apply a tapered trench relates to the characteristics of the device. For example for Flash Memory devices, in some process steps following the STI formation, trench sidewalls are exposed to doping implantation: the doping is quite impossible to obtain with vertical sidewalls.
If TCR is formed before the tapered trench, this latter step needs the development of a multiple sub-steps (STM patent pending), working as polymerization compensation. This is due to the fact that the polymer coming from the trench step deposits on that coming from TCR step: the result of these overlapping polymers is bowed sidewalls. This kind of sidewalls is not acceptable for the following process steps of oxidation and filling of the trench (Fig.6).
In some specific configuration it is necessary to deposit an hard mask (HM) on the Nitride layer: the HM is typically oxide (SiO_2) and has the function to help the photoresist to perform its job of masking the etching of underlying layers. The use of an HM adds complications to the etch recipe and hence is not a preferred solution. However, for the 193nm lithographic photoresist generation, which use is foreseen for 90 nm technology node, the application of the HM is almost obliged: the bad performances of this photoresist forces this solution in order to avoid excessive CD loss, Nitride tapering and faceting.

Conclusion

For manufacturing microelectronics devices, the definition of STI structures is a fundamental step, not only related to its function of isolation. Dimensions and shapes are directly related to the electrical performance of devices. The multi-level film stack needs to be etched by specific developed etch steps and each steps must be integrated together and have specific issues to be taken account for the final result.

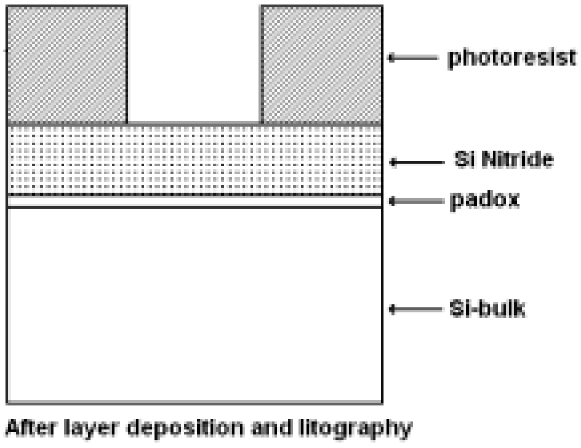	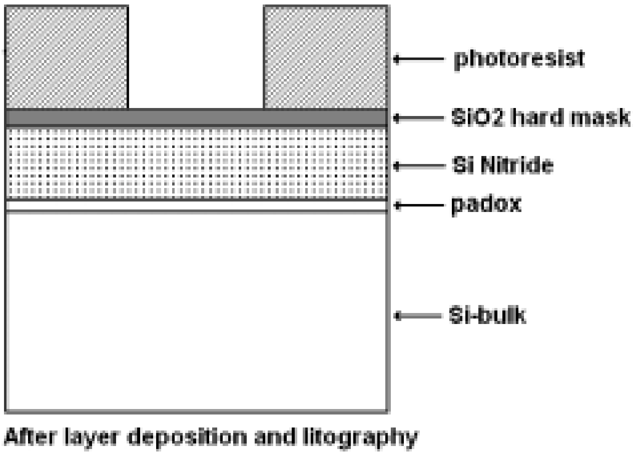
Fig.1a) Standard STI film stack	Fig.1b) STI film stack with SiO_2 hard mask

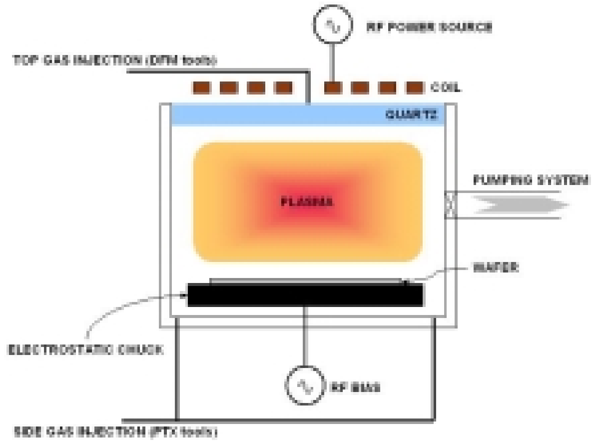

Fig.2a) Schematic drawing of the Lam dry plasma etch chamber (PTX or DFM)

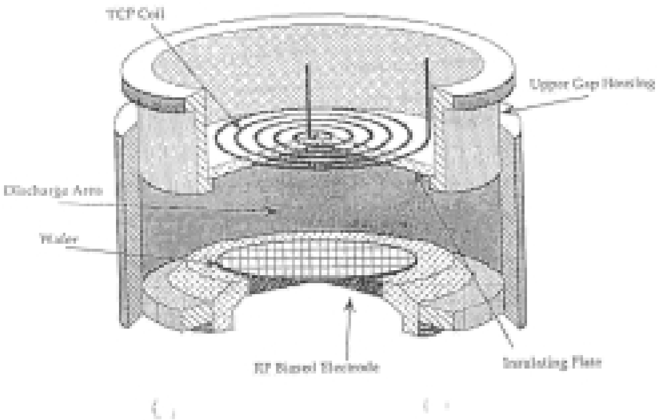

Fig.2b) Chamber layout (courtesy of Lam)

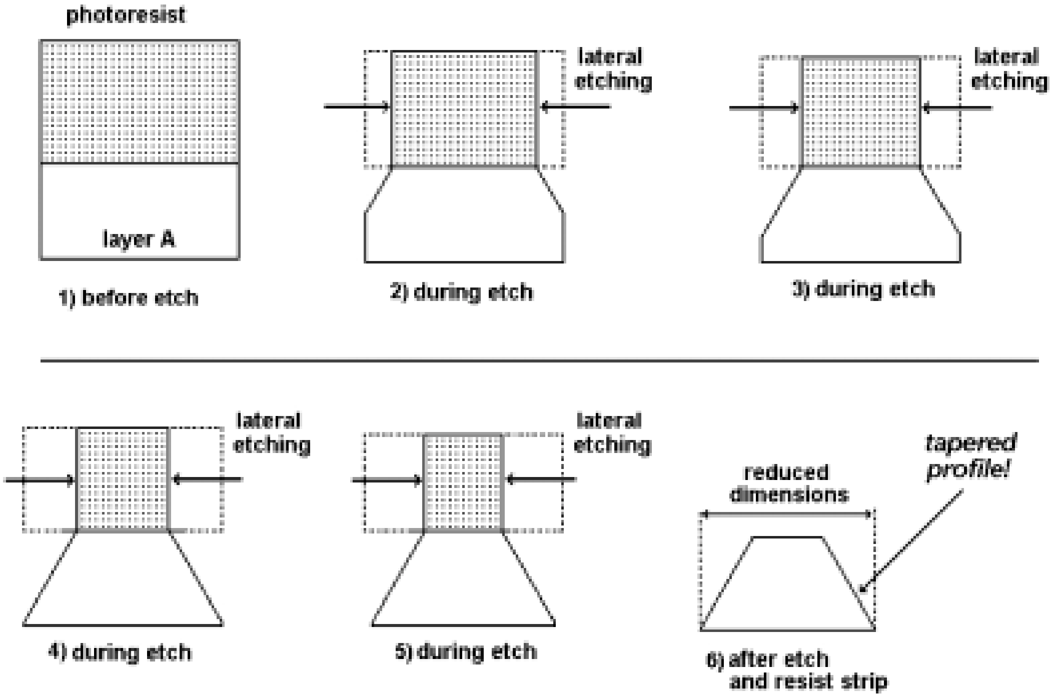

Fig.3) How the lateral consumption of the photoresist causes tapered profile of the underlying layer.

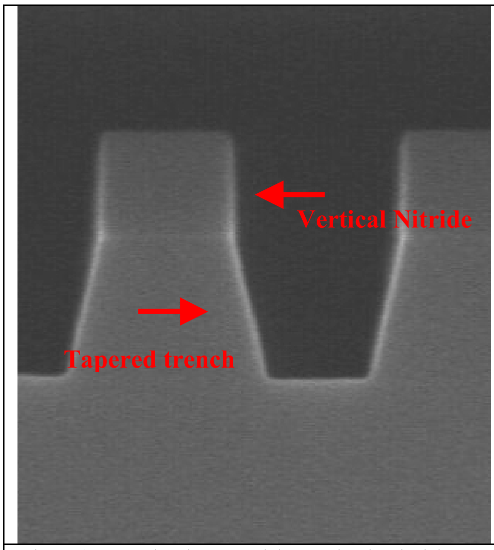

Fig.4a) Standard STI with vertical Nitride and tapered trench

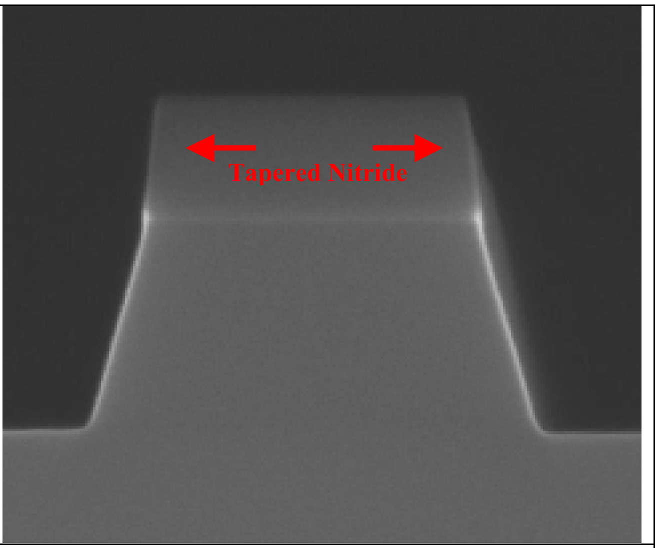

Fig.4b) Standard STI with tapered Nitride and trench

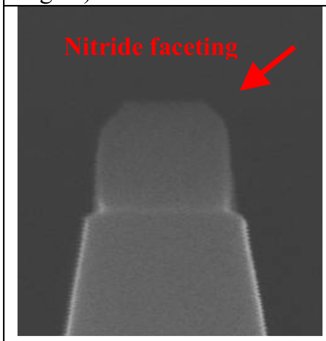

Fig.4c) Nitride faceting due to excessive photoresist consumption

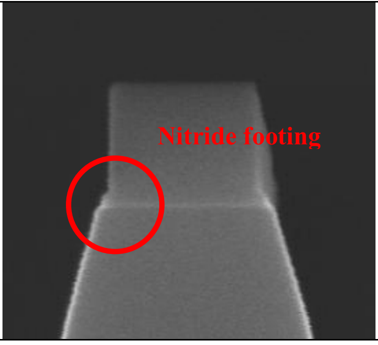

Fig.4d) Nitride footing due to slightly incomplete Nitride etch.

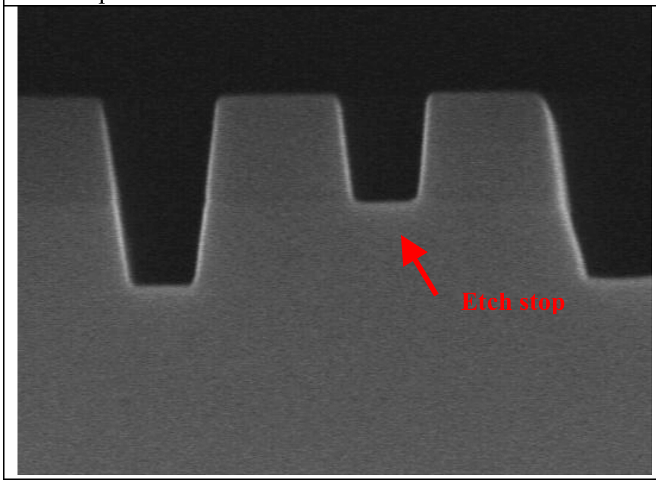

Fig.4e) Cross section of STI with etch-stop due to incomplete Nitride etch or padox etch.

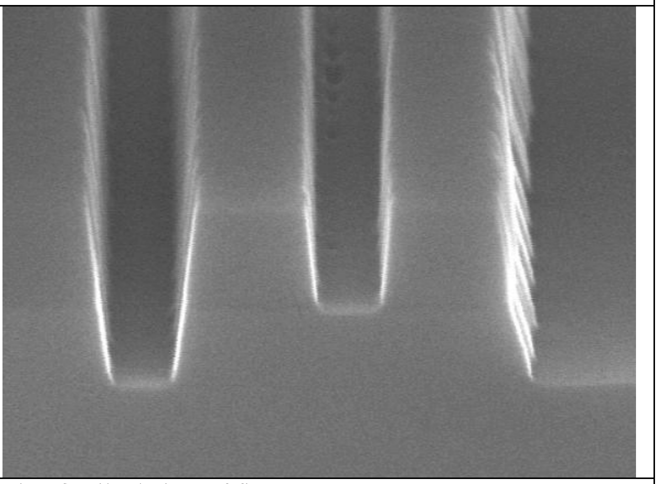

Fig.4f) Tilted view of fig.4e.

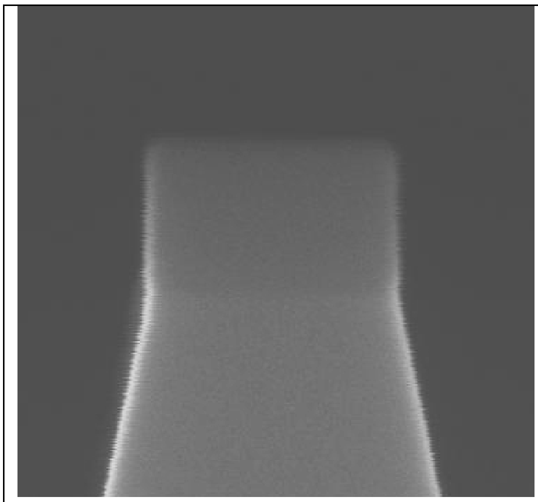

Fig.5a) Cross section of the usual padox etch step, that guarantees a vertical profile before the trench etch.

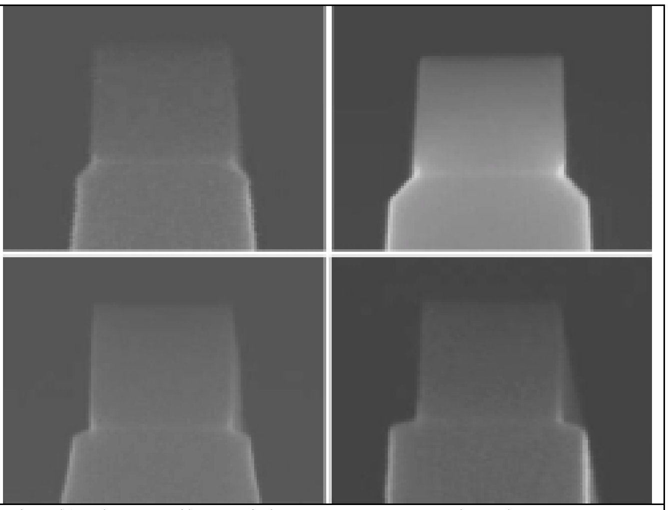

Fig.5b) Photo gallery of the TCR step: varying the parameters of the step is possible to obtain different dimensions (left to right) and shapes (top to bottom).

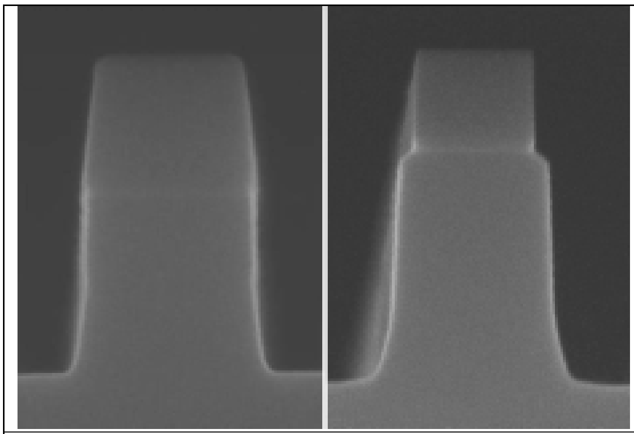

Fig.6a) Vertical profile trench without and with the application of TCR. The bottom rounding of the trench helps the following Oxide filling steps.

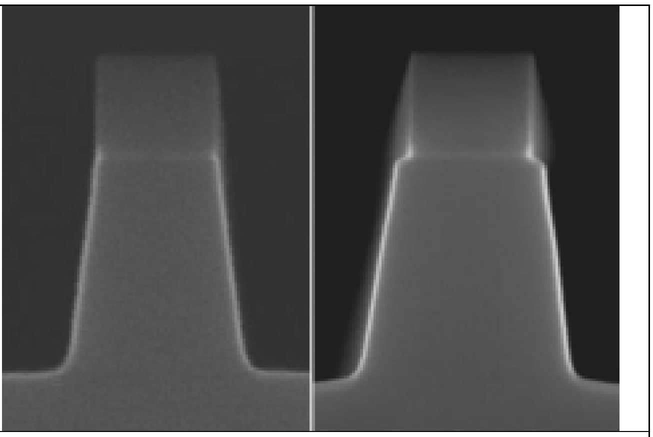

Fig.6b) Tapered profile without and with the application of TCR. The Sacociov approach (STM patent request pending) is needed to obtain a straight profile in this latter solution.

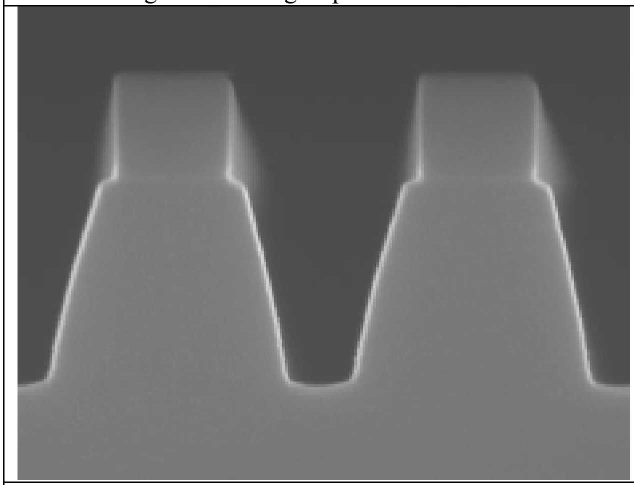

Fig.6c) The effect of TCR on the tapered trench when applied without Sacociov etch steps.

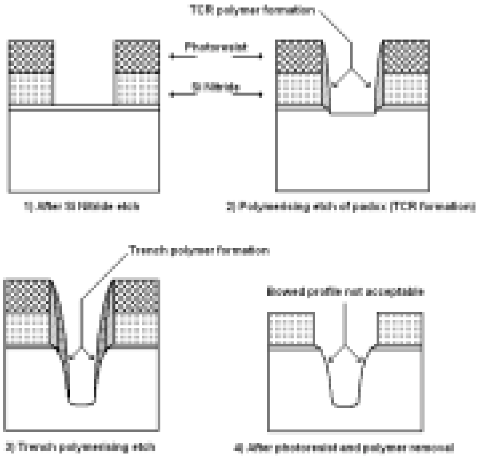

Fig.6d) Explanation of the resulting bowed profile of the trench showed in fig.6c.

Glow discharge for killing insects in rice

W.R. Rutgers, H. van Houten, H.A. Jenner

KEMA-TDC Arnhem, IV-Consult Papendrecht, KEMA-KPS Arnhem, The Netherlands

Dry matter such as foodstuffs that are transported in bulk (rice, cereals, flour etc.) frequently contain entomology (insects, insect larvae and insect eggs), which feed on the dry matter. To kill this entomology at present use is made of treatment of the dry matter with chemical agents such as methyl bromide. In this paper we introduce an environmentally friendly alternative treatment for killing entomology by glow discharge plasma, which prevent the use of toxic substances.

To demonstrate the glow discharge treatment of rice a glow discharge plasma chamber with 10 and 49 electrodes above a copper plate was build. To make a uniform glow discharge each electrode is connected to a HV power supply via a 100 kOhm series resistor. The air pressure in the chamber is between 10 and 45 mBar. For initial trials with the 10 electrode system a DC power supply, an AC power supply (50 Hz) and a pulsed power supply were used. Short HV pulses of 0.1 msec duration and 100 Hz repetition frequency gave the best results in killing insects. The experiments were continued with 49 electrodes (7*7 array), pulses of 0.1 msec duration, 1 kHz repetition frequency and a gas pressure of 15 mBar. 100% killing was obtained for *Sitophylus orizae* and *Tribolium castaneum* as well as for their larvae with a glow discharge of 500 Volt and (total) current of 200 mA during the pulse. Because of the low power input the temperature increase and loss of moisture of the rice is limited. No change in taste of the rice after cooking was established. After successful experiments in batch treatment a flow system has been designed to investigate up scaling of the glow discharge plasma technique for killing entomology.

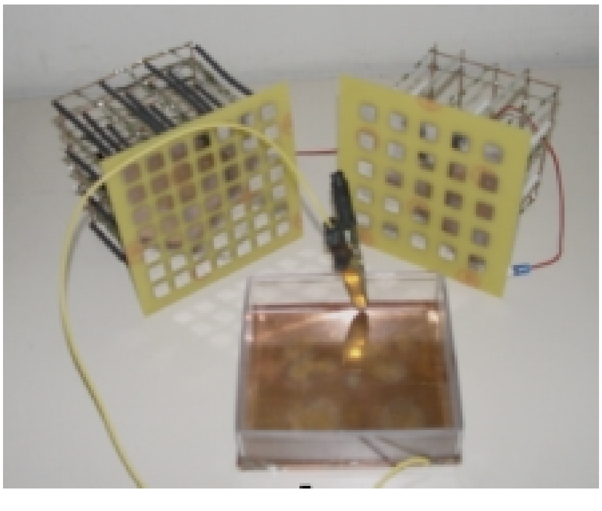

7*7 (left) and 5*5 (right) electrode arrays with series resistors for the production of uniform glow discharge

Control of a DC-RF Hybrid Plasma Flow System for Particle In-flight Treatment

K. Kawajiri, K. Ramachandran and H. Nishiyama

Institute of Fluid Science, Tohoku University, Sendai, 980-8577, Japan

Abstract

A DC-RF hybrid plasma flow has complex flow structure owing to the strong interaction between an RF-ICP flow and a DC plasma jet. A DC-RF hybrid plasma flow is ignited easily and becomes stable when the central gas ratio is low and the swirl gas ratio is high. Nitrogen should be injected with the central gas, and its injection limit can be increased by decreasing the central gas ratio and increasing the swirl gas ratio. Regression relations are obtained for different variables from the experimental results.

1. Introduction

A radio frequency inductively coupled plasma (RF-ICP) flow has many advantages, a large plasma volume, low gas velocity, and its purity. Then an RF-ICP flow has been investigated intensively [1-2], and used for material processing such as spraying and fine particles synthesis [3-5]. However, an RF-ICP flow is very sensitive to the flow conditions or a mixed reactive gas and becomes unstable easily. Then a DC-RF hybrid plasma flow has been expected to overcome these disadvantages of an RF-ICP flow. It is composed of an RF-ICP flow and a direct current (DC) plasma jet as a supplement to an RF-ICP flow. In a DC-RF hybrid plasma flow, a DC plasma jet is used to ignite and maintain an RF-ICP flow stably. So far, its applications have been investigated by Yoshida et al intensively [6-8]. However, there are few papers that clarified the effect of the flow condition on the plasma characteristics.

In the present study, we consider the injected gas conditions as an input, and consider the following parameters, plasma stability, appearance voltage of an RF-ICP flow, upper limit of the injected reactive gas flow rate and particle residence time in the plasma core region as outputs. And the effects of the inputs and their interactions on the outputs are clarified statistically by Taguchi method [9-10].

2. Experimental apparatus and procedures

Figure 1 shows the schematic of the experimental apparatus and Figure 2 shows the schematic of the DC-RF hybrid plasma torch and the gas injection system. The DC-RF hybrid plasma torch consists of 3-turn RF induction coil, water-cooled quarts tube of 44 mm inside diameter, and DC electrodes mounted on the torch head. There are three modes of gas injections to control the plasma flow characteristics. The sheath gas is the most fundamental gas to produce an RF plasma flow. The central gas, which is discharged to produce a DC plasma jet, is

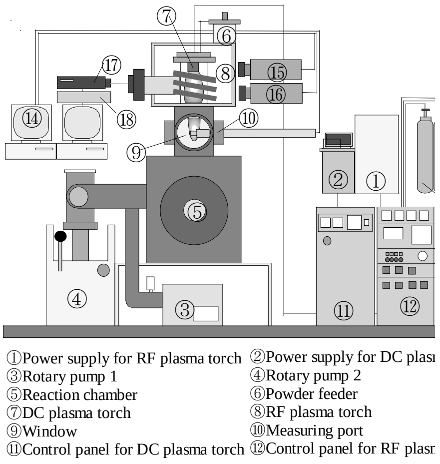

Figure 1. Schematic of the experimental apparatus

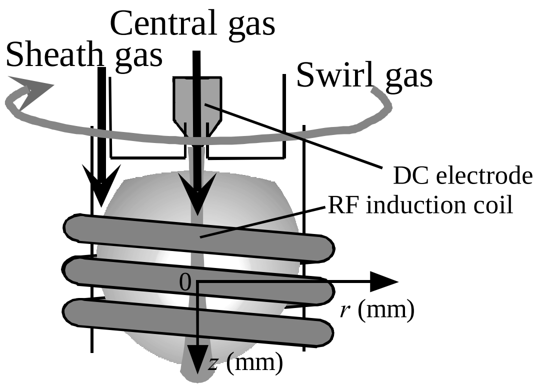

Figure 2. Schematic of a DC-RF hybrid plasma torch and a gas injection system

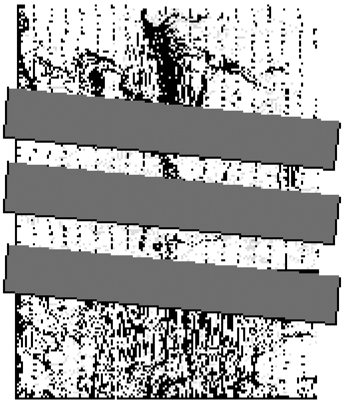

Figure 3 Particle trajectory in the coil region

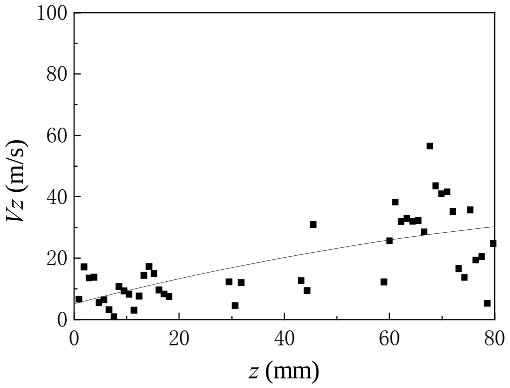

Figure 4 Particle velocity in the centerline region of Figure 3

Table 1 (a) Particle residence time in the coil region for each condition

		R_{Sw}				
		20	30	40	50	Total
R_C	20	0.005126	0.005539	0.008196	0.009051	0.027912
	30	0.005442	0.003375	0.006948	0.006168	0.021933
	40	0.003233	0.003716	0.003257	0.003865	0.014072
	50	0.00282	0.002489	0.003365	0.002982	0.011656
	Total	0.016622	0.015119	0.021766	0.022066	0.075573

(b) ANOVA for particle residence time

	f	S	V	$F0$	F	$F0'$	F'	$\rho(\%)$
R_{Cl}	1	0.00004009	0.00004009	65.71285	0.00003970	52.43442	0.00001027	66.15307
R_{Cq}	1	0.00000079	0.00000079	1.301033	0.28701838			
R_{Cc}	1	0.00000067	0.00000067	1.099675	0.32498226			
R_{Swl}	1	0.00000660	0.00000660	10.81962	0.01103325	8.633326	0.01241222	10.8921
R_{Swq}	1	0.00000020	0.00000020	0.332745	0.57991208			
R_{Swc}	1	0.00000263	0.00000263	4.305411	0.07167576			
R_{Cl}*R_{Swl}	1	0.00000474	0.00000474	7.763208	0.02369485	6.194517	0.02849062	7.815215
e	8	0.00000488	0.00000061					
T	15	0.00006060	0.00005633					100
(e)	12	0.00000917	0.00000076		0.00000076			15.13961

injected through the nozzle of the DC torch whose diameter is 2mm. The swirl gas is injected with the sheath gas to rotate the sheath gas. We used nitrogen as a reactive gas. Nitrogen is injected into the plasma torch by being mixed with the central gas or the sheath gas selectively. Alumina particles of 10 μm diameter, which are injected into the centerline region, are used as a tracer for the particle image velocimetry (PIV) system.

Appearance and disappearance voltages are measured from the plate voltage of the RF induction coil at a moment when an RF-ICP flow is ignited and extinguished in a DC-RF hybrid plasma flow. Upper limits of an injected nitrogen flow rate are measured when an RF-ICP flow is extinguished in a DC-RF hybrid plasma flow. Particle residence time in the core region is obtained from particle velocity measured with a PIV system. Figure 3 shows the particle trajectory in the core region. Figure 4 shows the particle velocity in the centerline region (Figure 3). Operating conditions are as follows. RF power is 5.5 kW at 4MHz oscillator frequency. DC power is 1 kW and gas is Argon or mixture of Ar/N_2. Total gas flow rate is fixed to 20 l/min to keep the constant operating pressure at 9000 Pa. R_C and R_{Sw}, whose levels are adopted at four levels (20, 30, 40, 50 %), stand for the ratio of the central gas flow rate and that of the swirl gas flow rate to the total gas flow rate respectively.

3. Results and discussion

3.1 Particle residence time

Tables 1 (a) shows a particle residence time T_R (s) in the coil region for each condition and Table 1 (b) shows the analysis of variance (ANOVA) for T_R; where subscript l, q and c indicate linear, quadratic and cubic in Chebyshev's orthogonal polynomial respectively, and asterisk indicate the interaction. f stands for degrees of freedom and S for sum of squares of a effect of R. V stands for a variance obtained by dividing a mean sum of squares of source R by its f. $F0$ is the variance ratio to V of error e. F stands for F-possibility, which is significant if this value is less than 0.05, and the value shows a possibility that it happens accidentally. $F0'$ and F' stands for modified $F0$ and F respectively by adding not significant f and V values to e's one, which is shown in *(e)* column.

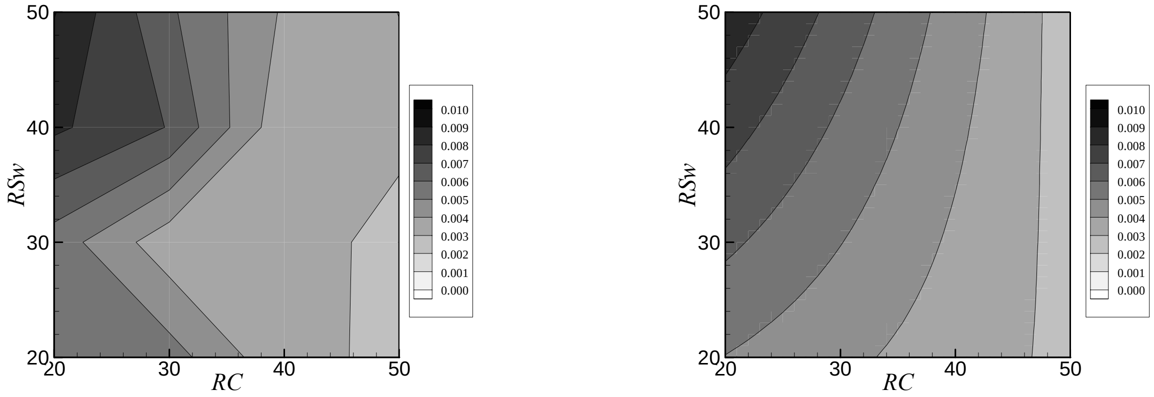

Figure 5 (a) Contour map of T_R obtained by the experiment (b) Contour map of T_R obtained by the equation (1)

Table 2 (a) Appearance voltage for each condition

		R_{Sw}				
		20	30	40	50	Total
R_C	20	4.5	3.8	3.5	3.1	14.9
	30	4.8	4.2	4.1	3.8	16.9
	40	5.1	4.6	4.3	4.1	18.1
	50	5.1	5.1	4.7	4.7	19.6
	Total	19.5	17.7	16.6	15.7	69.5

(b) ANOVA for appearance voltage

	f	S	V	$F0$	F	$F0'$	F'	$\rho(\%)$
R_{Cl}	1	2.926125	2.926125	203.5565	0.00000057	176.0075	0.00000002	55.63636
R_{Cq}	1	0.015625	0.015625	1.086957	0.32762515			
R_{Cc}	1	0.015125	0.015125	1.052174	0.33501999			
R_{Swl}	1	1.953125	1.953125	135.8696	0.00000267	117.4812	0.00000015	37.13607
R_{Swq}	1	0.050625	0.050625	3.521739	0.09740910			
R_{Swc}	1	0.003125	0.003125	0.217391	0.65346725			
$R_{Cl}*R_{Swl}$	1	0.180625	0.180625	12.56522	0.00756725	10.86466	0.00638603	3.434343
e	8	0.115	0.014375					
T	15	5.259375	5.15875					100
(e)	12	0.1995	0.016625		0.01662500			3.793226

ρ shows a strength of a source influence on obtained results.

As shown in Table 1 (b), the influence of the central gas on the particle residence time is much stronger than that of the swirl gas because particles in the centerline region are accelerated mainly by the central gas. The influence of error is somewhat large because the influence of R_{Swq} on V_A, which is neglected and added to the effect of error, is large. Then the regression analysis is conducted from the results in Table 1 (a) and (b), and the following equation is obtained.

$$T_R = 4.72\times10^{-3} - 1.42\times10^{-4}(R_C - 35) + 5.74\times10^{-5}(R_{Sw} - 35) - 4.35\times10^{-6}(R_C - 35)(R_{Sw} - 35) \quad (1)$$

Figure 5 (a) shows the contour map of T_R obtained from the experiment and Figure 5 (b) shows the contour map obtained from the equation (1). As compared with Figure 5 (a), Figure 5 (b) has the different tendency at the area of R_{Sw}=30 %. This is because T_R is not calculated accurately by equation (1) owing to the effects of the neglected sources, particularly R_{Swq}. From these results, it can be concluded that the central gas ratio should be kept lower and the swirl gas ratio should be kept higher to increase the particle residence time in the plasma core region.

3.2 Appearance and disappearance voltages

The appearance voltage V_A (kV) is shown in Table 2 (a) and its ANOVA is shown in Table 2 (b). The disappearance voltage V_D (kV) is shown in Table 3 (a) and its ANOVA is shown in Table 3 (b). The influences of the central gas and the swirl gas on V_A (Table 2 (b)) are similar to that of the central gas and the swirl gas on V_D (Table 3 (b)). The effect of the central gas on V_A and V_D is rather larger than that of the swirl gas. There are two reasons for it. The first reason is that the axial gas velocity is increased by the central gas effectively. Therefore, the temperature in the skin effect region of an RF-ICP flow, which plays an important role to ignite an RF-ICP flow and to stabilize it, is decreased owing to the strong heat diffusion to downstream region. The second reason comes from that specific enthalpy of a DC plasma jet increases with decreasing the central gas ratio, and electron density in the coil region increases. From the two tables, the following equations are obtained from regression analysis.

Table 3 (a) Disappearance voltage for each condition

		R_{Sw}				
		20	30	40	50	Total
R_C	20	3.8	3.5	3.5	3.1	13.9
	30	3.9	3.8	3.8	3.6	15.1
	40	4.2	3.9	3.8	3.8	15.7
	50	4.2	4.2	4	3.8	16.2
	Total	16.1	15.4	15.1	14.3	60.9

(b) ANOVA for disappearance voltage

	f	S	V	$F0$	F	$F0'$	F'	$\rho(\%)$
R_{Cl}	1	0.703125	0.703125	63.63122	0.00004459	65.23194	0.00000201	56.27814
R_{Cq}	1	0.030625	0.030625	2.771493	0.13452271			
R_{Cc}	1	0.003125	0.003125	0.282805	0.60931424			
R_{Swl}	1	0.406125	0.406125	36.75339	0.00030172	37.67797	0.00003554	32.50625
R_{Swq}	1	0.000625	0.000625	0.056561	0.81799418			
R_{Swc}	1	0.010125	0.010125	0.91629	0.36648053			
$R_{Cl}*R_{Swl}$	1	0.007225	0.007225	0.653846	0.44212181			
e	8	0.0884	0.01105					
T	15	1.249375	1.172025					100
(e)	13	0.140125	0.010779		0.01077885			11.21561

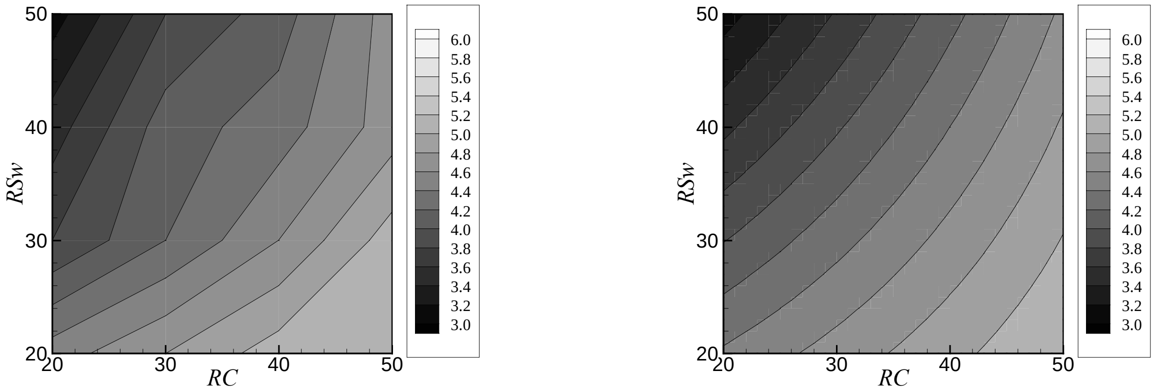

Figure 6 (a) Contour map of V_A obtained by the experiment (b) Contour map of V_A obtained by the equation (2)

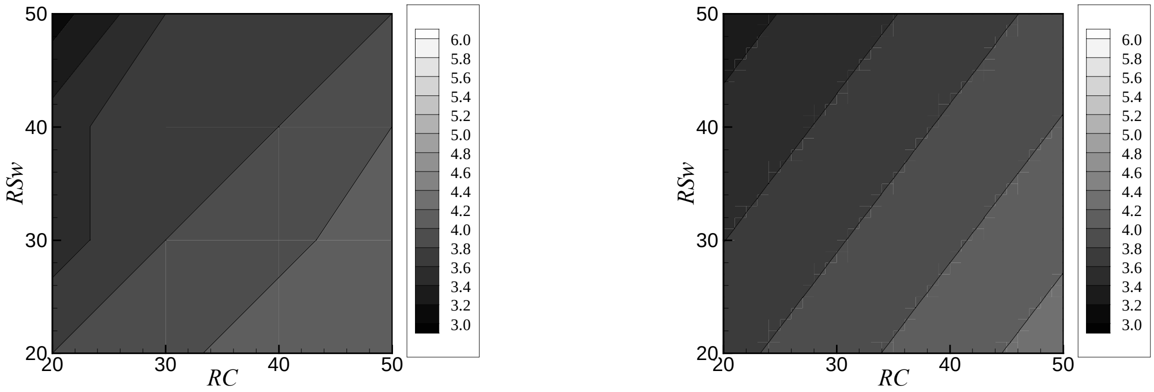

Figure 7 (a) Contour map of V_D obtained by the experiment (b) Contour map of V_D obtained by the equation (3)

$$V_A = 4.34 + 3.83\times10^{-2}(R_C - 35) - 3.13\times10^{-2}(R_{Sw} - 35) + 8.50\times10^{-4}(R_C - 35)(R_{Sw} - 35) \tag{2}$$

$$V_D = 3.81 + 1.88\times10^{-2}(R_C - 35) - 1.43\times10^{-2}(R_{Sw} - 35) \tag{3}$$

Figure 6 (a) shows the contour map of V_A obtained from the experimental results, and Figure 6 (b) shows the contour map obtained from the equation (2). Figure 7 (a) shows the contour map of V_D obtained from the experiment, and Figure 7 (b) shows the contour map obtained from the equation (3). From the results in Tables 2 and Tables 3, V_A and V_D are calculated accurately by the each equation because the influences of error on the results are low. From the results of these figures, an RF-ICP flow is ignited easily and kept stably in a DC-RF hybrid plasma flow by keeping the central gas ratio lower and the swirl gas ratio higher.

3.3 Upper limit of injected nitrogen flow rate

Tables 4 (a) and (b) show the upper limits of injected nitrogen flow rate L_C (l/min) and the ANOVA for L_C respectively in case of nitrogen is injected with the central gas. Tables 5 (a) and (b) show the upper limits of injected nitrogen flow rate L_{Sw} (l/min) and the ANOVA for L_{Sw} in case of nitrogen is injected with the sheath gas. As shown in Table 4 (a) and Table 5 (a), L_C is much larger than L_{Sw}. The main reason for that depends on the position where

Table 4 (a) Upper limit of injected nitrogen flow rate for each condition in case of nitrogen is injected with the central gas

		R_{Sw}				
		20	30	40	50	Total
R_C	20	1.3	2	2.6	6	11.9
	30	1.2	1.4	1.8	2	6.4
	40	1.2	1.2	1.5	1.6	5.5
	50	1.1	1.1	1.5	1.6	5.3
	Total	4.8	5.7	7.4	11.2	29.1

(b) ANOVA Upper limit of injected nitrogen flow rate

	f	S	V	$F0$	F	$F0'$	F'	$\rho(\%)$
R_{Cl}	1	5.356125	5.356125	11.17198	0.01019397	10.15716	0.00781850	25.40329
R_{Cq}	1	1.755625	1.755625	3.661939	0.09201641			
R_{Cc}	1	0.190125	0.190125	0.396569	0.54642685			
R_{Swl}	1	5.460125	5.460125	11.3889	0.00971701	10.35438	0.00738425	25.89655
R_{Swq}	1	0.525625	0.525625	1.096365	0.32566684			
R_{Swc}	1	0.021125	0.021125	0.044063	0.83898338			
$R_{Cl}*R_{Swl}$	1	3.940225	3.940225	8.218647	0.02093098	7.4721	0.01814802	18.68789
e	8	3.8354	0.479425					
T	15	21.08438	17.7284					100
(e)	12	6.3279	0.527325		0.52732500			30.01227

Table 5 (a) Upper limit of injected nitrogen flow rate for each condition in case of nitrogen is injected with the sheath gas

		R_{Sw}				
		20	30	40	50	Total
R_C	20	0.22	0.28	0.46	0.36	1.32
	30	0.22	0.33	0.3	0.3	1.15
	40	0.21	0.29	0.3	0.33	1.13
	50	0.19	0.24	0.29	0.32	1.04
	Total	0.84	1.14	1.35	1.31	4.64

(b) ANOVA Upper limit of injected nitrogen flow rate

	f	S	V	$F0$	F	$F0'$	F'	$\rho(\%)$
R_{Cl}	1	0.009245	0.009245	4.581269	0.06473709	4.817034	0.04694580	13.79851
R_{Cq}	1	0.0004	0.0004	0.198216	0.66796520			
R_{Cc}	1	0.000605	0.000605	0.299802	0.59894574			
R_{Swl}	1	0.032805	0.032805	16.25619	0.00377807	17.09279	0.00117512	48.96269
R_{Swq}	1	0.007225	0.007225	3.580278	0.09510885			
R_{Swc}	1	0.00032	0.00032	0.158573	0.70088990			
$R_{Cl}*R_{Swl}$	1	0.000256	0.000256	0.126858	0.73092232			
e	8	0.016144	0.002018					
T	15	0.067	0.052874					100
(e)	13	0.02495	0.001919		0.00191923			37.23881

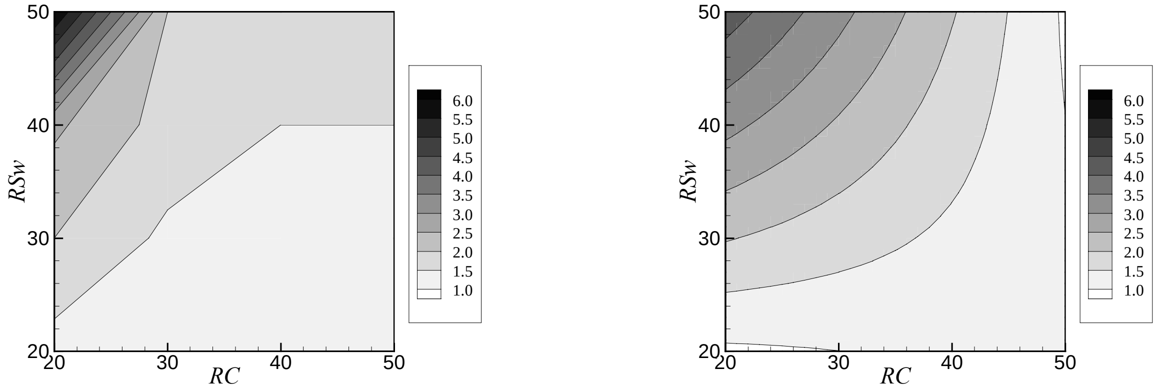

Figure 8 (a) Contour map of L_C obtained by the experiment (b) Contour map of L_C obtained by the equation (4)

nitrogen gas is dissociated in a plasma flow. An RF-ICP flow is kept stable by high temperature in the coil region. If nitrogen is injected into the skin effect region directly by the sheath gas, it takes much energy to dissociate nitrogen from an RF-ICP flow. As a result, an RF-ICP flow becomes unstable. The dissociation in case of nitrogen is injected with the central gas is lower than the dissociation in case of nitrogen is injected with the sheath gas in the coil region. Therefore, if we need to inject a large amount of nitrogen, nitrogen should be injected with the central gas. The influences of the central gas and the swirl gas in Tables 4 (b) are drastically changed from that in Table 5 (b). This is reasonable because the influence of the central gas becomes stronger when nitrogen is injected with the central gas, and the influence of the swirl gas becomes stronger when nitrogen is injected with the sheath gas. The influences of R_{Cq} (Table 4 (b)) on L_C and that of R_{Swq} (Table 5 (b)) on L_{Sw} are rather large. However their values are neglected because F values are less than 0.05, and this results in the increases in the influences of errors on L_C and L_{Sw}. The following equations are obtained from regression analysis of these tables.

$$L_C = 1.82 - 5.18\times10^{-2}(R_C - 35) + 5.23\times10^{-2}(R_{Sw} - 35) - 3.97\times10^{-3}(R_C - 35)(R_{Sw} - 35) \tag{4}$$

$$L_{Sw} = 0.29 - 2.15\times10^{-3}(R_C - 35) + 4.05\times10^{-3}(R_{Sw} - 35) \tag{5}$$

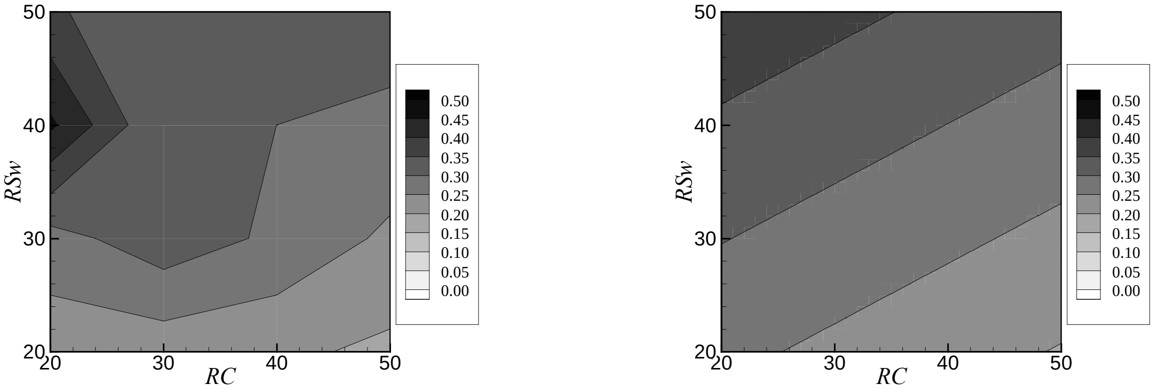

Figure 9 (a) Contour map of L_{Sw} obtained by the experiment (b) Contour map of L_{Sw} obtained by the equation (5)

Figures 8 (a) and (b) show the contour map of L_C obtained from the experimental results and that obtained from the equation (4) respectively. Figure 9 (a) and (b) show the contour map of L_{Sw} obtained by the experiment and from the equation (5) respectively. As compared with Figure 9 (a), Figure (b) has the different tendency overall because L_{Sw} is not calculated accurately by the equation (5) owing to the strong influence of error. From the results shown in Figures 8 and Figures 9, it is concluded that the central gas ratio should be kept lower and the swirl gas ratio should be kept higher to inject a large amount of nitrogen.

4. Conclusion

Statistical method has been applied to analyze the obtained experimental results, and the following conclusion was obtained to optimize the operating conditions. The particle residence time increases with decreasing the central gas ratio and increasing the swirl gas ratio, and particularly, the controlling of the central gas ratio is important. By keeping the central gas ratio lower and the swirl gas ratio higher, an RF-ICP flow can be ignited easily and kept stably in a DC-RF hybrid plasma flow. A large amount of nitrogen can be injected with the central gas, and nitrogen flow rate increases with decreasing the central gas ratio and increasing the swirl gas ratio.

References

[1] M. I. Boulos, *IEEE Tran. Plasma Science*, **4** (1) (1976), 28-39.
[2] J. Lesinski and M. I. Boulos, *Plasma Chem. and Plasma Processing*, **8** (2) (1988), 133-144.
[3] M. Sugasawa, N. Kikukawa, N. Kayano and T. Kimura, *Proc. 15th Int. Symp. Plasma Chem.* , **2** (2001), 691-696.
[4] P. Bushner, H. Ferfers, H. Schubert and J. Uhlenbusch, *Plasma Sources Sci. Technol.* , **6** (1997), 450-459.
[5] J. H. Park and S. H. Hong, *IEEE Tran. Plasma Science*, **23** (4) (1995), 532-537.
[6] T. Yoshida, T. Tani, H. Nishimura and K. Akashi, *J. Appl. Phys.* , **54** (2) (1983), 640-646.
[7] T. Yoshida, T. Okada, H. Hamatani and H. Kumaoka, *Plasma Sources Sci. Tech.* , **1** (1992), 195-201.
[8] N. Yamaguchi, T. Hattori, K. Terashima and T. Yoshida, *Thin Solid Films*, **316** (1998), 185-188.
[9] G. Taguchi, *Systems of Experimental Design*, Japanese Standards Association, vol. **1**, **2** (1976, 1977).
[10] N. Logothetis and H. P. Wynn: *Quality Through Design* (Clarendon Press, Oxford, 1994).

Low temperature deposition of microcrystalline silicon films by PECVD under high etching selectivity

A. Grimaldi[1], A. Sacchetti[2], M. Losurdo[2], M. Ambrico[2], P. Capezzuto[1,2] and G. Bruno[2]

[1] *Department of Chemistry, University of Bari, INSTM Unit, Via Orabona 4, 70126 Bari, Italy*
[2] *Institute of Inorganic Methodologies and of Plasmas, IMIP-CNR, Via Orabona 4, 70126 Bari, Italy*

Abstract

Hydrogenated microcrystalline silicon, μc-Si:H, is an important material for TFT applications. PECVD growth from SiF_4-H_2-He mixtures was performed in order to get fully μc-Si:H structures for very thin (<100nm) layers at temperatures as low as 100°C, instead of conventional silane based techniques. Results are discussed on the basis of an etching-deposition growth model controlling the amorphous to microcrystalline phase transition.

1.Introduction

Hydrogenated microcrystalline silicon, μc-Si:H, is attracting considerable interest as a material for thin film transistors, TFTs [1], because it has stability and electron mobility higher than that of amorphous silicon, a-Si:H. Thin layers (<100nm) with low hydrogen content (<2%) [2] and high crystalline volume fraction (>90) [3] are required for TFT applications. Furthermore, a growing market potential for lightweight and flexible devices has pushed research towards flexible substrates such as plastic foils. Standard μc-Si deposition, as derived from amorphous silicon technology, was optimised at a temperature of 200-250° that is higher than most low cost plastics can withstand. Therefore, it is important to develop μc-Si:H growth and processes at low temperature. Microcrystalline silicon films have been directly deposited by plasma enhanced chemical vapor deposition, PECVD, from silane, SiH_4, and hydrogen, H_2, plasmas using highly hydrogen diluted mixtures [4] or alternating deposition and etching by hydrogen plasma treatments in what is called the layer-by-layer, LBL, technique [5]. Depending on plasma conditions, different growth models have been proposed in order to explain the crystalline phase formation by SiH_4-H_2 PECVD: i) the surface diffusion model assumes that the growing surface is covered by hydrogen that enhances the surface mobility of film precursors that are incorporated at favourable places [6]; ii) the chemical annealing model is based on the fact that H atoms permeate the growth zone and yield a structural rearrangement of the amorphous network [7, 8]; iii) the partial chemical equilibrium or etching model states that the preferential etching of the disordered (amorphous) phase leads to the growth of predominantly crystalline structures [9, 10]. Indeed, μc-Si:H layers from SiH_4-H_2 exhibit a growth dynamics, i.e., an increase of crystalline fraction with film thickness [11], with an amorphous incubation layer of about 20nm [12] formed at the initial stage of film growth. Moreover, under a huge variety of deposition conditions [13-16], a decrease of crystallinity was always found out with temperature decrease. For instance, Matsuda [17] took into account just this temperature behaviour to introduce the surface diffusion model, since the lower the temperature, the lower the surface diffusivity. Roca y Cabarrocas [18] argues that lower substrate temperatures hinder the hydrogen diffusion into the film and the silicon network relaxation, supporting the chemical annealing mechanism. A deeper insight into the growth mechanism is hence needed in order to grow thin fully microcrystalline layers.

The use of halogenated sources (tetrafluorosilane, SiF_4 [19], dichlorosilane, SiH_2Cl_2 [20]) instead of SiH_4 has been investigated to enhance crystallinity of silicon thin films. Previous studies demonstrated that PECVD from SiF_4-H_2 plasmas can be able to suppress the amorphous incubation layer, yielding crystalline volume fractions higher than 90% [21], and to reduce the hydrogen content to 3% [22]. An increasing of film crystallinity at lower temperatures was recently found from SiH_2Cl_2 mixtures [23].

In this contribution, we present the growth of undoped μc-Si:H thin films from SiF_4-H_2-He plasma mixtures in the temperature range 100°C-180°C. The dependence of film microstructure on the deposition temperature is investigated. Fully microcrystalline films with low hydrogen content are deposited at temperature as low as 100°C. The temperature dependence of film etching by H and F atoms has also been investigated in order to clarify the role of etching. The chemistry and kinetics of the amorphous-to-microcrystalline phase transition is discussed in the frame of a model based on the deposition/etching competition.

2. Experimental methods

A. FILM GROWTH

μc-Si:H films were deposited by PECVD from SiF_4-H_2-He mixtures in a parallel plate reactor. Depositions were performed at 13.56 MHz, at a plasma power of 20W and at a pressure of 0.3 Torr. The flow rates of SiF_4, H_2, He were 20, 10 and 45 sccm, respectively. Corning 7059 glass was used as substrate. A dry cleaning of the substrate was run using SiF_4 plasmas. Depositions were performed at substrate temperatures Ts=180°C, 120°C, 100°C. The substrate temperature was monitored with a thermocouple touching the heater. A substrate temperature calibration was done using interferometric thermometry [24] to correlate the actual substrate temperature with the temperature of the thermocouple; actual substrate temperatures are reported here. Laser reflectance interferometry, LRI, was used to evaluate in real time growth kinetics, growth rate and surface modifications [25]; a He/Ne laser, λ=632.8 nm, at an incidence of 70° was used for it.

Film microstructure was investigated by X-ray diffractometry (XRD) and spectroscopic ellipsometry (SE). The crystal size of the samples have been determined by the Sherrer formula (H1) using (111) peak. SE spectra were acquired with a phase-modulated ellipsometer (UVISEL- Jobin Yvon) in the energy range 1.5-5.0 eV and analyzed using the Bruggerman effective medium approximation (BEMA) [26] to derive the volume fractions of the microcrystalline and amorphous phases.

Dark and photo (AM1) conductivity measurements have been performed in coplanar configuration (Ag evaporated contacts). a-Si:H layers were also deposited by PECVD from SiF_4-H_2 to study the etching rate dependence of the amorphous phase. Details on a-Si:H deposition can be found elsewhere [27].

B. FILM ETCHING

Etching processes of amorphous and microcrystalline silicon films between 300°C and RT were run using nitrogen trifluoride, NF_3, plasmas as sources of F atoms. A NF_3 flux of 5 sccm, a power of 5 Watt and a pressure of 0.04 mbar were used.

3. Results & discussion

A. μc-Si:H FILM DEPOSITION

Figure 1 shows the XRD spectrum of a film grown at 120°C. Diffraction peaks are observed at angles (2θ) of about 28° and 47° due to (111) and (220) orientations respectively, showing the formation of a crystalline phase. A grain size of about 12nm was estimated from the FWHM of (111) peak.

Figure 2 shows the ellipsometric spectra of the imaginary part, $<\varepsilon_2>$, of the pseudodielectric function of films deposited at temperatures between 100°C and 180°C. All films show the E_1 and E_2 interband critical points indicative of film crystallinity consistently with XRD data. The SE spectra have been fitted to optical model based on the Bruggeman effective medium approximation, that allows estimation of the volume fraction of the various film constituents. As shown in Fig. 2, a simple two-layer model, substrate/film/surface roughness fits to SE spectra. The film is considered a BEMA mixture of μc-Si, a-Si phases and voids (voids are to take into account the effect of grain boundaries and/or microvoids induced by hydrogen inclusion). Surface roughness is modelled as 50% bulk material and 50% voids according to an approach already consolidated in literature [28]. Data of film microstructure as derived by the ellipsometric analysis are reported in Figure 3 as a function of deposition temperature. Microcrystalline phase volume fraction increases from 77% to 90% as the deposition temperature decreases from 180°C to 100°C. Meanwhile, both a-Si:H and voids percentages lower till 5-6%, values which take into account the grain boundaries structure in microcrystalline silicon layers.

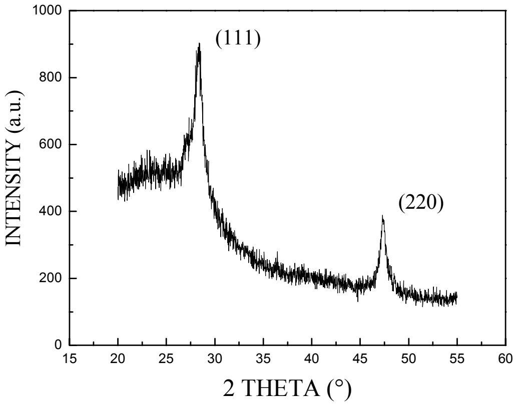

Figure 1. XRD spectrum of a μc-Si:H film grown at 120°C

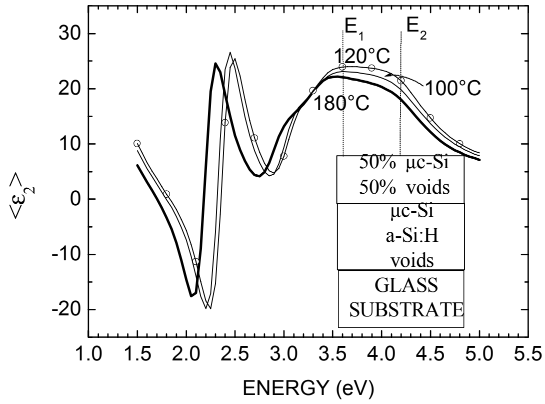

Figure 2. SE spectra of the imaginary part, $<\varepsilon_2>$, of the pseudodielectric function of films deposited at various temperatures.

In this contest, the low void fraction can be explained by a low hydrogen content, c_H, in the film. In fact, a very low hydrogen content (<1%) was measured trough integration of the wagging SiH mode band by FTIR measurements [29]. The film microstructure can be related to the growth kinetics, as shown in Figure 4. Here the temperature dependence of the deposition rate, r_D, and of the crystalline fraction is reported. It is worthy to note that the deposition rate is in the range 0.2 - 0.38 Å/sec when varying the temperature from RT to 180°C.

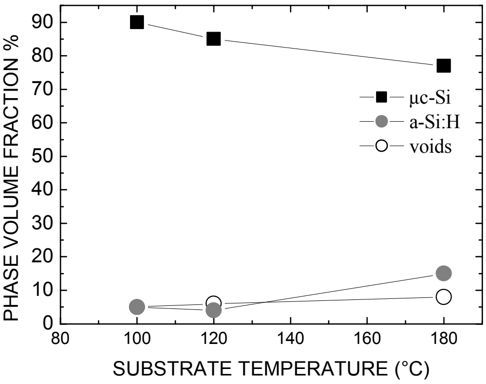

Figure 3. Composition of films deposited at different temperatures in terms of volume fraction of the μc-Si, a-Si phases and voids.

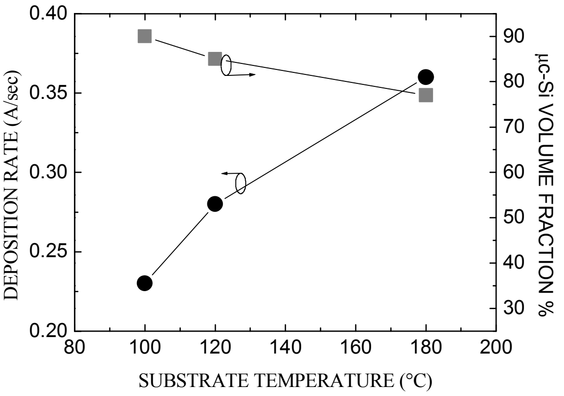

Figure 4. Temperature dependence of the deposition rate, r_D, and the crystalline volume fraction.

These rate values are higher than typical values of 0.1-0.2 Å/sec obtained in the same temperature range from Alpium et al. [16] by PECVD using conventional SiH_4-H_2 plasmas. However, in both systems the deposition rate decreases with temperature. The electrical properties of the deposited films have also been measured. Specifically, dark conductivity is in the range $1\text{-}30\times10^{-3}\ \Omega^{-1}\text{cm}^{-1}$ for films with crystallinity higher than 80%; correspondingly the photo-to-dark conductivity ratio is in the range 1-3. These values are typical for films with very high crystallinity and are used as an evidence of the amorphous to microcrystalline phase transition [16].

B. FILM ETCHING

Figure 5 shows the Arrhenius-like plot for amorphous and microcrystalline silicon etching by F-atoms. H atoms etching values, taken from Wanka et al. [30], are added for comparison. Silicon etching rate is described by the regression equation:

$$r_E \propto e^{-Ea,F(H)/kT}[X] \qquad X = F, H \qquad (1)$$

Etching activation energies, as derived from equation (1), are shown in the inset. The activation energy for fluorine atoms etching, $E_{a,F}$, is positive, thus the etching rate increases with the increase of temperature. Moreover, $E_{a,F}$ is higher on microcrystalline silicon than on amorphous silicon, resulting in a much higher a-Si:H etching rate than µc-Si as temperature decreases. For H atoms etching, the activation energy $E_{a,H}$ is negative, while its absolute value is still lower for the a-Si phase than for the crystalline phase, resulting in an opposite behaviour than the F atoms case: the etching rate increases with the decrease of temperature and the a-Si-to-µc-Si etching rate ratio becomes higher as temperature increases.

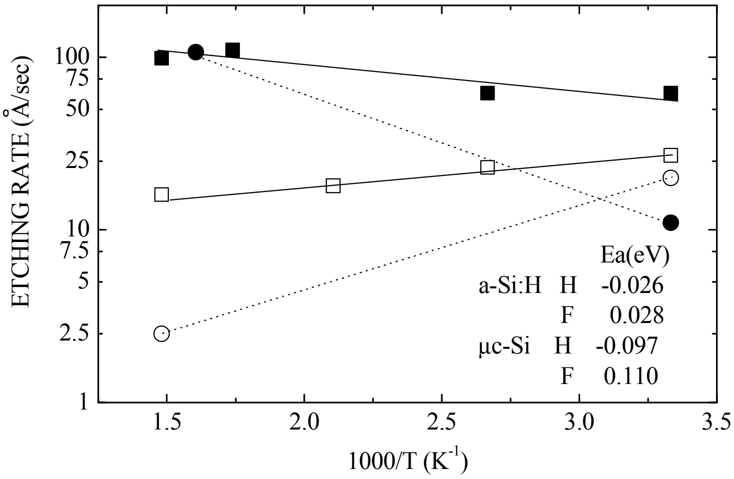

Figure 5. Arrhenius plot of silicon materials etching rate by F, full symbols (■, ●), and H, hollow ones (□, ○). Etching rates of amorphous and microcrystalline silicon are indicated by squares and circles, respectively.

The temperature dependence of the crystallinity in our system, thus, can be explained on the basis of the etching/deposition model of µc-Si:H deposition from SiF_4-H_2 mixtures [31]. According to this model, the deposition results from two competitive processes: i) the growth of both a-Si:H and µc-Si phases film, which involves the chemisorption of SiF_x and the formation of free-bond silicon species, ii) the selective etching of the amorphous phase with respect to the microcrystalline phase operated by fluorine atoms, which involves the desorption of SiF_2/SiF_4 from the surface. The microcrystalline structure results from a faster a-Si:H etching than for the microcrystalline phase. The enhancement of the crystalline volume fraction found between 180°C and 100°C and the small content of amorphous phase (<6%) even in the first stages of the growth are due to the highly selective etching activity of F atoms for a-Si:H with respect to µc-Si. On the contrary, in conventional SiH_4-H_2 systems a high selectivity in favour of crystalline phase growth is accomplished at higher deposition temperature. Thus, the a-Si:H to µc-Si:H etching selectivity S ($S = r_E$(a-Si:H)/r_E(µc-Si:H)), shown in Fig. 6, rules on the film microstructure. As shown in Fig. 6 S, in our fluorine based system, has the value of about 1.5 at 250 °C, allowing only a slight enrichment in the crystalline phase, while at room temperature a-Si etching rate is 6 times higher than to µc-Si:H, leading to a fully microcrystalline structure. Therefore, µc-Si:H depositions from SiF_4-H_2-He plasmas represent an approach to get highly ordered silicon films in the low temperature regime.

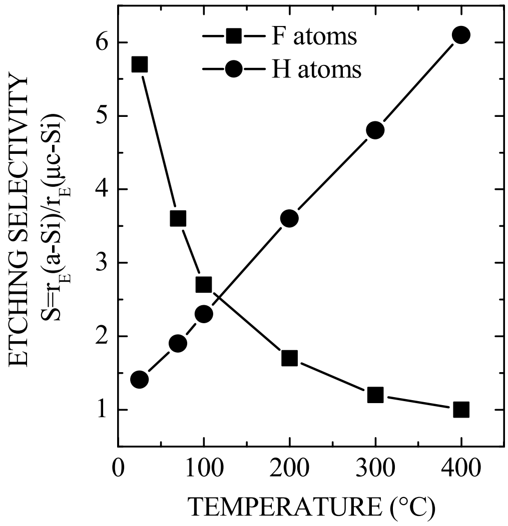

Figure 6. Temperature dependence of amorphous-to-microcrystalline phase etching selectivity. F atoms case, squares, H atoms case, circles.

4. Conclusions

μc-Si:H films has been deposited by PECVD, starting from non conventional SiF_4-H_2-He mixtures. The analysis of the layers has been performed by spectroscopic ellipsometry and it was found that a fully microcrystalline film can be deposited at the substrate temperature of 100°C. An increase in the crystalline phase was observed at lower temperatures, in contrast with μc-Si:H layers deposited from SiH_4. The role of the etching process by fluorine atoms in controlling the amorphous-to-microcrystalline selectivity was found out, supporting the etching model for the μc-Si films deposition. a-Si phase formation is limited in favor of μc-Si phase by the high etching activity of F atoms and this discrepancy grows up as the temperature lowers. This behaviour can be quantified by a selectivity parameter S, corresponding to the a-Si/μc-Si etching rate ratio. The same model accomplishes the opposite temperature dependence of crystallinity observed in SiH_4 based systems.

5. Acknowledgments

The authors are grateful to Dr. D. Barreca for the XRD measurements. The financial support by CNR, Progetto Finalizzato MSTA II, is also acknowledged.

6. References

[1] V. Foglietti, L. Mariucci, G. Fortunato - J. Appl. Phys. **84**, 616 (1999)
[2] A. M. Brockhoff, E.H.C. Ullersma, H. Meiling, F.H. Habraken, W.F. Van der Weg - Appl. Phys. Lett. **73**, 244 (1988)
[3] U. Kroll, J. Meier, A.Shah, S. Mikhailov, J. Weber - J. Appl. Phys. **80**, 4971 (1996)
[4] J. Meier, R. Fluckiger, H. Keppner, A. Shah - Appl. Phys. Lett. **65**, 860 (1994)
[5] N. Layadi, P. Roca i Cabarrocas, B. Drevillon, I. Solomon - Phys. Rev. B **52**, 5136 (1995)
[6] A Matsuda - J. Non-Cryst. Sol. **59-60**, 767 (1983)
[7]Y.H. Yang, M. Katiyar, G.F. Feng, N. Maley, K.R. Abelson - Appl. Phys. Lett. **65,** 1789 (1994)
[8] N. Shibata, K. Fukuda, H. Otoshi, J. Hanna, S. Oda, I. Shimizu - MRS Symp. Proc. **95**, 225 (1987)
[9] J.J. Wagner, S. Veprek - Plasma Chem. Plasma Proc. **2**, 95 (1982)
[10] C.C. Tsai, G.B. Anderson, R. Thompson, B. Wacker - J. Non-Cryst. Sol. **114**, 151 (1989)
[11] S. Hamma, P Roca y Cabarrocas - Thin Solid Films **296**, 11 (1997)
[12] C. Niikura, R. Brenot, J. Guillet, J. E. Kleider, R. Bruggemann, C. Langeaud - Sol. Energy Sol. Mater. **66**, 421 (2001)

[13] E.I. Terukov, V.K. Kudoyarova, V.Y. Davydov, K.V. Koughia, G. Weiser, H. Mell - Mater. Sci. Eng. B **69–70**, 266 (2000)
[14] J. Kondo, A. Tabata, T. Kawamura, T. Mizutani - Vacuum **66**, 40 (2002)
[15] A. Terasa, M. Albert, H. Gruger, A. Haiduk, A. Kottwitz - J. Non-Cryst. Sol. **266-269**, 95 (2000)
[16] P. Alpuim, V. Chu, J.P. Conde - J. Appl. Phys. **86**, 3812 (1999)
[17] A. Matsuda - Thin Sol. Films **337**, 1 (1999)
[18] S. Hamma, P. Roca y Cabarrocas - J. Non-Cryst. Sol. **227-230,** 852 (1998)
[19] S. Ishihara, D. He, M. Nakata, I. Shimizu - Jpn. J. Appl. Phys. **32**, 1539 (1993)
[20] T. Wang, C.C. Wu, J.J. Wu - J. Crystal Growth **243,** 419 (2002)
[21] M. Losurdo, R. Rizzoli, C. Summonte, G. Cicala, P. Capezzuto, G. Bruno - J. Appl. Phys. **88**, 2408 (2000)
[22] Ray, S. Mukhopadhyay, S.C. Saha, S. Hazra - Thin Solid Films **337**, 7 (1999)
[23] L.Guo, M. Kondo, A. Matsuda - Sol. Ener. Mat. Sol. Cells **66**, 405 (2001)
[24] V. M. Donnelly, J. A. McCaulley - J. Vac. Sci. Technol. A **8**, 84 (1990)
[25] M. Losurdo, A. Grimaldi, M. M. Giangregorio, P. Capezzuto, G. Bruno - J. Phys.IV France **11**, Pr3-1175 (2001)
[26] D. G. Bruggemann - Ann. Phys. (Leipzig) **24**, 636 (1935)
[27] G. Bruno, P. Capezzuto, G. Cicala - J. Appl. Phys. **69,** 7265 (1991)
[28] H. Fujiwara, J. Koh, P.I. Rovina, R.W. Collins - Phys. Rev. B **36**, 4821 (1987)
[29] A. Grimaldi, A. Sacchetti, M. Losurdo, M. Ambrico, P. Capezzuto, G. Bruno - Proc. EURO CVD XIV (accepted)
[30] H.N. Wanka, M. B. Schubert - J. Phys. D **30**, L28 (1997)
[31] G. Cicala, P. Capezzuto, G. Bruno - Thin Solid Films **337**, 59 (1999)

Er-doped nanostructured silicon films by plasma-enhanced chemical vapor deposition

M.M. Giangregorio,[1] M. Losurdo,[1] A. Sacchetti,[1] P. Capezzuto,[1,2] G. Bruno[1]

[1] *Institute of Inorganic Methodologies and of Plasmas IMIP-CNR, via Orabona, 4-70126, Bari, Italy*
[2] *Department of Chemistry, University of Bari, via Orabona, 4-70126 Bari, Italy*

Abstract

Erbium doped silicon thin films have been grown at low temperature (200°C) from SiF_4-H_2-Ar plasmas and sputtering of a metallic erbium target. Both the Er sputtering and the plasma enhanced chemical vapor deposition (PECVD) processes have been investigated, through the parametric study of the effect of pressure, radiofrequency power, and bias potential on Er incorporation yield in thin silicon films.
Different silicon matrixes, going from a-Si:H,F,O to SiO_2:F, have been deposited depending on reactant flow rates, and it has been found that the Er inclusion strongly depends on the silicon matrix composition. In the a-Si:H,O,F matrix, an Er-concentration one order of magnitude higher than in SiO_2 is found.
The present study is also characterized by the definition of the correlation between growth chemistry/kinetics and structure/properties of Er-doped silicon thin films. Spectroscopic Ellipsometry is used to establish the interplay between nanostructure and optical properties of Si:Er thin films. SE is used to analyze non-destructively Er-doped nc-Si thin films with different crystallinity and nanocrystallites size that cannot be detected by conventional structural techniques such as X-ray diffraction and Raman spectroscopy. The nanostructure of Si:Er films is correlated to photoluminescence properties.

1. Introduction

Silicon is traditionally considered a material not suitable as light emitter because of its indirect band gap. Indeed, there are several attempts to obtain luminescence from Si-based materials, such as incorporation of rare-earth metal atoms (RE) into the Si lattice for using an intra-4f-shell transition characteristic of the triply ionized state, RE^{3+}. For the Er^{3+} ion, the transition $^4I_{13/2} \rightarrow {}^4I_{15/2}$ gives light emission at 1.54μm. The absorption in silica-based optical fibers has a minimum at this wavelength, which makes Er an interesting candidate to be incorporated into Si for obtaining infrared light emission [1]. Therefore, a strong effort is addressed to depositing Er-doped silicon films.

Erbium embedded in a host matrix assumes the trivalent Er^{3+} state [1]. Electric dipole transitions are not allowed in the metallic Er°, while they are allowed in Er^{3+}, where the presence of the surrounding atoms perturbs the 4f states and mixes with states of opposite parity. Co-dopants such as oxygen, fluorine and hydrogen affect the Er^{n+} ionicity, and change the local Er environment that determines its optical activity. This is because the magnitude of the crystal-field splitting, which determines the transition probability, depends on the symmetry and chemical nature of the ligands bound to Er. Therefore, among other factors, the Er luminescence intensity strongly depends on the Er concentration itself [2], on Er ionicity [1], on the Si-based matrix host that control energy transfer mechanism, [3-4], on the lattice position of Er in the Si matrix [5], and on the concentration of co-dopants, such as oxygen and fluorine [6]. Previous studies [7] show that the addition of oxygen and fluorine to Er-doped silicon matrix enhances the Er luminescence intensity and reduces its thermal quenching. So far, the majority of studies concern Er-doped SiO_2 [8] and oxygen as co-dopant. Few studies on fluorine co-doped Si:Er films grown by metalorganic chemical vapor deposition (MOCVD) and plasma enhanced chemical vapor deposition (PECVD) have been reported [9], showing that the addition of fluorine to Er-doped silicon matrix improves the light intensity output of erbium by 100 times, compared to erbium in silicon oxide. This has been explained by the electronegativity of fluorine, which is larger than that of oxygen, and results in a stronger ligand field surrounding the Er^{3+} ion. Furthermore, the fluoride environment of erbium leads to a less distortion of the silicon lattice and to narrowing of the 1.54μm emission line.

In this contribution, we report on the PECVD process using SiF_4-H_2-Ar plasmas to deposit at low temperature (200°C) a-Si:H,F films that are doped with Er using simultaneous sputtering of a pure metallic erbium target. The effect of pressure, RF power, bias potential, and electrode geometry on Er incorporation yield and on the silicon matrix composition has been studied. Silicon-based films going from amorphous to microcrystalline have been deposited by changing the SiF_4-H_2 gas flow ratio. It has also been found that the structure of the silicon matrix, i.e., the presence, fraction and size of silicon crystallites affects the Er photoluminescence. In particular, silicon nanocrystallites with a diameter lower then 3 nm have been found effective in enhancing the Er photoluminescence at 1.54 μm. A study of the correlation between matrix structure and optical properties has been carried out by spectroscopic ellipsometry (SE) and photoluminescence (PL) measurements.

2. Experimental methods

Growth experiments were performed in a sputtering assisted PECVD system that has asymmetric electrodes in the vertical configuration. In particular, the substrate is positioned on the ground electrode (that is also temperature controlled) with a diameter of 4”. The r.f. (13.56MHz) sputtering electrode with a diameter of 2” holds the metallic Er target. The distance between the sputtering and ground electrode has been varied from 18 mm to 118 mm to obtain films with different Er concentration. In fact, the inter-electrodes distance affects the bias potential of the sputtering electrodes and, hence, the Er sputtering yield.

Er-doped silicon thin films were deposited from SiF_4 -H_2-Ar plasmas. Argon was used for sputtering the metallic erbium target. For O co-doping, 0.2 sccm of air was flowed through a leak valve. Corning glass and crystalline Si (100) were used as substrates.

Experimental conditions, such as pressure, bias potential and plasma composition were changed in order to deposit films with different composition and structure. The r.f. power was set at 30 watt and the substrate temperature at 200°C during experiments. Other parameters are reported in Table 1.

Ar (sccm)	SiF_4 (sccm)	H_2 (sccm)	P (mbar)	$-V_{bias}$ (V)	Er By SIMS
4	8.8	1.7	0.085	710	$2.87x10^{19}$
			0.1	690	$3.74x10^{19}$
			0.175	600	$1.10x10^{19}$
3	3.5	0.7	0.09	680	$3.18x10^{18}$
2	4.4	0.9	0.09	685	$3.18x10^{18}$
			0.175	608	$2.20x10^{18}$

Table 1. Experimental conditions for the deposition of silicon films at a fixed temperature of 200°C and a r.f. power of 30watt. The Er concentration measured by SIMS in the films deposited under the various conditions is also reported.

Si deposition and Er sputtering processes were monitored in real time by Laser Reflectance Interferometry (LRI) for the estimation of the deposition rate, r_D, and of the film thickness [10].

The optical characterization of Er-doped silicon thin films has been performed by photoluminescence measurements. Chemical composition was determined by secondary ion mass spectrometry (SIMS). Structural characterization was performed by spectroscopic ellipsometry by measuring the pseudodielectric function, $<\varepsilon>=<\varepsilon_1>+i<\varepsilon_2>$ in the range 1.5-5.0 eV with a phase modulated ellipsometer (UVISEL-Jobin Yvon) at an incidence angle of 70.57°. The experimental energy dependence of the ellipsometry angles Ψ and Δ were converted to the ratio, ρ, between the complex reflectance coefficients of the two components of the light, r_p and r_s, polarized, respectively, parallel and perpendicular to the plane of incidence, according to the equation:

$$\rho=r_p/r_s=\tan\Psi\exp(i\Delta) \tag{1}$$

where Ψ is the amplitude ratio ($\tan\Psi=|r_p|/|r_s|$), and Δ is the phase difference ($\Delta=\delta_p-\delta_s$) between the p and s components. The pseudodielectric function, $<\varepsilon>$, was derived from the ρ parameter through the following equation:

$$<\varepsilon>=\varepsilon_0\sin^2\phi_0[1+\tan^2\phi_0(1-\rho)^2/(1+\rho)^2] \tag{2}$$

where ϕ_0 is the angle of incidence of light and ε_0 is the ambient dielectric function.

SE spectra were analyzed in terms of optical models based on the Bruggeman effective medium approximation (BEMA) [11] applying the least-squares regression method for the fitting, where the fit goodness was estimated by the parameter χ^2 defined in ref. [12]. The 95% confidence limit of fit parameters was also evaluated. Standard dielectric functions of the silicon phases (a-Si, microcristalline silicon and silicon oxides) reported in Ref. [13] were used in the BEMA model. The nc-Si phase was parameterized by the Tauc-Lorentz expression [14]. SE models were corroborated by measurements of X-ray photoelectron spectroscopy (XPS) for the evaluation of the presence of the native oxide layer and of atomic force microscopy (AFM) for the determination of the surface roughness. High-resolution transmission electron microscopy (HRTEM) measurements were performed to establish the presence of silicon nanocrystallites.

3. Results and Discussion

a) Growth process characterization

Figures 1(a) and 1(b) show the Er content into the silicon matrix as a function of bias potential, plasma composition, pressure and total flux. The Er sputtering process depends on the Ar pressure that determines the ion bombardment onto the sputtering electrode and, hence, its bias potential, V_{bias}.

Figure 1(a) shows the dependence of Er sputtering rate as a function of the bias potential, V_{bias}, at the sputtering electrode. The extrapolation of the straight line gives the lowest bias potential value (~–540 V) to have Er sputtering. Therefore, to have a significant Er concentration into films, silicon deposition has been run at a pressure lower then 0.2 mbar.

Figure 1(b) shows that, at a constant plasma composition, the more negative the bias potential, the larger the Er content in the silicon matrix; at a constant V_{bias}, the Er content in the silicon matrix increases with the increase of total flux, because of the increase of mass transport.

Furthermore, we found from SIMS measurements that at lower total flux ($Ar:SiF_4:H_2$=2:4.4:0.9, air flux=0.5sccm), a silicon oxide matrix, SiO_2:H,F, is mainly deposited, while at higher total flux ($Ar:SiF_4:H_2$=4:8.8:1.7), a silicon matrix, Si:H,F,O is deposited. Therefore, from data of figure 1(b) it is inferred that the Er content in the SiO_2:F matrix is about $3\text{x}10^{18}$ at/cc, while the Er content incorporated in the a-Si:H,F,O matrix is about $3\text{x}10^{19}$ at/cc, i.e. one order of magnitude higher than in SiO_2. Figure 1(b) also shows that at a constant plasma composition ($Ar:SiF_4:H_2$=4:8.8:1.7), a decrease of pressure leads to an a-Si to SiO_2 matrix transition. From SIMS measurements, it also results that [H]=$3\text{x}10^{21}$ at/cc and [F]=$7\text{x}10^{21}$ at/cc are incorporated as co-dopants using $SiF_4:H_2:Ar$ plasmas

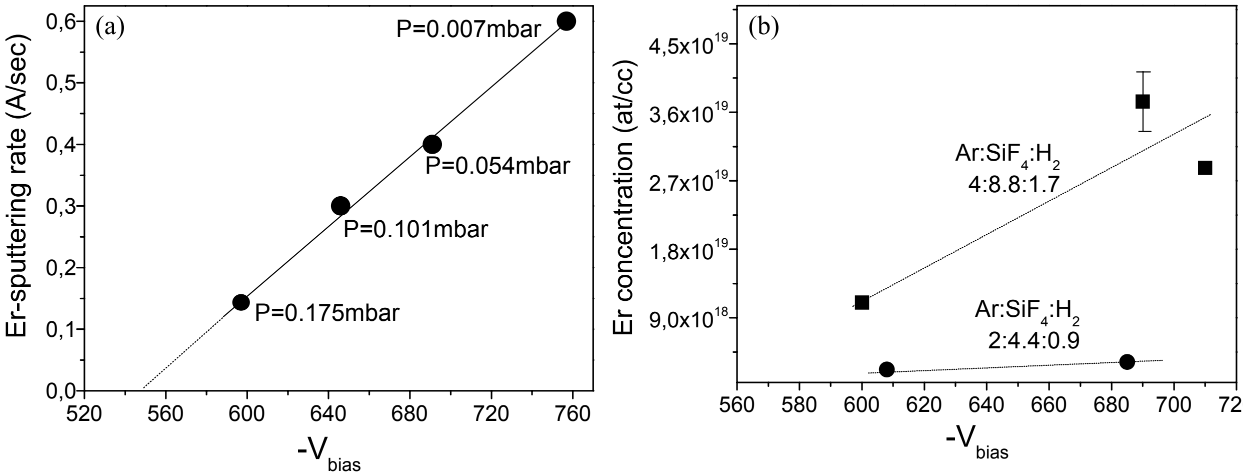

Figure 1. (a) Dependence of Er sputtering rate on self-bias potential of the r.f. sputtering electrode. The pressure is also indicated. (b) Effect of bias potential, plasma composition and total flux on Er concentration in the film, as determined by SIMS analysis.

b) Film Characterization

The different stoichiometry of the silicon based matrix deposited at different total flow rate and pressure has also been confirmed by infrared FTIR measurements shown in Figure 2.

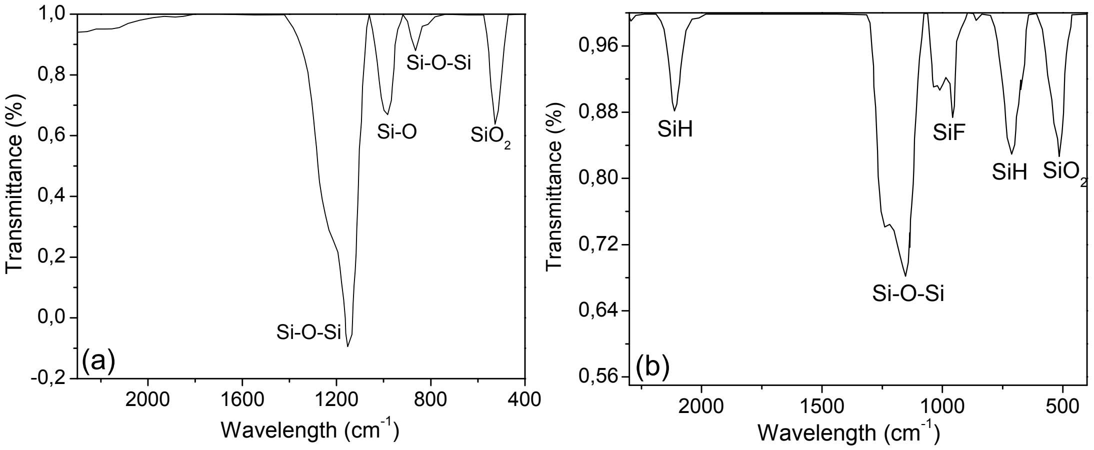

Figure 2. FTIR spectra of (a) SiO$_2$ matrix grown at low flow rate (Ar:SiF$_4$:H$_2$=2:4.4:0.9) and (b) a-Si:H,F,O matrix grown at high flow rate (Ar:SiF$_4$:H$_2$=4:8.8:1.7).

For both silicon matrixes, that were amorphous, spectroscopic ellipsometry has revealed that erbium is included in the ionic forms. In fact, figure 3 contrasts the spectra of the refractive index and extinction coefficient derived for the erbium included in the deposited silicon matrix and that measured for a standard metallic erbium target. Two peaks in the energy range below 2.5eV characterize the extinction coefficient of erbium in the deposited silicon matrix. These peaks are consistent with the Er^{3+} absorption transitions $^4I_{15/2} \rightarrow {}^2H11_{/2}$ at 2.29eV and $^4I_{15/2} \rightarrow {}^4I_{9/2}$ at 1.55eV that are not allowed in metallic erbium. Therefore, we confirmed by SE that erbium was included in the silicon matrix in the ionic form and not as inactive metallic clusters.

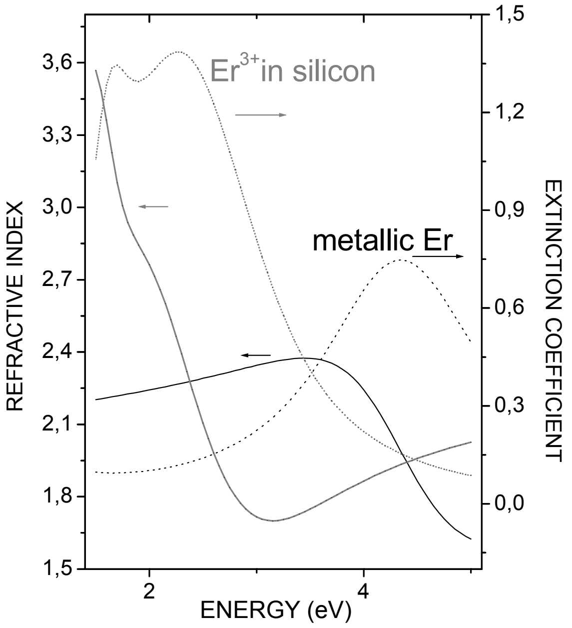

Figure 3. Comparison between refractive index (continuous line) and extinction coefficient (dashed line) of a metallic Er target and that derived for Er^{3+} ions in silicon matrix

The highest PL intensity of Er3+ at 1.54 μm has been found for nanocrystalline films. SE and HRTEM have confirmed the nanocrystallinity. Figure 4a contrasts the SE spectra of the imaginary, $<\varepsilon_2>$, part of the pseudodielectric function of typical Er-doped amorphous, a-Si:H, and nanocrystalline, nc-Si:H, films with [H]=34% and 28%, respectively, as estimated by RBS analysis; other co-dopants concentration is <1%. SE spectra put in evidence the extension of the interference system to energy values higher than 2 eV for the sample that was suspected to be nc-Si. A HRTEM image of the same nc-Si:H sample is shown in fig. 4b, providing evidence of nanocrystallites whose size distribution is also reported in the inset of figure 4b, being in the range 1-3 nm. These nanometer size crystallites well explain the bandgap value found by SE spectra, as expected by quantum confinement effects. The peculiarity of these samples is the presence of PL at 1.54 μm from Er^{3+} ions as shown in fig. 5a.

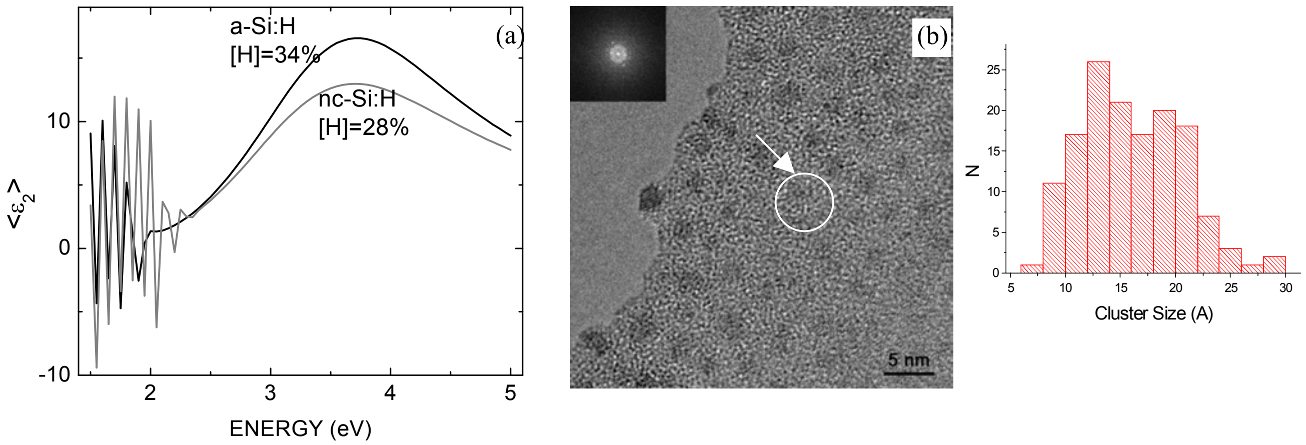

Figure 4. Experimental SE spectra of the imaginary part, $\langle\varepsilon_2\rangle$, of the pseudodielectric function of a-Si:H with %H = 34% and of a nc-Si film with %H = 28%. (b) Cross-sectional TEM image of the nc-Si film. The arrow points out the (111) oriented nanocrystallite; (b) Si nanocrystallite size distribution.

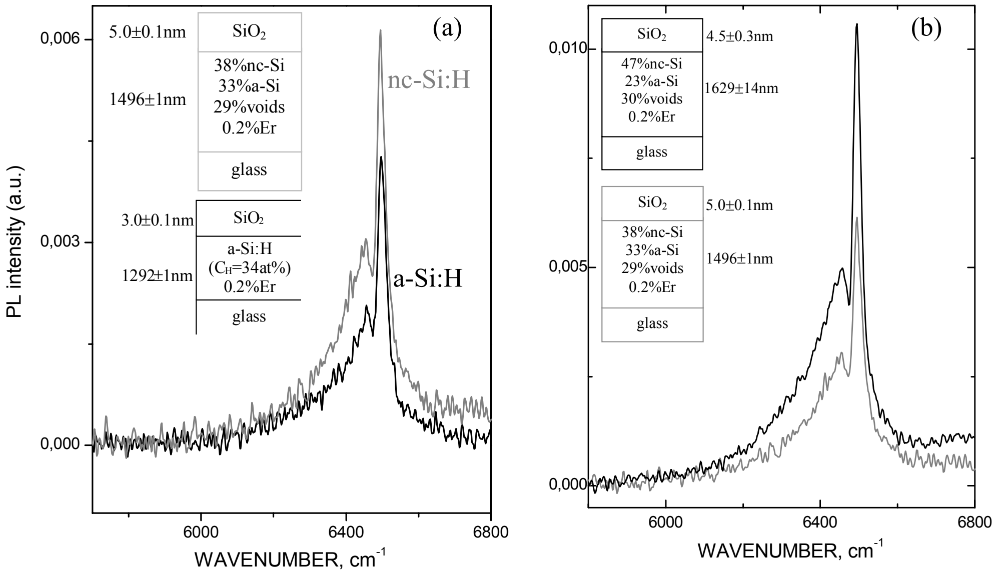

Figure 5. (a) Photoluminescence spectra of a-Si:H with %H = 34% and of a nc-Si film with %H = 28%; the structure and thickness of films is shown in the inset; (b) PL spectra of Er-doped (%Er = 0.1%) nc-Si:H (%H = 27-28%) films with different nc-Si density as indicated by their volume fraction reported in the sketched structural model derived by the ellipsometric analysis.

It is found that the Er PL at 1.54 μm increases going from an amorphous to a nanocrystalline matrix, and the larger the volume fraction of nanocrystallites, the higher the PL intensity because of the efficient transfer of energy from nanocrystals to Er^{3+}, as reported by others [15-17]. Thus, the very small nanocrystals play the main role in the Er^{3+} activation. Further PL investigations are in progress to clarify better the role of nanocrystals as Er sensitizers and the role of co-dopants.

4. Conclusions

In conclusion, we have explored the feasibility of the sputtering assisted PECVD system using SiF_4-H_2-Ar plasma in depositing silicon-based matrixes with composition going from a-Si:H,O,F to SiO_2:F and structure going from amorphous to nanocrystalline.

Non-destructive optical characterization of nanostructure has been carried out by spectroscopic ellipsometry and corroborated by HRTEM. It is found that a higher Er concentration is incorporated in the a-Si:H,F,O matrix. Ellipsometric spectra can be used to predict and/or discriminate the photoluminescence properties of nc- and a-Si:Er,H,O,F thin films. In particular, very small nanocrystallites with a size in the range 1 – 3 nm embedded in an amorphous hydrogenated silicon matrix give a higher Er^{3+} PL at 1.54 μm.

Acknowledgements

Authors are grateful to Prof. M.F. Cerqueira from Universidade do Minho, Portugal and Dr. M. Stepikova from Institute for Physics of Microstructures RAS, Russia for photoluminescence and RBS measurements and helpful discussion.

References

[1] A.Polman, J. Applied Physics **82** (1997) 1

[2] Y.H.Xie, E.A.Fitzgerald, Y.J.Mii, J. Appl. Phys., **70** (1991) 3223

[3] M.S.Bresler, O.B.Gusev, V.Kh.Kudoyarova, A.N.Kuznetsov, P.E.Pak, E.I.Terukov, I.N.Yassievich, B.P.Zakharchenya, Appl. Phys. Lett. **67** (1995) 3599

[4] G.Franzò, D.Pacifici, V.Vinciguerra, F.Priolo, F.Iacona, Appl. Phys. Lett. **76** (2000) 2167

[5] A.Terrasi, F.Priolo, G.Franzò, S.Coffa, F.D'Acapito, S.Mobilio, J. Luminescence, **80** (1999) 363

[6] D.L.Adler, D.C.Jacobson, D.J.Eaglesham, M.A.Marcus, J.L.Benton, J.M.Poate, P.H.Citrin, Appl. Phys. Lett. **61** (1992) 2181

[7] S.Coffa, G.Franzò, F.Priolo, A.Polman, R.Serna, Phys. Rev. B, **49** (1994) 16313

[8] F.Priolo, G.Franzò, S.Coffa, A.Polman, E.Snoeks, G.N.van den Hoven, S.Libertino, S.Lombardo, S.U.Campisano, A.Carnera, NIM in Phys. Res. B, **116** (1996) 77

[9] V.B.Voronkov, V.G.Golubev, A.V.Medvedev, A.B.Pevtsov, N.A.Feoktistov, N.I.Gorshkov, D.N.Suglobov, Phys. Sol. St., **40** (1998) 1301

[10] C.D.Zuicker, D.M.Gruen, A.R.Krauss, MRS Bulletin, May 1995, 29

[11] D.G. Bruggeman, Ann. Phys. (Leipzig) **24**, 636 (1965)

[12] G.E. Jellison, Thin Solid Films **313-314**, 33 (1998)

[13] D.E. Aspnes, A.A. Studia, E. Kimnsbron, Phys. Rev. B, **29**, 768 (1984)

[14] G.E. Jellison, F.A. Modine, Appl. Phys. Lett. **69**, 371 (1996); **69**, 2137 (1996).

[15] G.Franzò, V.Vinciguerra, F.Priolo, Appl. Phys. A, 69, 3 (1999)

[16] P.G.Kik, M.L.Brongersma, A.Polman, Appl. Phys. Lett., 76, 2325 (2000)

[17] J.H.Shin, M.Kim, S.Seo, C.Lee, Appl. Phys. Lett., 72, 1092 (1998)

Advances in AlCu plasma etching

A. Spandre[1], S. Alba[1]

[1] *ST Microelectronics, Agrate Brianza, Italy*

Abstract

The upcoming requirements on microelectronic device performances have exacerbate the role of conductive lines in semiconductor manufacturing. Different applications (Flash memories, embedded Flash, high power BCD) require the definition of metal strips with very different geometries and thickness. Plasma etching processes for defining conductive lines of AlCu (Cu 0.5 wt%) have thus become a challenge. Conductive lines dimensions have followed the deep down scaling of cell size, and minimum interline spacing has gone down to up to 120 nm. A standard metal etching approach proved to be successful to define 160 nm spaced lines and process robustness was achieved with a standard 470 nm thick DUV photoresist. The patterning of aggressive 120 nm spaced lines required the introduction of a new generation of photoresists, the 193 nm DUV, less selective with respect to the metal etching. The introduction of a hard mask and improvements in selectivity allowed definition of 250 nm thick lines and spaced 120 nm. Beyond critical dimensions, high power devices require 3000 nm thick metallization, with an 800 nm of minimum spaces. The challenge of this etching was the arising strong microloading effects and has been solved by tuning the process pressure and optimizing the gas fluxes. Another application concerned the etching of intermetallic capacitors (MIM), in which a dielectric layer of about 100 nm is placed between two metal plates of 150 and 550 nm of thickness respectively. Key issue during patterning of the first metal plate was sidewall etching. The large exposed area, together with the exothermic reaction of AlCu etching where kept under control by reducing gas fluxes and by improving sidewall polymerization. The uniformity of the dielectric etching was a crucial issue during patterning of both metal plates. The intermetallic dielectric left after partial etching during the patterning of the 150 nm thick metal plate, acts as hard mask during the etching of the beneath 550 nm thick metal plate. Dielectric breakthrough must be uniform to avoid the onset of micro masking issues and consequent metal shorts. A metal etching chemistry was found to be suitable to etch the dielectric within 5% of uniformity.

Introduction

Etching processes were developed in an LAM TCP 9600 PTX low-pressure, high-density, inductively coupled plasma metal etch system. A planar inductive coil (TCP) of rectangular cross section is placed on top of the dielectric roof (made of Al_2O_3). Both the inductive coil and the wafer electrode (the bottom electrode) are powered at 13.56 MHz. Reactant gases are introduced through a top mounted gas ring just below the dielectric plate and exhausted via a turbomolecular pump. The wafers are clamped to the bottom electrode by means of an electrostatic bipolar chuck. There, a helium pressure is maintained to assure efficient heat dissipation from the wafer during the exothermic etching of the AlCu. Typical process conditions are: discharge pressure: 6 – 20 mTorr; TCP power: 400 – 780 Watt; Cl_2: 30 – 150 sccm; BCl_3: 20 – 60 sccm; Ar: 50 – 100 sccm; N_2: 5 – 15 sccm. Under these conditions the AlCu etchrate ranges from 500 to 1000 nm/min.

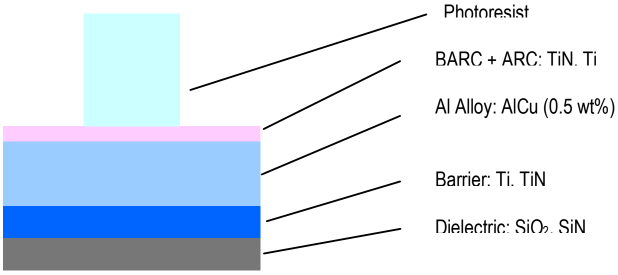

Fig. 1. Cross section of a typical interconnect layer structure.

8” diameter wafers were etched with a Cl_2, BCl_3, N_2 and Ar gas mixture, which composition varied depending on the size and the aspect ratio of the structures to be defined. The figure 1 depicts the basic sequence of layers composing the stacks to be etched, which are, starting from the mask patterning photoresist, an organic antireflective coating (the BARC) and/or an inorganic antireflective layer (a non-stoichiometric titanium nitride layer), the AlCu layer and a barrier, made of a combination of titanium and titanium nitride layers.

The composition of the stack is basically the same for all the processes treated hereinafter. The requirements for the device layout and functionality determine the thickness and sequence of the layers. A key point of the etching process is the ratio between the width and depth of the trench to be defined. This parameter, known as aspect ratio, is crucial, since impacts the downstream flux of the reacting and polymerizing species. Provided that the goal of metal etching is to define vertical conductive lines, every developed process should be a compromise between the AlCu removal rate and the sidewall protection necessary to avoid sidewall etching and guarantee the integrity of the structures. The sidewall protecting film, known as polymer, builds-up as a consequence of side-reactions involving the combination of the etching products, sputtered photoresist and the reactive species. The deposition of the protecting film may e enhanced by adding suitable polymerizing components such as N_2 or CH_xF_y.

After etching, the metal sidewalls are soak of the reaction product $AlCl_3$, which in presence of humidity, hydrolyzes to a highly corrosive hydrochloric acid that can destroy the entire patterned structures. Treating the etched wafer with water plasma corrosions may be prevented, since gaseous hydrochloric acid is still formed, but readily pumped away (plasma discharge occurs at low pressure), while the metal sidewall is oxidized to a protecting Al_2O_3. This process, known as passivation, occurs by means of a microwave discharge plasma in a dedicated chamber, separated but connected to the metal etcher in a such a way that the wafers never get in contact with the humidity. To assure a wafer-to-wafer repeatability, the metal etching tool is equipped with an end point detection system. The progress of the etching reaction is monitored through a plasma emission spectroscopy of the reaction products.

Etching of a 30000 Å thick metal layer, spaced 0.8 micron

Main issues concern the tight aspect ratio and the strong microloading effects arising from the topology of the patterning mask, where very dense zones (spaced ≤1 micron) face larger areas to be cleared (≥ 2 micron). In order to minimize the microloading (defined as the difference in the etchrate between dense and open zones) high process pressure (~20 mTorr) and high gas fluxes were chosen (the etching was carried out using a Cl_2, BCl_3, N_2, Ar based chemistry). The introduction of Ar into the AlCu and barrier etching chemistry assured a vertical profile by diluting the highly isotropic Cl_2. Moreover, a 3:1 Cl_2 to Ar ratio helped to keep under control Cl_2 isotropy without compromising selectivity towards the photoresist.

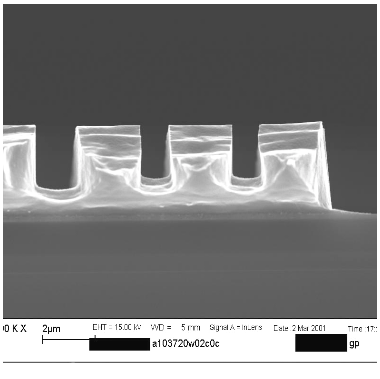

Fig. 2. Cross section of the 30000 Å thick, 8000 Å spaced AlCu lines at metal etch endpoint.

A Cl_2:BCl_3 ratio close to 2:1, with high fluxes and high discharge pressure allows to leave less than 1 micron of AlCu within the dense zones, while clearing the AlCu in the open areas (see fig. 2).

During etching of the residual AlCu and the underneath barrier within the dense zones, Cl_2 ratio with respect to Ar and BCl_3 is diminished to keep the profile vertical.
Optimized Cl_2 to BCl_3 ratio should range within 1.3 – 1.7. Beyond these limits, isotropic etching (>2.4) or loss in photoresist selectivity may occur (<1.7). Fluxes and discharge pressure are kept high, in order to play against microloading in the dense zone (see fig. 3). Finally, in the overetch step a low-pressure discharge is set to get rid of grain boundaries footsteps and residues mainly left in the open zones (fig. 4).

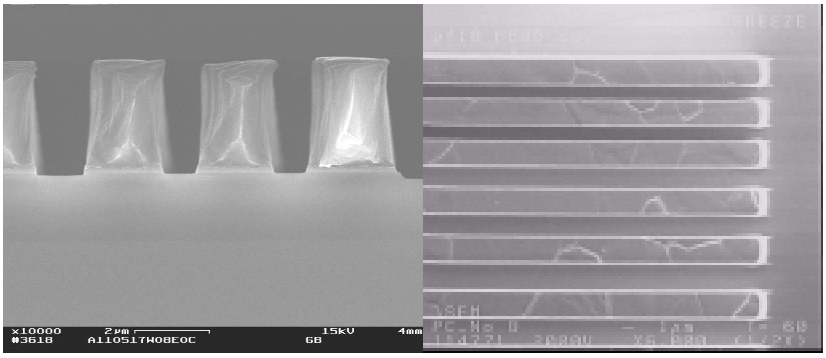

Fig. 3. (a) Cross section of the fully etched 30000 Å thick, 8000 Å spaced AlCu lines. (b) top view of the same dense zone showing perfect clearance of any AlCu, barrier or oxide residues.

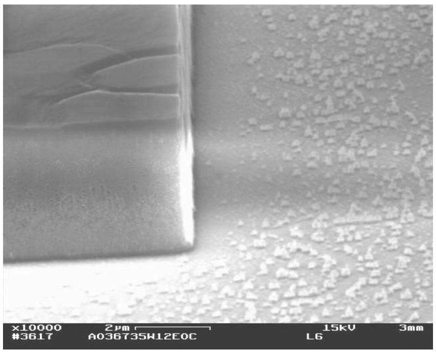

Fig. 4. Residues in open zones after non-optimized overetch step.

Etching of an intermetallic capacitor

The intermetallic (MIM) capacitor consists of a dielectric layer placed within two metal plates. The dielectric made of either 350 Å of SiN or 420 to 1000 Å of SiO_2, is position between an upper 1500 Å AlCu layer and an underneath metal layer with a varying thickness from 5500 to 8800 Å. Both AlCu stacks are etched separately as depicted in the figure 5:
In a first step the upper metal level is defined. Some dielectric etching is desirable in order to help the breakthrough of the oxide prior to the definition of the second metal level. In a second step, after the key dielectric breakthrough, the beneath metal level is patterned. Fig 9 and 10 show MIM capacitors, where on top can be seen the thin metal layer.

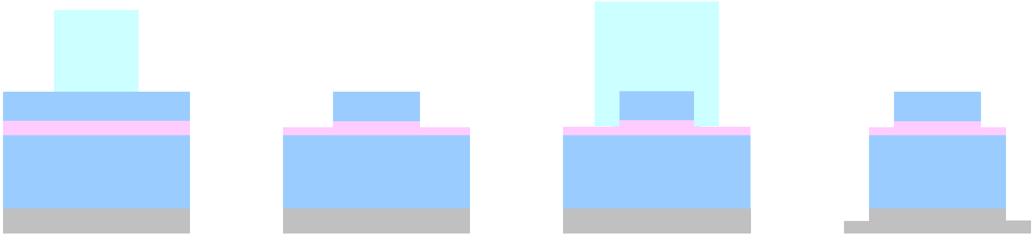

(a) (b) (c) (d)

Fig. 5. Step sequence for the definition of the MIM capacitor. (a) mask patterning of the upper capacitor metal plate, (b) definition of the 1500 Å metal level, (c) patterning of the underneath capacitor metal plate and (d) etching of the 5500 – 8800 Å metal layer.

Usually the area of a MIM capacitor is a small percentage (5%) of the total area of the wafer, whereas in a standard etching process is typically comprised between 40 and 60%. Since AlCu etching is highly exotermic, etching a wafer with a large exposed area (as in the case of MIM) will dramatically increase the wafer temperature with a consequent increase in Cl_2 isotropy. Etching isotropy, enhanced by the temperature, together with a lack of polymerization will give the sidewall overetching profile shown in figure 6.

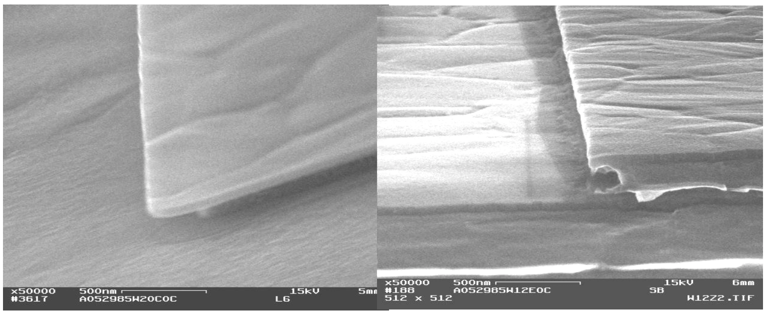

(a) (b)

Fig. 6. Negative profile for the upper MIM capacitor plate (a and b), arising from inadequate heat dissipation during AlCu etching and insufficient sidewall polymerization.

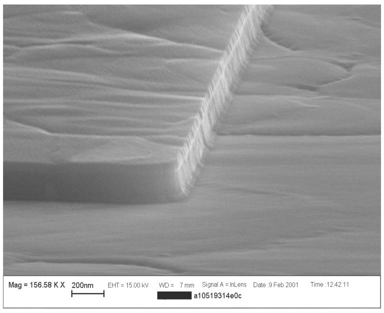

Fig. 7. Tilted and rotated view of a upper MIM capacitor plate etched.

Since the bottom electrode cooling cannot be improved without deeply compromising the center-to-border wafer uniformity, the major issue is to diminish the etchrate (and consequently the wafer temperature) and improve the sidewall polymerization. The etchrate was thus halved (~9000 to ~4500 Å/min), by both decreasing the amount of Cl_2 and the total flow rate. Further improvement was achieved by increasing sidewall polymerization by adding N_2. Figure 7 shows the improved sidewall quality with the above described process improvements.

In the etching of the beneath metal level the dielectric breakthrough should be carried out with an adequate sputtering component, in order to shun residues that may be drag through the beneath metal stack giving rise, in a worse case, to metal shortcuts (figure 8).

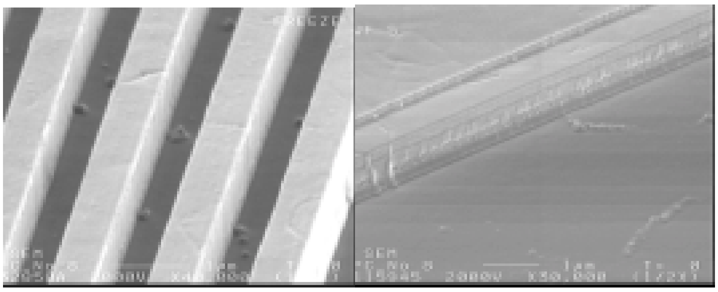

(a) (b)

Fig. 8. Underneath MIM capacitor plate etching: micro-masking residues are present in dense (a) and open zones (b) when the sputtering component during AlCu etching is insufficient.

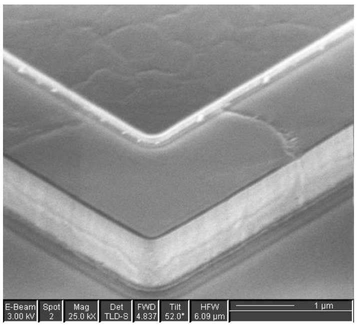

Fig. 9. Micro-masking issues are solved by increasing the sputtering component during AlCu etching, either by increasing the BCl_3 fraction or by raising the RF BIAS.

Raising the bottom electrode power can increase the sputtering component. Moreover, the sputtering component may be further improved if the fraction of BCl_3 within the total gas flow is raised. Figure 9 shows the optimized process, where can be seen the whole intermetallic capacitor.

Patterning of aggressively spaced lines - Introduction

The upcoming requirements on microelectronic device performances have exacerbate the role of conductive lines in semiconductor manufacturing. Plasma etching processes for defining conductive lines of AlCu (Cu 0.5 wt%) become a challenge, when conductive lines dimensions have to accomplish for the deep down scaling of geometries, and minimum interline spacing has gone down to up to 120 nm. A standard metal etching approach proved to be successful to define 160 nm spaced lines, where process robustness was achieved with a standard

470 nm thick 248 nm DUV photoresist. However, the patterning of the aggressive 120 nm to 100 nm spaced lines required the introduction of a new generation of photoresists, the 193 nm DUV, whose less selectivity against metal etching required the introduction of an oxide hard mask.

Patterning of 160 nm spaced lines

For the patterning of 160 nm lines was essential the introduction of a dedicated BARC/ARC etching step, in order to guarantee a CD BIAS[1] close to 0. ARC etching step is carried out with a Cl2/Ar isotropic etching chemistry (see figure 10), with small additions of BCl_3, in order to prevent etch stop arising from ARC oxidation during occurring lithographic reworks. Intermetallic dielectric filling may be dramatic if the dense zones are characterized by negative profiles. The use of a 470 nm thick, 248 nm DUV photoresist required the notable improvements of selectivity against photoresist. This was achieved by lowering the gas fluxes, decreasing the TCP power to the minimum required to ignite the plasma and to reduce RF BIAS. Cl_2 to BCl_3 ratio was increased up to 3:1 to guarantee clearance of the dense zones and improve the microloading. Furthermore, high amounts of N_2 were required to guarantee sidewall polymerization. Improvement of selectivity were not put in place for barrier etch and overetch step since sputtering was mandatory to clear any risk of metal shortings between adjacent conductive lines.

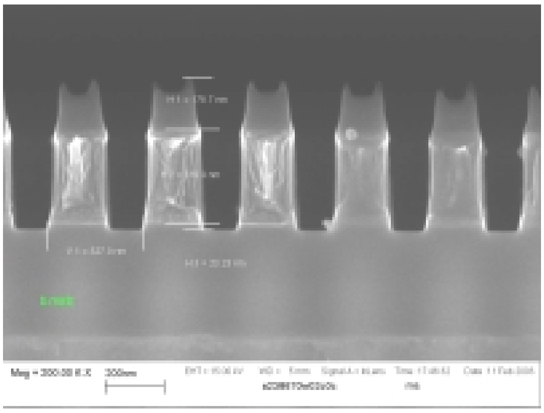

Fig. 10. Cross section of 260 nm thick AlCu lines, spaced 160 nm. Photoresist on top of the line was not stripped to show the selectivity reached during the etching.

Patterning of 120 nm spaced lines

From the lithographic point of view the definition of 120 nm spaced line required the implementation of the new the 193 nm DUV photoresist generation. Since photoresist thickness is reduced accordingly to shrinking of the dimensions to be defined, 240 nm thick resist is spin for 120 nm spaced lines. This has obviously required the introduction of SiO_2 hard mask. Thickness was dictate by the fact that during AlCu etching, photoresist must still be present to allow suitable sidewall polymerization. Furthermore, hard mask thickness was set to give the smaller impact during the etching process to what concerns the dimensions to be defined. A thin hard mask <50 nm was successfully open by employing a $C_xH_yF_z$/Ar chemistry, with a CD BIAS close to 0 (see fig. 11) and very high selectivity to the underneath TiN layer. More than 180 nm resist were left, which allowed performing the AlCu etching with an almost vertical profile. Again, etching parameters were set in order to give the maximum reachable selectivity. Low RF BIAS was set, while a close 3:1 Cl_2 to BCl_3 ratio with a high content of

---

[1] CD BIAS accounts for the difference between the line width measured after mask development and the line width measured after etching.

N_2 was chosen, to achieve vertical profile and assure sidewall polymerization. Subsequent steps were safely carried out using the hard mask as protecting layer (fig. 13).

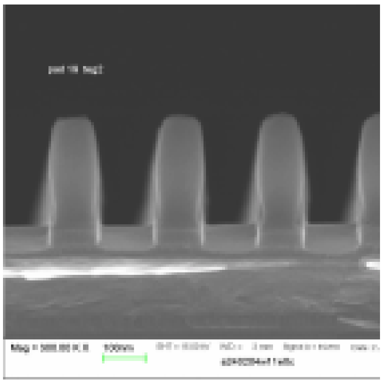

Fig. 12. Cross section of the 120 nm spaced lines after hard mask opening. Above 180 nm of photoresist are left, while the hard mask profile is vertical.

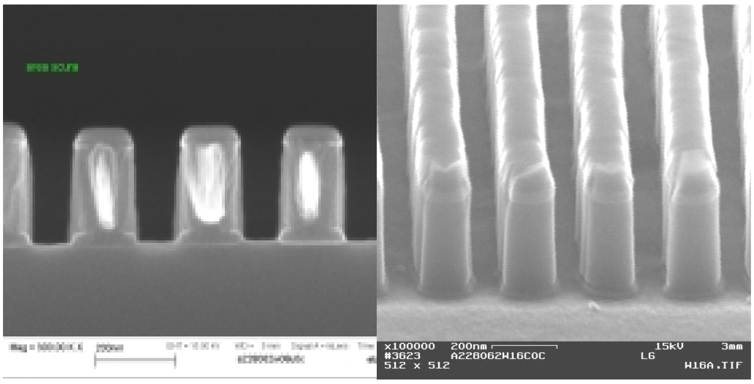

Fig. 13. Cross section and tilted view of the 220 nm thick AlCu lines, spaced 120 nm. The stack was etched up to the barrier. Note that the hard mask has been almost fully preserved. .

Conclusions

Etching requirements for defining conductive lines for new devices require innovative solutions. In the present work are described four original cases.

The key point of patterning thick metal levels (~3 micron) is to improve the microloading, which can be achieved by raising the discharge pressure.

In the case of MIM structures, the key parameter to defining the upper metal plate is to reduce the ethchrate, to accomplish for the high exposed area.

For tight geometries (160 nm) the selectivity against the photoresist plays the fundamental role; improved selectivity may be obtained by decreasing TCP and bottom electrode powers, together with a decrease in the total flow rate.

For smaller dimensions (120 nm), the introduction of a 193 nm DUV photoresist required the implementation of a SIO_2 hard mask.

The Borderless approach in Flash Memory technology: critical parameters and their effect in Local Interconnect Layer (LIL) etch

S.Alba[1], O.Donghi[1], R.Morandi[1], D.Piumi[1]

[1]ST Microelectronics, Agrate Brianza, Italy

Abstract

The new Flash technologies stress the problem of contact overlay because of the tight layout rules: to relax the overlay control the condition is to have a stopping layer (Si_3N_4) to preserve the field oxide from contact etch. The introduction of this new layer to etch implies a new approach for contact etch: contact etch stops on this layer and then switches to a second step, highly selective vs oxide. This contact approach is named borderless. The greatest difficulty of the oxide etch is to develop a chemistry that permits to increase the oxide vs nitride selectivity. In this work it will be showed what one the critical parameters to be considered during the development of a etch recipe and the critical points of this approach.

Introduction

The increased density requirements both in Flash stand alone Memory in Flash and Memories embedded in a CMOS logic core, demand for strong scaling of active area pitches. Shallow Trench Isolation (STI) with its zero field encroachment, better planarity, parasitic immunity and low junction capacitance, together with borderless contacts is the preferred isolation and contact scheme for these applications. This approach is necessary for 0.15μm technology and below: the contact dimensions can vary between 0.25μm and 0.1μm for the advanced application.

Borderless approach description

To explain the difference between a standard contact hole process and a borderless process, see figure 1.

The borderless approach permits to relax the overlay control; to achieve this, the process involves the use of a stop layer (typically Si_3N_4) deposited below the PMD (Pre-Metal Dielectric) (see figure 1).

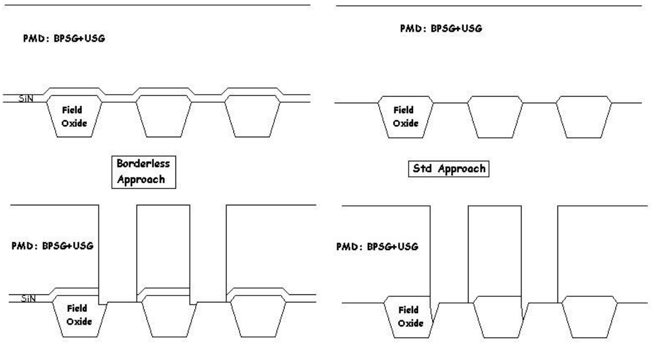

Figure 1: Comparison Borderless and no borderless approach

The etch recipe consist a two step process, performed with a different chemistry (see figure 2): the first step selectively etches the oxide film (generally BPSG and USG) and thus stops on the silicon nitride, and then switches to a second step to etch the nitride, highly selective versus field oxide (usually obtained with Shallow Trench Isolation (STI)) and $TiSi_2$ or Si (depending on application).

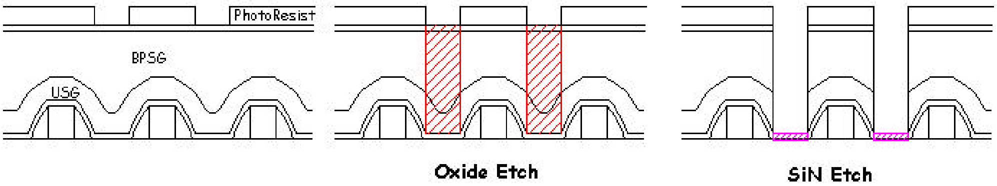

Figure 2: Etching recipe structure in borderless approah

The advantage of borderless process lies in the fact that a contact can be made with zero or negative overlap towards the field isolation without being penalized with an increase in diode leakage. This is due to a short-circuit between a S/D region and its “well” caused by the vertical penetration of contact into the field oxide. Due to this characteristic, the contact is not delimited towards the active/field edge and becomes “borderless” (no respect for borders!).

The limit of standard approach process is the unavoidable field oxide consumption during the contact etching step in case of misalignment. The misalignment of contact mask may cause an unwanted oxide removal in cuvette region, thus discovering a poorly doped silicon region. For STI isolation, the dig into the field oxide produces a deeper dig respect to LOCOS isolation because the STI trench slope near to be vertical. In this case the contact doping, using with successful effect on LOCOS isolation, is not always effective to recover the induced leakage.

The integration of Borderless contact process requires several controls both regarding the physical and morphological characteristics of stopping layer (Si_3N_4). An important characteristic of nitride layer is the film step coverage, that is the difference of nitride thickness between the top of the gate and the drain chain.

The main silicon nitride layer deposition techniques currently available are PECVD (Plasma Enhanced Chemical Vapor Deposition) e HDPCVD (High Density Plasma Chemical Vapor Deposition). The morphological drawback of PECVD nitride layer is mainly due to the poor step coverage (50%); this cause the need to depositing a high quantity of material to obtain a good coverage in any region. In order to solve the problems correlated to PECVD nitride deposition, the introduction of HDPCVD nitride has been suggested taking into account that this deposition technique allows to obtain an acceptable step coverage (80%).

The minimum nitride thickness will be determined by uniformity control during the deposition and by the borderless etch process constraint.

Equipment description

The tool used for this process (LAM Exelan HP) is a dual frequency oxide etcher in which both the 27 MHz and 2 MHz RF generators are applied to the bottom electrode, while the top electrode is grounded. It is a fixed gap chamber with movable confinement rings that allow a dynamic control of the WAP - wafer area pressure. A dual channel chiller is installed to allow using different temperatures between top and bottom electrode.

The termal excange between chuck and wafer is assured by an helium flow backside of the wafer: it is possible to tune the wafer-temperature, changing the He pressure of this flow.

The gas usually used includes C_xF_y, CH_xF_y, CO, O_2, Ar, N_2.

In Figure 3 it is showed the LAM Exelan HP chamber schematic and has been reasumed the tipical process condition.

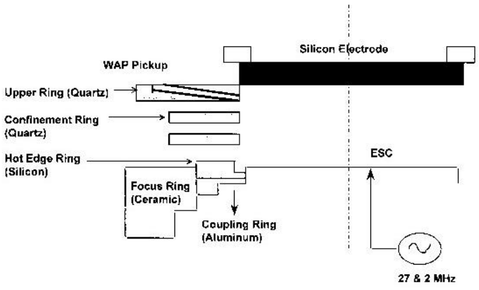

Parameter	Min Val	Max Val
RF 27 MHz	0W	2000W
RF 2 MHz	0W	2000W
Pressure	60mT	100mT
He flow	8T	15T

Figure 3 - LAM Exelan HP chamber schematic and work parameters

Borderless etching characteristics

The etch recipe consist a two step process, performed with a different chemistry (see figure 2): the first step selectively etches the oxide film (generally BPSG and USG) and thus stops on the silicon nitride, and then switches to a second step to etch the nitride, highly selective versus field oxide.

The greatest difficulty of the oxide etch is to develop a chemistry that permits to increase the selectivity oxide vs nitride. This aim has been obtained using a chemistry rich in carbon-containing gases (C_xF_y): possible gases are , for example C_4F_8, C_4F_6, C_5F_8, C_3F_6.

Two important parameters to take into account developing this etch process are the nitride step coverage and the thickness uniformity of oxide. In fact the selectivity requirements are related to the percentage of OE necessary to compensate the difference of oxide thickness on wafer and to the minimum nitride thickness on wafer.

It is possible to reach an optical end point monitoring the variation on 390nm (CN line) and 440nm (SiF line) wavelengths.

On the other hand, the difficulty of nitride etch is to obtain a high selectivity nitride to oxide. This aim is obtained using a CH_3F/O_2 chemistry at high pressure and low power. This reduces the ion bombardment energy, so that selectivity is reached based on the fact that nitride binding energy is lower than oxide one.

It is possible to reach an optical end point monitoring the variation on 390 nm (CN line) and 440nm (SiF line) wavelengths.

Borderless application on Local Interconnect Layer (LIL) approach

The borderless approach is used also in a particular application, the Local Interconnect Layer (LIL). The peculiarity of LIL etch is that in the same mask are opened holes and trenches (see Figure 4). This approach is used to substitute the traditional approach of Self-Aligned Source (SAS) in the memory cell and permits to remove a mask level.

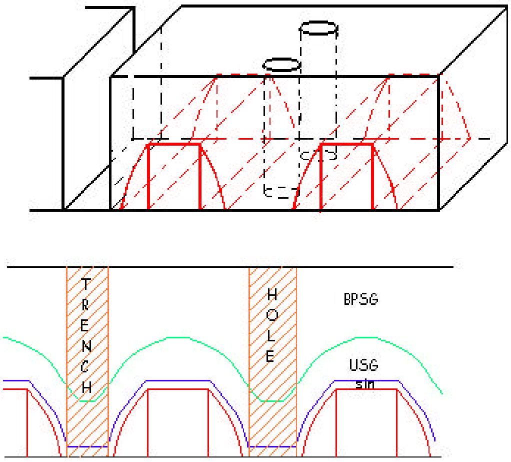

Figure 4a:Schematic LIL approach

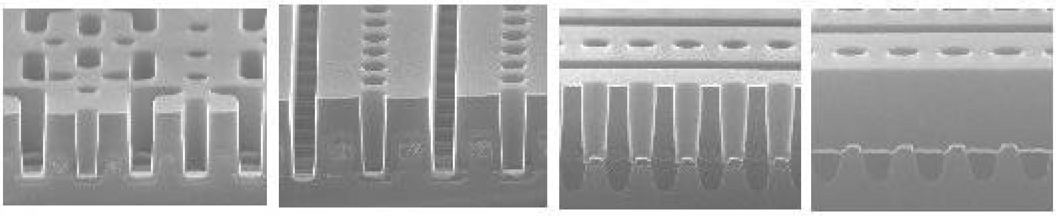

Figure 4b: LIL etch; example of different structures (trenches and holes) and different cuts (parallel orthogonal at the source or drain line). Hole and trench dimensions: 0.25 µm.

The greatest difficulty of LIL etch is to etch holes and trenches with a very low µ-loading (difference in term of etch rate between hole and trench) to preserve the nitride layer in the trench while the hole etch is not still completed.

Clearly, in this case, the planarity of oxide layer and the nitride step coverage play a very important role. To compensate the non uniformity of film planarity (8%) and the non uniformity of center and edge etch rate (5%) and the µ-loading effect (5%) it is necessary to fix OE at 60% on EP of oxide etch step.

The influence of several critical recipe parameters (pressure, polymerising –fluorocarbide– and depolymerising gases –O_2–) on different etch parameters (etch stop, selectivity oxide vs nitride, µ-loading, verticality of hole and trench profile) has been studied.

In particular, the fine tuning on ratio C_xF_y/O_2 has permitted to develop a recipe with a sufficient selectivity oxide vs nitride and that does not show the etch stop problem. In particular we have seen the etch stop when the ratio C_xF_y/O_2 is higher than 1 and a not sufficient selectivity vs nitride when the ratio C_xF_y/O_2 is lower than 0.8.

It has been studied four recipe parameters of the oxide etching step: pressure, C_xF_y and O_2 flow and He flow and the variation of four different process parameters (ER & EP time, selectivity oxide vs nitride, trench and hole verticality, trench and hole bottom dimensions (figure 5)).

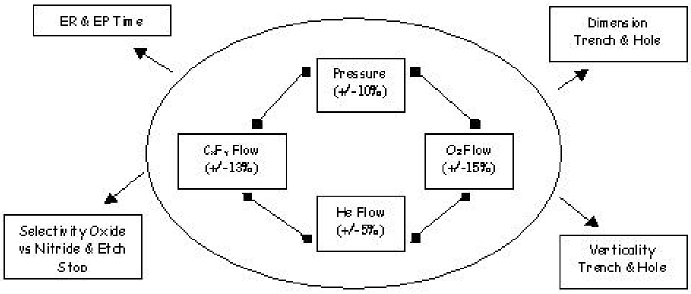

Figure 5: Trial summary

The model selected to analyse the data is a polynomial of 2nd order for all data except for selectivity oxide vs nitride data where best fit is obtained with a linear model. All wafers has been etched at end point (optical) with 60% OE.

It has been showed that with a more polymerising chemistry (increasing C_xF_y and decreasing O_2) the hole (figure 6b) and the trench dimension decrease (figure 6a). In figure 6a and figure 6b the Delta CDs are represented: this is the difference between dimension after etch and after litho development.

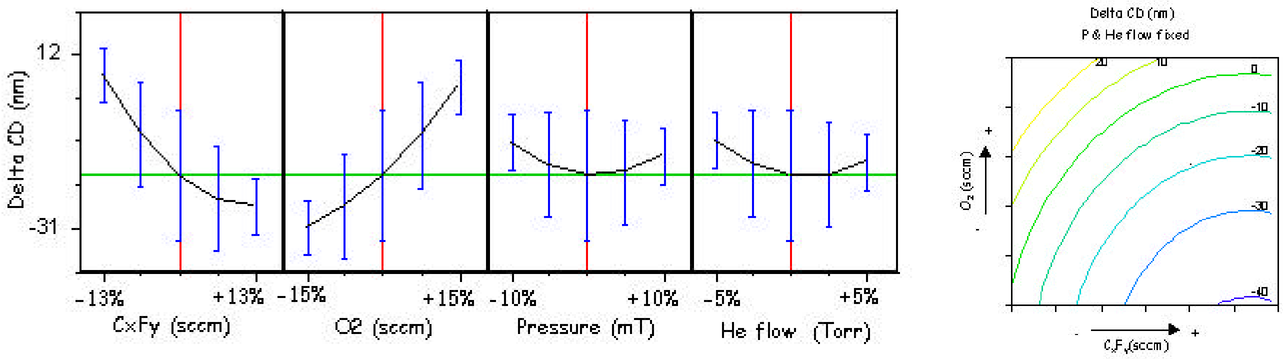

Figure 6a: Trench - Delta CD

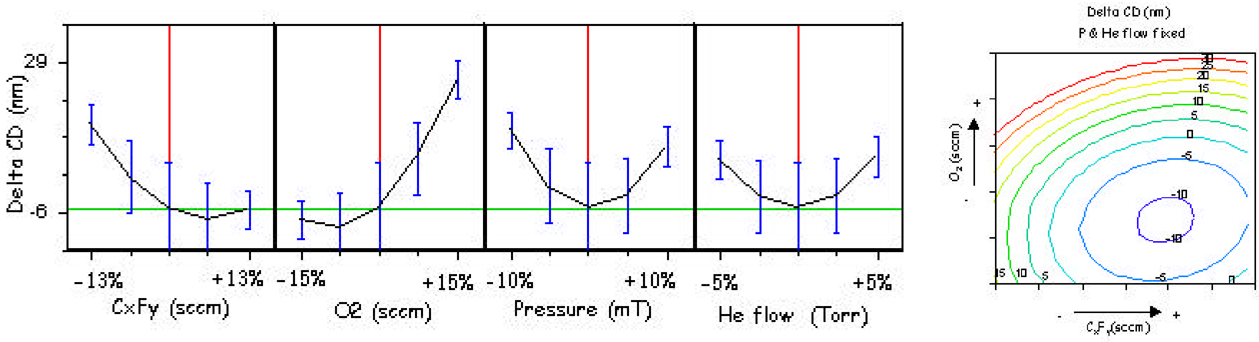

Figure 6b: Hole - Delta CD

The same trend can be seen for the hole and the etch rate values (figure 7).

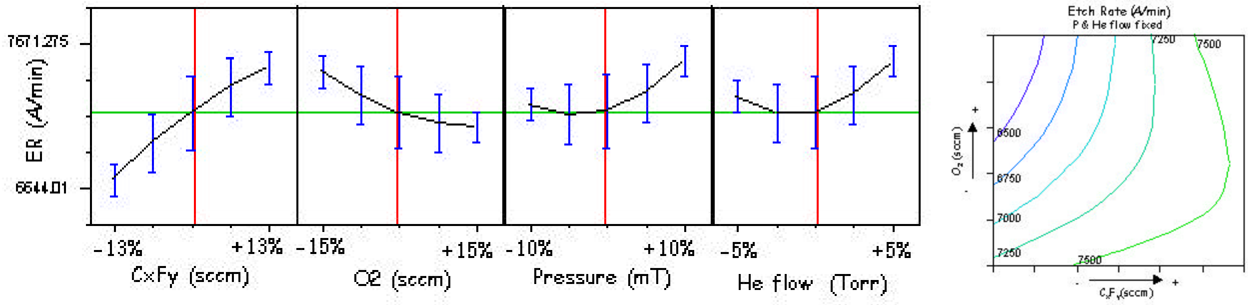

Figure 7: Etch Rate

The main variable to increase the selectivity oxide vs nitride is the O_2 flow. In the figure 8a it is showed that the effect of O_2 flow dominates respect to C_xF_y flow in the trench. The same situation can be seen on hole (figure 8b)

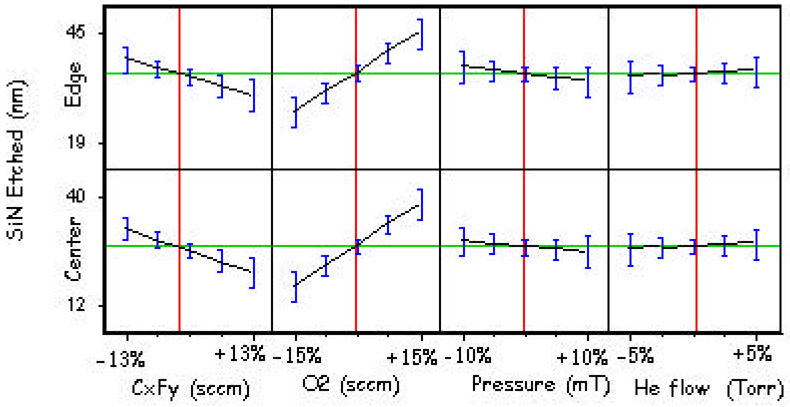

Figure 8a: Trench - Nitride etched @ edge and center of wafer. All trial have the same % of OE

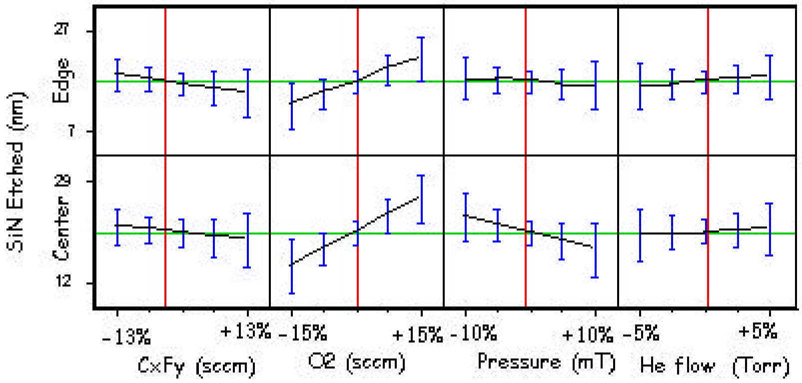

Figure 8a: Hole - Nitride etched @ edge and center of wafer. All trial have the same % of OE

The etch stop problems occurs for low O_2 flow and when the ratio C_xF_y/O_2 is higher than 1. The insufficient selectivity vs nitride occurs for higher O_2 (figure 9) flow and when the ratio C_xF_y/O_2 is lower than 0.8.

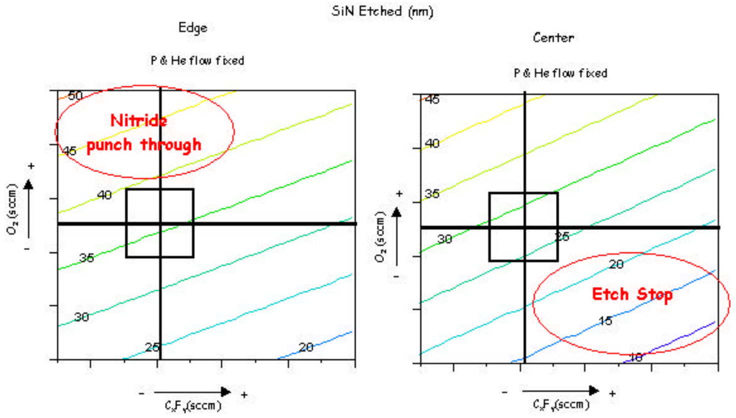

Figure 9: Trench – Etch stop problem and Nitride selectivity

It is clear that it is very difficult to reconcile the high selectivity requirements, the more straight profile of trench and holes and the dimension of structures.

Nitride etched on hole is very little while the correlation with process parameters is poor because the EP is seen on trench.

Finally in the range explored it has been seen a little effect of He backside cooling and pressure.

Conclusion

The borderless approach represents the future on contact etch: this study has showed the limits and the difficulties of this method. It is necessary to make an accurate study of parameter space to have a good and reliable process window.

Acknowledgements

The authors would like to thank P.Colpani and B. Zanderighi for the support in the DOE work.

Sacrificial layers for the tailored growth by PECVD of oxide thin films with controlled porosity

A.Barranco[1], J. Cotrino[2], F. Yubero[1], A.R. González-Elipe[1]

1)Instituto de Ciencia de Materiales de Sevilla (CSIC- Univ. Sevilla). Avda. Américo Vespucio s/n. 41092 Sevilla (Spain)
2)Departamento de Física Atómica, Molecular y Nuclear. Universidad de Sevilla, Sevilla (Spain)

Fabrication of porous metal oxide thin films is interesting because of their use as antireflective coatings for photovoltaic and other applications in optics, low-k materials for their use in electronics, diffusion membranes for separation and purification of fluids or porous layers used as substrate for biomaterials to grow living cells in a controlled way.

In the present paper we propose a new PECVD procedure for the room temperature synthesis of porous oxide thin films. The novelty of the method consists of the deposition of an organic sacrificial layer that is removed during the deposition of the oxide thin film. The procedure resembles a template approach since it uses a sacrificial organic material for the control of the porous microstructure of the film. The final porosity of the oxide thin film directly correlates with the thickness of the deposited organic layer.

Here we present some results about the deposition method of the porous oxide thin films, in particular SiO_2 and Al_2O_3, focussing the attention on the characteristics and deposition procedure of the organic sacrificial layer. This one is prepared by plasma polymerisation in a microwave plasma of pure oxygen by using toluene as precursor. The layer was formed by a highly oxygenated polymeric material. Besides describing the particular experimental procedure developed to prepare this sacrificial layer, characterisation results by FT-IR, RBS, XPS and UV-vis absorption spectroscopy are presented. The characteristics and relative concentration of the different functional groups (i.e., C-OH, C=O, COO^-, etc.) present in the layer have been determined through this analysis.

It is shown that a critical feature of this material when used as a sacrificial layer is that it has a high content of oxygen in its structure. The deposition of the oxide thin films proceeds after that of the sacrificial layer by changing the operating deposition conditions of the microwave reactor. By properly adjusting these conditions it is possible to get the removal of the organic material while the inorganic one is being deposited. Either the deposition of the sacrificial layer or that of the oxide thin films take place at room temperature.

A careful analysis of the deposition processes and properties of the oxide thin films (SiO_2 and Al_2O_3) reveal that a direct correlation can be established between the porosity of the oxide thin films and the thickness of the previously deposited sacrificial layer. A good adhesion and mechanical stability is obtained for all the oxide thin films, even if their porosity is very high.

Application examples of the final oxide thin films as optical sensors of humidity or as gas diffusion membranes are reported and correlated with the microstructure of the films.

Model reactions of NO, O_2, CH_4 and mixtures of these gases in a surface wave plasma.

J.L. Hueso[1], J. Cotrino[2], A. Yanguas[1], A. Caballero[1], A.R. González-Elipe[1]

1)Instituto de Ciencia de Materiales de Sevilla (CSIC-Univ. Sevilla). Avda. Américo Vespucio s/n. 41092 Sevilla (Spain)
2)Departamento de Física Atómica, Molecular y Nuclear. Universidad de Sevilla, Sevilla (Spain)

This paper shows plasma reactions results for a series of molecules (O_2, NO, CH_4) diluted in Ar as a carrier gas. These molecules are present as pollutants in Diesel and other exhausts and the experiments are carried out to model their reactivity in a plasma according to different basic parameters of the process as electron temperature, pressure, etc. The intention is to be able to extrapolate the reaction schemes to predict the removal efficiency under real conditions. In this respect, preliminary results are also shown for these molecules diluted in nitrogen as a carrier gas.

In all cases, the mixtures reproduce the concentrations typically found in this type of exhausts. Since the removal of the particles of soot coming from Diesel engines posses a critical problem for the cleaning of this type of exhausts, attention is given to the formation/removal of carbon during the reaction of gases containing methane.

A surface wave microwave applicator is used to induce the plasma. Reaction yields are monitored by analyzing the gas composition before and after the reaction as a function of composition, pressure and microwave power. This study was complemented with the analysis by Optical Emission spectroscopy (OES) of the emission lines coming from the intermediate species of the plasma.

The evaluation of the reaction products, the percentage of decomposition of the pollutant molecules, as well as the identification of the intermediate species detected in the plasma enable the proposal of a reaction scheme to account for the removal of NO in the gas stream.

The plasma reaction results under our experimental conditions can be summarized as follows:

- NO dissociates into N_2 and O_2
- For mixtures O_2+NO the yield of formation of N_2 decreases
- Total decomposition of NO with formation of N_2 is detected for mixtures NO + CH_4. Other products are H_2, CO_2 and some CO.
- A plasma of CH_4 produces H_2 and C. Incorporation of O_2 to the mixture leads to a progressive formation of CO_2. Formation of H_2O starts to be important with a high excess of O_2 in the reaction mixture.
- The products obtained from a mixture NO+CH_4+O_2 were H_2O, H_2, CO_2, CO and N_2 in different proportions according to the working conditions. No traces of NO_2 could be detected

A model is developed to explain the previous observations and the evolution of intermediate species detected by OES as well as to account for the preliminary results obtained when using N_2 as a carrier gas. A proposal is made about the use of surface wave reactors for the cleaning of gas exhaust by means of plasmas.

Modelling of an argon atmospheric capillary surface-wave discharge

A. Yanguas[1], J. Cotrino[2], J.L. Hueso[1], A. R. González-Elipe[1]

1)Instituto de Ciencias de Materiales de Sevilla (CSIC-Univ. Sevilla). Avda. Américo Vespucio s/n. 41092 Sevilla. Spain
2)Departamento de Física Atómica, Molecular y Nuclear. Universidad de Sevilla, Sevilla (Spain)

Surface wave discharges have been proved to be suitable in many technological procedures. Due to the wide range of applications of high frequency surface-wave-excited plasmas and the importance of improving a particular process, a better understanding of some features of the discharge is needed. Our aim in this work is to reproduce the argon kinetics main features by using a collisional-radiative model and a two-temperature model for non-equilibrium plasmas. Thirty-one argon atomic levels are considered. The production of electrons and excited states atoms in a flowing non-equilibrium plasma will be determined taken into account all important collisional and radiative processes. The atom-atom collisions, as a potential source of production of electrons and excited atoms, is also included. A numerical analysis is also carried out to determine the main characteristics of microwave frequency surface waves along atmospheric pressure plasma columns, when they are sustained in ambient air by an argon discharge excited by 2.45 GHz microwaves in an open-ended dielectric discharge tube. The axial behavior of plasma parameters, the energy available and the thermodynamic equilibrium in the discharge are analyzed as a function of microwave power and gas flow.

Experimental investigation of the splashing processes at impact in plasma sprayed coating formation

J. Cedelle, S. Bansard, C. Escure, M. Vardelle, , B. Pateyron, P. Fauchais

Laboratoire Science des Procédés Céramiques et Traitements de Surface, Université de Limoges, Limoges, France

Abstract :

This paper is devoted to an experimental investigation of the different splashing phenomena (impact and flattening)when a plasma sprayed single particle impacts on a flat substrate. This research is carried out using an imaging technique with a fast CCD camera aimed either parallel to the substrate for impact splashing or almost orthogonal to it for flattening splashing. The correlation of the image with the results of a set allowing to determine particle parameters in flight just prior to their impact allows a better understanding of the splashing processes.

Introduction :

Thermal spray coatings are built up by the layering of splats formed by the flattening and solidification of individual molten droplets [1]. Coating properties depend on the contact of those splats with the underlying substrate surface or already solidified passes [1,2]. This contact is a function of several parameters linked both to impacting particles : size, velocity, material, degree of melting, and chemical state (for example degree of oxidation in the case of metal droplets) and substrate or previously deposited layers: roughness, chemistry,oxide layer thickness for metals, desorption of adsorbates and condensates.

Fauchais and al. [3] showed that when a particle hits a substrate, the splashing phenomena are two fold : the first one is impact splashing, resulting in the ejection of tiny droplets (1µm) in the impact direction and which seems to occur immediately after the impact. The other one, called flattening splashing results in extensively fingered splats [4,5], the fingers having a poor adhesion with the substrate or the previously deposited layers. As shown by imaging experiments performed with millimeter sized particles [4], it occurs at the end of the flattening stage with a splashing parallel to the substrate surface. Splashing phenomena play an important role concerning the contact quality between splats and underlying surface, i.e the coating adhesion / cohesion. For the splashing occuring at the end of the flattening process on a smooth surface (Ra < 0,05), named flattening splashing in the following, it has been shown that below a preheating temperature , named transition temperature Tt, splats are extensively fingered while over it they are disk shaped [6]. Even when spraying on rough substrates, as in industrial conditions, the coating adhesion is significantly enhanced when spraying is performed with the substrate preheated over Tt [7]. It explains why these last years many studies (modelling and experiments, [3]) have been devoted to the phenomena related to particles flattening and solidification and the resulting splat formation. To study a single particle flattening together with the measurement of its parameters prior to its impact : velocity, surface temperature and diameter, it's necessary to use an imaging device to visualize it. Such measurements are very complex because the mean particle velocity is around 200-250 m/s, its mean diameter 30µm and its surface temperature over 3000 K for oxides. The particle image at impact is obtained by a fast CCD camera (exposure/ delay time 100 ns to 1ms) with possible multi-exposures and its parameters prior to impact are measured with a fast (50 ns) two-color pyrometer and a phase Doppler Anemometer [8].

Alumina and Zirconia particles with different sizes are used in conjunction with glass and stainless steel substrates maintained at specific temperatures to study these splashing phenomena.

Experimental procedure :

Plasma spraying is carried out using a direct current (dc) plasma torch (PTF4 type) with a 7 mm internal nozzle diameter. The plasma torch is operated between 300A and 600A, and the inlet plasma gas flow consists of a mixture of 45 L/min Ar and 15 L/min H2. An yttria partially stabilized zirconia powder (8% Y2O3) and an alumina one with particle sizes ranging between 5µm and 20 µm and 22µm and 45 µm respectively are used in this study.

The powder is injected 2 mm upstream of the nozzle exit and the argon carrier gas flow rate is adjusted to the working parameters in order to achieve a mean trajectory making an angle of about 3,5° with the torch axis (optimum value). The internal diameter of the injector tube is 1.8 mm. Splats are collected on a substrate at a distance of 100 mm. Only particles following the trajectory close to the plasma jet axis are collected thanks to a moving heat shield positioned at 70mm of the torch nozzle exit and a fixed one where a 1.5mm hole is drilled and which is positioned at 20 mm upstream of the substrate (Fig 1).
The experimental set-up is composed of two parts : for a single particle in flight characterisation, a measurement device ,consisting of a phase Doppler particle analyzer and for its flattening, a fast (50ns) two-color pyrometer and an imaging system, i.e., a fast CCD camera triggered by the velocity signal.

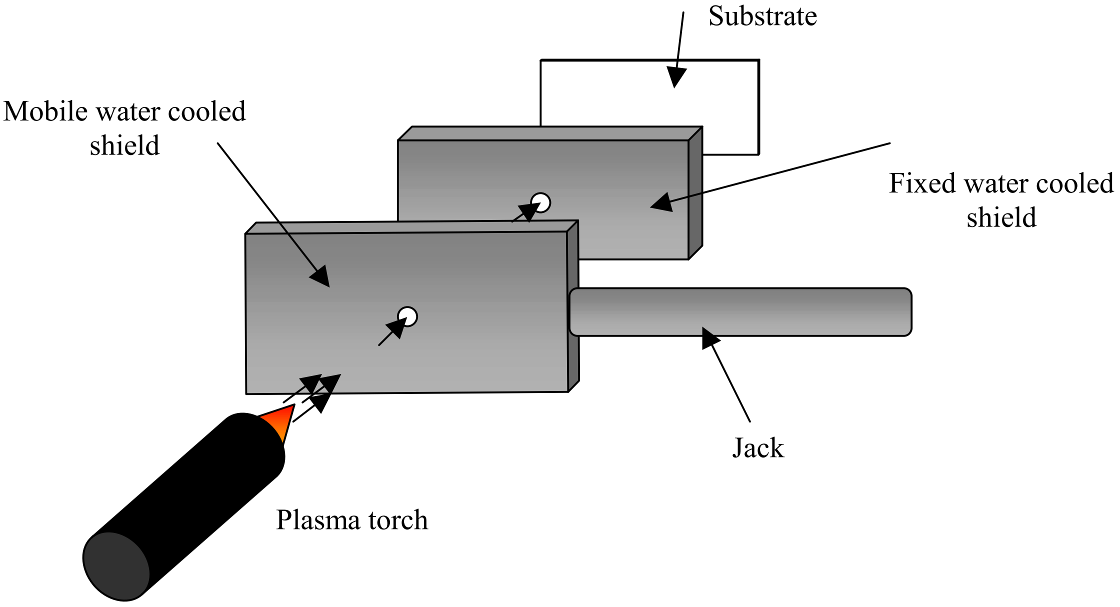

Figure 1 : Experimental set-up to select particles

Measurement techniques :
-Particle parameters
The parameters of a single molten droplet parameters are measured prior to its impact, with the experimental set-up shown in Figure 2.

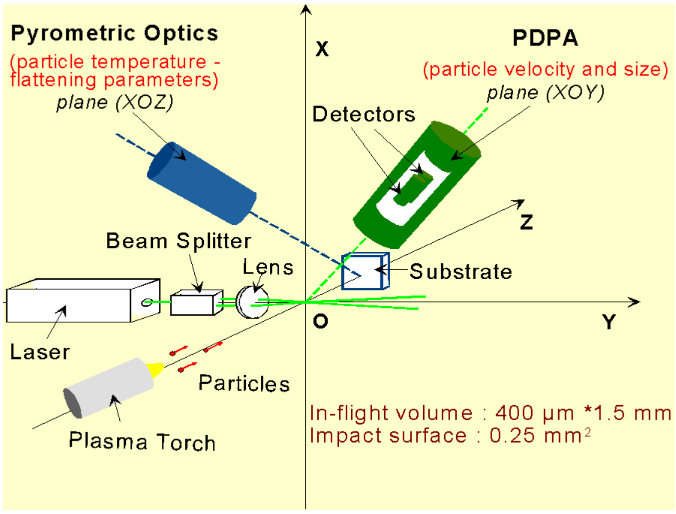

Figure 2 : Experimental set-up to obtain particle parameters

The size and the velocity of a single particle in flight are determined from the light scattered by the particle passing through an interference fringe pattern (8 µm) generated at the intersection of two coherent laser beams whose wavelength is 514.5 nm. The velocity is deduced from the time frequency of the Doppler burst generated by the particle crossing the fringe pattern (5% of precision). The size is computed from the phase shift between the light signals collected by two sensors looking at the probe volume from two different angles (10% of precision for size measurement). This phase shift is linearly related to the particle size. In the PDA system, the two sensors are avalanche diodes. After amplification, the signals from the diodes are recorded using a digital oscilloscope. Algorithms based on across spectral density method are used to obtain the frequency and the phase shift of signals. The probe volume is limited using a spatial filter placed before the photo detectors. It corresponds to a cylinder (1.5 mm in lenght and 0.4 mm in diameter) whose axis is orthogonal to plasma jet axis.

The temperature of the particle prior to its impact, and the time-evolution of the resulting splat temperature are determined from the thermal radiation emitted by the particle in flight and at impact (10% of precision for temperature measurement). This radiation is collected by a two-color pyrometer head focused on the substrate and filtered at two- wawe -lengths (632,8 and 832,8 nm).

The temperature of a particle just prior to its impact and that of the resulting splat, are derived, after calibration, from the ratio of the photo detector outputs of the pyrometer, by assuming that the material behaves as a grey body . The main cooling rate of the splat is estimated from the time- temperature evolution of the lamella.

-Imaging technique

The experimental observation of the droplet's impact on a substrate is carried out by an imaging technique composed of a rapid CCD camera (PCO SENSICAM) and a long distance microscope (QUESTAR).[8] Figure 3 describes the experimental set-up of the imaging technique.

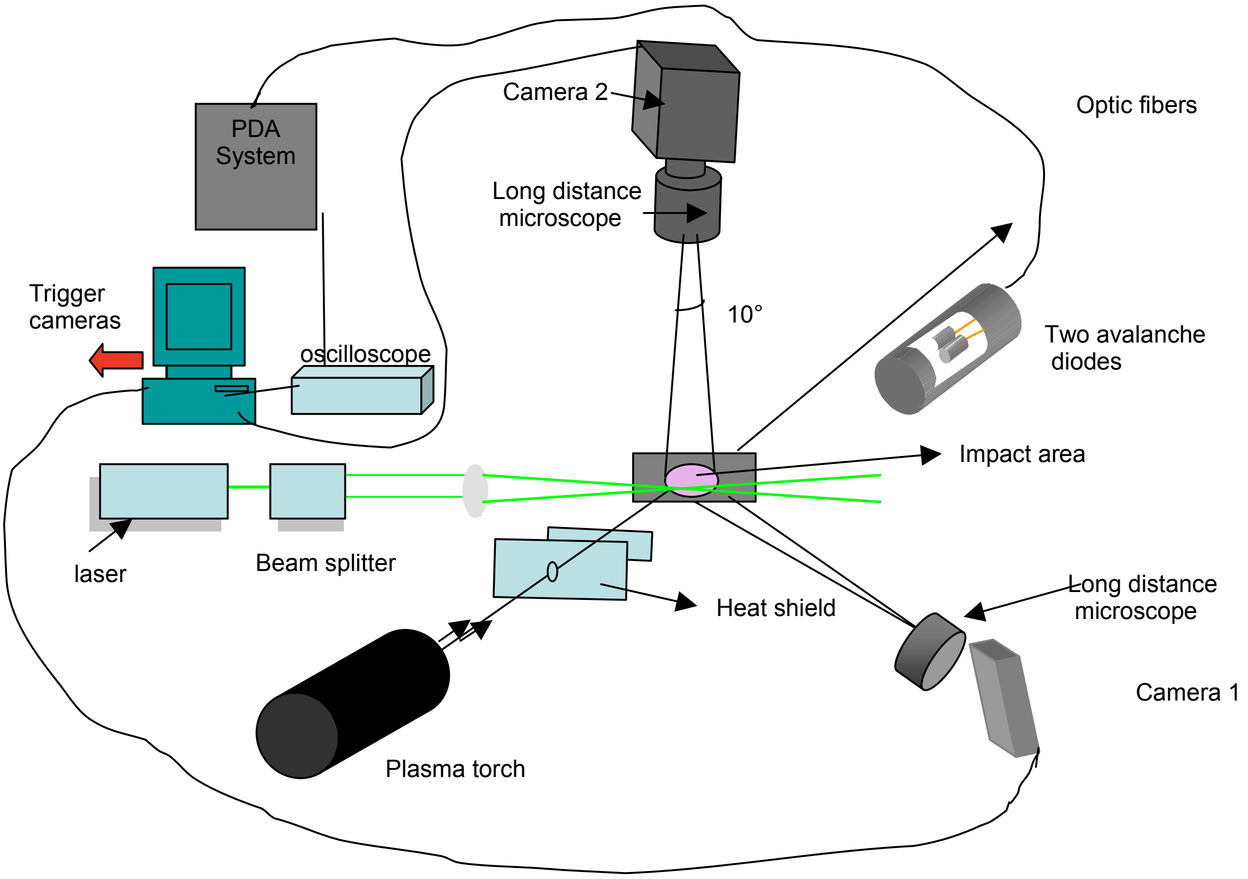

Figure 3: Experimental set-up of the imaging technique

Two imaging systems are used. One is aimed parallel to the substrate axis in order to visualize the impact splashing in the direction orthogonal to the substrate. Having a camera parallel to the substrate axis allows to visualize impacts on inclined substrates. The second camera is aimed orthogonal to the substrate in order to follow the flattening splashing occurring generally when the flattening process is almost completed ,i.e., in the µs time range. A long distance microscope is necessary for two reasons : the object to visualize is in the tens µm size range and the environment close to it is very harsh with hot gases (2000-3000 K) and dusts. Each imaging system is positioned at a distance of 55 cm from the impact point.The images given by the cameras on a computer screen are 1.5 mm in width and 2 mm in length. Cameras triggering are generated by external TTL (5 V) signals at the impact moment.The latters are produced by a Labwiew program wich creates TTL pulses (with a choice of different delays) from the velocity signal obtained by the PDA system. This procedure allows to be sure that the images come from the same particle wich velocity has been calculated. A cooling system, consisting in injecting compressed air in a thin slot (300µm width for 5 cm length) is positioned in the visual field of view of the microscope in order to take hot gases away from the lens and have a clear image.

Results and discussion :

Previous studies realized by C.Escure at the SPCTS laboratory [8] showed that it was possible to visualize droplets impacting a substrate with an imaging technique and a laser lighting. In the present set up, the synchronisation system has been improved and the substrate is fixed on a mobile support in order to avoid the splats overlapping and keep a smooth substrate at each impact. The laser lighting is mandatory because in spite of its high temperature (> 3000 K) the particle is very small (a few tens µm) and the long distance microscope reduces significantly (more than 90%) the transmitted light. The camera is positioned in order to give a side view of the phenomena. For these studies the substrate used is made of stainless steel AISI 304 L.
-Present results

a) Impact splashing

In this study, substrate surface is brought up to a temperature superior to the transition temperature in order to avoid the flattening splashing, i.e., disk shaped splats are observed on the substrate at the end of the experiments. In these conditions, splashing is exclusively due to the impact phenomena.

Thanks to the PDA system, the Sommerfield parameter value can be calculated and associted to the impact's photography. It appears from this study that alumina behaves according to the Sommerfeld rules : deposition for low Sommerfeld parameter (K) values and splashing for high values (figure 4). With ethanol droplets, Mundo and al [9] found that the transition between deposition and splashing occured at K = 57.7. In our experimental conditions, the precision on the K value is about 20% wich allow to say that results obtained with alumina particles at impact follow the same trend as that of ethanol droplets

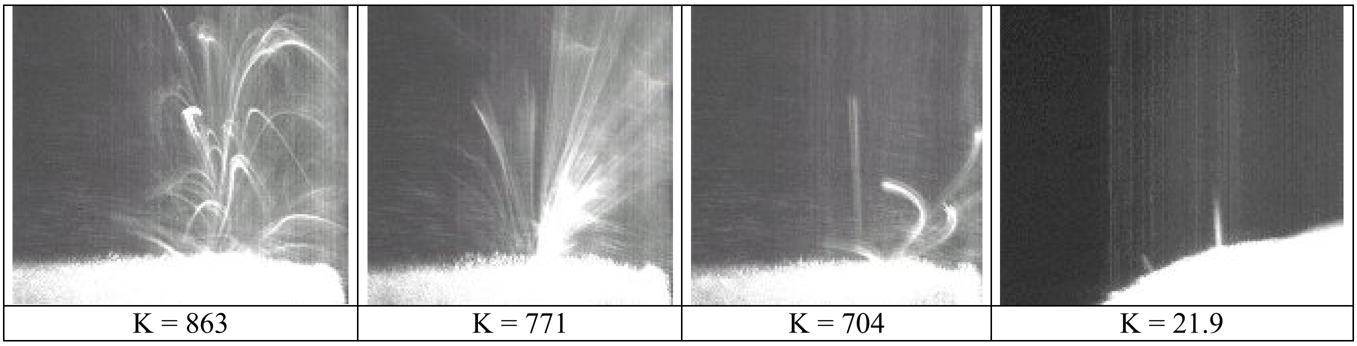

K = 863	K = 771	K = 704	K = 21.9

Fig 5 : *examples of splashing and deposit mode*

This first study attests that impact splashing phenomenon is closely linked to the Sommerfield value and not to the substrate temperature contrary to the flattening splashing. In our spraying conditions, using a dc plasma torch and an alumina powder, high values of Sommerfield parameters are expected (60<K<1800) and at impact, splashing is more the rule than the exception. In that case, droplets reach distances from the substrate superior to 3 mm, i.e., out of the boundary layer. It may be hoped that most of them will thus be entrained by the plasma plume flow.

These results allow to differentiate two folds of splashing: impact one and flattening one.

b) Flattening splashing

The second camera, aimed orthogonal to the substrate will give information on the flattening characteristics wich depend on several parameters: droplet's parameters at impact and substrate properties.Exept for the work of Moreau et al [9] related to plasma sprayed molybdenum particles impacting on glass plates and wich diameter evolution was followed by laser shadography, all the other experiments in the field have been made on millimeter sized droplets [4]. In this second part of our study, our goal is to link images on the one hand to droplet's velocity, temperature and size and in the other hand to substrate temperature. The problem lies at the fact that it's difficult to synchronise the two cameras with the PDA system. At the moment, work is in progress.

Conclusion

A new experimental investigation of the splashing processes at impact is studied using an imaging technique composed by two rapid CCD cameras and two long distance microscopes. The experimental set-up of C.Escure et al [8] has been modified in order to improve the synchronisation system for the study of impact splashing. Substrates are fixed on a mobile support in order to avoid overlapping of splats and keep a smooth impact surface. Results concerning impact splashing confirm those of Escure ones and present the same tendency as that of millimeter sized ethanol droplets. Many questions concerning the second fold of splashing, i.e. the flattening behaviour have still no answers. In order to work on the flattening splashing wich depends on the substrate temperature and the particle parameters at impact, a new imaging system composed by a camera allowing the flattening visualisation has been settled. At the moment, works related to the numerous adjustments for the camera synchronisation are in progress.

References :

[1] P.Fauchais, A.Vardelle and B.Dussouds, Quo Vadis Thermal Spray, J. Of Thermal Spray Technology, 2001,vol 10(1)pp 44-66.

[2] A.Vardelle, C.Moreau and P.Fauchais, The Dynamics of Deposit Formation in Thermal-Spray Processes, MRS Bulletin, July 2000, Volume 25, N°7 pp 32-37.

[3] P.Fauchais, M. Fukumoto, A.Vardelle, M.Vardelle, Knowledge concerning splat formation, J. Of Thermal Spray Technology, 2003.

[4] M. Fukumoto, E. Nishioka and T. Nishiyama, Effect of surface morphology of substrate on flattening behaviour of freely fallen metal droplet, in Proc. Of Int.Thermal Spray, Conf Essen 2002, (ed.) E. Lugsheider (pub.) DVS Düsseldorf, Germany, 2002, pp 37-41.

[5] L. Bianchi, A.C. Leger , M. Vardelle, A. Vaedelle and P.Fauchais, Microstructural investigation of plasma sprayed ceramic splats, Thin solid films 305 (1997) 35-47.

[6] M. Fukumoto and Y.Huang, J.of Thermal Spray Technology, 1999, vol 120-121, pp 124-130.

[7] N. Shakakibara, H. Tsukuda and A. Notomi, The splat morphology of plasma sprayed particles and the relation to coating properties, in Thermal Spray: Surface Engineering via Applied Research (ed.) C.C. Berndt (Pub.) ASM, Int. Materials Park OH, USA, 2000, pp 753-758.

[8]C.Escure, M.Vardelle and P.Fauchais, Experimental and Theoretical study of the impact of alumina droplet on cold and hot substrates, Plasma Chem. Plasma Process., 2003, vol 23(2).

[9] C. Moundo, M. Sommerfeld and C.Tropea, Frpolet-wall collisions: experimental studies of the deformation and break-up process, Int. J. Multiphase Flow, 1995, vol 21, pp 151-173.

SYNTHESIS OF CATHODE MATERIALS FOR SOLID OXIDE FUEL CELLS IN AN INDUCTIVE RF NON- EQUILIBRIUM PLASMA.

M. NIKRAVECH[1], F. ROUSSEAU[1], D. MORVAN[1], J. AMOUROUX[1].

[1]*Laboratoire de Génie des Procédés Plasmas et Traitements de surfaces*
ENSCP, 11 rue Pierre et Marie Curie, 75231 Paris Cedex 05.

Abstract

Lanthanum manganite perovskites doped with strontium are known as promising SOFC cathode materials. A non-equilibrium plasma reactor equipped with convergent nozzle permitted to achieve synthesis and deposit of $La_{1-x}Sr_xMnO_{3+\delta}$ in one step. Fine droplets of nitrate solutions used as the starting materials are injected in the reactor by the means of an ultrasonic sprayer. Characterization of the deposits was performed by XRD, SEM, TEM and IR techniques.

1.Introduction

The fuel cells have known for a few years a renewed interest on behalf of the research laboratories and industrialists. Their qualities (strong energetic efficiency, respect of the environment) seem to be able to bring answers to the two following problems : the emission of polluting gases and the evolution of the energy resources.

Solid Oxide Fuel Cells permit the transformation of chemical energy into electrical and thermal energy, without emission of pollutants like NOx, and with a very important efficiency. The materials of this cell are usually elaborated by screen printing, Spray-drying, Freeze-drying, sol-gel techniques…and so on [1]. Those techniques often lead to a formation of pollutants and undesired phases, which reduce the performances of the cell. Moreover, conventional techniques require several processing steps that take time and high investment.

Development of SOFC depends on manufacturing costs of its components, but also depends on their quality. In particular the cathode, which allows the reduction of oxygen for the cell, has to be synthesised in a medium meeting the following conditions:

- high purity, absence of undesired phases like $La(OH)_3$, MnO, strong adherence of the deposit on the substrate.

In order to fill these requirements, a low-pressure RF plasma wave shock reactor, which is able to synthesise $LaMnO_3$ used as cathode material, has been developed in the laboratory [2]. This perovskite is elaborated from nitrate precursors ($Mn(NO_3)_2$ and $La(NO_3)_3$) and deposited on a substrate of quartz or YSZ (Y_2O_3-ZrO_2). However, it is necessary to investigate the role of influent parameters in order to enhance the quality of deposits. It is known that doping the $LaMnO_3$ by strontium improves the performances of cathodes [3]. So strontium nitrate ($Sr(NO_3)_2$) was added to nitrate precursors, in the plasma process, in order to elaborate thin layers of lanthanum manganite doped with Strontium. Reactional parameters of the nitrate transformation into perovskite have been studied. IR spectroscopy, XRD, SEM, TEM and Impedance measurements permitted the physicochemical characterisation of the deposits.

2.Experimental

Principles of this process :

The starting solution is realised according to the composition of the perovskite that one wants to obtain. Precursors nitrated are obtained with ICP grade solutions (Aldrich Company) of $Mn(NO_3)_2$, $La(NO_3)_3$ and $Sr(NO_3)_2$ dissolved in water (1-2 wt. % HNO_3) with concentration of 10000 µg / ml. The starting solution is placed in a nebullizer at the entry of the reactor. The ultrasonic sprayer produces fine droplets which contain nitrated precursors. A carrier gas is added in order to allow the transport of the precursors toward the reactor. The carrier gas causes a difference in pressure on both sides of the pulsed valve (around 500 mbar). When the valve opens, the pressure difference projects droplets through the plasma on the surface of the substrate.

Oxygen and argon are used as plasma gas. During our experiences, the total maximum output plasma gas didn't exceed 100 cc / min in order to have 1 mbar pressure in the reactor. When the nitrated precursors pass in the nozzle, they are subjected to a strong local electronic density and a frequency of electronic collisions significant responsible for their transformation into perovskite.

Experimental set up :
Plasma reactor consists in a glass tube (external diameter 50 mm and length 650 mm) (figure 1). The tube is provided with a convergent nozzle, that focuses the aerosol on the substrate. A vacuum pump makes it possible to lower the pressure in the reactor until approximately 1 mbar. The pressure is controlled by a MKSA gauge of pressure. A dust filter equips the pump in order to avoid the penetration of dust.

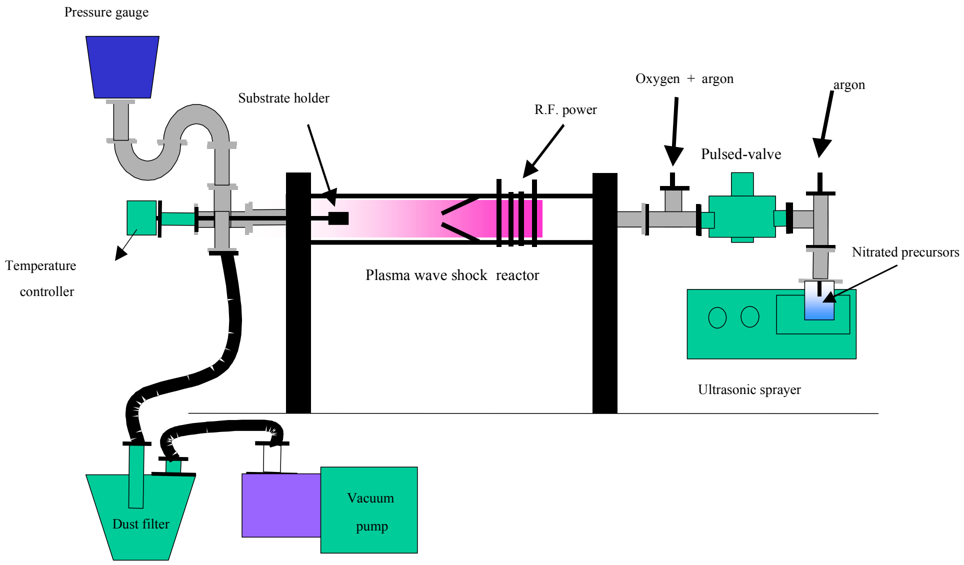

Figure 1 : Experimental Set up

A high frequency power supplier (6 KW, 40 MHz) permits to produce the plasma by the intermediary of an inductive coil surrounding the glass tube. The voltage is adjustable between 2 and 3,6 kV. The current varies between 0,4 and 1 A.
The aerosol, which is injected in the plasma, is produced by an ultrasonic sprayer. A flow of argon carries the aerosol in the reactor by the intermediary of pulsed valve (injection during 0,25 seconds every 10 seconds). The substrate holder, on which the layer of perovskite is deposited, can be heated by an internal resistance. A thermocouple type K permitted to measure the evolution of temperature of the substrate.
A gas distributor equipped with mass flow-meters allows the control of plasma gas (O_2 and Ar) and carrier gas (Ar).

The analysis techniques :
The SEM (Scanning Electron Microscopy) (S440 LEICA apparatus) and the TEM (Transmission Electron Microscope) were used to observe the surface of the deposits. X Ray Diffraction was used to control the purity and the cristallinity of the layers. Infrared spectroscopy (BRUKER IFS 48) permitted to perform a method to quantify the conversion rate of nitrate precursors into perovskite. On-line mass spectroscopy (PFEIFFER Prisma) permitted to identify the gaseous by-products of the reaction. Impedance measurements carried out with a Solartron Frequency Analyser 1250 permitted the electrical characterisation of the deposits.

3.Characteristics of plasma Ar-O_2

Our results show that the reactive species produced in Ar-O_2- H_2O plasma permit to transform the nitrate precursors into perovskites.. In a previous study, spectroscopy emission analysis made it possible to highlight the presence of Ar* and $O^{\bullet}$ [2]. Argon facilitates the production of plasma, involving the dissociation of molecular oxygen by electronic collisions and energy transfer between molecules

(Penning effect). The atomic oxygen resulting from the dissociation of O_2 in the plasma is one of the reactive and oxidant species which allows the nitrates elimination and the formation of perovskite.
The decomposition of water in the plasma leads to the apparition of OH radicals, which are oxidant species too [4]. In a previous article [5], Optical Emission Spectroscopy investigations were made to detect the formation of OH radicals and estimate the rotational temperature produced during the dissociation of water in the argon plasma. This study shows that the light intensity of OH° at 309,11 nm increases during the injection of nitrated precursors corresponding to the evaporation and dissociation of water. The reactivity of OH° with the those of oxygen radicals granting high oxidant properties to plasma. The effect of oxidant properties of O° and OH° on the conversion rate are demonstrated in this paper.

4.Results and discussion

Aspect and composition of the deposits :

The observation of a sample of $La_{0.7}Sr_{0.3}MnO_3$ (annealed during 2 h) by SEM shows that the layer has a compact and homogeneous aspect. A more significant enlarging (fig 2) highlights the presence of a significant porosity. This porosity is due to the agglomeration of particles which have a diameter ranging between 0.1 and 1 µm. The size of the particles obtained by MEB was confirmed by TEM micrograph (fig 3). Moreover, the figure 2 shows that the particles which form the layer are well welded between them. The particles, resulting from the transformation of nitrated solution, coagulate in plasma and stick the ones to the others when they arrive on the substrate. Thus, this phenomena involves the formation of a layer with strong adherence on YSZ surface.

Fig 2

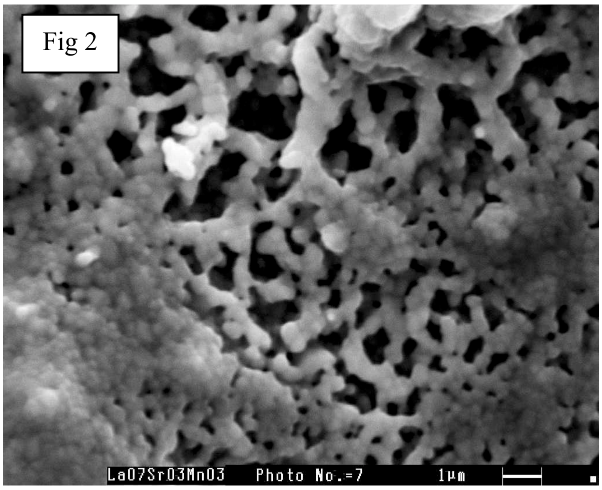

Fig 3

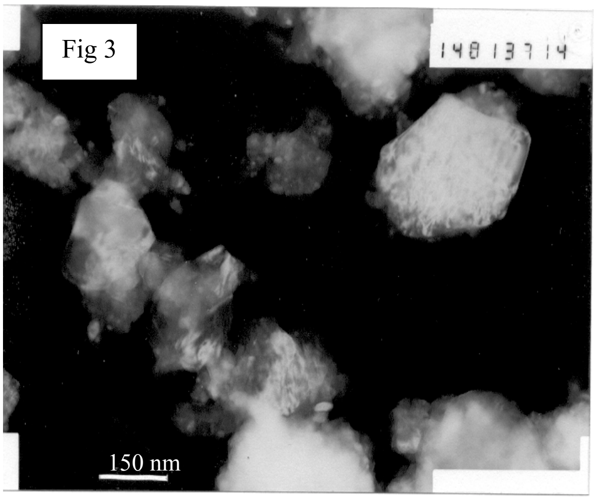

Figure 2 : Micrograph of $La_{0.7}Sr_{0.3}MnO_3$ deposited in following conditions : Power = 2340 W, Ar / O_2 = 50 / 50 cc. min^{-1}, carrier gas pressure = 500 mbars. The deposit was annealed at 1473 K during 2 h.

Figure 3 : TEM's Photograph of $La_{0.7}Sr_{0.3}MnO_3$ deposited in following conditions : Power = 2340 W, Ar / O_2 = 50 / 50 cc. min^{-1}, carrier gas pressure = 500 mbars. The deposit was annealed at 1023 K during 2 h.

XRD analysis of $La_{0.7}Sr_{0.3}MnO_3$ permitted to know that the deposits without annealing are amorphous Perovskite annealed at 750°C during 1 h in air present a crystalline structure. The peaks corresponded to a single phase perovskite structure in agreement with the synthetic spectrum of $La_{0.7}Sr_{0.3}MnO_3$.In the two cases, no phases like $La(OH)_3$, MnO, $La_2Zr_2O_7$ or $SrZrO_3$, being able to be formed during the synthesis and the annealing, were detected (detection limit : 2 %). So, the layer obtained does not contained undesirable phases. It is important to notice that the annealing involves changes of properties in the deposit. Changes of structure during the annealing leads to a better cohesion of the particles and to a better adherence on YSZ. Moreover, samples annealed present magnetic properties, non-detectable in amorphous $La_{0.7}Sr_{0.3}MnO_3$.

Electrical characteristics of the deposits

The conductivity of the deposits measured under different experimental conditions is plotted versus temperature in figure 4. In all cases, the conductivity increases from around 15 S.cm-1 at 400 °C to more than 275 S.cm-1 at 750 °C. At 3,6 kW plasma power, the conductivity of the deposit processed with a plasma gas containing 50% of oxygen is higher than that of the deposit processed with 25% oxygen. These results confirm that both high power and high concentration of oxygen in the plasma gas improves the conductivity of the layer. These results show that the plasma parameters influence directly the reactions of transformation of nitrate precursors into perovskite. A comparison with the conductivity of powders achieved by a thermal method [6] shows that the conductivity of plasma deposits is more sensitive to temperature and is higher beyond 700 °C . The results presented on figure 5 show that the electrical resistance of $LaMnO_3$ is higher than that of $La_{0.7}Sr_{0.3}MnO_3$. As expected these results confirm that doping with strontium increases the conductivity of deposits.

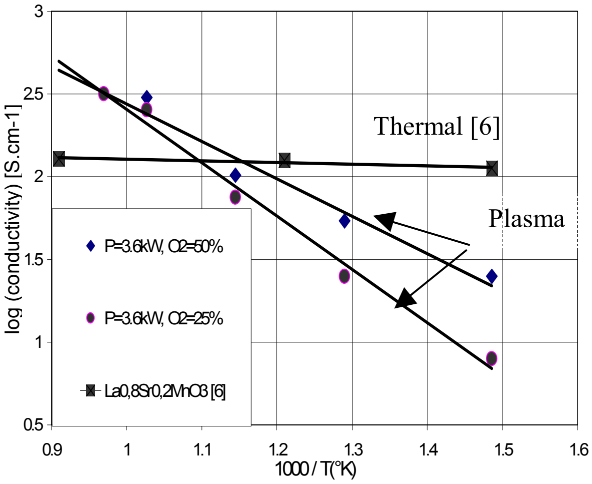

Figure 4 : Arrhenius plots of conductivity for $La_{0.7}Sr_{0.3}MnO_3$ deposited at oxygen rate 25% and 50% in plasma gas, plasma power = 3.6 kW. Comparison with the conductivity of $La_{0.8}Sr_{0.2}MnO_3$ achieved by liquid mixture method [6].

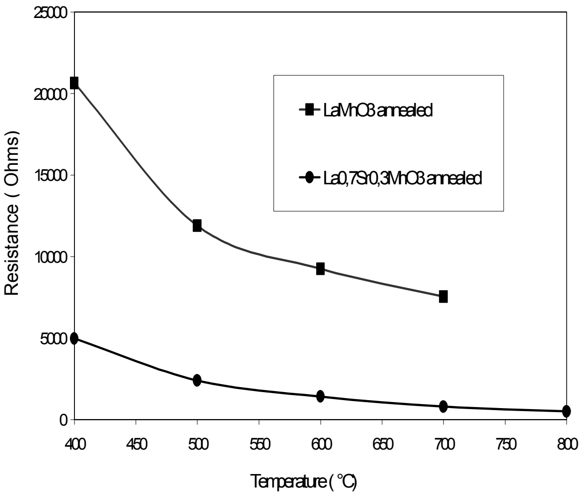

Figure 5. The electrical resistance measured in air versus temperature for deposits of $LaMnO_3$ and $La_{0.7}Sr_{0.3}MnO_3$.

<u>Influence of plasma parameters on the conversion rate of nitrate precursors into perovskite :</u>

Both high power and high oxygen yield in plasma involve a significant apparition of atomic oxygen. This species is well known to have oxidant properties, which allow the transformation of the nitrate precursors into perovskite oxide.

The figure 6 shows an IR spectrum of $La_{0.6}Sr_{0.45}MnO_3$, without annealing. We can note the presence of two intense bands at 420 and 600 cm-1, which can be attributed at the La-O and Mn-O vibrations. Two other bands were distinguished, at 1370 and 1480 cm-1, attributed to NO_3^-. The presence of nitrates in the deposit shows that all the precursors are not transformed into perovskite in the plasma.

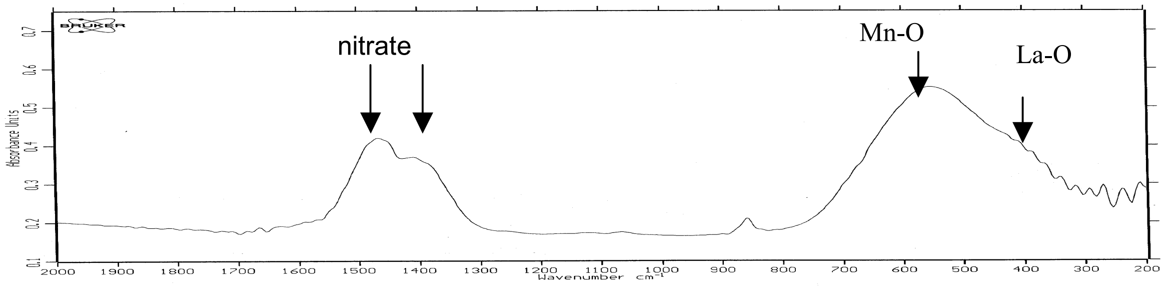

Figure 6 : IR spectrum of $La_{0.6}Sr_{0.45}MnO_3$ (plasma without oxygen)

In order to quantify the effect of plasma parameters (plasma generator power, O_2 quantity in plasma-producing gas) on the conversion rate, an analyse technique based on IR spectroscopy was performed. By making mixtures of La, Mn, Sr nitrates and commercial $La_{0.7}Sr_{0.3}MnO_3$ in various proportions, and by using the intensity of the bands at 1370 and 600 cm-1, we obtained a calibration curve. By this technique, we could determine the conversion rate of the nitrated precursors into perovskite as a function of experimental parameters.

The curve on figure 8 shows the evolution of the conversion rate versus plasma generator power. The conversion rate increases with the power (nearly 50 % to 71 %). Indeed, the high power involves a significant apparition of activated species (for example O radicals and OH°), which could oxidize more significant quantity of nitrated precursors into perovskite. The curve on figure 9 shows that the oxygen yield in plasma is an important parameter too. The conversion rate increases from 59 % to 77% for oxygen quantity ranging between 25 and 75 %. For more than 75 % O_2, the conversion rate remains constant at 77 %.

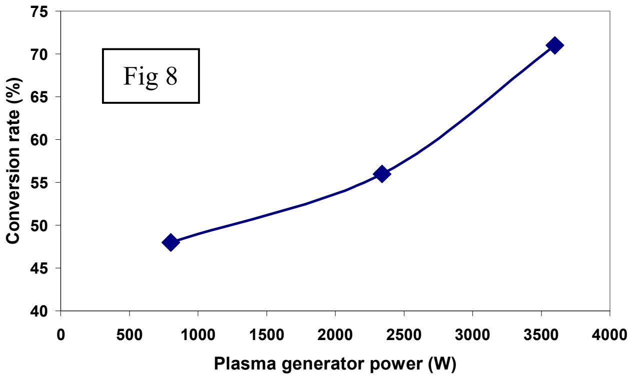

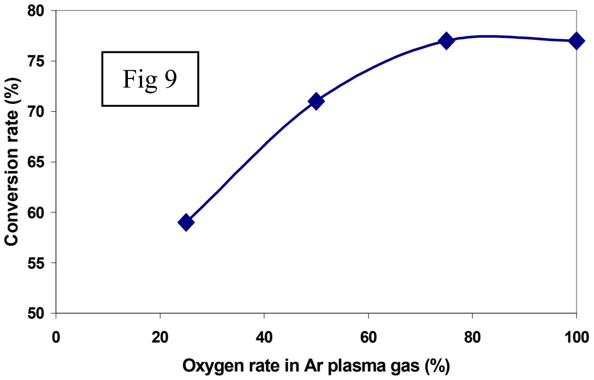

Figure 8 : Evolution of the conversion rate versus plasma generator power (Ar/O_2 = 50%/50%)
Figure 9 : Conversion rate versus oxygen rate in Ar plasma gas (Power = 3600 W).

The role played by water in oxidisation of the nitrate precursors into perovskite was studied. We evaporated 10 µl of the starting solution (stoichiometrie $La_{0.7}Sr_{0.3}MnO_3$) under a pressure of 0.7 mbar. Thus, the solid obtained was installed on the substrate holder in order to be treated by two types of plasma :

1) plasma with O_2 / Ar (50 cc.min-1 / 50 cc.min-1), generator power = 1200 W
2) plasma with O_2 / Ar (50 cc.min-1 / 50 cc.min-1), generator power = 1200 W, injection of water droplets during 0.25 s every 10 s.

Several samples treated in these conditions permitted to obtaine the two following curves (figure 10).

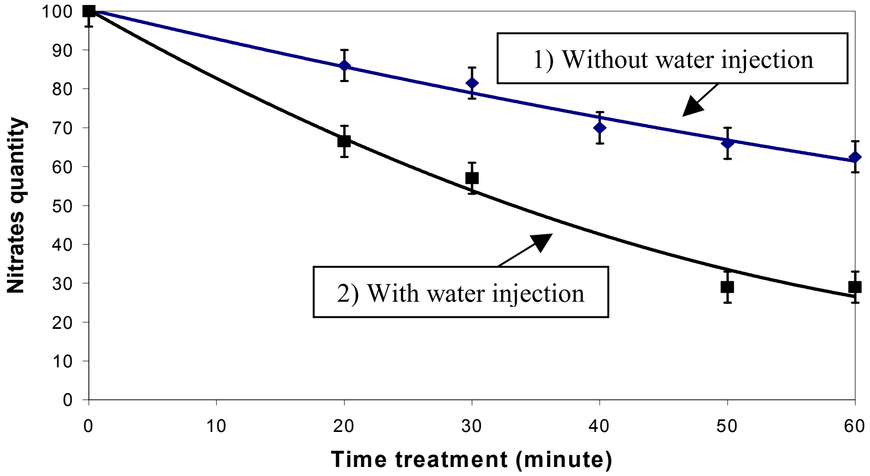

Figure 10 : Evolution of nitrates quantity as a function of time treatment.

These results show that the nitrate quantity decreases with the time of treatment. The curves clearly indicate that the introduction of water into the plasma enhances the nitrates transformation into perovskite. In this process, the water of the starting solution plays a significant role in the oxidisation phenomena, due to the apparition of OH° radicals resulting from the water decomposition in the plasma.

As the thermal decomposition of metallic nitrates requires temperatures higher than 600K these results confirm the role of reactive species in cold plasma. Elastic electron-molecule collisions cause an increase in the kinetic energy of the molecules. The transfer of energy in inelastic collisions leads to dissociation and ionisation of molecules and formation of plasma species such as free radicals, excited metastables and ions. In low pressure plasmas containing Ar, O_2 and H_2O numerous reactions lead to the formation of OH, O radials and ionic species. The following reactions are among the most important. As it was noted above, the production of these species leads to control the reactivity of plasma and thus the quality of the deposits.

$e + O_2 \rightarrow O + O^-$ $(E = 4{,}4\ eV)$ $k= 0{,}774\ 10^{-11}\ cm^3/s$ (1)
$e + O_2 \rightarrow e + O + O^*$ $(E = 8{,}4\ eV)$ $k= 0{,}182\ 10^{-12}\ cm^3/s$ (2)
$e + O_2 \rightarrow e + O_2\ {}^1\Delta_g$ $(E = 0{,}98\ eV)$ $k = 0{,}341\ 10^{-9}\ cm^3/s$ (3)
$e + Ar \rightarrow e + Ar^*({}^3P_{2,1})$ (4)
$Ar^*({}^3P_{2,1}) + H_2O \rightarrow OH^*\ A({}^2\Sigma^+) + Ar + H$ (5)

In order to understand the reaction mechanisms, the on-line mass spectroscopy was used, that permitted to confirm the formation of NO and NO_2 during the conversion of nitrate precursors into perovskite. This study is actually under focus, the results will be published later.

5. Conclusion :

The deposits obtained with this plasma process seem to be used as SOFC cathode. Indeed, the layers deposited don't contain undesirable phase or pollutants. Moreover, a strong adherence is noted on YSZ and a high porosity, which can enhance gas exchanges. We underline the fact that the plasma parameters have important effect on the conversion rate of the precursors. A high plasma generator power associated with an important O_2 yield in the plasma, permits to obtain a very strong oxidisation and a high conversion rate of the nitrate precursors into perovskite. It was proved that the water plays a very significant role in the oxidisation phenomena by the production of OH°. In a next study, an analyse of the activated species will be proceeded in the plasma by the emission spectroscopy and mass spectroscopy. Thus, a numerical model, which is under development, will be compared with LDA (Laser Doppler Anemometry).

References :

[1] R. J. Bell, G. J. Millar, J. Drennan, Solid State Ionics, 131 (2000), pp 211-220.
[2] S. F. Miralaï, Développement d'un nouveau réacteur plasma basse pression, à tuyère convergente, pour le dépôt de couches minces d'oxydes perovskite. Application aux piles à électrolyte solide, Thèse à l'Université Pierre et Marie Curie, Paris, 1995.
[3] H. Ullmann, N. Trofimenko, F. Tietz, D. Stöver, A. Ahmad-Khanlou, Solid State Ionics, 138 (2000), pp 79-90.
[4] F. Collier, Réactivité dans les plasmas, école d'été d'Aussois, Ed. de Physique, 1983, pp 173-241.
[5] M. Nikravech, N. Baudouin, D. Morvan, J. Amouroux, 15th International Symposium on Plasma Chemistry, Symposium proceedings, Volume V, 2nd July session Thursday 12, 2001, Eds A. Bouchoule, J. M. Pouvesle, A. L. Thomann, J. M. Bauchire and E. Robert, GREMI, CNRS / University of Orléans, pp 1971-1976.
[6] J.H. Kuo. Journal of solid state chemistry 87, pp 55-63 (1990).

STUDY OF THE REACTIVE SPECIES IN NON EQUILIBRIUM PLASMA PROCESS USED FOR THE SYNTHESIS OF $La_{1-x}Sr_xMnO_{3\pm\delta}$. APPLICATION TO SOFC CATHODE.

Mehrdad Nikravech, Frederic Rousseau, Daniel Morvan and Jacques Amouroux

Laboratoire de Génie des Procédés Plasmas et Traitement de Surfaces, University of Pierre and Marie Curie, Ecole Nationale Supérieure de Chimie de Paris, 11 rue Pierre et Marie Curie 75005 Paris, France.
Mehrdad-nikravech@enscp.jussieu.fr

Deposits of $La_{1-x}Sr_xMnO_{3+\delta}$ are obtained by the means of a non equilibrium RF plasma reactor equipped with a convergent nozzle. Reactive species produced by plasma together with the action of the wave shocks produced by the nozzle lead to the decomposition of nitrate precursors into perovskite and to deposit on the electrolyte yttria-stabilized zirconia substrate.

Recently we demonstrated that the power induced and the oxygen concentration in the plasma improve the oxidation mechanisms. It is well known that metastable oxygen $^1\Delta_gO_2$ and charged oxygen O^- and radicals OH are the major reactive species in the plasma. These species are considered to be responsible of the oxidation process. In previous work the rotational, temperature of radicals OH was determined by optical emission spectroscopy. In this contribution the results concerning electronic temperature and vibrational temperature measured by emission spectroscopy will be presented. This study will be completed by measuring the evolution of the particles seize and velocity by means of Laser Dopler Anemomtry and Granulomtery. A mathematical model is under development.

OPTICAL SPECTROSCOPIC DIAGNOSTIC OF AN Ar+H_2 RF THERMAL PLASMA USED TO THE SILICON POWDER PURIFICATION. EFFECT OF THE EVAPORATION PHENOMENA

M.Benmansour [1], M.Nikravech[1], S.Darwiche[1], D.Morvan[1], J.Amouroux[1], J.Chapelle[2]

1. *LGPPTS - ENSCP, 11, rue Pierre et Marie Curie, 75005 Paris (France)*
2. *GREMI, Université d'Orléans, 14 rue d'Issoudun, B.P 6744, 45067 ORLEANS, (France)*

Abstract

The Ar+H_2 RF thermal plasma spraying is used to melt, purify and hydrogenate metallurgical silicon particles in order to elaborate a thin layer for photovoltaïcs applications. Hydrogenation and purification phenomena have been analysed by a spectroscopic diagnostic. Transitions of excited argon, hydrogen and silicon detected have been used to calculate the electronic density, electronic temperature and silicon vapour content in the plasma flow.

1. Introduction

Several works have proved the improve of the photovoltaïc properties of the silicon layers after their hydrogenation[1-2]. In our case, the hydrogenation of silicon is made by an Ar/H_2 thermal plasma. This technique has the advantage to avoid the post hydrogenation of the silicon layers. Indeed, silicon particles are injected in the plasma and are simultaneously purified and hydrogenated during their residence time in the plasma and finally on a ceramic substrate, under plasma jet[3]. The final concentration of hydrogen in the silicon deposit determined by exodiffusion technique is around 2.10^{15} cm^{-3}. So it's clear that we have interaction between excited hydrogen species of plasma and melted silicon. The aim of this work is therefore to characterise the physical properties of the Ar/H_2/Si in order to understand the interactions between the silicon particles and the reactive species of the plasma. Spectroscopic measurements have been undertaken in order to identify the high excited states of the atomic hydrogen and to obtain the electronic density, the electronic temperature and evaporation ratio of the silicon particles along the plasma jet and particularly in the induction zone.

2. Experimental setup

The spectroscopic measurements have been realised with the experimental setup described in figure -1-. The plasma jet is generated in a plasma torch by a RF generator (4,9 MHz) with a power fixed between 18 kW and 21 kW. The torch is equipped with 8 water cooled copper fingers. This torch permits to inject inside an effective power up to 10 kW in the plasma. A slit of 5 mm width between 2 fingers permit to make optical observations inside the torch. The plasma gas consists of a mixture of three argon flows: the sheath gas Q_3 which serves to protect the wall of the torch, the intermediate gas Q_2 serves to stabilise plasma and is mixed with 1% of H_2, and finally the carrier gas Q_1 which serves to introduce axially the silicon particles in the plasma gas.

The measurements have been realised from the point of injection (Z=0 cm) until Z=9,3 cm. The signal is simultaneously collected with three optical fibres and is transmitted to a CCD spectrometer detector. Three positions have been recorded in order to cover the total distance of the plasma jet in the water cooled torch.

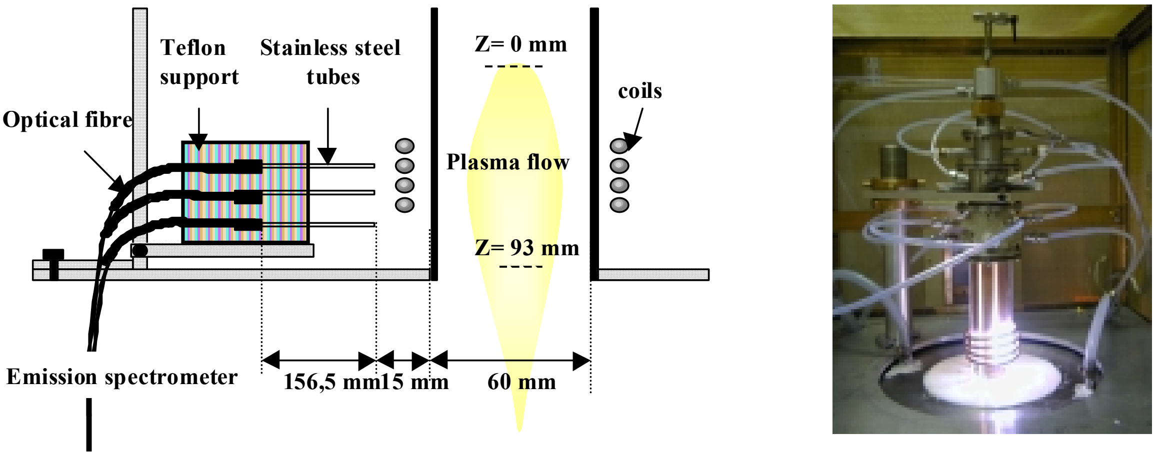

Figure 1 : Experimental setup

Table 1: Experimental plasma conditions

Argon			Hydrogen (% vol)	Powder rate (g.mn^{-1})	Power (kW)
Q_1 (L.min^{-1})	**Q_2 (L.min^{-1})**	**Q_3(L.min^{-1})**			
5	15	25	1%	0,3	18
3 acquisition, 50 msec. Scan^{-1}					

3. Determination of electronic density

Spectroscopic measurements proves the presence of the excited atomic hydrogen species (Balmer lines). The Balmer lines, particularly the H_β transition, have been used to determine the electronic density given by the Griem equation[4] :

$$N_e = C(N_e,T)\ .\ \Delta\lambda_S^{3/2} \quad \text{where} \quad \left| \begin{array}{l} \Delta\lambda_S \ \text{ is the Stark broadening of the atomic line} \\ C(N_e,T) \ \text{ is a coefficient given by Griem} \end{array} \right.$$

We can underline that this method doesn't require the Local Thermodynamic Equilibrium assumption. The Stark broadening of the atomic hydrogen line is due to the electromagnetic field and is equal to the entire broadening of the line. The variation of the electronic density along plasma jet is presented in figure-2-.

The results show in a first time an increase of the electronic density from 1,5.10^{15} cm^{-3} at the exit of the injector (Z=0), reaches to a maximum of 1,1.10^{16} cm^{-3} in the middle of the inductive coils, and in a second time a decrease when we go away the coils. This confirms that the region in the inductive coils is the most reactive zone of the plasma. When silicon particles are injected in the plasma, we observe that an evaporation phenomenon occurs but it doesn't modify the electronic density profile.

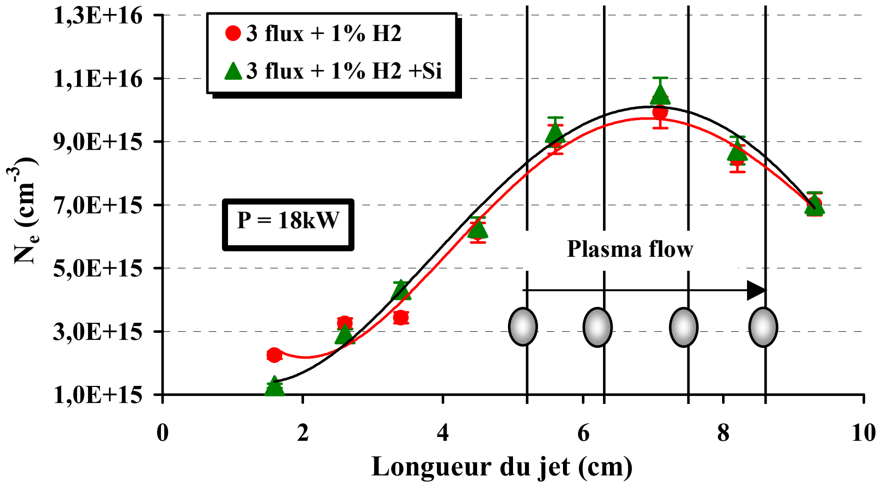

Figure 2 : Variations of N_e along plasma for the hydrogenated argon plasma calculated with hydrogen atomic lines

4. Determination of electronic temperature

Assuming the LTE state, the plasma temperature can be obtained using the equation :

$$\ln\left(\frac{\varepsilon_{mn}}{A_{mn}\,\nu_{mn}\,g_m}\right)=\ln K-\frac{E_m}{k.T_e}$$

where ε_{mn}, ν_{mn} and A_{mn} are respectively the emission coefficient, the frequency and the transition probability of the transition; E_m and g_m are the energy and the statistical weight of the upper state of the transition, respectively; k is the Boltzmann constant, and K is a constant for all the ArI lines. Differents ArI lines have been chosen in order to cover the maximum energy area so as to increase the precision of the method. The slope of the obtained straight lines is inversely proportional to the electronic temperature. A typical Boltzmann plot obtained for the hydrogenated argon plasma is presented on the Figure -3-. We can show that the points are very well aligned and we can therefore means that our plasma is in the LTE.

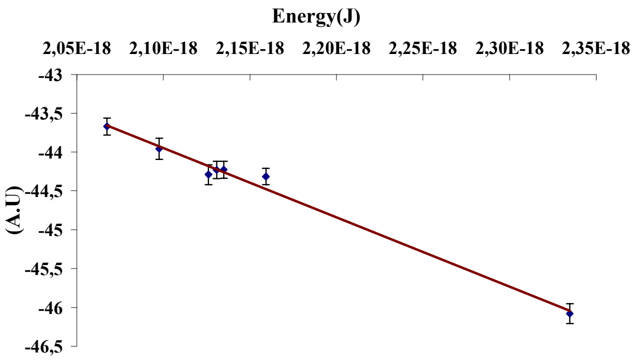

Figure 3 : Typical Boltzmann plot

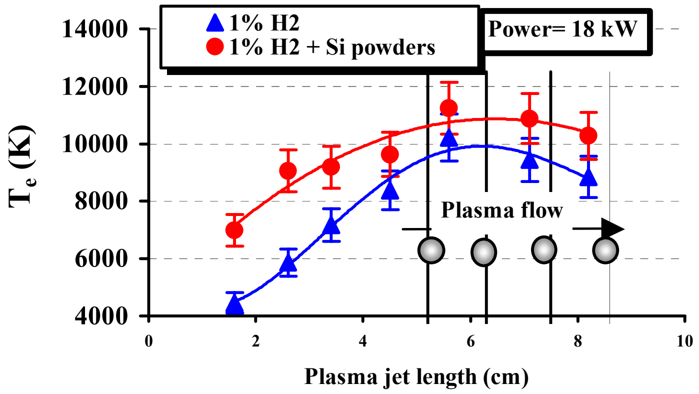

Figure 4 : Electronic temperature variations. Measurements with argon lines

However, the accuracy of this method is quite sensitive to the determination of the line intensity that were sometimes bad resolved, so it's difficult to conclude about temperature values. The results, presented figure-4-, show that the electronic temperature is around 10500 K in the inductive zone.

The second method used for the determination of the T_e is based on the equation[5] :

$$y = \frac{h^4 C}{8\pi C_1 (2\pi m_e k)^{3/2}} . \frac{g_m}{g_I} . A_{mn} . \frac{\lambda}{\Delta\lambda} . \frac{\exp[(E_\infty - E_m)/kT_e]}{T_e \xi(\lambda, T_e)} . \left(1 - \frac{\Delta E_\infty}{kT_e}\right)$$

where *h* is the Planck's constant; *C* is the light velocity; m_e is the electronic weight; g_I is the statistical weight of the fundamental level of ArII ion, E_∞ and ΔE_∞ are the ionisation energy and the lowering of ionisation potential, respectively; and C_I is a constant for all the ArI lines.

This equation gives the value of T_e versus the ratio of a line's intensity at the wavelength λ to the adjacent continuum intensity in a given spectral range $\Delta\lambda$=1nm. This ratio has been determined from the experimental data for different ArI lines. The obtained results are presented in the Figure -5-.

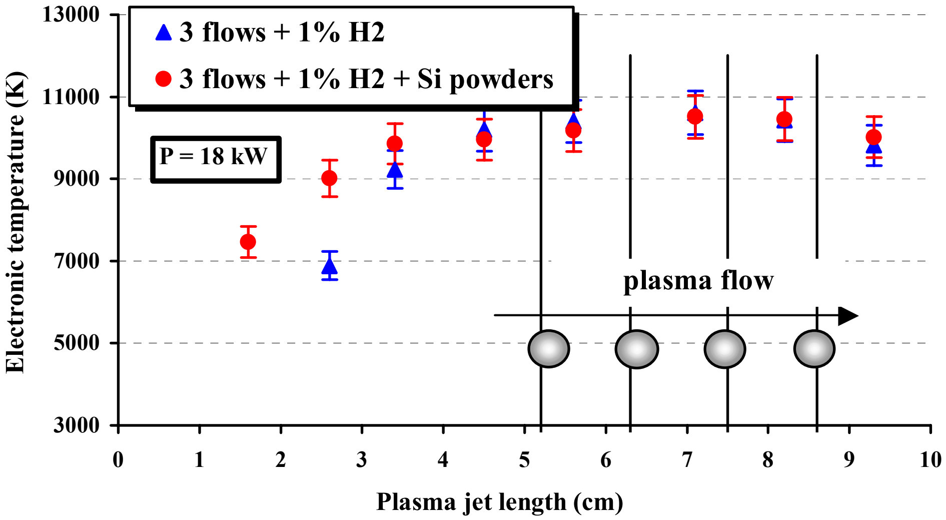

Figure 5 : Electronic temperature variations for hydrogenated argon plasma

The variations show that the electronic temperature increases from 7000K in the exit of the injector to a maximum of 10800K in the inductive zone. At last, the temperature decreases when we go away this zone. This result confirms those previously obtained by the Boltzmann plot method. The addition of the silicon particles in the plasma flow doesn't modify the temperature profiles.

The third and last method consists to obtained the electronic temperature from the expression of the intensities ratio of the excited and ionised silicon lines versus the temperature.

$$y = \frac{I_{ij}}{I_{mn}} = \frac{\nu_{ij}}{\nu_{mn}} \frac{A_{ij}}{A_{mn}} \frac{2g_i^+}{g_m} \frac{1}{N_e} \left(\frac{2\pi m_e kT_e}{h^2}\right)^{3/2} \exp\left(-\frac{E_i^+ - E_m}{kT_e}\right)$$

where ε_{mn}, ν_{mn} and A_{mn} are respectively the emission coefficient, the frequency and the transition probability of the transition; E_m and g_m are the energy and the statistical weight of the upper state of the transition, N_e the electronic density, and E_i energy of the ionised states.

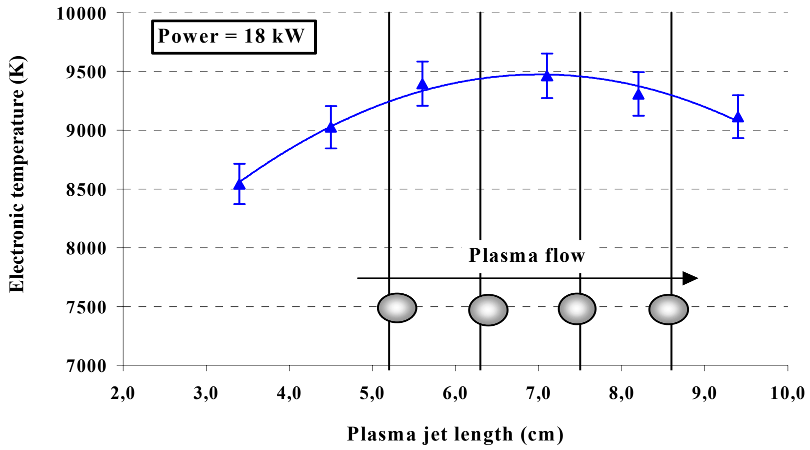

Figure 6 : Electronic temperature variation of the hydrogenated argon plasma with silicon particles

The obtained result, presented in figure-6-, shows that the electronic temperature of the hydrogenated argon plasma with silicon particles have a maximum of 9500K in the middle of the inductive coils. This result, obtained by the Boltzmann plot and by the line-to-continuum ratio method, confirms that the inductive zone is the most reactive zone of the plasma

5. Determination of the evaporation rate

The fraction of the silicon vapour in the plasma can be obtained using excited argon, excited and ionised silicon lines. Expressions of the excited silicon and argon ration, and ionised silicon and excited argon ratio versus temperature and silicon fraction are presented below:

$$y(x,T_e)=\frac{I_{SiI}}{I_{ArI}}=\frac{\lambda_2}{\lambda_1}\,\frac{A_1}{A_2}\,\frac{g_1}{g_2}\,\frac{Z^0_{ArI}(T_e)}{Z^0_{SiI}(T_e)}\,\frac{N^0_{SiI}(T_e,x)}{N^0_{ArI}(T_e,x)}\exp\left(-\frac{hc(\sigma_1-\sigma_2)}{kT_e}\right)$$

$$z(x,T_e)=\frac{I_{SiII}}{I_{ArI}}=\frac{\lambda_2}{\lambda_1}\,\frac{A_1}{A_2}\,\frac{g_1}{g_2}\,\frac{Z^0_{ArI}(T_e)}{Z^+_{SiII}(T_e)}\,\frac{N^+_{SiII}(T_e,x)}{N^0_{ArI}(T_e,x)}\exp\left(-\frac{hc(\sigma_1-\sigma_2)}{kT_e}\right)$$

Where: $N°_{ArI}$, $N°_{SiI}$ are the densities of silicon and argon atoms in the fundamental state, N^+_{SiII} density of the first ionised silicon level, $Z°_{ArI}$, $Z°_{SiI}$ and $Z°_{SiII}$ the partition functions of excited argon and excited and ionised silicon, $x = N_{Si} / N_{Ar}$ the faction of silicon in the argon plasma.

The intersection of the y(x,Te) and z(x,Te) gives the concentration of silicon vapour and temperature of plasma. The results are presented in figure-7-. We can observe that the evaporation phenomena have a maximum in the middle of the coils where the fraction of silicon vapour is around $2{,}5.10^{-4}$. In this zone, the electronic temperature is around 9500K.

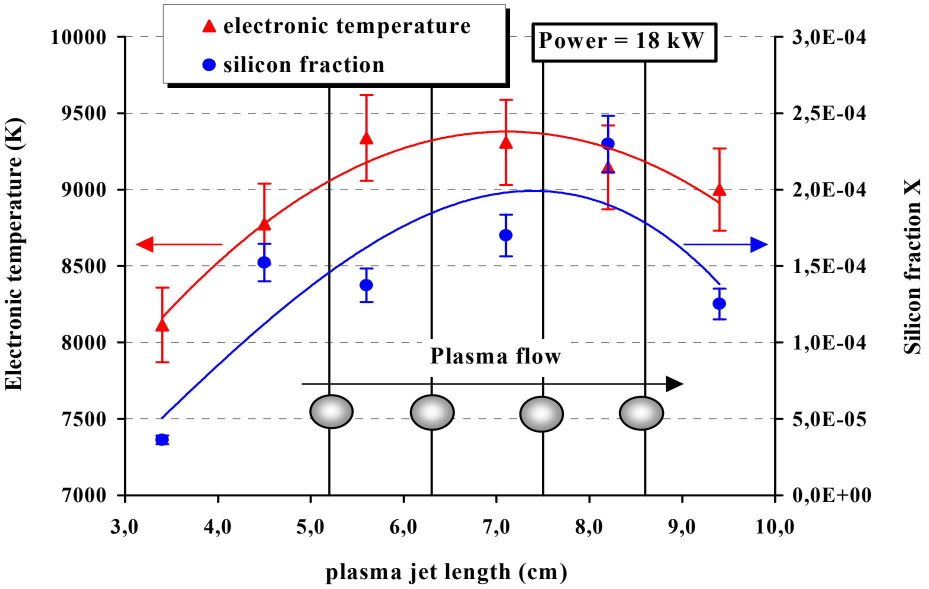

Figure 7 : Variations of the silicon vapour ratio along plasma jet

6. Conclusion

The energetic characterisation of an inductive Ar-H_2 thermal plasma torch has been obtained by Optical Emission Spectroscopy. Different emission lines have been detected : high excited states of atomic hydrogen (n=7 of Balmer serie), excited argon, excited and ionised silicon when particles are injected in the plasma flow. These lines permit to calculate electronic density and temperature. Results show that the maximum of electronic temperature of the hydrogenated plasma, determined by three different methods, is around 10500 K in the inductive zone for an electronic density $N_e=10^{16}$ $e^{-}.cm^{-3}$. The introduction of the silicon powder doesn't modify the electronic density and temperature profiles. In this zone, the evaporation phenomena is maximum and the fraction of the silicon vapour is around $2,5.10^{-4}$ in the middle of the inductive coils. All these results are in good agreements with numerical model and the measurements by LDG described in another papers[6]

References

[1] B.Pajot, B.Clerjaud, J.Chevallier
Bulletin de la SFP (131) Octobre 2001, 26-31
[2] J.Chevallier, B.Pajot
Solid State Phenomena, Vols 85-86 (2002), pp 203-284
[3] M. Benmansour, E. Francke, D. Morvan, J. Amouroux, D.Ballutaud
Thin solid film, Vol 403-404, pp 112-115, 2001
[4] Hans R. Griem (Mc Graw-Hill Book Company)
[5] F.Bourg, D.Morvan, J.Amouroux, S.Pellerin, J.Chapelle
Solar Energy Materials and Solar Cells, Vol 72/1-4, 2001, pp361-371
[6] M.Benmansour, S.Darwich, E.Francke, D.Morvan, J.Amouroux, S.Dresvin
To be published in Proceedings of ISPC 16, Taormina, Italy, June 2003

Evolution of chemical process of carbon plasma created by an excimer laser in nitrogen ambience

S. Abdelli-Messaci, T. Kerdja, S. M-Aberkane, A. Bendib[1], S. Lafane, K.Yahiaoui and S. Malek

Laboratoire d'Interaction Laser-Matière, Centre de Développement des Technologies Avancées
Alger, Algérie
[1] Laboratoire d'Electronique Quantique, Faculté de Physique,USTHB, Alger, Algérie

In order to understand the CN molecule formation and to obtain a well quality and properties of deposited carbon nitride thin films, a spatio-temporal evolution study of carbon plasma surrounded by nitrogen atmosphere is investigated. In this work, we present the experimental result obtained from spectroscopic emission diagnostic of carbon plasma created by an excimer laser KrF (248nm, 25 ns) at three different laser fluences (12, 25 and 32 J/cm^2) and at 1 mbar of nitrogen pressure.

1. Introduction

In order to synthesise carbon nitride films ($C_{x-1}N_x$), some authors have studied laser-produced carbon plasma in reactive ambient nitrogen (N_2) and/or ammoniac (NH_3) [1-4] at low laser fluences (3, 6, 12 J/cm^2) and in low pressures. The films deposited at 3-6 J/cm^2 were completely amorphous, while those deposited at 12 J/cm^2 presented microcrystals of a new CN_x phase dispersed in an amorphous matrix [5]. Although several results are obtained from these studies to understand the kinetics of plasma species surrounded by a reactive gas, some chemical and physical processes involved in plasma remain not completely understood yet. In this context, at high laser fluences the investigation is rather low. In this paper we present the spatio-temporal evolution of CN and C_2 for high enough laser fluences and the chemical process which could lead to CN formation.

2. Experimental setup

The carbon plasma is induced by a KrF excimer laser (λ= 248 nm, τ = 25 ns, E = 300mJ, f = 10Hz). The laser beam is focused on rotating graphite target at an incidence angle of 45° through a set of lenses. Two crossed cylindrical lenses of 1 m focal length aligned with 0. 5 m of spherical lens focal length in order to obtain a smallest spot size (0.66 10^{-2} cm^2) and then a high enough laser fluence. The target chamber is evacuated to a pressure of 10^{-6} mbar and then is filled with nitrogen gas. The plasma emission is optically imaged on the 100 µm entrance slit of Spex spectrometer with a magnification of 1 at a right angle to the normal of the target surface. The spectral lines and molecular band emissions of different species of carbon surrounded by a nitrogen gas with a spectral resolution of 0.08 nm, are collected by a fast photomultiplier with 2.2 ns rise time. This latter is connected to a digital oscilloscope (TDS3032).

3. Results and discussion

Emission of plasma species

The time integrated plasma emission spectra of laser ablated carbon in the presence of nitrogen at a pressure of 0.5 mbar has been recorded and analysed at 3 mm from the target surface between 250 and 750 nm. The plasma emission spectrum is well dominated by CN molecular emission of violet system ($B^2\Sigma^+ \rightarrow X^2\Sigma^+$) of the sequence ($\Delta$v = -1, 0, 1) followed by the C_2 emission of Swan system ($d^3\Pi_g \rightarrow a^3\Pi_\mu$) of the sequence ($\Delta$v =-1, 0), C^+, neutral carbon, N_2^+, N^+ and neutral atomic nitrogen. The occurrence of these species emission depends on laser fluence.

For that, the dependence of the temporal profile on the laser fluence of the (0, 0) band head of CN, C_2, and N_2^+ at 388.3, 516.5 and 391.4 nm respectively and C, C^+, N^+ lines at 247.8, 426.7 and 399.5 nm respectively has been followed at a distance from the target surface of 4 mm and for the laser fluences range from 1 to 32 J/cm^2 under 0.5 mbar nitrogen pressure.

We found that CN, N_2^+, C_2 and neutral carbon emissions appear at 1 J/cm^2 and CN emission intensity does not vary with laser fluence. Whereas C^+, N^+ emissions appear at 6, 10 J/cm^2 respectively and their intensities increase with laser fluence. Neutral atomic nitrogen emission at 745.2 nm appears at 25 J/cm^2 and its emission intensity is very weak.

The dependence of the relative intensity of emissions of the (0, 0) band head of CN, C_2, and C, C^+, N^+ lines on laser fluence in the range of 10 to 35 J/cm^2 is represented on figure 1.

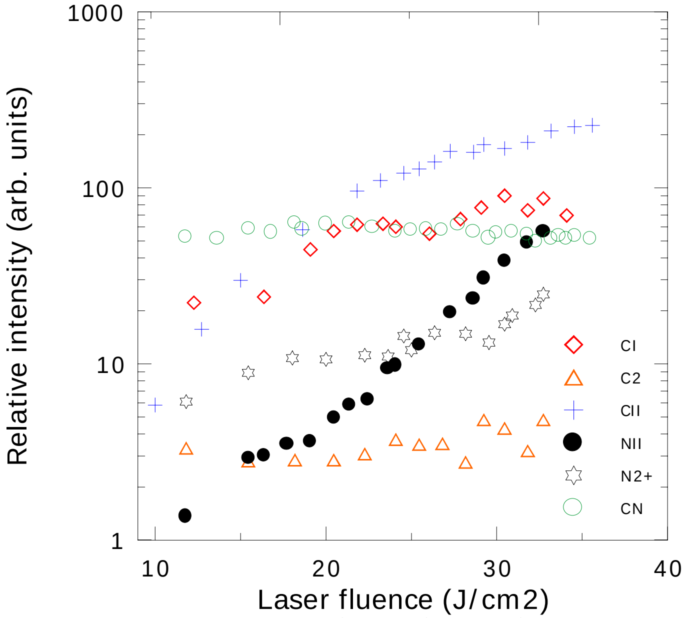

Figure 1: Maximum emission intensity of CN, C_2, N_2^+, C, C^+ and N^+ as a function of laser fluence for 0.5 mbar nitrogen pressure and at 4 mm from the target surface.

The temporal profile of the emission of N_2^+ molecules is characterised by a prompt emission when the laser beam reaches the target surface, followed by a broad emission with time evolution similar to that of N^+ and C^+. Only the intensity of N_2^+ broad emission is presented in figure 1.

Emission intensity of plasma species

To avoid the continuum emission contribution in the plasma emission, the emissions species has been recorded from 2mm of the target surface.

The maximum emission intensity of CN and C_2 and the corresponding observation distance are plotted on figure 2 for three laser fluences and at a nitrogen pressure of 1 mbar.

We observe a decrease of C_2 emission intensity, which at 6 mm from the target surface becomes very weak, and beyond 7 mm no C_2 emission is observed.

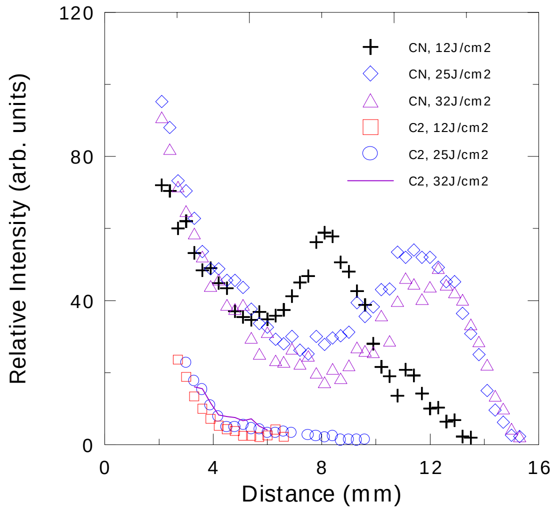

Figure 2: The maximum emission intensity of CN and C_2 as a function of the distance from the target surface and for N_2 pressure of 1 mbar.

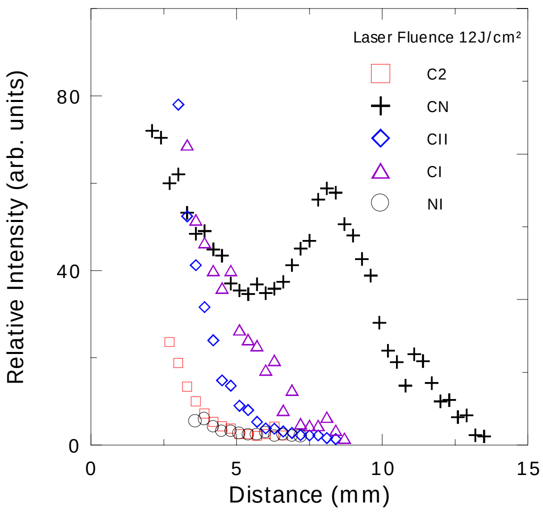

Figure 3: The maximum emission intensity of CN, C_2, C, C^+ and N^+ as a function of the distance for N_2 pressure of 1 mbar.

Concerning the CN emission intensity the decay is also observed till 6mm for 12 J/cm^2 and 8 mm for 25 and 32 J/cm^2.

Beyond these distances we note an important enhancement in the CN emission intensity and the maximum of this enhancement moves far from the target surface as the laser fluence increases from 12 to 25 J/cm^2. This could be interpreted as a presence of a high chemical reactivity in this region.

In figure 3, we report the maximum emission intensity of C^+, C, N^+, C_2 and CN as a function of the distance for a fluence of 12 J/cm^2. An emission intensity decreasing of C^+, C and N^+ is also noted. For any distance of observation, we remark that the CN emission dominates all emissions and the same behaviour is obtained at 25 and 32 J/cm^2.

Spatio- temporal evolution of plasma species

Figure 4 shows the z-t plot of CN and C_2 at three different laser fluences 12, 25 and 32 J/cm^2 and at 1 mbar of nitrogen pressure. From the figures we note that C_2 and CN evolutions have the same behaviour up to 4 mm from the target surface which means that they have the same velocity.

Beyond 4.5 mm, the C_2 species is decoupled from the CN ones. CN velocity is greater than C_2 one for the three laser fluences.

The C_2 velocity at 12 J/cm^2 is greater than that at 25 and 32 J/cm^2. We could explain this by the fact that C_2 molecules come from clusters dissociation, and the important mass of these clusters will result in the longer delays of C_2 emission observed. Such a velocity decrease has been also observed by other works [6, 7].

The figure 4 shows clearly that C_2 emission disappears after 6 mm from the target surface but the CN one persists up to 16 mm. This confirms that there is an important reactivity between carbon plasma species and nitrogen gas.

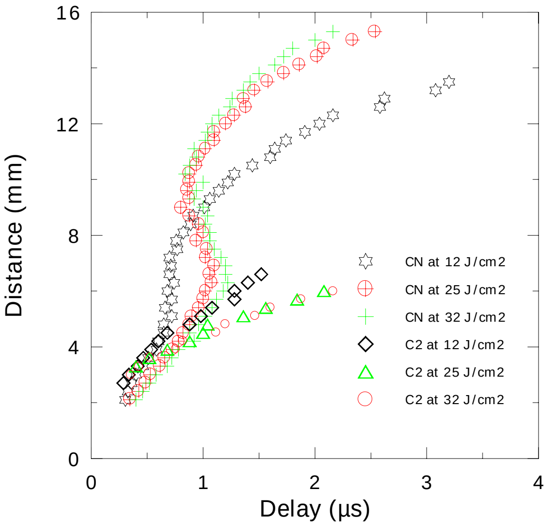

Figure 4: The z-t plot of the (0,0) band head of CN and C_2 for N_2 pressure of 1 mbar.

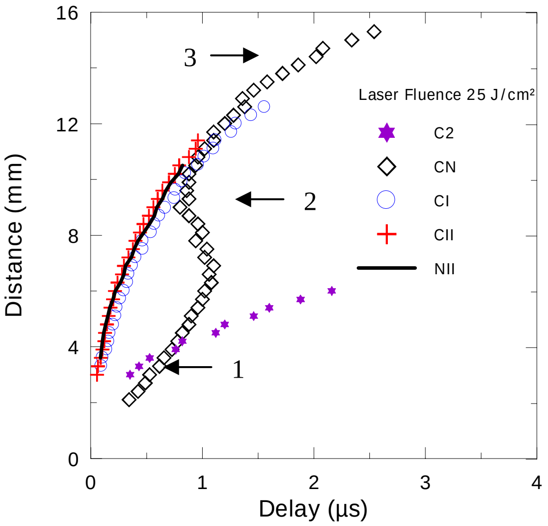

Figure 5: The z-t plot of the (0,0) band head of CN and C_2 and lines of C, C^+, N^+ for N_2 pressure of 1mbar.

We note also on the figure 4 that the CN evolution can be divided into three branches. The first and the third branch correspond to the CN evolution respectively up to 5 mm and beyond 8 mm from the target surface. This difference is attributed to different processes leading to the CN formation. The second branch has not a physical signification. In fact, it corresponds to the overlapping of the two kinds of the CN evolution.

Furthermore, for distances above 8 mm from the target surface the CN evolution follows the C, C^+ and N^+ evolutions as shown in figure 5. We can deduce therefore that for these distances CN molecules formation come from chemical reactions between atomic carbon plasma species and atomic nitrogen gas. The atomic nitrogen species are formed by the dissociation and ionisation of gas molecules by collisions in plasma front. The same behaviour of figure 5 is obtained at 12J/cm² and 32J/cm².

By comparing the results obtained on figures 3 and 5 concerning the CN of the third branch, it can be established that the CN molecule formation could follow the three body reaction given below:

$$C_{(gas)} + N_{(gas)} + M \longrightarrow CN_{(gas)} + M \qquad (1)$$

The particle M could be atomic carbon (C) or atomic nitrogen (N) since in this kind of three body recombinaison process the mass of M must be comparable to the mass of one of the first two particles of the reaction 1[8]. The rate of this reaction is of the order of 10^{-32} cm^6 s^{-1}.
Concerning the CN evolution involved in the first branch, since it follows the C_2 one and the CN and C_2 evolution is well decoupled from C and C^+ ones as shown in figure 5, the CN formation could either come directly from the target surface following the reaction 2 or probably from the reaction 3:

$$C_{(solid)} + N_{(gas)} \longrightarrow CN_{(gas)} \qquad (2)$$

$$C_{2\,(gas)} + N_{2\,(gas)} \longrightarrow 2\,CN_{(gas)} \qquad (3)$$

The reactions 2 and 3 have been proposed on references [3,1] for laser fluences less than 12 J/cm^2 and have been discussed in our previous work [7] where the carbon plasma has been induced by a Nd-Yag laser beam (λ = 1.06 µm) at 8 and 35 J/cm^2. In that study the spatio-temporal evolution of CN and C_2 is completely decoupled from atomic carbon evolution on overall propagation distance. It was found that the CN velocity is either equal or less than the C_2 one. In that case we can not apply the reaction 1.

4. Conclusion

The excimer laser ablated carbon plasma under nitrogen ambience is investigated by emission spectroscopy at high enough laser fluences. We found that CN dominates the emitted spectrum and that CN, C_2, C^+ and N_2^+ emissions do not depend on laser fluences.
According to the spatio-temporal evolution of CN, C_2, C^+, C and N^+ different chemical reactions leading to CN formation are proposed.

References

[1] C. Vivien, J. Hermann, A. Perrone, C. Boulmer-Leborgne and A. Luches, J. Phys. D: Appl. Phys. **31**, 1263, (1998).

[2] C. Vivien, J. Hermann, A. Perrone and C. Boulmer-Leborgne, J. Phys. D: Appl. Phys. **32**, 518, (1999).

[3] S. Acquaviva, A. P. Caricato, M. L. De Giorgi, G. Dinescu, A. Luches and A. Perrone, Phys. B: At. Mol. Opt. Phys. **30**, 4405, (1997).

[4] S. S. Harilal, Riju C. Issac, C. V. Bindhu, Pramod Gopinath, V. P. N. Nampoori, and C. P. G. Vallabhan, Spectrochimica Acta Part A **53,** 1527, (1997).

[5] S. Acquaviva and M.l. De Giorgi, Applied Surface Science, 186, 329 (2002).

[6] S. S. Harilal, Riju C. Issac, C. V. Bindhu, V. P. N. Nampoori, and C. P. G. Vallabhan, J. App. Phys., **80**, 3561, 1996.

[7] S. Abdelli-Messaci, T. Kerdja, A. Bendib and S. Malek J. Phys. D: Appl. Phys. **35**, 2772, (2002).

[8] B. M. Smirnov, Introduction to plasma physics, Mir Publishers, Moscow, (1977).

PLASMA TREATMENT OF SOLID WASTE

S. Dmitriev[1], V. Gnedenko[2], D. Pegaz[3], A. Suris (Souris)[4]

[1]*MOS NPO "Radon", Russia,*
[2]*RNC "Kurchatov Institute", Russia,*
[3]*Environmental Energy Resources Ltd., Israel,*
[4]*Moscow State University of Ecological Engineering, Russia*

Modern methods of thermal processing of solid wastes are based usually on Incineration Processes. Low temperatures of combustion, high consumption of air (in excess of stoichiometric requirement), low efficiency of Power Generating Unit (18 to 24%), large quantity of fly ash as well as products of incomplete combustion in the bottom ash make the Incineration Process incapable of complying with the more and more stringent environmental standards. The most environmentally "clean" technology for treatment of the incineration solid residues is vitrification, which requires considerable amount of additional electric energy for melting this secondary solid waste in a special installation.

Plasma process for treatment of solid waste was investigated in this work. Investigation was performed using installations of different capacity. The Plasma reactor is a vertical shaft furnace lined inside with refractory material. The waste is loaded into the upper part of the shaft through a system of seals (shutters), which prevent air ingress into the reactor. In the lower part of the reactor, plasma torches, ports and devices for introduction of oxidizing agents (air, steam or other gases), and provisions for release of the molten slag are located.

During its residence inside the reactor, the waste passes through successive zones:

- Drying zone;
- Pyrolysis zone;
- Gasification zone;
- Combustion zone;
- Melting zone.

In the Drying zone, the moisture content of the waste is reduced and partial melting/softening of some waste also occurs.

In the Pyrolysis zone, disassociation of waste takes place, which results in generation of gaseous products containing C_mH_n, CO, CO_2, H_2O, H_2, H_2S, HCl and others. Based on the operating conditions, temperature and residence time, varying quantities of pyrolytic gas, pyrolytic tar and char (carbonaceous residues of organic matter) are formed. The pyrolytic gases exiting the reactor can carry with them some amount of dust. It's quantity depends on the flow rate of wastes and correspondingly on the flow rate of oxidizing gases.

In the Gasification zone, interaction of char with products of combustion and steam occur, and conversion to mostly CO and H_2 takes place.

In the Combustion zone, some quantity of char is oxidized to CO_2 and H_2O.

In the Melting zone, the inorganic components of MSW are melted by the plasma jets, and the molten material accumulates in the bottom part of the reactor from which it is periodically or continuously removed in the form of liquid slag/metal mixture. This material does not contain any organic residues and is environmentally "clean".

Theoretical and experimental investigation of the process has shown that the actual composition of the gaseous products, their temperature and heating value varies as a result of changes in ratios of steam (G_s) and air (G_a) supplied to the reactor, as well as due to modulated power of the plasma torches (P_t) and the enthalpy of the plasma jet (I_j).

The process parameters G_s, G_a, P_t, I_j are additional degrees of freedom enabling control of the process and its optimization according to composition and moisture content of the waste treated. In this connection it is capable of processing wastes with high contents of inorganics, high moisture content and varying composition.

The process permits to treat different types of waste (medical, industrial, radioactive, municipal).

Process parameters have to be chosen according to the aim of technology (economics of the process, as well as improvement of the environmental aspects).

Parylene-like plasma deposited films: plasma emission, infrared and UV-VIS absorption spectroscopy

B. Mitu[1], S. Bauer-Gogonea[2], I. Volintiru[1], S. Bauer[2], G. Dinescu[1]

[1] *National Institute for Lasers, Plasma and Radiation Physics. Magurele MG-16, Bucharest Romania;*
e-mail: dinescug@alpha1.infim.ro
[2]*Angewandte Physik, Johannes Kepler Universitat Linz, Altenberger Str. 69, A-4040 Linz, Austria;*
e-mail: sbauer@jk.uni-linz.ac.at

Abstract

This work reports on the deposition of parylene - like thin films by RF plasma polymerization of di – para – xylylene vapors. The film properties are investigated by FTIR and UV – VIS measurements and are correlated to the plasma characteristics as resulted from Optical Emission Spectroscopy. It is shown that the properties of deposited layers are sensitive to the average energy applied to the unit of monomer mass and are gradually changing from dimer – like to hydrogenated carbon – like films.

1. Introduction

Thin poly-para-xylylene (parylene) films offer a range of useful properties, like low dielectric constant and low dissipation factor over a large frequency range, good conformality, and low permeability to moisture and other corrosive gases [1]. Parylene films have found widespread use in packaging, microelectronics, MEMS and biomedical devices [2]. In comparison to the conventional vacuum vapor deposition polymerization of di-para-xylylene (DPX), the plasma polymerization process and the properties of the obtained plasma parylene-like films were not yet investigated in detail. Plasma polymerization of DPX can be advantageous for several reasons, as example for the fabrication of composite layers or for an inexpensive incorporating of fluorine within the films in order to obtain parylene – F- like films. On the other hand, some drawbacks may appear, as plasma polymer films have no simple repetition unit, but are highly reticulated [3]. Additionally the polymeric character, for example the maintenance of the aromatic structure of the monomer in the plasma polymer has to be demonstrated.

In this work results concerning the plasma deposition and the properties of parylene-like films are reported. The film characteristics as resulted from FTIR and UV - Vis – NIR measurements are presented and discussed in correlation to the plasma characteristics. The present work is focused on the study of aromatic character retention and the introduction of impurities in the structure and to the optical properties of the films.

2. Experimental

A capacitively coupled RF plasma set-up (13.56 MHz) consisting of a tubular reactor with external electrodes was used. A schematic view of the experimental set – up is presented in Figure 1. The plasma was generated in argon (0.1-10 sccm) at various RF power (10-350 W). The heating of the DPX dimer, in solid phase in normal conditions of temperature and pressure, is insured by an external oven mounted on the glass reactor. The DPX vapors (mass flow rate up to 200 mg/min) produced by sublimation were introduced in the discharge at a controlled rate through the open end of a heated glass ampoule. The system is pumped down to 10^{-3} mbar by a rotary mechanical pump which is protected from contamination by a cold trap. The substrate holder has been placed in the vicinity of the active RF electrode and the dissociation products resulted from the DPX fragmentation in plasma are condensed on Si (100) and quartz substrates.

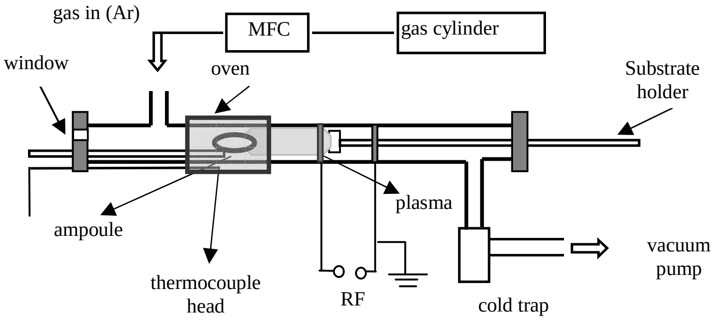

Figure 1. Schematic view of the experimental set-up

The emission characteristics in the 200 – 600 nm of the Ar/ DPX plasma in different conditions of dimer flow and RF applied power have been monitored by a typical OES chain consisting of quartz lens, optical fiber, monochromator with grating (1200 lines/mm), amplifier and acquisition system. The deposited films have been investigated by absorption spectroscopy in IR region (400 – 4000 cm^{-1}) in order to determine the chemical bonds, by using a Bruker Equinox 55 apparatus with a resolution of 2 cm^{-1}. The transmission characteristics in the UV – VIS – NIR region (175 – 3300 nm) have been measured with a Cary 500 spectrometer working in the double beam mode.

3. Results and discussion

It is known that in plasma polymerization processes a key parameter that determines the material properties is the ratio between the applied RF power and the dimer mass flow rate W/F [4]. In a previous work [5], the structural and morphological properties as resulted from SEM, AFM, XRD, and FTIR investigations on parylene- like films deposited in different experimental conditions were presented. According to them, the deposited materials will belong to three categories: dimer like at low W/F ratio, polymer – like at intermediate W/F and hydrogenated carbon – like at high W/F values. Smooth transitions between these categories can be obtained by changing gradually the power level or the dimmer mass flow values. The estimations of the transitions from low W/F to intermediate W/F regions and from intermediate to high W/F regions have led to values of approximately 0.1 and 3 $W.min.mg^{-1}$, respectively. Consequently, the experimental results are presented and discussed according to these values.

3.1. FTIR measurements

In Figure 2 is presented the FTIR spectrum in the regions 400 – 2000 cm^{-1} and 2600 – 3200 cm^{-1} in the case of a film obtained without plasma, by recondensation of the dimer onto a silicon substrate. Vibrations corresponding to both aromatic and aliphatic bonds of the dimer have been identified. The fingerprint of the methylene groups in the dimer is proved by the νCH_2 symmetric and asymmetric deformations at 2852.66 cm^{-1} and 2925.96 cm^{-1} respectively [6], and of the in – plane deformation γCH_2 at 719.43 cm^{-1}. In aromatic hydrocarbons the νCH stretching vibrations appear in the 3000 – 3100 cm^{-1} region, as compared to the saturated hydrocarbons which absorb below 3000 cm^{-1} [7]. Therefore this region is useful for differentiating the aromatic from aliphatic compounds. In the present spectrum, the vibration at 3031.94 cm^{-1} (present in all the aromatic compounds) and those at 3012.75 cm^{-1} and 3089.5 cm^{-1} corresponding to para – xylene have been identified. As concerning the out of plane deformation vibrations, γCH, the para-substituted compounds have one band in the region 800 – 810 cm^{-1} (in this case at 806.23 cm^{-1}). Additionally, due to the distortions of the benzene ring and to the interstitial resonances that appear in the particular geometry of the paracyclophane systems, two other new γCH vibrations at 894.95 cm^{-1} and 936.34 cm^{-1} are present. The vibrations at 1020.32 cm^{-1}, 1087.83 cm^{-1} and 1178 cm^{-1} correspond to the in - plane

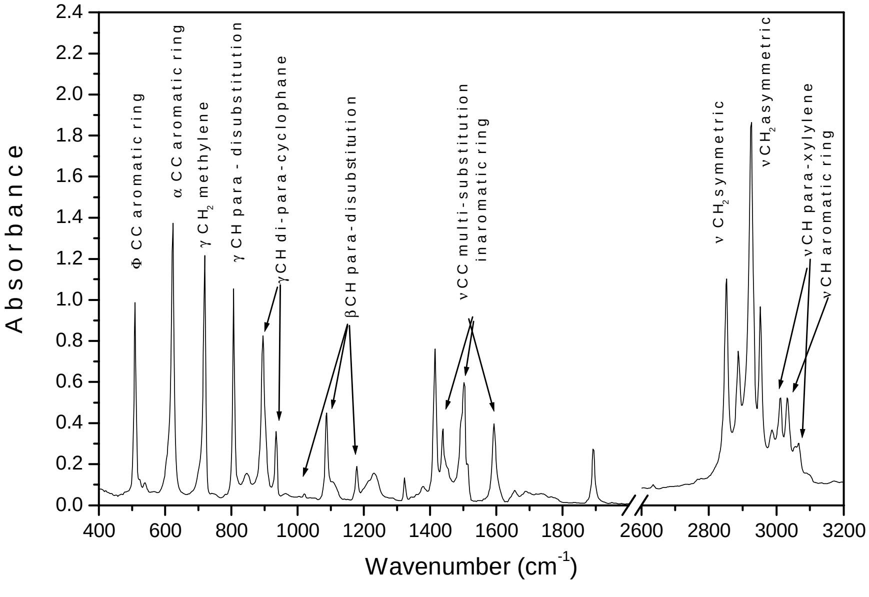

Figure 2. The FTIR spectrum of an DPX film obtained by recondensation of dimer on Si substrate

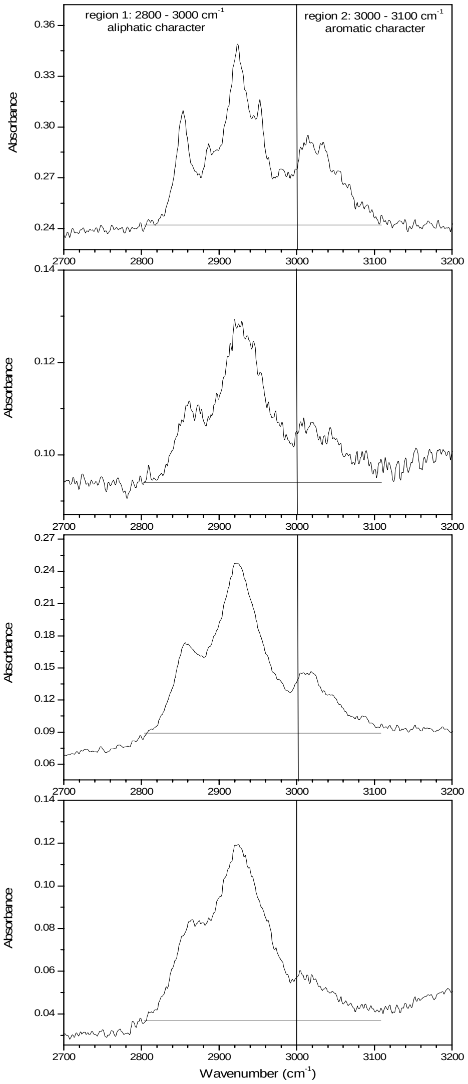

Figure 3. The evolution of the 2800 – 3100 cm^{-1} absorbtion region of the FTIR spectra due to the increase of the W/F ratio

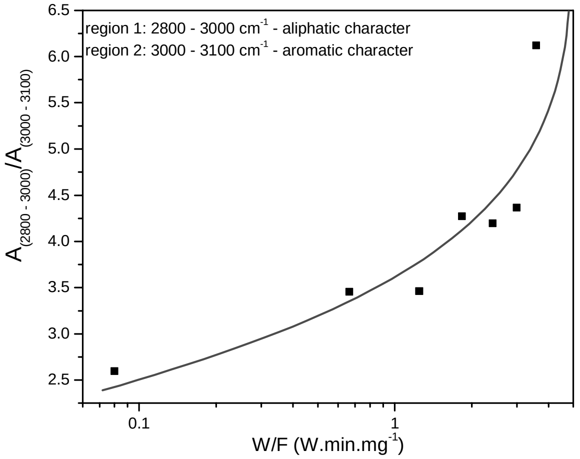

Figure 4. The ratio of the absorbances of the aliphatic to aromatic – related region of the FTIR spectra as function of W/F ratio

deformations of the CH bonds in the benzene ring of the para – substituted compounds (βCH) [1]. The multi-substituted aromatic compounds show the presence of four bands in the region 1400 – 1650 cm^{-1}, corresponding to the stretching νCC vibrations, the most important one being around 1500 cm^{-1} (here at 1502.52 cm^{-1}), while those at approximately 1571 ± 11 cm^{-1} and 1620 ± 8 cm^{-1} are in most of the cases insufficient separated to allow a distinct observation (here one band at 1593.69 cm^{-1} is observed). Moreover, the carbon atoms forming the aromatic ring vibrate as a whole, giving rise to in – plane deformation αCC at 623 cm^{-1} and out of plane deformation ΦCC at 509.2 cm^{-1}.

The FTIR spectra of the films deposited by using plasma are modified in respect to the case discussed above. At low RF applied power or at high dimer flow, corresponding to low W/F ratio, the energy available for dimer fragmentation is low and part of the dimer vapors which enter into the discharge will not be fragmented. Consequently the deposited film will contain both polymerized fragments and re-condensed dimer. In the FTIR spectrum the vibrations described earlier are present, but the bands widths are larger due to the less ordered structure, while the relative absorbances of the bands are changing. By increasing the RF power or decreasing the dimer flow, the dimer fragmentation is more pronounced and a polymeric parylene – like film is obtained. Although the vibrations in the region 3000 – 3100 cm^{-1} and the triad in the region 1400 - 1650 cm^{-1} have lower absorbance, their existence confirms that part of the aromatic rings are still present in the deposited film. In order to have a view of the gradual modifications of the film composition due to the increase of the W/F ratio, in Figure 3 the FTIR spectra of the region 2800 – 3100 cm^{-1} are presented. This absorption region can be interpreted by considering the absorbance in the 2800 – 3000 cm^{-1} region as related to the aliphatic character, while the absorbance in the region 3000 – 3100 cm^{-1} gives a measure of the aromatic character. It can be seen that going from low W/F values (case a) toward intermediate (case b and c) and high W/F values (case d), the bands in the region 3000 – 3100 cm^{-1} are less and less pronounced. For a quantitative description of the absorption behavior, the Beer law has been considered [8]:

$$A = \varepsilon l c, \qquad (1)$$

where A is absorbance, ε is the absorptivity, l is the film thickness and c is the concentration. The absorptivity is a constant for a given molecule at a given wavenumber, it actually depends on the absorption cross section of the IR radiation in the film. The concentration is related to the number of the oscillators (the number of bonds) excited by a given energy in the system. The absorbance was determined by integration of the curve for the considered regions, respectively by summing all the absorption bands present in each region. Consequently, the ratio $A_{2800-3000}/A_{3000-3100}$ for one sample will give a measure of aliphatic/aromatic behavior for the deposition conditions (W/F) of that sample. In Figure 4 the dependence of this ratio as function of W/F parameter is presented. One can see that although the ratio of the absorbencies in the aliphatic and aromatic regions is always higher than 1, the aromatic character of the films gradually diminishes as the ratio W/F is increased.

By increasing the RF power at very high values, the electron density and the electron temperature increase. The plasma becomes more energetic and consequently the dimer bonds are completely destroyed in the discharge and small carbon containing radicals are formed. As it was previously shown, these conditions leads to deposition of hydrogenated carbon – like films [5]. Indeed, in the FTIR spectrum of such a film, presented in Figure 5, the signature of the aromatic compounds completely disappears, at the same time the vibrations corresponding to C=C stretching mode at 1630 cm^{-1} and to the CH_3 bending modes (1380 cm^{-1} and 1460 cm^{-1}) and stretching modes (2962 cm^{-1}) are present [9]. Moreover, some impurities are incorporated in the films, as proved by the presence of NH and CO deformation vibrations. The problem of impurities presence in the film as observed from FTIR measurements was addressed by Optical Emission Spectroscopy measurements.

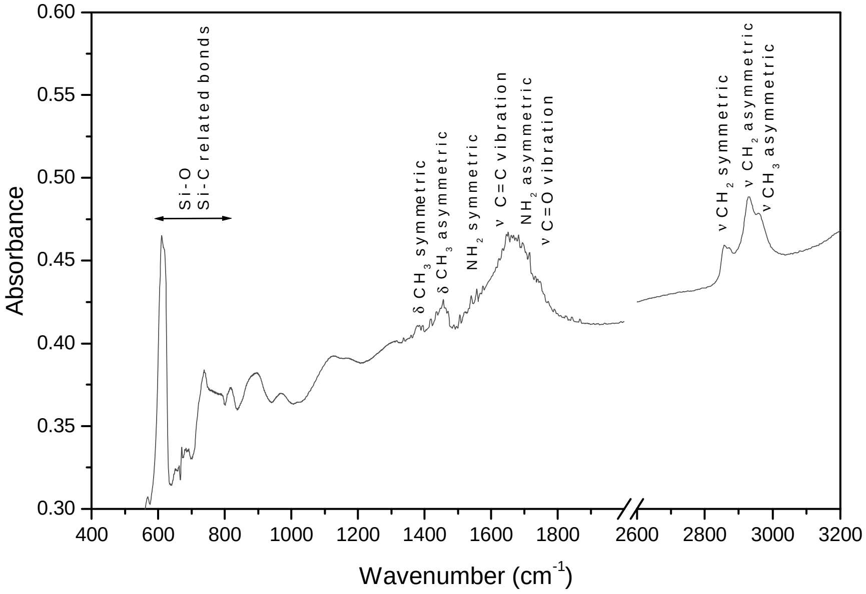

Figure 5. A typical FTIR absorption spectrum for films deposited at high W/F values

3.2. Optical Emission Spectroscopy

Optical emission spectroscopy measurements have been performed in order to elucidate the species contributing to the deposition and to relate plasma conditions with film properties. The emission of carbon containing radicals (CH, C_2) which are typical for deposition of carbonic materials and impurity radicals (CN, OH, NO, and NH) were observed.

Selections of OES spectra of the plasma generated in Ar and Ar/DPX vapors corresponding to high W/F deposition conditions are presented in Figure 6a. The presence of the impurities as nitrogen and water vapors is obvious even for the discharge sustained in Ar at 50 W, probably due to the low vacuum and to the fed gas. The introduction of the gaseous dimer into plasma leads to the appearance of CH, C_2 and CN radicals and to the quenching of Ar lines. Small carbon fragments and radicals are obtained from the dissociation of the di – para - xylylene vapors induced by the interaction of DPX with electrons, Ar metastables and ions. The CN radical is formed by chemical reaction of these carbon fragments with the nitrogen traces present in the residual gas. The relative increase of the emission intensities for the impurities species by increasing the RF power at constant dimer mass flow rate is presented in Figure 6b. The general increase of the emission intensities of impurities is mainly related to the power increase, as can be seen from the behavior of Ar lines as well. The preferential excitation of CN radicals is related to its high stability (dissociation energy of 7.55 eV) compared to those of CH (dissociation energy of 3.47 eV) and C_2 radicals (dissociation energy of 6.25 eV) [10]. Nevertheless, this increase is not enough high to explain the strong incorporation of impurities in the growing film. Consequently, for explaining the appearance of the impurities – related bonds in the IR spectra of the films deposited at high W/F, an active oxidation process subsequent to the deposition step have to be considered.

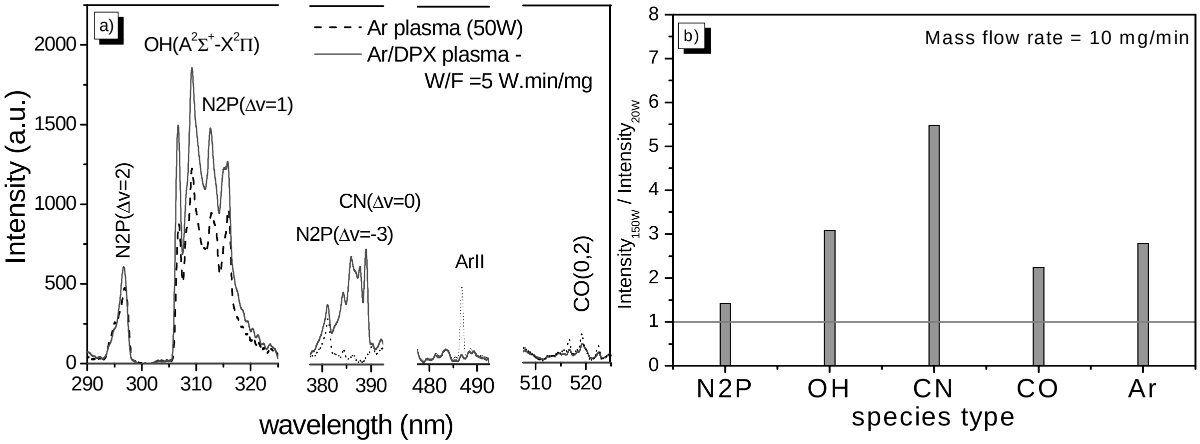

Figure a) The optical emission spectra of the discharge generated in Ar and Ar/DPX vapors at 50 W; b) The relative increase of the emission intensities of the species

3.3. UV – Vis – NIR absorption

The rough crystalline structure at W/F = 0 and the presence of large dimer crystallites embedded in the film at low W/F values induce a large scattering effect of the light in the UV – VIS region and the transmission spectra might be not quantitatively reliable. The UV – VIS – NIR spectra of the films deposited at intermediate and high W/F values are further discussed. A typical example is presented in Figure 7a. It can be seen that the films are transparent in the wavelength interval 400 - 2700 nm. The absorption coefficient is in fact the optical quantity characterizing the material ($\alpha = \Sigma\varepsilon_i c_i$, where ε_i are the absorptivities of the chemical groups composing the material and c_i are their concentrations that absorb at a given wavelength). Consequently, in Figure 7b is presented its dependence on the wavelength for different W/F values. For all spectra, the absorption coefficient decreases from aproximatelly 10^5 cm^{-1} at 200 nm to 2.10^2 cm^{-1} at 600 nm. In addition, the absorption coefficient increases as the W/F increases, probably due to the gradual loss of the polymeric character of the deposited material. There is no clear evidence of specific absorption of some chemical groups as the maxim observed on the curves may be related to an oscillatory behavior which can be caused by the interference due to the multiple reflections of the light in the film.

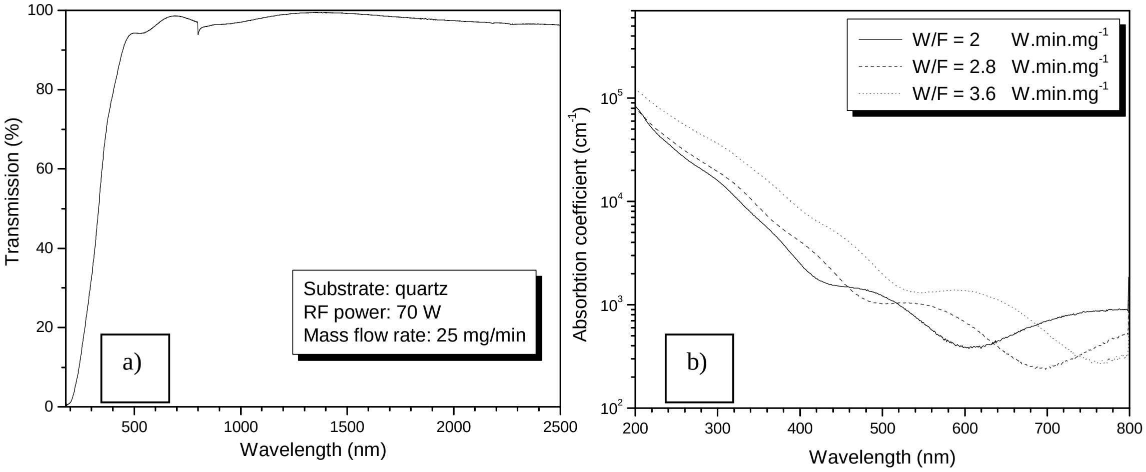

Figure 7. Optical characteristics of parylene – like films deposited at intermediate and high W/F values in UV – VIS – NIR region a) A typical example of transmission spectra; b) The dependence of the absorption coefficient on wavelength

4. Conclusions

We have used the DPX (di-para_xylylene) sublimation as method for precursor injection in the plasma polymerization technique aiming to obtain parylene-like plasma polymer films.

By FTIR measurements we have shown that polymeric character of the films, as indicated by the aromatic related bonds in the material, which is pronounced at intermediate W/F values, gradually diminishes by increasing W/F ratio. At the same time, the amount of the bonds corresponding to the aliphatic character increases.

Hydrogenated carbon–like films that contain oxygen and nitrogen as impurities are obtained under high W/F conditions. The level of impurities relates rather to a subsequent oxidation step than to the deposition environment, as Optical Emission Spectroscopy indicates.

The films are highly transparent in visible and NIR region. The absorption coefficient increases slightly with the W/F values.

References

[1] S. Rane, G. Beaucage, Poly(p-xylylene), in Polymer Data Handbook, Ed. J.E. Mark, Oxford University Press, 1999, p. 965

[2] W. F. Beach, C. Lee, D.R. Basset, T.M. Austin, R. Olson, Xylylene Polymers, Encyclopedia of Polymer Science and Engineering, Vol. 7, 2nd edn., Willey 1989, pp. 990-1023

[3] H. Biederman, Y. Osada, Plasma Polymerization Processes, Elsevier, Amsterdam, London, NY, Tokyo, 1992, p.78

[4] H. Yasuda, “Glow Discharge Polymerization”, in J.L. Vossen, W. Kern (eds.) Thin Film Processes, Academic Press, New York, San Francisco, London, 1978, p 361-400.

[5] B. Mitu, S. Bauer – Gogonea, H. Leonhartsberger, M. Lindner, S. Bauer, G. Dinescu, Surf. Coat. Tech., in press, 2003

[6] A. Zocco, A. Perrone, A. Luches, R. Rella, A. Klini, I. Zergioti, C. Fotakis, Thin Solid Films, **349** (1999), 100-104

[7] M. Avram, Gh. D. Mateescu, Infrared Spectroscopy. Applications in Organic Chemistry, Wiley – Interscience, Bucharest, Technical Ed., 1971, p 213-216.

[8] B.C. Smith, Fundamentals of Fourier Transform Infrared Spectroscopy, CRC Press, Boca Raton, Florida, p.140, 2000

[9] J. Coates, Interpretation of Infrared Spectra, A Practical Approach, in Encyclopedia of Analytical Chemistry: Applications, Theory, and Instrumentation, R.A. Meyers, Ed., John Wiley &Sons, 2000

[10] R. Mavrodineanu, H. Boiteux, Flame Spectroscopy, John Wiley &Sons, 1965, p.339

Comparative analysis of supersonic plasma jets formed by DC arc and ICP torch

S.E. Selezneva[1], V. Sember, M.Rajabian, D.V. Gravelle and M.I. Boulos

Department of Chemical Engineering, Université de Sherbrooke, Sherbrooke, Québec, Canada
[1] present address: C&MT, General Electric Global Research Center, Niskayuna, NY USA

Abstract

In the present paper, we analyze the common features and differences between the supersonic jets of argon flowing from the DC and ICP torches with slightly subatmospheric pressures through the supersonic nozzles (with the outlet Mach numbers 1.1 and 1.5). The jets discharge into a 2kPa chamber. The analysis is performed by means of the optical emission spectroscopy combined with the numerical modeling. In the paper, we show that the physical properties of supersonic plasmas depend on the generation method and location of plasma formation region. The results show that substantial interrelated deviations from the thermal, ionization and Boltzmann equilibria can be found in both jets. We demonstrate also that the ratio of the static pressure at the chamber inlet to the chamber pressure together with the Mach number at the nozzle outlet and the rarefaction parameter define the supersonic jet structure, and not the chamber pressure alone.The obtained results are useful for the optimization of plasma reactors for plasma chemistry and plasma processing applications.

1. Introduction

Direct current (DC) arc and inductively coupled plasma (ICP) torches [1] working in a supersonic regime are two plasma systems that widely used in plasma spaying, PECVD and simulation of re-entry conditions. Both of these plasma systems have been extensively studied over the past several decadeds [2] with the aid of experimental diagnostics [3-4] and mathematical modeling [5-8]. In practice, an engineer often has to choose the most appropriate mode of plasma generation for the required application of plasma system. We believe that the DC arc and ICP torch are substantially different because the plasma generation mode and operating conditions. It is interesting to make a comparative analysis of the under-expaned supersonic plasma jets formed by these two systems and to answer the following questions:

- What are the parameters that determine the gas dynamical and physical properties of supersonic jets?
- What properties of under-expanded supersonic plasma jets do not depend on the specific plasma system?
- Does the mode of plasma formation affect the supersonic jet structure and equilibrium conditions?

In the present article, we compare the plasmas flowing from the DC and ICP torches fixed at slightly subatmospheric pressures through the supersonic nozzles (with the outlet Mach numbers M = 1 and 1.5) into reactors having the same pressure (2kPa). The analysis is performed by means of optical emission spectroscopy combined with the numerical modeling.

2. DC arc and ICP torch experimental set-ups.

In this section we will describe the DC arc and ICP facilities operating in the University of Sherbrooke.

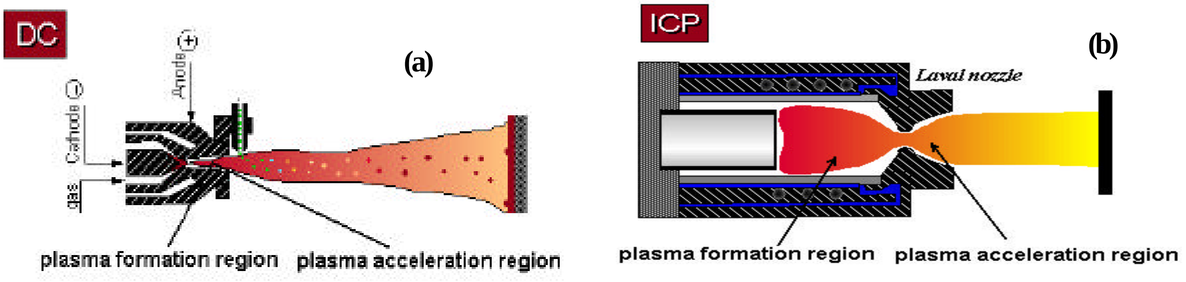

Fig.1 Schematic of supersonic plasma systems a) DC arc, b) ICP torch

The DC arc [6] is formed inside the convergent- straight nozzle (Fig.1a). The pressure at the torch inlet is 1.2 atm. The torch operates with the central tungsten cathode and a water-cooled annular copper anode. The plasma gas is injected into the gap between the two electrodes. Typical torch currents are in the range of a few hundreds amperes. The torch voltage depends on the nature of the working gas and can vary between 25 and 30V for pure argon. As the gas passes around the arc through the anode nozzle construction, it is heated and partially ionized and forms a high velocity jet. So, the plasma is formed in the region, where the gas flow is already accelerated up to almost sonic velocity. The static pressure in the plasma formation region is about 50kPa and it does not change much in the anode cylindrical part. Because of the shape of the nozzle the plasma exhausts into 2kPa working chamber with a velocity that is only slightly larger than sonic velocity.

In ICP discharge the plasma is formed by means of Tekna PL35 torch. The typical plasma velocities in the discharge region do not exceed 200m/s. The pressure in the discharge can be 0.5-2atm. Downstream of the discharge the plasma is accelerated in the convergent- divergent nozzle [7-8]. The schematic of the torch with the supersonic nozzle is shown in Fig.1b. Passing through the convergent-divergent nozzle the plasma flows into the working chamber where the pressure value P_{ch}=2kPa is maintained. The plasma exhausts with supersonic velocity in the chamber inlet. The Mach number and the static pressure at the chamber inlet depend on the nozzle design. Note that if the ICP nozzle Mach number is about 1.5 than this number is close to the Mach number of the plasma produced by the DC torch, which is typically about 1-1.2

3. Spectroscopic measurements.

The spectroscopic measurements [6],[8] are performed using 1m Jobin-Yvon monochromator with a 1200 grooves/mm grating. The image of the plasma jet is projected by means of two lenses and two mirrors into the monochromator entrance slit. This image, reduced 0.2 times, is oriented perpendicular to the input slit. This configuration enabled the measurement of radial profiles of spectral intensities by means of CCD detector with the spectrum and radius resolved along the horizontal and vertical axis of the detector, respectively. The width of the input slit gives the step of the measured radial profile 0.13 mm per pixel. The output signal is received by a photodiode array in the monochromator output plane. Measurements at several spectral windows are made to cover a selection of frequencies of different energy levels to allow for a good estimate of the temperature. Spectral intensities are calibrated by means of a tungsten filament lamp placed into the chamber. Background noise and dark noise is recorded for each individual optical and spectroscopic configuration. In spite of this procedure, there still remains relatively intensive optical and electronic noise. The optical noise is reduced using longer exposure time and the electronic noise is reduced by means of performing 50 shots per one measurement. A special technique of OES data interpretation based on the introduction of two excitation temperatures T_{exL} and T_{exH} describing the populations of the upper and lower excited states is used instead of a single excitation temperature T_{ex} [8].

4. Model.

The model used in the present paper is described in details in [6,7] and is based on fluid dynamic code FLUENT with incorporated two-temperature model. Computational aspects of DC arc and ICP jet models are given below.

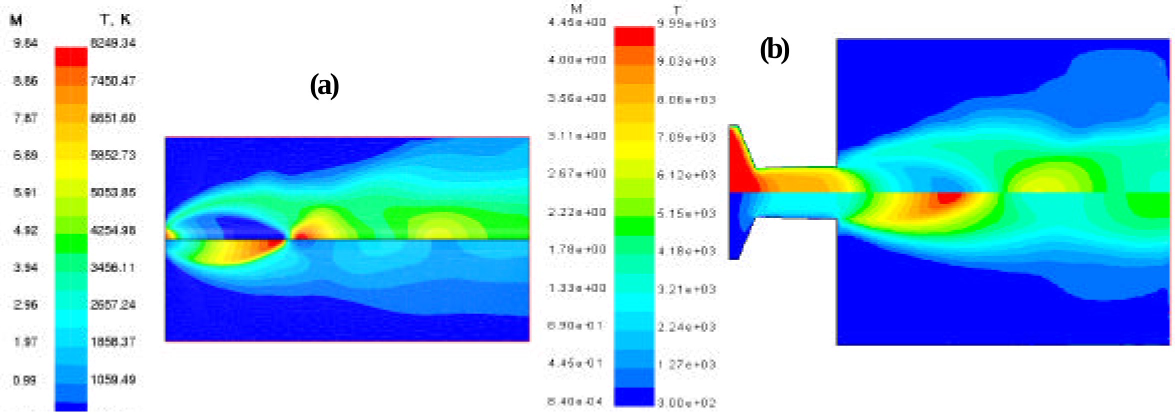

Fig.2 Contours of gas temperature (top) and Mach number (bottom) in the supersonic jet generated by a) DC arc, b) ICP torch

DC arc jet. The computational domain used for the modeling the stationary axisymmetric DC arc jet of argon is shown in Fig.2a. As it was mentioned we use the results of the emission spectroscopy study to assign the inlet boundary conditions. These conditions are as follows: the electron temperature 11000K is supposed to be out of equilibrium with the argon heavy particle temperature 7500K. Constant profiles of the temperatures are set at the torch outlet with the radius R_{in} =2.5mm. The equilibrium value of the electron number density calculated at the electron temperature 11000K and the static pressure P_{in} = 48kPa is assigned at the torch outlet. The turbulence intensity is assumed to be 0.5% with its length scale is of 0.005m at the chamber inlet. The computational area radius is R_{ch} = 0.5cm and length is L_{ch} = 0.1m. The parameters defining the structure of supersonic jets are the nozzle Mach number M and the ratio of the static pressure at the chamber inlet P_{in} to the ambient chamber pressure P_{ch}. Our analysis is limited to the jets exhausting from the convergent-straight nozzle (with M ≈ 1), having the static pressure P_{in}= 48 kPa, the chamber pressure P_{ch} = 2 kPa and the argon flow rate of 50 slm. The supplied electrical power in the corresponding experiments is about 17kW. It is assumed that 30% of this power is dissipated by the plasma. In the model we use a constant wall boundary condition for the heavy particle temperature T_w = 300K, a zero normal derivative condition for the electron temperature and non-slip velocity boundary condition. For electron mass fraction equation zero diffusion flux is set at the torch wall. Constant ambient pressure conditions are set at the outlet boundaries. The calculations are performed for the ambient pressure 2k Pa. The computations start using the first order upwind scheme on nonstructural grid. The grid consists of two parts. The inner part of the grid represents a region from the axis till the value of the radial coordinate r = 2.5 mm. The outer part is a region in the radial direction from r = 2.5 mm till r = 4.5 cm. In the beginning of the calculations, the grid contains 6400 quadrilateral cells in the inner region and 10631 triangular cells in the outer region. Then the grid is adapted: 1600 quadrilateral cells are added in the inner region and 560 triangular cells are added near the torch wall in the outer region.

ICP jet. The computational domain used for ICP axisymmetric jet modeling flowing from the convergent-divergent nozzles is shown in Fig.2b. The axial coordinate x=0 corresponds to the nozzle outlet, the nozzle inlet values correspond to x = -0.0244m for M = 1.5 nozzle. The radius of the nozzle inlet is 0.0175 m , the radius of the simulated chamber region is R_{ch}=0.04m for M = 1.5 nozzle, the length of the simulated chamber part is L_{ch} = 0.08m. Boundary conditions set in the present study are as follows. At the nozzle inlet the total mass flow rate 0.00174 kg/s (60 slm) is given. The constant heavy particle temperature 10000K is assumed to be equal to the electron temperature and the equilibrium value of the electron number density is assigned at the nozzle inlet. The value 10000K is the maximal possible value of the temperatures that can be attained at the nozzle inlet assuming that the plasma power input is 8kW (20kW in the torch). This observation also follows from the plasma flow modelling in the induction discharge tube. Note that with these inlet boundary conditions, the model results can give the evaluation of the maximal possible electron and heavy particle temperatures in the jet region. The turbulence intensity is assumed to be 0.1% at the nozzle inlet, where the flow velocity is less than 100m/s and the static pressure is about P_{nozzle} = 0.4 atm. At the wall we use a constant condition for the heavy particle temperature (300K), a zero normal derivative condition for the electron temperature and non-slip velocity boundary condition. At the chamber outlet the pressure P_{ch} = 2kPa is specified. The computations start on a nonstructural grid containing 9856 cells of two types: quadrilateral and triangular. After performing several hundreds iterations the grid is adapted: about 1000 cells are added near the walls and in the jet region. In both cases the calculations proceed using the second order accuracy scheme until the residuals of all the equations become less than 10^{-4}.

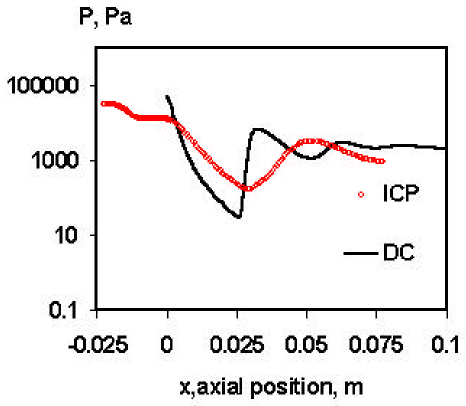

Fig.3 Static pressure along the axis

5. Results

The results show that at the chamber pressure inlet the static pressure in ICP jet is about 12kPa, while in the DC jet this pressure is about 48 kPa (Fig.3). The ratio n of the static pressure at the chamber inlet to the chamber pressure is about $n \approx 6$ for the ICP jet and $n \approx 24$ for the DC jet. Because of this difference in the pressure ratio, the ICP jet is mildly under-expanded, while the DC jet is strongly under-expanded. In the first expansion zone, in both jets the plasma is accelerated until the velocity of about 3300 m/s is reached (Fig.4a). However, within the DC arc jet, the velocity drops sharply in the region of normal shock wave (Mach disk) and the centerline flow contains a small subsonic region (Fig.4b). In the ICP jet, however, the drop in the velocity is not so abrupt in the compression region, which is free of the normal shock wave (i.e. it contains only oblique shock). Due to the greater degree of under-expansion in the DC arc jet, the drop in the axial pressure and static temperature in the first expansion zone is more pronounced in this jet than in the ICP jet (Fig.5). Because of the lower value of axial gas temperature at the end of the first expansion zone in the DC jet than in the ICP jet, the maximal Mach number as reached in the DC jet is higher than in the ICP jet. It can be seen from

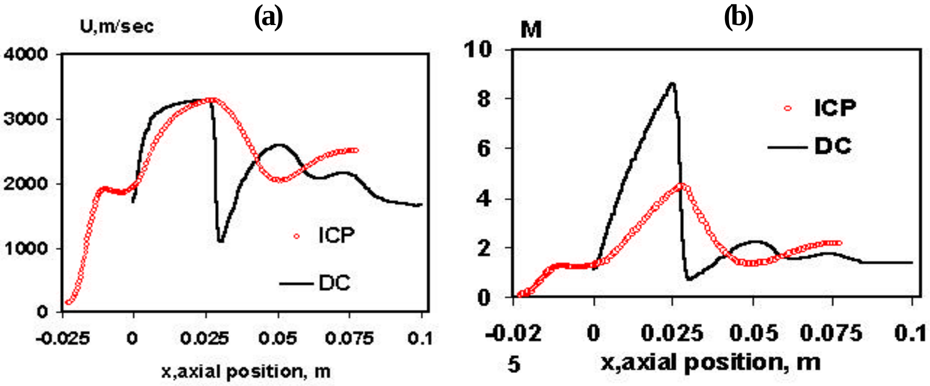

Fig.4 Axial profiles of (a) velocity (b) and Mach number

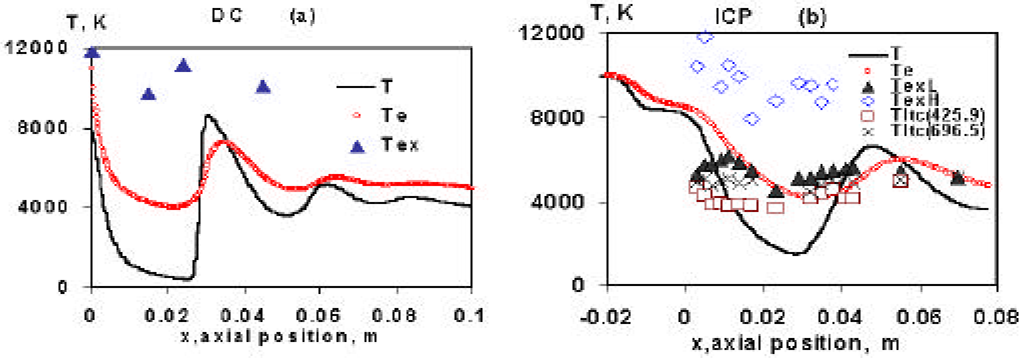

Fig.5 Comparison of the axial profiles of predicted by the model heavy particle temperature T and electron temperature T_e with the experimentally measured excitation temperaturesTex, $T_{ex\,L}$, $T_{ex\,H}$, and T_{ltc}, in supersonic DC (a) and ICP (b) plasmas .

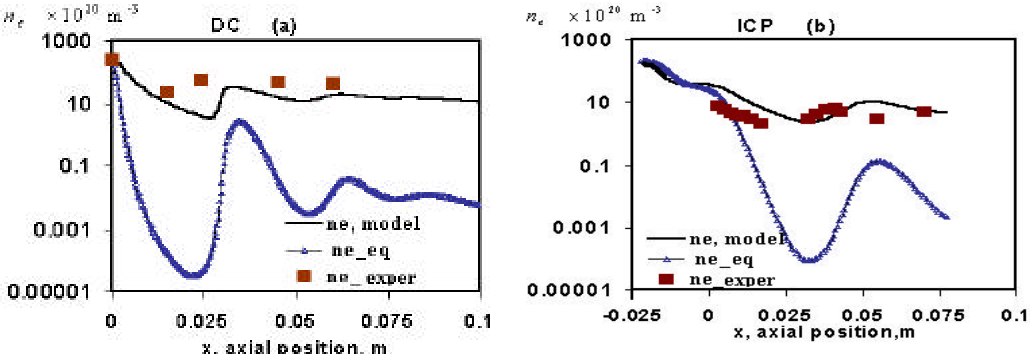

Fig.6 Comparison of the axial profiles of predicted by the model electron number density n_e with the experimentally measured electron number densities n_{e_cont} and with the equilibrium ne_{eq} and frozen ne_{-fr} values in supersonic DC (a) and ICP (b) plasmas.

Fig.5 that in both jets, the axial heavy particle and electron temperatures drop in the expansion. In DC jet, and due to higher degree of under-expansion, the axial heavy particle temperature drops to lower values than in the ICP jet; the electron temperature, however reaches the same minimal values at the end of the first expansion zone in both jets. In this region, and within the DC jet, the three-particle recombination, with electrons acting as third bodies, is a more essential process than that in the ICP jet, and this recombination heats the electrons, preventing their temperature from experiencing a substantial decrease. The electron number density at the chamber inlet is higher in the DC jet than in the ICP jet (Fig.6). In the expansion zone, however, this density drops more significantly in the DC jet (due to the larger degree of under-expansion) than in the RF jet, so that the average axial value of the electron number density does not practically differ in these jets. As may be seen from Fig.6, this value is several orders of magnitude higher than the equilibrium value in both cases. The spectroscopic measurements give reliable data on electron number density, however, the electron temperature appears to be overestimated if one assumes local Saha equilibrium utilizing Boltzmann plot technique (Fig.5a).

6. Analysis of the results

The main findings can be summarized as follows.

1. The place of plasma formation, the type of discharge and the static pressure in the plasma formation region are the differences between plasmas formed in different supersonic plasma configurations. Let us consider these differences in detail.

a) Plasma formation region

In ICP supersonic configuration, thermal plasma is firstly formed in the RF discharge and is then ccelerated in the nozzle. In DC arc on the contrary, the plasma is formed inside the supersonic nozzle, i.e. in the region of acceleration (Fig.1a). Due to this fact this plasma chan be slightly under-ionised comparing with the equilibrium values of the ionisation degree. Besides, this plasma can deviate substantially from the thermal equilibrium already at the chamber inlet.

b) Static pressure in the torch

We should mention that the pressures in the plasma formation region are different depending on the plasma set-up. For instance, in ICP discharge, the static pressure in plasma formation region is 0.5-2 atm. In DC arc the pressure in the discharge regions are slightly sub-atmospheric: and 0.4-0.5 atm in DC arc. The mentioned pressure differences should be taking into consideration when one compares the supersonic plasmas formed by these sources.

c) The type of discharge

It is well known that different discharges produce plasma with different properties. The maximal temperature attained in ICP discharge plasma is about 10000K; this plasma is usually very close to LTE. In the DC arc discharge, however, the plasmas can slightly deviate from LTE due to the fact that the plasma is accelerated in the formation region. This is why we have assumed that the temperature of electrons at the outlet of DC plasma nozzle is about 11000-12000K while the heavy particle temperature is 7500-8000K. Probably, it is not a big mistake to assume that all the mentioned discharges ionise plasma up to equilibrium values of the ionisation degree. With these assumptions in mind, we obtain the results showing that the ionisation degree reached in the DC plasma is slightly higher than the ionisation degree reached in the plasma produced by ICP discharge.

2. The pressure in the expansion chamber, the nozzle design (its outlet Mach number) and the rarefaction parameter as well as the Reynolds number are the important parameters for every supersonic plasma system. The nondimensional parameters defining the structure of weakly ionised supersonic plasma jet are the pressure ratio $n = P_{in}$ ▯ P_{ch} the nozzle outlet Mach number M, and the Reynolds number Re, as well as the Prandtl number Pr, the Schmidt number Sc, the ratio of the stagnation temperature in the jet to the ambient temperature $T_0 / T_¥$ and the isentropic exponent g. Note that the nozzle geometry also influences the jet structure mainly because of the fact that this geometry defines the nozzle outlet Mach number. It is important to understand that the physical state of a nonequilibrium plasma jet flow depends on the flow history, i.e. it depends on the flow properties upstream of the chamber inlet described in the previous paragraph.

a) Chamber pressure (rarefaction degree)

To categorize pressure regimes one can use a rarefaction parameter $x = d\,(P_{st}\,P_{ch})^{1/2} / T_{in}$, where d is the chamber inlet diameter, P_{st} is the stagnation pressure at chamber inlet, T_{in} is the heavy particle temperature at the chamber inlet [9]. The values of $x > 5{\cdot}10^{-3}$ N/m/K correspond to the continuum regime, the values of $x < 3{\cdot}10^{-4}$ N/m/K correspond to the scattering regime. For the DC arc flow regime the values of the rarefaction parameter are about $x = 0.2$ N/m/K, which corresponds to the essentially continuum flow. For the ICP supersonic flow regime the values of the rarefaction parameter are in the diapason of x from 0.5 to 1 N/m/K. These values are slightly larger than for DC plasma.

b) Reynolds number

In order to categorize the flow regimes one can take the following value of the Reynolds number [2] $\mathrm{Re}_L = \mathrm{Re}_* / \sqrt{N}$, where $N = P_{st}/P_{ch}$, $\mathrm{Re}_* = r_* U_* d_* / m_*$; r_*, U_*, m_* are the values of density, velocity and viscosity in the nozzle critical section that has a diameter d_*.. For the DC arc flow regime the values of the Reynolds numbers are about Re_L=100, which corresponds to the laminar regime in the mixing boundary layer in the initial region of the jet. For the ICP supersonic flow regime the values of the Reynolds numbers are in the diapason of Re_L from 30 to 60. These values are slightly lower than the Reynolds numbers of DC plasma. This range of Reynolds numbers also corresponds to the laminar regime in the mixing boundary layer in the initial region of the jet, however they show that some effects of the rarefaction can be noticeable as the Knudsen number is proportional to M / Re $_L$.

7. Summary and conclusions

The common features between DC and ICP under-expanded supersonic plasmas are as follows:

- A structure of alternating expansion and compression zones can be found in both cases.
- Both under-expanded supersonic plasma jets are characterized by the electron overpopulation (comparing with LTE values) and by the occurrence of thermal and Boltzmann nonequilibrium.
- Typical operating regime of both set-ups corresponds to the continuum regime.
- The Reynolds numbers corresponds to the laminar regime of the mixing boundary layer in the initial region of the jet.

The important differences between these two supersonic plasma configurations are as follows:

- In the DC torch the plasma is formed and accelerated at the same time in the sub-atmospheric conditions. Due to this fact, the plasma deviates from local thermodynamic equilibrium (LTE) in the formation region. The ICP torch with supersonic nozzle a thermal plasma is firstly formed and it is then accelerated.
- The ionization degree reached in the DC plasma is slightly larger than the ionization degree reached in the plasma produced by ICP discharge.
- For under-expanded jets, the pressure ratio n = P_{in}/P_{ch} has a significant impact both on the hydrodynamic structure of the jet core and on the physical properties of the plasma. Because of the difference of the pressure ratio, the ICP jet is mildly under- expanded (containing only oblique shock waves in the core region), while DC jet is strongly under-expanded (containing a strong normal shock on the core region).
- In a DC jet due to higher degree of under-expansion, the axial heavy particle temperature drops down to smaller values than in ICP jet, the electron temperature, however reaches the same minimal values at the end of the first expansion zone in both jets. In this region of the DC jet the role played by three-particle recombination with electron as a third body is more important than in the ICP jet, and this recombination heats the electrons preventing their temperature from the substantial decreasing.
- The electron number density at the chamber inlet is larger in DC jet than in ICP jet. In the expansion zone, however, this density drops more significantly in DC jet (due to the larger degree of under-expansion) than in RF jet, so that the average axial value of the electron number density practically does not differ in these jets.
- The effect of the nozzle design on DC and ICP supersonic plasma properties is expected to be different because in DC torch the plasma is formed and accelerated in the nozzle while in ICP configuration the plasma is only accelerated there.

Based on the presented results, we conclude that the ratio of the static pressure at the chamber inlet to the chamber pressure together with the Mach number at the nozzle outlet, the Reynolds number and the rarefaction parameter define the structure of under-expanded supersonic plasma jet while its physical properties depend on the history of the flow.

References

[1]Boulos, M.I., Fauchais, P. and Pfender, E. Thermal Plasma Fundamentals and Applications, Plenum Press, vol. 1 (1994)
[2] Luk'yanov, G.A. Supersonic plasma jets, Leningrad, Mashinostroenie, 269p (1985) (in Russian)
[3] Sabsabi, M., Vacquié, S., Gravelle, D.V. and Boulos, M. I. J. Phys. D: Appl. Phys. 25 425 (1992)
[4] van de Sanden, M.C.M., van den Bercken, R. and Schram, D.C. Plasma Sources Sci. Technol. 3, 511 (1994)
[5] George, C., Candler, G., Pfender, E. J. Phys. D: Appl. Phys, 31, 2269 (1998)
[6] Selezneva, S.E., Rajabian, M., Gravelle, D., and Boulos, M. I. J.Phys.D: Appl. Physics, 34, 2862 (2001)
[7] Selezneva, S.E. and Boulos, M.I. J.Appl.Phys 91, 5 (2002)
[8] Selezneva, S.E., Sember, V., Gravelle, D.V., Boulos, M.I J. Phys. D: Appl. Physics, 35, 12, 1338 (2002)
[9] Muntz, E. P., Hamel, B.B., Maguire, B.L. AIAA Journal 8 (9) 1651 (1970)

Plasma surface modification of engineering thermoplastics: Relevance to adhesion of electroless Ni or Cu films

M. Charbonnier, Y. Goepfert, M. Romand and A. Fares-Karam

Laboratoire de Sciences et Ingénierie des Surfaces, Université Claude Bernard - Lyon 1, 69622 Villeurbanne, France

Abstract

This paper deals with plasma treatments of thermoplastics (30 % glass-reinforced poly(butylene terephthalate) and poly(phenylene sulfide)) in a nitrogenated atmosphere (N_2 or NH_3) and with electroless metallization (Ni or Cu) on the surface of such materials. The original approach implemented in this work has allowed to coat substrates which are known to be very resistant to metal deposition when standard electroless procedures operating exclusively in wet-chemical baths and solutions are used. This economically attractive and environmentally friendly process involves successively: (i) grafting of nitrogenated functionalities on plasma-treated surfaces, (ii) catalyst attachment on the so-functionalized surfaces, through a direct chemisorption, of palladium species in a simple, acidic palladium chloride solution, and (iii) reduction of the so-chemisorbed Pd(+2) species to the Pd(0) state in a hypophosphite solution. This last step is required to initiate the electroless metallization in commercial electroless plating baths to get rid of catalytic sites poisoning due to the presence of stabilizers. Adhesion tests are used to prove the "quality" of the formed metal / polymer interface, i.e. the efficiency of the proposed method.

1. Introduction

The electroless metallization of engineering thermoplastics has found a wide variety of applications over the last two decades, particularly in the electrical and electronics industries. For example, this deposition process is currently employed in the manufacturing of flexible printed circuit boards, ohmic contacts, lightweight connectors as well as in that of housings for electronic units or systems which must be able to work without generating outside disturbing electromagnetic waves [1, 2]. Regardless of the nature of these applications, it is clear that both performances and lifetime of devices implemented from electroless plating techniques are largely dependent on the adhesion of metal to plastic substrates. Unfortunately, the standard procedures of electroless metallization are often responsible for detrimental effects which lead to poor product performances and premature system failure. Furthermore, some new materials available today have proved to be very resistant to metal deposition by the conventional chemical way. In addition, the standard procedures involve, to a large extent, the use of many chemicals which cause a lot of environmental problems and are, in part, responsible for excessive processing costs.

For a better understanding of what follows, it is useful to remind that the electroless process takes place in a solution containing ions of the metal to be deposited (generally Ni or Cu), a strong reducing agent which provides electrons necessary to the chemical reduction of the metal ions, and buffering and complexing agents which are required to inhibit an in-service bath decomposition and control the parameters of the deposition process. The specificity of the latter is that the chemical reduction is catalysed by the deposited metal itself, hence the "autocatalytic" term also in use to name the plating method. However, concerning dielectric substrates, initiation of the chemical reduction occurs only if the material surface has been previously rendered catalytically active. This step is generally carried out using some more or less complex ways which lead to the attachment of palladium containing particles to the material surface.

The industrial surface preparation of plastic parts for electroless plating is today relatively complex and specialized. Figure 1 (A) represents a simplified scheme of the procedures which are required to perform the chemical preparation of plastic surfaces prior to the electroless plating itself. During these procedures (preplate cycle) the plastic parts are usually subjected to various operations including: cleaning and/or "predipping", etching, neutralization, catalysis and acceleration. Briefly cleaners (often mild alkaline solutions) are used to remove light soils. "Predips" are appropriate solvents used to attack or swell the surface of plastics which are normally hard to etch. Etchants are generally highly concentrated solutions of chromic and sulphuric acid used to produce a micro-roughened oxidized surface able to provide anchoring sites for the deposited metal. After etching, the plastic components are thoroughly rinsed, and then immersed in a neutralization bath (usually an alkaline solution) in order to remove (neutralize) the oxidizing agents (coming from the etching solution) which are harmful to the subsequent operation. After rinsing, the substrates are subjected to an activation step which is performed to introduce the catalytic nuclei on the material surface. For this purpose, the use of a colloidal solution containing tin chloride ($SnCl_2$), palladium chloride ($PdCl_2$) and hydrochloric acid is in common industrial practice. After rinsing, the "activated" substrates are dipped in an acceleration (or solubilizing) bath (usually an organic or mineral acid) with a view to removing the excess of stannous species which prevent palladium from acting as a catalyst able to initiate the electroless plating. Note that the sequence of operations described above can include up to fifteen or so steps, depending on the specific conditions and materials involved. As we can imagine it, the preplate cycle leading to electroless plating requires the consumption of many chemicals and specialty formulations, hence the need to take into consideration many problems such as bath control and replacement, and chemical waste disposal. In addition, such a preplate cycle is very time-consuming. Under these conditions, it is highly desirable to develop alternative approaches for preparing substrate surfaces before the electroless deposition. These new approaches should be technologically, ecologically and economically more attractive than those in common use in the present time. It is the aim of the present work which describes the development of new routes involving, prior to the plating step itself, the surface modification of some thermoplastics via a plasma treatment and the direct adsorption of palladium species making the treated surface catalytic for the electroless reaction. The process needs a reduced number of steps which are reported in figure 1 (B). They involve the direct exposure of the plastic substrates to a reactive low pressure plasma in a nitrogenated atmosphere (N_2 or NH_3) with a view to grafting specific functionalities (mainly amino groups) on the treated surfaces. Subsequently, the catalysis of the so-functionalized surfaces is made through a simple immersion in a dilute, acidic palladium chloride ($PdCl_2$) solution [3-16]. When industrial plating baths are used, an additional step consisting of a Pd(+2) to Pd(0) pre-reduction is necessary [15]. Of course, it is very important to understand how the catalytic species are attached at the substrate surfaces and how they operate at the time of the deposit initiation step, in order to elaborate a strong adhesion at the metal / polymer interface. This is also, in part, the objective of the present work.

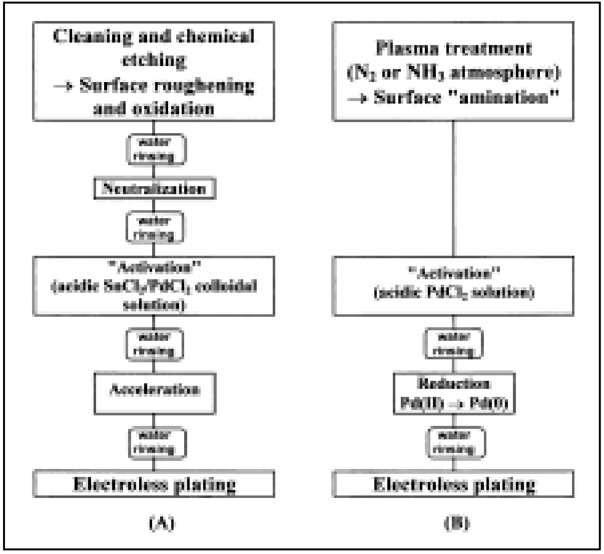

Figure 1: Schematic diagram of the electroless plating process according to: (A) the conventional industrial method involving, among others, an etching / oxidizing chemical treatment of the plastic substrates and the subsequent activation and acceleration steps and (B) the proposed method involving the plasma treatment of the plastic substrates, the direct "activation" in an acidic $PdCl_2$ solution, i.e. through the use of a tin-free catalyst process and a reduction step.

2. Experimental

Surface pretreatments and subsequent electroless metallizations were carried out on injection-moulded thermoplastics, namely on 30 % glass-reinforced poly(butylene terephthalate) and poly(phenylene sulfide) substrates (denoted in the following as PBT and PPS, respectively). Before processing, these substrates were ultrasonically cleaned in ethanol.

Plasma treatments were performed in a parallel plate RF reactor operating in the reactive ion etching mode (RIE 80 from Plasma Technology, England) under N_2 or NH_3 atmosphere (100 mTorr, 100 sccm, 0.5 W cm^{-2}). Subsequently to plasma treatments, polymer surfaces were subjected to an "activation" step by immersion in an acidic palladium chloride solution (0.1 g dm^{-3} $PdCl_2$ + 0.1 cm^3 dm^3 HCl), which causes the chemisorption of Pd(+2) species, and then to a chemical reduction of the grafted Pd(+2) species to the Pd(0) state by immersion in a hypophosphite solution (10 g dm^{-3} $NaH_2PO_2 \cdot H_2O$) [15]. Finally, electroless metallization was performed using commercial Ni or Cu plating solutions supplied by Enthone-OMI, France. After metallization, the coated samples were rinsed and dried under a nitrogen flow.

X-ray photoelectron (XPS) analyses were performed with a Riber SIA 200 spectrometer using a non-monochromatized Al K_α X-ray source and a take-off-angle of 65° with respect to the specimen surface. All spectra were referenced to the C 1s peak at a binding energy of 285.0 eV characteristic of C-C and C-H bonds. Wettability and surface energy measurements were performed using the static sessile drop method with an automatic apparatus (GBX Scientific, Instruments, Romans/Isère, France). Adhesion measurements were carried out using the ASTM D-3359 cross-hatch tape test and a conventional tensile test (pull-off test) in which a force applied to a glued element is exerted perpendicular to the surface of the metal coating.

3. Results and discussion

Figure 2 shows XPS wide-scan spectra of (a) an ethanol-cleaned PBT substrate, (b) and (c) the same material as (a) after a plasma treatment for 1 min in N_2 and NH_3, respectively. Clearly, these spectra reveal the occurring of significant surface modifications. As shown from data in Table 1, the plasma treatments have mainly caused a decrease in the carbon surface concentration and an increase in the nitrogen surface concentration. For the purpose of the present work, the most important point to emphasize is the relatively high surface concentration in nitrogen (8.2 at. %) grafted by the NH_3 plasma treatment under the experimental conditions used. These changes in surface composition are associated with a cleaning / etching of the substrate surface [17] and a grafting of nitrogenated polar groups (above all amino-groups) (see for example [18]). As a result, the plasma-treated surfaces have become more reactive as shown by the large increase of the surface wettability, the water contact angle decreasing from 86.6° to about 10° for a NH_3-plasma treatment of 1 min (Fig. 3). In other respects, figure 4 represents XPS wide-scan spectra of the plasma-treated substrates after the "activation" step, i.e. after their immersion for 1 min in a simple acidic $PdCl_2$ solution, rinsing and drying. Spectra (b) and (c) are relative to plasma-treated substrates in N_2 and NH_3, respectively. They show that palladium species are adsorbed (0.7 and 2.0 at. % in (b) and (c) experiments, respectively) to the surfaces carrying nitrogenated functionalities. Again, these experiments confirm that NH_3 plasma treatments are more efficient than N_2 plasma treatments to graft nitrogenated species, and therefore Pd species. Note that such an attachment of palladium (in the Pd(+2) form as shown by XPS) corresponds, in fact, to a true chemisorption on the nitrogenated groups present at the surface of the treated substrates. Indeed, we have shown that this Pd(+2) chemisorption operates specifically on nitrogen atoms given that it does not occur on surfaces grafted with oxygenated functionalities by plasma treatment (cf. Fig. 4, spectrum (a)), VUV-irradiation or chemical oxidation [15]. In addition, we have also evidenced that the surface concentration in Pd varies concomitantly with that of the grafted nitrogenated species (experiments carried out on polyimide substrates (Kapton® HN 500) by plasma treatments in N_2 or NH_3 atmosphere, or VUV-irradiation in NH_3 for different treatment times) [14, 15]. In other words, the higher the surface concentration in nitrogenated species, the higher that of the adsorbed Pd(+2) species. This means that the attachment of Pd(+2) species at the surfaces carrying nitrogenated groups results in no case from physisorption phenomena. Indeed, the latter would not lead to the observed selectivity and the Pd(+2) species should be then equally attached at surfaces carrying nitrogenated and oxygenated functionalities. For all these reasons, the basis mechanism of the Pd(+2) species attachment would rather consist in the formation of coordinate covalent bonds, N atoms giving their lone pair of electrons to Pd(+2) ions so as to complete their 4d electronic level [16].

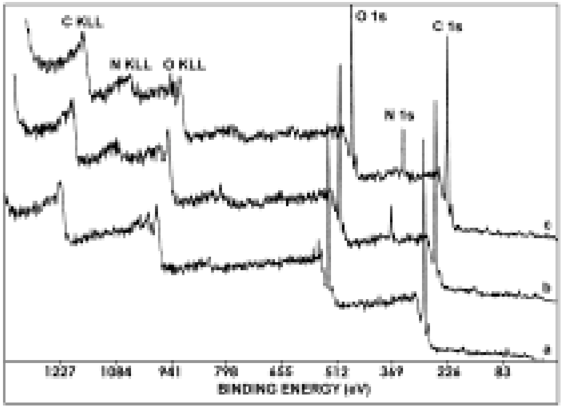

Figure 2: XPS wide-scan spectra of PBT substrates: (a) ethanol cleaned, (b) and (c) the same as (a) after plasma treatment in N_2 and NH_3, respectively. Note that the energy scale is associated with the bottom spectrum (a). Other spectra are shifted for sake of convenience.

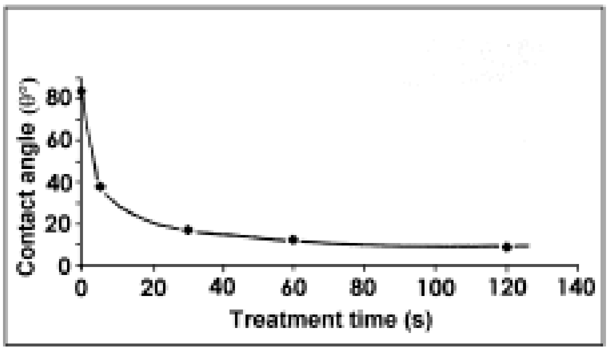

Figure 3: NH_3 plasma treatment of PBT substrates. Influence of the plasma treatment time (100 sccm, 100 mTorr, 0.5 W cm^{-2}) on the water contact angle (θ in degrees). Note that similar results are obtained in the case of a N_2 plasma treatment.

Table 1: Surface atomic concentrations (XPS analysis) of PBT substrates after plasma treatment for 1 min in N_2 or NH_3, then after "activation" by immersion in a $PdCl_2$ solution for 1 min and water-rinsing

Surface treatment	Surface composition (at. %)				
	C	O	N	Pd	Cl
Ethanol-cleaned substrate	77.5	22.5			
N_2 plasma	66.3	28.7	5.0		
N_2 plasma + Pd "activation"	72.3	23	3.6	0.7	0.4
NH_3 plasma	70.2	21.5	8.2		
NH_3 plasma + Pd "activation"	68	23	5.8	2	1.2

As already noted, palladium is chemisorbed on the N_2 or NH_3 plasma-treated surfaces in the Pd(+2) form. When such substrates are dipped in a home-made electroless Ni solution (bath containing only the Ni salt ($NiSO_4{\cdot}6H_2O$), the reducing agent (sodium hypophosphite $Na_2H_2PO_2$) and a complexing agent (lactic acid)), the plating is initiated after an incubation time of about 10-15 s. On the other hand, when the same substrates are dipped in a home-made electroless Cu solution (bath containing only the Cu salt ($CuSO_4{\cdot}5H_2O$), the reducing agent (formaldehyde, HCHO) and a complexing agent (sodium potassium tartrate, $KNaC_4H_4O_6{\cdot}4H_2O$ and ethylenediamine tetraacetic acid, EDTA) no metal deposition is observed. As shown by XPS, the reducing agent present in the home-made Ni plating bath is quite able to reduce the Pd(+2) species to the Pd(0) state, while that present in the Cu plating bath is not strong enough to provoke this same reduction or, at least, is inoperative for kinetic reasons. In other words, this result means that Pd(0) operates as the actual catalyst capable of initiating the electroless plating [15]. In other respects, when the N_2 or NH_3 plasma-treated substrates are activated in $PdCl_2$ and dipped in the commercial electroless Ni or Cu bath used in the present work, no metal plating occurs. Comparison between experiments carried out with home-made and commercial electroless Ni solutions underlines the fact that some additives present in the commercial solutions prevent Pd(+2) reduction from taking place. As a result, this means that such a reduction must be performed prior to immersion of the "activated" substrates in the plating baths. When this reduction is performed, plating with the home-made electroless Ni or Cu solutions occurs without any initiation time [16], while only a few seconds are necessary to initiate the deposit with the commercial baths. Figure 5 is relative to PBT substrates which are NH_3 plasma-treated for 1 min, activated in a $PdCl_2$ solution, and then subjected to a reduction of the Pd(+2) species by immersion for different times in a simple hypophosphite solution operating under the same conditions (concentration, pH and temperature) as those used for the electroless Ni bath. It shows that the Pd 3d XPS spectra are progressively shifted towards the low binding energy side as the treatment time in the hypophosphite solution increases. This proves that an increasing number of Pd(+2) species (Pd $3d_{5/2}$ peak at 338.0 eV) is reduced to the Pd(0) state (Pd $3d_{5/2}$ peak at 335.5 eV). Under these conditions, substrates with a sufficient surface density of palladium in the Pd(0) state can be plated in the industrial baths which contain stabilizers with a very short initiation time. Commonly, bright and well-adherent Ni or Cu films are obtained when the "activated" substrates are treated for only 1 or 2 min in the

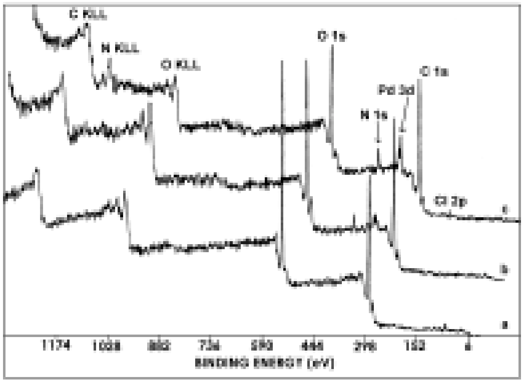

Figure 4: XPS wide-scan spectra of PBT substrates grafted with nitrogenated functionalities via the surface treatments (b) and (c) described in figure 2, and subsequently "activated" by immersion in an acidic $PdCl_2$ solution, rinsed and dried. For comparison, spectrum (a) is relative to a PBT substrate plasma-treated in O_2 and subsequently immersed in the same acidic $PdCl_2$ solution. Note that the energy scale is associated with the bottom spectrum (a). Other spectra are shifted for sake of convenience.

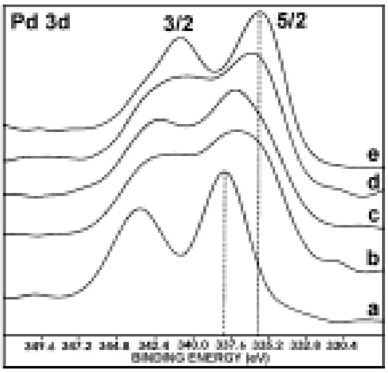

Figure 5: Pd 3d XPS spectra of PBT substrates (a) after surface functionalization by NH_3 plasma treatment and "activation" by an acidic $PdCl_2$ solution, (b), (c), (d) and (f), the sames as (a) after immersion in a hypophosphite solution for 3, 5, 10 and 15 min, respectively.

hypophosphite solution and further dipped in the plating baths. On the other hand, it is interesting to note that the Pd(+2) reduction does not occur when the "activated" substrates are dipped in a simple formaldehyde solution operating also under the same conditions (concentration, pH and temperature) as those used for the electroless Cu bath. This confirms that formaldehyde cannot reduce the Pd(+2) species in the electroless Cu baths, and therefore emphasizes the need to operate this reduction in a previous step. In addition, note that, as soon as the Cu deposition is initiated due to the presence of Pd(0) species, Cu plating progresses by autocatalysis since formaldehyde is capable of reducing Cu(+2) ions to Cu(0). Finally, it is important to highlight that stabilizers and other additives present in commercial plating solutions can act as poison of the Pd(+2) "catalytic" sites when the reduction step is not carried out. In conclusion, the reduction step in a solution containing hypophosphite (or another suitable reducing agent) is therefore an essential operation to perform electroless plating in industrial conditions.

From a practical point of view, it is now important to observe that the results described above and dealing with PBT substrates can be extended to many other engineering thermoplastics. For example, figure 6 is relative to PPS, a polymer-based material containing a relatively high concentration in sulphur. It shows XPS wide-scan spectra of (a) an ethanol cleaned PPS substrate, (b) the same material as (a) after a plasma treatment in NH_3 for 1 min, and (c) the same material as (b) after "activation" by immersion in the acidic $PdCl_2$ solution. These spectra confirm that a NH_3 plasma treatment is efficient for grafting nitrogenated species at the substrate surface and that a relatively high surface concentration in palladium (1.8 at. % in this experiment) is chemisorbed on the grafted nitrogenated species.

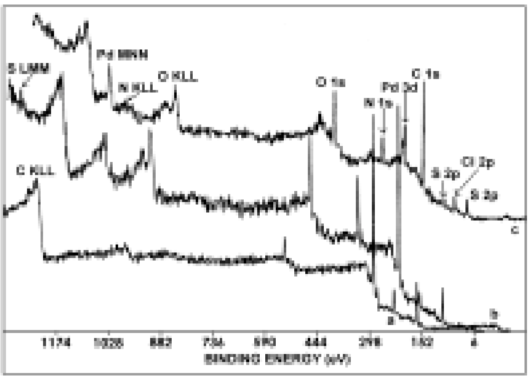

Figure 6: XPS wide-scan spectra of PPS substrates before (a) and after (b) surface functionalization via plasma treatment in NH_3. Spectrum (c) is the same material as (b) after "activation" by immersion in an acidic $PdCl_2$ solution. Note that the energy scale is associated with the bottom spectrum (a). Other spectra are shifted for sake of convenience.

Examples previously described deal with engineering thermoplastics which can hardly be metallized via the conventional electroless methods using, in full, wet-chemical processes. Figure 7 represents a photomicrograph of a complex plastic housing for electronic equipments after electroless metallization via the original approach developed in the present work. This part was coated successively with a 12 µm thick electroless Cu layer and a 3 µm thick electroless Ni layer. Metal coatings achieved in this way are bright and without apparent defects. Note also that after a first electroless deposition of a thin metal film (Ni or Cu) the metallization can be pursued by using a conventional electroplating process, and even, completed by deposition of a second electroless film (e.g. Ni to protect the underlying Cu against oxidation).

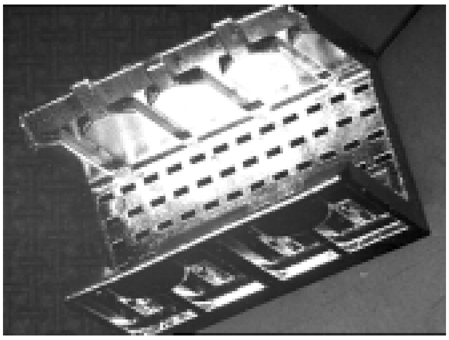

Figure 7: Photograph of a housing for electronic unit coated with a combination of electroless Cu and Ni deposit (15 µm in thickness).

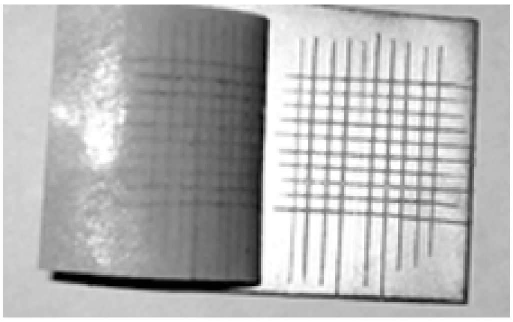

Figure 8: Photograph of a 3 µm thick Ni deposit subjected to a Scotch®-tape test.

Grafting of nitrogenated groups on carbon atoms at the polymer surface and further chemisorption of palladium species on these nitrogenated functionalities lead to the formation of C-N-Pd covalent bonds. As a result, this suggests that the so-formed catalytic species are strongly attached to the polymeric substrate, and therefore that a high adhesion can be achieved at the metal / polymer interface. The fact that relatively thick metal coatings (cf. Fig. 7) can be deposited without any delamination appears to support the previous statement. However, there is great practical importance to get more information about the "quality" of the metal / polymer interface and to determine the actual locus of failure if the latter occurs, for example, during a mechanical test. In a first series of experiments, adhesion of Ni and Cu coatings to their substrates was investigated using a Scotch® tape peel test (cross-hatched peel test). Figure 8 is relative to the case of a 3 µm thick Ni film deposited on a PBT substrate. As can be seen, a good practical adhesion is obtained since no metal part is stripped off by the tape. Unfortunately, this simple test is only qualitative in nature since it is only capable of discriminating low and high adhesion levels. For obtaining more quantitative data, composite systems were subjected to a pull-off test. These specimens were elaborated by coating PBT substrates with a first electroless Ni film which was successively covered with Cu and Ni films deposited via different combinations of electroplating or electroless processes. In each case, the whole thickness of the metal coating is about 12-13 µm. Results from the test show that practical adhesion strengths are about twice the values required for the concerned industrial applications, and in other respects, that fracture is not at the metal / substrate interface but within the polymeric material below the interface. Good practical adhesion is also confirmed by using thermal shocks.

Conclusions

The work reported in this paper confirms the specific interest of plasma-assisted processes in order to graft nitrogenated functionalities on polymeric substrates which have to be subsequently rendered catalytically active (via the chemisorption of palladium species) toward electroless metallization (Ni or Cu deposition). In this study, the proposed method is shown to be very efficient for depositing relatively thick metal films (10-15 µm or more) on the surface of PBT and PPS thermoplastics which are very resistant to electroless plating when standard electroless procedures operating exclusively in wet-chemical way are used. In comparison with the surface conditioning steps of these wet-chemical procedures, plasma treatments such as those performed in the present investigations, have many significant advantages as they are economically attractive and environmentally friendly.

References

[1] G.O. Mallory and J.B. Hadju - "Electroless plating: Fundamentals and Applications", American Electroplaters and Surface Finishers Society, Orlando, FL, USA, 1990.

[2] J.J. Kuzmik - In "Electroless plating: Fundamentals and Applications", G.O. Mallory and J.B. Hadju, Eds., American Electroplaters and Surface Finishers Society, Orlando, FL, USA, 1990, pp. 377-399.

[3] M. Charbonnier, M. Alami, M. Romand - J. Electrochem. Soc. **143** (2), 472-480 (1996).

[4] M. Alami, M. Charbonnier, M. Romand - J. Adhesion **57**, 77-90 (1996).

[5] M. Alami, M. Charbonnier, M. Romand - Plasmas Polym. **1** (2), 113-126 (1996).

[6] M. Charbonnier, M. Alami, M. Romand - J. Appl. Electrochem. **28**, 449-453 (1998).

[7] M. Romand, M. Charbonnier, M. Alami, J. Baborowski - In "Metallized Plastics 5 & 6: Fundamental and Applied Aspects", K. L. Mittal Ed., VSP, Utrecht, The Netherlands, 1998, pp. 3-23.

[8] M. Charbonnier, M. Romand, M. Alami, Tran Minh Duc - In "Polymer Surface Modification: Relevance to Adhesion", Vol. 2, K.L. Mittal Ed., VSP, Utrecht, The Netherlands, 2000, pp. 3-27.

[9] M. Charbonnier, M. Romand, M. Alami - In "Polymer Surface Modification: Relevance to Adhesion", Vol. 2, K.L. Mittal Ed., VSP, Utrecht, The Netherlands, 2000, pp. 29-43.

[10] M. Charbonnier, M. Romand, G. Stremdoerfer, A. Fares-Karam - Recent Res. Devel. Macromol. Res. **4**, 27-43 (1999)

[11] M. Charbonnier, M. Romand, E. Harry, M. Alami - J. Appl. Electrochem. **31**, 57-63 (2001).

[12] M. Charbonnier, M. Romand, H. Esrom, R. Seeböck - J. Adhesion **75**, 381-404 (2001).

[13] M. Charbonnier, M. Romand, U. Kogelschatz, H. Esrom, R. Seeböck - In "Metallized Plastics 7: Fundamental and Applied Aspects", K.L. Mittal Ed., VSP, Utrecht, The Netherlands, 2001, pp. 3-26.

[14] M. Romand, M. Charbonnier, Y. Goepfert - In "Metallization of Polymers 2", E. Sacher Ed., Kluwer Academic / Plenum Publishers, New York, 2002, pp. 191-205.

[15] M. Charbonnier, Y. Goepfert, M. Romand - In "Polyimide and Other High Temperature Polymers", Vol. 2, K.L. Mittal Ed., VSP, Utrecht, The Netherlands, 2003, pp. 1-26.

[16] M. Charbonnier, M. Romand - Int. J. Adhesion Adhesives (in press).

[17] R. d'Agostino - "Plasma Deposition, Treatment and Etching of Polymers", Academic Press, Boston, 1990.

[18] J.E. Klemberg-Sapieha, O.M. Küttel, L. Martinu, M.R. Wertheimer - J. Vac. Sci Technol. **A 9**, 2975-2981 (1991).

XPS Study of Silicon Surface Modifications Induced by CF_4/O_2 Plasma Exposure

G.Arena[1], C.Donato[1], P.Vasquez[1], A.Scandurra[2], A.Fichera[3] and O.Puglisi[3,4]

[1]*STMicroelectronics – Stradale Primosole 50, 95100 Catania, Italy*

[2]*Laboratorio Superfici ed Interfasi - Consorzio Catania Ricerche c/o STMicroelectronics, Stradale Primosole 50, 95100 Catania, Italy*

[3]*Dipartimento di Scienze Chimiche dell'Universita' di Catania, V.le A. Doria 6, 95100 Catania, Italy*

[4]*Istituto Nazionale per la Fisica della Materia Unità di Catania*

Abstract

Reactive Ion Etching (RIE) of silicon oxide is largely used in electronic devices fabrication for contacts formation and vias opening processes. At contact levels, highly selective removal of SiO_2 over Si processes are achieved by the use of carbon rich fluorocarbon plasmas ($CF_4/CHF_3/Ar$). This method is useful for deposition of a thick layer of fluorocarbon film on the sidewall in order to protect it from the etchant species and to guarantee the required anisotropic etch behaviour. On the other hand, as SiO_2 etching reactions occur under ion bombardment, implantation of C-containing species into the Si substrate results during the overetch step. This leads to a degradation of the quality of metal/silicon interface affecting the device electrical performances.

In order to remove the damaged region, an *in situ* soft silicon etch is performed after the oxide bulk etch step. This process is usually performed using a fluorine based plasma at high process pressure and low RF power, in order to minimize the ion bombardment effects.

In this paper the $CF_4/CHF_3/Ar$ plasma treated silicon surfaces have been analyzed by X-ray Photoelectron Spectroscopy (XPS) and the presence of *teflon-like* polymers have been observed without any softetch step. Several softetch conditions have been investigated and the silicon surface compositions are shown in this work. Moreover, the importance of the O_2 addition for the softetch effectiveness is also demonstrated.

Introduction

The anisotropic selective ion etching of SiO_2, widely used in microelectronic manufacturing and microstructure fabrication, is known to induce damage in both the silicon surface and sub-surface regions exposed at the end of the etching process.

Reactive ion Etching is carried out in a reactor where reactive species (electrons, ions, photons) have energies in the range of tens to several hundred electronvolt(1). The bombardment of the substrate by energetic ions generated in the plasma, ensures the directionality of the pattern transfer. The electrons and photons are by-products of these reactions.

Three types of SiO_2 dry etching damage mechanisms have been identified: residue and surface film formation, contamination by the etching species, impurities and lattice damage, due to the ion bombardment and radiation exposure. Moreover, dry etching can roughen the silicon surface(2).

These damage and contamination effects produce an anomalous electrical behaviour of metal/silicon interface contacts, affecting the contact resistance.

For these reasons damage formation and its removal are critical issues in modern electronic devices manufacturing.

In the reactive ion etching systems, characterized by a narrow gap parallel plate (1.2 cm), typically 200Å deep crystal defects region is created, due to the ion bombardment and carbon implantation. In particular Si-C species can be formed at a depth up to 200Å, while C-O species can be formed up to 400Å(3,4).

Therefore, it is important that a recovery treatment follows the dry etch process, in order to remove the silicon damaged region without imparting any other damaging and/or contamination to the silicon surface. This technique is typically an *in-situ* process in the same plasma etcher, in a step following the bulk oxide etch. This dry treatment is usually defined as soft-silicon etch (SSE) and it is performed in a high-pressure / low-power CF_4/O_2 containing plasma.

In this work the impact of the oxygen concentration in the SSE plasma has been investigated by XPS and by AFM techniques Moreover, thermal wave measurements of the treated silicon surface have been also performed.

Experimental

N-type silicon substrates were used for sample preparation. The used reactor was a commercial LAM Rainbow 4526i etch tool. A sketch of the etching chamber is showed in Figure 1.

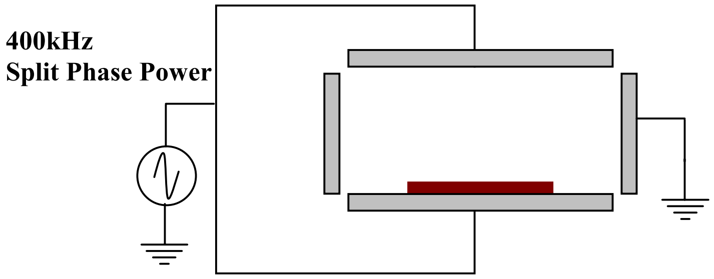

Fig. 1. Reactor chamber sketch.

The tool uses a low frequency power supply (400 kHz) and a small gap between the electrodes, providing a power density of about 4 Watt/cm^2. Split phase technology allows to eliminate current flow from either electrodes to the chamber wall and maximising the current flow between the two electrodes. To achieve this, the 400kHz power is equally split between upper and lower electrodes and at same time the phase is shifted so that the two electrodes are 180^o out of phase. The upper electrode is silicon made, while the wafer is mechanically clamped by a ceramic ring and cooled by a backside helium flow.

A mixture of CF_4, CHF_3, and Ar was used as reaction gas. In order to create the damaged layer, the used conditions were: Pressure 500mTorr, RF power 550 Watt, CF_4 flow 25 sccm, CHF_3 flow 25 sccm and Ar flow 100 sccm, etching time 60sec.

After the etching process every samples was in situ treated with another plasma step, in order to remove the damaging created in the previous step. The used conditions for this step are shown in Table 1.

	Sample #1	**Sample#2**	**Sample #3**	**Sample #4**	**Sample #5**	**Sample #6**
Pressure (mTorr)	NOT Treated (no SSE step)	800	800	800	800	800
RF Power (Watt)		75	75	75	75	75
CF_4 flow (sccm)		**50**	**53**	**50**	**45**	**40**
O_2 flow (sccm)		**0**	**2**	**5**	**10**	**15**
time (sec)		10	10	10	10	10

Table 1. Process conditions used for sample preparation.

For each sample the total gas flow was kept constant at 55 sccm.

The surfaces of treated samples were analysed by XPS with the Spectrometer AXIS-HS by Kratos; the instrument is equipped with Mg and Al dual anode X ray source; the pass energy of 40 eV was used (Fixed Analyser Transmission mode). The spectra were acquired using $Mg_{K\alpha}$ radiation of 1253.6 eV. Silicon surface roughness, induced by CF_4 and CF_4/O_2 containing plasmas (samples #2 and #4) has been determined by AFM analysis. A silicon untreated wafer has been used as reference for all the analysis. Finally, Thermal Wave (TW) measurements of the modulated optical reflectance, were performed and the TW signal has been correlated with the surface chemical state.

The apparatus employed for these analysis was a commercial Therma-Probe 200 System (Therma-Wave, Inc, Fremont California). A simplified block diagram of this tool is showed in figure 2.

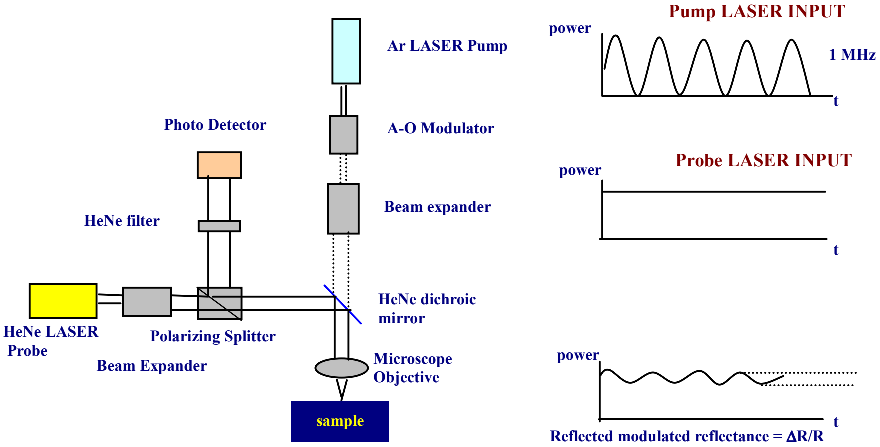

Fig. 2. Simplified block diagram of Thermal Wave apparatus.

In this apparatus, thermal waves are generated and detected by two low-power laser beams auto focused to a 1 µm spot diameter on the wafer surface. Absorption of light from an acoustic-optically modulated (1 MHz) Ar-ion pump laser generates thermal and plasma waves within the surface region of the silicon down an effective depth of about 3µm. These waves are then detected by He-Ne probe laser through the pump induced, 1 MHz modulation of the sample reflectivity at the wavelength of the probe laser. The effect of the thermal and plasma waves on the reflectivity of silicon result in a net modulated reflectivity signal that is very sensitive to the presence of disorder or defects in the surface region of the wafer(6).

Results and Discussion

XPS Analysis

XPS survey spectra show the O, F, C and Si signals in all the samples. The spectrum of sample etched with CF_4/O_2 flow ratio of 45/10 is shown in Fig. 3 as an example.

The F1s and C1s signals together are useful for the chemical characterization of these surfaces. Fig. 4a reports the F1s expanded regions of surfaces obtained after etching done using different CF_4/O_2 flow ratio as well as for the sample obtained with only overetch (no SSE, see Tab. 1 in the experimental section). The spectra can be deconvoluted by using two Gaussian components centred at binding energy of about 686.3 and 688.6 eV. These components are assigned to SiFx/SiOFx and to CFx respectively(7).

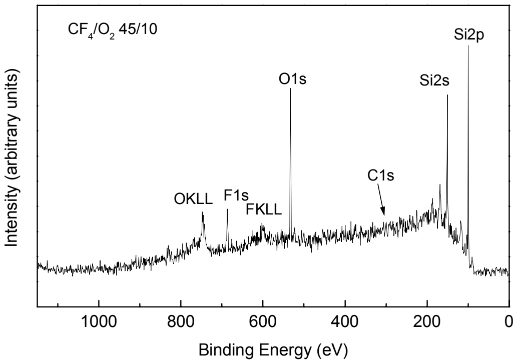

Fig. 3. Typical survey spectrum of sample etched using a CF_4/O_2 flow ratio of 45/10.

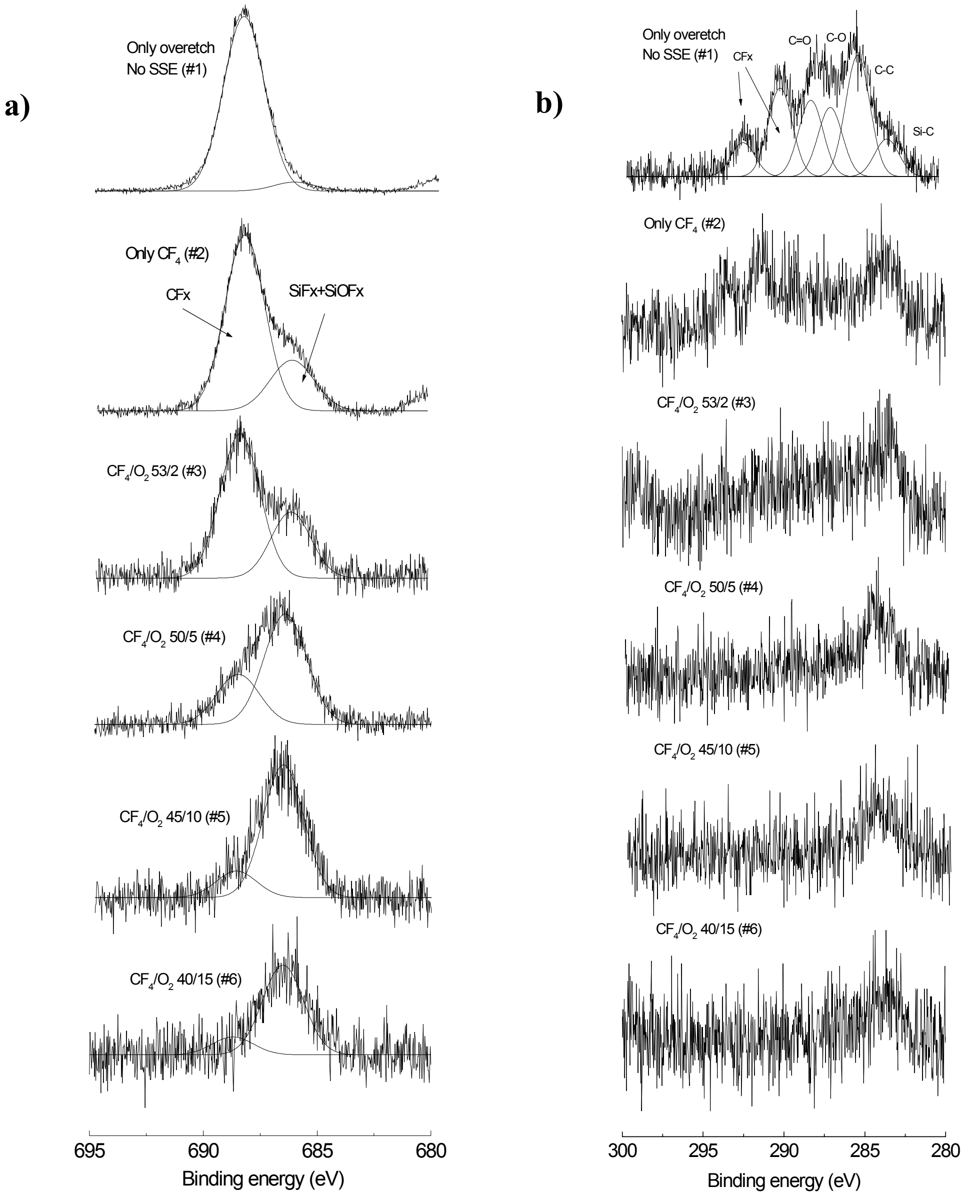

Fig. 4. F1s a) and C1s b) XPS spectra of samples obtained at different CF_4/O_2 flow ratio.

The spectra show a remarkable variation of the intensity ratio of CFx/SiFx-SiOFx components as function of the CF_4/O_2 gas flow ratio used during etching. The spectrum of the sample obtained without softetch process exhibits nearly a single component due to CFx species.

Fig. 4b reports the corresponding C1s spectra regions. The spectrum of sample #1 can be deconvoluted by using 6 Gaussian components centred at 283.2, 285.0, 286.7, 288.2, assigned to Si-C, C-C, C-O, C=O respectively, and 289.8 e 292.1 assigned to CFx. Increasing the O_2 content in the SSE plasma almost all the C1s components present in the spectra disappear, except the component centred at about 283.2 eV. Tab. 2 reports the quantitative chemical compositions of these surfaces.

Sample	%F (CFx)	% F (SiFx)	%C tot.	% Si	% O
#1	44.9	≈ 0	39.2	8.9	7.0
#2	27.6	10.6	12	33.7	16.1
#3	10.3	5.3	9.4	40.6	34.4
#4	6.5	11.2	8.5	54.9	18.8
#5	1.5	7.3	7.5	54.0	29.6
#6	0.9	2.7	10.2	48	38

Tab. 2. Surface composition as obtained by XPS analysis.

AFM Measurements

In order to evaluate the impact of the O_2 presence in the SSE plasma environment on the silicon surface AFM analysis has been performed, as described above. The results are shown in figure 5a, 5b and 5c. An untreated silicon wafer has been also analysed as reference and the result is shown in Fig. 5a. The evaluated samples roughness is reported in Table 3.

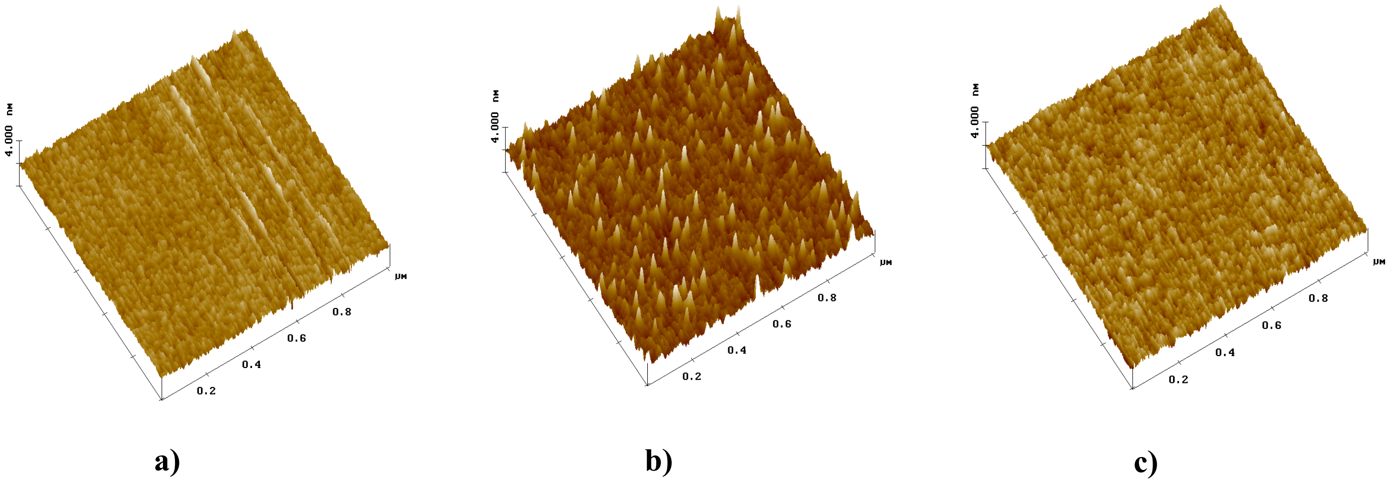

a) **b)** **c)**

Fig. 5. AFM images of: a) untreated Si sample; b) CF_4 treated sample; c) CF_4 / O_2 treated sample.

	Untreated (reference)	CF_4 (sample #2 of Table 1)	CF_4 / O_2 (sample #4 of Table 1)
Mean Roughness (nm)	0.105	0.205	0.136
RMS (nm)	0.131	0.291	0.171

Table 3. AFM analysis results.

Data of Table 3 show that the CF_4 plasma exposed sample exhibits the highest roughness, while the O_2 presence in the SSE reduces the surface roughness.

Thermal-Wave Measurement

The graph of Figure 6 reports TW signal variation against surface plasma treatments.

TW signal data agree with the previous XPS results. In particular, it increases with silicon surface

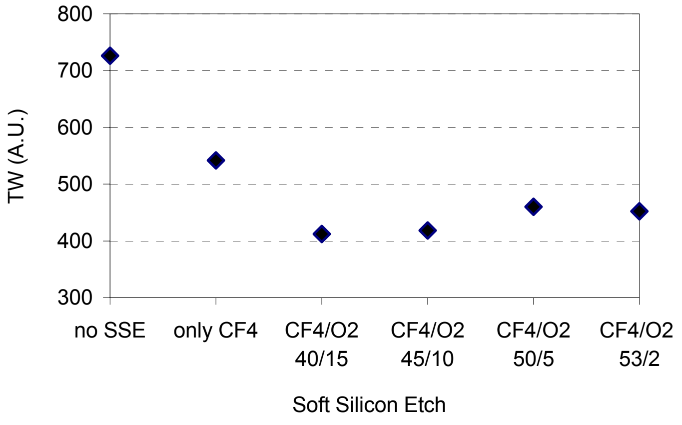

Fig. 6. TW signal variation versus surface treatments.

contamination by teflon-like polymers (no SSE step), while it is reduced performing the CF_4 based soft silicon etch. Adding O_2 in the plasma environment TW value is reduced again. However it remains almost constant increasing oxygen concentration in the plasma

Processes Characterization

The processes already reported in Table 1, were characterized in terms of both silicon etch rates and etch non- uniformity. The obtained values are reported in Table 4. Maximum ER value was obtained for CF_4/O_2 flow ratio of 10 (50/5).

SSE step	Etch Rate (Å/min)	Non-Uniformity (%)
CF_4/O_2 53/2	798	5.5
CF_4/O_2 50/5	916	2.1
CF_4/O_2 45/10	866	8.1
CF_4/O_2 40/15	782	8.3
only CF_4	600	4.0

Table 4. SSE etch rate versus plasma composition.

Conclusions

After the SiO_2 contact etch an in-situ soft-silicon etch (SSE) step is performed in order to remove the silicon damaged region. This is usually achieved by mean a CF_4 or CF_4/O_2 plasma at low-power and high pressure working conditions. In this work the impact of the oxygen concentration in the SSE plasma has been investigated by XPS and by AFM techniques. By performing the overetch step only a teflon-like polymer was observed on the silicon surface. By increasing O_2 concentration in the plasma, the ability of SSE step in polymer removal increases and, at the same time, the surface roughness is reduced. Moreover, a correlation between the surface chemical state and thermal wave measurements has also achieved. In particular, TW signal increases with silicon surface contamination by teflon-like polymers, while it is reduced increasing the O_2 concentration during the SSE step. This is a demonstration that damage induced to silicon surface and sub-surface during SiO_2 plasma etch can be readily detected and quantified using a rapid, non-contact and non-destructive thermal wave modulated reflectance analysis.

Acknowledgements

The authors wish to thank G.F.Indelli for technical assistance in the part of the work done at "Laboratorio Superfici ed Interfasi" of Consorzio Catania Ricerche.

References

1) F. Mohhdam and Xiao Chun Mu, IEEE Trans. on Electron Devices Vol.36, No. 9, pp 1602-1609 (1989).
2) M.Biavati, I.Perez-Quintana, A.Poggi and A.Susi, J.Vac Sci Technol. B 13(5), pp 2139-2141 (1995).
3) H. Komeda, M.Sato, A.Ishihama, K. Sakiyama and T. Ohmi, 3rd International Symposium on Plasma Process-Induced Damage, June 4-5 Honolulu, HI, USA (1998).
4) K.Miyamoto, K.Sugihara and A. Asai 2nd International Symposium on Plasma Process-Induced Damage, May 13-14 , Monterey , CA, USA (1997).
5) S. Deshmukh and M.Nelson 1997 2nd International Symposium on Plasma Process-Induced Damage, May 13-14 , Monterey , CA, USA (1997).
6) P.Geraghty and W.L.Shith Mat.Res. Symp.Proc.Vol. 68 1986 – Material Research Society
7) D. Briggs and M.P. Seah, (Eds.) *Practical Surface Analysis*, Second Edition, Vol. 1, John Wiley & Sons, Chichester, (1990).

Double d.c. plasma torch system used for the simulation of composite material degradation in segmented solid rocket motors

S. Bansard, E. Legros, G. Mariaux, M. Vardelle and A. Vardelle

Sciences des Procédés Céramiques et Traitements de Surface, Université de LIMOGES, ENSIL, 16 rue Atlantis, 87068 LIMOGES, FRANCE.

Abstract

This study deals with a plasma system used to experimentally simulate the degradation of carbon composite subjected to a flux of alumina droplets. The system included 2 d.c. plasma torches discharging in a chamber filled with argon or air at 10^5 or 0.5 10^5 Pa. They were used, both, to spray alumina droplets on the carbon-composite sample and maintain liquid the alumina film that formed on the sample surface. This paper is focused on the measurement and calculation of the temperature fields in the chamber and substrate.

Introduction

In the European Ariane V rocket, the propulsion at take-off is provided by aluminum-enriched propergol. The adding of 18 to 20% of aluminum makes it possible to increase the specific impulsion by 6 to 8%. The design of the proper geometry of the nozzle requires a good knowledge of the heat transfer process and recession behavior of the base material. The nozzle material is a carbon/carbon or carbon/phenolic resin composite. The latter associates good mechanical and thermal performance with a light weight. In operation three phenomena are involved in the degradation of such material : erosion, oxidation and ablation [1]. Various studies have shown that the recession rate is, to a large extent, controlled by the diffusion of water vapor and carbon dioxide to the nozzle surface [2,3,4]. In addition, the combustion of the propergol fuel results in the formation of alumina droplets that impinge on the nozzle wall where they form a liquid film. This film can react with the substrate contributing to the nozzle degradation [5]. If the reduction process of alumina by carbon has been the subject of different studies [6], very few works are concerned with the mechanical interaction between the alumina droplets and composite. Among the most advanced studies, Chiba [7] carried out an experimental observation of the composite recession and established empirical laws of mechanical mass removal and Yang et al [8,9] developed a numerical model of the ablation of the materials taking into consideration the mechanical erosion phenomenon.

To validate the aerothermochemical model developed by Snecma "Propulsion Solide" (SPS), an experimental simulation of the harsh conditions undergone by the nozzle material has been developed. It combines two d.c. plasma torches that are used both to form the alumina film and maintain it liquid. The plasma flows must exhibit a low momentum at the substrate surface so that they do not perturb the liquid layer and they must have a high enthalpy and thermal conductivity to ensure the melting of alumina either in powder and film form. The experimental simulation will result in correlations that link a parameter characteristic of the ablation phenomenon (recession rate) with the substrate temperature and the size, velocity and number of impinging droplets.

This study examines the operating of the double plasma torch system. The experimental part involves the determination of the plasma temperature fields using an imaging technique, and the study of the substrate temperature thanks to pyrometry and thermocouples. The experimental results are compared and completed with the projections of a mathematical model that computes the gas/particle velocity and temperature fields within the jet envelope and projects the rate of heat transfer at the substrate surface.

1. Experimental set-up

The configuration of the experimental device is shown in figure 1. The plasma torches operated in a water-cooled chamber under air or argon atmosphere at 10^5 or 0.5 10^5 Pa. The latter permitted to improve the stability of the plasma jet and get more homogeneous thermal flux on the substrate. In addition, argon atmosphere helped to avoid the oxidation of the substrate so that, only the degradation of the carbon material resulting from the interaction with the alumina droplets was investigated.

The alumina powder used in this study had a particle size distribution of 10-40 µm. The powder was injected in both torches through a 1.8-mm diameter port located at 3 mm upstream of the nozzle exit. The particles were melted in the plasma jet and sprayed onto the target located at 78 mm from the torch front.

The latter was made in a “two-dimension composite” : the carbon fibers were weaved into sheets that were coated with resin and piled together. The substrate was manufactured so that its revolution axis was perpendicular to the carbon fiber layers. The geometry of the substrate (figure 2) and its position in the chamber were optimized with the result that the heat and particle flux were as homogeneous as possible and did not perturb the substrate temperature measurement.

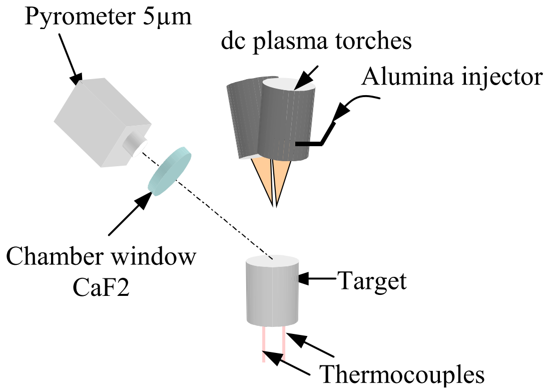

Figure 1 : Experimental set-up and target temperature measurement

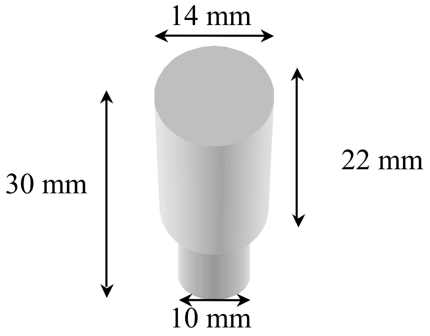

Figure 2 : Geometry of the substrate

2. Measurement techniques

Plasma jet characterization

A diagnostic technique based on the image processing of jet photographs was developed. This technique permitted the optimization of the operating of the plasma torches and monitoring of the stability and reproducibility of experiments. The procedure consisted in the taking of plasma flow photographs over one minute at the rate of 25 shots per second in the wavelength range 509.5- 519.5 nm thanks to an interferential filter. The latter range corresponds, in particular, to some neutral lines of argon. The temperature zones of the plasma flow were derived from the pictures using a calibration with spectroscopic measurements based on the absolute line intensity of a neutral line of argon (ArI at 774.2 nm) [10]. An example of a calibration curve that associates temperature with the gray levels of the picture is shown in figure 3. This method gives reliable results above 10,000 K. Below this value, temperature measurements may be over-estimated. Indeed the spectroscopic technique assumes local thermodynamic equilibrium and departures from the thermal equilibrium may occur in the fringes of the jet where high gradients take place.

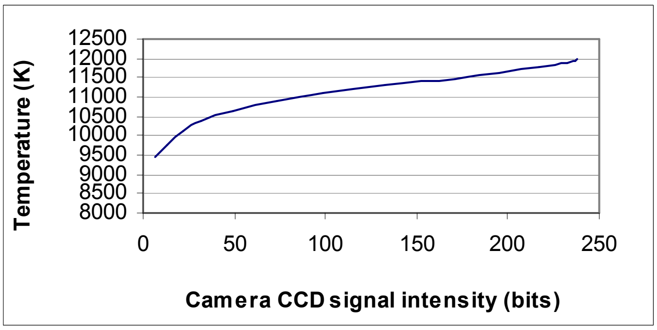

Figure 3 : Temperature calibration of the gray levels of pictures

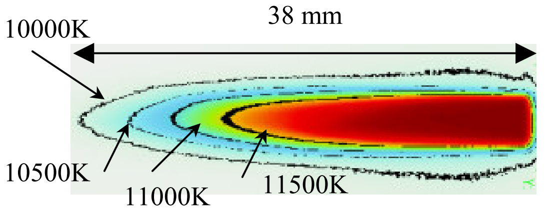

Figure 4 : Isotherms deduced from the picture gray levels. Torch operating conditions: gas mixture: 45 slm Ar + 15 slm H_2; 600 A, torch nozzle diameter : 7 mm , environment : air at 10^5 Pa

Target temperature

The temperature of the surface exposed to the plasma and particle heat flux was determined by using a single-color infrared pyrometer IRCON™ Modline 3 at 4.8-5.2 µm (figure 1). The minimum analyzed surface was 10 mm in diameter. A special calibration, under the conditions of this study, made it possible to perform measurements over 3000K. The calibration took into consideration the angle of the measurement axis with the target surface and light absorption by the chamber window (CaF_2). The emissivity was supposed to be 0.8 as this value corresponds to the emissivity of both alumina [11] and carbon composite at 5µm.

The inside temperature of the substrate was estimated from three thermocouples sunk in the substrate; they were located at 10, 14 and 18 mm, respectively, from the top surface. Nonstandard types of thermocouples formed from W-Re (5%) and W-Re (26%) alloys were used. Their measurement range was 200 to 2000°C and the accuracy +/- 30°C at 2000°C. However, in the presence of carbon, they had to be changed after each experiment.

3. Modeling

The 3-D numerical modeling of the two plasma jets impinging on the carbon target was carried out using the CFD commercial code ESTET 3.4 [12]. This code is dedicated to steady or unsteady, subsonic, turbulent, multi-component reactive flows. It solves the conservation equations of mass, species, momentum, energy and turbulence with an hybrid scheme using finite difference and finite volume methods applied to a mono-bloc structured mesh grid. The tracking and heating of particles injected in the flow are performed with a Lagrangian scheme.

The modeling of the plasma flow was based on the assumptions of local thermodynamic equilibrium, optically thin plasma and chemically inert gas. In addition, the flow was supposed steady and the arc movement inside the nozzle and its effects on the plasma flow were not taking into account [13, 14]. The loading effect by the processed powder was also neglected. The latter assumption is reasonably accurate as the particle loading was less than 20% under the spraying conditions of this study.

The multi-component flow was supposed to be made of the plasma-forming gas (Ar/H_2), powder carrier (Ar) and ambient gas (air or argon). The thermodynamic (specific heat, enthalpy and density) and transport properties (viscosity and thermal conductivity) of the gas mixture were calculated using the laws of mixtures and the data of pure gases expressed in terms of temperature [15]. The flow was modeled by a k-ε model with the correction of Launder and Sharma for low Reynolds numbers.

Figure 5 shows the 3-D calculation domain (114 x 120 x 54 mm^3) and curvilinear computational grid. The number of mesh nodes in the x, y and z directions was 93, 73 and 47, respectively, with a finer mesh close to the walls (anode and substrate) to have an accurate calculation of the heat flux and friction to the anode and the substrate.

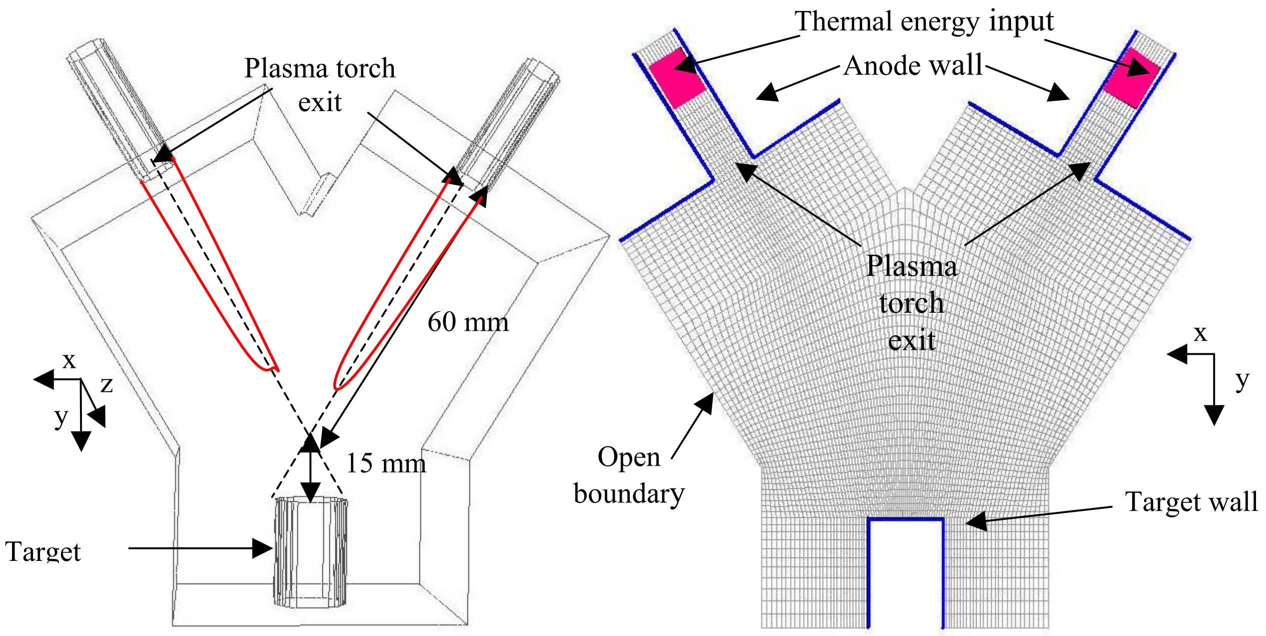

Figure 5 : 3-D calculation domain and mesh grid

The plasma-forming gas entered the computation domain through the two nozzles with a uniform temperature of 27 °C and laminar velocity profile. The conversion from electrical to thermal energy in the gas flow was assumed to occur uniformly throughout the medium and a volumetric generation rate (W/m^3) was imposed in a fixed portion of the nozzle at the entrance of the computation domain, as shown in figure 5 (red domain). This enthalpy generation rate was calculated from the electric power V.I divided by the volume of a cylindrical portion of the nozzle [16, 17]. The heat generation was, then, taken into account as a source term in the heat conservation equation. This model resulted in an acceptable estimation of the effective power of the plasma torch under the spraying conditions of this study.

The shear stress at the anode wall was calculated from the "law of the wall" through a friction coefficient. The heat transfer to the nozzle and target was deduced from the momentum and heat transfer analogy in the wall boundary layer using the functional relation of Prandtl-Taylor and assuming that the surface temperature of the anode was maintained at a constant temperature of 800 °C and the surface of the target at 2000°C.

4. Results and discussion

The optimization of the system geometry and torch operating conditions was carried out thanks to the imaging technique of the jet flows. The objective was to get a uniform heating of the substrate with a temperature high enough to maintain liquid the impinging alumina droplets. The investigated parameters were the angle between the torch axes, composition of the plasma forming gas mixture, arc current and chamber pressure.

Preliminary studies in air with the torch operating conditions used at the laboratory to spray alumina (gas mixture of 45 slm Ar + 15 slm H_2 – 600 A – sample distance: 100 mm) showed that the two plasma jets were too short and did not interact while the substrate temperature was below the melting point of alumina (figure 6). In addition, the chemical erosion due to the chemical reaction between the oxygen and the surface was the predominant mechanism of ablation.

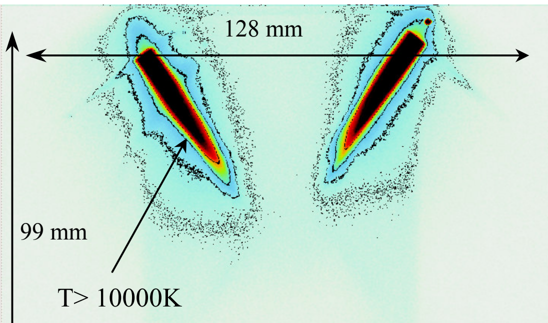

Figure 6 : Temperature isocontours .Torch operating conditions : 45 slm Ar + 15 slm H_2- 600 A– chamber pressure : air at 10^5 Pa

The imaging technique showed, as expected, that a decrease in the chamber pressure resulted in a lengthening of the plasma jet and an increase in surface target temperature. Also, the plasma expanded when discharging in argon atmosphere instead of air.

The optimized spraying parameters are summarized in table 1. The angle between the torch axes was fixed at 65°.

Table 1 : Plasma torch parameters

PLASMA TORCH PARAMETERS			
Plasma torch	F4-MB	Torch nozzle diameter	8 mm
Plasma-forming gas	(1) 45 slm Ar + 9 slm H_2 (2) 45 slm Ar + 15 slm H_2	Arc current	600 A
Gas mass flow rate	(1) 1.349 10^{-3} kg.s^{-1} (2) 1.358 10^{-3} kg.s^{-1}	Arc voltage	(1) 60 V (2) 65 V
Torch thermal efficiency	(1) 50 % (2) 53 %	Effective power input to the gas	(1) 18000 W (2) 20600 W
Location of the sample	78 mm from torch exit, perpendicular to the symmetry axis of the 2 torches		
Environment	argon at 0.5 bar		

Figure 7 shows the predicted (a) and experimental (b) temperature fields of the plasma jets in the axial plan of the torches. The agreement between calculations and measurements is fair. Both exhibit a dissymmetry in the shape of the two jets. In the actual system, this dissymmetry may be explained by differences in the dynamic behavior of the two torches and turbulence phenomena. However, in calculations, the mesh grid was symmetric and the torches operated under the same steady conditions. Therefore, only turbulences and swirls enhanced by the impacting of jets onto the target prevented the stabilization of the flows. It should be noted that the color zones in the target give an idea of the temperature gradients but no absolute temperature as the temperature calibration was carried out for the gas flow and not the material. However, such images should be used to optimize the location of the composite samples in front of the plasma guns.

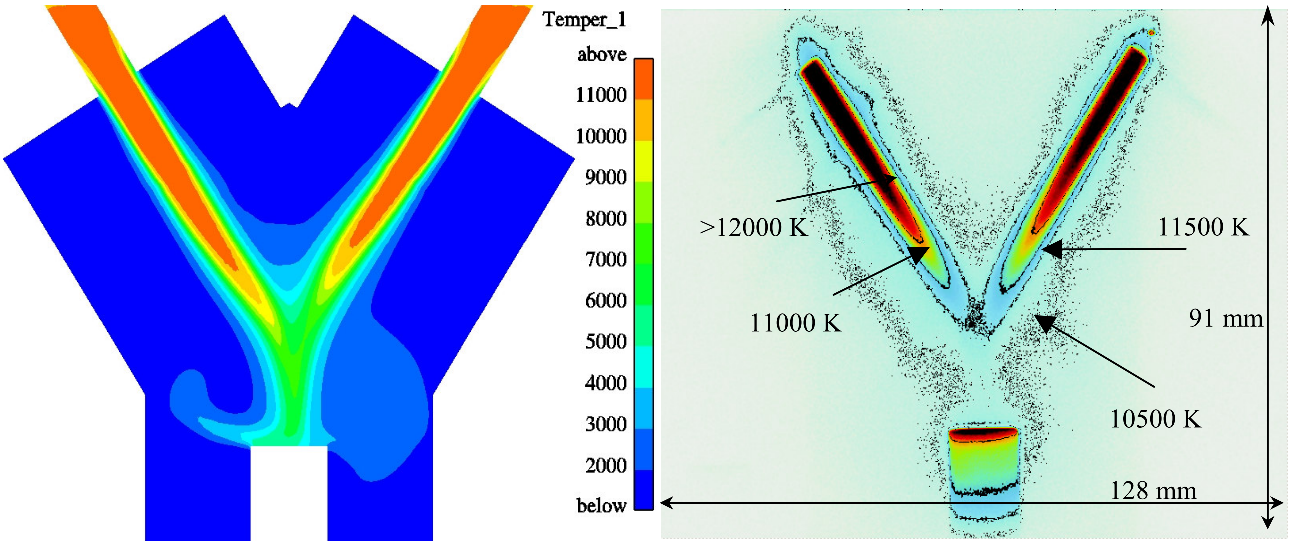

(a) (b)

Figure 7 : Calculated (a) and experimental (b) temperature isocontours
Torch operating conditions : set 1 – chamber pressure : argon at 0.5 10^5 Pa

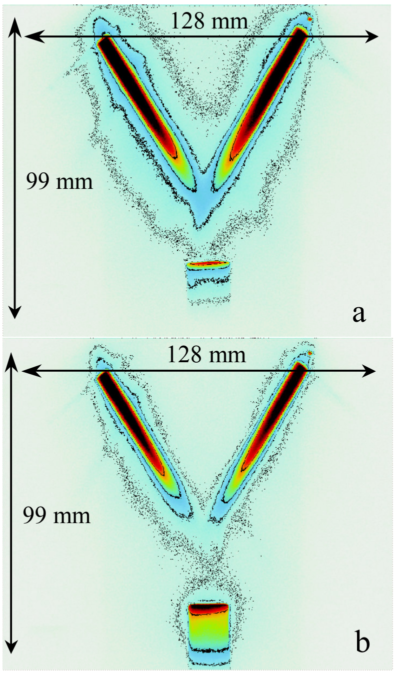

Figure 8 : Torch operating conditions : 600 A ;
chamber pressure : argon at 0.5 10^5 Pa
a)- 45 slm Ar + 3 slm H_2 b)- 45 slm Ar + 15 slm H_2

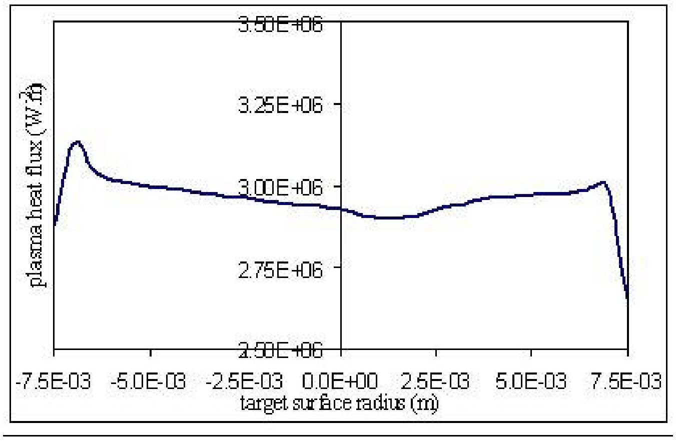

Figure 9 : Predicted heat flux transferred
to the substrate by plasma jet

An increase in the hydrogen content from 3 to 15 slm gave rise to a decrease in the plasma flow length. However, the internal and external temperature of the substrate increased because of a more efficient heat transfer to the material as shown in figure 8 : the target surface temperature measured by the pyrometer increased from 2,700K to 3,300K. The calculation of the plasma flow fields and heat flux to substrate with different hydrogen contents agree well with the experimental observations.

Figure 9 shows the predicted heat flux to the substrate brought by the two plasma flows. It varied between 2 and 3 $MW.m^{-2}$ and is consistent with calorimetric measurements under identical spraying conditions [10]. The heat flux was more important on the edges of the substrate. This can be explained by the position of the torches in relation to the target. Experimental observations also showed a more significant ablation on the edges.

5. Conclusion

An experimental system has been developed for studying the erosion of carbon composite materials subjected to the impact of high velocity alumina droplets. The system involves 2 plasma spray torches that are used to spray alumina particles onto the composite substrate and maintain a liquid film of alumina on the top of the substrate. An imaging technique and a CFD model of the 2 flow jets were used to optimize the operating conditions : angle between the 2 plasma torches, pressure and atmosphere in the chamber, working parameters of the torches.

Under the optimized conditions, the system makes it possible to melt and spray the 10-40 μm alumina particles and get a uniform heating of the sample that reaches a temperature of 3300 K on the top surface.

In addition, the CFD model enables the calculation of the heat flux to substrate by plasma jet and particles. It should help to quantify the mechanical erosion of the carbon composite by the impinging particles.

The next step of the study deals with the onset and maintenance of the melt layer on the sample surface.

6. References

[1] K. Klager, Aerojet-General, Sacramento, California 95813 (USA)

[2] K.K. Kuo, S.T. Keswani,, Combustion Science and Technology, **42**, pp. 145-164, 1985

[3] S.T. Keswani, E. Andiroglu, J.D. Campbell, K.K. Kuo, Journal of Spacecraft and Rockets, **22**, pp. 396-397, 1985

[4] S.T. Keswani, K.K. Kuo, Combustion Science and Technology, vol. **47**, pp. 177-192, 1986

[5] V. Borie, Y. Maisonneuve, D. Lambert et G.Lengellé, "Ablation des matériaux de tuyères de propulseurs a propergol solide", ONERA report in french, ISSN 0078-3781

[6] A. VARDELLE, D. Sc., “Numerical study of heat, momentum and mass transfer between dc plasma jet and particles”, in french, 29-87, 1987, University of Limoges, France

[7] Z. Chiba, "Particulate impact erosion in entrance-throat region of solid rocket nozzles", Accurex corporation, Aerotherm Division, Mountain view, California

[8] B.C. Yang, F.B. Cheung, J.H. Koo, "Numerical Investigation of Thermo-chemical and Mechanical Erosion of Ablative Materials", AIAA/SAE/ASME/ASEE 29th Joint Propulsion Conference and Exhibit, June 1993/Monterey,CA

[9] B.C. Yang, F.B. Cheung, J.H. Koo, Journal of Applied Mechanics, **20**, pp. 1027-1032, 1993

[10] O. Betoule, Ph. D. thesis, "Relationships between the distributions of particle velocity and temperature and coating properties", in french, 24-1994, 1994, University of Limoges, France

[11] O. Rozenbaum, D. De Sousa Meneses, Y. Auger, S. Chermanne and P. Echegut, Review of Scientific Instruments, volume 70, number 10 (octobre 1999), pp. 4020-4025

[12] ESTET ASTRID 3.4, manual, Simulog, Paris, France, 2000

[13] B. Dussoubs, G. Mariaux, A. Vardelle, M. Vardelle, Journal of High Temperature Materials and Processes, 3 (2-3), 1999, pp. 235-254

[14] G. Mariaux, P. Fauchais, A. Vardelle, B. Pateyron, Journal of High Temperature Materials and Processes, 5 (1), 2001, pp. 61-85

[15] M. Boulos., P. Fauchais, and E. Pfender, “Thermal Plasmas, Fundamental and Applications”, vol. 1, (Pub.) Plenum Press, New York, 1995

[16] G. Mariaux, E. Legros, A. Vardelle, in the Proceedings of 10th CIMTEC, July 2002, Firenze, Italy, International Ceramics Congress, vol. F

[17] K. Remesh, Effect of carrier gas on particle in-flight characteristics during the plasma spray process with external injection, 35th National Heat Transfer Conference, California 2001

Measurement of the Species Spatial Distribution in an IPVD Reactor by Optical Spectroscopy

P.Vašina[1,2], L.de Poucques[1], C.Boisse-Laporte[1], O.Leroy[1], D.Pagnon[1], L.Teulé-Gay[1], M.Touzeau[1]

[1] *Lab. Physique des Gaz et des Plasmas, Bat. 210, Université Paris-Sud, 91405 Orsay Cedex, France*
[2] *Department of Physical Electronics, Masaryk University, 61137 Brno, The Czech Republic*

Abstract

In this paper absorption spectroscopy results are presented for an IPVD reactor, consisting of a magnetron sputtering device assisted by two microwave systems devoted to the ionization of the sputtered titanium atoms. For 4 Pa pressure and magnetron current of 2 A, applying of 800 W into each microwave device increases the titanium ionization degree by factor 4 and the titanium ion flux to the substrate by factor 15.

1. Introduction

Ionized physical vapour deposition, or IPVD, is of current interest to improve the quality of deposited film coatings obtained with conventional sputtering techniques [1-3]. One of the aim of IPVD is to collimate depositing particle fluxes by ionizing a significant fraction of the incident metal vapour sputtered from a magnetron and applying an electric potential bias to the substrate. Most of the IPVD reactors use RF coils to create additional ionization [1-2], in this paper, we present the results of absorption spectroscopy measurements in a original IPVD reactor with an additional microwave source of ionization.

The cathode (22 x 9 cm) can be moved between 4.5 and 10 cm from the centre of the reactor.

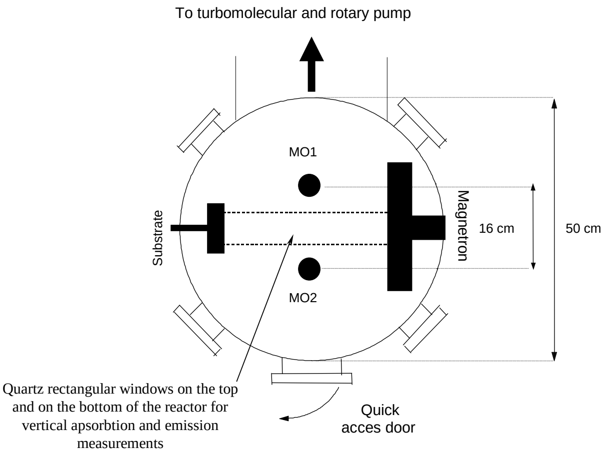

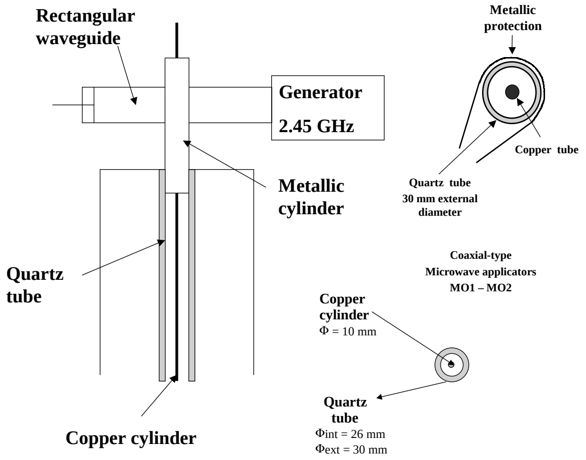

Figure 1: Configuration of the experimental setup.

Figure 2: Configuration of coaxial microwave system.

2. Experimental Setup

The apparatus for plasma analyzing and studying the elementary processes in the microwave assisted magnetron sputtering is presented in Figure 1. It consists of a cylindrical metallic vessel, 50 cm in diameter and 45 cm high, a planar titanium cathode, 21 cm long and 9 cm large, supplied by a 1.5 kW DC generator and of two coaxial-type microwave applicators. These applicators are located perpendicularly to the magnetron-substrate axis, 4.5 cm from magnetron, 8 cm from the axis, supplied by 1.2 kW 2.45 GHz generator and covered by metallic protection to avoid titanium deposition on the quartz tubes. The schematic drawing of the microwave alimentation is presented in Figure 2. The working gas is argon, apparatus is pumped by turbomolecular and rotary pumps. Working pressure is measured by MKS baratron and controlled by flow and exhaust throttle valve MKS type 655B.

The reactor is designed in order to allow optical diagnostic and Langmuir probe measurement. Spatially resolved absorption measurement was carried out using a pulsed titanium hollow cathode lamp. Lens was used to transform the light coming from the lamp in a parallel beam. Along the magnetron-substrate axis a moving mirror is used to reflect the beam into the reactor. The light crosses the plasma vertically and is focused by another lens in an optical fiber. The light is then analysed by a Jobin-Yvon HR1000 spectrometer equipped by a photomultiplier tube. Signal from desired component is measured by Tektronix TDS 340A oscilloscope synchronized with the lamp excitation.

3. Spatial distribution of titanium species

3.1. Experimental determination of titanium groung state densities

The absorption measurement was carried out to determine the density of titanium neutral atoms in ground ^{3}F and metastable ^{5}F state and the density of titanium ions in ground state ^{4}F.

The absorption measurement at wavelengths 363.5, 364.2, 365.3 and 398.1 was carried out. A numerical iteration program [4] was used to obtain simultaneously the neutral titanium ground state density n_{Ti}, the temperature of lamp and the titanium temperature T_{Ti}, corresponding to Boltzmann distribution in the ground state sublevels.

The titanium metastable atom density $n_{Ti,m}$ and titanium ion density $n_{Ti,i}$ was obtained by measuring the absorption coefficient for the wavelengths 498.1 and 338.4 nm and by assuming a Boltzmann distribution with same temperature T_{Ti} estimated for titanium ground state sublevels under the given conditions.

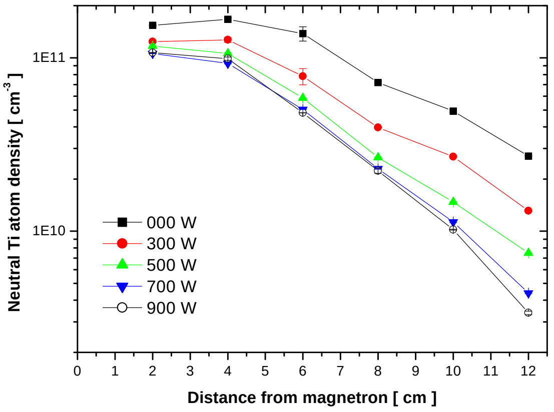

Figure 3: Spatial distribution of titanium ground state density for pressure 4 Pa, argon flow 200 sccm, magnetron current 0.5 A and variable microwave power.

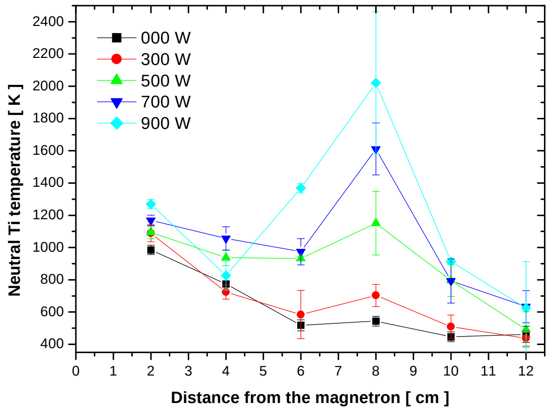

Figure 4: Spatial distribution of neutral titanium atom temperature for pressure 4 Pa, argon flow 200 sccm, magnetron current 0.5 A and variable microwave power.

3.2. Results

Spatial distribution of titanium ground state density n_{Ti} and neutral titanium atoms temperature T_{Ti} for pressure 4 Pa, argon flow 200 sccm and magnetron current 0.5 A is presented in Figure 3 and Figure 4 as a function of microwave power. From the Figure 3, we can observe that for all position increasing microwave power results into decreasing of n_{Ti}. Applying of 900 W of microwave power results into 50 percents decrease of n_{Ti} at distance of 2 cm from magnetron and into decrease of n_{Ti} by a factor 5 at distance of 10 cm with respect to no applied microwave power. The spatial evolution of T_{Ti} in Figure 4 can be divided into two parts: the magnetron region (distance from magnetron is less than 4 cm) and the region of microwave influence (distance from magnetron is more than 4 cm). In the magnetron region, the T_{Ti} is about 1000 K and does not change with microwave power. It is attributed to a magnetron heating. In the microwave region, the T_{Ti} increases with microwave power and on all curves, there is significant maximum of T_{Ti} at distance about 8 cm, which corresponds to a maximum of electron density, measured by Langmuir probe.

For the same conditions (pressure 4 Pa, argon flow 200 sccm and magnetron current 0.5 A), the spatial distribution of neutral titanium metastable (state ^{5}F) atom density as a function of microwave power is shown in Figure 5. In the microwave area, we can observe for all microwave powers almost the same increase of $n_{Ti,m}$ with respect to the value without microwave. This behavior can be explained by the fact, that the metastables atoms are created by electron collision with the neutral titanium atoms. It reflects the variation of neutral titanium atoms (Figure 3) and of the electron density (which increases with microwave power). In the magnetron area, where the electron density can be excepted to be almost independent of microwave power, applying of microwave power results into decrease of $n_{Ti,m}$ due to decrease of n_{Ti}. It can be noted that the density of metastable can be of the same order of magnitude then the ground state one.

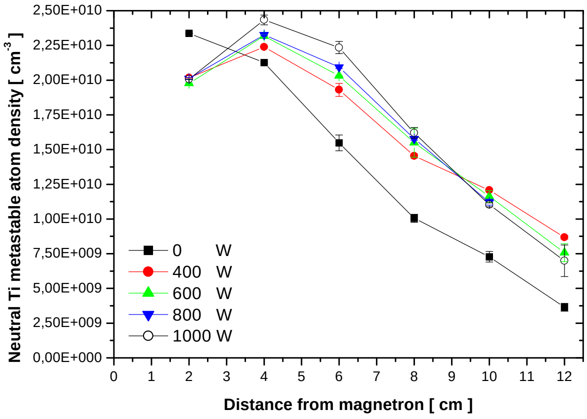

Figure 5: Spatial distribution of titanium neutral metastable atom density for pressure 4 Pa, argon flow 200 sccm, magnetron current 0.5 A and varied microwave power.

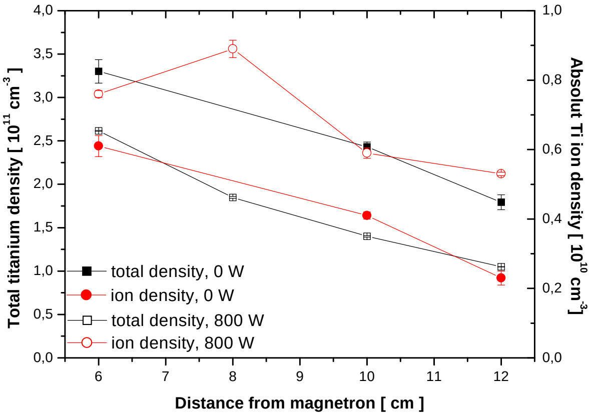

Figure 6: Spatial distribution of total titanium and ion densities for pressure 4 Pa, argon flow 200 sccm, magnetron current 2 A and microwave power 0 and 800 W.

For the magnetron current 0.5 A the absorption was very weak to determine the value of $n_{Ti,i}$ properly. Increasing the magnetron current to 2 A raised the absorption coefficient to a reasonable value to determine $n_{Ti,i}$. For pressure 4 Pa, argon flow 200 sccm, magnetron current 2 A and without and with 800 W of microwave power, the spatial distributions of n_{Ti}, $n_{Ti,m}$ and $n_{Ti,i}$ were determined. In Figure 6, are plotted the spatial distributions of total titanium density $n_{Ti,tot} = n_{Ti} + n_{Ti,m} + n_{Ti,i}$ and $n_{Ti,i}$ in the microwave area for no and 800 W of microwave power. Without microwave power we can observe the same relative decrease of $n_{Ti,tot}$ and $n_{Ti,i}$ with the distance from the magnetron. It was attributed to the diffusion losses of titanium atoms. However applying microwave power increases $n_{Ti,i}$ and decreases $n_{Ti,tot}$ and it results into an increase of ionization degree, which is presented in Figure 7. For 800 W of microwave power, we can observe that as the distance from the magnetron increases the ionization degree increases too and at the 12 cm distance from the magnetron, which corresponds to substrate holder position it reachs the value of 5 percents, which is 4 times higher ionization degree than for no microwave power.

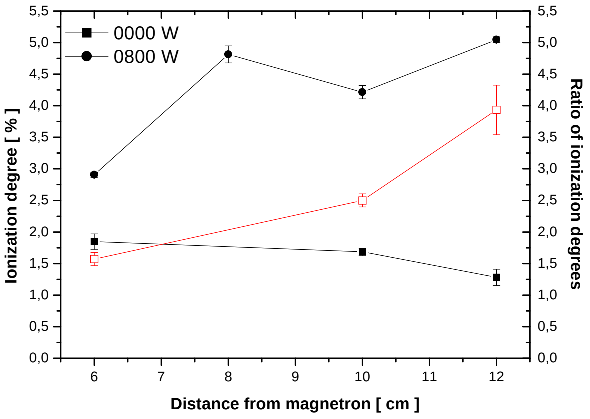

Figure 7. Spatial distribution of ionization degree and ratio of ionization degree for pressure 4 Pa, argon flow 200 sccm, magnetron current 2 A and microwave power 0 and 800 W.

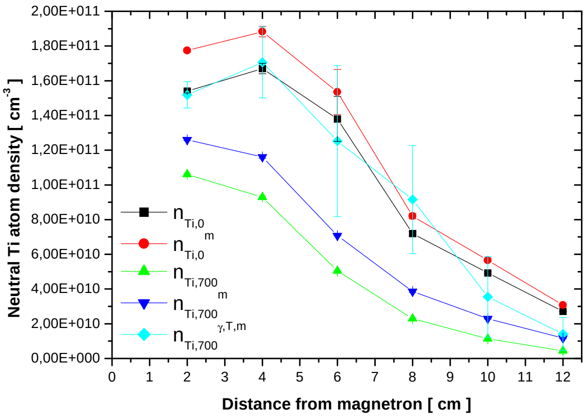

Figure 8: Explication of various effects causing the decreasement of titanium ground state density with applied microwave power. Results of local model.

4. Variation of titanium ground state density with microwave power

In this section, a simple local model for explanation of n_{Ti} decrease with microwave power is presented. The goal of this model is to obtain from spatial distribution of titanium ground state density $n_{Ti,x}$, measured for the applied microwave power of x Watts, the spatial distribution of $n_{Ti,0}$ without microwave power. The conditions corresponding to applied microwave power 700 W was chosen to demonstrate the influence of microwave power on n_{Ti}. The loss of $n_{Ti,x}$ due to excitation of metastable ^{5}F levels was taking into account by adding the concentration of metastable titanium atoms $n_{Ti,m,x}$ to $n_{Ti,x}$ to obtain $n^m_{Ti,x}$.

$$n^m_{Ti,x} = n_{Ti,x} + n_{Ti,m,x} \tag{1}$$

From Figure 8, it is obvious, that the excitation of titanium metastable ^{5}F levels is not the main effect leading to the decrease of n_{Ti} with microwave power.

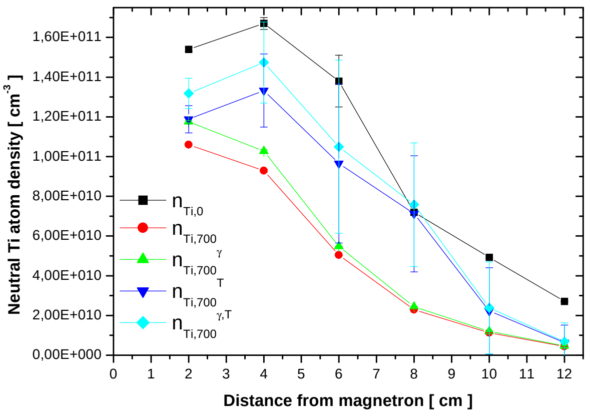

Figure 9: Explication of various effects causing the decreasement of titanium ground state density with applied microwave power. Results of local model.

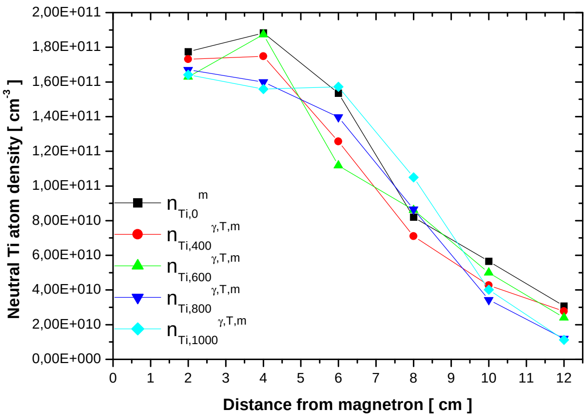

Figure 10: Spatial distribution of titanium ground state density after taking into account all effects of its decreasement with microwave power. Results of local model.

Next, two effects were taken into account. During the experiments a magnetron current was kept constant. It was observed, that increase of the microwave power resulted into decrease of magnetron voltage U$_{\text{mag}}$ to keep the same current to the magnetron cathode. The decrease of voltage, applied on the magnetron cathode results into reduction of the energy of argon ions bombarding the cathode and then into reduction of the pulverisation coefficient γ [5] (for no applied microwave power U$_{\text{mag}}$=231 V, γ_0=0.23; for 800 W of applied microwave power U$_{\text{mag}}$=215 V, γ_{800}=0.20). The loss of $n_{Ti,x}$ due to the change of γ was taking into account to obtain $n^{\gamma}_{Ti,x}$

$$n^{\gamma}_{Ti,x} = n_{Ti,x}\frac{\gamma_0}{\gamma_x} \tag{2}$$

For a given pressure, we assumed, that the change of neutral gas temperature T_{Ti} results into decrease of n_{Ti} according to ideal gas equation of state. The loss of $n_{Ti,x}$ due to changing T_{Ti} was taken into account to obtain $n^{T}_{Ti,x}$

$$n^{T}_{Ti,x} = n_{Ti,x}\frac{T_x}{T_0} \tag{3}$$

Because all these effects take place simultaneously, we used all equations at the same time to obtain $n_{Ti,0}$ from $n_{Ti,x}$. Order of the upper index indicates the order of the effects taken into account. Then $n^{\gamma,T,m}_{Ti,700}$ means that $n_{Ti,m,700}$ was added into $n_{Ti,700}$ after taking into account the γ and T_{Ti} effects.

In Figure 9, are plotted spatial distributions of $n_{Ti,0}$ (black square), $n_{Ti,700}$ (red circle), $n^{\gamma}_{Ti,700}$ (green up triangle), $n^{T}_{Ti,700}$ (dark blue down triangle) and $n^{\gamma,T}_{Ti,700}$ (light blue diamond). In Figure 8, are plotted spatial distributions of $n^{m}_{Ti,0}$ (red circle) and $n^{\gamma,T,m}_{Ti,700}$ (light blue diamond). From these figures, we can observe, that in the microwave area the decrease of n_{Ti} is caused by the neutral gas heating. However in the magnetron area, where the influence of microwave is weak the γ effect is more significant. Adding $n_{Ti,m}$ into n_{Ti} shows that excitation of titanium metastable levels does not play an important role, as it was discussed previously. In Figure 10, are plotted the spatial dependencies of $n^{m}_{Ti,0}$ and $n^{\gamma,T,m}_{Ti,x}$ for various applied microwave powers. For simplicity, the error bars were extracted. The fact that for all experimental conditions $n^{\gamma,T,m}_{Ti,x}$ obtained from $n_{Ti,x}$ well corresponds to $n^{m}_{Ti,0}$, supports the validity of the local model which allows to explain the decrease of n_{Ti} with microwave power and quantify the γ, T_{Ti} and metastable excitation effects.

3. Conclusion

In this paper, an original IPVD reactor consisting of a magnetron assisted by an additional microwave source of ionization is studied. The spatial distribution of sputtered species in this IPVD reactor has been obtained by optical absorption measurements: densities of neutral titanium atom in ground (^{3}F) and metastable (^{5}F) state and density of titanium ions in ground (^{4}F) state.

For pressure of 4 Pa, magnetron current of 2 A and no applied microwave power, the ionization degree near the substrate holder is about 1.5 percents, for 800 W the ionization degree increase of factor 4 with respect to the value without microwave up to the value of 5 percent. For 2 A, the flux of all titanium atoms to the substrate is almost the same for 800 W of microwave power $(2.5 \cdot 10^{15}\text{cm}^{-2}\text{s}^{-1})$ and no applied microwave power $(2.7 \cdot 10^{15}\text{cm}^{-2}\text{s}^{-1})$, however applying 800 W of microwave power increases the ion flux by factor 15 in respect to no applied microwave power from value $3.4 \cdot 10^{13}\text{cm}^{-2}\text{s}^{-1}$ to $5.9 \cdot 10^{14}\text{cm}^{-2}\text{s}^{-1}$. The decrease of titanium ground state density n_{Ti} with microwave power was observed. A local model, taking into account the gas heating, metastable levels excitation and changing of pulverization coefficient γ with applied microwave power correctly describs the decrease of n_{Ti}, the main effect of n_{Ti} decrease in magnetron area is the changing of γ, in microwave area, it is mainly due to gas heating.

References

[1] S. M. Rossnagel, J. Vac. Sci. Technol. B 16, 2585 (1998)
[2] M. Yamashita, Y. Setsuhara, S. Miyake, M. Kumagai, T. Shoji and J. Musil, Jpn. J. Appl. Phys. Vol. 38, 4291 (1999)
[3] J. Lu and M. J. Kuschner, J. Vac. Sci. Technol. A 19, 2652 (2001)
[4] O. Leroy, L. de Poucques, C. Boisse-Laporte, M. Ganciu, L. Teulé-Gay and M. Touzeau, submitted to J. Vac. Sci. Technol. A, (2003)
[5] Y. Yamamura and T. Tawora, Atomic Data and Nuclear Data Tables, 62, (1996), p. 149-253

Modeling of arc formation in a dc plasma spray torch

C. Baudry[1], G. Mariaux[1], A. Vardelle[1], C. Delalondre[2] and E. Meillot[3]

[1]*Laboratoire Sciences des Procédés Céramiques et de Traitements de Surface, University of Limoges, Limoges, France*
[2] *Electricité De France,Research and Development, Chatou, Fance*
[3] *Commissariat à l'Energie Atomique, Le Ripault, Monts, France*

Abstract

This work deals with the 3-D transient simulation of the arc behavior and plasma flow in a d.c. plasma spray torch. Two approaches are proposed to consider the conversion from electrical to thermal energy in the plasma-forming gas. The first approach involves a uniform time-dependent heat source in a certain zone of the nozzle. The volumetric generation rate is, then, used as a source term in the energy conservation equation. Even if this approach does not take into account the physics of arc formation, it provides a good estimate of the gas velocity and temperature profiles at the nozzle exit. However, it requires the knowledge of the torch efficiency to give reliable results. The second approach consists in solving simultaneously the gas flow and current density conservation equations and Maxwell and Ohm's laws using arc boundary conditions derived from experimental observations. It makes it possible to investigate the dynamic behavior of the arc when using a new anode.

Introduction

A key aspect of the behavior of a d.c. plasma torch is the stochastic aspect of arc formation inside the nozzle. This unsteady phenomenon results in instabilities in the jet flow fields that are enhanced by the turbulent mixing with the ambient gas when the plasma jet issues in the quiescent surrounding gas. In addition, the wear of electrodes and possible drifts in nominal process conditions contribute also to make the flow time-dependent. A comprehensive model of high-intensity arcs in d.c. plasma guns must address the interaction between electric, magnetic, fluid dynamics and thermal phenomena. It is still a topical and challenging subject that has received a renewed attention during the last years [1-4].

This paper addresses the modeling of the transient conversion from electrical to thermal energy in the plasma-forming gas. The term objective of the work is to develop a fully predictive numerical simulation of the plasma spray process using as sole input data the process parameters fixed by the operator. In this study, two approaches to arc formation are proposed:

- The first approach assumes that the power generation occurs uniformly throughout a given volume inside the nozzle. The transient volumetric generation rate is used as a source term in the energy conservation equation of the fluid [5].
- The second approach consists in a 3-D transient modeling of the arc column and its attachment on the anode wall. It is based on the simultaneous solutions of the conservation equations of mass, momentum energy and current and the electromagnetism equations and uses experimentally derived arc boundary conditions.

Torch operating conditions

The calculations are performed with a torch geometry corresponding to the F4-MB plasma spray torch of Sulzer-Metco. The spraying parameters combine high arc current and hydrogen content in the plasma-forming gas so as to favor the restrike mode for the arc movement. This mode voltage is characterized by a saw-tooth shaped time-evolution of the arc voltage that can be easily modeled by a periodic function V(t). The set of operating conditions are listed in table 1 and the actual time-evolution of the torch voltage under this set of working conditions is shown in figure 1.

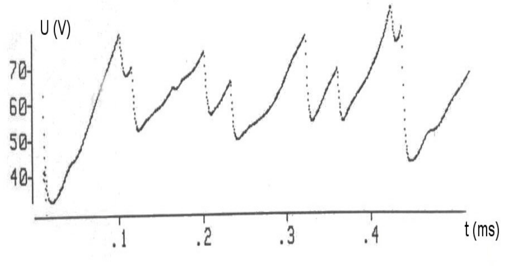

Figure 1 : Time-evolution of arc voltage under the spraying conditions of table 1

Table 1: Plasma spraying parameters

Torch nozzle exit	7 mm
Plasma-forming gas	45 slm Ar + 15 slm H_2
Gas mass flow rate	1.25 $g.s^{-1}$
Arc current **I**	600 A
Actual torch effective power	21,450 W
Environment	Air at atmospheric pressure

Plasma-flow modeling

The model is based on the following assumptions:

- The arc is unsteady and three-dimensional.
- Local Thermodynamic Equilibrium (LTE) prevails in the whole computational domain. If this assumption is acceptable in the arc column, appreciable deviations from LTE may occur in the anode and cathode regions. However, LTE assumption is used in this study to simplify the analysis.
- The plasma is optically thin.
- The flow is incompressible. This hypothesis is reinforced by a preliminary numerical simulation under the same torch operating conditions (table 1) with the assumption of a compressible flow that resulted in a pressure field ranging between 1.013 10^5 and 1.275 10^5 Pa and a Mach number always lower than 0.4.

Under these assumptions, the conservation equations may be expressed as:

Mass:

$$\frac{\partial \rho}{\partial t} + div\, \rho\vec{v} = 0 \qquad (1)$$

where ρ is the plasma density and $\vec{v}$ is the local instantaneous velocity.

Momentum:

$$\rho\frac{\partial \vec{v}}{\partial t} + \left(\rho\vec{v}.\overrightarrow{grad}\right)\vec{v} = -\overrightarrow{grad}\, p + div\,\vec{\tau} + \rho\vec{g} + \vec{S} \qquad (2)$$

where p is the local pressure, g is the gravitational acceleration, $\vec{\tau}$ is the momentum diffusion tensor and $\vec{S}$ is a source term.

Energy balance:

$$\rho\frac{\partial H}{\partial t} + \rho\vec{v}.\overrightarrow{grad}\, H = -div\, Q - S_{rad} + \overset{o}{q} \qquad (3)$$

where h is the enthalpy, Q is the heat diffusion flux, S_{rad} is the radiation term and $\overset{o}{q}$ is a source term.

Species:

$$\rho\frac{\partial X_i}{\partial t} + \rho\vec{v}.\overrightarrow{grad}\, X_i = div\left(\rho D_{ij}\,\overrightarrow{grad}\, X_i\right) \qquad (4)$$

where Xi is the mass fraction of species i. and Dij the diffusivity of species i in the mixture j.

The thermodynamic and transport properties of the argon-hydrogen gas mixture are calculated using the laws of mixtures and the data of pure gases [6].

The set of governing equations (1-4) expressed in curvilinear coordinates in a structured mesh grid is solved using the commercial ESTET 3.4 CFD finite volume code [7- 8] that is based on the SIMPLEC algorithm [9].

Modeling of thermal energy generation in the plasma-forming gas

The conversion from electrical to thermal energy in the plasma-forming gas is modeled by a heat source in a given volume V_{olume} inside the nozzle. The thermal energy generation is supposed to occur uniformly throughout this volume. The transient volumetric generation rate q° is then taken into account as a source term in the energy conservation equation. It is equal to the instantaneous electric power V(t).I divided by V_{olume}. The latter corresponds to a cylinder with a diameter equal to the diameter of the nozzle and a length that is adapted so as to predict the right torch thermal efficiency under the spraying conditions of the study.

The calculation domain and boundary conditions required for the solution of the set of conservation equations are shown in Figure 2 and Table 2. The calculation domain (42 x 125 x 42 mm^3) includes the torch nozzle in the internal field and the plasma free jet and substrate in the external field. The numerical grid consists of 147,825 nodes: 45, 73 and 45 in the x-, y- and z-direction, respectively, with a finer mesh closed to the walls (anode and substrate) to have an accurate calculation of the heat flux to the anode and the part. The gas flow is supposed to be made up of three gases: the plasma-forming gas (Ar-H$_2$), ambient gas (air) and powder carrier gas (Ar).

The plasma-forming gas enters the domain with a uniform temperature (27°C) and a laminar velocity profile that fits the conic shape of the tip of the cathode. The shear stress at the anode wall is calculated from the "law of the wall" through a friction coefficient. The heat transfer to the nozzle is deduced from the momentum and heat transfer analogy in the wall boundary layer using the functional relation of Prandtl-Taylor and assuming that the surface temperature of the anode is maintained at 1,000°C.

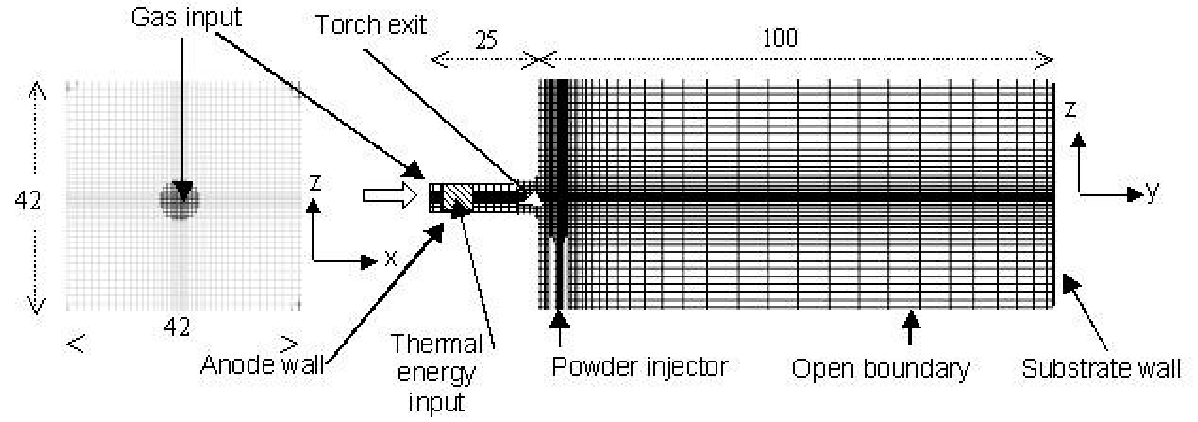

Figure 2 : Calculation domain, grid and boundaries conditions (all dimensions are in millimeters)

Table 2 : Boundary conditions (subscript n stands for normal and τ for tangential)

	Enthalpy H (J.kg^{-1})	Velocity v (m.s^{-1})	Pressure p (Pa)	Mass fraction
gas input	$H = H_0$	$v = v_{max}\left(1-\left(\frac{r}{R}\right)^2\right)$	$p = p_0$	$X_{Ar} = X_{Air} = 0$ $X_{ArH_2} = 1$
anode wall	$H = H_w$	$v = 0$	$\frac{\partial p}{\partial n} = 0$	$\frac{\partial X_i}{\partial n} = 0$
open boundary	$\frac{\partial H}{\partial n} = 0 \quad if\ v_n > 0$ $H = H_0 \quad if\ v_n < 0$	$\frac{\partial v_\tau}{\partial n} = \frac{\partial v_n}{\partial n} = 0$	$p_{atm} = p + \frac{1}{2}\rho v^2 \quad if\ v_n < 0$ $p_{atm} = p \quad if\ v_n > 0$	$if\ v_n > 0 \quad \frac{\partial X_i}{\partial n} = 0$ $if\ v_n < 0$ $X_{air} = 1, X_{Ar} = X_{ArH_2} = 0$

Figures 2 and 3 show the predicted and experimental gas velocity and temperature profiles at 2 mm from the nozzle exit. The gas temperature is determined by emission spectroscopy and velocity by a "time of flight" method applied to the luminous fluctuations of the plasma jet [10, 11]. As both measurement techniques provide time-averaged information, steady-state calculations were performed to compare the experimental and projected data. From these two figures, it can be seen that the temperature profile is correctly predicted by the model while the velocity profile is too flat. This may results from the assumption of a uniform heat generation in the nozzle that is not representative of the arc geometry.

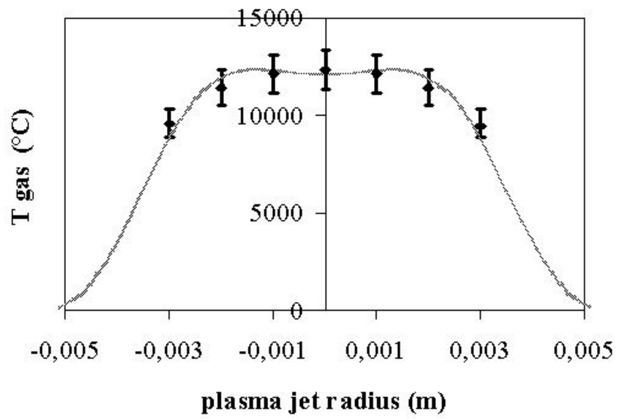

Figure 3 : Predicted and measured gas temperature at 2 mm from nozzle exit

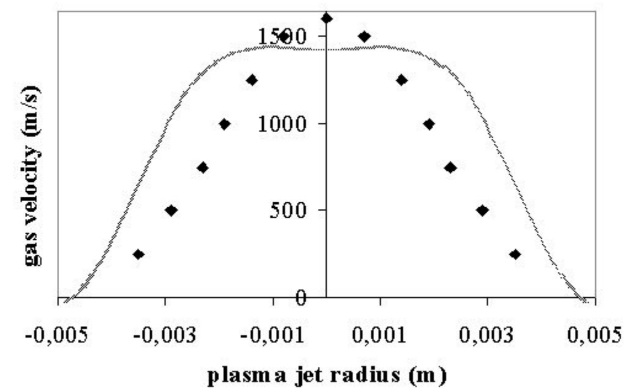

Figure 4 : Predicted and measured gas velocity at 2 mm from nozzle exit

Modeling of the arc by using a MHD model

The model is based on the simultaneous solution of the fluid dynamics and electromagnetism equations. The source terms in equations 2 and 3 are expressed as :

$\overset{o}{q} = \vec{j}.\vec{E}$ (5) and $\vec{S} = \vec{j} \wedge \vec{B}$ (6)

where $\vec{B}$ is the magnetic field, $\vec{E}$ is the electric field and $\vec{j}$ is the current density. They are calculated from the equation of current continuity, Ohm's law and Maxwell's equations under the assumptions of electric neutrality and quasi-stationary state for electromagnetism. The latter assumption is admitted to be pertinent in arc plasmas [12-13]. No specific treatment of anodic and cathodic sheath has been taken account.

The calculation domain is shown in figure 5. The 3-D grid comprises 99,937 nodes : 37, 73 and 37 in the x-, y- and z-direction, respectively. The plasma-forming gas enters the computation domain with a uniform temperature (27°C) and a vortex velocity profile. The boundary conditions are resumed in table 3.

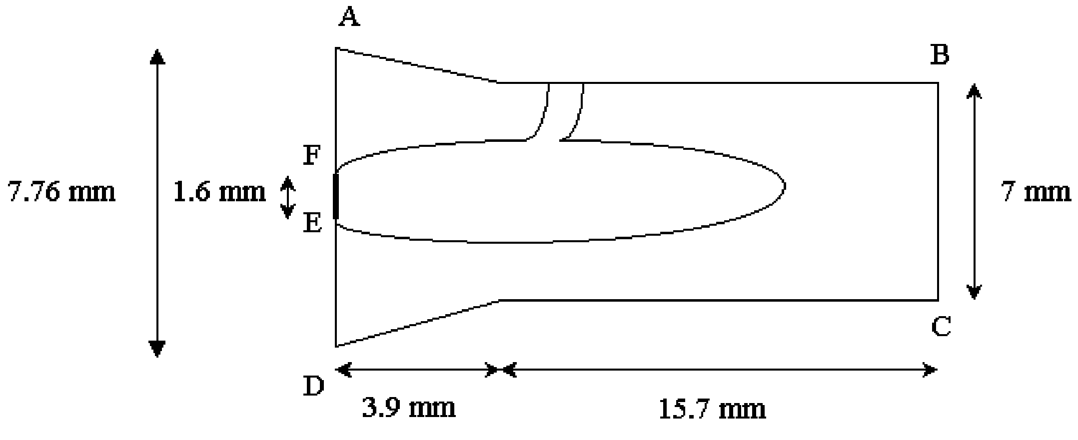

Figure 5 : Calculation domain

A hot gas column is used to initiate the calculation : a gas flow rate at 10% of the nominal value (table 1) and 200 A at 11,000 K simulates the initiation. Once the arc is initiated, the arc current and gas flow rate are increased up to the nominal values over 400 calculation time steps that is $4\ 10^{-5}$ s.

A breakdown of the arc occurs when the electric field is higher than a specific value (E_b=$1.6.10^5$ V.m^{-1}). The creation of a new attachment spot by re-arcing is favored by the modification of the boundary condition for the electrical potential at the anode wall: the potential reached by the arc just before breakdown is imposed on a ring on the anode wall, closed to the location where the maximum electric field value was observed. After a few time steps (about 2-3), the electric potential at the anode wall is stabilized and the decrease in arc voltage is observed as expected after an upstream re-arcing.

Table 3 : Boundary conditions

	Magnetic potential A (T.m)	Enthalpy H (J.kg^{-1})	Velocity v (m.s^{-1})	Pressure P (Pa)	Electrical Potential Pot (V)
[AF],[DE] (inflow)	$\frac{\partial A}{\partial n}=0$	$H=H_0$	Vortex profile	$p=p_0$	$\frac{\partial Pot}{\partial n}=0$
[EF] (cathode tip)	$\frac{\partial A}{\partial n}=0$	$\frac{\partial H}{\partial n}=0$	$v=0$	$\frac{\partial p}{\partial n}=0$	$Pot=0$
[BC] (outflow)	$A=A^{(n)}$	$\frac{\partial H}{\partial n}=0$	$\frac{\partial v_r}{\partial n}=\frac{\partial v_x}{\partial n}=0$	$if\ v_x>0 \quad p_{atm}=p$ $if\ v_x<0$ $p_{atm}=p+\frac{1}{2}\rho v^2$	$\frac{\partial Pot}{\partial n}=0$
[AB],[DC] (anode wall)	$\frac{\partial A}{\partial n}=0$	$-\frac{k}{C_p}\frac{\partial H}{\partial n}=h_{eq}\left(T_w-T_{ext}\right)$	$v=0$	$\frac{\partial p}{\partial n}=0$	$Pot=DPOT$

In this table, k and Cp are the thermal conductivity and specific heat of the gas, respectively, h_{eq} is a heat transfer coefficient, T_{ext} is the temperature of the cooling water and DPOT is the calculated value of the electrical potential at the previous time step. In the present calculations, h_{ef} is set at 10^5 W. m^{-2}K^{-1}.

Figure 6 shows the electrical potential distribution along a 16,000K isotherm just after an upstream "restriking". The new and old attachment spots can be seen on the figure. The life time of the two spots co-existence is around 2 µs in this case. The persistence of the older is explained by a hot zone at this location after the arc breakdown. At the attachment point, the predicted current density is at the order of 10^7 Wm^{-2}.

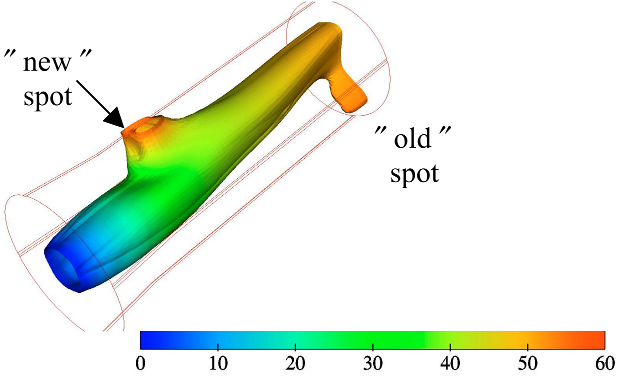

Figure 6: electrical potential field along a 16,000 K after a breakdown

Figures 7 to 10 show the onset of the arc followed by the lengthening of the arc column until breakdown. Under the conditions of this study, the arc operates in the restrike mode. Due to the magnetic body force witch does not balance the gas dynamic forces that act on the arc column, the arc exhibits a strongly transient behavior. In addition, as in the model, the anode wall is supposed to be smooth, the arc spot slides continuously on the anode wall in the direction of the flow until a breakdown occurs and a new spot is created upstream in the anode channel.

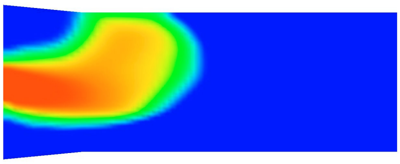

Fig. 7: temperature field at t=5 10^{-5} s

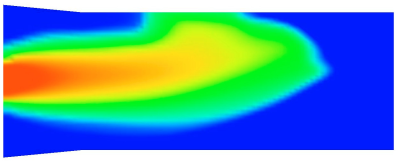

Fig. 8: temperature field at t=8 10^{-5} s

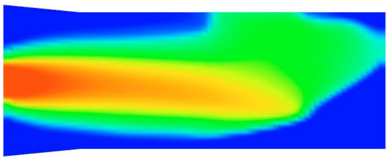

Fig. 9: temperature field at t= 10^{-4} s

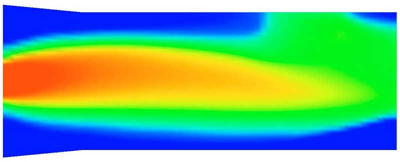

Fig. 10 : temperature field at t=1,1 10^{-4} s

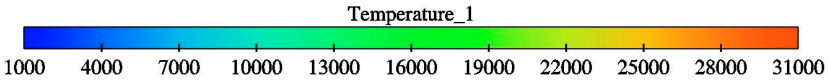

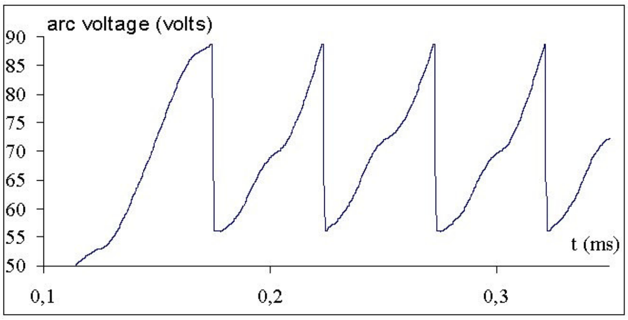

Figure 11 : Time-evolution of arc voltage

Figure 11 shows the projected time-evolution of the arc voltage. It exhibits the characteristic saw-tooth variation of the restrike mode at a frequency of about 20 kHz. The limits of the arc voltage are a little bit to high, as well as the frequency value. Further investigation will be performed about E_b and the anode thermal boundary condition (h_{eq}). The arc movement inside the anode gives rise to time-variation of the gas temperature and velocity at the nozzle exit that fluctuate around 16000 K and 2000 m/s for the calculations presented in this paper.

Conclusion

On the basis of this 3- D numerical study of the transient conversion from electrical to thermal energy in the plasma-forming gas, the following conclusions can be drawn:

- The use of a heat source in the energy equation makes it possible to project the gas velocity and temperature profiles at the nozzle exit and calculate the flow fields outside the torch. However, this approach requires an accurate calculation of the heat transfer to the anode wall and the "right" length of the volume located inside the nozzle in which the heat conversion proceeds. The knowledge of the actual torch thermal efficiency in the operating conditions of the study or the use of a 1-D energy balance in the arc column can help to project the arc length and, therefore, get an estimate of the length of this volume. This simple approach can be easily implemented in a model of the plasma spray process.
- The arc behavior predicted by the simultaneous solution of the transient equations of fluid flow and electromagnetism is reasonably consistent with experimental observations. The calculated arc voltage and current density at the anode wall are reasonable. However, the model overestimates the gas temperature and velocity. It is believed that it is, to a large extent, explained by the boundary conditions of the model. The coupling of the flow calculations with a thermal model calculating the heat diffusion in the anode wall is in progress. Also, the condition used for the arc breakdown has to be improved and validated.

References

[1] A. Kaddani, S. Zahrai, C. delalondre, O. Simonin, J. Phys. D: Appli. Phys. 28 (1995), 2294
[2] L. Schlitz, S. V. Garimella, S. H. Chan, J. Appli. Phys. 85 (1999), 2547
[3] J.J. Gonzalez, P. Freton, A. Gleizes, J. Phys. D: Appli. Phys. 35 (2002), 3181-3191
[4] He-Ping Li, E. Pfender, Xi Chen, J. Phys. D: Appli. Phys. 36 (2003), 1084-1096
[5] G. Mariaux, E. Legros, A. Vardelle, in the Proceedings of 10th CIMTEC, July 2002, Firenze, Italy, International Ceramics Congress, vol. F
[6] Boulos, M. and P. Fauchais, E. Pfender: Thermal Plasmas: Fundamental and Applications, 1995, Plenum Press, New York
[7] ESTER-ASTRID, SIMULOG , 1 rue James Joule, 78286 Guyancourt Cedex, France, http://www.simulog.fr
[8] Kaddani, Ph. D thesis, Paris VI, France "2-D and 3-D modeling of electric arcs in argon at atmospheric pressure" (1995), in french
[9] S. V. Patankar,"Numerical heat transfer and fluid flow", (1980), Mc Graw Hill, New York (1980)
[10] M.P. Planche, Ph. D. thesis, "Experimental study of fluctuating plasma jets", in French (1995), University of Limoges, France
[11] O. Betoule, Ph. D. thesis, "Relationships between the distributions of particle velocity and temperature and coating properties", in French (1994), University of Limoges, France
[12] S. Vacquié, “L’arc électrique”, in French, Eyrolles, (2000)
[13] M. Gonzales, Ph. D. thesis, "Three-dimensional and unsteady simulations of the interaction between an electric arc and a surrounding flow", in French (1999), University of Toulouse, France

Deposition of carbon films from plasma of a secondary discharge supported by RF discharge

V. Chernyak[1], I. Mozharovskij[1], M. Fedorchenko[2], I. Babich[1], V. Zrazhevskij[1]

[1]*Department of Physical Electronics, Taras Shevchenko Kyiv University, Kyiv, UKRAINE*
[2]*Department of Microelectronics, Taras Shevchenko Kyiv University, Kyiv, UKRAINE*

The work includes the results of researches of the plasma parameters of the secondary discharge supported by the RF discharge in argon and mixture of molecular and hydrocarbon gases; the deposition of carbon films in plasmachemical systems with RF discharge; the deposition of carbon films on an anode and a cathode of the secondary discharge supported by the RF discharge; the electronic and emission properties of carbon films.

Probe technique was used for the definition of parameters of plasma. Spectroscopy analysis of electron energy loss and Raman spectroscopy were used for the analyses of properties of carbon films.

Plasma destruction of persistence organic pollution in water

V. Chernyak[1], I. Babich[1], V. Zrazhevskij[1], V. Yukhymenko[1], A. Trokhymchuk[1], E. Molozhenova[2], Ya. Tarasova[3], I. Molozhenov[4],

[1]*Department of Physical Electronics, Taras Shevchenko Kyiv University, Kyiv, UKRAINE*

[2]*Institute of Toxicology of Ukrainian National Academy of Science, Kyiv, Ukraine*

[3]*Institute of Biocolloidal Chemistry of Ukrainian National Academy of Science, Kyiv, Ukraine*

[4]*Medical Institute, UANM, Kyiv, Ukraine*

The creation principles of non-equilibrium plasmachemical technology for destruction of the high active chemical multicomponent agents will be considered. The plasma method will be shown with conversion of phenol and 1,1 –di(4- chlorphenol)-2,2,2-threechlorethane (DDT) in water solution.

The work includes the results of researches: The toxicity of plasma destroys of DDT in water solution with added of organic solvent; the influence of plasma creation gas (an air, a water vapour and mixture of an air with aerosol of treating solution), of the "liquid" electrode polarity, the material of electrodes and the concentration of the initial toxic organic agent in a water solution on effectiveness of destruction stimulated by plasma of a secondary discharge in a plasma stream with a liquid electrode.

The absorption and Raman spectroscopies and reagent methods were used for the analyses of destruction of the organic agents. Vegetable tests for investigation of toxicity of plasma destroys products were used. The efficiency of plasma systems for water cleaning with secondary discharges is compared with effectiveness of water treatment by ozone.

Varnished SiO_2 films PECVD deposited on OT 59 brass as anti-corrosion layers

G. Moretti[1], F. Guidi[1], R. Canton[2], M. Battagliarin[3]

[1] Department of Chemistry, University Ca' Foscari Venezia, D.D. S. Marta 2137 - 30123 Venezia, (Italy)
[2] MOMA s.r.l., via Pastore, 1 - 42026 Reggiolo (Reggio Emilia - Italy)
[3] CNR - IENI, Corso Stati Uniti, 4 - 35127 Padova (Italy)

Specimens of an industrial brass substrate (BS) (OT 59; diameter: 8 cm) were treated in a cylindrical process chamber at 0.1 mbar with O_2 and hexamethyldisiloxane (HMDSO) with a 13.56 MHz radio frequency source and at about 35°C. Varying the PECVD deposition time, different layer thicknesses were obtained. One half of the obtained PECVD treated (PT) specimens were varnished with an industrial powder paint and the different specimens were evaluated from the corrosion point of view in a standard medium: (aerated 1 N sulphuric acid at 25°C from 1 to 168 h).
Secondary Ion Mass Spectrometry (SIMS) technique was used to evaluate the element profiles and the coating obtained thickness, while DC (Tafel curves) and AC techniques (Electrochemical Impedance Spectroscopy - EIS) were used on BS, PT and painted PT specimens to examine their corrosion performance. The polarization curves (DC data) obtained at the different immersion times for the painted PT and PT specimens respectively yielded very small exchange current densities and more noble potentials than those observed for the bare BS both in the short (24h) and long time (168h) tests. This was confirmed by AC data. EIS measurements were interpolated by means of an equivalent circuit model proposed by Kendig et al [1] in which high frequency and low frequency contributes to the impedance spectra are distinguished in order to separately evaluate the variation of coating properties over time (168h tests) [2].
The obtained data was used to tune the process parameters to industrially apply an appropriate PECVD SiO_2 layer to objects whose life-time had to be at least 5-10 years corrosion resistant for quality motivations. Some of these varnished PT objects, undergone to the ASTM B117/97 protocol tests, resisted until 1000h (and more) of salt spray (fog) chamber time.

References

[1] M.W. Kendig, H.-S. Ryang, T.-L. Liao, and S.L. Jeanjaquet, Corrosion, **55 No. 3**, 222 (1999).
[2] E. Angelini, S. Grassini, F. Rosalbino, F. Fracassi, R. d'Agostino, Proc. of 15th International Corrosion Congress, Granada (Spain), September 22-27, 2002, Paper n° 362.

Two-dimensional pattern formation in Dielectric-Barrier Discharge

A. Chirokov[1], A. Gutsol[1], A. Fridman[1],
K. D. Sieber[2], J. M. Grace[2], K. S. Robinson[2]
[1]*Drexel University, College of Engineering, Drexel Plasma Institute*
[2]*Eastman Kodak Company*

Abstract:

Formation of regular pattern by filaments in dielectric-barrier discharge at atmospheric pressure was studied. Innovative micro-discharge interaction model in dielectric-barrier discharge was proposed. Monte-Carlo simulation of microdischarge interaction in discharge gap was developed on the basis of proposed model. Analysis and comparison between modeled and experimental patterns was performed by several methods: 2D correlation function, Voronoi Polyhedra and Fourier transform.

Introduction:

Dielectric-barrier discharge (DBD), also referred to as silent discharge, have found a number of interesting industrial applications in addition to the well know ozone generation. In particular, DBD is very effective in plasma treatment of polymer surfaces to promote wettability, printability and adhesion [1, 2]. Such discharge is an extremely non-equilibrium and usually operates at atmospheric pressure with ambient temperature, and this makes it advantageous for industry. The silent discharge is a good generator of atoms, free radicals and chemically active species, such as O, N, O_3 and OH. Most of physical and chemical processes occur within the microdischarges. In our case we study a silent discharge system for polymer web treatment. A thin polymer web moves with 5 m/sec speed on the surface of one electrode and is treated by filaments to activate the surface of the web and further to cover it by an emulsion. The goal of our study was to investigate the conditions when the surface treatment is more efficient. Surface treatment efficiency may depend on different parameters such as specific power, driving voltage amplitude, waveform and frequency. It was noticed experimentally that changes in these parameters lead to different pattern formations, i.e. a different efficiency results. In this paper we limit ourselves by detailed description of proposed discharge model and comparison of it with experimental results. We also introduce the numerical approach for examination of micro-discharge patterns, means of analyzing and interpreting time-averaged microdischarge patterns.

Experimental Setup and Results

A humid air ($N_2/O_2/H_2O$) with room temperature 300K and variable flow rate flows between two parallel electrodes, which connected to the altering power supply with the following parameters: power W= 20-150 Watt, frequency f = 10-40 kHz. Upper electrode is made of titanium and lower electrode is made of aluminum. Aluminum electrode is covered by dielectric (quartz glass) with thickness of 1 mm. The distance between upper electrode and dielectric (discharge gap) d = 0.89 mm. The system operates at atmospheric pressure (p = 1 atm). The Figure 1 shows the 8-bit image of a dielectric barrier discharge in air obtained from the experimental setup. The real discharge area was 5×5 cm. The image was taken using a storage phosphor screen that was placed on the surface of the isolator in the discharge gap. Note, that imaging plate was exposed directly to the discharge (as opposed to most other methods such as Lichtenberg figures). The storage phosphor screen was an unovercoated SO-390 storage phosphor screen and the image was scanned using a Molecular Dynamic Storage Imager with Molecular Dynamics Image Quant software. Discharge image presented in Fig. 2 was obtained using one excitation cycle at 20.4 kHz. Digital oscilloscope traces from the secondary side of the transformer indicate that the high voltage transformer shows some ringing after the initial amplified waveform is applied to the primary side. There were actually 20 half cycles of voltage occurring during the discharge used to make this image. The SO-390 storage phosphor screen employs a complex barium fluorohalide storage phosphor that is sensitive to both electron bombardment as well as UV photons. The minimum excitation required to form an imaginable center in the phosphor system is defined by the energy required to form an excitation. This energy is around 4.5 eV and sets the lower limit of energy sensitivity for this imaging system. In Figure 1 the sharper black points corresponds to more intense treatment. The existence of micro-discharge pattern is obvious. As a result, the surface treatment is not uniform. More importantly, we found that the different discharge conditions such as driving voltage frequency and amplitude result in different microdischarge patterns.

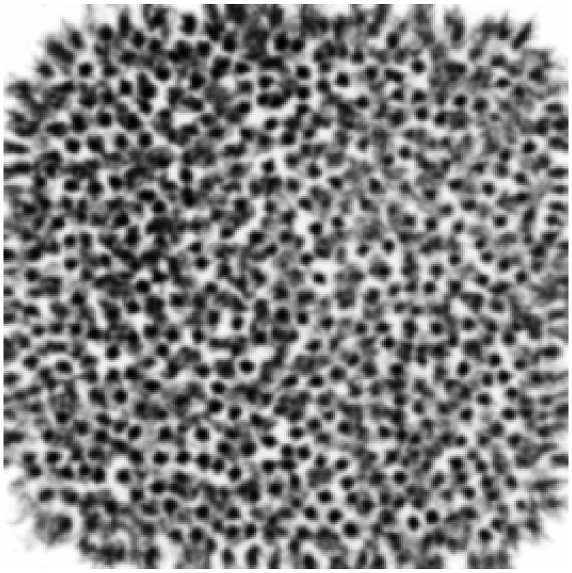

Figure 1: The top-view image of filaments in dielectric barrier discharge gap in air obtained from experimental setup using 20 excitation cycles at 20.9 kHz.

Multiple Streamer Interaction Model

As streamers are the main causers of plasma chemical processes in DBD, so it is extremely important to understand the nature of an individual streamer. The general streamer description is based on the consideration of multiple avalanches formation and propagation (Fig. 4, left side). Within the framework of avalanche propagation, the simplest set of equations containing the basic physics necessary for description of streamer propagation was considered [3, 4, 5]. This consideration, taking into account gas composition, pressure, power and current, gives us the main characteristics of the streamer, the first Townsend coefficient, electron concentration and temperature profiles in channel volume. Average characteristics of the streamer are: propagation time – 10 ns; the charge transferred by streamer – about 10^{-10} C; diameter of the plasma channel formed by streamer – about 0.1 mm; initial electron concentration in the plasma channel – about 10^{14}cm^{-3}; time of channel disappearance due to diffusion and ion mobility – 10^{-3} s. Streamer formation depends only on the local value of the electric field and the discharge gap.

In this paper, the innovative Monte-Carlo model of multiple streamer interactions is introduced. The assumption is based on a fact that space charge in the microdischarge channel decreases electric field and prevents streamer formation in vicinity of this space charge (Fig. 4, right side). The next discharge won't be expected in this region. Formation of streamer also decreases the average voltage drop in the discharge gap and consequently prevents formation of the next streamer just after the previous one. Consider two types of applied voltage in DBD: unipolar voltage and alternative voltage. In first type, one of the electrodes keeps positive and another negative. The streamer always moves in one direction, so that another streamer has small probability to break through in the same place until the first one gets enough dispersal. The totally different picture appears in case of alternative voltage. There is no need to wait until first streamer gets enough dispersal, instead, when the voltage is switched the probability of appearance of the second streamer in that place increases. After the voltage is switched, the electric field of the space charge increases the strength of the applied electric field giving the opportunity for streamer to strike. As a result, the most streamers break through the channels (or their vicinity) formed before voltage switching. In literature, this effect is called *memory effect* [6]. Each of these two types of voltage leads to the different pattern pictures. The difference in pattern pictures is visible from our simulation results and is presented and discussed below. In both cases filaments will stay separated by distance corresponding to the length scale of the field inhomogeneity. All simulation results as well as experimental correspond to alternative voltage type. For given applied voltage amplitude, adjacent filaments can get close enough that no additional filaments can squeeze between them. If the applied electric field is high enough, it will cause streamers to develop in all the untaken spaces, so that the gap becomes filled from end to end.

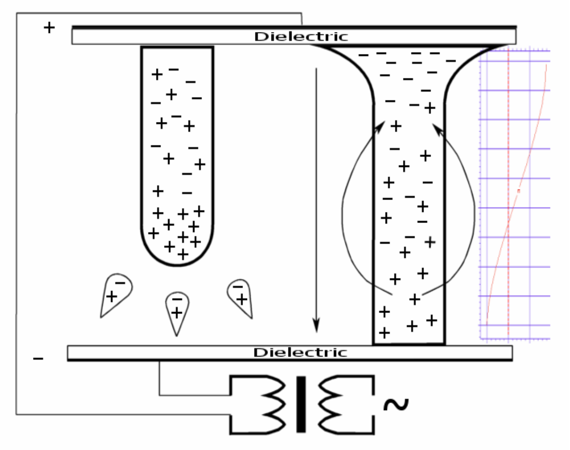

Figure 2: Streamer formation and interaction due to electric field distortion**.**

For present modeling, the probability driven cellular automata (CA) was used [10]. A cellular automation consist of

- A lattice of cells; this lattice can be any dimensional and have arbitrary size. At each time cell can be in one state.
- Local rules of transformation from one state to another, which depend on state of transformed cell as well as states of neighbor cells.

In this work, a two dimensional stochastic CA was employed. Space between electrodes in DBD was divided into cells. Thus, lets define $S_{i,j}$ as an array of states of the cellular automata. We used so-called extended form of CA, in which not only the discrete states of CA, but also some data about real physical values (charge density, electric field, energy release, random fluctuations, etc) were kept in each cell. CA transformation rules define a new state of cell at the next time step using not only data on the states of the CA but also external to CA information such as driving voltage wave. It was assumed that the probability of next streamer to occur depends only on the local value of the electric field. We determine the position of microdischarge strike based on a Monte-Carlo decision for given probability values in each automata cell. However, since streamers could appear randomly in time as well as in space, additional Monte Carlo simulation to decide whenever streamer will occur this time or not was employed. Figure 3 shows the flow chart for this procedure.

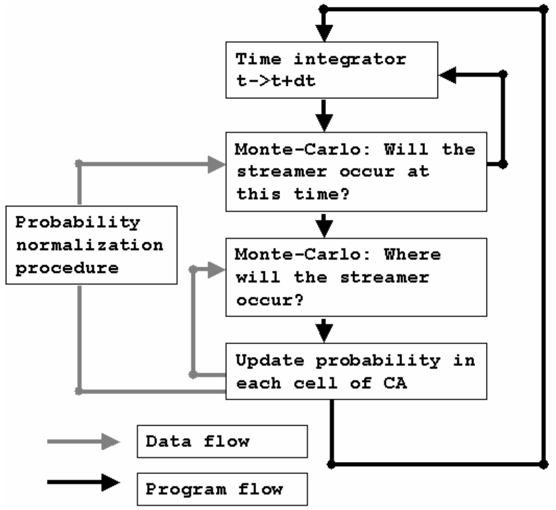

Figure 3: Flow chart for the space and time coupled Monte Carlo simulation.

Simulation and Results

The simulation code of CA was developed in C++ and works with arbitrary voltage form. The input parameters to the program are the simulation time (number of periods with period length given for the case of AC voltage), driving voltage waveform, size of CA and geometry of the discharge gap. The charge transferred by the streamer is not specified as an input parameter instead it dynamically calculated during simulation based on local electric field strength. The charge transferred by individual streamer decreases electric field inside the micro discharge channel because it creates local electric field opposites to the outer electric field. We assume that the total charge transferred by the streamer is the charge that decreases the local electric field to zero (electric current through the channel exists until the electric field drops to zero). Probability of streamer to strike in CA is calculated from local electric field by the following formula (1).

$$P(E) = 1 - \frac{1}{1 + \exp(S \cdot \frac{E - E_0}{E_0})} \quad (1)$$

Where E-electric field in the cell, E_0-critical electric field necessary for streamer formation from Meek condition, S-is DBD's ability to accumulate memory about previous streamers. In case of large S, memory effect has negligible effect on operation of DBD, thus probability function will be step function that represents Meek's condition for streamer formation [11]. In case of small S, *memory effect* significantly affects probability of streamer formation. Streamer could be formed in the weaker electric fields that required by Meek's law in the presence of ions and metastables in the gap. Value of S represents the cumulative *memory effect* and should be determined from the experiment. We used experimental data [12] to estimate value S for our system. High operation frequencies tend to decrease value of S as well as other factors that increase memory effect. The output parameters from the program represented in the density map of streamer activity on the surface of the web. For given voltage the model can calculate the dependence of current on time. Typical result of simulation obtained for the end of 20th period is shown on Figure 4, this particular simulation was performed on CA size of 50×50, DBD cell was driving by sine voltage with 4.5kV amplitude and 20 kHz. The darker the point, the more streamers strike this point. It is possible to see that streamers strike non-uniformly: some regions are well treated by streamers and some are not treated at all. This uniformity is the result of interactions between streamers and micro discharge channels.

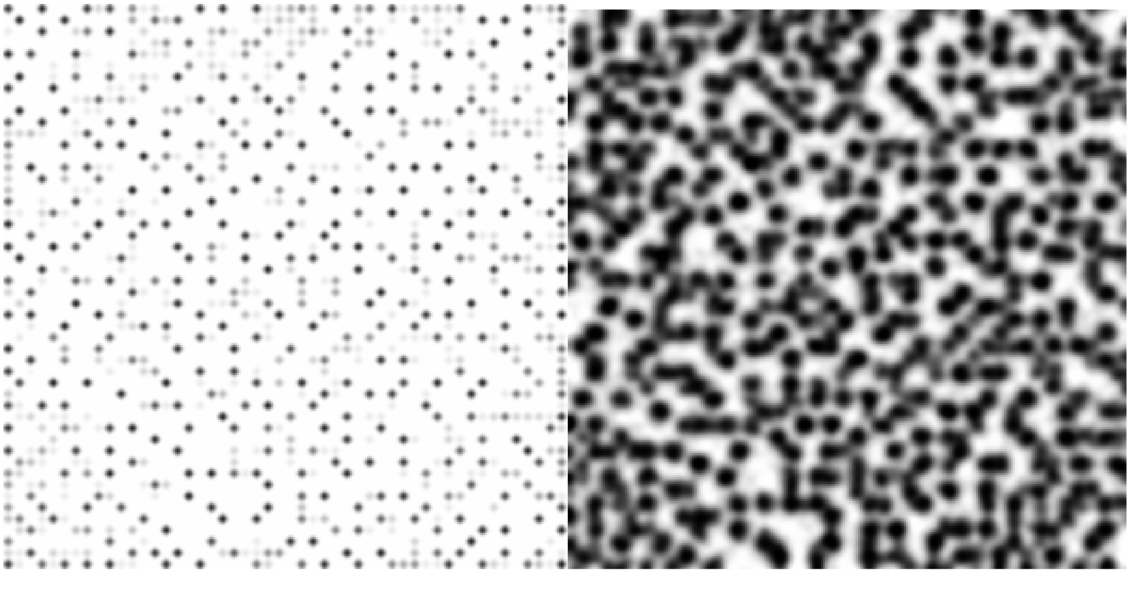

Figure 4: Simulation result on CA size 50×50. This matrix represents the number of streamers strike recorded in CA. Total number of streamers recorded is 17462 (left). Simulation result with added noise for visual comparison with experimental data (right).

Most of the cells in CA were not treated by streamers at all while some cells were treated by more than 20 times. Results of simulation as well as experimental results show non-evenly treatment in DBD.

Comparative analysis of experimental and simulated patterns

In order to describe the multiple streamer patterns and compare them with patterns obtained experimentally, three methods of analysis were used: 2D correlation function of the pattern averaged over the observed space [7], Voronoi Polyhedron approach [8] and Fourier transformation (FFT) [9].

Voronoi Polyhedra analysis of experimental data (Figure 5a) shows that most of the cells in pattern have six angles. The same result we have for the image obtained during simulation (Figure 5b). Comparison of these results with random dot distribution (Figure 6) shows that the distribution of experimentally obtained pattern looks very similar to simulated pattern, but not to the random one.

The correlation function, which is widely used for post processing in crystallography, gives us idea about an order in pattern, for example, if one can construct the correlation function of gas as a material where the position of centers are random, it would looks like in Figure 7(c), so the function would not have a periodic oscillations. The correlation function for the liquids with the local forces looks like on Figure 7(a), the oscillations exists only at the beginning, because there is no long-range order. For ideal crystal, this function has the oscillations up to infinity, Figure 7(b). From experiment, the pattern behaves, as a liquid (Fig. 7(a)) and the oscillations are smoothed by the noise. In simulation obtained image (Fig. 7(b)), the oscillations are more pronounced, but have the same liquid characteristic. From the above facts, one can conclude, the DBD pattern is of liquid type, this validates by experiment and modeling.

Two-dimensional Fourier transform was computed on the simulated pattern with added noise (Figure 4b) to make a fair comparison with experimental one. The FFT power spectrum images (Figure 8) of both experimental and simulated image are similar and have a “donut” in the center. The power spectrum image of random distribution is totally differing from experimental and simulated ones. “Donut” in power spectrum means a local order caused by streamer interactions [9]. Donut in experimental power spectrum is bigger because of the noise presence.

Conclusion

In this article we made the first attempt in modeling of DBD *memory effect* and multiple streamer interaction. The memory effect and multiple streamer interaction result in a streamers pattern formation. The compatible analysis made above verified the validation of our model of multiple streamer interaction, and this model is ready for the further investigations.

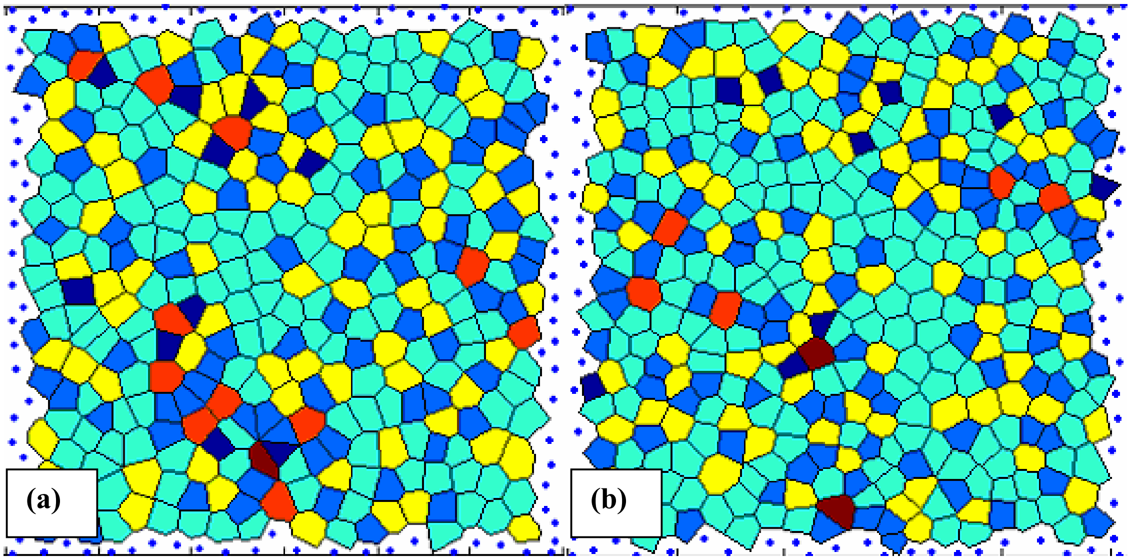

Figure 5: Voronoi Polyhedra analysis of the simulated microdischarge locations from image shown on Figure 4 (a) (left) and for the experimentally obtained microdischarge locations from image shown on Figure 1 (b) (right). Polyhedra cells are angle colored. The cells on both images obtained in simulation are mainly six-sides cells.

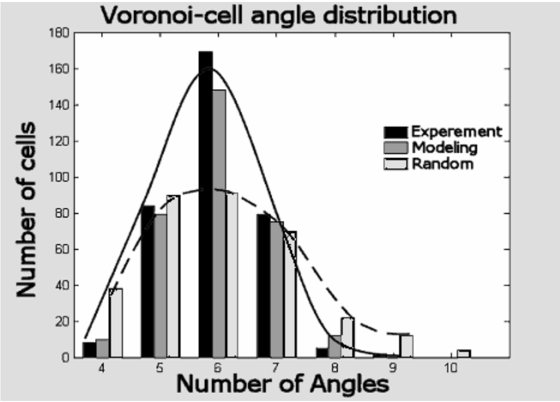

Figure 6: Distribution of Voronoi-cell angles. The experimental data (Figure 5a), simulation data (Figure 5b) and data from random-point distribution are shown for comparison.

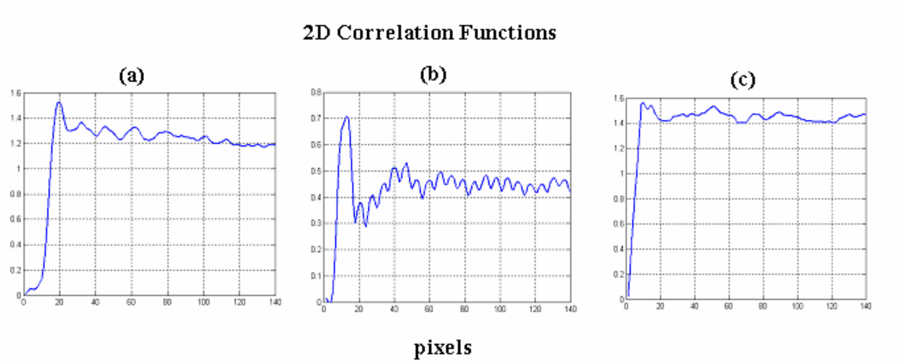

Figure 7: 2D correlation functions: (a) of experimental image from Figure 1; (b) of simulation data from Figure 4a; (c) of data form random-point distribution (shown for comparison).

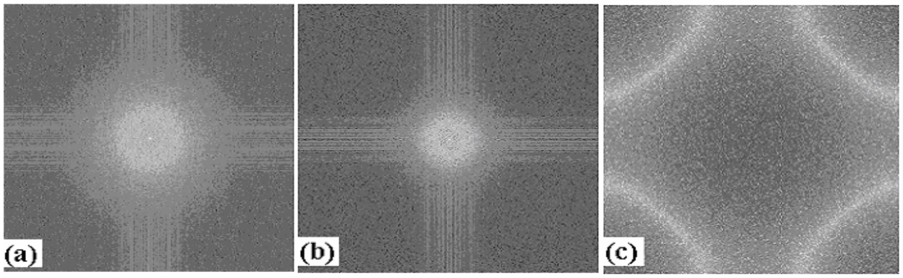

Figure 8: 2D Fourier transforms: (a) of experimental data from image in Figure 1; (b) of simulation data from Figure 4a; (c) of data from random-point distribution (shown for comparison).

References:

[1] J.L Linsley Hood, Int. Conf. On Gas Discharges and their Applications, Edinburgh (1980) 86-90

[2] T. Uehara in: Adhesion Promotion Techniques, K.L. Mittal, A. Pizzi (Eds.), Marcel Dekker, New York (1999) 139-174

[3] R Morrow, JJ Lowke “Streamer Propagation in air” J. Phys. D:Appl. Phys. 30 (1997) 614-627

[4] A. Kulikovskiy IEEE Transactions on Plasma Science, vol. 25, NO. 3, June 1997.

[5] Gunter Steinle and etc. J. Phys. D: Appl. Phys. 32 (1999) 1350-1356

[6] B.Eliasson, M.Hirth, U.Kogelschatz, J. Phys. D: Applied Phys. 20 (1987) 1421-1437

[7] M. Zuzic et al., Phys. Rev. Lett., November 6, 2000, Volume 85, Issue 19, pp. 4064-4067

[8] H. Thomas et al., Phys. Rev. Lett., August 1, 1994, Volume 73, Number 5

[9] Harburn, Taylor, Welbeny, Atlas of Optical Transforms.

[10] L. Niemeyer, L. Pietronero, H. J. Wiedmann Phys. Rev. Letters 52, 12 (1984)

[11] J. M. Meek “A theory of Spark Discharge” Physical review, volume 57 (1940)

[12] A. Aints, Ahaljaste, K Kudu, T Plank J. Phys. D: Appl Phys 30 (1997) 210-220

STUDY ON FLUORINE CONTAINING MIXTURES IN LOW PRESSURE RF ICP PLASMA

A. Gutsol, K. Iskenderova, A. Fridman

Drexel University, College of Engineering, Drexel Plasma Institute, Philadelphia, PA, USA

Abstract

The numerical studies of plasma-chemical processes in the mixtures containing NF_3/CF_4/ C_2F_6/N_2/O_2/Ar were performed using CHEMKIN gas-phase libraries. The NF_3 decomposition is almost 100 % in all cases considered and this gas is preferable to CF_4 and C_2F_6 ones. But, due to the fact that NF_3 is expensive gas, we considered the ways for its partial or total replacement on another gases such as CF_4, C_2F_6. The presence of O_2 in discharges is found to be very important.

Introduction

In the production of integrated circuits the cleaning of treatment chambers is the very time consuming operation because deposits of silicon oxides are difficult to remove from surfaces of treatment chamber. The cleaning is usually achieved by etching chamber surfaces by active particles, among which atomic fluorine is the most effective one. Atomic fluorine can be conveniently produced from stock gases as NF_3, CF_4, C_2F_6 and SF_6 in low temperature discharge plasma. Chemical Downstream Etch (CDE) used in the integrated circuits manufacture is a system that generates etching atoms in a remote plasma chamber. The typical CDE system can be divided in three parts: plasma reactor, transport tube and deposition chamber (DC).

We have developed kinetic model to describe the atomic fluorine production from NF_3, CF_4, C_2F_6 in ICP plasma source and provided comparison of effectiveness in decomposition of these parent molecules. Dilution of each fluorine-based molecules with O_2 is also studied and found to be very important. The presence of O_2 in discharges (NF_3 and C_xF_y) gives the various effects that in different plasma parameters can be treated differently. The reaction mechanism containing 216 reactions includes reactions of neutrals, ionization, dissociation, excitation, relaxation, electron-ion recombination, ion-ion recombination, dissociative attachment and ion-molecular reactions. To estimate the rate constants of electron-neutral reactions, the electron energy distribution function (EEDF) must be found. The Boltzman equation for EEDF was solved in [1], and the obtained data for the rate constants were presented in the Arrhenius expressions as a function of the electron temperature, while for neutral-neutral reactions the dependence on gas temperature is only considered.

Simulation Results

The focus of this part of the work was on analyzing of several aspects of plasma source operation including destruction of SiF_4 in NF_3/O_2 plasma, influence of O_2 on fluorine production and NO_x formation, the efficiency of CF_4 and C_2F_6 in comparison with NF_3 in DC cleaning. The performance measures emphasized are the dissociation efficiency of the parent molecule in the discharge.

We have used a plug flow reactor model. Gas residence time in plasma source is 0.5 sec and the gas temperature is supposed equal to 300K. In this model the nature of the discharge is taken into account in calculation of electron temperature and concentration. The electron temperature (T_e = 3 eV) and electron concentration were computed from simplified equation of energy consumption:

$$W = k_{eV} \cdot n_e \cdot n_0 \cdot \varepsilon_0 \cdot V$$

Where W is power of the source, V - plasma volume, n_e - electron concentration, n_0 - gas concentration, $\varepsilon_0 \approx$ 0.1 eV - characteristic value of energy transfer from electron to molecule in one collision, , $k_{eV} \approx 3\times10^{-8}$ cm^3/sec - rate coefficient of the electron-vibrational relaxation.

The dissociation efficiency in pure NF_3 gas is presented in Fig.1. The atomic fluorine yield in this case is 0.4. Dissociation of NF_3 in a discharge approaches 100%, resulting in higher F atom concentrations and higher etch rates in comparison with fluorocarbon gases.

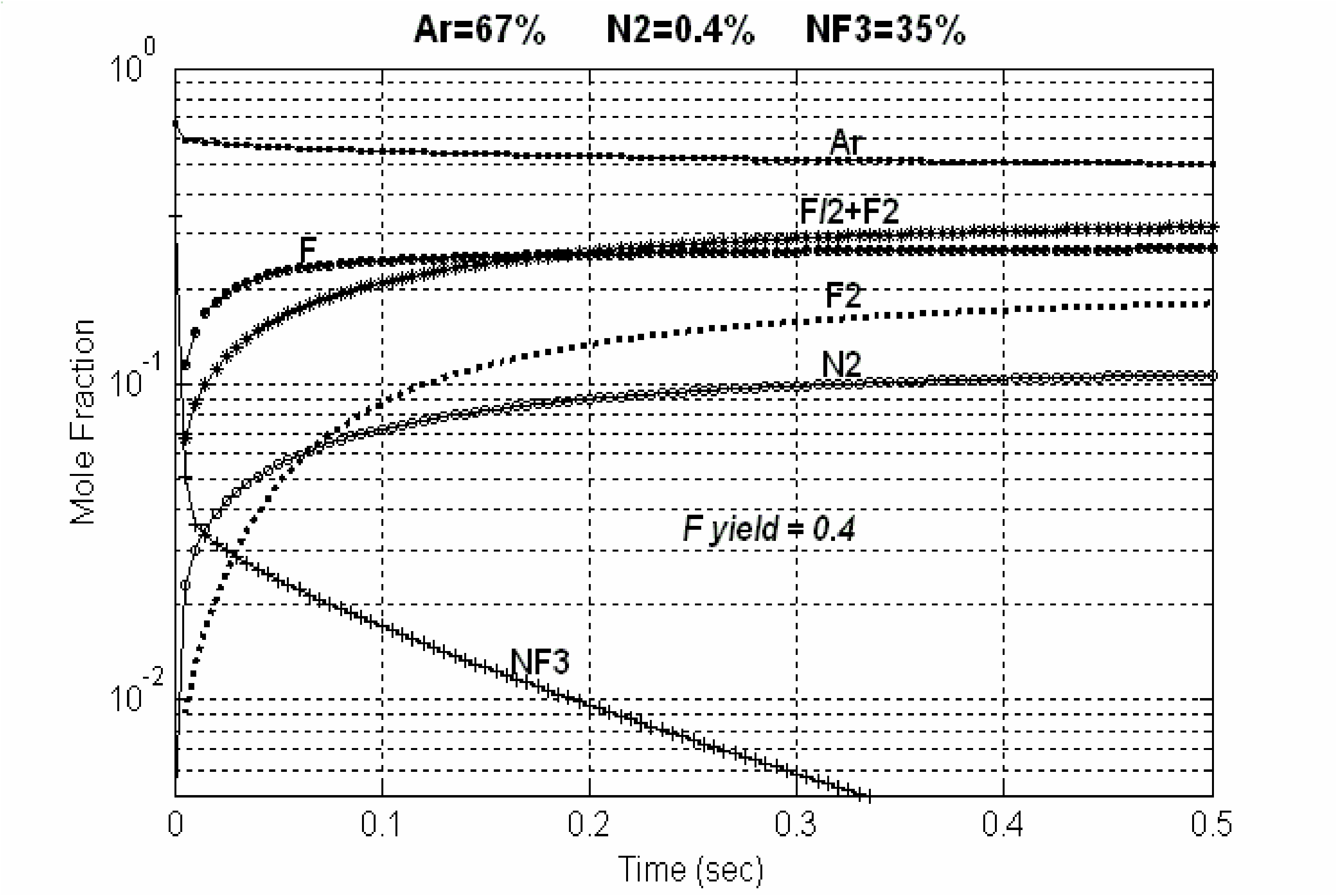

Figure 1. Numerical simulation of NF_3 dissociation in discharge. Time dependence of the main species concentration.

As one can see from Fig. 2, O-atoms enhance production of atomic fluorine but the concentration of F is not increased as O_2 added because of dilution effect. This effect can be explained in terms of the reactions. In the absence of O_2, the NF_x daughter species recombine according to:

$$NF+NF \Rightarrow N_2+2F \qquad (1)$$

$$NF+NF_2 \Rightarrow N_2+F_2+F \qquad (2)$$

The recombination mechanism of the NF_x is different in the presence of O. Oxygen atoms react quickly with NF_x species:

$$O+NF_2 \Rightarrow NF+OF$$

$$O+NF \Rightarrow NO+F$$

which leads to a reduced NF density. OF is very reactive and is lost in the discharge immediately to O_2 and F:

$$2OF \Rightarrow 2F+ O_2$$

$$O+OF \Rightarrow O_2+F$$

Therefore, in the presence of oxygen atoms in the discharge the occurrence of the recombination reactions (1) and (2) is reduced, the concentration of their products N_2 and F_2 is smaller, and production of atomic fluorine is enhanced by O atoms.

The dissociations of CF_4 and C_2F_6 in gas discharge in presence of oxygen are shown on Fig.3-4. The discharges of fluorocarbon gases produce significant amounts of molecules and radicals that do not contribute to etching reactions and even cause fluorocarbon deposition, such as CF_3, COF_2, and larger carbon chain molecules like C_2F_6. The O_2 addition into CF_4 discharge plays the significant role [2]. It increases the atomic fluorine concentration due to the oxidation of CF_x molecules. The dissociation of C_2F_6 is less dependent on the O_2 but more dependent on power consumption. Also, CF_4 molecule dissociates faster then the C_2F_6 because of shorter lifetime in discharge. Such tendency is observed in the systems with the high-energy input (200 J/cm^3) [2]. Our modeling was performed for low energy input (60 J/cm^3). It can explain why the dissociation degree of C_2F_6 is smaller then observed in our simulation results, see Fig.3-4.

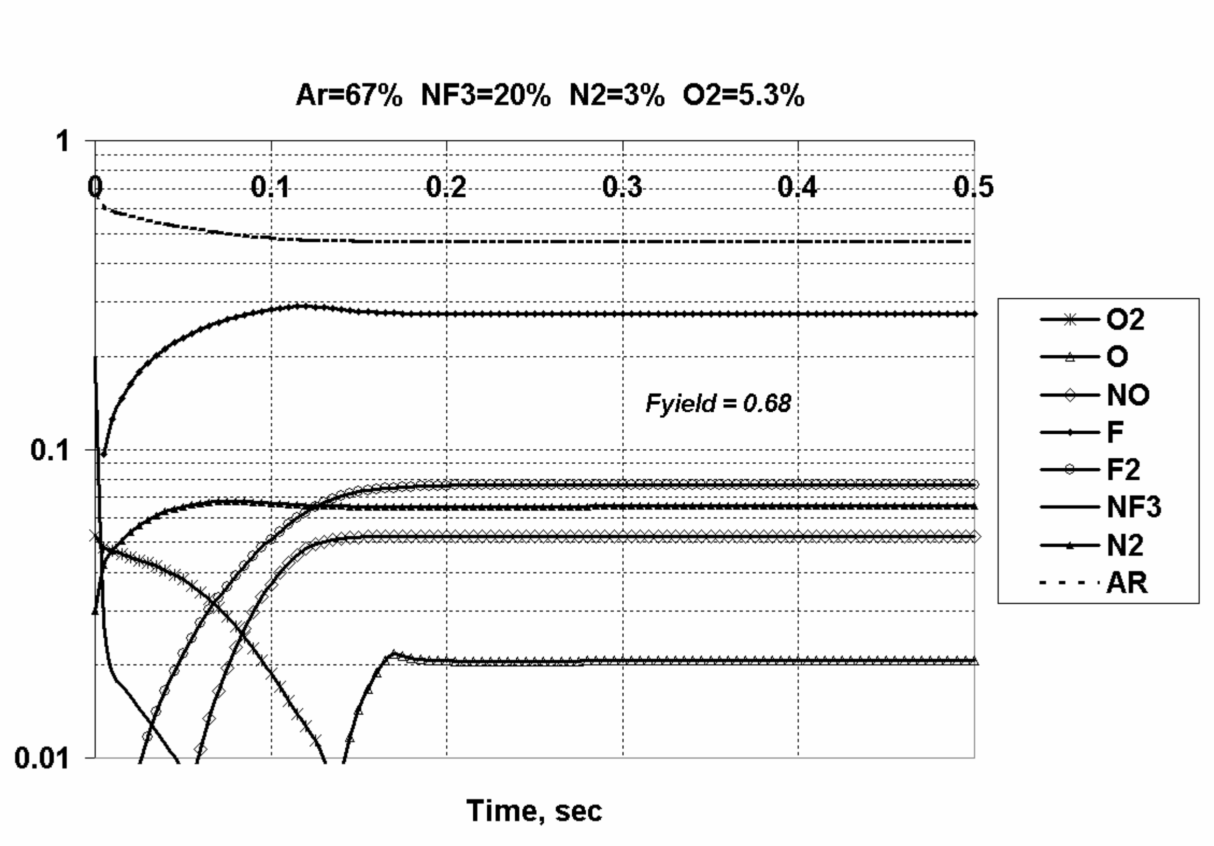

Figure 2. Numerical simulation of $NF_3/N_2/O_2$ plasma chemistry. Time dependence of the main species concentration.

The summary of F yield in discharge for different parent molecules is placed in Table 1. The F yields for different parent molecules were calculated as following:

$$\text{For (Ar/NF3 /N2)}: \qquad F_{yield} = \frac{(F)_{out}}{3(NF_3)_{in}} \cdot \frac{(Ar)_{in}}{(Ar)_{out}}$$

$$\text{For (Ar/CF4/N2)}: \qquad F_{yield} = \frac{(F)_{out}}{4(CF_4)_{in}} \cdot \frac{(Ar)_{in}}{(Ar)_{out}}$$

$$\text{For (Ar/C2F6/N2)}: \qquad F_{yield} = \frac{(F)_{out}}{6(C_2F_6)_{in}} \cdot \frac{(Ar)_{in}}{(Ar)_{out}}$$

Results in Table 1 shows that nitrogen trifluoride is environmentally preferable to CF_4 and C_2F_6 because it has a shorter atmospheric lifetime and also it can approach 100% dissociation, resulting in higher F atom concentrations and higher etch yields as compared to fluorocarbon gases.

Table 1. F-yield in discharges with different parent molecules.

	NF_3	CF_4	C_2F_6
Ar / N_2	0.4	0.27	0.1
Ar / N_2 / O_2	0.68	0.34	0.15

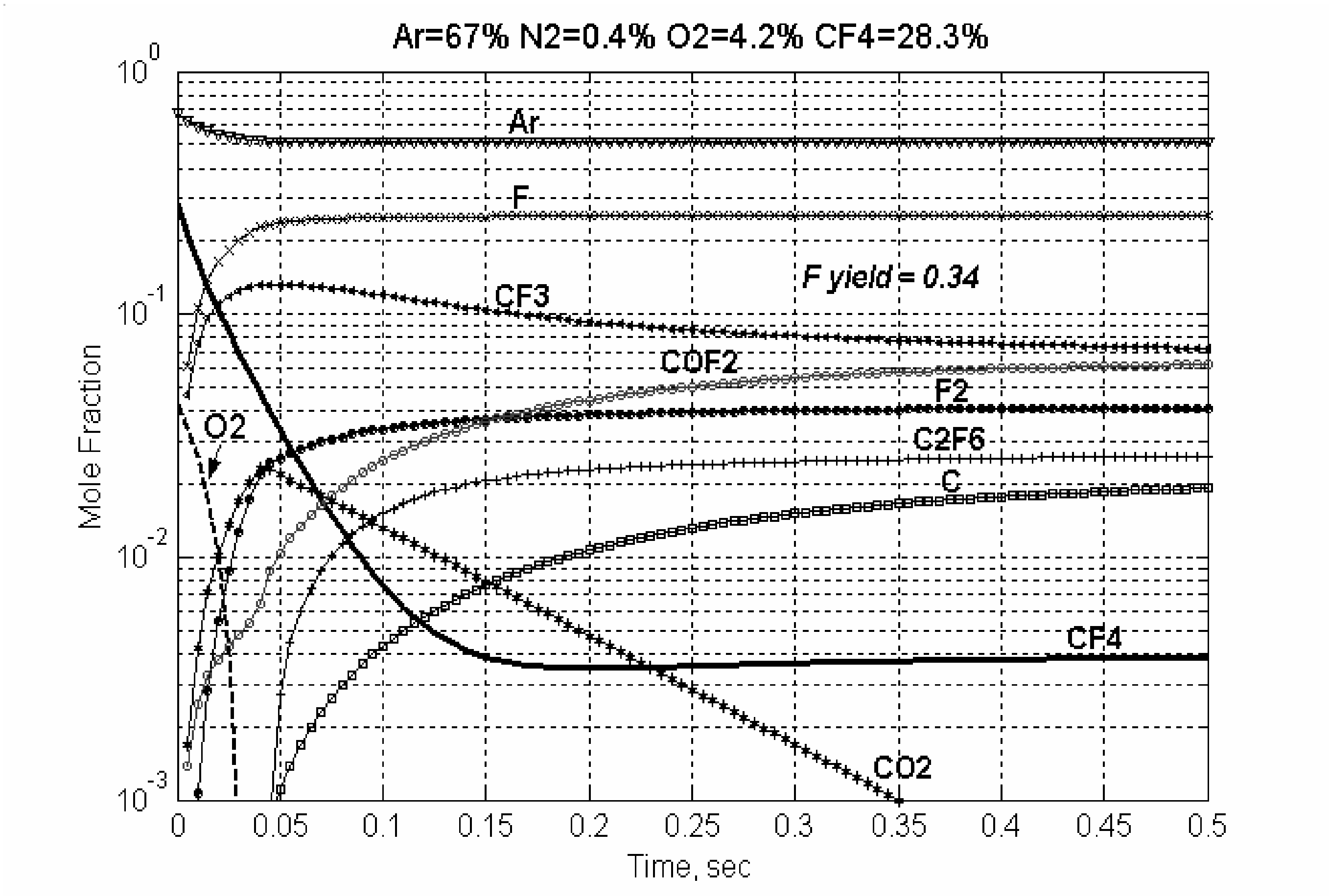

Figure 3. Numerical simulation of CF_4/O_2 plasma chemistry. Time dependence of the main species concentration.

Summary

The important issues of the plasma source performance and major species balance has been addressed in this study. We found that NF_3 decomposition is complete in all cases considered. The NF_3 is preferable to CF_4 and C_2F_6 gases. The presence of O_2 in discharges (NF_3 and C_xF_y) gives the various effects that in different plasma parameters can be treated differently.

References

[1] E. Meeks, R.S. Larson, S.R. Vosen, J.W. Shon - J. Electrochem. Soc. **144**, 1 (1997)
[2] B.E. Kastenmeier, G.S. Oehrein, J.G. Langan, W.R. Entley - J.Vac.Sci.Technol. A **18**(5), 2102 (2000).

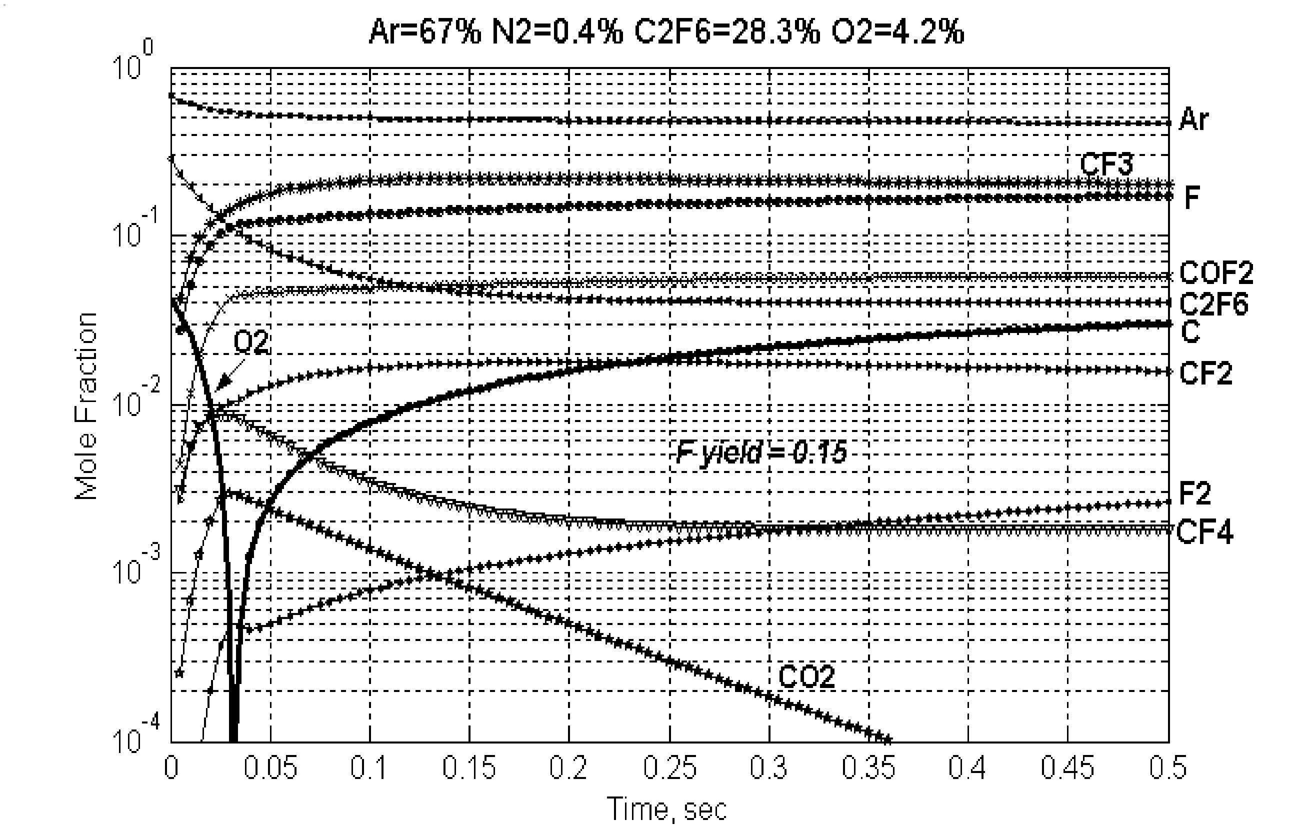

Figure 4. Numerical simulation of C_2F_6/O_2 plasma chemistry. Time dependence of the main species concentration.

Generation and Diagnostics of Non-Equilibrium Plasma in Gliding Arc Discharge

Mikhail Kossitsyn, Alexander Gutsol, Alexander Fridman

Drexel University, College of Engineering, Drexel Plasma Institute

Abstract:

The gliding arc (GA) is an intermediate system between thermal and non-thermal discharges, and is able to provide simultaneously high plasma density, power and operating pressure with high level of non-equilibrium, high electron temperature, low gas temperature and possibility of stimulation selective chemical processes without any quenching. The main peculiarities of GA are the "memory effect" and essential influence of convective heat and mass transfer on plasma properties and the space/time arc evolution.

1. Introduction

One of the critical challenges of modern plasma chemistry is to unite the advantages of thermal and non-thermal plasma systems by developing powerful and high-pressure discharges generating non-equilibrium cold plasma, which can be applied in particular for large scale exhaust gas cleaning, pollution control, fuel conversion, hydrogen production and surface treatment. One of the possible ways to create such hybrid plasma is to use the transient type of arc – the gliding arc (GA) discharge [1 - 3]. The non-equilibrium gliding arc is a very sophisticated physical phenomenon: this transitional quasi-equilibrium/non-equilibrium discharge is essentially non-uniform in time and in space, and includes "mysterious" internal transition from thermal to non-thermal mechanism of ionization. Although some success in practical application is already achieved, the wide-range application of the discharge requires deeper understanding of its physics and chemistry, particularly of the "memory effect" and heat/mass transfer in the transitional regime.

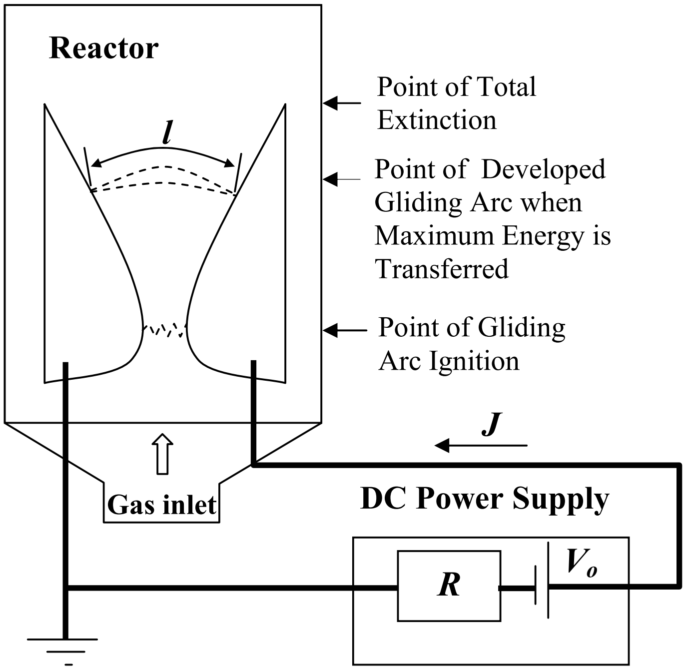

Fig 1. Electrical scheme of the DC Gliding Arc.

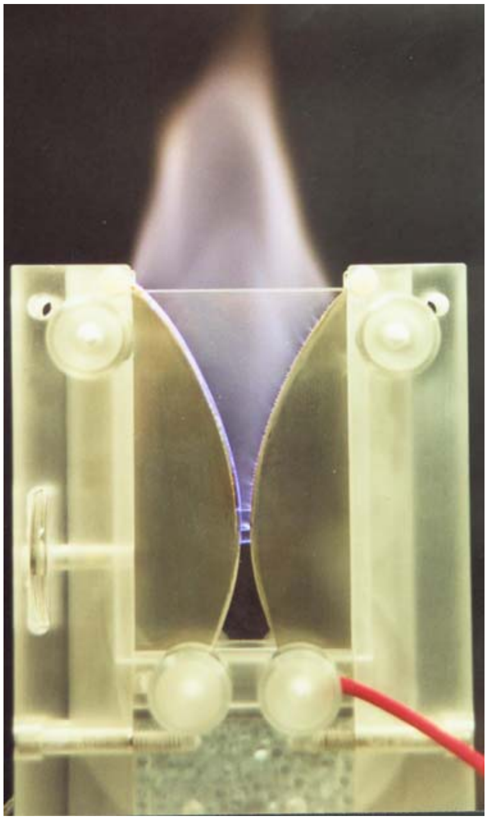

Fig. 2. Photo image of the Gliding Arc in the Parallel flow reactor.

The conventional gliding arc (GA, Fig. 1) starts in a narrow gap between two or more diverging electrodes in a gas flow, when the electric field in this gap reaches approximately 3 kV/mm in air [4], the arc current increases very fast and the voltage on the arc drops. If the gas flow is strong enough, it forces the arc to move along the diverging electrodes and to elongate. The growing arc demands more power to sustain itself. At the moment when its resistance becomes equal to the total external resistance, the discharge consumes one-half of the power delivered by the source. This is the maximum power that can be transferred to the arc from the constant-voltage power supply. Next, the length continues increasing, but the supplied power is insufficient to balance energy losses of the thermal plasma to the surrounding gas. The arc cools down and either extinguishes or changes ionization mechanism to non-thermal one - if electric field is sufficient for that. The non-thermal plasma channel formed after the "equilibrium/non-equilibrium" transition keeps growing until extinguishing anyway closing a cycle. The next cycle starts immediately after the voltage reaches the breakdown value, usually just after the fading of the previous arc. A typical repetition rate of the arc is in the range of 10 Hz to 100 Hz and changes with the gas flow rate: the higher is the flow rate, the higher is the frequency. Due to high repetition rate of the arc discharge it is visually observed as a quasi-uniform plasma layer (Fig. 2).

2. New experimental and theoretical results

2.1. We have studied experimentally the gas temperature variation during the GA evolution in parallel air flow. The experimental set-up included a parallel flow Gliding Arc reactor operating at atmospheric pressure and flow rates 2-l0 l/s. Maximal voltage of the low-ripple (0.1%) power supply (Universal Voltronics, Inc.) operating in a voltage stabilized mode was 10 kV. The maximal current was limited by external resistor bank and in different regimes was 0.05-0.15A. The spectroscopic system included Acton Research SpectraPro 500i monochromator with a focal length of 0.5m and a 1200 grooves/mm grating. Photo detection was accomplished with a Princeton Instruments camera with a 512 x 512 matrix CCD array. Light emitted by the Gliding Arc was focused using a quartz lens on the entrance slit (width = 10μm) of the monochromator in such way that spatially resolved (in the direction of arc propagation) spectra could be obtained.

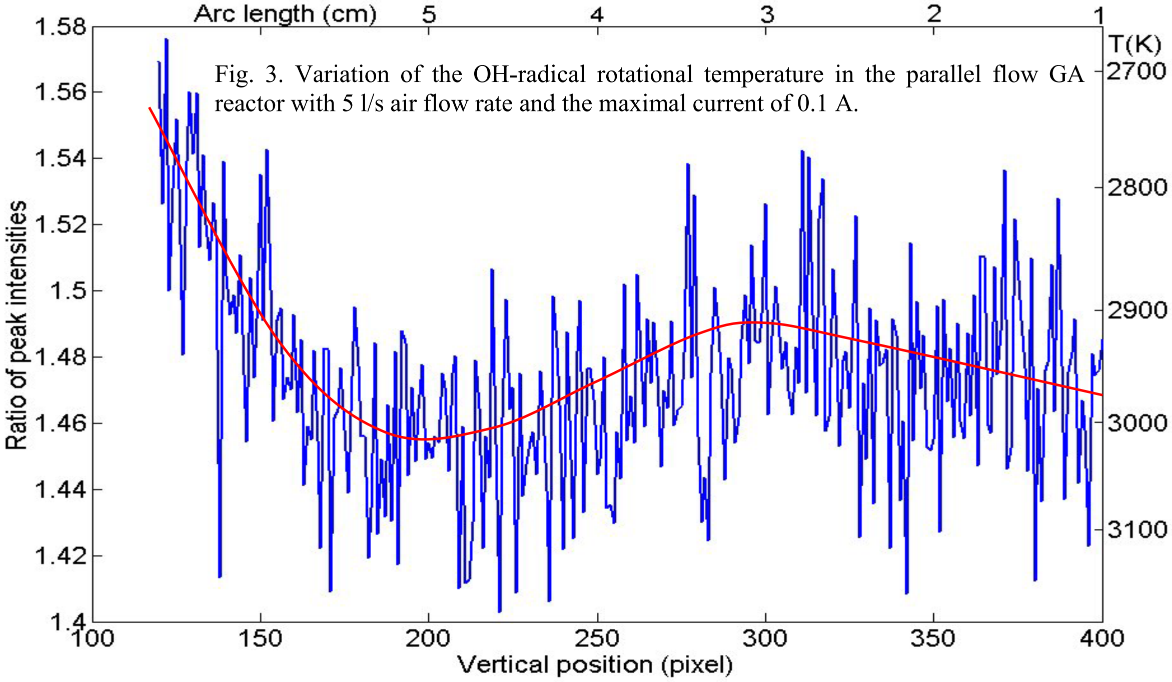

Fig. 3. Variation of the OH-radical rotational temperature in the parallel flow GA reactor with 5 l/s air flow rate and the maximal current of 0.1 A.

Two different spectral groups were observed: one corresponding to UV OH band (transition $A^2\Sigma$, $v=0 \rightarrow X^2\Pi$, $v'=0$) in the region 306-312 nm and another corresponding to N_2 molecule in wide region 330-390 nm (having 3 subgroups corresponding to transitions between different vibrational levels). Most of results reported here were obtained using UV OH band and in one regime both spectral groups yielded similar results. Unfortunately in most of operating regimes N_2 spectra were not satisfactory due to low signal and high noise levels. Obtained OH radical spectra were treated according to well known technique [5, 6]. First, the intensities of separate spectral lines in the region 306-310nm were computed at different temperatures using approach described in the above publications and the data from [7]. Then these lines were convoluted with different apparatus functions to get the best agreement with experimentally observed spectra Thus, obtained model spectra were then used to get the calibration graph, on which the ratio of intensities of two distinct spectral peaks was plotted versus temperature. Finally the peaks ratio was calculated for experimental spectra and the temperature was found using the calibration graph. Typical results are shown in Fig. 3. It is possible to see that in the case of temperature measurement inside the parallel flow GA reactor the overall GA temperature decrease with the GA length growth is not monotonic. This is a simple appearance of the "memory effect": GA propagates through the air preheated by the discharge and its temperature raises while the current and power drop.

2.2. The traditional microwave technique to determine electron densities is based on measurement of the MW radiation absorption and phase shift [8]. This method works only when characteristic length of plasma is much greater than the wavelength of probing microwave radiation. In the case of Gliding Arc the diameter of plasma column is 2-5mm and the wave length should be considerably less than the GA radius. In that case we should work already with IR radiation. The electron density in the GA was expected on the order of 10^{11} - 10^{12}cm^{-3}. In that case the expected phase shift along the GA diameter should be very small for measuring with any reasonable accuracy. More over, hardware for this technique in the mentioned wave length rage is very expensive.

We have used another method described in a number of old publications [9, 10] (Fig. 4). The idea of this old method is very simple: transmitting and receiving antennas are immersed into plasma (Fig. 4b) and the amount of microwave power transmitted through plasma is measured. At the frequency equal to the plasma frequency (directly depended on electron density) resonant absorption is observed. As mentioned above in the case of Gliding Arc the electron density is expected on the order of 10^{11} - 10^{12} cm^{-3} corresponding to the electron plasma frequency in the range of 3 - 10GHz (wavelengths 3 - 10cm).

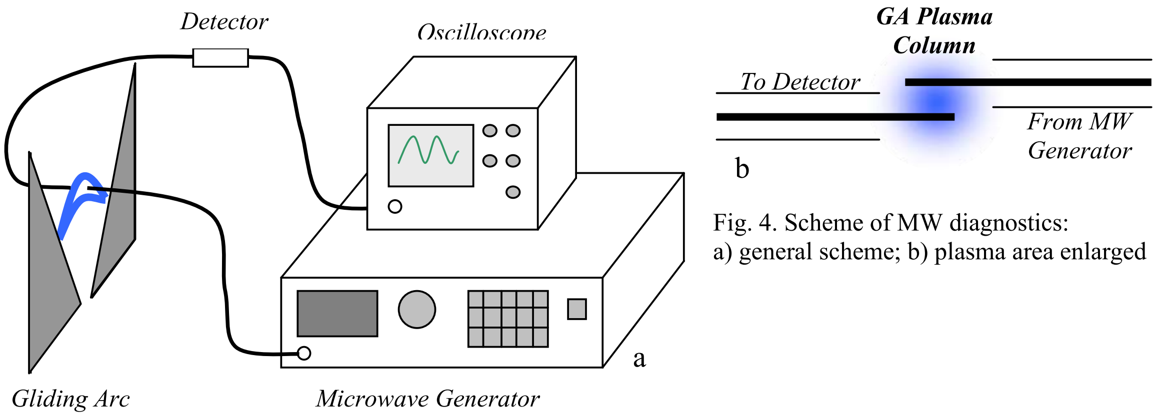

Fig. 4. Scheme of MW diagnostics:
a) general scheme; b) plasma area enlarged

Serious experimental difficulty was caused by very high electric potential (1-5kV) of the plasma with respect to ground. So, it was not possible to use commercially available coaxial cables and connectors for microwave signal transmission due to the fact that the central conductor of the cable would have very high potential of the arc thus applying this potential to Synthesized Sweep Generator (Anritsu 68169B 10MHz – 40 GHz) and detector, and due to the possibility of breakdown in the cable or connector. This difficulty was overcome by breaking the central conductor of the coaxial cable. As soon as it's broken some or the most part of transmitted microwave power is lost due to parasitic reflections. We succeeded to construct a special coaxial connector with transmission about 30 - 50%, which is high enough to get a measurable signal (Fig. 5).

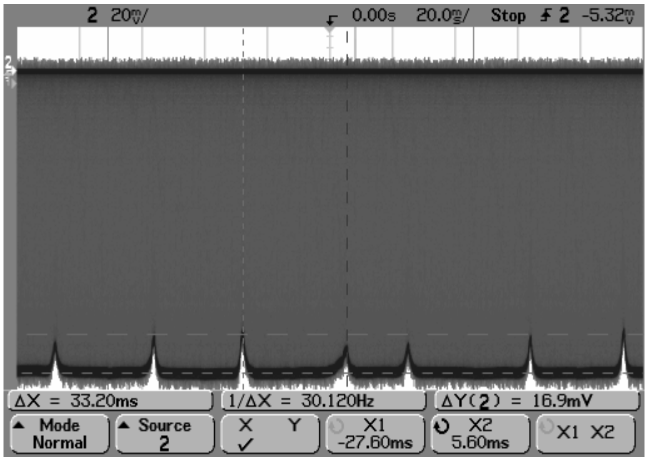

Fig. 5. Oscilloscope screen image in the case of MW diagnostics: RF modulated MW signal passes from transmitting antenna to receiving one. Width of the gray band in the screen corresponds to the amplitude of RF signal from the MW detector. White pikes correspond to absorption of the MW signal by the GA plasma passing between the antennas.

Results obtained using this method $n_e = (1 - 3)\cdot10^{11}$ cm^{-3} are in good agreement with the estimations based on voltage-current data and plasma volume measurements made with the help of shot exposition photo images of the GA.

2.3. We found that NO_x generation in the conventional GA strongly depends on the GA current. We made a series of measurements of NO_x generation in Gliding Arc. Some changes were made to the experimental set-up to include NO_x analyzer. High voltage power supply was operated in the regulated current regime. In this regime the current in the beginning stages of gliding arc development is limited by the power supply, the arc starts with the preset current value, which is lower than if it would be restricted only by the external resistance. In this case changing the restricting current we could vary power supplied to the GA and study the dependence of NO_x generation on GA power consumption. The experimental results are shown in Fig. 6.

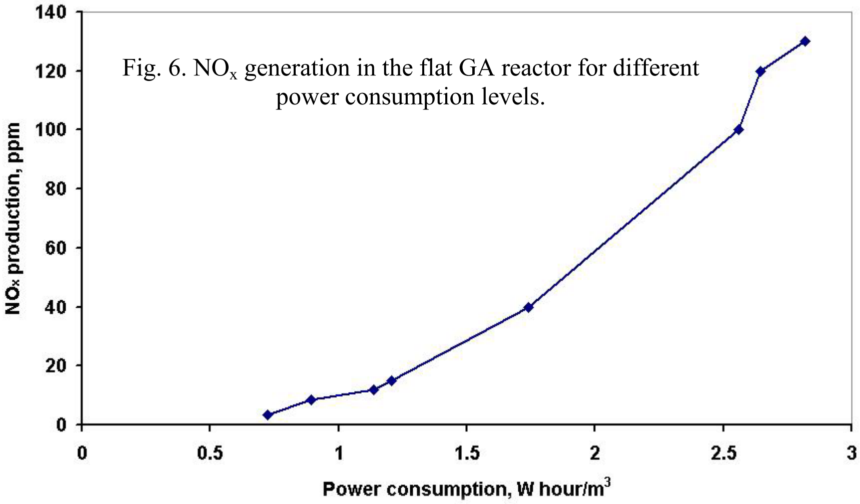

Fig. 6. NO_x generation in the flat GA reactor for different power consumption levels.

2.4. A linear stability analysis of the low-current gliding arc discharge in the transitional regime was performed in [11, 12]. It was shown that the transitional GA remains stable even after the maximal discharge power point ("overshooting" effect) and gradually transforms during the evolution into a more non-equilibrium discharge. Analytical and numerical solutions explain the general behavior of the low-current gliding arc and are in a good agreement with our preliminary experiments [3] (Fig. 7).

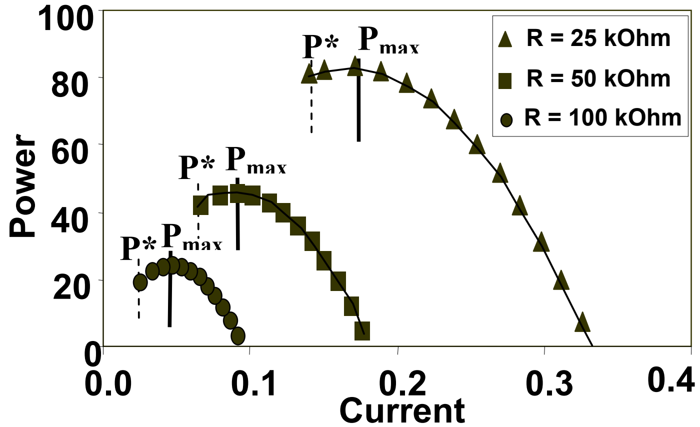

Fig. 7. Calculated power-current dependence of the gliding arc. The results are in a very good agreement with experimental results [13]. A stable solution exists beyond the point of the maximal power P_{max}.

2.5. Analysis of the kinetic balance of the transient regime shows that during the transition, translational and electron temperatures are strongly coupled and changes together but in a small range, which is in good agreement with our temperature measurements.

Since spectral diagnostics using OH and N_2 spectra showed very small change in gas temperature during the evolution of GA we conclude that gas and electron temperatures are stabilized at the level of about 3000 K and 10000-15000 K respectively. This result confirms our assumption that we have transition regime in which both direct electron impact ionization (sensitive to electric field) and thermal ionization (sensitive to gas temperature) play significant role. To describe this regime we will write balance equation for electron concentration n_e. Electron concentration is affected in two types of processes: ionization and attachment. Ionization rate coefficient must be proportional to the concentration of excited neutral atoms n^*

and electron concentration n_e: $k_i \sim n^* n_e$. We assume that the concentration of excited atoms and electron concentration obey Boltzman distribution $n^* \sim \exp(-\frac{E^*}{T_{elex}})$, $n_e \sim \exp(-\frac{I-E^*}{T_e})$, where T_e is the electron temperature, T_{elex} and E^* is temperature and the energy of electronic excitation. So,

$$k_i \sim \exp(-\frac{E^*}{T_{elex}})\exp(-\frac{I-E^*}{T_e})$$

In general the gas temperature $T_0 < T_{elex} < T_e$. Since we have a relatively cold plasma we can assume that $T_{elex} \approx T_0$ and $n^* \sim \exp(-\frac{E^*}{T_0})$. The dependence of T_e (E) can be approximated by $T_e \sim \left(E/n_0\right)^k$. Here we use $k = 1$ and $T_e \sim E/n_0$. So, $k_i \sim \exp\left(-\frac{A}{ET_0} - \frac{B}{T_0}\right)$, where A and B are some constants. Using similar procedure we can write for attachment rate coefficient $k_a \sim \exp(-\frac{A'}{ET_0})$. In a steady state ionization must be balanced by attachment: $k_{i0}\exp(-\frac{A}{ET_0} - \frac{B}{T_0}) = k_{a0}\exp(-\frac{A'}{ET_0})$. Regrouping terms in this equation we can get: $\exp(-\frac{A''}{ET_0} - \frac{B}{T_0}) = const$, and finally: $\frac{E'+E}{E} = CT_0$

In the extreme case of $E \to \infty$ (glow discharge) our formula must give the temperature equal to the glow discharge temperature, which is on the order of a room temperature, and we find $C = (T_{room})^{-1}$ and $E' \approx E_{glow}$ (here E_{glow} is a parameter on the order of the field of a glow discharge).

In the case of low electric field $E \to 0$ (arc) we should make a small correction to the denominator and the formula becomes $\frac{E+E_{glow}}{E+E_{arc}} = \frac{T}{T_{room}}$. E_{arc} here is some parameter on the order of the field in the arc discharge, $E_{arc} << E_{glow}$, so that at $E = 0$ we have $\frac{E_{glow}}{E_{arc}} = \frac{T_{arc}}{T_{room}}$. Taking into account that $T_{room} \approx 300$K, $T_{arc} \simeq 10000$K we find that $E_{glow}/E_{arc} \cong 30$.

Fig. 8 shows the calculated E vs. T dependence in the range where it's valid ($E_{arc} << E << E_{glow}$, solid line) and a typical behavior in the ranges of thermal arc and glow discharge (dashed line). As expected the electric field decreases with increasing temperature.

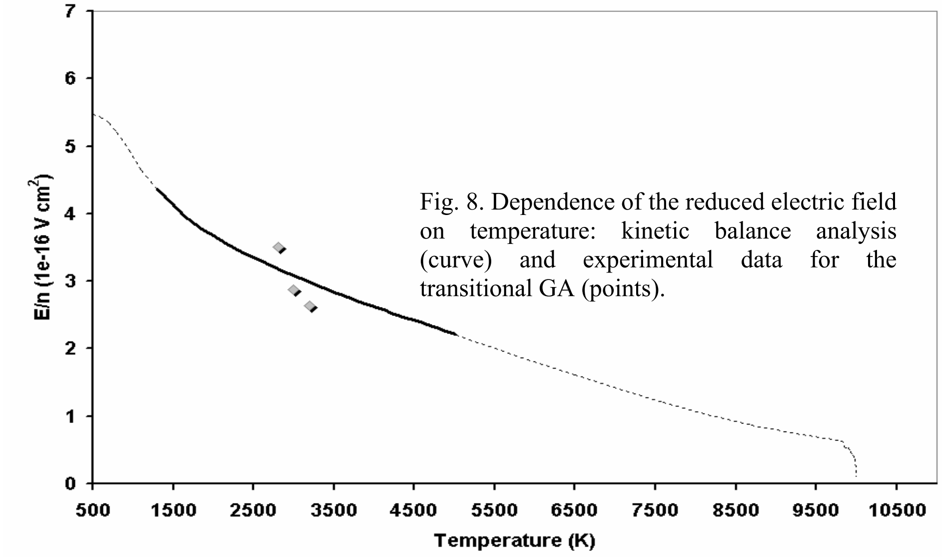

Fig. 8. Dependence of the reduced electric field on temperature: kinetic balance analysis (curve) and experimental data for the transitional GA (points).

3.6. Better understanding of the GA phenomenon permitted us to enhance the non-equilibrium plasma parameters using the newest GA design – Tornado GA (Fig. 9). Details regarding this design are presented in another paper [14].

3. Conclusion

Basic understanding of the non-equilibrium gliding arc achieved today determines the following three steps of the GA investigations. First of all, the GA "memory effect", which is responsible for high density of charged and excited species after transition to strong non-equilibrium phase, should be clarified. Second, the non-equilibrium GA behavior during the long transitional period results in essential influence of convective heat and mass transfer on the space/time non-stationary arc evolution. This strong effect was already observed experimentally and should be investigated to understand the non-equilibrium GA plasma local interaction with gas flow. Last but not the least, - optimization of macroscopic gas flow interaction with the GA plasma requires investigation of different organization of the discharge geometry. Preliminary analysis brings us to a spiral GA organization in the reverse vortex flow, where a rotating gliding arc is trapped inside of "the tornado". Such "non-equilibrium GA-Tornado", demonstrated excellent results in preliminary experiments, providing good plasma/gas contact and keeping most of generated active species in the flow for further effective plasma-chemical reactions.


Fig. 3. Photo image of the Tornado GA

References:

[1] A. Czernichowski - Pure & Appl. Chem. 66(6), pp. 1301-1310 (1994)

[2] A. Fridman, A. Czernichowski, J. Chapelle, J.M. Cormier, H. Lesueur, J. Stevefelt - Journal de Physique, 4, pp. 1449 (1994).

[3] A. A. Fridman, S. Nester, L.A. Kennedy, A.V. Saveliev, O. Mutaf-Yardimci - Progress in Energy and Combustion Science, 25, pp. 211-232 (1999).

[4] Y. P. Raizer, "Gas discharge physics" (Springer, Berlin, 1997).

[5] S. Pellerin, J. M. Cormier, F. Richard, K. Musiol, J. Chapelle - J. Phys. D: Applied Physics 29 pp. 726-739 (1996)

[6] Charles de Izarra - J. Phys D: Applied Physics 33 pp. 1697-1704 (2000)

[7] G. H. Dieke and H. M. Crosswhite - J. Quant. Spectrosc. Radiat. Transfer, Vol. 2 pp. 97-199 (1961)

[8] V. Jivotov, V. Rusanov, A. Fridman, "Diagnostics of Non-Equilibrium Chemically Active Plasma", Atomizdat, Moscow, 216 p. (1985) (in Russian).

[9] L. M. Levitski and I. P. Shashurin - 1963, J. of Technical Physics, Vol.XXXIII-4 (in Russian).

[10] V. Golant, "Microwave methods plasma study", Moscow, Nauka (1968) 328 p. (in Russian)

[11] I. V. Kuznetsova, N. Y. Kalashnikov, A. F. Gutsol, A. A. Fridman, L. A. Kennedy ISPC-15, Orleans, July 9 – 13, 2001, Vol. IV, pp. 1509 - 1514.

[12] I. V. Kuznetsova, N. Y. Kalashnikov, A. F. Gutsol, A. A. Fridman, L. A. Kennedy - Journal of Applied Physics, 2002, V. 92, No. 8, pp. 4231-4237.

[13] O. Mutaf-Yardimci, A. Saveliev, A. Fridman, L. A. Kennedy - J. of Applied Physics, vol.87, pg.1632-1641, 2000.

[14] C. S. Kalra, M. Kossitsyn, K. Iskenderova, A. Chirokov, Y. I. Cho, A. Gutsol, A. Fridman - ISPC-16, Taormina, Italy, 2003.

Electrical discharges in the Reverse Vortex Flow – Tornado Discharges

Chiranjeev S. Kalra, Mikhail Kossitsyn, Kamilla Iskenderova, Alexandre Chirokov,
Young I. Cho, Alexander Gutsol, Alexander Fridman

Drexel University, College of Engineering, Drexel Plasma Institute

Abstract:

Properties of the electrical discharges in the Reverse Vortex Flows (Tornado Discharges - TD) differ significantly from the prosperities of discharges in the flows of conventional geometries. This difference is the most considerable for the non-equilibrium discharges. The reason of the difference is an intensive convective cooling of the discharge zone and a perfect thermal insulation of the discharge zone from the walls. This difference makes TD very attractive for many applications.

1. Introduction

It is relatively easy to realize the Reverse Vortex Flow (RVF), which is very similar to the natural tornado, in the cylindrical volume. It is necessary to direct an outlet of the flow from the volume along the axis to the swirl generator side, and the diameter of the outlet should be considerably less than that of the cylindrical vessel (Fig. 1).

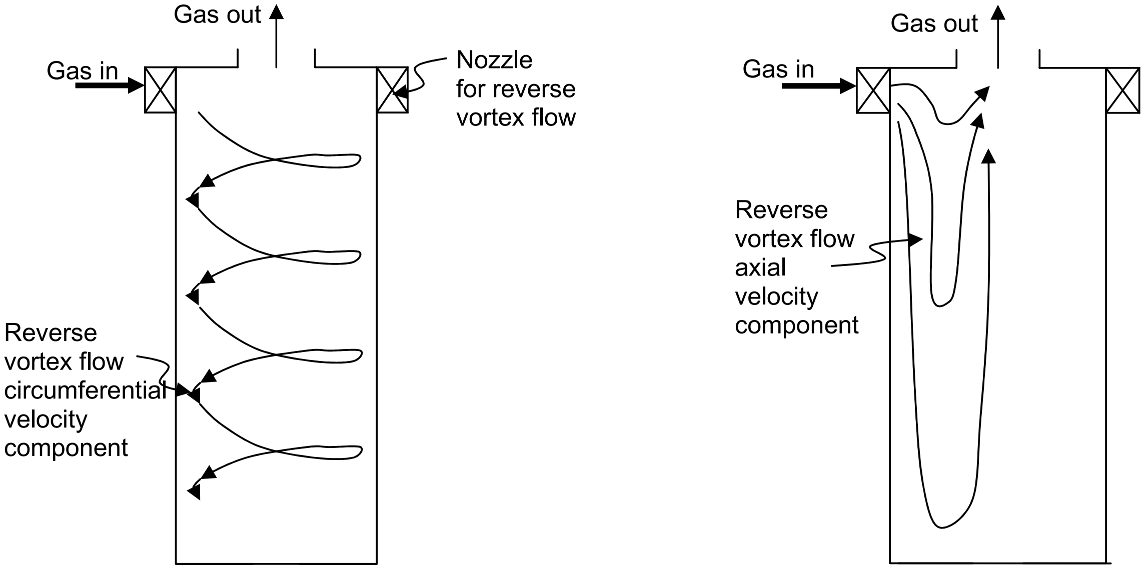

Figure 1: Reverse Vortex ("Tornado") flow in a cylindrical reactor.

Several kinds of atmospheric pressure electrical discharges were already realized in the RVF: microwave (MW) discharge [1 - 6], RF ICP [6 - 9], arc and gliding arc. Gaseous flame, which could be also considered as low temperature plasma, was also realized in tornado geometry [5, 10 - 14]. In the cases of MW and RF ICP plasma generators and gas combustion chamber, the RVF have been compared experimentally (calorimetric investigations) and numerically with conventional "forward" vortex flow (FVF). Here we present some new results regarding simulation of RF ICP generator and experiments with arc and gliding arc in RVF, and discuss all obtained results from the unified point of view.

2. Self-consistent simulation of RF ICP generator with Reverse Vortex Flow

Argon ICP generator with RVF was studied experimentally earlier [7 - 9]. Also we have published already the results of simplified simulation of this generator [6 - 8], where gas-dynamic problem was solved in assumption about place and size of energy release zone. Today we have and present results of self-consistent modeling. Plasma is assumed to be in local temperature equilibrium and optical thin.

Electromagnetic field calculation was based on a current loop method. Consider a cylindrical loop of radius *R* carrying a current *I*, as shown on a Fig.1. The vector potential will be equal to $A_\theta(r,z)=\frac{\mu_0 I}{2\pi}\sqrt{\frac{R}{r}}G(k)$

Where

$$G(k)=\frac{(2-k^2)K(k)-2E(k)}{k}$$

$$k^2=\frac{4Rr}{(R+r)^2+(z-z_c)^2}$$

K and *E* are the complete elliptic integrals.

Therefore, the electromagnetic field can be calculated from these equations:

$$A_R(r,z)=\frac{\mu_0 I}{2\pi}\sqrt{\frac{R}{r}}\sum_{i=1}^{coil}G(k_i)+\frac{\mu_0\omega}{2\pi}\sum_{i=1}^{C.V.}\sqrt{\frac{r_i}{r}}\sigma_i A_{I,i}S_iG(k_i)$$

$$A_I(r,z)=-\frac{\mu_0\omega}{2\pi}\sum_{i=1}^{C.V.}\sqrt{\frac{r_i}{r}}\sigma_i A_{R,i}S_iG(k_i)$$

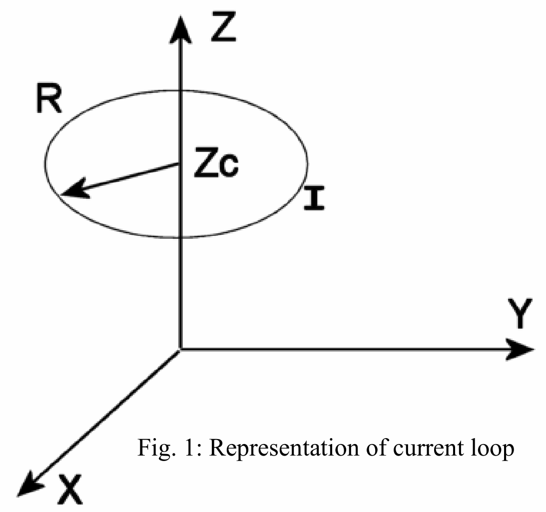

Fig. 1: Representation of current loop

These equations were solved by successive iterations to get real and imaginary part of vector potential. Lorenz force, *F*, and local energy dissipation rate, *P*, were calculated using vector potential [15]. We assumed radiation losses are the function of the local temperature [16]. Gas flow coupled together with electromagnetic field equations was solved by FLUENT (Version 6) in axially symmetric 2D case. Build-in Reynolds Stress turbulence model was employed. The coupling scheme is shown on a Fig.2.

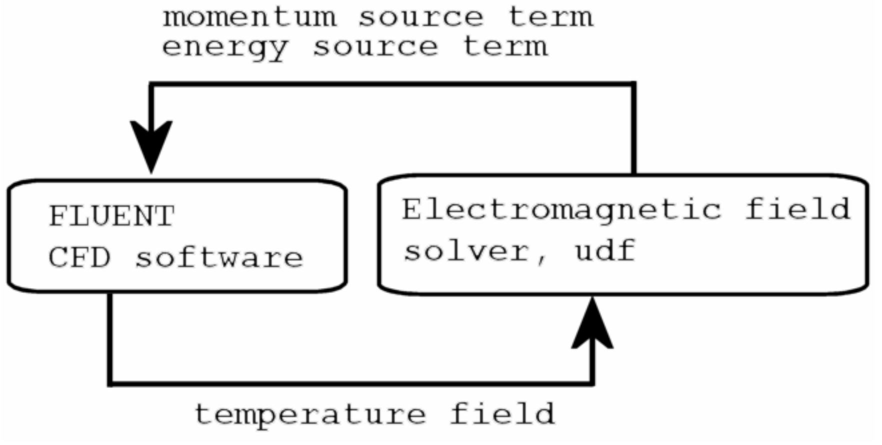

Figure 2: Coupling framework

Results of simulation are in a good agreement with experimental data obtained previously (Fig. 3). If we compare the results of self-consistent simulation with the results of simplified simulation of this generator [6 - 8], it is possible to see that the main difference is larger diameter of the energy release zone (heating zone). Convergence of self-consistent simulation was obtained with plasma only for the cases with low efficiency (Fig. 4, the temperature fields for the cases marked by red circles in Fig. 3), where the recirculation zone near the closed end of the generator still exists. This recirculation zone formed because of Ampere force, results in formation of the central plasma “tail” (Fig. 3a) of disturbance of the temperature field (Fig.3b). Attempts to simulate more efficient regimes (with lower power or higher flow rates) results in going out of plasma (temperature of the plasma drops, consequently conductivity drops and power absorption drops too). It was possible to improve the situation by assuming that conductivity depends not only on gas temperature but on electric field also (assumption of non-equilibrium). This assumption results in better agreement with the experiments but permits to move into the higher flow rates very little, then plasma goes out again. We suppose that in experiments we have diffusion of electrons to the outer layer of plasma, and there conductivity is much higher then that in assumption of equilibrium or temperature dependence. Probably it is possible to simulate this in two-liquid assumption (electron gas and argon should be considered separately along with ambipolar diffusion). Such simulation is in our plans for future.

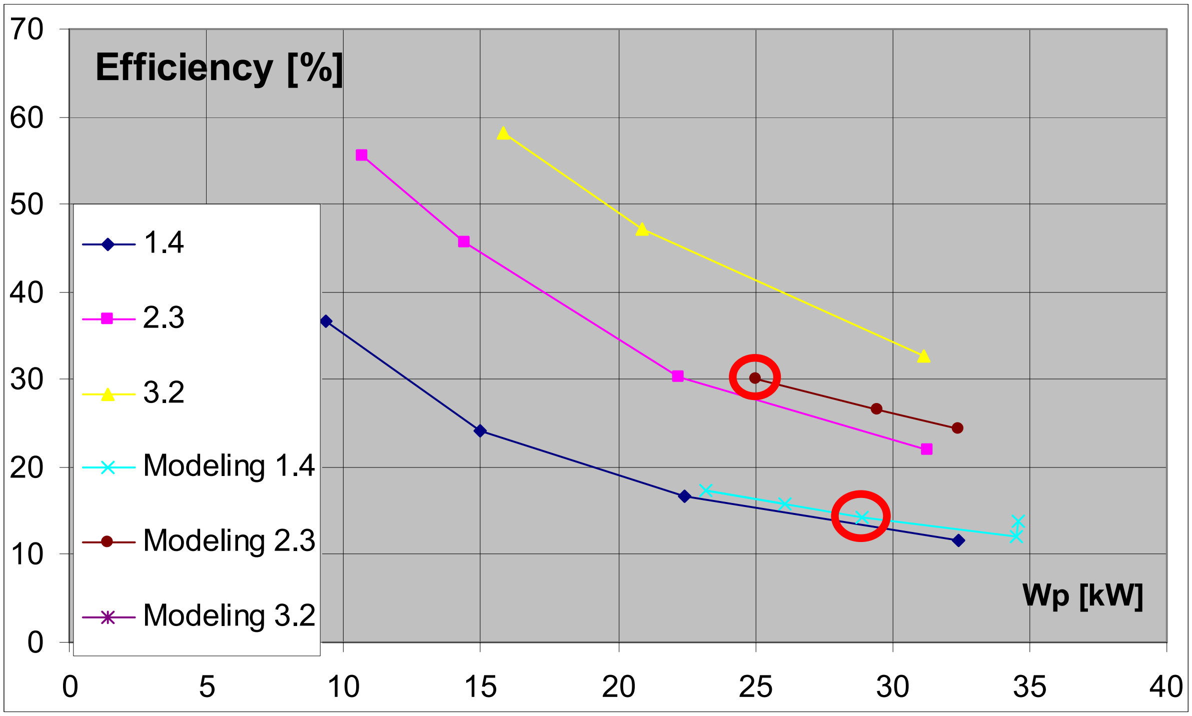

Figure 3: Comparison between the experimental data [9] and simulation for three levels of argon flow rate 1.4, 2.3 and 3.2 g/s. Red circles mark the points presented in Fig. 4.

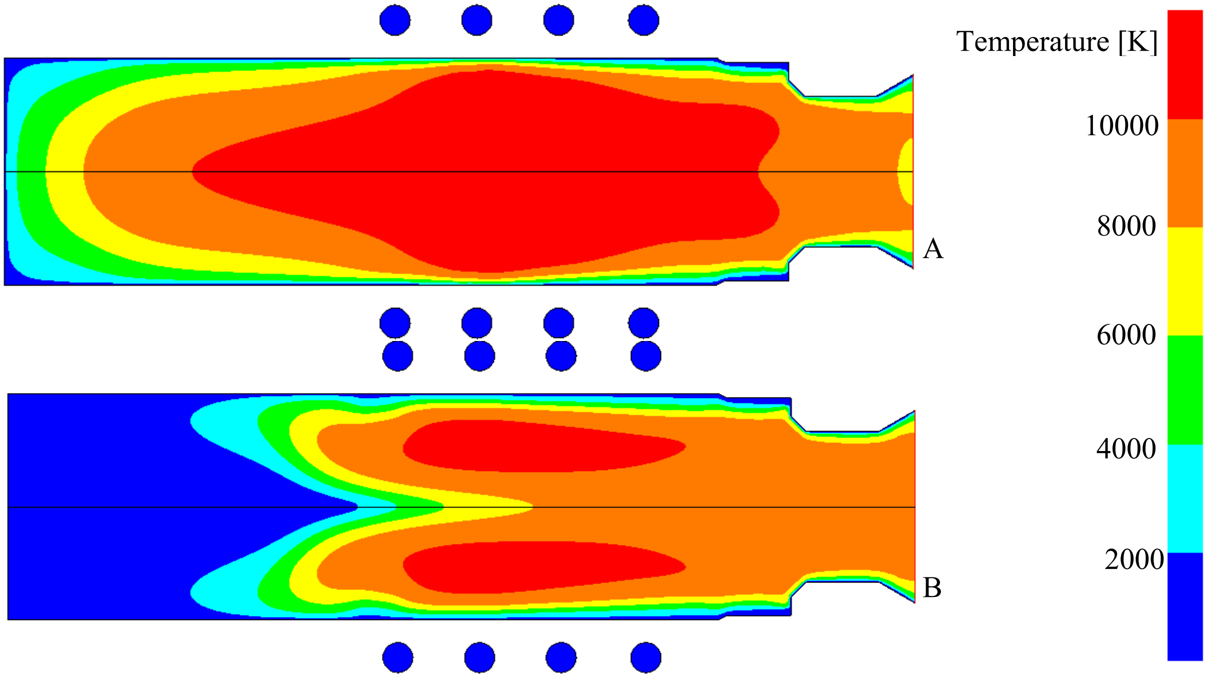

Figure 4: Temperature field for two simulated cases marked by red circles in Fig. 3: (A) – 1.4 g/s of argon and 28 kW of plasma power; (B) – 2.3 g/s of argon and 25 kW of plasma power.

3. Experiments with arc and gliding arc in Reverse Vortex Flow

Conventional gliding arc is a high-pressure gas non-stationary discharge [17, 18]. The arc starts in a narrow gap between two or more diverging electrodes in a gas flow, after breakdown when the electric field in this gap reaches approximately 3 kV/mm in air. The arc current increases very fast and the voltage on the arc drops. If gas flow is strong enough, it forces the arc to move along the diverging electrodes and elongate. The growing arc demands more power to sustain itself. It continues to elongate till the power supply can no longer compensate the energy lost in heat transfer to the surrounding gas. The arc cools down and finally extinguishes. The next cycle starts immediately after the voltage reaches the breakdown value, usually just after fading of the previous arc.

The gliding arc can operate in non-equilibrium regimes and have relatively low gas temperatures [17, 18]. Previously gliding arc has been reported for applications in the field of plasma-catalytic conversion of organic compounds, etc [19, 20]. Gliding arc requires velocities high enough to move the discharge along diverging electrodes but plasma catalytic conversions require high residence time for higher degree of completion of chemical reactions. Specific power delivered remains low in case of non-equilibrium regime and conventional (flat, in the case of two electrodes) geometry. Also a large amount of gas passes around the arc resulting in no residence in the discharge zone. Thus the gliding arc looks to have potentially a number of application and attractive for plasma-catalytic conversions but unable to give expected results. That is why we use a new approach to get gliding in circular geometry in the reverse vortex flow.

Gliding Arc in Tornado works in a Reverse Vortex Flow setup in a cylindrical volume (ϕ 40mm; L=150mm) (Fig. 5). A circular and spiral electrode is placed in the plane of the flow near the cylinder walls. The flow conditions and the characteristics of the power supply determine the shape of the spiral electrode. Based on experimental flow visualization and numerical modeling of the flow conditions the spiral shape and characteristics are determined. The voltage, 10 kV, from Voltronics power supply gives power as high as 2.5 kW per discharge in laboratory experiments.

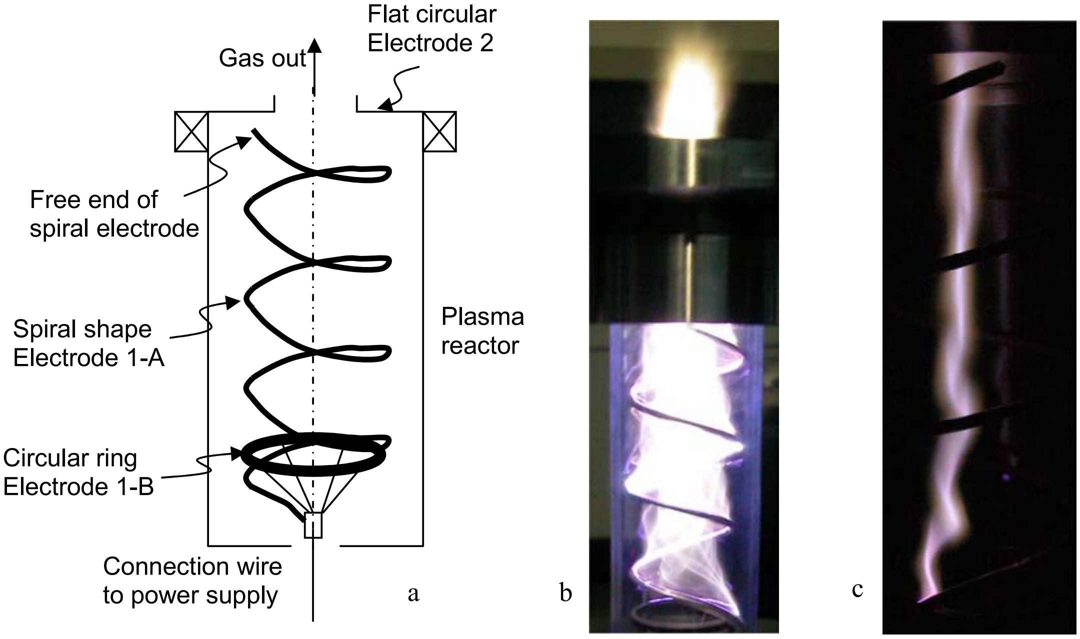

Figure 5: Tornado Gliding Arc (TGA), a – schematic of TGA reactor; b - photo image of gliding arc with normal exposition time; c - photo image of gliding arc with shot exposition time (1/1000 s).

The reactor as shown in the figure 5a essential consists of a cylindrical volume, with metal flange at the outlet. This metal flange at the outlet also acts as anode and is connected to the ground terminal. The flange also houses 4 tangential inlets into the cylindrical tube. Gas enters through these tangential inlets (2mm x 2mm) into the tube generating a strong reverse vortex inside. Typical inlet velocities vary from 10m/s to 50m/s. An additional axial inlet is provided to add more gas flow for additions of reactants in case of plasma-catalytic conversions. The spiral electrode is connected axially in the tube and acts as the cathode. The end of the spiral turns to form a ring smaller in diameter than the spiral itself. In fact the diameter of the spiral goes on decreasing as it moves away from the anode.

When high potential is applies across the electrodes (about 3kV/mm in air) electrical breakdown ignites the gliding arc. The strong vortex flow forces this arc to move around the tube axis. The arc thus elongates along the spiral. Eventually the elongated arc reaches the ring shaped end of the spiral electrode (Fig. 5b and Fig 6. In the second case the discharge was formed by elongating the distance between two electrodes). Now the arc is in the central zone of the reactor, this zone has relatively less disturbances. This is the central discharge zone or the center column.

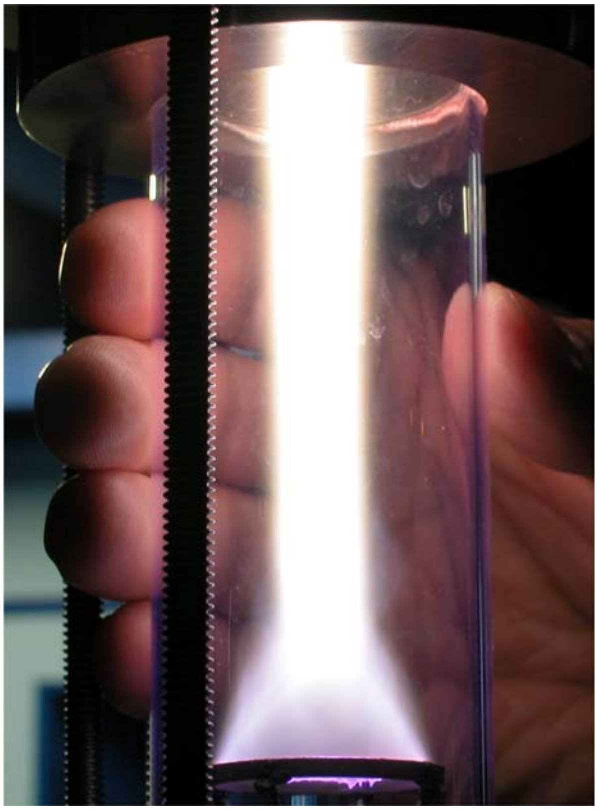

Figure 6: Tornado Gliding Arc (TGA) between circular electrode and flange (flat circular electrode).

The discharge zone has very intensive convective cooling due to the vortex flow around it and the central flow through it. At the same time this discharge zone because of the same vortex flow is in perfect thermal insulation form the reactor wall (Fig. 6). Very fast movement of the electrode spots results in no electrode erosion or deterioration. The elongation of the arc in this case is not due to the shape of the electrodes, instead the arc moves on two parallel electrodes. This elongation is due to the different velocities of the gas flowing near the electrodes (Fig. 7). Due to this the arc elongates and finally reaches a point where the thermal losses due to elongation of the arc can no longer be compensated by the power supply. At this point the plasma supported re-ignition of the arc is observed. This is possible because of the circular geometry.

Figure 7: Elongation of arc on parallel electrodes but with different gas flow velocities near the two electrodes

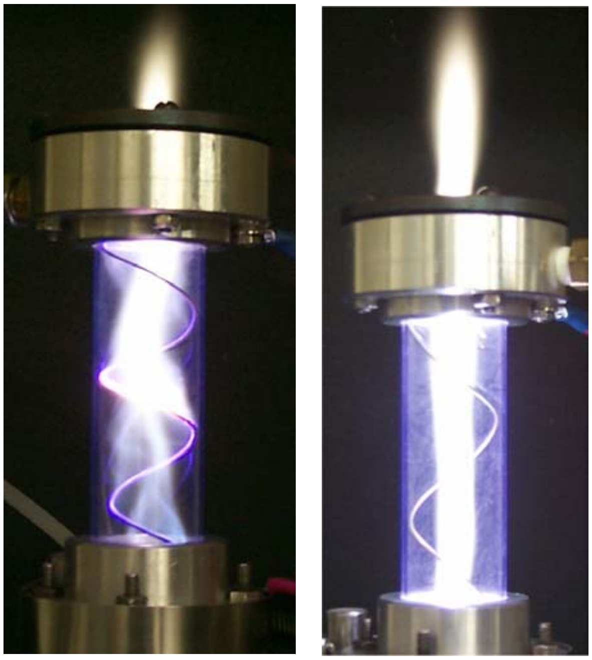

Figure 8: Tornado Gliding Arc (left) may transform to the high voltage atmospheric pressure discharge inside the Reverse Vortex Flow (right).

It is also possible to stabilize the ordinary arc in RVF. Fig. 8 demonstrates transformation of the TGA to the high voltage atmospheric pressure discharge inside RVF.

4. Discussion and Conclusion

Perfect thermal insulation properties of RVF were emphasized earlier [1 - 14]. Here we'd like to emphasize the influence of convective cooling of the central zone on the plasma properties. Between thermal plasmas (arcs, ICP) and cold plasmas (DBD, corona) of atmospheric pressure it is a range where relatively hot non-equilibrium (transitional) plasmas exist. Such kind of plasmas can be realized in the case of microwave discharge or gliding arc [21]. In transitional plasmas electric field is relatively strong, translational and electron temperatures are strongly coupled and changes together [12]. Decrease of translational temperature results in increase of plasma electric field and electron temperature, and plasma becomes more non-equilibrium. This effect can be easily realized in the reverse vortex flows because of intensive convective cooling of central zone by turbulence and axial flow (see Fig. 4B for example). The first example of such effect is the temperature drop (at least according to simulation) in the Reverse Vortex Stabilized microwave discharge [2 - 5]. Gliding Arc and High Voltage atmospheric Pressure Discharge in RVF is another example. In RVF gliding arc exists in conditions corresponded to extremely elongated gliding arc between two divergent electrodes, means in the most non-equilibrium state [18, 21]. In contrast to conventional thermal and non-thermal discharges, the transitional discharges are able to provide simultaneously high plasma density, power and operating pressure (typical for thermal systems) with high level of non-equilibrium, high electron temperature, low gas temperature and possibility of stimulation selective chemical processes without any quenching (typical for non-thermal systems). That is why transitional discharges in the Reverse Vortex Flows and Tornado Gliding Arc particularly, combining high extent of non-equilibrium with high residence time, are very attractive for many applications.

References:

[1] V. T. Kalinnikov and A. F. Gutsol - Doklady Akademii Nauk, 1997, V. 353 (4), p. 469-471. (Physics - Doklady, Vol. 42, No. 4, 1997, pp. 179 - 181).
[2] A. Gutsol, J. A. Bakken - ISPC-13, Beijing, China, Aug.18-22, 1997. Vol. 1, p. 155-160.
[3] A. Gutsol, J. A. Bakken - J.Physics D: Applied Physics , 1998 , V. 31, No. 6, pp. 704 - 711.
[4] A. Gutsol, J. A. Bakken - In: Thermal Plasma Torches and Technologies. Edited by O. P. Solonenko. Vol. 1. Plasma Torches: Basic Studies and Design. CISP, Cambridge, England. 1998.
[5] A. Gutsol, A. Fridman, L. Kennedy – HEFAT- 2002: 1st International Conference on Heat Transfer, Fluid Mechanics, and Thermodynamics, Kruger Park, South Africa, 2002. Vol. II, pp. 987 – 992.
[6] A. Chirokov, A. Gutsol, A. Fridman, L. Kennedy – ISPC-15, Orleans, 2001, Vol. I, pp. 167 – 172.
[7] A. Gutsol, J. Larjo, R. Hernberg – ISPC-14, Prague, 1999, Vol. 1, pp. 227 - 231.
[8] A. Gutsol, J. Larjo, R. Hernberg - Teplofizika vysokikh temperatur, Vol. 39, No. 2, 2001, pp. 187-197. (High Temperature, Vol. 39, No. 2, 2001, pp. 169 - 179.)
[9] A. Gutsol, J. Larjo, R. Hernberg - Plasma Chem. and Plasma Proc., Vol. 22, No. 3, 2002, p. 351-369.
[10] V. T. Kalinnikov and A. F. Gutsol - Doklady Akademii Nauk, 1998, V. 360 (1), p. 49-52. (Physics - Doklady, Vol. 43, No. 5, 1998, pp. 302 - 305).
[11] V. T. Kalinnikov and A. F. Gutsol Reverse - Teplofizika vysokikh temperatur, Vol. 37, No. 2, 1999, pp. 194 - 201. (High Temperature, Vol. 37, No. 2, 1999, pp. 172 - 179.)
[12] A. F. Gutsol - Matematicheskoe modelirovanie (Math. Modeling), 1999. V. 11. No. 6. pp. 38 – 44.
[13] A. Gutsol - In: Progress in Plasma Processing of Materials 1999. Editors: Pierre Fauchais and Jacques Amouroux. Begell House, Inc., NY, 1999. P. 81 - 86.
[14] A. Gutsol, A. Fridman, L. Kennedy – 29th Int. Symp. on Combustion, Sapporo, Japan, July 21-26, 2002, Abstract 1-14-1065, p. 92.
[15] J. Mostaghimi, M. I. Boulos - Plasma Chem. and Plasma Proces., Vol. 9, 1, (1989).
[16] T.G. Owano, M.H. Gordon, C.H. Kruger - Phys. Fluids, B 2 (12), (1990).
[17] I. Kuznetsova, N. Kalashnikov, A. Gutsol, A. Fridman, L. Kennedy – ISPC-15, Orleans, 2001. Vol. IV, pp. 1509 - 1514.
[18] I. Kuznetsova, N. Kalashnikov, A. Gutsol, A. Fridman, L. Kennedy – Journal of Applied Physics, 2002, V. 92, No. 8, pp. 4231-4237.
[19] A. Czernichowski - Pure & Appl. Chem. **66(**6), pp. 1301-1310 (1994)
[20] K. Iskenderova, P. Porshnev, A. Gutsol, A. Saveliev, A. Fridman, L. Kennedy, T. Rufael – ISPC-15, Orleans, 2001. Vol. VII, pp. 2849 - 2854.
[21] M. Kossitsyn, A. Gutsol, A. Fridman - ISPC-16, Taormina, Italy, 2003.

THE COMPUTER THERMODYNAMIC MODELING OF PLASMACHEMICAL SYSTEMS AT UTILISATION OF INDUSTRIAL TOXIC WASTE.

S. Sosnovckyi, V. Vlasov, A. Zorin

Physicotechnical Department, Tomsk Polytechnic University, Tomsk, Russia

The results of the thermodynamic analysis plasmachemical process of reception from solutions of fluoride aqueous-saline metals in conditions of air, inert and reducing plasma are submitted. These solutions are formed as processing of less-common and refractory metals as industrial toxic waste.

The common plasmachemical processing of liquid industrial toxic waste is carried out by thermal decomposition. As a result the metal oxides are formed. We offer to use reaction of plasmachemical hydrolysis for treatment of fluoride salts solutions. The water vapour from solution, and water contained in crystals should participate in the given reaction.

We carried out thermodynamic accounts of equilibrium compositions of plasmachemical process of reception nanopowder and acids from a mix of loosened fluoride aqueous-saline solutions. The account of equilibrium compositions was carried out on the computer at various pressure, temperatures, initial proportions of solution and plasma thermofor. The initial concentration of metals salts in researched system were varied.

The method, offered us, allows to reduce amount of technological operations, response time and decrease total power inputs in comparison with traditional technologies of nanopowder reception. Received nanopowder are reduce temperature and time of fine ceramics. It allows to remove losses of oxides from sintered weight and to improve ecological compatibility of production.

The carried out theoretical and practical researches show perspectivity to use the thermodynamic analysis for plasmachemical process of reception nanopowder from fluoride of aqueous-saline metals in conditions of air, inert and reducing plasma.

Effect of Plasma Turbulent Temperature Fluctuations on Particle Heating in DC Plasma Spray

Maher Hady, Javad Mostaghimi, and Sanjeev Chandra
Centre for Advanced Coating Technologies
Faculty of Applied Science and Engineering
University of Toronto
Toronto, Canada

Abstract

This paper investigates dc plasma spraying processes by addressing the influence of plasma temperature fluctuations on particle heating in atmospheric plasma spraying. Previous works have considered the effect of plasma velocity fluctuations on particle trajectories and have concluded that dispersion of particle trajectories is most significant for small particles. The effect of temperature fluctuation on particle temperature has not yet been considered, although this could be as significant as dispersion of particle trajectories.

We calculated particle temperature distribution by implementing a two-dimensional mathematical/numerical turbulent model. In addition to average flow properties, the model calculates the variance of the plasma temperature field. Particle trajectory and temperature field was calculated by a Lagrangian model. Effect of plasma temperature fluctuation on particle temperature was considered by a stochastic model.

Computations were carried out for a standard APS system with nickel and alumina particles. Dispersion of particle temperature was shown to be significant; e.g., for 80-micron nickel particles, temperature dispersion could be more than 500 K. This is significant as it increases the possibility of more unmelted particles at the spraying point.

Introduction

Thermal spray deposition is a process that combines particle melting, quenching, and solidification in a single operation. Two techniques commonly used in industry to form coatings are plasma spraying and High Velocity Oxy-Fuel (HVOF) spraying. Plasma jets are created by heating an inert gas in an electric arc confined within a water-cooled nozzle. HVOF jets are produced by reacting fuel and oxygen in a high pressure combustion chamber, with the combustion products being accelerated through a constricting nozzle. Coatings are produced by injecting powders (metallic, ceramic, or a mixture) into the high temperature jet, where particles rapidly melt while being accelerated towards the workpiece. Molten droplets undergo rapid solidification when they impact on the substrate, with cooling rates of typically 10^6 to 10^8 K/s, producing deposits with fine grained (~0.5 μm) homogeneous microstructures. Thermal sprayed deposits have been used as protective coatings in corrosion and wear applications and as thermal barriers. Deposits have also been used for building up worn bearing surfaces, and for making free-standing relatively thin-walled structures such as refractory rocket nozzles.

Conventional thermal spraying is normally carried out at atmospheric pressure. Typical metallic deposits include some oxides, and also have some porosity due to incomplete melting, wetting, or fusing of deposited particles. The production of dense, high strength thermal sprayed deposits requires that: *a*) injected powder particles be heated sufficiently to melt them before they impinge on the substrate; *b*) particles have high enough velocities so that they spread out and flow into the irregular surface of the previously deposited layer; and *c*) strong inter-particle or particle/substrate bonds be formed.

Sophisticated mathematical models have been developed to predict the thermal history of injected particles in a dc plasma jet. In particular, the pioneering works of Lee and Pfender [1-2] are of great importance in this regard. They developed a turbulent model of dc plasma spraying and considered turbulence dispersion effects on particle trajectories. Lee and Pfender accounted for fluctuations in plasma density, velocity, and temperature fluctuations using a Favre-averaged k-ε model. While the effect of velocity fluctuations on particle trajectories were considered, the effect of temperature fluctuations on particle thermal history were not. The objective of the present work is to include such an effect and study its effect on particle heating.

Mathematical Model

The dc plasma jet is assumed to be quasi-steady, axi-symmetric and turbulent. Furthermore, the plasma is in local thermodynamic equilibrium, optically thin, with negligible viscous dissipation. The presence of particles may affect plasma fields as they exchange momentum and energy with each other. The governing equations for the conservation of mass, momentum, and energy along with the turbulence model is described in [1, 2] and will not be repeated here. We note that in order to account for the effect of plasma temperature fluctuations on particle heating, we must also calculate plasma temperature variance $\widetilde{T}''^2$ as well and its dissipation rate ε_T as described in [1-3].

Particle trajectories and thermal histories are calculated using the well-known Lagrangian approach [1-2]. In order to consider the effect of temperature fluctuations on particle heating, a stochastic approach is employed.

The solutions provided by the governing equations of the plasma flow include temperature variance profile $\sqrt{\widetilde{T}''^2}$ and the mass weighted average plasma temperature $\widetilde{T}$. Assuming a normal plasma temperature distribution and employing a Monte Carlo model, at each time step, the instantaneous plasma temperature can be calculated.

In order to separate the effect of temperature fluctuations on particle temperature from the effect of flow turbulence, turbulent dispersion effect on particle trajectories were not considered. In addition, since the particle sizes considered are equal to or greater than 40 μm, trajectory dispersion is not strong.

Results and Discussion

Computations were carried out for two particle types; metallic (nickel (Ni)) and ceramic (alumina (Al_2O_3)), for different sizes 40, 60, 80, and 100 μm, also for different Argon flow rates 50, 80, and 120 cf/hour. These cases were modeled for a constant torch power input of 10.5KW (35Volts, 300Amps) with 50% efficiency. Powder feed rate was of the order of 16g/min. Figure 1 shows a schematic of the computational domain. Due to the limitations on the length of this paper, we will only discuss the results for nickel.

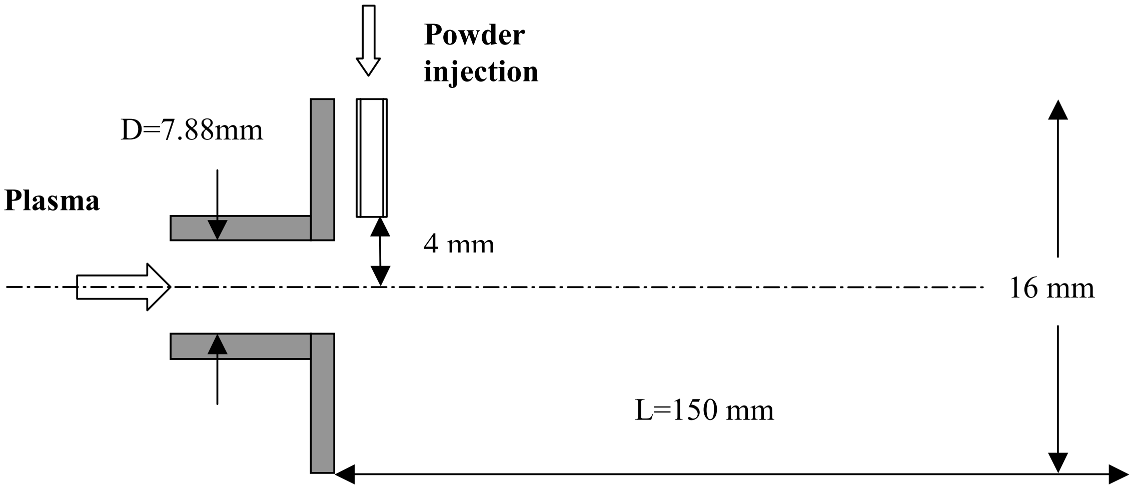

Figure 1 Domain of Computation

Predicted particles average temperature and trajectories are shown in Figure 2. Particles smaller than 80 μm reach boiling point temperature and partially evaporate. The ratio of the predicted standard deviation in particle temperature to the mean particle temperature is a reflection of the fluctuations in temperature fluctuations of the particles. The results, shown in Figure 3, indicate a maximum of 4% in normalized standard deviation. Each graph in Figure 3 has two parts: the first represents the heating zone where solid particle temperature increases to the melting temperature, while the second is the superheating of the melted particle up to its boiling point. The gap between the two parts indicates the melting zone where particle melting temperature is constant. In the melting zone, plasma temperature fluctuations will only influence the melting speed, not the particle temperature. For smaller particles (40 and 60 μm) particle temperature will reach the evaporation stage and the curves drop to zero. Note that according to these results, standard deviation peaks in the superheating zone are larger than the one in the heating zone. Smaller particles have a higher value of standard deviation over the mean temperature. We may conclude that – as was the case for particle trajectories - smaller particles are more influenced by plasma temperature fluctuations than larger particles.

This effect is evident in Figure 4 where distribution of nickel particles temperature for a sample of 2000 particles is depicted. The profile is broadened as particle size is reduced.

Conclusions

It is shown that fluctuations in plasma temperature may result in a broad distribution of particle temperatures. The broadening is stronger for smaller particles.

Acknowledgements

Financial support by NSERC, MMO and members of the Thermal Spray Consortium is gratefully acknowledged.

References

1. Y.C.Lee, 1984, “Modeling Work in Thermal Plasma Processing”, University Of Minnesota.
2. Y.C. Lee and E. Pfender, 1985, “Particle Dynamics and Particle Heat and Mass Transfer in Thermal”, Plasma Chemistry and Plasma Processing, Part I, 5, N^{o}.3, pp. 211-237.
3. B.E. Launder, D.B. Spalding, 1974, “The numerical Computation of Turbulent Flows”, Computer Methods in Applied Mechanics and Engineering, 3, pp. 269-289.

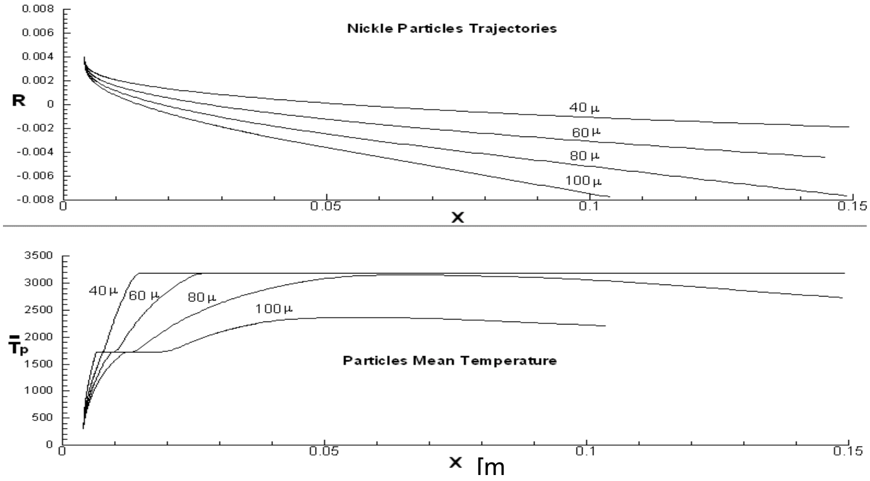

Figure 2 Particle Trajectories and Mean Temperature in K (Ni, 50cf/hour ~ 25 liter/min)

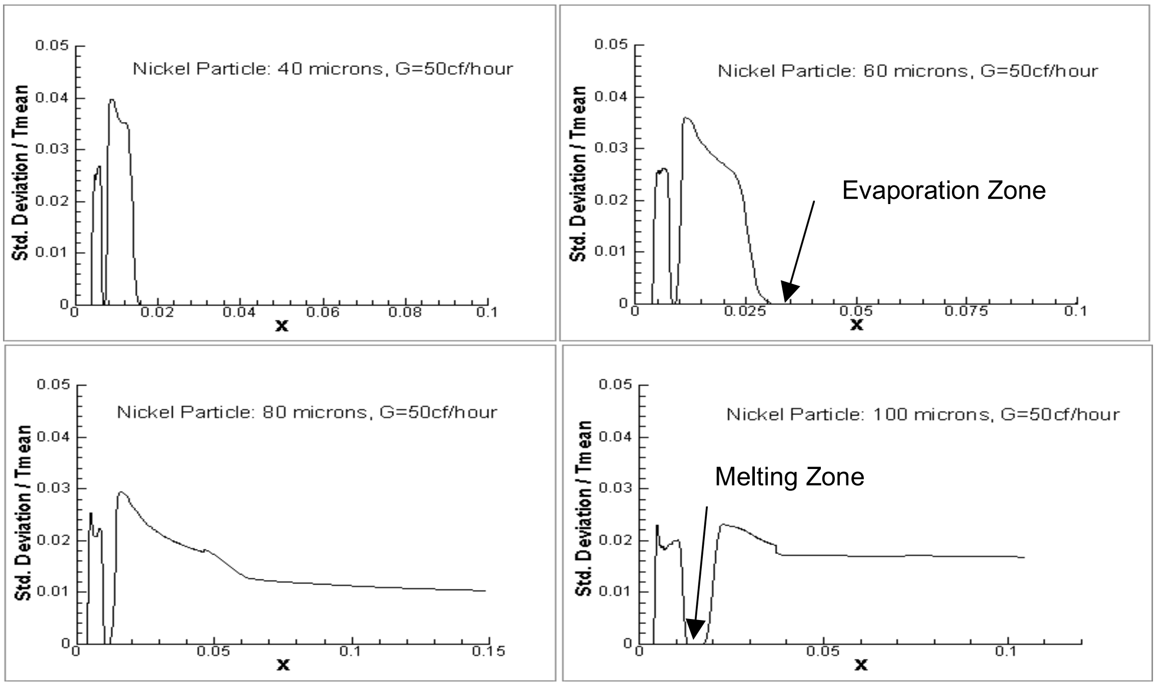

Figure 3 Particle Temperature Standard Deviation /T_{mean} (Ni, 50cf/hour~25liter/min)

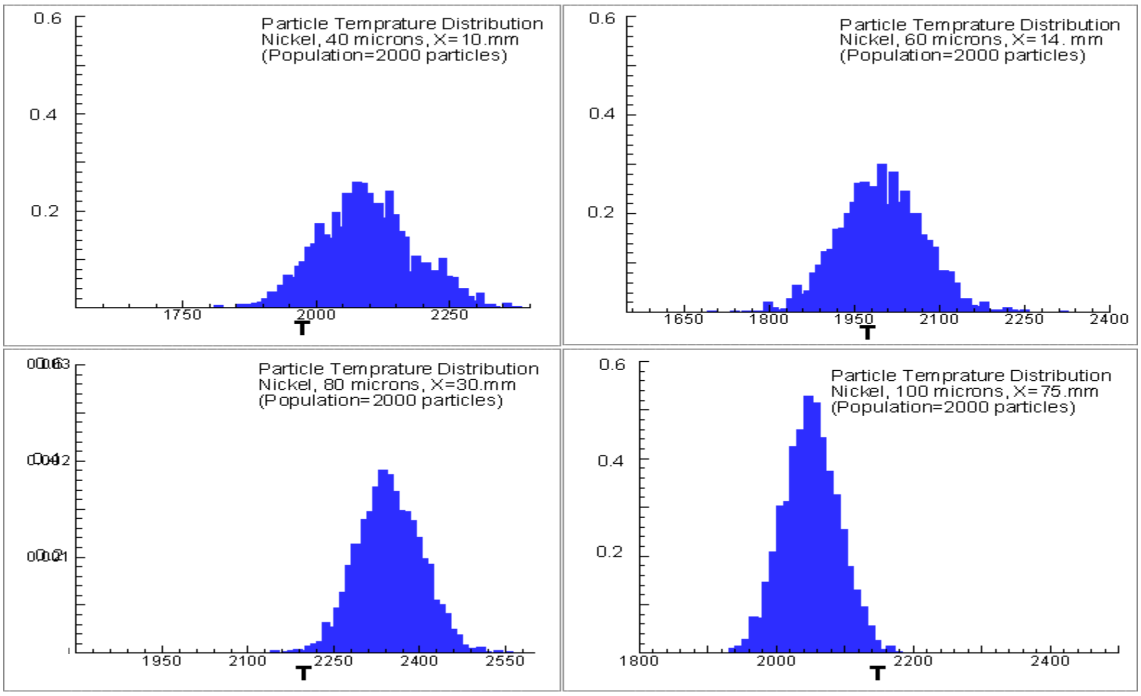

Figure Errore. Nel documento non esiste testo dello stile specificato.**4** - Nickel Particle Temperature

Electric modelling of a N_2O-He RF reactor for SiO_2 thin film deposition

G.Younis, M.Yousfi[1], B.Despax[2], H. Caquineau[2], K. Radouane

[1]CPAT-UMR 5002, [2]LGET-UMR 5003, Email: yousfi@cpat.ups-tlse.fr
Université Paul Sabatier, 118 Route de Narbonne 31062 Toulouse, France

Abstract :

The is paper is devoted to the simulation of the electrical RF discharge behaviour in the case of N_2O, He and N_2O/He under different gas pressures and applied voltages. This is based on a particle model using a Monte Carlo technique for the collision treatment and a Poisson equation solution for electric field determination. The power densities calculated for various conditions (pressure, voltage and gas composition) show a quite good agreement with measurements. The effects of He addition in N_2O are also analysed.

1. Introduction :

The RF discharges studied in the framework of this paper can be used to deposit SiO_2 thin films which are very useful for the microelectronic industry. In the present case, the RF reactor already described elsewhere [1,2] is filled with a ternary gas mixture involving a small fraction of SiH_4 with N_2O as the oxygen donor and He in order to improve the film homogeneity in comparison the N_2O-SiH_4 case.

The optimisation of such a reactor needs more particularly a better knowledge of the electric, energetic, hydrodynamic and mass transfer processes and phenomena. The first step of our work is to perform the modelling and the simulation of the electric and energetic phenomena occurring in the RF reactor because the formation of the deposition precursors are completely conditioned by this discharge behaviour. Furthermore, it is expected that the electric behaviour of the RF reactor is certainly dominated by the more important gas component of the mixture. This is why the present work has been devoted to the electric modelling of an N_2O-He reactor. This mixture choice allows us also to complete and validate the numerous basic data not available in the literature on the electrons and ions transport and reaction in the case of N_2O-He. In fact in order to complete progressively the needed basic data, we have started first of all with studying discharges in a pure N_2O and then in pure He before the case of binary mixture N_2O-He discharges. The electric model results are partly validated from the measurements of the dissipated RF power density of our simulated RF reactor in N_2O, He and N_2O-He mixtures.

The next section is devoted to a short description of the simulated reactor followed by information about the used electric discharge model and the associated electron and ion basic data. Then, we first show some comparisons between calculated and measured RF power density. This is followed by several results on the electric characteristics of our RF reactor in pure gas (N_2O and He) and also N_2O-He mixtures in order to show the effect of He addition on the electrical behaviour of the RF reactor.

2. Discharge model and basic data:

2.1 RF power measurements:

The simulated reactor is already described elsewhere [1]. The inter-electrode distance is 3.95 cm and the electrode length is 25.6 cm. The gas temperature inside the reactor is about 503 K. For the different filling gases (N_2O or He or N_2O/He mixtures) and the chosen gas pressures (about from 0.4 Torr up to 1 Torr), the RF power dissipated in the discharge is measured by a classical subtractive method [2]. Then, the power density (in mW/cm^2) is obtained from the real power injected by dividing this later by the mean electrode area recovered by the plasma discharge.

2.2 Discharge model:

A powerful particle model based on Monte Carlo method coupled with Poisson equation [1],[2] is used in the present work. Monte Carlo method is used for the treatment of the collisions between the various considered charged particles (electrons and ions) and neutral atoms and molecules of the gas. Between the successive collisions, the different charged particles are accelerated by the electric field which is calculated from the solution of Poisson equation in order to take into account the high charge space effect. Our particle model involves several optimisation techniques (variable pseudo-particle, null collision, etc.) which hugely reduce the computation time.

2.3 Basic data:

The basic data needed in our discharge model are the collision cross sections for the different particles interacting with the neutral gas. The considered particles are the electrons, the main ions in N_2O gas (i.e. N_2O^+, O^- and NO^-), in He gas (i.e. He^+) ion and also the metastable state of He (i.e. He_m). Each of these particles can undergo collisions with either N_2O or with He gas during the simulation of RF discharge in the case of our N_2O/He mixture. The different interactions taken into account in the present work are summarized in the following.

Electron gas interactions:

$e + N_2O \rightarrow e + N_2O$	elastic collision
$e + N_2O \rightarrow N_2^* + O + e$	inelastic collisions
$e + N_2O \rightarrow N_2 + O + e$	dissociation
$e + N_2O \rightarrow NO + N + e$	dissociation
$e + N_2O \rightarrow N_2O^* + e$	excitation
$e + N_2O \rightarrow N_2(A^3\Sigma_u^+) + O(^3P) + e$	dissociative excitation
$e + N_2O \rightarrow N_2 + O^* + e$	dissociative excitation
$e + N_2O \rightarrow N_2(X^1\Sigma_g^+) + O(^1S) + e$	dissociative excitation
$e + N_2O \rightarrow N_2O(1 \leq v \leq 3) + e$	vibrational excitation
$e + N_2O \rightarrow O^-(^2P) + N_2(X^1\Sigma_g^+)$	attachment
$e + N_2O \rightarrow N_2O^+ + 2e$	ionization

$e + He \rightarrow e + He$	elastic collision
$e + He \rightarrow e + He_m$	metastable formation
$e + He \rightarrow e + He^*$	excitation
$e + He \rightarrow 2e + He^+$	ionization
$e + He_m \rightarrow 2e + He^+$	ionization stepwise

Ion gas interactions

$O^- + N_2O \rightarrow O^- + N_2O$	elastic collision
$O^- + N_2O \rightarrow NO^- + NO$	NO- formation
$O^- + N_2O \rightarrow O_2^- + N_2$	ion conversion
$O^- + He \rightarrow O^- + He$	elastic collision
$O^- + He \rightarrow O + He + e$	detachment

$NO^- + N_2O \rightarrow NO^- + N_2O$	elastic collision
$NO^- + N_2O \rightarrow N_2O^- + NO$	ion conversion
NO- + $N_2O \rightarrow O^- + N_2 + NO$	O- formation
$NO^- + N_2O \rightarrow N_2O + NO + e$	detachment
$NO^- + He \rightarrow NO^- + He$	elastic collision
$NO^- + He \rightarrow NO + He + e$	detachment

$N_2O^+ + N_2O \rightarrow N_2O^+ + N_2O$	elastic collision
$N_2O^+ + N_2O \rightarrow N_2O + N_2O^+$	charge transfer
$N_2O^+ + He \rightarrow N_2O^+ + He$	elastic collision

$He^+ + He \rightarrow He^+ + He$	elastic collision
$He^+ + He \rightarrow He + He^+$	charge transfer
$He^+ + N_2O \rightarrow He^+ + N_2O$	elastic collision
$He^+ + N_2O \rightarrow He + N_2O^+$	charge transfer

Penning ionizations:

$He_m + N_2O \rightarrow He + N_2O^+ + e$
$He_m + He_m \rightarrow He + He + e$

The collision cross section of electron-N_2O and electron-He systems are quite well known even though it has been necessary to solve some problems concerning the bad knowledge of for example electron attachment and dissociation in N_2O and also stepwise ionisation in He (see figure 1 showing the stepwise ionisation cross section for e-He_m impacts). Collision cross sections are mainly taken from previous works (e.g. Radouane [3] for electron-N_2O) and completed in the present work.

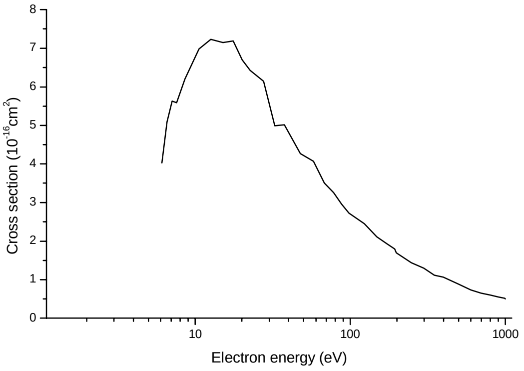

Figure 1: Stepwise ionisation collision cross section for e-He_m impact from [4]

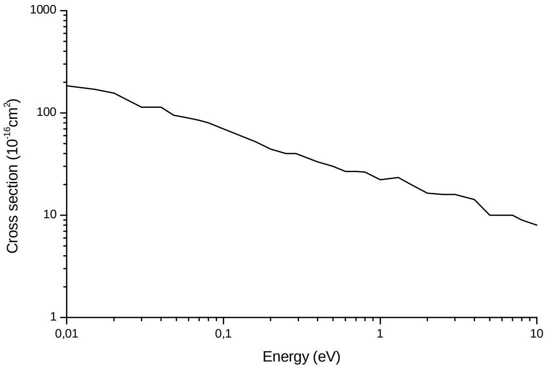

Figure 2: Penning and associative ionisation for the reaction He_m + He_m from [6]

However, the ion-neutral case is much more problematic because the collision cross sections for the main ions formed by electron impacts on N_2O or He (i.e. N_2O^+, NO^-, O^- and He^+) and interacting either with N_2O or with He in the mixture case are not well known. Therefore, a specific method [5] has been used to obtain the missed collision cross sections in our different ion-neutral systems involved in the N_2O/He reactor and previously listed. Noting that Penning ionisations are also considered in our model (see e.g. Penning ionisation cross section for He_m+He_m reaction in figure 2 taken from reference [6]).

Collision cross sections for N_2O^+, NO^- and O^- ions interacting with N_2O are taken from [3] while those of He^+/He system are taken from [7]. He^+ ion interacting with N_2O and N_2O^+ ion interacting with He are completed in the frame of this work with the help of Hennad [8].

3. Results:

Calculations of the electrical discharge characteristics have been undertaken from our particle model using the previous basic data. The simulation conditions of our 13.56 MHz RF reactor are an electrode separation of 3.95 cm, applied voltages varying from about 40 up to 160 Volts and two gas pressures (0.5 and 1 Torr). Calculations are performed for N_2O, He and N2O/He mixtures at a gas temperature of 503 K [9]. The RF voltage is defined by: $V_{RF}(t) = V_{max} \cos(\omega_{RF} t)$, V_{max} being the input voltage, ω_{RF} the angular frequency in rad s^{-1} and t the time.

The calculated electrical characteristics are the space charge electric field, the charged particle densities and current densities, the electron and ion mean energies, the electron and ion reaction rates (for ionisation, dissociation, detachment, etc.), the electron and ion distribution functions and also the RF power density.

Figures 3a and 3b show the total RF power density as a function of the applied voltage in the case of respectively N_2O and He for two gas pressures (0.5 and Torr).

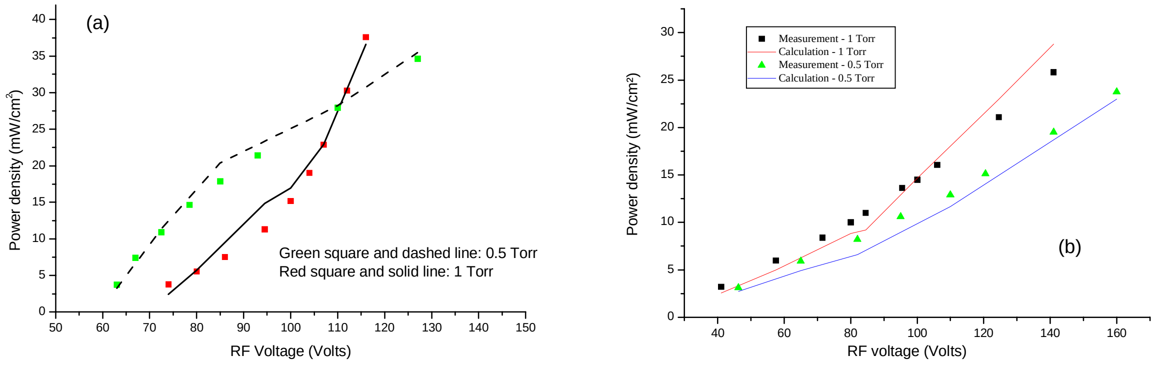

Figure 3: Power density dissipated in the reactor as a function of the RF voltage for two pressure cases (0.5 and 1 Torr): Lines: Calculation, Symbols: measurements: (a) N2O case, (b) He case

Figure 4 shows the power density for two RF voltages as a function of proportion of He in N_2O.

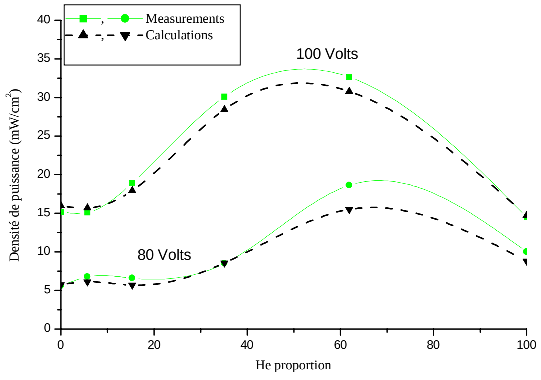

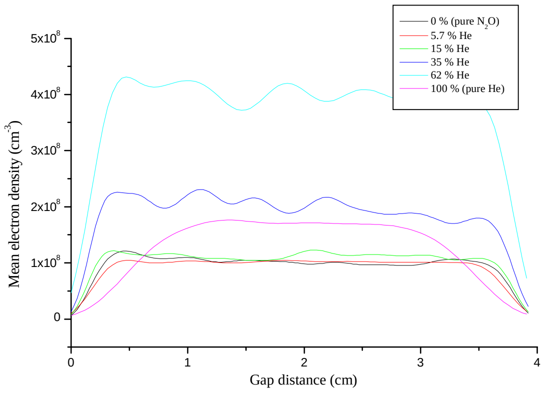

Figure 4: Power density dissipated in the reactor as a function of the proportion of He in N2O for two RF voltages (80 and 100 Volts) at 1 Torr

Figure 5: Mean electron density at 1 Torr and 80 Volts

First of all, we can observe in these figures (Fig. 3 and 4) that the calculated power densities are in a quite good agreement with the measured ones. This coherence can be considered as a confirmation of our choice and determination of the different electron and ion basic data. As already shown in reference [2] power density is directly and mainly proportional to then electron density. So according to [2], results of figure 3a in pure N_2O can be explained in terms of ionisation, attachment, ion conversion and detachment processes, i.e.:

$e + N_2O \rightarrow N_2O^+ + 2e$, $e + N_2O \rightarrow O^- + N_2$, $O^- + N_2O \rightarrow NO^- + NO$ and $NO^- + N_2O \rightarrow N_2O + NO + e$

Indeed at 0.5 Torr, power density mainly depends on ionization and attachment processes while at 1 Torr NO^- formation becomes quite large leading to a great role of electron detachment from NO^- which contribute to reinforce the power density so that this later at 1 Torr becomes larger than the power density at 0.5 Torr from about 110 Volts for the RF voltage (see Fig. 3a). In the case of pure He, the electron density are mainly due to ionization processes (direct and stepwise) which are more important at lower pressure because electrons are more energetic and therefore have a larger ionization efficiency. Penning ionization between metastable of He does not really play an important role under our discharge conditions.

Figure 4 shows the power density as a function of proportion of He in N2O for two RF voltages. The maximum of the power density observed in both cases around respectively 60% of He and 65% of He are due here also to a balance of the processes of creation and loss of electrons. Indeed as the proportion of He in N2O increase, this automatically leads to a reduction of the weight of the numerous excitation (vibrational, optical and dissociation) processes which therefore allow to the electron to gain more energy from the field between successive collisions. Under these conditions, the ionization efficiency of electron is more large and in the same time the attachment efficiency can decrease due to the lower N2O concentration in the mixture. So, the conjunction of these two phenomena leads to a rise of the power density with the rise of He proportion. Then above a certain proportion of He, when the effect of N2O becomes weak due to its low concentration, the discharge is mainly dominated by the processes in He gas in which the electron creation processes need further electronic energy to ionizes atoms (24.6 eV in He rather than 12.6 eV in N2O). The behavior is confirmed by the mean electron density shown in figure 5. This is a mean density because it is integrated over all the RF cycles. We observe in figure 5 that the electron density first increases as a function of He proportion and then decreases above a certain proportion of He in N2O (e.g. about 65% at 80 Volts). Figure 6 confirms also the tendency of electrons to have larger energy because the reduced electric field (E/N) increases in the sheath region (near the electrodes) as a function of the He proportion up to about 65% before to observe its decrease in the case of the pure He.

We observe in the same time in figure 7 showing the dissociation rate of N2O in the case of N2O/He mixtures, that this dissociation rate increases up to 65 % of He and then it decreases. The dissociation rate is defined as the product of the collision frequency and the electron density. The rise up to 65 % of He is explained by the rise of the electron density. Such a result also shows that the addition of He in N2O does not affect the efficiency of the deposit precursor formation which directly depends on the N2O dissociation rates as is shown in reference [3].

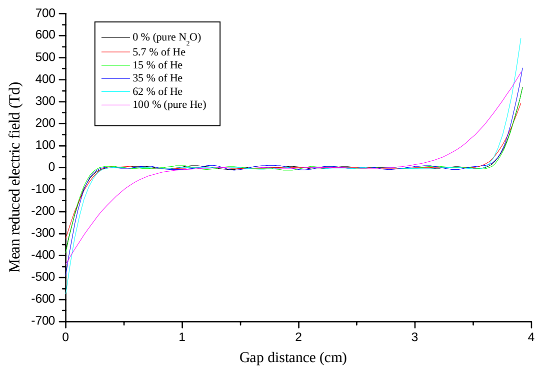

Figure 6 : Mean reduced electric field as a function of gap distance for different proportions of He in N2O at 80 Volts.

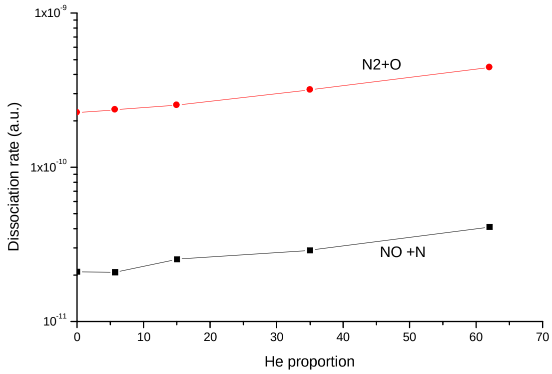

Figure 7: Dissociation rate of N2O for different proportions of He in N2O at 80 Volts.

The next step of this work is to study the ternary mixture case (N_2O, He and SiH_4) using the data already obtained in the present work. This study will also concern the hydrodynamic and mass transfer phenomena.

Reference:

[1] K. Radouane, L. Date, M. Yousfi, B. Despax, H. Caquineau J. Phys. D :Appl. Phys. , **33**, 1332 (2000)

[2] L. Date, K. Radouane, M. Yousfi, B. Despax, H. Caquineau , A. Hennad, J. Phys. D :Appl. Phys. , **32**, 1478 (1999)

[3] K. Radouane, PhD thesis, n° 3559, Université Paul Sabatier (1999)

[4] H. Deutsch, K. Becker, S. Matt, T.D. Märk, J. Phys. B, **32**, 4249, (1999)

[5] M. Yousfi, A. Hennad, O. Eichwald, J. Appl. Phys, **84**, 107, (1998)

[6] R.H. Neynaber, G.D. Magnuson, S.Y. Tang, J. Chem. Phys. , **68**, 5112, (1978)

[7] A. Himoudi, PhD thesis, n° 1547, Université Paul Sabatier, (1993)

[8] A. Hennad, PhD thesis, 2458, Université Paul Sabatier, (1996)

[9] M. Chayani, PhD thesis, to be published, (2003)

Electrical characterization of a d.c. non-transferred plasma torch

E. Vassallo, A. Cremona, L. Laguardia, N. Spinicchia

Istituto di Fisica del Plasma, National Research Council, Milan, Italy

Abstract
Non transferred arc plasma torches are often used as plasma sources for the treatment of toxic and hazardous halogenated substances. At the IFP-CNR in Milan, a research program has been carried out for the development of some types of plasma torches with integrated waste injection systems. In this paper the electrical characterization of the Hollow Cathode Plasma Torch is studied.

1. Introduction

The main purpose for the development of a non transferred arc plasma torch, with an integrated waste injection system, is to maximize the plasma-waste interaction and to transfer the maximum electrical power to the plasma. The thermal efficiency κ_{eff} is the parameter which gives information about the real power transferred to the plasma. This work has been addressed to identify the operative conditions in which the thermal efficiency of the torch device is optimized.

The designed non-transferred plasma torch [1] is a direct current type, water cooled, with nominal power of 50 kW. The controllable parameters of the torch are the electrical current, the cooling water and the carrier gas flow rate. The hollow cathode is made by a copper rod with an insertion of a tungsten cone on the top. The anode is made by a conical shaped copper protected by a hollow cylinder of tungsten of 6 mm of inner diameter as shown in Fig. 1. Both the electrodes are cooled by a single close circuit of forced deionised water. The distance between the electrodes is variable with a minimum of 1.2 mm. The carrier gas is argon injected by a swirl system. Table 1 shows the main experimental conditions.

Table 1	
Torch power	0-25 kW
Water flow rate	15 l/min
Water flow rate temperature	18°C
Argon flow rate	30-50 l/min
Arc currents	150-700 A

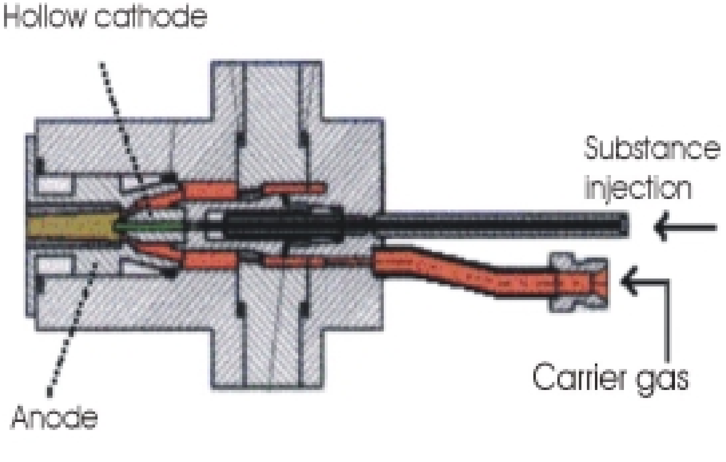

Fig. 1: Torch layout

2. Experimental results

Current-Voltage Characteristics

In order to define the torch thermal efficiency, the current-voltage characteristics must be investigated. Only a few reports are available in literature [2;3] on the I-V characteristics of DC plasma torches and, in any case, they are limited to arc current ranges lower than 400 A. The present paper reports values until 700 A, as a result of experimental measurements carried out in our institute.

Fig. 2 shows the variation of arc voltage as a function of arc current for different argon flow rates. Two types of analysis can be developed:

A) for a fixed flow rate
B) for a fixed current

A) For a fixed flow rate the arc voltage decreases with increasing in arc current for arc current less than about 450 A and then increases with increasing of arc current. The relationship connecting the arc voltage V and the arc current I is approximately parabolic. The value 450 A is characteristic for the Hollow Cathode Plasma Torch and can shift to lower or higher arc currents depending on the structural features of the torch.

In order to explain the behaviour of the I-V characteristics in the first range of current it must take the increase of electric conductivity with gas temperature into account. It's well known that the analytical form for the electrical conductivity is given by [4]:

$$\sigma_e = \frac{n_e e^2}{\sqrt{2\pi T m_e}\, n_0 \sigma_{e0}} \tag{1.1}$$

where n_e, n_0 are the the electrons and neutral particle number densities rispectively and σ_{e0} the electron-neutral collision cross section. The ratio n_e/n_0 can be determined by Saha equation. In consequence the behaviour of σ_e with temperature is given by :

$$\sigma_e(T) \propto (KT)^{3/4} \exp\left(-eE/2KT\right) \tag{1.2}$$

where E is the ionization potential of atoms.

In the particular case of argon plasma [4] σ_e is negligibile for $T < 5000$ K and then increases steeply until reaching values of about 10^4 A/Vm for $T \geq 17000$ K, keeping around this value also for higher temperatures. The growth of σ_e with increasing in current is resposible for the voltage falling trend in the plasma torch.

In order to explain the rise of voltage at currents larger than 450 A, it is necessary to consider the magnetohydrodynamics (MHD), according to which, as a result of an increase in current density, a larger $\boldsymbol{J} \times \boldsymbol{B}$ body force acts on the plasma arc. The Lorentz force $\boldsymbol{F} = \boldsymbol{J} \times \boldsymbol{B} = -\mu_0 J_z^2 r\,\hat{\mathbf{r}}$ is radially inward, tending to pinch the arc to a smaller diameter. The decreasing of the section of the arc brings about a smaller electrical conductance. Moreover, at arc currents larger than 450 A, phenomena of turbolence and instability [5] reduce the conductivity of plasma resulting in an increase in arc voltage. A critical kinetic Reynolds number can be introduced in order to distinguish between the range of the low arc current in which the plasma is in a laminar flow state and the range of the high arc current in which phenomena of turbulence occur. Reynolds number R_e can be defined as:

$$R_e = \frac{4}{\pi \eta d} \cdot \frac{M}{RT} \cdot F \tag{1.3}$$

where M is the argon molar mass, F the volumetric flow rate $p \cdot dV/dt$, η the argon viscosity, d the arc diameter, R the universal constant of gases and T the average temperature in the torch. From experimental measurements [6] it is possible estimate that T increases from 10000 K to 15000 K when the arc current increases from 200 A to 600 A. In this range of temperature and at atmospheric pressure the argon viscosity decreases from 2.7×10^{-4} Pa·s to 5.7×10^{-5} Pa·s [7]. With regard to this range of current and temperature and at a fixed flow rate $dV/dt = 40$ l/m, that is 6.7×10^{-4} m^3 s^{-1} in SI units, pressure increases from its nominal value 3×10^5 Pa to 6×10^5 Pa, as it has been taken in previous experimental measurement carried out in our institute. The values so calculated for Reynolds number are the following:

$R_e = 454$ at T 10000 K ($I = 200$ A)
$R_e = 1433$ at T 15000 K ($I = 600$ A)

where it has been assumed $d = 2 \times 10^{-3}$ m (this number has been reasonably estimated by the anode inner diameter that, as mentioned in the introduction, is of 6 mm).

In general a gas is considered in a laminar flow state when $R_e \leq 1200$ and in a turbulent flow state when $R_e \geq 2200$ while for $1200 \leq R_e \leq 2200$ the features of the two types of flow coexist. Therefore for arc current of about 200 A the argon flow inside the torch is surely laminar but for arc current of 600 A the torch works in an intermediate regime in which laminar and turbulent behaviours coexist. This change of flow regime together with the possible decreasing of the size of the arc induced by magnetic effects explains the different trend of the I-V characteristics at low and high arc currents.

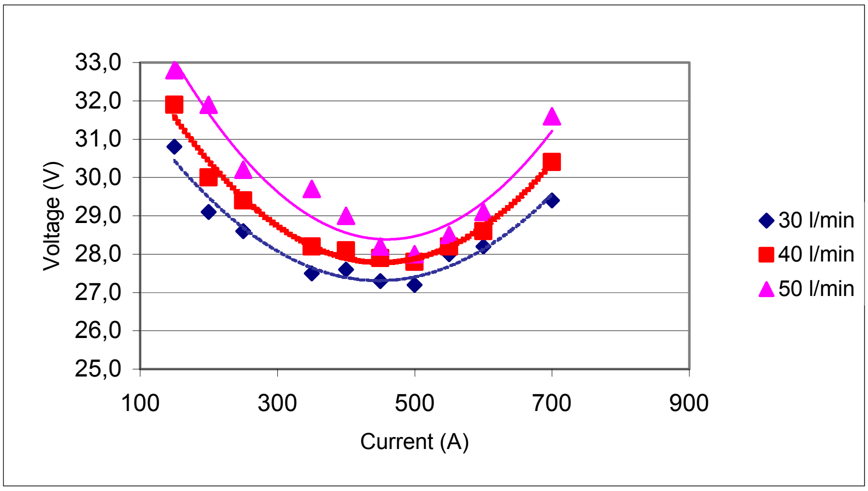

Fig. 2: Variation of arc voltage as a function of arc current for different flow rates of carrier gas

B) For a fixed current the arc voltage grows as the argon flow rate grows (Fig. 3) [8].This behaviour can be attributed to the decrease of the electrical conductivity as a result of the temperature decrease and to the lengthening of the arc column.

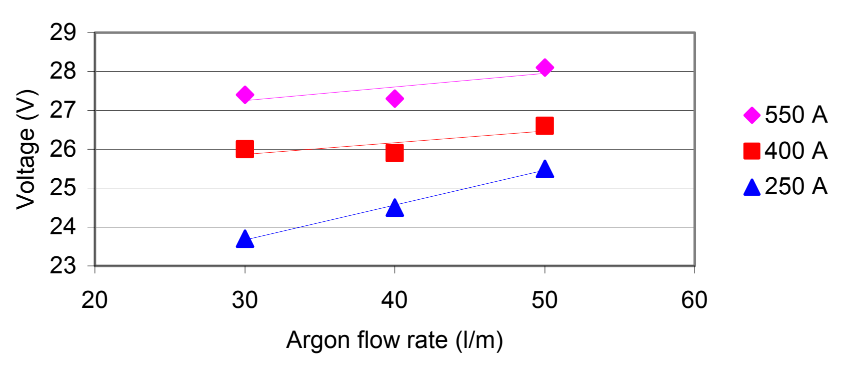

Fig. 3: Arc voltage as a function of argon flow rate at different currents

Thermal efficiency

The thermal efficiency κ_{eff} % of the torch has been determined by a calorimetric method, that requires the evaluation of the power transferred to the arc plasma (Q_{pl}) and of the power supplied ($P_{arc} = V_{arc}I$) to the torch. The arc power P_{arc} is converted into heat and goes into heating the cathode (Q_C), the anode (Q_A) and the plasma column, according to the equilibrium equation:

$$P_{arc} = V_{arc}I = Q_C + Q_A + Q_{pl} = Q_{torch} + Q_{pl} \tag{1.4}$$

The thermal efficiency is defined by the equation:

$$\kappa_{eff} = \frac{Q_{pl}}{V_{arc}I} = 1 - \frac{Q_{torch}}{V_{arc}I} \tag{1.5}$$

and Q_{torch} can be calculated as:

$$Q_{torch} = G_w C_p \left(T_{wi} - T_{wf}\right) \tag{1.6}$$

where C_p is the water specific heat at constant pressure, G_w the flow rate of the cooling water, and T_{wi}, T_{wf} its initial and final temperatures respectively.

Fig. 4 shows the thermal efficiency as a function of the power supplied to the torch for different argon flow rates. The curves exhibit a maximum that shifts to higher values of the input power with increasing of argon flow rate. The decrease of the thermal efficiency at high input powers due to high energy losses is in accordance to the temperature dipendence of the thermal conductivity [4] that, for an argon plasma in the temperature range from 5000 to 15000 K, rises to 2.3 W/m·K in consequence of the increasing of ionization and of the high translational energy of the electrons. Vice versa the low thermal efficiency at low input powers can be attributed to different interaction conditions between the gas and the electric arc. In general, at very low current the electric arc interacts only partially with the process gas due to its reduced dimensions and to instability phenomena.

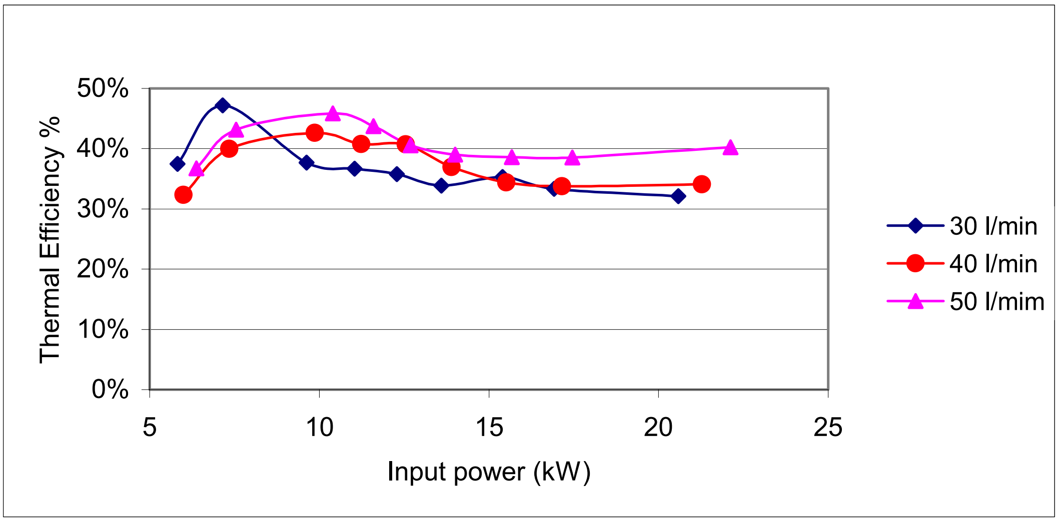

Fig. 4: Variation of thermal efficiency as a function of input power for different flow rates of argon

3. Conclusions

In this work the I-V characteristics and the thermal efficiency of a d.c. non trasferred arc plasma torch have been investigated. Every torch has a range of optimal thermal efficiency depending on the operative conditions and on the structural parameters of the torch. In the case of the Hollow Cathode Plasma Torch used in these experimental measurements the highest thermal efficiency is around 9 kW for argon flow rates of 40 or 50 l/min and around 7 kW for argon flow rates of 30 l/min.

References

[1] F.E. Beretta, E. Vassallo, *"Design Criteria for Integrated Injection Systems in a d.c. Plasma Source"*, Proceedings of the 14th International Symposium on Plasma Chemestry, (1999)

[2] A. K. Das, K.P. Sreekumar, N. Venkatramani, Plasma Sources Sci. Technol. 3 (1994) 108-113

[3] R. Ramasamy, V. Selvarajan, Eur. Phys. J. D 8, 125-129 (2000)

[4] M. I. Boulos, P. Fauchais and E. Pfender, *"Thermal Plasmas"*, Vol. 1, Plenum Press (1994)

[5] O. P. Solonenko and M. F. Zhukov, *"Thermal Plasma and New Materials Technology"*, Vol. 1, Cambridge Interscience Publishing, (1995)

[6] M. I. Boulos, P. Fauchais, J. Heberlein, M. Hrabovský, E. Pfender, *"Thermal Plasma Technology"*, Vol. 1, 14th International Symposium on Plasma Chemestry, Prague, (1999)

[7] B. Bottin, D. Vanden Abeele, M. Carbonaro, G. Degrez, G.S.R. Sarma, *"Thermodynamic and Transport Properties for Induction Plasma Modelling"*, Joint Thermophysics and Heat Transfer Conference, Albuquerque, NM, USA, (1998)

[8] A. Capetti, E. Pfender, Plasma Chem. Plasma Process. 11, 379, (1993)

Simulation of gas dynamics effects on NOx removal in a typical flue gas corona discharge

O.Eichwald, M. Yousfi, M. Benhenni, D. Nelson.

CPAT-UMR du CNRS n° 5002, Université Paul Sabatier, 118 Route de Narbonne,
31062 Toulouse Cédex 04, France (email: olivier.eichwald@cpat.ups-tlse.fr)

Abstract

A 1D mass transfer model for the post discharge phase, including radial diffusion, gas temperature variation and chemical kinetics, is developed to follow the spatio-temporal evolution of the main chemical species in a pulsed corona discharge used for NO pollution control in a typical flue gas (76% N_2, 12%CO_2, 6% O_2, 6% H_2O). The obtained results shows that the classical simplified models (i.e. 0D models) neglecting thermal and transport phenomena induced by the discharge leads necessary to an overestimation of the NO removal in the discharge channel.

1. Introduction

The pulsed corona discharge is one of the nonthermal plasma technique which can be used to remove toxic oxides (such as NO_x or SO_x or VOC) from the polluted industrial flue gases [1]. In this technique, the harmful oxides can react with primary radicals (such as O, N, OH) created during the discharge phase (i.e. streamer formation and propagation) by electron-molecule and ion-molecule impacts. Then during the post discharge phase, reactions involving secondary radicals (HO_2 or O_3, etc.) can lead to NOx removal, acid formation (e.g. HNO_3 which can be transformed into salt by adding a base) and other harmless atoms and molecules. During the pollution control process, the time needed to remove oxides by reactions with radicals is larger than the diffusion time of the main chemical species. This means that the chemical kinetics is therefore necessary affected by the radial expansion of the gas mixture in the discharge channel ([2],[3]). Furthermore, a fraction of the dissipated power in the plasma channel relaxes into a thermal form. The resulting gas temperature rise induces also a significant perturbation on the chemical kinetics and the diffusion phenomena ([2],[3],[4]). In fact, this means more generally that the electric, energetic, hydrodynamics and chemical processes and phenomena occurring inside the reactor are very dependant and strongly coupled.

In the present work the reactive gas model is a 1D mass transfer model including radial diffusion, gas temperature variation and chemical kinetics. It is used in order to follow the spatio-temporal evolution of the main neutral chemical species in a pulsed corona discharge used for NOx pollution control from a typical flue gas (76%N_2, 12% CO_2, 6%H_2O, 6%O_2) at the atmospheric pressure and ambient temperature (300 K) with an initial NO concentration of 400ppm. Concerning the present model, it is important to notice that the temperature variations take into account the vibrational energy relaxation into the random thermal energy. The initial concentration of each reactive species as well as the power dissipated in the flue gas by the discharge are obtained from a 1.5D streamer model coupled to the chemical kinetics model which also includes the charged species ([3]). The article is organized as follow: section 2 is devoted to a rapid description of our modelling of the discharge phase and the post-discharge phase including radial diffusion and gas temperature variation. In section 3, we describe our simulation conditions and then in section 4, some obtained results are shown and discussed before giving our concluding remarks.

2. Electrical discharge and reactive gas dynamics models

The discharge phase dynamics is analyzed from a 1.5D electrical model for the simulation of the positive streamer formation and propagation coupled with a chemical kinetics model in order to follow for example the radical and metastable species formation. The formalism and the physical assumptions for the streamer dynamics are already detailed elsewhere [3]. The 1.5D model means that the transport equations are solved along the discharge propagation axis while the electric field is calculated for a 2D cylindrical geometry in order to take into account the space-charge effect due to the filamentary structure of the corona discharge. The radial shape of the charged particle densities in the streamer channel is assumed gaussian with a constant radius. The charged particle transport equations are solved with the help of a powerful numerical method which is a space and time second order MUSCL method [5] while Poisson equation for the charge space electric field calculation is solved by using a fast Fourier transform analysis along the propagation axis and a cyclic reduction method along the radial direction [6].

The 1D fluid model used to follow the reactive gas dynamics during the post-discharge phase is detailed in reference [3]. This model allows us to analyse the radial expansion (i.e. in the direction transverse to the discharge channel) of the main neutral chemical species during the post discharge phase after the streamer propagation. The model takes into account the radial mass diffusion of each neutral chimical species and the gas temperature variation. It is assumed that there is no initial convective flow and that the gas pressure remains constant. The modelling of the gas temperature variation includes the relaxation of electronic and vibration excitation energy into a random thermal energy. The reactive gas transport equations are integrated in a one-dimensional cylindrical geometry along the radial direction r and solved by a second order space and time algorithm. The diffusive flux is corrected by the MUSCL superbee scheme [5] in order to limit the numerical diffusion.

3. Simulation conditions

In this work, the electrical discharge modeling has been carried out in the case of a wire-to-plane electrode configuration close to the conditions of the non thermal pollution control devices [1]. We consider a typical flue gas (76% N_2, 12%CO_2, 6%O_2, 6%H_2O) at atmospheric pressure and ambiant temperature polluted by 400ppm of NO. The distance between the anode (wire) and the cathode (plane) is 0.55 cm, the anode curvature is 500µm, and the applied voltage is 18kV. The streamer radius is choosen as 200µm according to, for example, the results of Babaeva and al [7] under similar simulation conditions. The discharge phase model involves 17 positive and negative charged species (e, O^-, O_2^-, N^+, N_2^+, N_4^+, NO^+, NO_2^+, H^+, H_2^+, H_2O^+, O^+, O_2^+, O_4^+, OH^+, CO_2^+, CO^+) and 26 neutral species (atoms H, N, O, molecules N_2, O_2, CO_2, H_2O, OH, H_2, HO_2, O_3, NO, NO_2, NO_3, N_2O, N_2O_5, N_2O_4, HNO, HNO_2, HNO_3, HO_2, H_2O_2, $O(^1D)$, $N_2(A^3\Sigma_u^+)$, $N_2(a'^1\Sigma_u^-)$, $O_2(a^1\Delta g)$) reacting following 147 selected chimical reactions. The electron swarm data needed for the electrical discharge model (mobility and diffusion coefficients, ionization, attachment and dissociative frequencies) as well as the fractions of the energy transferred from charged to neutral particles via elastic and inelastic processes are given from a Boltzmann equation solution [8].

The post-discharge reactive gas dynamics model takes into account the previous 26 neutral chemical species reacting following 70 selected chemical reactions. The discharge model gives the density of each considered species along the propagation axis z while the reactive gas dynamics model needs the initial radial profile i.e in the direction perpendicular to the discharge channel. Therefore it has been assumed, as in the case of charged particles, a radial gaussian shape with a radius of 200µm for each neutral particle. The thermal conductivity of the flue gas was calculated using a relation already given in reference [4]. The Lennard-Jones parameters values used to calculate the binary diffusion coefficients of all species in the mixture were taken from [9] and [10]. Finally, the vibration relaxation time is chosen equal to 50µs according to reference [11] while the electronic excitated radiative levels are assumed to relax instantaneously into thermal form.

4. Results and discussion

4.1 Discharge phase results

Figures 1(a), 1(b), 1(c) and 1(d) show respectively the reduced electric field E/n (where E is the electrical filed and n the gas density) , some positive and negative charged species densities and certain neutral radical densities along the discharge propagation axis. The reduced electric field exhibits the classical shape of an cathode directed streamer (see figure 1a) with a quite high electric field on the streamer head (more than 2000Td at 8ns). This electrical field is partly responsible of the high electron and ion densities along the discharge propagation axis (see figure 1b and figure 1c). In fact, during the streamer propagation, the different ions (N_2^+, CO_2^+, H_2O^+, O_2^+, N^+, O^+ and CO^+) are mainly created in the streamer head by the energetic electrons during direct ionization (dissociative or not) of the dominant gas molecules (N_2, CO_2, O_2, and H_2O). For example, due to the high proportion of N_2 (76%) in the flue gas, N_2^+ and electron densities reach a maximum value of around 10^{15}cm^{-3} in the streamer head (see figure 1b and 1c) following the reaction (5) $e+N_2^+ \rightarrow 2e+N_2^+$. Hovewer, just after the streamer head crossing, N_4^+ ion play an leading role in the evolution of the main positive ions. In fact, the three body reaction (97) $N_2^+ + 2N_2 \rightarrow N_4^+ + N_2$ enhance the N_4^+ ion density up to 10^{15}cm^{-3} just behind the streamer head to the detriment of N_2^+ ion concentration which fall down rapidly in the ionized channel (see the corresponding curves figure 1b). Then, due to the efficiency of reactions (99) $N_4^+ + CO_2 \rightarrow 2N_2 + CO_2^+$ and (100) $N_4^+ + H_2O \rightarrow 2N_2 + H_2O^+$, the CO_2^+ and H_2O^+ ion densities increase in the ionized channel as long as the N_4^+ ion concentration remain high enough. Hovewer, the creation of CO_2^+ by reaction (99) is balanced by the ion conversion reaction (60) $CO_2^+ + H_2O \rightarrow CO_2 + H_2O^+$ which contributes also to enhance the H_2O^+ ion concentration. Finally, the reactions (116) $N_2(A^3\Sigma_u^+) + H_2O \rightarrow OH + H + N_2$, (25) $e + H_2O^+ \rightarrow H + OH$ and (27) $e + H_2O^+ \rightarrow 2H + O$ favor the formation of OH and H radicals in the ionized channel while the reaction $e + O_2^+ \rightarrow 2O$ maintains the O radical formation. All the previous radicals as well as the N radical are first created in the streamer head by dissociative reactions on the main molecule such as reactions (7) $e + O_2 \rightarrow O + O$, (13) $e + H_2O \rightarrow e + H + OH$ or (3) $e + N_2 \rightarrow e + 2N$.

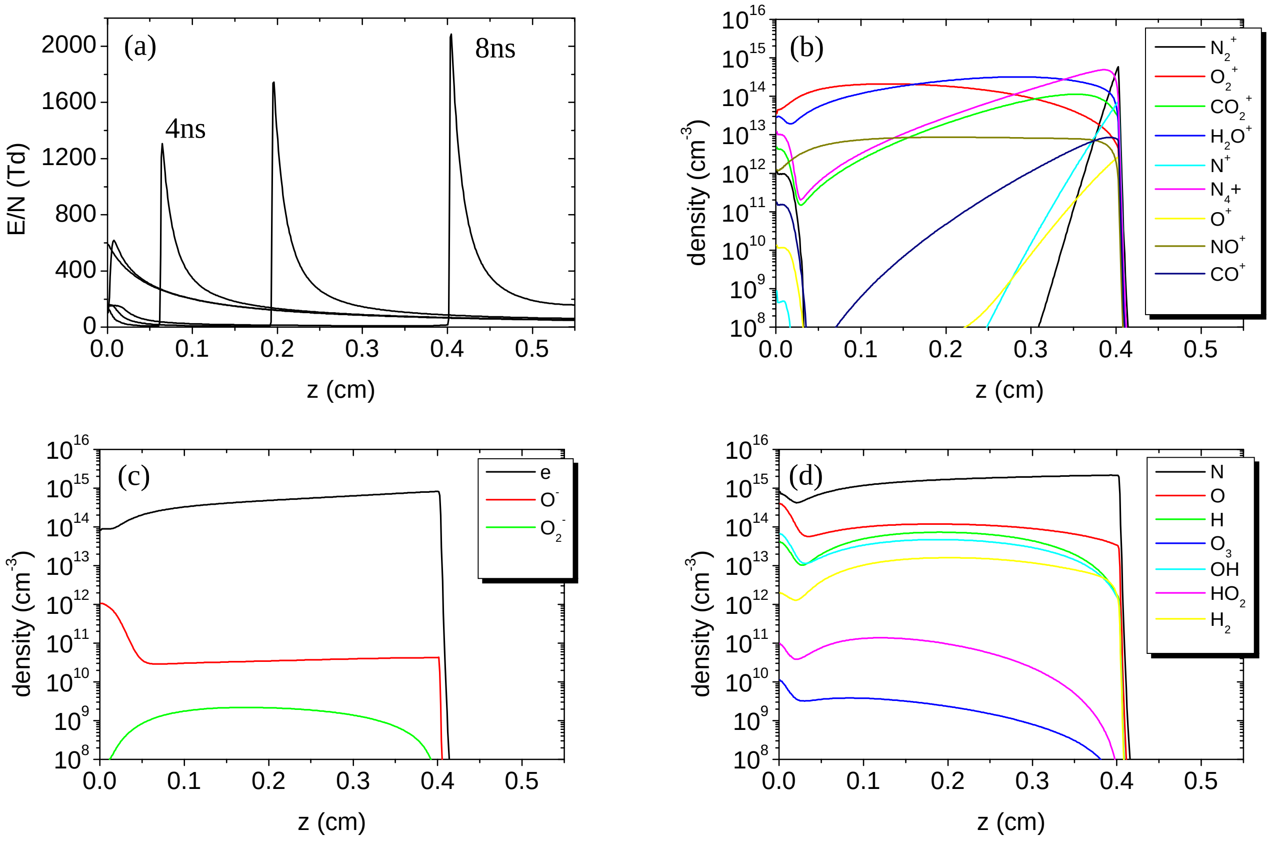

Figure 1 : Spatial variation from anode (z=0) towards the cathode (z=0.55cm) of (a) reduced electric field at time t=0,2,4, 6 and 8ns, (b) some positive charged species at t=8ns, (c) some negative charged species at t=8ns and (d) some radical species at t=8ns.

4.2 Post discharge phase results

In the post-discharge phase, the radial gas expansion is analysed from 10ns up to 10ms at a fixed position of the discharge axis (i.e. z= 0.25cm). This peculiar position is chosen far enough from the anode to neglect the convective phenomena and close enough to the anode to have a non negligible gas temperature effect. The shape of the initial radial profile of each neutral species is assumed gaussian with a half width of 200µm. The maximum value of the density on the axis is determined from the discharge model.

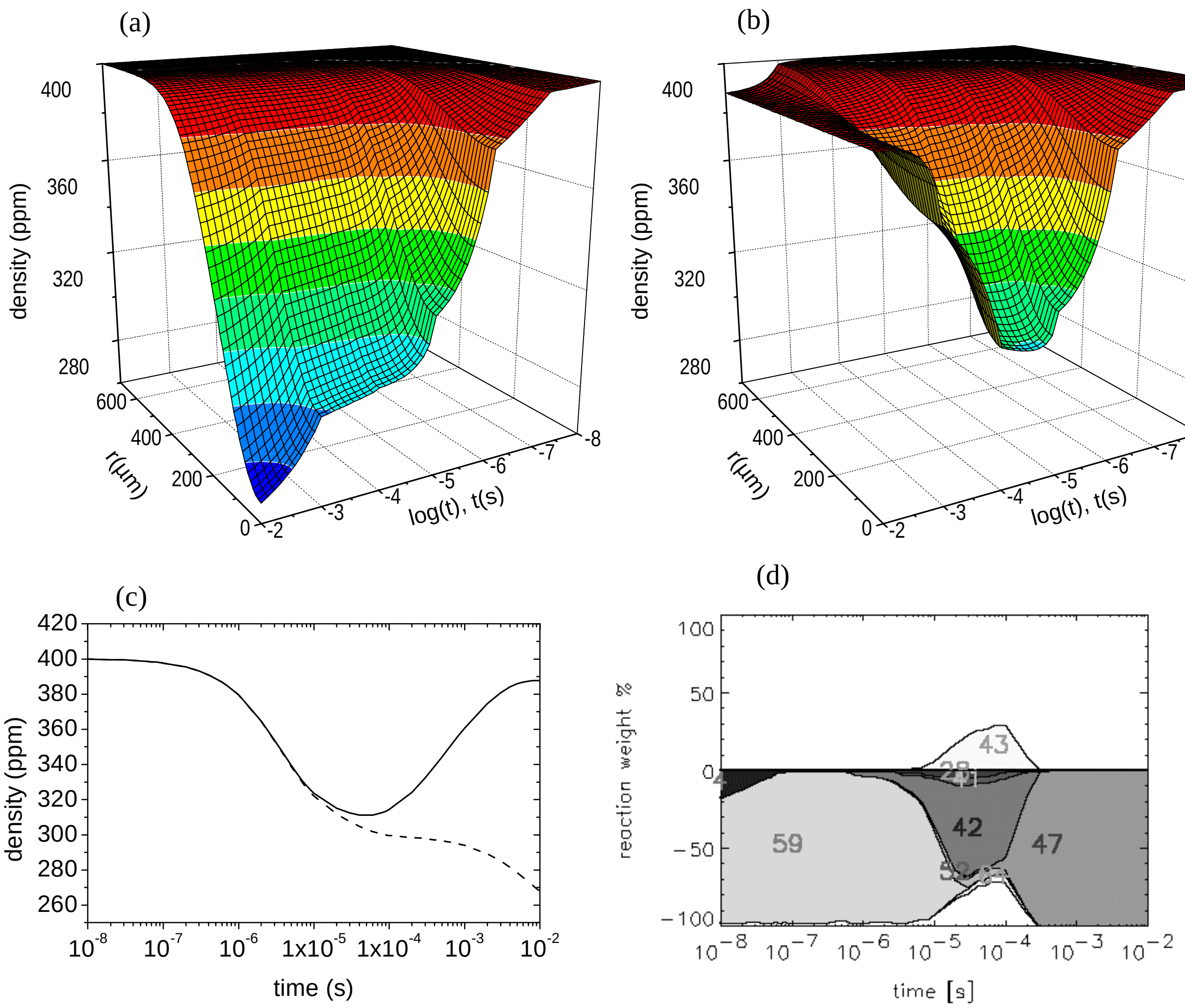

Figure 2: Radial evolution of NO at 0.25 cm from the anode (a) without the gas dynamics consideration and (b) with the gas dynamics consideration. (c) Time evolution of the NO density with (dashed curve) and without (solid curve) the gas dynamics consideration on the discharge axis and at 0.25 cm from the anode. (d) NO normalized reaction efficiency without the gaz dynamics consideration on the axis at 0.25cm from the anode. The numbers are associated to the following reactions : (4) $N_2(a'^1\Sigma_u^-)+NO \rightarrow N_2+N+O$, (28) $HO_2+NO \rightarrow NO_2+OH$, (41) $O+NO+O_2 \rightarrow NO_2+O_2$, (42)$O+NO+N_2 \rightarrow NO_2+N_2$,(43) $O+NO_2 \rightarrow NO+O_2$, (47) $O_3+NO \rightarrow O_2+NO_2$, (52) $OH+NO+N_2 \rightarrow HNO_2+N_2$, (59) $N+NO \rightarrow N_2+O$, (63) $N_2O_4+N_2 \rightarrow NO_2+N_2$, (64) $NO+NO_3 \rightarrow 2NO_2$,(67) $2NO_2+N_2 \rightarrow N_2O_4+N_2$

In order to clearly show the gas dynamics effects, two distinct simulations have been undertaken. The first one (i.e. 0D model) takes into account only the gas reactivity while the second one (based on the reactive gas dynamics model) includes in addition both the mass diffusion phenomena and the gas temperature variations.

The gas temperature on the axis at 0.25 from the anode is 320°K at t=10ns (i.e after the streamer gap crossing). The gas temperature increase is confined inside the ionised channel and extends up to r=200µm. The enhance of the temperature during the discharge phase results from the direct Joule heating and from the relaxation of electronic excitated state into thermal form. The gas temperature reaches its maximum value (330°K) on the discharge axis around 50µs. The corresponding thermal energy is then brought by the relaxation of the vibration excitation states created in the ionised channel during the discharge phase. After 50µs, the gas temperature on the axis decreases because of the thermal diffusion which also enlarges the radial gas temperature profile.

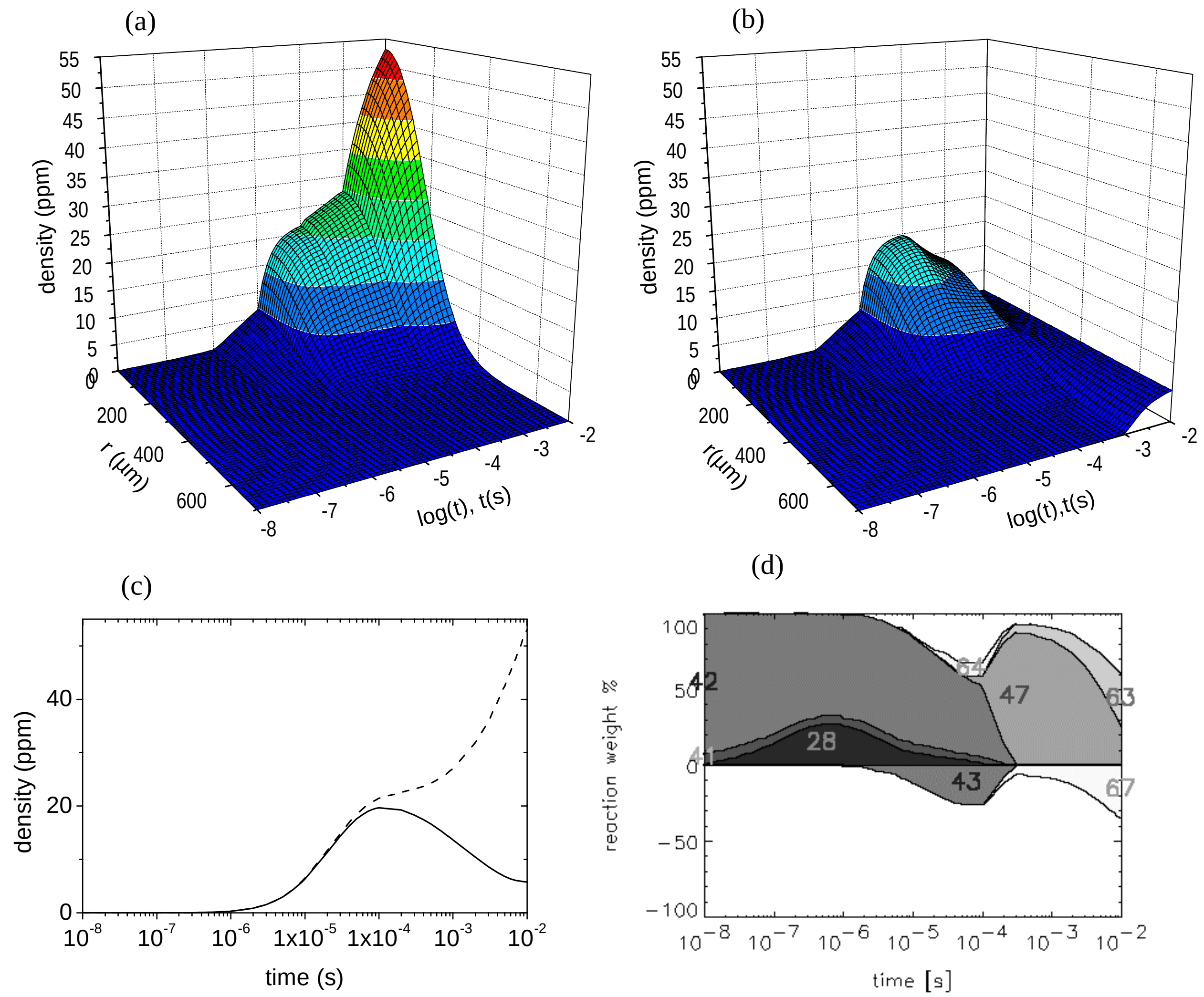

Figure 3: Radial evolution of NO_2 at 0.25 cm from the anode (a) without the gas dynamics consideration and (b) with the gas dynamics consideration. (c) Time evolution of the NO density with (dashed curve) and without (solid curve) the gas dynamics consideration on the discharge axis at 0.25 cm from the anode. (d) NO normalized reaction efficiency without the gaz dynamics consideration on the axis and at 0.25cm from the anode. The numbers are associated to the following reactions : (4) $N_2(a'^1\Sigma_u^-)+NO\rightarrow N_2+N+O$, (28) $HO_2+NO\rightarrow NO_2+OH$, (41) $O+NO+O_2\rightarrow NO_2+O_2$, (42)$O+NO+N_2\rightarrow NO_2+N_2$,(43) $O+NO_2\rightarrow NO+O_2$, (47) $O_3+NO\rightarrow O_2+NO_2$, (52) $OH+NO+N_2\rightarrow HNO_2+N_2$, (59) $N+NO\rightarrow N_2+O$, (63) $N_2O_4+N_2\rightarrow NO_2+N_2$, (64) $NO+NO_3\rightarrow 2NO_2$,(67) $2NO_2+N_2\rightarrow N_2O_4+N_2$

The diffusive mass transport and the gas temperature variations quite affect the gas evolution in the ionized channel as is shown by comparing for example figures 2a and 2b for NO and figures 3a and 3b for NO_2. However, the efficiency of the main reactions (shown in figures 2d and 3d) is rather similar under our simulation conditions with or without the gas dynamics consideration untill 10ms. The diffusion phenomena become sensitive after a delay time of 10µs as it can be observed from the comparison of the density expansion shown in figures 2a and 2b for NO or figures 3a and 3b for NO_2. In the case of NO oxide, the density evolution before 1µs is mainly governed by reaction (59) $N+NO\rightarrow N_2+O$ (see figures 2d) whose the efficiency is not altered by the gas temperature rise.

After 10µs, NO and NO_2 species progressively diffuse from the high density region to the low density region as shown in figures 2b and 3b. The expansion of these oxide and radical species inside and outside the ionized channel limits the maximum value of their concentration. For example, the density maximum reached for NO_2 is of 20ppm at 100µs with the gas dynamics consideration while it is more than 45ppm at 10ms without (see figure 3c). With the gas dynamics consideration (even if the NO density considerably increases in the ionised channel due to the diffusion phenomena), reactions (42) $O+NO+N_2 \rightarrow NO_2+N_2$ and (47) $O_3+NO \rightarrow O_2+NO_2$ are not able to locally compensate the NO_2 decay due to the diffusion transport. In fact, the densities of the main radicals (O, N, OH, H, HO_2, O_3) after 100µs become lower then 0.1ppm. Finally, the present results show (see for example figures 2b and 3b) that the densities of all the species involved in our study become homogeneous from about 10ms.

Conclusion

The present work is devoted to the analysis of the effect of the radial gas expansion on NO removal in a typical flue gas mixture initially stressed by a pulsed corona discharge.

This work emphasizes the large influence of N_4^+ ion during the discharge phase which considerably limits the concentration of N_2^+ ion but in the same time this increases the CO_2^+ and H_2O^+ ion densities by ion conversion reactions. However, the high radical N formation in the streamer head due to reaction $N_2+e \rightarrow e+2N$ limits the influence of the other radicals such as OH and H which are mainly created in the ionized channel through H_2O^+ ion recombinaison with electrons.

During the discharge phase, the comparisons between results obtained with or without the gas dynamics consideration show as espected that the gas temperature rise and the mass diffusion transport significantly affect the evolution of the neutral chemical species during the post-discharge phase. It was also shown that a delay time of about 10ms is required to have a quasi homogeneous density for all species. The corresponding densities can then be used (only after this time of about 10 ms) in a 0D chemical kinetics model in order to follow the oxide evolution for longer times .

References

[1] Non thermal plasma techniques for pollution control, edited by B.M. Penetrante, and S.E. Schultheis, Part A and B, (Springer New York 1992)
[2] A. C. Gentile and M. J. Kushner, J. Appl. Phys. 79 (8), 3877 (1996),
[3] O. Eichwald, N.A. Guntoro, M. Yousfi, M. Benhenni, J.Phys. D : Appl. Phys. 35, 439-450 (2002), N.A. Guntoro, "Modélisation de la dynamique des neutres et de la cinétique chimique dans les réacteurs plasmas de dépollution des gaz d'échappement", Ph. D. Université Paul Sabatier, (2001)
[4] O. Eichwald, M. Yousfi, A. Hennad, and M. D. Benabdessadok, J. Appl. Phys. 82 (10), 4781 (1997).
[5] B. Van Leer, J. Comput. Phys. 32, 101 (1979)
[6] Numerical recipes, Cambridge University Press, second edition (1992)
[7] N Yu Babaeva and G V Naidis, J.Phys. D : Appl. Phys. 29, 2423-2431 (1996)
[8] M. Yousfi and M.D. Benabdessadok, J. Appl. Phys. 80, 6619 (1996)
[9] J.O. Hirschfielder, F.E. Curtiss and R.B. Bird, "Molecular Theory of Gases and Liquids", (John Wiley-New York, Chapman et Hall, London, 1954)
[10] A.R. Svehla and R.S. Brokaw, NASA Lewis Research Center, Cleveland, Ohio, NASA Technical Note, NASA TN D-3327, (1966)
[11] Y.L.M Creyghton, Thesis Eindhoven, Nugi 812 (1994)

Determination of the arc spot parameters as function of the magnetic field by thermal and spectroscopic methods

D. A. Bublievsky§, A. Marotta, A. M. Essiptchouk§, and L. I. Sharakhovsky§

Instituto de Física "Gleb Wataghin", Universidade Estadual de Campinas, Unicamp, 13083-970,
Campinas, São Paulo, Brasil
§Permanent address: The Luikov Heat & Mass Transfer Institute, P. Brovki street, 15, 220072,
Minsk, Republic of Belarus

Abstract

In this work, the main arc spot parameters of copper cathode, the thermal volt-equivalent U and the current density j, have been measured as functions of the magnetic field by using thermal and spectroscopic methods. These parameters are very important for the prediction of cold electrode erosion. Experiments were carried out in a magnetically driven arc setup. We show that the thermal volt-equivalent increases linearly with magnetic field. A new, more sensitive diagnostic technique – the thermo-spectroscopic one – was developed and applied for the determination of arc spot current density. The obtained results showed a strong increase of current density for low values of magnetic field. By using the present report, a recently published erosion model has been validated. This work can be used for better calculations of cold electrode erosion.

1. Introduction

One of the most important parameters determining erosion is the arc spot heat flux density $q_0 = jU$, where j is the arc spot current density and U is the volt-equivalent of the heat flux. Usually, one measures current I and arc spot diameter d in order to obtain j. For cold electrodes, the electric arc is not stationary, and the arc spot presents a complex internal structure (see [1,2]), that makes measurements of U and j extremely difficult. We overcame these difficulties by using thermal methods for their determination, introducing the concept of effective arc spot current density. In this approach, the current density is related to its thermal effect and not to the area of the spot, as in the traditional methods of detection of erosion tracks or arc spot luminosity. Actually, by the thermal approach we measure the spot macrofusion onset, i.e., the transition point from the microerosion regime to the macroerosion one. This new type of current density definition allows a straightforward calculation of erosion electrode regimes, for the continuous and step-wise modes of arc spot motion. Further, we combined the thermal method with spectroscopic measurements of copper vapor line emission intensity, thus, improving the sensibility of the arc spot current density measurements.

2. The experimental setup

Two similar setups, described in detail elsewhere [3,4] and in a companion paper, have been used. They have cylindrical ring commercial copper electrodes, being the outer ring the investigated cathode, and axial air gas flow (no vortex motion). Current I, arc rotation velocity v and cathode surface temperature T_0 were recorded in all experiments. A broad range of currents I, axial air velocities v_a and magnetic fields B have been used: 100-1760 A, 0.2-33 ms^{-1} and 0.01-3.9 T, respectively.

For the measurement of $U(B)$, only unsteady experiments, with uncooled electrodes, were carried out, while for $j(B)$ both, unsteady and steady experiments (the latter one, with cooled electrodes) have been carried out. The unsteady installation was designed for short-term (1-2 s) experiments, while the steady one, for longer experiments (10 min or more), after which the cathode was weighed for the erosion measurement.

As all cathode ring surfaces are thermally-insulated, except the inner one, the heat flux into the inner cathode surface behaves like an infinitely long ring submitted to a given heat flux density q at its inner surface area. From the general analytical solution (see [4]) one obtains the heat flux density q into the cathode surface for unsteady experiments as:

$$q = \frac{\lambda}{a}\frac{R_2^2 - R_1^2}{2R_1}\frac{dT}{d\tau}, \qquad (1)$$

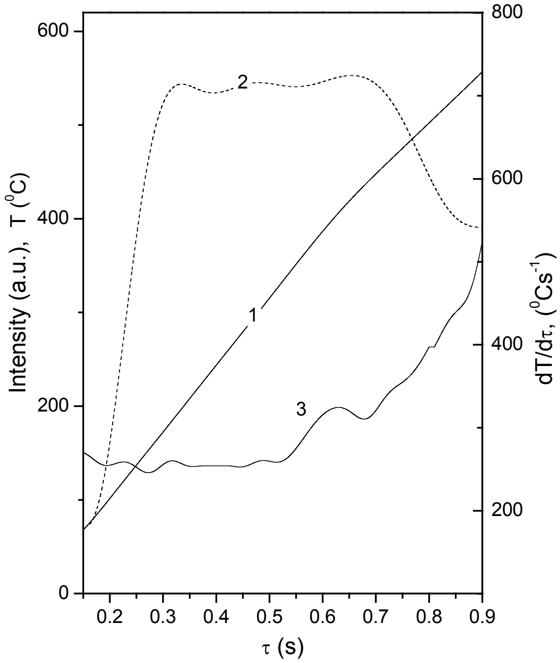

Figure 1. Typical records of cathode surface temperature T_0 (line 1), derivative $dT_0/d\tau$ (line 2) and copper vapor spectroscopic line emission intensity (line 3) versus time in an unsteady experiment.

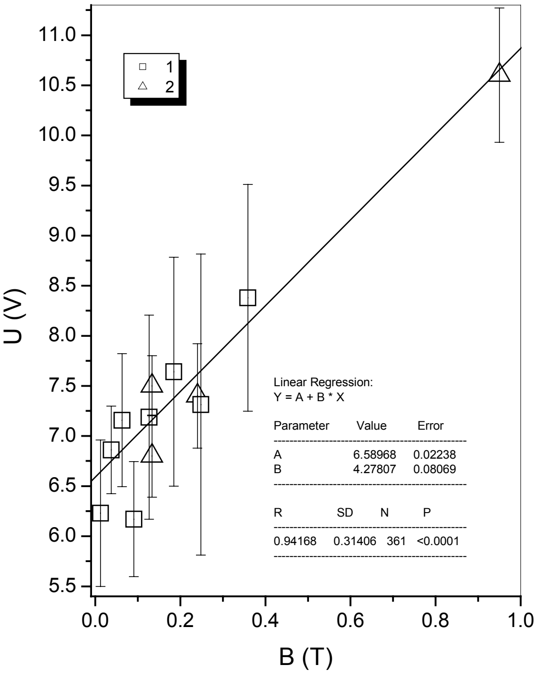

```
Linear Regression:
Y = A + B * X

Parameter      Value      Error
------------------------------------------
A            6.58968    0.02238
B            4.27807    0.08069
------------------------------------------

R          SD        N      P
------------------------------------------
0.94168    0.31406   361   <0.0001
------------------------------------------
```

Figure 2. Volt-equivalent of the arc spot heat flux *U* versus magnetic induction *B*, obtained in an unsteady thermal experiment. 1 – the present data; 2 – data from [4]; *R* – correlation coefficient, *SD* – standard deviation, *N* – number of points.

where λ and a are the cathode material thermal conductivity and thermal diffusivity, respectively, and R_1, R_2 are the inner and outer ring radius, respectively. The evolution of the cathode temperature $T(\tau)$ was measured by a cromel-alumel thermocouple, placed side-on in the cathode, at 1-2.5 mm from the internal electrode surface. A typical experimental result of $T(\tau)$ is shown in Figure 1. The heat flux density q is obtained from Figure 1, from the linear section of $T(\tau)$ (regular regime, $dT/d\tau = \text{Const}$), using equation (1).

3. The thermal volt-equivalent of the arc spot

The thermal volt-equivalent of the arc spot heat flux U can be measured by using equation $U = Q_0/I$, where Q_0 is the arc spot heat flux. The total heat flux entering the cathode Q consists of Q_0 and heat coming from the arc column, the walls, the gas, etc, by convection-radiation processes Q'. Whereas Q_0 is supplied only within the limits of the spot area, Q' depends on the total surface of the electrode. Two thermally and electrically isolated cathode rings, with given diameter $2R_1$ and different widths, b_1 and b_2 were considered. Two consecutive experiments were carried out, measuring the total Q_i fluxes into these rings. Consider $Q'_i = 2\pi R_1 b_i q'_i$, where q'_i is the convection-radiative heat flux density to the ring with width b_i that will be assumed constant over the area of both rings. We calculate q_i from (1) and obtain the total heat fluxes Q_i into these rings. Then, the arc spot heat flux Q_0 can be calculated by the formula [4]

$$Q_0 = (Q_1 b_2 - Q_2 b_1)/(b_2 - b_1), \tag{2}$$

Many other similar experimental setups can be used for measuring Q_0 and obtaining U. A plot of U experimental data versus B is shown in Figure 2. The linear fitting to points in Figure 2 leads to the relationship:

$$U = r + sB \tag{3}$$

where $r = (6.59 \pm 0.02)$ V (0.3 %) and $s = (4.28 \pm 0.08)$ V/T (2 %). The correlation coefficient obtained for the linear fitting was 0.94168.

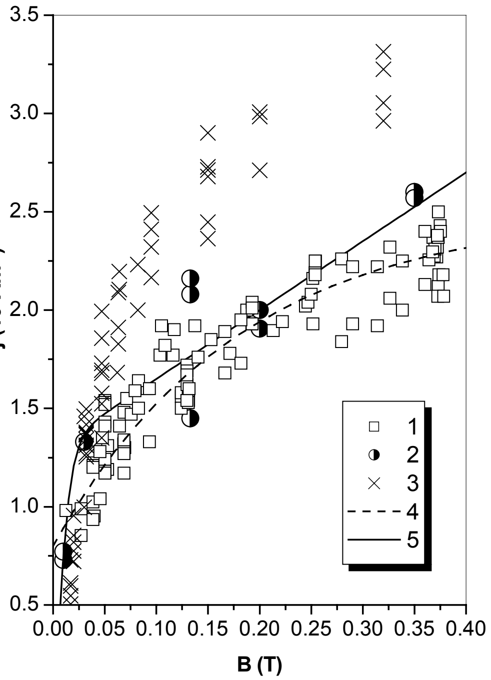

Figure 3. Arc spot apparent current density j_s versus magnetic induction B: 1- unsteady thermal data; 2 - steady thermal data; 3 - unsteady spectroscopic/ thermal data; 4 – fitting to unsteady data (6); 5 – fitting to steady data (7).

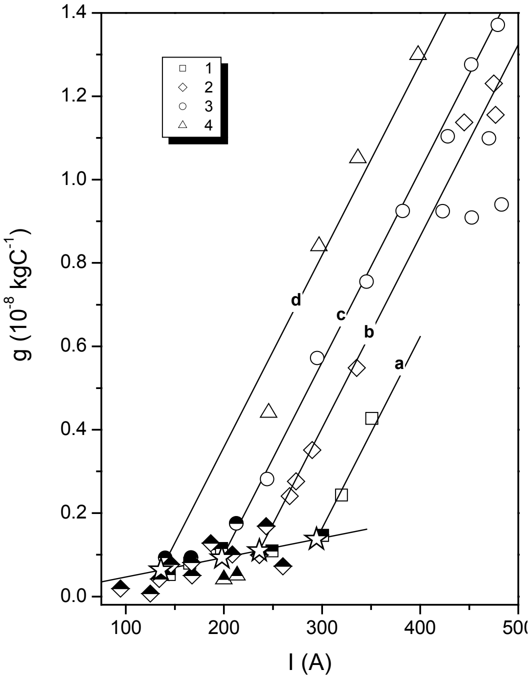

Figure 4. Typical data of specific erosion g versus current I. Points corresponding to I_{cr} (stars), were chosen for the calculation of the steady value of j_s. Lines a, b, c, d are linear approximations of macro-erosion regime: $a - B = 0.01$ T, $b - B = 0.137$ T, $c - B = 0.2$ T, $d - B = 0.35$ T.

4. The arc spot current density

We describe here a thermal method for obtaining the effective arc spot current density j. From the solution of the heat diffusion equations one can obtain τ_0, the time the spot needs to reach the melting temperature T_f [4]:

$$\tau_0 = \frac{\pi}{4a}\left[\frac{(T_f - T_0)\lambda}{q_0}\right]^2. \tag{4}$$

The onset of macroscopic scale erosion in the spot can be obtained if the spot residence time $\tau_r = \tau_0$. In the erosion model, the parameter $f = \tau_0/\tau_r$ is used to distinguish the microerosion ($f > 1$) from the macro-erosion regime ($f < 1$), with $f = 1$ corresponding to the onset of macroerosion. For the step-wise erosion model, the spots are located at a distance L one from the other and the spot residence time can be given as $\tau_r = L/v$, where v is the mean arc spot velocity (see [5]). Using equation (4), and introducing $n = L/d$, one can write for f the expression

$$f_s = \frac{\pi^{1.5} v \lambda^2 (T_f - T_0)^2}{8 a j_s^{1.5} U^2 I^{0.5}}, \tag{5}$$

where we define $j_s = jn^{2/3}$ as the new apparent step-wise arc spot current density and j, as the effective (or thermal) arc spot current density. Both, j and j_s extend the meaning of the common, or real arc spot current density (defined by the spot diameter). They average the thermal effect of the internal spot micro-structure and of the spot motion (with stops, for the case of j_s) on the electrode surface. In fact, it is very difficult to define unambiguously the real current density, due to the internal microstructure of the spot.

Figure 1 is a typical result of the unsteady experiment for measuring j. We observe that at $\tau \sim 0.55$ s the derivative $dT/d\tau$ starts to decrease. This, most probably, is due to the onset of surface fusion within the arc spot, i.e., $\tau_r = \tau_0$ ($f_s = 1$). Then, by using I, v and T_0 experimental data for such point one can calculate j_s from (5). Figure 3 shows the unsteady j_s versus B data (in crosses) and the best fitting non-linear function

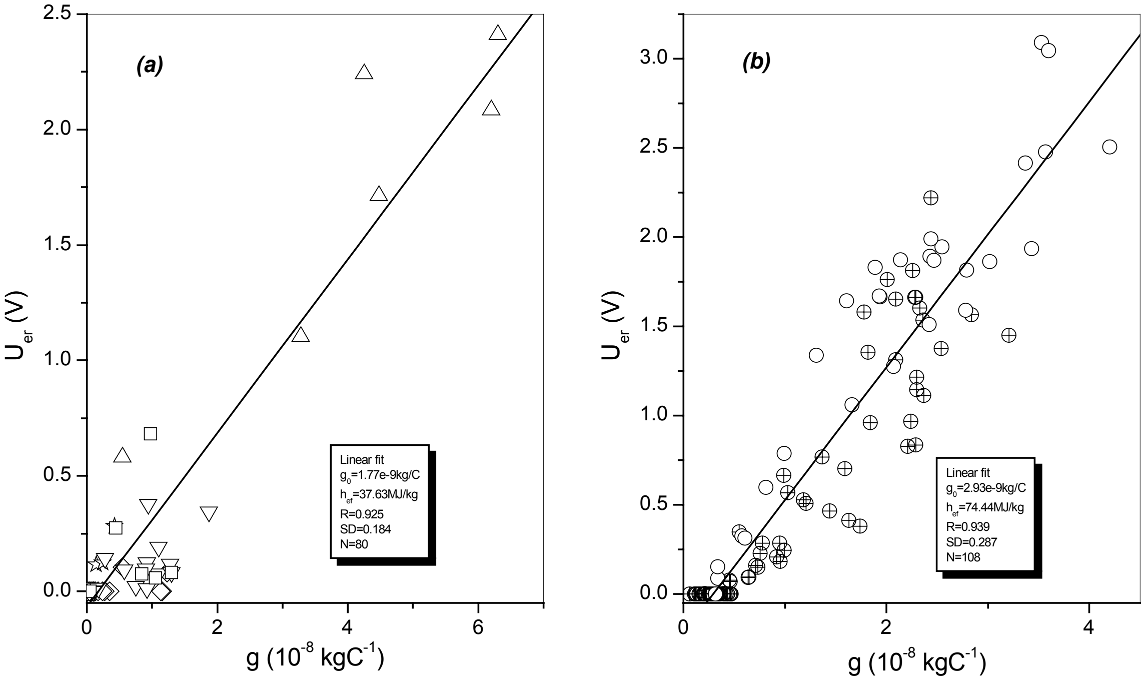

Figure 5. a) $U_{er} = UW$ versus specific erosion g for the present data; b) idem, data taken from [4]. Symbols see in Figure 6.

$$j = \left[2.5 - 1.7\exp(-B/0.18)\right] \times 10^{9}, \qquad (6)$$

with B given in T and j in Am^{-2}. These unsteady values of j correspond to clean surfaces, where the arc spot motion is almost continuous.

Another indirect method for measuring the apparent current density j_s in erosion experiments is the steady method. This provides a value of j_s for dirty surfaces, where the arc spot approximates more to a step-wise arc motion. The steady j_s can be obtained taking into account the I_{cr} values of current in plots like $g(I)$, where a sharp increase of erosion occurs (a typical plot is shown in Figure 4). Here, g is the specific erosion (kgC^{-1}). We ascribe to these points f_s = 1, allowing to calculate the steady values of j_s from (5). The mean values of j_s, obtained for I_{cr} points, taken from plots like those in Figure 4, are shown in Figure 3 with crossed rhombuses. As one can see in Figure 3, the unsteady results lie noticeably below the steady ones. The best fitting to the steady data is shown as a solid curve in Figure 3 and is given by the formula:

$$j_s = \left[1.3 - 2.8\exp(-141.3B) + 1.665\exp(-292B) + 3.5B\right] \times 10^{9}. \qquad (7)$$

Figure 3 shows results of $j(B)$, for unsteady (1 and 3) and steady (2) data. The difference between the 1 and 3 data is in the method of registration of the critical temperature T_{crit} for spot fusion onset. In 1, T_{crit} is taken at the temperature when the derivative dT/dt of the thermocouple straight line starts to decrease, and in 3, by observing a sudden increase of the copper vapor spectroscopic line emission intensity (wavelength 5218 Å) (see Figure 1). It was shown in [7], that the copper spectral line intensity, radiated by the arc from near cathode region, is proportional to the erosion rate. It was assumed that the fusion onset corresponds to the onset of intense evaporation of electrode material. The steady data can be considered as the most relevant for erosion calculations. One can see that spectroscopic data 3 fall higher even than steady data 2. This might be the effect of the decomposition of the unstable oxide Cu_2O at 250° C [8]: $Cu_2O = CuO+Cu$, giving rise to Cu emission from plasma at a lower temperature T_{crit} than the copper cathode begins to melt. To check this hypothesis it is necessary to make experiments with no oxygen in the plasma gas.

5. Validation of the results

For the validation of our data on j and U and testing its applicability to practical calculations of erosion we carried out a comparison between the theoretically calculated and the measured experimental erosion data. We used the continuous model taken from [4] and the relationships (3), (7) for U and j_s, respectively. From [4] we have the following expression for the specific erosion:

$$g = g_0 + \frac{UW}{h_{ef}}, \tag{8}$$

where g_0 is the micro-erosion term, h_{ef} is the effective erosion enthalpy (in $\mathrm{Jkg^{-1}}$) and $W(f)$ is the nondimensional erosion energy (which is a function of the nondimensional parameter f). For the continuous model, we have [4]

$$W \approx 1 - f\left(\frac{7.13}{2.457 + f} + \frac{0.442}{0.04 + f} - 1.477\right). \tag{9}$$

From (8), we note that the volt-equivalent of the erosion heat $U_{er} = UW$ is a linear function of g: $U_{er} = (g - g_0)h_{ef}$. By plotting U_{er}, calculated from experimental data versus experimentally measured g, and making a linear fit, one obtains the erosion parameters g_0 and h_{ef}. Figure 5 shows this plot for both the present data (80 points, Figure 5a) and data taken from [4] (108 points, Figure 5b). From the straight-line fits we obtain $g_0 = 1.8 \times 10^{-9}$ $\mathrm{kgC^{-1}}$ and $h_{ef} = 38$ $\mathrm{MJkg^{-1}}$ for the present data and $g_0 = 2.9 \times 10^{-9}$ $\mathrm{kgC^{-1}}$ and $h_{ef} = 74$ $\mathrm{MJkg^{-1}}$ for the data taken from [4]. The different obtained values might be attributed to the type of commercial used copper and to the different methodology for measuring g. Figure 6 shows the theoretical erosion g_{th} versus the experimental g_{ex}. One can see a good agreement between g_{th} and g_{ex}. The coefficients of the straight line in $g_{th} = f(g_{ex})$ are $b = 0.99996$, which is close to 1, and $a = 9.7 \times 10^{-13}$, which is close to zero for a correlation coefficient $R = 0.935$.

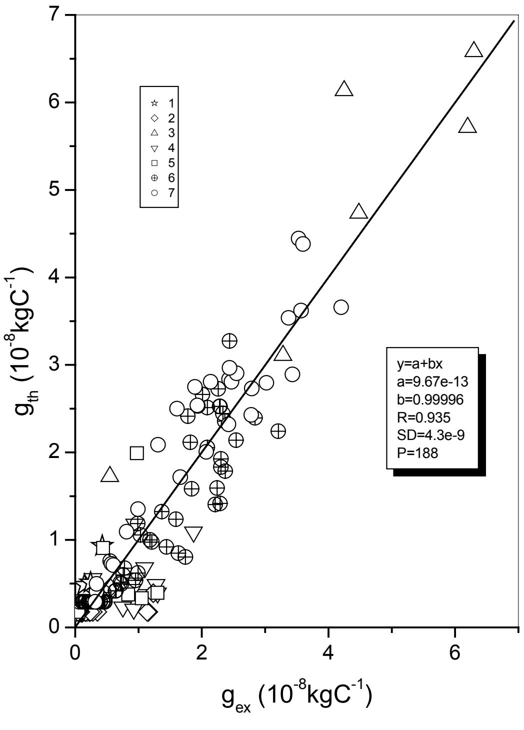

Figure 6. Comparison between calculated erosion g_{th} and experimental erosion g_{ex}. 1 - $B = 0.01$ T; 2 – $B = 0.133$ T; 3,4 – $B = 0.2$ T (see symbols and caption of Figure 4 for details); 5 – $B = 0.35$ T; 6,7 – points from [4] for $B = 0.03$ T, and randomly distributed B within $0.133 < B < 0.24$ T, respectively.

6. Conclusion

In this report, functions $U(B)$ and $j(B)$ for copper cathode in air have been obtained by thermal methods. It has been shown that U grows linearly with B and j, nonlinearly. Difference in $j(B)$, obtained by thermal and spectral methods, we explain by the decomposition of the unstable copper oxide film on the electrode surface. We have also shown good agreement between the erosion model and experimental results, enabling one to predict cold cathode erosion with reasonable accuracy.

Acknowledgments

The authors gratefully acknowledge Prof. R. A. Clemente for valuable help in proof reading the manuscript and Mr. A. A. B. do Prado for his technical assistance. The work was supported by CNPq, FAPESP and FINEP of Brazil.

References

[1] V.I. Rakhovskii, IEEE Transactions on Plasma Science, **PS-4**, 2 (1976).

[2] P. Siemroth, T. Schulke, and T. Witke, IEEE Transactions on Plasma Science, **23**, 6 (1995).

[3] A.M. Essiptchouk, L.I. Sharakhovsky, and A. Marotta, J. of Phys. D: Appl. Phys., **33**

(2000).

[4] A. Marotta and L.I. Sharakhovsky, IEEE Transactions on Plasma Science, **25** (1997).

[5] A. Marotta and L. I. Sharakhovsky, “Application of Heat Diffusion Theory to Cold Electrode Erosion for Nonstationary Arc Spots”, *in collection* “*Thermal Plasma Torches and Technologies, vol. 1: Plasma Torches, Basic Studies and Design*”, Cambridge International Science Publishing (2000).

[6] J. J. Kiselev, and V. K. Pogora, J. of Eng. Phys., **53**, 2 (1987) in Russian.

[7] J-L. Meunier and N. Desaulniers-Soucy – J. Phys. D: Appl. Phys. **27** (1994).

[8] A.E. Guile and A.H. Hitchcock - J. Phys. D: Appl. Phys. **7** (1974).

Cold cathode erosion in a magnetically driven arc as function of current, velocity and electrode surface temperature.

A. M. Essiptchouk[§], A. Marotta, and L. I. Sharakhovsky[§]

Instituto de Física "Gleb Wataghin", Universidade Estadual de Campinas,Unicamp, 13083-970,
Campinas, São Paulo, Brasil
[§]*Permanent address: The Luikov Heat & Mass Transfer Institute, P. Brovki street, 15, 220072,*
Minsk, Republic of Belarus

Abstract

A study of copper cathode erosion is carried out in this report using a magnetically driven arc setup, as function of arc current, arc velocity and electrode surface temperature. The experiments showed the presence of two different erosion regimes: a microerosion and a macroerosion one. The first occurs for low currents (or low electrode surface temperatures), with erosion slowly rising with arc current, and the second, for high currents, with erosion suddenly increasing at a certain critical point. We show that the critical current is a linearly decreasing function of the applied magnetic field. A critical temperature of about 500-600 K was found for magnetic fields in the range 0.01-0.35 T. The report shows that low velocities or low magnetic fields can decrease erosion, but high ones can increase it, contrary to what was expected. We also show that erosion experimental data can be represented as an exponential function of the time for the electrode surface to reach the fusion temperature. A reasonable agreement to predictions of a previously published erosion model is obtained.

1. Introduction

Many researchers investigated the influence of current on erosion and empirical power formulas of the type $g \propto I^a$ have been proposed, with the exponent a changing from 2.24 in [1] to 4.5 in [2], depending on electrode surface conditions. In [3], an attempt of analysis of the erosion dependence on current was carried out for copper cathode. Guile et al. [4] were the first to suggest the electrode surface temperature as the main parameter involved in cold electrode erosion. They found that the process of electrode substrate fusion plays a dominant role in copper erosion. Usually, for decreasing electrode erosion, a magnetic field is used for rotating the arc [5]. However, at high magnetic fields erosion increases, as shown in this report. So, there is a range of magnetic fields for which erosion is minimum. In a recently published paper [6], a model has been proposed for cold electrode erosion. In this model, the arc current I, the arc spot velocity v and the electrode surface temperature T_0, are the main parameters determining erosion. The study of the influence of these parameters on copper cathode erosion behavior is the main goal of this report. By measuring cathode erosion in a magnetically driven arc, our results confirm the importance given by Guile et al. to the electrode surface temperature.

Many authors have shown that the arc spot in a cold cathode is composed of many, high current density (10^{10}-10^{12} Am^{-2}) micro-spots (see, e.g., [2,7] and references therein). Rakhovsky [2] observed the existence of two erosion regimes, one for low currents and low temperatures, with the micro-spots leaving no visible erosion tracks on the electrode surface. The second, for high currents and high temperatures, with overlapping thermal fields of the micro-spots. This erosion regime leaves strong melted areas on the electrode surface, easily identified visually. These two regimes confirm Rakhovsky's observations. We call these regimes as micro- and macroerosion regimes, respectively.

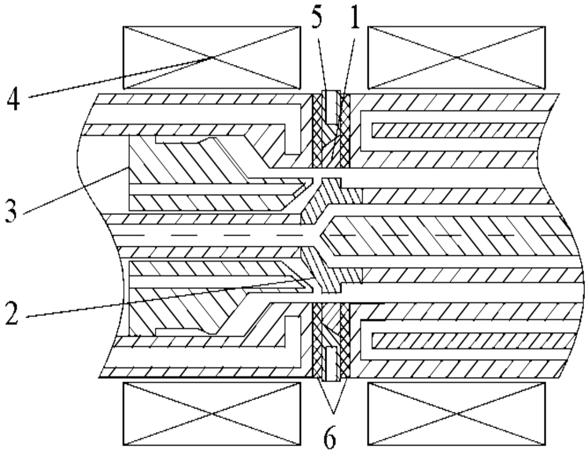

Figure 1. The diagram of the experimental setup. 1 - the investigated cathode; 2 - the anode; 3 - the auxiliary cathode for arc ignition; 4 - solenoid; 5 - water cooling jacket; 6 - heat- and electro-insulating spacers.

2. The experimental setup

A coaxial experimental setup, with a magnetically driven arc, was used for the cathode erosion measurements (see Figure 1). The system was equipped with water-cooled commercial copper ring electrodes placed in an axial magnetic field. The outer electrode was the investigated cathode, with $2R_1 = 40$ mm inner diameter and 5 mm width. It was isolated by heat- and electro- insulating spacers and placed inside a water-cooled ring jacket, embracing the cathode ring insert at its outer diameter. Most of the experiments were carried out with a cathode ring thickness of 10 mm (outer ring diameter of $2R_2 = 60$ mm). For safety purposes, the water-cooling flow rate was maintained constant. In order to increase the cathode surface temperature, some experiments were carried out with a different cathode ring of $2R_2 = 120$ mm. After 10 min of arc burning, the cathode ring insert was extracted for weighing and obtaining the average mass erosion rate G (kgs^{-1}). Compressed air, without vortex flow, was used as the working gas. Current I, rotational arc velocity v, cathode surface temperature T_0, and the integral heat flux Q supplied to the inner ring cathode surface were recorded in the experiments.

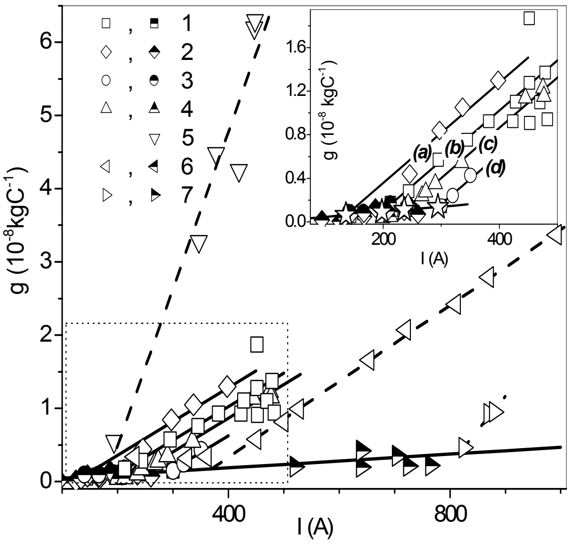

Figure 2. Specific erosion g of copper cathode versus current I: 1-4 - same points shown in Figure 3; 5 - idem, but cathode with inner diameter $2R_1 = 40$ mm, outer diameter $2R_2 = 120$ mm, magnetic field of 0.2 T; 6 - points taken from [9], cathode with inner diameter of $2R_1 = 50$ mm, magnetic field of 0.133 T; 7 - idem, cathode with inner diameter of 90 mm and magnetic field of 0.03 T. Lines a, b, c, d: linear approximations to points 1-4. The half-painted points relate to the micro-erosion regime. Stars—intersections of lines a,b,c,d and microerosion fit line.

Four values of magnetic fields were used for the study of arc current influence: $B = 0.01$; 0.02; 0.137 and 0.35 T. The arc current range was 95-480 A. The axial gas velocity in the interelectrode gap was 7.6 ms^{-1}. For the arc velocity influence study, the arc current was maintained constant at 290 A and the arc velocity varied from 6 to 320 ms^{-1} via variation of the magnetic field from 0.005 to 0.417 T.

The arc velocity v was obtained by analyzing the fast Fourier transform of the voltage induced in a magnetic probe, made up by the single-loop thermocouple wires, used for measuring the cathode surface temperature, and placed side-on in the cathode at 1-2.5 mm from the internal electrode surface. As shown in [5], the rotational arc velocity v in magnetically driven arcs can be expressed by the empirical formula (in SI units):

$$v = 78 I^{4/9} B^{0.6} \rho_0^{-8/9} \varphi^{-1/3} \tag{1}$$

where ρ_0 is the free stream gas density, $\varphi = (1 + v_a)^{-1} + v_a$ and v_a is the axial gas velocity in the interelectrode gap. Thus, for a given gas and constant current, v depends only on B and v_a.

As both lateral plane surfaces of the cathode ring are insulated, the thermal flux behaves similarly to an infinitely long hollow cylinder under a given heat flux density q at its inner surface. Then, the cathode surface temperature T_0 at the radius R_1 can be calculated from measurements made by a thermocouple $T(r)$ by the formula (see [6] and [8]):

$$T_0 = T(R_1) = T(r) + (qR_1/\lambda)\ln(r/R_1),$$

where $q = Q/(2\pi R_1 h)$, h is the electrode width, R_1 is the inner cathode radius, and λ is the cathode material thermal conductivity.

3. Results and discussion

Figure 2 shows data for $g(I)$, where g (kgC^{-1}) is the specific erosion. Different experimental setups and magnetic fields were used (see details in the figure caption). In the inset are shown results only for the setup described above (inner cathode diameter $2R_1 = 40$ mm). We observe clearly a sudden increase of erosion at a critical current value I_{cr}. This I_{cr} divides the plot in two parts, one with slowly increasing erosion (called micro-erosion regime) and the other one (called macro-erosion regime), with a fast increase of erosion. From

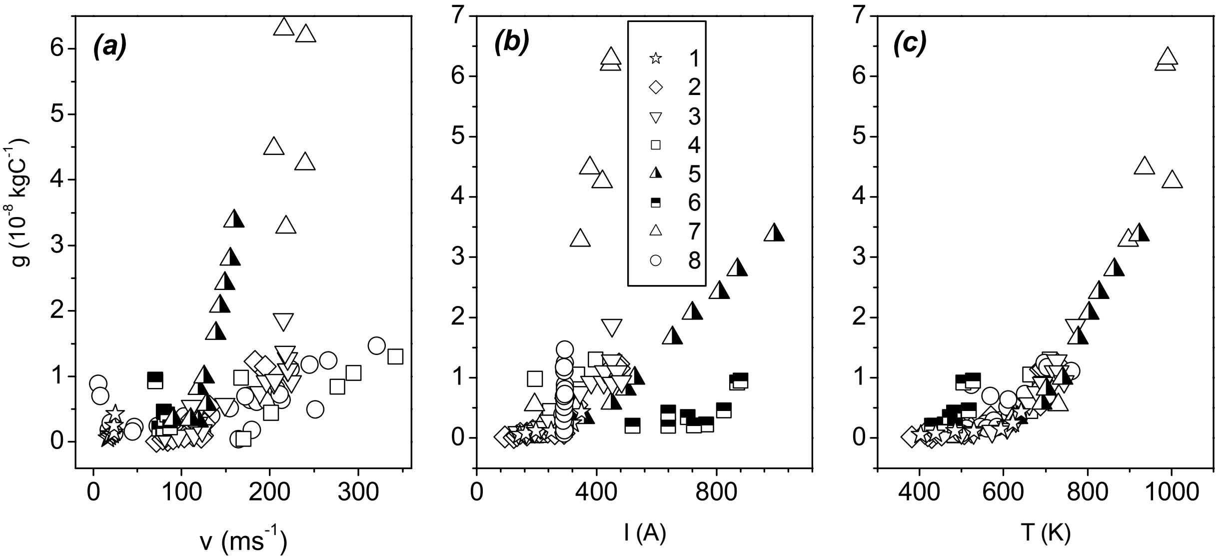

Figure 3. a, b, c - Specific mass erosion g versus arc velocity v, arc current I and electrode surface temperature T_0, respectively. 1-4 experimental points for 40 mm cathode inner diameter and 10 mm cooled wall thickness: 1- B = 0.01 T, 2- B = 0.137 T, 3- B = 0.2 T and 4- B = 0.35 T; 5 - experimental points, taken from [9] for 50mm cathode inner diameter, B = 0.133 T; 6 - experimental points taken from [9] for 90mm cathode inner diameter, B = 0.03 T; 7 - the same as points 3, but for 40 mm cooled wall thickness; 8 - points obtained at constant current of 290 A and magnetic field changing from 0.005 to 0.417 T.

Figure 2 we see that $I_{cr} \sim$ 300-350 A for cathodes with 40-50 mm diameter, and $I_{cr} \sim$ 800 A for cathodes with 90 mm. We fitted linear functions $g(I)$ for each B, for the micro- and macro-erosion points. It is possible to show that the critical current values I_{cr} and the critical erosion values g_{cr} are decreasing linear functions of the magnetic field value B. Figure 2 shows that deterioration in the water cooling of the cathode inner surface, due to a thicker cooling wall, leads to erosion changing from micro- to macro-erosion with a lower critical current. However, the slope dg/dI of the macro-erosion regime is higher when cooling is less efficient (compare points 5 in Figure 2 with points 1-4).

Figures 3. a, b, c present a comparison between the specific copper cathode erosion g as functions of v, I and T_0, respectively. We observe that, while $g(T_0)$ shows an unambiguous erosion behavior (following almost a single curve), the other plots for $g(v)$ and $g(I)$ show a high spread of data, confirming Guile et al. observation that temperature is the most relevant parameter in cold cathode erosion. In the case of Figure 1c, $T_{0cr} \sim$ 600 K for cathodes with 40-50 mm diameter and $T_{0cr} \sim$ 500 K for cathodes with 90 mm diameter. Such critical temperatures are almost independent of the applied magnetic field.

It can be expected that thermal processes are the principal erosion mechanisms for both the macro- and micro-erosion regimes. A evidence of this is shown in Figure 4, where g is potted as function of $(1 - \theta)^2$. Here, $\theta = T_0/T_f$, where T_f = 1356 K is the fusion temperature. Parameter $(1 - \theta)^2$ is a function of τ_0, the time necessary for the electrode surface to reach the melting temperature T_f. As shown in [6],

$$\tau_0 = \frac{\pi}{4a}\left[\frac{\lambda(T_f - T_0)}{q_0}\right]^2 = k\theta^2,$$

where $k = (\pi\lambda^2 T_f^2)/(4aq_0^2)$ and a is the thermal diffusivity of the electrode material, and $q_0 = jU$ is the arc spot heat flux density. Present micro- and macro-erosion data (points 1) and data from [9] (points 2) can be fitted to two different straight lines. This allows to ascribe the same thermal erosion mechanism for both regimes. The different angular coefficients for g versus $(1 - \theta)^2$ might be related to different heat resistances of the electrode materials and also to different procedures applied in measuring the erosion rate. Extrapolating the linear approximations in Figure 4, it is possible to obtain the maximum erosion which can be expected at the copper fusion temperature T_f (i.e., for $(1 - \theta)^2 = 0$): $g_{\max} = 1.4 \times 10^{-7}$ kgC^{-1} and 0.5×10^{-7} kgC^{-1} for points 1 and 2, respectively. We compare these values with the case of vacuum pulsed discharges with stationary arc spots [2]: $g_{\max} = 1.2 \times 10^{-7}$ kgC^{-1}. It is also possible to show that a linear fit can represent the best behavior of $T_0(B)$:

$$T_0 = 545 + 383B\,, \tag{2}$$

Figure 5 shows $g(v)$ for the present data (points 1) and for other authors' data [10, 11] (see figure caption for details). As shown, there is a range of optimum arc spot velocities (between 30 to 150 ms^{-1}) for minimum electrode erosion: below $v = 30\ \mathrm{ms}^{-1}$ erosion decreases with increasing v and above $v = 150\ \mathrm{ms}^{-1}$ erosion increases. For our data the minimum erosion occurs for $0.01 < B < 0.13$ T. In order to obtain the theoretical curve $g = f(v)$ we used eq. (1) for $v(B)$. As shown in [6], g is given by the equation

$$g = g_0 + \frac{UW}{h_{ef}} \tag{3}$$

where g_0 is the minimum erosion, here taken as constant, $W(f)$ is the non-dimensional erosion energy, given by the approximated expression [6]

$$W \approx W' = 1 - f\left(\frac{7.13}{2.475 + f} + \frac{0.442}{0.04 + f} - 1.477\right), \tag{4}$$

h_{ef} is the effective erosion enthalpy and f, a non-dimensional parameter characterizing the fusion zone extent in the arc spot (or the residence time), is given by the formula [6]

$$f = \frac{\pi^{1.5} v \lambda^2 (T_f - T_0)^2}{8 a j^{1.5} U^2 I^{0.5}}. \tag{5}$$

We have taken for copper $T_f = 1356$ K, the mean values (at $T = 700$ K) $\lambda = 377\ \mathrm{Wm^{-1}K^{-1}}$ and $a = 10^{-4}\ \mathrm{m^2s^{-1}}$. From the present experimental setup, we obtained the minimal erosion rate $g_0 = 2.1 \times 10^{-9}\ \mathrm{kgC^{-1}}$ and the effective enthalpy $h_{ef} = 36\ \mathrm{MJkg^{-1}}$. These values differ somewhat from values obtained in [9] ($g_0 = 3 \times 10^{-9}\ \mathrm{kgC^{-1}}$ and $h_{ef} = 66\ \mathrm{MJkg^{-1}}$), where a different copper may have been used. For calculating f, we have to obtain $U(B)$ and $j(B)$. We used the empirical dependences

$$U = 6.6 + 4.3B \tag{6}$$

and

$$j = 2.5 - 1.7\exp(-B/0.18) \times 10^9 \tag{7}$$

taken from a companion paper [13]. Using formula for $T_0(v)$ and all the parameters as functions of v, we calculated the central theoretical curve $g = f(v)$ and the two boundary curves for $T_{\max} = T_0$ plus minus 45 K. These three theoretical curves of $g = f(v)$ are shown in Figure 5. A quite reasonable agreement between theoretical calculations and the experiment is evident.

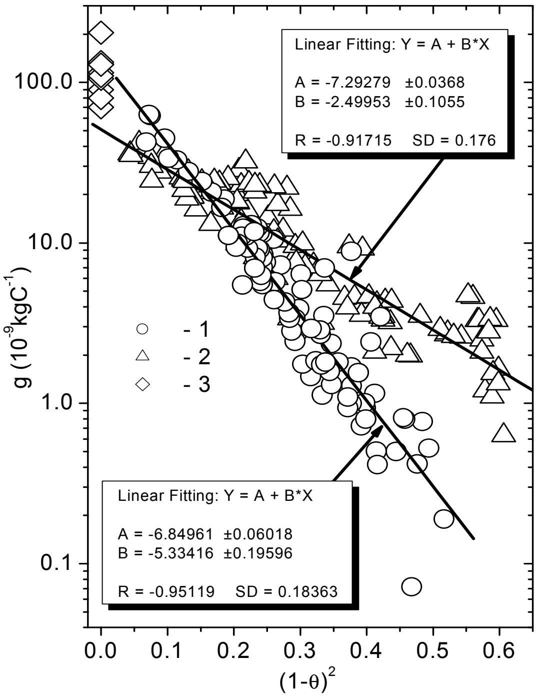

Figure 4. Specific mass erosion g versus $(1 - \theta)^2$, where $\theta = T_0/T_f$, temperatures in K. 1 - the present data; 2 - data taken from [9]; 3 - data for pulsed discharge in vacuum taken from [2]. R – correlation coefficient: SD – standard deviation.

4. Conclusion

This report concerns the study of cold cathode erosion of a magnetically driven arc in a coaxial setup as function of the operating arc parameters, current, cathode surface temperature and velocity. The erosion rate clearly shows the presence of two erosion regimes, one for low parameter values and the other for high ones. For low currents and temperatures there is little dependence of erosion from these parameters. Then, at certain critical parameter values a sudden increase of erosion occurs. We found that the critical temperature is about 500-600 K for magnetic fields in the range of 0.01-0.35 T. These two erosion regimes are called as micro- and macro-erosion regimes, respectively. The critical current and erosion values are decreasing linear functions of the magnetic field. Confirming Guile et al. observations, we also show that temperature is the most relevant parameter in cold cathode erosion, as almost a single curve is obtained for erosion as function of temperature, independently of magnetic field and for different experimental setups. We also found that we can fit a single straight line to experimental points of erosion versus the time for the surface under the arc spot to reach the fusion temperature $(1 - T_0/T_f)^2$, for both micro- and macro-erosion points. This confirms that thermal processes are the principal erosion mechanisms for both regimes. Investigating erosion versus arc velocity, we found that the range of optimum arc spot velocities is $30 < v < 150$ ms^{-1} or $0.01 < B < 0.13$ T for minimum electrode erosion. Below this range, erosion decreases with increasing velocity and above it erosion increases. This behavior can be explained as a consequence of increasing electrode wall temperature versus magnetic field due to two different factors: enhanced heat transfer from the arc to the electrode wall and the ascending functions of the arc spot thermal volt-equivalent *U* and arc spot current density *j* on magnetic field. A good qualitative agreement was obtained between experimental results and the theoretical predictions using the present and other authors' experimental data.

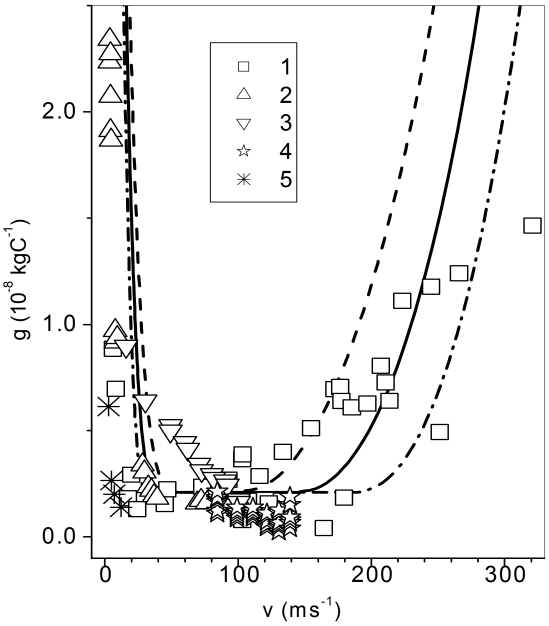

Figure 5. Specific mass erosion rate g_0 versus velocity of the arc *v*. 1- author's data for air; 2- data taken from [10] for argon-nitrogen mixture; 3- data taken from [10] for pure nitrogen; 4- data taken from [11] for air; 5- data taken from [12], obtained with vortex air heater (gas dynamic vortex displacement of spot without magnetic field). Lines: theoretical prediction of erosion rate. Solid line: linear approximation of the cathode surface temperature T_0 as function of *B*. Dashed line: idem for $T_{max} = T_0 + 45$ K. Dotted line: idem for $T_{min} = T_0 - 45$ K.

Acknowledgements

The authors gratefully acknowledge Mr. A. A. B. do Prado for the technical assistance. The work was supported by CNPq, FAPESP and FINEP of Brazil.

References

[1] M.G. Fey and J. McDonald, Proc. of AIChE Plasma Chemical Processing Symposium (1976).
[2] V.I. Rakhovskii, IEEE Transactions on Plasma Science, **PS-4**, 2 (1976).
[3] A.E. Guile and B. Jüttner, IEE Transactions on Plasma Science, **8**, 3 (1980).
[4] A.E. Guile, A.H. Hitchcock, K. Dimoff, and A.K. Vijh, J. of Phys. D: Appl. Phys., **15** (1982).
[5] A.M. Essiptchouk, L.I. Sharakhovsky, and A. Marotta, J. of Phys. D: Appl. Phys., **33** (2000).
[6] A. Marotta and L.I. Sharakhovsky, IEEE Transactions on Plasma Science, **25** (1997).
[7] B. Jüttner, J. of Phys. D: Appl. Phys., **34** (2001).
[8] E.P. Trofimov, Inzhenerno-Fizicheskij Journal, **3**, 10 (1960). in Russian.
[9] L.I. Sharakhovsky, A. Marotta and V.N. Borisyuk, J. of Phys. D: Appl. Phys., **30** (1997).
[10] R.N. Szente, R.J. Munz, and M.G. Drouet, J. of Phys. D: Appl. Phys., **21** (1988).
[11] J.E. Harry, J. of Appl. Phys., **40**, 1 (1969).
[12] A.S. Anshakov, A.N. Timoshevsky, and E.K. Urbakh, Izvestiya of Siberian Department of USSR Acad. of Sci., Techn. Sci., **2**, 7 (1988). in Russian.
[13] A. M. Essiptchouk, A. Marotta, L. I. Sharakhovsky, and D. A. Bublievsky, see these Proceedings.

Comparison of spectroscopic and enthalpy probe measurements in H_2O-Ar thermal plasma jet

V. Sember[1], T. Kavka[1], V. Kopecký[1], M. Hrabovský[1]

[1] *Department of Thermal Plasma, Institute of Plasma Physics AS CR, Prague, Czech Republic*

Abstract

Optical emission spectroscopy (OES) and enthalpy probe (EP) have been applied to study an atmospheric pressure H_2O-Ar dc arc thermal plasma jet. Differences between temperatures and composition obtained by respectively OES and EP measurements are explained mainly by the mechanism of air entrainment. The effect of departures from LTE and temperature and space fluctuations is reduced by choosing a suitable method for evaluation of spectroscopic data.

1. Introduction

In thermal plasma spraying, heat and momentum transfer between flowing plasma and injected particles is the crucial parameter that influences properties of the sprayed coating. It is therefore of great importance to know properties of the plasma jet, such as temperature, velocity and composition, along the whole possible path of treated particles. In atmospheric thermal plasma jets, this is usually impossible to measure by a single diagnostic technique because of great change in parameters and entrainment of cold gas.

In investigation of turbulent plasma flows of high intensity arcs, OES and EP are the most widely used diagnostic techniques, the main advantage of which is their simplicity and robustness. OES gives more accurate results in laminar flows for temperatures above 10 000 K, difficulties may, however, occur in the jet's fringes because of departure of excited and ionized species from their equilibrium populations. EP is said to be more reliable in colder and turbulent regions, below 10 000 K, although the temperature limit can be significantly lower in the case of high enthalpy plasma flows. While OES is sensitive only to high temperature species, EP gives average values of the enthalpy and temperature of hot and cold entrained gases [1].

Besides the departures from LTE and entrainment of cold gas, the interpretation of both OES and EP measurements can be complicated by fluctuations and instabilities of the plasma flow, which in the case of the arc torches is typically caused by anode attachment phenomena. The data measured by standard OES and EP are time averaged and the derivation of true mean values of the quantities such as temperature is not always straightforward. This can be demonstrated, for instance, for the case of absolute emission coefficient method: the direct Abel inversion of measured lateral intensity profiles $I(r)$ does not necessary give true mean radial profiles of emission coefficient $\varepsilon(r)$ and the true mean temperature $T(r)$ ($\varepsilon(r) = K(T)\cdot\exp(-E_{exc}/kT)$) is not simply given by the mean emission coefficient [2]. A detailed theoretical study of the influence of both space and temperature fluctuations on the determination of temperature with the method of absolute emission coefficient has been reported in [3].

Although interpretation of EP data seems to be more trivial and, in contrast to OES, the measured data represent the local values, there are a few studies suggesting that in jets with fluctuating temperature and flow regime (pockets of hot and cold gas) EP may suffer from the same shortcoming. Simple theoretical reasoning in [4], for instance, shows that the manner in which EP averages temperatures may give rise to large deviations from the true mean.

In this paper we report on OES and EP measurements in H_2O-Ar dc arc thermal plasma jet. All the measurements are time averaged and no special data treatment is undertaken to deal with the jet fluctuations. The possible error in evaluated temperatures and composition is discussed at the end of the article.

2. Plasma Source

The hybrid H_2O-Ar plasma torch is based on the water dc arc plasma torch, in which the arc is stabilized by the vortex of water injected tangentially into the arc chamber. In the hybrid torch the arc chamber is divided into short cathode part, where the arc is stabilized by tangential argon flow, and the longer part similar to the water torch. This arrangement not only provides additional stabilization of the cathode region and protection of the cathode tip, but also offers the possibility of controlling plasma jet characteristics in significantly wider range than that of pure gas or liquid stabilized torches [5, 6]. In contrast to the gas torches, the arc is attached to the external water-cooled rotating disc anode a few mm downstream of the torch exit nozzle. The position of the attachment changes quasi-periodically due to the restrike mode, causing the arc voltage to fluctuate within the range of tens of volts. In addition, an anode jet forms at the place of the arc attachment and its interaction with the main plasma jet, approximately 20 mm downstream of the nozzle, causes a significant acceleration of the air entrainment and transition of the main plasma jet from a quasi-laminar to a fully turbulent flow regime [7].

Typical parameters of the torch are: arc current of 150-500 A, voltage of 160-270 V, and argon flow rate of 12-28 slm. The volume percentage of argon in the plasma flow at the torch exit depends not only on the argon flow rate, but also on the arc current as the evaporation rate of stabilizing water increases with an input power. The volume percentage of argon can thus vary approximately from 20 to 80%. The centreline plasma flow velocity at the torch exit, increasing with both current and argon flow rate, ranges approximately from 1500 m/s (150 A, 15 slm Ar) to 6000 m/s (500 A, 28 slm Ar). The exit temperature is almost independent of argon flow rate [6, 9] and varies between 14 000 and 22 000 K.

3. Diagnostics

EP measurements were performed with an enthalpy probe system Tekna equipped with a quadruple mass spectrometer Balzers QMS 200. The outer and inner diameters of the probe tip are respectively 4.76 and 1.27 mm. Details of the Tekna system, measurement and data evaluation can be found in [8] and [9]. Because of more complex plasma than that in common gas torches, our EP measurements were restrained by two circumstances. First, extremely high enthalpy of the plasma flow restricted our measurements to positions with the temperature lower than 6000 K. Second, to prevent condensation of water inside the Tekna system, a freezer had to be used and thus the content of hydrogen and oxygen could not be measured directly. True composition was then obtained by assuming composition of the plasma at the torch exit determined from OES measurement. The mole fraction of entrained air was derived from the mole ratio of argon to nitrogen.

Emission spectra from the plasma jet were measured with a monochromator Jobin Yvon HR-320 (f = 0.32 m) equipped with a linear photodiode array detector. The plasma jet was imaged onto an entrance slit of the monochromator with the jet axis oriented along the slit. Radial scans of the spectral intensities were obtained by moving the torch fixed to a positioning device. The optical path was calibrated with a tungsten ribbon lamp and the radial profiles of the spectral intensities were transformed to the local emission coefficients using a standard Abel inversion transform. Because the arc attachment to the outer anode gives rise to a departure from a cylindrical symmetry of the plasma jet, the Abel inversion was modified by a special procedure [10]. This procedure assumes that the jet keeps a cylindrical shape within which an asymmetrical distribution of radiation exists only perpendicular to the direction of observation. This assumption is fairly fulfilled upstream of the anode attachment, fails in the attachment region, and is partially retrieved more downstream. Because the departure from cylindrical symmetry is not significant for the purposes of this study, all the presented radial profiles are obtained by folding the asymmetrical profiles as usual in most literature.

The electron number density was obtained from Stark broadened H_β line by fitting the experimental profile with the simulated one using the tables published in [11]. The procedure has been described elsewhere [12]. The method is independent of the assumption of LTE and it requires only a rough assessment of the temperature.

To determine the plasma temperature and composition, a variety of atomic and ionic lines of different species were recorded in several spectral regions. The temperature (T_{Saha}) was calculated from the ratios of various argon atomic to ionic line emission coefficients by using Saha equation and the measured electron number density. The ionic lines were: 434.81, 440.1, 442.75, 460.96, 473.59 and 480.6 nm, and in some cases also 723.35 nm; and the atomic lines were: 696.54, 706.72, 826.45, and 852.14 nm. In colder parts, where there were no ionic lines detected, the temperature was estimated from the approximate LTE composition and measured electron number density (T_{LTE}). Figure 1 shows radial profiles of the temperature at the torch exit obtained by both the approaches for two arc currents and the argon flow rate of 22.5 slm. Note that T_{Saha} represents a mean of all values obtained by all the ratios of Ar II/Ar I emission coefficients. The corresponding temperature profiles appear to be in reasonably good agreement, slight deviation can be seen only for the case of 300 A which can be explained by increasing error in T_{LTE} for temperatures above 16 000 K where the dependence of n_e on T_{LTE} starts to become flat.

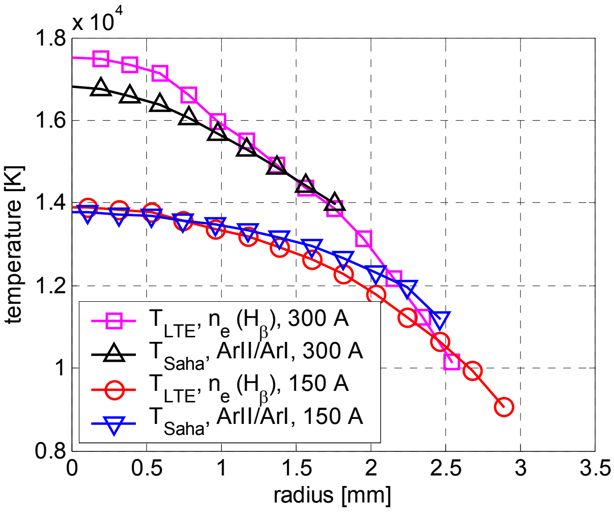

Figure 1. Comparison of radial profiles of the temperature obtained from the ratio of Ar II/Ar I emission coefficients and Stark broadening of H_β line assuming LTE.

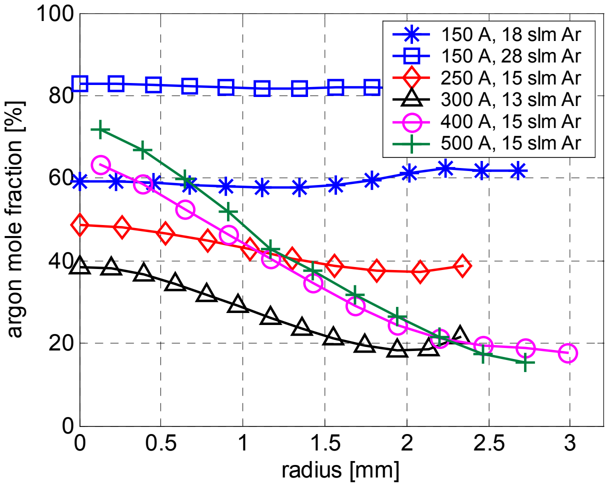

Figure 2. Radial profiles of the mole fraction of argon at the torch exit.

Concentrations of atomic species at the torch exit were determined from emission coefficients of various argon and oxygen (715.67, 844.65, 822.68 nm) atomic lines, and H_β line assuming Boltzmann distribution of atomic level populations. The emission coefficient of H_β line was obtained either from the fitting procedure or by a standard line-integral method. The first approach was used for higher temperatures when H_β line was too broad and superimposed by Ar II lines. Both the calculations proved, however, fairly compatible. In this way we obtained concentrations with unrealistically low values and unrealistic shape of radial profile. This discrepancy can be explained as a result of both jet fluctuations and departures from LTE. Another shortcoming may be connected with an imperfect subtraction of background stray light originating in hottest plasma regions. An attempt to limit the stray light by diaphragms was successful only partially at the torch exit, downstream of the anode in turbulent region, however, the stray light was still very intensive.

The following procedure was, therefore, applied. A commercial code T&T Winner [13] was used to calculate tables of LTE composition of homogeneous H_2O-Ar mixture as a function of temperature and initial mole fraction of argon. The mole fraction of argon in the plasma jet was then assessed by comparing average experimental mole ratios of atomic hydrogen and oxygen to argon, obtained using corresponding emission coefficients as described above, with the LTE tables. Figure 2 shows radial profiles of the mole fraction of argon at the torch exit for various arc currents and argon flow rates. The results reveal that, except the lowest arc current, the components of plasma are not fully mixed and the concentration of argon in the jet core increases with the arc current. The resulting plasma composition was then used to correct T_{LTE}.

To determine concentrations of atomic species downstream of the anode, we calculated tables of LTE composition as a function of temperature and mole fraction of entrained air assuming homogeneous mixture of plasma components with the mole fraction of argon taken as an average of that measured at the torch exit. The mole fraction of air was then obtained from an averaged measured mole ratio of atomic nitrogen to argon. We used the following Ar I lines: 696.54, 706.72, 750.93, 826.45, 840.82, 842.46, and 852.14 nm; and N I lines: 742.36, 744.23, 818.64, 821.63, 824.24, 856.77, 859.4, and 862.92 nm.

For each distance from the nozzle, the composition of all atomic species was assessed by solving conservation equation for number density of particles together with a condition of macroscopic electrical neutrality. The input parameters were the measured temperature, electron number density and mole ratios of H I/Ar I, O I/Ar I and N I/Ar I, and the total number of atomic neutral and ionized species including electrons taken from LTE tables.

4. Results

First it should be noted that all EP measurements refer to a fully turbulent part and OES measurements to a quasi-laminar part of the jet including transition between both the flow regimes. The quasi-laminar part of the jet was too hot for EP and the turbulent region too noisy for OES, as indicated in the previous section.

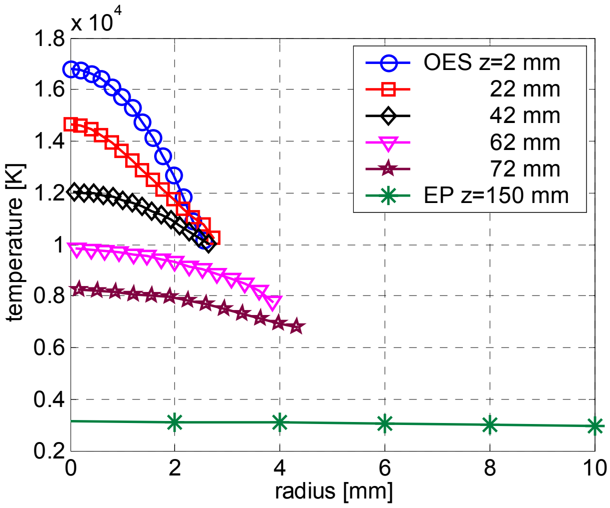

Figure 3. Radial profiles of the temperature for various distances from the torch exit; arc current 300 A, argon flow rate 22.5 slm.

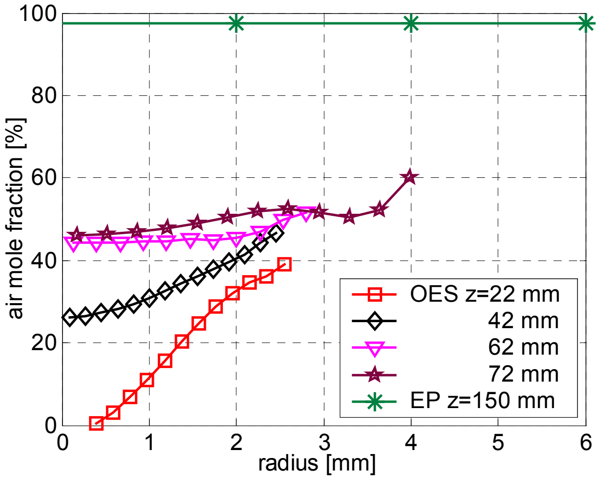

Figure 4. Radial profiles of the air mole fraction for various distances from the torch exit; arc current 300 A, argon flow rate 22.5 slm.

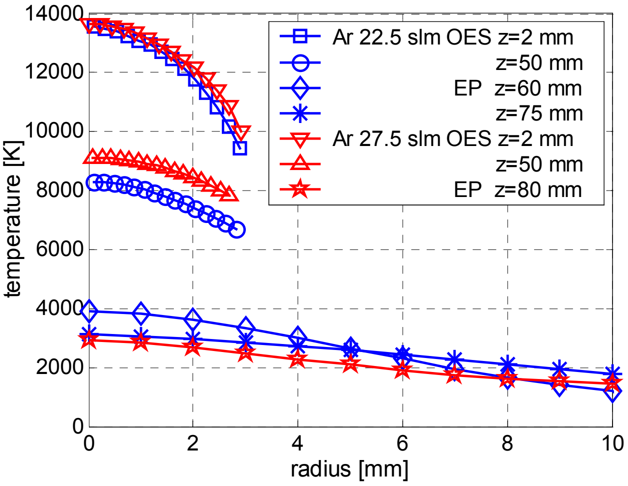

Figure 5. Radial profiles of the temperature for various distances from the torch exit; arc current 150 A, argon flow rate 22.5 and 27.5 slm.

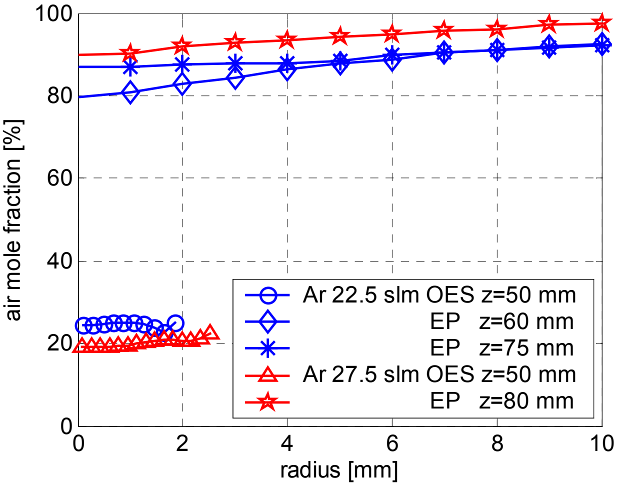

Figure 6. Radial profiles of the air mole fraction for various distances from the torch exit; arc current 150 A, argon flow rate 22.5 and 27.5 slm.

Figures 3, 5 and 4, 6 show radial profiles of respectively temperature and air mole fraction at various distances from the torch exit for arc currents of 300 and 150 A and argon flow rates of 22.5 and 27.5 slm obtained by both OES and EP measurements. The corresponding axial profiles, including two other results of EP, are shown in figures 7 and 8.

Evolution of temperature and amount of entrained air along the quasi-laminar part of the jet is demonstrated in figures 3 and 4 for the current of 300 A and argon flow rate of 22.5 slm. The first measurement of the air concentration is taken just behind the anode region (22 mm) and it shows that small fraction entrained air already approaches the centreline at this position. The transition to the fully turbulent regime occurs, however, about 60 mm downstream of the torch exit, as confirmed by other optical observations [9], where both temperature and air concentration profiles becomes flat. Because of lack of EP measurements for this particular case, the EP measurements are represented only by one result showing that in the axial distance of 150 the jet is composed almost completely of air. Figures 5 and 6 show similar results for the current of 150 A and two different argon flow rates with more results from EP. The transition to the turbulent flow regime occurs approximately at the axial distance of about 50 mm in this case.

From the first comparison of all the figures, it is evident that both axial and radial profiles of the measured

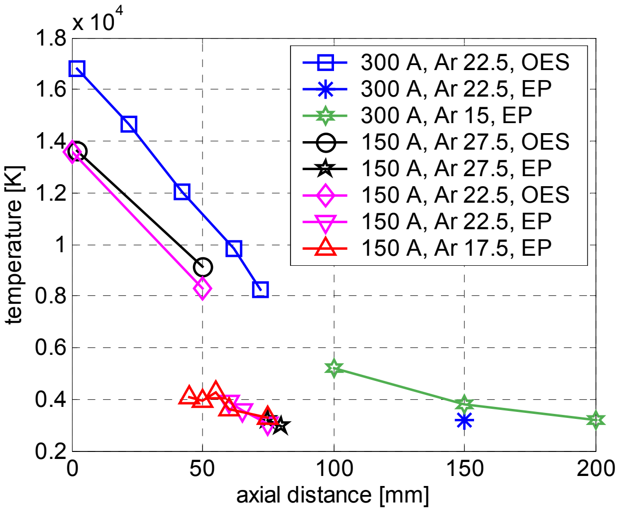

Figure 7. Comparison of centreline temperatures obtained by OES and EP.

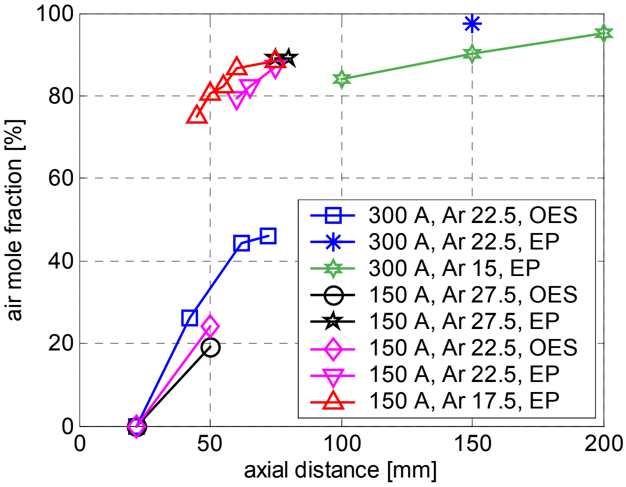

Figure 8. Comparison of centreline air mole fraction obtained by OES and EP.

quantities are almost independent of the argon flow rate. This is rather surprising since an increase in argon flow rate leads to an increase in plasma mass flow rate and thus to an increase in velocity and mass and heat fluxes. The reasons for this effect are discussed in [6, 9], the question remains, however, still open. Nevertheless, it turns out that the increase in argon flow rate results approximately only in an elongation of the quasi-laminar jet core, i.e., in a shift of the transition to a turbulent flow more downstream, which allows us to compare all the results for the same current together.

The comparison of axial profiles in figures 7 and 8 for the current of 150 A reveals significant discrepancy between OES and EP measurements at the position of the flow transition $z = 50$ mm. The temperature measured by OES is about 4000 K higher and the mole fraction more than three times lower than the values measured by EP. The two points of EP measurement 150 A, 17.5 slm Ar for $z \leq 50$ mm can be attributed to a shift of the transition to a fully turbulent flow more upstream as compared to OES measurements taken at higher argon flow rates. The discrepancy may be explained by three reasons: departures from LTE, temperature and/or space fluctuations, and mixing of cold air bubbles into a hot plasma flow. On the other hand, the same comparison for 300 A shows much less difference between OES and EP measurements. In fact, the axial profiles of temperature and air mole fraction composed of both the measurements are similar to those measured in other comparable experiments using only EP diagnostics, e.g. [14], with the same change in the slope of both centrelines at the position in which the flow becomes fully turbulent. The fact that an increase in the arc current leads to a more gradual air entrainment may suggest that the discrepancy for the current of 150 A can be ascribed mainly to the mixing of cold air with hot plasma bubbles which is significantly steeper for this low arc current.

It has been shown for this kind of torches that a standard deviation of the temperature fluctuation in the plasma jet at the torch exit is approximately 1500 K [15]. In our case this could lead to an overestimation of the centreline temperature at the torch exit of about 1700 K and underestimation at jet fringes approximately of the same value [3].

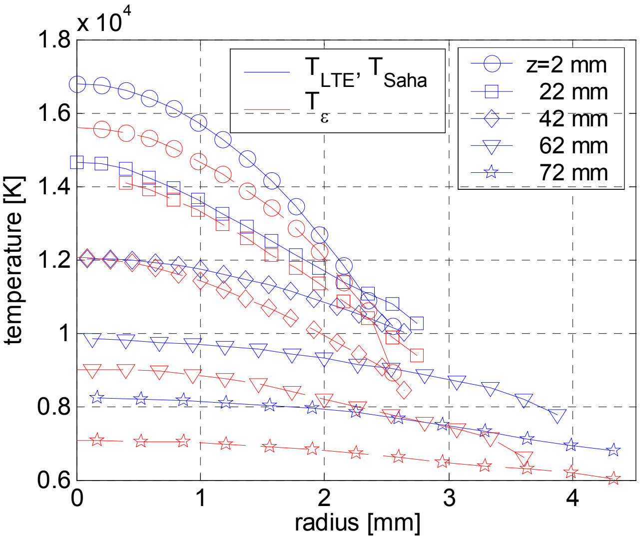

Figure 9. Comparison of radial profiles of the temperature obtained from ratios Ar II/Ar I emission coefficients and H_β line and from absolute emission coefficients of argon atomic lines.

This reasoning is, however, valid for the method based on the absolute emission coefficient of a spectral line. In our case we used either relative emission coefficients of atomic and ionic lines or the profile of H_β line. The difference between these two approaches is demonstrated in figure 9 that compares radial profiles of the temperature obtained from the ratio of ionic and atomic emission coefficients and Stark broadening of H_β line (T_{Saha}, T_{LTE}) with those calculated from absolute emission coefficients of argon atomic lines (T_ε) using the plasma composition derived as described in the section 3. At the torch exit, which is the only position where T_{Saha} was used, the centreline temperature T_ε is about 1200 K lower. Downstream of the nozzle the comparison resembles the results published in [1]. In this article the difference between the temperatures obtained from H_β line and absolute emission coefficient of argon atomic line is explained as an overpopulation of free electrons due to the frozen flow effect. However, as shown in the section 3 and demonstrated in figure 1, the temperatures derived from absolute emission coefficients correspond to those obtained from H_β line.

The space fluctuations become important downstream of the anode region as the arc anode attachment and anode jet cause whipping and surging of the main plasma jet. This may result in underestimation of the centreline temperature in the range of several hundreds K if using the method of absolute emission coefficient. Although both the temperature and space fluctuations are supposed to affect the results of OES measurements, it seems that their effect as assessed above is too small to explain the difference between OES and EP found in the case of 150 A.

5. Conclusion

In this article we have compared time averaged OES and EP measurements of the temperature and mole fraction of entrained air in the atmospheric pressure H_2O-Ar dc arc thermal plasma jet. It is shown that choosing an appropriate method of evaluation of spectroscopic data may reduce the effects of fluctuations and departures from equilibrium and lead to more realistic results. The differences between OES and EP measurements are explained mainly as a result of entrainment of cold air.

Acknowledgement

This work was supported by the Grant Agency of the Czech Republic under the project No. 202/01/1563 and by the Grant Agency of Academy of Sciences CR under the project No. A1057202.

References

[1] W.L.T. Chen, J. Heberlein, E. Pfender, Plasma Chem. Plasma Proc. **14**, 317 (1994).

[2] J.F. Coudert, M.P. Planche, P. Fauchais, Proc. of 12th ISPC, Minneapolis, 1619 (1995).

[3] R. Thoukvatoulline, G. Feldmann, J. Phys. D: Appl. Phys. **33**, 2420 (2000).

[4] J.B. Cox, F.J. Weinberg, J. Phys. D: Appl. Phys. **4**, 877 (1971).

[5] V. Březina, M. Hrabovský, M. Konrád, V. Kopecký, V. Sember, Proc. of 15th ISPC **III**, 1021 (2001).

[6] M. Hrabovský, V. Kopecký, V. Sember, Effect of Gas Properties on Characteristics of Hybrid Gas/Water Plasma Spraying Torch, Proc. of 16th ISPC, in this volume.

[7] A. Chumak, M. Hrabovský, V. Kopecký, Investigation of Anode Attachment in dc Arc Plasma Spraying Torch with External Anode, Proc. of 16th ISPC, in this volume.

[8] T. Kavka, M. Hrabovský, Czechoslovak Journal of Physics **52**, Suppl. D, D637-D642 (2002).

[9] T. Kavka, M. Hrabovský, M. Konrád, V. Kopecký, V. Sember, O. Chumak, Entrainment of Ambient air into H_2O/Ar Arc Plasma Jet, Proc. of 16th ISPC, in this volume.

[10] Y. Yasutomo, K. Miyata S. Himeno, T. Enoto, Y. Ozawa Y, IEEE Trans. on Plasma Sci. **9**, 18 (1981).

[11] C.R. Vidal, J. Cooper, E.W. Smith, Astrophys. J. Supp. Ser. **25**, 37 (1973).

[12] V. Sember, Czechoslovak Journal of Physics **52**, Suppl. D, D643 (2002).

[13] B. Pateyron, G. Delluc, Computer code T&T Winner, ADEP, University of Limoges, France.

[14] J.R. Fincke, C.H. Chang, W.D. Swank, D.C. Haggard, Int. J. Mass Transfer. **37**, 1673 (1994).

[15] V. Sember, J. Hlína, V. Kopecký, Proc. of 22th ICPIG - Contrib. Papers **1**, 57 (1995).

Plasma surface treatment of carbon nano-fibres for improved binding in polymer composites

V. Brüser[1], M. Heintze[1], W. Brandl[2], G. Marginean[2], H. Bubert[3], S. Haiber[3]

[1] *Institut für Niedertemperatur-Plasmaphysik e.V., Friedrich-Ludwig-Jahn-Str. 19, 17489 Greifswald, Germany*
[2] *Fachhochschule Gelsenkirchen, Neidenburger Str. 10, 45877 Gelsenkirchen, Germany*
[3] *Institut für Spektrochemie und Angewandte Spektroskopie (ISAS), Bunsen-Kirchhoff-Straße 11,*
44139 Dortmund, Germany

Abstract

Carbon nano-fibres (vapour grown carbon fibres, VGCF) were treated in RF plasma to enhance the surface energy and thus to improve the bonding to the matrix in polymer composites. Oxygen and nitrogen containing groups were introduced into the surface of these fibres using. To achieve a homogeneous treatment of VGCF in large enough quantities for the preparation of polymer composite samples three different reactors were used and compared.

1. Introduction

Carbon nano-fibres (vapour grown carbon fibres, VGCF) are a potentially interesting material to be used as filler in polymers adjusting their thermal, electrical and mechanical properties. However, in the as-grown state the surface of the fibres is essentially graphitic and does not permit covalent bonding to a polymer matrix. The plasma treatment is a useful tool to modify the surface properties and to enhance the surface energy. Thereby, oxygen and nitrogen containing groups may be introduced into the surface of VGCF. The use of cold plasma for the surface functionalisation of carbon blacks, PAN based carbon fibres, thermally treated VGCF as well as VGCF nano-fibres was shown [1-5]. To achieve a homogeneous treatment of VGCF in large enough quantities to prepare polymer-fibre test samples appropriate techniques have to be developed. It can be done by fluidising the fibres in the plasma zone. In first investigations the oxygen plasma treatment in vibrating bed reactor and fluidised bed reactor was carried out [5-7].

The aim of this work is to investigate and compare different fluidisation methods for plasma treatment of VGCF. In three different reactors the fibres were fluidised in the plasma zone. The process parameters pressure, plasma power and gas composition were investigated. The surface energy and surface composition of the fibres were characterise before and after the treatment by contact angle measurement, XPS and SEM.

2. Experimental

Nano-VGCF (Pyrograf®-III Applied Sciences, Inc., Cedarville, USA) with a diameter between 50 and 200 nm and a length in the range from 10 to 200 µm were used.

The plasma treatment was carried out in three reactors in which the fibres were agitated by different means: mechanical vibration (vibrating bed reactor), a gas stream (fluidised bed reactor) and a rotating drum, respectively. The fluidised bed reactor allows both continuous and discontinuous (batch) processing. These methods allow a homogeneous treatment of large fibre samples.

2.1 Vibrating bed reactor

The sample is held in a stainless steel dish with a diameter of 105 mm, which is made to vibrate by an electromagnet at 50 Hz (Fig. 1). In this way the fibres (up to 20 g) are fluidised during the process ensuring a homogeneous treatment. The 27.12 MHz RF plasma is inductively coupled into the reactor through a quartz glass window.

NH_3 and two gas mixtures, Ar-O_2 and Ar-CO_2 in the ratio of 1:1 were used in the pressure range of 0.01 – 40 mbar. The plasma power was 80 and 150 W and the treatment time between 5 and 40 min.

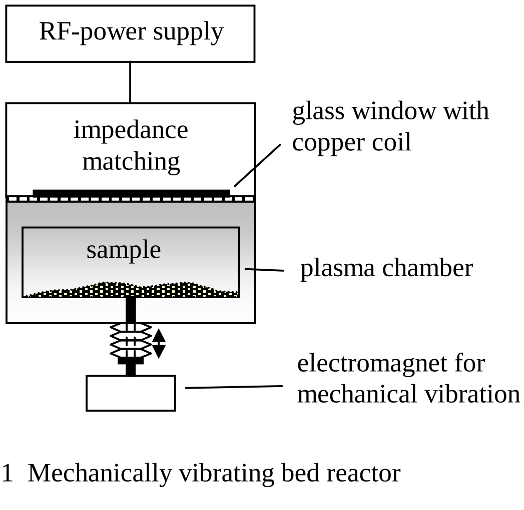

Fig.1 Mechanically vibrating bed reactor

2.2 Fluidised bed reactor

In this reactor (Fig. 2) a process gas stream through the plasma is maintained by a circulating pump. The fibres are fed into the gas stream using a screw feeder. The gas velocity in the plasma zone is sufficiently high to carry the fibres through the plasma zone into a separation zone. There the diameter of the vessel is 3 times wider than in the plasma zone and hence the gas velocity is reduced to approx. 1/10th, leading to settling of the fibres. Because of the laminar gas flow through the plasma zone fibres move upward only in the centre of the tube and fall downward near the tube wall. The riser has a diameter of 70 mm and a length of 1.2 m.

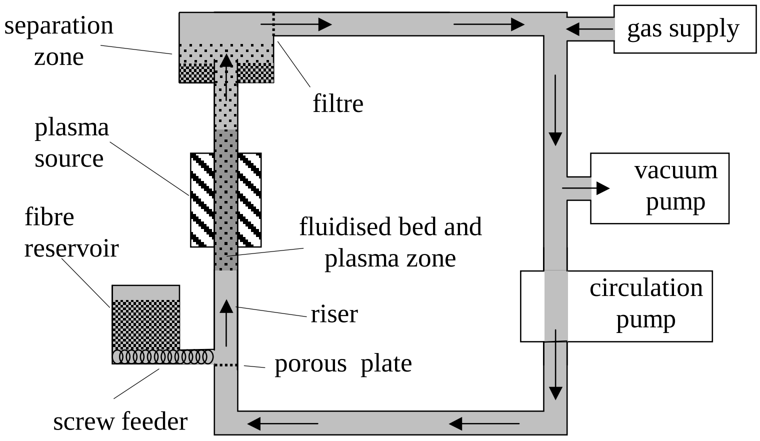

Fig.2 Fluidised bed plasma reactor

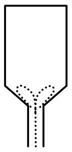

a

- separation zone without particle trap
- the particles that reach the separation zone fall back in the plasma zone, all fibres circulate during the entire treatment time
- discontinuous (batch) procedure
- 25 g VGCF per hour can be treated

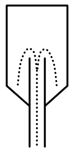

b

- all fibres that reach the separation zone are trapped by the cylinder inserted into the lower conical section
- only a single pass through the plasma is possible
- continuous treatment of larger samples is possible
- approx. 3 g VGCF can simultaneously be kept in a fluidised state

Fig.3 Two modifications of the separation zone

The separation zone was modified in two different ways, allowing to control the treatment time (Fig. 3).

The functionalisation was carried out with a gas composition of Ar : O_2 = 2 : 1 in a pressure range of 1.5 to 2.5 mbar and at 10 mbar. The plasma power was 30, 50, 80, 150 and 250 W. The 27.12 MHz RF plasma is inductively coupled into the reactor through a glass tube by a copper coil.

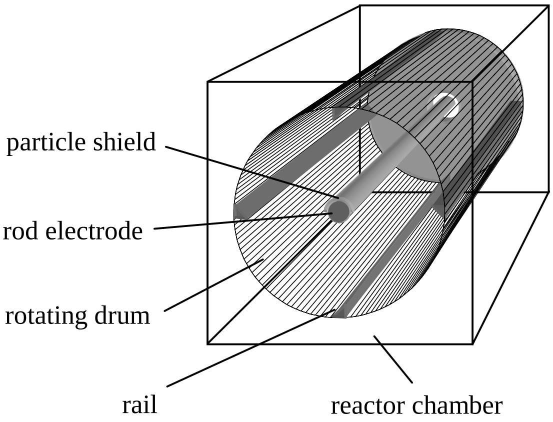

Fig. 4 Rotating drum reactor

2.3 Rotating drum reactor

The fibres are loaded into an aluminium drum (Fig. 4). The closed drum rotates in roll axis and thereby the fibres are mixed. To improve the mixing process four rails are mounted on the wall inside. The 13.56 MHz RF plasma is capacitively coupled by a rod electrode, which is arranged in the longitudinal axis of the drum.

The drum has a diameter of 250 mm and a length of 390 mm.

2.4 Methods of surface analysis

The surface energy of the fibres was obtained from contact angle measurement [4] using a Tensiometer (DCAT 11, DataPhysis Instruments GmbH Filderstadt, Germany). A constant volume of carbon fibres is put into a glass tube, which is attached to a microbalance. The sample is brought into contact with several liquids (water, isopropyl alcohol and di-iodomethane). The penetration velocity measured through the weight increase is a function of the contact angle. The total surface energy γ is the sum of the dispersive component γ^d and the polar component γ^p. The dispersive component γ^d represents the surface roughness and the fluctuation of the charge distribution whereas the polar component γ^p is determined by the concentration of oxygen containing functional groups on the surface. Surface concentrations of these groups were also measured by XPS (AXIS-HS spectrometer, Kratos, Manchester, UK) [5]. The spectra obtained from untreated and treated carbon fibres show O1s and N1s photoelectron signals from oxygen or nitrogen containing groups, respectively. Some of these groups like C-OH, C=O, COOH can be distinguished by the energetic position of C1s photoelectron signal from carbon. But other groups like C-OH, C-N=O and C-NH_2 cannot be distinguished because the position of the signals are nearly the same. The quantification was carried out by a standard procedure using sensitivity factors from polyethyleneglycol and polystyrene.

3 Results and discussion

3.1 Plasma treatment in CO_2-Ar gas mixture

The plasma treatment in CO_2-Ar gas mixtures was only carried out in the vibrating bed reactor.

The effect of this treatment on the surface energy γ of carbon nanotubes is shown in Fig. 5. It leads to a significant enhancement of the surface energy. This is mainly effected by the polar component γ^p. With increasing gas pressure during plasma treatment the surface energy decreases. At pressures over 1 mbar the plasma contracts into the space near coupling window. Therefore, the plasma power was increased to 150 W in order to reach a better interaction between plasma and sample.

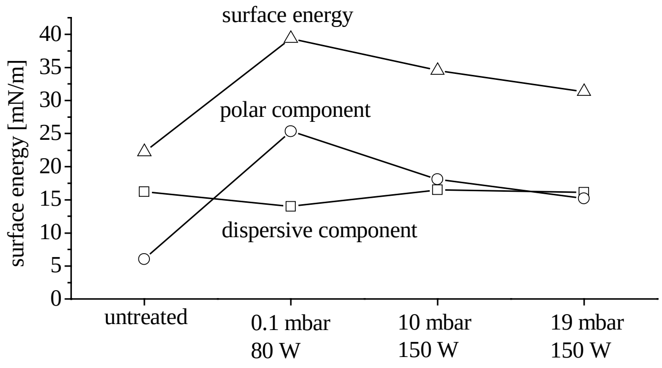

Fig. 5 Surface energy at different pressures and plasma power; treatment time: 10 min; gas composition: Ar : CO_2 = 1 : 1

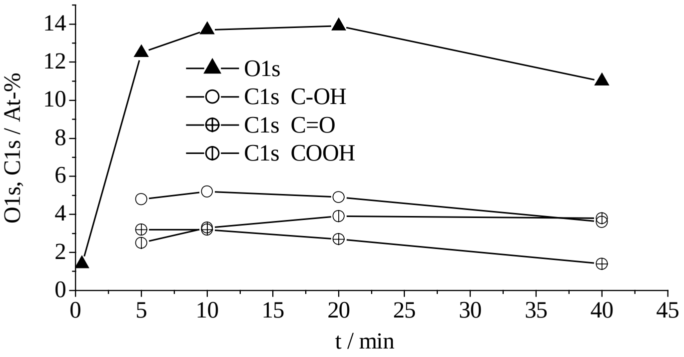

Fig. 6 O1s and C1s values at 1.2 mbar and 80 W gas composition: Ar : O_2 = 1 : 1

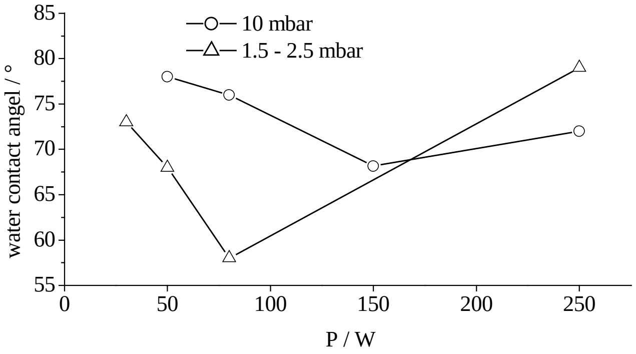

Fig. 7 Water contact angle at different plasma power and pressures gas composition: Ar : O_2 = 2 : 1

3.2 Plasma treatment in O_2-Ar gas mixtures

The oxygen-argon treatment in the vibrating bed reactor leads to an enhancement of oxygen concentration on the surface after 5 min and decreases slightly at longer times (Fig. 6). But the concentration of COOH groups increases during the entire treatment time. The COOH groups are probably formed from C=O and C-OH groups, the concentration of which decreases.

In the fluidised bed reactor the effect of plasma power and pressure on the water contact angel was investigated in the continuous mode (Fig. 7). The lowest water contact angel was obtained in the pressure range of 1.5 to 2.5 mbar and a plasma power of 80 W. During the plasma treatment two processes take place simultaneously: a) functionalisation by reactions of molecular or atomic gas species at the surface of the sample and b) etching of the surface caused by ion bombardment or reaction of oxygen with substrate. It depends on the plasma parameters which process dominates. In both investigated pressure ranges at 250 W the etching process is more effective than the functionalisation and hence the water contact angle at 250 W is higher than at 80 or 150 W, respectively.

In the vibrating bed reactor, the fluidised bed reactor (in discontinuous mode) and the rotating drum reactor carbon nanotube samples were treated for different times. The influence of the treatment time on the water contact angle can be seen in Fig. 8. The rotating drum reactor requires the longest treatment time to reach the same water contact angles compared to the other two reactors because the mixing process is slower. In the vibrating bed reactor a shorter treatment time than 5 min leads to an inhomogeneous treatment. In the fluidised bed reactor there is the best contact between the free floating carbon fibres and the plasma.

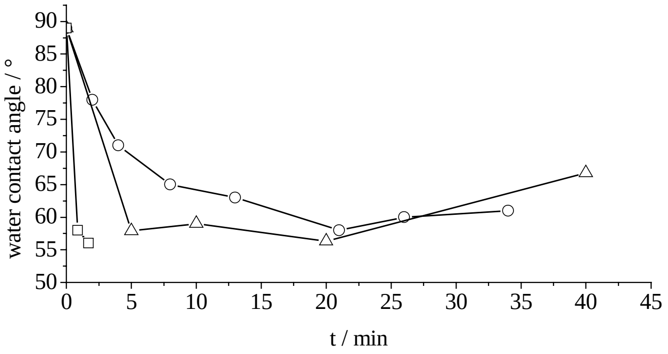

Fig. 8 Comparison of treatment times measured on plasma processes in three different reactors

○ rotating drum reactor; 80 W; 0.1 mbar;
20 sccm O_2 + 12 sccm Ar; 2 g VGCF

△ vibrating bed reactor; 80 W; 1.2 mbar;
35 sccm O_2 + 35 sccm Ar; 4.5 g VGCF

□ fluidised bed reactor: 50 W; 1.5…2.5 mbar;
10 sccm O_2 + 20 sccm Ar; 2.5...3 g VGCF

3.3 Plasma treatment in NH_3

For the NH_3 plasma treatment the vibrating bed reactor was used. The dependency on process pressure was investigated at a plasma power of 50 W and a treatment time of 4 min (Fig 9.). With decreasing pressure the nitrogen concentration on the surface increases. However, the values of nitrogen is not so high as the oxygen concentration after O_2-Ar treatment (Fig 6.).

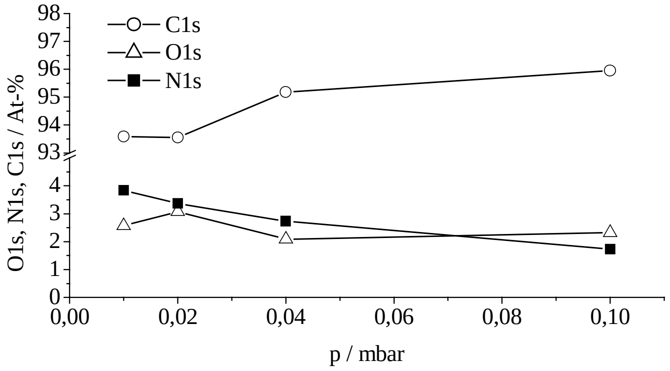

Fig. 9 N1s, O1s and C1s values at 50 W; NH_3 plasma

Additionally, it was investigated if the NH_3 plasma treatment leads to higher nitrogen concentrations on the surface if fibres pre-treated in oxygen are used. Two nanotube samples with different surface compositions of oxygen containing functional groups were used for ammonia plasma treatment. As it is shown in Fig. 6, different distributions of C-OH, C=O and COOH groups on the surface can be realised by different treatment times. In the first step the samples of carbon fibres were treated 10 and 40 min in an oxygen-argon plasma in the rotating drum reactor (Tab.1). The sample treated for 10 min contains more C-OH and less C=O and COOH groups than the 40 min treated sample. In a second step, these samples were treated in an ammonia plasma at 0.01 mbar and 50 W in the vibrating bed reactor. During this treatment the contents of C=O groups

Table 1 XPS data of oxygen and additionally ammonia treated carbon nanotubes

1	2	3	4	5	6	7
Sample	C1s C=O [at-%]	C1s COOH [at-%]	C1s C-OH* [at-%]	O1s [at-%]	N1s [at-%]	N1s + O1s [at-%]
O_2 + Ar treated (10 min)	2.01	2.13	5.15	10.10	0.47	10.57
additionally NH_3 treated	1.93	1.20	1.45	7.95	2.78	10.73
O_2 + Ar treated (40 min)	2.79	2.63	4.80	12.86	0.55	13.41
additionally NH_3 treated	2.51	2.59	1.93	9.66	2.87	12.53

* in case of NH_3 treated sample the difference between the measured C-OH and the N1s signals is given

of both samples and the content of COOH groups of 40 min treated sample changed only slightly. The 10 min treated sample contains less COOH groups after ammonia treatment. The content of nitrogen containing groups of both samples increased. The signals of C-OH and nitrogen containing groups like $C-NH_2$ and C-N=O can not be distinguished as above mentioned. Only a sum signal can be measured. To obtain the C-OH content the values of N1s signals were subtracted from the sum signals. The calculated values show that during the ammonia treatment the content of C-OH groups significantly decreases. The oxygen containing groups, which are lost during the ammonia treatment, are replaced by nitrogen containing groups (see column 7 in Tab. 1). However, the NH_3 plasma treatment of oxygen treated carbon nanotubes does not lead to higher nitrogen concentrations on the surface than when using untreated fibres.

3.4 SEM images of freeze-fractured samples

Two samples of polymer compound were produced by mixing of polyethylene with a) five percent untreated and b) five percent argon-oxygen treated VGCF. These samples were fractured at low temperatures and investigated by SEM (Fig.10a). The fibres were treated 20 min at 80 W and 35 sccm O_2 + 35 sccm Ar in the vibrating bed reactor. The image of the sample with untreated nanotubes shows some fibres and lot of holes indicated by the dark spots (Fig.10b). This means that during the break the fibres are not fractured because of the bad bonding to the polymer matrix. However, by using treated fibres not so match holes are visible. The bonding between fires and polymer matrix is better.

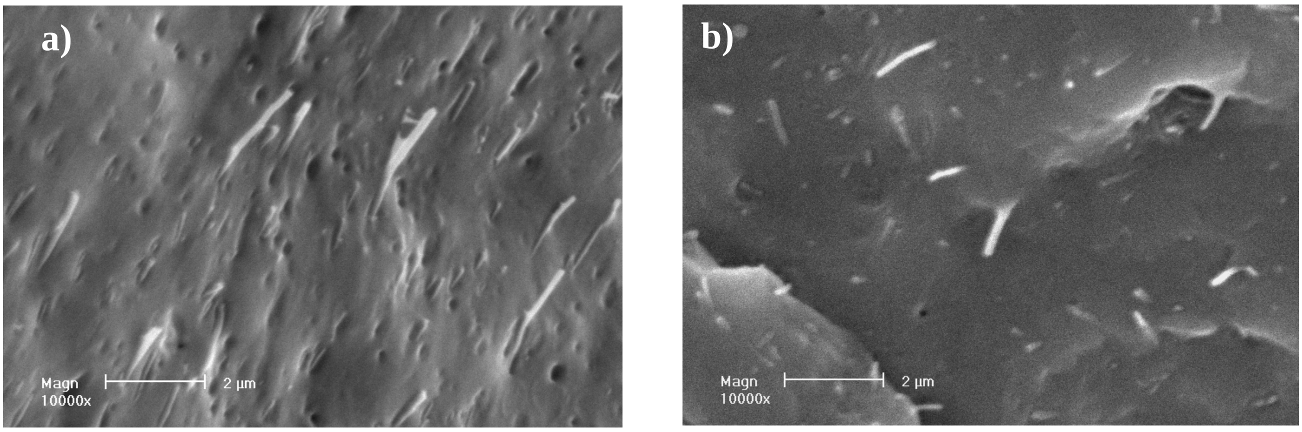

Fig. 10 SEM images of freeze-fractured samples of polypropylene a) + untreated VGCF and b) + oxygen plasma treated VGCF

4 Summary

The surface of VGCF can be functionalised in RF-plasma using CO_2, O_2, or NH_3 containing gasses. The surface composition of oxygen functional groups during oxygen plasma processing can influenced by the treatment time. At ammonia treatment with decreasing process pressure the nitrogen concentration on the surface increases. The oxygen plasma treatment of carbon nanotubes leads to good bonding between fibres and polymer matrix.

The fluidised bed reactor and the vibrating bed reactor provide shorter treatment times as the rotating bed reactor.

References

[1] I. H. Loh, R. E. Cohen, R.F. Baddour, "Modification of carbon surfaces in cold plasma", J. Mat. Sci. **22**, 2937 (1987)

[2] E. Pasch, S. Strehle, "Plasmabehandlung von VGCF Kohlefasern", Proceedings 9th Workshop Plasmatechnik, Ilmenau, 123 (2001)

[3] A. Bismarck, M. E. Kumru, J. Springer, "Influence of Oxygen Plasma Treatment of PAN-Based Carbon Fibres on Their Elektrokinetic and Wetting Properties", J.Colloid Interface Sci. **210**, 60 (1999)

[4] Marginean, G., Brandl, W., Toma, D., Bubert, H., Jenett, H., “Surface Characterisation of Vapour Grown Carbon Fibres (VGCF) Treated by Oxygen Plasma“, Proceedings of the 15th International Symposium on Plasma Chemistry, Orleans, France, 527 (2001)

[5] H. Bubert, X. Ai, S. Haiber, M. Heintze, V. Brüser, E. Pasch, W. Brandl, G. Marginean, “Basic analytical investigation of plasma-chemically modified carbon fibers”, Spectrochimica Acta B **57**, 1601 (2002)

[6] M. Heintze, V. Brüser, W. Brandl, G. Marginean, H. Bubert, “Funktionalisierung von Kohlenstoff-Nanofasern (VGCF) durch Plasmabehandlung,“ Proceedings 10th Workshop Plasmatechnik, Ilmenau, 81 (2002)

[7] M. Heintze, V. Brüser, W. Brandl, G. Marginean, H. Bubert, S. Haiber, “Surface functionalization of carbon nano-fibers in a fluidized bed plasma”, to be published in Surface & Coatings Technology

Temperature measurement of arc plasma jet by the oxygen single-band model LIF thermometry

Yang Furong , Yue Bin , Su Tie , Yu Fuming

China Aerodynamics Research &Development Center,P.O.Box 211,Mianyang,Sichuan,China,621000

Amongst quantitative measurements for high temperature and high enthalpy gases, LIF is a technology initiated from 1980's to perform laser spectroscopy diagnostics. Very high temporal and spatial resolutions are involved in this technology, so it can acquire abundant information of flow field and be used to make measurements of temperature, digital density, velocity, pressure and other significant parameters, and simultaneous measurements of multiple parameters at various points can be realized. Because of this, many researchers were greatly attracted by the LIF technology at the beginning of development. This paper presents applications of LIF in the flow of high temperature and high enthalpy gases: We have adopted ArF excimer to excite the rot-vib absorption lines near 193.3nm for Schumann-Runge system of Oxygen and used ultraviolet PMT to detect the fluorescence near 256nm to establish a set of LIF flow field measuring system based on ArF excimer. We have obtained the radial temperature distribution of the arcjet of oxygen and argon mixture gases by using the single-band thermometry LIF model on the basis of the fluorescence signal of. Oxygen Schumann-Runge system. The established O2 LIF system based ArF excimer can be applied in the diagnosis on the flow field of high enthalpy facility.

[1] M.P. Lee, R.K. Hanson," Calculation of O2 Absorption and Fluorescence at Elevated Temperatures for A Broadband Argon-fluoride Laser Source at 193 nm", J.Quant.Spectrosc.Radiat.Transfer, 36(5):425-440 (1986).
[2] Allen M.G., Parker T.E., Reinecke W.G., Legner H.H., Foutter R.R., Rawlins W.T., and Davis S.J., Instantaneous Temperature and Concentration Imaging in Supersonic Air Flow behind A Rear-Facing Step with hydrogen Injection, AIAA92-0137(1992).
[3] Allen M.G., Cronin J.F., Davis S.J., Foutter R.R., PLIF Imaging Measurements Compared to Model Calculations in High-Temperature Mach 3 Airflow Over A Sphere, AIAA 93-0092(1993)
[4] Palmer J.L. and Hanson R.K., PLIF Measurements of Temperature and Velocity in A Reacting Supersonic Free Jet With OH, AIAA-94-0618(1994)

Numerical simulation of blistering fluctuation stage.

A.L. Bondareva, G.I. Zmievskaya

Keldysh Institute of Applied Mathematics Russian Academy of Sciences

Understanding of processes of interaction between solids surfaces and plasma has huge significance for development technologies which concern with cosmophysics, controlled thermonuclear fusion, nanotechnologies. Such problems as blistering, flecking and others near-surface processes, which take place under irradiation solids surfaces by ions beams, result in solids properties change, plasma pollution and plasma properties change as result it. In connection with high cost and complexity of laboratory experiments with plasma, computer simulation of interaction between plasma and solids surfaces takes on special significance.

Fluctuation stage of high-temperature blistering is examined in this work. Formation of gas-vacancy pores, which were named blisters, into Ni crystal lattice under the influence of He ions is discuss. He ions have energy from 10 keV to 100 MeV, radiation dose is from 10^{16} to 10^{19} ions/sm^2, the temperature of material ***T*** is $0{,}4T_{melt} \le T \le 0.6T_{melt}$, T_{melt} is melting temperature of Ni. Fluctuation stage is very short, its duration is approximately 10^{-4} sec. But this stage determinants all following development of blistering.

Authors suggest stochastic model of fluctuation stage of high-temperature blistering. The model under discussion is based on Brownian motion model. Blistering is considered as first-order phase transition on its fluctuation stage. Bubbles have size approximately several angstorm and its are considered Brownian particle with sphere form and variable mass. Blisters can interact with each other, solid lattice and solid surface. Splitting on physical processes is used in this work. The evolution of bubbles is presented as a superposition of the stochastic processes of size increase and bubbles migration in crystalline lattice. It is possible since processes of bubble size increase and bubble migration in lattice have appreciably different time scales. Characteristic time for blisters size increasing is 10^{-9} sec, typical time for its migration in lattice is 10^{-8} sec. Kinetic equations of Brownian motion model are very difficult for solve. The method of stochastic analog is used for solve this problem. The main idea of the method is change of kinetic equations its stochastic analogs and solve stochastic differential equations. Author apply not only splitting on physical processes but splitting on coordinate too [1,2]. Received kinetic equation and its stochastic analogs display below. Kinetic Fokker-Plank-Kolmogorov equation for evaluation of blister size is

$$\frac{\partial f_r(g,t)}{\partial t} = \frac{\partial\left[D_g(g,t)\frac{\partial f_r(g,t)}{\partial g}\right]}{\partial g} + \frac{1}{kT}\,\frac{\partial\left[D_g(g,t)f_r(g,t)\frac{\partial\{\Delta\Phi(g,\vec{r},t)\}}{\partial g}\right]}{\partial g}$$

$$f_r(g,0) = f_{0g} \qquad \left.\frac{df_r(g,t)}{dg}\right|_{g=2} = 0 \qquad f_r(g,t)\,|_{g<2} = 0$$

g is number of He atoms in bubble, f_r is distribution function, $D_g(g,t)$ is diffusion coefficient in space of bubbles sizes, $\Delta\Phi(g,\vec{r},t)$ is Gibs potential.

The stochastic analog of Fokker-Plank-Kolmogorov equation is

$$\frac{dg}{dt} = -\frac{1}{kT}D_g(g,t)\frac{\partial\Delta\Phi(g,\vec{r},t)}{\partial g} - \frac{1}{2}\frac{\partial D_g(g,t)}{\partial g} + \sqrt{2D_g(g,t)}\,\xi(t)$$

$$t_0 \le t \le T_k \quad g(t_0) = g_0 \in [g_{\min};g_{\max}] \quad g(t) > 2$$

T_k is full time of computation, $\xi(t)$ is stochastic function, $D_g = D_{g0} g^{2/3}$

$$\Delta\Phi(g,\vec{r},t) = \begin{cases} -(a_{\Delta\Phi} - c)g + bg^{2/3} + \Delta\Phi_r, & \Delta\Phi(g,\vec{r},t) < \Delta_{break} \\ -(a_{\Delta\Phi} - c)g + bg^{2/3} + \Delta\Phi_r - \Delta\Phi_{break}, & \Delta\Phi(g,\vec{r},t) > \Delta_{break} \end{cases}$$

$$\Delta\Phi_r = k_x \cos(2\pi(x - \varphi_x)) + k_y \cos(2\pi(y - \varphi_y)) + k_z \cos(2\pi(x - \varphi_z))$$

$$\Delta_{break} = 6E_{lat} \qquad \Delta\Phi_{break} = N_{br}\Delta_{break}$$

We to take into account the difference between chemical potentials of two phase, surface tension on bubble – metal surface, elastic force of lattice reaction [3], disparity between locations in lattice points and internodes, relcases in crystalline lattice [1,2]. The difference between chemical potentials is consisted in coefficient $a_{\Delta\Phi}$, b depends on surface tension on bubble –metal surface, elastic force of lattice reaction is considered in c, $\Delta\Phi_r$ determines the disparity between locations in lattice points and internodes, $\Delta\Phi_{break}$ deals with relcases in crystalline lattice. N_{br} is number single relcases, Δ_{break} is energy of single relcase, E_{lat} is binding energy in lattice. $\left.\frac{d(\Delta\Phi)}{dg}\right|_{g=g_{cr}} = 0$, g_{cr} is critical size of bubble, $\Delta\Phi(g_{\min}) = \Delta\Phi(g_{\max}) = \Delta\Phi(g_{cr}) - kT$, $g_{\min} < g_{cr} < g_{\max}$.

The Gibs potential has form which is presented on figure 1.

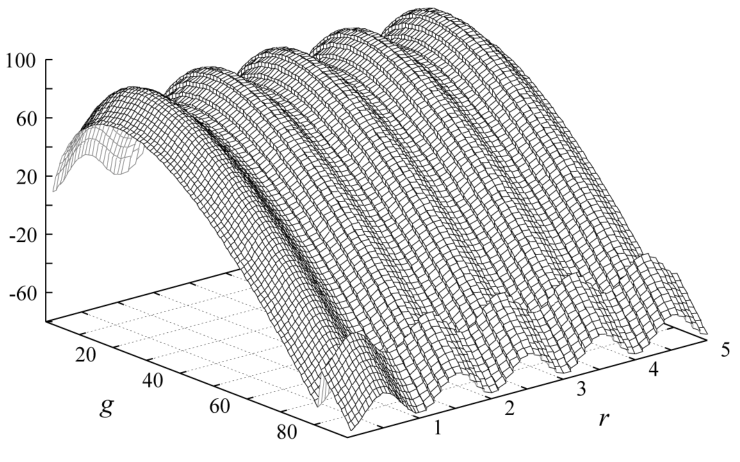

Fig.1 The dependence of Gibs potential (Joule/atom) from blister size (g) and place crystal lattice (r). Blister size is measured in number of helium atoms in bubble. r is measured in lattice parameter. The break on g ≈80 corresponds the first break of lattice and concerns with increase of blister size.

The kinetic equation for motion of blisters is following

$$\frac{\partial f_g(\vec{r},t)}{\partial t}=\frac{\partial\left[D_r(\vec{r},t)\frac{\partial f_g(\vec{r},t)}{\partial r}\right]}{\partial\vec{r}}-\frac{\partial\left[\frac{\vec{F}(\vec{r},t)}{M_g\gamma}f_g(\vec{r},t)\right]}{\partial\vec{r}}$$

$$f_g(\vec{r},t)|_{t=0}=f_{0r}\qquad f_g(\vec{r},t)|_{z=z_{\max}}=0\qquad f_g(\vec{r},t)|_{z<z_2(g)}=0$$

$$f_g(\vec{r},t)|_{x=x_{left}}=f_g(\vec{r},t)|_{x=x_{right}}\qquad f_g(\vec{r},t)|_{y=y_{left}}=f_g(\vec{r},t)|_{y=y_{right}}$$

$$x_{left}=-200,\quad x_{right}=200,\quad y_{left}=-200,\quad y_{right}=200,\quad z_{\min}=0,\quad z_{\max}=400,$$

$$z_2(g)=\frac{2}{3}r_{He}\sqrt[3]{g}.$$

We consider that blister comes out surface and perishes on it if $z\leq z_2$.
x,y,z are measured in lattice parameter, $z_{\min}$ is surface, $z_{\max} = 2\ R_p$, R_p is middle depth of projection run, origin of coordinates is in point {x=0, y=0, z=0}, $f_g(\vec{r},t)$ is distribution function, $D_r(\vec{r},t)$ is diffusion coefficient in lattice space, M_g is mass of blister, γ is dissipative factor, $F_x=-\frac{\partial U(x,y,z)}{\partial x}$, $U(x,y,z)$ is potential of indirect interaction between bubbles by way of phonons and oscillation of electron density.

$$U(x,y,z)=\sum_{i\neq j}^{N}\frac{b_r\left[\frac{3}{5}-\frac{(x_i-x_j)^4+(y_i-y_j)^4+(z_i-z_j)^4}{(\vec{r}_i-\vec{r}_j)^4}\right]+a_r\cos(\vec{c}_r(\vec{r}_i-\vec{r}_j))}{|\vec{r}_i-\vec{r}_j|^3}$$

The stochastic analog of the kinetic equation for one coordinate is following.

$$x(t)=x(t_0)+\int_{t_0}^{t}H_x(\tau,x(\tau),y(\tau),z(\tau))d\tau+\int_{t_0}^{t}\sigma(\tau,x(\tau),y(\tau),z(\tau))dW(\tau)$$

$$H_x=-\frac{1}{\gamma M_g}\frac{\partial U(x,y,z)}{\partial x}-\frac{1}{2}\frac{\partial D_x}{\partial x};\sigma=\sqrt{2D_x},D_x=\frac{D_0e^{-E_m/kT}}{\gamma M_g}(1+\alpha(x-x_0)^2)$$

E_m is energy of migration, dW is increment of Viner stochastic process.

The fusion of blister is considered in model under discussion. The fusion of two bubbles is made approximately. Two bubbles interflow if following condition is realized: distance between centers of mass bubbles is less than sum of blisters radiuses and some model parameter Δ_f. $0\leq\Delta_f\leq a$, *a* is lattice parameter [1,2].

Used model allows to find the distribution functions of bubbles from size and place in lattice at different moment of time. Such characteristics as middle size of bubbles, porosity of layers, tension in layers, number of blasted blisters and dependence of these values from time can be find as a result of processing of these distribution functions.
Distribution functions from most interesting parameters, bubble radius and distance from surface under irradiation, are shown on figure 2 and 3. The dependence of porosity from depth of layer at moment of finish of fluctuation stage is presented on figure 4. Tensions in solid layers at finish time are shown on figure 5.

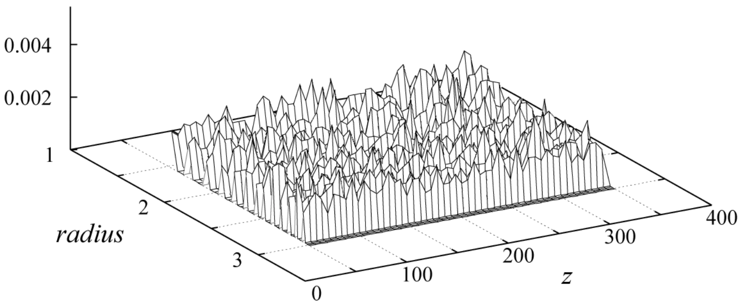

Fig.2 Two dimensional distribution function $f(R_{bl},z)$ at initial moment of time $t = 0$ is presented on this figure. Radius of blister is shown in Å, distance from surface under irradiation (z) is measured in lattice parameter.

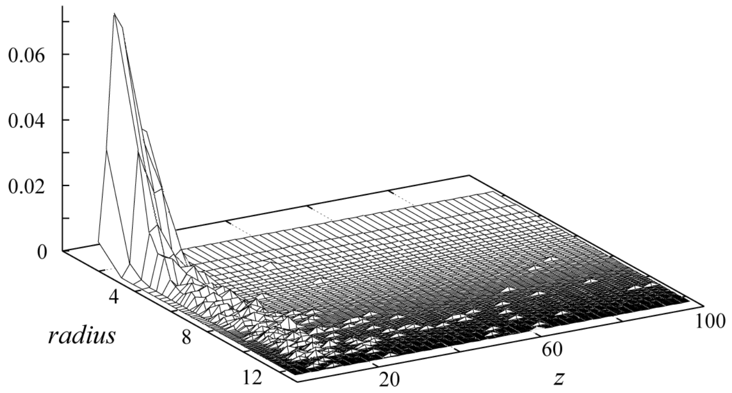

Fig. 3 presents the $f(R_{bl},z)$ at finish moment of time.

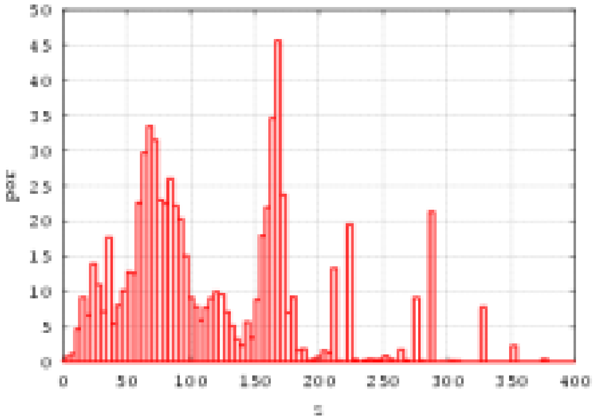

Fig.4. The dependence of porosity from depth of layer at moment of finish of fluctuation stage is presented on the picture. The porosity of layer on this figure is determined as ratio of layer porosity from total porosity of all sample at initial moment of time. The distance from surface under irradiation (z) is measured in lattice parameter

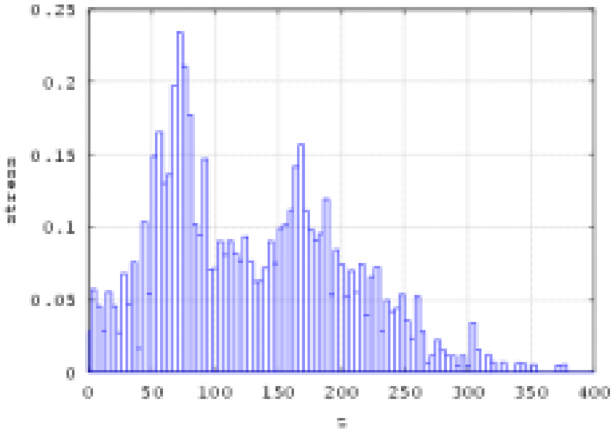

Fig.5. Tensions in solid layers at finish time are shown. Tension is measured in 2 10^9 Pa.

Conclusions.

1. According classical theory bubbles must destroy if them sizes less than g_{cr}. However bubbles can increase if $g_{min} \leq g \leq g_{cr}$ and blisters can degrade if $g_{cr} \leq g \leq g_{max}$. Majority of blisters, which sizes $g_{min} \leq g \leq g_{max}$ increase.
2. If radius of bubble is larger than 5 Å then bubble does not migrate on crystal lattice, if bubble size is less than 5 Å then bubble moves to surface under irradiation.
3. Layer-like structure of near-surface layer is observed.
4. The greatest porosity is observed on depths ~ 0.85 R_p and ~ 0.35R_p.
5. Increase of bubble size reduces after size reaches 12 Å.
6. Largest tensions are observed on depths ~ 0.85 R_p and ~ 0.35 R_p.
7. The distribution function of bubbles from sizes and depths is nonequilibrium.

This work is partially supported by RFBR grant 02–01–01004.

References.

1. Bondareva A.L., Zmievskaya G.I. // Proceeding. XXV ICPIG, 2001, Nagoya, Japan, Vol.3, pp. 187-188
2. Bondareva A.L., Zmievskaya G.I. // Doklady Physics, 2002, V.66, № 7 pp. 994-997
3. Bondareva A.L., Zmievskaya G.I // book Mathematical Models of Non-Linear Excitations, Transfer, Dynamics and Control in Condensed Systems and Other Media, Plenum Publishing Corporation, 1998, editor L. Uvarova, New-York pp. 241-250

Resist Plasma Etching for 157 nm Lithography

D. Eon[1], G. Cartry[1], M.C. Peignon[1], Ch. Cardinaud[1], E. Tegou[2], N. Vourdas[2], V. Bellas[2], P. Argitis[2], E. Gogolides[2], A. Tserepi[2]

[1] IMN LPCM, 2 rue de la Houssinière, BP 32229, 44322 Nantes Cedex 3, FRANCE
[2] Institute of Microelectronics, NCSR “Demokritos”, Aghia Paraskevi, 15310 Athens, Greece

Abstract

This work concerns the etching of silicon containing copolymers in oxygen plasmas. Such copolymers are candidate materials for the next generation optical lithography. In this aim, we need a good resistance to oxygen plasma and a high selectivity with respect to carbon containing resist. Etch rates and selectivity are measured by in-situ ellipsometry. We investigate etching mechanisms using both ellipsometry and quasi in-situ XPS.

1. Introduction

International efforts are presently being conducted to develop the 157 nm lithography, which is expected to be the next generation optical lithography, allowing to meet the 70 nm node and possibly go beyond. We are involved in an European IST program (157 CRIPIES), joining several national laboratories and industrials, to address resist challenges associated with the 157 nm lithography.

Resist absorbance is a major problem at 157 nm, “usual” carbon containing resists having too high absorbance at this wavelength. A possible way to face this issue is to use silicon containing resists, which present a suitable absorbance at 157 nm. However, their too low resistance to chloro or fluorocarbon plasma etching does not allow to use them in a single layer scheme. They must be associated with a “usual” resist in a bilayer scheme (figure 1): the top layer is made of a silicon containing copolymer used as imaging material for 157 nm lithography; after irradiation and wet development of the top layer, the bottom layer (carbon containing resist) is opened in oxygen plasma.

Our aims are to identify the etch mechanisms and to measure and understand the resist/resist selectivity, which is one of the most important parameter of the bilayer process. To achieve this goal, we measure etch rates in real time by in-situ ellipsometry. We characterise the resist surface before and after etching by quasi-in situ XPS analysis and by angular XPS analysis. We then correlate surface characterisation to the plasma phase and try to identify interaction mechanisms between etching agents and surface.

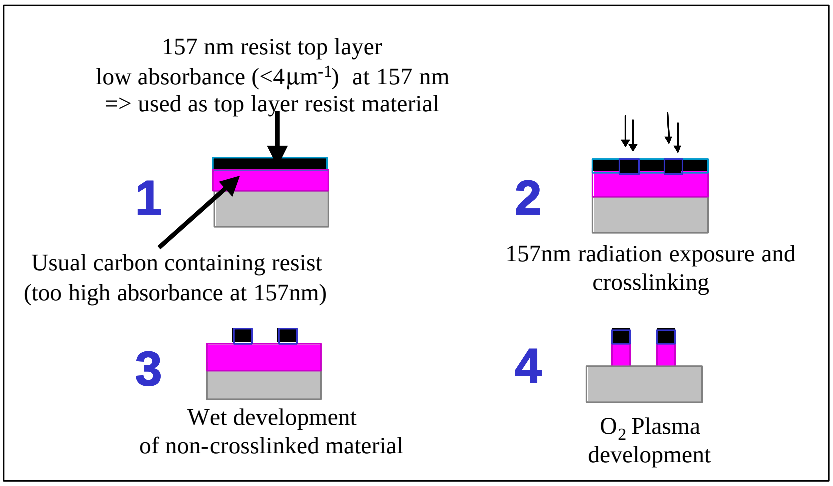

Figure 1: The bilayer resist scheme

2. Materials

In a first attempt, we used PolyDiMethylSiloxane (PDMS) and PolyMethylSilsesQuioxane (PMSQ) as silicon containing polymer (figure 2). These materials exhibit a negative tone behaviour. Then, we started to study other materials allowing positive tone behaviour: within the present European program a novel and very promising class of copolymers have been developed for the bilayer resist scheme [1-2].

They consist of a silicon-based inorganic cage (Si_8O_{12}, Polyhedral oligomeric silsesquioxanes monomer, POSS, figure 2) surrounded by eight organic corner groups. This monomer is associated with reactive polymerizable organic groups (TBMA, MA, IA, figure 2). The silicon cage provides etch resistance to oxygen plasmas and ensure a low absorbance at 157 nm while the organic monomers offer desirable resist requirements (positive tone behaviour…) (figure 2 and table 1).

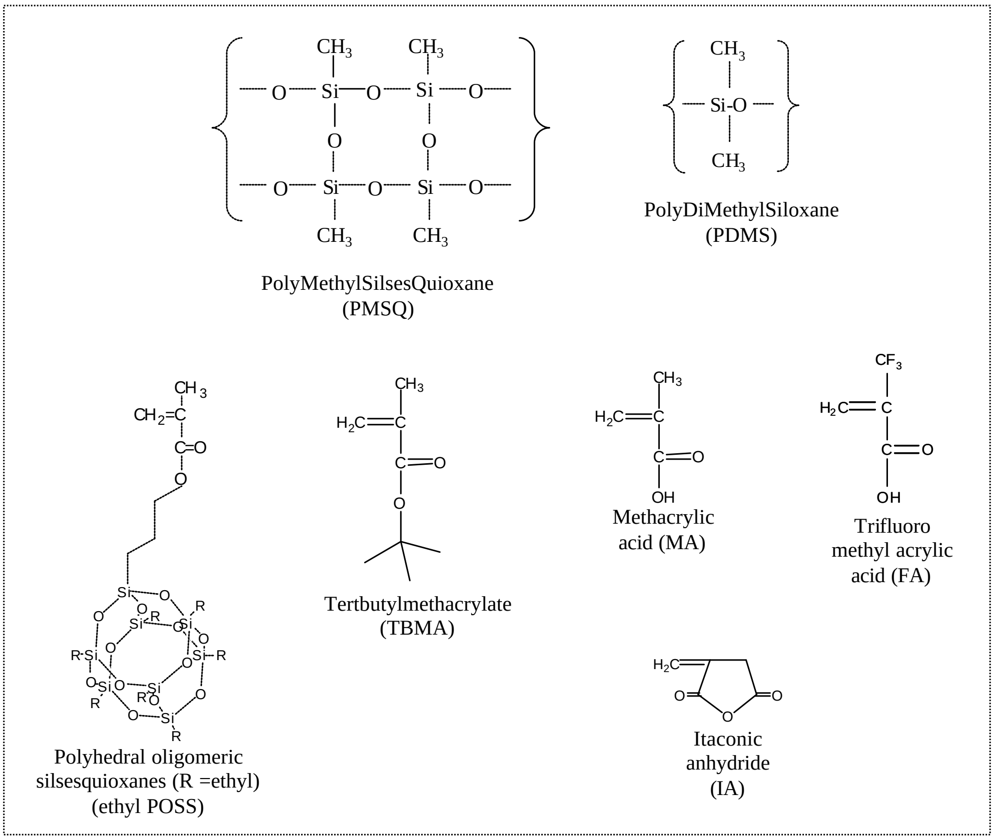

PolyMethylSilsesQuioxane
(PMSQ)

PolyDiMethylSiloxane
(PDMS)

Polyhedral oligomeric
silsesquioxanes (R =ethyl)
(ethyl POSS)

Tertbutylmethacrylate
(TBMA)

Methacrylic
acid (MA)

Trifluoro
methyl acrylic
acid (FA)

Itaconic
anhydride
(IA)

Figure 2: Materials studied: PDMS, PMSQ and POSS based copolymers including TBMA, MA, IA and FA.

Name	S1	S2	S3	S4	S5	S6	S7	S8
<u>Weight percentage</u>:								
POSS	100	60	40	30	20	40	30	30
TBMA	0	40	60	50	80	40	40	40
MA	0	0	0	20	0	20	10	0
IA	0	0	0	0	0	0	20	0
FA	0	0	0	0	0	0	0	30

Table 1: Chemical composition of the different copolymers studied

3. Experiments

Etching is made in a ICP reactor composed of a quartz dome (180 mm diameter) surrounded by a circular antenna connected to a 13.56 MHz generator. A substrate holder is placed at the bottom of the diffusion chamber (200 mm height). The wafer can be RF biased (13.56 MHz) independently from the source power and its temperature is controlled by cooling the sample holder at 20°C using a cryostat (HUBERT unistat 385) and helium circulation. Etching is made under a pressure of 10 mTorr (1.33 Pa), for a flow rate of 40 sccm, a source power of 800 W and different bias power leading to 0V, -50V or -100V DC bias.

Resist thickness versus etching time is measured by in-situ multi-wavelength ellipsometry (Woolam M88). Etch rates and selectivity are deduced from these measurements. XPS (Leybold LH11) is used to determine surface chemical composition before and after plasma exposure. Etch mechanisms are investigated combining ellipsometry and quasi in-situ XPS.

4. Results

4.1. PDMS and PMSQ etching

Thickness versus etching time is presented in figure 3 for PDMS (results are identical for PMSQ). We observe a very fast etching during the first seconds followed by a slower etching. XPS has been used to understand plasma surface interaction during these two phases. We have shown [3-4] that during the first seconds, oxygen atoms coming from the plasma etch carbon and hydrogen atoms of the surface. This leads to the very fast etching observed during the first seconds. The PDMS surface is rapidly converted into a silicon oxide like surface that is etch resistant in oxygen plasma. This leads to the slow etching observed during the second phase (figure 3). For -100 V DC bias the etch rate during this second phase is 7 nm/min and is controlled by the silicon oxide sputtering by oxygen ions. For 0 V DC bias, the etch rate drops to 0.3 nm/min during the second phase. Such a weak variation of thickness versus time is most probably due to a densification of the material rather than to a real etching. Indeed, ion energy (V_p-V_f is about 15 V) is too low to induce sputtering of silicon oxide like material. Oxygen atoms diffuse through the silicon oxide like top layer, etch carbon and hydrogen atoms and lead to oxidation, densification and a to low thickness loss.

On what concerned selectivity with respect to usual carbon containing resist (AZ Novolac 5214), results are very encouraging since selectivity as high as 90 and 157 are reached for respectively PDMS and PMSQ with -100 V DC bias.

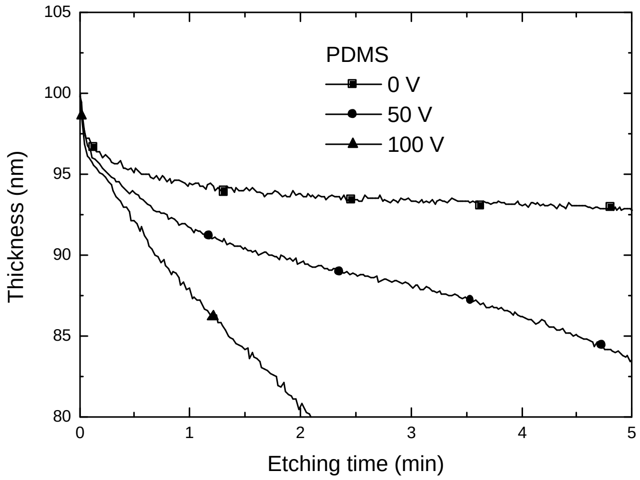

Figure 3: Thickness versus etching time for PDMS. O_2 plasma, 800 W, 40 sccm, 10 mTorr.

4.2. POSS containing copolymers etching

We investigated several materials containing various amount of POSS monomer (see table 1). POSS containing copolymers have been synthesised at IMEL (Athens) [1-2]. Some of the copolymers synthesised have presented unusual bad wet development and we have suspected them to develop a surface segregation of the POSS molecule. As surface segregation could have a great impact on etching mechanisms, we analysed POSS containing copolymers before etching by XPS to investigate this point. This is the aim of the first paragraph.

i) XPS analysis before etching

If POSS molecules reside preferentially at or close to the surface, the surface chemical composition and structure should be different from the average chemical composition and structure of the material. Particularly, the Si-C and Si-O bond percentages should be higher than expected since Si atoms are present only in the POSS molecule. In a similar way silicon atomic percentage should be higher and the C=O bond percentage should be lower than expected. Si-C, Si-O, C=O and Si percentages were determined from XPS spectra. Table 1 summarizes results obtained. We indicate the difference between the measured percentage (labelled “meas”) and the expected one (labelled “th”). The first column give results for the pure POSS monomer (sample S1) for which no surface segregation is expected. One can see that differences do not exceed 1%. On the contrary, for POSS-containing copolymers, the measured Si, Si-C and Si-O percentages are systematically higher than expected ones. For example, for sample S5 (20/80/0), we can see that the measured silicon concentration exceeds the expected one (the concentration without surface segregation) by more than 6%, and the carbon to silicon and oxygen to silicon bond percentages exceeds the expected ones by about 13 and 35 % while the C=O double bond percentage is 18% lower than expected from a copolymer without surface segregation.

Copolymer composition: POSS/TBMA/MA weight percentages	100/0/0 (S1)	60/40/0 (S2)	40/60/0 (S3)	30/50/20 (S4)	20/80/0 (S5)	40/40/20 (S6)
$\%(Si)_{meas} - \%(Si)_{th}$	1.3	3.6	4.1	1.1	6.3	3.2
$\%(C\text{-}Si)_{meas} - \%(C\text{-}Si)_{th}$	-1.1	4.9	12.4	12.5	13.5	19.9
$\%(O\text{-}Si)_{meas} - \%(O\text{-}Si)_{th}$	-0.01	15.7	31.1	21.2	35.7	21.2
$\%(C{=}O)_{meas} - \%(C{=}O)_{th}$	-0.04	-7.8	-15.5	-10.6	-17.9	-10.6

Table 2: Difference between measured percentages by XPS (meas) and calculated ones from the chemical structure of the copolymer (th), for different copolymers (POSS/TBMA/MA, see figure 2). For C-Si, O-Si and C=O, the measured percentage is the ratio of the C-Si, O-Si or C=O component area over the whole peak area, respectively C1s, O1s and C1s.

XPS analysis of the copolymers before etching clearly shows that the POSS molecules reside preferentially on the surface and point out a surface segregation phenomenon [5]. To determine if POSS molecules aggregate on surface forming islands or an homogeneous layer we used AFM in phase mode. No difference of contrast was observed on the surface. Our interpretation is that POSS molecules aggregate forming an (almost) homogeneous layer. Moreover, as the carbon etch rate under oxygen plasma is much larger than the silicon etch rate, an island like aggregation phenomenon should lead to a very rough surface after oxygen etching (almost no etching of islands and fast etching of carbon containing monomers). On the contrary, very smooth surfaces (rms < 1 nm) are observed by AFM after etching.

We expect the surface segregation phenomenon to modify considerably the nature of the interaction between the plasma and the surface. Indeed, the composition of the material to etch is closer to PMSQ than it should be.

ii) Etch rates, selectivity and etch mechanisms

POSS copolymer etching rates versus etching time present a two slopes behaviour in oxygen plasmas (figure 4). During the first seconds of the plasma a fast etch rate is observed, then the etch rate goes slower. The etch rate during first seconds is almost the same whatever the POSS percentage in the copolymer. However, the duration of this first phase increases with decreasing the POSS percentage.

For POSS rich materials (> 40%), we can imagine that the phenomenon observed is almost the same as was observed for PDMS and PMSQ. Oxygen atoms etch carbon and hydrogen atoms, allow bonding between the polyhedral silsesquioxanes groups, and by ending the work started by surface segregation convert the top surface into a SiO_x like layer. This process is of course faster if the surface initially contains a lot of silicon oxide cages (high POSS percentage). The SiO_x layer is etch resistant in oxygen plasmas and acts as a protective layer. As the top copolymer layer becomes etch resistant, the etch rate decreases and the selectivity versus AZ 5214 reaches high values, from 27 (20% POSS) to 390 (100% POSS) for -100 V DC bias.

We have performed XPS measurements after 10 seconds etching. For all materials, XPS analysis reveals an oxidation of the surface; silicon and oxygen percentages increase and carbon percentage decreases.

As was explained before, because of surface segregation, materials containing a high percentage of POSS molecules present a surface “similar” to PDMS and PMSQ. Hence, for theses materials, etch mechanisms are most probably close to those of PDMS and PMSQ. The etch rate is controlled by ion sputtering for -100 V DC bias and by diffusion, oxidation and densification for 0 V DC bias. Concerning low POSS percentage materials, more studies are needed to understand the etch mechanisms

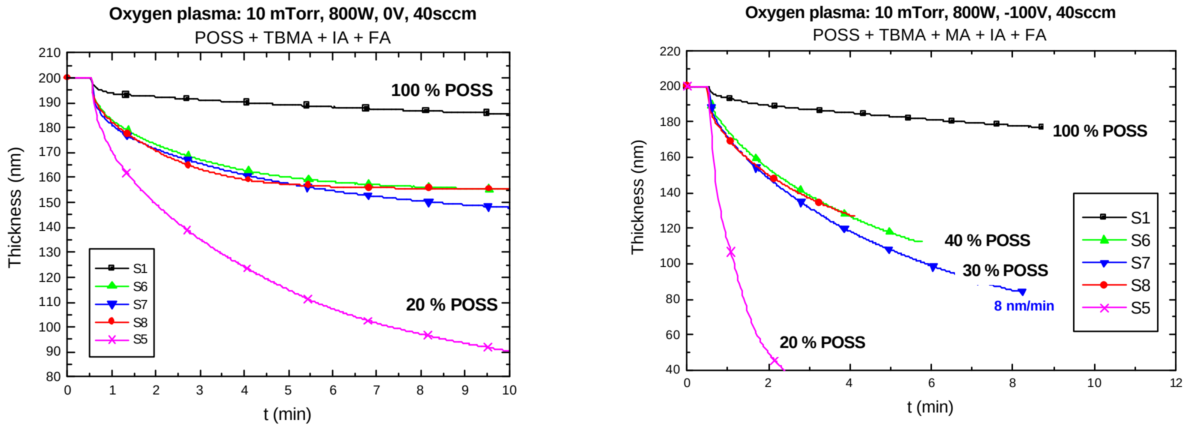

Figure 4: Thickness versus etching time for different POSS containing copolymers. O_2 plasma, 800 W, 40 sccm, 10 mTorr, 0 V DC bias (on the left), -100 V DC bias (on the right)

5. Conclusion

We investigated etching of silicon containing polymers in oxygen plasmas. We shown that these materials are suitable for a bilayer resist scheme; they present a low etch rate and a high selectivity with respect to carbon containing resist in oxygen plasmas.

Furthermore we tried to understand etching mechanisms of these polymers using quasi in-situ XPS and in-situ ellipsometry. We shown that during the first seconds of oxygen plasma, a silicon oxide like layer is formed onto PolyDiMethylSiloxane (PDMS) and PolyMethylSilsesQuioxane (PMSQ) polymers. This layer is etch resistant in oxygen plasma and acts as a protective layer. We also investigated a novel class of copolymers based on the POSS monomer (Si_8O_{12}, Polyhedral oligomeric silsesquioxanes). We shown that etching mechanisms are very similar to those obtained for PDMS and PMSQ for copolymers with high percentage of POSS molecules. More studies are needed to determine etch mechanisms for low POSS percentage materials.

6. Acknowledgments

We wish to thank the European Community Program IST for supporting this work under the project 157 CRISPIES (IST n° 2000-30143).

7. References

[1] V. Bellas, E. Tegou, I. Raptis, E. Gogolides, P. Argitis, H. Iatrou, N. Hadjichristidis , E. Sarantopoulou, A.C. Cefalas, J. Vac. Sci. Technol. B, to appear.

[2] E. Gogolides, E. Tegou, N. Vourdas, V. Bellas, O. Brani, P. Argitis, A. Tserepi, D. Eon, G. Cartry, C. Cardinaud, this conference ISPC-**509**.

[3] A. Tserepi, G. Cordoyiannis, G.P. Patsis, V. Constantoudis, E. Gogolides, E.S. Valamontes, D. Eon, M.C. Peignon, G. Cartry, Ch. Cardinaud, and G. Turban, J. Vac. Sci. Technol. B, **21**, 174 (2003).

[4] D. Eon, L. de Poucques, M.C. Peignon, Ch. Cardinaud, A. Tserepi, G. Cordoyiannis, E.S. Valamontes, I. Raptis, E. Gogolides., Microelectrical Engineering, **61-62,** 901 (2002).

[5] D. Eon et al, to be submitted to J. Vac. Sci. Technol. B

Low-k etching in high density fluorocarbon plasmas

V. Raballand, D. Eon, G. Cartry, M-C. Peignon- Fernandez, Ch. Cardinaud

LPCM-IMN, Université de Nantes, 2 rue de la Houssinière, BP 32229, 44322 Nantes cedex 03, France

Abstract

This work concerns etching of low-k materials (SiOC and porous SiOC) in high density fluorocarbon plasmas. Such materials may be used as interlevel dielectric in integrated circuits. In this aim, high etch rates are needed and high selectivity with respect to the etch stop layer made of SiC is required. Etch rates and selectivity are measured by in-situ ellipsometry while etch mechanisms are investigated combining ellipsometry, quasi in-situ XPS and plasma diagnostics.

1. Introduction

At present, performance in integrated circuit (IC) are no longer limited by feature size, which approach 0.1µm and beyond, but by the increase of interconnection delay. Signals through metal interconnects are delayed by the resistance R of the metal lines and the capacitance C between adjacent lines. To optimize IC devices, interconnection delay must inevitably be reduced. One solution is to diminish the parasitic capacitance between levels by replacing SiO_2 (k=4.5) conventional interlevel dielectric by a low dielectric constant material (low-k). Methylsilsesquioxane polymers (SiOC) are candidate materials to replace SiO_2 as interlevel dielectric. However, the global dielectric constant is also affected by the permittivity of the etch stop layer. For this reason, amorphous hydrogenated silicon carbide (SiC) materials are used as etch stop layer instead of the standard SiN (k=7) [1].

Our laboratory is concerned with the etching of the low-k materials SiOC (k=2.9) and SiOC with 40% of porosity (k=2.2) and by the etching of the etch stop layer SiC (k=4.5). The etch selectivity of the low-k with respect to SiC is an important criterion to obtain. Furthermore, one must ensure that the etching does not adversely affect the dielectric constant of the films. To satisfy these properties, etching mechanisms are studied in details.

The etch is performed with fluorocarbon gases, since they have proven to be very successful in the etch of conventional SiO_2 [2-4]. We used a 13.56 MHz Inductively Coupled Plasma (ICP) source, consisting of a quartz dome with an external loop antenna surrounding a diffusion chamber. The substrate can be biased with a second RF generator providing 600W. Low-k etch rates have been measured in real time by in-situ multi-wavelength ellipsometry. Surface composition and modification are then analyzed by quasi in-situ X-ray Photoelectron Spectroscopy. Plasma analysis are also performed with optical emission spectroscopy.

2. Results

The present work is focused on the effect of the process parameters on the etching of SiOC and porous SiOC and on their selectivity with respect to the SiC etch stop layer. Our main aim is to identify and understand the etch mechanisms.

First, the etch rates of SiOC, porous SiOC, and SiC are measured in C_2F_6 plasma, 800W, 10mTorr for various bias voltage (figure 1). The etching starts at about 20V and the etch rate of the three materials are increasing with the bias voltage. Selectivity of SiOC or porous SiOC with respect to SiC is also calculated (figure 2). The selectivity of porous SiOC with respect to SiOC is close to 1.4 for bias voltage superior to 200V, which approximately corresponds to the two material densities ratio ($\rho_{SiOC}/\rho_{porous\ SiOC} = 1.3 /0.8 = 1.6$). Thus, the higher etch rate of porous SiOC compared to the one of SiOC is simply due to the lower density of porous SiOC. The two materials present the same evolution of etch rate and selectivity. So, in the following, we focus mainly on SiOC.

The selectivity of SiOC with respect to SiC is almost constant and equal to 1.8, which also corresponds to the material densities ratio (ρ_{SiC}= 2 g.cm^{-3}). Thus, better plasma conditions have to be found to improve selectivity. In this aim, mixtures of C_2F_6 with different percentage of hydrogen, argon or oxygen are studied. SiOC and SiC etch rates are shown respectively in figure 3 and figure 4, and the selectivity of SiOC with respect to SiC is presented in figure 5. One can see that oxygen addition leads to an increase of the etch rate for less than 50% of oxygen and a decrease beyond. However, selectivity remains almost constant (S=2). Adding argon to C_2F_6 keeps etch rate and the selectivity constant. The best selectivity is obtained by addition of hydrogen but unfortunately this improvement comes with a decrease of the low-k material etch rate.

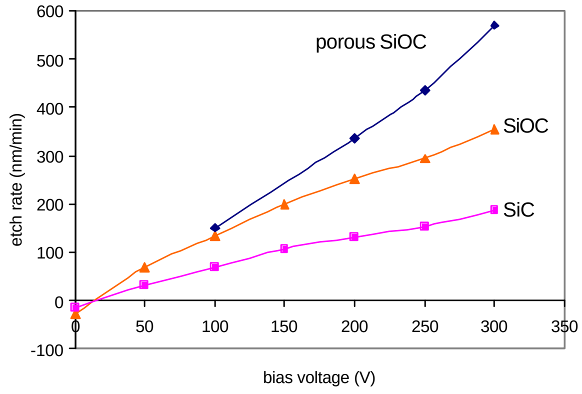

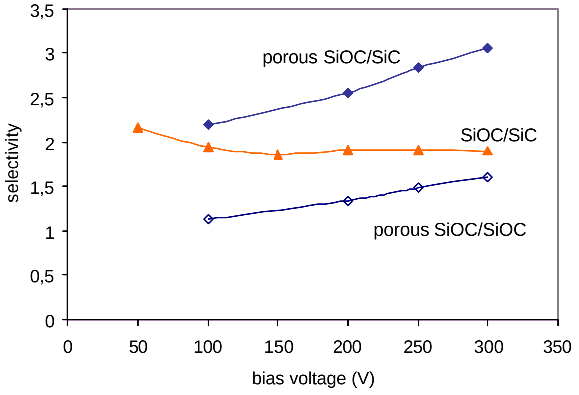

Figure 1:Etch rate versus bias voltage in C_2F_6 plasma 800W 40sccm 10mTorr

Figure 2: Selectivity versus bias voltage in C_2F_6 plasma 800W 40sccm 10mTorr

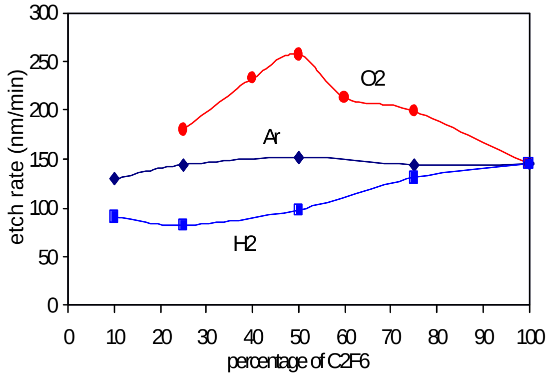

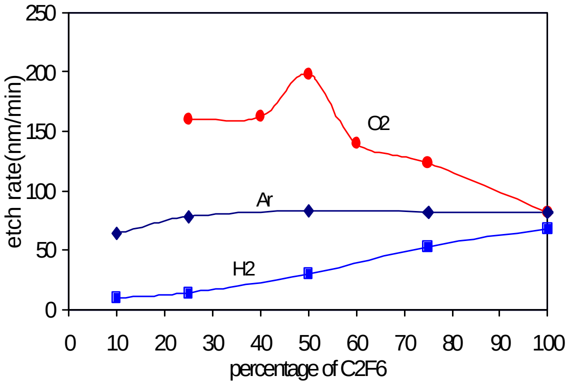

Figure 3: SiOC etch rate versus C_2F_6 percentage in C_2F_6 mixtures with O_2, Ar, or H_2 800W 10mTorr 40sccm -100V

Figure 4: SiC etch rate versus C_2F_6 percentage in C_2F_6 mixtures with O_2, Ar, or H_2 800W 10mTorr 40sccm -100V

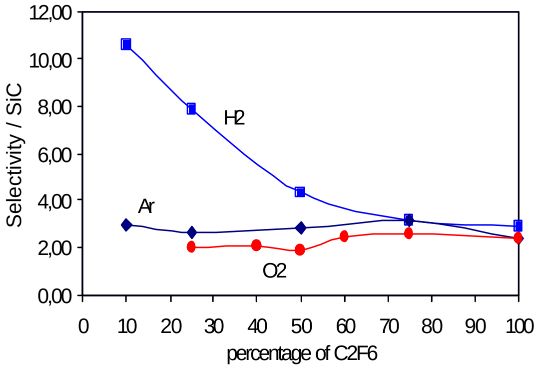

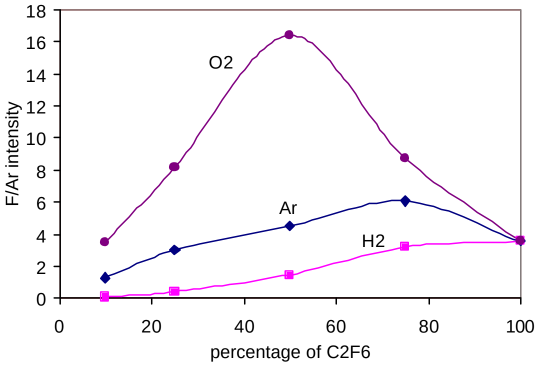

Figure 5:SiOC/SiC selectivity versus C_2F_6 percentage in C_2F_6 mixtures with O_2, Ar, or H_2 800W 10mTorr 40sccm -100V

Figure 6: Evolution of fluorine intensity versus C_2F_6 percentage in C_2F_6 mixtures with O_2, Ar, or H_2 800W 10mTorr 40sccm

Etch rates and selectivity for this kind of materials are mainly controlled by three parameters [3-4]: the ion flux, the neutral flux, and the passivation layer onto surfaces. The ion flux brings energy on surface to break bonds. Then, impinging ions and neutrals can form volatile compounds with surface atoms leading to etching, or can form a passivation layer deposited onto the surface. The passivation layer usually protect more or less the surface from etching. A fluorine rich layer will favour etching while a carbon rich layer will block etching. As the passivation layer composition can be different for two materials (SiOC and SiC for example), the passivation layer influences strongly etching and more precisely etching selectivity. Therefore, in order to analyse etch mechanisms, these three parameters (ion flux, neutral flux and passivation layer thickness and composition on all materials) should be measured.

To obtain the neutral flux, and especially the fluorine flux, analysis of the plasma by optical emission spectroscopy are performed. The behaviour of the normalized atomic fluorine line (normalisation with argon) is followed and shown in figure 6. One can see that the fluorine to argon ratio shows a peak for the mixture C_2F_6/O_2 (50%/50%). This maximum fluorine concentration may explain the higher etch rates obtained for the mixture C_2F_6/O_2 (50%/50%). To check this hypothesis, the surface composition of SiOC is investigated. X-ray Photoelectron Spectroscopy (XPS) points out the absence of a fluorocarbon layer on SiOC. This tends to confirm the better etch rates obtained with oxygen than those with argon or hydrogen and the weaker value of selectivity. However, the evolution of the ion flux is needed to fully understand the etching mechanisms in C_2F_6/O_2 mixtures.

Adding argon to C_2F_6 leads to the decrease of the fluorine concentration in the plasma because of the dilution of C_2F_6. This should decrease the etch rate. However, decreasing the percentage of C_2F_6 leads to an increase of the ion flux, because of a higher electronic density in argon plasma than in fluorocarbon plasmas [5]. This stronger ion flux should increase the etch rates. The opposite influence of these two parameters may lead to the almost constant etch rates observed (figure 3 and 4).

The atomic fluorine concentration is less important in C_2F_6/H_2 plasma than in C_2F_6/Ar plasma. Hydrogen reduces the fluorine abundance in the plasma, probably by forming HF [3]. Furthermore, the carbon XPS peak indicates the presence of a fluorocarbon layer on SiC and SiOC after C_2F_6/H_2 and C_2F_6/Ar plasma. Figure 7 presents etch rate variations versus carbon percentage in the fluorocarbon layer, for C_2F_6/H_2 and C_2F_6/Ar plasma. As expected, etch rate decreases linearly with the increase of the carbon percentage in the fluorocarbon layer. So, adding H_2 to C_2F_6 leads to a decrease of the etch rates because of a decrease of the fluorine flux and because of passivation layers containing a higher percentage of carbon.

According to these results, we study thoroughly the C_2F_6/H_2 (25%/75%) mixture. Figure 8 presents SiOC etch rate and the normalized fluorine emission line versus the flow rate. Etch rates noticeably decrease as the flow rate increases whereas the fluorine emission increases. To understand these evolutions, that seem contradictory, further analysis have to be made. Mass spectrometer analysis are presently carried out in order to better correlate plasma diagnostics and surface analysis.

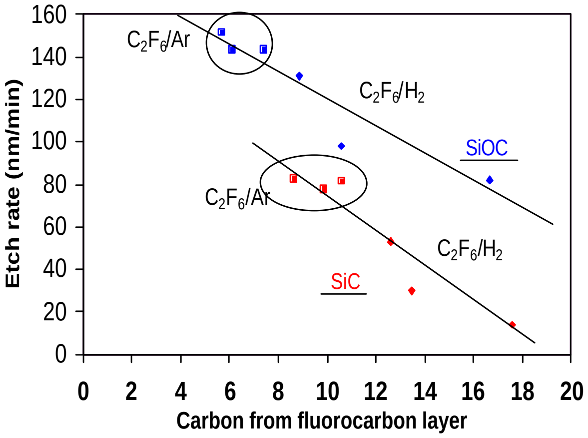

Figure 7: SiOC and SiC etch rates versus carbon percentage in the fluorocarbon layer for various mixtures of C_2F_6/Ar and C_2F_6/H_2 800W 10mTorr 40sccm -200V

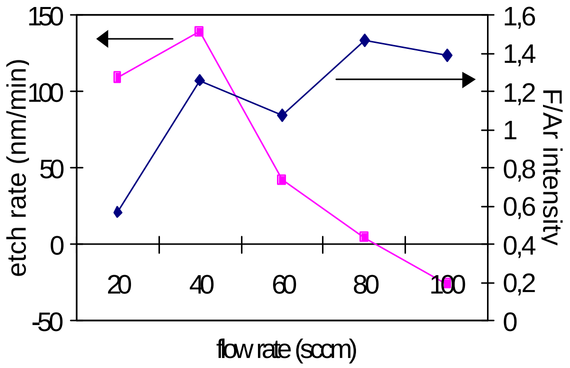

Figure 8: SiOC etch rate and fluorine intensity versus flow rate in C_2F_6/H_2 (25%/75%) plasma 800W 10mTorr (-200V)

Finally, etching have to do not affect the dielectric constant of the films. An important change in the dielectric constant value should be correlated with a bulk modification of the material. FTIR measurements have been performed in order to check that etching do not affect the material. Figure 9 presents the SiOC infra-red spectra before and after etching. No clear modification of the material is seen. So, we assume that the dielectric constant is almost not affected by fluorocarbon etching. This conclusion have to be verified.

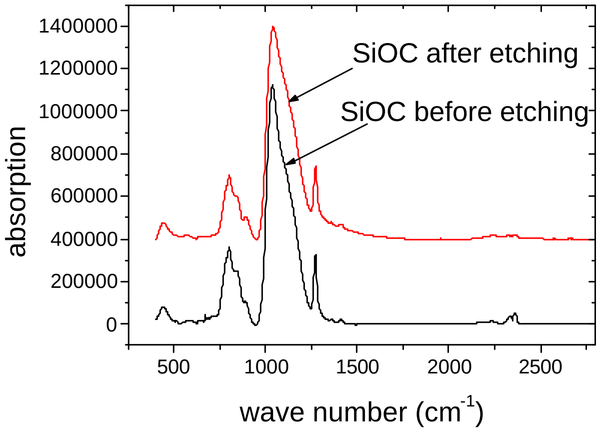

Figure 9 : SiOC FTIR spectra before etching and after etching in C_2F_6/H_2 (25%/75%) plasma, 800W, 40sccm, 10mTorr.

3. Conclusion

We studied etching of low-k materials in high density fluorocarbon plasmas. Particularly, we paid attention to the influence of the process parameters on SiOC, porous SiOC and SiC etch rates and selectivity. Etch rates increase with bias voltage up to 600 nm/min for SiOC in C_2F_6 plasmas, while selectivity (SiOC/SiC and porous SiOC/SiC) remains quite low (<2) . Mixtures of C_2F_6 with oxygen, argon, and hydrogen have been studied. The C_2F_6/O_2 (50%/50%) plasma, give the best etch rate but the lowest selectivity. Adding argon to C_2F_6 does not modify either etch rate or selectivity. On the contrary, selectivity increases up to 10 with addition of hydrogen but at the same time, the etch rate decreases. To understand these evolutions, we measured fluorine concentration by optical emission and passivation layer composition by XPS. A high atomic fluorine concentration in C_2F_6/O_2 (50%/50%) is well correlated with the largest etch rates obtained. A more important fluorocarbon layer on SiC than on SiOC explained the better selectivity observed with hydrogen.

4. References

[1] R. A. Donaton, et al. – Microelectron. Eng. **55**, 277 (2001)

[2] T. E. F. M. Standaert, P. J. Matsuo, S. D. Allen, G. S. Oehrlein, T. J. Dalton – J. Vac. Sci. Technol. A **17**, 741 (1999)

[3] F. Gaboriau, PhD thesis, Nantes University, France (2001), *in french*

[4] F. Gaboriau, G. Cartry, M.C Peignon and Ch. Cardinaud, J. Vac. Sci. Technol. B, **20**, 1514 (2002)

[5] Gaboriau F., Peignon M.C., Cartry G., Rolland L., Eon D., Cardinaud Ch. and Turban G., J. Vac. Sci. Technol. A **20-3**, 919-927 (2002)

Arc Discharge in Water as a Source of Carbon Nanostructures

H. Lange, A. Huczko, M. Sioda and M. Bystrzejewski

Department of Chemistry, University of Warsaw, Warsaw, Poland

Abstract

Carbon nanostructures (onions, nanotubes and encapsulates) were generated by arc discharge in water between pure and catalyst-doped graphite electrodes. The obtained structures were of fine crystalline morphology, similar to those formed in He arc plasma. Emission spectroscopy was performed to assess the plasma components (H, O, C and C_2) and temperatures. C_2 radicals were determined quantitatively, between 10^{15} and 10^{16} cm^{-2} depending on graphite anode composition. The temperature was between 4000 and 6500 K.

1. Introduction

Since the discoveries of the novel carbon nanostructures the study of high current carbon arc discharge has become of interest because it appeared to be the most efficient source of fullerenes and nanotubes [1, 2]. Synthesis of fullerenes and other carbon nanostructures are routinely carried out in a helium arc plasma. Discharges in liquid media were also investigated as a route to carbon nanomaterials: e.g., fullerenes in toluene or benzene [3], carbon nanotubes (CNTs) in aromatic hydrocarbons.

Hsin *et al.* [4] reported the first low-temperature, solution-phase production of CNTs in water. Sano et al. [5] described the large scale formation of carbon nano-onions using relatively low discharge currents (30 A), the graphite electrodes being submerged in deionized water. Their study showed that the resulting nanoparticles, floating on the water surface, consisted of C_{60} cores wrapped in graphenes (*ca.* 7-15 layers, *ca.* 25-30 nm diameter). Under similar discharge conditions Zhu et. al. [6] investigated the formation of CNTs using also salt solutions as the medium. The authors obtained nanotube-rich material.

High yield, large-scale, and cost-efficient approaches to such nanostructures should not only boost fundamental research but will also foster industrial applications, eg. lubrication technology. Therefore, it is of interest to carry out detailed studies of the carbon arc discharge process in water. First, we focused our attention on the plasma process identifying intermediate species and determining the plasma temperature. Second, we tried to establish the selectivity of this process in nanomaterial generation, i.e. which types of nanostructure would form concurrently during the bulk production of carbon nano-onions. Pure graphite electrodes, as well as Y–, Gd–, Ce–, Co/Ni–, Fe– and B-doped, were employed. These dopants play a critical catalytic role in CNTs formation [7].

2. Experimental

The anode and cathode (6 mm diam.) were immersed to a depth of *ca.* 3 cm in deionized water (1 dm^3) contained in a transparent glass vessel. The electrodes were aligned horizontally. The brass electrode holders were free to move, forward and backward, which enabled proper electrode gap adjustment to be made during the arc discharge. The discharge in water (Fig. 1) is rather unstable and it is critical to control precisely the arc gap in order to run the arc continuously. The electrode gap was maintained at *ca.* < 0.7 mm. We used a digital controllable power supply with constant voltage output equal to 90 V. Optimum arc performance was achieved at current of 40 A with voltage drop between 21 – 30 V.

The erosion rates of the doped electrodes, consisting of 0.6 - 0.8 at % of catalysts, was higher comparing to the pure graphite anodes. The respective values are given in the Table 1.

During discharge, the spectroscopic features of the plasma emission were monitored optically using a ST8 CCD camera coupled to a high-resolution spectrograph, in order to identify the atomic lines and molecular bands. Considering the quantitative diagnostics, such a task in the case of the arc discharge in water is rather a very difficult one because of high arc fluctuation, small arc gap, and progressing decrease of water transparency caused by carbon particles dispersed in water. Therefore, the information characterizing the plasma was inferred only from C_2 radical radiation which is mainly associated with the Swan band system d $^3\Pi_g \rightarrow$ a $^3\Pi_u$. The emission band 0-0 (516.5 nm) was used for temperature assessment and contribution of carbon in the plasma phase evaluation. The C_2 contents was determined applying the method based on the

Fig. 1. Arc discharge in water.

phenomenon of self-absorption which highly influences the intensity of the band head with respect to the intensity of the non-overlapped rotational components. It is clearly seen in Fig. 2 showing the 0-0 band emitted by the arc discharge in helium between pure graphite electrodes (A) and in water with Y–doped graphite anode (B).

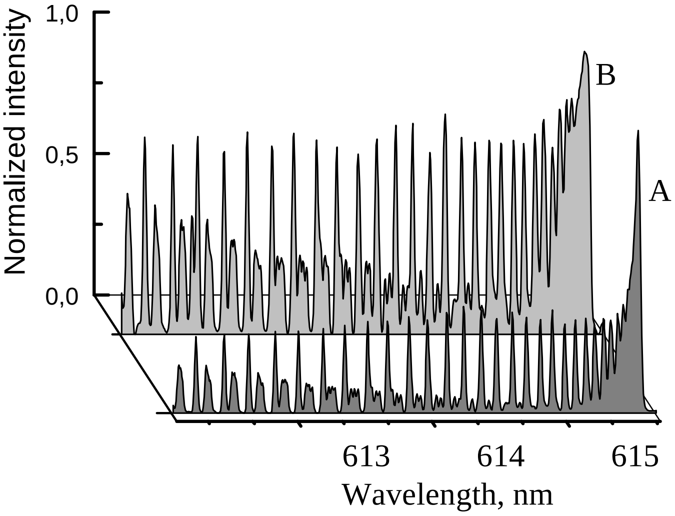

Fig. 2. Profiles of C_2(d-a, 0-0) emission band under low and high self-absorption.
A – arc discharge in He, anode: graphite. B – arc discharge in water, anode: graphite + 0.8 at% Y.

For the sake of comparison a reference test was carried out in He under atmospheric pressure and the same arc discharge current (40 A). The plasma diagnostic procedure was described earlier [8].

The products were analyzed using scanning and transmission electron microscopy (ultra high resolution field-emission SEM, Leo 1530 and HRTEM JEOL 3010).

3. Results and discussion

3.1 Plasma spectroscopy

The arc discharge in water is similar to some extent to that of a carbon arc discharge in He. The strongest radiation is still associated with C_2 radicals (d $^3\Pi_g \rightarrow$ a $^3\Pi_u$, e.g., 516.5 nm), carbon atoms and ions. However, the presence of atomic hydrogen, *e.g.*, H_α, and oxygen (e.g., 777.2, 777.4 and 777.5 nm) lines, appears to be a new feature. In the cases of doped electrodes, characteristic lines of metal admixtures are also readily detected. The bands associated with CH, OH and CO molecules could not be detected. Meanwhile, the discharge was accompanied by strong continuum radiation covering the visible and UV range.

Because of a continuous displacement of the arc in the electrode gap during discharge, light refraction and scattering, caused by bubbles dispersed in water (Fig. 1), the spectroscopic measurements were averaged across and along the arc channel, i.e., within *ca.* 6 and 1 mm, respectively. The arc operating parameters, electrode composition, erosion rate and average temperature and C_2 content (in the units of column density) values are given in Table 1.

Table 1 Operational parameters and plasma characteristics

Anode composition (at %)	Voltage [V]	Anode erosion rate [mg s^{-1}]	Average temperature [K]	C_2(a $^3\Pi_u$, v =0) column density nl [10^{15} cm^{-2}]
Arc discharge in He, p = 950 mb, i = 40 A				
C	21	> 0.3	4200	1.4
Arc discharge in water, p = 950 mb, i = 40 A				
C	26	1	5400	2.5
C/Co(0.6)-Ni(0.6)	28	6.5	5400	6.4
C/Ce(0.8)	26	6	5200	7.7
C/Y(0.8)	25	8	6400	14.7
C/Gd(0.8)	24	7	5000	15.4
C/Fe(0.7)	29	4	5600	5.2
C/B(1.0)	28	2,4	5000	2.1

The average plasma temperature in water was quite high, between 5000 - 6000 K. The temperature values were *ca.* 1500 K higher than for the discharge in He. Even at higher arc power input (> 2 kW) in He the temperatures are still a few hundreds degrees lower [9]. It is apparent that the higher plasma temperature in water results from the bubbles, which are small in number and volume, leading to high energy density. Meanwhile, reactions among carbon, oxygen and hydrogen are highly exothermic. Under atmospheric pressure, the degree of dissociation of water into atomic oxygen and hydrogen is higher than 99% at *ca.* 5000 K. Thus, the average plasma temperature in water is higher than in He. Table 1 reveals also that for pure and doped graphite anodes, C_2 contents are different. The erosion rate of pure graphite is much lower, thus the C_2 column density is lower than that of the doped electrodes. Generally, the amount of C_2 produced in water discharge, despite a relatively low current, is higher than that formed in the presence of He. Similar C_2 content in He was observed only at much higher arc current [9].

Two main factors influencing the C_2 density are the anode erosion rate and diffusion process. Since the plasma is surrounded by water, diffusion is limited within the bubbles volume and carbon species are trapped within the bubbles. Hence, the carbon vapor pressure in the plasma bubbles is higher than that in the He-carbon arc plasma where carbon species can expand freely.

3.2 Carbon nanostructures

The use of pure or doped anodes manifested itself not only in diverse anode erosion rates (Table 1) but also in different behavior with respect to the cathode deposit growth. For pure graphite the cathode surface was etched by active species e.g., such as H or O. However in the case of a doped electrode, a deposit grew on the cathode tip similar to the carbon arc discharge in He. Independent of the type of anode, a layer of soot appeared on the water surface but with different wettability properties.

The collected floating products were examined by SEM and HRTEM. The results in the case of pure graphite electrodes are shown in Fig. 3. Evidently the product contains carbon nano-onions (Fig. 3c), and it confirms the finding of the other authors [5]. However, additionally there is also large amount of multi-walled carbon nanotubes (Figs. 3a and 3b). These nanotubes are *ca.* 20-30 nm in diameter, and a few micrometers in length, with a *ca.* 0.34 nm layer separation, and exhibited no significant differences from those generated by arc discharge in He. Samples obtained from the bottom of the tank also contained many large carbon ball-shaped structures (*ca.* 1-5 µm diam.) and pieces of the starting material.

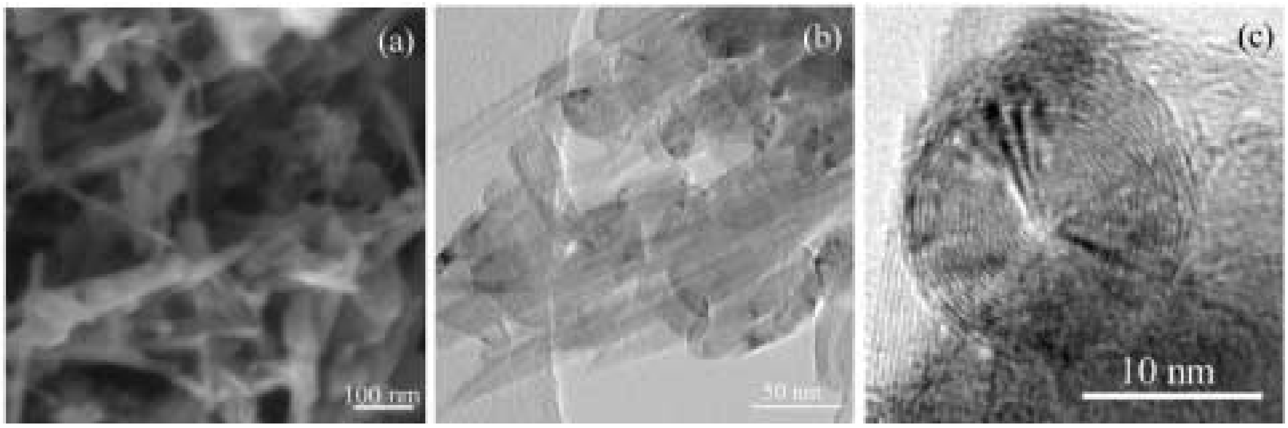

Fig. 3. SEM (a) and HRTEM (b and c) images of carbon nanostructure. Electrode: pure graphite.

When Gd-doped electrodes were used, various carbon structures were produced with high yields including the formation of many polygonal encapsulated crystals (Figs. 3b and 3c). Such encapsulations resemble the morphology of those produced in He arc discharge; they appear to be regular and to adopt the inner curvature of the carbon cages. The single crystal feature of the fillings has also been confirmed by TEM. Linear isolated NTs were found, some of which were fully or partly filled with catalyst.

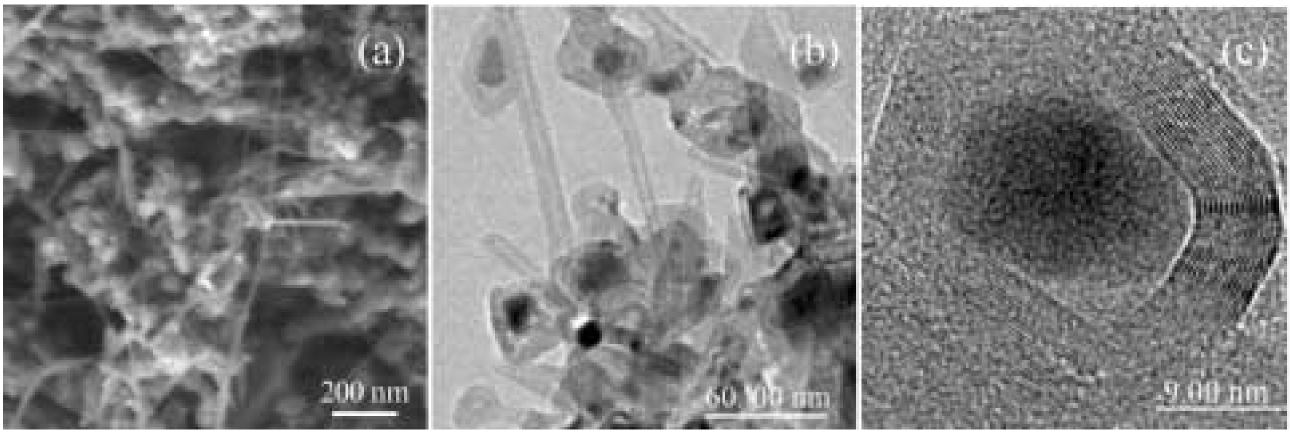

Fig. 4. SEM (a) and HRTEM (b and c) images of carbon nanostructures floating on water surface. Electrode composition: C + 0.8 at. % Gd.

Selected images of floating and cathode deposit products formed when Y–doped anode was arced in water are shown in Fig. 5. The percentage of filled structures is higher than that when Gd– doped electrodes were used. We found two types of carbon nanotube: (i) partly filled with Y or its carbide, usually partially defected; (ii) normal carbon arc nanotubes, hollow, straight, long and well crystallized, also accompanying with polyhedral particles. Fig. 5c shows a metal nanoparticle occupying ca. half of the cavity of a polyhedral carbon-shell.

The examples of SEM images of products obtained using other electrodes listed in Table 1 are shown in Fig. 6.

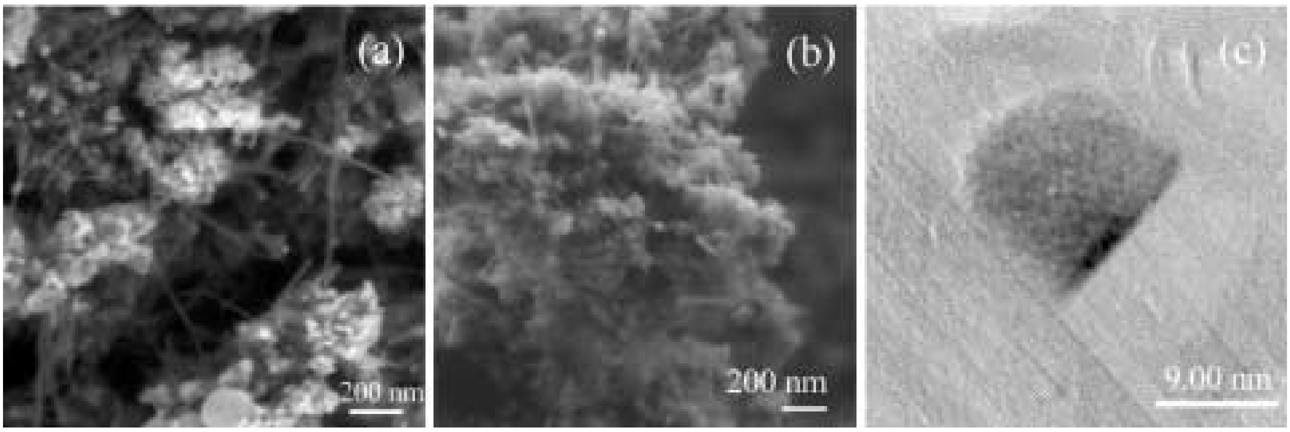

Fig. 5. SEM (a and b) and HRTEM (c) images of carbon nanostructures: Electrode composition: C + 0.8 at % Y.
(a) cathode deposit and (b and c) products floating on water surface.

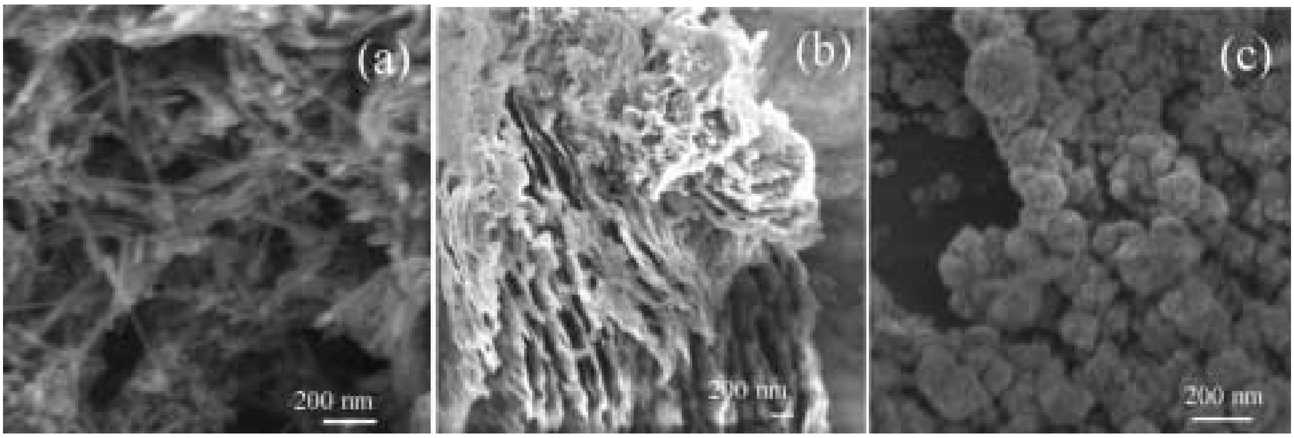

Fig. 6. SEM images of carbon nanostructures: Electrode composition:
C + 1 at% B, products collected from the bottom (a) and floating on water surface (b);
C + 0.6 at % Co + 0.6 at % Ni, floating products (c).

The elongated carbon nanostructeres which could be detected by SEM were only found when B–doped anode was used (Fig. 6a). The HRTEM analyses of solid products formed during arc sublimation of anodes doped with Ce, Ni–Co, Fe and B are under way.

Acknowledgment

The work was supported by the Committee for Scientific Research (KBN) through the Department of Chemistry, Warsaw University, under Grant No. 4 T08D 021 23.

References

1] W. Krätschmer, L. D. Lamb, K. Fostiropoulos and D. R. Huffman: Nature **347,** 354 (1990).
[2] S. Iijima: Nature **354** 56 (1991).
[3] M.T. Beck, Z. Dinya, S. Keki and L. Papp, Tetrahedron **49**, 285 (1993).
[4] Y.L. Hsin, K.C. Hwang, F.R. Chen and J.J. Kai, Adv. Mater. **13,** 830 (2001).
[5] N. Sano, H. Wang, M. Chhowalla, I. Alexandrou and G.A. J. Amaratunga, Nature **414,** 506 (2001**)**.
[6] H.W. Zhu, X.S. Li, B. Jiang, C.L. Xu, Y.F. Zhu, D.H. Wu and X.H. Chen. Chem. Phys. Lett. **366**, 664 (2002).
[7] C. Journet and P. Bernier, Appl. Phys. A **A67**, 1 (1998).
[8] H. Lange, K. Saidane, M. Razafinimanana ,A. Gleizes, J. Phys D: Appl. Phys. **32,** 1024 (1999).
[9] A. Huczko, H. Lange, T. Sogabe. J. Phys. Chem. A **104,** 10708 (2000).

A study of fluctuations in the dc cylindrical magnetron discharge using Langmuir probes

P. Kudrna[1,2], M. Holík[1,2], O. Bilyk[1], A. Marek[1], J.F. Behnke[2], E. Martines[3], M. Tichý[1,2]

[1] *Charles University in Prague, Faculty of Mathematics and Physics, Department of Electronics and Vacuum Physics,*
V Holešovičkách 2, 180 00 Prague, Czech Republic
[2] *University of Greifswald, Institute of Physics, Domstrasse 10a, 17487 Greifswald, Germany*
[3] *Consorzio RFX, Associazione Euratom-ENEA sulla Fusione, corso Stati Uniti 4, 35127 Padova, Italy*

Abstract

Floating potential fluctuations in the cylindrical magnetron DC discharge were characterized using the data from single and double cylindrical Langmuir probes positioned in the plane perpendicular to the discharge axis. The power density spectra were calculated from the experimental data in the range of magnetic fields 10 to 40 mT, pressures 1.5 to 7 Pa and discharge currents 100 and 200 mA. Spatial changes of plasma parameters with magnetic field and their correlation with observed fluctuations are also discussed.

1. Introduction

In many plasmatic systems stochastic fluctuations, i.e. stochastic changes of plasma parameters, have been experimentally detected. Among the most interesting systems we can cite the stationary plasma thrusters (SPT), where the fluctuations are supposed to aid the transport of electrons across the magnetic field, which is applied radially at the exit of the SPT [1]. So-called turbulence-driven charged particle transport across the magnetic field in the scrape-off layer in tokamaks is supposed to be a process of primary importance in the study of fusion plasmas since it influences plasma confinement by the magnetic field [2].

Cylindrical magnetrons are nowadays widely used as technological systems e.g. for creating thin films of superconductive or special magnetic properties. In the cylindrical magnetron the symmetry and homogeneity of the magnetic field simplifies both the theoretical and experimental investigations. In our previous experimental studies we already reported the presence of fluctuations of the plasma potential in our cylindrical magnetron system [3,4]. Fluctuations manifest as the unwanted noise added to the Langmuir probe floating potential when measuring with the floating probe and in the increased noise of the measured current when measuring the V-A probe characteristic. The amplitude of the floating potential fluctuations in our cylindrical magnetron system significantly increased when the magnetic field increased above the value of approximately 20 mT.

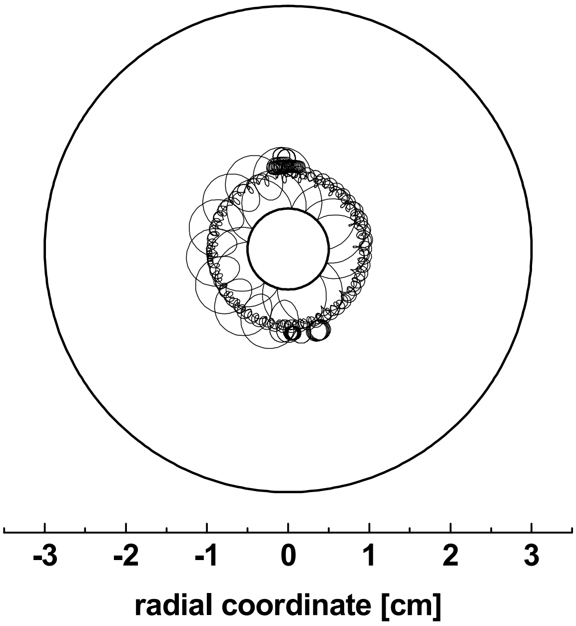

Figure 1. The typical trajectory of one electron in the DC discharge in cylindrical magnetron in argon for first 300 ns. Anode voltage U = 500 V, intensity of magnetic field B = 20 mT, the pressure of argon neutral gas p = 0.5 Pa. From [5].

In our former paper we performed Monte-Carlo simulations of radial charged particle transport in the ExB field of cylindrical magnetron [5]. In the model we did not include the effect of stochastic oscillations. The model clearly shows that at lower pressures the electrons from the cathode cannot reach the anode, see Figure 1, while in experiment at similar conditions the discharge burns (and stochastic oscillations are present). It is therefore very probable that also in DC discharge plasma in cylindrical magnetron the stochastic fluctuations help the transport of charged particles across the magnetic field. In this manner the research performed on a simple, small and cheap experimental magnetron system may be relevant for tokamak edge plasma research and in general for research on all fusion devices with magnetic confinement. Stochastic oscillations in a DC discharge plasma in planar magnetron have already been studied and the relevant experimental methods developed [6]. We applied these methods for the more detailed experimental study of the floating potential fluctuations in the DC discharge in cylindrical magnetron system in argon.

2. Experimental system

The cylindrical magnetron in the so-called post configuration of the DC discharge consists of cylindrical cathode mounted coaxially inside of the cylindrical anode. The discharge volume is axially limited by means of two disc-shaped limiters, which are connected to the cathode potential. In our device the diameters of the cathode and anode are 18 mm and 60 mm respectively. The length of the discharge volume is 300 mm. The homogeneous magnetic field is created by six coils and is parallel with the common axis of the system. To prevent overheating the coils and cathode, are water-cooled.

The system is constructed in high-vacuum technology. The pumping unit consists of the combination of the turbomolecular and rotary pumps. The ultimate pressure in the discharge vessel is in the order of 10^{-3} Pa. During the operation of the magnetron discharge the working gas, in this case argon slowly flows into the system and through the valve reducing the pumping speed of the pumps leaves the system. The typical flow rate is below 1 sccm and is adjusted by means of the MKS flow controller in order to keep the pressure in the discharge volume constant.

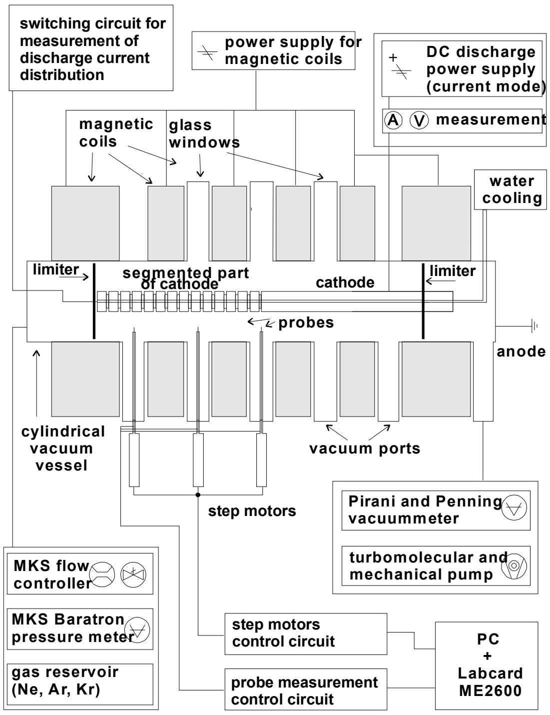

Figure 2. Schematic diagram of the cylindrical magnetron system.

The system is equipped with 5 ports for inserting the Langmuir probes, see Figure 2. Ports are distributed at the distances of 60 mm from each other in between the magnetic coils along the discharge vessel. The probes could be inserted radially through vacuum ports into the system. In the following figures we denote the probe in the middle of the discharge vessel length as probe 1 and the other two as probes 2 and 3 respectively. Apart from the three cylindrical probes, which were radially movable by means of stepping motors, we used also in one of the ports the double probe with two cylindrical tips separated by the distance Δx=1.6 mm. We used tungsten cylindrical probes with diameter 47 μm and length 2-4 mm.

3. Estimation of the power spectra

The Langmuir probes used for monitoring the floating potential were floating - did not have applied the bias voltage. The floating potential signal from the probes was sampled using the digital oscilloscope (Tektronix TDS 610) and samples h_n in 8-bit resolution were transferred to the computer over the GPIB interface:

$$h_n = h(n \cdot \Delta t), \tag{1}$$

where $h(t)$ is the probe voltage with respect to the anode, Δt is the sampling interval and integer n ranges from 0 to the number of samples N-1. Then the discrete Fourier transform of the sampled data was calculated by means of the FFT:

$$H_k = \sum_{n=0}^{N-1} h_n \exp \frac{-2\pi \mathrm{i} kn}{N}. \tag{2}$$

The guess of the Fourier transform of the voltage $h(t)$ at the discrete frequencies $k\Delta f$ is given by

$$H(k \cdot \Delta f) = \Delta t \cdot H_k, \tag{3}$$

where $\Delta f = 1/(N\Delta t)$. The power density is then

$$S(f) = \frac{1}{N\Delta t} \left| H(f) \right|^2. \tag{4}$$

In order to decrease the scatter of the calculated spectrum estimate several realizations (typically 100) were averaged into the resulting power density curve. The number of samples was limited by the amount of the oscilloscope memory to 50 000 samples, the sampling frequency was chosen to be 2.5 MHz.

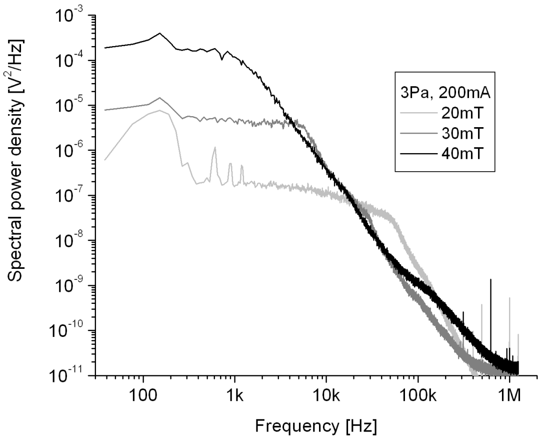

Figure 3. Example of power signal density spectrum with the magnetic field strength as parameter. Argon pressure 3 Pa, discharge current 200 mA.

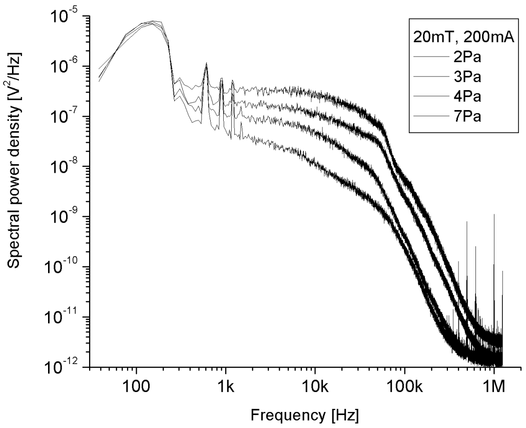

Figure 4. Power signal density spectrum changes with the argon pressure at fixed magnetic field of 20 mT and the discharge current of 200 mA.

Examples of the measured spectra are in the two figures above. Figure 3 shows the dependence of the measured power density spectrum on the magnetic field at the pressure of 3 Pa and the discharge current 200 mA. In the range up to several kHz there appears notable increase of the amplitude of fluctuations with increasing magnetic field. The peaks on the curve corresponding to the 20 mT are probably connected to the discharge power-supply noise. Figure 4 shows the changes of the power density spectrum with the pressure at fixed magnetic field of 20 mT and the discharge current 200 mA. The increase of the pressure leads to the decrease of the amplitude of fluctuations.

4. Spatial changes of plasma parameters with magnetic field

It is interesting to compare the effect of magnetic field to the fluctuations (temporal changes of plasma parameters) with the effect of magnetic field to the spatial distribution of plasma parameters in radial and axial direction within the discharge vessel. The radial changes of plasma parameters have been measured by radially movable probes the estimate of axial changes has been determined by measuring with three probes at three different axial positions within the discharge vessel.

Figure 5 shows the radial dependences of electron density at three different positions along the discharge vessel and at three different magnetic fields. It is seen that the magnetic field affect significantly radial as well as axial distribution of electron density within the discharge vessel.

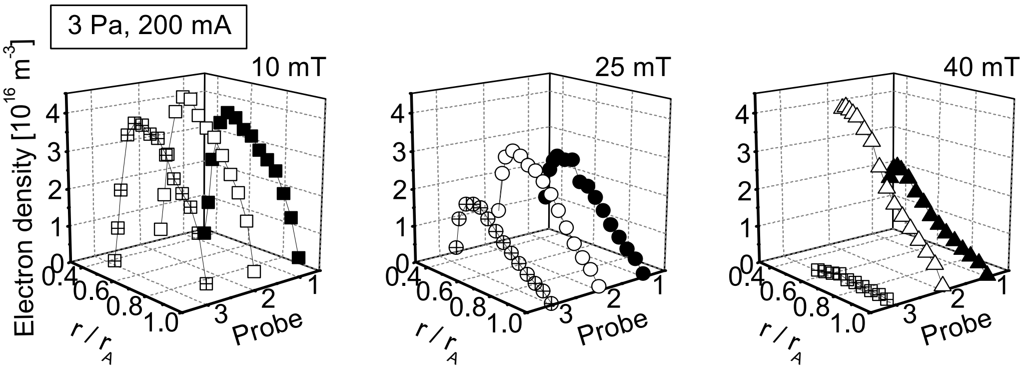

Figure 5. Dependence of radial and axial electron density distribution on the magnetic field.

The procedure of destruction of the axial homogeneity we can also follow in Figures 6 and 7, which depict the radial profiles of electron density at the probe 1 and 2 with magnetic field strength B as a parameter. It is interesting to note that while in the middle of the discharge vessel the peak electron density monotonously decreases with increase of the magnetic field strength, at the probe 2, i.e. 6 cm apart the peak electron density at first decreases and then increases again.

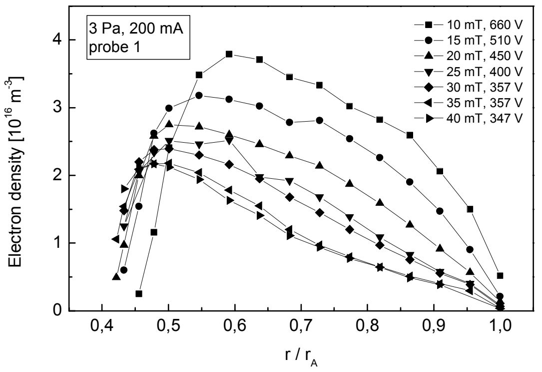

Figure 6. Radial profile of electron density measured at the central axial position (probe 1).

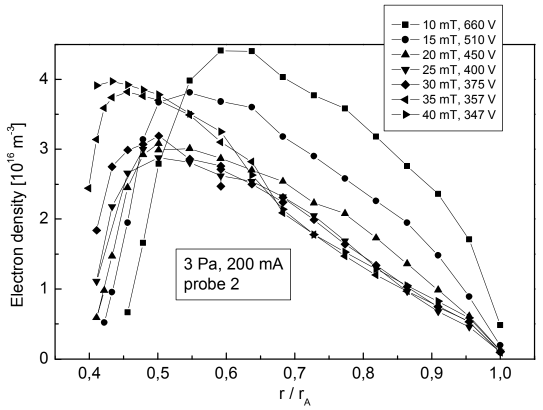

Figure 7. Radial profile of electron density measured at 6 cm from the central axial position (probe 2).

Figures 8 and 9 show the measured profiles of the plasma potential and electron mean energy at the position of probe 1 respectively. The plasma potential has been determined from the zero-crossing point of the second derivative of the probe characteristic with respect to the probe potential. Second derivative has been computed numerically from the measured probe characteristic. The mean electron energy has been determined by numerical integration over the second derivative. One can note the increase of the radial electric field with increase of the magnetic field strength in Figure 8, which is accompanied by the increase of the electron mean energy (Figure 9).

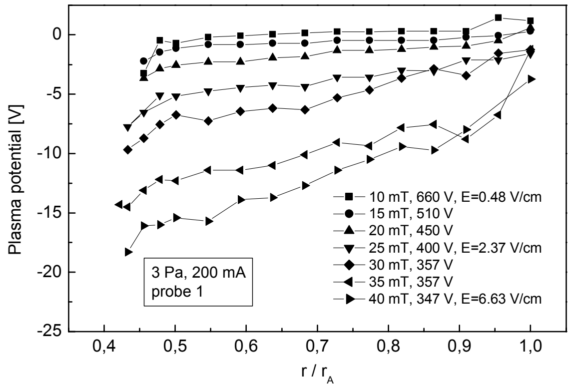

Figure 8. Radial profile of plasma potential measured at probe 1. Also indicated are the radial electric field E in V/cm and the discharge voltage.

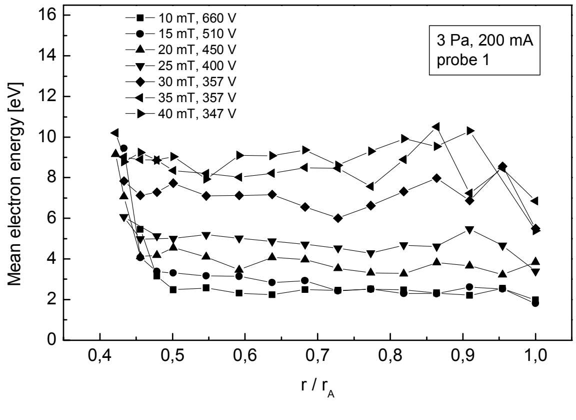

Figure 9. Radial profile of the mean electron energy (probe 1). Noted is also the discharge voltage.

5. Frequency vs. wave number spectra

In order to analyze the wave-like behaviour of the potential fluctuations of the DC discharge plasma in cylindrical magnetron the power density spectra derived from the fluctuations measured simultaneously on two Langmuir probes were evaluated according to the method described in [6]. For this purpose a double probe was inserted into position of the probe 1 (central position). Cylindrical tips of the double probe were aligned in the plane perpendicular to the discharge vessel axis, see Figure 10.

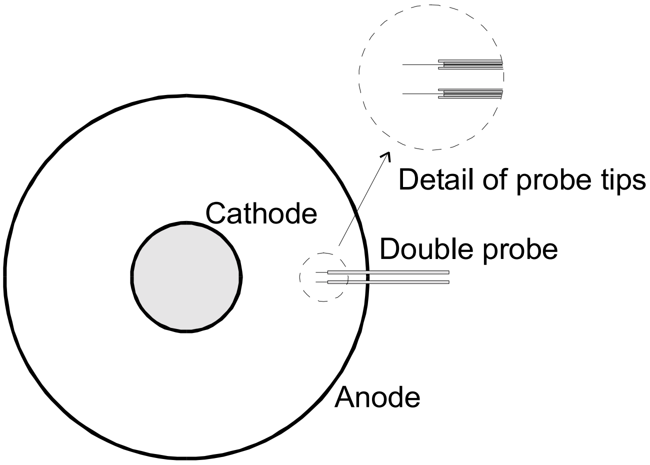

Figure 10. Position of the double probe inside cylindrical magnetron discharge vessel and detail of the probe tips. Probe material and dimensions: tungsten, diameter 47 µm, length 2 mm.

At first the wave number was calculated for each frequency from the phase shift between the signals at the two probes and the known distance Δx=1.6 mm between the probes:

$$k(f)=\frac{\arg H^{(2)}(f)-\arg H^{(1)}(f)}{\Delta x}, \qquad (5)$$

where $H^{(1)}$ and $H^{(2)}$ are the Fourier transforms of the signals $h^{(1)}$ and $h^{(2)}$ measured simultaneously at both tips of the double probe. Using the wave number and the average power density $S^{(12)}(f)$ at the two probes

$$S^{(12)}(f)=\frac{S^{(1)}(f)+S^{(2)}(f)}{2} \qquad (6)$$

the histogram $S(f,k)$ can be built. For each frequency f the bin corresponding to the wave number k was increased by the amount $S^{(12)}(f)$.

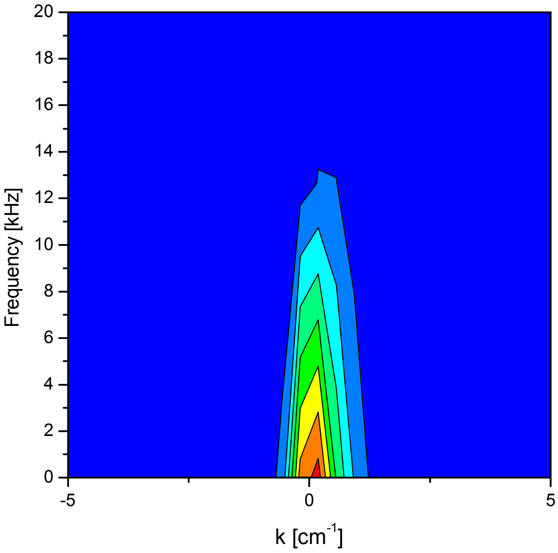

Figure 11. $S(k,f)$ histogram at 30 mT, 1.5 Pa and 200 mA.

Figure 11 shows the typical frequency vs. wave number histogram. It is seen from the figure that the phase shift between fluctuations measured at the two probe positions is negligible i.e. the fluctuations at the positions of both the probes are well correlated. In comparison with the work [6], which studied fluctuations in planar magnetron, no fluctuations modes have been found in our cylindrical magnetron configuration.

6. Discussion and conclusion

When the magnetic field is applied to plasma the similarity parameter is considered to be the quantity B/p. This follows from the dependence of the diffusion coefficient of electrons in the direction perpendicular to B, which depends on the ratio ω_c/ν (frequency of the electron cyclotron motion over the collision frequency of electrons with neutrals). Figures 3 and 4 demonstrate qualitatively that B/p seems to be similarity parameter also for the power of fluctuations - at least in a limited range of lower frequencies: At constant pressure the fluctuations power density increases with magnetic field strength, at constant magnetic field the same decreases with increasing the pressure. With regard to spatial changes of the electron density the decrease of the electron density at higher magnetic fields at the ends of the discharge vessel (see Figure 5) has been satisfactorily explained by a recent kinetic model [7]. This kinetic model takes into account the effect of disc-shaped limiters - additional walls - that terminate the discharge vessel axially. What remains unclear yet is the decrease of the electron density with increasing magnetic field in the middle of the discharge vessel, which seems to be compensated - since the discharge current was kept constant - by the increase of the electron density in the intermediate position between middle and end of the discharge vessel (at the position of probe 2). This axial dependence of the electron density is neither included nor described by the model [7]. From our experimental results follows, however, that the discharge current at higher magnetic fields is mostly axially constrained to two areas lying symmetrically around the middle of the discharge vessel. Simultaneously the discharge voltage with increasing the magnetic field monotonically decreases (see notes in Figures 8 and 9). It is therefore very probable that at higher magnetic fields the radial transport of electrons from cathode to anode is enhanced by the fluctuations. This conclusion is further supported by comparison of the experimentally measured radial course of the plasma potential with the plasma potential computed using the 1-D PIC model [8]. The PIC model calculates the plasma parameters for discharge running-times up to about 100 μs after the discharge switch-on and hence it cannot encompass the role of fluctuations. The experimentally measured radial electric field is always several times smaller than the electric field computed from the PIC model. This result also suggests that there is another mechanism, which contributes to the radial transport of electrons in our system, and the observed (and in this paper characterized) fluctuations may well represent a kind of such mechanism.

Acknowledgment

The work in Greifswald was financially supported by the Deutsche Forschungs-Gemeinschaft (DFG) in frame of the project SFB 198 Greifswald "Kinetik partiell ionisierter Plasmen" and by DAAD trilateral project of the University in Greifswald, Paris-Sud and St. Petersburg. The work in Prague was partially financially supported by the Grant Agency of Czech Republic, Grant No. 202/03/0827 and 202/01/D095, by the Grant Agency of Charles University, Grant No. 173/2002/B FYZ /MFF, by project COST action 527.70 and by the Ministry of Education, Youth and Sports, Research plan MSM 113200002.

References

[1] A. Bouchoule, A. Cadiou, A. Heron, M. Dudeck, M. Lyszyk, Contrib. Plasma Phys., **41** (2001) 573-588.

[2] E. Martines, V. Antoni, R. Cavazzana, G. Regnoli, G. Serriani, M. Spolaore, N. Vianello, M. Hron, J. Stöckel, Czech. J. Phys. **52** (2002) D13-D24.

[3] J.F. Behnke, P. Kudrna, J. Rusz, M. Tichý, Czech. J. Phys. **50/S3** (2000) 419-426.

[4] P. Kudrna, E. Passoth, Contrib. Plasma Phys. **37** (1997) 417-429.

[5] J.F. Behnke, E. Passoth, C. Csambal, M. Tichý, P. Kudrna, D. Trunec, A. Brablec, Czech. J. Phys. **B49** (1999) 483-498.

[6] E. Martines, R. Cavazzana, G. Serianni, M. Spolaore, L. Tramontin, M. Zuin, V. Antoni, Phys. of Plasmas **8** (2001) 3042-3050.

[7] I.A. Porokhova, Yu.B. Golubovskii, P. Kudrna, M. Tichy and J.F. Behnke, Kinetic modeling of the axially non-uniform cylindrical magnetron discharge, Proc. ICPP, 15. – 19. 7. 2002, Sydney (Australia), in print.

[8] P. Kudrna, M. Holík, C. Csambal, I.A. Porokhova, Yu.B. Golubovskii, M. Tichy, J.F. Behnke, PIC-MCC modeling of the cylindrical magnetron discharge, Proc. ICPP, 15. – 19. 7. 2002, Sydney (Australia), in print.

Decontamination of drinking water and liquid media by cold plasma

Alexander A. Pivovarov

Ukrainian State Chemical-Technolgy University
8, Gagarin av., Dnepropetrovsk, Ukraine 49005
pivovar@id.ru

Now there is a set of problems connected with decontamination pathogenic micro-organisms. The known methods can not be always applied to resistant-steady bacteria, as well as always effective known antiseptics and disinfectants are not. As a result of bacterial pollution of water the epidemics of dysentery, cholera or typhoid are possible. Contamination with the viruses can also cause hepatitis B and poliomyelitis. For destruction of them there is a need to chlorinate water more intensively, which generates new problems. Intensive chlorination can form haloidform compounds that are dangerous for health and which in a number of countries are not monitored at all.

New plasmachemical processes of decontamination of the biologically polluted water and liquid media are the ones with one of the most potential for theoretical and applied research.

The preliminary research at the establishments of the Ministry of Public Health of Ukraine and Russia has shown that as a result of processing of water media containing various kinds of pathogenic and conditionally - pathogenic bacteria complete disinfection of them is achieved. This allows to apply the given technology for decontamination of a wide spectrum of bacteria from the polluted media.

After the decontamination of water in accordance with the conclusions of Research Institute Practical Toxicology and Disinfection, located in Moscow, it has been found that the microbiological parameters of water matches the requirements of the state standard of "Drinking Water".

Such technology can become reliable guarantee of safe consumption of drinking water during massive epidemics of cholera, plague, etc.

Preliminary experiments with liquid media containing poliomyelitis and hepatitis B testify that they can be decontaminated or these viruses can be concentrated with their subsequent separation from liquid medium suitable for its further utilisation. Other areas of possible application of the given technology in microbiology and medicine as well as in the military with the purpose of utilisation of the weapons of a mass destruction are also obvious.

The application of non-equilibrium low temperature plasma with the purpose of activation of chemically pure water also can represent practical interest.

Such water can be used in medicine, pharmacology, biology and chemistry as a bactericidal preparation, conservant, disinfectator, sterilizer, bio-stimulator, and intensificator of the oxidant-lyrestoration processes.

The modern level of development of plasma equipment allows to carry out liquid-phase processes at a qualitatively new technological level that inevitably requires realisation of fundamental theoretical and experimental research in order to create new technological processes.

Effect of Gas Properties on Characteristics of Hybrid Gas/Water Plasma Spraying Torch

M. Hrabovský, V. Kopecký, V. Sember

Institute of Plasma Physics, Academy of Sciences of CR, Praha, Czech Republic

Abstract

The paper presents results of experimental investigation of effect of gas composition and flow rate on characteristics of arc in a new type hybrid plasma torch with combined stabilization of arc by gas and water vortex. The experiments were performed with various flow rates of argon, nitrogen and mixtures of argon with hydrogen. Effect of gas flow rate and composition on arc voltage, power, efficiency, plasma temperature and velocity is studied.

1. Introduction

Plasma jets generated in dc non-transferred arc torches are utilized in several plasma processing technologies like plasma spraying, plasma cutting, plasma synthesis and decomposition of persistent chemical substances. In commonly used plasma torches the arc is stabilized by gas flow along the arc column. Plasma jets with substantially different characteristics, which cannot be achieved in gas torches, are generated in arcs stabilized by a water vortex [1, 2]. Besides apparent advantage of water-stabilized generators that no gas supply is needed, there is many other differences between gas and water torches in plasma processes, plasma properties and especially in performance characteristics in plasma processing. Water torches are characterized by extremely low plasma mass flow rates and thus plasma enthalpy is several times higher than enthalpy achieved in common gas torches [3]. Water torches have been industrially applied especially for plasma spraying.

Physical limits of the two principles, gas- and liquid- arc stabilization, do not allow generation of plasmas with parameters in a wide region between the two principles. In hybrid gas/water torch [4] a new method of arc stabilization is utilized that is based on combination of principles of liquid and gas arc stabilization. The principle offers possibility of control of plasma jet characteristics in a wide range from values typical for liquid-stabilized torches to values typical for gas-stabilized torches. It was shown in [4] that plasma mass flow rate, velocity and momentum flux in the jet can be controlled by changing gas flow rate in the gas-stabilized section while thermal characteristics like enthalpy flux and plasma temperature are determined by processes in water-stabilized section.

This paper presents results of further experimental investigation of effect of gas composition and flow rate on characteristics of gas/water-stabilized arc.

2. Experimental set-up

The schematic diagram of hybrid plasma torch is shown in Fig. 1. A cathode part of the torch is arranged similarly like in gas torches. Gas is supplied along the cathode tip, vortex component of gas flow that is injected tangentially assures proper stabilization of arc in the cathode nozzle. Gas plasma flows through the nozzle into the second part of arc chamber where arc column is surrounded by a vortex of water. The vortex is formed in a chamber with tangential water injection in a same way like in water-stabilized torch. Steam plasma mixes in this chamber with plasma produced in the cathode section of the torch. Anode is created by a rotating copper disc with internal water cooling.

The arc column is composed of three sections. Short cathode section is stabilized by vortex gas flow. The most important section is water-stabilized part, where arc column interact with the water vortex. The third part between exit nozzle and anode attachment is an arc column in free jet. We measured potentials of the both electrodes, cathode nozzle and exit nozzle. From these measurements voltage drops on the three sections were evaluated. From calorimetric measurements on cooling system power loss to electrodes and to the stabilizing water vortex were determined.

Profiles of plasma temperature and composition at the nozzle exit were determined by emission spectroscopy. The electron number density was obtained from Stark broadened H_β line. The temperature was calculated from the ratio of various argon atomic and ionic lines assuming Saha equilibrium. In colder parts, where there were no ionic lines detected, the temperature was estimated from the approximate LTE composition and measured electron number density. The plasma composition was determined from ratios of emission coefficients of argon, oxygen and hydrogen.

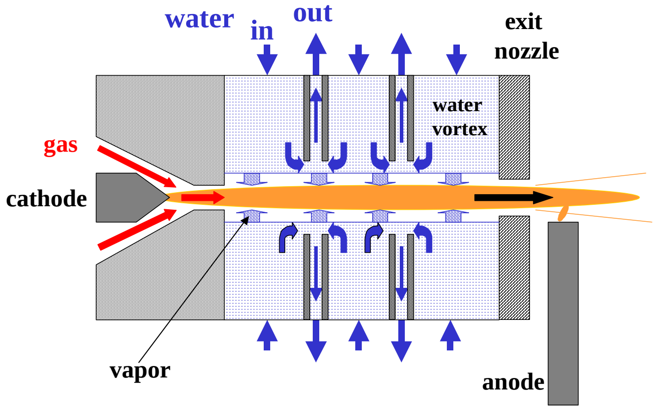

Fig. 1. Schematics of hybrid plasma torch.

3. Results

Effect of argon flow rate.

Measured voltage drop on two stabilized parts of the arc column in dependence on argon flow rate for various arc currents are shown in Fig. 2. The potential difference between cathode and cathode nozzle was in all cases between 7 and 9 V. Thus, the dependences of measured voltage on arc current and gas flow rate are determined by processes in water-stabilized part. For higher arc currents the voltage, and thus also arc power, is almost independent of argon flow rate while for lower currents arc voltage and power decrease with increasing gas flow rate.

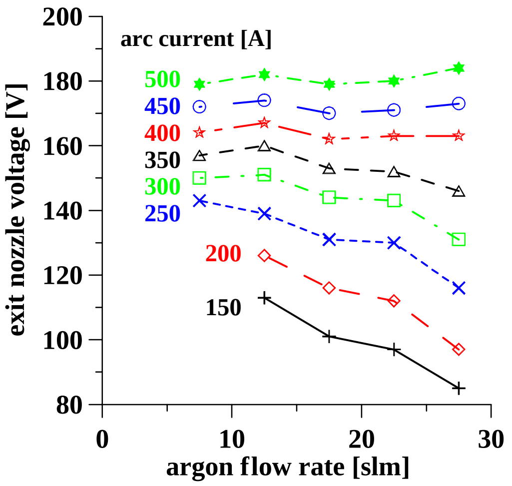

Fig. 2. Dependence of potential difference between cathode and exit nozzle on flow rate of argon for various arc currents.

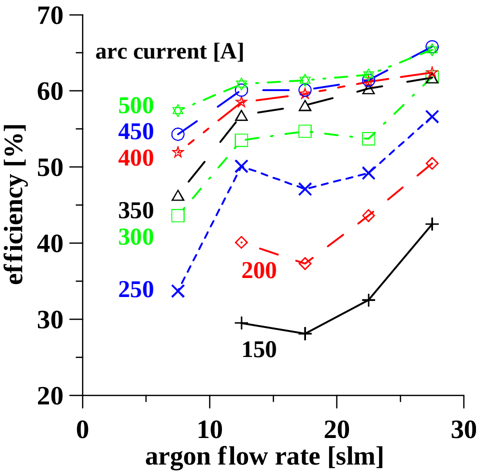

Fig. 3. Dependence of efficiency η on flow rate of argon for various arc currents.

Efficiency of the stabilized part of plasma torch was then determined as

$$\eta = \frac{U.I - P}{U.I} \qquad (1)$$

where U is potential difference between exit nozzle and cathode and P power loss to stabilizing water vortex and to the cathode. The dependence of efficiency on argon flow rate for various arc currents is in Fig. 3.

Fig. 4 presents percentage of argon at the plasma measured 2 mm downstream of exit nozzle for several argon flow rates and arc currents. The concentrations were determined from spectroscopic measurements from ratio of lines of hydrogen and argon. Values of concentration of argon for 13 slpm and 25 slpm correspond to increase of argon flow rate, non-homogeneous distribution of argon was found for two cases where towards the arc centerline argon concentration increases. It seems that in these cases the mixing of evaporated steam with plasma was not complete and higher concentration of steam existed in the arc fringes than in the arc centerline.

Temperature profiles measured 2 mm downstream of exit nozzle are shown in Fig. 5. As can be seen, the temperature profile is almost independent of change of argon flow rate from 12.5 slm to 22.5 slm. Of course plasma temperature increases with increasing arc current.

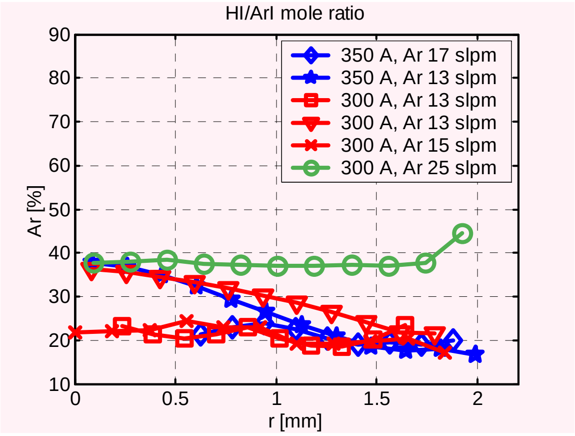

Fig. 4. Profiles of concentration of argon for arc currents 300 A and 450 A and argon flow rates 13, 17 and 25 slpm.

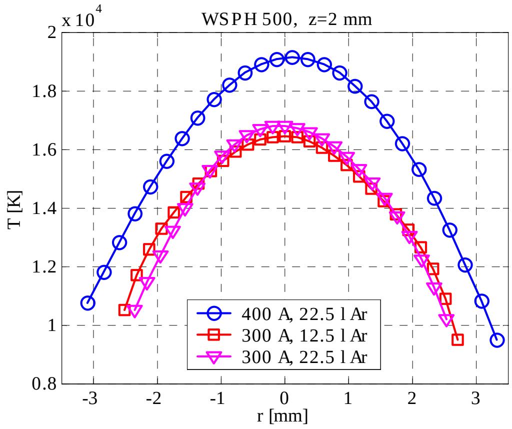

Fig. 5. Profiles of plasma temperature for arc currents 300 A and 400 A and argon flow rates 12.5 and 22.5 slpm.

Effect of gas flow rate and arc current on plasma velocity is illustrated in Fig. 6, where average velocity of plasma in the jet region close to anode attachment at distances 0-15 mm from the exit nozzle is plotted in dependence of arc current. The velocity was determined from the speed of propagation of sound waves in stream-wise and counter-stream-wise direction [5].

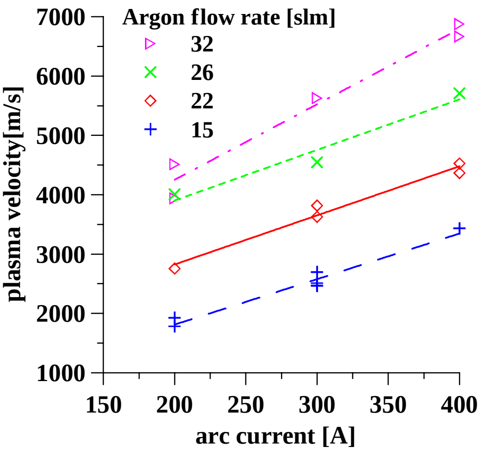

Fig. 6. Centerline plasma velocity in the anode region as a function of arc current for various argon flow rates.

It is clear from the presented results that plasma composition, flow rate and velocity changed substantially due to changes of gas flow rate, while changes of plasma temperature and power balances, especially for higher currents, were not significant. Due to increase of mass flow rate of plasma with increasing gas flow rate the plasma jet was visibly prolonged and it was more stable than the jet generated in water torch. Measurements of effect of gas flow rate on characteristics of plasma jet are described more in detail in [6].

Effect of composition of gas on gas/water arc.

Measurements were performed for pure argon, mixtures of argon with hydrogen and for nitrogen as plasma gas in gas-stabilized section. Dependence of the potential difference between exit nozzle and cathode on arc current measured for various plasma gases is shown in Fig. 7. Measurements were made for total gas flow rates of 12.5 slm and 17.5 slm, for nitrogen also 8.5 slm. Volt-ampere arc characteristics were increasing for all gases in the range of currents from 200 A to 400 A, arc power varied from 28 kW to 75 kW. Both the arc voltage and the efficiency are increased with the increasing content of hydrogen in argon/hydrogen mixture, the highest arc voltages and efficiencies were found for nitrogen.

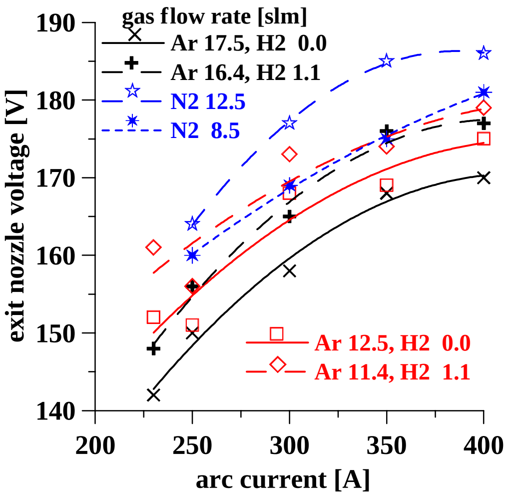

Fig. 7. Dependence of potential difference between cathode and exit nozzle on arc current for mixtures of argon with hydrogen and for nitrogen.

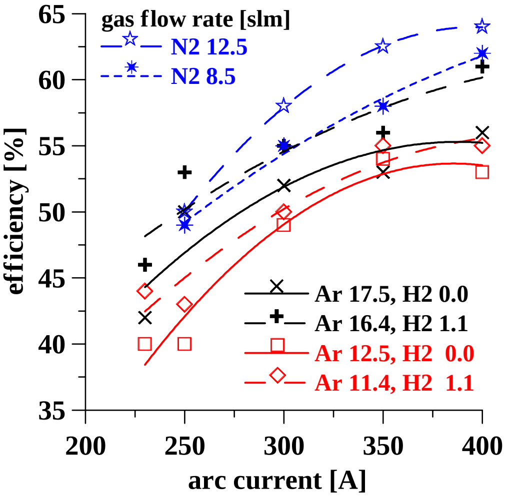

Fig. 8. Dependence of efficiency η on arc current for mixtures of argon with hydrogen and for nitrogen.

4. Discussion and conclusions.

The experimental results were analyzed on the basis of following simple model of water-stabilized section of arc column. The conducting arc channel is represented by isothermal cylinder of length L and cross section A. The gas enters axially the cylinder with the total flow rate G_0. Due to evaporation of inner surface of stabilizing water vortex a steam flows into the column radially with the flow rate per unit length m. The heat dissipated in the column by Joule heating is spent partially for heating of inflowing steam to temperature in the column, fraction α of the heat is transferred radially by heat conduction and radiation to the water vortex. Part of this radially transferred heat is absorbed in the steam flowing from the water surface. This part of heat is returned back to the column. The absorption is represented by coefficient ε. Power balance in the conducting column can be written as

$$\frac{d(\rho v h A)}{dz} = IE - P \tag{2}$$

where ρ is plasma density, h enthalpy and v axial velocity, I arc current and E electric field intensity, P is power loss to the stabilizing water vortex. This loss includes also power needed for evaporation from the inner surface of the vortex. According to the above specified assumptions the power loss P can be expressed as $P = (1 - \varepsilon).\alpha.IE$. We then obtain following relation between efficiency η and coefficients α, ε that characterize radial heat transfer:

$$\eta = 1 - \alpha(1 - \varepsilon) \tag{3}$$

Equation (2) can be easily integrated if coefficients α, ε are supposed independent of z. After substitution $E = dU/dz$ we can derive equation for potential of the nozzle of stabilizing channel in the form

$$U = \frac{(\rho v h A)_e}{\eta I} \tag{4}$$

Total mass flow rate at the exit nozzle of arc chamber is $(\rho v A)_e = G_0 + mL$. Enthalpy of plasma created by mixture of gas with steam can be expressed as

$$h = \frac{G_0 h_{gas} + m L h_{H_2O}}{G_0 + m L} \tag{5}$$

Equation (5) is valid with good accuracy for high temperatures in the conducting arc column where effect of chemical reactions between gas and steam plasma on enthalpy of gas mixture need not be considered.

Arc current is given by the equation

$$I = \sigma A E = \sigma A \frac{U}{L} \tag{6}$$

where E was supposed constant along the column.

The equation for voltage between exit nozzle and cathode can be then written as

$$U = \left(\frac{L}{A\eta}\right)^{\frac{1}{2}} \left(G_0 \frac{h_{gas}}{\sigma} + mL \frac{h_{H_2O}}{\sigma}\right)^{\frac{1}{2}} \tag{7}$$

All measured dependences can be explained by differences in contribution of individual heat transfer mechanisms that are caused by differences in material properties of steam, argon, hydrogen and nitrogen plasmas. The efficiency η given by (3) is dependent on coefficients α and ε representing relation between radial and axial heat transfer and intensity of heat absorption in the vapor respectively. The arc voltage is determined by value of η, by flow rate of gas and evaporation rate of steam and by ratios of enthalpy of components to the electrical conductivity.

Addition of argon into the arc chamber reduces thermal conductivity of the mixture while radiation properties and absorption of radiation in the colder zones are affected only slightly. Therefore radial heat transfer described by coefficient α is reduced due to increase of argon flow rate, ε is not changed significantly. The reduction of α is significant for lower currents when heat conductions is dominant, while for higher currents radiation component prevails and α is almost unchanged. Therefore efficiency η increases with argon flow rate at lower currents. As enthalpy of argon plasma is one order lower than enthalpy of steam plasma while electric conductivity is changed only slightly with change of content of argon in plasma, the effect of argon flow rate on the term in the second bracket of (7) is small. Thus arc voltage is decreased due to increase of η and from the reasons given above it is significant at lower currents. The addition of argon into water stabilized arc thus does not influence enthalpy flux in the axial plasma flow, changes of arc power are related dominantly to changes of radially transferred energy. Therefore plasma temperature and total heat flux are almost constant while mass flow rate and plasma velocity are increased due to increase of argon flow rate.

Addition of hydrogen or nitrogen to arc plasma influences not only radial heat transfer but also plasma enthalpy, as enthalpy of nitrogen is comparable with enthalpy of steam and enthalpy of hydrogen is much higher. This leads to increase of arc voltage with increasing flow rates of hydrogen or nitrogen. At the same time also efficiency is increased due to increase of ε as addition of both molecular gases leads to increase of absorption due to photo-dissociation of ultraviolet radiation, which is intensive especially at higher currents. As total enthalpy flux increases, the fraction of radially transferred arc power α is decreased which also results in increase of efficiency.

Thus, arc characteristics and plasma properties can be adjusted through choice of composition and flow rate of plasma gas in the gas-stabilized torch section. Use of gas with low enthalpy like argon offers possibility of control of mass flow rate and velocity of plasma with little effect on arc power and plasma temperature. If hydrogen or nitrogen were used as plasma gases, all characteristics of arc were changed.

Acknowledgement

The authors gratefully acknowledge the support of this work by the Grant Agency of the Czech Republic under the project No. 202/01/1563 and by the grant Agency of Academy of Sciences CR under the project No. A1057202.

References

[1] Hrabovský M., Konrád M., Kopecký V., Sember V., Processes and properties of electric arc stabilized by water vortex, IEEE Trans. on Plasma Science **25** (1997), No. 5, 833-839.

[2] Hrabovský M., Konrád V., Kopecký V., Sember V., Properties of Water Stabilized Plasma Torches, in Thermal Plasma Torches and Technologies (ed. O.P. Solonenko), Vol. 1, Cambridge Int. Sci. Publ., Cambridge, 1998, pp. 240 – 255.

[3] Hrabovský M., Water-stabilized plasma generators, Pure & Applied Chemistry **70** (1998), No. 6, 1157 - 1162

[4] Brezina V., Hrabovsky M., Konrad M., Kopecky V. and Sember V., New plasma spraying torch with combined gas-liquid stabilization of arc, Proc. of 15th Int. Symp. on Plasma Chemistry (ed. A. Bouchoule et al.), Vol. III, 9-13 July 2001, Orleans, 1021 – 1026.

[5] Hrabovský M., Kopecký V. and Macura P., Investigation of propagation of perturbations in thermal dc arc plasma jet, in Progress in Plasma Processing of Materials 2001 (ed. P. Fauchais), Begell House, New York –Wallingford 2001, 223 – 228.

[6] Kavka T, Hrabovsky M., Konrad V., Kopecky V., Sember V., Chumak A., Entrainment of ambient air into H_2O/Ar arc plasma jet, Proc. of ISPC16, in this volume.

Characterization of magnetron sputtering process of NiO by using flow modulation of oxygen

I. Hotovy[1] and J. Huran[2]

[1] *Microelectronics Department, Slovak University of Technology, Ilkovicova 3, 812 19 Bratislava, Slovakia*
[2] *Institute of Electrical Engineering, Slovak Academy of Sciences, Bratislava, Slovakia*

Abstract

We present the pulsed dc magnetron sputtering method in which a nickel target is sputtered in a mixture of argon and reactive gas oxygen. The flow rate of oxygen is modulated periodically in time and during deposition when oxygen flows is cut off to remove the oxide formed on the target. Modulated deposition process was monitored directly by optical emission spectroscopy, the deposition rate and partial pressure measurement. The variations of atomic ratio in NiO films were revealed by SIMS method.

1. Introduction

Nickel oxide (NiO) is an attractive material for use as an antiferromagnetic layer, p-type transparent conducting films, in electrochromic devices and as a functional sensor layer for chemical sensors. In the bulk, NiO has a cubic (NaCl-type) structure with a lattice parameter of 0.4195 nm. NiO is considered to be a model semiconductor of hole-type conductivity. These films have been fabricated by various physical and chemical vapour deposition techniques such as reactive sputtering and plasma-enhanced chemical vapour deposition because chemical stability of the layers as well as their optical and electrical properties is excellent. Reactive sputter deposition involves the sputtering of metal, alloy or compound in a reactive gas mixture in order to deposit a compound film composed of the sputtered material and the reactive species. A wide variety of compounds have been formed in this way, with a wide range of properties. In this method, it is well known that the deposition can be unstable due to the competition between the target sputtering and the consumption of the reactive gas either by target or by the deposited film.

We present the pulsed dc magnetron sputtering method in which a nickel target is sputtered in a mixture of argon and reactive gas oxygen. The flow modulation of oxygen is proposed to enhance the deposition process of preparation of the oxide films [1]. The flow rate of oxygen is modulated periodically in time and during deposition when oxygen flows is cut off to remove the oxide formed on the target [2, 3]. This leads to oscillating oxygen concentration during the sputtering process and causes the variation of the atomic ratio in growing film. Modulated deposition process was monitored directly by optical emission spectroscopy, the deposition rate and partial pressure measurement. The effect of the different oxygen flow periodically changes in time on the selected Ni and O_2 emission intensities and the deposition rate were investigated. The variations of atomic ratio in NiO films were revealed by SIMS method.

2. Experiment

The experiments were carried out in the experimental apparatus (Fig. 1), which contained of a dc custom-built magnetron sputtering source with a Ni target. Measurements of flow conditions were realized at constant total pressure of the working mixture and its value was 0,5 Pa. The oxygen flow rate was regulated with computer operated experimental unit in conjunction with a mass flow controller. The flow rate of oxygen was modulated periodically in time. During one period (50 s), first, oxygen flow was on 45 s and second, O_2 flow was cut off (5 s). The discharge power was maintained at 600 W.

The light emitted from discharge was collected from a certain point near the target by two UV lenses and 1 mm aperture (mounted in between) onto the entrance slit 0.3 m monochromator Bentham M300E. A photomultiplier Hamatsu R955 was mounted just behind the exit slit of the monochromator. The photomultiplier signal was sent to current supply, then to analogue-digital converter and the spectra stored on a microcomputer. This optical system was mounted upon a vertically moving table, which enables us to observe the emitted light from plasma along the target. The spectral range between 300 and 900 nm was investigated. In order to study the influence of oxygen flow 10, 30 and 50 sccm, respectively, on the OES spectra, we selected Ni (352.4 nm), Ar (751.4 nm) and O (777.0 mm) lines on which to focus. Partial pressure measurements were realized at the constant values of pumping speed and of chamber volume by a capacitance manometer (MKS Baratron). The changes of deposition rates ware monitored by a thin film thickness and deposition rate monitor (Inficon) with a quartz crystal sensor head. A quadrupole SIMS instrument Physical Electronics PHI ADEPT 1010 with primary ion beam Cs^+ was used to depth compositional analysis of NiO films prepared by this process.

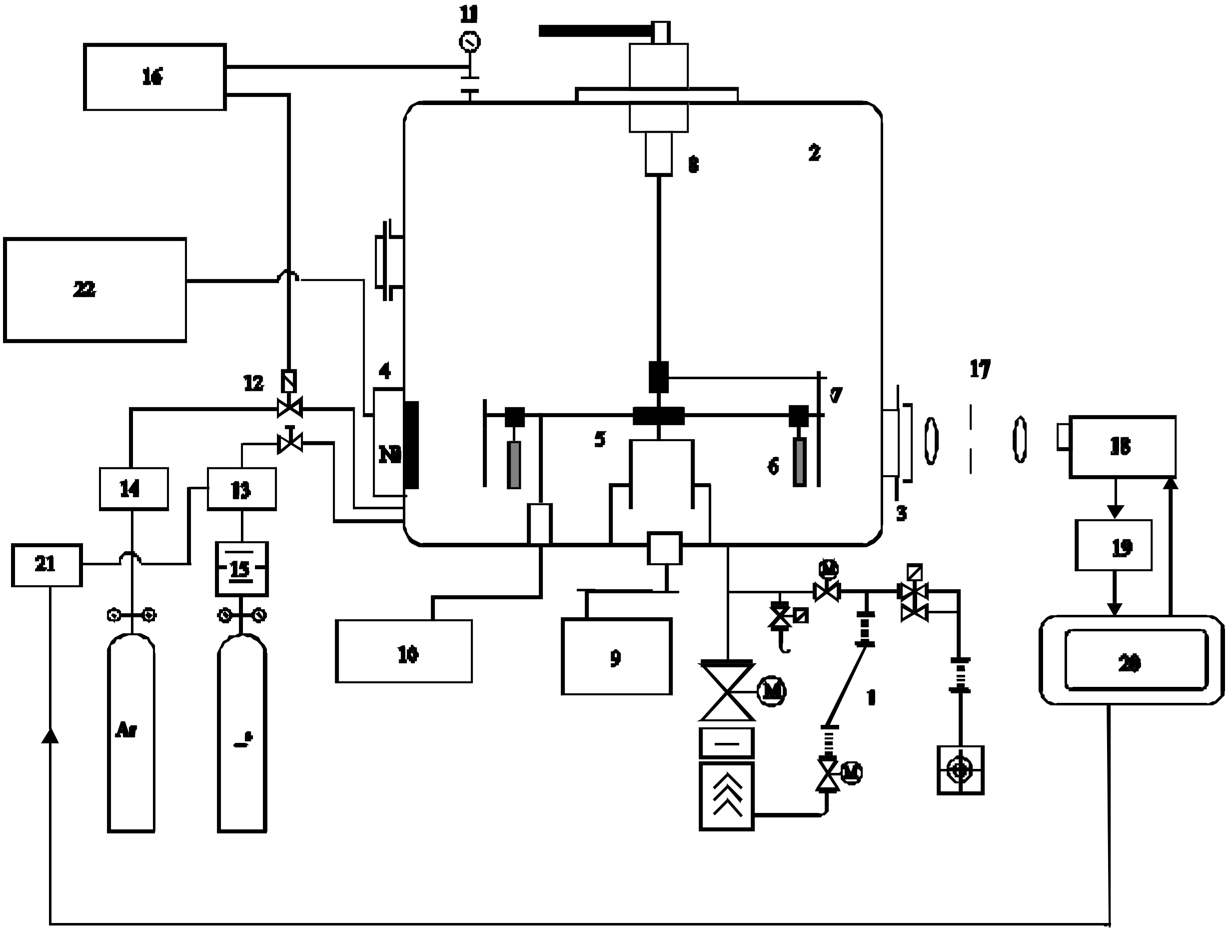

Fig. 1: Block schema of the experimental apparatus: 1) -vacuum pumping system, 2) - vacuum chamber, 3) - quartz window, 4) - magnetron sputtering source with Ni target, 5) - carrousel holder of samples, 6) - carrier of substrates, 7) - shield, 8) - shield operator, 9) - step engine, 10) - bias, 11) - Pirani gauge, 12) - needle valve, 13) - mass flowmeter, 14) - mass flowmeter, 15) - LN_2 trap, 16) -total pressure controller, 17) - optical system, 18) - monochromator, 19) - current amplifier, 20) - PC, 21) - modulation unit, 22) - power supply

3. Experimental results

In our previous study were defined the sputtering modes for continuous addition of oxygen at NiO deposition [4]. According to these results were chosen the oxygen flow rates. The conditions of the oxygen flow rates and period in Fig. 2a were respectively 10 sccm and 50 s, 30 sccm and 50 s, 50 sccm and 50 s. The first condition corresponds to the experimental observation for metal-sputtering mode while the other conditions are valid for oxide-sputtering mode for the continuous addition of oxygen. The figures help to characterize the effects of the oxygen modulation on the parameters and the properties of sputtering process.

In Fig. 2b, the modulation causes the oscillation of oxygen partial pressure. The partial pressure measurements were realized at the constant values of pumping speed and of chamber volume without plasma. Fig. 2b shows the change of the partial pressure of oxygen during an oxygen-on and oxygen-off period for various oxygen flows. The time for increase and decrease of the partial pressure is determined by pumping speed, chamber volume and oxygen flow. Using the modulation unit, we controlled oxygen flow and this lead to an oscillating oxygen concentration during the sputtering process. When the oxygen flow is cut off, the partial pressure will be decreased and the decrease in the partial pressure will enhance the deposition rate.

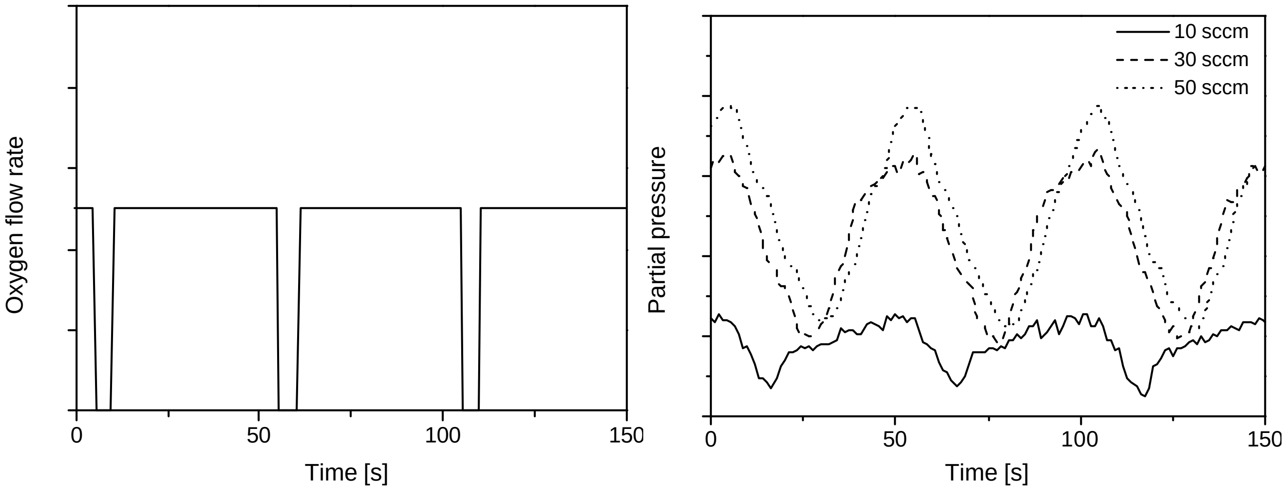

Fig. 2: (a) Schematic representation of pulsed oxygen flow rate and (b) partial pressure of oxygen in deposition chamber during an oxygen-on and oxygen-off period at the different oxygen flow. Total pressure was 0.5 Pa.

OES yields interesting information on excited species, atoms, molecules and radicals present in the plasma as well as qualitative variations of these species with respect to the discharge conditions. The corresponding variations of the intensities of Ni (352.4 nm), O (777.0 nm) and Ar (751.4 nm) lines against the oxygen flow rate are given in Fig. 3. We note that the changes are due to the oxygen modulation and they reflect the coverage of the target. During the oxygen-off period the peak intensity from Ni line rapidly increases while the oxygen OES signal indicating the concentration of excited oxygen molecules in the plasma decreases.

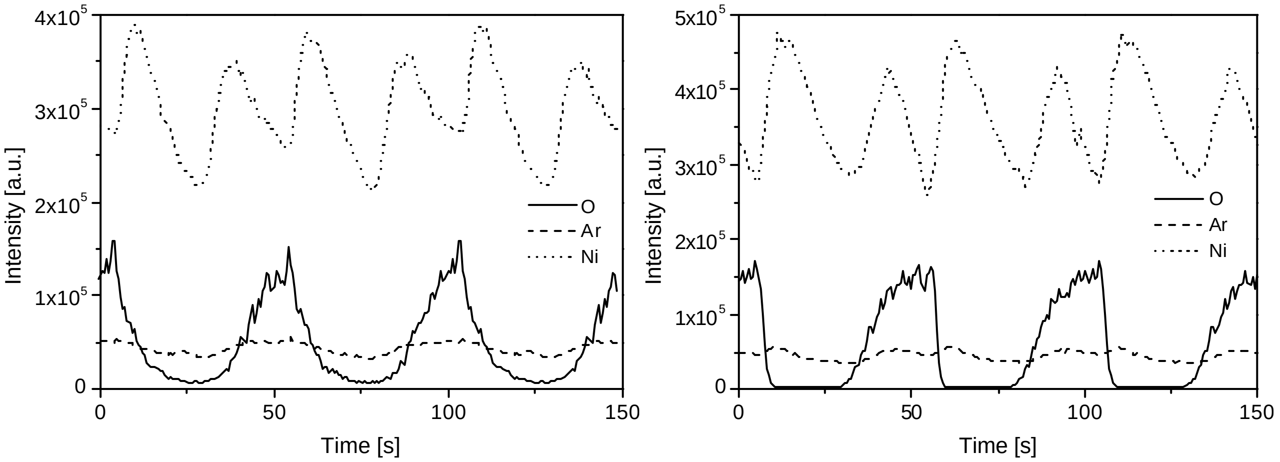

Fig. 3: Time dependencies of OES signals of nickel, oxygen and argon for periodic oxygen addition (a) 30 sccm, (b) 50 sccm.

The variations of the target voltage (Fig. 4) show the regions correspond to the three regimes: 1) oxide-sputtering mode with low value of the target voltage (318-325 V), 2) transition-sputtering mode characterized by an abrupt increase in the value of the target voltage, 3) metal-sputtering mode when the discharge voltage increases to 430-440 V. In the oxide-sputtering mode the poisoning of the target becomes serious because of the higher secondary electron emission coefficient of the oxide compared to that of pure metal, the total number of electrons near the target increases and hence higher target current can be achieved at lower voltage.

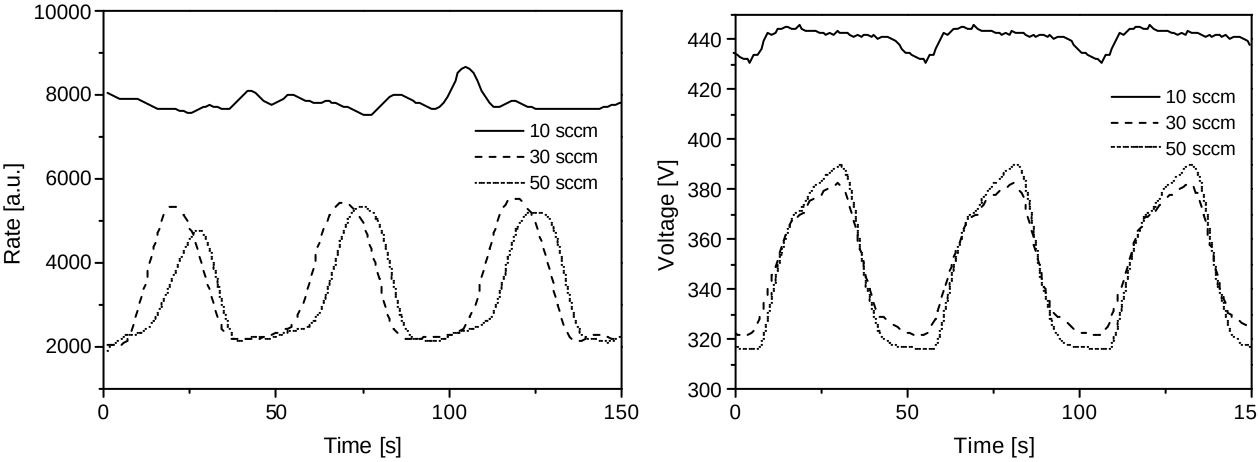

Fig. 4: (a) Time variation of the deposition rate experimentally observed and (b) real time measurements of nickel target potential for periodic oxygen addition.

Some samples on silicon substrates have been deposited by repeated oxygen-on and oxygen-off cycles. In the case of sample prepared at 10 sccm oxygen flow rate (Fig. 5) the SIMS depth profiling show that the level of Ni and O is constant and is not affected by periodic oxygen addition. On the other hand, SIMS measurements from samples prepared 30 and 50 sccm oxygen flow rate clearly record the oscillation of Ni and O in the depth profile (Fig. 6).

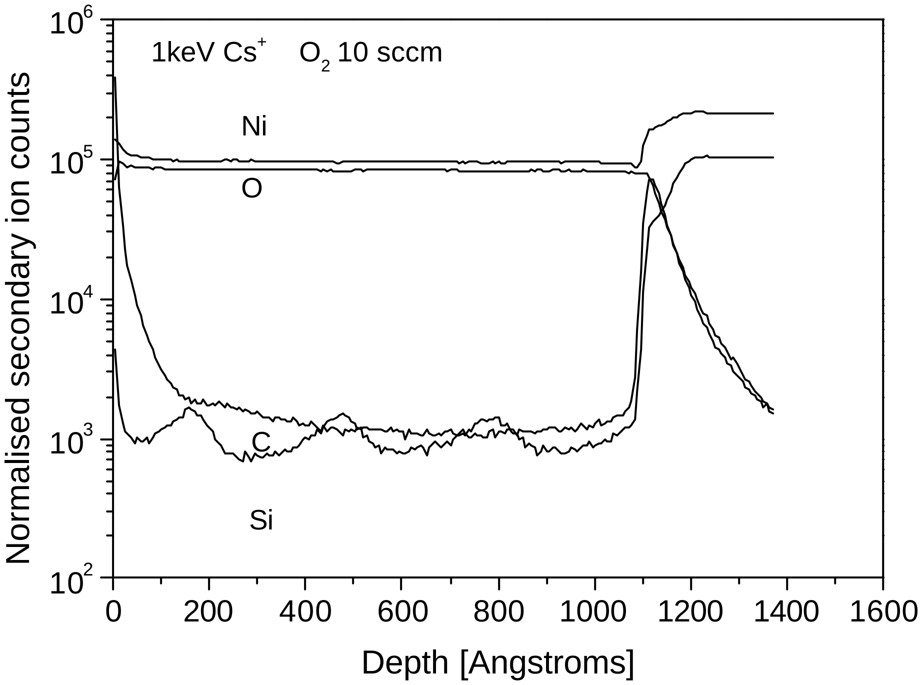

Fig. 5: SIMS depth profile taken from NiO film prepared at 10 sccm oxygen flow.

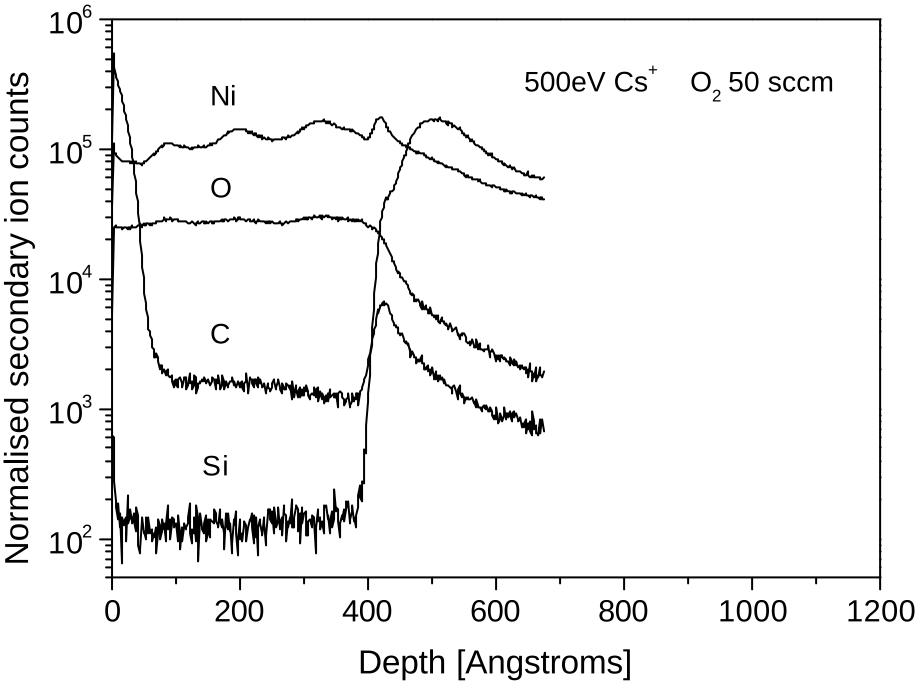

Fig. 6: SIMS depth profile taken from NiO film prepared at 50 sccm oxygen flow.

4. Conclusion

A sputtering process to enhance and change the deposition rate of NiO in reactive magnetron system was proposed using flow modulation of oxygen. This study also concluded that this process could be used for control of deposition film compositions. Thin NiO films with the different oxygen content can be deposited by this process alternatively and the multilayered film results.

Acknowledgement

The work was supported by Scientific Grant Agency of the Ministry of Education of the Slovak Republic and the Slovak Academy of Sciences, No. 1/0170/03.

References

[1] N. Martin, A.R. Bally, P. Hones, R. Sanjines, F. Levy, J. Thin Solid Films **377-378** (2000), 550-556.
[2] H. Sekigichi, T. Murakami, A. Kanzawa, T. Imai, T. Honda, J. Vac. Sci. Technol. **A14** (1996), 2231-2234.
[3] S. Kimura, T. Honda, D. Fukushi, J. Vac. Sci. Technol. **A17** (1999), 3312-3316.
[4] I. Hotovy, J. Huran, J. Janik, A.P. Kobzev, Vacuum **51** (1998), 157-160.

Carbon-containing Species Concentrations in a Moderate Pressure H_2/CH_4 Microwave Plasma- Modelling versus Infrared Diagnostics

G. Lombardi[1], K. Hassouni[1], J. Röpcke[2], A. Gicquel[1]

[1] Laboratoire d'Ingénierie des Matériaux et des Hautes Pressions, CNRS UPR 1311, Université Paris Nord
99, avenue J.B. Clément, 93430 Villetaneuse, France
[2] Institut für Niedertemperatur-Plasmaphysik e.V. Greifswald,Friedrich-Ludwig-Jahn-Str.19, 17489 Greifswald, Germany

Abstract

Concentration measurements of carbon-containing species in a moderate pressure H_2/CH_4 microwave plasma used for diamond deposition were performed by IR Tuneable Diode Laser Absorption Spectroscopy (TDLAS). The information deduced from this line of sight technique is analysed by a 1D radial modelling of the plasma reactor, and the results of the measurements are used for the validation of a 1D axial model of the plasma.

1. Introduction

In this paper we present experimental and numerical investigations of moderate pressure H_2/CH_4 microwave plasmas. These plasmas are processed under discharge conditions usually adopted for diamond deposition experiments, i.e. pressure in the range 25 - 150 mbar and input microwave power between 0.6 and 3 kW for 2.45 GHz microwave excitation. The plasma is activated in a quartz bell-jar reactor. The most relevant characteristic parameter of the investigated plasma is the Micro-Wave Power Density (MWPD) defined as the ratio of the input power to the plasma volume. The volume is in fact maintained constant by a simultaneous change of the input power and the pressure in the vessel. Typically, MWPD varies from 9 to 38 W cm^{-3}. The gas flow is maintained constant at 200 sccm. Several models, i.e. a 1D axial H_2/CH_4 [1] and 2D self-consistent H_2 [2], of the discharge obtained under these conditions were previously developed and partially validated by laser spectroscopy to reach some process key-parameters such as gas temperature and H-atom mole fraction [3]. However, the chemical kinetics models still need to be validated for the carbon-containing species. In particular, the methyl radical CH_3 was investigated by UV absorption spectroscopy, but a discrepancy was found with a previous 1D transport model that described the axial distributions of species densities and plasma temperatures[4]. This 1D model was substantially improved in this work and to complete the model validation, we measured carbon-containing species concentrations like CH_4, C_2H_2, C_2H_4 and C_2H_6 and the methyl radical CH_3 using IR TDLAS technique.

2. Experimental approach

The concentration measurements were made using an Infra-Red Multi-Acquisition system (IRMA) described in [5]. It is based on four IR Tuneable Diode Lasers that allow an almost simultaneous analysis of at least four species. The acquisition time is in the range of few seconds, and the sensitivity in term of mole fraction is typically some 10^{-5}. The data acquisition is carried out by a special software package that makes use of an advanced form of sweep integration. The area under a transition is integrated using non-linear least squares fitting to the known spectral line shapes and positions. The resulting spectrum is fitted to a set of Voigt line functions, the shape of which depends on the pressure and temperature. Absolute species concentrations are determined from the non-linear least squares fits. A schematic of the experimental setup is depicted in figure 1. Quartz bell Jar with KBr windows allowing IR transmission were used in these experiments. A double path optical mount enabled us to reach 10 cm of absorption length in the discharge. Note that the IRMA system was previously used in the same gas mixture, but at lower pressure [6]. IR measurements were performed in this work under actual diamond deposition conditions. The IR absorption of five species have been investigated in a wide wavelength range. CH_4 absorption at 1302.4515 cm^{-1} was indeed measured in order to reach methane dissociation degree as a function of MWPD and methane percentage in the feed gas. The 1302.5968 cm^{-1} absorption of C_2H_2, which was shown to be the major carbon-containing species in the investigated discharges [1], was systematically recorded. The IR absorptions of C_2H_4 and C_2H_6 at 935.1209 cm^{-1} and 3000.06 cm^{-1} was also measured to determine the concentrations of these species for more complete validation of the model. Finally, the density of CH_3-radical which is considered as the main precursor of diamond growth was determined using the 612.41344 cm^{-1} IR absorption of this radical. Note that the methyl radical density was also measured by UV Broadband Absorption Spectroscopy, and good agreement was obtained between the density-values obtained from UV and IR absorption techniques [7]. Since a significant chemistry may take place outside the visible discharge region, the measurements were carried out on the whole bell-jar (inside and outside the discharge). for this purpose several quartz bell-Jars with different optical axis were used. A typical example of IR absorption line (CH_4 and C_2H_2) is given figure 2.

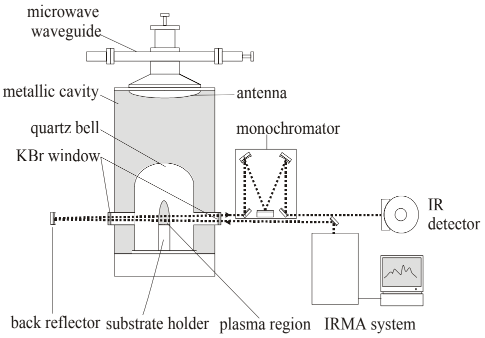

Figure 1: TDLAS experimental arrangement around the Bell-jar reactor, with the IRMA system

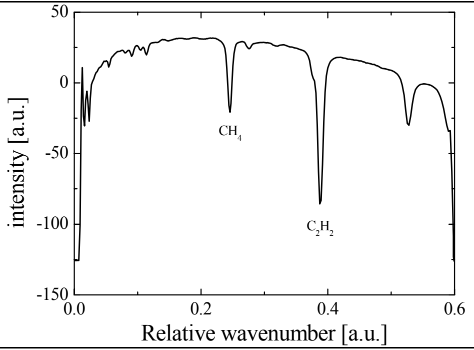

Figure 2: Example of IR spectrum of CH_4 (1302.4515 cm^{-1}) and C_2H_2 (1302.5968 cm^{-1}) MWPD= 9 $W.cm^{-3}$, p= 25 mbar, P= 0.6 kW

The effect of methane percentage in the feed gas on the densities of the investigated carbon containing species are shown figure 3, for a MWPD= 9 $W.cm^{-3}$ (i.e. p= 25 mbar, P= 0.6 kW). Since the absorption measurements are integrated over the line of sight, the measured density values are actually the averages of the density radial distribution. The estimation of the species densities requires the knowledge of the gas temperature which is actually non uniform over the plasma volume. The methyl radical is assumed to be mainly obtained in the discharge region, and its mole fraction is calculated by using the gas temperature value in the bulk of the discharge (i.e. 2200 K in the probed zone). On the other hand, stable species like C_2H_4 or C_2H_6 are mainly produced outside the discharge by recombination of smaller molecules or radicals. The temperature used to derive their concentrations was therefore taken equal to 300 K. Results show that the main conversion product is C_2H_2 and CH_3 mole fraction varies from 4 to 9.10^{-4} in the investigated range of methane percentage. Finally, the concentrations of C_2H_4 and C_2H_6 are much smaller than those of the other species. The dissociation degree of the methane introduced in the feed gas is shown in figure 4, it decreases when methane percentage in the feed gas is increased.

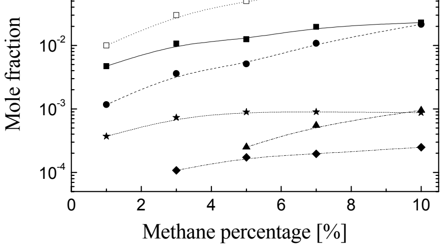

Figure 3: Averaged measured mole-fractions of 5 carbon-containing species along an optical path through the plasma bulk, in function of methane percentage MWPD= 9 $W.cm^{-3}$, p= 25 mbar, P= 0.6 kW

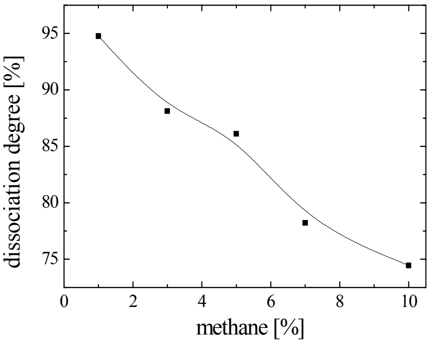

Figure 4: Dissociation degree of methane in function of the methane added in the feed gas MWPD= 9 $W.cm^{-3}$, p= 25 mbar, P= 0.6 kW

The effect of MWPD on the hydrocarbon-species of interest are reported in figure 5 which shows that the increase of MWPD favours the conversion of CH_4 to C_2H_2. The density of CH_3-radical tends to decrease in the plasma bulk with MWPD.

The interpretation of absorption measurements is in fact quite difficult, since the plasma is probed over a line of sight, which does not allow to take into account the spatial non-homogeneity of gas temperature and species densities. We therefore developed discharge models that enabled us to estimate the radial distribution of the plasma parameters and interpret the density-values as determined from TDLAS.

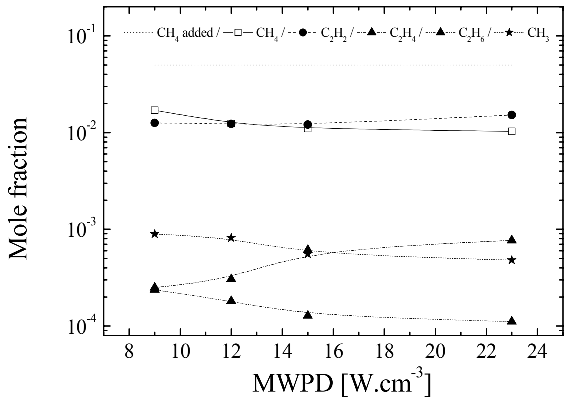

Figure 5: Averaged measured mole-fractions of 5 carbon-containing species along an optical path through the plasma bulk, in function of MWPD (5% CH_4)

3. Modelling approach

In principle the interpretation of TDLAS measurements requires the development of 2D model for thermochemically non-equilibrium H_2/CH_4 moderate pressure microwave plasmas. This is however very difficult due to the large number of species involved in the chemical model and to the strong stiffness of the system. This difficulty was overcome by developing two models. First a 1D axial model was developed to describe the plasma flow on the reactor axis. This model was used to determine the thermal and species density diffusion boundary layer thickness and estimate the overall species and energy losses at the diamond substrate surface. These loss are then used as a source term in a second transport model that describes the plasma diffusion along the line of sight of the IR laser beam.

In both these models H_2/CH_4 microwave discharges are treated as a 28 species/131 reactions, thermo-chemically non equilibrium medium. We distinguished between the heavy species energy modes which are characterized by the gas temperature T_g and the translational mode of electron that is characterized by the electron energy distribution function (eedf). The chemical species taken into account in the present model involve the neutral species, H_2, H(n=1), H(n=2), H(n=3), C_xH_y (x=1-2 and y=0-6), hydrogen and hydrocarbon ions, H^+, H_2^+, H_3^+, $C_2H_6^+$, $C_2H_5^+$, $C_2H_4^+$, $C_2H_3^+$, $C_2H_2^+$ and electrons. The chemistry that links these species consists of three sets of reactions. The first one describes the thermal hydrocracking in hydrogen-methane mixture [8-9], the second group involves the electron-impact dissociation and ionization processes of hydrocarbons and molecular and atomic hydrogen [10], the third group is related to ion conversion and dissociative recombination of ions [11].

The axial distribution of the plasma species-densities and temperatures are computed by solving the coupled set of species continuity, electron energy and total energy equations. Actually, in order to minimize the computation time, the simulation procedure involved two steps. First the transport equation were solved for pure hydrogen discharge. Then the gas temperature profile obtained from this simulation was used as an input parameter for the simulation of the more complex H_2/CH_4 models. The total energy equation was therefore decoupled from species continuity and electron energy equations. This simplification should not affect the simulation results since previous experimental measurements showed that the gas temperature does almost not vary with the methane amount in the discharge as long as this remains less then 10 % [12].

3.1. Radial model

The radial model is used to determine the species distribution from the reactor axis to the quartz wall. The solution of the corresponding transport equations requires the knowledge of the radial distribution of MWPD. This was estimated from a 2D self consistent model [2]. As discussed in the last section, the radial model takes into account the losses on both the diamond substrate (T_s= 1000 K), and the top wall of the quartz bell jar (T_q= 600 K). The loss probabilities for the different species are taken from [13].

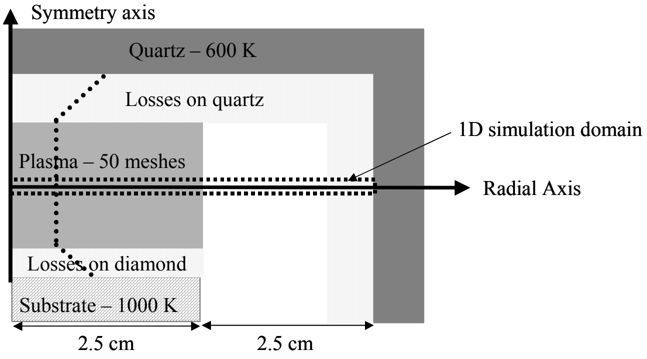

Figure 6: Principle of the radial model

3.2. Axial model

The 1D axial transport model is used to determine species density distribution between the quartz top wall and the substrate surface The microwave power coupled to the plasma was measured experimentally by following the emission intensity of the plasma [1].
This 1D axial model is based on the one discussed in [1] with the following significant improvements : (i) the radial losses on quartz are now taken into account, (ii) the numerical scheme has been strengthen in order to reach MWPD up to 23 $W.cm^{-3}$ for which the system of transport equations becomes very stiff, and (iii) the thermodynamic and transport data have been improved.

3.3. Results of the models

The calculated axial and radial distributions of gas temperatures in pure hydrogen mixture are given in figure 7-a and 7-b, respectively. The substrate is located at z= 0 cm and has a radius of 2.5 cm. The results are consistent, and yield to the same T_g values in the plasma bulk. These vary from 2250 K at 9 $W.cm^{-3}$ to 3200 K at 30 $W.cm^{-3}$.

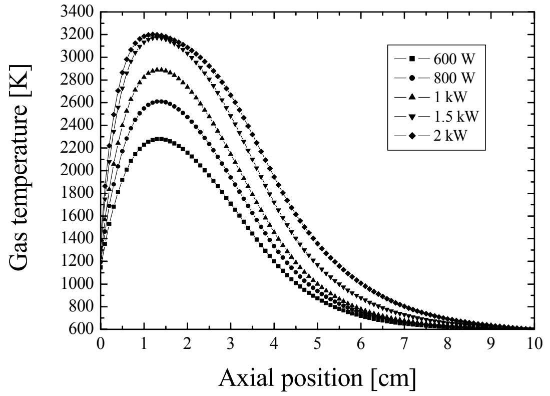

Figure 7-a: Axial gas temperature profile calculated in hydrogen plasmas in function of the MWPD (substrate: z= 0 cm)

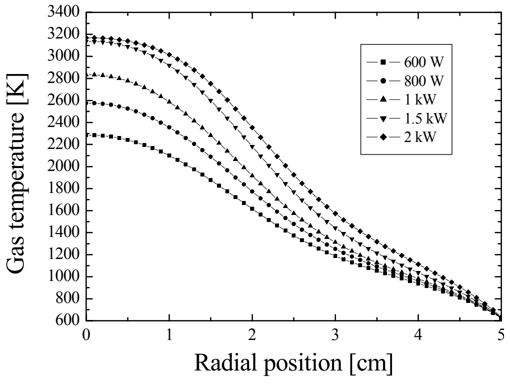

Figure 7-b: Radial gas temperature profile calculated in hydrogen plasmas in function of the MWPD (substrate: r= 0 to r= 2.5 cm)

This high T_g-values lead to an enhanced production of H-atom which is a key species for diamond deposition. A good agreement was found between the H-atom mole fractions predicted by the radial and axial models, as shown in figure 8-a, b.

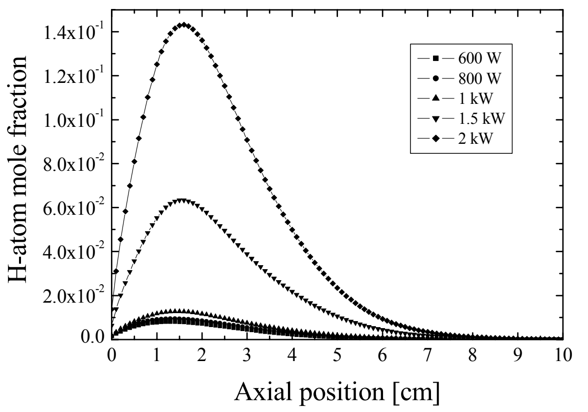

Figure 8-a: Axial H-atom mole fraction profile calculated in hydrogen plasmas in function of the MWPD (substrate: z= 0 cm)

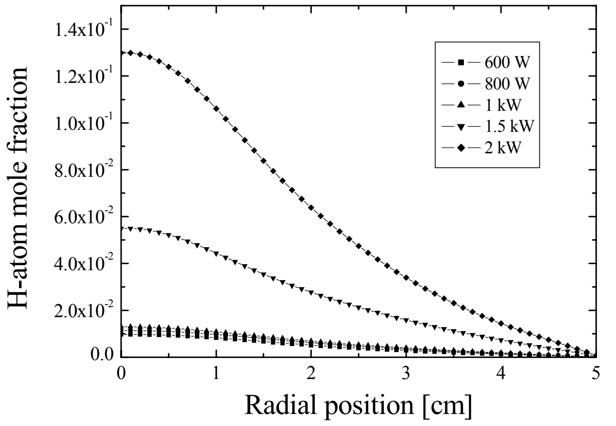

Figure 8-b: Radial H-atom mole fraction profile calculated in hydrogen plasmas in function of the MWPD (substrate: r= 0 to r= 2.5 cm)

The methyl radical is considered as an important precursor for diamond growth. Therefore, a special attention was devoted to its diagnostic and modelling. A comparison between experimental values obtained by means of IR TDLAS and the averaged values of the radial model are given figure 9-a, as function of MWPD. A reasonable agreement was obtained between, showing typical mole fraction of 10^{-4}.

Figure 9-b shows a comparison between the line-of-sight averaged mole fractions obtained from the model and from IR measurements. The calculated value of CH_4 dissociation rate are twofold smaller than those obtained from measurements. This discrepancy may come from the fact that the radial model uses approximate estimates of species and energy losses at diamond surface. In particular the H-atom recombination on the substrate may be overestimated, which would lead to underestimate the rate of $CH_4 + H \rightarrow CH_3 + H_2$ reaction which represents the main dissociation channel of CH_4 and production channel of CH_3. Note however that the model prediction remains satisfactory when we consider that several reaction rate constants are not well known over all the temperature range that characterizes diamond deposition system (600-3300 K). Note also that IR TDLAS measurements were performed in the plasma bulk, 2 cm above the substrate with a spatial resolution of 0.5 cm where the gas temperature is the higher, and where CH_4 thermal dissociation is maximal, whereas the radial model is axially averaged. Nevertheless, the agreement can be considered as reasonable since the hierarchy of the 5 carbon-species detected are well predicted by the model, with C_2H_2 as major species, followed by C_2H_4, CH_3 and C_2H_6.

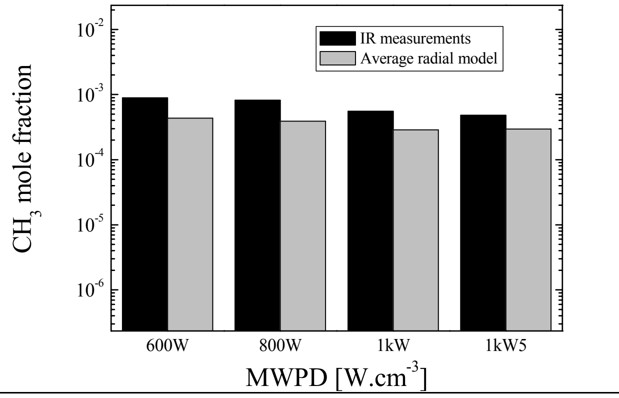

Figure 9-a: CH3 radical measured by IR TDLAS and averaged radial model mole fraction (5% CH_4) in function of the MWPD

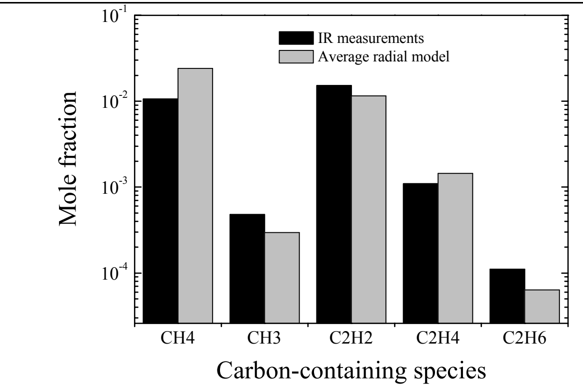

Figure 9-b: Carbon-containing species measured by IR TDLAS and averaged radial model mole fraction (5% CH_4, P=1.5 kW, p= 80 mbar)

The experimental difficulties associated with the use of IR TDLAS for a strongly non uniform discharge are highlighted when looking at the axial and radial species profiles in figure 10-a,b. The discharge zone which presents the region of interest can be analysed with the axial model. Indeed, when looking the radial distribution of species densities, one can see a strong increase of stable species like CH_4, C_2H_4 and C_2H_6 in the cold region of the reactor, i.e. outside of the plasma bulk and the plasma/surface boundary layer. For such species, the mole fraction in the active region can only be reached by the models, since the measured radially-averaged values of density are mainly representative of the cold gas outside the discharge zone. This shows the limits of the IR line of sight technique in a strongly non-uniform discharge like the one investigated here. Nevertheless, the CH_3 radical which is mainly present in the hot region of the discharge was found in satisfactory agreement with measurements, when taking into account an absorption length equal to the visible plasma region (i.e. 5 cm).

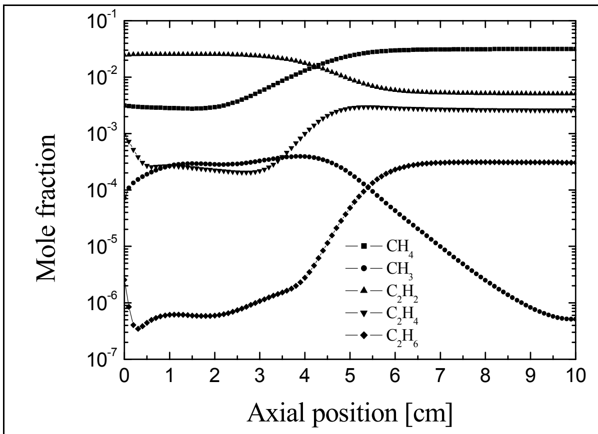

Figure 10-a: Axial H-atom mole fraction profile
P= 1.5 kW, p= 80 mbar, MWPD= 23 W.cm^{-3}, 5 % CH_4
(substrate: z= 0 cm)

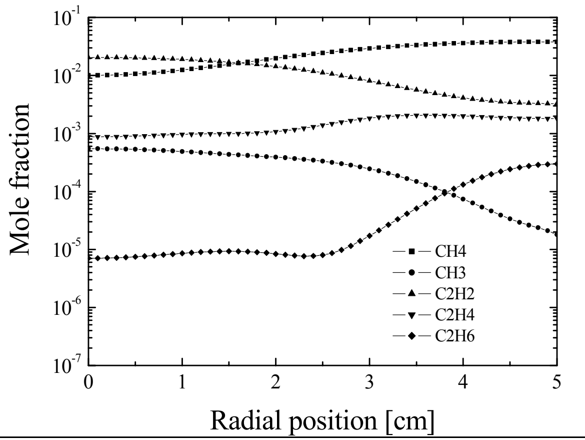

Figure 10-b: Radial H-atom mole fraction profile
P= 1.5 kW, p= 80 mbar, MWPD= 23 W.cm^{-3}, 5 % CH_4
(substrate: r= 0 to r= 2.5 cm)

The maximum of the axial distribution of CH_4 dissociation yield is much greater than the dissociation yield estimated from the radial model. This confirms the fact that the axial averaging performed when using the radial model may significantly affect estimated dissociation yield and species density. We may conclude that the radial model may be used only for the determination of the relative radial variation of species densities, while the axial model can be used for more quantitative prediction.

Conclusion

The chemistry that occurs in a moderate pressure microwave H_2/CH_4 discharge used for diamond deposition has been experimentally analysed with IR Tuneable Diode Laser Absorption Spectroscopy. The densities of 5 important carbon-containing species CH_4, CH_3, C_2H_2, C_2H_4 and C_2H_6 were systematically measured. This technique being line of sight integrated, a radial model of the discharge was developed along the optical path in order to analyse the experimental results and especially the effect of the strong temperature and concentration gradients on the line-of-sight measured densities. Reasonable agreement were obtained between the radial model and the IR measurements in a wide range of diamond deposition processes.

References

[1] K. Hassouni, O. Leroy, S. Farhat, A. Gicquel, Plasma Chem. Plasma Process. **18-3**, 325 (1998).
[2] K. Hassouni, T.A. Grotjohn, A. Gicquel, J. Appl. Phys. **86-1**, 134 (1999).
[3] A. Gicquel, M. Chenevier, K. Hassouni, A. Tserepi, M. Dubus, J. Appl. Phys. **83**, 7504 (1998).
[4] M.A. Cappelli, T.G. Owano, A. Gicquel, X. Duten, Plasma Chem Plasma Process. **20**, 15 (2000).
[5] J. Röpcke, L. Mechold, M. Käning, J. Anders, F.G. Wienhold, D. Nelson, M. Zahniser, Rev. Sci. Instrum. **71**, 3706 (2000).
[6] L. Mechold, J. Röpcke, X. Duten, A. Rousseau, Plasma Source Sci. Technol. **10**, 52 (2001).
[7] G. Lombardi, G.D. Stancu, F. Hempel, A. Gicqual, J. Röpcke, submitted in Plasma Source Sci. Technol.
[8] S.L. Girshick, C. Li, B.W. Yu, H. Han, Plasma. Chem. Plasma Process., **13**, 169 (1993).
[9] B.W. Yu, S.L. Girshick, J. Appl. Phys., **75**, 3914 (1994).
[10] H. Tawara, Y. Itakawa, H. Nishimura, H. Tanaka, Y. Nakamura, NIFS-DATA Res. Rep., **6**, 1 (1990).
[11] H. Tahara, K.I. Minami, A. Murai, T. Yasui, T. Yoshikawa, Jpn. J. Appl. Phys, **34**, 1972 (1995).
[12] Y. Breton, PhD Thesis, University Paris North (1997).
[13] L.N. Krasnoperov, I.J. Kalinovski, H.N. Chu, and D.J. Gutman, *J. Phys. Chem.*, **97**, 11787 (1993).

Secondary electron emission by nitrogen metastable states in atmospheric-pressure glow discharge

C. Khamphan[1], P.Ségur[1], F. Massines[2], M.C. Bordage[1], N. Gherardi[2] and Y.Cesses[1]

[1] Centre de Physique des plasmas et de leurs Applications de Toulouse(CPAT), UMR CNRS n°5002
[2] Laboratoire de Génie électrique de Toulouse(LGET), UMR CNRS n°5003
Université Paul Sabatier, 118,route de Narbonne ,31062 Toulouse Cedex France

Abstract

The aim of this work is to contribute to a better understanding of the formation of a glow dielectric barrier discharge in nitrogen at atmospheric pressure. To this end, a time dependent, one-dimensional fluid model of the discharge is used. The influence of secondary electron emission due to metastable states of nitrogen is investigated and the introduction of this phenomenon into the model gives results in excellent agreement with experiment.

1. Introduction

Dielectric barrier discharges (DBD) at atmospheric pressure are widely used in various applications such as ozone production, depollution, surface treatment and thin film deposition. At atmospheric pressure, these discharges are usually filamentary. This does not allow the injected energy to be correctly controlled and leads to non-uniform surface treatments. Under some specific conditions, it is possible to obtain a glow discharge similar to the one obtained at low pressure. This kind of discharge is very interesting for applications related to surfaces (treatment or coating).

Dielectric barrier discharges at atmospheric pressure have been under study both theoretically (CPAT) and experimentally (LGET) for a considerable time in Toulouse and a glow discharge in nitrogen has been in use for a few years in LGET[1]. In order to understand the physical mechanisms involved in the appearance of a glow discharge regime in nitrogen, a numerical model has been developed at CPAT.

The first results of this model [2] revealed the major role played by the lowest metastable states of nitrogen ($N_2(A^3\Sigma_u^+)$ and $N_2(a'^1\Sigma_u^-)$). Through reactions 21 and 22 (see. Table 1), they enable the creation of electrons and N_4^+ in between two discharges by Penning ionisation. Thus, this slowly growing space charge, starting at weak fields, avoids the formation of large electron avalanches leading to filamentary discharges.

However, recent work [3] has pointed out that $N_2(a'^1\Sigma_u^-)$ density could not be sufficient to supply enough charged particles between two discharges and the excited states could be quenched by collision with nitrogen molecules (reaction 20) [4]. So it is possible that Penning ionisation between two metastable states of nitrogen is not the only physical mechanism playing an important role in the production of charged particles. Other processes must be investigated.

For a glow discharge to occur, a source of secondary electrons is necessary when the electric field is low. In their work, Golubovskii et al.[3] introduced spontaneous electron desorption on the cathode. When an electrode is the anode, the dielectric surface is charged with electrons. During the following half cycle, those electrons desorb and give rise to a desorption current. Golubovskii et al. obtained results corresponding qualitatively to the experimental data. We will explain later why we think that spontaneous electron desorption is not the main process occurring in an atmospheric-pressure glow discharge in nitrogen.

Another possible source of charged particles is secondary emission due to the impact of nitrogen metastable states on the electrodes. We present the experimental evidence and observations which led us to consider this process below. The results obtained from the numerical modelling will then be presented.

2. Secondary emission due to nitrogen metastable states

2.1 Secondary emission induced by metastable states

The secondary emission coefficient due to metastable impact (γ_m) on a metallic cathode can be high [5,6]. Little[6] reports that γ_m may be between 0.1 and 1 in a glow discharge in the case of metallic cathodes. For a dielectric surface, the problem is more complicated because of the charge-up effect. If the dielectric surface is not charged, the secondary emission coefficient induced by metastables (but also by ions) can be calculated from Hagstrum's theory [18]. Motoyama et al. have made such calculations[7]. In their work, it can be seen that the maximum value of the secondary emission coefficient is 0.5. However, the influence of the charge-up effect on the secondary emission coefficient value is not known. In our case, as the dielectric surface has been charged by electrons during the previous breakdown, it is likely that secondary emission may be high, both from metastables and ions. Based on the above comments, we will use the maximum value of 0.5 for the secondary emission coefficient in this work.

2.2 Role of nitrogen metastable states

The importance of secondary electron emission due to $N_2(A^3\Sigma_u^+)$ metastable impact on a metallic cathode has been reported already [8]. Furthermore, experimental investigations carried out at LGET have provided evidence that $N_2(A^3\Sigma_u^+)$ plays an important role in the occurrence of a glow dielectric barrier discharge in nitrogen[1,9]. Optical emission spectroscopy measurements clearly show that the concentration of metastable states is always large, even between two breakdowns [9]. Hence, metastable states created during the breakdown can produce electrons by secondary emission whatever the value of the electric field inside the discharge. Another important observation is that adding a gas able to quench $N_2(A^3\Sigma_u^+)$ states to nitrogen induces a transition from a glow discharge to a filamentary one. Oxygen plays this quenching role and it is thus impossible to obtain a glow discharge in air. If electron desorption is assumed to be the main process of production of electrons at low field, a glow discharge could be obtained even with strong quenching of metastable states. This feature is the main drawback of Golubovskii et al.'s model[3].

3. Numerical modeling

The numerical model has already been described elsewhere [2,10]. As the discharge is radially homogenous, a one-dimensional model is used. It is based on the solution of the continuity equations for every species (electrons, ions and excited states) coupled to the Poisson equation. This self-consistent model gives the spatiotemporal variation of the particle densities and of the electric field. The time variations of current and voltages are also obtained. A model describing the current in the external circuit of the LGET experiment was added in order to correctly compare modelling results with measurements. The model was an RLC circuit in which the element values had been measured.

In the kinetic description, the four positive ions of nitrogen N^+, N_2^+, N_3^+, N_4^+, the two lowest metastable states $N_2(A^3\Sigma_u^+)$ and $N_2(a'^1\Sigma_u^-)$ and the radiative state $N_2(C^3\Pi_u)$ were taken into account. The set of reactions considered and the corresponding kinetic rates are given in table I. Reactions 1 and 2 characterise the direct ionisation of nitrogen molecules by electrons. Reactions 3-5 characterise the direct and inverse excitation of the two main metastable states of nitrogen, $N_2(A^3\Sigma_u^+)$ and $N_2(a'^1\Sigma_u^-)$, and of the radiative state $N_2(C^3\Pi_u)$. The corresponding reaction rates were computed using a numerical solution of the equilibrium

Table 1. Reactions and corresponding reaction rates used in the model (see references in [20])

Electron-molecule collisions					
Ionisation			***Recombination***		
1	$e^- + N_2 \rightarrow N_2^+ + 2e^-$	f(E/N)	6	$N_4^+ + e^- \rightarrow N_2(C^3\Pi_u) + N_2$	k=2.0 10^{-6} $(Tg/Te)^{1/2}$ $cm^3.s^{-1}$
2	$e^- + N_2 \rightarrow N^+ + N + 2e^-$	f(E/N)	7	$N_3^+ + e^- \rightarrow N_2 + N$	k=2.0 10^{-7} $(Tg/Te)^{1/2}$ $cm^3.s^{-1}$
Excitation			8	$N_2^+ + e^- \rightarrow 2N$	k=2.8 10^{-7} $(Tg/Te)^{1/2}$ $cm^3.s^{-1}$
3	$e^- + N_2 \leftrightarrow N_2(A^3\Sigma_u^+) + e^-$	f(E/N)	9	$N_2^+ + e^- \rightarrow N(^2D) + N$	k=2.0 10^{-7} $(Tg/Te)^{1/2}$ $cm^3.s^{-1}$
4	$e^- + N_2 \leftrightarrow N_2(a'^1\Sigma_u^-) + e^-$	f(E/N)	10	$N_2^+ + 2e^- \rightarrow 2N + e^-$	k=1.0 10^{-19} $(Tg/Te)^{4.5}$ $cm^6.s^{-1}$
5	$e^- + N_2 \leftrightarrow N_2(C''\Pi_u) + e^-$	f(E/N)	11	$N_2^+ + e^- + N_2 \rightarrow 2N_2$	k=6.0 10^{-27} $(Tg/Te)^{1.5}$ $cm^6.s^{-1}$
Ion-molecule collisions					
12	$N_2^+ + 2N_2 \rightarrow N_4^+ + N_2$	k=5.0 10^{-29} $cm^6.s^{-1}$	16	$N_3^+ + N \rightarrow N_2^+ + N_2$	k=6.6 10^{-11} $cm^3.s^{-1}$
13	$N_2^+ + N_2 + N \rightarrow N_3^+ + N_2$	k=3.4 10^{-29} $cm^6.s^{-1}$	17	$N_4^+ + N_2 \rightarrow N_2^+ + 2N_2$	k=2.4 10^{-15} $cm^3. s^{-1}$
14	$N_2^+ + N_2(A^3\Sigma_u^+) \rightarrow N_3^+ + N_2$	k=3.0 10^{-10} $cm^3.s^{-1}$	18	$N_4^+ + N \rightarrow N^+ + 2N_2$	k=1.0 10^{-11} $cm^3. s^{-1}$
15	$N_2^+ + N \rightarrow N^+ + N_2$	k=7.3 10^{-13} $cm^3.s^{-1}$	19	$N + N_2 + N^+ \rightarrow N_2^+ + N_2$	k=1.0 10^{-29} $cm^6.s^{-1}$
Reactions involving metastable states					
20	$N_2(a'^1\Sigma_u^-) + N_2 \rightarrow N_2(X) + N_2(X)$		k=2.0 $10^{-13}$$cm^3.s^{-1}$		
21	$N_2(a'^1\Sigma_u^-) + N_2(a'^1\Sigma_u^-) \rightarrow N_4^+ + e^-$		k=1.0 $10^{-11}$$cm^3.s^{-1}$		
22	$N_2(A^3\Sigma_u^+) + N_2(a'^1\Sigma_u^-) \rightarrow N_4^+ + e^-$		k=1.5 $10^{-11}$$cm^3.s^{-1}$		
23	$N_2(A^3\Sigma_u^+) + N_2(A^3\Sigma_u^+) \rightarrow N_2(B) + N_2(X)$		k=7.7 $10^{-11}$$cm^3.s^{-1}$		
24	$N_2(A^3\Sigma_u^+) + N_2(A^3\Sigma_u^+) \rightarrow N_2(C) + N_2(X)$		k=3.0 $10^{-10}$$cm^3.s^{-1}$		
25	$N_2(A^3\Sigma_u^+) + N \rightarrow N_2 + N$		k=4.0 $10^{-11}$$cm^3.s^{-1}$		
26	$N_2(C) + N_2 \rightarrow N_2(a'^1\Sigma_u^-) + N_2$		k=1.0 $10^{-11}$$cm^6.s^{-1}$		
27	$N_2(C) \rightarrow N_2(B) + h\nu$		k=2.7 $10^{+7}$$s^{-1}$		

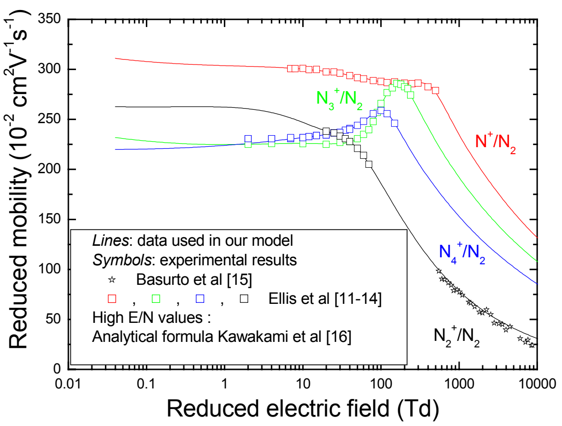

Figure 1 : Ion mobilities used in the model

form of the Boltzmann equation. As electrons and ions are assumed to be in equilibrium with the electric field, the reaction rates are functions of the reduced electric field E/N, where N is the density of the background gas. Reactions 6-10 characterise the different recombination processes between electrons and ions. Reactions 12-19 correspond to ion - molecule collisions. And finally, reactions 20-27 present processes involving the metastable and excited states of nitrogen. The mobility and diffusion coefficients for electrons were determined from the numerical solution of the Boltzmann equation. Mobility of ions was obtained from the reports published by Ellis et al.[11-14]. However, as the E/N range of the available data was insufficient, values were extrapolated to low field using the Langevin formula and to high field using the Kawakami analytic formula[16]. The mobilities computed are given in figure 1. They are functions of the reduced electric field E/N expressed in Townsend ($1\text{Td}=1.10^{-17}\text{V.cm}^2$). The diffusion coefficients for ions were obtained using Einstein's relationship and the diffusion coefficients for metastable states were estimated from the data reported in [17]. Photoemission at the cathode was not taken into account in our model because, in our type of discharge, few UV photons are emitted by N_2 radiating states due to low E/N values and the influence of this process is small [6,3]. For all nitrogen ions, the secondary emission coefficient was assumed constant and equal to 0.01.

4. Results

4.1 $\gamma_{metastables}=0.5$ / $\gamma_{ions}=0.01$

Figure 2 shows the time variation of the calculated and measured electrical characteristics over a cycle for discharge current, applied voltage and gas voltage. Measurements are represented with symbols while model results are represented by lines. The calculated electrical characteristics show excellent agreement with measurements indicating that the physical mechanisms included in the model are realistic.

Figure 3 presents the spatial distribution over the gas gap of the reduced total electric field and of the densities of electrons and N_4^+ ions (the dominant ion in the discharge). These spatial distributions are given at the maximum of the discharge current. The pure space charge field is also represented, by a dashed line. The discharge is a pure weak cathode fall with no negative glow. The space charge being small, this structure is typical of a Townsend discharge. The electric field is quasi-constant over the gas gap because the ionisation level in the discharge is not high enough to induce a strong distortion of the electric field. As the density of electrons is maximum at the anode, the production of excited states is also maximum there. $N_2(A^3\Sigma_u^+)$ states are created close to the anode, which will become the cathode in the next half cycle.

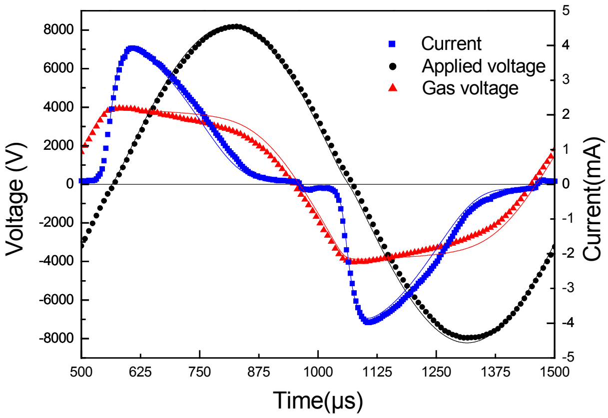

Figure 2 : Electrical characteristics of the discharge $\gamma_m=0.5$ (Measurements : symbols – Model : Lines)

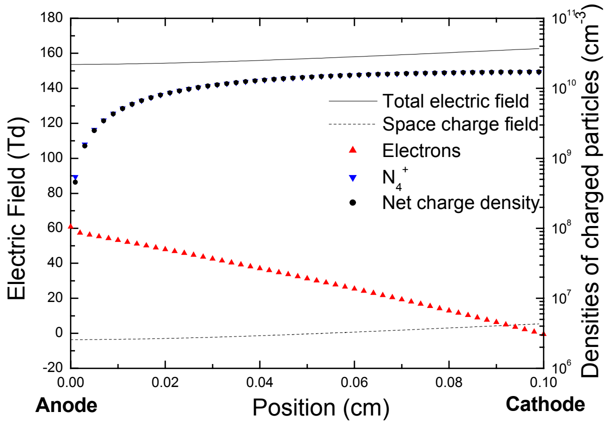

Figure 3 : Space variation of electrons, ions densities and of reduced electric field at the maximum of discharge current

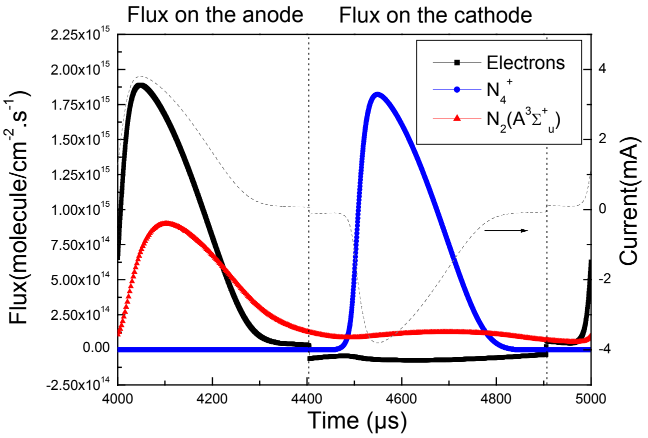

Figure 4: Discharge current, and electrons, N_4^+ and $N_2(A^3\Sigma_u^+)$ fluxes on one of the dielectric surfaces

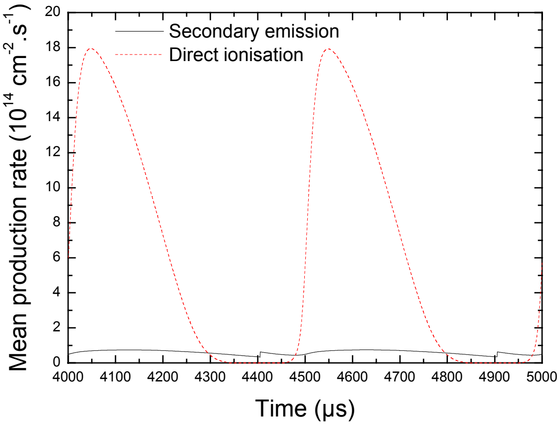

Figure 5: Electrons production rates : flux of electrons emitted by secondary emission (line) and spatially integrated ionisation rate (dashed line)

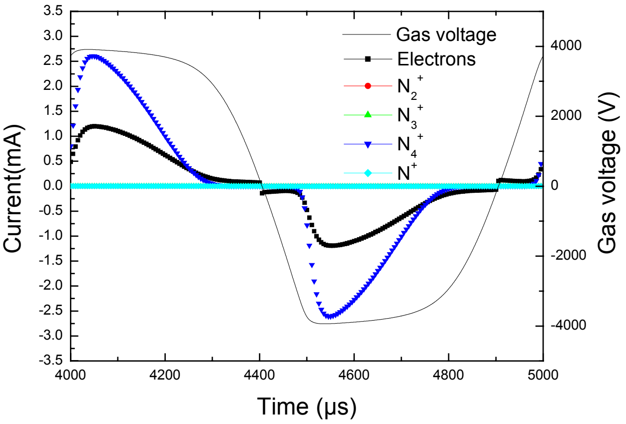

Figure 6: Current due to each charged particle and gas voltage over a cycle

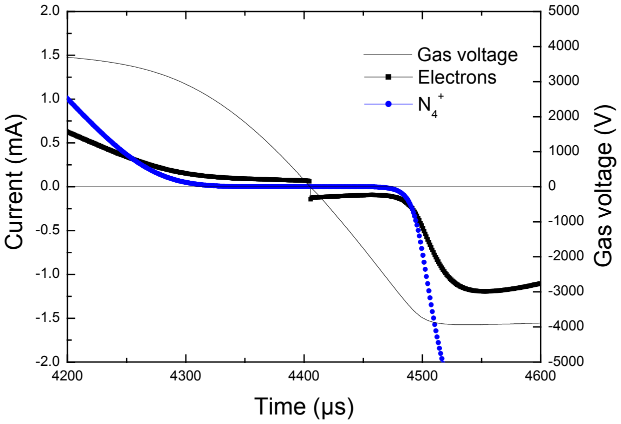

Figure 7: Current due to electrons and N_4^+ at V$_g$ inversion (enlargment of the previous figure)

To evaluate the influence of secondary emission of metastable states, we have plotted the fluxes of $N_2(A^3\Sigma_u^+)$ metastables, N_4^+ ions and electrons on one of the electrodes (figure 4). This electrode is the anode during the first half cycle and becomes the cathode when the gas voltage(V$_g$) polarity changes. We can see that, before the breakdown, the metastable flux on the cathode is much higher than the ion flux. Hence, at this time, secondary emission of electrons due to metastables is very efficient. This can be observed by looking at the variation of the electron flux. In the first half period, the electron flux is maximum during the current peak and then decreases. When V$_g$ polarity changes, the electron flux becomes negative, which means that electrons are emitted from the cathode. Secondary emission due to ions is negligible because, on the one hand, before the breakdown, the value of the ion flux is very low and on the other hand, during the breakdown, γ_{ions} value is small.

In figure 5, the mean production rates of electrons by secondary emission at the cathode and by direct ionisation are compared. Direct ionisation is two orders of magnitude higher than secondary emission. The indirect ionisation rate by Penning ionisation is several orders of magnitude lower and is not represented on the figure. The direct ionisation rate is high during the current peak but vanishes between two discharges when the electric field is low. The secondary electron emission rate is low compared to direct ionisation but its value is quasi-constant at low electric field.

Figure 6 shows the currents for all the charged particles. Only the N_4^+ and electron currents can be observed. This is due to the fact that N_2^+ ions created by direct ionisation are quickly converted into N_4^+ ions (reaction 12). During the current peak, the N_4^+ current is higher than the electron current. Figure 7 shows details of the current inversion. We note that the electron current dominates. Electrons come from secondary emission at the cathodes as already shown in figure 5. We observe that the variation of current is very steep when V_g polarity changes. However, this variation is smoother on the experimental curve. This difference may be due to the fact that, in our model, γ_m does not depend on the reduced electric field E/N. It is likely that, when the electric field is small, γ_m would be low and would increase with E/N [7]. In figure 8, we plot the value of the reduced electric field on the dielectric which is the anode during the first half cycle and the cathode during the next one. We observe that E/N is low at current inversion and then rises rather quickly before breakdown. Hence, taking into account the dependence of γ_m on E/N could lead to a less steep current inversion. It could also be interesting to correlate γ_m with surface electron density. This surface density is also plotted on figure 8. As already mentioned, this density is maximum before breakdown.

4.2 $\gamma_{metastables}$=0.01 / γ_{ions}=0.01

In order to investigate the influence of secondary emission of metastable states, we strongly decreased the γ_m coefficient and analysed the results of the model. Figure 9 shows the time variation of the electrical characteristics calculated in this new configuration. In this case, the structure of the discharge is very different. Oscillations can be observed on the current curve. Figure 10 and 11 clearly show that no electrons are emitted at the cathode. The breakdown voltage is about 900V higher than in the previous case ($\gamma_{metastables}$=0.5 / γ_{ions}=0.01). Then, the current rise is very steep and oscillations related to the power supply appear. Indeed, the variation of the load seen by the power supply varies during the ignition of the discharge. In this case, as the variation of the power supply load is too fast, instabilities appear[19].

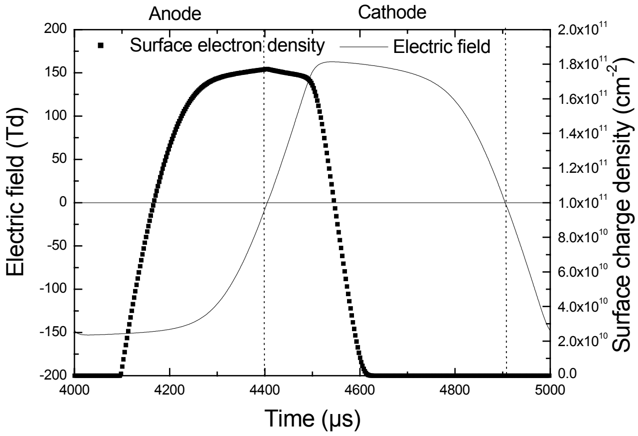

Figure 8 : Variation of electron surface density and reduced electric field on one of the dielectric surfaces

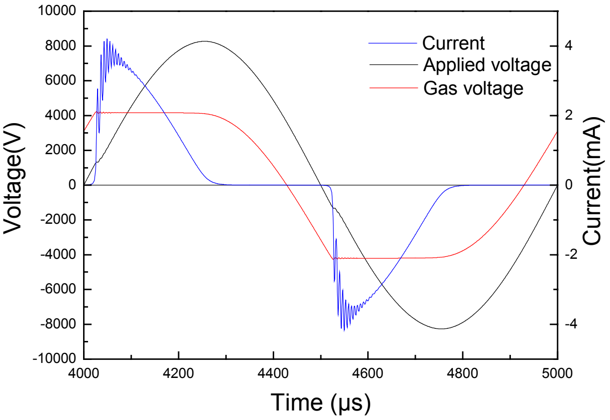

Figure 9 : Electrical characteristics of the discharge γ_m =0.01

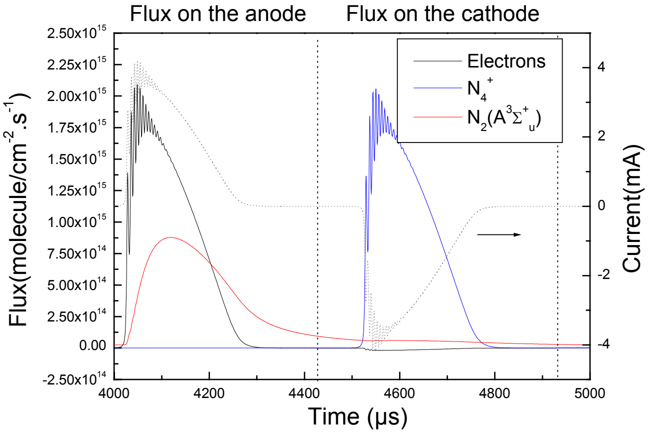

Figure 10 : Discharge current, and electron, N_4^+ and $N_2(A^3\Sigma_u^+)$ fluxes on one of the dielectric surfaces

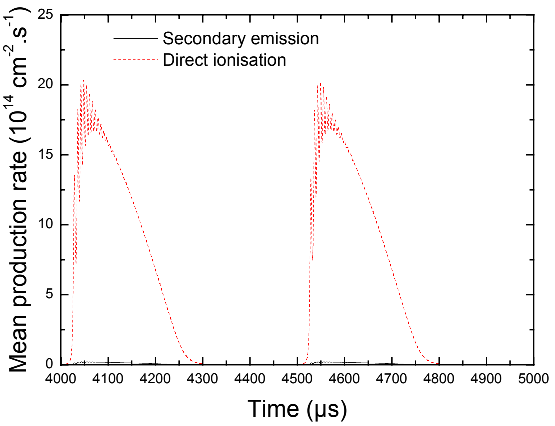

Figure 11 : Electron production rates : flux of electrons emitted by secondary emission (line) and spatially integrated ionisation rate (dashed line)

According to the above results (§4.1 and §4.2), it clearly appears that secondary emission induced by metastables allows a continuous creation of electrons before the breakdown. This process limits the increase of the electric field in the discharge and thus avoids the formation of large electron avalanches.

5. Conclusion

In this work we used numerical modelling to investigate the influence of secondary emission induced by metastable states on a dielectric barrier discharge in nitrogen at atmospheric pressure. It clearly appears that this phenomenon is important in the formation of a glow discharge in nitrogen. Indeed, the continuous creation of electrons at the cathodes allows a Townsend breakdown to be initiated.

To improve our understanding of this type of discharge, it would be interesting to calculate a secondary emission coefficient taking into account the influence of charges on the dielectric surface and also the influence of backscattering of emitted electrons at weak electric field.

References

[1] N.Gherardi, G.Gouda, E.Gat, A.Ricard and F.Massines, Plasma Sources Sci. Technol. **9** (2000), 340

[2] P.Ségur and F.Massines, Proc.13th Int.Conf. on Gas Discharges and their Applications, p15 (2000)

[3] Y.B.Golubovskii, V.A. Maiorov, J.Behnke and J.F. Behnke, J.Phys.D:Appl.Phys. **35** (2002), 751-761

[4] Piper L.G., J. Chem. Phys, **87** (3), 1987

[5] Y.P.Raizer,in: Gas discharge physics, Springer Verlag, (1991), 71

[6] P.F.Little, in: Electron Emission Gas Discharges I, Springer Verlag, (1956), 574

[7] Y.Motoyama,H.Matsuzaki and H.Murakami IEEE Trans. on electron devices **48(8)** (2001) 1568

[8] D.A.Bosan, T.V.Jovanovic and D.M. Krmpotic, J.Phys.D:Appl.Phys. **30** (1997), 3096-3098

[9] F.Massines, P.Ségur, N.Gherardi, C.Khamphan and A.Ricard, Proc. 8th International Conference on Plasma Surface Engineering(PSE 2002), To be published

[10] F.Massines, R.Ben Gadri,P.Decomps,A.Rabehi,P.Ségur,C.Mayoux, J.Phys.D:Appl.Phys **38** (1998), 2950

[11] H.W.Ellis, R.Y.Pai, E.W.McDaniel, E.A.Mason and L.A.Viehland, Atomic Data and Nuclear Data Tables **17** (1976), 177-210

[12] L.A.Viehland and E.A.Mason, Atomic Data and Nuclear Data Tables **60** (1995), 37-95

[13] H.W.Ellis, E.W. McDaniel, D.L. Albritton, L.A.Viehland, S.A Lin and E.A. Mason, Atomic Data and Nuclear Data Tables **22** (1978), 179-217

[14] E.W.McDaniel and E.A.Mason,The mobility and diffusion of ions in gases, John Wiley and Sons (1973)

[15] E.Basurto, J. de Urquijo, I.Alvarez and C. Cisneros, Physical Review E **61(3)** (2000) 3053

[16] R.Kawakami, S.Okuda,T.Miyazaki,N. Ikuta, Journal of the physical Society of Japan **65** (1996) 1270

[17] G.N.Hays, C.J.Tracy, A.R.Demonchy and H.J.Oskam, Chemical Physics Letters **14** (1972),352-355

[18] H.D.Hagstrum, Physical Review **96(2)** (1954), 336-365

[19] N.Naudé, J.P. Cambronne, N.Gherardi, F.Massines, Proceedings of this conference.

[20] S.LeMoing, A.Rabehi, J. Potin, P.Ségur, M.C.Bordage, E.Croquesel, F.Massines, Proc.13th Int.Conf. on Gas Discharges and their Applications (2000), 363

Differences between 2D and 3D modelling of thermal plasma torches

P. Freton, J.J. Gonzalez, A. Gleizes

C.P.A.T., UMR5002 C.N.R.S., Université Paul Sabatier, 118, route de Narbonne 31062 Toulouse Cedex 4 – France
Freton@cpat.ups-tlse.fr

Abstract:

A cutting plasma torch is studied by a numerical approach. Due to the complexity of this geometry the 2D models of the literature classically use several assumptions. The aim of this paper is to study the validity of two specifics points: the description of the air injected by the vortex and the arc root attachment. The temperature fields obtained by the 2D and the 3D models are then presented in the entire domain. The results between the two models are very close and validate the use of a 2D model in a supersonic cutting torch: for the vortex injection description due to the nozzle constriction and for the arc attachment due to the supersonic arc behaviour. Nevertheless a 3D model is needed to study the heat transfer in the metal work piece.

1. Introduction

Thermal plasma processes, in order to be improved, need a better understanding of the plasma behaviour. Two complementary approaches can be used: experimental and theoretical. Since the nineties, modelling becomes more and more important and numerous papers report numerical models in one or two dimensions. Nevertheless, the three dimensional models remain scarce due to the limited computing possibilities. Sometimes, the assumption of 2D is sufficient for optimising, but the new computer power makes it possible to develop and characterise, when necessary, the plasma medium in three dimensions (3D), using geometries closer to reality. Indeed, some specific points like for example the vortex gas injections or some complex geometries requires a 3D co-ordinate system. The aim of this paper is to present a cutting configuration developed in 3D, to compare the results with the classically used 2D approach, which necessitates several assumptions, and to determine the limitation of the 2D model.

For this communication, two main points are studied in the cutting transferred arc: the vortex injection and the arc attachment description on the metal plate. The two points will be studied in 2D (with some classical assumptions) and in 3D. In the first part of this paper, the model is presented. It considers the plasma like a stationary laminar fluid at L.T.E. governed by the Navier Stokes conservation equations. These equations are solved using the commercial code Fluent v4 adapted for taking into account the plasma characteristics (electrical aspect, transport coefficients…). In a second part, the cutting geometry and its representation in 2D and 3D are presented. Finally, in the last part of this paper, the results show the validity of the 2D model on plasma characteristics prediction on the axis and the limitation of the 2D approach with the famous assumption of the porous anode is underlined for the case of the lateral arc attachment. We compare in the two cases the temperature evolution.

2. Mathematical model

The model assumes the plasma to be a laminar Newtonian fluid, in steady state, described by the Navier – Stokes equations. These equations traduce the conservation of the energy, momentum, total mass and oxygen mass fraction. In order to take into account the electrical aspect of the plasma, Poisson's law for the electrical potential and Maxwell's law for the potential vector components are solved. Joule heating and Lorentz's forces are added respectively in source terms of the energy and momentum equations. As the cutting torch uses oxygen gas discharging in an air environment, the air is considered as a non-reacting melt of 21% of oxygen and 79% of nitrogen. The transport coefficients are obtained using the assumption of LTE [1] and the Wilke laws [2]. The radiation of the plasma is taken into account with the net emission coefficient [3]. Commercial CFD code Fluent V4.5 is used to solve the differential equation system. Additional users subroutines are developed in Fortran to take into account the properties and additional equations. All the equations are written in 2D and 3D in the general form of a Patankar's equation [4]:

$$\mathrm{div}(\rho\vec{v}\phi) = \mathrm{div}\left(\Gamma_\phi \overline{\mathrm{grad}}(\phi)\right) + S_\phi \qquad (1)$$

ρ : Mass density, Γ_ϕ : diffusion coefficient, ϕ the variable (enthalpy, velocities…), S_ϕ : the source term and $\vec{v}$ the fluid velocity. The variables solved are h: the enthalpy, m_{O2} the mass fraction of oxygen, v_r, v_θ, v_z respectively the radial, azimuthal and axial velocity for the 2D model and v_x, v_y, v_z the components of the velocity for the 3D model. For electrical equations, we solve: V the electric potential, A_r, A_z (2D) or A_x, A_y, A_z (3D) the components of the potential vector (to obtain the magnetic field B). More details for each solved equation can be found in [5].

3. The cutting configuration – Assumptions on the geometry

The cutting torch used is an OCP 150 system with a Nertajet HP 120 stabilised current generator supply. This device is commercialised by Air Liquide. The cutting gas is oxygen discharging in an air environment, the current intensity equal to 60A, and a swirl injection is used. The nozzle diameter is equal to 1mm. The geometry of the torch is presented in figure 1 as it was modelled in 3D.

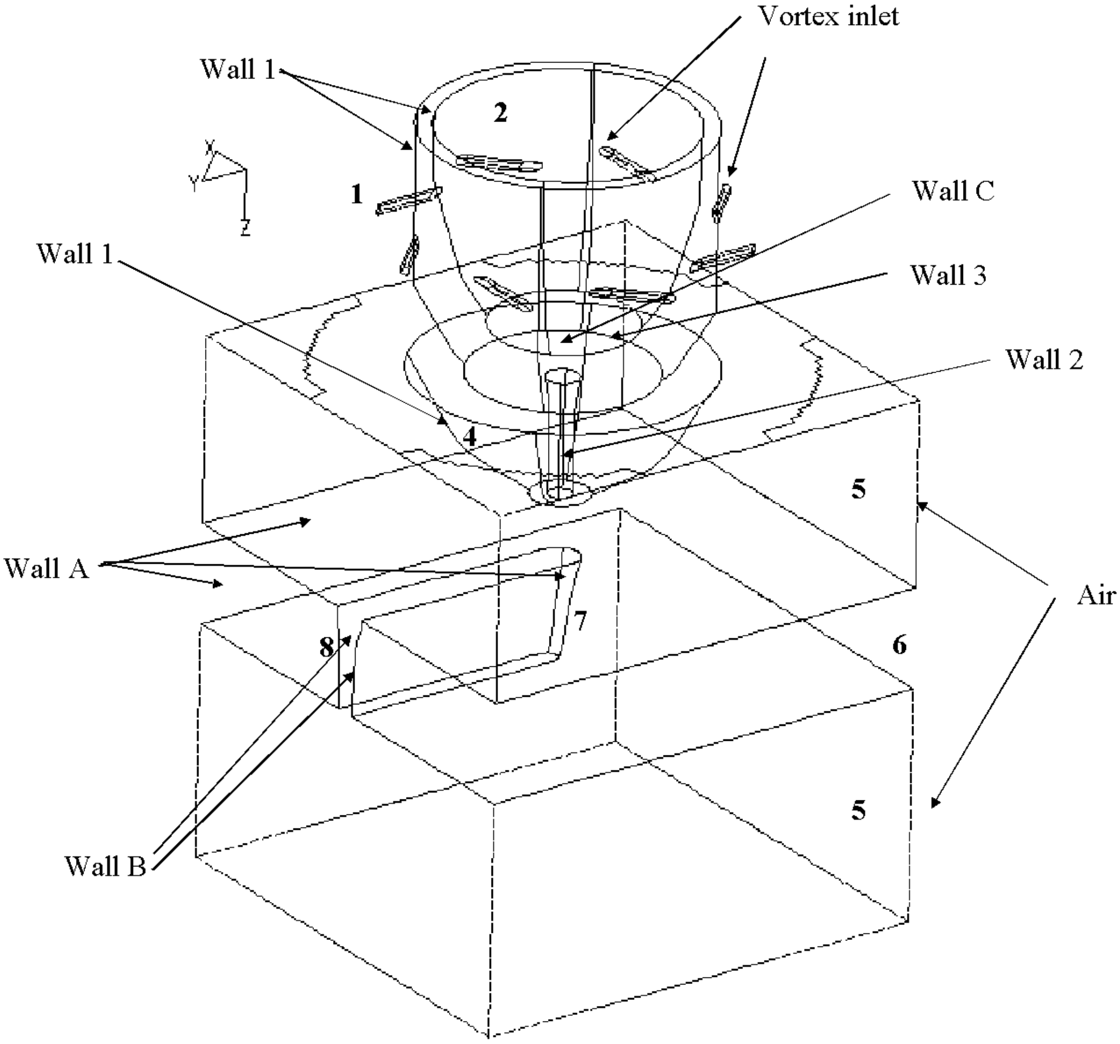

Figure 1: 3D geometry of the cutting configuration.

Part 1 corresponds to the 8 oxygen vortex injectors and part 2 to the flat cathode. Part 3 is the nozzle, par 4 the cap of the torch. Part 5 represents the surrounding air. Part 6 is the metal plate to be cut. In this plate, part 7 represents the front of the cut and part 8 the hole in the metal plate. The thickness of the plate is 4mm and the distance between the nozzle exit and the top of the plate is 3mm. The size of the hole has been chosen according to experimental results obtained by Air Liquide.

In three dimensions, no assumptions are made on the eventual symmetry of the jet. The system of equations is solved in a Cartesian repair (x,y,z). The entire domain is divided into 420000 cells. The same geometry in two dimensions is presented in figure 2. As there is an axis of symmetry, the hole cannot be well described in 2D. We make so the assumption of a cylindrical hole witch has the same diameter as the width of the hole for the 3D case. The volume under the plate is not represented in the 2D configuration and 13500 cells are used to represent the whole domain.

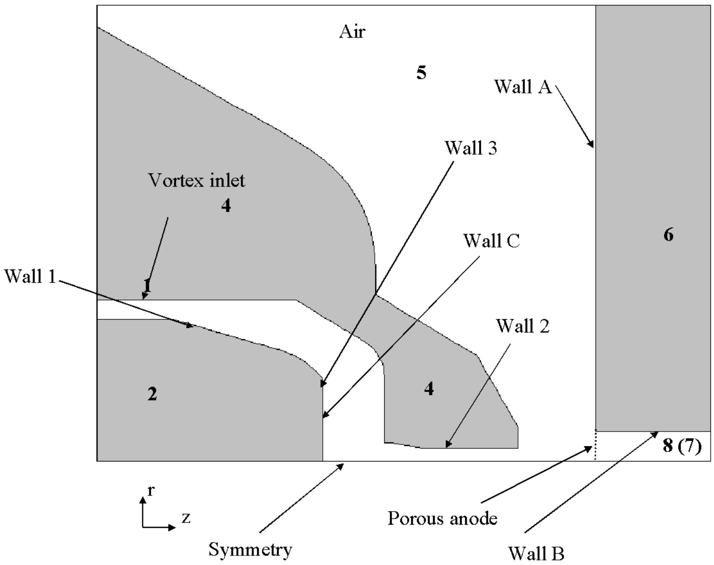

Figure 2: 2D geometry.

	Pressure P	v_i	T	m_{O2}	V	A_i
Wall 1	$\frac{\partial p}{\partial \vec{n}} = 0$	0 m/s	300K	$\frac{\partial m}{\partial \vec{n}} = 0$	$\frac{\partial V}{\partial \vec{n}} = 0$	$\frac{\partial A_i}{\partial \vec{n}} = 0$
Wall 2	$\frac{\partial p}{\partial \vec{n}} = 0$	0 m/s	700K	$\frac{\partial m}{\partial \vec{n}} = 0$	$\frac{\partial V}{\partial \vec{n}} = 0$	$\frac{\partial A_i}{\partial \vec{n}} = 0$
Wall 3	$\frac{\partial p}{\partial \vec{n}} = 0$	0 m/s	1000K	$\frac{\partial m}{\partial \vec{n}} = 0$	$\frac{\partial V}{\partial \vec{n}} = 0$	$\frac{\partial A_i}{\partial \vec{n}} = 0$
Wall A&B	$\frac{\partial p}{\partial \vec{n}} = 0$	0 m/s	1000K	$\frac{\partial m}{\partial \vec{n}} = 0$	0	$\frac{\partial A_i}{\partial \vec{n}} = 0$
Wall C	$\frac{\partial p}{\partial \vec{n}} = 0$	0 m/s	3500K	$\frac{\partial m}{\partial \vec{n}} = 0$	$J_z(x,y)/\Delta z$	$\frac{\partial A_i}{\partial \vec{n}} = 0$
Inlet (1)	P	$\frac{\partial v_i}{\partial \vec{n}} = 0$ (3D) cosinus director (2D)	300K	1	0 V	0 T.m
Exit (5)	1atm	$\frac{\partial v_i}{\partial \vec{n}} = 0$	$\frac{\partial T}{\partial \vec{n}} = 0$	0.233	0 V	$\frac{\partial A_i}{\partial \vec{n}} = 0$

Table 1: Boundary conditions in 2D and 3D.

The boundary conditions are given in table 1 for 2D and 3D cases. They are “classical” boundary conditions. At the cathode, the condition for the electrical potential is imposed through a parabolic profile of the current density. For the 2D boundary conditions, two points need to be highlighted. The first one is the condition for the eight vortex injectors. As the real vortex geometry cannot be taken into account in two dimensions, they are replaced by an injection corona, which has an area equivalent to the one of the eight injectors [6]. The direction of the velocity components is taken in order that it corresponds with the direction of the vortex. The second point to be highlighted is the arc attachment. In 3D, we not impose the arc root attachment. So, the arc can be transferred anywhere on the front cut. In 2D this condition is not possible and we use a porous anode through witch the plasma can flow. On this porous anode, situated at the top of the plate, we impose the electrical potential to be zero. In order to see the influence of these two points, we have separated our study in two cases. A first case where the calculations are made only in the torch device (and not in the volume under the nozzle exit) and a second where the whole configuration presented on figure 1 is studied. The results for the two cases are presented below.

4. Results in the torch

For the first case, the intensity is taken equal to 40A and the inlet pressure P=3.5atm. With this pressure, the mass flow rate obtained in 2D and 3D is the same and is about 3.2Slm. The potential fall in the torch is found to be 80V in the two cases. The temperature field obtained in 3D is presented in figure 3 for two perpendicular planes. The two fields are identical in the two planes and are symmetrical to the axis (Oz). The temperature is maximum in the nozzle, on this axis. This maximum, situated at the entry of the straight part, is 20 360K. Near the cathode, there is a radial expansion of the arc. Below, the plasma is constricted by the vortex in order to enable the arc to flow in the straight part of the nozzle. In this straight part, the arc seems to be fully developed and occupies all the nozzle. At the exit, the temperature is about 16000K.

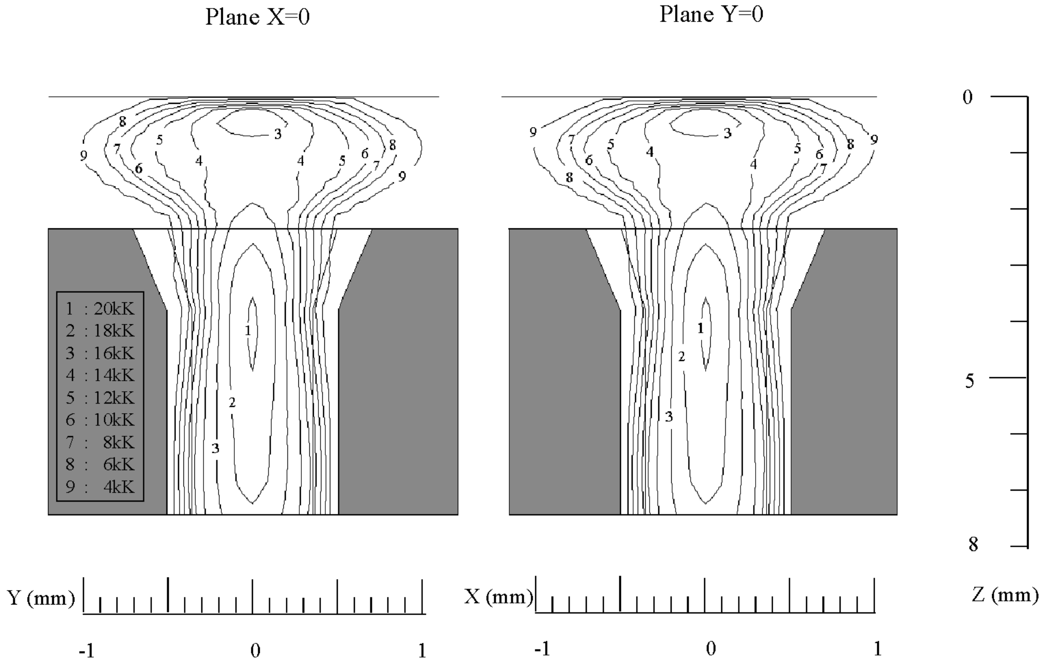

Figure 3: Temperature field for plane X=0 and plane Y=0

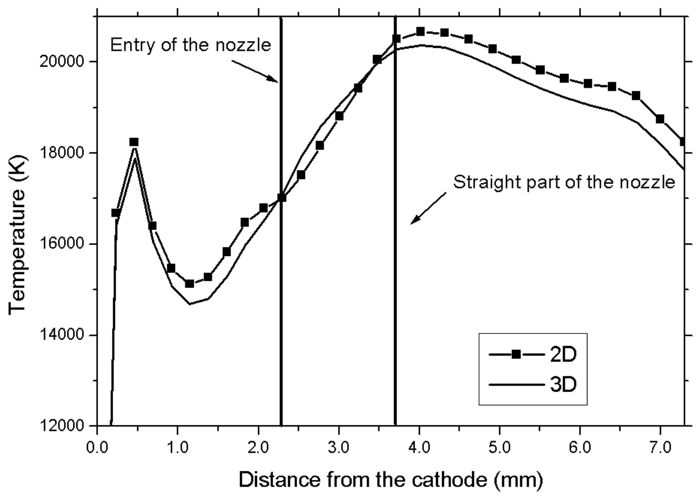

Figure 4: Axial temperature in the torch for 2D and 3D calculation

In figure 4, a comparison is made between the 2D axial temperature and the 3D one. The two curves are very close with a maximal difference of 500K. Between the cathode and the nozzle entry, there is a minimum of the temperature, which corresponds to a radial expansion of the plasma. Below, the arc is constricted by the vortex and the same value of the temperature is reached at the entry of the nozzle for 2D and 3D modelling. A local maximum is reached in the straight part of the nozzle. This maximum is 20300K for 3D and 20600K for 2D. After, the temperature decreases and is around 17500K at the nozzle exit. Concerning the velocities obtained, the differences are also very weak and we can say that in the torch device, the 2D calculation and 3D one give very similar results.

5. Results in the total cutting configuration

For this second case, we take a current intensity of 60A and an inlet pressure of 4.5atm. A mass flow rate of 4.2slm is obtained in 2D and 3D. For this case an electrical potential fall of 122V is found in 3D. The 2D value is slightly higher. The arc obtained is supersonic and presents a shock wave at the nozzle exit.

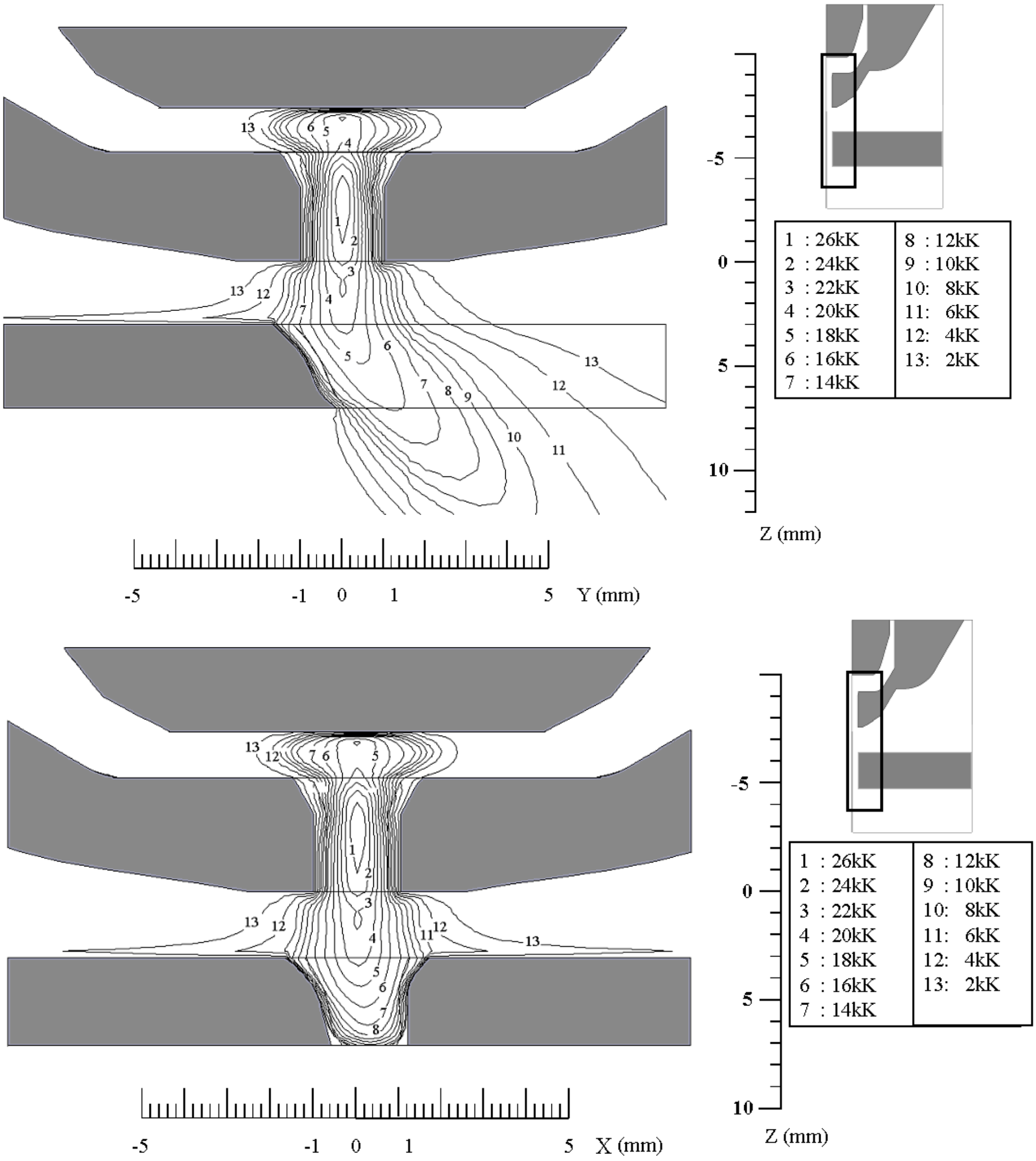

Figure 5: 3D Temperature fields for plane X=0 and Y=0.

Figure 5 show the 3D temperature field for plane X=0 and Y=0. In the nozzle, results are very close to those of the previous section. At the nozzle exit, there is a local maximum of the temperature (around

22000K) due to the presence of a shock wave. In the plane X=0 the plasma is deflected by the impact of the flow on the front of the cut and there is an expansion to the opposite side. In the plane Y=0, the plasma is confined and presents strong temperature gradients near the walls.

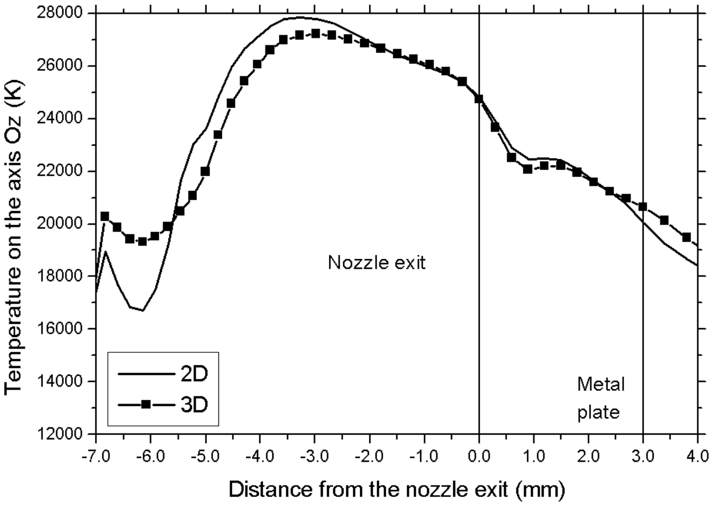

Figure 6: Axial temperature in the cutting configuration for 2D and 3D calculation

A comparison between 2D and 3D temperature on the axis is made in figure 6. Over the metal plate, the two profiles are similar. After the metal plate, in the hole the two temperature profiles cannot really be compared because the real geometry does not present any symmetry. Nevertheless the arc attachment in 3D and the porous anode in 2D give over the plate the same results. This is probably due to the very high velocity of the plasma (over 9000m/s). Effectively, due to this velocity, the boundary conditions near the anode seems to not influence the upper part of the flow.

6. Conclusion

We have presented in this paper a comparison between 2D and a 3D calculation for a cutting device. Two points were studied. The first is the vortex injection in the torch and the second the arc attachment near the metal plate to be cut. The results found for the first studied point in 2D and 3D are very close and for this kind of configuration where the arc is very constricted by the nozzle, the equivalent surface in 2D is a good simplification to study the plasma behaviour in the nozzle. Concerning the second point, as the plasma has a very high velocity, it seems that the arc attachment condition does not influence the plasma characteristics over the plate. So for obtaining the plasma properties in the torch and over the plate, a two dimensional approach is sufficient. Nevertheless, if one wants to study now the whole process (torch + metal plate) with the heat transfer, a 3D calculation is needed.

[1] Boulos I., Pfender E., Fauchais P., « Thermal plasma, Fundamentals and applications », v1, Plenium Press-New york, (1994).
[2] R. Byron Bird , Warren E. Stewart, Edwin N. Lightfoot , « Transport phenomena », Wiley (1960)
[3] Naghizadeh-Kashani Y., Cressault Y., Gleizes A., « Net emission coefficient of air thermal plasmas », J Phys D 35, 2925-2934 (2002)
[4] Patankar S. V., « Numerical heat transfer and fluid flow » McGraw-Hill, (1980)
[5] Freton P., Gonzalez J.J., Gleizes A., « Comparison between a two- and a three-dimensional arc plasma configuration », J Phys D 33, 2442-2452 (2000)
[6] Gonzalez J.J., Freton P., Gleizes A., « Comparisons between two- and three-dimensional models: gas injection and arc attachment», J Phys D 35, 3181-3191 (2002)

Influence of doped graphite and diamond electrode electric arc on the single-wall carbon nanotubes synthesis

M. Razafinimanana(1), M. Pacheco(1), M. Monthioux(2),
L. Donnadieu(2), H. Allouche(2), N. Caprais(2), H. Lange(3), A. Huczko(3),
A. Gleizes(1), J.J Gonzalez(1)
[1] CPAT, UMR 5002 CNRS, Université Paul Sabatier, 113 Route de Narbonne, 31062 Toulouse cedex, France.
[2] CEMES, UPR A-8011 CNRS, BP 4347, F-31055 Toulouse cedex 4, France
[3] Department of Chemistry, ul. Pasteura 1, Warsaw, Poland

Abstract.

The formation of single-wall carbon nanotubes (SWNTs) and other carbon nanophases by the electric arc method was correlated to the plasma characteristics (temperature and C_2 radical concentration fields) by *in-situ* emission spectroscopy, for various conditions such as electrode gap, catalyst type and anode type. Conditions have been found which are able to produce preferentially either SWNTs, or double-wall nanotubes (DWNTs), or single wall nanocapsules (SWNCs).

1. INTRODUCTION

Among the numerous processes allowing the production of carbon nanostructures, the electric arc method is now widely used to synthesize single wall carbon nanotubes (SWNTs). Up to day this technique is still one of the most common ways to prepare either commercial of laboratory grades of single-wall carbon nanotubes (SWNTs). Since the discovery of the SWNTs [1,2] in 1993, the effect of varying the usual parameters of the process, i.e., the type of catalysts, the type of neutral atmosphere, the pressure value, and the arc current have been more or less extensively investigated [3,4]. However, two parameters have attracted little attention so far, i.e., the catalyst dispersion, and the type of carbon source. Since the effect of varying any parameter was rarely related to the physical modifications subsequently brought to the plasma, we report in this paper the changes brought to the carbon phase typology and proportion which occured in our arc chamber while changing the fabrication method of the doped anode. Usually, catalyst(s) are introduced into the graphite rod anode. In order to provide some dispersion of the catalysts with respect to the carbon source, a co-axial hole is drilled in the anode, subsequently filled with a mixture of the catalysts powder and a large amount of graphite powder. However, an homogeneous dispersion is not really achieved, obviously due to the existence or the surrounding pure graphite anode body which also acts as a carbon source. Some results concerning the anodes with homogeneously dispersed catalysts instead of regular "drilled" anodes have been investigated, and reported in this paper.
For all the processes involving solid carbon to synthesize carbon nanotubes (electric arc, laser ablation, solar light vaporisation, …), graphite, i.e., pure *sp*^{2} carbon was chosen as the carbon source so far. However, it seems interesting to study the effect of using *sp*^{3} carbon as the carbon source, both in the type of carbon nanotube obtained and the plasma characteristics. We started investigating this point by incorporating some diamond powders in addition to catalysts in the graphite anode of an electric arc device.

2. EXPERIMENTAL

The arc chamber, a hollow cylinder of 30cm diameter and 1m height is presented in figure1. The two graphite electrodes of 6mm diameter are located vertically in the centre of the arc chamber. The anode is in the upper position. Modification of the distance between the two electrodes and striking of the arc by contact was made possible from outside the chamber by means of a system allowing independent moving of the electrodes. Two quartz windows having 6 cm in diameter were placed along an optical axis perpendicular to the arc axis allowing observation of the discharge. It is necessary for the spectroscopic diagnostic of the arc to maintain the electrode gap constant during the experimental run. For this purpose, the image of the arc was projected on a photodiodes array coupled with a P.C type microcomputer which drives the adjustment of the anode and cathode positions by independent motors.

The light emitted by the plasma was focused onto the entrance slit of a monochromator with a focal length of 1m and 1200 grooves/mm grating. On the outlet focal plane was placed a CCD array allowing analysis of plasma radiation. Radial exploration of the arc was made possible by means of a mirror enabling displacement in two directions. The whole spectroscopic analysis set up was driven by a PC microcomputer. Electrical power was supplied by three DC sources of 100V and 100A each. Common working conditions for all the experiments reported here were (except when specifically mentioned): 80 A current intensity, 1mm arc length and helium ambient gas at pressure of 60-65 kPa. Parameters investigated were mainly the catalyst type (Ni/Co, Ni/Y), the catalyst dispersion in the anode (homogeneous, heterogeneous), and the anode composition (graphite + catalyst, or graphite + catalyst + diamond). Catalysts heterogeneously dispersed in the anode corresponds to standard graphite anode with a co-axial hole drilled at the center of it, subsequently filled with graphite powder and catalyst(s), whose particle sizes are <400 nm. Such anodes were prepared either in our laboratory or kindly obtained from P. Bernier and S. Tahir (GDPC, Montpellier, France). Anodes with catalysts homogeneously dispersed were specifically prepared by a pressureless sintering technique [5] and, resulting in Ni-Co alloy particles whose sizes range from 30 to 200 nm. All the solid products formed in the four main sampling areas of the reactor (cathode deposit, collaret, web, and soot) were investigated by transmission electron microscopy as raw materials, i.e., without any subsequent chemical treatment. Emission spectroscopy methods based on the use of the Swan $C_2(0,0)$ rotational system emission spectra was carried out to determine the plasma temperature. The self-absorption effect in the d $^3\Pi_g$, v'= 0 → a $^3\Pi_u$, v''= 0 C_2 band was used for the C_2 radicals column density determination under various arc discharge conditions. At strong arc currents the C_2 content is so high that the (0-0) band exhibits self-absorption. This effect was used here for C_2 column density determination [6].

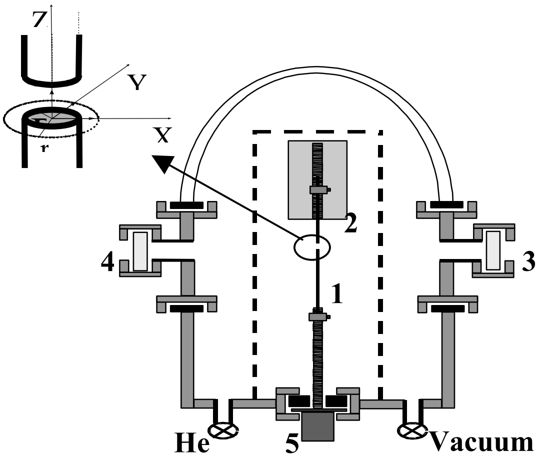

Figure 1. The arc chamber 1: Anode – 2: Cathode; 3 – 4: Windows; 5: Motors

3. RESULTS

3.1. Influence of catalyst dispersion

Comparison of the carbon nanostructures obtained when using either homogeneous anode or heterogeneous anode is summarised in Table 1. One can note a remarkable difference of the carbon nanophases obtained with the use of identical catalysts

Table 1. Morphologies of the carbon nanophases obtained with homogeneous and heterogeneous Ni/Co doped anodes. Proportions of catalysts are in atom %.

Catalysts	0.6%at.Ni/0.6%at.Co Homogeneous	0.6%at.Ni/0.6%at.Co Heterogeneous	4.2%at.Ni/1%at.Y Heterogeneous
Cathode deposit	•**POPAC** et SWNC •**Catalysts** ϕ~5-300nm + MWS •MWNT ϕ<50nm •[*SWNT*] ϕ~1.6nm clean + Cn ,isolated or ropes	•**MWS**, catalysts free •**MWNT** ϕ<35 nm •POPAC et SWNC •[*SWNT*], isolated or **ropes** •[*Catalysts*] ϕ~3-30nm	•**SWNT** ϕ~1.4-4.1nm, **POPAC** or **AC** (+ catalysts ϕ<30nm, MWS, Cn, [MWNT])
Collaret	•**POPAC** et **SWNC** •Catalysts ϕ~3-250nm, **<50nm** + MWS •SWNT ϕ 1-1.2nm, [*opened*], isolated or **ropes** ϕ<15nm, + **Cn** •[*AC*]	•**Catalyts** ϕ~3-170 nm + MWS •AC ou POPAC + **catalysts** ϕ~3-50nm •**SWNT ϕ~1.4 nm propres + Cn** isolated or **ropes ϕ<20nm**	**SWNT** ϕ~1.4-2.5nm (+Cn, POPAC or AC, catalysts ϕ<30nm, [MWS])
Web	•[*MWNT*], **DWNT**, ϕ 2.7-**4**-5.7nm SWNT ϕ 1.2-1.8nm, isolated or **ropes** ϕ<15nm, + POPAC ± **Cn** •AC + catalysts ϕ~3-40nm+MWS •[*NANF*]	None	**SWNT** ϕ~ 1.4nm, **AC** (+POPAC, catalysts ϕ<40nm)
Soot	• **MWNT**+ **MWS**+ **PAC** or **Cn** ±catalysts ϕ~3-35nm • NANF + catalysts • AC + catalysts •[*DWNT*], [*SWNT*], ropes or isolated + POPAC	• **AC** et POPAC + catalysts ϕ~3-35nm •**NANF** + catalysts ϕ~4-15nm •[*SWNT*] ϕ~1.2nm, isolated or ropes	**POPAC, AC** (+catalysts ϕ<30nm, SWNT ϕ~1.4nm, Cn, [SWNC])

Glossary: AC: amorphous carbon; PAC: polyaromatic amorphous carbon; Cn: fullerene-like structure, including C$_{60}$; NANF: nearly amorphous nanofiber; MWS: multi-wall sell; SWNT: single-wall nanotube; DWNT: double-wall nanotube, MWNT: multi-wall nanotube; SWNC: single-wall nanocapsule.
Abundant – Present – [*Rare*]

Results corresponding to Ni/Y heterogeneous doped anode is given for reference since corresponding to conditions for high SWNT production [3]. Results are consistent with published data [3], with SWNTs found as the main products either in the cathode deposit, collaret, or the web.

The results obtained from a standard Ni/Co-doped anode (column 3) are consistent with previous studies [3], since the formation of SWNTs is not favoured and no web is formed. However, as soon as a homogeneously dispersed anode is used, dramatic changes occur in the type of carbon nanophases formed. Though SWNTs are also present, single-wall nanocapsules (SWNCs), together with poorly-organized polyaromatic carbon (POPAC), spontaneously form as one of the main products found in the collaret, instead of SWNTs for standard anode (heterogeneous Ni/Y anode). SWNCs can actually be considered as non isometric, giant fullerenes resulting from "failed" nanotubes whose tubular morphology was missed due to an inappropriate display of some of the pentagons. They are usually formed using a laser vaporisation process [7]. Another dramatic change brought by the use of a homogeneously dispersed anode is that a web has formed. Moreover, as shown in figure 2, the nanotubes forming the web are mainly double-wall nanotubes (DWNTs), added with some SWNTs and triple-wall nanotubes, instead of SWNTs only as usual. DWNTs were already reported to form in electric arc, but some partial pressure of H$_2$ introduced in the reactor was necessary [8]. Because π electrons are internally satisfied by the occurrence of the two co-axially superimposed graphene tubes which allows van der Waals bonds to develop, DWNTs tend not to gather into large ropes but remain isolated or gather by few entities only.

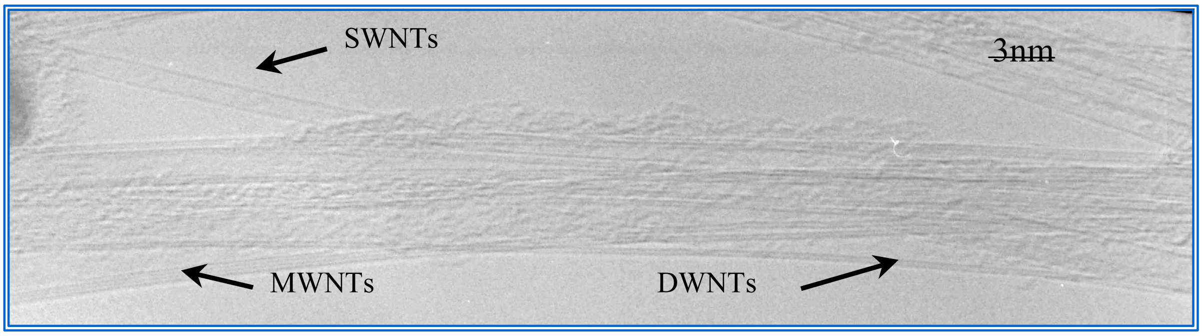

Fig. 2: HRTEM image of a small rope showing the prevalent occurrence of DWNTs, but regular SWNT (1.4 nm diameter, up left) and MWNTs (3-walls, bottom left) are also present as minor components.

It is noteworthy that the production of both SWNCs and DWNTs since they are interesting nano-morphologies of carbon, whose potential applications have been discussed elsewhere [7,9]. It is our belief that the spontaneous formation of DWNTs by the arc method has not been reported by another Group yet Since the erosion rate for identical working conditions is systematically higher with homogeneous doped anode than that with the heterogeneous one, the resulting plasma characteristics (temperature field and C_2 density) for both cases are different as shown in figure 3 when Ni/Co are used as catalysts. Reasons for such discrepancies brought in the results by a better dispersion of the catalysts in the anode are possibly related to the difference in the subsequent relative homogeneity of the moieties within the plasma (i.e., small size and better dispersion of metal atoms with respect to carbon species). In fact, one can note that the plasma temperature obtained with homogeneous anode is lower than that of with heterogeneous one. In contrary C_2 densities obtained with homogeneous anode are much higher ($25\times10^{15}\text{cm}^{-2}$) with a radial profile presenting a marked gradient. One can also note that the discrepancy between the temperatures and the C_2 densities close to the electrodes for both cases (homogeneous and heterogeneous) are higher with heterogeneous doped anode. This statement supports the idea that high C_2 densities in the plasma are not necessary conditions for building the nanotubes, either SWNTs or DWNTs, but could more likely be the bricks for building the MWNTs in the cathode deposit [10].

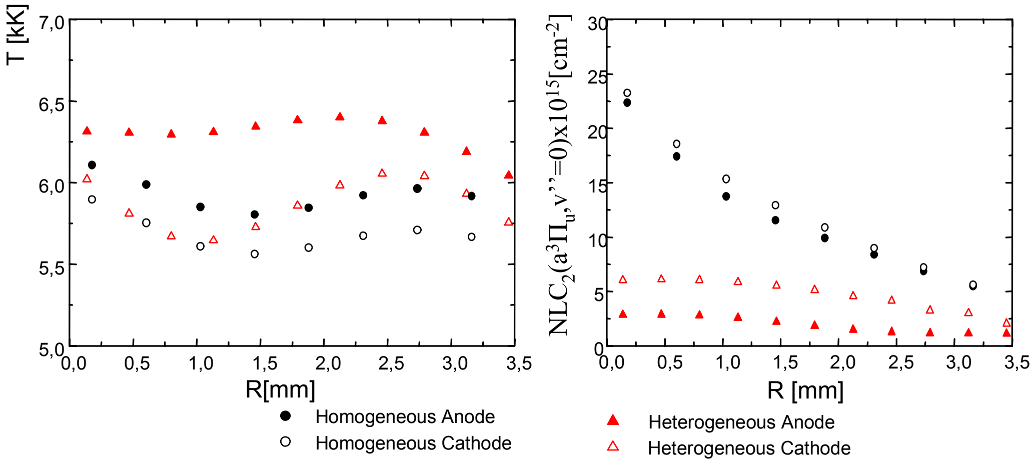

Figure 1 : Influence of the anode configuration on the temperature and C_2 density profiles

3.2. Influences of the electrode gap and diamond with Ni/Y as catalysts

All the anodes used were prepared by us following the standard way (i.e., co-axial hole drilled in the anode subsequently filled with either Ni, Y and graphite powders or Ni, Y, and diamond powders). Catalyst proportions were Ni in the 3.5-4.2 % range and Y in the 0.8-1 % range (atomic). For the diamond-doped anodes, the diamond/graphite weight or atomic ratio is 0.4-0.5. The most remarkable result is a systematic increase in the web yield when diamond is added to the anode, as opposed to regular all-graphite Ni/Y-doped anodes, whatever the electrode gap. The web yield is actually increased corresponding to increasing factor of x 3.7, x 4.1, and x 2.9 for the electrode gap of 1, 2, and 10 mm respectively. All the web samples were checked to contain SWNTs as the major phase (together with remnants of catalysts). For some conditions (gap = 2 mm) the yields in collaret (which also contains SWNTs as the major phase) is also increased, by +27%. The soot yield is increased and surprisingly appeared to also be a SWNT-rich material. Another interesting feature of the SWNT-rich materials obtained from diamond-doped anodes is that, beside catalyst remnants which are inevitable, other carbon impurities are limited to amorphous or poorly organised polyaromatic carbon materials, i.e., MWSs and MWNTs do not exist in the material collected, except in the cathode deposit material. This is likely to allow less aggressive and complex purification procedures to be used, leaving the SWNTs undamaged, as opposed to what is currently observed when mineral acids like HNO_3 and H_2SO_4, among other oxidising agents, are used [11].Whatever, the results reported here open interesting perspectives regarding an unexpected way to increase significantly the yield in SWNTs for all SWNT production processes using solid carbon materials as carbon source (e.g., electric arc, laser vaporisation, solar light vaporisation,..) [12].

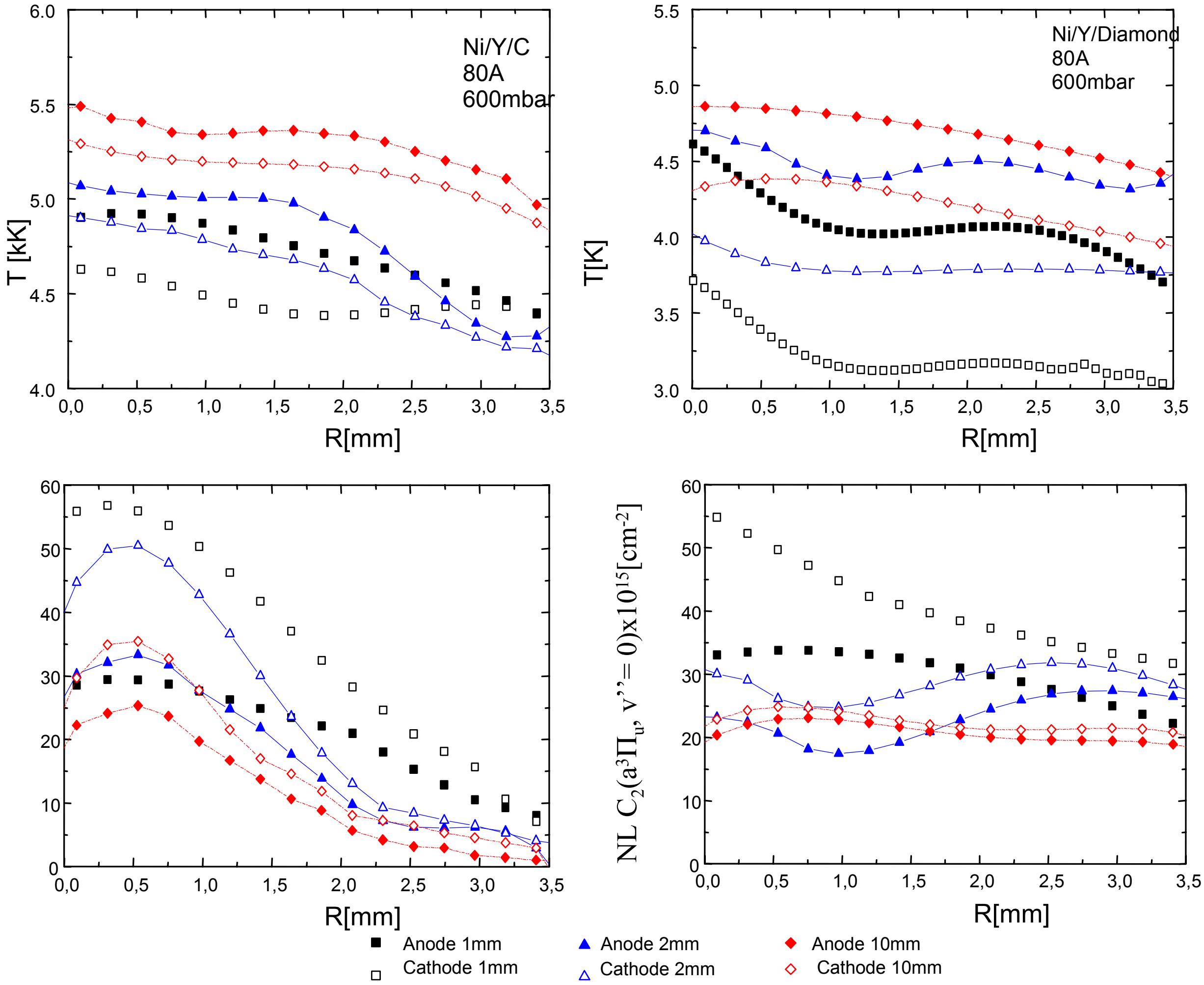

Figure 2 : Temperature and C_2 density profiles (Ni/Y/C and Ni/Y/diamond) for different electrode gaps (1, 2 and 10mm)

The temperature and C_2 density profiles for different values of electrode gap (1, 2 and 10mm), for 80A arc current intensity and pressure of 600mbar are reported in figure 2. Globally, an increase of the electrode gap for the two configurations considered (Ni/Y/C and Ni/Y/diamond) leads to reduce the discrepancy of the temperatures close to the electrodes, this effect being more marked with the presence of diamond. The increase of the electrode gap with both Ni/Y and Ni/Y/diamond leads to a certain uniformity of the plasma characteristics and also to an increase of nanotubes yield.

The presence of diamond in the doped anode, whatever the electrode gap, not only leads to a cooling of the plasma (about 500K) but allows in the same time to obtain a certain uniformity of the plasma. In fact, the temperature profiles are relatively flat and the discrepancy of the temperature profiles obtained close to the electrodes remains constant along the whole radial profile. One also can note that the C_2 densities obtained with diamond are lower than those obtained with graphite and present clearly a flat radial profile except for the electrode gap of 1mm. Since the high yield of SWNTs we have obtained when substituting graphite by diamond corresponds to electrode gap of 10mm, the main conditions of the plasma characteristics favourable for high production of SWNTs seem clearly resulting from the combination of a low plasma temperature with a flat radial profile with equally a low C_2 density with flat radial profile. Finally, it is worthy to note that the increase of the electrode gap does not change the morphology of the carbon nanotubes any way.

4. CONCLUSIONS

We have showed that adding diamond to the anode of an electric arc allows to increase significantly the SWNTs yield, up to three times higher, compared to standard conditions, with no well-organised, polyaromatic, carbon-shells as by-products. Depending on the conditions, this has allowed an increase in SWNT yield or the prevalent formation of other interesting carbon nanophases such as double-wall nanotubes or single-wall nanocapsules to be achieved. Impurities are therefore only catalyst remnants and amorphous – or nearly – carbon, suggesting that subsequent purification procedures could be simplified and less severe, with both higher efficiency and lower harmfulness towards SWNT structure. These results were correlated to the plasma characteristics (temperature and C_2 density profiles) more homogeneous than those corresponding to standard (Ni/Y/C) doping anode. In the electric arc method, the transport properties of the anode appear to be of an utmost importance regarding the type and quality of the carbon nanophases obtained. Further experiments will include the study of the variation of the sp^3/sp^2 ratio to tentatively identify the relevant mechanisms and determine whether optimising these preliminary results is possible.

References

[1] S. Ijima, T. Ishihashi. Nature, **363**, 603 (1993).

[2] D.S. Bethune, C.H. Kiang, M.S. De Vries, G. Gorman, R. Savoy, et al. Nature, **363**, 605 (1993).

[3] C. Journet, W.K. Maser, P. Bernier, A. Loiseau, M. Lamy de la Chapelle, et al. Nature;**388**,756(1997).

[4] C. Journet, La production de nanotubes de carbone, Ph-D Dissertation, Université Montpellier II, France, (1998).

[5] T. Sogabe, T. Matsuda, K. Kuroda, Y. Hirohata, T. Hino, T. Yamashina, Carbon, **33**, 1783 (1995).

[6] H. Lange, K. Saidane, M. Razafinimanana and A. Gleizes, J. Phys D: Appl. Phys., **32**, 1024 (1999)

[7] S. Iijima, R. Yudasaka, S. Yamada, K. Bandow, F. Suenaga, et al., Chem. Phys. Lett., **309**,165(1999).

[8] J.L. Hutchison, N.A. Kiselev, E.P. Krinichnaya, A.V. Krestinin, R.O. Loufty et al. Carbon, **39**, 761(2001).

[9] M. Monthioux, Carbon 2002, in press.

[10] M. Pacheco, H. Allouche, M. Monthioux, M. Razafinimanana, A. Gleizes. Extended Abstracts, XXVth Biennial Conference on Carbon, Lexington (Kentucky, USA), July 14-19, 2001; Novel/14.1 (CD-ROM).

[11] M. Monthioux, B.W. Smith, B. Burteaux, A. Claye, J.E. Fischer, D.E. Luzzi, Carbon,**39**,1251(2001).

[12] M. Monthioux, M. Razafinimanana, French Patent, 2002, submitted.

Modelling of a Dielectric Barrier Glow Discharge at Atmospheric Pressure in Nitrogen

M Madani[a, b], A. Bogaerts[a], R. Gijbels[a]. D. Vangeneugden[b] , N. Baguer[a]

[a] *University of Antwerp (U.I.A.), Department of Chemistry, Universiteitsplein 1, B-2610 Wilrijk, Belgium*

[b] *Flemish Institute for Technological Research (VITO), Materials Department, Boeretang 200, B-2400 Mol, Belgium*

Abstract: *In this paper the description of a two-dimensional fluid model used for simulations of a dielectric barrier discharge at atmospheric pressure in nitrogen is presented. In the first section we discuss the different equations and their solving mechanism. The second part describes the reactor that is simulated and in the last section some results such as reaction rates coefficients and electron transport coefficient are given.*

1. DESCRIPTION OF THE MODEL

1.1. Introduction

For modelling a Dielectric Barrier Glow Discharge at atmospheric pressure we use a 2 dimensional fluid model [1]. In this kind of model we assume that the plasma species form a continuum in equilibrium with the electric field. The different species present in the plasma, such as electrons, ions and neutrals are described by balance equations (based on conservation laws) and flux equations of diffusion and migration in the electric field. For the electrons an energy balance equation is also solved. The electric field is calculated self-consistently using the Poisson equation. The collision rates and electron transport coefficients can be obtained by solving the Boltzmann equation for the EEDF (electron energy distribution function).

1.2. Fluid model

A gas discharge consists of a number of particles (neutrals, ions, radicals and electrons). For each species a density balance is solved, given by following equation:

$$\frac{\partial n_k}{\partial t} + \overline{\nabla}.\overline{\Gamma}_k = S_{reac,k} \tag{1}$$

The flux for each particle is caused on one hand under influence of the electric field (migration) and on the other hand due to a concentration gradient (diffusion). These contributions are described by the flux equations. The loss and gain of energy has to be taken into account in the model by means of an energy balance equation, for ions this is negligible because of their large masses they can equilibrate with the electric field.

For the electrons the energy equation has following form:

$$\frac{\partial n_e \varepsilon}{\partial t} + \overline{\nabla}.\overline{\Gamma}_w = -e\overline{\Gamma}_e \overline{E} - k_{ion} n_e N_b H_{ion} \tag{2}$$

The first term on the right-hand side gives de Ohmic heating and the second term describes the loss of energy due to collisions. Γ_w is the energy flux and is again described by a drift-diffusion approximation.

By calculating the Poisson equation (3) we obtain the potential. The electric field can then be obtained as the negative gradient of this potential.

$$\Delta V = -\frac{e}{\varepsilon_0}\left(n_i - n_e\right) \tag{3}$$

---

[a] Madani@uia.ua.ac.be, Myriam.Madani@vito.be

This system of non-linear differential equation is discretised by the sharfetter-Gummel scheme. Convergence is reached when the errors on the calculated parameters are less than 10^{-6}.

1.3. The EEDF

As mentioned before the collision rates, electron transport coefficient and the average electron energy are obtained by solving a two-term Boltzmann equation for the EEDF. The EEDF or electron energy distribution function specifies the number of electrons at a certain position, with a certain velocity and at a given time. For this Boltzmann solver the background neutral densities are needed as input, these are obtained from the fluid model. The two parts of the model are run alternately until the changes in the density of the background neutrals at two succeeding RF cycles are less than 10^{-4}.

1.4. The boundary conditions

In order to solve the system of differential equation some boundary conditions need to be specified for the potential and density profiles. The presence of the dielectrics has to be taken into account in the model. Therefore the surface charge on the substrate on the side of the discharge is calculated and the corresponding change in electric field is included in the model. Furthermore electron desorption and secondary electron emission were implemented in the model.

2. INPUT DATA FOR THE MODEL

2.1. Geometry

We use a parallel plate configuration, consisting of two disk-shaped stainless steel electrodes with a diameter of 150 mm. Both electrodes are covered with an alumina plate of 2mm thickness. The gap can vary from 1mm to 5 mm. An AC voltage is applied with amplitudes that can go up to 20kV peak and a frequency in the range of 50Hz-500kHz

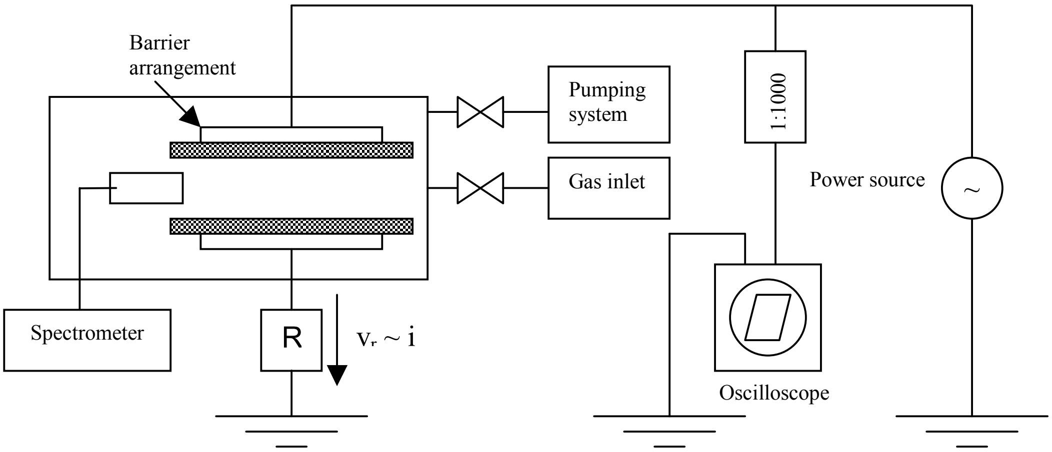

Figure 1: reactor geometry used for simulations.

2.2. Nitrogen species

The nitrogen species that are taken into account are the ground state, the two first metastable states, two radiative states, the atom and four ions (N^+, N_2^+, N_3^+,N_4^+).

2.3. Reactions

In the model several reactions are taken into account such as electron collisions, neutral-neutral and neutral-ion reactions. The cross sections used for the electron reactions are taken from Phelps and the reaction rates coefficients for the other reactions are taken from [2-4].

table 1.: Nitrogen reactions included in the model

Reaction	rate coefficient (cm^{-3}.s^{-1})
Electron reactions:	
$N_2 + e^- \rightarrow N_2^+ + 2e^-$	f(E/N)
$N_2 + e^- \rightarrow N_2\left(A^3\Sigma_u^+\right) + e^-$	f(E/N)
$N_2 + e^- \rightarrow N_2\left(a'^1\Sigma_u^-\right) + e^-$	f(E/N)
$N_2 + e^- \rightarrow N_2\left(C^3\Pi_u\right) + e^-$	f(E/N)
$N_2 + e^- \rightarrow N_2\left(B^3\Pi_g\right) + e^-$	f(E/N)
$N_2\left(A^3\Sigma_u^+\right) + e^- \rightarrow N_2^+ + 2e^-$	f(E/N)
$N_2\left(a'^1\Sigma_u^-\right) + e^- \rightarrow N_2^+ + 2e^-$	f(E/N)
$N_2 + e^- \rightarrow N^+ + N + 2e^-$	f(E/N)
ion-neutral reactions:	
$N_2^+ + N_2\left(A^3\Sigma_u^+\right) \rightarrow N_3^+ + N$	3.0x10^{-10}
$N_2^+ + N \rightarrow N^+ + N_2$	7.0x10^{-13}
$N_3^+ + N \rightarrow N_2^+ + N_2$	6.6x10^{-11}
$N_4^+ + N_2 \rightarrow N_2^+ + 2N_2$	2.4x10^{-15}
$N_4^+ + N \rightarrow N^+ + 2N_2$	1.0x10^{-11}
neutral-neutral reactions:	
$N_2\left(A^3\Sigma_u^+\right) + N_2\left(A^3\Sigma_u^+\right) \rightarrow N_2\left(B^3\Pi_g\right) + N_2$	1.0x10^{-11}
$N_2\left(A^3\Sigma_u^+\right) + N_2\left(A^3\Sigma_u^+\right) \rightarrow N_2\left(C^3\Pi_u\right) + N_2$	1.0x10^{-10}
$N_2\left(A^3\Sigma_u^+\right) + N_2\left(a'^1\Sigma_u^+\right) \rightarrow N_4^+ + e^-$	5.0x10^{-11}
$N_2\left(a'^1\Sigma_u^+\right) + N_2\left(a'^1\Sigma_u^+\right) \rightarrow N_4^+ + e^-$	2.0x10^{-10}
$N_2\left(A^3\Sigma_u^+\right) + N \rightarrow N_2 + N$	4.0x10^{-11}
$N_2\left(a'^1\Sigma_u^+\right) + N_2 \rightarrow N_2 + N_2$	2.0x10^{-13}
$N_2\left(C^3\Pi_u\right) + N_2 \rightarrow N_2 + N_2$	1.0x10^{-11}

3. RESULTS

Typical results that can be obtained by numerical modelling are spatio-temporal distributions of densities, potential, electric field and mean electron energy. The fluxes of the different plasma species can also be obtained. We can also obtain information on the different ionisation processes, and the relative importance of the different loss and production processes of the species. In the figures below some of the results from the EEDF model (see § 1.3.) are given.

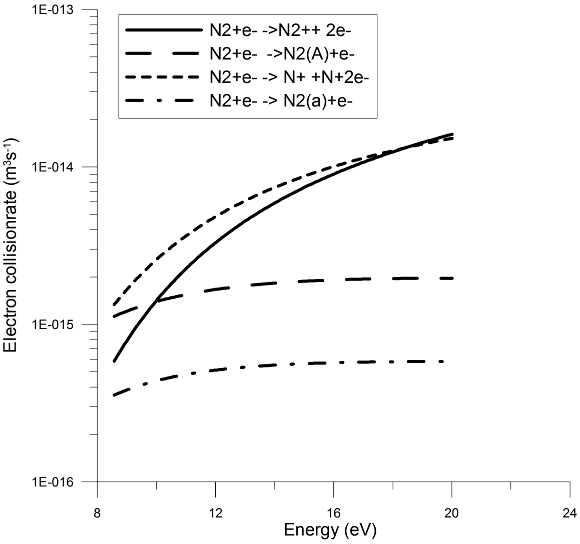

figure 2: reaction rates versus energy

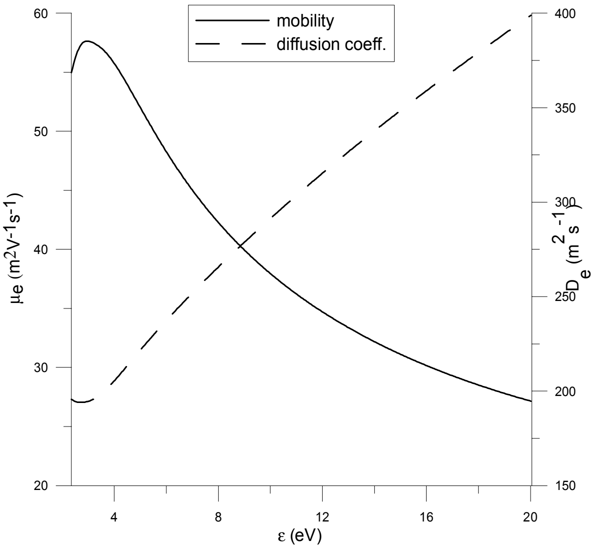

figure 3 : transport coeff. versus energy

In the first graph the electron collision rates are given for some reactions, we can see that the dominant reactions are the ionization and dissociation of N_2. These rates have also been calculated in function of the electric field. In the second figure de electron transport coefficients are given in function of their mean energy.

ACKNOWLEDGMENTS

We would like to acknowledge VITO for its financial support and V.A. Maiorov, W. Goedheer and F. Massines for some interesting discussions.

REFERENCES

[1] GJ Nienhuis, Ph.D. thesis, Utrecht University 1998

[2] N. Gherardi, E. Gat, F. Massines, S. Lemoing, P. Segur, Proceedins ISPC-15

[3] A.A. Matveyev, V.P. Silakov, PSST, 1999, **8**, p.162

[4] Y.B. Golubovskii, V.A. Maiorov, J. Behnke, J.F. Behnke, Proceedings ISPC-15

Plasma Enhanced Chemical Vapour Deposition of Silicon Rich Oxide (SRO) films for optoelectronics applications

L.Caristia [a], E.Castagna [b], A. Costa [a], S. Coffa [b], S.Ravesi [a]

STMicroelectronics, [a]DSG R&D, [b]Corporate R&D, Stradale Primosole 50, 95121 Catania, Italy

The synthesis of silicon nanocrystals in oxide matrixes has a considerable importance for technological applications, mainly in optoelectronics. It is possible to obtain silicon nanocrystals in SiO_2 by ionic implantation of Si in thermal oxide matrixes and by silicon rich oxide (SRO) layers deposition either. This latter solution has the advantage to allow high thickness film deposition in a short process time and with a good repeatability. Moreover silicon is uniformly distributed throughout the whole film. A following thermal process causes silicon diffusion and nucleation of nanocrystals.

In this work SRO films have been synthesized from SiH_4 and N_2O as gas precursors in an industrial plasma enhanced CVD equipment.

The deposition parameters have been changed in order to have silicon oxide films with silicon in excess. An important role has been played by the $[N_2O]/[SiH_4]$ flow ratio. The synthesis of SRO has been monitored by FTIR spectra (figure 1) that highlight a chemical composition change, varying progressively the gas ratio. The spectra of the sample deposited with $[N_2O]/[SiH_4]=24$ was very similar to the one of pure SiO_2. A decrease in the $[N_2O]/[SiH_4]$ ratio has determined a shift of the 1070 cm^{-1} peak (Si-O-Si symmetrical stretch) to a smaller value and an increase of its left end shoulder. Correspondingly, the 800 cm^{-1} peak (Si-O-Si asymmetrical stretch) has increased and shifted toward higher wave numbers. As reported in literature, these are proofs of a silicon enrichment of the film [1-3].

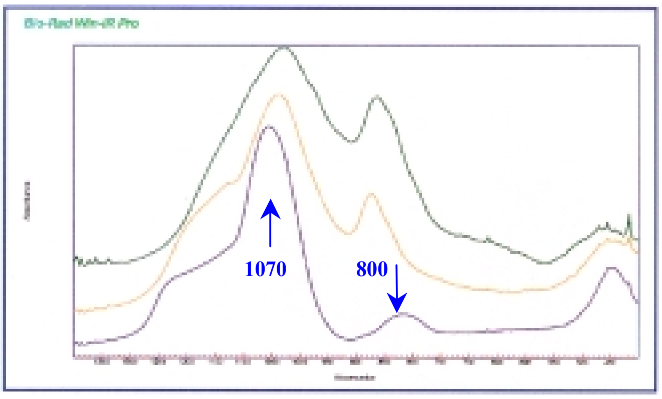

Figure 1: SRO films FTIR spectra as a function of $[N_2O]/[SiH_4]$ ratio.

After deposition, the films have been annealed at 1000 ºC to obtain the nucleation, growth and crystallization of Si nanocrystals.

The nanostructures have been characterized by TEM (Transmission Electron Microscopy) analysis. The crystallites have been found to be a few nanometers in size and spherically shaped. The optical properties of the SRO layers will be showed.

[1] Chi-Fa Lin, Wei-Tsu Tseng, Ming Shiann Feng, J. Of Appl. Phys., Vol. 87, No 6.
[2] A. J. Kenyon, P. F. Trwoga, C. W. Pitt, G. Rehm, J. Of Appl. Phys., Vol. 79, No 12.
[3] L. Doucet, H. Jaousen, J. Jimenez, STM Central Technical Library

Control of a DC Plasma Torch for CNT Production

J. Pacheco-Sotelo[1,3], E. Gutiérrez-Ocampo[1,3], J. Benítez-Read[1,3] , C. Torres[3], R. Valdivia[3]
M. Razafinimanana[2], J. J. Gonzalez[2], A. Gleizes[2], P. Teulet[2]

[1] *Instituto Nacional de Investigaciones Nucleares, México* jps@nuclear.inin.mx
[2] *Centre de Physique des Plasmas et Applications de Toulouse (CPAT), France.*
[3] *Instituto Tecnológico de Toluca, México*

Abstract
In this paper, a plasma torch and the assembling of its peripheral components such as the electrical power supply, the gas feeding system, the reactor and the measuring devices, are presented. These components are virtually reassembled in a unique PC monitor for control and recording of all the variables involved in the plasma treatment processes. The results obtained by Optical Emission Spectroscopy (OES) and analysis of the byproducts by Transmission Electron Microscopy (TEM) technique are also presented.

1. Introduction

Plasma torches have become an irreplaceable part of various processes in different industrial fields, like metallurgical applications (smelting, cutting and welding processes), synthesis of new materials (carbon nanotubes), environmental processes (hazardous wastes treatment), electrical processes (lighting, circuit-breakers) among others.

In these applications, it is desirable to attain stable operating conditions, since fluctuations in the plasma jet would lead to insufficient treatment of the product. Having the plasma a very high activity, rapid chemical reaction and short overall processing times are important to obtain a very accurate controllability against plasma disturbances during its operation. To achieve this task, a simple but practical control system has been developed [**1**], based on a PC screen, where more than twelve variables can be measured and recorded in real-time mode. A important feature of this control system, is the continuous availability of all the data of each variable, thereby, the operating condition of particular tests are rapidly consulted to compare and to establish the best conditions according to the byproducts obtained.

In these processes, four groups of variables are measured: (1) Pressure in several points inside the plasma reactor, (2) Some electrical parameters like plasma current, arc tension, plasma power and current of the transverse magnetic field, (3) Gas flux parameters: Flux of argon, methane, acetylene and mixtures of these gases, (4) The temperature in two points, at the reactor near the nozzle torch and at the gas exhaust, are registered. The registration and storage of these twelve variables was obtained by using a graphical programming language (LabVIEW™), which possess many useful tools [**2**], and options for the creation of virtual instrumentation and support facilities found in web [**3**].

An additional advantage of this control screen is its simplicity to improve or add other options (like the powder injection control), without affecting significantly the sampling time, since the routines and instructions in the main program run in parallel mode.

This work also reports the results obtained in the syntheses of CNT by plasma torch during several tests with different gaseous mixtures of argon-acetylene-catalyst, or argon-acetylene-catalyst feded into the plasma torch.

It has been established that the size of the catalyst particle defines the diameter of the nanotube formed [**4**], and that the nanotube diameter decreases, as a result of the formation of smaller ion clusters, when the ferrocene concentration, and hence the rate of iron deposition, is reduced [**5**]. The catalyst precursor used in our experiments was ferrocene powder previosly seeded at 75µm and fed at a very low rates (1.26gpm).

2. Experimental Facilities

In all the experiments realized, the plasma was generated by a DC plasma torch assembled in a reactor, as is showed in figure 1, with 10 kW of power capacity.

The pressure in the reactor can be controlled, by a pumping system and a special valve, within a 10-100kPa range. The DC current, from 80 to 150 A, is applied between the cathode and the torch nozzle (anode). The plasma reactor is also provided with a special sightseeing port for OES measures. The luminous signal coming from the plasma is shaped and focused by a convergent lens towards the entry slit of the monochromator (320mm of focal length), provided with a halographic grating with 1800 *grooves/mm*, and a CCD detector (122 x 1024 pixels). The spectra for different ranges of intensities and wavelengths can be obtained using a special software [**6**]. The optical signal of the plasma is guided by an optical fiber mounted in a XY electromechanical system [**7**] as is showed in the front part of figure 1, to make vertical and horizontal scanning of the plasma with very precise incremental steps.

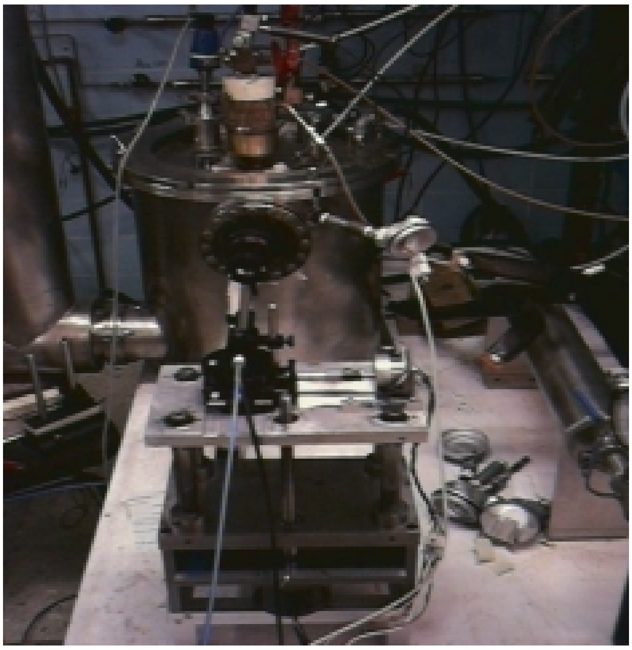

Figure 1.- Plasma torch facilities

A schematic of the “Control Screen” of the plasma process is shown in figure 2. On the left side there is a section (a) for the register of up to five electrical parameters. In the middle-upper part (b), there are three gas flux meters. In the middle-lower section, the pressure and temperature of the reactor plasma can be read. The right-lower side (c) is reserved to the power injector to control the feeding rate of catalyst used. In the upper-right section (d), the ignition of the plasma can be obtained just by pushing a virtual button that activates the plasma torch igniter. With this system, an intermittent high voltage discharge is generated to form a pilot arc between cathode and anode of the plasma torch, the details of this ignition system have been described elsewhere[**8**]. The high conductivity of this arc is a condition for a subsequent sustained electrical arc by the 10kW power supply.

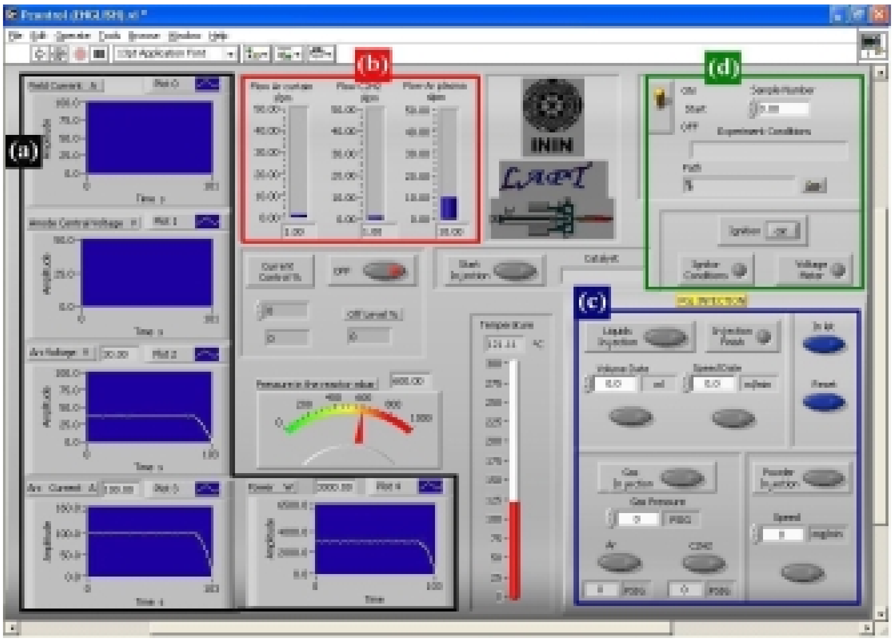

Figure 2.- Control screen for the synthesis of materials by plasma torch

Before the execution of the program, some security conditions and operating parameters have to be set, for instance the minimum gas flux, minimum plasma current, the number of samples to be acquired and averaged for each variable (14,000 points by default), the name of the file where these points will be stored, and some other security conditions that must be satisfied in order to initiate the process.

Once the plasma has been formed, there will begin the register and storage of all the parameters. If a malfunction occurs, a corresponding error message is displayed and maintained until the problem is corrected or the program is stopped. Stopping or aborting a test is always possible, by touching the switch located on the left side of the control of current. This will cause that plasma current will begin to decrease until it becomes zero.

Several tests where carried out for different gaseous mixtures and catalyst, feded into the plasma to obtain the synthesis of carbon nanotubes. The byproducts obtained were collected and prepared for subsequent analysis. The structures of the products were examined using Transmission Electron Microscopy (TEM) (JEOL 2010, operated at 200kV) and X-Ray Diffraction (XRD) (SIEMENS, D5000, operated at 35kV).

3. Results and discussion

Concerning the electrical parameters, the attention was concentrated on the voltage and current of the plasma. These parameters reflect pretty much the state of the plasma and are relatively easy to measure.

The recorded data of these measures parameters are shown in figure 3.
The current trace (fig 3a) shows that a stable condition of the plasma is rapidly reached (within the first 4 seconds), and it remains stable at 100 A during the rest of the experiment. The injection of the catalyst is clearly indicated, with a feed rate of 1.26g/min and a total mass of 2.451 grams of ferrocene injected.

The amplified area of figure 3b, manifests some voltage fluctuations in the plasma caused by the powder catalyst entering into the plasma.

The relation between argon flux (9LPM) and CH_4 flux (1LPM) injected, can also be noticed in figure 3c. This rate (9%) is maintained stable during the most part of the test and it is very important, to make energy and mass balance calculations.

By multiplying the data stored in figure 3a and 3b, the DC power in the plasma can be also obtained (2600Watts).

Therefore, by using these data previosuly stored in files, it is possible to determine the main operating conditions ocurring during any test.

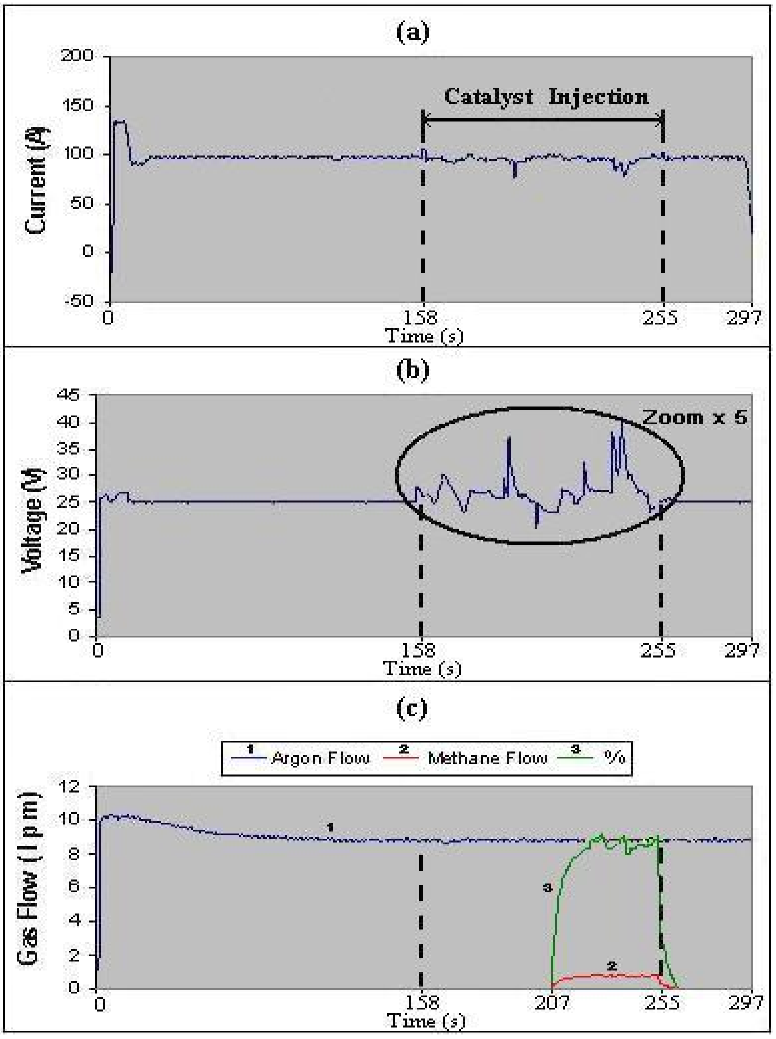

Figure 3.- Register of current(a), voltage (b) and flux rates (c) in The DC plasma torch.

4. OES Measurements

Optical emission spectroscopy (OES) is one of the most used techniques for plasma diagnosis, because chemical species participating in the plasma can be characterized. The information gathered can be processed to deduce the temperature distribution. Spectroscopic investigation was realized using the facilities described in the preceding section. In order to obtain reliable information, several measures in different positions of the plasma were realized.

Figure 4 shows the radial distribution of the plasma for a certain wavelength range. The peaks obtained clearly identifies the C_2 Swan band located from 513.1 to 516.3nm. The maximal values are obtained in the centre axe. The plasma jet has a diameter of 5mm and its radial scan was obtained during the catalyst-methane injection covering the entire diameter with displacements of 0.2 mm each step. This scan was realized at 8mm of the torch nozzle, where the maximal intensities of C_2 radical was detected

The resolution of the monochromator used was approximately of 0.11nm which represents a low resolution for our intentions. This was reflected mainly in the C_2 detection tests where the resolution needed must be as least of 0.05 nm to define more clearly the peaks in the spectra..

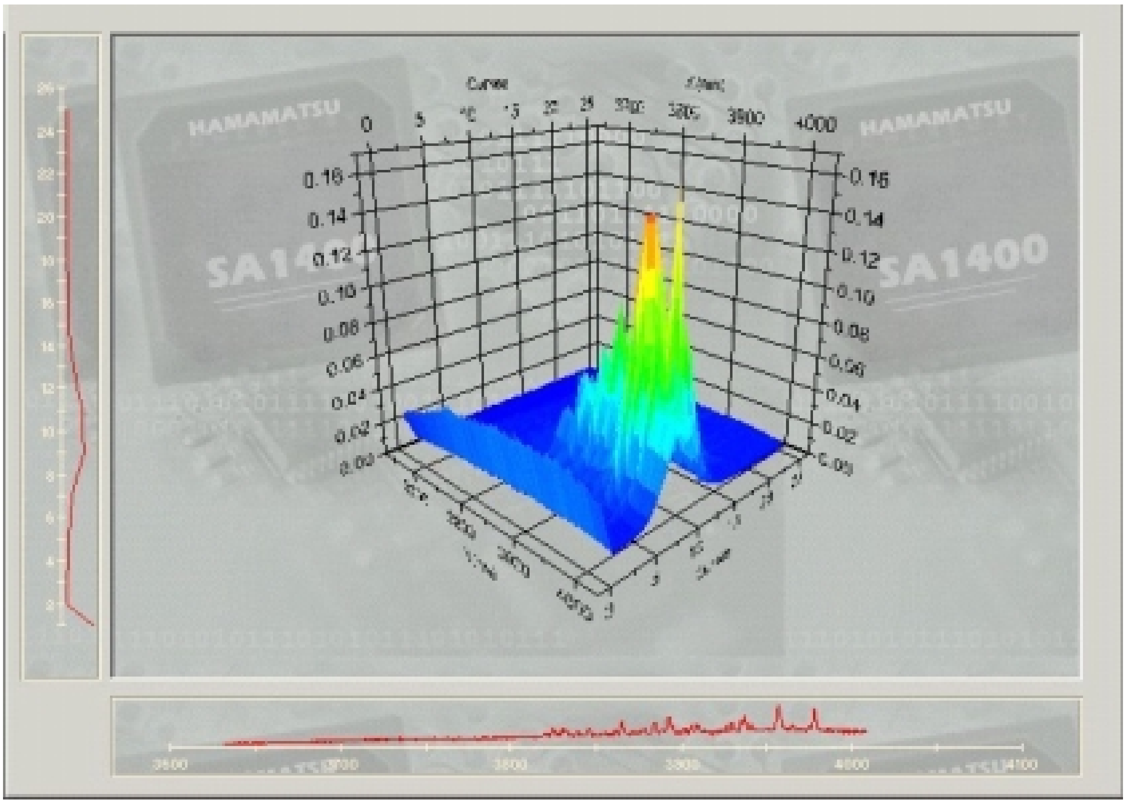

Figure 4 Radial scan of plasma in the Swan Band range.

The experimentally observed spectra was compared with simulated spectra. These comparisons are useful in determining various parameters of molecules such as the rotational temperature, even if monochromators with insufficient resolution are used. This method has been used in many other papers [**9, 10, 11**]. The spatial distribution of temperature was also deduced and these results are fully described in [**12**].

5. TEM Analysis:

The product was characterized using Transmission Electron Microscopy (TEM) to analyze the morphological structure of the samples. Several samples where analyzed. The TEM image shown in Figure

5a corresponds to a sample taken from the middle section of the reactor. In this image, there is no trace of nanotubes; however, it exhibits hexagonal nanoparticles of 30-40nm of diameter, probably conformed by graphitized carbon black.
The second lot of samples was collected at the outlet of the reactor. The TEM image (Figure 5b), shows that almost all the material consists of MWCNT with an average diameter of about 5nm, the spacing between the layers is approximately 0.673nm. The transmission electron microscope has an EDS device relied, the analysis obtained by EDS shows that the samples consist solely of C and Fe.

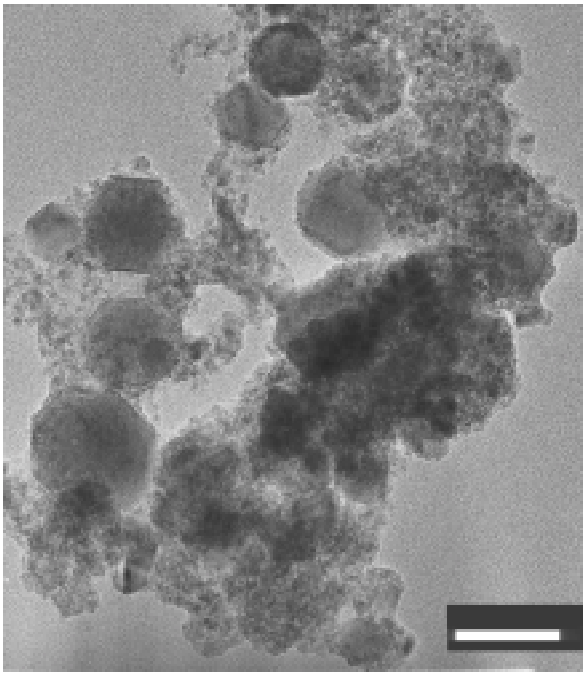

Fig 5(a) Sample from the middle part of reactor
Scale bar 50 nm

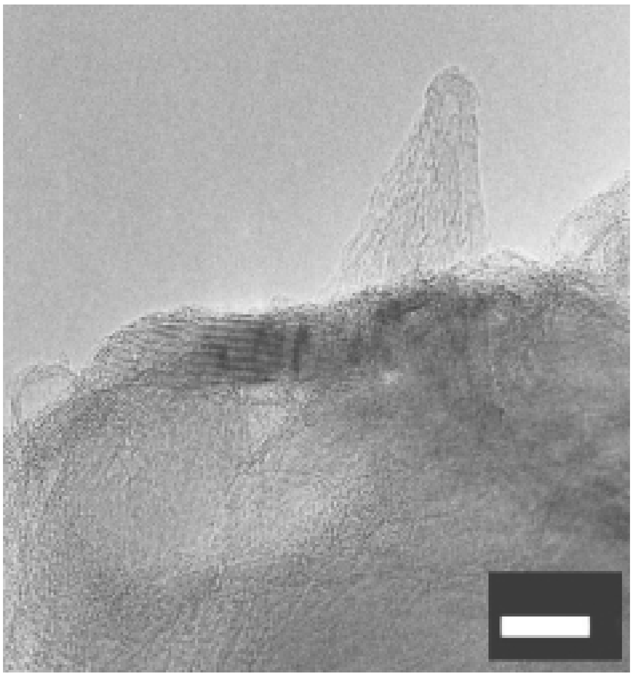

Fig 5(b) Sample from the exit of the reactor
Scale bar 10 nm

6. Conclusion

A precise knowledge of the DC plasma behavior, during different operating conditions can be obtained by using the “control screen” here described.
This system was tested with experiments oriented to the synthesis of carbon nanotubes by DC thermal plasma, but it can also be used in other applications such as hazardous waste degradation (ashes and askareles) and material surface treatment.

The product obtained by the pyrolisis of the described gas mixture and catalysis in thermal plasma, consists of amorphous carbon, graphite, nanoparticules and nanotubes. The comparison of the results obtained for several mixtures, shows that some presence of carbon nanotubes (CNT) exists when the mixture of Ar-CH_4-ferrocen is used. In the case of Ar-C_2H_2-ferrocene mixture, a large quantity of amorphous carbon was obtained, making difficult to obtain reliable OES measures; no traces of CNT were detected in the analyzed samples.

The yield of each product has not been estimated yet. As it was indicated, the reaction time of plasma is very short and every test lasts no more than 5 minutes.

7. Acknowledgments

The supports obtained from CONACyT (grant # 33424-U), ECOS/ANUIES (grant # MOO-P04), and COSNET (grant #619.02PR) are gratefully acknowledged. The authors would also thank I. Martínez, for his valuable help in the microscopy analysis and to F. Ramos, A. Cruz, M. Durán for their assistance during plasma tests.

8. References

[1] Carlos Eduardo Torres Reyes "*Control Screen for a DC thermal plasma torch*", Electronic engineering thesis, Instituto Tecnológico de Toluca , México, (2002).
[2] LabVIEW, measurement and automation catalogue, National Instruments, (1999).
[3] National Instruments official WEB, www.ni.com
[4] Y.M. Li, W. Kim, Y.G. Zhang, M. Rolandi, D.W. Wang, H.J. Dai, "*Growth of single walled carbon nanotubes from discret catalytic nanoparticles of various sizes*", J. Phys Chem. B; **105**,46, (2001)11424-31,
[5] Charanjeet Singh, M. S. P. Shaffer, A.H. Windle "Production of controlled architectures of aligned carbon nanotubes by an injection chemical vapour deposition method", Carbon **41**, (2003),359-368
[6] SA1400, Hamamatsu software for card and program SA1400, Version 3.0.(1999).
[7] Joel Martínez Adame, "*Determination of spectral lines of H2 and C by using CCD detector*", Electronic Engineering Thesis, Instituto Tecnológico de Toluca, México, (2002).
[8] J. Pacheco, R. Peña, L. Peña, A. Segovia; G. Cota "*Plasma Torch ignition by a half bridge resonant converter*"; IEEE Trans. Pl. Sc. **27**, 4, (1999), 1124-1130.
[9] H. Lange, K. Sadaine, M. Razafinimanana, A. Gleizes, "*Temperature and C_2 column densities in a carbon arc plasma*" J. Phys, D: Appl. Phys. **32**, U.K., (1999), 1024-1030.
[10] S. Pellerin, K. Musiol, O. Motret, B. Pokrzywka, J. Chapelle, "*Application of the (0,0) Swan band spectrum for temperature measurement",* J. Phys D: Appl. Phys **29**, UK. (1996), 2850-2865.
[11] A.Okada, K. Kijima, "*Measurement of C_2 rotational temperature en Ar-SiH_4-CH_4 inductively coupled plasma flame with Abel inversion*", J. Phys. D: Appl. Phys. **35,** (2002), 2126-2132.
[12] E. Gutiérrez, M. Razafinimanana, J Pacheco, M. Pacheco, H. Lange, R. López "*Evaluation of temperature in an argon-acetylene plasma by C_2 Swan Band method*", ISPC16, Taormine Italy, (2003)

EVALUATION OF TEMPERATURE IN AN ARGON-ACETYLENE PLASMA BY C2 SWAN BAND METHOD.

E. Gutiérrez[1], M. Razafinimanana[2], J. Pacheco[1], M. Pacheco[2], H. Lange[3], R. López[1]

[1]*Instituto Nacional de Investigaciones Nucleares (ININ), Instituto Tecnológico de Toluca (ITT), México*
[2]*Centre de physique des plasmas et de leurs applications de Toulouse (CPAT), Francia,*
[3]*Department of Chemistry, Warsav University.Poland.*

Abstract

The emission of spectra in the Swan Band of the C2 molecule was employed for the evaluation of the temperatures and column densities in a DC plasma torch in the state $d^3\Pi_g$, $v'=0$ → $a^3\Pi_u$, $v''=0$ $a^3\Pi_u$, $v''=0$. This method is based on a comparison of experimental data obtained by Optical Emission Spectroscopy (OES) with the calculated spectrum for temperatures within the range of 2750-11000K and column densities of $(0.5\text{-}8)\times10^{15}$ cm^{-2} where the previous parameters depend on the current of the plasma and the coordinates in the plasma jet as well as of the composition of the plasma gases.

1. Introduction

The aim of the present work is to obtain the temperature and column density distributions in a mixture of argon-acetylene plasma by using the Swan Band technique [1]. The spectra obtained experimentally was compared with the simulated spectra. These comparisons are useful in determining various parameters of molecules such as the rotational and vibrational temperatures.

Optical emission spectroscopy (OES) is one of the most used techniques for plasma diagnosis. The optical emission measurements of the Swan Band, caused by the C_2 radicals, are commonly used in the diagnosis of high temperature processes (thermal plasma or electrical arc) or even in low temperature processes (combustion furnace) by introducing carbon materials in the medium.

The C_2 has an important role in the synthesis of new materials; therefore, it is of great interest the quantitative study of these radicals produced in the DC plasma.

Special attention was concentrated in the measurement of the column density of C_2 radicals and temperature distribution in the jet of a DC plasma torch under conditions that favorize the production of Carbon Nanotubes (CNT) [2].

2. Swan Band of molecule C2

The Swan Band of molecule C_2 was discovered in 1856 when studies were carried out on flames containing carbon components. Since then, this technique has been applied by numerous investigators for the determination of temperatures [1,2,3,4].
This band corresponds to the transition between the electronic states $d^3\Pi_g$ to $a^3\Pi_u$, at 2.08 and 0.09 eV respectively.

For plasmas in departure from local thermal equilibrium, the rotational, vibrational and excitation temperatures from electrons can differ from those of the heavy species temperatures. Taking into account the relation between the rotational and translational states, the rotational temperature is derived generally from the temperature of heavy particles. Then, the temperature of heavy particles can be obtained from the measurement of the rotational temperature using the swan band at 516,611 nm [5].

A theoretical determination of the Swan band in the wavelength range from 513 nm to 516,8 nm is shown in figure 1 for different densities. The spectrum was constructed with 205 points according to the number of pixels from the CCD.

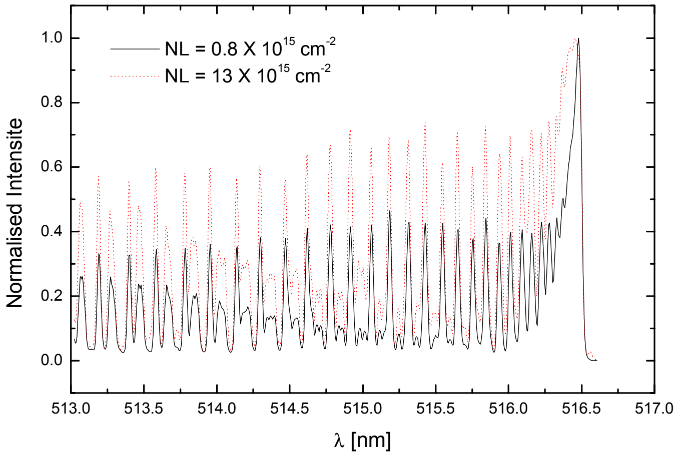

Figure 1. Simulated Spectrum for T = 6000 K

3. Swan Band diagnostic method

The rotational peaks appearing in the spectra have the particularity that are very sensitive to temperature changes. This characteristic allows the use of the superposition method and the Boltzman diagram method to measure temperatures in a plasma jet that contains carbon, since its theoretical emissivity is proportional to the carbon contents in the plasma jet.

3.1 Superposition method

The spectrum superposition method compares the spectrum of the Swan Band, experimentally obtained by OES, with those spectra simulated at standard intensities and temperatures within the interval from 2750 up to 11000 K, (with 125 K of increment). The emission and absorption coefficient used in the computation were based in reference [1] for a temperature of 4400K and a pressure of 13 kPa . By using MatLab^{TM} routines which call the Boltzman methode in order to have the first aproach to the more approximate temperature, and then the superposition method compares the simulated spectra with the experimental one to determine the temperature with a very close margin. The resultant data are processed by Origin to obtain the corresponding graphs of temperature and column density of the plasma.

The sequence of the superposition method is:
a). - Data acquisition by the spectroscopy system described below.
b). – Data processing and comparison of the spectra using Matlab routines.
c). - Edition and graphical presentation using the software Origin.

3.2 Boltzman diagram method

The Boltzman diagram can be applied to the spectral lines obtained in the Swan band to get the rotational temperatures in the plasma. The relative emission coefficient of two rotational lines within a band is given by [3]

$$\ln \frac{\varepsilon}{\sigma^4 \sum S_{K'',J''}^{K',J'}} = -\frac{hcF_v(J)}{k_B T} + \ln C \qquad (1)$$

Thus, for a given value of temperature, the first term of the equation is a linear function of the superior level of emission of the rotational ray. The coefficient on the right has a value of *-1/kBT*. Then, the temperature can be determined by constructing the so called Boltzman diagram [3]. This method is also called of relative intensities, since the temperature can be obtained from the slope of the straight line of figure 2, without calibration of the spectral lines.

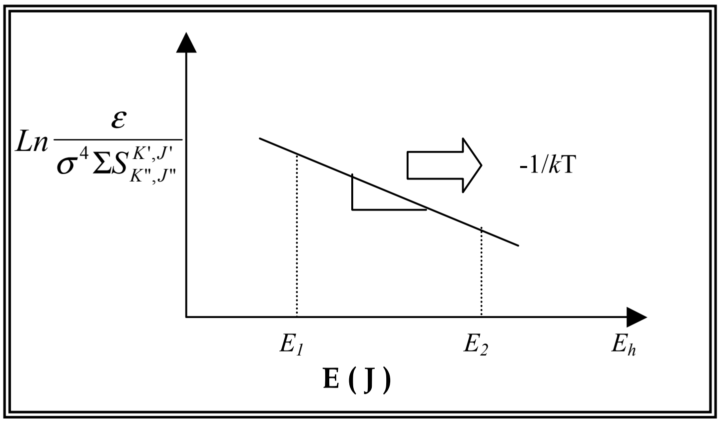

Figure 2. The Boltzman Diagram.

4. Experimental Set-up for the DC plasma

The ignition of the plasma can be obtained by an intermittent high voltage discharge [6], and then sustaining the plasma by means of three parallel current sources SDR/TH (100 A/120V), which have a current capacity up to 300 Amperes.

The arrangement of the plasma torch, reactor and peripheral devices is shown in figure 3.

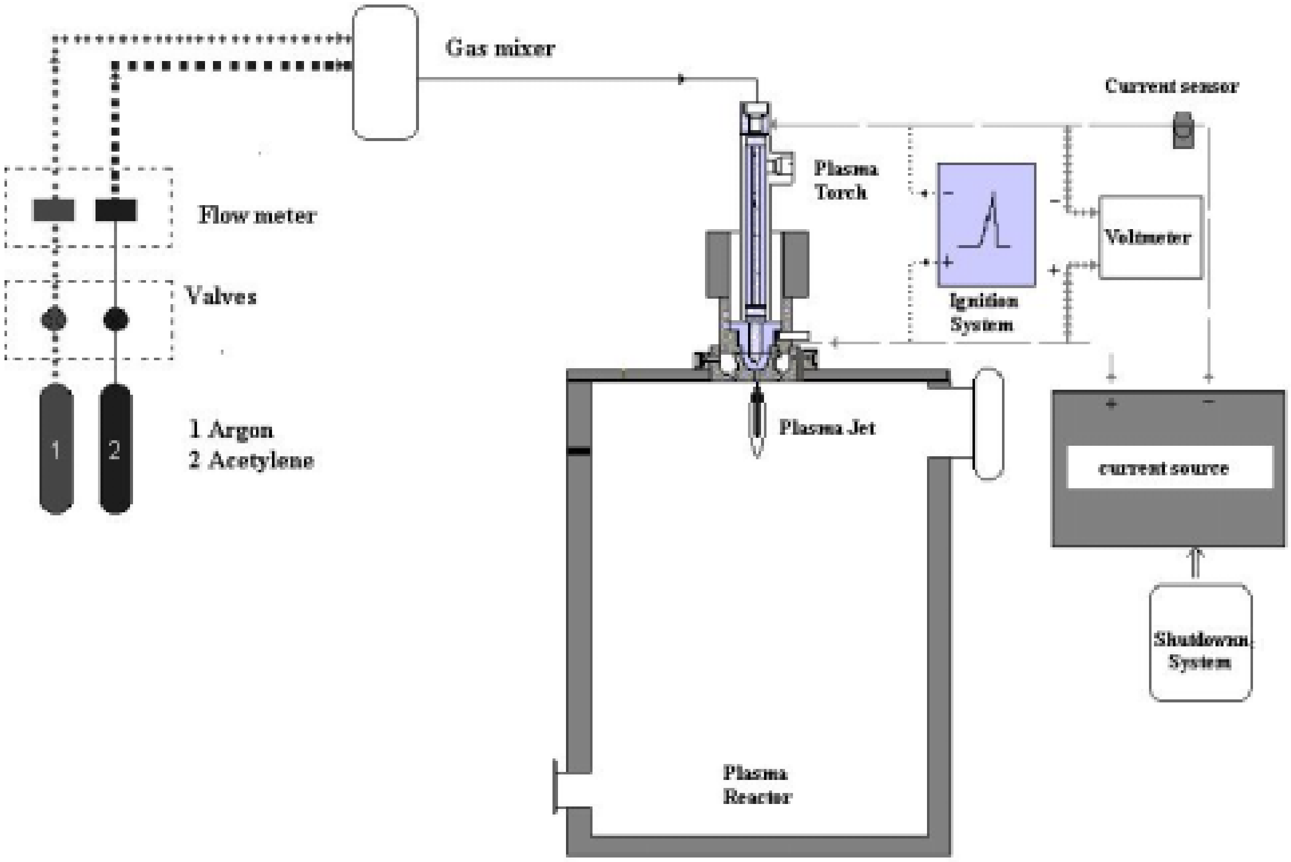

Figure 3. Expermimental set-up for the DC Plasma.

5. Optical emission spectroscopy System for diagnostic of Temperatures

The optical alignment is a very important factor in order to obtain a reliable diagnostic of the plasma jet. The alignment of the system was made with a He-Ne laser with a wavelength of 632 nm. The whole experimental setup is shown in figure 4.

The luminous signal coming from the plasma jet is "one to one" reproduced and focused by a convergent lenses towards the entry slit of the monochromator (THR 1000 1m of focal length), provided with a grating having 1200 grooves/mm, and a CCD detector (512 x 512 pixels). The length of each diode in the CCD is of 25 µm and the exposition time is controlled by a shutter from the PC. The width of the apparatus function was 0.03nm. The experiments were performed under stable operational conditions at 80A of current and 100kPa of pressure.

The spectra for different ranges of intensities and wavelengths can be obtained using the special software Winspec of Princenton which controls the data acquisition during the horizontal scanning of the plasma with very precise incremental steps, displacing the mirror horizontally, covering the whole diameter of the plasma. The vertical scanning was manually controlled covering 2 cm from the torch nozzle.

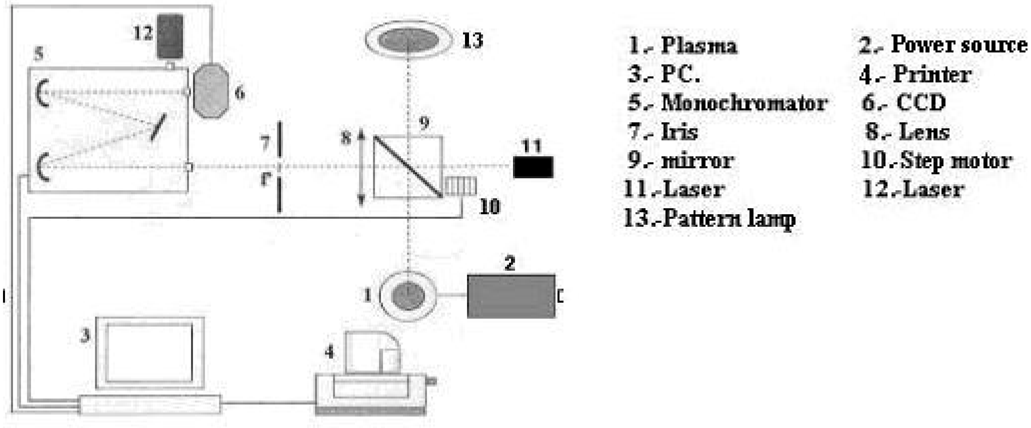

Figure 4. Optical emission spectroscopy System for plasma diagnostic.

6. Experimental results

Figure 5 shows the experimental spectrum of the C_2 band at normalized intensities, acquired during the OES measures and processed with Matlab subroutines. All the measures were obtained at the center of the plasma. Comparing these spectra with the simulated one (figure 1), it is evident that the rotational temperatures are very similar.

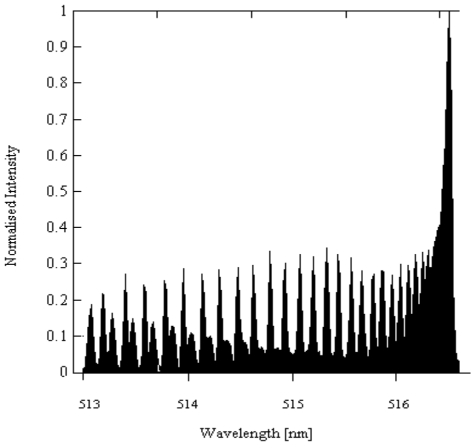

Figure 5.- The experimental Spectrum (Ar-C_2H_2, 80 A.)

After obtaining the spectrum of the system, the C_2 temperatures and densities were calculated from the (0,0) Swan band, using Boltzmann and Superposition methods, with a current of 80 A, and a gas mixture of Ar-C_2H_2.

The distribution of the axial temperature in the plasma jet for the C_2 is shown in figure 6, where the maximum temperature is located at the center of the jet ($5.5x10^3$ to $11x10^3$ K). The temperature decreases at the bottom and on the sides of the plasma jet. Figure 7 shows the fields of temperature in the plasma jet, where the highest temperature is found at the output of the torch, the cold zones between the hotter zones are there because the acetylene is injected into the plasma in these zones.

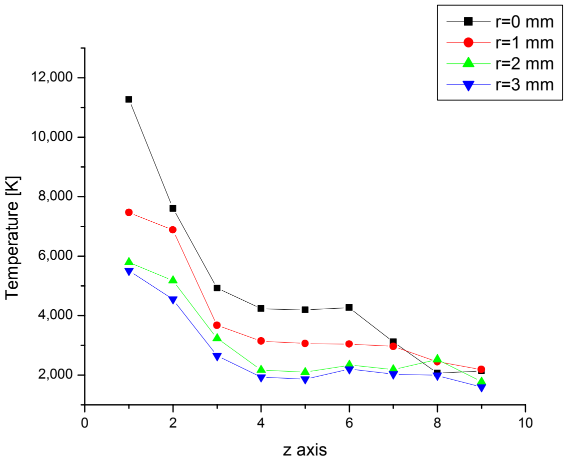

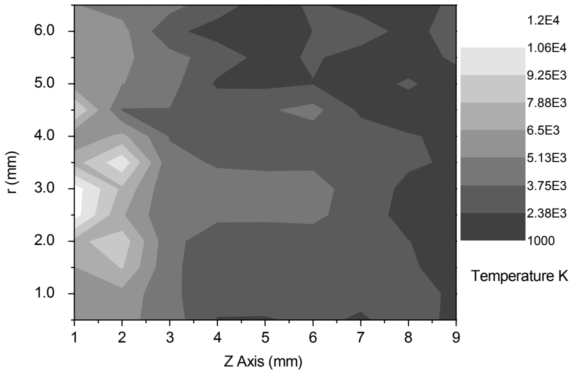

Figure 6. Radial profiles of temperature

Figure 7. Temperature field at the Plasma DC, Ar-C_2H_2

Figure 8 shows the column densities distribution of C_2 in argon-acetylene plasma, with a current of 80A. The greatest density of C_2 occurs at the output of the torch and decreases towards the bottom and the sides of the plasma jet .

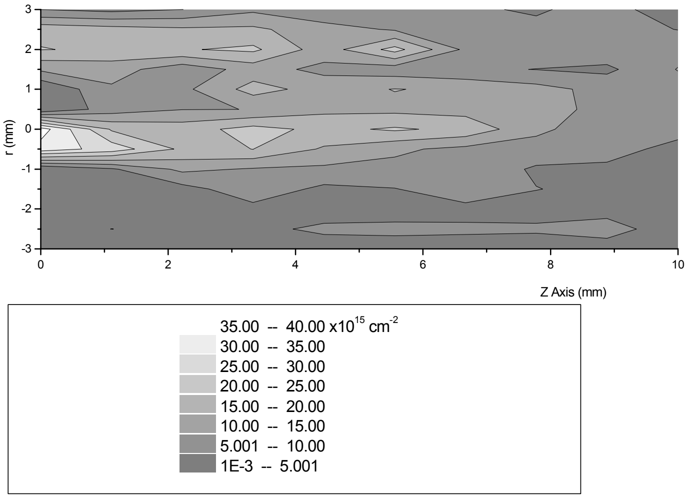

Figure.8 Densities fields of C_2 with the mixture Argon-Acetylene.

7. Conclusions

The method used in this work can be used as a very practical thermometer for the determination of temperatures in the DC plasma.

Molecules of C_2 appear in different zones of the plasma, and this chemical radical provides enough information to obtain the temperature of gas according to its emission. The range of temperatures covered was between 2750 and 11000 K and for column densities of $(0.5\text{-}8)\text{x}10^{15}$ cm^{-2}. The obtained results proved the importance of the C_2 (0,0) Swan band for the diagnostic of plasmas.

Acknowledgments

The authors would like to thank ECOS-ANUIES (grant # MPOO-004), ININ and ITT in Mexico and CPAT in France, for the support given to this work.

References

[1] H. Lange, K. Sadaine, M. Razafinimanana and A. Gleizes,*Temperature and C_2 column densities in a carbon arc plasma*, J. Phys, D: Appl. Phys. 32, (1999)
[2] P. Byszewski, H. Lange, A. Huczko and J. Behnke, *" Fullerene and Nanotube Synthesis. Plasma Spectroscopy Studies"*, J. Phys. Chem Solids, Vol.58, pp. 1679-1683, (1997).
[3] S. Pellerin, K. Musiol, O. Motret, B. Pokrzywka and J. Chapelle, *Application of the (0,0) Swan band spectrum for temperature measurements,* J. Phys D: Appl. Phys 29, (1996).
[4] N.G. Bycova, S.A. Vasil'evskii, I.S: Pershin, M.I. Yakushin, "*Temperature Measurements of Inductive Plasma subsonic flow from emission spectra"*, 45-50, ISPCXV, (2001)
[5] M. Pacheco, *"Synthèse des nanotubes de carbone par arc électrique",* These Doctoral ,Université Paul Sabatier ,Toulouse, Francia (2003).
[6] J. Pacheco, R. Peña, L. Peña, A. Segovia; G. Cota "*Plasma Torch ignition by a half bridge resonant converter*"; IEEE Trans. Plas. Sc. **27**, Nº 4, 1124-1130 (1999).

Plasma and Surface Chemistries for Advanced Gate Etch Processes

A. Sano, K. Ono, K. Takahashi, Y. Setsuhara

Department. of Aeronautics and Astronautics, Graduate. School of Engineering., Kyoto Univeristy, Kyoto, Japan

As integrated circuit device dimensions continue to be scaled down, increasingly strict requirements are being imposed on plasma etching technology. The requirements include the etch anisotropy, profile control, feature size or critical dimension (CD) control relative to the mask layer, selectivity to the underlying layers, and also microscopic uniformity of these etch parameters. The precise control of the profile and critical dimension (CD) of microstructural features is still one of the most important issues to be addressed, particularly in gate etch process for gate definition of microelectronic devices. In practice, the gate width of advanced microelectronic devices is projected to be scaled down to much less than 0.1 μm (or < 100 nm) in a few years, where a nanometer-scale control is indispensable for the profile and CD of gate electrodes. In developing the technology to meet these demands, a better understanding of the behavior of reaction and inhibitor layers on feature surfaces is particularly important, which also requires a better understanding of the behavior of etch products and surface inhibitors as well as reactants for etching in the plasma and in microstructures on the substrate.

This paper presents a comparative study of profile simulation and etch experiment, to achieve a nanometer-scale control of the profile and CD in etching of poly-Si gate electrodes. Attention is focused on the evolution of trenches etched in silicon with high-density chlorine-containing plasmas. The simulation employs a phenomenological model which relies on a full matrix approach with the volume density function in the entire computational domain for the materials being etched. This model enables us to take into account multilayer adsorption or reaction kinetics on feature surfaces which the usual string algorithm with Langmuir adsorption scheme is hard to deal with. The model takes into account the transport and surface chemistry of ions and neutrals in microstructures, based on our present understanding of the physics and chemistry underlying the processing: neutral adsorption, surface reemission or reflection of ions and neutrals, purely chemical etching, physical sputtering, ion-assisted reactions, and surface inhibitor deposition. The numerical results indicated that a thin passivation layer of surface inhibitors on feature sidewalls plays a key role in achieving the nanometer-scale control of the profile and CD through main etch and overetch processes, which qualitatively agrees with the etch experiment using two-step processes. In practice, the surface inhibitors through main etch rely on etch products desorbing from feature surfaces, while the inhibitors during overetch time come from the plasma and rely on polymerized particles originating from additive bromine-containing gases.

A second important issue to be addressed in gate etch process for advanced microelectronic devices is the fabrication of gate structure using high-permittivity (high-*k*) gate dielectrics. In practice, as the thickness of SiO_2 gate oxides approaches ~2 nm, a number of serious problems (such as increased gate leakage current and reduced oxide reliability) arise, which may ultimately prevent the device scaling. Hence, high-*k* insulating metal oxides such as Al_2O_3, ZrO_2, and HfO_2 are currently under consideration as novel gate dielectric materials in the 0.05 μm (or 50 nm) technology node and beyond, because they provide the required specific capacitance at a considerably larger thickness (~20 nm) than SiO_2, thus allowing the reduction of gate leakage current. In the fabrication of high-*k* gate stack structures, the etching of high-*k* thin gate dielectric films as well as gate electrodes is an important issue for pattern transfer. This paper also presents a comprehensive study of the etching characteristics of high-*k* materials with high-density fluorocarbon plasmas, in terms of plasma and surface chemistries and plasma parameters. Emphasis is placed on a better understanding of the physics and chemistry underlying the processing to achieve a high etch selectivity over Si substrate. The experiments indicated that the selectivies over Si are far less than unity with CF_4 plasmas owing to enhanced etch rates of Si by F radicals, and that the increased etch rates of high-*k* materials and etch selectivities over Si can be achieved with Ar/fluorocarbon mixture plasmas using C-rich fluorocarbon molecules owing to increased surface inhibitor deposition on Si.

Plasma Chemical Behavior of Reaction Products during Inductively Coupled CF_4 Plasma Etching of Si and SiO_2

I. Fujikake, K. Ono, K. Takahashi, and Y. Setsuhara

Department of Aeronautics and Astronautics, Graduate School of Engineering, Kyoto University, Kyoto, Japan

Abstract

A two-dimensional plasma fluid model including surface reactions has been developed for self-consistent treatment of plasma evolution and surface chemistry. The simulation was used to study the plasma chemical behavior and surface chemistry of reaction products during Si and SiO_2 etching in an inductively coupled CF_4 plasma. Numerical results indicated that the major ion species incident on the substrate is not CF_3^+ but SiF_3^+ at higher pressures > 50 mTorr.

1. Introduction

Radio-frequency discharges in low-pressure fluorocarbon gases have been widely used for the etching of SiO_2 layers on Si in the fabrication of microelectronics devices [1]. During plasma etching, several different kinds of reactive species (ions and neutrals) occur in the plasma, which are incident onto the substrate surface being etched: feedstock gas species and their fragmments (or reactants), reaction products (or etch products) from the substrate, impurities from chamber walls, and mask materials. In particular, the plasma chemical behavior of etch products is important as well as that of reactants, because the etch products desorbed from the substrate surfaces participate in gas-phase reactions, resulting in a change of plasma properties near the substrate; moreover, some of them reenter the substrate surface, which in turn significantly influence the etching characteristics such as etch rate, profile, and their microscopic as well as macroscopic uniformity. Thus, a better understanding is strongly required of the behavior of etch products in the gas phase as well as on the substrate surfaces, to further develop an advanced plasma etching technology for advanced microelectronics and microelectromechanical system (MEMS) devices.

The modeling of inductively coupled plasmas (ICPs) has been extensively studied as one of high-density plasma sources; however, little work has successfully taken into account the etch product chemistry in the gas phase and on the surfaces. Lee *et al.* investigated the role of etch products during Si etching in chlorine plasmas, using the so-called global model [2]. The volume-averaged global model can easily treat the complicated chemistry owing to the simplicity of the model; however, the model cannot provide the information on spatially nonuniform plasma properties and also the process uniformity. In practice, to address the process uniformity, a model is required with at least two-dimensional description. This paper presents a two-dimensional plasma fluid model combined with a surface reaction model including the chemistry of etch products, to take into account the plasma and surface chemistry in a self-consistent manner.

2. Model

A schematic of the ICP reactor presently studied is shown in Fig. 1. The plasma reactor consists of a cylindrical chamber R=15 cm in inner radius and H=9 cm high, a dielectric window at the top, a substrate holder R_w=10 cm in radius at the bottom with a wafer on it. The dielectric window is equipped with a five-turn planar rf coil for generation of ICPs. The coil current induces a time-varying magnetic field which in turn induces the electric field that couples the rf power to plasma electrons within a skin depth layer near the plasma-dielectric interfaces. The substrate holder can be rf biased to control the energy of ion bombardment onto the substrate surfaces. Feedstock gas is supplied through a gas inlet ring located just under the dielectric window, being pumped away through an annular ring port for pumping.

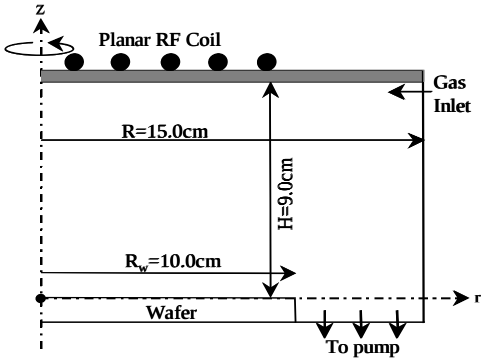

Fig.1. A schematic of the ICP reactor studied in the present simulation.

Maxwell's equations are solved to obtain the spatial profile of the rf induced field in the plasma, which is employed to evaluate that of the power deposition into the plasma. The profile of the power deposition is then given to the electron energy equation to calculate that of the electron temperature. The rate coefficients for electron-impact processes including ionization and chemical reactions are functions of the electron temperature, being given to source and sink terms of the rate equations for charged and neutral species in the plasma fluid model. At the plasma-surface boundaries, the surface site balance model is used with the flux of reactants from the plasma to the substrate as an input, to take into account the surface reactions and to determine the surface coverages and the flux of reaction products desorbing from the substrate. The product fluxes obtained are subsequently placed back to the plasma fluid model as boundary conditions, and the plasma electron density and thus the plasma conductivity is then obtained and given to Maxwell's equations. By iterating these procedures until a solution converges, a self-consistend steady state solution can be obtained.

In more detail, the electromagnetic fields are obtained by solving Maxwell's equations, where the rf spiral coil is approximated by a set of concentric coils. Assuming the axisymmetric configuration, we only consider the azimuthal component of the inductive electric field E_θ:

$$\nabla^2 E_\theta = j\omega\mu_0\sigma E_\theta \tag{1}$$

where ω is the angular frequency of the driving rf field, μ_0 is the permeability of vacuum, and σ is the plasma conductivity depending on the electron density n_{e}.

The diffusion and chemical reactions are taken into account for neutral species, where Fick's law is employed instead of solving the full momentum equation. This reduces the computational time significantly as compared to solving the Navier-Stokes equation. The flux of the kth neutral species is given by

$$\mathbf{\Gamma}_k = -D\nabla n_k \,, \tag{2}$$

where D is the diffusion coefficient and n_k is the kth neutral density. The continuity equation for the kth neutral species is then expressed as

$$\frac{\partial n_k}{\partial t} = -\nabla\cdot\mathbf{\Gamma}_k + \sum_j R_{kj} \,, \tag{3}$$

where R_{kj} is the generation and/or loss rate for the kth neutral species through the reaction event j. Neutral species also flow into and out of the discharge region as a result of pumping. As for the feedstock gas, the inflow has to be considered through the gas inlet to the reactor chamber. The gas temperature is assumed to be spatially uniform at a room temperature ($T_{\mathrm{n}} = 300$ K = 0.026 eV).

The fluid approach is also employed to model the behavior of charged species, assuming the electron energy distribution function (EEDF) to be Maxwellian. Kimura *et al.* performed Langmuir probe measurements in an inductively coupled CF_4 plasma source, and they reported that the EEDF was Maxwellian even at a pressure of 2 mTorr [3]. Then, the electron energy balance is expressed as

$$\frac{\partial}{\partial t}\left(\frac{3}{2}n_{\mathrm{e}}k_{\mathrm{B}}T_{\mathrm{e}}\right) = W - \nabla\cdot\mathbf{q}_{\mathrm{e}} - \nu_{\mathrm{m}}\frac{3m_{\mathrm{e}}}{M}n_{\mathrm{e}}k_{\mathrm{B}}(T_{\mathrm{e}} - T_{\mathrm{n}}) - \sum_j R_j\Delta H_j \,, \tag{4}$$

where T_{e} is the electron temperature, ν_{m} is the electron momentum transfer collision frequency, M_{n} is the mass of neutral species, $R_{\mathrm{e}j}$ is the rate for the inelastic electron-impact collision j, $\Delta H_{\mathrm{e}j}$ is energy gain and/or loss through the jth inelastic electron-impact collision, and k_{B} is the Boltzmann constant. The electron energy flux $\mathbf{q}_{\mathrm{e}}$ consists of heat conduction and convection as

$$\mathbf{q}_{\mathrm{e}} = -\kappa_{\mathrm{e}}\nabla T_{\mathrm{e}} + \frac{5}{2}k_{\mathrm{B}}T_{\mathrm{e}}\mathbf{\Gamma}_{\mathrm{e}} \,, \tag{5}$$

where $\mathbf{\Gamma}_{\mathrm{e}}$ is the electron flux, and κ_{e} is electron thermal conductivity given by

$$\kappa_e = \frac{3}{2}k_B D_e n_e \,. \tag{6}$$

The drift diffusion approximation is employed to model the electron and ion fluxes in the reactor chamber. To avoid solving the plasma sheath structure, we assume the continuity equation to cover all of the chamber area except for the sheath region. Based on the assumption of quasi-neutrality

$$\sum\nolimits_{+} n_{+} = \sum\nolimits_{-} n_{-} \,, \tag{7}$$

and congruence of flux

Table.I. Suraface reactions for Si etching in fluorocarbon plasma considered in the simulation.

1	$Si + X^+$	$\rightarrow Si + Si + X$	Physical sputtering	$1\text{-}\Theta_{tot}$
2	$Si + 2F + X^+$	$\rightarrow SiO_2\_F_2 + X^+$	Adsorption	$1\text{-}\Theta_{tot}$
3	$Si\_F_2 + 2F + X^+$	$\rightarrow SiF_4 + Si + X^+$	Ion enhanced etching	Θ_F
4	$Si\_F_2 + X^+$	$\rightarrow SiF_2 + X^+$	Ion enhanced sputtering	Θ_F
5	$Si\_F_2 + 2F$	$\rightarrow SiF_4$	Thermal etching	$1\text{-}\Theta_{CFx}\text{-}\Theta_p$
6	$Si + CF_x$	$\rightarrow Si\_CF_x$	Chemisorption	Θ_p
7	$Si\_CF_x + X^+$	$\rightarrow Si + CF_x + Si + X$	C sputtering	Θ_{CFx}
8	$Si\_CF_x + F$	$\rightarrow Si + CF_{x+1}$	Recombination	Θ_{CFx}
9	CF_x^+ at $E < E_{th}$	$\rightarrow$ polymer	Direct ion deposition	1
10	$Si\_CF_x + X^+$ at $E < E_{th}$	$\rightarrow$ polymer + X	Ion enhanced deposition	Θ_{CFx}
11	$P\text{-}F + X^+$	$\rightarrow$ etching of polymer	Ion enhanced etching	$\Theta_p\Theta_{F/P}$
12	$P\text{-}CF_x + X^+$	$\rightarrow$ more polymer	Ion enhanced deposition	$\Theta_p\Theta_{CFx/P}$
13	SiF_x	$\rightarrow$ more polymer	Re-deposion of etch products	1

Table.II. Suraface reactions for SiO_2 etching in fluorocarbon plasma considered in the simulation.

1.	$SiO_2 + X^+$	$\rightarrow Si + 2O + SiO_2 + X$	Physical sputtering	$1\text{-}\Theta_{tot}$
2.	$SiO_2 + 2F + X^+$	$\rightarrow SiO_2\_F_2 + X^+$	Adsorption	$1\text{-}\Theta_{tot}$
3.	$SiO_2\_F_2 + 2F + X^+$	$\rightarrow SiF_4 + O_2 + SiO_2 + X^+$	Ion enhanced etching	Θ_F
4.	$SiO_2\_F_2 + X^+$	$\rightarrow SiF_2 + O_2 + SiO_2 + X^+$	Ion enhanced sputtering	Θ_F
5.	$SiO_2\_F_2 + 2F$	$\rightarrow SiF_4 + O_2$	Thermal etching	$1\text{-}\Theta_{CFx}\text{-}\Theta_p$
6.	$SiO_2 + CF_x$	$\rightarrow SiO_2\_CF_x$	Chemisorption	Θ_p
7.	$2SiO_2\_CF_x + X^+$	$\rightarrow SiF_x + 2CO_2 + SiO_2 + X$	Ion enhanced etching	Θ_{CFx}
8.	$SiO_2\_CF_x + X^+$	$\rightarrow Si + 2COF_x + SiO_2 + X$	C sputtering	Θ_{CFx}
9.	$SiO_2\_CF_x + F$	$\rightarrow SiO_2 + CF_{x+1}$	Recombination	Θ_{CFx}
10.	CF_x^+ at $E < E_{th}$	$\rightarrow$ polymer	Direct ion deposition	1
11.	$SiO_2\_CF_x + X^+$ at $E < E_{th}$	$\rightarrow$ polymer + X	Ion enhanced deposition	Θ_{CFx}
12.	$P\text{-}F + X^+$	$\rightarrow$ etching of polymer	Ion enhanced etching	$\Theta_p\Theta_{F/P}$
13.	$P\text{-}CF_x + X^+$	$\rightarrow$ more polymer	Ion enhanced deposition	$\Theta_p\Theta_{CFx/P}$
14	SiF_x	$\rightarrow$ more polymer	Re-deposion of etch products	1

$$\sum\nolimits_+ \Gamma_+ = \sum\nolimits_- \Gamma_- \,, \tag{8}$$

which means that the total positive ion flux out of any region is equal to the sum of the negative ion and electron fluxes, and that the plasma is treated with an ambipolar model. Here, the subscripts '+' and '–' indicate positive ions and negative ions/electrons, respectively. The continuity equation for the *i*th charged species is then described as

$$\frac{\partial n_i}{\partial t} = -\nabla \cdot (\mu_i n_i \mathbf{E} - D_i \nabla n_i) + \sum_j R_j \,, \tag{9}$$

the summation is taken over the collisions for generation and/or loss of the *i*th ion species. With the drift-diffusion approximation, the *i*th ion flux is given by

$$\boldsymbol{\Gamma}_i = \mu_i n_i \mathbf{E} - D_i \nabla n_i \,. \tag{10}$$

where **E** is the plasma electrostatic field derived from the flux balance of charged species. The diffusion coefficient D_i and the mobility μ_i of the *i*th ions are given by

$$D_i = \frac{k_B T_i}{M_i \nu_{in}}, \;\; \mu_i = \frac{q}{M_i \nu_{in}} \,, \tag{11}$$

where q, M_i, T_i are the charge, mass, and temperature of the *i*th ion species, and ν_{in} is the ion-neutral collision frequency. Substituting eq.(10) into eq.(8), we have

$$\mathbf{E} = \frac{\sum_+ D_+ \nabla n_+ - \sum_- D_- \nabla n_-}{\sum_+ \mu_+ n_+ + \sum_- \mu_- n_-} \,. \tag{12}$$

The reaction mechanisms for Si and SiO_2 etching have been studied for years. We follow the surface model of Gogolides *et al.* [4], to formulate the reactions on Si and SiO_2 surfaces; in practice, we add the re-deposition process of etch products in the surface chemistry, to take into account the effect of enhanced polymer deposition. The surface reactions on Si and SiO_2 surface considered in this study are summarized in Tables I and II, respectively. The removal of substrate atoms is attributed primarily to the ion-enhanced etching reactions during simultaneous exposure of reactive neutrals and energetic ions: the neutral atoms or molecules adsorbed react on substrate surfaces and produce reactive layers, which are then enhanced to be etched out of the surface under energetic ion bombardment. For fluorocarbon plasma etching, we assume that fluorine atoms, fluorocarbon radicals, and polymer are simultaneously bonded to surface atoms, where the surface coverage is assigned for all these species in mixed surface layers. As long as the polymer does not cover the entire surface site, the etching is assumed to proceed.

3. Results and Discussion

The nonlinear partial differential equations were discretized in space with finite-volume approximations. Then, we integrated the set of ordinary equations with a fully implicit scheme, assuming an initial two-dimensional profile for the electron density and temperature and the densities of ion and neutral species. When the time variations of these quantities disappear, the calculated values give a solution for the steady state. The rf source for ICP was taken to be operated at 13.56 MHz, and CF_4 pure gas was supplied into the reactor chamber. The nominal operating conditions were: a gas pressure of 10 mTorr, a mass flow rate of 200 sccm, an rf power of 250 W, and a dc self-bias voltage of 100 V on the substrate.

Figure 2 shows the volume-averaged neutral composition with Si and SiO_2 wafers and without a wafer for the nominal operating conditions, indicating that the density of etch products builds up to a substantial fraction of the total gas density. Since the total pressure is defined as $p = \Sigma_j n_j k_B T_j$, the increased products density corresponds to the decrease of the density of reactants at a given pressure.

Figures 3(a) and 3(b) show the surface coverage of F atoms, CF_x radicals, and polymer on Si and SiO_2 wafer surfaces, respectively, for the nominal conditions. The coverage of polymer is lowered near the edge of the wafer, being attributed to the decreased flux of CF, CF_2, and SiF_x owing to pumping which contributes to the polymer deposition; in practice, the polymer deposition on surfaces suppresses the etching. Note that

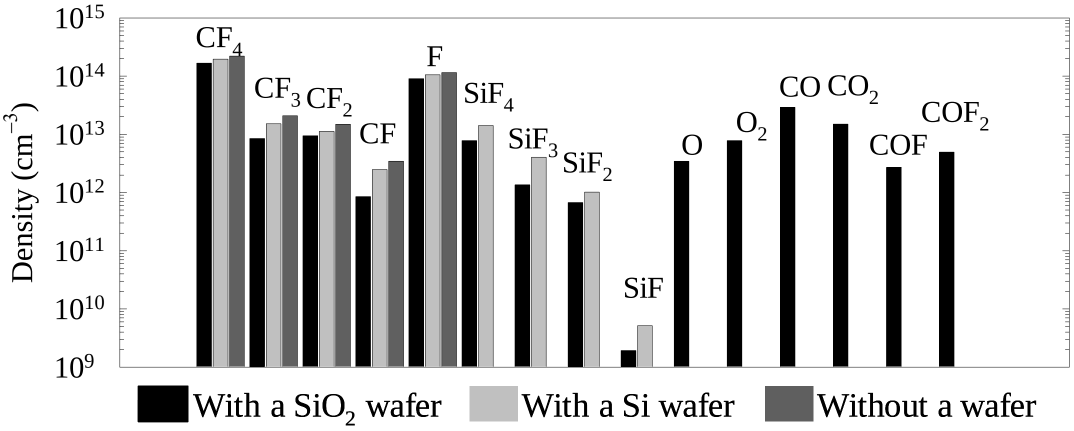

Fig.2. Comaprison of the volume-averaged neutral composition with Si and SiO_2 wafers and without a wafer for the nominal conditions (250 W rf power for ICP, CF_4 10 mTorr, 200 sccm, 100 V self bias).

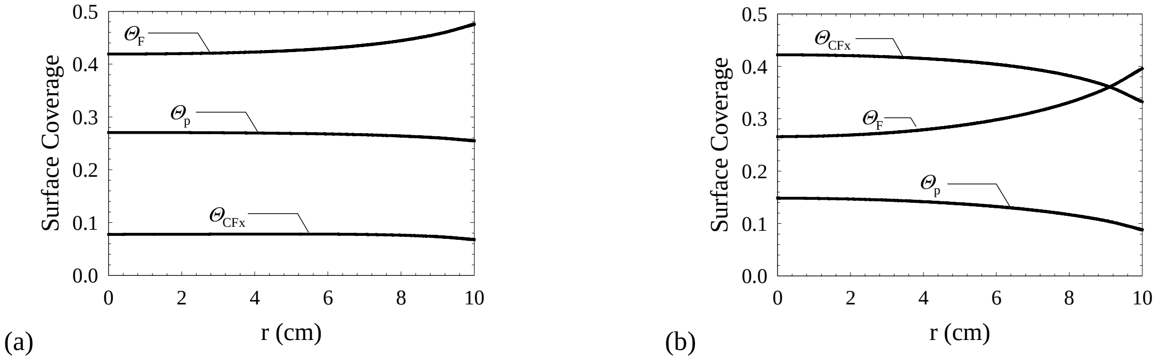

(a) (b)

Fig.3. Surface coverages on (a) SiO_2 and (b) Si surfaces as a function of wafer radius for the nominal operating conditions: the coverage Θ_F of F atoms, Θ_{CFx} of CF_x radicals, and Θ_p of polymer.

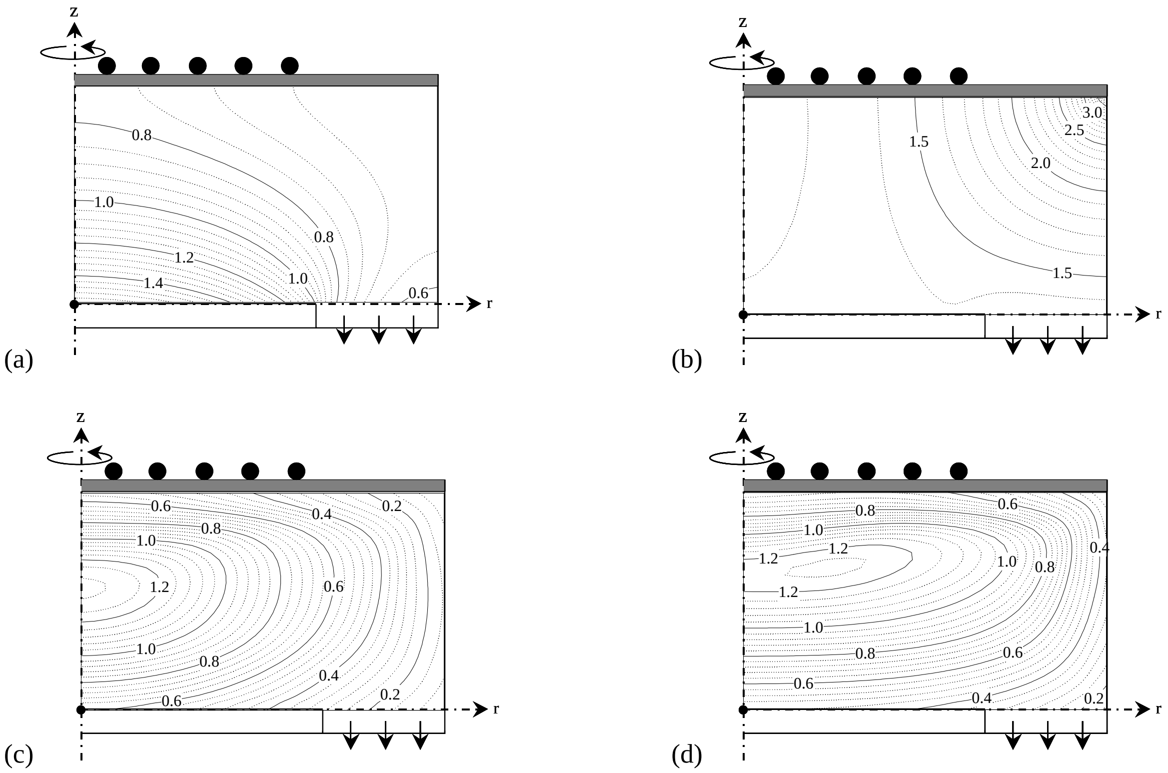

Fig.4. Density profiles in the gas phase during SiO_2 etching for the nominal operating conditions at 10 m Torr: (a) SiF_4 ($\times 10^{13}$ cm^{-3}), (b) CF_4 ($\times 10^{14}$ cm^{-3}), (c) SiF_3^+ ($\times 10^{10}$ cm^{-3}), and (d) CF_3^+ ($\times 10^{11}$ cm^{-3}).

the plasma properties in the bulk are different between the two cases, as can be seen in Fig. 2.

Figure 4 shows typical plasma properties in the bulk during SiO_2 etching for the nominal operating conditions, where the spatial distribution of density is shown for etch product SiF_4, feedstock gas CF_4, and their fragment ions SiF_3^+ and CF_3^+. The distribution of SiF_4 is fairly nonuniform, owing to a large amount of SiF_4 produced on substrate surfaces and to a small value of the diffusion coefficient of SiF_4. It is further noted that the product density decays smoothly away from the substrate surface, implying that the surface reaction is faster than the diffusion process. Considering the small amount of feedstock gas CF_4 which reaches the substrate surface, the mass flow rate of etch products desorbed from the surface is significant (corresponding to 13 sccm). The distribution of SiF_3^+ and CF_3^+ ions has a peak near the center of the chamber, because the diffusive transport dominates at low pressures. Since one of the major reaction processes for generation of CF_3^+ is the electron impact ionization of the feedstock CF_4 whose density is highest near the gas inlet ring, the peak density region for CF_3^+ ions spreads in larger radii. Note that the density of SiF_3^+ ion has a peak density of 1.3×10^{10} cm^{-3}, which is not negligible compared to that of 1.3×10^{11} cm^{-3} for major ions CF_3^+.

Figures 5(a) and 5(b) show the density profiles of major ions CF_3^+ and product ions SiF_3^+, respectively, at a higher pressure of 50 mTorr during SiO_2 etching, with the other operating conditions being the same as the nominal conditions. Compared with the results of Fig. 4 at 10 mTorr, the distribution is significantly localized; the density of CF_3^+ has an off-axis peak under the rf coils where the power deposition into plasma is highest, while that of SiF_3^+ builds up near the substrate. This is attributable to the ion-neutral collision frequency increased at increased pressures, resulting in a decrease of the ion diffusion coefficient and ion mobility as in eq. (11). Figure 6 shows the ion fluxes incident onto the substrate surface during SiO_2 etching at 10 and 50 mTorr. The major incident ion is CF_3^+ at 10 mTorr, while that is SiF_3^+ at higher 50 mTorr, implying that the etch reaction products may play an important role not only in gas-phase kinetics but also in the ion bombardment that contributes to the ion-enhanced surface reactions.

4. Conclusions

A two-dimensional fluid simulation has been performed for an inductively coupled CF_4 plasma source during Si and SiO_2 etching, taking into account the etch products chemistry along with gas-phase and surface reaction models. The plasma fluid model consisted of Maxwell's equation, rate equations for neutral and charged particles, and an energy balance equation for electrons. The surface reaction model assumed the Langmuir adsorption kinetics on surfaces, including the surface coverage of fluorine atoms, fluorocarbon radicals, and polymers which are simultaneously bonded to surface atoms. By coupling these models, steady state solutions were obtained in a self-consistent fashion.

The numerical results indicated that the etch products give a significant fraction of reactive species that occur in the chamber during etching. The presence of products tend to decrease the amount of reactants in the chamber at constant operating pressures. Moreover, the electron-impact processes for these products in the gas phase lead to the formation of ions and radicals of product species, which in turn play an important role during processing in the gas-phase and on surfaces.

Uncertainties of the model arise from the approximation contained, such as the ohmic heating mechanism, drift-diffusion approximation at low pressures, and the reaction processes with their rate parameters such as a sticking coefficient on surfaces. The sticking coefficient of reactive species may change depending on surface conditions. Parametric study of such uncertain parameters is required to acquire further insight into the picture that occur in the plasma reactor chamber.

References

[1] M. Schaepkens and G. S. Oehrlein: J. Electrochem. Soc. **148**, 211 (2001).

[2] C. Lee, D. B. Graves and M. A. Lieberman: Plasma Chemistry and Plasma Processing **16**, 99 (1996).

[3] T. Kimura and K. Ohe: Plasma Source Sci. Technol. **8**, 553 (1999).

[4] E. Gogolides, P.Vauvert, G. Kokkoris, G. Turban and A. G. Boudouvis: J. Appl. Phys. **88**, 5570 (2000).

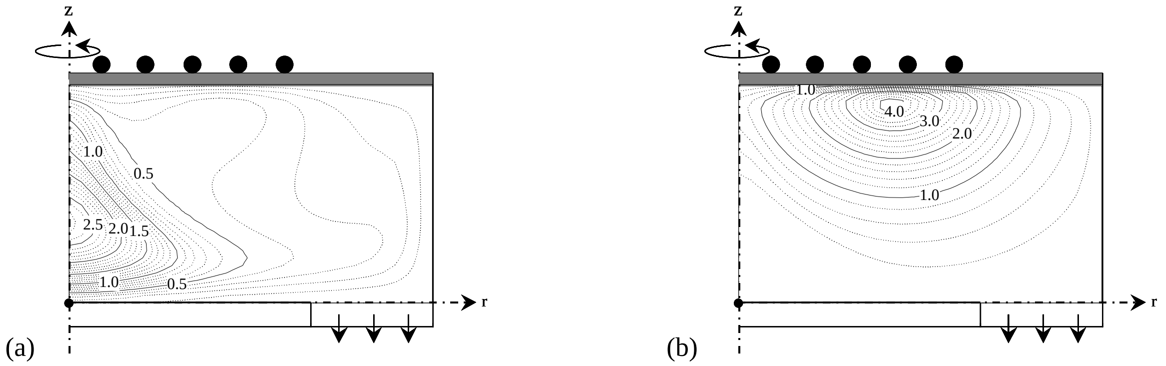

Fig.5. Density profiles of SiF$_3^+$ and CF$_3^+$ ions during SiO$_2$ etching at a pressure of 50 mTorr: (a) SiF$_3^+$ (×10^{11} cm^{-3}) and (b) CF$_3^+$ (×10^{11} cm^{-3}). Other operating conditions are the same as the nominal conditions.

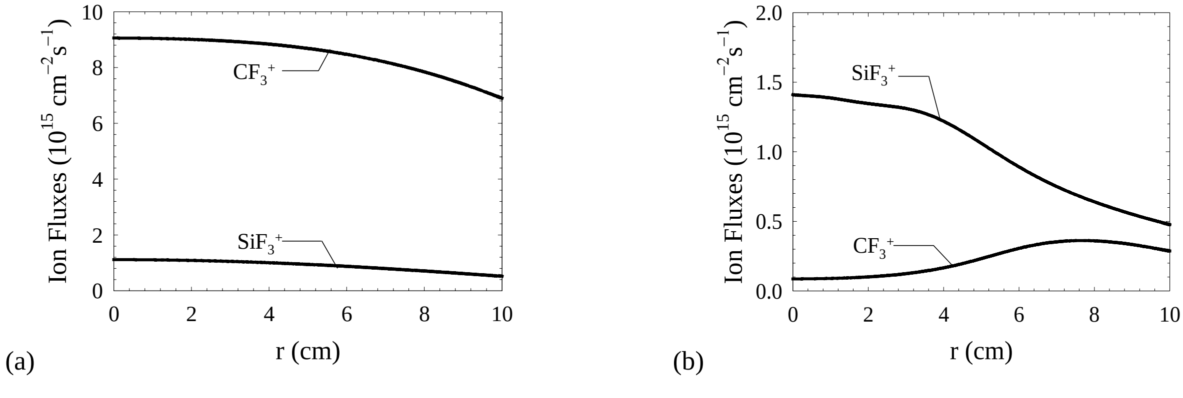

Fig.6. Flux distributions of CF$_3^+$ and SiF$_3^+$ ions incident onto the substrate surface during SiO$_2$ etching at a gas pressure of (a)10 mTorr and (b) 50 mTorr. Other operating conditions are the same as the nominal conditions.

ORGANIC AND MINERAL WASTE SOLIDIFICATION BY ARC PLASMA TECHNOLOGY

J.B. Bien, J D. Bien, W.Bialczak, K.Wystalska[1], M.Rozpondek[2]

[1]Institute of Environmental Engineering, Technical University of Czestochowa, Poland
[2]Department of Extraction and Recycling of Metals, Technical University of Czetochowa, Poland

Abstract

The paper presents a prototypical plasma reactor that has been started up in the Institute of Environmental Engineering, Technical University of Czestochowa. It also presents preliminary research results. The research included tests on plasma utilization of residues after thermal treatment of sewage sludge, medical and industrial waste. Introduction of oxygen into the reaction zone facilitated both after-incineration of combustible matter and solidification achieved in one system.

Introduction

Waste treatment is achieved by means of conventional as well as alternative thermal methods. Conventional methods are well known and have been applied for many years. As for alternative methods based on low-temperature pyrolysis, they are currently subject to investigation. Although thermal methods of treatment are considered the most fundamental they do not completely solve the problem with waste management and the number of opponents against these methods increases. It is due to the fact that the temperature range and oxygen presence in a process leads to formation and atmospheric release of SO_2, NO_x, CO_2 and the most hazardous compounds such as dioxins and furans. Furthermore, solid residues after thermal treatment which have to fulfill the appropriate standards and be transformed before landfilling need to be handled as well [1].

Utilization of hazardous waste is carried out by means of arc plasma technology. On commercial scale, production of titanium white by oxidation of titanium tetrachloride, acetylene from methane and cyanogen from coke and nitrogen can serve as an example of plasma application. In the USA, there research on iron extraction from hematite and magnetite ores in a pilot installation with power of 1 MW is conducted. Arc plasma technology for waste utilization was initially employed for toxic and radioactive waste. However with time, research was focused on less noxious waste. It resulted in constructing treatment plants using arc plasma technology [2],[3].The pilot installation with capacity of 500 kg/h for hospital waste treatment serves as an example [4]. The installation can be also used for out-of-date medicines and chemical waste treatment. Due to flexibility of a plasma process its economical indexes may be improved by reducing costs of waste selection. The investigations on utilization of ash [5], [6], both untreated and incinerated medical waste are available in literature. There is a number of plasmatron advantages: the size is 30 times smaller in comparison to an incineration plant, plasmatron modularity results in efficiency, cost-effectiveness, low maintenance and management costs.

Although plasma technology is associated in most cases with high operating costs due to significant energy consumption, a treatment plant employing plasma technology can be profitable [7]. Research carried out in the plasma reactor in the Institute of Environmental Engineering, Technical University of Czestochowa deals with residues from wastewater treatment plants [8],[9] and medical and industrial waste [10].

2. Experimental setup

The research included tests on plasma utilization of residues after thermal treatment of sewage sludge, medical and industrial waste. The aim of the research was to obtain solid, glassy end-products.

2.1. Plasma reactor

Chemical plasma reactor designed and constructed in the Institute of Environmental Engineering, Technical University of Czestochowa is used for thermal plasma utilization of hazardous waste (Figure 1). The reactor is hermetic and can operate at wide range of pressure (from partial vacuum to overpressure up to 0.05 MPa) due to that, the process is carried out in controlled atmosphere conditions. The installation consists of direct current (DC) plasma torch. The maximum plasma arc power reaches 150 kW at 50 to 1300 A for different voltage values up to 350 V which enables melting any kind of material. A torch inside the reactor can be modified and the length of plasma arc can be altered up to 0,35 m. Ceramic or graphite crucibles with capacity up to 10 dm^3 can be placed on arc-furnace electrode (anode). Argon with flow rate of 0,015 ÷ 0,060 Nm^3/min is applied as a plasma forming gas but oxygen can be also introduced into the reaction zone. At present, the reactor is operating in batch system, however tests with continuous material feed are planned to run as well.

The unique properties of the installation are following:

- the reactor can operate at partial vacuum and overpressure due to its hermetic installation,
- tests can be run in inert and redox conditions,
- any kind of material can be processed,
- high temperature (1000 – 3000°C) can be applied to heat up the material.

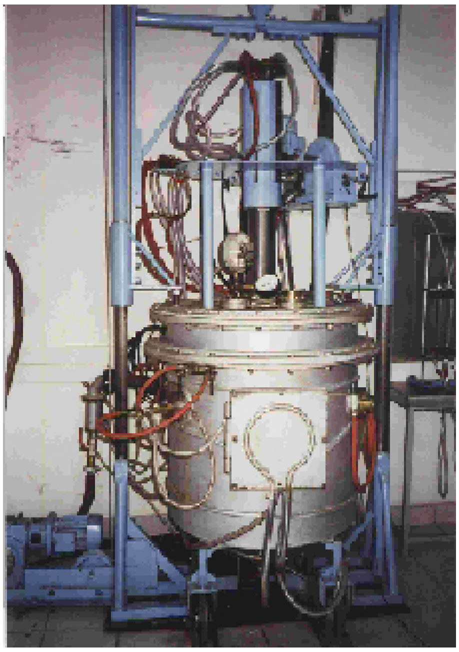

Figure 1. Plasma reactor

The installation is also equipped with gas analyzers determining CO, CO_2, SO_2, NO_x, C_xH_y. Introducing control units for gas flow rates with data logging system is planned. Due to that the research scope will be expanded and targeted changes of parameters in time will be reached properly.

2.2. Research procedure

Samples of fermented sewage sludge were provided by the Central Wastewater Treatment Plant in Czestochowa. The samples were dried and the process of pyrolysis was carried out. Residues from medical waste thermal treatment obtained by Purotherm two-stage incineration technology were subject to the research as well. Purotherm technology is based on pyrolysis i.e. controlled waste degassing and gasification in atmosphere of low oxygen content. Industrial waste was treated in rotary and multiple-hearth furnaces in a waste incineration plant. Test samples were subject to physico-chemical analysis (Table 1). For laboratory

tests residue samples were treated with plasma technology in specified I-U characteristics. The test was run for 15 minutes. During the first 10 minutes the treatment process was carried out at 200-300 A, then the power was gradually increased (max. 40 kW) in order to solidify the samples (350-400 A).
In cases of samples with high content of carbon (carbon content in sewage sludge samples after pyrolysis and medical waste samples after treatment was 36,48% and 22% respectively), oxygen was introduced into the reaction zone.

Table 1. Physico-chemical analysis of test samples

Analysis	Unit	Sewage sludge	Medical waste	Industrial waste
Ignition loss 550ºC	%	53,70	48,18	9,63
800ºC	%	-	4,82	2.27
SiO_2	%	23,27	15,9	45,80
CaO	%	8,36	12,24	11,87
Al_2O_3	%	1,96	4,69	6,40
MgO	%	1,82	2,24	2,76
Fe_2O_3	%	5,57	6,25	12,60
P_2O_5	%	0,59	1,19	0,29
TiO_2	%	0,2	0,9	1,69
CoO	%	<0,015	0,02	0.02
CuO	%	0,062	0,09	0,31
NiO	%	<0,015	0,23	0,05
ZnO	%	0,60	0,39	4,62
CdO	%	<0,015	<0,01	<0,01
S_{og}	%	1,89	1,37	1,38
PbO	%	-	-	-
Na_2O	%	2,0	-	-
K_2O	%	-	-	-
Mn_2O_3	%	0,043	-	-

3. Results & discussion

The research resulted in formation of the following products:

- ceramic phase was obtained from residues after sewage sludge pyrolysis (Figure 2.) and in case of one sample both ceramic and metallic phases were obtained,
- vitreous phase (Figure 3.), insignificant amounts of unsolidified product and little isolated metallic phase were obtained from residues after medical waste treatment,
- vitreous phase (Figure 4.) was obtained from residues after industrial waste treatment.

Ceramic phase density (obtained from residues after sewage sludge pyrolysis) is 2,5 g/cm^3 and is similar to the density of glass. According to chemical composition (Table 2.) this phase can be classified into slag category as blast furnace slag (Table 3.) that is used for production of metallurgical cement. Metallurgical cement is further applied for production of different kinds of concrete fulfilling severe design requirements on strength, leakproofness, chemical and physical corrosion resistance. Although metallic phase density is 7 g/cm^3 it may be in fact lower due to presence of air bubbles. This phase shows also significant hardness that may result in formation of carbides. Metallic phase can be considered as alloy cast steel due to exceeded concentration of the following particles (Table 4.): Cr – 0,4%, Cu – 0,3%, Si – 0,5%. Carbon content is a parameter for alloy cast steel as well.

Table 2. Concentration (%mass) of selected compounds for slag phase

CaO	SiO_2	Al_2O_3	MgO	Fe_2O_3
38,06	36,98	14,95	4,83	2,37

Table 3. Comparison of selected compound concentration (%mass) for slag and blast furnace slag

	CaO	SiO_2	Al_2O_3	MgO	Fe_2O_3
Slag phase	38,06	36,98	14,95	4,83	2,37
Granulated slag	44,80	38,70	8,10	5,20	1,30

Table 4. Concentration (%mass) of selected particles for metallic phase

Fe	Si	C	Cr	Cu	Ni	Mn	Ti	S
75,9	20,5	1,17	1,0	0,5	0,3	0,3	0,3	<0,0003

Figure 2. Slag and metallic phases obtained from residues after pyrolysis of sewage sludge

Vitreous phase obtained from residues after thermal treatment of medical and industrial waste (Figure 4.) showed compact and hard structure with vitreous surface. Apart from vitreous phase some unsolidified products and a metallized pellet were formed from residues after medical waste treatment. Vitrified end-products were analyzed for heavy metal leaching (Table 5.).

Figure 3. Vitreous phase obtained from residues after medical waste treatment

Figure 4. Vitreous phase obtained from residues after industrial waste treatment

Table 5. Aqueous extract analysis

Analysis	Unit	Value
pH	-	5,7-7,5
Chloride	mg/l	12-36
Cu	mg/l	<0,4
Zn	mg/l	<0,4
Ni	mg/l	<0,4
Mn	mg/l	<0,4
Cd	mg/l	<0,4

4. Summary

Utilization by means of arc plasma technology allows for solidification of residues after thermal waste treatment. It can be achieved without any additives which decrease melting point. Utilization of organic waste requires oxygen presence during the process. Oxygen supplied to the reaction zone enables after-incineration of combustible matter as well as solidification in one system. Melting process requires selection of suitable parameters of the reactor. According to the analysis of aqueous extracts prepared for different kinds of waste, utilization using plasma technology causes significant decrease in heavy metal leaching. Vitrified products and metallic matrix can be applied in building and metallurgic industries. The advantage of plasma technology is relatively low power consumption of the installation (max. 40 kW).

5. Conclusions

Application of arc plasma technology for utilization of residues after thermal waste treatment results in :

- significant reduction of material volume,
- material reuse,
- industrial application of slag and metallic phases,
- decrease in mobility of heavy metals found in waste,
- complete vitrification of material (in case of residues from industrial waste treatment) without any additives that increase costs of the process.

References:

[1] Rozporządzenie Ministra Gospodarki z dn.21.10.1998 r. w sprawie szczegółowych zasad usuwania, wykorzystywania i unieszkodliwiania odpadów niebezpiecznych (Dz.U. Nr 145, poz.942, Zmiana : Dz.U. z 2001 r. Nr 22, poz. 251).

[2] L.N. Toumanov, A.F. Galkin, V.D. Rousano, Plasma pyrolysis in technology of recovery of municipal solid waste: pre-rated preparation of a plant having capacity of 200000t. MSW/a, International Symposium on Plasma Chemistry, Prague, Czech Republic, 1999.

[3] S. Abramczyk, Plazmowanie nową metoda utylizacji odpadów, AURA 4/1999.

[4] R.N. Szente, R.F. Cuevas, C. K. Suzuki, Charakteristic of the Ceramic Matrix Obtained from the Plasma Treatment of Hospital Wastes, International Sympsium on Plasma Chemistry, Orleans, France, 1999.

[5] S. Bernard, P. Fauchais, J. Jarrige, J.P. Lecompte, A. Grimaud, Control on line of lead and zinc evaporation in the the treatment by transferred arc of fly ashes from wastes incenerator, International Symposium on Plasma Chemistry, Prague, Czech Republic, 1999.

[6] S. Robert, K. Couliabaly, E. Francke, S. Cavadias, M.F. Gonnord, Analysis of metalic oxide and chloride emission during thermal plasma process for fly ash vitryfication, International Symposium on Plasma Chemistry, Prague, Czech Republic, 1999.

[7] K. Brodowicz, J. Jerzy, M. Mikoś, M. Pilawski, T. Siekierski, Plazmowa metoda utylizacji odpadów niebezpiecznych termiczne metody „samolikwidacji" odpadów niebezpiecznych, III Międzynarodowa Konferencja „Spalanie odpadów – technologie i problemy" Szczyrk 1997.

[8] J.B. Bień, M. Sanitsky, J.D. Bień, W. Białczak, Plazma niskotemperaturowa jako rodzaj utylizacji i odzysku osadów ściekowych, Nowe Spojrzenie na Osady Ściekowe Odnawialne Źródła energii, II

Międzynarodowa i XIII Krajowa Konferencja Naukowo-Techniczna, Wydawnictwo Politechniki Częstochowskiej, Częstochowa, 3-5 lutego 2003.

[9] J.B. Bień, W. Białczak, K. Wystalska, Plazmowa utylizacja stałej frakcji po przekształceniu osadów ściekowych metodą pirolizy, Konferencja Nauk. – Techniczna nt. Gospodarka Odpadami Komunalnymi, Koszalin 2003.

[10] J.B. Bień, K. Wystalska, W. Białczak, T. Rozpondek, Witryfikacja pozostałości po termicznej utylizacji odpadów medycznych w reaktorze plazmowym, Konferencja Nauk. – Techniczna nt. Gospodarka Odpadami Komunalnymi, Koszalin 2003.